

The international journal of science / 30 January 2020

**outlook**  
The gut  
microbiome

# nature



## MAPPING THE FUTURE

How the brain keeps track of  
everything that might happen next

**Solid evidence?**  
Hints of metallic  
hydrogen seen in  
diamond anvil cell

**Flash drive**  
Bulk-scale graphene  
production from  
cheap carbon sources

**Pigment problems**  
Stress can sap stem  
cells to turn hair  
prematurely grey

Vol. 575, No. 7792  
nature.com



# nature

## Au revoir

**As Britain leaves the European Union, a future research relationship must be built on continued collaboration – and compromise.**

**A**t the stroke of 11 p.m. on 31 January, researchers will be among those lighting candles to mark the United Kingdom's departure from the European Union. Most scientists didn't want Brexit. Scientists co-founded a national campaign for a second referendum on the country's EU membership, fearing that the split would destroy a union that has promoted collaboration and the advancement of knowledge for the past 47 years.

They were unsuccessful – and the next 11 months will be an uncertain time as the United Kingdom enters a transition period in which it must negotiate the terms of its future links with the EU. UK researchers do not yet know if they will be part of joint EU research programmes. However, in one piece of welcome news, the futures of the many EU researchers who want to make their lives in Britain now lie in the hands of the UK Research and Innovation agency, and not the UK Home Office – an institution that, for much of the past decade, enacted and implemented policies to reduce immigration to the United Kingdom.

But it's not only the act of separation that will be so painful. Research has always been central to European unity. Back in 1973, Britain joined much more than the 'European Economic Community', which is what later became the EU. It joined an organization that had been founded to further a number of principles – that it is better for nations in the same neighbourhood to make decisions together; that conflicts must be resolved through negotiation and compromise; and that it benefits everyone if richer countries can assist poorer ones.

Each of these principles was rooted in the same goal – to avoid a repeat of the brutal war from which the EU's founders had emerged. The continent's scientists were very much part of the Second World War, which is why the bloc's architects deliberately planned for joint research – and especially technology – to be part of the glue for European integration. The idea that research cooperation can assist peace-building has inspired other regional unions, from Africa to Latin America and the Caribbean.

As the EU was taking shape, some of Britain's scientific leaders were sceptical about collaborating with European colleagues. But scepticism faded as the benefits of a European research area – not unlike that of the United States – with pooled funding and freedom of movement became clear. Britain's researchers received the second largest share of their country's EU funds (after farmers), and as of June 2019, this was more than €1 billion (US\$1.1 billion) a year. Much of this went towards collaborative projects with societal impact, such as the European Social Survey, which tracks changing social attitudes in 38 European

 **The EU exists to protect democracy and the rule of law.”**

nations; the Clean Sky programme, in which researchers from 27 countries work together to reduce aircraft carbon emissions and noise; or the Innovative Medicines Initiative, where researchers collaborate to develop medicines for under-served conditions such as tuberculosis.

### Free movement

Mindful of what it could lose, the government is investigating whether Britain could pay to join – or be 'associated' with – EU programmes. But at the same time, ministers have been preparing for the possibility that this will not happen. That's because UK membership of EU research programmes will require some form of freedom of movement and, so far, the UK government has said freedom of movement must end in its current form. Joining EU programmes also depends on the wider terms of the United Kingdom's future EU relationship to be thrashed out this year. Within government, there are varying views as to how close Britain should remain to the laws and regulations of its former EU partners – what is called 'alignment'. But from the perspective of researchers and society as a whole, there are more benefits in alignment than in moving out of the EU's orbit, at least for now.

It's in everyone's best interests that Britain should continue to align, to some degree, with the continent's carefully crafted decision-making frameworks on the environment, data, employment, food safety and the broader life sciences. Environmental issues are international by their very nature, so there is no sense, nor logic, in Britain creating its own standards, or aligning with a minority of countries. The same applies for regulations on technologies such as those involved in gene editing and artificial intelligence. UK researchers must be part of global efforts.

### Regional aid

The United Kingdom should also consider continuing to contribute to what is called 'cohesion funding'. These are EU funds that go to poorer regions, and include funding for research. Between 2014 and 2020, Britain's less developed regions – including those in Wales, Cornwall and the north-east of England – received €10.6 billion in cohesion funding. Under EU rules, this contribution must be matched from national sources, doubling the available money.

The government has pledged to replace some cohesion funding through a 'Shared Prosperity Fund', and on a visit to northeast England last week, science minister Chris Skidmore promised to "level up" research funding between the UK regions. Such an announcement could not have come sooner. The government's own data show that, in 2017–18, the northeast and Wales each received 2% of Britain's gross expenditure on research and development. By contrast, 35% went to institutions in London and the southeast of England.

But at a conference organized by the Institute for Public Policy Research in Newcastle upon Tyne, UK, on 22 January, it was pointed out that the various regions will be required to compete with each other for this new funding – creating winners and losers. And there were fears that UK funding for the poorest communities would be less than what has been obtained through EU funding. "Nothing I've



heard says the government knows what to do to solve the problems of the North of England,” said political scientist Anand Menon, director of the UK in a Changing Europe research programme.

The government needs to listen to these warnings if it is to make good on its promises. As the prime minister and his senior advisers start to make decisions in the coming months, leaders of the research community must continue to use their influential voice and ensure that UK researchers are generously funded, that under-served communities do not lose out and that research policies continue to reflect an international consensus.

### Dahrendorf's wish

“The European Union is seen by many as a model. And Britain must be part of that model.” The German–British philosopher Ralf Dahrendorf wrote these words in frustration in 1995 when a previous Conservative UK government found itself in turmoil over Britain's relationship with the EU.

Dahrendorf was unusually placed in that he could see Britain's relationship with the EU from many sides. He could see how EU membership was being interpreted by some as a loss of sovereignty in a post-imperial nation. But as a refugee from Nazi Germany who had been welcomed by Britain, he also understood the EU's crucial importance as the backstop against a return to authoritarianism in continental Europe.

Dahrendorf's wish will be denied. But it is essential that both the United Kingdom and the remaining 27 EU member states and EU institutions do not let Brexit diminish that mission. The EU exists to protect democracy and the rule of law. It ensures continued peace and prosperity through negotiation and compromise, through the freedom to travel and trade, and by the strong helping the weak – all catalysed by knowledge, research and innovation. These are values to which every nation must aspire, including the United Kingdom even if it is no longer part of the EU.

 We're delighted to see so many readers urge us to focus on global challenges. You're right.”

## What you want *Nature* to do next

**We asked readers what we should focus on in the next decade. Here is what you said.**

**L**ate last year, as *Nature* marked its 150th anniversary, we spent time reflecting on our values and how we could improve. We were keen to hear from you, our readers, so we put up a survey that asked: “What activity do you think is most important for *Nature* to focus on over the next decade?”

More than 500 of you responded (thank you!) and four things stood out. You would like *Nature* to make papers and data easier to access; help readers to find and digest research more easily; work to improve research integrity; and publish and communicate research that addresses global challenges. These responses and the many additional comments you sent will guide us as we chart a course into the new decade.

Some readers urged us to improve accessibility in its broadest sense. We should make research “easier for very curious but non-specialized people to read”, wrote one. We strive to ensure that abstracts to research articles and all our news and opinion content are clear and engaging for readers from different fields and at different career stages. But it's important to be reminded, as another reader told us, that palaeontology should be accessible to a neuroscientist and vice versa. It's equally important, as a reader from Mexico said, that we maintain “truthfulness and impartiality in the global dissemination of science”.

We're pleased that many readers complemented *Nature's* daily Briefing, our round-up of essential reading in research news from across the world. We want to do more to help readers make sense of what can be an overwhelming volume of information about new research.

Respondents also urged us to do more to make science open by further embracing open access, open data and reproducibility – including publishing peer-reviewed work that reproduces the results of previous studies. These views are informing our direction. And quite a few readers asked why *Nature* covers policy and politics in science; we see this as an essential part of what we do because policy decisions affect research and researchers' lives, and because the outcome of research affects policy decisions, too.

We're delighted to see so many readers urge us to focus on global challenges. You're right. *Nature* is committed to publishing and reporting in the areas that fall under the United Nations Sustainable Development Goals, and 2020 will be a busy year. In October, countries that belong to the UN Convention on Biological Diversity will meet in Kunming, China, to update global goals to reduce biodiversity loss. The following month, world leaders will gather in Glasgow, UK, to agree on a new and hopefully more ambitious set of climate targets. Before that, in June, representatives of many nations will convene in Lisbon with scientists, businesses and campaign groups for the UN Oceans Conference. We'll be covering all of these events.

You also told us in our poll that we should focus on increasing the diversity of our authors and contributors. We are redoubling our efforts here – and also reiterate our commitment from last December to having no more male-only speaker panels and organizing committees for *Nature* events. At the same time, we fully recognize that there is much more that we need to do.

Science, as one reader reminds us, is an essential part of humanity's heritage. “I hope that *Nature* can keep improving, and make [an] effort to preserve and select important information in a way that future generations can access them easily.”

We very much agree.



# World view

## Remember what science owes to child refugees

**Callous policies in Brexit's wake will ill serve a nation that claims to cherish innovators – learn from 1930s Britain, says Georgina Ferry.**

**W**hen the British House of Commons voted this month not to uphold child refugees' right to join family members in the United Kingdom, I was reminded of something. As a scientific biographer and obituarist (for *Nature* and the newspaper *The Guardian*), I'm regularly struck by how much leading scientific nations have gained from people to whom they once gave sanctuary.

Every life – whether of an adult or a child – is valuable, and people should be saved for humanitarian reasons alone. But it's worth remembering that the country benefits.

Take three pioneering researchers who all died in December 2019, and all had one other thing in common: they came to Britain in 1938–39 as unaccompanied child refugees from Europe. Hans Kornberg elucidated the reactions that microbes use to exploit carbon sources; Hannah Steinberg identified some of the effects of psychoactive drugs and drug combinations on behaviour; and Leslie Brent recognized a mechanism underpinning immune tolerance.

Current British policy on child refugees is callous. There are perhaps a few hundred such children waiting to join siblings, uncles, aunts or grandparents in the United Kingdom. Most have either lost their parents or left them behind in their war-ravaged countries.

Under European Union law they currently have the right to rejoin their families, but this is set to be revoked now that the Withdrawal Agreement Bill that sets terms for Britain's relationship with the EU after Brexit on 31 January has passed its final stage. After winning a convincing electoral victory in December, Conservative lawmakers ditched a key amendment guaranteeing the rights of child refugees; an attempt to reinstate it earlier this month failed.

Contrast this with the action of the British government in 1938. In November that year, on what has become known as Kristallnacht, Jewish homes, businesses and synagogues were ransacked across Germany with the connivance of the Nazi government. Days later, the UK House of Commons debated the situation, and the home secretary agreed to admit an unspecified number of Jewish children from Germany and neighbouring countries through a system later known as the Kindertransport. Most of the children travelled by train from Vienna, Berlin or Prague. In the months leading up to the outbreak of war in September 1939, around 10,000 came to the United Kingdom.

Steinberg fled Vienna aged 14, in 1938. She stayed with relatives and then a foster family; her mother took her own life and her father fled to Israel. In Britain, Steinberg was

**All would probably have perished but for a political decision."**

**Georgina Ferry** is a science writer and obituarist based in Oxford, UK. Her books include biographies of Dorothy Crowfoot Hodgkin, Max Perutz and John Sulston. e-mail: mgf@georginaferry.com



By Georgina Ferry

able to study psychology at University College London, where she went on to hold one of the world's first chairs in psychopharmacology. In retirement, she continued her research, helping to establish an evidence base on the psychological effects of exercise.

Kornberg, later knighted for his services to science, arrived in 1939 from northern Germany. Aged 11, he went to live with an uncle; both his parents died in the Holocaust. On leaving school, he took a job as a technician with Hans Krebs, a Jewish biochemist fired in 1933 by the University of Freiburg, Germany, because of his heritage. Krebs had just discovered the cycle of energy transformation in cells, for which he later won a Nobel prize. Kornberg went on to reach heights of distinction he could not have dreamt of on the cold, crowded train from Berlin, including gaining the chair in biochemistry at the University of Cambridge, UK.

Brent (born Lothar Baruch) was a key contributor to Peter Medawar's Nobel-prizewinning work on induced immune tolerance. At age 13, Brent was on the first Kindertransport from Berlin. Both his parents were transported to Latvia and shot. He came to the United Kingdom without any family to greet him, and worked as a laboratory assistant before achieving academic success.

Others who endured appalling upheavals in their childhoods and yet thrived after the Kindertransport are still alive, most notably Steve Shirley, who shattered the glass ceiling for women in computing and pioneered home-based programming. Made a dame for services to information technology in 2000, she says: "I determined at a ridiculously young age to make mine a life that had been worth saving." Others moved to the United States, of whom three – Walter Kohn, Arno Penzias and Jack Steinberger – won Nobel prizes in chemistry or physics. All would probably have perished but for a political decision.

In 1938, Britain had only recently emerged from a recession. It was heading into a war, and national debt remained stubbornly high. Yes, more could have been done, but for child refugees common humanity prevailed. It should do so again, in Britain and beyond. (As an aside: there is abundant evidence that immigration benefits economies, and that people overestimate true levels of migration by orders of magnitude. The argument that wealthy nations must safeguard their economies from becoming 'overwhelmed' by 'uncontrolled' immigration has no evidence base.)

Without a legal means to access the United Kingdom, children will risk their lives in the unseaworthy craft that are increasingly trying to cross the busy and often wind-tossed English Channel, or stow away in the kind of lorry in which 39 Vietnamese people suffocated in October 2019.

Out of simple human compassion – and in honour of the huge contributions made by refugee researchers – should not scientists speak up for these children?



# News in brief

## SOFTWARE TRACKS RIGOUR OF SCIENTIFIC PAPERS OVER TIME

Researchers are getting better at communicating science in a rigorous and reproducible way, according to a text-mining analysis of around 1.6 million papers. But the findings have also sparked fears that progress is too slow.

The study used software called SciScore, which gives papers a mark out of ten for 'rigour and transparency' (J. Menke *et al.* Preprint on bioRxiv <http://doi.org/dkg6>; 2020). SciScore searches the text in papers' methods sections for around 20 pieces of key information, which act as proxies for how rigorous the experiments are, and how easy it would be for other researchers to reproduce them. The software can flag where authors have specifically identified the reagents and tools they use, such as antibodies, software, cell lines or transgenic organisms. It also checks whether they have discussed factors such as sample sizes, how tests have been blinded or the sex of animals used.

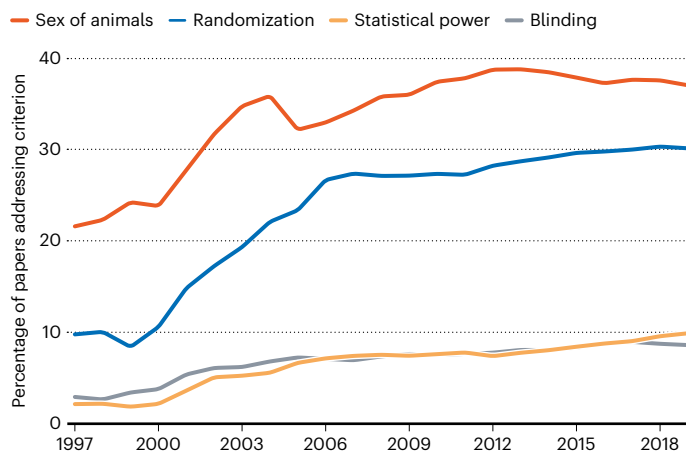
The researchers who created SciScore – led by Anita Bandrowski, an information

scientist at the University of California, San Diego – analysed 1.58 million freely available life-sciences papers indexed in the PubMed Central database. They found that between 1997 and 2019, the average score across all papers more than doubled, from 2 out of 10 to 4.2. The analysis also showed that individual measures of rigour are on the rise. For example, less than 10% of papers published in 1997 discussed randomization in the methods; this had risen to around 30% in 2019 (see 'Rigorous research').

But the numbers overall haven't increased as much as some researchers would like. By calculating the average SciScore rating for all the papers in a given journal, Bandrowski and her colleagues created a metric they dubbed the Rigor and Transparency Index. Although the study finds that all journals' average scores have increased since 1997, no title among those analysed has an index of more than five out of ten. This suggests that "less than half of the rigor and reproducibility criteria are routinely addressed by authors", the study says.

## RIGOROUS RESEARCH

Scientists are increasingly publishing details about the rigour and reproducibility of their experiments.



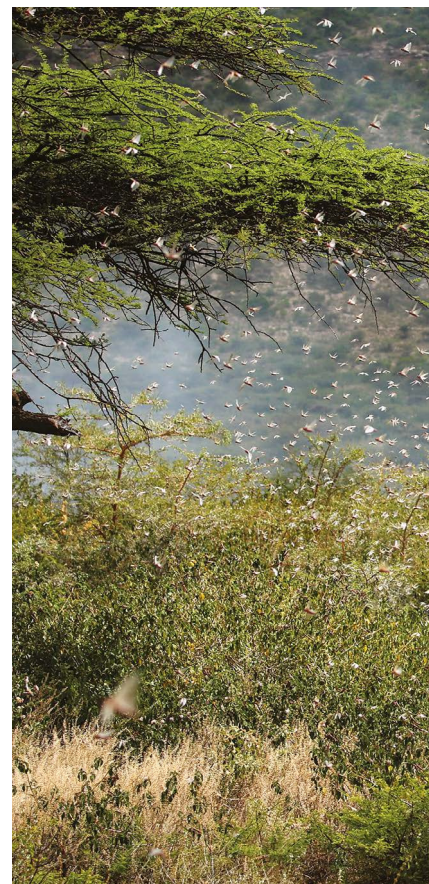
## ANCIENT AFRICAN GENOMES OFFER GLIMPSE INTO EARLY HUMAN HISTORY

Researchers have sequenced the genomes of four children who lived in what is now Cameroon several thousand years ago.

Their genomes – the first to be collected from any ancient human in West Africa – raise questions about the origins of a migration called the Bantu expansion, which carried languages and agriculture across the continent around 3,000–5,000 years ago. They also hint at older events in human history, such as the emergence of *Homo sapiens* and its spread out of Africa.

David Reich, a population geneticist at Harvard Medical School in Boston, Massachusetts, and Mary Prendergast, an archaeologist at Saint Louis University – Madrid Campus, analysed remains from a rock shelter in Cameroon called Shum Laka. They generated full genomes for two young boys, who lived 8,000 and 3,000 years ago, and collected more limited genome data from a boy and a girl from the same periods, respectively.

A genetic analysis, published on 22 January (M. Lipson *et al.* *Nature* <http://doi.org/dkh4>; 2020), showed that all four children descended from a group of *Homo sapiens* that branched off from the common ancestors of our species more than 200,000 years ago.



## United Nations appeals for locust help





Hundreds of millions of desert locusts, in swarms larger than cities, are ravaging East Africa. The Food and Agriculture Organization of the United Nations and a number of aid agencies are appealing for urgent help to deal with the crisis. Kenya has been worst hit – it has not seen locusts on this scale for 70 years – but the infestation has also struck Ethiopia (pictured) along with Somalia. Desert locusts (*Schistocerca gregaria*) have been breeding in large numbers because of unusual weather patterns, including heavy rains. The UN says that they need to be controlled by pesticides dropped from the air. If left unchecked, the locust population could grow 500-fold by June. A swarm the size of Paris will eat the same amount of food in a day as half the population of France.

## US OFFICIALS REVISIT RULES FOR RISKY DISEASE EXPERIMENTS

US disease researchers are pushing the government to be more transparent about federally funded research that involves making pathogens more deadly or more transmissible.

Several scientists who attended a meeting of the National Science Advisory Board for Biosecurity (NSABB) on 23–24 January say that the US government should offer a public explanation when it approves such ‘gain-of-function’ experiments, which are designed to help improve responses to outbreaks. The scientists also call for the government to disclose who decided to fund such research, and make a broad public announcement when a study begins. Others say that greater transparency could make it harder to approve necessary research.

The NSABB is reviewing guidelines for sharing information on gain-of-function research at the request of the National Institutes of Health (NIH) and the White House. The board is an independent panel that advises the NIH’s parent, the Department of Health and Human Services.

The debate over how much to disclose is revving up because the government is preparing to revisit rules that guide gain-of-function research – especially with regard to communication with the public.

“We’re not trying to say the policy is wrong – we’re trying to say the policy is ambiguous,” says Marc Lipsitch, an epidemiologist at the Harvard T.H. Chan School of Public Health in Boston, Massachusetts, and one of the researchers calling for more transparency.



## ABORIGINAL SITES PROBABLY DAMAGED IN AUSTRALIAN FIRES

Indigenous communities and archaeologists fear thousands of historic Aboriginal sites and artefacts have been damaged by fires that have ravaged Australia.

Since September, fires have razed more than 10 million hectares, mostly in the eastern states of Queensland, New South Wales and Victoria.

Much of that land is in national parks and other forests, where tens of thousands of important Indigenous sites are found, including many that have not been officially recorded, says Tiina Manne, an archaeologist at the University of Queensland in the Gold Coast and president of the Australian Archaeological Association (AAA).

These sites show where people lived and how they moved over tens of thousands of years, and help to reveal the development of cultural practices such as rock art (pictured).

Researchers have yet to do a formal assessment, but Manne says thousands of Aboriginal sites will have been affected. The AAA is calling on the government to conduct assessments of cultural sites as part of its fire-recovery plans.

The fires might also have opened up densely vegetated areas, potentially revealing undocumented sites, says Paul Taçon, who studies rock art at Griffith University, Gold Coast.



# News in focus



SLAM YIK FEI/NTT/REDUX/EVEMINE

Paramedics transport a man thought to be the first person in Hong Kong to have contracted the new coronavirus.

## WHAT SCIENTISTS WANT TO KNOW ABOUT THE CORONAVIRUS OUTBREAK

Researchers have sequenced the deadly pathogen's genome – and are now rushing to find out how it spreads and how deadly it is.

By Ewen Callaway and David Cyranoski

**T**he world is racing to learn more about the outbreak of a new viral infection that was first detected in Wuhan, China, last month and is causing increasing alarm around the world.

As *Nature* went to press, officials in China had confirmed more than 4,500 cases of the virus, which causes a respiratory illness, and some 100 deaths. Around 50 cases had also been confirmed in other countries, in Asia, the United States and Europe.

Researchers fear similarities to the 2002–03 epidemic of severe acute respiratory syndrome (SARS), which emerged in southern China and killed 774 people in 37 countries. Both are members of a large virus family, called coronaviruses, that also includes viruses responsible for the common cold.

China has taken unprecedented action to try to halt the outbreak – including putting Wuhan and nearby cities on 'lockdown', restricting travel in and out of the cities. For now, the World Health Organization (WHO) has held off declaring a public-health emergency of

international concern – the agency's highest level of alarm – after a meeting of officials last week, but that could change.

*Nature* rounds up the questions at the heart of scientists' efforts to understand the virus.

### How does the virus spread?

This is the most urgent question surrounding the outbreak. Chinese authorities have confirmed that it spreads from person to person after identifying clusters of cases among families, as well as transmission from patients to health-care workers. Monitoring the rate at



## News in focus

which new cases appear, and when symptoms began for each case, should reveal how easily the virus passes between humans and whether the outbreak has the potential to persist.

One figure that epidemiologists want is the number of people that someone with the virus tends to infect – known as  $R_0$ . An  $R_0$  of more than 1 means that countermeasures, such as quarantine, will be needed to contain the spread. The WHO last week published an estimated  $R_0$  of 1.4–2.5. Other teams suggest slightly higher values<sup>1,2</sup>. These estimates are similar to the  $R_0$  of SARS during the early stages of the 2002–03 outbreak, and of the novel strain of H1N1 influenza that caused a pandemic in 2009. But they are higher than  $R_0$  values estimated during outbreaks of the Middle East respiratory syndrome (MERS) virus, a coronavirus similar to SARS.

“Now it’s in the range of these other important epidemics, and that indicates the potential that it will cause a similar scale of public-health concern if nothing else happens,” says Mark Woolhouse, an epidemiologist at the University of Edinburgh, UK.

But researchers caution that  $R_0$  estimates come with large uncertainties because of gaps in the data, and the assumptions used to calculate the figure. They also point out that the  $R_0$  is a moving target and that estimates of the figure change over the course of an outbreak – as control measures are implemented. In the coming days, health authorities and researchers will be looking for signs that the travel restrictions in Wuhan and other Chinese cities, and other steps taken by to stem transmission, have reduced the  $R_0$  there.

### Can infected people spread the virus without showing symptoms?

Another major unanswered question is whether – and how extensively – people

without symptoms can infect others. A study<sup>3</sup> of a cluster of six infections in a family in Shenzhen identified a child who was infected with the virus but showed no symptoms. If such asymptomatic cases are common and these individuals can spread the virus, then containing its spread will be much more difficult, researchers say. Key to controlling the SARS virus was the fact that few cases were asymptomatic.

“Defining the scale of asymptomatic transmission remains key: if this is a rare event then its impact should be minimal in terms of the overall outbreak,” Jonathan Ball, a virologist at the University of Nottingham, UK, said in a statement distributed by the UK Science Media

### “Defining the scale of asymptomatic transmission remains key.”

Centre. “But, if this transmission mode is contributing significantly then control becomes increasingly difficult.”

One way to determine whether symptom-free people can spread the virus would be to study its spread in individual households in China, says Sheila Bird, a biostatistician at the University of Cambridge, UK. By monitoring all the members of a household in which one person is infected, it should be possible to determine who else contracts the virus and how. Such studies would also be helpful for identifying ways of stopping spread in households, Bird adds.

Raina MacIntyre, an epidemiologist at the University of New South Wales in Sydney, Australia, says that although the rise in cases probably reflects an increase in testing for

and detecting the virus, the dramatic jump is concerning. “It’s very much a dynamic picture, and until we have an indication that cases are declining, it’s going to continue to be of concern,” she says.

But MacIntyre also notes that researchers are struggling to accurately model the outbreak, and to predict how it might unfold, because the case-report data being released by Chinese authorities are incomplete. “What we need to identify is when people got sick, not when the cases were reported, and all we’ve seen so far is when the cases were reported.”

### How deadly is the virus?

High rates of pneumonia among the first people infected had many researchers worried that the Wuhan virus was especially pernicious. Those concerns have receded slightly, as more mild cases have turned up. With some 100 deaths in more than 4,500 reported cases, the virus does not seem to be as deadly as SARS – which killed around 10% of the people it infected. But “It’s too early to be sanguine about the severity”, says Neil Ferguson, a mathematical epidemiologist at Imperial College London.

### Where did the virus come from?

Authorities are working on the theory that the virus originated in an unidentified animal or animals, and spread to humans at an animal and seafood market in Wuhan, which is now closed. Identification of the animal source of the virus could help officials to control the current outbreak and gauge its threat – and potentially prevent future epidemics, say researchers.

Genetic sequencing suggests that the Wuhan virus is related to coronaviruses that circulate in bats, including SARS and its close relatives. But other mammals can transmit these viruses – SARS was probably spread to humans by civet cats.

The market in Wuhan also sells wild animals. And in a controversial study<sup>4</sup> published last week, a team of researchers in China who had performed a genetic analysis suggested that the virus jumped to humans from snakes. But other scientists were sceptical of the study, and said that there is no proof that viruses such as those behind the outbreak can infect species other than mammals and birds. “Nothing supports snakes being involved,” says David Robertson, a virologist at the University of Glasgow, UK.

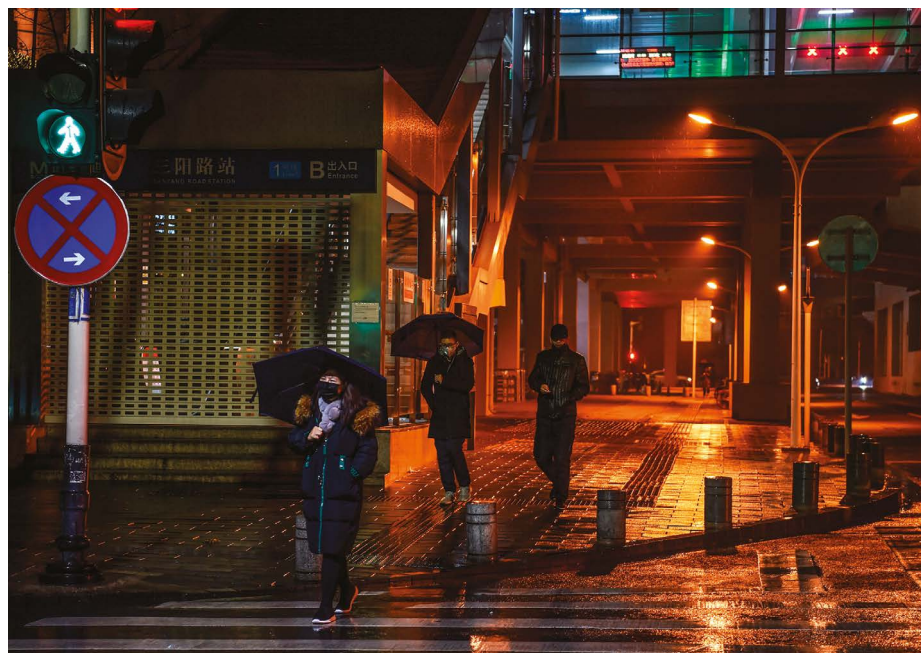
Many researchers think that the animal host or hosts of the virus won’t be identified without further field and laboratory work. And many hope that genetic tests of animals or environmental sources will turn up clues.

A mammal is the most likely candidate, says Cui Jie, a virologist at the Pasteur Institute of Shanghai who was part of a team that identified SARS-related viruses in bats from a cave in Yunnan province in southwestern China



Public-health staff check the temperatures of people arriving from China at Bangkok airport.





The city of Wuhan, China, is on lockdown in an attempt to halt the coronavirus outbreak.

in 2017. SARS and the new virus are part of a subgroup known as betacoronaviruses. Fieldwork in the wake of the SARS outbreak has found such viruses only in mammals, Cui says.

### What can we learn from the virus's genetic sequence?

Genetic sequencing of the Wuhan coronavirus offers clues to its origins and spread. Labs in China and Thailand have sequenced the genomes of more than 20 strains found in infected people and have made them publicly available. That's "pretty remarkable", says Trevor Bedford, an evolutionary geneticist at the Fred Hutchinson Cancer Research Center in Seattle, Washington, who is analysing the sequences as they come in. "People are extremely fast and excellent about data sharing," he adds.

Bedford and other geneticists are using the data to determine when the virus emerged — current estimates point to November 2019. Viral sequences, Bedford adds, could identify any genetic changes that might have helped the virus make the jump from animals to humans. And if there is extensive human-to-human transmission, Bedford and other geneticists will be looking for signs that the virus has gained further mutations that are enabling it to spread more efficiently in humans.

Bedford cautions that any conclusions are preliminary, because so few data are available. "Adding a few key samples can change the story significantly," he says.

### Can a drug be developed to treat the coronavirus?

No drugs have been shown to be effective in treating SARS or other coronavirus infections in humans, and no vaccines aimed at preventing

these infections have been licensed.

A team at China's National Engineering Research Center for the Emergence Drugs in Beijing is working on finding therapies that would work by blocking the receptor on human cells that the virus latches on to and uses to infect the cells. A comparison of the SARS and new China virus sequences, published on 16 January, found that they probably bind to the same receptor. The team is hoping to revive efforts to develop treatments for SARS and adapt them in a bid to develop a drug that could work against the latest virus.

Another researcher who has been developing drugs for coronaviruses since the SARS outbreak is hoping to test drug candidates in

**"People are extremely fast and excellent about data sharing."**

animal models of the Wuhan virus (see 'Q&A: Rolf Hilgenfeld').

Chinese authorities are also testing whether existing HIV drugs can treat the infection. Ritonavir and liponavir, which are approved to treat HIV, are being given to people with pneumonia caused by the coronavirus, according to media reports and a 26 January statement by the Beijing branch of China's National Health Commission.

1. Read, J. M. et al. Preprint at MedRxiv <https://www.medrxiv.org/content/10.1101/2020.01.23.20018549v1> (2020).
2. Liu, T. et al. Preprint at BioRxiv <https://www.biorxiv.org/content/10.1101/2020.01.25.919787v1> (2020).
3. Chan, J. F.-W. et al. *Lancet* [https://doi.org/10.1016/S0140-6736\(20\)30154-9](https://doi.org/10.1016/S0140-6736(20)30154-9) (2020).
4. Ji, W., Wang, W., Zhao, X., Zai, J. & Li, X. *J. Med. Virol.* <https://doi.org/10.1002/jmv.25682> (2020).

## Q&A

## Rolf Hilgenfeld

**Structural biologist Rolf Hilgenfeld has been trying to develop a cure for coronaviruses since the 2002–03 outbreak of severe acute respiratory syndrome (SARS). Hilgenfeld, who is based at the University of Lübeck in Germany, is hoping to get into the locked-down city of Wuhan in China to test drug compounds in animals infected with the new coronavirus. He tells *Nature* about his quest.**

### Why are you visiting China?

After this virus emerged, I contacted collaborators in Wuhan. I have two compounds to test against the new virus, so I am seeking collaborators who have samples of the virus.

### At what stage of development are your compounds?

We have been preparing them for testing in a mouse model of Middle East respiratory syndrome (MERS). In cell culture, we know they work against the SARS and MERS coronaviruses.

### Could they help to subdue the new virus?

The problem with antiviral drugs is that when the compound is ready, there are no patients. After six months, we could have data showing that one of our compounds works against the new virus, and would be able to develop a drug. But if the outbreak is over, there will be no patients, so how can you do clinical trials?

### What do your compounds do?

They are active against coronaviruses and a family of enteroviruses, which include hand, foot and mouth disease. Every year, half a million children get enterovirus-71, so we'd aim to go into clinical trials for these diseases. We can involve pharma. If we have something approved for those, we can use the drug in the next coronavirus outbreak. The compounds are directed at viral proteases, which have common features in coronaviruses and enteroviruses.

### Interview by David Cyranoski

This interview has been edited for length and clarity.



## Brexit is happening: what does it mean for science?

At 11 p.m. on 31 January, the United Kingdom will leave the European Union. Although an 11-month transition period means the milestone will bring few immediate changes for researchers, the moment marks the start of negotiations over the country's future relationship with the bloc, including the United Kingdom's role in the EU's next seven-year research programme, Horizon Europe, which will start on 1 January 2021 and is set to be worth €100 billion (US\$110 billion). As Brexit begins, *Nature* takes a look at how 2020 negotiations could shake out for science.

### What will change immediately after 11 p.m. on 31 January?

The United Kingdom will enter a transition period that will freeze its relationship with the EU for the rest of the year. Until 2021, scientists will still be free to take up jobs and travel between the United Kingdom and other EU countries. British researchers will be able to apply for European research funding and take part in exchange schemes.

### Will the United Kingdom seek to join Horizon Europe?

On 20 January, UK science minister Chris Skidmore told Parliament that he wanted the UK to 'associate' with Horizon Europe — a status that could allow UK scientists to participate on similar terms to those they experience today. But he stressed that association would depend on the final shape and content of the programme, which has yet to be agreed by European legislators. Wider negotiations — including agreements on immigration — are also likely to affect whether this kind of association is possible. Any such agreement would normally come only after countries have agreed a trade deal.

### What other factors will affect the United Kingdom's participation in Horizon Europe?

Skidmore will have to convince the UK treasury that participation is worth the cost. The country has long taken more out of the EU research pot than it puts in, but that will almost certainly change, probably to a model in which the United Kingdom pays into the programme in line with what it receives.



An anti-Brexit protest outside the Houses of Parliament in London.

### How can the UK associate if freedom of movement between the United Kingdom and the EU ends?

Under the existing Horizon 2020 research programme, Norway and Switzerland — both non-EU countries that wanted to associate — have to allow the free movement of people across their borders. This is something that the UK government has already ruled out. But the EU has suggested that it might be more flexible on the conditions of entry for the next programme. Beth Thompson, head of UK and EU Policy at the London-based biomedical-research funder Wellcome, says a UK system that guarantees mobility for researchers — such as the fast-track visa for researchers that the UK government announced on 27 January — could be enough to secure an agreement. The Global Talent visa route will open from 20 February, upgrading and expanding the underused 'exceptional talent' visa and allowing the country's main research funder, UK Research and Innovation, to endorse candidates.

### Can the scientific relationship between the United Kingdom and the EU be agreed by the end of the transition period on 31 December?

It's possible, says Thompson, but it will be a challenge. A mock negotiation exercise carried out by Wellcome and the Brussels-based economic think tank Bruegel found that there

is only a "remote" chance that the United Kingdom and the EU will be able to agree a wider trade deal in 11 months. But the report, published on 28 January, concluded that it might be possible to agree an unprecedented standalone deal for science. For this to happen, both sides would need to agree to make an exception for science, for example by establishing special visas for researchers and setting up a system that allows UK organizations to opt in to EU data standards.

### What if the United Kingdom doesn't manage to join Horizon Europe before the end of 2020?

This would be disruptive. "Both the UK and EU will lose out," warns Thompson. Without association, UK researchers would be able to take part in Horizon Europe only as members of a 'third country': they could participate in some EU-funded projects but not lead them, and only if the government agreed to pay their costs. If there is no wider trade deal, it could affect travel, data sharing and laboratory supplies. UK researchers will almost certainly need visas to take up jobs in EU nations, whether or not the United Kingdom can craft a new immigration system in time.

By Elizabeth Gibney



# THE BATTLE TO EMBED ETHICS IN AI RESEARCH

Bias and the prospect of societal harm increasingly plague the field of artificial intelligence.

By Elizabeth Gibney

**D**iversity and inclusion took centre stage at one of the world's major artificial-intelligence (AI) conferences in 2018. But at last month's Neural Information Processing Systems (NeurIPS) conference in Vancouver, Canada, attention shifted to another big issue in the field: ethics.

The focus comes as AI research increasingly deals with ethical controversies surrounding the application of its technologies – such as in predictive policing or facial recognition. Problems include tackling biases in algorithms that reflect existing patterns of discrimination in data, and avoiding disproportionately affecting already-vulnerable populations. “There is no such thing as a neutral tech platform,” warned Celeste Kidd, a developmental psychologist at the University of California, Berkeley, during her NeurIPS keynote talk about how algorithms can influence human beliefs. At the meeting, which hosted a record 13,000 attendees, researchers grappled with how to meaningfully address the ethical and societal implications of their work.

Ethicists have long debated the impacts of AI and sought ways to use the technology for

good, such as in health care. But researchers are now realizing that they need to embed ethics in the formulation of their research and understand the potential harms of algorithmic injustice, says Meredith Whittaker, an AI researcher at New York University and founder of the AI Now Institute, which seeks to understand the social implications of the technology. At the latest NeurIPS, researchers couldn't “write, talk or think” about these systems without considering possible social harms, she says. “The question is, will the change in the conversation result in the structural change we need to actually ensure these systems don't cause harm?”

## Meetings matter

Conferences such as NeurIPS, which, together with two other annual meetings, publishes the majority of papers in AI, bear some responsibility, says Whittaker. “The field has blown up so much there aren't enough conferences or reviewers. But everybody wants their paper in. So there is huge leverage there,” she says.

But research presented at NeurIPS doesn't face a specific ethics check as part of the review process. The pitfalls of this were encapsulated by the reaction to one paper presented

at the conference, in which faces – including aspects of a person's age, gender and ethnicity – were generated on the basis of voices. Machine-learning scientists criticized it on Twitter as transphobic and pseudoscientific.

One solution could be to introduce ethical review at conferences. For the first time, NeurIPS 2019 included a reproducibility checklist for submitted papers. In the future, once accepted, papers could also be checked for responsibility, says Joelle Pineau, a machine-learning scientist at McGill University in Montreal, Canada, and at Facebook, who is on the NeurIPS organizing committee and developed the checklist.

NeurIPS says that an ethics committee is on hand to deal with concerns during the existing review process, but it is considering ways to make its work on ethical and societal impacts more robust. Proposals include asking authors to make a statement about the ethics of their work. The organizers of the annual International Conference on Learning Representations – another of the major AI meetings – said it was discussing the idea of reviewing papers with ethics in mind.

AI Now goes a step further: in a report published last month, it called for all machine-learning research papers to include a section on societal harms, as well as the provenance of their data sets. Such considerations should centre on the perspectives of vulnerable groups, which AI tends to affect disproportionately, Abeba Birhane, a cognitive scientist at University College Dublin, told NeurIPS's Black in AI workshop. Developers should ask not only how their algorithm might be used, but also whether it is necessary, she said.

## Business influences

Tech companies – which are responsible for vast amounts of AI research – are also addressing the ethics of their work. But activists say that they must not be allowed to get away with ‘ethics-washing’. Tech firms suffer from a lack of diversity, and although some companies have staff and entire boards dedicated to ethics, campaigners warn that these often have too little power. Their technical solutions – which include efforts to ‘debias algorithms’ – are also often misguided, says Birhane. The approach wrongly suggests that bias-free data sets exist, and fixing algorithms doesn't solve the root problems in underlying data, she says.

Forcing tech companies to include people from affected groups on ethics boards would help, said Fabian Rogers, a community organizer from New York City. Rogers represents a tenants' association that fought to stop its landlord from installing facial-recognition technology without residents' consent. “Context is everything, and we need to keep that in mind when we're talking about technology. It's hard to do that when we don't have necessary people to offer that perspective,” he said.



Facial-recognition algorithms have been at the centre of privacy and ethics debates.





# THE CLIMATE LINK TO AUSTRALIA'S FIRES

Researchers race to decipher how global warming has influenced the record bush fires that have ravaged much of Australia. **By Nicky Phillips and Bianca Nogrady**





**Haze blankets Canberra on 5 January as visitors walk by Australia's parliament building.**

of the world, they were stunned by the scale and severity of the fires ravaging Australia (see 'A country aflame'). Since September, more than 10 million hectares have burnt – an area greater than the size of Austria – and the fire season doesn't end for several months in some states. So far, the conflagrations have killed at least 32 people and destroyed more than 2,000 homes across 3 states. Through it all, people have been asking Lewis: did climate change have a role in these catastrophic fires?

Lewis and a handful of her collaborators were busy discussing that very question. They work in a small but growing field called attribution science, which calculates the likelihood that an extreme event such as a heatwave, a flood or a catastrophic bush-fire season was made worse by climate change. In a study published last December<sup>1</sup>, Lewis and her colleagues linked catastrophic 2018 fires in northeastern Australia to climate change, and they are now planning an attribution study for the fires that have gripped large parts of the country over the past few months.

The work is being led by researchers in Europe who have conducted multiple rapid analyses of global warming's role in extreme events. The team first has to grapple with how it will define the fire event for the purpose of its study: it is tricky to model the various weather conditions that increase fire risk, and the blazes haven't yet died out. But once that is decided, the team could produce results as early as February.

Coming up with answers will be difficult. "Fire is probably the most complex physical and societal system known," says Tim Brown, a climatologist at the Desert Research Institute in Reno, Nevada. "There're so many different aspects of it, from the fuels and the people to the management practices."

But Australia and other countries need to know what they are facing. If attribution studies can quantify the role of climate change in particular extreme events, scientists can better forecast the chances that the catastrophes will strike again. Such information is vital for emergency-response managers as they prepare for a warmer Earth. Firefighters in many countries have noticed, for instance, that big blazes are getting hotter and more dangerous, so modelling studies of future risks would help them train for and respond to the conflagrations to come.

### Burning lands

Australia has always had fires – catastrophic ones, too. The really devastating ones earn their own name, such as Black Friday in 1939, Ash Wednesday in 1983 and Black Saturday in 2009. The last of those killed 173 people: the

continent's deadliest fire on record. All three – as well as the current crisis – happened amid or at the end of long, intense droughts.

This year's unusually hot and dry conditions are driven in part by a natural meteorological phenomenon called the Indian Ocean Dipole (IOD), which is defined by differences in sea surface temperatures across the ocean. In its positive phase, warmer waters congregate near Africa, and rainfall is reduced over the southern and most northerly regions of Australia. This year saw one of the strongest positive swings in the IOD in recent history. Coupled with these events was a shift in the polar winds above Antarctica – also a natural phenomenon, but much rarer than a positive IOD. This sudden stratospheric warming, as it is known, contributed to bringing hot, dry weather to much of Australia. On top of all this natural variation, global warming is making the country even hotter and drier, says Sarah Perkins-Kirkpatrick, a climate scientist at UNSW Sydney.

Evidence has been growing for decades that climate change will exacerbate Australia's fire seasons. A prescient paragraph in a 2008 government-commissioned climate report that compiled evidence from the previous 30 years warned that fire seasons would start earlier, end later and be more intense<sup>2</sup>. "This effect increases over time, but should be directly observable by 2020," noted the report, authored by Ross Garnaut, an economist at the University of Melbourne.

Lewis says we don't need attribution studies to say that climate change is generally making fires in Australia worse. But as extreme events become more frequent – and the pace

**"Fire is probably the most complex physical and societal system known."**

of warming shows no signs of falling – people want to know whether climate change had a hand in a specific extreme event.

Lewis's study on the 2018 event looked at 130 bush fires that razed nearly 750,000 hectares over 5 days. On one climate model, the researchers ran thousands of simulations of future conditions, and they compared a world with current greenhouse-gas concentrations against one with pre-industrial levels. Those runs suggest that climate change had made the extreme temperatures – a major driver of fire weather – 4.5 times more likely. A second model showed that the below-average rainfall was also linked to increased greenhouse-gas concentrations, but only in some climate scenarios. The researchers say the study is one of many that connect climate change to increasing fire risks in eastern Australia. The work helps to confirm what many suspect

**O**n 1 January, the air in Canberra was the worst of any city in the world. With unprecedented bush fires raging nearby, a thick blanket of smoke smothered Australia's capital for weeks, sending a surge of residents to the hospital with breathing problems. The toxic haze got so bad that Sophie Lewis, a climate scientist at the University of New South Wales (UNSW) Canberra, took her toddler and boarded a plane to Tasmania.

"I almost wept with relief in Melbourne, on the way to Hobart, simply from seeing the sky," she says. After weeks in the smoke, her daughter had grown used to all the people walking around with "bird beaks", Lewis's name for the masks everyone was wearing.

From Hobart, Lewis fielded e-mails from concerned colleagues overseas. Like the rest

## Feature

about the impacts of the major warming in Australia, says Perkins-Kirkpatrick, one of the authors of the report. Nine of Australia's ten hottest years on record have occurred in the past 15 years.

### Cause and effect

Friederike Otto, a climate modeller at the University of Oxford, UK, started contemplating an attribution study on the Australian fires after she saw satellite images peppered with conflagrations and smoke plumes stretching across the continent. The event was too big to ignore, says Otto, who is a co-investigator at World Weather Attribution (WWA), a partnership led by the university's Environmental Change Institute and the Royal Netherlands Meteorological Institute that analyses the effects of climate change on extreme weather. WWA decided to do a rapid attribution study, and invited Lewis, Perkins-Kirkpatrick and other researchers in Australia to join.

The first step in any attribution study is to set out the limits of the event (see 'A country aflame'), which is tricky in the Australian case because of the size of the area that has burnt and the time span over which it happened, says Perkins-Kirkpatrick. Once that has been done, the team will analyse whether temperature, rainfall and a 'fire-weather' index (FWI) – which includes those two variables and others – during the event were outside normal ranges. Last year was the country's driest and hottest on record, and a heatwave that affected most of the country in December smashed the record for the hottest day ever recorded in Australia. The average maximum temperature across the country reached 41.9 °C on 18 December.

To see whether climate change had a role in these extremes, the group will use half a dozen climate models to run thousands of simulations, some reflecting current greenhouse-gas concentrations and others using pre-industrial levels. The group will also determine whether climate change made fire weather worse during the event.

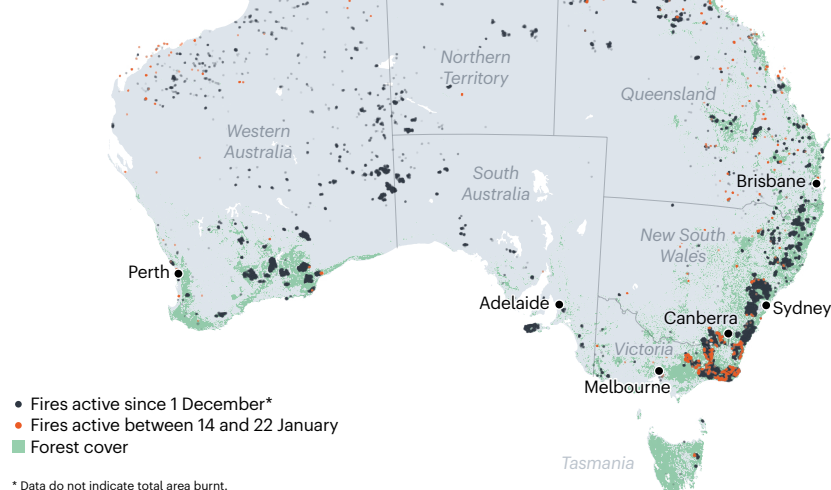
Perkins-Kirkpatrick is confident the study will pinpoint the influence of climate change on extreme temperatures, but its effects on dryness, humidity and winds are much harder to assess. That's why it's important to analyse the extent to which global warming influenced both the FWI and the individual components, says Otto.

The team plans to publish its results in an open-review journal, as soon as they're ready, and probably in the next couple of weeks. "For an event like this, where a lot of people have a lot of opinions on the role of climate change, it is important to make the scientific process as transparent as possible," says Otto.

The study could also feed into future attribution work on fires, for which there has been a shortage of work. Hundreds of

## A COUNTRY AFLAME

Infrared data from NASA satellites capture the location of fires in Australia.



attribution studies have shown that climate change increased the risks of specific heatwaves – including a record one in Europe last year. But only a small fraction have looked at extreme fires, partly because fires are much more complex than heatwaves or droughts, says Brown. A report examining major fires in British Columbia in Canada in 2017 found that climate change made extreme fire weather two to four times more likely and increased the area of the province that burnt by at least a factor of seven<sup>3</sup>. And a couple of studies have explored the factors driving a fivefold increase in the area burnt in California since the 1970s<sup>4</sup>, and a twofold increase in burnt area in the western United States since the mid-1980s<sup>5</sup>. Both studies found that the particular trend was probably driven by increased drying of leaves, twigs, tree branches and other 'fuels' as a result of global warming.

### Incendiary behaviour

Most fire-attribution studies have focused on answering relatively straightforward questions, such as how much climate change contributed to, or exacerbated, the event. But Brown, whose team specializes in studying fire, wants to look deeper, and investigate how climate change is altering the behaviour of fires. In particular, he and his colleagues are looking at night-time warming, a factor he thinks might link global warming to bush-fire risk. When temperatures drop sharply at night, humidity tends to increase and that can help firefighters to suppress blazes. But when overnight temperatures remain high, fire managers have less success in combating fires, he says. Night-time temperatures have been climbing around much of the globe<sup>6</sup>, and Brown is exploring whether that change is raising the risk of fires.

Scientists are also interested in examining whether fires are getting more severe. The increased fuel aridity makes fires burn hotter, which increases the chances that a blaze will create its own weather system, sparking lightning and throwing embers kilometres ahead of the fire front<sup>7,8</sup>.

Smoke from these events can be so thick that it turns the sky an eerie red, or plunges everything into darkness. The haze travels for hundreds of kilometres, and can be seen from space. Lewis worries there isn't enough attention on the health impacts for the millions of Australians who've endured months of thick smoke. Beyond the damage to people's lungs, the fires can take a psychological toll. When residents are stuck indoors for weeks, Lewis says, the smoke "makes you feel stressed and anxious and on edge. Everything smells of smoke."

Lewis and her family stayed in Tasmania for almost two weeks. Now back in Canberra, she's seeing the effects this wild summer has had on her toddler, who has started asking where the red Sun went and what happened to all the bird-beak masks.

**Nicky Phillips** is *Nature's* Asia-Pacific bureau chief. **Bianca Nogrady** is a freelance writer in Australia's Blue Mountains.

1. Lewis, S. C. et al. *Bull. Am. Meteorol. Soc.* **December**, S15–S21 (2019).
2. Garnaut, R. 'Projecting Australian climate change' in *The Garnaut Climate Change Review* 105–120 (Cambridge Univ. Press, 2008).
3. Kirchmeier-Young, M. C., Gillett, N. P., Zwiers, F. W., Cannon, A. J. & Anslow, F. S. *Earth's Fut.* **7**, 2–10 (2019).
4. Williams, A. O. et al. *Earth's Fut.* **7**, 892–910 (2019).
5. Abatzoglou, J. T. & Williams, A. P. *Proc. Natl Acad. Sci. USA* **113**, 11770–11775 (2016).
6. Alexander, L. V. et al. *J. Geophys. Res.* **111**, D05109 (2006).
7. Liu, Y. *Ecohydrology* **10**, e1760 (2017).
8. Matthews, S., Sullivan, A. L. & Williams, R. J. *Glob. Change Biol.* **18**, 3212–3223 (2012).

SOURCES: MODIS FIRE DATA COURTESY OF NASA; FIRMS; FOREST DATA FROM ESA



# Books & arts

## Isaac Asimov: centenary of the great explainer

The chemist and science-fiction visionary championed rationality in 20 million published words. **By David Leslie**

**O**n 24 December 1968, astronaut William Anders took a photograph of Earth from the observation window of Apollo 8. The picture, now known as *Earthrise*, became one of the most iconic images in human history – later credited with catalysing the environmental movement. Is *Earthrise* a product of science or a work of art? Isaac Asimov, the Russian-born chemist and science-fiction colossus (1920–92), had an answer: the two are, in fact, the same.

Asimov spent more than half of the twentieth century cultivating that transformative unity of art and science. He wrote and edited around 500 books and penned myriad stories, articles and essays. They spanned the rich microscopic worlds of cytoplasm, cells and subatomic particles, and ventured into the boundless wilds of space. Throughout, Asimov razed the make-believe boundary between imagination and reason. As he wrote in the gemlike 1978 essay ‘Art and Science’, the artist’s work suffers if knowledge is deficient; the scientist’s suffers if leaps of intuition, which so often outpace the leaden trot of rationality, are ignored. Advance in these arenas is often synergistic, and scientists can “make great leaps into new realms of knowledge by looking upon the universe with the eyes of artists”.

For Asimov, nurturing ingenuity and insight through exploration, learning and communication was an ethical imperative and crucial for human progress. It was an ethos he promoted through 20 million printed words.

### Life of wonder

Asimov was central to science fiction’s Golden Age, as the writer of iconic works such as *I, Robot* (1950), the *Foundation* series and *The Gods Themselves* (1972). As a scientist, he was a popularizer who often drew comparisons with H. G. Wells. The leitmotif of his life was an unstinting thirst for knowledge. In *Asimov’s New Guide to Science* (first published as *The Intelligent Man’s Guide to Science* in 1960), he wonderfully characterized the deep history of

life on Earth as an adventure of curiosity. The book takes us from the clumsy inquisitiveness of an upstart paramecium searching for food several hundred million years ago to the restless seeking that propelled big-brained *Homo sapiens* into the space age. That brain, the “most magnificently organized lump of matter in the known universe”, generates the “curiosity surplus” shaping human culture, he wrote.

Asimov’s curiosity was first sparked in the windowless back rooms of a string of Brooklyn sweet shops. Born in 1920 in Petrovichi in Soviet Russia, Asimov was three when he and his family arrived at Ellis Island and began to scrape a living in New York. Three years later, his father had saved enough money to set up the first shop. Young Isaac spent long days delivering newspapers, schlepping boxes and magazines – and reading voraciously. By the age of five, he had taught himself to read by studying street signs. At six, he got his first library card from the Brooklyn Public Library; he would eventually wangle a second one from the neighbouring borough of

Queens, doubling his weekly intake. By his early teens, Asimov was horrifying neighbours as he wended his way blindly down busy streets with his nose in a book and one more under each arm.

Asimov started reading science-fiction at nine, just as the genre had begun a journey from pulp extravagance to a more science-centred era. He had convinced his father that Hugo Gernsback’s magazine *Science Wonder Stories* contained serious stuff, despite the covers’ motley depictions of space ships and aliens. From then on, he would regularly abscond to the shop’s storeroom to immerse himself. Thus began a lifelong habit of exploring the open frontiers of possibility in enclosed, electric-lit spaces – not unlike the time-travelling Andrew Harlan (in his 1955 novel *The End of Eternity*), who zooms across thousands of centuries in a humming “kettle”.

### The flag of reason unfurled

A prodigy, Asimov graduated from high school at 15. He was, however, rejected by Columbia College in Manhattan and directed to Seth Low Junior College, a satellite school in Brooklyn. Anti-Semitism was at work. Undeterred, he plodded through his studies. Meanwhile, a distinctive vision of science fiction as “the literature of social change” took shape in his mind. In 1938, he joined a remarkable sci-fi fan club, the Futurians, along with authors Frederik Pohl, Cyril Kornbluth and Donald Wollheim. The group was progressive and political, opposing the interwar rise of barbarism and militaristic ideologies. It called for science fiction to raise “the torch of science” and unfurl



Isaac Asimov published around 500 books, including science-fiction and popular science.



Isaac Asimov in 1982 on Ellis Island, New York.

“the flag of reason” to foster a more united and humane society.

Although he embraced this vision, Asimov felt that an impetus to change needed to be grounded in an understanding of its historical complexities and enabling conditions. He became a student researcher for sociologist Bernhard J. Stern, a co-founder of the journal *Science and Society* who was completing a book on the social resistance to technological change – *Society and Medical Progress*, published in 1941. Asimov began to perceive technology as a social institution entangled with others, such as politics and the economy.

He realized that the processes of innovation, which make possible both science fiction and technological progress, are in struggle with the norms and institutions that constrain them. He saw that the modern “era of change” was the crucible for this struggle, as scientists and artists envisioned and created futures and realities radically different from the past.

This conflict became Asimov’s creative launchpad. Science fiction in his hands dove headlong into the eye of the societal storm, where future-facing human ingenuity

## “Science fiction in his hands dove headlong into the eye of the societal storm.”

confronts the prevailing cultural patterns and historical conditions that determine the possibilities of the present.

### To the stars

Asimov’s star began its spectacular rise. While still an undergraduate, he published his first sci-fi piece, ‘Marooned Off Vesta’, in the magazine *Amazing Stories*. The freshly shaven 18-year-old Asimov had also shown up, manuscript in hand, at the door of the legendary editor of *Astounding Science Fiction*, John W. Campbell. Although Campbell gracefully turned down the story, he became Asimov’s greatest literary mentor. Their relationship ended up tense and complicated, however, with Asimov explicitly rejecting Campbell’s fascist politics and belief in racial superiority. (It must be noted here that Asimov had his

own egregious behaviour: the unapologetic harassing of women.)

With Robert Heinlein and Arthur C. Clarke, among others, Asimov ushered in a turn towards technically sophisticated science fiction, inspiring readers to move beyond the escapist era of ray guns and romance to critically embrace the computer revolution and the coming space age.

Asimov’s *annus mirabilis* spanned 1941 and 1942. He published ‘Nightfall’ in *Astounding*, a metaphor for humankind’s devastating psychological confrontation with its own cosmic insignificance. In 1968, the Science Fiction Writers of America voted it one of the greatest sci-fi stories ever penned. He also produced several of his celebrated robot stories – such as ‘Reason’, ‘Liar’ and ‘Runaround’ – in which he coined the term robotics (after the robots of *R.U.R. (Rossum’s Universal Robots)*, a play by Czech writer Karel Čapek, published 100 years ago) and famously invented the field’s three ethical laws. Those accomplishments are honoured every April in the United States, during National Robotics Week.

And 1942 saw the publication of ‘Foundation’,



## Books & arts

the inaugural instalment of Asimov's eponymous series and a masterwork of future history modelled on Edward Gibbon's eighteenth-century classic, *The History of the Decline and Fall of the Roman Empire*. In the series, humanity battles against a galactic descent into 30,000 years of barbarism, foretold by the statistical science of 'psychohistory'. The epic is rife with the struggles of human agency against the "dead hand of social inevitability" – themes still unnervingly relevant in today's algorithm-driven 'big data' society. In 1966, the Foundation trilogy won a Hugo Award for the best science-fiction series ever written.

### Responsibility of communication

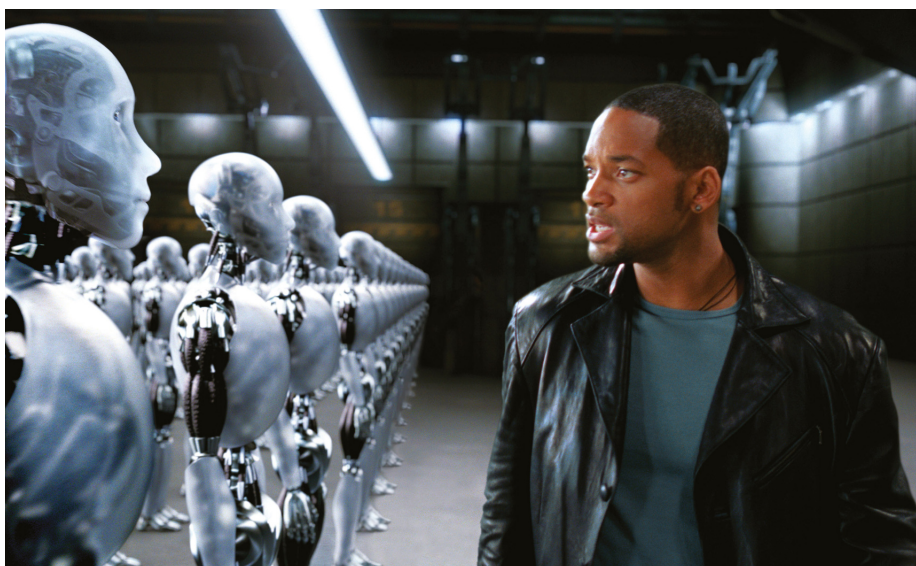
The next decade was a busy one. Asimov worked as a scientist for the US Navy during the Second World War; completed a doctorate in chemistry at Columbia; and, in 1949, took a post teaching biochemistry at Boston University School of Medicine in Massachusetts. Even as his science-fiction career gathered pace, his academic role nudged him towards science writing, beginning with the co-authored 800-page *Biochemistry and Human Metabolism* in 1952. Six books on chemistry followed, along with a run of sparkling popular-science essays with beguiling titles such as 'The Explosions Within Us' and 'The Abnormality of Being Normal'.

On 4 October 1957, the world was galvanized as the Soviet Union propelled the 84-kilogram satellite Sputnik 1 into elliptical Earth orbit. In the United States, panic rose over the gap in research progress. As US citizens turned on short-wave radios to listen for its eerie 'beep-beep', Sputnik mania sparked a massive demand for educational popular-science writing – and a shift towards a more unified vision of Earth. Nature ended and Ecology was born, the media theorist Marshall McLuhan later noted: "The planet became a global theater in which there are no spectators but only actors. On Spaceship Earth there are no passengers; everybody is a member of the crew."

Asimov plunged into both educating the public and advocating a sustainable future. In 1958, he switched to mainly writing science books. The following year, he wrote half a million words in eight months, culminating in *The Intelligent Man's Guide to Science*, nominated for the 1960 National Book Award.

Across his non-fiction, Asimov dedicated himself to initiating lay readers into the world of scientific exploration through unadorned but wonder-filled writing. The aim was to allow them to weigh up the prospects and challenges of scientific advance lucidly and capably. Astronomer and science communicator Carl Sagan's obituary of Asimov in *Nature* calls him "one of the great explainers of the age", motivated by a "profoundly democratic impulse" (*C. Sagan Nature* 357, 113; 1992).

Asimov himself dubbed that impulse the



Will Smith in Alex Proyas's film *I, Robot* (2004), based on Asimov's fiction.

"responsibility of communication". In a 1988 interview, he explained that it rested on the fact "that science is tentative, that it is not certain, that it is subject to change". Therefore, no voice can have the last word, and open, inclusive and rational communication is the only option for advancement. The public, meanwhile, bears the "responsibility of listening".

These strains of Enlightenment thinking made him a staunch critic of pseudoscience,

### "Asimov wrote: 'Science gathers knowledge faster than society gathers wisdom.'"

intolerance and superstition. He spent a good part of his final years championing secular reason in an age when, he believed, the candle of critical thinking had dimmed. In 1988, he observed: "the saddest aspect of life right now is that science gathers knowledge faster than society gathers wisdom".

### The good Earth is dying

Asimov recognized that this troubling disconnect had grave planetary consequences. In his perceptive 1971 essay 'The Good Earth Is Dying', he pointed out that, with accelerating technological advancement, harmful impacts on society and the environment had already reached a global scale. Meanwhile, attitudes such as the reverence for limitless growth and the embrace of tribalism persisted – dictated by antiquated parochial beliefs and local conventions, rather than being transposed in a global key and altered accordingly. Asimov wrote: "What was common sense in a world that once existed has become myth in the totally different world that now exists, and suicidal myth at that".

Many decades before the rise of idioms of anxious sociotechnical reflection such as 'the sixth extinction', or the 'Anthropocene epoch', Asimov was writing about how "anthropogenic processes" were poisoning the planet. From the 1970s onwards, he wrote about how atmospheric pollution was destroying the ozone layer, acidifying the oceans and exacerbating the scale of natural catastrophes. He described human-driven global warming and its probable effects on the biosphere. He noted how overpopulation and the sweep of reckless human activities were prompting a "great die-off" of species at an unprecedented rate.

Asimov called for global solutions to global problems, anchored in a vision of humanity united by a common aim. That stance drove him from the start. More than a decade before *Earthrise* so stirringly revealed our planetary home, Asimov, in the 1953 essay 'Social Science Fiction', reflected on how literature portraying a multitude of worlds puts ours into perspective. In a conceptually vast Universe, Earth shrinks, to beneficial effect: subdivisions that ordinarily polarize can become much harder to perceive or conceive, and humanity can be seen as faced with "common dangers and common tasks".

A century after Asimov's birth, forests burn from Australia to California. Shorelines are swallowed by rising seas, towns ravaged by unearthly storms. Humanity's insatiable appetites continue to crush the diversity of life, and conflicts draw us ever closer to a fiery end. At such a juncture, we might do well to pick up Asimov's writings and take flight with him. Perhaps then we can together peer back at our pale blue island, suspended in the void, and gain a saner, more humane and more rational point of view.

**David Leslie** is the Ethics Fellow at the Alan Turing Institute in London.  
e-mail: dleslie@turing.ac.uk

### **Correction**

#### **Isaac Asimov: centenary of the great explainer**

This article should have noted that Asimov had his own egregious behaviour: his unapologetic harassing of women.

See <https://doi.org/10.1038/d41586-020-00176-4>



# Correspondence

## Swift visas for post-Brexit science

As the UK government's chief scientific adviser, I welcome the announcement of a new fast-track immigration scheme for researchers to help ensure that the United Kingdom remains a top destination for scientific talent after it leaves the European Union later this year. The scheme – which is being incorporated within a reformed and rebranded Global Talent Route – will go live on 20 February.

The fast-track scheme applies to all eligible overseas researchers and their team members who receive peer-reviewed grants from recognized funding bodies. The national funding agency, UK Research and Innovation, will oversee the eligibility of funding bodies and establish a new criterion for automatic endorsement. Dependents will continue to have full access to the labour market. There will also be an accelerated path to settlement. There is no cap on the number of researchers who can benefit.

The scheme will allow UK-based researchers to recruit overseas talent to their teams. Attracting the best international scientists at all career stages is an important part of the government's strategy to boost research and development. This first phase of changes goes a long way towards ensuring that the United Kingdom remains a global leader in science excellence.

**Patrick Vallance** Government Office for Science, London, UK.  
contact@go-science.gov.uk

## Crop revolutions must reach poor

As researchers who recognize that plant science underpins food security, we applaud the development of genetic strategies that could sustainably improve crop yields (J. Bailey-Serres *et al. Nature* **575**, 109–118; 2019). However, the socio-economic implications of such technologies could prevent farmers and consumers from adopting them, particularly in developing countries hit hardest by climate change.

Commercial interests typically drive the implementation of crop technologies. Advances in crop science are more about integrating technology with global economic realities, which can include poverty, poor governance, lack of market access and inefficient supply chains (A. A. Adenle *et al. Nature Biotechnol.* **36**, 137–139; 2018).

Taking such limitations into account, along with public unease about genetic modification and the use of the gene-editing tool CRISPR in food production (J. L. Lusk *et al. Food Pol.* **78**, 81–90; 2018), we consider that a broader range of technologies should be explored in parallel. Innovative approaches to plant breeding strategies, for example, could deliver a new green revolution.

**Christine H. Foyer\*** University of Birmingham, UK.  
c.h.foyer@bham.ac.uk  
\*On behalf of 5 correspondents; see [go.nature.com/38hcjiv](https://go.nature.com/38hcjiv).

## Research funding gloom for Catalexit

I disagree with Joan Martínez Alier's view that Catalonia's research funding could increase if the region were to become independent of Spain (*Nature* **576**, 384; 2019). For a start, Catalonia would lose out on future European research grants because it would cease to be a member of the European Union. And, contrary to Alier's suggestion, discontinuing fiscal transfers to Spain would make little difference in its landscape of bulging public debt, departing businesses, and no access to European Central Bank financing.

Madrid has a comparable weight in Spain's economy. Although fiscal transfers from Madrid to the rest of Spain are much higher than those from Catalonia, its absolute and per capita public debt are less than half those of Catalonia. Since 2012, Catalonia has drawn more than €70 billion (US\$78 billion) in favourable-term loans from Spanish public sources such as the Regional Liquidity Fund. To make matters worse, an independent Catalonia might need to add its share of Spanish public debt – around another €200 billion – to its regional debt (see [go.nature.com/37kqc1c](https://go.nature.com/37kqc1c)).

**José M. Rojo** Margarita Salas Biological Research Center, CSIC Madrid, Spain.  
jmrojo@cib.csic.es

## Genentech not first biotech company

In his illuminating history of corporate research, Paul Lucier repeats the common mistake of calling Genentech the first biotechnology firm (*Nature* **574**, 481–485; 2019). Cetus was founded five years earlier, in 1971, by Nobel-prizewinner Donald Glaser and others. It initially developed microbial processes for producing chemical feedstocks, including propylene oxide and antibiotic intermediates. The corporation later pivoted to therapeutics.

Genentech was backed by venture capital. Cetus was funded largely by other means, including support from Standard Oil. Consequently, Cetus and a few other early biotech companies – Irvine Scientific, Gamma Biologicals and Cell Associates among them – have been overlooked or long forgotten because of a history that equates biotech with venture-capital-funded drug discovery.

**William Bains** Five Alarm Bio, Cambridge, UK.  
[william@fivealarmbio.com](mailto:william@fivealarmbio.com)

## HOW TO SUBMIT

Correspondence may be submitted to [correspondence@nature.com](mailto:correspondence@nature.com) after consulting the author guidelines and section policies at [go.nature.com/cmchno](https://go.nature.com/cmchno).

# News & views

## Stem cells

# Fight or flight turns hair white

Shayla A. Clark & Christopher D. Deppmann

Signalling from the sympathetic nervous system of mice when subjected to stress leads to the depletion of a stem-cell population in their hair follicles. This discovery sheds light on why stress turns hair prematurely grey. **See p.676**

It has been said that Marie Antoinette's hair went completely white on the night before her beheading. This story might be apocryphal, but rapid greying of the hair is now widely referred to as Marie Antoinette syndrome. It is often assumed to be caused by stress – a phenomenon perhaps best exemplified by photographs of heads of state before and after they held office. However, the relative contributions of ageing, genetic factors and stress to greying are not known – in part owing to a lack of mechanistic understanding of the process. On page 676, Zhang *et al.*<sup>1</sup> identify the mechanism governing premature greying in mice that have experienced stress.

The average human scalp has 100,000 hair follicles, and a wide range of hair colours can be found across the human population. Hair colour is determined by cells called melanocytes, which produce different combinations of light-absorbing melanin pigments<sup>2</sup>. Melanocytes are derived from melanocyte stem cells (MeSCs), which are located in a part of the hair follicle called the bulge<sup>3</sup>. The normal hair cycle is divided into three stages: hair-follicle regeneration (anagen), degeneration (catagen) and rest (telogen). Melanocyte production begins early in the anagen phase (Fig. 1a). As people age, the pool of MeSCs is gradually depleted – and so pigmented hair becomes 'salt and pepper' coloured, and then turns to grey and finally to white after a complete loss of pigment in all hair follicles<sup>4</sup>.

Aside from ageing, there are several factors that bring about premature greying, including dietary deficiencies<sup>5</sup>, disorders such as alopecia areata or vitiligo<sup>6,7</sup>, and stress<sup>8,9</sup>. Zhang *et al.* set out to test the role of stress in the greying process in mice. They exposed the animals to three different stressors – pain, restraint and a model of psychological

stress – during different phases of hair growth. Each stressor caused depletion of MeSCs from the bulge region, eventually leading to the development of patches of white hair.

Prevailing theories posit that stress-induced greying involves hormones (such as corticosterone) or autoimmune reactions<sup>10</sup>. Zhang and colleagues examined these potential mechanisms, first by preventing corticosterone

signalling and next by stressing animals that had compromised immune systems. In both cases, greying occurred after stress, indicating that neither corticosterone nor autoimmune reactions cause MeSC depletion. However, the authors found that MeSCs express  $\beta_2$ -adrenergic receptors, which respond to noradrenaline – a neurotransmitter molecule involved in the 'fight or flight' response to stress. Loss of this receptor specifically in MeSCs completely blocked stress-induced greying.

Adrenal glands are the main source of circulating noradrenaline. But, surprisingly, the researchers discovered that removing these glands did not prevent greying in response to stress in the mice.

Another source of noradrenaline is the sympathetic nervous system (SNS), which is highly active in response to stress, and which drives the fight-or-flight response. Zhang and colleagues showed that bulge regions are highly innervated by sympathetic neurons, and that ablating the SNS using a neurotoxin molecule, or blocking the release of noradrenaline from sympathetic neurons, prevented stress-induced greying. Next, the authors

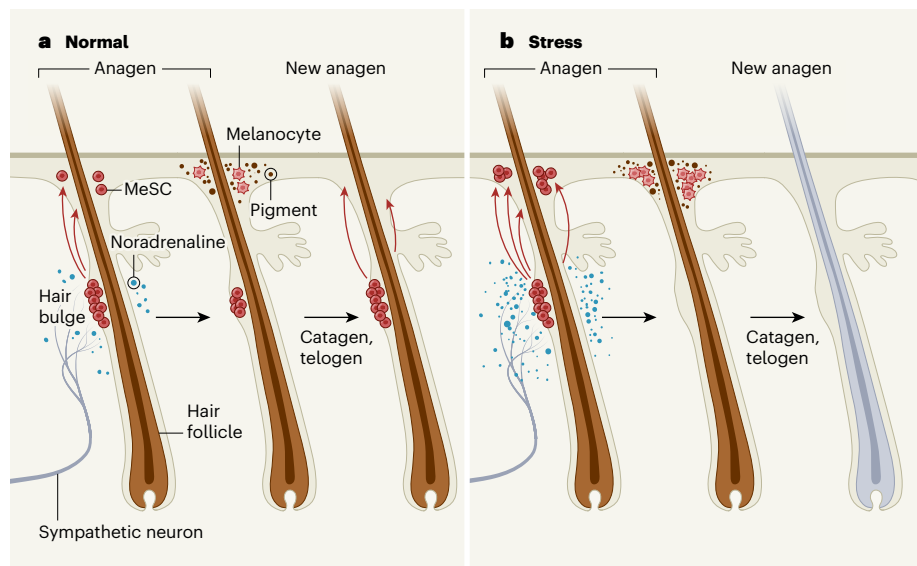


**Figure 1 | Melanocyte stem cells and stress.** Melanocyte stem cells (MeSCs) are located in the bulge of the hair follicle, which is innervated by neurons of the sympathetic nervous system that release the neurotransmitter molecule noradrenaline. The follicle cycles through three phases: regeneration (anagen), degeneration (catagen) and rest (telogen). **a**, Under normal conditions, MeSCs migrate away from the bulge (red arrows) and differentiate into melanocytes during anagen. Melanocytes synthesize pigments that add colour to the regenerating hair. During catagen and telogen, they begin to die and migrate out of the niche (not shown). However, plentiful MeSCs remain to replace the melanocytes in the next anagen phase. **b**, Zhang *et al.*<sup>1</sup> show that stressful stimuli activate the sympathetic nervous system, increasing noradrenaline release in hair follicles. Noradrenaline causes complete conversion of MeSCs into melanocytes, which migrate out of the niche in catagen and telogen. The hair follicle is depleted of MeSCs that would have differentiated to replace these melanocytes. Without any pigment cells to colour the hair in the next anagen phase, it begins to look grey or white.



generated mice in which sympathetic neurons could be acutely activated, and found that overactivation of the SNS in these mice caused greying in the absence of stress. Together, these results indicate that noradrenaline released from active sympathetic neurons triggers MeSC depletion (Fig. 1b). Interestingly, Zhang *et al.* found that the propensity of an area to turn grey correlates with its level of sympathetic innervation.

Exactly how does sympathetic activity cause depletion of MeSCs from hair follicles? Normally, these stem cells are maintained in a dormant state until hair regrowth is required. However, when the researchers tracked MeSCs labelled with a fluorescent protein, they discovered that MeSC proliferation and differentiation increase markedly under extreme stress or exposure to a high level of noradrenaline. This results in mass migration of melanocytes away from the bulge, and leaves no remaining stem cells. To further confirm this result, the researchers suppressed MeSC proliferation pharmacologically and genetically. When proliferation was dampened, the effects of stress on MeSC proliferation, differentiation and migration were blocked.

Zhang and colleagues' work raises several questions. For instance, is the mechanism underlying MeSC depletion in response to stress the same as that which causes greying during ageing? Future experiments modulating SNS activity over a longer period would determine whether age-related greying can be slowed or hastened. Perhaps, in the absence of sympathetic signals, MeSCs have the capacity for unlimited replenishment, pointing to a way to delay age-related greying.

Are other pools of stem cells similarly susceptible to stem-cell depletion in response to stress, if they or the cells that make up their niche express  $\beta_2$ -adrenergic receptors? In support of this idea, haematopoietic stem and progenitor cells (HSPCs), which give rise to blood and immune lineages, reside in a bone-marrow niche that contains stromal cells, and stimulation of those cells by the SNS causes HSPCs to leave their niche<sup>11,12</sup>. Perhaps, like MeSCs, stress depletes HSPCs – which could partially explain why immune function is impaired in response to chronic stress<sup>13,14</sup>. Whether this type of relationship extends beyond MeSCs and HSPCs is an open question.

It is fascinating to consider what possible evolutionary advantage might be conferred by stress-induced greying. Because grey hair is most often linked to age, it could be associated with experience, leadership and trust<sup>15</sup>. For example, adult male silverback mountain gorillas (*Gorilla beringei beringei*), which get grey hair on their backs after reaching full maturity, can go on to lead a gorilla troop<sup>16</sup>. Perhaps an animal that has endured enough stress to 'earn' grey hair has a higher place in the social order than would ordinarily

be conferred by that individual's age.

Connecting the dots between stress, fight or flight, stem-cell depletion and premature greying opens up several avenues for future research. Beyond developing anti-greying therapies, Zhang and colleagues' work promises to usher in a better understanding of how stress influences other stem-cell pools and their niches.

**Shayla A. Clark** and **Christopher D.**

**Deppmann** are in the Neuroscience Graduate Program, University of Virginia, Charlottesville, Virginia 22903, USA. **C.D.D.** is also in the Departments of Biology, Biomedical Engineering, Cell Biology and Neuroscience, University of Virginia.

e-mail: deppmann@virginia.edu

1. Zhang, B *et al.* *Nature* **577**, 676–681 (2020).

## Cardiovascular biology

# Suspect that modulates the heartbeat is ensnared

**Xiaohan Wang & Richard W. Tsien**

The activity of calcium channels in the heart increases during what is called the fight-or-flight response. An investigation into the 50-year-old mystery of how this occurs has captured a previously overlooked suspect. **See p.695**

In the Sherlock Holmes tale *The Adventure of the Dancing Men*, the detective runs a heart-pounding race to try to save his client's life. The thumping of the sleuth's heart – a literary example of the 'fight-or-flight' effect<sup>1</sup> – reflects the changes that occur when the entry of calcium ions into the heart rises<sup>2</sup>. On page 695, Liu *et al.*<sup>3</sup> provide a solution to the long-standing riddle of how this occurs, through deductions worthy of Sherlock Holmes.

Some aspects of how calcium enters the heart during a fight-or-flight response are known. The process is mediated by the hormone adrenaline acting on  $\beta$ -adrenergic receptors – proteins that reside in the surface membrane of heart cells called cardiomyocytes. Receptor activation leads to an increase in the opening of what is called an L-type voltage-gated calcium channel. This occurs through a mechanism that involves the molecule cyclic AMP (cAMP)<sup>4,5</sup> and an enzyme called protein kinase A (PKA) that requires cAMP for its function<sup>6</sup>. Similar types of PKA-mediated processes are found in other contexts. For example, some neurons use cAMP and PKA to enhance calcium entry through L-type calcium channels<sup>7</sup>.

- Riley, P. A. *Int. J. Biochem. Cell Biol.* **29**, 1235–1239 (1997).
- Nishimura, E. K. *et al.* *Nature* **416**, 854–860 (2002).
- Nishimura, E. K., Granter, S. R. & Fisher, D. E. *Science* **307**, 720–724 (2005).
- Shaw, N. A., Dickey, H. C., Brugman, H. H., Blumberg, D. L. & Witter, J. F. *Lab. Anim.* **8**, 1–7 (1974).
- Nahm, M., Navarini, A. A. & Kelly, E. W. *Int. J. Trichol.* **5**, 63–68 (2013).
- Daulatabad, D., Singal, A., Grover, C. & Chhillar, N. *Int. J. Trichol.* **9**, 19–24 (2017).
- King, C., Smith, T. J., Grandin, T. & Borchelt, P. *Appl. Anim. Behav. Sci.* **185**, 78–85 (2016).
- Akin Belli, A., Etgu, F., Ozbas Gok, S., Kara, B. & Dogan, G. *Pediatr. Dermatol.* **33**, 438–442 (2016).
- Paus, R. *Pigment Cell Melanoma Res.* **24**, 89–106 (2011).
- Katayama, Y. *et al.* *Cell* **124**, 407–421 (2006).
- Mendez-Ferrer, S., Enikolopov, G. N., Lira, S. & Frenette, P. S. *Blood* **112**, 4 (2008).
- Glaser, R. & Kiecolt-Glaser, J. K. *Nature Rev. Immunol.* **5**, 243–251 (2005).
- Heidt, T. *et al.* *Nature Med.* **20**, 754–758 (2014).
- Cunningham, M. R., Druen, P. B. & Barbee, A. P. in *Evolutionary Social Psychology* (eds Simpson, J. A. & Kenrick, D. J.) Ch. 5 (Erlbaum, 1997).
- Robbins, M. M. *Behaviour* **132**, 21–47 (1995).

This article was published online on 22 January 2020.

phosphorylation sites were converted to an amino acid (alanine) that can't be phosphorylated, and when this channel was studied alone, PKA-mediated enhancement of L-type channels nevertheless persisted. The authors therefore looked elsewhere for the elusive mediator of PKA's ability to regulate the fight-or-flight effect.

Reasoning that some unknown factor must come into close proximity to the calcium channel during this regulatory process, the authors conducted a systematic search. Using proximity proteomics, Liu and colleagues engineered channel subunits to contain an enzyme that adds a tag called biotin to any protein within a radius of approximately 20 nanometres<sup>15</sup>. Tagged proteins were then identified by mass spectrometry. Hundreds of proteins in proximity to the calcium channel were analysed, and the authors found that the protein Rad was enriched in the channel microenvironment under resting conditions, but was noticeably depleted during stimulation of the  $\beta$ -adrenergic receptor. This dovetailed with an earlier clue – Rad is known to inhibit L-type voltage-gated calcium channels<sup>15</sup>, and, in mice, deletion of the gene that encodes Rad mimics the effect of  $\beta$ -adrenergic stimulation and eliminates further adrenaline-mediated enhancement of the activity of L-type channels<sup>16</sup>.

Liu *et al.* investigated whether PKA could prevent Rad-mediated channel inhibition. The authors tested whether phosphorylation of amino-acid residues on Rad would enable it to move away from the vicinity of the calcium channel. They narrowed the candidate residues down to four serines (in some experiments, just two), which, if replaced by alanine, abolished PKA-mediated regulation of calcium entry.

The calcium channel's  $\beta$ -subunit was the prime suspect as the target of Rad inhibition. Ablation of the interaction between the calcium channel's  $\alpha_{1C}$ -subunits and its  $\beta$ -subunits fully eliminates PKA-mediated modulation of channel activity<sup>17</sup>. Indeed, the authors' measurements, using a technique called fluorescence resonance energy transfer, showed that the interaction between Rad and the calcium-channel  $\beta$ -subunit was inhibited by PKA phosphorylation of the key serines in Rad that the authors had identified. Further tightening the noose around Rad's metaphorical neck, electrical recordings demonstrated that all of the biophysical fingerprints of modulation by  $\beta$ -adrenergic signalling – such as the activity of previously inactive calcium channels and a shift in the voltage dependence of their activation<sup>18</sup> – were prevented by eliminating Rad phosphorylation.

The results make a compelling case for the following scenario (Fig. 1). Adrenaline binds and activates the  $\beta$ -adrenergic receptor. This, in turn, results in the activation of an enzyme

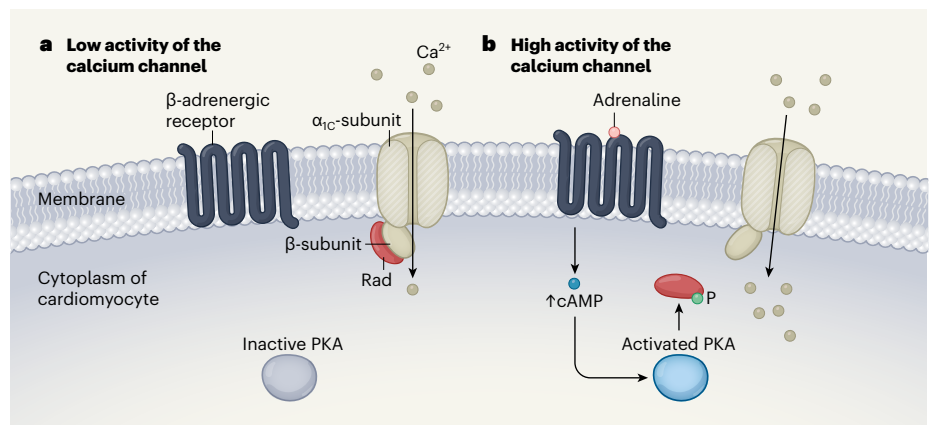


**Figure 1 | Modulation of the cardiac calcium channel.** In heart cells called cardiomyocytes, the activity of calcium-ion channels increases during what is called the fight-or-flight response. Activation of the enzyme protein kinase A (PKA) is required for this process, and, in mouse studies, Liu *et al.*<sup>3</sup> reveal that its elusive target is the protein Rad. **a**, In the absence of a fight-or-flight response, the  $\beta$ -adrenergic receptor is not stimulated and PKA is inactive. Rad binds to a subunit of the calcium channel (beige; only the  $\alpha_{1C}$ - and  $\beta$ -channel subunits are shown) and calcium-ion ( $\text{Ca}^{2+}$ ) entry into cardiomyocytes is low. **b**, During the fight-or-flight response, the hormone adrenaline activates the  $\beta$ -adrenergic receptor. This leads to the production of cyclic AMP (cAMP) molecules, which activate PKA. Activated PKA adds a phosphate group (P) to Rad, causing Rad to dissociate from the channel and enabling channel activity to increase. This elevation of  $\text{Ca}^{2+}$  in the cytoplasm boosts the heartbeat.

that produces cAMP, which activates PKA. PKA phosphorylates Rad and causes it to leave the vicinity of the calcium channel, thereby preventing it from inhibiting the channel.

The study puts Rad and other members of this family of proteins front and centre as players in calcium-channel modulation. Is Rad the entire missing chapter in the story of PKA's role in the heart, given Liu and colleagues' compelling arguments that other potential PKA targets are unnecessary? Sceptics will want

### “The study puts Rad and other members of this family of proteins front and centre as players in calcium-channel modulation.”

further *in vivo* evidence from a type of mouse model termed a knock-in – animals whose original Rad sequence is replaced either with a version in which Rad's own PKA-phosphorylation sites are mutated or with a version in which the part of Rad needed for the interaction with the  $\beta$ -subunit is eliminated – to see whether any PKA-mediated modulation of the calcium channel still occurs. Hints of differences between channel regulation in the embryonic and adult heart<sup>13</sup> also warrant further study.

Might cardiac regulation by Rad be of clinical value? Heart failure in humans is associated with loss of regulation of calcium channels by  $\beta$ -adrenergic receptors. Rad levels fall during heart failure<sup>19</sup>, perhaps providing a temporary increase in the strength of heart contraction<sup>16</sup>. However, this would also

reduce the heart's ability to further increase its strength<sup>20</sup>, what is known as its functional reserve, which would be a severe price for a person's heart to pay.

There will undoubtedly be debate about how PKA modulation of calcium channels operates in neurons, such as in PKA-responsive CA1 pyramidal cells in which Rad is essentially absent. In those neurons, the mutation of a particular serine (serine 1928) to alanine in the L-type channel eliminates channel modulation and L-type channel-dependent strengthening of inter-neuronal (synaptic) connections<sup>7</sup>. Here, PKA might be phosphorylating the calcium channel, after all.

Organ-specific pathways for regulation would make functional sense. Rad can completely inhibit calcium-channel activity, and so modifying such inhibition would give heart cells a wide range of regulatory capability<sup>18</sup>, suitable for a brief flight-or-flight response. Perhaps other cell types needing a more sustained but subtler boost to their calcium-channel activity might operate better without Rad-mediated regulation and rely instead on milder, more direct modulation of a subunit of the calcium channel.

Liu and colleagues have set a high bar for future detective work on cellular signalling in the heart. Their work shows the power of a systematic round-up of suspects and relentless interrogation of their roles.

**Xiaohan Wang** and **Richard W. Tsien** are at the Neuroscience Institute, New York University Grossman School of Medicine, New York, New York 10016, USA, and in the Department of Neuroscience and Physiology, New York University.



e-mails: richard.tsien@nyulangone.org;  
xiaohan.wang@nyulangone.org

1. Cannon, W. B. *Bodily Changes in Pain, Hunger, Fear, and Rage: An Account of Recent Researches into the Function of Emotional Excitement* (Appleton, 1915).
2. Reuter, H. J. *Physiol. (Lond.)* **192**, 479–492 (1967).
3. Liu, G. *et al. Nature* **577**, 695–700 (2020).
4. Tsien, R. W., Giles, W. & Greengard, P. *Nature New Biol.* **240**, 181–183 (1972).
5. Reuter, H. J. *Physiol. (Lond.)* **242**, 429–451 (1974).
6. Osterrieder, W. *et al. Nature* **298**, 576–578 (1982).
7. Qian, H. *et al. Sci. Signal.* **10**, eaaf9659 (2017).
8. De Jongh, K. S. *et al. Biochemistry* **35**, 10392–10402 (1996).
9. Bunemann, M., Gerhardtstein, B. L., Gao, T. & Hosey, M. M. *J. Biol. Chem.* **274**, 33851–33854 (1999).
10. Fuller, M. D., Emrick, M. A., Sadilek, M., Scheuer, T. &

- Catterall, W. A. *Sci. Signal.* **3**, ra70 (2010).
11. Lemke, T. *et al. J. Biol. Chem.* **283**, 34738–34744 (2008).
12. Brandmayr, J. *et al. J. Biol. Chem.* **287**, 22584–225924 (2012).
13. Fu, Y., Westenbroek, R. E., Scheuer, T. & Catterall, W. A. *Proc. Natl Acad. Sci. USA* **110**, 19621–19626 (2013).
14. Rhee, H.-W. *et al. Science* **339**, 1328–1331 (2013).
15. Finlin, B. S., Crump, S. M., Satin, J. & Andres, D. A. *Proc. Natl Acad. Sci. USA* **100**, 14469–14474 (2003).
16. Manning, J. R. *et al. J. Am. Heart Assoc.* **2**, e000459 (2013).
17. Yang, L. *et al. J. Clin. Invest.* **129**, 647–658 (2019).
18. Bean, B. P., Nowycky, M. C. & Tsien, R. W. *Nature* **307**, 371–375 (1984).
19. Chang, L. *et al. Circulation* **116**, 2976–2983 (2007).
20. Chen, X. *et al. Circ. Res.* **91**, 517–524 (2002).

This article was published online on 22 January 2020.

## Condensed-matter physics

# A milestone in the hunt for metallic hydrogen

Serge Desgreniers

An optical study of cold solid hydrogen at extreme pressures indicates that electrons in the material are free to move like those in a metal. This suggests that the long-sought metallic phase of hydrogen might have been realized. **See p.631**

Hydrogen is the most abundant element in the Universe. Its molecular-gas state is simple, but its solid state has proved to be complex. In 1935, it was predicted that solid hydrogen should behave like an electrical conductor at elevated pressures, owing to its molecules being separated into their atomic constituents<sup>1</sup>. This prediction heralded a race to prove experimentally that solid hydrogen displays such metallic behaviour under ultrahigh compression. However, although there have been many claims of proof (for example, refs 2–4), these studies have been challenged. Now, on page 631, Loubeyre *et al.*<sup>5</sup> report that dense hydrogen shows a discontinuous and reversible change in optical reflectivity at extreme pressure and low

temperature that can be attributed to a phase transition into a metallic state.

It is common practice to use a device called a diamond anvil cell to achieve ultrahigh compression of a material and to study changes in the material's physical properties at high density. A diamond anvil cell squeezes a sample, which is confined to a microscopic chamber in a thin metal foil, between two diamond anvils (Fig. 1a). The device operates on a deceptively simple physical concept: pressure is inversely proportional to the area of a surface over which a force is applied. In the present case, this simplicity comes with an inherent drawback: reaching extreme pressures inevitably implies working with tiny sample volumes.

Conventional techniques have been the bottleneck in applying extreme pressures to highly compressible materials such as hydrogen. Over the past few decades, research groups around the world have pushed the boundaries of pressure generation. They have also refined the tools and methods needed to accurately estimate pressures applied to a microscopic sample of compressed gas. Nevertheless, debate continues over the accuracy of reported pressures and the interpretation of results drawn from measurements of physical properties.

Recognizing this long-standing problem, Loubeyre and colleagues' research group developed an innovative approach that involves the precise sculpting of diamond-anvil surfaces using a stream of massive ions<sup>6</sup> – a technique called focused ion-beam milling. A similar experimental development has also been reported<sup>7</sup>. The profiled anvils produce extreme pressures that can be reliably estimated, reaching more than 400 gigapascals (about 4 million times Earth's atmospheric pressure). Moreover, the shape of the anvils helps to confine dense hydrogen samples that are suitable for optical measurements.

Under increasingly extreme pressures, dense hydrogen becomes more and more opaque to visible light. For pressures in excess of about 300 GPa, solid hydrogen becomes penetrable only by electromagnetic radiation of lower energy than visible light<sup>2–4,8</sup>, such as infrared radiation (Fig. 1b). Loubeyre *et al.* measured the optical transparency of solid hydrogen at pressures much higher than those reached previously, using the near-to-mid-infrared emission from a source of synchrotron radiation – electromagnetic radiation that is produced when charged particles are accelerated in a curved path.

The authors found that a compressed sample of hydrogen blocks all light and exhibits an abrupt increase in optical reflectivity when the pressure is raised above 425 GPa (Fig. 1c). Moreover, they discovered that this transition is reversible. The authors

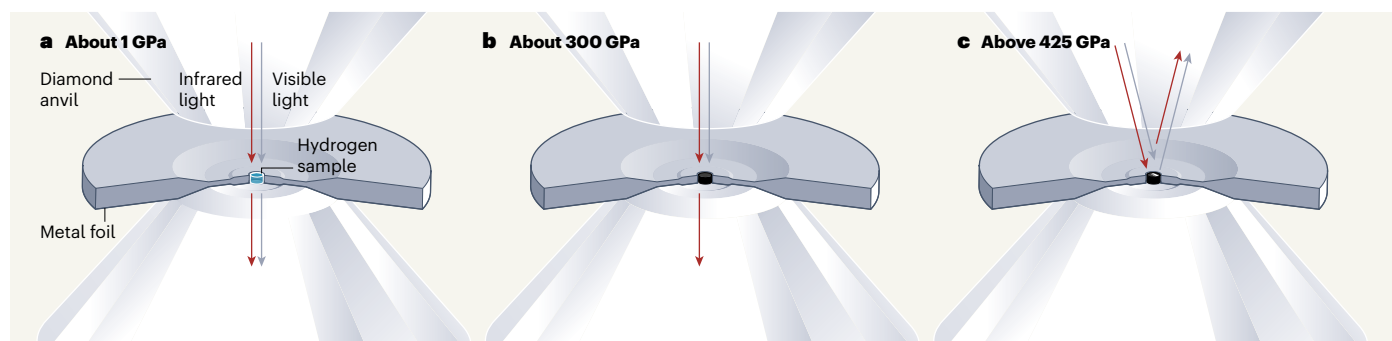


**Figure 1 | Effect of increasing pressure on cold solid hydrogen.** **a**, Loubeyre *et al.*<sup>5</sup> have studied solid hydrogen at extreme pressure and low temperature using a device known as a diamond anvil cell. This device compresses a sample of the material, which is confined to a microscopic chamber in a thin metal foil, between two diamond anvils. At first when the pressure is applied, the sample

is transparent to both infrared and visible light (GPa, gigapascals). **b**, When the pressure is raised to roughly 300 GPa, the dense hydrogen loses its transparency to visible light. **c**, Finally, when the pressure is above 425 GPa, the sample becomes reflective to both infrared and visible light, indicating a shift into the long-sought metallic state of hydrogen.

attribute the change in optical reflectivity to a pressure-induced phase transition in which electrons in the sample become free to move like those in a metal. Hydrogen remains as a molecular solid up to the transition pressure; it possibly stays in this state above 425 GPa, but it is difficult to confirm this by spectroscopy because there is a reduced coupling between light and matter in these extreme conditions.

It can certainly be argued that a definite proof for metallic hydrogen would come only from a measurement of the sample's electrical conductivity at high pressure as a function of temperature. Solid hydrogen should exhibit a high level of electrical conduction that should then decrease as the sample temperature is raised. However, even with experimental techniques developed in the past few decades to study condensed matter in extreme conditions, electrical-transport measurements of hydrogen remain a huge challenge<sup>9,10</sup>.

Nevertheless, Loubeyre and co-workers' findings should be considered as a close-to-definite proof of dense hydrogen reaching a metallic state in extreme-pressure conditions. Computational predictions of the pressure at which molecular hydrogen enters a metallic state still lack accuracy, because they require many different quantum-mechanical corrections that are difficult to address. However, the experimental value of 425 GPa agrees with calculations<sup>11</sup> that predict a transition in hydrogen to a different solid phase at a similar pressure.

Loubeyre and colleagues' study has combined innovative techniques for ultra-high-pressure generation with advanced experimental methods using synchrotron radiation. In doing so, it has raised expectations for the discovery of other remarkable properties of solid hydrogen at extreme density. For the time being, many questions remain. For instance, could electrical resistivity be measured across the metallic transition? Could superconductivity at a record-high temperature be achieved in hydrogen? And could the molecular order be disrupted under ultrahigh pressure and lead to an atomic phase in the solid state?

Competition is still strong between different research groups seeking to answer these questions, and to further unveil and understand the characteristics of hydrogen at extreme density. More exciting findings are sure to come at every stage of the race.

**Serge Desgreniers** is in the Department of Physics, University of Ottawa, Ottawa, Ontario K1N 6N5, Canada.  
e-mail: serge.desgreniers@uottawa.ca

3. Eremets, M. I., Troyan, I. A. & Drozdov, P. Preprint at <https://arxiv.org/abs/1601.04479> (2016).
4. Dias, R. P. & Silvera, I. F. *Science* **355**, 715–718 (2017).
5. Loubeyre, P., Occelli, F. & Dumas, P. *Nature* **577**, 631–635 (2020).
6. Dewaele, A., Loubeyre, P., Occelli, F., Marie, O. & Mezouar, M. *Nature Commun.* **9**, 2913–2922 (2018).
7. Jenei, Zs. et al. *Nature Commun.* **9**, 3563 (2018).

8. Loubeyre, P., Occelli, F. & LeToullec, R. *Nature* **416**, 613–617 (2002).
9. McMinis, J., Clay, R. C. III, Lee, D. & Morales, M. A. *Phys. Rev. Lett.* **114**, 105305 (2015).
10. Azadi, S., Drummond, N. D. & Foulkes, W. M. C. *Phys. Rev. B* **95**, 035142 (2017).
11. Eremets, M. I. & Troyan, I. A. *Nature Mater.* **10**, 927–931 (2011).

## Computational biology

# Protein-structure prediction gets real

Mohammed AlQuraishi

Two threads of research in the quest for methods that predict the 3D structures of proteins from their amino-acid sequences have become fully intertwined. The result is a leap forward in the accuracy of predictions. **See p.706**

Proteins perform or catalyse nearly all chemical and mechanical processes in cells. Synthesized as linear chains of amino-acid residues, most proteins spontaneously fold into one or a small number of favoured three-dimensional structures. The sequence of amino acids specifies a protein's structure and range of motion, which in turn determine its function. Over decades, structural biologists have experimentally determined thousands of protein structures, but the difficulty of these studies has made the promise of a computational approach for predicting protein structure from sequence alluring. On page 706, Senior *et al.*<sup>1</sup> describe an algorithm, AlphaFold, that takes a leap forward in solving this classic problem by bringing to bear modern machine-learning techniques.

The diversity of protein structures precludes the possibility of obtaining simple folding rules, making structure prediction difficult. Protein folding is ultimately driven by quantum mechanics. Were it possible to compute the exact energy of protein molecules from quantum theory, and to do so for every possible conformation, then predicting a protein's most energetically favoured structure would be easy. Unfortunately, a quantum treatment of proteins is computationally intractable (quantum computers might change this), and the total set of possible conformations that any protein can take is astronomical, prohibiting such a brute-force approach.

This has not stopped scientists from attempting a direct attack on the problem. Physical chemists have devised tractable, but approximate, energy models for proteins<sup>2</sup>, and computer scientists have developed ways to explore protein conformations<sup>3</sup>. Much progress has been made on the first problem but

the second has proved more recalcitrant.

The set of shapes that a protein might take can be likened to a landscape: different locations in the landscape correspond to different shapes, with nearby locations having similar shapes. The height of a location corresponds to how energetically favourable the associated shape is, with the lowest point being the most favoured. Natural proteins evolved to have funnel-shaped landscapes that enable newly synthesized proteins, jostled by the thermal fluctuations of the cell, to cross the landscape and find their way to a favoured conformation in physiologically relevant timescales (milli-

**“The algorithm outperformed all entrants at the most recent blind assessment of methods used to predict protein structures.”**

seconds to minutes)<sup>4</sup>. Algorithms can search the landscape to find favoured conformations by following the landscape's inclination, but the ruggedness of the terrain causes them to get stuck in troughs and valleys far from the lowest basin.

The course of the structure-prediction field changed nearly a decade ago with the publication of a series of seminal papers<sup>5–7</sup> exploring the idea that the evolutionary record contains clues about how proteins fold. The idea is predicated on the following premise: if two amino-acid residues in a protein are close together in 3D space, then a mutation that replaces one of them with a different residue (for example, large for small) will probably induce, at a later time, a mutation that alters

1. Wigner, E. & Huntington, H. B. *J. Chem. Phys.* **3**, 764–770 (1935).  
2. Mao, H. K. & Hemley, R. J. *Science* **244**, 1462–1465 (1989).



the other residue in a compensatory direction (in our example, swapping small for large). The set of co-evolving residues therefore encodes valuable spatial information, and can be found by analysing the sequences of evolutionarily related proteins.

By transforming this co-evolutionary information into a matrix known as a binary contact map, which encodes which residues are proximal, the set of conformations that merit consideration by algorithmic searches can be restricted. This in turn makes it possible to accurately predict the most favourable protein conformation, especially for proteins for which many evolutionarily related sequences are known. The idea was not new<sup>8</sup>, but the rapid growth in available sequence data in the early 2010s, coupled with crucial algorithmic breakthroughs, meant that its time had finally come.

Co-evolutionary analysis has been responsible for most progress in protein-structure prediction in the past few years, but it has not obviated the need for algorithms to search the energy landscapes of proteins: binary contact maps constrain the search space, but do not pin down a single 3D structure. Furthermore, the mathematics underpinning the conversion of co-evolutionary data into contact maps is restricted by the types of input used and the output generated. The initial injection of deep learning (a type of machine learning) into co-evolutionary analyses improved matters by incorporating richer inputs<sup>9</sup>. AlphaFold takes things a step further by changing the outputs.

In lieu of binary contact data, AlphaFold predicts the probabilities of residues being separated by different distances. Because probabilities and energies are interconvertible, AlphaFold predicts an energy landscape – one that overlaps in its lowest basin with the true landscape, but is much smoother. In fact, AlphaFold's landscape is so smooth that it nearly eliminates the need for searching. This makes it possible to use a simple procedure to find the most favourable conformation, rather than the complex search algorithms employed by other methods.

The idea that a complex search could be unnecessary for structure prediction is, in hindsight, unsurprising. Mathematically, the distances between points determine their relative locations. Predictions of distances can therefore predict structure. Moreover, relatively simple models of protein energy landscapes known as *Gō* potentials, in which experimentally determined distances between residues are favoured, can lead to protein-folding pathways that resemble ones experienced by real proteins<sup>10</sup>. This suggests that proteins fold more like simple origami than like an intricate knot – all parts can come together at once. My own work has shown that folding can be predicted implicitly using a deep-learning model without searching<sup>11</sup>,

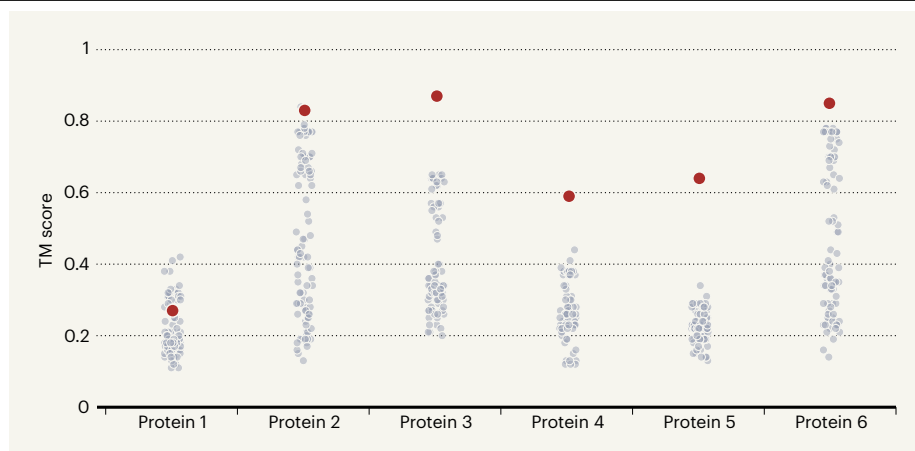


**Figure 1 | Predictions of protein structures.** Senior *et al.*<sup>1</sup> report a machine-learning system called AlphaFold, which predicts the 3D structures of proteins from their amino-acid sequences. Template modelling (TM) scores measure how well a predicted structure matches the overall shape of the actual structure, on a scale from 0 to 1. TM scores for AlphaFold were better than those of other prediction systems for 25 out of 43 proteins in a blind test. Here, the TM scores for AlphaFold (red) are compared with those of other prediction systems (grey) in the blind test for six proteins whose 3D structures could be modelled only on the basis of their amino-acid sequences – no 3D structures of proteins that have similar amino-acid sequences were available to use as a starting point for modelling. AlphaFold made the most accurate predictions for five of these six proteins. (Adapted from Fig. 1b of ref. 1.)

and minimal search procedures have also been embedded within another deep-learning model to predict protein structures<sup>12</sup>.

What is notable about AlphaFold is that it predicts distances with sufficient accuracy to outperform state-of-the-art search methods (Fig. 1). Senior *et al.* used advances in deep learning to extract as much structural information as possible from protein sequences. The resulting algorithm outperformed all entrants at the most recent blind assessment of methods used to predict protein structures (the CASP13 event), generating the best structure for 25 out of 43 proteins, compared with 3 out of 43 for the next-best method. AlphaFold's predictions had a median accuracy of 6.6 ångströms on this set of proteins – that is, for the middle-ranked protein in this set, the atoms in the proposed structures were on average 6.6 Å away from their actual positions.

Challenges remain. AlphaFold is not yet accurate enough for most applications, such as working out the catalytic mechanisms of enzymes or how drugs bind to proteins (which both typically require 2–3 Å resolution). And although AlphaFold's search procedure is much simpler than most modern methods, it can still be slow, taking tens to hundreds of hours to make a single prediction. For applications such as protein design, which require the structures of many different protein sequences to be modelled, the lack of speed is an impediment.

Nevertheless, this is a watershed moment for the field. Given continued growth in the number of available protein sequences, it is possible that the coarse structures (about 4 Å resolution) of most proteins that consist of a single folded domain will become available in

the next five years from structure predictions. Such broad availability of structural information might transform the life sciences, just as sequence information did in the preceding decades. This could mean that, combined with the rapid advances in protein-structure determination enabled by cryo-electron microscopy, we are entering a golden age of structural biology – one that makes possible a quantitative and mechanistic basis for the life sciences, broadly grounded in firm structural hypotheses.

**Mohammed AlQuraishi** is in the Laboratory of Systems Pharmacology, Department of Systems Biology, Harvard Medical School, Boston, Massachusetts 02115, USA.  
e-mail: alquraishi@hms.harvard.edu

1. Senior, A. W. *et al.* *Nature* **577**, 706–710 (2020).
2. Guvench, O. & MacKerell, A. D. Jr *Methods Mol. Biol.* **443**, 63–88 (2008).
3. Maximova, T., Moffatt, R., Ma, B., Nussinov, R. & Shehu, A. *PLoS Comput. Biol.* **12**, e1004619 (2016).
4. Bryngelson, J. D., Onuchic, J. N., Socci, N. D. & Wolynes, P. G. *Proteins* **21**, 167–195 (1995).
5. Marks, D. S. *et al.* *PLoS ONE* **6**, e28766 (2011).
6. Jones, D. T., Buchan, D. W. A., Cozzetto, D. & Pontil, M. *Bioinformatics* **28**, 184–190 (2012).
7. Kamisetty, H., Ovchinnikov, S. & Baker, D. *Proc. Natl Acad. Sci. USA* **110**, 15674–15679 (2013).
8. Lapedes, A. S., Giraud, B. G., Liu, L. & Stormo, G. D. *IMS Lecture Notes Monogr. Ser.* **33**, 236–256 (1999).
9. Wang, S., Sun, S., Li, Z., Zhang, R. & Xu, J. *PLoS Comput. Biol.* **13**, e1005324 (2017).
10. Hills, R. D. & Brooks, C. L. *Int. J. Mol. Sci.* **10**, 889–905 (2009).
11. AlQuraishi, M. *Cell Syst.* **8**, 292–301 (2019).
12. Ingraham, J., Riesselman, A., Sander, C. & Marks, D. in *7th Int. Conf. Learn. Represent.* <https://openreview.net/forum?id=Byg3y3C9Km> (2019).

This article was published online on 15 January 2020.

# Single-cell maps of the human heart

Ragini Phansalkar & Kristy Red-Horse

Three methods for gene-expression profiling have now been combined to produce spatially defined single-cell maps of developing human organs from limited sample material, overcoming a major hurdle in studying human development.

People are often curious about how their bodies work. So, it is no surprise that single-cell RNA sequencing (scRNA-seq) – which has the power to map all the cell types in the human body<sup>1–3</sup> – has drawn great interest from scientists and funding agencies alike. But a major limitation of scRNA-seq is that it cannot provide information about where in the original tissue each cell was located. Writing in *Cell*, Asp *et al.*<sup>4</sup> demonstrate a way of overcoming this hurdle by combining scRNA-seq with other sequencing methods that retain location information. They use this approach to create a spatially defined cell atlas of the developing human heart.

scRNA-seq involves dissociation of a tissue into hundreds or thousands of individual cells, each of which is analysed to determine its gene-expression profile. This profile indicates the proteins and pathways that are active in that cell – information that computational methods can then use to sort thousands of cells into different types or states at once. However, the tissue-dissociation protocol breaks the link between single cells and their original positions in the tissue. Without this information, interpretation of the data is incomplete. Asp *et al.* set out to bridge this gap by combining scRNA-seq with two approaches that produce spatially defined gene-expression maps, although at a lower resolution than scRNA-seq.

The first is a technique called spatial transcriptomics<sup>5</sup>. Thin slices of tissue are placed on a specially prepared microscope slide that has been dotted with circular ‘patches’. Each patch contains many copies of a nucleic-acid probe that binds to messenger RNA in the tissue sample and carries a sequence called a barcode. Each patch has a different barcode, so that a specific label is attached to the mRNA in the area of tissue sitting on top of that patch. When the mRNA from each region is sequenced, the barcode acts as a record of the cells’ original locations in the tissue. A limitation of this method is that single-cell analysis is compromised, because gene sequences are pooled from approximately

30 cells in each patch. Nonetheless, a non-biased description of gene-expression profiles at discrete locations is obtained.

The second method is *in situ* sequencing (ISS), in which the expression of preselected genes is probed directly on a tissue slice on a microscope slide<sup>6,7</sup>. DNA probes are designed to bind to mRNA transcribed from genes of interest, with each probe carrying a unique barcode. When these probes are introduced into a tissue, they bind to their target mRNAs in the tissue’s cells and – after further processing steps – a fluorescent-imaging-based

sequencing method is used to detect the barcodes while they remain in place in the tissue. This technique can provide information about the expression of 50–100 genes in individual cells at high spatial resolution. But the genes must be preselected, which requires some knowledge about which genes will be informative.

Asp and colleagues ultimately used ISS to achieve cell-level mapping of heart development. But to determine which genes they should select for ISS, they needed to perform scRNA-seq and spatial transcriptomics (Fig. 1). The authors’ scRNA-seq analysis revealed genes correlating with cell type – genes expressed only in smooth-muscle cells, for instance. And their spatial transcriptomics analysis revealed groups of genes that broadly correlated with certain locations in the heart – genes specifically expressed in cells in a region called the outflow tract, for example.

The researchers then created a panel of 69 ISS probes – some corresponding to the location markers identified by spatial transcriptomics, some to the cell-type markers identified by scRNA-seq, and some to genes previously reported to be important for heart development. They combined the data produced by this ISS screen with their scRNA-seq data using a recently developed algorithm<sup>8</sup> that assigns each RNA molecule detected by

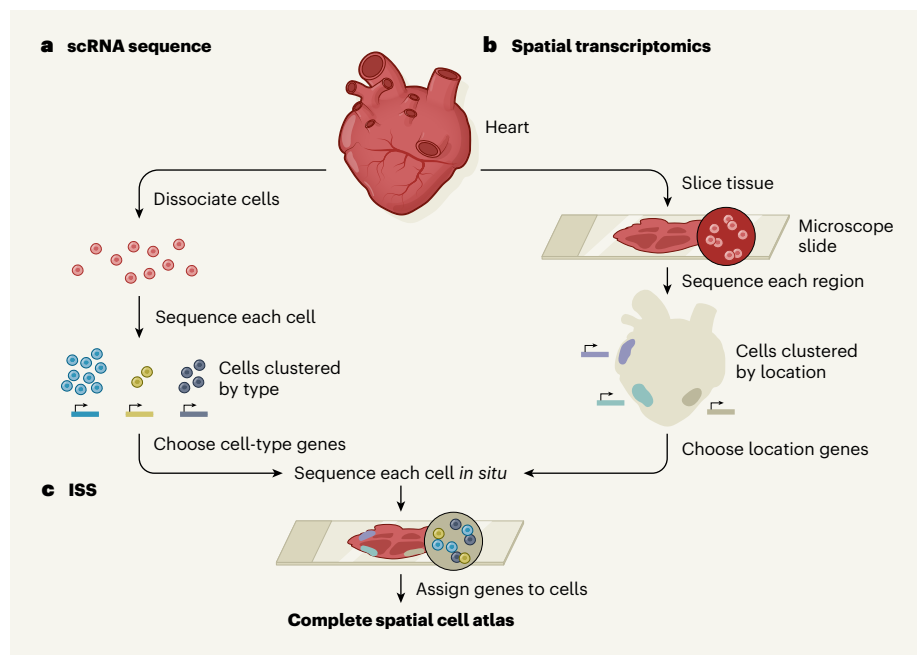


**Figure 1 | A framework to map human development.** Asp *et al.*<sup>4</sup> combine three methods to produce single-cell maps of the developing human heart that retain spatial information. **a**, In single-cell RNA sequencing (scRNA-seq), a heart is dissociated into single cells and the RNA of each cell is sequenced to generate a gene-expression profile. A computer algorithm assigns a type to each cell, clustering together those that have similar gene-expression profiles. However, no information is retained about the original position of each cell in the tissue. **b**, In spatial transcriptomics, slices of heart tissue are placed on microscope slides and many small regions of about 30 cells are sequenced. This provides information about gene expression in specific locations, but not at the single-cell level. **c**, The authors used the results of these screens to choose a panel of 69 genes that mark specific cell types or locations in the heart. They used a third sequencing approach, *in situ* sequencing (ISS), to analyse expression of these genes at the single-cell level across slices of human heart tissue. An algorithm assigns each RNA molecule to a cell within the tissue slice, generating spatially resolved maps of cell type.



## News & views

ISS to a specific cell nucleus, and each nucleus to a specific cell type. The final result was the first spatiotemporal cell atlas of the embryonic human heart between 6.5 and 7 weeks of development. Anybody can explore the atlas using a searchable online tool (see [go.nature.com/3rj6dtf](https://go.nature.com/3rj6dtf)).

Beyond a technical proof-of-principle, the authors also gained insights into heart development. For example, a previous study<sup>9</sup> described several distinct, but transcriptionally similar, clusters of fibroblast-like cells – a structural cell type that is not fully understood, but which is known to participate in a pathological tissue-scarring process called fibrosis. Asp *et al.* demonstrated that these fibroblast subgroups are located in distinct parts of the heart, providing a clue as to how they might function differently.

As another example, Asp and colleagues described a previously unknown human equivalent of a subpopulation of cardiac muscle cells found in mice that expresses high levels of the gene *Myoz2* (ref. 10). Finally, the researchers performed a cellular analysis of a tissue called the atrioventricular mesenchyme, and identified the time point at which Schwann cells (neuron-associating cells that ensure proper electrical transmission) arise in this tissue. Such knowledge of human heart cells can be used to inform follow-up experiments

aimed at defining those cells' functions.

However, limitations in Asp and colleagues' study highlight that pre-existing knowledge is still required to fully appreciate single-cell data. For instance, some of their cell populations seem to be misidentified. One population is deemed by the authors to be cells that line capillary blood vessels (coronary endothelium). But on the basis of the cells' marker-gene expression and location, we would suggest that they

**“The techniques have the crucial advantage of providing a wealth of information from limited tissue.”**

are instead endocardial cells that line the heart chamber. Furthermore, the authors' approach could not be used to distinguish between all of the subtypes or substates in particular populations, such as the coronary endothelium, which is a mixed population that lines the arterial, venous and capillary blood vessels leading to and from the heart. However, the authors' workflow is certain to be refined as advanced techniques are developed for directly profiling the spatial gene expression of tissues<sup>11,12</sup>.

A major strength of Asp and colleagues'

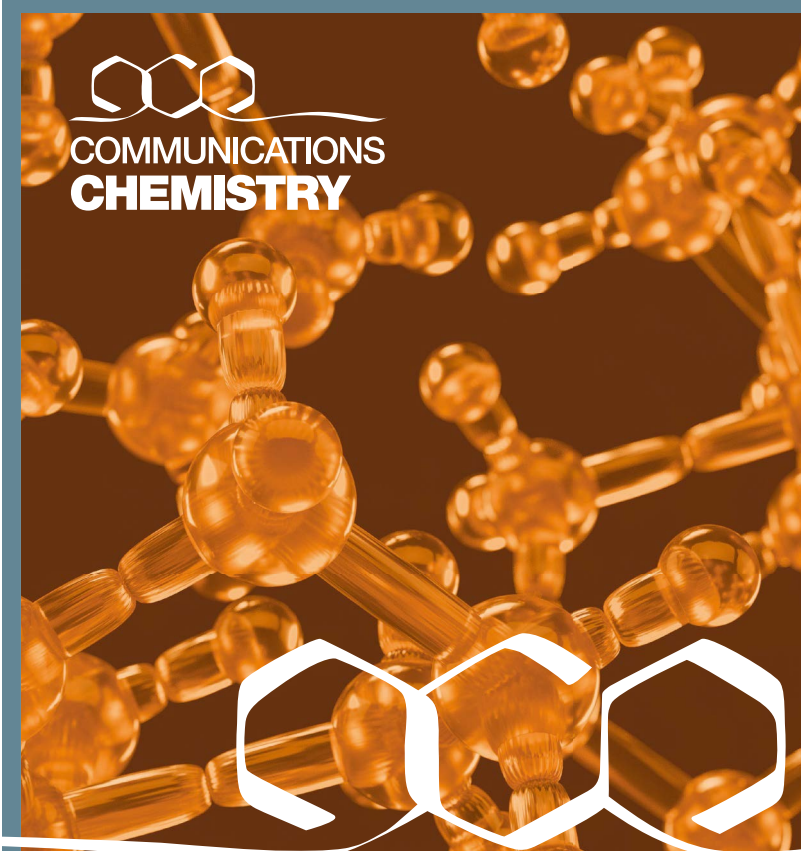
study is that it provides a framework for maximizing the power of scRNA-seq. Anyone who begins experiments to understand human biology faces the challenge of limited sample availability, particularly when assessing embryonic development. The techniques presented here have the crucial advantage of providing a wealth of information from limited tissue. Asp and co-workers' strategy is likely to benefit efforts such as the Human Cell Atlas ([www.humancellatlas.org](http://www.humancellatlas.org)) and HuBMAP (<https://hubmapconsortium.org>) projects, which are both seeking to fully define the human body.

Ragini Phansalkar is in the Department of Genetics, and Kristy Red-Horse is in the Department of Biology, School of Humanities and Sciences, Stanford University, Stanford, California 94305, USA.

e-mail: [kredhors@stanford.edu](mailto:kredhors@stanford.edu)

1. Camp, J. G., Platt, R. & Treutlein, B. *Science* **365**, 1401–1405 (2019).
2. HuBMAP Consortium. *Nature* **574**, 187–192 (2019).
3. Regev, A. *et al.* *eLife* **6**, e27041 (2017).
4. Asp, M. *et al.* *Cell* **179**, 1647–1660 (2019).
5. Ståhl, P. L. *et al.* *Science* **353**, 78–82 (2016).
6. Ke, R. *et al.* *Nature Methods* **10**, 857–860 (2013).
7. Lee, J. H. *et al.* *Science* **343**, 1360–1363 (2014).
8. Qian, X. *et al.* *Nature Methods* **17**, 101–106 (2019).
9. Cui, Y. *et al.* *Cell Rep.* **26**, 1934–1950 (2019).
10. Gladka, M. M. *et al.* *Circulation* **138**, 166–180 (2018).
11. Rodrigues, S. G. *et al.* *Science* **363**, 1463–1467 (2019).
12. Eng, C. L. *et al.* *Nature* **568**, 235–239 (2019).

This article was published online on 27 January 2020.



COMMUNICATIONS  
CHEMISTRY

## Open access chemical sciences journal from Nature Research.

*Communications Chemistry* publishes high-quality research, reviews and commentary in all areas of the chemical sciences.

Research papers published by the journal represent significant advances for a specialized area of research.

Submit your research and benefit from:

- Fast decisions, easy submission
- Rigorous, balanced peer review
- Nature Research editorial standards
- Global visibility, fully open access
- Expert in-house editors and editorial board

[nature.com/commschem](https://nature.com/commschem)

[@CommsChem](https://twitter.com/CommsChem)

nature research

# Synchrotron infrared spectroscopic evidence of the probable transition to metal hydrogen

<https://doi.org/10.1038/s41586-019-1927-3>

Received: 12 April 2019

Accepted: 26 November 2019

Published online: 29 January 2020

Paul Loubeyre<sup>1\*</sup>, Florent Occelli<sup>1</sup> & Paul Dumas<sup>1,2</sup>

Hydrogen has been an essential element in the development of atomic, molecular and condensed matter physics<sup>1</sup>. It is predicted that hydrogen should have a metal state<sup>2</sup>; however, understanding the properties of dense hydrogen has been more complex than originally thought, because under extreme conditions the electrons and protons are strongly coupled to each other and ultimately must both be treated as quantum particles<sup>3,4</sup>. Therefore, how and when molecular solid hydrogen may transform into a metal is an open question. Although the quest for metal hydrogen has pushed major developments in modern experimental high-pressure physics, the various claims of its observation remain unconfirmed<sup>5–7</sup>. Here a discontinuous change of the direct bandgap of hydrogen, from 0.6 electronvolts to below 0.1 electronvolts, is observed near 425 gigapascals. This result is most probably associated with the formation of the metallic state because the nucleus zero-point energy is larger than this lowest bandgap value. Pressures above 400 gigapascals are achieved with the recently developed toroidal diamond anvil cell<sup>8</sup>, and the structural changes and electronic properties of dense solid hydrogen at 80 kelvin are probed using synchrotron infrared absorption spectroscopy. The continuous downward shifts of the vibron wavenumber and the direct bandgap with increased pressure point to the stability of phase-III hydrogen up to 425 gigapascals. The present data suggest that metallization of hydrogen proceeds within the molecular solid, in good agreement with previous calculations that capture many-body electronic correlations<sup>9</sup>.

The search for metal hydrogen has a unique place in high-pressure physics. Indisputably, metal hydrogen should exist. Owing to increase in electron kinetic energy because of quantum confinement, pressure should turn any insulator into a metal, as observed for molecular oxygen around 100 GPa some 20 years ago<sup>10</sup>. At first, the prediction of the insulator–metal transition in dense hydrogen was intertwined with the molecular dissociation<sup>2</sup>. However, it was later suggested that metal hydrogen may exist as a proton-paired metal<sup>11</sup>. Quantitative predictions of the stability domain and of the properties of metal hydrogen remain challenging because many contributions could be in effect and should be self-consistently treated<sup>3,4</sup>; for example, many-body electronic correlations, nuclear quantum effects, nuclear spin ordering, coupling between protons and electrons (as suggested by a large Born–Oppenheimer separation parameter), or anharmonic effects. The most advanced calculations, such as diffusion Monte Carlo (DMC) simulations<sup>4,9,12</sup>, now go beyond the electronic correlation mean-field description of density functional theory and try to capture many-body electronic correlations. Importantly, metal hydrogen should exhibit notable properties, such as room-temperature superconductivity<sup>13–15</sup>, a melting transition at a very low temperature into a superconducting superfluid state<sup>16</sup> and a mobile solid state<sup>17</sup>.

The change in the direct bandgap of solid hydrogen was previously measured up to 300 GPa by visible absorption measurements<sup>18</sup>. By extrapolating to zero the linear decrease of the bandgap with density, the transition to metal hydrogen was predicted to occur around 450 GPa. In this work, we extend the investigation of the direct bandgap decrease down to the near-to-mid-infrared energy range. Infrared measurements provide a non-intrusive method both to disclose structural changes and also to characterize the electronic properties of hydrogen up to its metal transition. Our approach is based on two experimental developments. First, in order to overcome the 400 GPa limit of conventional diamond anvil cells<sup>19</sup>, we used the recently developed toroidal diamond anvil cell (T-DAC)<sup>8</sup> that can achieve pressures of up to 600 GPa. Importantly, under extreme pressures, the T-DAC preserves the advantages of the standard diamond anvil cell in terms of stress distribution, optical access and sample size. Synthetic type-IIa diamond anvils were used to provide infrared transparency down to 800 cm<sup>–1</sup>. Second, an infrared horizontal microscope was designed to be coupled to a collimated exit port of a synchrotron-feed Fourier-transform infrared spectrometer at the SMIS beamline at the SOLEIL synchrotron facility. Such a high-brightness broadband infrared source is essential for measuring, by transmission, satisfactory signal-to-noise

<sup>1</sup>CEA, DAM, DIF, Arpajon, France. <sup>2</sup>Synchrotron SOLEIL, Gif-sur-Yvette, France. \*e-mail: paul.loubeyre@cea.fr



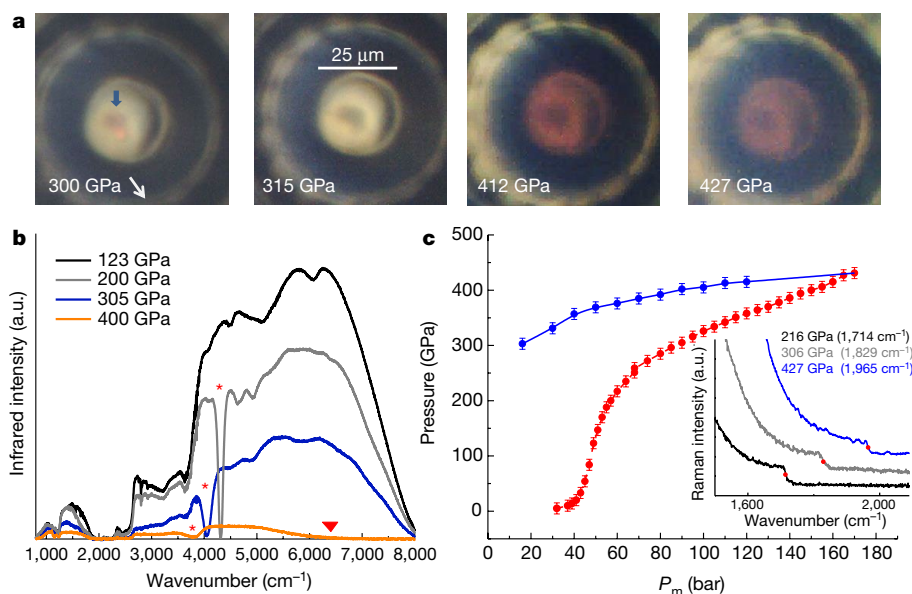


**Fig. 1 | A selection of measurements over the investigated pressure range.**

**a**, Photographs of the hydrogen sample taken at different stages of compression, under simultaneous front and back bright-light illumination. The hydrogen sample is indicated by the blue arrow. Around 310 GPa, the sample reversibly turns black, as illustrated by the photographs taken at 315 GPa for the increasing pressure path and at 300 GPa for the decreasing pressure path. At 427 GPa, the sample is in the metallic state and is still distinguishable from the rhenium gasket. The red-coloured aspect at the diamond tip centre is attributed to the decrease of the diamond bandgap<sup>8</sup>. **b**, Infrared transmission

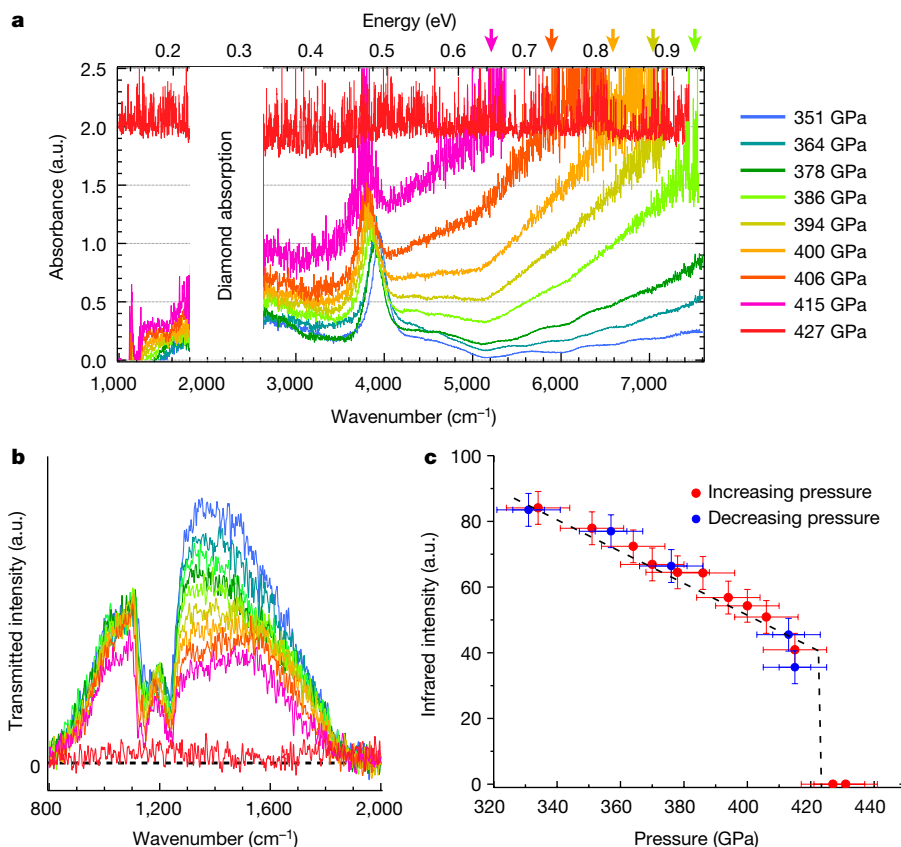
ratio spectra through a 5-μm diameter sample. Simultaneous Raman spectroscopy and visual observation could be performed.

Figure 1 illustrates selected data obtained for the hydrogen sample in the T-DAC at 80 K during different compression and decompression stages. Four photographs (Fig. 1a) show the changes in the sample appearance. The formation of black hydrogen—that is, the transformation of hydrogen from transparent to totally opaque in the visible range—is observed around 310 GPa, as previously reported<sup>18</sup>, and this was reversible upon pressure release. The visual transformation of the sample at the probable insulator–metal transition is less contrasted. The observed metal–hydrogen sample is not highly reflective, as it appears darker than the surrounding rhenium gasket. As discussed below, this is consistent with the formation of a molecular metal instead of an atomic metal. The infrared signal was collected over the 800–8,000 cm<sup>-1</sup> wavenumber range; several raw spectra are shown in Fig. 1b. Up to 360 GPa, the signal intensity decreased owing to the shrinkage of the hydrogen sample size and the deformation of the toroidal anvil tip<sup>8</sup>. However, after intensity normalization, from 123 GPa to 360 GPa all spectra display the same shape when the hydrogen vibron peak is discarded (see Extended Data Fig. 1). Consequently, the variation of the infrared transmittance of the diamond anvil itself should remain negligible up to the 400 GPa range. Therefore changes in the infrared spectra can only be due to intrinsic properties of hydrogen. In Fig. 1a, two interesting features are clearly seen: (1) the strong absorption peak around 4,000 cm<sup>-1</sup> is associated with the H<sub>2</sub> vibron that appears above 160 GPa upon the solid entering phase III, as reported previously<sup>20</sup>. This vibron mode broadens and shifts to lower wavenumbers with increasing pressure; (2) above 360 GPa, the shape of the infrared spectra display zeroing at high wavenumbers, evolving towards low values with pressure (see Extended Data Fig. 2), which indicates the decrease of the hydrogen direct bandgap in the infrared range. Importantly, a very discernible Raman diamond edge (see inset Fig. 1c), used as the pressure gauge, could be measured up to the maximum pressure and upon release, as a result of an elastic deformation at the diamond anvil tip

spectra at various pressures. Intrinsic absorption features associated with the vibron and with the closing of the bandgap are indicated by the red stars and the triangle, respectively. **c**, Pressure evolution in hydrogen versus the helium membrane pressure acting on the piston of the T-DAC, during pressure increase (red) and decrease (blue). Inset, the high-wavenumber part of the Raman diamond spectra collected at three pressures. The wavenumber at the step used to calculate pressure is indicated as a red dot, and noted in the key. Solid lines are guides to the eye. a.u., arbitrary units.

facilitated by the toroidal shape. In Fig. 1c, the evolution of the sample pressure versus the force on the piston features the expected trend<sup>8,19</sup>.

In Fig. 2a, absorbance spectra have been obtained by taking a direct ratio of the spectrum at a given pressure to that taken at 123 GPa (after intensity normalization). For infrared measurements of semiconductors under pressure, the direct excitonic level (in the case of hydrogen, the values of the excitonic and of the direct bandgap should be almost identical)<sup>21</sup> is positioned at the junction between the absorbance plateau and the lower energy tail, as done previously to position the hydrogen bandgap in the visible range<sup>18</sup>. In the present experimental configuration, a maximum absorbance value of just 2 could be measured. Hence, a lower bound for the bandgap should probably be inferred because the absorbance plateau might be at a higher value. However, because the hydrogen sample was about 1.6 (± 0.1) μm thick, the absorption coefficient associated with an absorbance of 2 is estimated to be about 28,000 cm<sup>-1</sup>, which is similar to the value obtained from the direct bandgap measurements in the visible range<sup>18</sup>. The bandgap underestimation should be smaller than 0.14 eV. Around 425 GPa, a transition to a total infrared absorption is observed, corresponding to an absorption coefficient greater than 25,000 cm<sup>-1</sup> over the whole infrared spectral range investigated. This is a necessary condition for the infrared observation of metal hydrogen but not definitive evidence, because the existence of a direct bandgap less than 0.1 eV—that is, below the 800 cm<sup>-1</sup> lower limit of the covered infrared spectral range—cannot be ruled out, although that seems unlikely because the nucleus zero-point energy is greater than this value. In Fig. 2c, the discontinuity of the transition is evidenced by the pressure evolution of the integrated infrared intensity over the 800–2,000 cm<sup>-1</sup> wavenumber range. Upon pressure release, the infrared spectral intensity and shape are reversibly recovered (see Extended Data Fig. 2). The C2/c structure with 24 atoms per unit cell, henceforth C2/c-24, has been calculated to be the most probable candidate in the pressure range of the present measurements<sup>22</sup>. If so, from electronic band structure calculations<sup>21</sup>, an indirect bandgap should close under pressure before the direct bandgap does. Consistent with



**Fig. 2 | Discontinuous pressure evolution in the infrared absorption and probable signature of metal hydrogen.** **a**, Absorption spectra of hydrogen at different pressures. Above 386 GPa, the direct electronic bandgap is indicated by arrows. For clarity, different colours are associated with different pressures. **b**, Transmission spectra over the infrared range 800–2,000  $\text{cm}^{-1}$ . The pressure

colourscale is as in **a**. **c**, Integrated transmitted intensity over the 800–2,000  $\text{cm}^{-1}$  infrared range for increasing (red) and decreasing (blue) pressure. Pressure uncertainty is  $\pm 10$  GPa. Errors are the random uncertainty estimated from different measurements at the same pressure, for typically three measurements. The dashed lines in **b**, **c** are guides to the eye.

this picture, hydrogen was recently reported<sup>23</sup> to start conducting above 350 GPa (or 330 GPa, if the diamond pressure scale used here is applied). Then up to 440 GPa (or 395 GPa in our case), the value of the resistivity (about  $5 \times 10^{-4} \Omega \text{ m}$ ), and its temperature dependence suggest a semimetal state with a low concentration of charge carriers. The associated plasma edge should be below 0.1 eV, which is why it could not be detected here. For comparison, the plasma edge of the low-density charge carriers conducting xenon could only be measured using the present synchrotron infrared setup<sup>24</sup> just above the xenon metallization pressure when the resistivity falls below  $1 \times 10^{-4} \Omega \text{ m}$  (ref. <sup>23</sup>).

Properties of solid hydrogen up to the metal transition are shown in Fig. 3. In Fig. 3a, the linear pressure shift of the vibron wavenumber from 160 GPa to 425 GPa indicates that no structural change occurs up to 425 GPa and that the solid hydrogen remains in phase III. The  $C2/c-24$  candidate structure for phase III was first proposed using an ab initio random structure searching method<sup>22</sup>. It consists of layers of molecules forming a slight monoclinic distortion of the hexagonal lattice. The  $C2/c-24$  structure has a specific infrared fingerprint<sup>22</sup>, exhibiting one intense vibron infrared mode as well as one intense phonon infrared mode, in good agreement with the present observation. The phonon mode is, to our knowledge, reported here for the first time but could be observed only up to 225 GPa, above which it becomes hidden by the strong absorption of the diamond anvils. The vibron wavenumber shift was reversibly observed upon pressure decrease (see Extended Data Fig. 3). Finally, the calculated<sup>22,25</sup> pressure evolutions of the vibron and of the phonon infrared wavenumbers for the  $C2/c-24$  structure are in very good agreement with the present experimental data. In Fig. 3b, the direct bandgap is seen to decrease linearly with pressure, and is well matched with the previous measurements in the visible range<sup>18</sup>.

In calculations, the bandgap is profoundly affected by the level of the description of electronic exchange–correlation and also by nuclear quantum effects. Previous work that has used local exchange–correlation density functional theory, for example using the Perdew–Burke–Ernzerhof (PBE) calculation<sup>21</sup> or implementing vdW-DF<sup>26</sup>, has obtained unreliable bandgaps, and has usually underestimated its value. The more advanced methods of quasi-particle computational approaches, GW<sup>22</sup> and DMC<sup>9</sup>, should be more reliable. In Fig. 3b, they are seen to give higher bandgap values than obtained by experiment. Accounting for nuclear quantum effects should lower the bandgap energy<sup>26</sup> by at least 1 eV and therefore a better agreement with the present data should be obtained. It is interesting to note that there is a confluence of the bandgap and of the vibron energy values, both about 0.5 eV, when the transition to the probable metal state occurs.

Currently, there are five experimentally described phases of hydrogen<sup>4,27</sup>. Recently, a single crystal X-ray diffraction study<sup>28</sup> at 300 K up to 254 GPa showed that the I, III and IV phases are isostructural, and the hydrogen molecules remain in the hexagonal close-packed crystal lattice structure. Phases IV and V exist only above 200 K (refs. <sup>23,27</sup>). An updated low-temperature phase diagram of solid hydrogen is shown in Fig. 4. In phase I, the molecules are in a quantum free-rotational state and arranged on a hexagonal close-packed lattice. Upon transitioning to phase II, very small discontinuities in the lattice parameters have been measured<sup>29</sup>. Quantum molecular rotations become restricted and phase II can be described as a quantum fluxional solid<sup>30</sup>. At 160 GPa, phase II transforms into an ordered molecular phase III. We suggest here that phase III has the  $C2/c-24$  structure up to 425 GPa, above which a discontinuous transition to metal hydrogen occurs. It should be noted that the infrared spectra in phase III at 300 K and at 100 K are reasonably



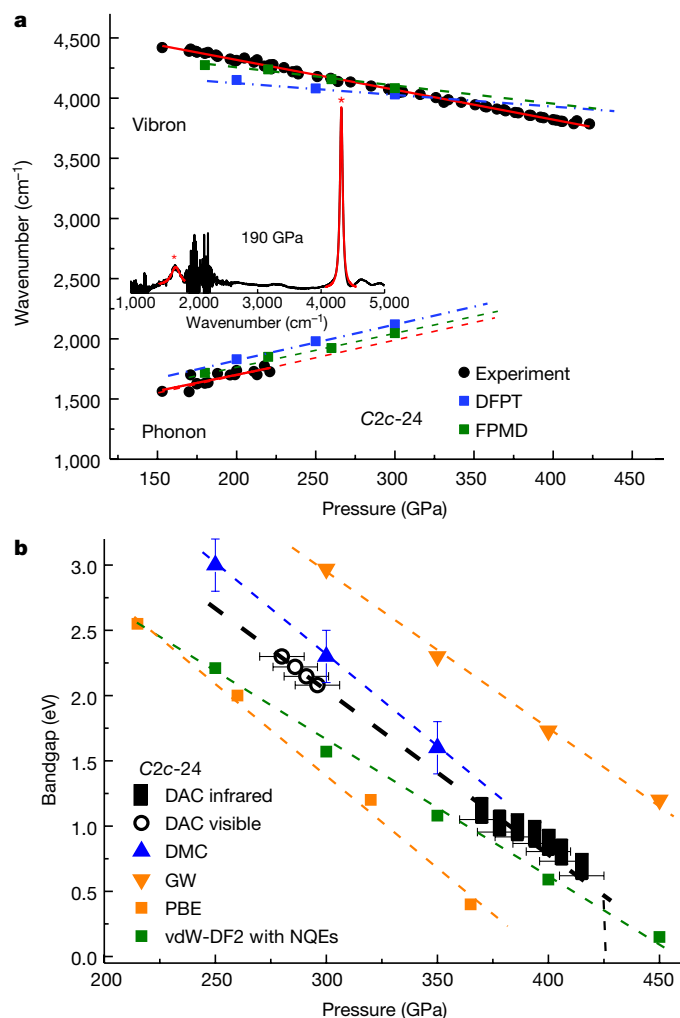


**Fig. 3 | Evolution of the molecular solid hydrogen properties up to the insulator–metal transition: comparison between experiment and calculations.** **a**, Wavenumbers of the vibron and of the phonon infrared active modes in phase III versus pressure. The black dots and the red lines represent experimental data and linear fits. The blue squares and the green triangles are the density functional perturbation theory<sup>21</sup> and first-principles molecular dynamics<sup>25</sup> calculations for the C2/c-24 structure, respectively. Inset, the infrared absorption spectrum at 190 GPa, showing the vibron and the phonon peaks. Comparison of the present data with previous experimental determinations of the infrared H<sub>2</sub> vibron wavenumber versus pressure is shown in Extended Data Fig. 4. **b**, The pressure evolution of the experimental bandgap (combining data in the visible range<sup>18</sup> and the present infrared data; black symbols), is compared to calculations for the C2/c-24 structure performed under a variety of approximations: within the DFT framework with local PBE (orange squares) and nonlocal vdW-DF2 (green squares) exchange–correlation functionals<sup>26</sup>; with the quasiparticle approach within the GW approximation<sup>9</sup> (orange triangles); and with the DMC method<sup>22</sup> (blue triangles). The vertical dashed line indicates the transition to metal hydrogen. The uncertainty on the bandgap is 0.14 eV, estimated from Fig. 2a by linearly extending the rising absorbance before the plateau of 2 to an absorbance value of 3. The dashed lines that follow the data are guides to the eye. Evolution of the direct bandgap versus density, using a revisited hydrogen compression curve to convert pressure into density, is shown in Extended Data Fig. 5. Vibron and bandgap data are presented in Extended Data Table 1.

different and are associated with a substantial temperature shift of the vibron wavenumber<sup>31</sup>. The orientational ordering of the molecules could be increased by lowering the temperature, hence inducing the monoclinic distortion from the hexagonal close-packed lattice at 300 K to form the C2/c-24 structure at 80 K. In the framework of PBE density functional theory, the C2/c-24 structure should be stable only up to

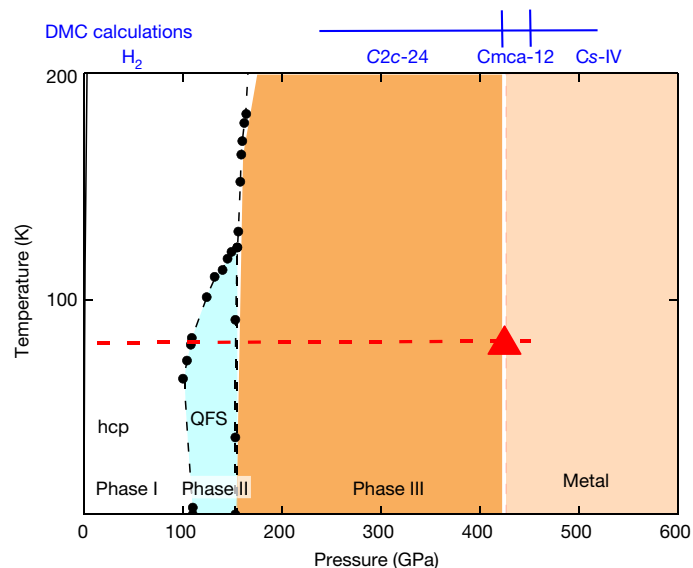


**Fig. 4 | Low-temperature phase diagram of solid hydrogen.** The red dashed line is the pathway of the infrared data collection and the red triangle indicates the transition to metal hydrogen. Boundary lines between phases I, II and III are from previous studies (as reviewed in ref. <sup>4</sup>). The sequence of phase transitions, determined by DMC calculations including nuclear quantum effects<sup>9</sup>, is displayed at the top of the graph.

270 GPa<sup>21</sup>. Using DMC calculations and including nuclear quantum effects, a transition from an insulating C2/c-24 structure to a metallic Cmca-12 structure is obtained at 424 GPa<sup>9</sup>, in good agreement with the pressure at which we observe total infrared absorption above 800 cm<sup>-1</sup>. That structural transition should be displacive, implying an orientation ordering in the layers of the H<sub>2</sub> molecules from nearly parallel to flat, which should induce a larger distortion from hexagonal packing. That could take place with almost no pressure hysteresis. Furthermore, the reflectivity in the visible range for the Cmca-12 molecular metal has been calculated<sup>32</sup> to be about 0.5, and so this molecular metal should appear darker than the rhenium gasket. Consequently, the full infrared absorption, the small hysteresis of the transition and the photograph of the sample above 425 GPa all suggest that we have observed the hydrogen insulator-to-metal transition in the molecular crystal, associated with a structural transition from C2/c-24 to Cmca-12. Following DMC calculations<sup>9</sup>, atomic metal hydrogen should be observed above 447 GPa.

More measurements are now needed to definitively prove the hydrogen transition to a metallic state. It seems particularly appropriate to try to observe the predicted high-temperature superconductivity of metal hydrogen in both the molecular and atomic hydrogen-metal phases, at 250 K (ref. <sup>14</sup>) and 350 K (ref. <sup>15</sup>), respectively. For doing so, a non-invasive infrared reflectivity measurement has recently been proposed<sup>33</sup>, and the sample size reachable using the T-DAC will improve our ability to make such a measurement.

## Online content

Any methods, additional references, Nature Research reporting summaries, source data, extended data, supplementary information, acknowledgements, peer review information; details of author contributions and competing interests; and statements of data and code availability are available at <https://doi.org/10.1038/s41586-019-1927-3>.

1. Rigden, J. S. *Hydrogen, the Essential Element* (Harvard Univ. Press, 2002).
2. Wigner, E. & Huntington, H. B. On the possibility of a metallic modification of hydrogen. *J. Chem. Phys.* **3**, 764–770 (1935).
3. Ashcroft, N. Dense hydrogen: the reluctant alkali. *Phys. World* **8**, 43–48 (1995).
4. McMahon, J. M., Morales, M. A., Pierleoni, C. & Ceperley, D. M. The properties of hydrogen and helium under extreme conditions. *Rev. Mod. Phys.* **84**, 1607–1653 (2012).

5. Mao, H. K. & Hemley, R. J. Optical studies of hydrogen above 200 gigapascals: evidence for metallization by band overlap. *Science* **244**, 1462–1465 (1989).
6. Eremets, M. I. & Troyan, I. A. Conductive dense hydrogen. *Nat. Mater.* **10**, 927–931 (2011).
7. Dias, R. P. & Silvera, I. F. Observation of the Wigner–Huntington transition to metallic hydrogen. *Science* **355**, 715–718 (2017).
8. Dewaele, A., Loubeyre, P., Occelli, F., Marie, O. and Mezouar, M. Toroidal diamond anvil cell for detailed measurements under extreme static pressures. *Nat. Commun.* **9**, 2913 (2018).
9. McMinis, J., Clay III, R.C., Lee, D. and Morales, M. A. Molecular to atomic phase transition in hydrogen under high pressure. *Phys. Rev. Lett.* **114**, 105305 (2015).
10. Desgreniers, S., Vohra, Y. K. & Ruoff, A. L. Optical response of very high density solid oxygen to 132 GPa. *J. Phys. Chem.* **94**, 1117–1122 (1990).
11. Johnson, K. A. & Ashcroft, N. W. Structure and bandgap closure in dense hydrogen. *Nature* **403**, 632–635 (2000).
12. Drummond, N.D. et al. Quantum Monte Carlo study of the phase diagram of solid molecular hydrogen at extreme pressures. *Nat. Commun.* **6**, 7794 (2015).
13. Ashcroft, N. W. Metallic hydrogen: a high-temperature superconductor? *Phys. Rev. Lett.* **21**, 1748–1749 (1968).
14. Cudazzo, P. et al. Ab initio description of high temperature superconductivity in dense molecular hydrogen. *Phys. Rev. Lett.* **100**, 257001 (2008).
15. Borinaga, M., Errea, I., Calandra, M., Mauri, F. & Bergara, A. Anharmonic effects in atomic hydrogen: superconductivity and lattice dynamical stability. *Phys. Rev. B* **93**, 174308 (2016).
16. Babaev, E., Sudbo, A. and Ashcroft, N.W. Observability of a new state of matter: a metallic superfluid. *Phys. Rev. Lett.* **95**, 105301 (2005).
17. Geng, H. Y., Wu, Q. & Sun, Y. Prediction of a mobile solid state in dense hydrogen under high pressures. *J. Phys. Chem. Lett.* **8**, 223–228 (2017).
18. Loubeyre, P., Occelli, F. & LeToullec, R. Optical studies of solid hydrogen to 320 GPa and evidence for black hydrogen. *Nature* **416**, 613–617 (2002).
19. Li, B. et al. Diamond anvil cell behavior up to 4 Mbar. *Proc. Natl Acad. Sci. USA* **115**, 1713–1717 (2018).
20. Hanfland, M., Hemley, R. J. & Mao, H. K. Novel infrared vibron absorption of solid hydrogen at megabar pressures. *Phys. Rev. Lett.* **70**, 3760–3763 (1993).
21. Azadi, M., Drummond, N. D. & Foulkes, W. M. C. Nature of the metallization transition in solid hydrogen. *Phys. Rev. B* **95**, 035142 (2017).
22. Pickard, C. J. & Needs, R.J. Structure of phase III of solid hydrogen. *Nat. Phys.* **3**, 473–476 (2007).
23. Eremets, M. I., Drozdov, A. P., Kong, P. P. & Wang, H. Semimetallic molecular hydrogen at pressure above 350 GPa. *Nat. Phys.* **15**, 1246–1249 (2019).
24. Dewaele, A., Loubeyre, P., Dumas, P. and Mezouar, M. Oxygen impurities reduce the metallization pressure of xenon. *Phys. Rev. B* **86**, 014103 (2012).
25. Zhang, C. et al. Finite-temperature infrared and Raman spectra of high-pressure hydrogen from first-principle molecular dynamics. *Phys. Rev. B* **98**, 144301 (2018).
26. Morales, M., Mc Mahon, J. M., Pierleoni, C. & Ceperley, D. M. Towards a predictive first-principles description of solid molecular hydrogen with density functional theory. *Phys. Rev. B* **87**, 184107 (2013).
27. Dalladay-Simpson, P., Howie, R. T. & Gregoryanz, E. Evidence for a new phase of dense hydrogen above 325 gigapascals. *Nature* **529**, 63–67 (2016).
28. Ji, C. et al. Ultrahigh-pressure isostructural electronic transitions in hydrogen. *Nature* **573**, 558–562 (2019).
29. Goncharenko, I. & Loubeyre, P. Neutron and X-ray diffraction study of the broken symmetry phase transition in solid deuterium. *Nature* **435**, 1206–1209 (2005).
30. Geneste, G., Torrent, M., Bottin, F. & Loubeyre, P. Strong isotope effect in phase II of dense solid hydrogen and deuterium. *Phys. Rev. Lett.* **109**, 155303 (2012).
31. Loubeyre, P., Occelli, F. & Dumas, P. Hydrogen phase IV revisited via synchrotron infrared measurements in H<sub>2</sub> and D<sub>2</sub> up to 290 GPa at 296 K. *Phys. Rev. B* **87**, 134101 (2013).
32. Zhang, X.-W., Wang, E.-G. & Li, X.-Z. Ab initio investigation on the experimental observation of metallic hydrogen. *Phys. Rev. B* **98**, 134110 (2018).
33. Carbotte, J. P., Nicol, E. J. & Timusk, T. Detecting superconductivity in the high pressure hydrides and metallic hydrogen from optical properties. *Phys. Rev. Lett.* **121**, 047002 (2018).

**Publisher's note** Springer Nature remains neutral with regard to jurisdictional claims in published maps and institutional affiliations.

© The Author(s), under exclusive licence to Springer Nature Limited 2020



### The toroidal diamond anvil cell

The toroidal shape of the synthetic single-crystal diamond anvil tip was prepared by focused ion beam machining. Scanning electron micrograph and profile of the toroidal tip are given in Extended Data Fig. 6. The central flat diameter, groove and depth are 25  $\mu\text{m}$ , 80  $\mu\text{m}$  and 4.6  $\mu\text{m}$ , respectively. The toroidal tip has been recovered intact upon full pressure release, indicating its purely elastic deformation up to the highest pressure reached. That indicates that no irreversible transformation of the anvil at tip in contact with the hydrogen sample has perturbed the absorption measurements. Breakage on the bevelled slope of the anvil is observed, as in standard DAC, but outside of the focused ion beam-machined central part.

High pressures were generated using the T-DAC, consisting of a LeToullec membrane diamond anvil cell equipped with Boehler–Almax type seats of polycrystalline diamond and equipped with toroid-shaped diamond anvils. The hydrogen sample was loaded in the T-DAC under a pressure of 140 MPa. A focused ion beam-drilled rhenium gasket was used. The sample pressure was slowly increased to enable the gradual elastic deformation of the anvil tip by changing the membrane pressure pushing the piston with a rate of 0.2 bar  $\text{min}^{-1}$ . The red colour of the diamond tip is gradually observed above 350 GPa, reversibly disappearing upon pressure release, owing to the diamond bandgap closing within the visible range at the diamond tip<sup>8,34</sup>.

The sample thickness,  $1.6 \pm 0.1 \mu\text{m}$ , was estimated by the conservation of the hydrogen mass between loading (33.6  $\text{cm}^3 \text{mol}^{-1}$  of hydrogen loaded in a gasket hole 14  $\mu\text{m}$  in diameter and 6  $\mu\text{m}$  thick) and the sample at 400 GPa (1.6  $\text{cm}^3 \text{mol}^{-1}$  in a diameter of about  $5.8 \pm 0.2 \mu\text{m}$ ).

The conversion between the membrane pressure,  $P_m$ , and the force on the piston,  $F$ , is  $F [\text{kN}] = 0.05 \times P_m [\text{bar}]$ .

### Pressure measurement

The high-frequency step of the  $T_{2g}$  Raman spectra of the stressed diamond anvil was used to measure the pressure at the hydrogen sample. The hydrogen sample pressure is related to the diamond-edge wavenumber by the Akahama calibration<sup>35</sup>. The revision<sup>36</sup> of this calibration curve up to the 400 GPa pressure range was discarded because the pressure appeared to be overestimated, on the basis of the following: (1) in our previous measurements with toroidal anvils using X-ray diffraction<sup>8</sup>, the rhenium pressure gauge gave values in better agreement with the original pressure scale; (2) as seen in Extended Data Fig. 7, the pressure evolution versus the membrane pressure and the infrared vibron wavenumber versus pressure exhibit unphysical behaviours when using the revised scale; and (3) the revised scale is based on the Pt equation of state<sup>37</sup> that has been recently shown to overestimate pressure<sup>38</sup>. The pressure of the bandgap data measured previously in the visible range<sup>18</sup> has been corrected using the same pressure calibration as in the present study ( $\sim 20$  GPa). No difference up to a pressure of 330 GPa, estimated with the diamond-edge Raman pressure gauge, could be observed between operating the toroidal anvils or the standard bevelled anvils, by looking at the infrared  $H_2$  vibron wavenumber versus pressure (see Extended Data Fig. 3). The error bars in the pressure measurements,  $\pm 10$  GPa, arise from the random uncertainties originating from the positional accuracy of the sample and the stress field at the tip. The systematic uncertainties owing to the pressure calibration scale are not taken into account. The estimated pressures may be corrected in the future if the diamond-edge pressure gauge calibration is refined. The pressure scale used here is:

$$P[\text{GPa}] = 547 \frac{\Delta\omega}{\omega_0} \left( 1 + 1,375 \frac{\Delta\omega}{\omega_0} \right)$$

where  $\Delta\omega$  is the frequency shift of the diamond edge and  $\omega_0 = 1,334 \text{ cm}^{-1}$ .

### Infrared bench

A photograph of the bench is shown in Extended Data Fig. 8. This bench was previously used to characterize the infrared vibrational modes of phase IV of hydrogen at 300 K<sup>31</sup>. The custom-made horizontal infrared microscope is equipped with two infinity-corrected long-working-distance Schwarzschild objectives (working distance, 47 mm; numerical aperture, 0.5; magnification, 15 $\times$ ) that produce a 23  $\mu\text{m}$  (full width at half maximum, FWHM) infrared spot at a wavelength of 10  $\mu\text{m}$ . This beam size is reduced inside the T-DAC owing to the effect of the diamond refractive index. The spatial and temporal stability of the broadband infrared beam enabled us to record transmission spectra, with a good signal-to-noise ratio over the range 800–8,000  $\text{cm}^{-1}$  for a hole of diameter 6  $\mu\text{m}$  (see Extended Data Fig. 8). One of the Schwarzschild objectives is mounted on a 300-mm translation stage to free up space behind the cryostat in order to insert the optical head for Raman spectroscopy measurements without moving the T-DAC. The Raman signal was excited by a 660-nm-wavelength laser limited to 3 mW power output above 300 GPa to prevent thermal heating and hence breakage of the toroidal tip. The Raman head is also equipped with a digital camera to take photographs of the sample at each pressure. The quality of the measurements obtained also relies on the high mechanical stability of the bench and on the high reproducibility in position upon swapping between the infrared and the Raman configurations. Infrared spectra were collected with a 4  $\text{cm}^{-1}$  resolution and 1,024 scans, with an electron beam current of 450 mA (top-up mode).

### Absorption spectra

All spectra were recorded using the transmission geometry and then divided by a reference transmission spectrum, here taken at 123 GPa. Such a pressure is high enough to avoid any Fabry–Perot interference signal coming from the two parallel diamond interfaces of high refractive index enclosing the sample, but with the absence of the strong  $H_2$  vibron absorption which appears above 160 GPa in phase III. The overall intensity (peak-to-peak value of the interferogram) of the spectra has been normalized by that at 310 GPa to take into account the change in the hydrogen sample diameter owing to its compression. It was observed that above 310 GPa, the sample size is almost constant upon pressure increase and decrease. The absorbance is defined as  $A = -\log_{10}(I(v)/I_0(v))$ , where  $I$  is the intensity of the raw spectrum at a frequency  $v$ .

In the present experimental configuration, the maximum absorbance value that could be reasonably measured is approximately 2, indicating that less than 1% of the reference spectrum signal is detected. Considering the small gasket hole, the detection of the signal remained challenging and required using the detector gain at maximum value, inducing an increase of the intrinsic detector noise.

### Data availability

The data that support the findings of this study are available from the corresponding author upon request.

34. Ruoff, A. L., Luo, H. & Vohra, Y. K. The closing diamond anvil optical window in multimegabar research. *J. Appl. Phys.* **69**, 6413–6416 (1991).
35. Akahama, Y. & Kawamura, H. Pressure calibration of diamond anvil Raman gauge to 310 GPa. *J. Appl. Phys.* **100**, 043516 (2006).
36. Akahama, Y. & Kawamura, H. Pressure calibration of diamond anvil Raman gauge to 410 GPa. *J. Phys. Conf. Ser.* **215**, 012195 (2010).
37. Holmes, N. C., Moriarty, J. A., Gathers, G. R. & Nellis, W. J. The equation of state of platinum to 660 GPa. *J. Appl. Phys.* **66**, 2962–2967 (1989).
38. Yokoo, M., Kawai, N., Nakamura, K. & Kondo, K. Ultrahigh-pressure scales for gold and platinum at pressures up to 550 GPa. *Phys. Rev. B* **80**, 104114 (2009).
39. Ishmaev, S. N. et al. Neutron structural investigations of solid parahydrogen at pressures up to 24 kbar. *Sov. Phys. JETP* **84**, 394–403 (1983).
40. Dewaele, A., Torrent, M., Loubeyre, P. & Mezouar, M. Compression curves of transition metals in the Mbar range: experiments and projector augmented-wave calculations. *Phys. Rev. B* **78**, 104102 (2008).
41. Vinet, P., Ferrante, J., Rose, J. H. & Smith, J. R. Compressibility of solids. *J. Geophys. Res.* **92**, 9319–9325 (1987).

42. Akahama, Y. et al. Evidence from X-ray diffraction of orientational ordering in phase III of solid hydrogen at pressures up to 183 GPa. *Phys. Rev. B* **92**, 060101 (2010).
43. Zha, C.-S., Liu, Z. & Hemley, R. J. Synchrotron infrared measurements of dense hydrogen to 360 GPa. *Phys. Rev. Lett.* **108**, 146402 (2012).

**Acknowledgements** We thank O. Marie for focused ion beam machining the toroidal anvils and the gasket holes. We are grateful to the SOLEIL director general, J. Dailant, for giving us regular access to the infrared beamline over the past six years. The inputs of S. Lefrançois in designing and assembling the horizontal infrared microscope and of the optics group at SOLEIL in aligning the Schwarzschild objectives are appreciated. We thank F. Borondics and F. Capitani for their assistance at the SMIS beamline.

**Author contributions** P.L. designed the project. P.L. and F.O. prepared and loaded the T-DAC. P.D., F.O. and P.L. developed the infrared microscope. P.L., F.O. and P.D. conducted the experiment and analysed the data. P.L. and P.D. wrote the manuscript. All authors discussed the results.

**Competing interests** The authors declare no competing interests.

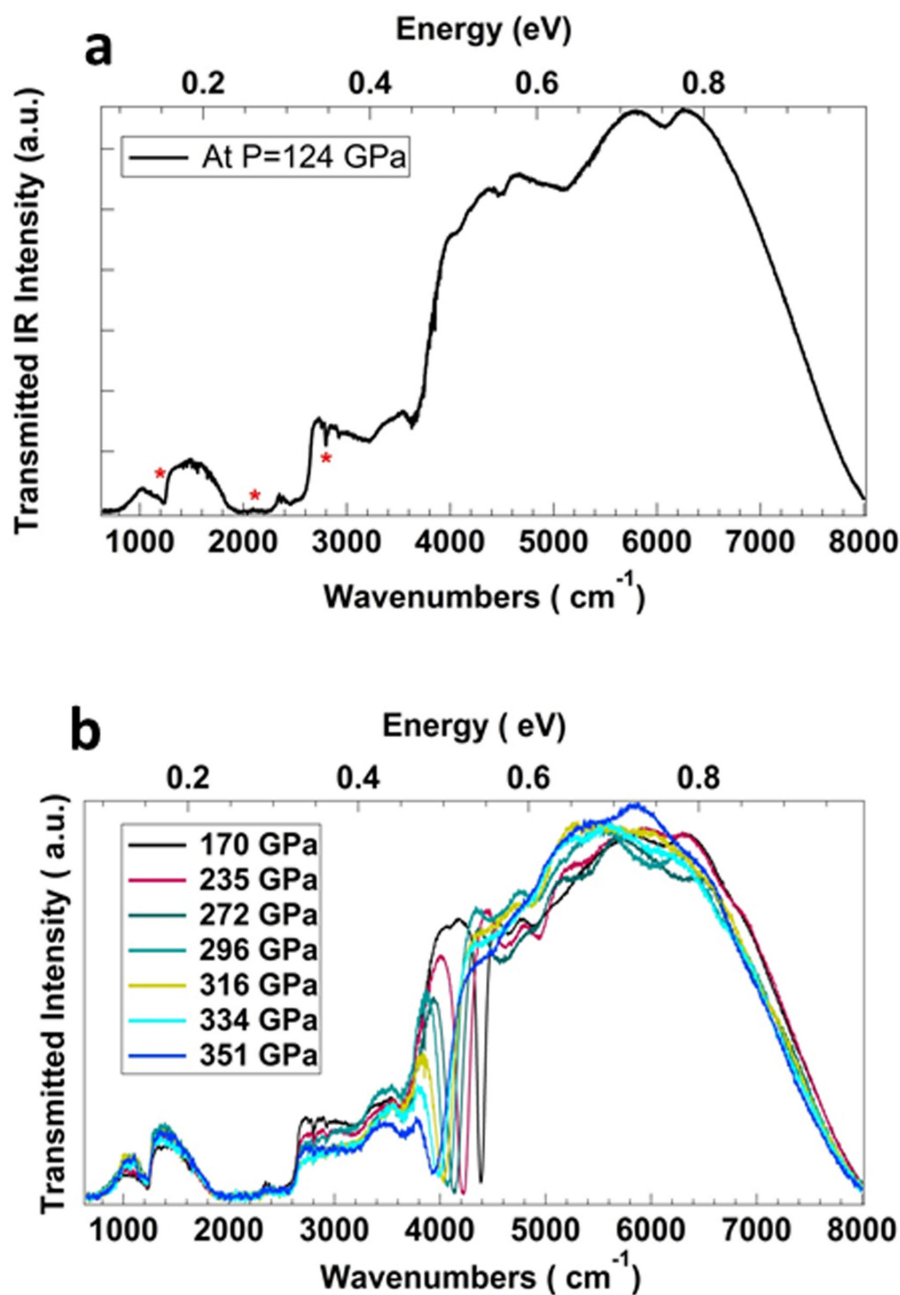
**Additional information**

**Supplementary information** is available for this paper at <https://doi.org/10.1038/s41586-019-1927-3>.

**Correspondence and requests for materials** should be addressed to P.L.

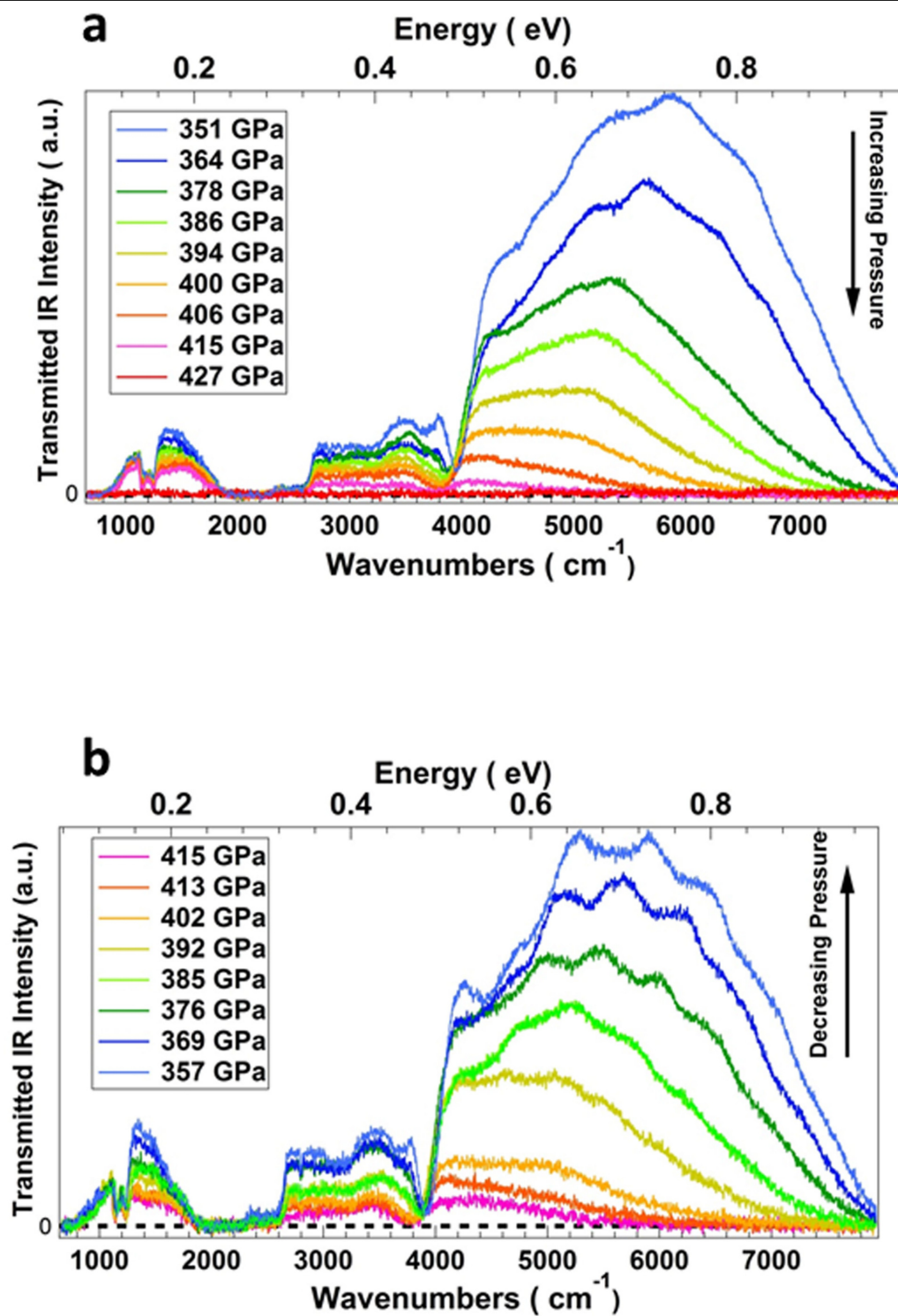
**Reprints and permissions information** is available at <http://www.nature.com/reprints>.





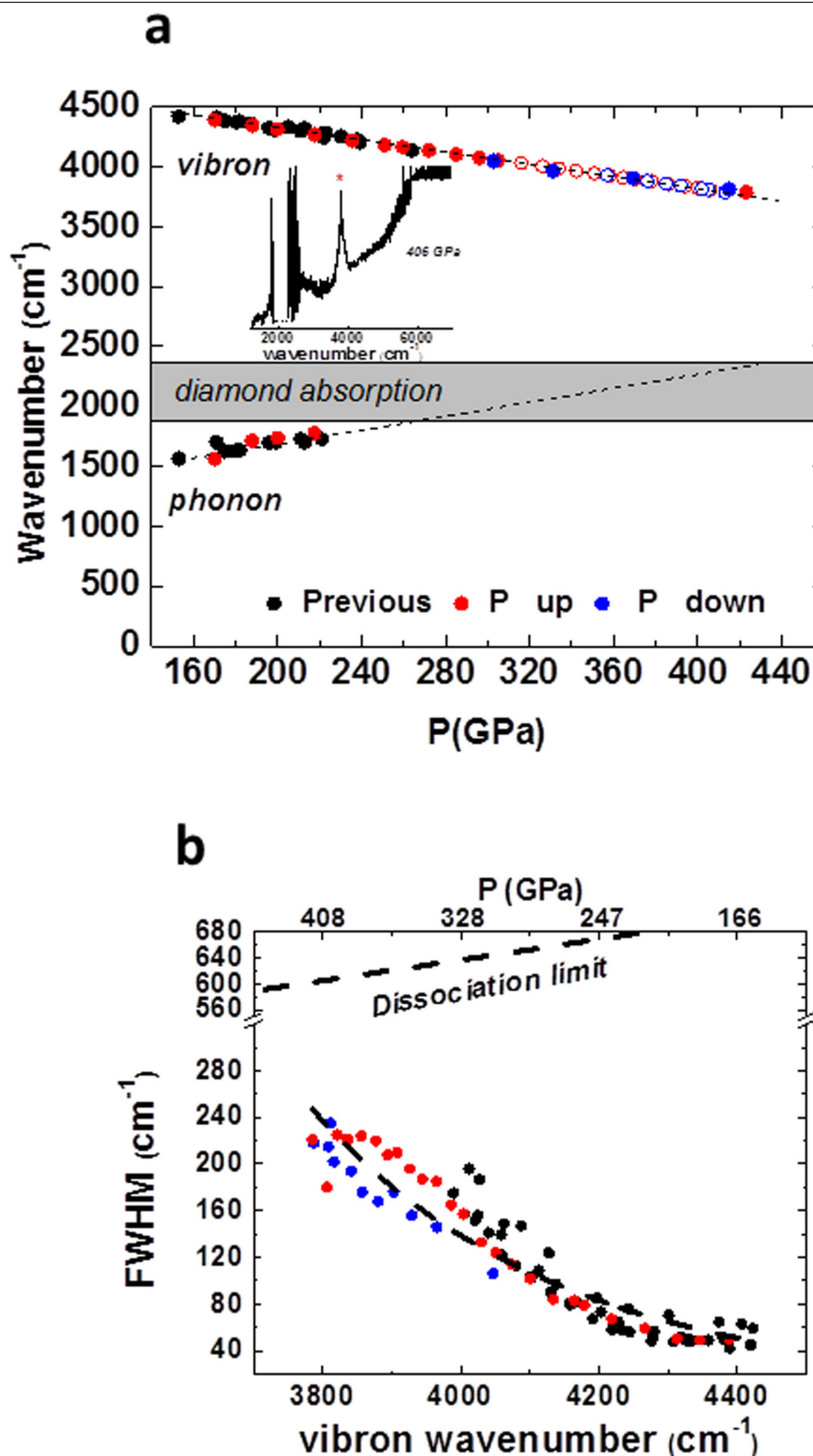
**Extended Data Fig. 1 | Infrared spectra below 350 GPa. a**, Single-beam spectrum at 123 GPa, used as the reference spectrum for the absorption spectra. The three red stars indicate parasitic effects corresponding to, from right to left, absorption peaks of impurities around 2,800 cm<sup>-1</sup>, a broad

absorption band from the diamond (1,900–2,300 cm<sup>-1</sup>), and a broad absorption around 1,200 cm<sup>-1</sup> from the protected layers of the aluminium mirrors of the beamline. **b**, Single-beam spectra, after intensity normalization (peak-to-peak value of their respective interferogram before Fourier transform). IR, infrared.



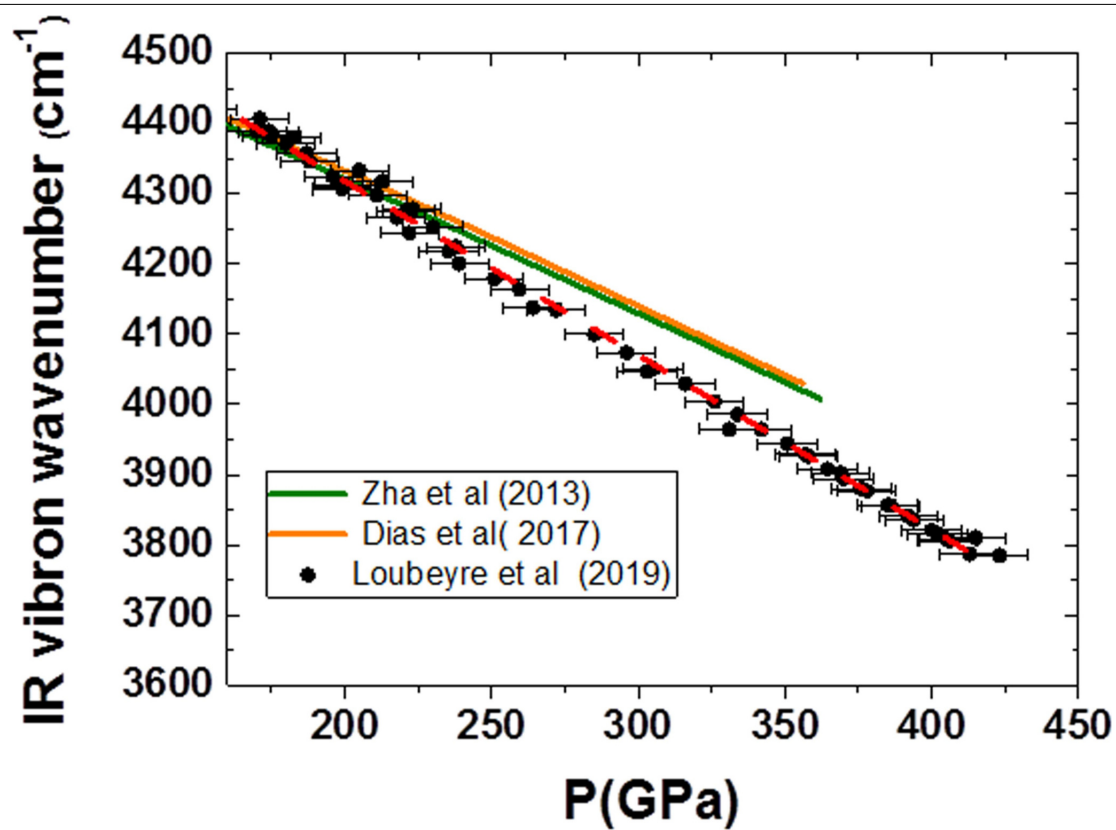
**Extended Data Fig. 2 | Infrared spectra above 350 GPa with pressure increase and pressure decrease. a, b,** These spectra show a zeroing at high wavenumbers, progressing towards low wavenumber values with pressure increase (a) and reversibly, to the opposite direction upon pressure release (b).





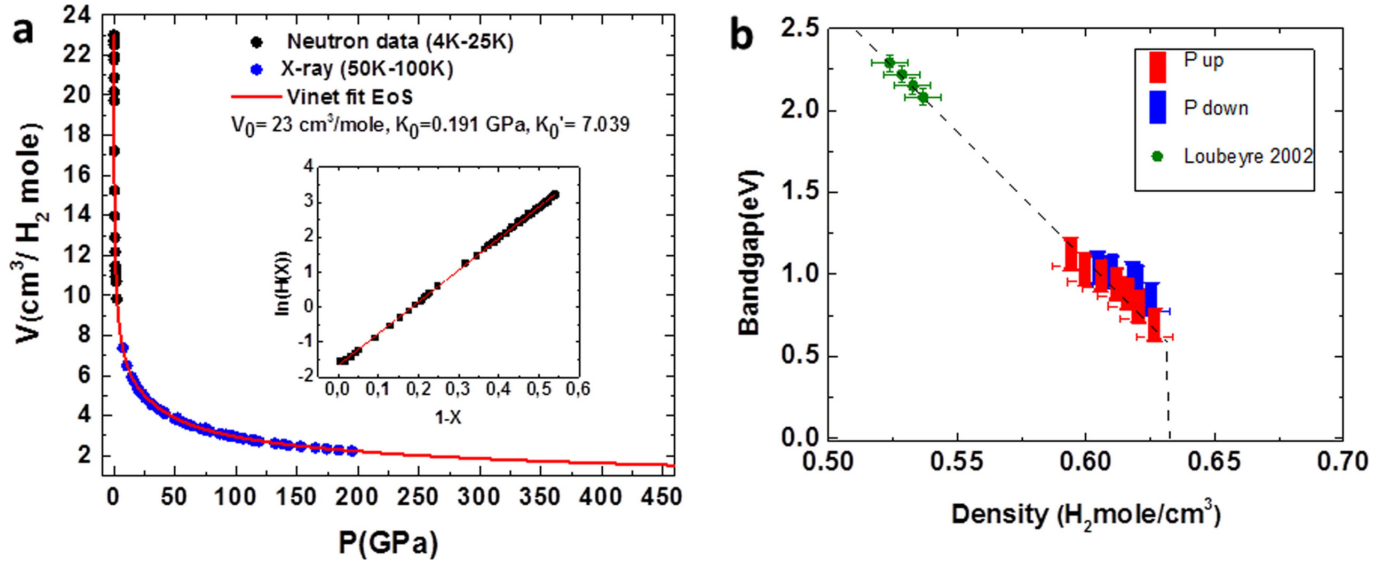
**Extended Data Fig. 3 | Infrared vibron and phonon wavenumbers versus pressure.** **a**, The symbols indicate: red, pressure increase; blue, pressure decrease; and black, previous work performed using standard diamond anvil cells. The filled dots indicate the pressure measured by the diamond pressure scale and the open symbols are the position according to the linear vibron shift as a function of pressure. Inset, infrared spectrum at 406 GPa, in arbitrary absorbance units, with the vibron peak indicated by a red star. The linear fit of the vibron wavenumber with pressure is given by:  $\nu_{\text{vibron}} [\text{cm}^{-1}] = 4,814 - 2.48P [\text{GPa}]$

and that of the phonon wavenumber by:  $\nu_{\text{phonon}} [\text{cm}^{-1}] = 1,163 + 2.69P [\text{GPa}]$ . **b**, FWHM of the vibron peak versus its wavenumber,  $\nu_{\text{vibron}}$ . The increase in the vibron linewidth with pressure remains well below the dissociation limit value, given by  $\text{FWHM} = E/2\pi$ , with  $E = h\nu_{\text{vibron}}$  the vibron energy and where  $h$  is the Planck constant. This limit is estimated by assuming that the lifetime of the vibron state (inferred by assuming it is the only contribution to the line broadening) is equal to the vibration period.



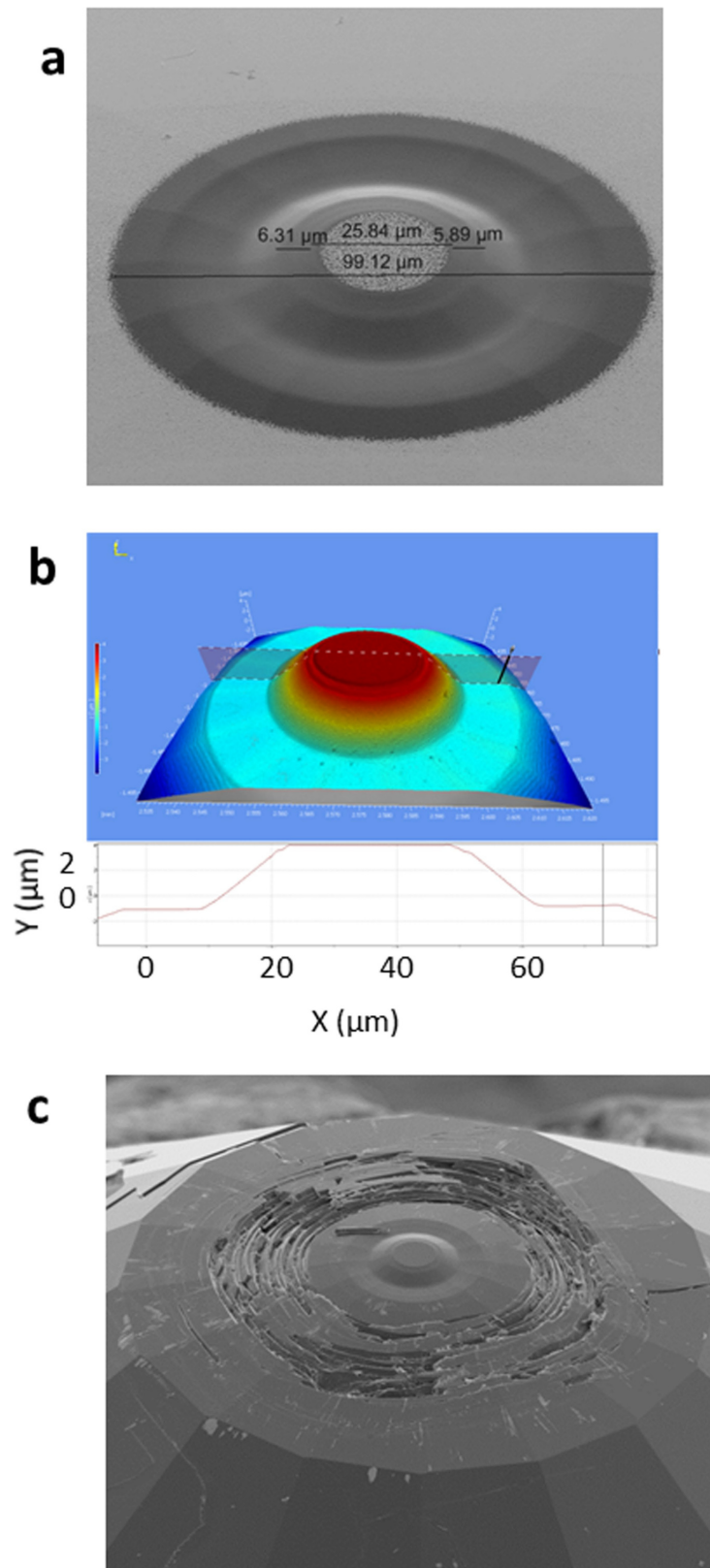
**Extended Data Fig. 4 | Infrared vibron wavenumber versus pressure.** The present data (black dots), and their linear fit (red dashed line) are compared to the linear fits of previous measurements<sup>743</sup> up to 360 GPa. Pressure uncertainty is  $\pm 10$  GPa.





**Extended Data Fig. 5 | Hydrogen equation of state and evolution of the direct electronic bandgap versus density. a,** Equation of state of solid hydrogen around 80 K. The black dots are neutron diffraction measurements<sup>39</sup>. The blue dots are our unpublished X-ray diffraction data obtained at the European Synchrotron Radiation Facility; the pressure scale is based on the revised ruby scale<sup>40</sup>. The red line is the fit of the experimental data by a Vinet form<sup>41</sup>:  $P = 3K_0(1-X)X^2 \exp[3/2(K_0' - 1)(1-X)]$ , with  $X = (V/V_0)^{1/3}$ ,  $K_0 = 0.191 \text{ GPa}$ ,  $K_0' = 7.039$  (where  $K_0' = dK_0/dP$ ), and  $V_0 = 23 \text{ cm}^3 \text{ mol}^{-1}$ . The present equation of state is in good agreement with that measured previously<sup>42</sup>. Inset, the Vinet form can be

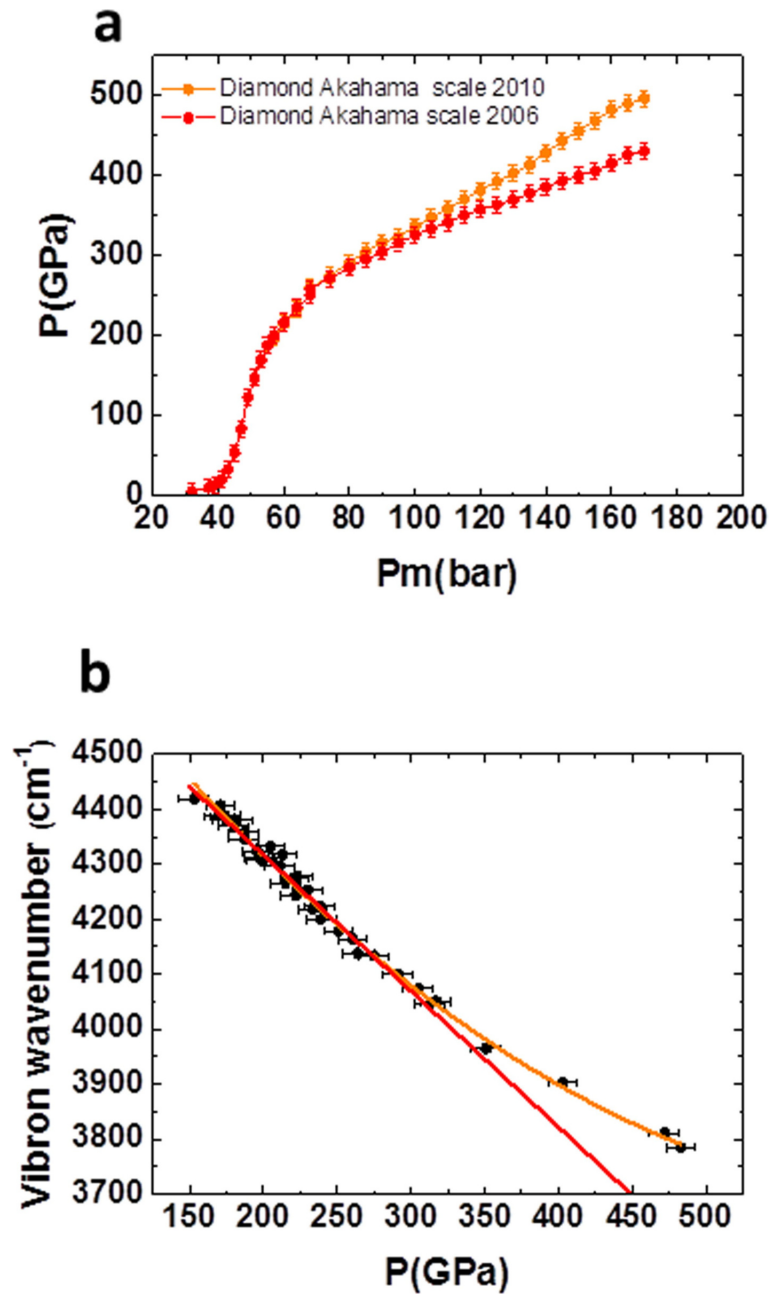
reformulated in terms of expressions analogous to normalized stress,  $\ln[H(X)] = \ln[PX^2/3(1-X)]$ , and Eulerian strain,  $(1-X)$ . This gives:  $\ln[H(X)] = \ln K_0 + 3/2(K_0' - 1)(1-X)$ . The linear fit of the data is shown. **b,** Evolution of the direct bandgap of solid hydrogen with density, for pressure increase (red), pressure decrease (blue) and from a previous study in the visible range<sup>18</sup> (green). The vertical rectangles indicate the maximum 0.14-eV underestimation of the bandgap owing to the limited absorbance value of 2 that could be measured. The density uncertainties ( $\pm 0.007 \text{ H}_2 \text{ mole cm}^{-3}$ ) are obtained by propagating the  $\pm 10 \text{ GPa}$  pressure uncertainties.



**Extended Data Fig. 6 | Geometry of the toroidal shape. a,** Scanning electron micrograph of the anvil. **b,** Profile of the toroidal diamond tip measured by interferometry. **c,** Scanning electron microscope image of the toroidal anvil

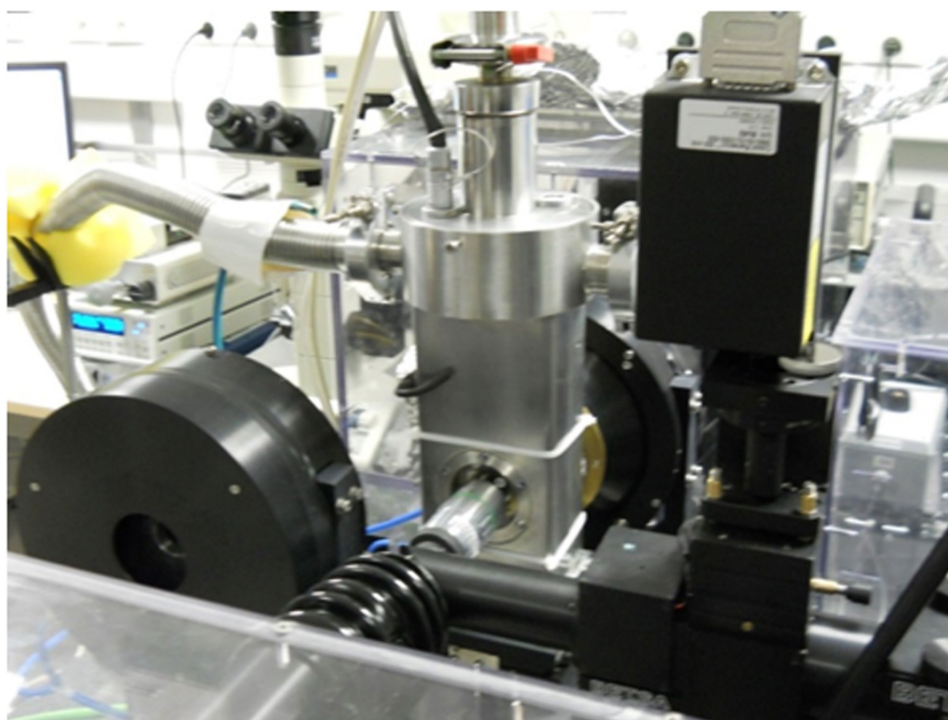
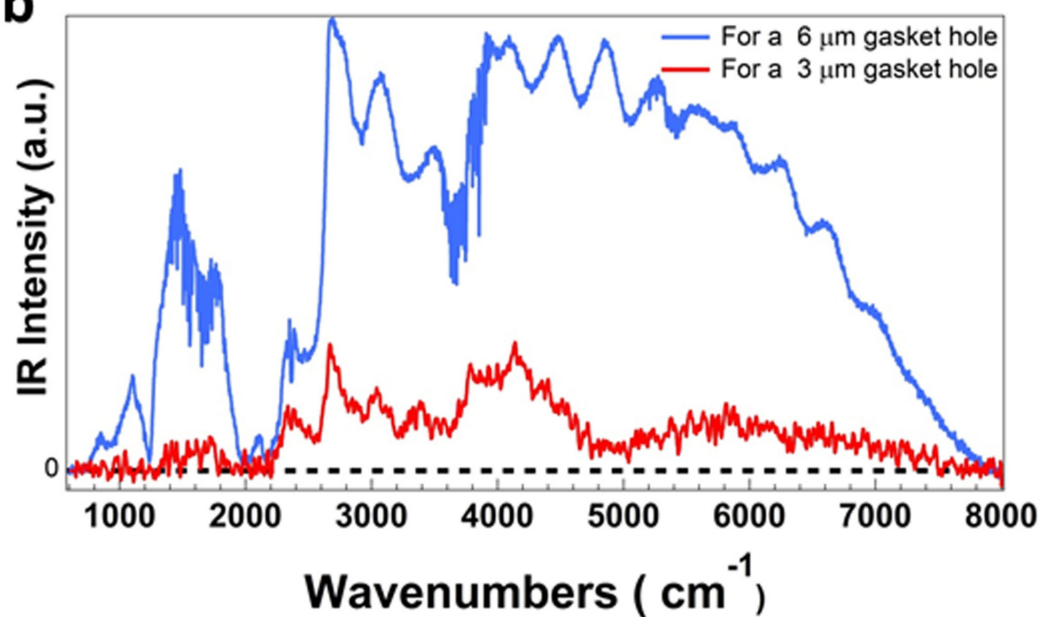
recovered after pressure release. The toroidal part of the anvil is intact. Ring cracks are seen on the bevel of the anvil, at a diameter of about 150  $\mu\text{m}$ .





**Extended Data Fig. 7 | Comparison of the original<sup>35</sup> and revised<sup>36</sup> Akahama diamond pressure scales for two measurements.** The two scales deviate above 300 GPa. **a**, Sample pressure–load curve. The force on the piston of the T-DAC is linearly related to the helium gas pressure inflating the membrane,  $F [kN] = 0.05 \times P_m [bar]$ . The revised scale (orange) gives a convex evolution above 300 GPa that is mechanically incorrect. **b**, Infrared  $H_2$  vibron

wavenumber versus pressure. Above 300 GPa, using the original scale (red), the shift is linear, in agreement with the calculated trend in phase III<sup>22,25</sup>; however, using the revised scale (dots and orange line), a sublinear shift is observed. The error bars in the pressure measurements ( $\pm 10$  GPa) arise from the random uncertainties originating from the positional accuracy of the sample and the stress field at the diamond anvil tip.

**a****b**

**Extended Data Fig. 8 | Experimental setup on the horizontal infrared microscope at the SMIS beamline of the SOLEIL synchrotron. a,** The L-N<sub>2</sub> flow cryostat containing the T-DAC sits between the two Schwarzschild objectives for infrared transmission measurements. In the Raman configuration, one of the Schwarzschild objectives is swapped by the Raman head. Both configurations are reproducibly recovered within about 2 μm,

because they are mounted on a precise, long-travel translation stage. **b,** Raw spectra recorded through two calibrated gasket holes 6 μm and 3 μm in diameter, made by focused ion beam machining in a rhenium gasket, and positioned between the two diamond anvils of the T-DAC. The spectra were recorded with a resolution of 4 cm<sup>-1</sup> and after 400 accumulations.

**a**

Vibron H2 (cm <sup>-1</sup> )	Energy gap(eV)	P (GPa)
3894	1.05 (+0.14)	370
3877	0.95 (+0.14)	378
3856	0.90 (+0.14)	386
3836	0.87 (+0.14)	394
3821	0.80 (+0.14)	400
3806	0.73 (+0.14)	406
3785	0.62 (+0.14)	415

**b**

Vibron H2 (cm <sup>-1</sup> )	Energy gap(eV)	P (GPa)
3787	0.77 (+0.14)	413
3808	0.87 (+0.14)	405
3816	0.90 (+0.14)	402
3841	0.94 (+0.14)	392
3857	0.96 (+0.14)	385

The pressure uncertainty is  $\pm 10$  GPa, the bandgap uncertainty is  $\pm 0.14$  eV and the vibron wavenumber uncertainty is  $\pm 4$  cm<sup>-1</sup>. Top, increasing pressure; bottom, decreasing pressure.



# Dualities and non-Abelian mechanics

<https://doi.org/10.1038/s41586-020-1932-6>

Received: 26 April 2019

Accepted: 11 November 2019

Published online: 20 January 2020

Michel Fruchart<sup>1,2\*</sup>, Yujie Zhou<sup>3</sup> & Vincenzo Vitelli<sup>1,2\*</sup>

Dualities are mathematical mappings that reveal links between apparently unrelated systems in virtually every branch of physics<sup>1–8</sup>. Systems mapped onto themselves by a duality transformation are called self-dual and exhibit remarkable properties, as exemplified by the scale invariance of an Ising magnet at the critical point. Here we show how dualities can enhance the symmetries of a dynamical matrix (or Hamiltonian), enabling the design of metamaterials with emergent properties that escape a standard group theory analysis. As an illustration, we consider twisted kagome lattices<sup>9–15</sup>, reconfigurable mechanical structures that change shape by means of a collapse mechanism<sup>9</sup>. We observe that pairs of distinct configurations along the mechanism exhibit the same vibrational spectrum and related elastic moduli. We show that these puzzling properties arise from a duality between pairs of configurations on either side of a mechanical critical point. The critical point corresponds to a self-dual structure with isotropic elasticity even in the absence of spatial symmetries and a twofold-degenerate spectrum over the entire Brillouin zone. The spectral degeneracy originates from a version of Kramers' theorem<sup>16,17</sup> in which fermionic time-reversal invariance is replaced by a hidden symmetry emerging at the self-dual point. The normal modes of the self-dual systems exhibit non-Abelian geometric phases<sup>18,19</sup> that affect the semiclassical propagation of wavepackets<sup>20</sup>, leading to non-commuting mechanical responses. Our results hold promise for holonomic computation<sup>21</sup> and mechanical spintronics by allowing on-the-fly manipulation of synthetic spins carried by phonons.

Symmetries and their breaking govern natural phenomena from fundamental particles to molecular vibrations<sup>22</sup>. They are also powerful tools to design synthetic materials from chemical compounds to metamaterials<sup>23–27</sup>. Here we start by asking a question almost deceptive in its simplicity: what is a symmetry? A symmetry is a transformation that maps a system onto itself, as illustrated by the threefold rotation  $C_3$  acting on the structure in Fig. 1a. A duality, on the other hand, relates distinct models or structures<sup>1–8</sup>. A celebrated example is the Kramers–Wannier order–disorder duality<sup>1,2</sup> between the low- and high-temperature phases of the two-dimensional Ising model, pictured in Fig. 1b. In self-dual systems, the distinction between dualities and symmetries is blurred: additional symmetries can emerge at a self-dual point even if the spatial symmetries are unchanged. This is what occurs in the critical configuration of the mechanical system shown in the middle panel of Fig. 1c. Here we show how such dualities can be harnessed to engineer material properties from wave propagation to static responses that are not predicted by a standard symmetry analysis based on space groups.

Mechanical structures are described at the linear level by normal modes of vibration and their oscillation frequencies. Both are determined by the dynamical matrix  $\hat{D}$ , which summarizes the Newton equations of motion in the harmonic approximation  $\partial_t^2|\phi\rangle = -\hat{D}|\phi\rangle$ . The vector  $|\phi\rangle$  has components  $\phi_p = u_p/\sqrt{m_p}$ , where  $u_p$  is the displacement of particle  $p$  with mass  $m_p$  from its equilibrium position. The eigenvectors  $|\phi_i\rangle$  and eigenvalues  $\omega_i^2$  of the dynamical matrix, such that  $\hat{D}|\phi_i\rangle = \omega_i^2|\phi_i\rangle$ , are the normal modes of vibration and the corresponding

angular frequencies. In a spatially periodic system, the spectrum of the Bloch dynamical matrix  $D(k)$  is organized in frequency bands with dispersion relations  $\omega_i(k)$  parameterized by quasi-momenta  $k$  forming the Brillouin zone of the crystal. Although our discussion is focused on mechanics, our analysis applies when  $\hat{D}$  is replaced by other linear operators, such as the Maxwell operator of a photonic crystal<sup>28</sup>, the mean-field Hamiltonian of a quantum system (in which case the eigenvalues are energies) or the dynamical matrix of an electrical circuit<sup>29–31</sup>.

Twisted kagome lattices are a family of structures obtained from a mechanical kagome lattice<sup>9–15</sup> by actuating a mechanism, called a Guest–Hutchinson mode<sup>9</sup>, that allows a global deformation of the unit cells (see Supplementary Video demonstrating this property). This family is parameterized by a twisting angle  $\theta$  described in Fig. 2. We denote by  $\hat{D}(\theta)$  the dynamical matrix of the structure with twisting angle  $\theta$ . To each twisted kagome lattice with a twisting angle  $\theta$  corresponds a dual mechanical structure, which is another twisted kagome lattice with a twisting angle  $\theta^* = 2\theta_c - \theta$ . Comparison of the lower panels of Fig. 2b, d reveals that two lattices related by a duality transformation share the same band structure despite their clear structural difference. Remarkably, there is a self-dual kagome structure with angle  $\theta_c^* = \theta_c + \pi/4$ , where the band structure is doubly degenerate over the entire Brillouin zone, as shown in the lower panel of Fig. 2c. We now prove that the explanation of these phenomenological observations can be traced to the existence of a mathematical duality between the dynamical matrices of pairs of kagome lattices. An application of our

<sup>1</sup>James Franck Institute, University of Chicago, Chicago, IL, USA. <sup>2</sup>Department of Physics, University of Chicago, Chicago, IL, USA. <sup>3</sup>Instituut-Lorentz, Universiteit Leiden, Leiden, The Netherlands. \*e-mail: fruchart@uchicago.edu; vitelli@uchicago.edu

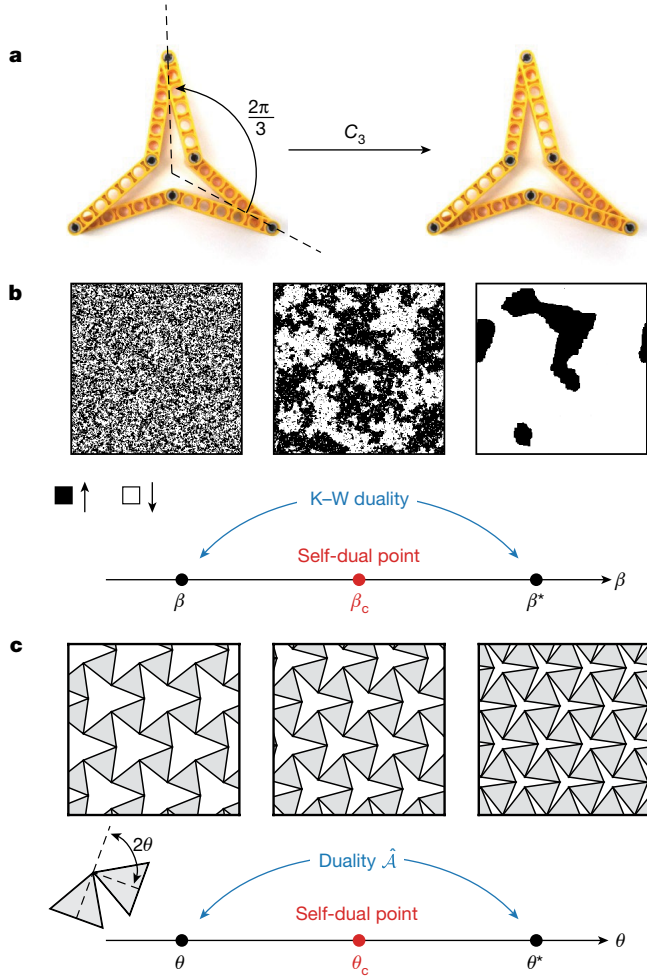


**Fig. 1 | Symmetries and dualities.** **a**, A star-shaped polygon in LEGO bricks illustrates threefold rotation symmetry: the mechanical molecule is mapped to itself by a  $2\pi/3$  ( $120^\circ$ ) rotation  $C_3$ . This is in contrast to a duality, which generically maps one system to another system. **b**, In the Ising model, spins on a two-dimensional lattice can take two values,  $\pm 1$ , represented by black (white) pixels. A phase transition separates an ordered ferromagnetic phase at low temperature in which spins align (right panel) from a disordered paramagnetic phase at high temperature (left panel). The Kramers and Wannier duality<sup>1</sup> associates to each (inverse) temperature  $\beta$  a dual temperature  $\beta^*$ , and the ratio of the partition functions at  $\beta$  and  $\beta^*$  is a known smooth function. The self-dual point  $\beta_c = \beta_c^*$  corresponds to the critical phase (middle panel), where the phase transition between the ferromagnet and the paramagnet occurs. **c**, Twisted kagome lattices form a family of mechanical structures parameterized by a variable  $\theta$  called the twisting angle. (See Fig. 2 for a model in LEGO bricks.) To each kagome lattice with angle  $\theta$  is associated a dual kagome lattice with angle  $\theta^* = 2\theta_c - \theta$ , resulting in strong relations between their mechanical properties. At the self-dual point, where  $\theta_c = \theta_c^* \equiv \pi/4$ , the duality becomes a symmetry.

general approach to electrical circuits is outlined in the Supplementary Information.

We first introduce a unitary transformation  $\hat{U}$  acting on the vibrational degrees of freedom of a twisted kagome lattice as represented in Fig. 3. A direct calculation (see Supplementary Information) shows that

$$\mathcal{U}(k)D(\theta^*, -k)\mathcal{U}^{-1}(k) = D(\theta, k) \quad (1)$$

where  $\mathcal{U}(k)$  is the Bloch representation of operator  $\hat{U}$ . Hence,  $\hat{U}$  should be viewed as a linear map between different spaces, describing the vibrations of the different mechanical structures with twisting angles

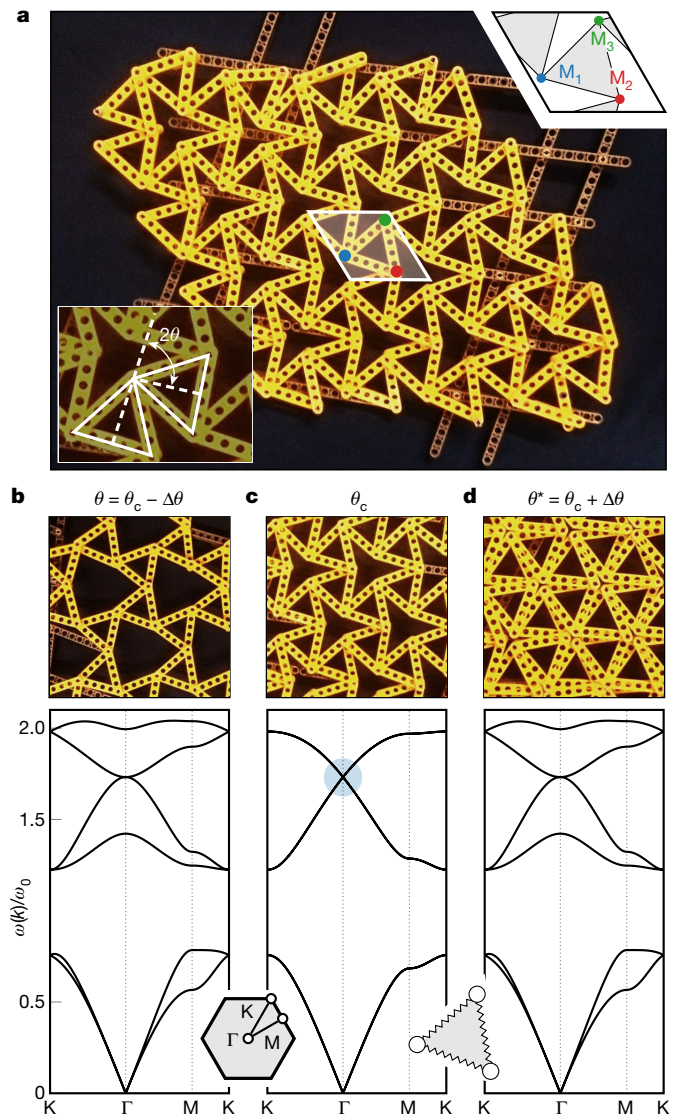


**Fig. 2 | Twisted kagome lattices and their band structures.** **a**, A LEGO bricks realization of the twisted kagome lattice tuned close to the critical point  $\theta_c$ . Lower inset: visualization of the twisting angle  $\theta$ . The angle between two triangles is  $\pi - 2\theta$ . Upper inset: unit cell of the mechanical structure. There are three inequivalent points (that is, not related by Bravais lattice translations) labelled  $M_1$ ,  $M_2$  and  $M_3$ . **b–d**, Band structures of the mechanical structures at different twisting angles. The physical frequencies are non-dimensionalized by a characteristic frequency,  $\omega_0 = \sqrt{k_0/m_0}$ , where  $k_0$  and  $m_0$  are the characteristic spring constant and the mass, respectively. The dual twisted kagome lattices with twisting angles  $\theta_c \pm \Delta\theta$  have the same band structure (**b** and **d**). The self-dual lattice with twisting angle  $\theta_c$  (**c**) has a twofold-degenerate band structure (including for points outside high-symmetry lines). At the  $\Gamma$  point, a double Dirac cone can be observed, highlighted by a blue shaded circle. The band structures are obtained by diagonalizing the Bloch dynamical matrices  $D(\theta, k)$ . The masses  $m_i$  of points  $M_i$  are set to unity in units of  $m_0$ . See Supplementary Information for details and a video demonstrating the collapse mechanism.

$\theta^*$  and  $\theta$  (compare the two lattices in Fig. 3). Note that  $\mathcal{U}(k)$  does not depend on the twisting angle  $\theta$ . As Newton equations are real-valued, the Bloch dynamical matrix satisfies  $\Theta D(\theta, k)\Theta^{-1} = D(\theta, -k)$  where  $\Theta$  is complex conjugation. Hence, by combining the anti-unitary operator  $\hat{\Theta}$  with  $\hat{U}$ , we get an anti-unitary operator  $\mathcal{A}(k) = \mathcal{U}(k)\Theta$ , which squares to  $\mathcal{A}(k)^2 = -\text{Id}$  (where  $\text{Id}$  is the identity matrix) and such that

$$\mathcal{A}(k)D(\theta^*, k)\mathcal{A}^{-1}(k) = D(\theta, k) \quad (2)$$

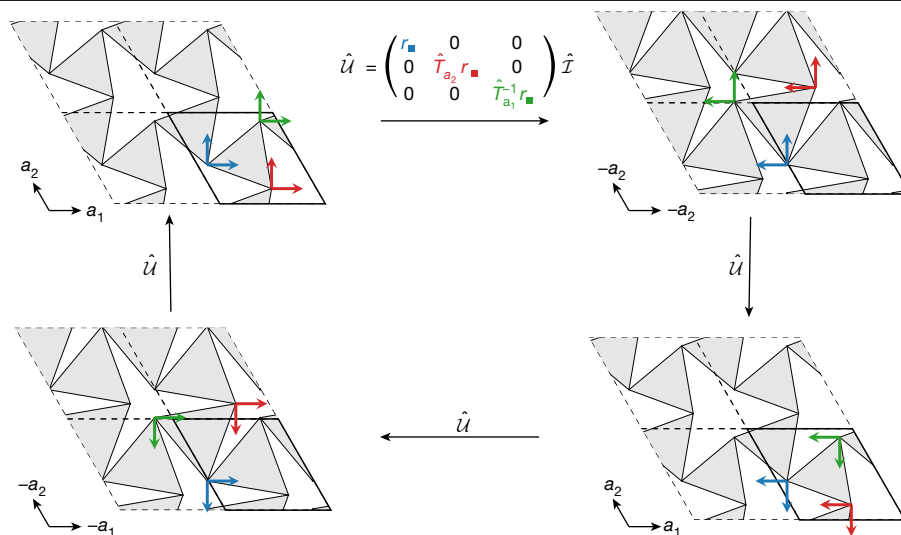


**Fig. 3 | Schematic action of the duality operator.** The duality operator maps the vibrational degrees of freedom of a twisted kagome lattice to the vibrational degrees of freedom of the dual kagome lattice. The vibrational degrees of freedom (in blue, red and green) in a unit cell (bold outline) are rotated by  $90^\circ$  counterclockwise and translated to another unit cell. Importantly, the translation depends on the degree of freedom: the vibrations of mass  $M_1$  (in blue) are not shifted, whereas the vibrations of mass  $M_2$  (in red) are shifted by one lattice vector  $a_2$  and the vibrations of mass  $M_3$  (in green) are shifted by another lattice vector  $-a_1$ . The operator  $\hat{U}$  is written as a block matrix; the different blocks describe the different masses in the unit cell (as represented by the colours), and the (real) matrices  $r_{\blacksquare} = i\sigma_y$  (the square

represents fourfold rotation on the degrees of freedom) act for each mass on the two orthogonal vibrations along  $x$  and  $y$ , mapping  $(u_x, u_y)$  to  $(u_y, -u_x)$ . The operator  $\hat{I}$  acts on the Bravais lattice as space inversion, but does not modify the internal degrees of freedom (see Supplementary Information). Iterated applications of  $\hat{U}$  show that  $\hat{U}^2 = -\text{Id}$ ,  $\hat{U}^3 = -\hat{U}$  and  $\hat{U}^4 = \text{Id}$ , showing that the symmetry has order 4. In the self-dual lattice, the transformation resembles a non-symmorphic symmetry composed of a  $90^\circ$  rotation followed by a non-integer lattice translation at first sight. However, further inspection shows that this operation is different from the duality operation, and is not a symmetry of the self-dual lattice (see Supplementary Information for a visual proof).

Equation (2) is the expression of a duality between the two lattices with twisting angles  $\theta$  and  $\theta^*$ , illustrated in Fig. 1c. The dynamical matrices of the two dual systems are related by an anti-unitary transformation. As a consequence, they have identical band structures (more precisely, the eigenvalues are related by complex conjugation, and are equal because they are also real) and the eigenvectors are related by  $\mathcal{A}$ . Equation (1) is also a duality between the same lattices. In contrast to equation (2), it is ruled by a unitary operator, but is non-local in momentum space (it relates  $k$  to  $-k$ ). Alone, it would ensure that the band structures of both lattices are the same only up to an inversion of momentum.

We now move on to explain the global twofold degeneracy observed in Fig. 2c. This degeneracy is reminiscent of a celebrated theorem from Kramers<sup>16,17</sup> stating that the energy states of time-reversal invariant quantum systems with half-integer spin are at least doubly degenerate. At first sight, this theorem does not apply here, as the mechanical degrees of freedom are neither quantum mechanical nor fermionic. Yet Kramers' theorem can still formally apply provided that some anti-unitary operator squaring to minus the identity matrix commutes with the dynamical matrix. At the critical twisting angle  $\theta_c = \theta_c^* \equiv \pi/4$ , the mechanical structure is self-dual. The duality shown in equation (2) acts as a hidden symmetry of the critical dynamical matrix  $D(\theta_c)$ , through  $\mathcal{A}(k)D(\theta_c, k)\mathcal{A}^{-1}(k) = D(\theta_c, k)$ . As  $\mathcal{A}^2 = -\text{Id}$ , Kramers' theorem can indeed be applied, and implies that the band structure is twofold degenerate at every point  $k$  of the Brillouin zone, as observed in Fig. 2c. Interestingly,  $\mathcal{A}$  acts in the same way as the combination of spatial inversion and a so-called fermionic time-reversal would in an electronic system, although neither is present in our mechanical system. Owing to the presence of the self-dual symmetry, the critical band structure exhibits exotic features. For instance, a finite-frequency linear dispersion (a double Dirac cone) is observed at the centre of the Brillouin zone (called  $\Gamma$ ; see Fig. 2c) that is uncommon in systems with time-reversal invariance (see Supplementary Information for a discussion and references).

When the self-duality is combined with the usual crystal symmetries, anomalous point groups can be realized. Consider paving the two-dimensional plane with a single regular polygon. This is possible with a triangle, a square or a hexagon, but not with a pentagon or a dodecagon. This is a manifestation of the crystallographic restriction theorem: the only point group symmetries compatible with lattice translations are of order 1, 2, 3, 4 or 6, in two dimensions. (The order of an operation  $g$  is the smallest integer  $n$  such that  $g^n$  is the identity matrix.) The point group  $C_{3v}$  of twisted kagome lattices at the centre  $\Gamma$  of the Brillouin zone contains threefold rotations (as visible in Fig. 2), perfectly compatible with this assertion. At the critical angle  $\theta_c$ , the duality relation (1) turns into an additional symmetry of the dynamical matrix. The point group at  $\Gamma$  has effectively to be supplemented with  $\mathcal{U}(\Gamma)$ , which has order 4 (see Fig. 3). Combined with a threefold rotation from  $C_{3v}$ , the self-dual symmetry  $\mathcal{U}(\Gamma)$  produces an anomalous symmetry of order  $3 \times 4 = 12$ , making the effective point group at  $\Gamma$  non-crystallographic (isomorphic to  $D_{12}$ ; see Supplementary Information). The emergence of this non-crystallographic point group is curious, as the twisted kagome lattices are indeed crystals, not quasicrystals. However, there is no contradiction with the crystallographic restriction theorem, because the self-dual symmetry is not a spatial symmetry.

Besides vibrational modes, the duality induces a relation between the elastic tensors  $c_{ijk\ell}(\theta)$  and  $c_{ijk\ell}(\theta^*)$  that describe the static mechanical response of dual structures in the linear regime (see Supplementary Information). A striking manifestation of the enhanced symmetry at the self-dual point is revealed by considering the elastic tensors of a twisted kagome lattice in which inequivalent springs have different stiffnesses. In this case, there are no spatial symmetries besides translations (the space group is  $p1$ ). In the Supplementary Information, we show that three distinct elastic moduli exist for  $\theta \neq \theta_c$ , whereas at the self-dual point  $\theta = \theta_c$  the elastic tensor becomes isotropic and only one non-vanishing modulus remains.



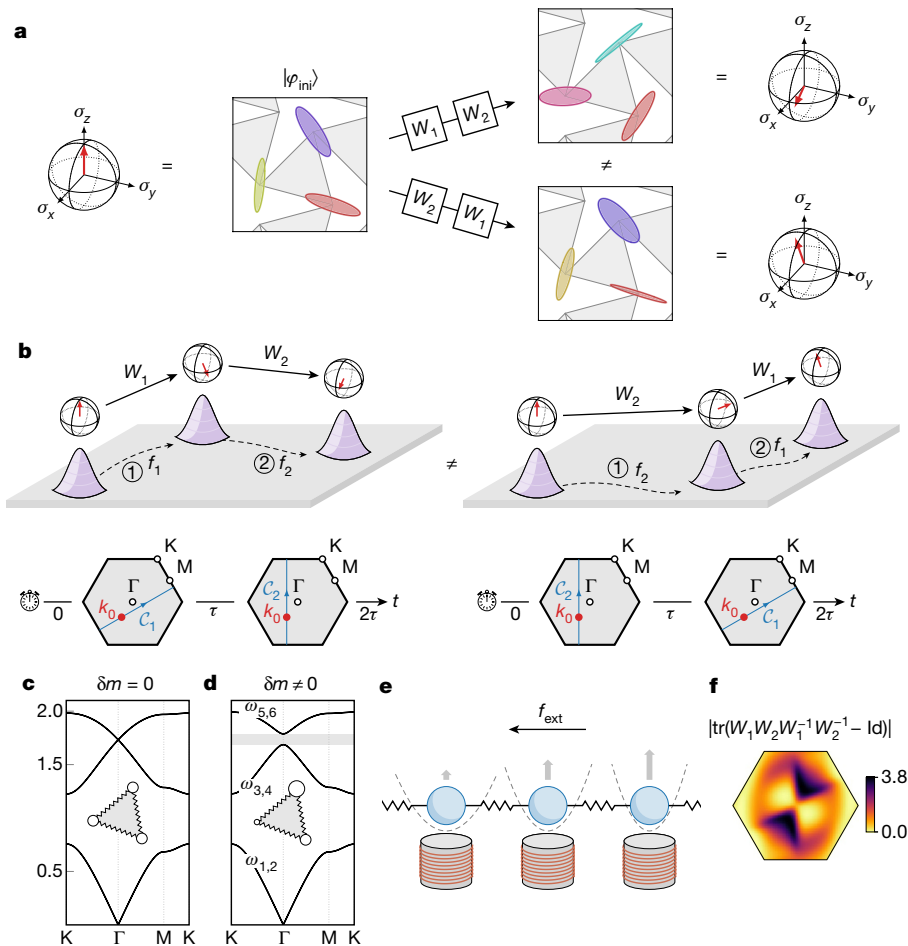


**Fig. 4 | Mechanical spintronics via non-Abelian geometric phases.** Pushing on a wavepacket with an effective force  $f$  makes it move in momentum space and changes its pseudo-spin state  $|\varphi\rangle$ . This is described by the holonomy  $W$  of a non-Abelian Berry connection, which acts on  $|\varphi\rangle$  as a single-qubit gate. **a**, The vibrational states  $W_2 W_1 |\varphi_{\text{ini}}\rangle$  ( $W_1 W_2 |\varphi_{\text{ini}}\rangle$ ) obtained after the sequence of forces ( $f_1, f_2$ ) (of ( $f_2, f_1$ )) were applied for a duration  $\tau$  such that  $f_i \tau = a_i^*$  are represented by ellipses describing the motion of the masses, with the colour representing their phases. They are equivalently represented on a Bloch sphere (see Supplementary Information for a definition of the momentum-dependent basis). **b**, Sketch of the real space and momentum space trajectories (see Supplementary Information for the numerically integrated solutions). **c, d**, To avoid non-adiabatic transitions, an asymmetry  $\delta m$  is introduced between the three masses in a unit cell ( $m_1, m_2, m_3$ ) = (1 -  $\delta m$ , 1, 1 +  $\delta m$ ),

illustrated by circles of different sizes. As a consequence, the double Dirac cone becomes massive, with a gap (in grey) proportional to  $\delta m$  at first order, while the global twofold degeneracy is preserved. **e**, An effective force  $f_{\text{ext}}$  acting on the wavepacket is produced by applying a spatially varying harmonic potential that essentially shifts the optical bands in frequency proportionally to the potential (see Supplementary Information). **f**, Comparing  $W_1 W_2 W_1^{-1} W_2^{-1}$  to the identity matrix provides a quantitative measure of the non-commutativity. The absolute value of the trace of their difference is plotted as a function of the starting point  $k_0$  of the protocol. In the numerical simulations, we have considered a wavepacket projected on the bands with dispersions  $\omega_3(k) = \omega_4(k)$ , and we have set  $k_0 = (2, 1)$  and  $\delta m = 0.1$  (see Supplementary Information for details on the numerical computation and orders of magnitude).

We now show how non-Abelian sound waves arise in our self-dual mechanical structures. Non-commuting (or equivalently non-Abelian) behaviour is pervasive in mechanics, from the moves of a Rubik's cube to the non-holonomic dynamics of rolling spheres and robotic arms. Here, we focus instead on a more subtle phenomenon: the non-commutative behaviour of the classical excitations (that is, sound waves) that propagate on top of a background configuration. Note that because our reasoning does not rely on a particular length scale, it should also apply to nanostructures with quantum phonons. The propagation of a wavepacket constructed out of vibrational modes can be affected by geometric (or Berry) phases. For a single isolated band, the Berry phases are complex numbers of modulus one that manifestly commute. To obtain non-Abelian Berry phases, a set of (at least) two degenerate bands is required. The geometric phases then become  $2 \times 2$  unitary matrices that do not need to commute<sup>18,19</sup>.

The self-dual kagome lattice is a suitable platform to realize non-Abelian sound because it has a global twofold-degenerate phonon spectrum, allowing us to realize a pseudo-spin mechanical degree of freedom  $|\varphi\rangle$ , represented by a Bloch sphere in Fig. 4a, b. To do so, we need to isolate a single twofold-degenerate band in the spectrum. This is done by assigning different values to the three masses in the unit cell to lift the threefold rotation symmetry of the lattice, creating a gap in the double Dirac cone at  $\Gamma$  (see Fig. 4c, d). This modification preserves the self-dual symmetry of equation (2), so the global twofold degeneracy persists regardless of the values of the masses. Consider an acoustic wavepacket constructed from the central set of twofold-degenerate bands with dispersions  $\omega_3(k) = \omega_4(k)$ , where dispersion relations  $\omega_i(k)$  with  $i = 1, \dots, 6$  are labelled with increasing frequencies (see Fig. 4d). As we apply external forces to the wavepacket as in Fig. 4b, it evolves within the twofold-degenerate subset of mechanical vibrations, as long as the external perturbation is small enough (see Supplementary Information

for orders of magnitudes). The wavepacket can then be treated as a particle-like object described by semiclassical equations of motion (see Supplementary Information and refs.<sup>20,32–34</sup>) that govern the evolution of its semiclassical position  $r(t)$ , momentum  $k(t)$  and pseudo-spin (that is, polarization)  $|\varphi(t)\rangle$ .

When a constant force is applied to the wavepacket, its momentum  $k(t)$  increases linearly in time while its pseudo-spin state changes from an initial value  $|\varphi_{\text{ini}}\rangle$  to  $W[C]|\varphi_{\text{ini}}\rangle$  (this situation is analogous to Bloch oscillations in solid-state physics). Here  $W[C] = P \exp\left(-\int_C A\right)$  is a Wilson line operator, the non-Abelian analogue of a Berry phase, that acts on  $|\varphi\rangle$  as a single-qubit gate, and  $A$  is the non-Abelian Berry connection<sup>18,19</sup> describing the twofold-degenerate band (see Supplementary Information). An effective force acting on wavepackets is not equivalent to a force acting on the elements of the mechanical lattice. The effective force on the wavepackets can be obtained through an additional harmonic potential imposed to each mass with a spatially dependent stiffness, as illustrated in Fig. 4e. This effective force is applied for a duration  $\tau$  chosen so that the momentum changes by exactly one reciprocal lattice vector  $a_i^*$ . As a consequence,  $C_i(\lambda) = k_0 + \lambda a_i^*$  is a closed loop starting and ending at  $k_0$  (see Fig. 4b), and the Wilson loop  $W_i = W[C_i]$  is the holonomy of the Berry connection along  $C_i$ .

Pictorially, pushing on the wavepacket changes its pseudo-spin state: this change is the holonomy  $W[C]$ . Here, the point is that the holonomies do not commute: when one pushes on the wavepacket in different directions, the order of the pushes matters because the pseudo-spin state keeps track of what happened. This is represented in Fig. 4b. After the forces  $(f_1, f_2)$  are sequentially applied during the appropriate duration, the pseudo-spin of a wavepacket initially at  $k_0$  changes from any initial state  $|\varphi_{\text{ini}}\rangle$  to  $W_2 W_1 |\varphi_{\text{ini}}\rangle$ . The reversed sequence  $(f_2, f_1)$  produces a different final pseudo-spin state  $W_1 W_2 |\varphi_{\text{ini}}\rangle$ , because the two Wilson loops typically do not commute:

$$W_1 W_2 \neq W_2 W_1 \quad (3)$$

These non-commuting mechanical responses share similarities with non-Abelian excitations such as anyons<sup>35–38</sup>. However, in the present study, non-commutativity arises from how independent wavepackets respond to external forces, whereas for anyons it is associated with the exchange (braiding) of these quasi-particles with each other. In Fig. 4f, we assess how the choice of the initial point  $k_0$  affects the non-commutativity of  $W_1(k_0)$  and  $W_2(k_0)$  by quantifying the deviation of  $W_1 W_2 W_1^{-1} W_2^{-1}$  from the identity matrix.

Our results raise the prospect of materials in which information is encoded and processed using non-Abelian mechanical excitations and can be seen as a first step towards an extension of phononics<sup>39</sup> including mechanical pseudo-spins, which we call mechanical spintronics. More broadly, our work illustrates the power of duality relations in mechanics and wave physics. The counterintuitive degeneracies of elastic moduli and phonon spectra at the self-dual point suggest that dualities and their breaking may play as crucial a role in the design of metamaterials as symmetries currently do.

## Online content

Any methods, additional references, Nature Research reporting summaries, source data, extended data, supplementary information, acknowledgements, peer review information; details of author contributions and competing interests; and statements of data and code availability are available at <https://doi.org/10.1038/s41586-020-1932-6>.

- Kramers, H. A. & Wannier, G. H. Statistics of the two-dimensional ferromagnet. *Part I. Phys. Rev.* **60**, 252–262 (1941).
- Savit, R. Duality in field theory and statistical systems. *Rev. Mod. Phys.* **52**, 453–487 (1980).
- Urade, Y., Nakata, Y., Nakanishi, T. & Kitano, M. Frequency-independent response of self-complementary checkerboard screens. *Phys. Rev. Lett.* **114**, 237401 (2015).
- Senthil, T., Vishwanath, A., Balents, L., Sachdev, S. & Fisher, M. P. A. Deconfined quantum critical points. *Science* **303**, 1490–1494 (2004).
- Louvet, T., Delplace, P., Fedorenko, A. A. & Carpentier, D. On the origin of minimal conductivity at a band crossing. *Phys. Rev. B* **92**, 155116 (2015).
- Devetak, I. Triangle of dualities between quantum communication protocols. *Phys. Rev. Lett.* **97**, 140503 (2006).
- Hull, C. M. & Townsend, P. K. Unity of superstring dualities. *Nucl. Phys. B* **438**, 109–137 (1995).
- Maldacena, J. The large- $N$  limit of superconformal field theories and supergravity. *Int. J. Theor. Phys.* **38**, 1113–1133 (1999).
- Guest, S. & Hutchinson, J. W. On the determinacy of repetitive structures. *J. Mech. Phys. Solids* **51**, 383–391 (2003).
- Souslov, A., Liu, A. J. & Lubensky, T. C. Elasticity and response in nearly isostatic periodic lattices. *Phys. Rev. Lett.* **103**, 205503 (2009).
- Sun, K., Souslov, A., Mao, X. & Lubensky, T. C. Surface phonons, elastic response, and conformal invariance in twisted kagome lattices. *Proc. Natl Acad. Sci. USA* **109**, 12369–12374 (2012).
- Kane, C. L. & Lubensky, T. C. Topological boundary modes in isostatic lattices. *Nat. Phys.* **10**, 39–45 (2013).
- Paulose, J., Gin-ge Chen, B. & Vitelli, V. Topological modes bound to dislocations in mechanical metamaterials. *Nat. Phys.* **11**, 153–156 (2015).
- Rocklin, D. Z., Zhou, S., Sun, K. & Mao, X. Transformable topological mechanical metamaterials. *Nat. Commun.* **8**, 14201 (2017).
- Ma, J., Zhou, D., Sun, K., Mao, X. & Gonella, S. Edge modes and asymmetric wave transport in topological lattices: experimental characterization at finite frequencies. *Phys. Rev. Lett.* **121**, 094301 (2018).
- Kramers, H. A. Théorie générale de la rotation paramagnétique dans les cristaux. *Proc. K. Akad. Wet. C* **33**, 959–972 (1930).
- Klein, M. J. On a degeneracy theorem of Kramers. *Am. J. Phys.* **20**, 65–71 (1952).
- Berry, M. V. Quantal phase factors accompanying adiabatic changes. *Proc. R. Soc. A* **392**, 45–57 (1984).
- Wilczek, F. & Zee, A. Appearance of gauge structure in simple dynamical systems. *Phys. Rev. Lett.* **52**, 2111–2114 (1984).
- Xiao, D., Chang, M.-C. & Niu, Q. Berry phase effects on electronic properties. *Rev. Mod. Phys.* **82**, 1959–2007 (2010).
- Zanardi, P. & Rasetti, M. Holonomic quantum computation. *Phys. Lett. A* **264**, 94–99 (1999).
- Coleman, S. *Aspects of Symmetry* (Cambridge Univ. Press, 1985).
- Khanikaev, A. B., Fleury, R., Hossein Mousavi, S. & Alù, A. Topologically robust sound propagation in an angular-momentum-biased graphene-like resonator lattice. *Nat. Commun.* **6**, 8260 (2015).
- Süsstrunk, R. & Huber, S. D. Classification of topological phonons in linear mechanical metamaterials. *Proc. Natl Acad. Sci. USA* **113**, E4767–E4775 (2016).
- Huber, S. D. Topological mechanics. *Nat. Phys.* **12**, 621–623 (2016).
- Matlack, K. H., Serra-Garcia, M., Palermo, A., Huber, S. D. & Daraio, C. Designing perturbative metamaterials from discrete models. *Nat. Mater.* **17**, 323–328 (2018).
- Fruchart, M. et al. Soft self-assembly of Weyl materials for light and sound. *Proc. Natl Acad. Sci. USA* **115**, E3655–E3664 (2018).
- Ozawa, T. et al. Topological photonics. *Rev. Mod. Phys.* **91**, 015006 (2019).
- Ningyuan, J., Owens, C., Sommer, A., Schuster, D. & Simon, J. Time- and site-resolved dynamics in a topological circuit. *Phys. Rev. X* **5**, 021031 (2015).
- Albert, V. V., Glazman, L. I. & Jiang, L. Topological properties of linear circuit lattices. *Phys. Rev. Lett.* **114**, 173902 (2015).
- Lee, C. H. et al. Topoelectrical circuits. *Commun. Phys.* **1**, 39 (2018).
- Culcer, D., Yao, Y. & Niu, Q. Coherent wave-packet evolution in coupled bands. *Phys. Rev. B* **72**, 085110 (2005).
- Shindou, R. & Imura, K.-I. Noncommutative geometry and non-Abelian Berry phase in the wave-packet dynamics of Bloch electrons. *Nucl. Phys. B* **720**, 399–435 (2005).
- Onoda, M., Murakami, S. & Nagaosa, N. Hall effect of light. *Phys. Rev. Lett.* **93**, 083901 (2004).
- Stern, A. & Lindner, N. H. Topological quantum computation—from basic concepts to first experiments. *Science* **339**, 1179–1184 (2013).
- Iadecola, T., Schuster, T. & Chamon, C. Non-Abelian braiding of light. *Phys. Rev. Lett.* **117**, 073901 (2016).
- Barlas, Y. & Prodan, E. Topological braiding of Majorana-like modes in classical metamaterials. Preprint at <https://arxiv.org/abs/1903.00463> (2019).
- Liu, Y., Liu, Y. & Prodan, E. Braiding flux-tubes in topological quantum and classical lattice models from class-D. Preprint at <https://arxiv.org/abs/1905.02457> (2019).
- Li, N. et al. Phononics: manipulating heat flow with electronic analogs and beyond. *Rev. Mod. Phys.* **84**, 1045–1066 (2012).

**Publisher's note** Springer Nature remains neutral with regard to jurisdictional claims in published maps and institutional affiliations.

© The Author(s), under exclusive licence to Springer Nature Limited 2020

## Methods

### Non-Abelian holonomies

Geometric phases<sup>18,40–42</sup> describe the residual influence of its environment on a subsystem considered in isolation. They typically arise when the system undergoes a slow cyclic change of its parameters. In this situation, the state of the system is transported over the parameter space to describe the evolution. The change in this state from before to after one cycle is a geometric phase factor. Formally, it is the holonomy of a connection along the closed loop travelled in parameter space: the connection provides a covariant derivative describing the parallel transport in the vector bundle of system states. The holonomies (geometric phase factors) are not necessarily mere  $U(1)$  phases, but can be matrices referred to as non-Abelian geometric phases<sup>43</sup>, because the formalism allows for non-commuting holonomies (phase factors). More precisely, let

$$W(C) = \mathcal{P} \exp \left( - \int_C A \right) \quad (4)$$

be the holonomy of the connection along the curve  $C$  in parameter space. Here,  $A$  is the connection form (see Supplementary Information for details), called a non-Abelian gauge field in the context of gauge theory<sup>43</sup>. The quantity  $W(C)$  is also called a Wilson loop operator<sup>44</sup>, and can be computed numerically (see Supplementary Information). We are interested in situations where two holonomies do not commute, that is, when  $W(C_1)W(C_2) \neq W(C_2)W(C_1)$  for two closed loops  $C_i$  starting (and ending) at the same point.

In the main text, we consider the propagation of wavepackets in a lattice of coupled mechanical oscillators. In this situation, the restriction to a subsystem described in isolation consists in assuming that the wavepacket stays in a given (set of degenerate) phonon bands, ignoring the bands with higher or lower frequencies. The parameter space is momentum space (that is, the Brillouin torus): the quasi-classical momentum changes because a force is applied to the wavepacket, and effectively acts as an external parameter from the point of view of the wavepacket (see Supplementary Information and refs.<sup>20,32–34,45–50</sup>). We emphasize that although the wavepacket moves both in momentum space and in position space, the non-Abelian geometric phase factors discussed in the main text are related to the trajectory in momentum space (not position space).

Non-Abelian holonomies arise in various physical contexts. The most common situation corresponds to an abstract parameter space<sup>51–54</sup>. In the situation analysed in the main text, the relevant parameter space is momentum space. This is similar to situations arising in the study of artificial spin–orbit coupling and non-Abelian gauge fields in optics<sup>46–56</sup> and in ultracold atomic gases<sup>57–61</sup>. Non-Abelian holonomies can also arise with position space as the relevant parameter space, such as in the non-Abelian Aharonov–Bohm effect<sup>43</sup> recently predicted and reported in optics<sup>62,63</sup>. Again, similar phenomena arise in ultracold atomic gases<sup>57–61</sup>. In another context, (non-Abelian) anyons<sup>35,64–69</sup> can also be understood as (non-Abelian) holonomies<sup>69–71</sup>, where the relevant parameter space is essentially describing the positions of the excitations. Interestingly, similar situations where classical excitations can be braided around one another were reported in optics and mechanics<sup>36–38,72</sup>.

A fascinating facet of non-Abelian holonomies is the possibility of harnessing them to realize holonomic computations<sup>21</sup>. This idea was developed with quantum computation in mind, but it can indeed also be applied to classical systems (and hence, classical computation). From this point of view, the non-Abelian holonomies described in the main text can be seen as single-qubit gates. This is not enough to realize any quantum computation, even with quantum degrees of freedom (phonons). For that, one would need two-qubit gates, which would require an interaction between the wavepackets ignored in our analysis. Nonetheless, a suitable design of the pattern generating the effective

forces should allow the realization of simple classical operations on the mechanical pseudo-spins carried by the wavepackets that would enrich the growing toolbox of phononic systems<sup>39,73</sup>.

### Semiclassical equations and Bloch oscillations

In the main text, we consider a wavepacket centred at a position  $r$  and a momentum  $k$ . We assume that this wavepacket is composed of a narrow band of frequencies corresponding to the two degenerate bands with dispersions  $\omega_3(k) = \omega_4(k)$  (the same analysis could be done on the upper bands  $\omega_5(k) = \omega_6(k)$ ). Its composition in the corresponding two-dimensional space is summarized by a pseudo-spin (polarization)  $|\varphi\rangle$ . In the context of wave physics, semiclassical approximations provide an approximate particle-like description of a wavepacket localized in both physical space and momentum space. For instance, geometrical optics can be viewed as a short-wavelength approximation of Maxwell equations<sup>74</sup>. Here, the position  $r$  and momentum  $k$  and the pseudo-spin  $|\varphi\rangle$  are promoted to the status of dynamical variables (called semiclassical variables) that evolve when the system is perturbed, for example when the wavepacket propagates in a non-uniform medium. The equations describing the semiclassical dynamics of the wavepacket in a (perturbed) spatially periodic structure can be systematically obtained from the underlying wave equations<sup>20,32,33,75–79</sup> (see also refs.<sup>34,45–50</sup> for application to classical waves). They read

$$\begin{aligned} \dot{r}^\mu &= \frac{\partial \Omega}{\partial k_\mu} + i[F^{\mu\nu}]_\varphi \dot{k}_\nu \\ \dot{k}_\mu &= -\frac{\partial V}{\partial r^\mu} \\ \dot{\varphi} &= -(i\Omega(k) + iV(r) + A^\mu \dot{k}_\mu)\varphi \end{aligned} \quad (5)$$

where  $\Omega(k) = \omega_3(k) = \omega_4(k)$  is the dispersion relation of the relevant degenerate bands,  $V(r)$  is an external potential, and  $A(k)$  and  $F(k)$  are the matrix-valued non-Abelian Berry connection and curvature forms of the degenerate band<sup>18,19,43</sup> (see Supplementary Information for more details).

The case of a constant (uniform) force  $f_0 = -\partial_r V$  considered in the main text describes so-called Bloch oscillations<sup>80</sup>, a situation realized in semiconductor superlattices<sup>81</sup> and in optical lattices of cold atoms<sup>82</sup> that provides a powerful tomographic tool for Bloch states<sup>83–88</sup>. In this case, the momentum equation  $\dot{k} = f_0$  can be integrated to  $k(t) = k_0 + f_0 t$ . The pseudo-spin can then formally be obtained up to a phase as a Wilson loop along the momentum space trajectory (see Supplementary Information for more details).

### Fabrication of the kagome lattices in LEGO bricks

The LEGO bricks realization of the kagome lattice allows us to demonstrate its collapse mechanism. It is composed of LEGO Technic liftarms connected by pins (see Supplementary Fig. 15).

Each pin can be attached to at most four liftarms, at different heights  $h_1, \dots, h_4$ ; and in the kagome lattice, it must be attached to exactly four liftarms. As the liftarms are rigid, they should not be bent, so the two pins connected by a liftarm should be attached at the same height. Amusingly, this constraint is similar to the ice rule of the six-vertex model. A practical consequence is that the unit cell of the kagome lattice has to be enlarged in the LEGO bricks realization. In our design, the unit cell is doubled with respect to the original lattice in order for the vertices to satisfy the ice-like rule. It is composed of 12 ‘liftarms  $1 \times 6$  thin’ (LEGO part 32063) and six ‘pins without friction ridges lengthwise’ (3673).

The presence of edges induces additional (unwanted) zero-energy mechanisms besides the global Guest–Hutchinson mechanism. They are suppressed as much as possible with an additional structure that prevents local motions without preventing the global deformation of the system.



## Data availability

No external data set was used during the current study.

## Code availability

The code used to compute the band structures and the holonomies, to perform the group-theoretical analysis, to integrate the semiclassical equations of motion and to verify the duality relations is available on Zenodo at <https://doi.org/10.5281/zenodo.3417426> under the 2-clause BSD licence.

40. Wilczek, F. & Shapere, A. *Geometric Phases in Physics* (World Scientific, 1989).
41. Chruściński, D. & Jamiołkowski, A. *Geometric Phases in Classical and Quantum Mechanics* (Birkhäuser Boston, 2004).
42. Cohen, E. et al. Geometric phase from Aharonov–Bohm to Pancharatnam–Berry and beyond. *Nat. Rev. Phys.* **1**, 437–449 (2019).
43. Wu, T. T. & Yang, C. N. Concept of nonintegrable phase factors and global formulation of gauge fields. *Phys. Rev. D* **12**, 3845–3857 (1975).
44. Wilson, K. G. Confinement of quarks. *Phys. Rev. D* **10**, 2445–2459 (1974).
45. Bliokh, K. Y. & Bliokh, Y. P. Modified geometrical optics of a smoothly inhomogeneous isotropic medium: the anisotropy, Berry phase, and the optical Magnus effect. *Phys. Rev. E* **70**, 026605 (2004).
46. Onoda, M., Murakami, S. & Nagaosa, N. Geometrical aspects in optical wave-packet dynamics. *Phys. Rev. E* **74**, 066610 (2006).
47. Bliokh, K. Y., Frolov D. Y. & Kravtsov Y. A. Non-Abelian evolution of electromagnetic waves in a weakly anisotropic inhomogeneous medium. *Phys. Rev. A* **75**, 053821 (2007).
48. Bliokh, K. Y. & Freilikher, V. D. Polarization transport of transverse acoustic waves: Berry phase and spin Hall effect of phonons. *Phys. Rev. B* **74**, 174302 (2006).
49. Mehrafarin, M. & Torabi, R. Geometric aspects of phonon polarization transport. *Phys. Lett. A* **373**, 2114–2116 (2009).
50. Torabi, R. & Mehrafarin M. Berry effect in acoustical polarization transport in phononic crystals. *JETP Lett.* **88**, 590–594 (2009).
51. Alden Mead, C. Molecular Kramers degeneracy and non-Abelian adiabatic phase factors. *Phys. Rev. Lett.* **59**, 161–164 (1987).
52. Zee, A. Non-Abelian gauge structure in nuclear quadrupole resonance. *Phys. Rev. A* **38**, 1–6 (1988).
53. Alden Mead, C. The geometric phase in molecular systems. *Rev. Mod. Phys.* **64**, 51–85 (1992).
54. Sugawa, S., Salces-Carcoba, F., Perry, A. R., Yue, Y. & Spielman, I. B. Second Chern number of a quantum-simulated non-Abelian Yang monopole. *Science* **360**, 1429–1434 (2018).
55. Bliokh, K. Y. Rodriguez-Fortuño, F. J. Nori, F. & Zayats, A. V. Spin–orbit interactions of light. *Nat. Photonics* **9**, 796–808 (2015).
56. Ma, L. B. et al. Spin–orbit coupling of light in asymmetric microcavities. *Nat. Commun.* **7**, 10983 (2016).
57. Dalibard, J., Gerbier, F., Juzeliūnas, G. & Öhberg, P. Artificial gauge potentials for neutral atoms. *Rev. Mod. Phys.* **83**, 1523–1543 (2011).
58. Goldman, N., Juzeliūnas, G., Öhberg, P. & Spielman, I. B. Light-induced gauge fields for ultracold atoms. *Rep. Prog. Phys.* **77**, 126401 (2014).
59. Wu, Z. et al. Realization of two-dimensional spin–orbit coupling for Bose–Einstein condensates. *Science* **354**, 83–88 (2016).
60. Huang, L. et al. Experimental realization of two-dimensional synthetic spin–orbit coupling in ultracold Fermi gases. *Nat. Phys.* **12**, 540–544 (2016).
61. Aidelsburger, M., Nascimbene, S. & Goldman, N. Artificial gauge fields in materials and engineered systems. *C. R. Phys.* **19**, 394–432 (2018).
62. Chen, Y. et al. Non-Abelian gauge field optics. *Nat. Commun.* **10**, 3125 (2019).
63. Yang, Y. et al. Synthesis and observation of non-Abelian gauge fields in real space. *Science* **365**, 1021–1025 (2019).
64. Leinaas, J. M. & Myrheim, J. On the theory of identical particles. *Nuovo Cimento B* **37**, 1–23 (1977).
65. Wilczek, F. Quantum mechanics of fractional-spin particles. *Phys. Rev. Lett.* **49**, 957–959 (1982).
66. Fröhlich, J. in *Nonperturbative Quantum Field Theory* (eds ’t Hooft, G. et al.) 71–100 (Springer, 1988).
67. Wen, X. G. Non-Abelian statistics in the fractional quantum Hall states. *Phys. Rev. Lett.* **66**, 802–805 (1991).
68. Moore, G. & Read, N. Nonabelions in the fractional quantum Hall effect. *Nucl. Phys. B* **360**, 362–396 (1991).
69. Nayak, C., Simon, S. H., Stern, A., Freedman, M. & Das Sarma, S. Non-Abelian anyons and topological quantum computation. *Rev. Mod. Phys.* **80**, 1083–1159 (2008).
70. Arovas, D., Schrieffer, J. R. & Wilczek, F. Fractional statistics and the quantum Hall effect. *Phys. Rev. Lett.* **53**, 722–723 (1984).
71. Lahtinen, V. & Pachos, J. K. Non-Abelian statistics as a Berry phase in exactly solvable models. *New J. Phys.* **11**, 093027 (2009).
72. Noh, J. et al. Braiding photonic topological zero modes. Preprint at <https://arxiv.org/abs/1907.03208> (2019).
73. Maldovan, M. Sound and heat revolutions in phononics. *Nature* **503**, 209–217 (2013).
74. Born, M. et al. *Principles of Optics* (Cambridge Univ. Press, 1999).
75. Karplus, R. & Luttinger, J. M. Hall effect in ferromagnetics. *Phys. Rev.* **95**, 1154–1160 (1954).
76. Arovas, D., Schrieffer, J. R. & Wilczek, F. Fractional statistics and the Hofstadter spectrum: semiclassical dynamics in magnetic Bloch bands. *Phys. Rev. B* **53**, 7010–7023 (1996).
77. Sundaram, G. & Niu, Q. Wave-packet dynamics in slowly perturbed crystals: gradient corrections and Berry-phase effects. *Phys. Rev. B* **59**, 14915–14925 (1999).
78. Panati, G., Spohn, H. & Teufel, S. Effective dynamics for Bloch electrons: Peierls substitution and beyond. *Commun. Math. Phys.* **242**, 547–578 (2003).
79. Chang, M.-C. & Niu, Q. Berry curvature, orbital moment, and effective quantum theory of electrons in electromagnetic fields. *J. Phys. Condens. Matter* **20**, 193202 (2008).
80. Zener, C. A theory of the electrical breakdown of solid dielectrics. *Proc. R. Soc. A* **145**, 523–529 (1934).
81. Mendez, E. E. & Bastard, G. Wannier–Stark ladders and Bloch oscillations in superlattices. *Phys. Today* **46**, 34–42 (1993).
82. Raizen, M., Salomon, C. & Niu, Q. New light on quantum transport. *Phys. Today* **50**, 30–34 (1997).
83. Price, H. M. & Cooper, N. R. Mapping the Berry curvature from semiclassical dynamics in optical lattices. *Phys. Rev. A* **85**, 033620 (2012).
84. Atala, M. et al. Direct measurement of the Zak phase in topological Bloch bands. *Nat. Phys.* **9**, 795–800 (2013).
85. Jotzu, G. et al. Experimental realization of the topological Haldane model with ultracold fermions. *Nature* **515**, 237–240 (2014).
86. Aidelsburger, M. et al. Measuring the Chern number of Hofstadter bands with ultracold bosonic atoms. *Nat. Phys.* **11**, 162–166 (2014).
87. Flaschner, N. et al. Experimental reconstruction of the Berry curvature in a Floquet Bloch band. *Science* **352**, 1091–1094 (2016).
88. Li, T. et al. Bloch state tomography using Wilson lines. *Science* **352**, 1094–1097 (2016).

**Acknowledgements** We thank B. Bradlyn, V. Cheianov, S. Huber, W. Irvine, P. Lidon, N. Mitchell, S. Ryu, C. Scheibner, D. Son, A. Souslov, P. Wiegmann and B. van Zuiden for discussions. V.V. was supported by the Complex Dynamics and Systems Program of the Army Research Office under grant no. W911NF-19-1-0268. M.F. was primarily supported by the Chicago MRSEC (US NSF grant DMR 1420709) through a Kadanoff–Rice postdoctoral fellowship and acknowledges partial support by the University of Chicago through a Big Ideas Generator (BIG) grant and the Netherlands Organization for Scientific Research (NWO/OCW) as part of the Frontiers of Nanoscience program. LEGO is a trademark of the LEGO Group of companies which does not sponsor, license or endorse its use in this work.

**Author contributions** M.F. and V.V. designed the research, performed the research, and wrote the paper. Y.Z. and M.F. fabricated the mechanical kagome lattices. All authors contributed to discussions and manuscript revision.

**Competing interests** The authors declare no competing interests.

### Additional information

**Supplementary information** is available for this paper at <https://doi.org/10.1038/s41586-020-1932-6>.

**Correspondence and requests for materials** should be addressed to M.F. or V.V.

**Peer review information** *Nature* thanks Muamer Kadac, Ronny Thomale and the other, anonymous, reviewer(s) for their contribution to the peer review of this work.

**Reprints and permissions information** is available at <http://www.nature.com/reprints>.

# Fully hardware-implemented memristor convolutional neural network

<https://doi.org/10.1038/s41586-020-1942-4>

Received: 25 November 2018

Accepted: 25 October 2019

Published online: 29 January 2020

Peng Yao<sup>1</sup>, Huaqiang Wu<sup>1,2\*</sup>, Bin Gao<sup>1,2</sup>, Jianshi Tang<sup>1,2</sup>, Qingtian Zhang<sup>1</sup>, Wenqiang Zhang<sup>1</sup>, J. Joshua Yang<sup>3</sup> & He Qian<sup>1,2</sup>

Memristor-enabled neuromorphic computing systems provide a fast and energy-efficient approach to training neural networks<sup>1–4</sup>. However, convolutional neural networks (CNNs)—one of the most important models for image recognition<sup>5</sup>—have not yet been fully hardware-implemented using memristor crossbars, which are cross-point arrays with a memristor device at each intersection. Moreover, achieving software-comparable results is highly challenging owing to the poor yield, large variation and other non-ideal characteristics of devices<sup>6–9</sup>. Here we report the fabrication of high-yield, high-performance and uniform memristor crossbar arrays for the implementation of CNNs, which integrate eight 2,048-cell memristor arrays to improve parallel-computing efficiency. In addition, we propose an effective hybrid-training method to adapt to device imperfections and improve the overall system performance. We built a five-layer memristor-based CNN to perform MNIST<sup>10</sup> image recognition, and achieved a high accuracy of more than 96 per cent. In addition to parallel convolutions using different kernels with shared inputs, replication of multiple identical kernels in memristor arrays was demonstrated for processing different inputs in parallel. The memristor-based CNN neuromorphic system has an energy efficiency more than two orders of magnitude greater than that of state-of-the-art graphics-processing units, and is shown to be scalable to larger networks, such as residual neural networks. Our results are expected to enable a viable memristor-based non-von Neumann hardware solution for deep neural networks and edge computing.

CNNs have become one of the most important deep neural networks (DNNs)<sup>5</sup> and play a vital role in image-processing-related tasks, such as image recognition<sup>11</sup>, image segmentation and object detection<sup>12</sup>. A typical computing procedure for a CNN involves a large number of sliding convolutional operations. In this respect, computing units that support parallel multiply–accumulate (MAC) calculations are highly desired. Such demand has led to the redesign of conventional computing systems to operate CNNs with higher performance and lower power consumption, ranging from general application platforms, such as graphics-processing units (GPUs)<sup>13</sup>, to application-specific accelerators<sup>14,15</sup>. However, further improvements in computing efficiency will ultimately be constrained by the von Neumann architecture of these systems, in which the physical separation of memory and processing units results in substantial energy consumption and large latency in data shuffling between units<sup>16</sup>. By contrast, memristor-enabled neuromorphic computing provides a promising non-von Neumann computing paradigm in which the data are stored, thus eliminating the cost of data transfer<sup>1,2</sup>. By directly using Ohm's law for multiplication and Kirchhoff's law for accumulation, a memristor array is capable of implementing parallel in-memory MAC operations, leading to analogue in-memory computing with greatly improved speed and energy efficiency<sup>3</sup>.

Studies on memristor-based neuromorphic computing have covered a broad range of topics, from device optimization to system implementation<sup>6,17–23</sup>. Several experimental demonstrations<sup>4,24–28</sup> related to practical applications of in-memory computing have been reported as well. The most recent studies report the demonstrations of two-layer<sup>4</sup> and three-layer<sup>27</sup> memristor multi-layer perceptrons for image recognition using the MNIST (Modified National Institute of Standards and Technology) handwritten-digit database<sup>10</sup>. However, a complete CNN, which is essential for more complex image-recognition tasks, has not yet been demonstrated in a fully memristor-based hardware system. The reason mainly pertains to the lack of an efficient solution for the implementation<sup>27</sup> of a memristor-based CNN (mCNN): first, the fabricated mCNN usually suffers from a poor yield and non-uniformity of memristor crossbar arrays<sup>4,7,8</sup>. Second, it is difficult to achieve a performance (for example, image-recognition accuracy) comparable to software results owing to device imperfections, such as variations, conductance drift and device state locking<sup>6–9</sup>. Third, the key convolutional operation in CNNs is time-consuming because of the need to slide over different input patches, which is usually a sequential process and results in speed mismatch between the memristor convolver and the memristor array for fully connected vector–matrix multiplication (VMM).

<sup>1</sup>Institute of Microelectronics, Beijing Innovation Center for Future Chips (ICFC), Tsinghua University, Beijing, China. <sup>2</sup>Beijing National Research Center for Information Science and Technology (BNRist), Tsinghua University, Beijing, China. <sup>3</sup>Department of Electrical and Computer Engineering, University of Massachusetts, Amherst, MA, USA. \*e-mail: wuhq@tsinghua.edu.cn

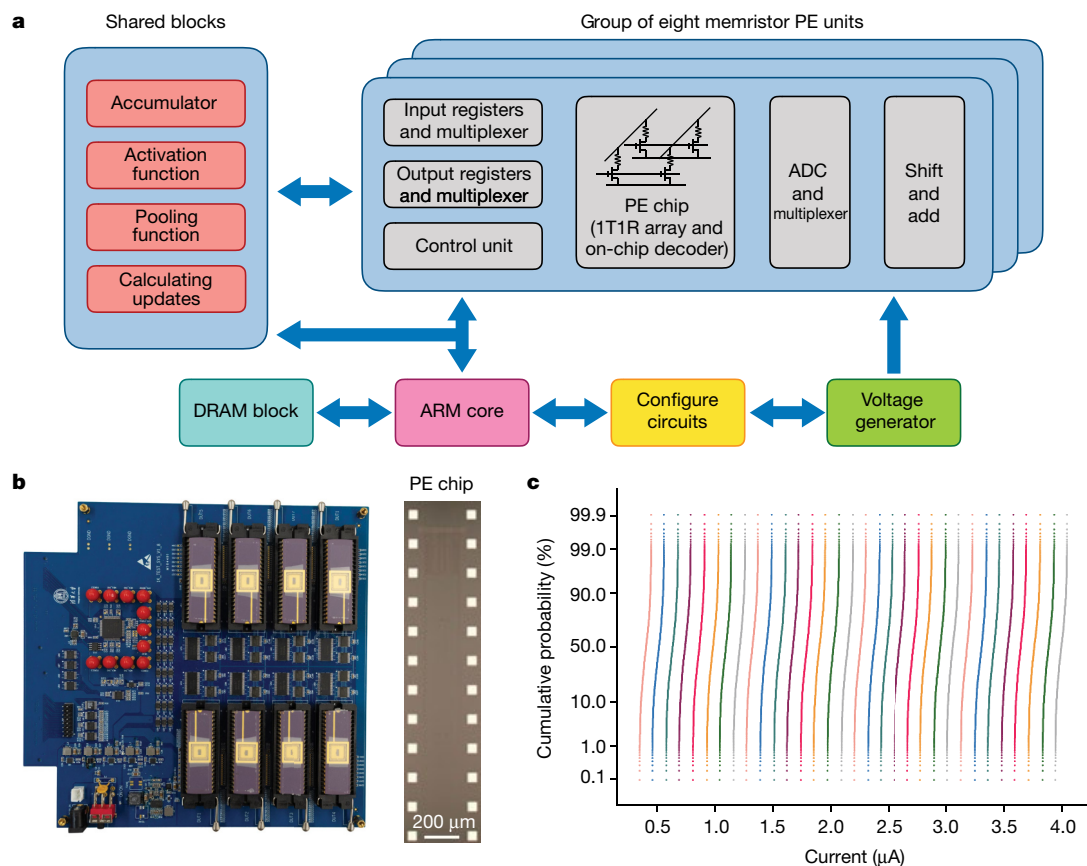


**Fig. 1 | Memristor-based hardware system with reliable multi-level conductance states.** **a**, Schematic of the system architecture with eight integrated memristor PE units and other functional blocks. DRAM, dynamic random-access memory; ARM core, control unit with ARM (Acorn RISC Machine) architecture. **b**, Left, photograph of the integrated PCB subsystem, also known as the PE board. Right, image of a partial PE chip consisting of a 2,048-memristor array and on-chip decoder circuits. **c**, Cumulative probability

distribution of 1,024 cells with respect to 32 independent conductance states. The conductance is equivalently represented by the read-out current under a 0.2-V voltage pulse. For programming, the SET conditions were  $V_{WL} = 1.8$  V for the word-line voltage,  $V_{BL} = 2.0$  V (50 ns pulse) for the bit-line voltage and  $V_{SL} = 0$  V for the source-line voltage; the RESET conditions were  $V_{WL} = 4.7$  V,  $V_{BL} = 0$  V and  $V_{SL} = 1.8$  V (50 ns pulse).

In this study, a complete five-layer mCNN for MNIST digit image recognition was successfully demonstrated. The optimized material stacks enabled reliable and uniform analogue switching behaviours in 2,048 one-transistor–one-memristor (1T1R) arrays. With the proposed hybrid-training scheme, the experimental recognition accuracy reached 96.19% for the entire test dataset. Furthermore, replication of the convolutional kernels to three parallel memristor convolvers was implemented to reduce the mCNN latency roughly by a factor of 3. Our highly integrated neuromorphic system provides a feasible solution to substantially improve the CNN efficiency by closing the throughput gap between memristor-based convolutional computation and fully connected VMM.

Realizing a practical memristor-based neuromorphic computing system usually requires the integration of multiple memristor crossbar arrays. In general, splitting the weights into different arrays is beneficial for parallel computing, which is increasingly needed with increasing network scales. However, previous memristor-based demonstrations relied on a single array<sup>4,24–26</sup>, mainly because of the challenge of producing highly repeatable arrays. The variability and non-ideal characteristics of memristive devices are considered as substantial hurdles to the application of neuromorphic computing<sup>7–9</sup>.

Here we propose a versatile memristor-based computing architecture for neural networks, shown in Fig. 1a. The memristor cell uses a material stack of TiN/TaO<sub>x</sub>/HfO<sub>x</sub>/TiN, and shows continuous conductance-tuning capability (see Supplementary Information) in both potentiation (SET) and depression (RESET) by modulating the electric

field and heat<sup>29</sup>. The materials and fabrication process (see Methods for details) are compatible with the conventional CMOS (complementary metal–oxide semiconductor) process, so that the memristor arrays can be conveniently built in the back end of line in a silicon fab to reduce process variations and achieve high reproducibility. The fabricated crossbar arrays exhibit uniform analogue switching behaviours under identical programming conditions. Hence, a multiple-memristor-array hardware system (see Supplementary Information) was built using a customized printed circuit board (PCB) and a field-programmable gate array evaluation board (ZC706, Xilinx). As the system schematic shows, the system mainly consists of eight memristor-based processing elements (PEs). Each PE has its own integrated 2,048-cell memristor array. Each memristor is connected to the drain terminal of a transistor, namely, in a 1T1R configuration (see Supplementary Information). The core PCB subsystem with eight memristor array chips is presented in Fig. 1b. Each memristor array (right inset of Fig. 1b) has an assembly of  $128 \times 16$  1T1R cells. There are 128 parallel word lines and 128 source lines horizontally, and 16 bit lines vertically (see Methods for details). This array exhibits remarkably repeatable multi-level conductance states, as shown by the test results in Fig. 1c and the measured data from the remaining 2,048-cell arrays in Extended Data Fig. 1. Figure 1c shows the distribution of 1,024 memristors in 32 different conductance states, where all the curves are separated without any overlap. Identical SET and RESET pulse trains with a pulse width of 50 ns were employed in the closed-loop programming<sup>24</sup> operations to reach a certain conductance state. The measurement flow is described in Methods.



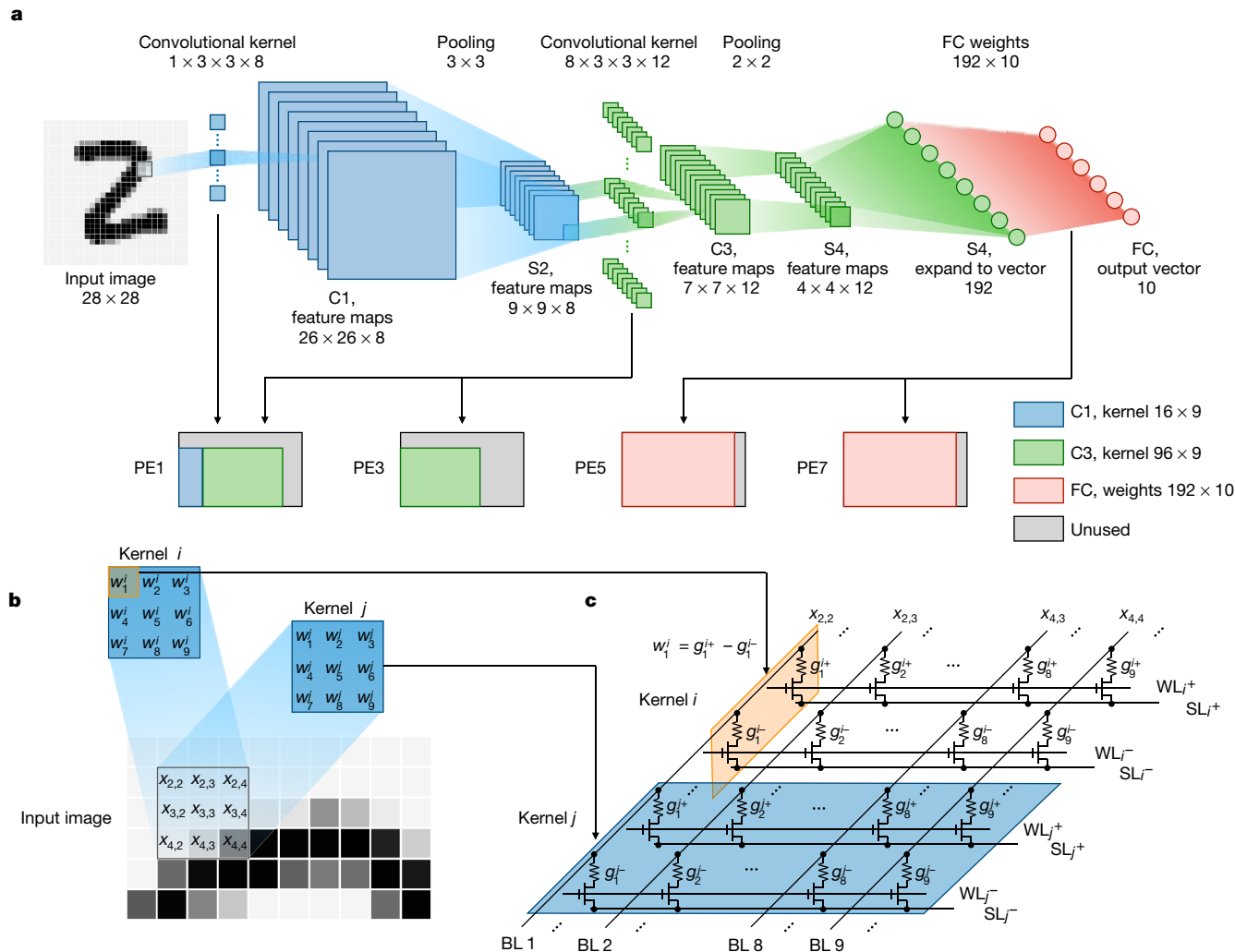


**Fig. 2 | Five-layer mCNN with memristor convolver.** **a**, Structure of the five-layer mCNN used for MNIST image recognition, with alternating convolutional (C1, C3) and subsampling (S2, S4) layers. The input is a  $28 \times 28$  greyscale (8-bit) digit image. The mapping relations between the weights of different layers and the independent PEs are illustrated (see Methods for details). The top labels give the kernel size (input channel depth  $\times$  filter height  $\times$  filter width  $\times$  filter batch size) for C1 and C3, the pooling size for S2 and S4 and the weight size for the FC layer (input neuron number  $\times$  output neuron number). The bottom labels provide the feature map dimension (height  $\times$  width  $\times$  channel depth) or the vector dimension. **b**, Typical convolutional case during the slipping

process. The grey box in the image confines the input patch of this sample case.  $x_{m,n}$  indicates the relevant pixel at the crossing of row  $m$  and column  $n$ . Kernels  $i$  and  $j$  each have a total of  $3 \times 3$  weights. **c**, The equivalent memristor convolver of the convolutional operation in **b**. Throughout the entire parallel computing process, all word lines (WL) are set to  $V_{wl} = 4.5$  V. The injected bit line (BL) pulses are 0.2 V, and the source lines (SL) are clamped at 0 V.  $w$  represents the element value in the weight matrix, and  $g^+$  and  $g^-$  represent the device conductance values for the positive and negative weights in the differential pair, respectively.

As shown in Fig. 2a, a five-layer CNN was constructed on a memristor-based hardware system to recognize MNIST handwritten-digit images. The detailed data flow in the CNN and the corresponding memristor mapping are described in Methods.

Realizing memristor-based convolutional operations requires performing sliding operations with various kernels. Memristor arrays are highly efficient in achieving parallel MACs under shared inputs for different kernels<sup>22</sup>. Figure 2b shows a typical convolution example at a particular slipping step, and Fig. 2c reveals the associated events in the 1T1R memristor array. The input value is encoded by the pulse number according to its quantized bit number (Extended Data Fig. 2). A signed kernel weight is mapped to the differential conductance of a pair of memristors. In this manner, all the weights of a kernel are mapped to two conductance rows: one row for positive weights with positive pulse inputs and the other for negative weights with equivalent negative pulse inputs. After inputting the encoded pulses into the bit lines, the output currents through the two differential source lines are sensed

and accumulated. The differential current is the weighted sum corresponding to the input patch and the chosen kernel. Different kernels with different weights are mapped to different pairs of differential rows, and the entire memristor array operates MACs in parallel under the same inputs. All the desired weighted-sum results are obtained concurrently.

In typical CNN training, it is necessary to propagate the objective derivative backwards with respect to the last outputs, to determine all weight updates<sup>10</sup>. This task requires highly complex operations to apply encoded read pulses to source lines from back to front and layer by layer. Furthermore, it is challenging to train a complicated memristor DNN, owing to non-ideal device characteristics, such as nonlinearity and asymmetric conductance tuning<sup>6,27</sup>. In contrast to the pure in situ training solution, the ex situ training method appears to be a shortcut that takes advantage of existing high-performing parameters. However, inevitable hardware imperfections, such as defective devices and parasitic wire resistance and capacitance, would blur the weights and degrade the system performance

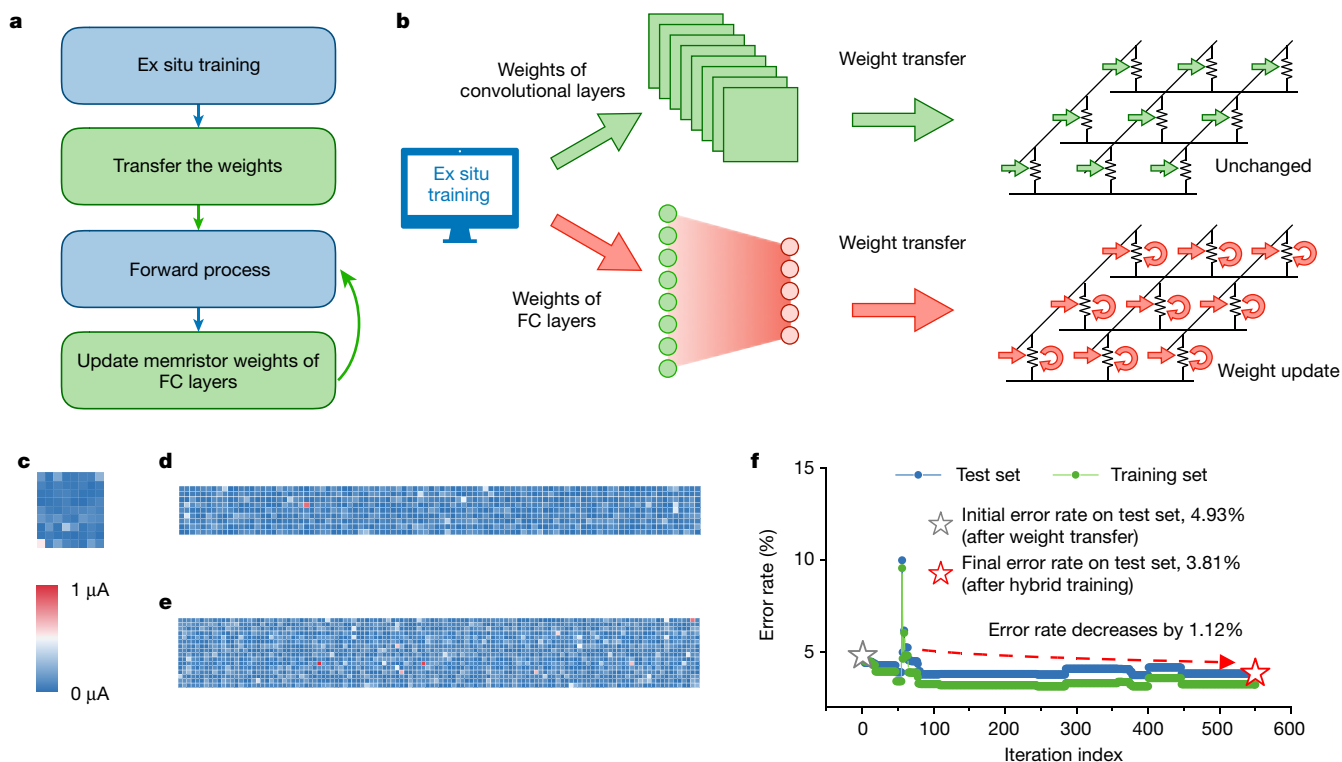


**Fig. 3 | Hybrid training on the mCNN.** **a**, Flowchart of the hybrid-training method used in this experimental demonstration. **b**, Diagram of the experimental mCNN demonstration with hybrid training. First, the system transfers the kernel weights of different convolutional layers and the  $192 \times 10$  FC weights to the memristor PEs. Next, the system maintains the kernel weights unchanged and updates only the FC weights through in situ training. **c–e**,

Distributions of weight-transfer error compared with the target values for the kernel weights in the C1 layer (**c**;  $8 \times 9$  in size), C3 layer (**d**;  $96 \times 9$  in size) and FC layer (**e**;  $120 \times 16$  in size). The colour bar shows the absolute value of weight-transfer error. **f**, Error-rate traces over 550 hybrid-training iteration cycles. The green curve indicates the trend for the 55,000 training images, and the blue curve shows the trend for the 10,000 test images.

when transferring the ex situ learned weights to memristor conductances<sup>4</sup>. Therefore, ex situ training normally requires prior knowledge of the hardware situation and learns weights on the basis of this costly awareness using software.

To circumvent various non-ideal device characteristics, a hybrid-training method is proposed to implement the mCNN. The entire flowchart, illustrated in Fig. 3a, includes two stages. First a CNN model is trained ex situ, and then all the determined weights are transferred to the memristor PEs by a closed-loop writing method. In the next step, the external input propagates forwards through the mCNN, and only the last fully connected (FC) layer is trained in situ afterwards to tune the memristor conductance. It should be pointed out that the proposed hybrid learning method is different from typical transfer learning<sup>27,30</sup>. Hybrid training aims to accommodate the device variations in the previous layers to implement the parallel mCNN efficiently through the in situ training of the memristor weights, whereas transfer learning typically retrains the weights of the FC layers (hereafter, FC weights) using software to obtain knowledge on a new dataset.

Here the hybrid-training technique emphasizes the training of FC weights to compensate for existing device imperfections, and it could be extended as a generic system approach to address device variations and other non-ideal device characteristics by in situ tuning of some memristor weights. Hybrid training is applicable to a wide range of neural network models and could be used to address non-ideal device characteristics regardless of the specific type of memristor device. However, it is worth mentioning that, compared with traditional ex situ training, hybrid training requires fetching the training data to realize in situ conductance tuning; therefore, additional memory blocks or data-transmission modules might be required.

A memristor model is established to validate that the in situ training of only the FC layer is generally adequate for compensating for device

imperfections and that it yields remarkable generalization results (see Methods for details). In this manner, hybrid training uses the advantages of both ex situ and in situ training, which complement each other.

To realize an mCNN with hybrid training (Fig. 3b), a model (Fig. 2a) was trained ex situ in Python with TensorFlow on a training set containing 55,000 images. The recognition accuracy for the 10,000 test digit images was 97.99%, which was taken as the baseline accuracy. The well trained weights were rescaled to meet the unified memristor conductance window and quantized from 32-bit floating type to 15-level fixed-point type (see Methods for details). Reasonable weight quantization caused a tolerable performance degradation; for example, the 4-bit quantization of kernel weights and 2-bit quantization of the FC weights for a typical CNN model, AlexNet, was shown to induce a 2.60% increase in the recognition error for ImageNet (a widely used image database for visual object recognition) classification compared with the 32-bit quantization of kernel weights and FC weights<sup>31</sup>. The quantization of the 15-level fixed point relaxed the conductance mapping requirements to speed up weight transfer, and ensured a high recognition accuracy of 96.92%, close to the software baseline.

Subsequently, the quantized kernel weights of the convolutional layers and the weights of the FC layer were transferred to the corresponding memristor conductance (Fig. 2a). The weight-transfer accuracy distributions of the convolutional layers C1 and C3 and the FC layer are shown in Fig. 3c–e. The error distributions probably arise from device variations, conductance drift and state locking. The memristor hardware system still achieves a recognition accuracy of 95.07% (see Methods for details) on the 10,000 test images—a 2.92% accuracy loss compared with the baseline value of 97.99%. After an epoch of 550 training iterations (a mini-batch of 100 training images was fed into the mCNN for one iteration) on the entire training database, the recognition error rate for the 10,000 test images decreased considerably from the

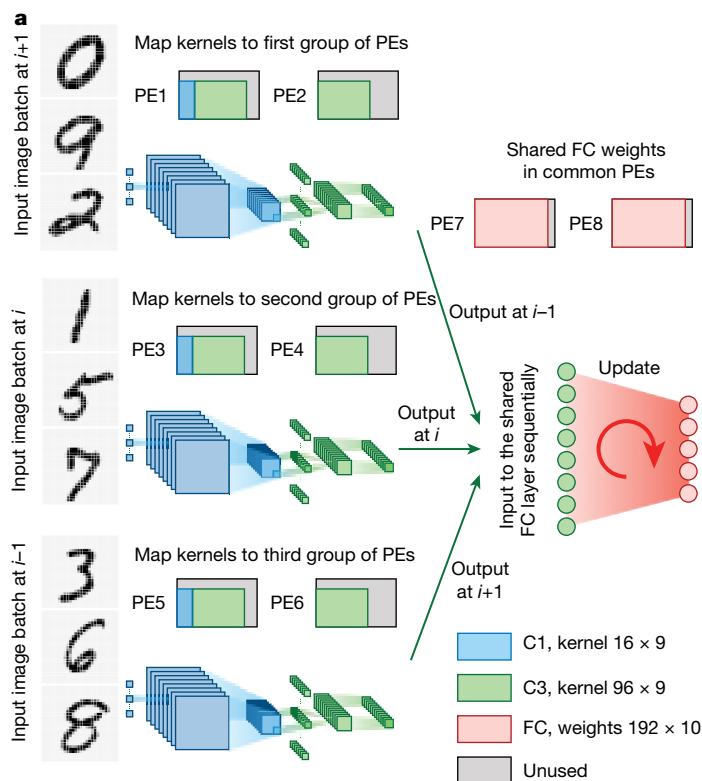


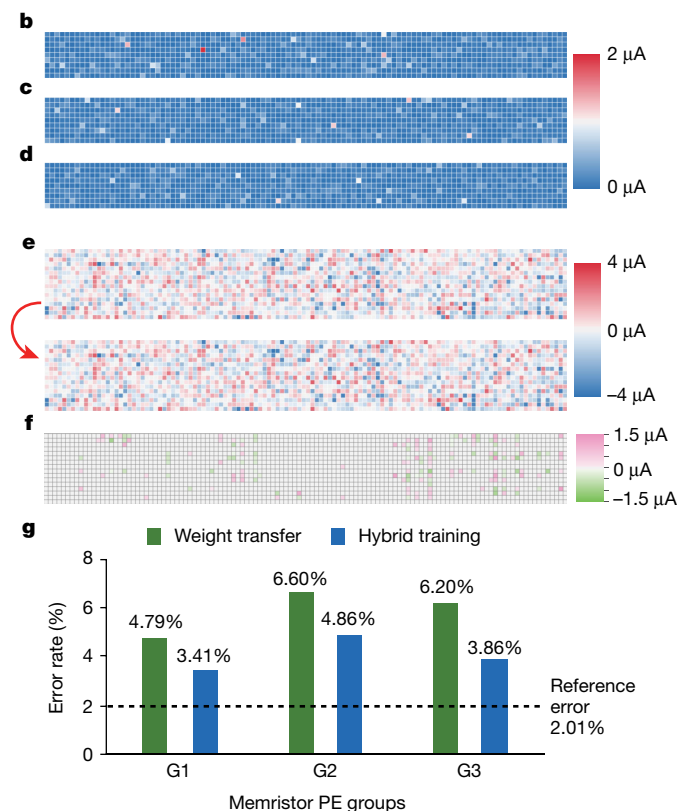
**Fig. 4 | Parallel memristor convolvers with hybrid training for improving convolutional efficiency.** **a**, Sketch of the hardware system operation flow with hybrid training used to accommodate non-ideal device characteristics for parallel memristor convolvers. Three batches of input images (handwritten digits on the left) are fed into three PE convolver groups. All the processed intermediate data are fed into the shared FC PEs to complete the in situ tuning. In the neural network schematic, the blue part represents convolutional layer C1 and subsampling layer S2, and the green part represents convolutional layer C3 and subsampling layer S4. In the PE diagram, the blue region represents the kernels of the C1 layer and the green region represents the kernels of C3 layer.

initial value of 4.93% to the final value of 3.81% (Fig. 3f). The error rate on the training set also dropped from 4.82% to 3.21%.

In a memristor-based neuromorphic computing system, the accuracy loss is mainly attributed to two factors: first, the presence of non-ideal device characteristics, such as device variations, array yield problems and device reliability issues; second, the limited precision due to weight quantization. Even though the accuracy is not fully recovered given the limited quantization precision, the experimental results suggest that the hybrid-training method could effectively recover high recognition accuracy by accommodating device variations across different memristor crossbars. It should be emphasized that in this in situ training process, only the FC weights are updated in an analogue fashion, instead of retraining all the conductance weights. The detailed training procedure is described in Methods.

Further experiments were conducted to show the effect of conductance drift on system performance (see Methods and Extended Data Fig. 3). According to the test results, the reliability of multiple conductance states needs to be further investigated and improved by material and device engineering, which remains an active research area.

Although a memristor convolver can realize the different kernels of a convolutional layer in parallel under shared inputs (Fig. 2b), operating an mCNN remains time-consuming owing to the need to provide different patches of input during the sliding process. Considering that memristor-based MAC computing is more efficient and straightforward when used as the VMM of the FC layer, the severe speed mismatch between the memristor FC implementation and the memristor



**b–d**, Weight-transfer error distributions for the mapping from the ex situ-trained kernel weights of the C1 and C3 layers onto three different groups: G1 (**b**), G2 (**c**) and G3 (**d**). The size of the colour map is  $104 \times 9$ . The colour bar represents the error in the transferred current values at a 0.2-V read pulse. **e**, Evolution of experimental FC weight distributions ( $120 \times 16$ ) before (top) and after (bottom) hybrid training. **f**, Distribution of conductance-weight changes corresponding to **e**. **g**, The error rate obtained on the test set after hybrid training is considerably lower than that measured immediately after weight transfer for each convolver group.

convolver<sup>27</sup> would induce sizeable efficiency loss. Replicating the same group of weights in multiple parallel memristor arrays appears to be a promising way to recognize an input image efficiently in an mCNN. Spatial parallelism of the memristor convolvers could expedite convolutional sliding tremendously. In practice, transferring the same weights to multiple parallel memristor convolvers is challenging because of unpredictable and inevitable device variations, conductance drift and state locking<sup>6–9</sup>, which would induce unavoidable and random mapping error distributions. This process could result in substantial system generalization loss and is therefore considered as a major bottleneck for the realization of an efficient mCNN<sup>27</sup>.

A five-layer CNN with three duplicated parallel convolvers on the eight memristor PEs was successfully established in our full hardware system. Hybrid training was again used to address the non-ideal device characteristics. The approach used to perform hybrid training in the parallel operating scheme is sketched in Fig. 4a. In the beginning, the ex situ trained weights were transferred to all eight memristor PEs. Specifically, the kernel weights of the C1 and C3 layers were mapped to three independent groups of PEs. All three parallel memristor convolvers were connected to common PEs of shared FC weights. The specific mapping details are shown in Fig. 4a. Figure 4b, c, d shows the accuracy distributions of the total kernel weights (both C1 and C3 layers) after the weight transfer with respect to the first, second and third groups of PEs. It is clear that inevitable mapping errors exist in each group. The subsequent in situ training of the FC weights (see Methods for details) compensates for the device imperfections naturally. We ran 100 rounds



(that is, 300 batches) to reach a stable recognition accuracy. Figure 4e illustrates the transition of the FC conductance weights before and after the in situ training, and Fig. 4f presents the related distribution of the change in FC weights. After the in situ training of the FC memristors, the error rate decreased accordingly. Figure 4g shows that the error rates with respect to the memristor PE groups G1, G2 and G3 decreased from 4.79%, 6.60% and 6.20% to 3.41%, 4.86% and 3.86%, respectively (see Extended Data Fig. 4 for results on the training set). By dividing one input into three fraction regions uniformly from top to bottom, the parallel memristor convolvers could accelerate the forward process on a single image. The three convolvers operated on their associated input parts simultaneously, and their outputs were fed together into the FC layer to complete the classification. The experimental results show that hybrid training could boost the recognition accuracy on the 10,000 test images from 93.86% to 95.83%. Moreover, we carefully evaluated the hardware performance of memristor-based neuromorphic computing using the experimental data (see Methods, Extended Data Fig. 5 and Extended Data Tables 1, 2). The performance benchmark of the memristor-based neuromorphic computing system shows 110 times better energy efficiency ( $11,014 \text{ GOP s}^{-1} \text{ W}^{-1}$ ;  $1 \text{ GOP} = 10^9$  operations) and 30 times better performance density ( $1,164 \text{ GOP s}^{-1} \text{ mm}^{-2}$ ) compared with Tesla V100 GPU<sup>27</sup>. It should be mentioned that some necessary functional blocks (such as the pooling function, the activation function, and the routing and buffering of data between different neural-network layers) were not considered in the comparison. These blocks could be integrated monolithically with the memristor arrays in the future and accounted for in the energy efficiency calculation.

These findings suggest that the parallel memristor convolvers are highly efficient in achieving a high recognition accuracy while greatly accelerating the mCNN. In addition, the method of replicating the same kernels to different memristor convolvers could be scalable to larger CNN models to boost the parallel computing efficiency. The associated expenditure of chip area could be minimized in the future by employing high-density integration of memristors<sup>32,33</sup>. A standard residual neural network, ResNET-56<sup>11</sup>, with a compact memristor model was explored on the CIFAR-10 database and exhibited only a slight accuracy drop of 1.49% compared with the software baseline of 95.57% (see Methods and Extended Data Fig. 6).

Here, we proposed a hybrid training method to maintain high training efficiency and accuracy in a multiple-crossbar memristor CNN system. We should mention that although a small subset of the training data is sufficient in hybrid training, additional memory or data-transfer modules might be required. Moreover, a higher weight quantization precision is needed to fully recover the system accuracy, but at the cost of more hardware resources. Meanwhile, the system performance could be further enhanced by optimizing the peripheral circuits—especially the analogue-to-digital converter (ADC) blocks—and improving device reliability.

In summary, we have experimentally demonstrated a complete mCNN with hybrid training and parallel computing on multiple memristor arrays. The hybrid-training method is a generic system-level solution that accommodates non-ideal device characteristics across different memristor crossbars for various neural networks, regardless of the type of memristor device. The parallel convolution technique, which replicates weights to multiple memristor arrays, is proposed to eliminate the throughput gap between memristor-based convolutional computation and fully connected VMM. Generally, this technique could be extended to other memristor-based neuromorphic systems to efficiently boost their overall performance. The benchmark of our memristor-based neuromorphic computing system shows more than two orders of magnitude better power efficiency and one order of magnitude better performance density compared with Tesla V100 GPU. We expect that the proposed approach will enable the development of more powerful memristor-based neuromorphic systems.

## Online content

Any methods, additional references, Nature Research reporting summaries, source data, extended data, supplementary information, acknowledgements, peer review information; details of author contributions and competing interests; and statements of data and code availability are available at <https://doi.org/10.1038/s41586-020-1942-4>.

1. Ielmini, D. & Wong, H.-S. P. In-memory computing with resistive switching devices. *Nat. Electron.* **1**, 333–343 (2018).
2. Wong, H.-S. P. & Salahuddin, S. Memory leads the way to better computing. *Nat. Nanotechnol.* **10**, 191–194 (2015); correction **10**, 660 (2015).
3. Williams, R. S. What's next? *Comput. Sci. Eng.* **19**, 7–13 (2017).
4. Li, C. et al. Efficient and self-adaptive in-situ learning in multilayer memristor neural networks. *Nat. Commun.* **9**, 2385 (2018).
5. LeCun, Y., Bengio, Y. & Hinton, G. Deep learning. *Nature* **521**, 436–444 (2015).
6. Wu, H. et al. Device and circuit optimization of RRAM for neuromorphic computing. In *2017 IEEE Int. Electron Devices Meeting (IEDM)* 11.5.1–11.5.4 (IEEE, 2017).
7. Xia, Q. & Yang, J. J. Memristive crossbar arrays for brain-inspired computing. *Nat. Mater.* **18**, 309–323 (2019); correction **18**, 518 (2019).
8. Ding, K. et al. Phase-change heterostructure enables ultralow noise and drift for memory operation. *Science* **366**, 210–215 (2019).
9. Welser, J., Pitera, J. & Goldberg, C. Future computing hardware for AI. In *2018 IEEE Int. Electron Devices Meeting (IEDM)* 1.3.1–1.3.6 (IEEE, 2018).
10. LeCun, Y., Bottou, L., Bengio, Y. & Haffner, P. Gradient-based learning applied to document recognition. *Proc. IEEE* **86**, 2278–2324 (1998).
11. He, K., Zhang, X., Ren, S. & Sun, J. Deep residual learning for image recognition. In *Proc. IEEE Conference on Computer Vision and Pattern Recognition* 770–778 (IEEE, 2016).
12. Ren, S., He, K., Girshick, R. & Sun, J. Faster R-CNN: towards real-time object detection with region proposal networks. In *Advances in Neural Information Processing Systems* 91–99 (NIPS, 2015).
13. Coates, A. et al. Deep learning with COTS HPC systems. In *Proc. 30th Int. Conference on Machine Learning* 1337–1345 (PMLR, 2013).
14. Jouppi, N. P. et al. In-datacenter performance analysis of a tensor processing unit. In *Proc. 44th Int. Symposium on Computer Architecture (ISCA)* 1–12 (IEEE, 2017).
15. Chen, Y.-H., Krishna, T., Emer, J. S. & Sze, V. Eyeriss: an energy-efficient reconfigurable accelerator for deep convolutional neural networks. *IEEE J. Solid-State Circuits* **52**, 127–138 (2017).
16. Horowitz, M. Computing's energy problem (and what we can do about it). In *2014 IEEE Int. Solid-State Circuits Conference Digest of Technical Papers (ISSCC)* 10–14 (IEEE, 2014).
17. Woo, J. et al. Improved synaptic behavior under identical pulses using  $\text{AlO}_x/\text{HfO}_2$  bilayer RRAM array for neuromorphic systems. *IEEE Electron Device Lett.* **37**, 994–997 (2016).
18. Burr, G. W. et al. Neuromorphic computing using non-volatile memory. *Adv. Phys. X* **3**, 89–124 (2017).
19. Yu, S. Neuro-inspired computing with emerging nonvolatile memories. *Proc. IEEE* **106**, 260–285 (2018).
20. Choi, S. et al. SiGe epitaxial memory for neuromorphic computing with reproducible high performance based on engineered dislocations. *Nat. Mater.* **17**, 335–340 (2018).
21. Burr, G. W. et al. Experimental demonstration and tolerancing of a large-scale neural network (165 000 synapses) using phase-change memory as the synaptic weight element. *IEEE Trans. Electron Dev.* **62**, 3498–3507 (2015).
22. Gao, L., Chen, P.-Y. & Yu, S. Demonstration of convolution kernel operation on resistive cross-point array. *IEEE Electron Device Lett.* **37**, 870–873 (2016).
23. Kumar, S., Strachan, J. P. & Williams, R. S. Chaotic dynamics in nanoscale  $\text{NbO}_2$  Mott memristors for analogue computing. *Nature* **548**, 318–321 (2017).
24. Yao, P. et al. Face classification using electronic synapses. *Nat. Commun.* **8**, 15199 (2017).
25. Prezioso, M. et al. Training and operation of an integrated neuromorphic network based on metal-oxide memristors. *Nature* **521**, 61–64 (2015).
26. Sheridan, P. M. et al. Sparse coding with memristor networks. *Nat. Nanotechnol.* **12**, 784–789 (2017).
27. Ambrogio, S. et al. Equivalent-accuracy accelerated neural-network training using analogue memory. *Nature* **558**, 60–67 (2018).
28. Serb, A. et al. Unsupervised learning in probabilistic neural networks with multi-state metal-oxide memristive synapses. *Nat. Commun.* **7**, 12611 (2016).
29. Gao, B. et al. Modeling disorder effect of the oxygen vacancy distribution in filamentary analog RRAM for neuromorphic computing. In *2017 IEEE Int. Electron Devices Meeting (IEDM)* 4.4.1–4.4.4 (IEEE, 2017).
30. Donahue, J. et al. DeCAF: a deep convolutional activation feature for generic visual recognition. In *2014 Int. Conference on Machine Learning* 647–655 (ACM, 2014).
31. Han, S., Mao, H. & Dally, W. J. Deep compression: compressing deep neural networks with pruning, trained quantization and Huffman coding. In *2016 International Conference on Learning Representations (ICLR)* (2016).
32. Xu, X. et al. Fully CMOS-compatible 3D vertical RRAM with self-aligned self-selective cell enabling sub-5-nm scaling. In *2016 IEEE Symposium on VLSI Technology* 84–85 (IEEE, 2016).
33. Pi, S. et al. Memristor crossbar arrays with 6-nm half-pitch and 2-nm critical dimension. *Nat. Nanotechnol.* **14**, 35–39 (2019).

**Publisher's note** Springer Nature remains neutral with regard to jurisdictional claims in published maps and institutional affiliations.

© The Author(s), under exclusive licence to Springer Nature Limited 2020

## Methods

### Fabrication of 1T1R memristor array

The fabricated memristor array has a 1T1R structure (see Supplementary Information) in which the memristor stacks are TiN/TaO<sub>x</sub>/HfO<sub>x</sub>/TiN. This array has a high operation speed of ~10 ns, a high yield (99.99%) and robust endurance performance.

All transistors and major metal interconnections and vias are fabricated in a standard CMOS foundry. The technology node is 130 nm. The back end of line—that is, the procedure used to complete the memristor stacks and the remaining top metal interconnections and vias—is processed in the laboratory. The bottom electrode layer of TiN, the switching layer of HfO<sub>x</sub>, the capping layer of TaO<sub>x</sub>, and the top electrode layer of TiN are deposited sequentially after receiving the wafers from the foundry. The capping layer is used as a thermally enhanced layer<sup>34</sup> to modulate the distribution of the electric field and heat in the switching layer for improved device behaviour. Afterwards, a lithographic process is adopted to form isolated 0.5 μm × 0.5 μm memristor stacks. Then, the SiO<sub>2</sub> dielectric is added and polished. The final steps of etching the vias, depositing aluminium and shaping the remaining interconnection patterns are performed to complete the fabrication process.

### Structure of memristor array

A PE chip (Fig. 1b) integrates on-chip encoder circuits and a 128 × 16 1T1R memristor array (see Supplementary Information). The memristor array is constructed by connecting the top electrodes of 128 memristor devices on the same column (that is, bit line) and the 16 transistor sources on the same row (that is, source line). The transistor gate ports facilitate fine memristor-conductance modulation by controlling the device's compliance current with a specific applied gate voltage. The gates in a row are connected to the same line (that is, word line), which is parallel to the source line. This memristor array acts as a pseudo-crossbar of two-port memristors by operating all transistors in the deep-triode region.

### Measurements of multi-level conductance states

To measure the reliability of multi-level conductance (see Fig. 1c) in the array, we used a closed-loop writing method with identical SET and RESET pulses. During the test, we supplied the programming pulses to 1,024 randomly chosen memristors from the array to reach 32 individual conductance targets. These target states were distributed within the switching window from 2 μS (that is, 0.4 μA at 0.2-V read voltage) to 20 μS (that is, 4 μA at 0.2-V read voltage) with a uniform interval of 0.58 μS (that is, 116 nA at 0.2-V read voltage). For any desired conductance state, such as  $I_t$  at a 0.2-V read voltage, we established the maximum programming pulse number to be 500. In addition, we set the defined target margin parameter  $\Delta I$  to be ±50 nA. When writing an individual cell to this conductance  $I_t$  from any initial state, we continuously applied operating pulses up to the maximum pulse number, and the real-time conductance value was sensed as  $I_{\text{read}}$  at a 0.2-V read voltage after each programming pulse. If  $I_{\text{read}}$  was within the desired range, from  $I_t - \Delta I$  to  $I_t + \Delta I$ , the procedure ended successfully. Otherwise, a subsequent SET or RESET pulse was applied accordingly (see Supplementary Information). This entire process was conducted repeatedly over the chosen memristors for the 32 conductance targets. The low-conductance switching range and succinct operation with identical programming pulses could be used to simplify the system design and achieve low-power monolithic integration.

### Structure of the five-layer CNN

As shown in Fig. 2a, a C1 layer measuring 26 × 26 × 8 (weight × height × depth) is acquired after convolution with kernel weights measuring 1 × 3 × 3 × 8 (depth × weight × height × batch). The result is subsampled by a pooling layer (S2), that uses a 3 × 3 max-pooling operation over the input with a sliding stride of 3. Then, a C3

layer is formed with 12 stacked feature maps after convolution with the 8 × 3 × 3 × 12 kernels. Another pooling layer (S4, 4 × 4 × 12) is subsequently formed using a 2 × 2 max-pooling operation with a stride of 2. Then, the expanding 192-element vector is passed into the FC layer to obtain the final 10 probability outputs, determining the class to which the input belongs. The inset (dashed box) clarifies how to map the total weights of different layers to memristor PE of the hardware system. In the experimental demonstration, 9 of 16 memristors in a row were used to realize a 3 × 3 kernel, and the residual cells remained unused. Hence, the 1 × 3 × 3 × 8 kernel weights of the C1 layer required 16 differential rows of memristors (PE1), and the 8 × 3 × 3 × 12 kernel weights of the C3 layer required 192 differential rows of memristors (PE1 and PE3). Owing to the limited number of memristors per row (that is, 16), we split the total 192 weights connected to an output neuron in the FC layer into 24 differential rows and gathered all the corresponding currents of the 12 positive weight rows and 12 negative weight rows (see Supplementary Information). Thus, we were able to map the total FC weights to PE5 (120 rows) and PE7 (120 rows) to carry out the equivalent VMM of the FC layer.

### mCNN demonstration

A typical CNN model is created by stacking convolutional and pooling layers repeatedly in series, followed by one or two FC layers at the end. Here we implemented a complete five-layer CNN with our memristor-based hardware system to recognize MNIST handwritten-digit images. The CNN model employed is shown in Fig. 2a. The model contains two convolutional layers, two pooling layers and one FC layer. The max-pooling and ReLU (rectified linear unit) activation functions are employed. The images in this dataset are categorized into 10 classes numbered 0 to 9. The input layer has 784 neurons, which is consistent with the number of pixels in the 28 × 28 input image. There are eight 3 × 3 kernel weights for the first convolutional layer (C1 layer in Fig. 2a) and twelve 3 × 3 × 8 kernel weights for the second convolutional layer (C3 layer in Fig. 2a). The convolutional operation is conducted by calculating the weight sums between the shared local kernel and the generated input patch of the input layer during continuous sliding with a fixed stride step. This operation could be decomposed into parallel MAC operations, which are naturally amenable to a memristor-based in-memory-computing architecture. The input patch is unrolled into a nine-dimensional vector. The hardware system then drives nine channels of pulses accordingly to be supplied to nine bit lines simultaneously. A weight is represented by two differential 1T1R memristor conductances, and thereby a kernel is mapped throughout to the corresponding positive and negative weight rows. The difference in the cumulative flowing currents through these two related source lines is precisely the desired weighted sum of the kernel weights and the input patch. The elements of the second pooling layer (S4 layer in Fig. 2a) are flattened and expended as a 192-dimensional vector to be passed into the last FC layer, and then the weighted-sum values are fed as the input of the softmax function to compute the classification probability. In this manner, the system leads to a map from the original digit image to the ten output probabilities of the last layer. Each output neuron is associated with a defined digital class. The largest among the outputs indicates that the CNN classifies the input image to the matching category accordingly. The associated pooling and ReLU activation functions, as well as the update-calculating modules (such as those computing softmax outputs and weight gradients), were realized by running the codes on ARM cores.

### Hybrid training on a subset of the training images

We trained the five-layer CNN model in Python and reached 97.99% recognition accuracy on the test set. The extracted memristor compact model was then used to validate that in situ learning of the FC conductance weights is generally adequate for tolerating device imperfections. After transferring the weights, the recognition accuracy dropped from

97.99% to 95.63% owing to the non-ideal memristor characteristics. Afterwards, all possible combinations of different layers of the weights were tuned—that is, we tried to train the FC weights only, the weights of C1 only, the weights of C3 only, the weights of the FC layer and the C3 layer together, etc. Five epochs of measurements were conducted on the entire training set for the arch trial. As shown in Extended Data Fig. 4b, tuning the FC conductance weights only is most efficient for regaining a remarkable generalization result. Essentially, this approach guarantees a high recognition accuracy and simplifies the original end-to-end training flow by skipping the backward propagation.

Furthermore, we experimentally validated that only a small subset of the training data is sufficient to recover the initial system accuracy using hybrid training, which helps to minimize the hardware resources needed for fetching training data. A five-layer CNN (shown in Fig. 2a) was employed to demonstrate that only 10% of the training dataset is enough to regain the high recognition accuracy of the system. Similarly to the experimental procedure, the trained weights were first transferred to the memristor PEs, and during the transfer some mapping errors were intentionally added by replacing 10% of the target weights with random values; accordingly, the recognition accuracy was reduced to 80.66%. Then 5,500 training images were randomly chosen from the total training dataset (that is, 10% of the 55,000 training images) to update the weights of the FC layer. After performing hybrid training as described in the main text, the accuracy was increased up to 94.40% after ten training epochs. To prove the robustness of our hybrid training technique, the experiment was conducted two more times, and the result is shown in Extended Data Fig. 6c.

Furthermore, a typical ResNET-56 model was used to validate that a small subset of the total training dataset is adequate for recovering the high initial accuracy of the system using hybrid training. The initial accuracy achieved using software was 95.57% (training with 32-bit single-precision floating-point weights), which was degraded to 89.64% after the quantization using 15-level weights. Subsequently, the quantized weights were mapped to the memristor arrays with the established device model in the weight-transfer stage, and the recognition accuracy dropped accordingly to 79.76%. Afterwards, we evaluated the system accuracy after hybrid training using 3% of the total training dataset, that is, 1,500 images from a total of 50,000 training samples. During the simulation, ten trials were made. The final result is plotted in Extended Data Fig. 6d, which depicts the recognition accuracy associated with the key phases of the whole simulation process. It was found that a small subset (3%) of the training data is enough to guarantee a high recognition accuracy (92%)—a 3.57% precision decline against the software result. This simulation result is consistent with the experimental results described above.

## The 15-level conductance weight

A 4-bit weight is generally sufficient to achieve a high recognition accuracy for CNNs<sup>31,35</sup>. In this work, an approximate 15-level fixed-point weight was adopted as the differential conductance of a pair of 8-level memristors. The smaller number of conductance states needed within the switching window leads to faster weight transfer because a larger target margin is permitted in the closed-loop writing. Writing an arbitrary 15-level fixed-point number to a differential pair of memristors obviously calls for a consistent ability to distinguish among eight conductance states in each device. In addition, such writing requires that these states be separated within the switching window over the same interval. During the corresponding experiment, the conductance was programmed from 2.5  $\mu\text{S}$  (0.5  $\mu\text{A}$  at a 0.2-V read pulse) up to 20  $\mu\text{S}$  (4  $\mu\text{A}$  at a 0.2-V read pulse) with a constant step of 2.5  $\mu\text{S}$ . The equivalent 15-level weight of the memristor pair was thus referred to the 15 individual differential conductance values that were uniformly distributed from negative 17.5  $\mu\text{S}$  (2.5  $\mu\text{S}$ –20  $\mu\text{S}$ ) to positive 17.5  $\mu\text{S}$  (20  $\mu\text{S}$ –2.5  $\mu\text{S}$ ). Moreover, the effect of read disturbance on the 15-level conductance weights after applying  $10^6$  read pulses (0.2 V) is investigated in Extended

Data Fig. 7. The experimental data from the array-level tests show that the read operations with the 0.2-V pulse do not disturb the conductance states markedly or systematically.

## Estimation of number of programming pulses and programming currents

It is critical to assess the required number of programming pulses in the closed-loop programming system to benchmark the system performance. To estimate the number of programming pulses required to stably converge the memristor to a desired conductance state, we randomly selected 24 rows of 1T1R memristor devices and programmed them to high conductance states, that is, >20  $\mu\text{S}$  (4.0  $\mu\text{A}$  at a 0.2-V read pulse). Afterwards, we divided these devices to eight groups, each with three rows. These eight groups of memristors were correspondingly written to eight different conductance states, from 0.5  $\mu\text{A}$  to 4.0  $\mu\text{A}$  with a uniform interval of 0.5  $\mu\text{A}$  under a read voltage of 0.2 V. The error margin was set as  $\pm 100$  nA for the eight states. Then the required pulse numbers were analysed statistically on the basis of the measured data, and they are shown in Extended Data Fig. 8a, b.

Even though the test only provides a rough estimation on the required number of programming pulses, it indicates that it strongly depends on the gap between the starting conductance and the desired state. The larger the gap is, the more pulses are needed. Besides, a higher programming resolution—for example, a greater number of required quantized conductance states within the switching window or a smaller desired error margin—would also require a larger number of pulses.

In addition, writing currents are crucial for system design, especially for the calculation of the system energy. However, the programming currents cannot be deduced directly based on the reading currents and writing voltages owing to the nonlinear current–voltage curve. To estimate the programming currents accurately, we swept the d.c. voltage on a single 1T1R cell to measure the write current.

The result is shown in Extended Data Fig. 8c, d. The SET current is around 60  $\mu\text{A}$  at 1.5 V and the RESET current is around 45  $\mu\text{A}$  at  $-1.2$  V. Both voltages are smaller than those measured during the pulse programming process in the array (that is, 2.0 V for SET pulse and  $-1.8$  V for RESET pulse). This is because the 50-ns pulse width used for pulse programming is much shorter than the voltage duration in the d.c. test.

## Evaluation of recognition accuracy

Although we have successfully demonstrated the mCNN using parallel operations, the test system crashes easily for long running periods owing to unstable interface connections—for example, the UART interface between the upper computer and lower computer and the FMC connector between the ZC706 board and the customized PE board (Supplementary Information). Besides, the specific implementation of the test system—such as the quantity and speed of the commercial ADC chips—is not optimized for a high-performance design. To facilitate a reliable accuracy analysis within a stable connection period, in this study the conductance of each memristor in different PEs is written first. Then, the current of each memristor is sensed, and this value is consequently used to calculate the recognition accuracy using the ARM core of the test system. The computation process is similar to that realized by the hardware.

## Learning and tuning of FC weights

During the second phase of hybrid training, we adopted in situ learning to adjust the FC memristor weights. A stochastic gradient descent (SGD)<sup>10</sup> with a batch size of 100 was used. Even though this mini-batch SGD technique may require extra memory resources to store the intermediate results, it could increase the converging speed and mitigate the overfitting issue. In addition, the memory overhead could be minimized by using the proposed hybrid training method to update the FC weights only and eliminate the demand for storing the intermediate results of all convolutional layers.



For a single iteration cycle, the 100 images drawn from the 55,000 training images were fed into the mCNN and processed from the initial to the final output layer. Then, the gradients of the objective function (here, the cross-entropy loss function) with respect to the FC weighted-sum outputs were determined using the softmax probabilities and the associated true image labels. Later, the quantitative updates of the FC weights were calculated from the intermediate FC inputs and the gradients as follows:

$$\Delta W = \eta \sum_{i=1}^{100} \mathbf{V}_i \times \delta_i \quad (1)$$

Here, the learning rate  $\eta$  is a constant;  $\Delta W$  describes the desired updates of the weight matrix;  $\mathbf{V}_i$  is the intermediate 192-dimensional column vector injected into the FC layer;  $\delta_i$  is the calculated ten-dimensional row vector representing the objective derivatives of the FC outputs; and  $i$  represents the image index in the batch of 100 images. The accumulated weight updates determine the conductance changes that are ultimately needed on the basis of the following threshold learning rule<sup>36</sup>:

$$\Delta W_{m,n} = \begin{cases} \Delta W_{m,n} & |\Delta W_{m,n}| \geq \text{Th} \\ 0 & |\Delta W_{m,n}| < \text{Th} \end{cases} \quad (2)$$

where  $\Delta W_{m,n}$  represents the update cell at the cross point of row  $m$  and column  $n$  in the weight-update matrix, and Th represents the predefined threshold value used to determine whether the corresponding memristor needs to be programmed. In this study, Th was equal to 1.5  $\mu\text{S}$  (that is, 0.3  $\mu\text{A}$  at a 0.2-V read pulse). This threshold learning rule tends to reduce the number of programming operations by filtering out the original tiny updates, and results in training acceleration and energy saving. Then, parallel programming of the FC memristors could be conducted row by row<sup>24</sup> to achieve the desired updates accordingly. The closed-loop writing method was introduced to circumvent the nonlinear and asymmetric conductance tuning issue, which could be addressed by exploring new basic weight units<sup>27</sup> and programming schemes<sup>4</sup>. Alternatively, if the device performance (for example, the linearity and symmetry) could be further improved, faithful in situ updating could be used with the SGD updating method. This could be more energy- and latency-efficient by encoding the residual error from the output side and the input data from the input side to the corresponding programming pulses directly.

### Degradation of conductance weight with time

In hybrid training, the kernel weights were programmed only during the weight-transfer stage. Thus, we set up this experiment by writing all the convolutional kernel weights onto two memristor PEs. After programming all the conductance weights smoothly, we read out these weights to assess how the conductance weights evolved within 30 days.

Extended Data Fig. 3a illustrates how the differential conductance weights (represented by the current read at 0.2 V) drifted with time. The cluster of grey curves in Extended Data Fig. 3a includes the evolution traces of all the conductance weights, where each line represents one individual weight. In the foreground, three typical evolution traces of the conductance weights are highlighted to show the general trend. Because the conductance weights were quantized and programmed using 15 levels, we divided all the weight cells in Extended Data Fig. 3a to these 15 different weight levels, and obtained the mean weight values for each level statistically, as shown in Extended Data Fig. 3b. It can be seen that the 15 levels are still accessible and there is no overlapping between adjacent levels over time.

Extended Data Fig. 3a indicates that the majority of cells can still maintain the weights well, even though there are some tail cells exhibiting noticeable weight drift with time. However, these tail cells could degrade the system accuracy, which will be discussed in the next section.

Hybrid training could be used to address the device reliability issue caused by conductance drifts to some extent, instead of adopting the expensive reprogramming strategy. However, the reliability of the multiple conductance states needs to be further investigated<sup>37</sup> and improved by device and material engineering<sup>38</sup>. The performance of memristor-based neuromorphic systems would benefit considerably from the improvement of device reliability and other non-ideal device characteristics.

### Effect of conductance weight degradation on recognition accuracy

By repeating the experiment described in Fig. 3, we investigated how the drifts of the conductance weights affect the system recognition accuracy after hybrid training. The inference accuracy and conductance weights were recorded at 10, 30, 60, 90 and 120 min after hybrid training.

Extended Data Fig. 3c illustrates how the system accuracy changes during the experiment. Similarly to Extended Data Fig. 3a, in Extended Data Fig. 3d we plot the state evolution curves of all the involved weights, including the convolutional kernels and the weights of the FC layer, and three typical lines. Most of the weight states are maintained well within the first 2 h after hybrid training; however, the conductance drifts of the tail cells lead to apparent accuracy degradation.

### Training process in parallel memristor convolvers

After transferring the weights, three fetched batches of training images were passed into the three convolver copies separately. By applying the input signal as described in the previous section, we captured three independent batches of interim output of the S4 layer and organized them as the input to the FC layer in a pipeline fashion. The training scheme sets the constraint that a batch of intermediate outputs will not be supplied as input until the previous batch has been used to calculate the desired weight updates and the corresponding FC memristor conductances have been well tuned. The desired updates of the FC weights with respect to the first input batch were calculated according to equation (1), and the relevant memristor conductances were modulated following the threshold learning rule of equation (2). Then, the FC conductances were updated after inputting the second input batch based on the well tuned FC weights of the previous phase. Afterwards, the third batch was used to tune the FC conductance weights sequentially. During this updating stage, another three batches were drawn from the training database and fed into the unoccupied memristor convolvers in parallel. These operations were repeated until the system converged to a stable recognition accuracy.

### Benchmarking of system metrics

We evaluated the hardware performance of the memristor-based neuromorphic computing system using the experimental data. Based on the calculation results, we can conclude that the system can achieve 110 times better energy efficiency and 30 times better performance density compared with Tesla V100 GPU.

To benchmark the performance of the memristor-based neuromorphic computing system, we propose a neural processing unit architecture (shown in Extended Data Fig. 5) corresponding to the structure in Fig. 1a. It consists of multiple memristor tiles and each tile contains four memristor cores. The memristor core comprises one  $128 \times 128$  memristor array and all the essential peripheral circuits, including drivers, multiplexer (MUX), MUX controller, sample-and-hold blocks and ADCs. Using the macro core, the typical energy efficiency and performance density are assessed by combining the experimental data (measured from the fabricated memristors at a 130-nm technology node) and simulation data obtained with the simulator XPEsim<sup>39</sup>.

In the memristor macro core, we maximize the computing parallelism by connecting two sample-and-hold blocks (S & H groups 1 and 2 in Extended Data Fig. 5) to each column of the array. Every four columns

share one common ADC converter to save chip area and power. When applying a 1-bit read pulse to all rows at 20 MHz, one of the S & H groups is turned on and is connected to the source lines in parallel to convert the accumulated current to voltage. During the next 1-bit read period, the S & H blocks are redirected to another S & H group. Meanwhile, at the beginning of this read phase, the stable voltage signals of the previous S & H group are passed to the ADC block through the control of the MUX-based data path, where every four stable voltages are converted in turn to a digital signal by the shared ADC at the MUX. The 8-bit ADC completes four conversions during the 1-bit inference stage and consumes 2.55 pJ of energy for each conversion. In this manner, there is no idle period for the ADCs and the input pulses are continuously fed into the array.

The detailed metrics, including the energy, latency and area of each block, are listed in Extended Data Table 1, which indicates the system performance for an input of a 1-bit read pulse (0.2 V, 50 ns). In Extended Data Table 1, the memristor-related metrics are evaluated with the measured memristor (130 nm technology node) characteristics. The parameters associated with the other peripheral circuitry blocks are extracted using the simulated circuits at the 65-nm technology node, except for the S & H block<sup>40</sup> and the 8-bit ADC block<sup>41</sup>. When inferring with a 0.2-V, 50-ns read pulse and considering all the 32 ADCs and other circuitry blocks, the energy consumption for 1-bit computing is 371.89 pJ, and the total occupied chip area is 63,801.94  $\mu\text{m}^2/90.69\% = 0.0704 \text{ mm}^2$  (the area efficiency is 90.69% for the layout of the macro blocks). Hence, we can assess the metrics of the memristor-based neuromorphic computing system when inputting an 8-bit integer by evaluating the performance, power, area, energy efficiency and performance density, as shown in Extended Data Table 2.

From the above calculations, we obtained an energy efficiency of 11,014  $\text{GOP s}^{-1} \text{W}^{-1}$  and a performance density of 1,164  $\text{GOP s}^{-1} \text{mm}^{-2}$ . Compared with the metrics of Tesla V100 GPU<sup>27</sup> (that is, energy efficiency of 100  $\text{GOP s}^{-1} \text{W}^{-1}$  and performance density of 37  $\text{GOP s}^{-1} \text{mm}^{-2}$  for 16-bit floating-point number computing), the memristor-based neuromorphic computing system shows roughly 110 times better energy efficiency and 30 times better performance density. It should be mentioned that some necessary functional blocks—such as the pooling function, the activation function, and the routing and buffering of data between different neural-network layers—were not considered in the comparison. Our system performance could be further improved by using more advanced technology nodes and optimizing the computing architecture and peripheral circuits.

Furthermore, in Extended Data Table 1, we break down the power consumption of each circuitry block in the macro core during the 1-bit inference period. The ADC accounts for 14.4 times the power of the memristor array; however, this number is expected to decrease when the memristor array size increases. For example, the ADC blocks (52 mW) would only account for 1.8 times the power of a  $1,024 \times 1,024$  memristor array (29 mW). This result suggests that both the array size and the ADC optimization should be carefully considered to achieve the best computing efficiency of memristor-based neuromorphic systems.

## Scalability demonstration using the ResNET model and the CIFAR-10 database

Replicating the same kernels to different memristor arrays is a crucial approach to improving the efficiency of memristor-based convolvers. This replicating method could mitigate the speed mismatch between the convolutional layer and the FC layer, and overcome the difference in the amount of convolution operations among different convolutional layers. In practice, we can duplicate a certain part of the kernels to realize efficient acceleration. For example, the first convolutional layer in a CNN normally contributes the greatest number of sliding convolutional operations because it has the largest input size; therefore, it causes the largest convolutional computing latency compared with the other layers. In the respect, it is reasonable to replicate only the kernels on

the first convolutional layer. Further studies are required to optimize the replicating strategy in the architecture design to yield the desired system performance.

To validate that the approach of replicating the same kernel to different memristor replicas, combined with the hybrid training method, is scalable to larger networks in the presence of intrinsic device variability, a standard residual neural network, ResNET-56, was tested on the CIFAR-10<sup>42</sup> database. We used the compact model incorporating the device variability to simulate the real device performance. Taking the programming error into consideration, a Gaussian distribution was employed to model it as  $\delta[\text{nA}] \sim N(0 \text{ nA}, 108 \text{ nA})$ . Here  $\delta$  is the programming error compared to the target conductance, and  $N(\mu, \sigma)$  denotes a Gaussian distribution with mean value  $\mu$  and standard deviation  $\sigma$ . The statistical parameters were extracted from the measurement results. During the simulation, the memristor was programmed at eight different levels during the weight-transfer stage. We then realized the equivalent 15-level weight by the differential technique as in the experiments. The kernels in the first convolutional layer were replicated into four copies of memristor arrays in the ResNET-56 model. Theoretically, this ResNET-56 model requires 782 memristor arrays with a size of  $144 \times 16$  to implement all the weights.

The initial accuracy achieved by the software was 95.57%, which was degraded to 89.64% after the quantization of the 15-level weights. Subsequently, the quantized weights were mapped to the memristor arrays in the weight-transfer stage, and the recognition accuracy further decreased to 80.06%. However, after the in situ training of the FC layer, the accuracy ultimately recovered to 94.08%—that is, a slight degradation of 1.49% compared with the baseline of 95.57%, as shown in Extended Data Fig. 6a. Extended Data Fig. 6b presents the error rates for the replicated G1, G2, G3 and G4 groups, which decreased from the initial values of 20.24%, 19.83%, 19.58% and 19.84% to 6.11%, 5.84%, 5.87% and 6.34%, respectively.

## Data availability

The datasets that we used for benchmarking are publicly available<sup>10,42</sup>. The training methods are provided in refs.<sup>10,36</sup>. The experimental setups are detailed in the text. Other data that support the findings of this study are available from the corresponding author upon reasonable request.

## Code availability

The simulator XPEsim used here is publicly available<sup>39</sup>. The codes used for the simulations described in Methods are available from the corresponding author upon reasonable request.

34. Wu, W. et al. A methodology to improve linearity of analog RRAM for neuromorphic computing. In *2018 IEEE Symposium on VLSI Technology* 103–104 (IEEE, 2018).
35. Cai, Y. et al. Training low bitwidth convolutional neural network on RRAM. In *Proc. 23rd Asia and South Pacific Design Automation Conference* 117–122 (IEEE, 2018).
36. Zhang, Q. et al. Sign backpropagation: an on-chip learning algorithm for analog RRAM neuromorphic computing systems. *Neural Netw.* **108** 217–223 (2018).
37. Zhao, M. et al. Investigation of statistical retention of filamentary analog RRAM for neuromorphic computing. In *2017 IEEE Int. Electron Devices Meeting (IEDM)* 39.34.31–39.34.34 (IEEE, 2017).
38. Kim, W. et al. Confined PCM-based analog synaptic devices offering low resistance-drift and 1000 programmable states for deep learning. In *2019 Symposium on VLSI Technology* T66–T67 (IEEE, 2019).
39. Zhang, W. et al. Design guidelines of RRAM-based neural-processing unit: a joint device–circuit–algorithm analysis. In *2019 56th ACM/IEEE Design Automation Conference (DAC)* 63.1 (IEEE, 2019).
40. O'Halloran, M. & Sarpeshkar, R. A 10-nW 12-bit accurate analog storage cell with 10-aA leakage. *IEEE J. Solid-State Circuits* **39**, 1985–1996 (2004).
41. Kull, L. et al. A 3.1 mW 8b 1.2 GS/s single-channel asynchronous SAR ADC with alternate comparators for enhanced speed in 32 nm digital SOI CMOS. *IEEE J. Solid-State Circuits* **48**, 3049–3058 (2013).
42. Krizhevsky, A. & Hinton, G. *Learning Multiple Layers of Features From Tiny Images*. Technical report (University of Toronto, 2009); <https://www.cs.toronto.edu/~kriz/learning-features-2009-TR.pdf>.

**Acknowledgements** This work is supported in part by the National Natural Science Foundation of China (61851404), the Beijing Municipal Science and Technology Project (Z191100007519008), the National Key R&D Program of China (2016YFA0201801), the Huawei Project (YBN2019075015) and the National Young Thousand Talents Plan.

**Author contributions** P.Y., H.W. and B.G. conceived and designed the experiments. P.Y. set up the hardware platform and conducted the experiments. Q.Z. performed the simulation work. W.Z. benchmarked the system performance. All authors discussed the results. P.Y., H.W., B.G., J.T. and J.J.Y. contributed to the writing and editing of the manuscript. H.W. and H.Q. supervised the project.

**Competing interests** The authors declare no competing interests.

**Additional information**

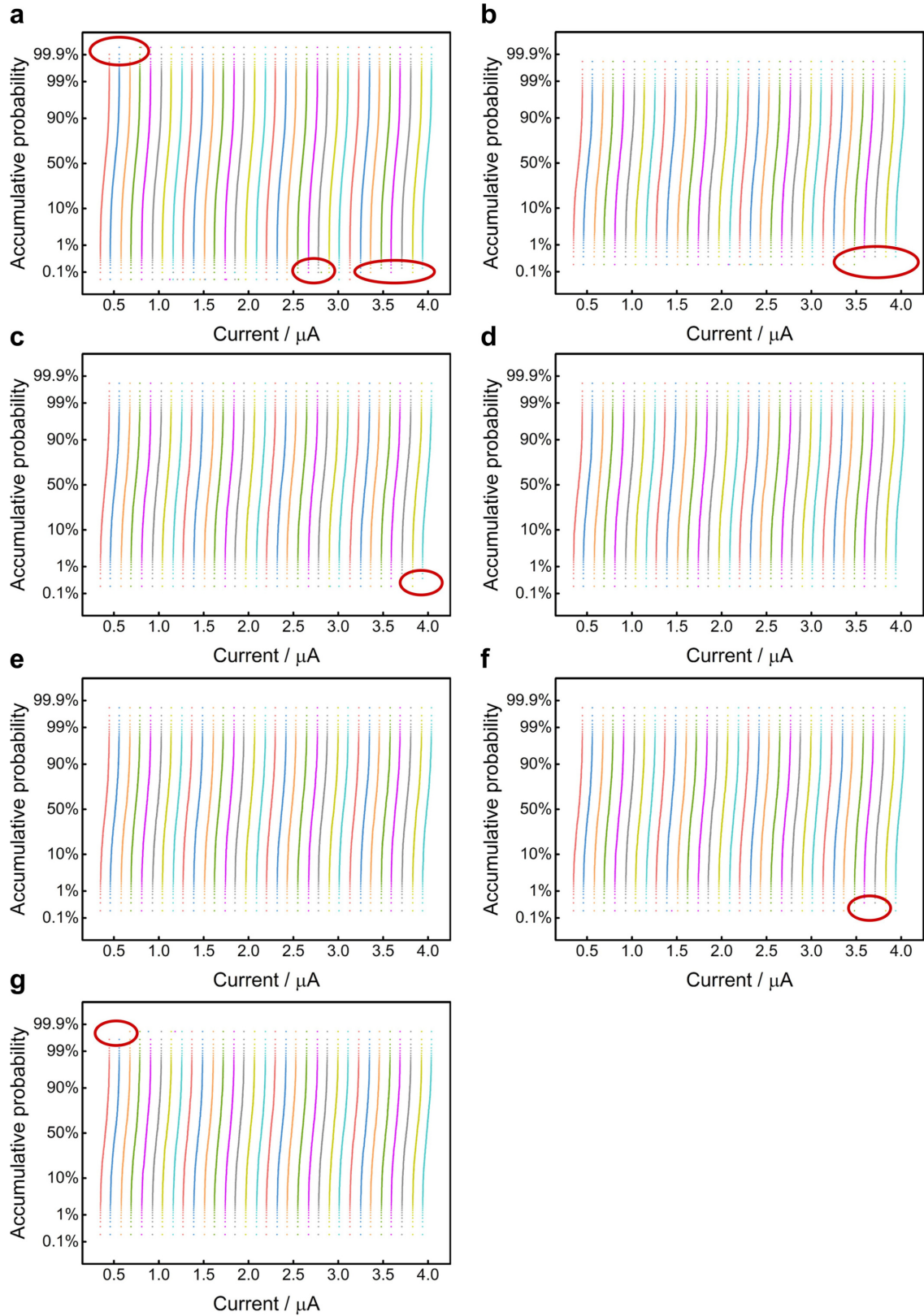
**Supplementary information** is available for this paper at <https://doi.org/10.1038/s41586-020-1942-4>.

**Correspondence and requests for materials** should be addressed to H.W.

**Peer review information** *Nature* thanks Darsen Lu and the other, anonymous, reviewer(s) for their contribution to the peer review of this work.

**Reprints and permissions information** is available at <http://www.nature.com/reprints>.





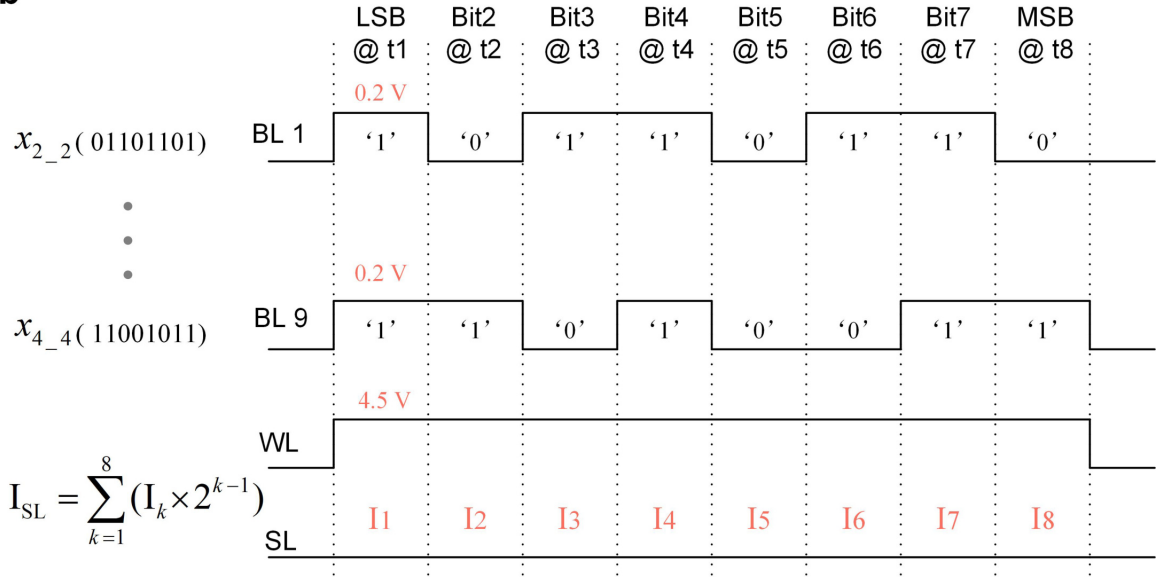
**Extended Data Fig. 1 | Cumulative probability distribution of memristor conductance for the remaining seven 2,048-cell arrays.** The red circles highlight abnormal data points, which deviate from their target conductance ranges owing to device variations. **a**, The 32-level conductance distribution on an entire 2,048-cell array. **b–g**, Conductance distributions for the first 32 rows

of memristors (namely, 512 devices) for each of the remaining 2,048-cell arrays. A small number of writing errors were observed during the programming procedure (red circles), which could be attributed to device variations. These results show good consistency with Fig. 1c.

**a**

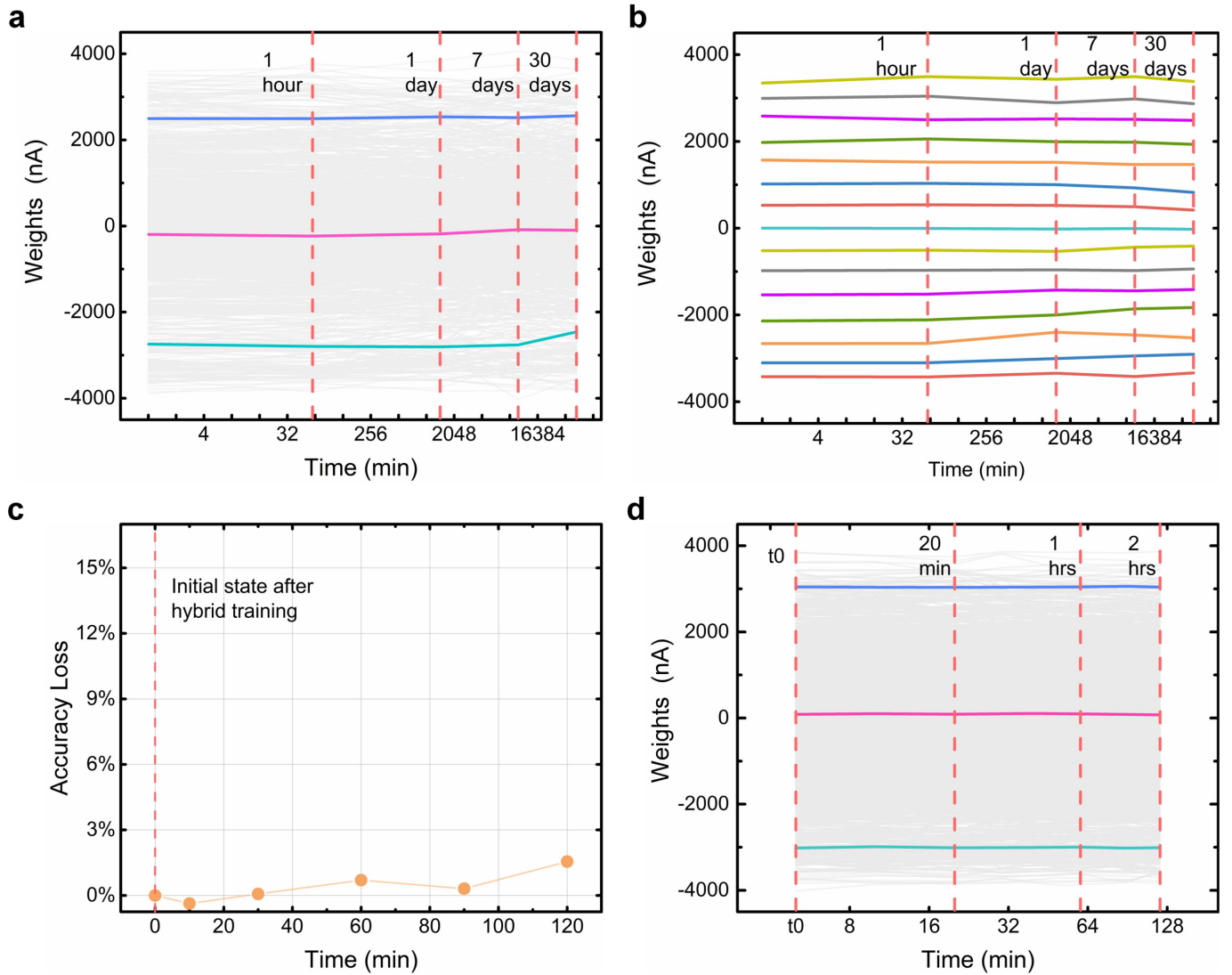
Input vector set

BL1	BL2	BL3	BL4	BL5	BL6	BL7	BL8	BL9
$x_{1\_1}$	$x_{1\_2}$	$x_{1\_3}$	$x_{2\_1}$	$x_{2\_2}$	$x_{2\_3}$	$x_{3\_1}$	$x_{3\_2}$	$x_{3\_3}$
$x_{1\_2}$	$x_{1\_3}$	$x_{1\_4}$	$x_{2\_2}$	$x_{2\_3}$	$x_{2\_4}$	$x_{3\_2}$	$x_{3\_3}$	$x_{3\_4}$
$\vdots$	$\vdots$	$\vdots$	$\vdots$	$\vdots$	$\vdots$	$\vdots$	$\vdots$	$\vdots$
$x_{2\_2}$	$x_{2\_3}$	$x_{2\_4}$	$x_{3\_2}$	$x_{3\_3}$	$x_{3\_4}$	$x_{4\_2}$	$x_{4\_3}$	$x_{4\_4}$
$\vdots$	$\vdots$	$\vdots$	$\vdots$	$\vdots$	$\vdots$	$\vdots$	$\vdots$	$\vdots$

**b**

**Extended Data Fig. 2 | Input patch set generated during the sliding process and input waveforms during the convolution.** **a**, Input nine-dimensional vectors unrolled from the input  $3 \times 3$  patch set.  $x_{m,n}$  indicates the relevant pixel at the crossing of row  $m$  and column  $n$ . The input patches are generated during the sliding convolutional process over the input feature planes and are subsequently injected into the memristor weight array. For a specific input vector, each element is encoded as the corresponding input pulse applied on the associated bit line. The red box indicates the current input vector, in agreement with the case illustrated in **b**. **b**, Input waveform sample in a memristor-based convolutional operation. Each element (an 8-bit binary

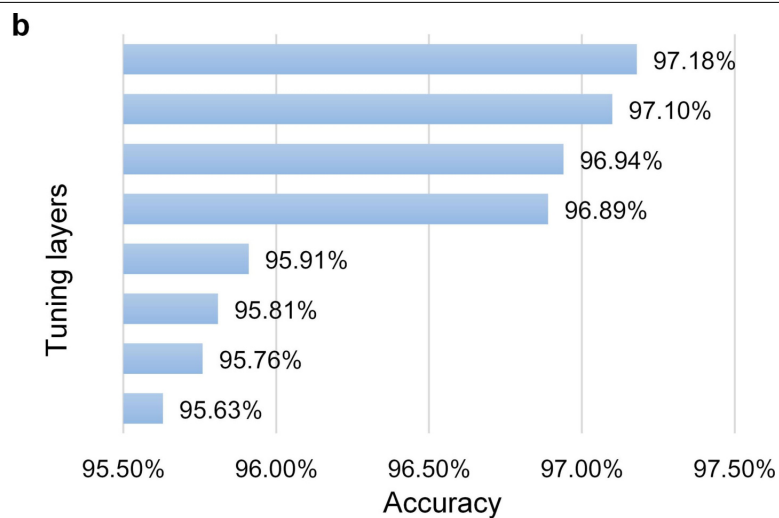
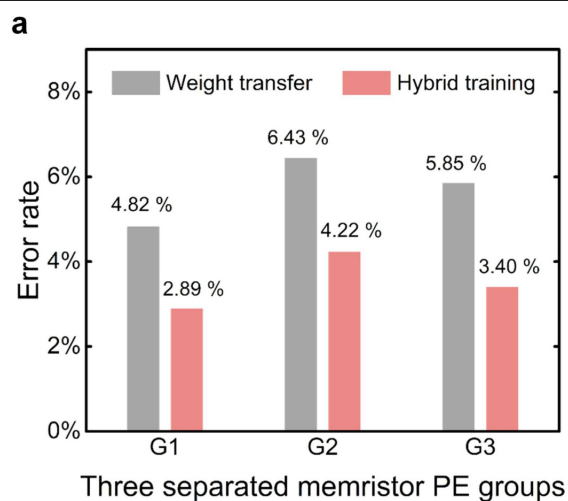
number) in the input vector is encoded as sequential pulses over eight time intervals ( $t_1, t_2, \dots, t_8$ ). For a particular period  $t_k$ , bit  $k$  determines whether a 0-V pulse or a 0.2-V pulse is used. Each '1' at a certain bit location implies the existence of a 0.2-V read pulse in the corresponding time interval, and a '0' indicates a 0-V read pulse. The corresponding output current  $I_k$  is sensed, and this quantized value is then left-shifted by  $k-1$ . Finally, the quantized and shifted results with respect to the same source line over the eight time intervals are summed together ( $I_{SL}$  in the inset equation). The difference between every two  $I_{SL}$  values from a pair of differential source lines is considered to be the expected weighted-sum result.



**Extended Data Fig. 3 | Drift of conductance weights in time and associated degradation in system accuracy.** **a**, Changes in the conductance weights with time, over 30 days after the transfer. The grey lines present the changing traces of all the cell weights, and the three coloured lines depict representative evolution trends. **b**, Mean weight value for the cells that belong to each of the 15 levels according to **a**. The 15 coloured traces show the 15 mean-value evolution traces as a function of time. **c**, Profile of accuracy loss during the experiment. The overall trend of the accuracy loss indicates how the conductance weight

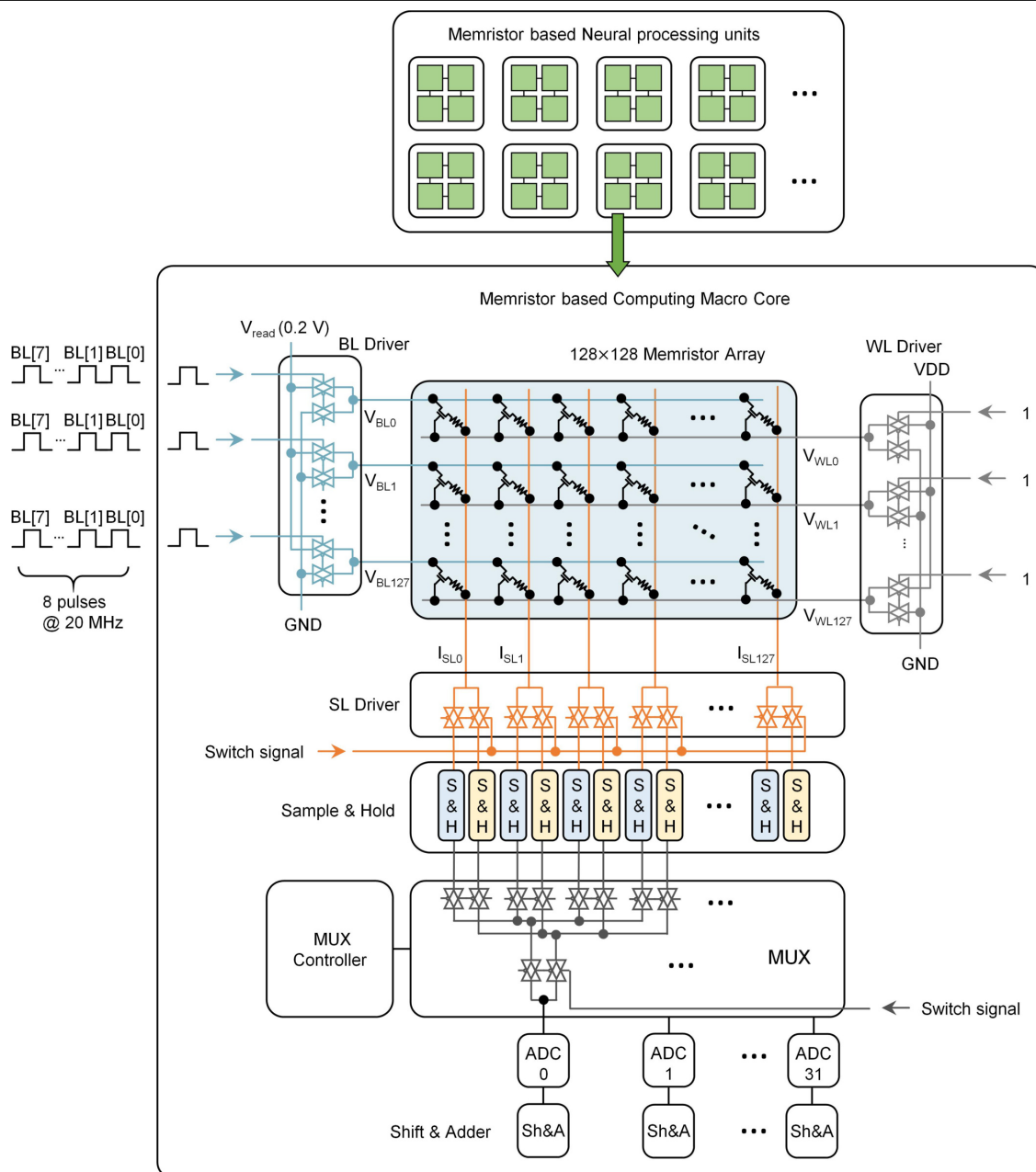
drifts deteriorate the recognition accuracy over time after hybrid training. Compared with the initial state, the recognition accuracy increases by 0.37% at  $t = 10$  min, owing to random device-state fluctuations. **d**, Evolution of the weights of the weight cells considered in **c** over 2 h.  $t_0$  denotes the moment when the hybrid training is completed. The grey lines show the changing traces of the states of the cells, and the three coloured lines depict representative evolution trends.



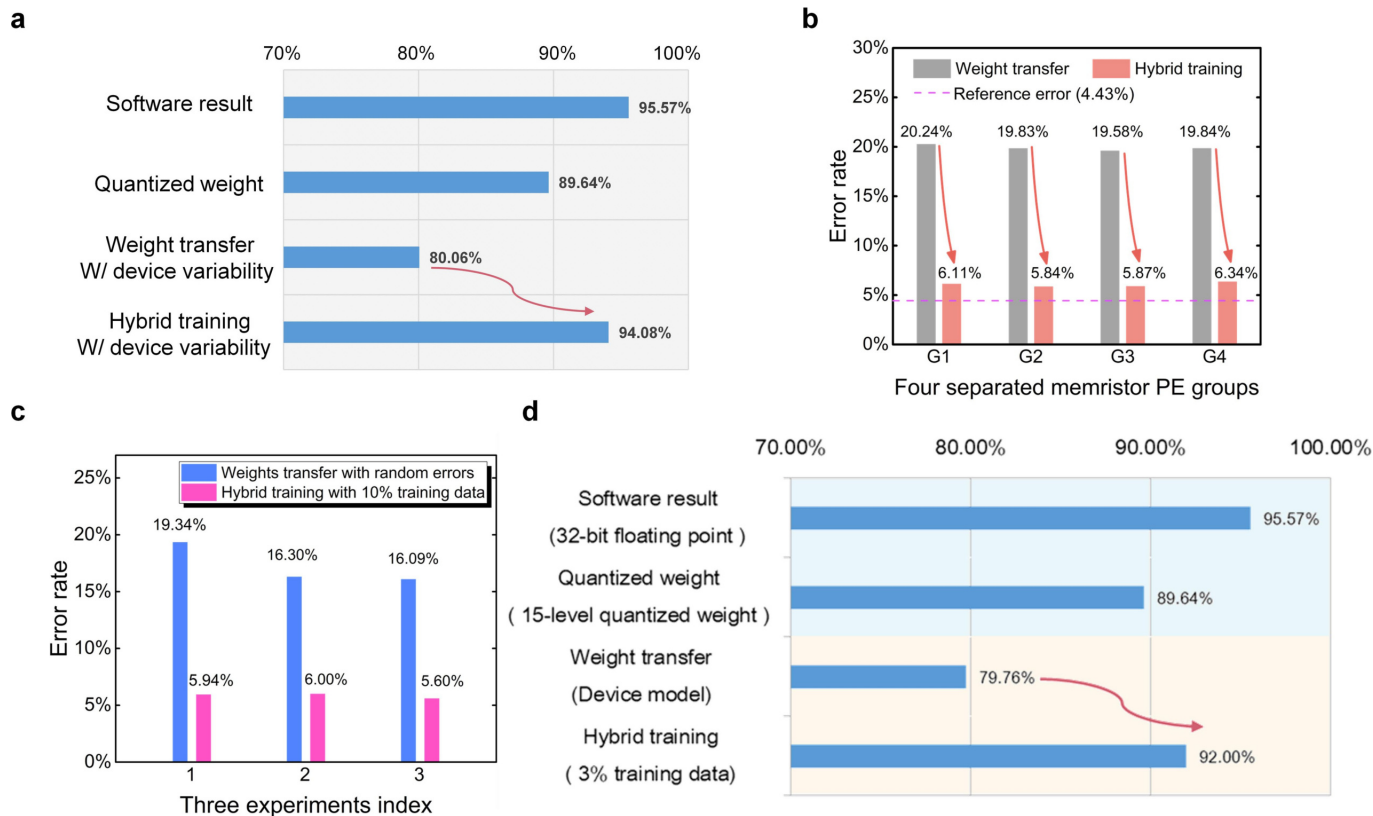


**Extended Data Fig. 4 | Experimental accuracy of parallel memristor convolvers after hybrid training, and simulated training efficiency of different combinations of tuning layers. a,** The error rate on the entire training set after hybrid training drops substantially compared with that achieved after weight transfer for any individual convolver group. The error

rates with respect to the G1, G2 and G3 groups decrease from 4.82%, 6.43% and 5.85% to 2.89%, 4.22% and 3.40%, respectively, after hybrid training. **b,** Simulation results for all combinations of tuning weights for different layers using hybrid training and the five-layer CNN.



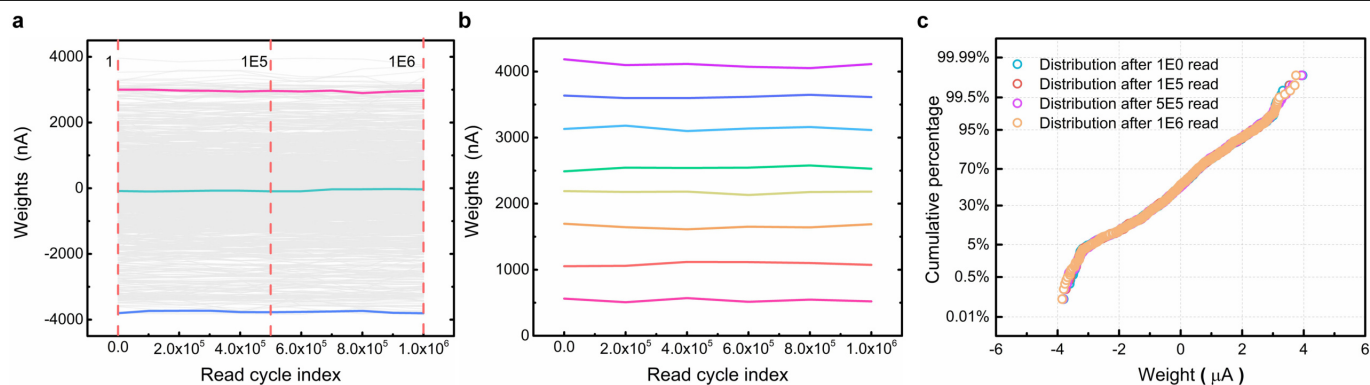
**Extended Data Fig. 5 | Architecture of the simulated memristor-based neural processing unit and relevant circuit modules in the macro core.**



**Extended Data Fig. 6 | Scalability of the joint strategy.** The joint strategy combines the hybrid training method and the parallel computing technique of replicating the same kernels. We show that a small subset of training data is sufficient for hybrid training. **a**, Recognition accuracies at different stages of the simulation process. During the simulation with ResNET-56, the kernel weights of the first convolutional layer are replicated to four groups of memristor arrays. **b**, After hybrid training the error rate on the test set drops substantially compared with that obtained immediately after weight transfer

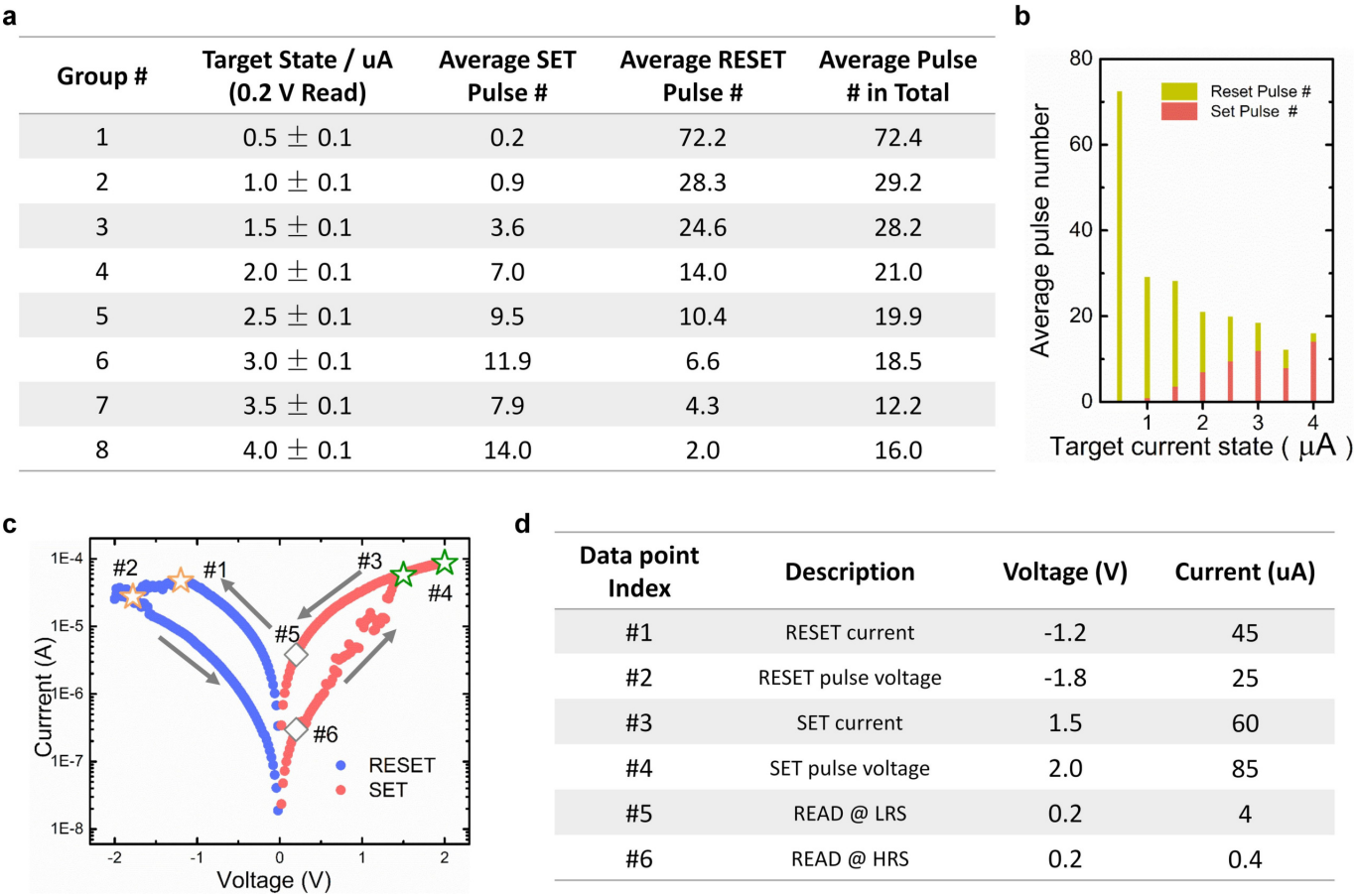
using each convolver group. **c**, The error rates drop considerably after hybrid training using 10% of the training data in the experiment with the five-layer CNN. The three experimental results show good consistency. **d**, Recognition accuracies at different stages of the simulation with ResNET-56. A high level of accuracy is achieved even when using 3% of the training data (1,500 training images) to update the weights of the FC layer. The mean accuracy for 10 trials is 92.00% after hybrid training, and the standard deviation is 0.8%.





**Extended Data Fig. 7 | Effects of read disturbance.** To investigate this effect, we set up this experiment by writing all the convolutional kernel weights to two memristor PEs. After programming all the conductance weights smoothly, we physically apply 1,000,000 read pulses (0.2 V) on all weight cells to see how the read operations disturb the weight states. **a**, Changes in the states of the 936

conductance weights while cycling read operations. The grey lines give the changing traces of the states of all cells, and the three coloured lines depict representative evolution trends. **b**, Conductance evolution of eight memristor states during  $10^6$  read cycles. **c**, Distributions of weight states after  $1, 10^5, 5 \times 10^5$  and  $10^6$  read cycles.



**Extended Data Fig. 8 | Test results of the required programming pulse number and programming currents. a,** Average pulse number required to reach each target conductance state. All the initial states were programmed to  $>4.0 \mu\text{A}$ . **b,** Stacked histogram distribution corresponding to the data in **a**. **c,** Current–voltage curve obtained during a d.c. voltage sweep. RESET and SET currents are measured at points #1 and #3, respectively. The conditions of

RESET and SET pulses in this study are marked by points #2 and #4, respectively. Point #5 labels the read current at the low-resistance state (LRS) and point #6 labels the read current at the high-resistance state (HRS). **d,** Typical programming parameters. The programming current is  $60 \mu\text{A}$  at  $1.5 \text{ V}$  during the SET process and  $45 \mu\text{A}$  at  $-1.2 \text{ V}$  during RESET.

Extended Data Table 1 | Detailed metrics of each circuitry module in the macro core with 1-bit input

Module	Area/ $\mu\text{m}^2$	Latency/ns	Energy/pJ
Array	1107.56	-	22.59
BL Driver	2104.36	0.002	1.99
WL Driver	2104.36	0.008	1.99
SL Driver	1686.3	0.38	0.11
Sample & Hold	10	-	0.13
Mux	1741.9	0.008	2.37
Mux Decoder	69.84	6.10	0.05
ADC	48000	-	326.4
Shift & Adder	6977.62	0.19	16.26
Sum	63801.94	-	371.89

BL, bit line; WL, word line; SL, source line.

**Extended Data Table 2 | Benchmark metrics of a single macro core with 8-bit input**

Performance	$(128 \times 128 \times 2) \text{ ops} / (8 \times 50 \text{ ns}) = 81.92 \text{ GOP s}^{-1}$
Power	$371.89 \text{ pJ} / 50 \text{ ns} = 7.438 \text{ mW}$
Area	$0.0704 \text{ mm}^2$
Energy efficiency	$81.92 \text{ GOP s}^{-1} / 7.438 \text{ mW} = 11,014 \text{ GOP s}^{-1} \text{ W}^{-1}$
Performance density	$81.92 \text{ GOP s}^{-1} / 0.0704 \text{ mm}^2 = 1,164 \text{ GOP s}^{-1} \text{ mm}^{-2}$

ops, operations.



# Gram-scale bottom-up flash graphene synthesis

<https://doi.org/10.1038/s41586-020-1938-0>

Received: 28 May 2019

Accepted: 22 October 2019

Published online: 27 January 2020

Duy X. Luong<sup>1,2</sup>, Ksenia V. Bets<sup>3</sup>, Wala Ali Algozeeb<sup>2</sup>, Michael G. Stanford<sup>2</sup>, Carter Kittrell<sup>2</sup>, Weiyin Chen<sup>2</sup>, Rodrigo V. Salvatierra<sup>2</sup>, Muqing Ren<sup>2</sup>, Emily A. McHugh<sup>2</sup>, Paul A. Advincula<sup>2</sup>, Zhe Wang<sup>2</sup>, Mahesh Bhatt<sup>4</sup>, Hua Guo<sup>3</sup>, Vladimir Mancevski<sup>2</sup>, Rouzbeh Shahsavari<sup>4,5\*</sup>, Boris I. Yakobson<sup>2,3,6\*</sup> & James M. Tour<sup>2,3,6\*</sup>

Most bulk-scale graphene is produced by a top-down approach, exfoliating graphite, which often requires large amounts of solvent with high-energy mixing, shearing, sonication or electrochemical treatment<sup>1–3</sup>. Although chemical oxidation of graphite to graphene oxide promotes exfoliation, it requires harsh oxidants and leaves the graphene with a defective perforated structure after the subsequent reduction step<sup>3,4</sup>. Bottom-up synthesis of high-quality graphene is often restricted to ultrasmall amounts if performed by chemical vapour deposition or advanced synthetic organic methods, or it provides a defect-ridden structure if carried out in bulk solution<sup>4–6</sup>. Here we show that flash Joule heating of inexpensive carbon sources—such as coal, petroleum coke, biochar, carbon black, discarded food, rubber tyres and mixed plastic waste—can afford gram-scale quantities of graphene in less than one second. The product, named flash graphene (FG) after the process used to produce it, shows turbostratic arrangement (that is, little order) between the stacked graphene layers. FG synthesis uses no furnace and no solvents or reactive gases. Yields depend on the carbon content of the source; when using a high-carbon source, such as carbon black, anthracitic coal or calcined coke, yields can range from 80 to 90 per cent with carbon purity greater than 99 per cent. No purification steps are necessary. Raman spectroscopy analysis shows a low-intensity or absent D band for FG, indicating that FG has among the lowest defect concentrations reported so far for graphene, and confirms the turbostratic stacking of FG, which is clearly distinguished from turbostratic graphite. The disordered orientation of FG layers facilitates its rapid exfoliation upon mixing during composite formation. The electric energy cost for FG synthesis is only about 7.2 kilojoules per gram, which could render FG suitable for use in bulk composites of plastic, metals, plywood, concrete and other building materials.

In the flash Joule heating (FJH) process, amorphous conductive carbon powder is lightly compressed inside a quartz or ceramic tube between two electrodes (Fig. 1a, Supplementary Fig. 1). The system can be at atmospheric pressure, or under a mild vacuum (~10 mm Hg) to facilitate outgassing. The electrodes can be copper, graphite or any conductive refractory material, and they fit loosely into the quartz tube to permit outgassing upon FJH. High-voltage electric discharge from a capacitor bank brings the carbon source to temperatures higher than 3,000 K in less than 100 ms, effectively converting the amorphous carbon into turbostratic FG. In high-resolution transmission electron microscopy (HR-TEM) analysis (Fig. 1b, c), the misoriented layers of FG exhibit the expected Moiré patterns, whereas FG derived from spent coffee grounds also shows hexagonal single-layer graphene (Fig. 1d).

High-quality graphene can be quickly identified by Raman spectroscopy<sup>7–10</sup>. FG from carbon black (CB-FG) has an intense 2D peak. As

seen in the Raman mapping of CB-FG in Fig. 1e, the intensity of the 2D band relative to the G band ( $I_{2D/G}$ ) is greater than 10 in many locations. The extremely low intensity of the D band indicates the low defect concentration of these FG products, which contributes to the amplification of the 2D band. Thus, the unusually high  $I_{2D/G} = 17$  (Fig. 1e) of CB-FG is the highest value reported so far for any form of graphene, and is probably an outcome of the extreme temperature reached in the flash process, which outgasses non-carbon elements from the system. Additionally, the two peaks  $TS_1$  and  $TS_2$  at  $-1,886\text{ cm}^{-1}$  and  $-2,031\text{ cm}^{-1}$ , respectively, confirm the turbostratic nature of FG (Supplementary Figs. 2, 3), which is discussed extensively in Supplementary Information and Supplementary Table 1<sup>11,12</sup>.

The X-ray diffraction (XRD) pattern of FG shows a well defined (002) peak indicating successful graphitization of the amorphous carbon. The (002) peak of FG occurs at diffraction angle  $2\theta = 26.1^\circ$ ,

<sup>1</sup>Applied Physics Program, Rice University, Houston, TX, USA. <sup>2</sup>Department of Chemistry, Rice University, Houston, TX, USA. <sup>3</sup>Department of Materials Science and NanoEngineering, Rice University, Houston, TX, USA. <sup>4</sup>C-Crete Technologies, Stafford, TX, USA. <sup>5</sup>Department of Civil and Environmental Engineering, Rice University, Houston, TX, USA. <sup>6</sup>Smalley-Curl Institute and the NanoCarbon Center, Rice University, Houston, TX, USA. \*e-mail: rouzbeh@ccretetech.com; biy@rice.edu; tour@rice.edu

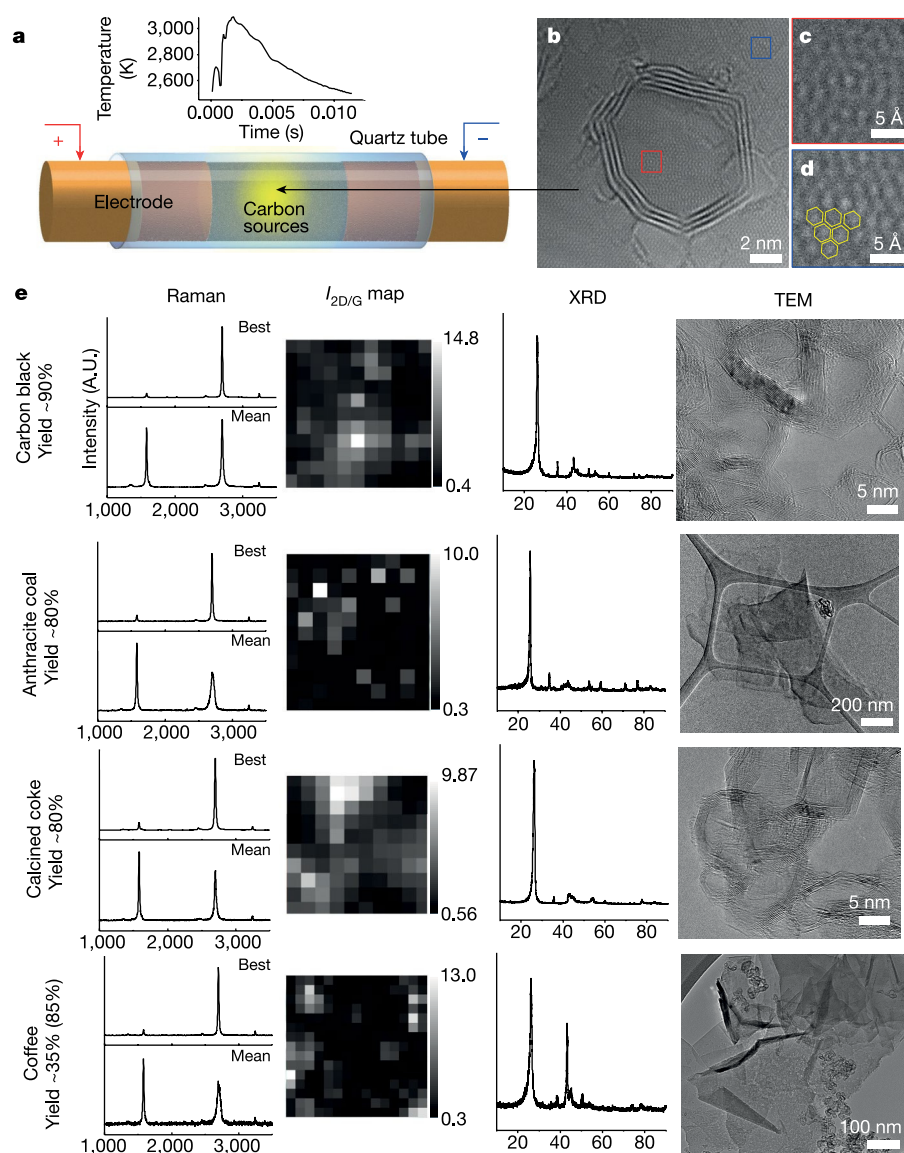


**Fig. 1 | FG synthesized from various carbon sources.** **a**, Schematic of the FJH process, and plot of the temperature rise versus time during flashing (inset). **b–d**, HR-TEM image of CB-FG on top of a single layer of coffee-derived FG. **e**, Characterization results, including Raman spectra (showing the best and the mean obtained spectra), XRD spectra and TEM images for FG derived from various carbon sources. The coffee-derived FG is made from used coffee grounds; the smaller graphene particles within large graphene sheets come

from the carbon black conductive additive. Each pixel in the Raman mapping is  $4 \mu\text{m}^2$  using a  $50\times$  magnification. All Raman samples were prepared from the powdered product after FJH; the samples were not exposed to the solvent before Raman analysis. Coffee is about 40% carbon, so the yield based on the starting carbon content is ~85%. The sample size for the mean Raman spectrum is 10.

which corresponds to an interlayer spacing of  $l_c = 3.45 \text{ \AA}$ . This spacing is larger than that in a typical Bernal (AB-stacked) graphite,  $3.37 \text{ \AA}$ , indicating the expanded and turbostratic structure of FG. The (002) peak was found to be unsymmetric, with a tail at small angles, which further suggests the turbostratic nature of FG<sup>13</sup>. The flash process is fast enough to prevent AB stacking. CB-FG has a surface area of  $\sim 295 \text{ m}^2 \text{ g}^{-1}$  with pore size  $< 9 \text{ nm}$ , as measured by Brunauer–Emmett–Teller analysis (Supplementary Fig. 4). Calcined petroleum coke (CPC) also works well for conversion to CPC-FG (Fig. 1e, Supplementary Table 2) which has a similar nanostructure to that of CB-FG. Together with carbon black, CPC is listed as a non-graphitized carbon source (Supplementary Table 3)<sup>14</sup>. The average size of CB-FG and CPC-FG is  $\sim 13 \text{ nm}$  and  $\sim 17 \text{ nm}$ , respectively (Supplementary Figs. 5, 6). The yield of the FJH process is as high as 80% to 90% from high-carbon sources such as carbon black, calcine coke or anthracite coal, and

the electric energy needed for their conversion is  $\sim 7.2 \text{ kJ g}^{-1}$  (Supplementary Information).

In the case of coffee grounds, the used grounds were mixed with 5 wt% carbon black to increase its conductivity—alternatively, we could use 2–5 wt% FG from a previous run as the conductive additive. Coffee grounds, being predominantly carbohydrate, are ~40% carbon. Hence, the yield of graphene of ~35% (Fig. 1e) would be ~85% conversion of the coffee carbon content into graphene, whereas the heteroatoms sublime out at these reaction temperatures ( $> 3,000 \text{ K}$ ). Anthracite can be sufficiently conductive to be used in the FJH reactor, but better results were obtained by adding 5 wt% carbon black. Although a black FG powder is produced regardless of the starting material, FG from graphitizing carbons—such as from used coffee grounds (C-FG) and anthracite coal (A-FG) (see Supplementary Information for definitions of graphitizing and non-graphitizing carbons; see also Supplementary Table 3)—has

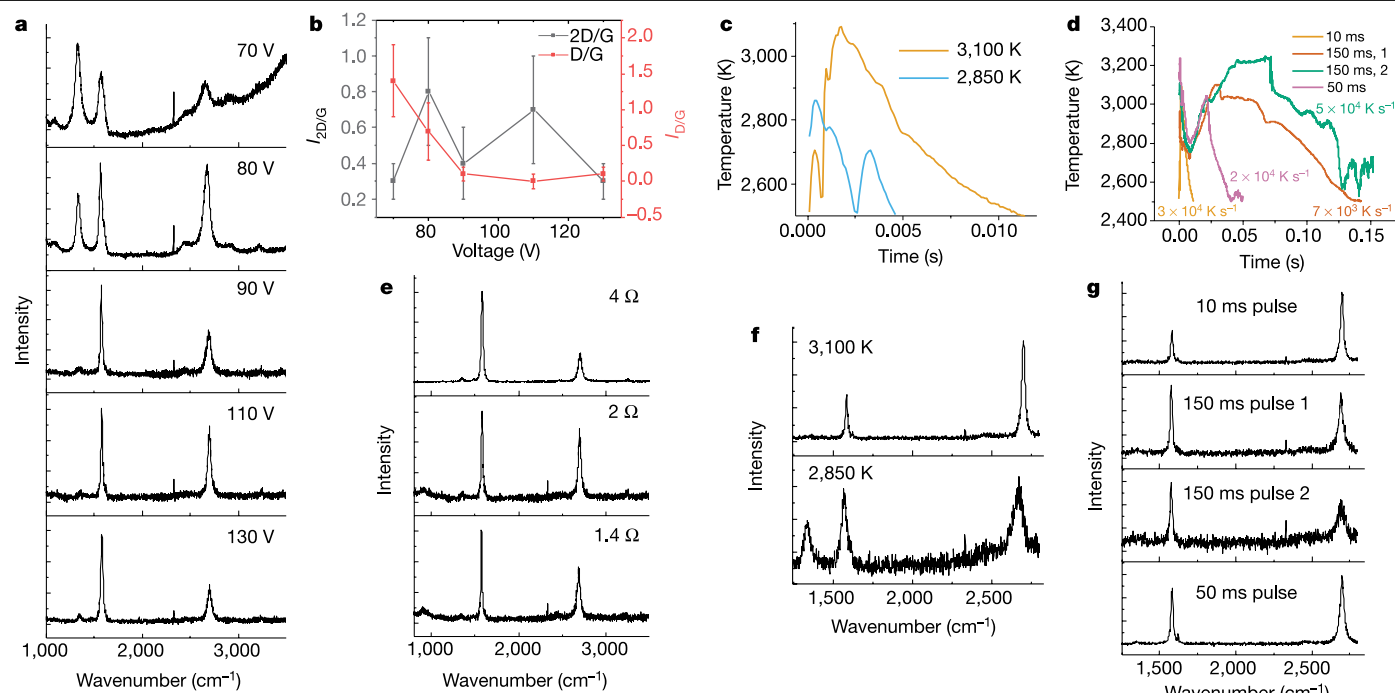


**Fig. 2 | FJH critical parameters.** **a**, Raman spectra of CB-FG with increasing flashing voltage (top to bottom). **b**,  $I_{2D/G}$  and  $I_{D/G}$  ratios of CB-FG at different flashing voltages. The bars represent 1 s.d. ( $n = 10$ ). **c**, Time–temperature graph of CB-FG reacted at different temperatures. The temperature is regulated by the flashing voltage. **d**, Time–temperature graph of CB-FG reacted at different flashing durations. The flashing duration is regulated by the sample compression between the electrodes, which affects the sample conductivity.

The numbers within the plot represent cooling rates. **e**, Raman spectra of CB-FG at different compression ratios. Higher compression provides lower resistance to the sample. **f**, Raman spectra of the CB-FG samples shown in **c**. **g**, Raman spectra of the CB-FG samples shown in **d**. The 150-ms pulses 1 and 2 have similar duration but different cooling rates, as shown in **d**. All Raman spectra in the figure were taken at low magnification ( $5\times$ ) to obtain a mean spectrum of the sample from 10 spectra.

different morphologies from CB-FG. Graphitizing carbons produce larger graphene sheets (Supplementary Fig. 7). XRD analysis of C-FG shows, in addition to the dominant (002) peak at  $2\theta = 26.0^\circ$ , a sharp (100) peak at  $2\theta = 42.5^\circ$ , which is associated with the in-plane interatomic spacing (Fig. 1e). The narrow full width at half-maximum of the (100) peak suggests larger in-plane sheet sizes relative to FG formed from some of the other starting materials. HR-TEM reveals folded graphene sheets in A-FG and C-FG (Fig. 1e) with an average size of  $0.5\ \mu\text{m}$  and  $1.2\ \mu\text{m}$  (Supplementary Fig. 7), respectively, similar to the size of graphene sheet obtained by exfoliation of graphite<sup>3,15,16</sup>. Selected-area electron diffraction measurements on these samples show both monolayer and turbostratic graphene (Supplementary Figs. 8–10).

Other carbons that are abundant, renewable or waste-sourced can be used, such as charcoal, biochar, humic acid, keratin (human hair), lignin, sucrose, starch, pine bark, olive oil soot, cabbage, coconut, pistachio shells, potato skins, rubber tyres and mixed plastic (Supplementary Fig. 11, Supplementary Table 4), including polyethylene terephthalate (PET or PETE), high- or low-density polyethylene, polyvinyl chloride, polypropylene and polyacrylonitrile. When converting synthetic polymers into FG, the non-carbon atoms sublime out as small molecules, leading to a very-high-carbon-content product, as shown here. However, polymer and rubber depolymerization can also ensue to afford oligomers that sublime before conversion; therefore, it is more economical to use a pyrolysis product where the volatiles are first industrially removed for fuel sources<sup>17</sup> and the residual carbon is converted into FG. This was demonstrated here with rubber-tyre-derived carbon black (Supplementary Fig. 11, Supplementary Tables 2, 4). None of these FG processes was optimized. Optimization was performed only on CB-FG, as described below. The FJH process can provide a facile route to convert these waste products into FG, a potential high-value building-composite additive<sup>18–21</sup>.

The graphene  $I_{2D/G}$  is optimized by adjusting the sample compression between the electrodes (which affects sample conductivity), the capacitor voltage and the switching duration to control the temperature and duration of the flash (Fig. 2a–g). Increasing the voltage will increase the temperature of the process. The temperature is estimated by fitting the black-body radiation spectrum in the 600–1,100 nm emission (Supplementary Fig. 12). We investigated the quality of CB-FG using Raman spectroscopy at low magnification (see Methods) by varying the time and temperature in the FG synthesis process. At  $<90\ \text{V}$  and  $<3,000\ \text{K}$ , FG has a high D peak, indicating a defective structure (Fig. 2a–c, f). By increasing the voltage output, CB-FG is formed at  $3,100\ \text{K}$ , which has a low number of defects and almost no D band in the Raman spectrum. Therefore,  $3,000\ \text{K}$  is a critical temperature for producing higher-quality graphene with a larger  $I_{2D/G}$  value.

By increasing the compression on the sample between the two electrodes, the conductivity of the carbon source increases, thus decreasing the discharge time (Fig. 2d, e, g). While maintaining the flash temperature between experimental runs at  $\sim 3,100\ \text{K}$ , a short flash duration of  $10\ \text{ms}$  results in a higher 2D band, whereas a flash of  $50$ – $150\ \text{ms}$  results in a lower 2D band product (Fig. 2g). This indicates that, given more time, the graphene flakes stack, orient and form more layers, lowering the 2D band of the resulting FG. A low cooling rate increases the flash duration and decreases the 2D band<sup>22</sup>. Therefore, to obtain a high  $I_{2D/G}$ , a thin quartz tube is chosen to accelerate the radiative cooling rate. Interestingly, although the internal temperatures exceed  $3,000\ \text{K}$ , the external walls of the quartz tubes are only warm to the touch ( $<60^\circ\text{C}$ ) after the flash process. Most of the heat exits as black-body radiation.

X-ray photoelectron spectroscopy analysis shows a considerable reduction of elements other than carbon in FG and increases in the  $sp^2$  carbon bond content (Supplementary Figs. 13, 14). Carbon has a

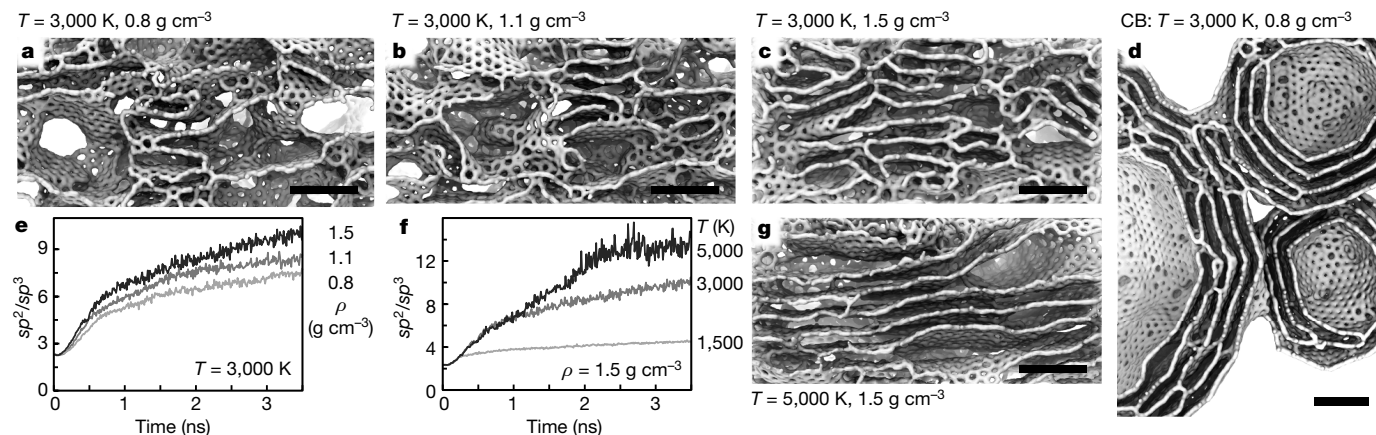


**Fig. 3 | Molecular dynamics simulations.** Structures with various characteristics (such as micro-porosity, misalignment and size of graphitic domains) kept at a given temperature range (1,500 to 5,000 K) for up to  $5 \times 10^{-9}$  s with a Nosé–Hoover thermostat. **a–c**, Sample structures for carbon materials of density  $0.8 \text{ g cm}^{-3}$  (**a**; sponge-like structure),  $1.1 \text{ g cm}^{-3}$  (**b**), and  $1.5 \text{ g cm}^{-3}$  (**c**; high degree of graphitization) after annealing at 3,000 K. **d**, Carbon black with

density  $0.8 \text{ g cm}^{-3}$  and large macro-porosity, after prolonged ( $5 \times 10^{-9}$  s) annealing at 3,600 K; polygonal fringes are apparent. **e–f**, Change of the structural composition of materials during annealing for materials of different densities  $\rho$  (**e**) and for annealing at different temperatures  $T$  (**f**). **g**, Structure of material with density  $1.5 \text{ g cm}^{-3}$  after annealing at 5,000 K; the initial structure is the same as that shown in **c**. All scale bars are 1.5 nm.

high sublimation temperature of  $\sim 3,900 \text{ K}$ ; other elements such as aluminium or silicon volatilize out at  $< 3,000 \text{ K}$ .

Thermogravimetric analysis in air shows that FG products are more oxidatively stable than the materials from which they are derived (Supplementary Fig. 15) and more stable than reduced graphene oxide obtained with Hummer's method<sup>23</sup>. In some cases, silicon oxide residues are detected, which come from worn out quartz tubes after multiples uses.

Previous studies have shown that graphene can be synthesized without catalysts at extremely high temperatures<sup>24–26</sup>. However, when FG is optimized as shown here, it can have exceptionally high quality when the reaction time and temperature are controlled. Furthermore, the electric current can facilitate the crystallization of graphene<sup>27</sup>. Degassing of hydrogen, nitrogen and oxygen during the FJH process might contribute to the formation of large and thin graphene sheets in coffee-derived FG because it could prevent stacking of graphene layers, thereby permitting further growth<sup>25,28,29</sup>.

To assess the mechanism of the rapid FG growth, we employ large-scale simulations with the AIREBO<sup>30,31</sup> interatomic potential as implemented in the LAMMPS package (see Methods)<sup>32</sup>. Some of the acquired structures are shown in Fig. 3a–d. The low-density materials yield a sponge-like structure (Fig. 3a) during annealing, whereas increased density leads to a high level of graphitization (Fig. 3c). We note the high level of graphitization in the low-density CB sample, where the substantially increased local density is combined with high macro-porosity (Fig. 3d). Additionally, the annealing process is quantified by the  $sp^2/sp^3$  ratio during simulation (Fig. 3e, f). We find that the graphene formation process is strongly impaired at lower temperatures ( $< 2,000 \text{ K}$ ) but greatly accelerated at higher temperature (5,000 K) (Fig. 3g)—a trend that is also suggested by experiments (Fig. 2f). In the case of carbon black, continuous defect healing during FJH results in the gradual conversion of initially roughly spherical centroid particles into polyhedral shapes (Fig. 3d) that appear as fringes at clearly defined angles in TEM images (see Fig. 1b, e), further confirming the low-defect nature of the produced materials.

The FJH process was scaled up by increasing the quartz tube size. With quartz tubes of 4 mm, 8 mm and 15 mm diameter, 30 mg, 120 mg and 1 g of FG can be synthesized per batch, respectively. Figure 4a shows the amount of CB-FG obtained with the three tube sizes. The shorter flash from the smaller tube results in FG with a higher  $I_{2D/G}$ . To increase the batch size while maintaining FG quality, flat tubes are helpful because they enable a higher cooling rate (Fig. 4a). For industrial production, we

envision that the process can be automated for continuous FG synthesis (Supplementary Fig. 16).

FG was found to be dispersible in water/surfactant (Pluronic F-127) to give highly concentrated dispersions reaching  $4 \text{ g l}^{-1}$  (Fig. 4b, Supplementary Fig. 17). Using organic solvents, FG has a high degree of dispersibility (Fig. 4c)<sup>33–35</sup>, which can be attributed to the turbostratic arrangement permitting efficient exfoliation; the interlayer attraction forces are much lower than in conventionally arranged AB-stacked graphene obtained by graphite exfoliation.

FG composites were explored, revealing considerably enhanced physical properties at small FG loadings. CB-FG–cement composites with 0.05% FG and cured for 28 days had  $\sim 25\%$  higher compressive strength than the FG-free control sample (Supplementary Fig. 18). This enhancement in the compressive strength is three times higher than the values reported recently for cement composites reinforced by electrochemically exfoliated graphene with the same graphene loading, and slightly larger than those of other cement–graphene composites<sup>36,37</sup>. The seven-day compressive and tensile strength of CB-FG–cement composites with 0.1% FG loading are  $\sim 35\%$  and  $\sim 19\%$  higher, respectively, than those of the FG-free control sample (Fig. 4d). These enhancements are almost three times larger than those of other reported graphene–cement composites with the same loading, demonstrating rapid strength development. Scanning electron microscopy images of CB-FG–cement composites (Supplementary Fig. 19) show a homogeneous distribution of FG in the cement matrix. The largely enhanced properties and rapid strength development of CB-FG–cement composites is again attributed to the high dispersibility of the turbostratic CB-FG, which results in greater homogeneity and robust composites (see Supplementary Information for further explanations).

In addition, CB-FG effectively enhances polymer properties. A 0.1 wt% CB-FG–polydimethylsiloxane (PDMS) composite showed  $\sim 250\%$  increase in compressive strength compared with PDMS without graphene (Supplementary Fig. 20).

To demonstrate its applicability in electrochemical energy storage devices, C-FG and CPC-FG were also used as electrode materials in a Li-ion capacitor and a Li-ion battery (Supplementary Fig. 21), demonstrating the potential to use FG in advanced energy applications.

In summary, a low-energy bottom-up synthesis of easily exfoliated turbostratic graphene was demonstrated from ultralow-cost carbon sources (such as coal and petroleum coke), renewable resources (such as biochar and rubber tyres) and mixed-waste products (including plastic bottles



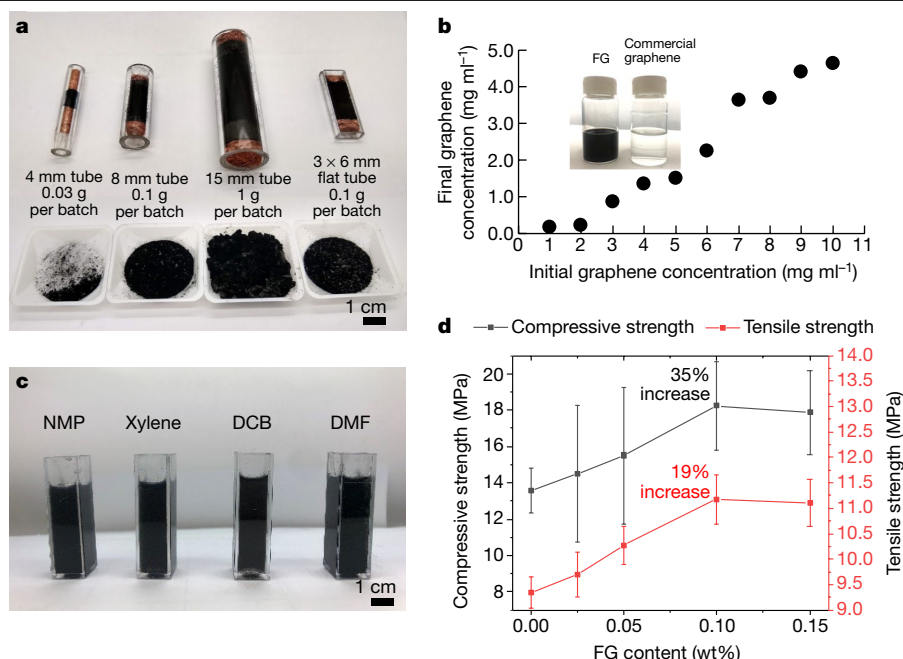


**Fig. 4 | Scaling up and applications of CB-FG.** **a**, FJH quartz tubes of different sizes and shapes, used to synthesize FG. Two separate synthesis processes were conducted with each tube, providing the samples in the tube and those in the plastic dishes. **b**, FG dispersion in a water-Pluronic (F-127) solution (1%). The photograph shows the supernatants of 4 g l<sup>-1</sup> of CB-FG and of 10 g l<sup>-1</sup> of a

commercial sample after centrifugation. The commercial graphene was not stable as a colloid at this concentration, resulting in a clear liquid in the supernatant after centrifugation. **c**, FG dispersion in various organic solvents at 5 g l<sup>-1</sup>. **d**, Mechanical performance of cement compounded with FG. The error bars represent one standard error ( $n = 3$ ).

and discarded food). Scaling up of the FG synthesis process could provide turbostratic graphene for bulk construction composite materials.

## Online content

Any methods, additional references, Nature Research reporting summaries, source data, extended data, supplementary information, acknowledgements, peer review information; details of author contributions and competing interests; and statements of data and code availability are available at <https://doi.org/10.1038/s41586-020-1938-0>.

- Allen, M. J., Tung, V. C. & Kaner, R. B. Honeycomb carbon: a review of graphene. *Chem. Rev.* **110**, 132–145 (2010).
- Yi, M. & Shen, Z. A review on mechanical exfoliation for the scalable production of graphene. *J. Mater. Chem. A* **3**, 11700–11715 (2015).
- Hernandez, Y. et al. High-yield production of graphene by liquid-phase exfoliation of graphite. *Nat. Nanotechnol.* **3**, 563–568 (2008).
- Eda, G., Fanchini, G. & Chhowalla, M. Large-area ultrathin films of reduced graphene oxide as a transparent and flexible electronic material. *Nat. Nanotechnol.* **3**, 270–274 (2008).
- Li, D. et al. Processable aqueous dispersions of graphene nanosheets. *Nat. Nanotechnol.* **3**, 101–105 (2008).
- Lin, L., Peng, H. & Liu, Z. Synthesis challenges for graphene industry. *Nat. Mater.* **18**, 520–524 (2019).
- Ferrari, A. C. et al. Raman spectrum of graphene and graphene layers. *Phys. Rev. Lett.* **97**, 187401 (2006).
- Ferrari, A. C. Raman spectroscopy of graphene and graphite: disorder, electron-phonon coupling, doping and nonadiabatic effects. *Solid State Commun.* **143**, 47–57 (2007).
- Malard, L. M., Pimenta, M. A., Dresselhaus, G. & Dresselhaus, M. S. Raman spectroscopy in graphene. *Phys. Rep.* **473**, 51–87 (2009).
- Ni, Z. H. et al. Probing charged impurities in suspended graphene using Raman spectroscopy. *ACS Nano* **3**, 569–574 (2009).
- Garlow, J. A. et al. Large-area growth of turbostratic graphene on Ni (111) via physical vapor deposition. *Sci. Rep.* **6**, 19804 (2016).
- Niilisk, A. et al. Raman characterization of stacking in multi-layer graphene grown on Ni. *Carbon* **98**, 658–665 (2016).
- Li, Z. Q. et al. X-ray diffraction patterns of graphite and turbostratic carbon. *Carbon* **45**, 1686–1695 (2007).
- Franklin, R. E. Crystallite growth in graphitizing and non-graphitizing carbons. *Proc. R. Soc. Lond.* **209**, 196–218 (1951).
- Stankovich, S. et al. Synthesis of graphene-based nanosheets via chemical reduction of exfoliated graphite oxide. *Carbon* **45**, 1558–1565 (2007).
- Cai, M., Thorpe, D., Adamson, D. H. & Schniepp, H. C. Methods of graphite exfoliation. *J. Mater. Chem.* **22**, 24992–25002 (2012).
- Miandad, R. et al. Catalytic pyrolysis of plastic waste: moving toward pyrolysis based biorefineries. *Front. Energy Res.* **7**, 27 (2019).
- Gibb, B. C. Plastics are forever. *Nat. Chem.* **11**, 394–395 (2019).
- Parfitt, J., Barthel, M. & Macnaughton, S. Food waste within food supply chains: quantification and potential for change to 2050. *Philos. Trans. R. Soc. B* **365**, 3065–3081 (2010).
- Gustavsson, J., Cederberg, C., Sonesson, U., van Otterdijk, R. & Meybeck, A. *Global Food Losses and Food Waste: Extent, Causes and Prevention* (FAO, 2011); <http://www.fao.org/3/a-i2697e.pdf>.
- Jambeck, J. R. et al. Plastic waste inputs from land into the ocean. *Science* **347**, 768–771 (2015).
- Yao, Y. et al. Carbothermal shock synthesis of high-entropy-alloy nanoparticles. *Science* **359**, 1489–1494 (2018).
- Advincula, P. A. et al. Accommodating volume change and imparting thermal conductivity by encapsulation of phase change materials in carbon nanoparticles. *J. Mater. Chem. A* **6**, 2461–2467 (2018).
- Chakrabarti, A. et al. Conversion of carbon dioxide to few-layer graphene. *J. Mater. Chem.* **21**, 9491–9493 (2011).
- Lin, J. et al. Laser-induced porous graphene films from commercial polymers. *Nat. Commun.* **5**, 5714 (2014).
- Nepal, A., Singh, G. P., Flanders, B. N. & Sorensen, C. M. One-step synthesis of graphene via catalyst-free gas-phase hydrocarbon detonation. *Nanotechnology* **24**, 245602 (2013).
- Huang, J. Y. et al. Real-time observation of tubule formation from amorphous carbon nanowires under high-bias Joule heating. *Nano Lett.* **6**, 1699–1705 (2006).
- Harris, P. J. F. Engineering carbon materials with electricity. *Carbon* **122**, 504–513 (2017).
- Luong, D. X. et al. Laser-induced graphene fibers. *Carbon* **126**, 472–479 (2017).
- Stuart, S. J., Tutein, A. B. & Harrison, J. A. A reactive potential for hydrocarbons with intermolecular interactions. *J. Chem. Phys.* **112**, 6472–6486 (2000).
- Brenner, D. W. et al. A second-generation reactive empirical bond order (REBO) potential energy expression for hydrocarbons. *J. Phys. Chem. Matter.* **14**, 783–802 (2002).
- Plimpton, S. Fast parallel algorithms for short-range molecular dynamics. *J. Comput. Phys.* **117**, 1–19 (1995).
- Xu, Y. et al. Liquid-phase exfoliation of graphene: an overview on exfoliation media, techniques, and challenges. *Nanomaterials* **8**, 942 (2018).
- O'Neill, A., Khan, U., Nirmalraj, P. N., Boland, J. & Coleman, J. N. Graphene dispersion and exfoliation in low boiling point solvents. *J. Phys. Chem. C* **115**, 5422–5428 (2011).
- Dong, L. et al. A non-dispersion strategy for large-scale production of ultra-high concentration graphene slurries in water. *Nat. Commun.* **9**, 76 (2018).
- Liu, J., Li, Q. & Xu, S. Reinforcing mechanism of graphene and graphene oxide sheets on cement-based materials. *J. Mater. Civ. Eng.* **31**, 04019014 (2019).
- Krystek, M. et al. High-performance graphene-based cementitious composites. *Adv. Sci.* **6**, 1801195 (2019).

**Publisher's note** Springer Nature remains neutral with regard to jurisdictional claims in published maps and institutional affiliations.

© The Author(s), under exclusive licence to Springer Nature Limited 2020

**FJH system**

The FJH set up is detailed in Supplementary Fig. 1. Inside a quartz tube, two loosely fitting electrodes compress the carbon source using two copper-wool plugs or graphite spacers to contact the carbon sources to allow degassing of volatile materials. The compressing force is controllable by a modified small vice so as to minimize the sample resistance to 1–1,000  $\Omega$ , and is key to obtaining a good flash reaction ( $0.004\text{--}4\text{ S cm}^{-1}$ ). To control the discharge time, a mechanical relay with programmable millisecond-level delay time is used. The entire sample reaction chamber is placed inside a low-pressure container (plastic vacuum desiccator) for safety and to facilitate degassing. However, the FJH process works equally well at 1 atm. The capacitor bank consists of 20 capacitors with a total capacitance of 0.22 F. Each capacitor is connected to the main power cable (or bus) by a circuit breaker that is also used as a switch to enable/disable each capacitor. The capacitor bank is charged by a d.c. supply capable of reaching 400 V. The first prototype system is placed conveniently on one plastic mobile cart (Supplementary Fig. 1b). Using a large 15-mm-diameter quartz tube, we achieve synthesis of 1 g of FG per batch using the FJH process.

Safety notice: the capacitor bank is capable of generating fatal electric pulses. Therefore, the following steps are taken to protect the operator as well as the circuit, and we strongly suggest that these measures be followed. Details of the circuit can be found in Supplementary Fig. 1a. Darkened safety glasses should be worn to protect eyes from the bright light during the discharge flashing process.

The voltage and current ratings for the circuit breaker are appropriate for the maximum voltage and the anticipated maximum current that will be supplied by each capacitor to the FJH discharge on the basis of a discharge time of 50–200 ms. We use the maximum charging and bleeding voltages at  $\sim 400\text{ V}$  with maximum currents of 0.7 A and 0.1 A, respectively. The pulse discharging voltage to the sample is  $\sim 400\text{ V}$  and current can reach up to 1,000 A in  $<100\text{ ms}$ . A 24-mH inductor is used to avoid current spikes while using the mechanical relay. Without the inductor, the mechanical relay could be prone to high-current arcing during the intermittent closing of the circuit. To protect the inductor from the spike voltage when shutting off the current, a diode and a low-resistance resistor with appropriate ratings are connected parallel to the inductor. Additionally, to protect the capacitor from reverse polarity in case of oscillatory decay (which can occur in a fast discharge), an appropriate diode is placed parallel to the capacitor bank.

**Characterization**

The resultant FG products were characterized by scanning electron microscopy (SEM) using an FEI Helios NanoLab 660 DualBeam SEM system at 5 kV with a working distance of 10 mm. X-ray photoelectron spectroscopy (XPS) data were collected with a PHI Quantera SXM Scanning X-ray Microprobe with a base pressure of  $5 \times 10^{-9}$  torr. Survey spectra were recorded using 0.5-eV steps with a pass energy of 140 eV. Elemental spectra were recorded using 0.1-eV steps with a pass energy of 26 eV. All of the XPS spectra were corrected using the C 1s peak (284.5 eV) as reference.

TEM images were taken with a JEOL 2100F field-emission gun TEM at 200 kV. Atomic-resolution HR-TEM images were taken with an FEI Titan Themis S/TEM system at 80 keV. Samples were prepared by dropping diluted dispersions ( $\sim 1\text{ mg ml}^{-1}$  in isopropanol) of the graphene sample ( $<200\text{ }\mu\text{l}$ ) on the TEM Cu grids. The dispersion was prepared using a bath sonicator ( $\sim 15\text{ min}$ ). Electron diffraction was calibrated by a diffraction standard (evaporated Al grid; Ted Pella).

All Raman spectra were collected with as-prepared FG samples atop a glass slide, before exposure to solvent, using a Renishaw Raman microscope and a 532-nm laser with a power of 5 mW. A  $50\times$  lens was used for the local Raman spectra in Fig. 1 and a  $5\times$  lens for the mean Raman spectra in Fig. 2.

**Atomistic modelling**

Atomistic simulations were carried out using periodic boundary conditions with  $\sim 15,000$  atoms per unit cell for all structures except the carbon black model, which contained  $\sim 55,000$  atoms. The initial configurations were created by random positioning and misorientation of small graphitic flakes of arbitrary shape and up to 8–12 Å in diameter, and subsequently adding randomly positioned individual carbon atoms (the atomic carbon content was  $\sim 50\%$  to represent a non-graphitized portion of the source material). Carbon black centroid particles were created by arranging randomly oriented graphitic flakes in roughly spherical shapes with hollow cores and diameters of up to 12 nm, and adding atomic carbon ( $\sim 50\%$ ). The initial configurations were subjected to preliminary annealing at 400 K for  $2 \times 10^{-9}\text{ s}$  to eliminate irregularities caused by the structure creation protocol, then heated to the target annealing temperature with a heating speed of  $0.5 \times 10^{-12}\text{ K s}^{-1}$  using a Nose-Hoover thermostat (canonical NVT ensemble) with a temperature damping parameter of  $0.025 \times 10^{-12}\text{ s}$ . The structures were held at the target annealing temperatures for  $5 \times 10^{-9}\text{ s}$  ( $15 \times 10^{-9}\text{ s}$  for carbon black).

**Preparation of flash graphene dispersion in water–Pluronic solution**

FG was dispersed in water–Pluronic (F-127) solution (1%) at concentrations of  $1\text{--}10\text{ g l}^{-1}$ . The mixture was sonicated in an ultrasonic bath for 40 min to obtain a dark dispersion. The dispersion was subjected to centrifugation at 1,500 rpm (470 relative centrifugal force) for 30 min to remove aggregates using a Beckman Coulter Allegra X-12 centrifuge equipped with a 19-cm-radius rotor. The supernatant was analysed via ultraviolet–visible spectroscopy (Shimadzu). The dispersions were diluted 500 times and the absorbance was recorded at 660 nm. An extinction coefficient of  $\alpha_{660} = 6,600\text{ l g}^{-1}\text{ m}^{-1}$  was used to calculate the concentration of graphene in the solution.

**Cement sample preparation**

FG at various concentrations was dispersed in 1% water–Pluronic (F-127) solution. The dispersion was agitated for 15 min at 5,000 rpm using a shear mixer (Silverson L5MA). The graphene suspension in water was mixed with Portland cement with a water-to-cement ratio of 0.40. The slurry was cast in  $5 \times 5 \times 5\text{ cm}^3$  cubic polytetrafluoroethylene moulds (for compressive strength measurements) and in  $2.5\text{ cm} \times 3.8\text{ cm}$  cylindrical moulds (for tensile strength measurements). All cubes and cylinders were taken out the moulds after 24 h and placed in water for curing for another 24 h. The compressive and tensile mechanical strengths were measured after 7 and 28 days. For each FG–cement ratio, three samples were cast and tested.

**Cement and PDMS testing procedures**

**Compressive strength.** The compression strength tests were performed using a Forney Variable Frequency Drive automatic machine with dual load cells for maximum accuracy.

**Tensile strength.** Owing to the brittle nature of cement-based materials, the tensile strength was calculated via a splitting test because it gives the most accurate measurement. Special jigs held the cylinders so that the uniaxial compressive force applied to the centre lines of the bottom and top surfaces of the samples caused tensile stress between the points of contact.

**Data availability**

The datasets generated and/or analysed during the current study are available from the corresponding author on reasonable request.

**Acknowledgements** We thank G. A. Lopez Silva for preparing the schematic of the FJH process, J. Li for preparing the olive oil soot, Oxbow Calcining International LLC for donating the calcined coke, Ergon Asphalt and Emulsions, Inc. for donating the rubber-tyre-derived carbon black, and Neroval LLC for donating the biochar. K.V.B. and B.I.Y. thank the National Science Foundation (NSF) for support (CBET-1605848) and B. Sastri of the US Department of Energy for discussions. R.S. thanks the partial support of NSF-DMR 1709051. J.M.T. thanks the US Air Force Office of Scientific Research (FA9550-19-1-0296) for support.

**Author contributions** D.X.L. discovered the FJH conversion of carbon materials to graphene, designed and built the FJH apparatus, designed and built the spectrometer for temperature determination, acquired most of the data, and wrote most of the manuscript. K.V.B. conducted the mechanistic theory calculations under the guidance of B.I.Y. W.A.A. and P.A.A. fabricated some FG samples, and blended and tested the polymer blends. M.G.S. obtained the SEM images and wrote parts of Supplementary Information, especially regarding FG morphology. C.K. assisted with the design of the FG apparatus and the spectrometer, and wrote parts of Supplementary Information regarding turbostratic graphene. R.V.S. obtained most of the TEM images and all of the selected-area electron diffraction data. W.C. and H.G. obtained some of the TEM images. M.R. built and tested the lithium-ion capacitor. C.K. and V.M. assisted D.X.L. in the design and safety features of the FJH system. E.A.M. performed the thermogravimetric analysis. Z.W. obtained the surface area. M.B. obtained the cement and polymer composite

data under the guidance of R.S. All aspects of the research were overseen by J.M.T., who co-wrote some sections of the manuscript.

**Competing interests** The FG synthesis process is the intellectual property of Rice University. J.M.T., D.X.L. and V.M. will be stockholders in Universal Matter Ltd, a company licensing the FG intellectual property of Rice University and scaling up this process. At the time of the writing and submission of this manuscript, the license to Universal Matter has not been consummated. C-Crete Technologies owns intellectual property on the strengthening of graphene-cement/concrete composites. V.M. is now employed by Universal Matter. D.X.L. and J.M.T. will remain full time with Rice University, whereas D.X.L. might be employed by Universal Matter in two years. All conflicts of interest for J.M.T. and D.X.L. are managed through regular disclosure to the Rice University Office of Sponsored Programs and Research Compliance.

#### **Additional information**

**Supplementary information** is available for this paper at <https://doi.org/10.1038/s41586-020-1938-0>.

**Correspondence and requests for materials** should be addressed to R.S., B.I.Y. or J.M.T.

**Peer review information** *Nature* thanks Loh Kian Ping and the other, anonymous, reviewer(s) for their contribution to the peer review of this work.

**Reprints and permissions information** is available at <http://www.nature.com/reprints>.

# Redox-switchable carboranes for uranium capture and release

<https://doi.org/10.1038/s41586-019-1926-4>

Received: 26 March 2019

Accepted: 30 October 2019

Published online: 22 January 2020

Megan Keener<sup>1</sup>, Camden Hunt<sup>1</sup>, Timothy G. Carroll<sup>1</sup>, Vladimir Kampel<sup>2</sup>, Roman Dobrovetsky<sup>2</sup>, Trevor W. Hayton<sup>1</sup> & Gabriel Ménard<sup>1\*</sup>

The uranyl ion ( $\text{UO}_2^{2+}$ ; U(VI) oxidation state) is the most common form of uranium found in terrestrial and aquatic environments and is a central component in nuclear fuel processing and waste remediation efforts. Uranyl capture from either seawater or nuclear waste has been well studied and typically relies on extremely strong chelating/binding affinities to  $\text{UO}_2^{2+}$  using chelating polymers<sup>1,2</sup>, porous inorganic<sup>3–5</sup> or carbon-based<sup>6,7</sup> materials, as well as homogeneous<sup>8</sup> compounds. By contrast, the controlled release of uranyl after capture is less established and can be difficult, expensive or destructive to the initial material<sup>2,9</sup>. Here we show how harnessing the redox-switchable chelating and donating properties of an *ortho*-substituted *closo*-carborane ( $1,2-(\text{Ph}_2\text{PO})_2-1,2-\text{C}_2\text{B}_{10}\text{H}_{10}$ ) cluster molecule can lead to the controlled chemical or electrochemical capture and release of  $\text{UO}_2^{2+}$  in monophasic (organic) or biphasic (organic/aqueous) model solvent systems. This is achieved by taking advantage of the increase in the ligand bite angle when the *closo*-carborane is reduced to the *nido*-carborane, resulting in C–C bond rupture and cage opening. The use of electrochemical methods for uranyl capture and release may complement existing sorbent and processing systems.

Known for over 50 years, carboranes have been extensively studied in coordination chemistry (including with U), catalysis, luminescence, and energy storage applications<sup>10–15</sup>. Studies have shown that reduction of substituted *closo*-carboranes to the *nido*-carboranes results in rupture of the C–C bond and cage opening, with a simultaneous increase in ligand bite angle,  $\theta$  (Fig. 1a; *closo* and *nido* refer to  $2n + 2$  and  $2n + 4$  framework bonding electrons, respectively, where  $n$  is the number of vertices)<sup>11,14,16–18</sup>. We rationalized that by incorporating donating groups to *ortho*-carborane, we could tune the chelating properties of the cluster switching from opened to closed conformations by redox control of the reduced and oxidized states, respectively, and enable the chemical or electrochemical capture and release of uranyl in solution (Fig. 1a).

The *closo*-carborane  $1,2-(\text{Ph}_2\text{PO})_2-1,2-\text{C}_2\text{B}_{10}\text{H}_{10}$  (**1**) was synthesized and fully characterized, including by X-ray diffraction (XRD) studies (Fig. 1a, Extended Data Fig. 1a)<sup>19</sup>. The cage C–C bond length (1.688(4) Å) and interatomic P...P distance (3.537 Å) are consistent with previous relevant reports<sup>19,20</sup> (all uncertainties are estimated standard deviations or standard uncertainties). These metrics will be used throughout to correlate coordinated and uncoordinated carboranes, both in lieu of—yet proportional to—the traditional bite angle  $\theta$  (Fig. 1a). The cyclic voltammogram of **1** in tetrahydrofuran (THF) revealed two quasi-reversible cathodic waves at  $-0.93$  V and  $-1.11$  V relative to the ferrocene/ferrocenium ( $\text{Fc}/\text{Fc}^+$ ) redox couple (Extended Data Fig. 2a). Reduction of **1** using 2.0 equiv. decamethylcobaltocene ( $\text{CoCp}_2^+$ ) afforded the direduced *nido*-carborane,  $[\text{CoCp}_2^+]_2[(\text{nido}-1,2-(\text{Ph}_2\text{PO})_2-1,2-\text{C}_2\text{B}_{10}\text{H}_{10})]$  (**2a**) (Fig. 1a). The solid-state structure revealed an open-cage *nido*-carborane with a

cleaved C–C bond (2.860 Å) and an elongated P...P distance (5.036 Å) relative to **1** (Extended Data Figs. 1b, c). An analogous salt,  $[\text{Bu}_4\text{N}]_2[(\text{nido}-1,2-(\text{Ph}_2\text{PO})_2-1,2-\text{C}_2\text{B}_{10}\text{H}_{10})]$  (**2b**) (Fig. 1a), relevant to the electrochemical experiments, was also synthesized by reduction of **1** with  $\text{KC}_8$ , followed by salt metathesis with  $[\text{Bu}_4\text{N}][\text{Cl}]$  (see Methods).

We next investigated the coordination chemistry of **1** and **2a**. Addition of 4 equiv. **1** to dimeric  $[\text{UO}_2\text{Cl}_2(\text{THF})_2]_2$  in deuterated dichloromethane ( $\text{DCM}-d_2$ ) resulted in a light-yellow solution from which two new equivalent-intensity  $^{31}\text{P}$  resonances appeared at 38.8 and 38.4 ppm in the nuclear magnetic resonance (NMR) spectrum, shifted downfield from **1** (22.8 ppm). The inequivalent P environments suggest either an octahedral geometry at U with two monodentate **1** ligands or a pentagonal bipyramidal geometry at U with two bidentate **1** and a chloride in the fifth equatorial site. Although attempts to obtain single crystals for XRD studies failed, the NMR data suggest that a 2:1 adduct is formed with a presumed formulation of  $[\text{UO}_2\text{Cl}_2(\text{THF})_2]_2$ . In contrast to **1**, treatment of 2 equiv. **2a** to  $[\text{UO}_2\text{Cl}_2(\text{THF})_2]_2$  led to clean formation of a single new resonance at 51.1 ppm in the  $^{31}\text{P}$  NMR spectrum, consistent with a bidentate coordination mode. XRD studies confirmed the composition as the uranyl salt  $[\text{CoCp}_2^+]_2[\text{UO}_2(\text{nido}-1,2-(\text{Ph}_2\text{PO})_2-1,2-\text{C}_2\text{B}_{10}\text{H}_{10})]$  (**3**) (Fig. 1a, c). A disubstituted uranyl salt was also obtained by addition of 4 equiv. **2a** to  $[\text{UO}_2\text{Cl}_2(\text{THF})_2]_2$ . Monitoring the reaction by  $^{31}\text{P}$  NMR spectroscopy revealed clean conversion to a new product with a single peak at 52.0 ppm. XRD studies on single crystals confirmed the composition as the disubstituted complex  $[\text{CoCp}_2^+]_2[\text{UO}_2(\text{nido}-1,2-(\text{Ph}_2\text{PO})_2-1,2-\text{C}_2\text{B}_{10}\text{H}_{10})_2]$  (**4**) (Fig. 1a, b). The bond metrics for **3** and **4** are similar (Extended Data Fig. 1c).

<sup>1</sup>Department of Chemistry and Biochemistry, University of California, Santa Barbara, CA, USA. <sup>2</sup>School of Chemistry, Raymond and Beverly Sackler Faculty of Exact Sciences, Tel Aviv University, Tel Aviv, Israel. \*e-mail: menard@chem.ucsb.edu



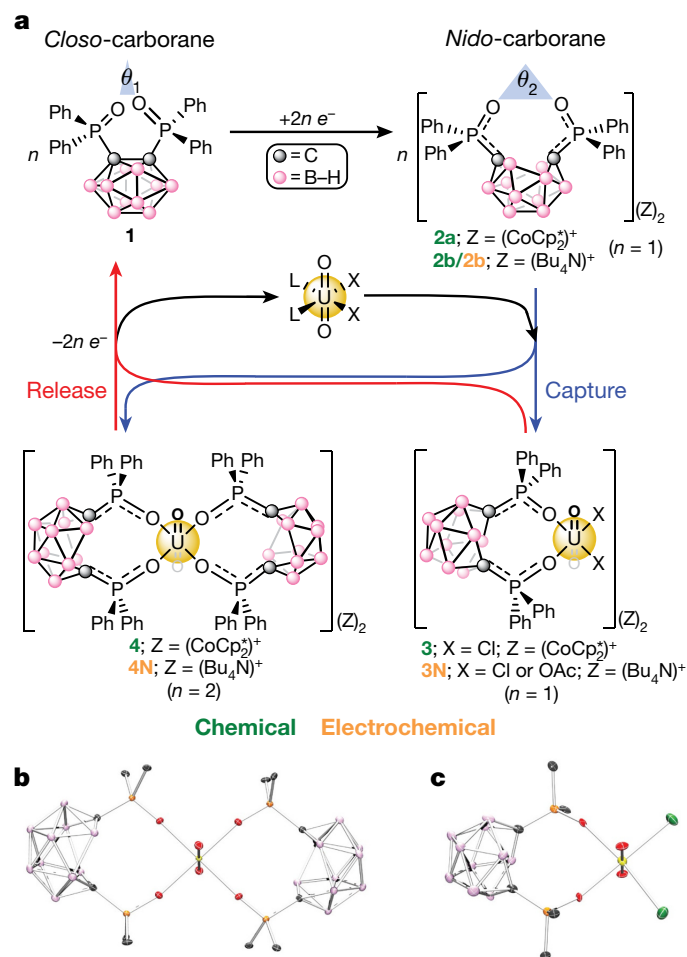


**Fig. 1 | Chemical or electrochemical capture and release of  $\text{UO}_2^{2+}$  with resulting complexes shown.** **a**, General chemical or electrochemical mono- or bi-phasic capture of uranyl from  $\text{UO}_2\text{X}_2\text{L}_2$  ( $\text{X} = \text{Cl}^-$ ,  $\text{OAc}^-$ ;  $\text{L} = \text{THF}$ ,  $\text{Ph}_3\text{PO}$ ) using the reduced 'open'-cage nido-carboranes (**2a/2b**) generated by reduction (for example,  $\text{CoCp}_2$  or negative bias) of the 'closed'-cage closo-carborane (**1**). The corresponding relative bite angles ( $\theta$ ) are also shown. Oxidation (for example,  $[\text{FeCp}_2][\text{PF}_6]$  or positive bias) of the captured products **3/4** or **3N/4N** leads to  $\text{UO}_2^{2+}$  release. Compounds labelled in green have been chemically isolated, whereas compounds in orange are proposed electrochemical products (see Methods). Blue and red pathways represent  $\text{UO}_2^{2+}$  capture and release, respectively. **b, c**, Solid-state molecular structures of **4** (**b**) and **3** (**c**) obtained from XRD studies. H atoms,  $[\text{CoCp}_2]^+$  counter cations, phenyl C-H linkages and all co-crystallized solvent molecules are omitted for clarity. See Extended Data Fig. 1 for the structures of **1** and **2a**.

Whereas **1** and **2a** coordinate to  $\text{UO}_2^{2+}$ , we postulated that a third ligand with a competitive binding affinity to **1**, but weaker than **2a**, could enable a pathway to  $\text{UO}_2^{2+}$  release. Competition experiments using **1**, **2a** and triphenylphosphine oxide (TPO), as part of  $\text{UO}_2\text{Cl}_2(\text{TPO})_2$  (ref. 21), were performed and monitored by  $^{31}\text{P}\{^1\text{H}\}$  NMR spectroscopy in  $\text{DCM-d}_2$ . Two equivalents of **1** were added to  $\text{UO}_2\text{Cl}_2(\text{TPO})_2$  for a 1:1 molar ratio of **1**:TPO. After an equilibration period, the  $^{31}\text{P}\{^1\text{H}\}$  NMR spectrum revealed broadened resonances for  $\text{UO}_2\text{Cl}_2(\text{TPO})_2$  and free TPO, as well as a set of sharp resonances for  $\text{UO}_2\text{Cl}_2(\text{1})_2$  and free **1**. The ratio of  $\text{UO}_2\text{Cl}_2(\text{1})_2$ :**1** was determined to be approximately 1:3, suggesting an equilibrium favouring the adduct,  $\text{UO}_2\text{Cl}_2(\text{TPO})_2$  (Extended Data Fig. 3a). The binding affinity of TPO was next compared to **2a** by addition of 1 equiv. **2a** to  $\text{UO}_2\text{Cl}_2(\text{TPO})_2$ . Rapid precipitation of products was observed. The  $^{31}\text{P}\{^1\text{H}\}$  NMR spectrum of the DCM supernatant revealed complete conversion to the products **3** and **4**, along with a sharp singlet for TPO, and a minor unknown singlet at 47 ppm. Analysis of the precipitate dissolved

in propylene carbonate (PC) by  $^{31}\text{P}\{^1\text{H}\}$  NMR spectroscopy revealed the presence of **4** (Extended Data Fig. 3b). These data are consistent with full dissociation of TPO from  $\text{UO}_2\text{Cl}_2(\text{TPO})_2$  in the presence of **2a**. The binding affinity of TPO was next tested against PC, a coordinating solvent<sup>22</sup>. An initial  $^{31}\text{P}\{^1\text{H}\}$  NMR spectrum of  $\text{UO}_2\text{Cl}_2(\text{TPO})_2$  dissolved in  $\text{DCM-d}_2$  revealed two singlets in a 3:1 ratio at 48.09 and 47.97 ppm, respectively, probably arising from *trans:cis* isomerism<sup>23</sup>. Whereas addition of 2 equiv. PC led to negligible changes, addition of 20 and 40 equivalents led to increasing broadness of the aromatic peaks in the  $^1\text{H}$  NMR spectra and broadening of the singlets in the  $^{31}\text{P}\{^1\text{H}\}$  NMR spectra (Extended Data Fig. 4). Together, these data suggest a weak equilibrium with PC that is heavily shifted towards  $\text{UO}_2\text{Cl}_2(\text{TPO})_2$ . Density functional theory (DFT) calculations further supported these observations. The electron density surfaces with integrated electrostatic potentials for **1** and **2a** clearly indicate increased electron density at the  $\text{P}=\text{O}$  bonds of **2a** upon reduction, accounting for its experimentally observed increased Lewis basicity (Extended Data Fig. 1d). This probably complements the increased bite angle (Fig. 1a) in rendering **2a** a stronger chelating agent than **1**. In silico isodesmic reactions of **2a**/TPO, TPO/**1** or **1**/PC with protons as a model for the uranyl cation were also calculated (see Methods and Supplementary Information). Together with the experimental data, these data support a relative Lewis basicity trend of: **2a**  $\gg$  TPO  $>$  **1**  $\gg$  PC.

We next investigated the in situ chemical capture and release of  $\text{UO}_2^{2+}$ . For optimal solubility, we used a 3:1 PC:benzene solvent mixture. A 2:4 solution of **1**:TPO was analysed by  $^{31}\text{P}\{^1\text{H}\}$  NMR spectroscopy, which revealed two sharp resonances (Extended Data Fig. 5a). Addition of 0.5 equiv.  $[\text{UO}_2\text{Cl}_2(\text{THF})_2]_2$  (1 equiv. U) resulted in no appreciable change to the resonance for **1**, but in substantial broadening to the resonance for TPO (Extended Data Fig. 5b). Only trace  $\text{UO}_2\text{Cl}_2(\text{TPO})_2$  is observed and is probably due to a combination of rapid exchange with excess TPO and the excess ( $\sim 2,000$  times) PC used relative to U. To initiate chemical capture of  $\text{UO}_2^{2+}$ , 4 equiv.  $\text{CoCp}_2$  was added. Analysis by  $^{31}\text{P}\{^1\text{H}\}$  NMR spectroscopy revealed the rapid and complete conversion of **1** to **4** with concomitant release of TPO (Extended Data Fig. 5c). To initiate  $\text{UO}_2^{2+}$  release, we first determined the oxidation potential of **4** by cyclic voltammetry, which revealed a quasi-reversible anodic event at  $-0.42$  V relative to  $\text{Fc}/\text{Fc}^+$  (Extended Data Fig. 2b). Thus, we exposed our in situ generated solution of **4** and TPO to 4 equiv.  $[\text{Fc}][\text{PF}_6]$ . Analysis by  $^{31}\text{P}\{^1\text{H}\}$  NMR spectroscopy revealed the full conversion of **4** back to **1**, along with the re-appearance of a broadened TPO resonance, similar to that of the pre-reduced solution (Extended Data Fig. 5d). Together, these results demonstrate the successful chemical capture and release of  $\text{UO}_2^{2+}$  in solution.

We next targeted the electrochemical capture and release of  $\text{UO}_2^{2+}$  by galvanostatic bulk electrolysis (GBE). This was conducted using a divided H-cell with coiled Pt electrodes, an anion-exchange membrane (AEM) and an excess of the  $\text{Fc}/\text{Fc}^+$  redox couple in the counter compartment (Fig. 2a). A 0.5:5:6 ratio of  $[\text{UO}_2\text{Cl}_2(\text{THF})_2]_2$ :**1**:TPO was used in PC:benzene (3:1) along with an internal standard for  $^{31}\text{P}$  NMR integration. Whereas the use of excess TPO is well reasoned (see above), the use of excess **1** was found to be necessary for optimal electrochemical performance (see Methods). An initial  $^{31}\text{P}\{^1\text{H}\}$  NMR spectrum revealed a sharp signal for **1** and a broadened signal for TPO (Fig. 2b, initial), analogous to the chemical capture/release experiments. Electrochemical capture of  $\text{UO}_2^{2+}$  was initiated by galvanostatically charging the solution to a 75% theoretical state of charge (SOC) relative to the  $\text{UO}_2^{2+}$  concentration (Fig. 2c, blue; see Methods). Analysis of the reaction mixture by  $^{31}\text{P}\{^1\text{H}\}$  NMR spectroscopy revealed the conversion of **1** to the captured products **3N** ( $\text{X} = \text{Cl}$ ) and **4N**—the analogues of **3** and **4**, but with  $[\text{Bu}_4\text{N}]^+$  cations (Fig. 1a)—with release of all TPO, as determined by integration versus the internal standard (Fig. 2b, cycle 1, blue; Extended Data Fig. 6a). To initiate the electrochemical release of  $\text{UO}_2^{2+}$ , the cell was galvanostatically discharged to a final SOC of 15% (Fig. 2c, red; the SOC extrema of 0% and 100% were not used, to avoid unwanted

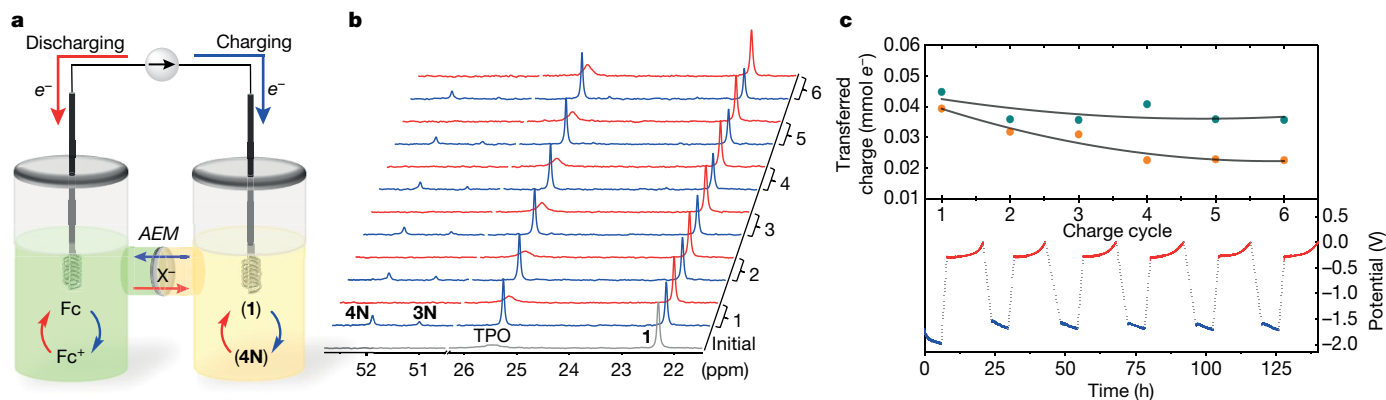


**Fig. 2 | Electrochemical setup and quantification data for the capture (blue) and release (red) of  $\text{UO}_2^{2+}$  in solution.** **a**, Illustration of the H-cell used, incorporating excess  $\text{Fc}/\text{Fc}^+$  (left) and **1**, TPO and  $[\text{UO}_2\text{Cl}_2(\text{THF})_2]$  (right) in a 3:1 PC:benzene solvent mixture. Charging the cell (blue) leads to the capture of  $\text{UO}_2^{2+}$ , converting **1** to **4N** (major product) and **3N** (minor product, not shown). **b**, Quantification of products and reactants by  $^{31}\text{P}\{^1\text{H}\}$  NMR spectroscopy against an inert internal standard,  $[\text{Ph}_3\text{PNPPh}_3][\text{PF}_6]$  (not shown). The initial spectrum is shown in grey, whereas spectra acquired during charge and

discharge cycles (1–6) are shown in blue and red, respectively. **c**, Bottom, applied galvanostatic potentials for charge (blue) and discharge (red) cycles. Dashed lines represent wait periods, which were necessary for  $^{31}\text{P}\{^1\text{H}\}$  NMR data acquisition. Each cycle is 24 h. Top, instrumental measure of delivered charge (teal) versus charge used for the reduction of **1**, measured by quantifying the total reduced products, **3N** and **4N**, by  $^{31}\text{P}$  NMR spectroscopy. See Methods and Extended Data Figs. 6, 8 for additional experimental details and data.

secondary electrochemical processes<sup>24</sup>). Analysis of the reaction mixture by  $^{31}\text{P}\{^1\text{H}\}$  NMR spectroscopy revealed the full conversion of **3N** and **4N** back to **1**, along with the presence of a broadened TPO resonance (Fig. 2b, cycle 1, red). The capture and release by GBE was carried out over the course of another five full cycles (Fig. 2c), with analyses of the reaction mixtures by  $^{31}\text{P}\{^1\text{H}\}$  NMR spectroscopy after each run (Fig. 2b). We observed that repeated cycling resulted in a loss of electrochemically generated **3N**, which we attribute to chloride migration to the counter compartment over time. The gradual appearance of a minor unknown product with a  $^{31}\text{P}$  resonance at 45 ppm was also observed after each charge cycle (Extended Data Fig. 6a). Analysis of the  $^{31}\text{P}\{^1\text{H}\}$  NMR integrations revealed approximate average losses of 0.3% per cycle for TPO, 3.4% per cycle for **4N** and 7.2% per cycle for **1**, perhaps attributable to electrochemical side reactions (Extended Data Fig. 6b)<sup>25,26</sup>. Lastly, analysis of the measured instrumental charge transferred relative to the total charge transferred for  $\text{UO}_2^{2+}$  capture (determined by  $^{31}\text{P}\{^1\text{H}\}$  NMR integrations) revealed a plateauing trend with increasing cycle number, with differences in charge attributed to Faradaic losses (Fig. 2c, top). Together, these results demonstrate the successful monophasic electrochemical capture and release of  $\text{UO}_2^{2+}$ .

A biphasic extraction scheme involving dissolved  $\text{UO}_2^{2+}$  (from  $\text{UO}_2(\text{NO}_3)_2(\text{THF})_2$ ) in the aqueous phase and **1** in the organic phase was next explored as a model system (Fig. 3a)<sup>27</sup>. We switched solvents from PC to water-immiscible 1,2-dichloroethane (DCE) and modified our H-cell design to include a physical glass-frit separator coupled with a heterogeneous carbon additive acting as a capacitive buffer, analogous to a previous report<sup>28</sup>, owing to the incompatibility of DCE with the anion-exchange membrane. The capture and release of  $\text{UO}_2^{2+}$  was simultaneously monitored by  $^{31}\text{P}\{^1\text{H}\}$  NMR and ultraviolet–visible absorption (UV-Vis) spectroscopy for the organic and aqueous layer, respectively. We note that the vibronic ligand-to-metal charge transfer absorption of  $\text{UO}_2^{2+}$  (425 nm) is pH-dependent, resulting in a variable extinction coefficient ( $\epsilon$ )<sup>29,30</sup>; therefore, a buffered solution of  $\text{UO}_2^{2+}$  was used. Figure 3 outlines the simplified experimental setup displaying half of the H-cell (see Methods and Extended Data Figs. 7, 8 for the full cell design and methodology). A DCE solution of **1** (1.0 equiv.) with  $[\text{Bu}_4\text{N}][\text{PF}_6]$  as the supporting electrolyte was galvanostatically charged to a ~75% theoretical SOC. Analysis of the solution by  $^{31}\text{P}\{^1\text{H}\}$  NMR spectroscopy revealed the clean conversion of most of **1** to **2b** (Fig. 3a, Extended Data Fig. 9a). A sodium acetate ( $\text{NaOAc}$ )-buffered (pH 5.4) water solution containing 1.25 equiv.  $\text{UO}_2(\text{NO}_3)_2(\text{THF})_2$  was

next added to the DCE layer with mixing. Approximately 0.9 equiv.  $\text{UO}_2^{2+}$  was captured from the aqueous phase, as evidenced by the comparison of the UV-Vis spectra obtained before and after mixing with the charged DCE solution (Fig. 3a, b, Extended Data Fig. 10a). Analysis of the DCE solution by  $^{31}\text{P}\{^1\text{H}\}$  NMR spectroscopy revealed the clean formation of a single resonance at 51.5 ppm (Fig. 3b, Extended Data Fig. 9b). Given the similar chemical shifts of isolated complexes **3** (51.1 ppm) and **4** (52.0 ppm), as well as the quantity of  $\text{UO}_2^{2+}$  captured (0.9 equiv.), we propose that the uranyl is probably the mono-ligated **3N** ( $\text{X} = \text{OAc}^-$  because of the buffer); however, **4N** cannot definitively be excluded (Fig. 1a). The aqueous phase was next removed and the cell was galvanostatically discharged to achieve a theoretical final SOC of ~0%. Mixing a fresh  $\text{NaOAc}$ -buffered solution (pH 5.4) into this solution led to the release of approximately 0.5 equiv.  $\text{UO}_2^{2+}$  from the DCE layer, as confirmed by UV-Vis spectroscopy (Fig. 3c, Extended Data Fig. 10b). Analysis of the DCE layer by  $^{31}\text{P}\{^1\text{H}\}$  NMR spectroscopy revealed the near-quantitative conversion to **1**, as well as the formation of minor (~20%) unknown byproducts (Fig. 3c, Extended Data Fig. 9c). We propose that the acetate ions probably act as the biphasic analogue of the monophasic TPO ligands by competitively binding with **1** to  $\text{UO}_2^{2+}$ . Control experiments revealed that negligible biphasic capture of  $\text{UO}_2^{2+}$  from the  $\text{NaOAc}$ -buffered solution occurred in the presence or absence of **1** (see Methods and Extended Data Fig. 10c–f). Together, these biphasic GBE experiments demonstrate the potential applicability of this redox-switchable capture and release chemistry.

In summary, we have introduced an approach to uranyl management involving its capture and—importantly—its release by controlled redox-switchable chelation using a derivatized *ortho*-carborane in monophasic or biphasic (organic/aqueous) environments. We anticipate that this fundamentally new direction in cluster carborane chemistry will have a considerable impact on nuclear fuel extraction and waste sequestration activities, and may lead to new research directions in related metal capture and release activities.

## Online content

Any methods, additional references, Nature Research reporting summaries, source data, extended data, supplementary information, acknowledgements, peer review information; details of author contributions and competing interests; and statements of data and code availability are available at <https://doi.org/10.1038/s41586-019-1926-4>.

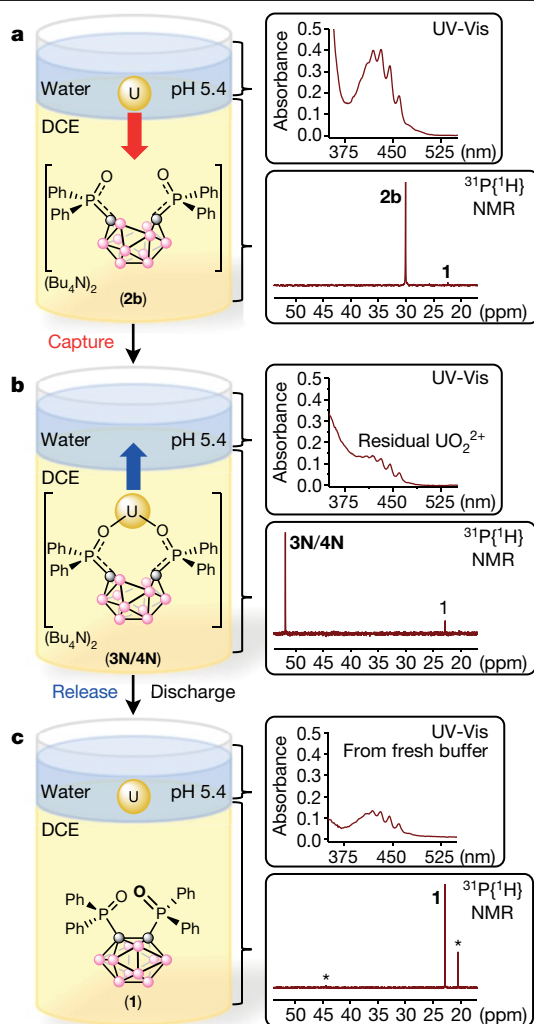


**Fig. 3 | Simplified depiction of half H-cell and spectroscopic measurements for the biphasic electrochemical capture/release of dissolved  $\text{UO}_2^{2+}$  (yellow sphere) from/to buffered aqueous solutions.** See Methods and Extended Data Fig. 7 for an expanded stepwise figure and all experimental details. **a**, Biphasic mixture of  $\text{UO}_2\text{X}_2$  dissolved in a NaOAc-buffered aqueous solution (pH 5.4) and of electrochemically generated **2b** from **1** ( $\text{X} = \text{OAc}^-$  or  $\text{NO}_3^-$ ). Inset, aqueous UV-Vis and organic  $^{31}\text{P}\{^1\text{H}\}$  NMR spectra after reduction of **1** to **2b**, but before phase mixing. Residual **1** is observed in the latter owing to the set SOC. **b**, Simplified depiction of the captured  $\text{UO}_2\text{X}_2$  in the form of **3N** and/or **4N**. Inset, aqueous UV-Vis spectrum showing the capture of  $\text{UO}_2\text{X}_2$  by the **2b**/DCE layer (top); the corresponding  $^{31}\text{P}\{^1\text{H}\}$  NMR spectrum of the DCE layer showing the captured major product (**3N/4N**) and minor residual **1** (bottom). **c**, Biphasic release of  $\text{UO}_2\text{X}_2$  from the DCE layer to a fresh NaOAc-buffered solution (pH 5.4), following electrochemical oxidation of **3N/4N**. Inset, aqueous UV-Vis and organic  $^{31}\text{P}\{^1\text{H}\}$  NMR spectra of free  $\text{UO}_2\text{X}_2$  and **1**, respectively—both consistent with the release of captured  $\text{UO}_2\text{X}_2$  from the DCE to the aqueous phase. A small amount (~20%) of unknown byproducts (marked by asterisks) is also observed in the  $^{31}\text{P}\{^1\text{H}\}$  NMR spectrum.

- Kim, J. et al. Recovery of uranium from seawater: a review of current status and future research needs. *Sep. Sci. Technol.* **48**, 367–387 (2013).
- Parker, B. F., Zhang, Z., Rao, L. & Arnold, J. An overview and recent progress in the chemistry of uranium extraction from seawater. *Dalton Trans.* **47**, 639–644 (2018).

- Xiong, L.-p. et al. Efficient capture of actinides from strong acidic solution by hafnium phosphonate frameworks with excellent acid resistance and radiolytic stability. *Chem. Eng. J.* **355**, 159–169 (2019).
- Sun, Q. et al. Bio-inspired nano-traps for uranium extraction from seawater and recovery from nuclear waste. *Nat. Commun.* **9**, 1644 (2018).
- Jang, J.-H., Dempsey, B. A. & Burgos, W. D. A model-based evaluation of sorptive reactivities of hydrous ferric oxide and hematite for  $\text{U}(\text{VI})$ . *Environ. Sci. Technol.* **41**, 4305–4310 (2007).
- Mellah, A., Chegrouche, S. & Barkat, M. The removal of uranium(VI) from aqueous solutions onto activated carbon: kinetic and thermodynamic investigations. *J. Colloid Interface Sci.* **296**, 434–441 (2006).
- Kim, J. H., Lee, H. I., Yeon, J.-W., Jung, Y. & Kim, J. M. Removal of uranium(VI) from aqueous solutions by nanoporous carbon and its chelating polymer composite. *J. Radioanal. Nucl. Chem.* **286**, 129–133 (2010).
- Mehio, N. et al. Quantifying the binding strength of salicylaldehyde–uranyl complexes relative to competing salicylaldehyde–transition metal ion complexes in aqueous solution: a combined experimental and computational study. *Dalton Trans.* **45**, 9051–9064 (2016).
- Kuo, L.-J. et al. Investigations into the reusability of amidoxime-based polymeric adsorbents for seawater uranium extraction. *Ind. Eng. Chem. Res.* **56**, 11603–11611 (2017).
- Fisher, S. P. et al. Nonclassical applications of closo-carborane anions: from main group chemistry and catalysis to energy storage. *Chem. Rev.* **119**, 8262–8290 (2019).
- Núñez, R., Tarrés, M., Ferrer-Ugalde, A., de Biani, F. F. & Teixidor, F. Electrochemistry and photoluminescence of icosahedral carboranes, boranes, metallocarboranes, and their derivatives. *Chem. Rev.* **116**, 14307–14378 (2016).
- Axtell, J. C., Saleh, L. M. A., Qian, E. A., Wixtrom, A. I. & Spokoyny, A. M. Synthesis and applications of perfunctionalized boron clusters. *Inorg. Chem.* **57**, 2333–2350 (2018).
- Fisher, S. P., Tomich, A. W., Guo, J. & Lavallo, V. Teaching an old dog new tricks: new directions in fundamental and applied closo-carborane anion chemistry. *Chem. Commun.* **55**, 1684–1701 (2019).
- Grimes, R. N. *Carboranes* 2nd edn (Elsevier Science and Technology, 2011).
- Xie, Z. Advances in the chemistry of metallocarboranes of f-block elements. *Coord. Chem. Rev.* **231**, 23–46 (2002).
- Weber, L. et al. Electrochemical and spectroelectrochemical studies of C-benzodiazaborolyl-ortho-carboranes. *Dalton Trans.* **42**, 2266–2281 (2013).
- Charmant, J. P. H. et al. A simple entry into nido- $\text{C}_2\text{B}_{10}$  clusters: HCl promoted cleavage of the C–C bond in ortho-carboranyl diphosphines. *Dalton Trans.* **11**, 1409–1411 (2008).
- Deng, L., Cheung, M.-S., Chan, H.-S. & Xie, Z. Reduction of 1,2- $(\text{CH}_2)_n$ -1,2- $\text{C}_2\text{B}_{10}\text{H}_{10}$  by group 1 metals. Effects of bridge length/rigidity on the formation of carborane anions. *Organometallics* **24**, 6244–6249 (2005).
- Popescu, A.-R. et al. Uncommon coordination behaviour of P(S) and P(Se) units when bonded to carboranyl clusters: experimental and computational studies on the oxidation of carboranyl phosphine ligands. *Chem. Eur. J.* **17**, 4429–4443 (2011).
- Sundberg, M. R. et al. Nature of intramolecular interactions in hypercoordinate C-substituted 1,2-dicarba-closo-dodecaboranes with short P...P distances. *Inorg. Chem. Commun.* **10**, 713–716 (2007).
- Bombieri, G., Forsellini, E., Day, J. P. & Azeez, W. I. Crystal and molecular structure of dichlorodioxobis(triphenylphosphine oxide)uranium(VI). *Dalton Trans.* **6**, 677–680 (1978).
- Brighli, M., Fux, P., Lagrange, J. & Lagrange, P. Discussion on the complexing ability of the uranyl ion with several crown ethers and cryptands in water and in propylene carbonate. *Inorg. Chem.* **24**, 80–84 (1985).
- Akono, S. B., Fawcett, J., Holloway, J. H., Russell, D. R. & Leban, I. Structures of cis- and trans-dichlorodioxobis(triphenylphosphine oxide)uranium(VI). *Acta Cryst. C* **47**, 45–48 (1991).
- Bard, A. J. & Faulkner, L. R. *Electrochemical Methods: Fundamentals and Applications* 2nd edn (Wiley, 2000).
- Liu, C. et al. A half-wave rectified alternating current electrochemical method for uranium extraction from seawater. *Nat. Energy* **2**, 17007 (2017).
- Chi, F., Zhang, S., Wen, J., Xiong, J. & Hu, S. Highly efficient recovery of uranium from seawater using an electrochemical approach. *Ind. Eng. Chem. Res.* **57**, 8078–8084 (2018).
- Paiva, A. P. & Malik, P. Recent advances on the chemistry of solvent extraction applied to the reprocessing of spent nuclear fuels and radioactive wastes. *J. Radioanal. Nucl. Chem.* **261**, 485–496 (2004).
- Hunt, C., Mattejat, M., Anderson, C., Sepanaru, L. & Ménard, G. Symmetric phthalocyanine charge carrier for dual redox flow battery/capacitor applications. *ACS Appl. Energy Mater.* **2**, 5391–5396 (2019).
- Quilès, F., Nguyen-Trung, C., Carteret, C. & Humbert, B. Hydrolysis of uranyl(VI) in acidic and basic aqueous solutions using a noncomplexing organic base: a multivariate spectroscopic and statistical study. *Inorg. Chem.* **50**, 2811–2823 (2011).
- Pant, D. D. & Khandelwal, D. P. The absorption and fluorescence spectra of uranyl nitrate solutions at room temperature. *P. Indian Acad. Sci. A* **50**, 323–335 (1959).

**Publisher's note** Springer Nature remains neutral with regard to jurisdictional claims in published maps and institutional affiliations.

© The Author(s), under exclusive licence to Springer Nature Limited 2020



## Methods

### General considerations

All manipulations were performed under an atmosphere of dry, oxygen-free N<sub>2</sub> or Ar by means of standard Schlenk or glovebox techniques (MBraun equipped with a –38 °C freezer, or VAC gloveboxes). Hexanes, pentane, DCM and benzene were dried on an MBraun solvent purification system. Acetonitrile (–H<sub>3</sub> and –D<sub>3</sub>) was dried over CaH<sub>2</sub> for several days before distillation. THF was dried over sodium benzophenone and distilled. PC was degassed by freeze–pump–thaw cycles and stored on activated 4-Å molecular sieves before use. DCE was initially distilled, followed by drying over CaH<sub>2</sub> for several days before a second distillation and subsequent storage on activated 4-Å molecular sieves. [FeCp<sub>2</sub>][PF<sub>6</sub>], [Bu<sub>4</sub>N][Cl] and TPO were purchased from Fisher Scientific; trimethylphosphine (Mes<sub>3</sub>P) was purchased from VWR International; *n*BuLi (1.6 M in hexanes) was purchased from Sigma Aldrich; all were used without further purification. *Ortho*-carborane was purchased from Boron Specialties and sublimed before use. Ph<sub>2</sub>PCl was purchased from Sigma Aldrich and vacuum-distilled before use. CoCp<sub>2</sub> was purchased from Sigma Aldrich and purified by filtration through celite using pentane, followed by recrystallization from pentane at –38 °C over several days. [Bu<sub>4</sub>N][PF<sub>6</sub>] was purchased from Oakwood Chemicals and purified by twice recrystallizing from hot ethanol. The recrystallized product was then washed with cold water, cold ethanol and pentane before drying at 100 °C under vacuum for 24 h. Sodium acetate (NaOAc) buffer was prepared from a stock solution purchased from Sigma Aldrich (pH 4.9) and adjusted to pH 5.4 using NaOH. The pH value was confirmed using a pH meter. Ketjenblack EC-600JD was purchased from a private supplier. UO<sub>2</sub>Cl<sub>2</sub>(TPO)<sub>2</sub> (ref. <sup>21</sup>), [UO<sub>2</sub>Cl<sub>2</sub>(THF)<sub>2</sub>]<sub>2</sub> (ref. <sup>31</sup>), [UO<sub>2</sub>(NO<sub>3</sub>)<sub>2</sub>(THF)<sub>3</sub>] (ref. <sup>32</sup>), KC<sub>8</sub> (ref. <sup>33</sup>) and bis(triphenylphosphoranylidene)ammonium hexafluorophosphate ([Ph<sub>3</sub>PNPPh<sub>3</sub>][PF<sub>6</sub>]) (ref. <sup>34</sup>) were prepared by procedures reported in the literature.

**NMR.** NMR spectra were obtained using a Varian Unity Inova 500 MHz or Agilent Technologies 400 MHz spectrometer, and were referenced to residual solvent resonances of acetonitrile (MeCN-*d*<sub>3</sub>) or dichloromethane (DCM-*d*<sub>2</sub>) or externally (<sup>11</sup>B, 85% (Et<sub>2</sub>O)BF<sub>3</sub>·<sup>31</sup>P, 85% H<sub>3</sub>PO<sub>4</sub>). Chemical shifts (δ) were recorded in parts per million. All <sup>11</sup>B NMR spectra were processed using MestReNova software to reduce a background signal with a linewidth of approximately 3,000 Hz from the Pyrex NMR tubes. The NMR time-domain data were first left-shifted to discard the first ~0.1 ms. To correct the linear phase change, a linear prediction was used to fill the initial discarded data before the Fourier transform or an appropriate linear phase correction was applied to the frequency-domain data after the Fourier transform. The relaxation times *T*<sub>1</sub> for <sup>31</sup>P nuclei were determined using the inversion recovery method. The delay times after the 180° inversion pulse were varied up to the maximum of five times of the expected *T*<sub>1</sub> values. The signal recovery curve was fitted with an exponential function to extract the *T*<sub>1</sub> values. Subsequent one-dimensional spectra were acquired with five times the longest *T*<sub>1</sub> value measured for accurate integrations (where *T*<sub>1</sub> values were determined for TPO: 2.3 s; Mes<sub>3</sub>P: 5.1 s; [Ph<sub>3</sub>PNPPh<sub>3</sub>][PF<sub>6</sub>]: 7.1 s; **1**: 0.51 s; **3**: 0.64 s; and **4**: 0.57 s).

**UV-Vis.** UV-Vis absorption spectra were collected using a Shimadzu UV-2401PC spectrophotometer. The UO<sub>2</sub><sup>2+</sup> extinction coefficient (ε) was experimentally determined to be 7.715 litres mol<sup>–1</sup> cm<sup>–1</sup> (460 nm) at pH 5.4.

**Elemental analyses.** Elemental analyses (C, N, H) were performed at the University of California, Berkeley using a Perkin Elmer 2400 Series II combustion analyser.

**Cyclic voltammetry.** Cyclic voltammetry was performed using a CH Instruments Electrochemical Analysis potentiostat, equipped with a

3-mm-diameter glassy carbon working electrode, a Ag-wire pseudo-reference electrode and a Pt-wire counter electrode using a [Bu<sub>4</sub>N][PF<sub>6</sub>] (0.1 M) solution as the supporting electrolyte. Cyclic voltammograms were referenced to the Fc/Fc<sup>+</sup> redox couple.

**Galvanostatic bulk electrolysis.** Galvanostatic bulk electrolysis cycling experiments were carried out inside an Ar glovebox using a Metrohm Autolab PGSTAT128N potentiostat/galvanostat. The full experimental setups for both the mono- and biphasic cycling experiments are described in sections ‘Monophasic electrochemical capture and release of UO<sub>2</sub><sup>2+</sup>’ and ‘Biphasic electrochemical capture and release of UO<sub>2</sub><sup>2+</sup>’.

**X-ray crystallography.** X-ray crystallography data were collected on a Bruker KAPPA APEX II diffractometer equipped with an APEX II CCD detector using a TRIUMPH monochromator with a Mo Kα X-ray source (wavelength α = 0.71073 Å). The crystals were mounted on a cryoloop under Paratone-N oil, and all data were collected at 100(2) K using an Oxford nitrogen-gas cryostream system. A hemisphere of data was collected using ω scans with 0.5° frame widths (ω, angle between the X-ray source and the sample). Data collection and cell-parameter determination were conducted using the SMART program. Integration of the data frames and refinement of the final cell parameters were performed using SAINT software. Absorption correction of the data was carried out using SADABS. Structure determination was done using direct or Patterson methods and difference Fourier techniques. All hydrogen atom positions were idealized and rode on the atom of attachment. Structure solution, refinement, graphics and creation of publication materials were performed using SHELXTL or OLEX<sup>2</sup>.

**Synthesis of closo-(1,2-(Ph<sub>2</sub>PO)<sub>2</sub>-1,2-C<sub>2</sub>B<sub>10</sub>H<sub>10</sub>) (1).** The synthesis of compound **1** was accomplished in two steps by modifications to literature procedures<sup>19,35</sup>.

**Step 1.** A solution of *n*BuLi in hexane (1.6 M, 28.2 ml, 45 mmol) was added dropwise to a solution of *ortho*-carborane (3.1 g, 21.5 mmol) in dry diethyl ether (250 ml) at –78 °C, resulting in the formation of a fine colourless precipitate. The reaction was slowly warmed to room temperature. After stirring for 30 min at room temperature, the mixture was cooled to 0 °C, and Ph<sub>2</sub>PCl (7.7 ml, 41.7 mmol) was added dropwise, resulting in a pale orange solution with a colourless precipitate. The mixture was stirred for 30 min at 0 °C. The solution was brought to room temperature and stirred for 30 min and was subsequently warmed to reflux and stirred for an additional 30 min. The solution was cooled to 0 °C, and water (30 ml) was slowly added to the mixture. The mixture was allowed to stir for 20 min and was filtered over a glass frit, where the resulting solid was washed with additional water (30 ml) and diethyl ether (20 ml). The solid was dried under vacuum at 100 °C for 2 h. The product was recrystallized from a mixture of hexane/toluene and was obtained in 81% yield (8.6 g, 16.7 mmol) <sup>1</sup>H NMR (400 MHz, CDCl<sub>3</sub>): δ 7.06–7.47 (m, 20H); 0.98–2.66 (broad, 10H). <sup>11</sup>B NMR (400 MHz, CDCl<sub>3</sub>): δ –0.40, –9.42. <sup>11</sup>B{<sup>1</sup>H} NMR (400 MHz, CDCl<sub>3</sub>): δ –0.40, –7.21, –9.42. <sup>31</sup>P{<sup>1</sup>H} NMR (400 MHz, CDCl<sub>3</sub>): δ 7.88.

**Step 2.** A solution of H<sub>2</sub>O<sub>2</sub> (30% in water, 1.8 ml, 58.7 mmol) was added dropwise to a solution of [closo-(1,2-(Ph<sub>2</sub>P)<sub>2</sub>-1,2-C<sub>2</sub>B<sub>10</sub>H<sub>10</sub>)] (from step 1) (2.1 g, 4.1 mmol) in THF (50 ml). The reaction was stirred for 3 h at room temperature. The reaction was monitored by <sup>31</sup>P NMR for formation of an unwanted side-product at 49 ppm. Once this product formed, the reaction was discontinued by addition of chloroform. The mixture was washed with water and brine, the phases were separated and the organic layer was dried with Na<sub>2</sub>SO<sub>4</sub>. The solvent was removed, and the solid was slowly recrystallized from acetonitrile to yield a colourless crystalline solid. The solid was dried under vacuum at 80 °C for several hours (1.4 g, 2.6 mmol, 60% yield). Single crystals suitable for X-ray crystallography were obtained by vapour diffusion of pentane in a saturated THF solution of **1**. <sup>1</sup>H NMR (400 MHz, MeCN-*d*<sub>3</sub>): δ 7.99 (m, 8H),



7.63 (m, 4H), 7.54 (m, 8H), 2.5 (broad s, 10H).  $^{11}\text{B}$  and  $^{11}\text{B}\{^1\text{H}\}$  NMR (400 MHz,  $\text{MeCN}-d_3$ ):  $\delta$  0.66, –8.75.  $^{31}\text{P}\{^1\text{H}\}$  NMR (400 MHz,  $\text{MeCN}-d_3$ ):  $\delta$  22.8. Anal. calc. for  $\text{C}_{26}\text{H}_{30}\text{B}_{10}\text{O}_2\text{P}_2$ : C, 57.35; H, 5.55. Found: C, 57.33; H, 5.66. Selected interatomic distances for **1** were C···C: 1.688(4) Å, P···P: 3.537 Å.

**Synthesis of  $\text{UO}_2\text{Cl}_2(\mathbf{1})_2$ .** A 20-ml vial equipped with a magnetic stirbar was charged with **1** (54.4 mg, 0.1 mmol) and 2 ml of DCM. In a separate vial,  $[\text{UO}_2\text{Cl}_2(\text{THF})_2]_2$  (24.2 mg, 0.025 mmol) was dissolved in 2 ml of DCM and added to the stirring solution of **1**, resulting in the formation of a light-yellow suspension. After 1 h, the reaction mixture became homogeneous. This was stirred for an additional 24 h at room temperature. The solvent was removed, yielding a yellow solid (62.5 mg). Multiple attempts were made to obtain single crystals suitable for XRD studies, but failed.  $^1\text{H}$  NMR (400 MHz,  $\text{DCM}-d_2$ ):  $\delta$  8.32–6.29 (m, 20H), 2.5 (broad s, 10H).  $^{11}\text{B}$  and  $^{11}\text{B}\{^1\text{H}\}$  NMR (400 MHz,  $\text{DCM}-d_2$ ):  $\delta$  5.84, –8.46.  $^{31}\text{P}\{^1\text{H}\}$  NMR (400 MHz,  $\text{DCM}-d_2$ ):  $\delta$  38.8 (s), 38.4 (s). Anal. calc. for  $\text{C}_{52}\text{H}_{60}\text{B}_{20}\text{Cl}_2\text{O}_6\text{P}_4\text{U}\cdot 1/2\text{CH}_2\text{Cl}_2$ : C, 43.05; H, 4.16. Found: C, 42.76; H, 4.32.

**Synthesis of  $[\text{CoCp}^*_2][\text{UO}_2\text{Cl}_2(\text{nido}-1,2-(\text{Ph}_2\text{PO})_2-1,2-\text{C}_2\text{B}_{10}\text{H}_{10})]$  (**2a**).** A 20-ml vial equipped with a magnetic stirbar was charged with **1** (54.4 mg, 0.1 mmol) and 6 ml of benzene. In a separate vial,  $\text{CoCp}^*_2$  (69.1 mg, 0.2 mmol, 2.0 equiv.) was dissolved in 4 ml of benzene and added dropwise to the stirring solution of **1**. Upon addition, a yellow solid immediately precipitated from the reaction mixture, and the mixture was stirred for an additional 4 h at room temperature. Stirring was discontinued and the solid was allowed to settle to the bottom of the vial. The supernatant was decanted and filtered on a plug of celite. The solids were washed with benzene ( $3 \times 6$  ml) and each washing was filtered over the same celite plug. The remaining solids were then dissolved in a minimal amount of MeCN (2 ml) and filtered on the same celite plug into a new vial. The MeCN filtrate was collected and the volatiles were removed in vacuo, yielding a shiny golden-yellow solid (114.3 mg, 0.95 mmol, 95% yield). Single crystals suitable for X-ray crystallography were obtained by vapour diffusion of  $\text{Et}_2\text{O}$  in a saturated MeCN solution of **2a** at  $-38^\circ\text{C}$ .  $^1\text{H}$  NMR (400 MHz,  $\text{MeCN}-d_3$ ):  $\delta$  8.05 (broad m, 8H), 7.24 (broad s, 12H), 1.62 (s, 60H). We note that carborane B–H resonances were too broad to be observed.  $^{11}\text{B}$  and  $^{11}\text{B}\{^1\text{H}\}$  NMR (400 MHz,  $\text{MeCN}-d_3$ ):  $\delta$  20.24, –0.62, –18.46, –22.06.  $^{31}\text{P}\{^1\text{H}\}$  NMR (400 MHz,  $\text{MeCN}-d_3$ ):  $\delta$  29.8. Anal. calc. for  $\text{C}_{66}\text{H}_{90}\text{B}_{10}\text{Co}_2\text{O}_2\text{P}_2$ : C, 65.88; H, 7.54. Found: C, 65.57; H, 7.67. Selected interatomic distances for **2a** were C···C: 2.860 Å, P···P: 5.036 Å.

**Synthesis of  $[\text{Bu}_4\text{N}]_2[(\text{nido}-1,2-(\text{Ph}_2\text{PO})_2-1,2-\text{C}_2\text{B}_{10}\text{H}_{10})]$  (**2b**).** The synthesis of compound **2b** was accomplished in two steps.

**Step 1.** In the glovebox, a 250-ml round-bottom flask equipped with a magnetic stirbar was charged with **1** (272.2 mg, 0.5 mmol) and 20 ml of THF, and cooled to  $-78^\circ\text{C}$ . In a separate vial,  $\text{KC}_8$  (182.4 mg, 1.35 mmol, 2.7 equiv.) was suspended in 20 ml of THF and added slowly dropwise to the stirring solution of **1**. Upon addition, the  $\text{KC}_8$  suspension began to turn grey, and was stirred for 30 min at room temperature. Stirring was discontinued and the mixture was filtered over a pad of celite on a fine glass frit. The graphite pad was washed additionally with MeCN ( $3 \times 5$  ml). The filtrate was collected and the volatiles were removed in vacuo, yielding a pale-yellow oil. The oil was redissolved in THF (5 ml) and layered with 5 ml of pentane, and was recrystallized at  $-38^\circ\text{C}$ , yielding a white solid (234.1 mg, 0.38 mmol, 75% yield).  $^1\text{H}$  NMR (400 MHz,  $\text{MeCN}-d_3$ ):  $\delta$  7.81 (broad m, 8H), 7.28 (broad m, 12H). Carborane B–H resonances were too broad to be observed.  $^{11}\text{B}$  NMR (400 MHz,  $\text{MeCN}-d_3$ ):  $\delta$  20.24, –0.62, –18.46, –22.06.  $^{31}\text{P}\{^1\text{H}\}$  NMR (400 MHz,  $\text{MeCN}-d_3$ ):  $\delta$  31.8. Anal. calc. for  $\text{C}_{26}\text{H}_{30}\text{B}_{10}\text{K}_2\text{O}_2\text{P}_2\cdot\text{THF}$ : C, 51.86; H, 5.51. Found: C, 51.09; H, 5.47.

**Step 2.** A 20-ml vial equipped with a magnetic stirbar was charged with  $[\text{K}]_2[(\text{nido}-1,2-(\text{Ph}_2\text{PO})_2-1,2-\text{C}_2\text{B}_{10}\text{H}_{10})\cdot\text{THF}]$  (655.4 mg, 0.94 mmol) (Step 1) and 15 ml of DCM, and was cooled to  $-78^\circ\text{C}$ . In a separate vial,

$[\text{Bu}_4\text{N}][\text{Cl}]$  (528 mg, 1.88 mmol, 2.0 equiv.) was dissolved in 10 ml of DCM and added dropwise to the stirring carborane suspension. Upon addition, the reaction mixture became homogenous, and after 1 h a white precipitate began to settle. This mixture was stirred for 2 h at room temperature. Stirring was discontinued and all volatiles were removed, yielding a pale-yellow solid. A minimal amount of DCM (3 ml) was added and the mixture was filtered on a celite plug. The solids were washed with chilled DCM ( $3 \times 2$  ml) and each washing was filtered over the same celite plug. The DCM filtrate was collected and the volatiles were removed in vacuo, yielding a pale-yellow residue; this was triturated with pentane (10 ml) and dried in vacuo to yield an off-white solid, which was recrystallized from DCM and pentane (690.4 mg, 0.67 mmol, 71% yield).  $^1\text{H}$  NMR (400 MHz,  $\text{MeCN}-d_3$ ):  $\delta$  8.03 (m, 8H), 7.25 (broad s, 12H), 3.08 (m, 16H), 1.59 (m, 16H), 1.35 (m, 16H), 0.96 (t, 24H). Carborane B–H resonances were too broad to be observed.  $^{11}\text{B}$  and  $^{11}\text{B}\{^1\text{H}\}$  NMR (400 MHz,  $\text{MeCN}-d_3$ ):  $\delta$  20.25, –0.65, –18.42, –22.05.  $^{31}\text{P}\{^1\text{H}\}$  NMR (400 MHz,  $\text{MeCN}-d_3$ ):  $\delta$  30.1. Anal. calc. for  $\text{C}_{58}\text{H}_{102}\text{B}_{10}\text{N}_2\text{O}_2\text{P}_2$ : C, 67.67; H, 9.99. Found: C, 66.81; H, 10.29.

**Synthesis of  $[\text{CoCp}^*_2][\text{UO}_2\text{Cl}_2(\text{nido}-1,2-(\text{Ph}_2\text{PO})_2-1,2-\text{C}_2\text{B}_{10}\text{H}_{10})]$  (**3**).** A 20-ml vial equipped with a magnetic stirbar was charged with  $[\text{UO}_2\text{Cl}_2(\text{THF})_2]_2$  (16.9 mg, 0.018 mmol) and 4 ml of MeCN. In a separate vial, **2a** (42.2 mg, 0.035 mmol) was dissolved in 4 ml of MeCN and then added dropwise to the stirring solution of  $[\text{UO}_2\text{Cl}_2(\text{THF})_2]_2$ , turning dark yellow. After stirring for 5 min, a yellow solid began to precipitate from the reaction mixture, and this was stirred at room temperature for 4 h. Stirring was discontinued and the mixture was passed over a celite plug, collecting a yellow solid and a yellow filtrate. The solvent was removed from the yellow filtrate, yielding a yellow solid, which was washed with THF ( $3 \times 2$  ml) and passed over another celite plug. The filtrate was collected and the volatiles were removed in vacuo, yielding a yellow powder. Residual  $[\text{CoCp}^*_2][\text{Cl}]$  was removed by selectively recrystallizing the mixture from pyridine/ $\text{Et}_2\text{O}$  at  $-38^\circ\text{C}$ . The supernatant was transferred and the volatiles were removed, collecting a yellow solid (36.3 mg, 0.024 mmol, 69% yield). Single crystals suitable for XRD studies were grown by vapour diffusion of  $\text{Et}_2\text{O}$  into a saturated MeCN solution of **3** at room temperature.  $^1\text{H}$  NMR (400 MHz,  $\text{MeCN}-d_3$ ):  $\delta$  8.13 (m, 10H), 7.35 (m, 10H), 1.66 (s, 60H). Carborane B–H resonances were too broad to be observed.  $^{11}\text{B}$  and  $^{11}\text{B}\{^1\text{H}\}$  NMR (400 MHz,  $\text{MeCN}-d_3$ ):  $\delta$  0.27, –16.90, –19.69.  $^{31}\text{P}\{^1\text{H}\}$  NMR (400 MHz,  $\text{MeCN}-d_3$ ):  $\delta$  51.12. Anal. calc. for  $\text{C}_{66}\text{H}_{90}\text{B}_{10}\text{Cl}_2\text{Co}_2\text{O}_4\text{P}_2\text{U}\cdot 2\text{MeCN}$ : C, 51.70; H, 5.95; N, 1.72. Found: C, 51.91; H, 5.88; N, 1.74. Selected interatomic distances and angles for **3** were C···C: 2.855 Å; P···P: 4.697 Å; O1–U–O2:  $86.5^\circ(3^\circ)$ .

**Synthesis of  $[\text{CoCp}^*_2][\text{UO}_2(\text{nido}-1,2-(\text{Ph}_2\text{PO})_2-1,2-\text{C}_2\text{B}_{10}\text{H}_{10})_2]$  (**4**).** A 20-ml vial equipped with a magnetic stirbar was charged with **2a** (26.6 mg, 0.022 mmol) and 1.5 ml of MeCN. In a separate vial,  $[\text{UO}_2\text{Cl}_2(\text{THF})_2]_2$  (5.3 mg, 0.0055 mmol) was dissolved in 1.5 ml of MeCN and then added dropwise to the stirring solution of **2a**. After stirring for 5 min, a yellow solid began to precipitate from the reaction mixture, and this was stirred at room temperature for 24 h. Stirring was discontinued and the solid was allowed to settle to the bottom of the vial. The supernatant was decanted and filtered on a celite plug. The solids were washed with MeCN ( $3 \times 2$  ml) and each washing was filtered over the same celite plug. The remaining solids were then dissolved in a minimal amount of pyridine and filtered on the same celite plug into a new vial. The pyridine filtrate was collected and the volatiles were removed in vacuo, yielding a light-yellow powder (35.5 mg, 0.018 mmol, 80% yield). Single crystals suitable for XRD analysis were grown from a small-scale reaction in a J. Young NMR tube, which was charged with a solution of **2a** (12.0 mg, 0.01 mmol) in  $\text{MeCN}-d_3$  (0.25 ml). A solution of  $[\text{UO}_2\text{Cl}_2(\text{THF})_2]_2$  (2.4 mg, 0.0025 mmol) in  $\text{MeCN}-d_3$  (0.25 ml) was added to this, whereupon crystals suitable for XRD analysis slowly formed on the walls of the NMR tube.  $^1\text{H}$  NMR (400 MHz,  $\text{MeCN}-d_3$ ):  $\delta$  8.13 (m, 15H), 7.38 (m, 10H), 7.24 (m, 15H), 1.68 (s, 60H). Carborane B–H

resonances were too broad to be observed.  $^{11}\text{B}$  and  $^{11}\text{B}\{^1\text{H}\}$  NMR (400 MHz,  $\text{MeCN-d}_3$ ):  $\delta$  0.26, -17.15, -20.66.  $^{31}\text{P}\{^1\text{H}\}$  NMR (400 MHz,  $\text{MeCN-d}_3$ ):  $\delta$  52.0. Anal. calc. for  $\text{C}_{97}\text{H}_{120}\text{B}_{20}\text{Co}_2\text{O}_6\text{P}_4\text{U}$ : C, 54.76; H, 5.99. Found: C, 55.22; H, 6.36. Selected interatomic distances and angles for **4** were C...C: 2.857 Å; P...P: 4.806 Å; O1-U-O2: 89.7° (17°).

### Chemical capture and release of $\text{UO}_2^{2+}$

**Formation of in situ generated  $[(\text{UO}_2)(\text{TPO})_2\text{Cl}_2]$ .** A 20-ml vial equipped with a magnetic stirbar was charged with **1** (2.0 equiv., 5.4 mg, 0.01 mmol), TPO (4.0 equiv., 5.6 mg, 0.02 mmol) and  $\text{Mes}_3\text{P}$  (4.0 equiv., 7.7 mg, 0.02 mmol) and dissolved in a 3:1 PC:benzene (3 ml) solvent system. A 500- $\mu\text{l}$  aliquot was taken from this mixture and placed in an NMR tube equipped with a  $\text{MeCN-d}_3$  capillary tube. A  $^{31}\text{P}\{^1\text{H}\}$  NMR spectrum was collected and the relative integrations were recorded (Extended Data Fig. 5a). The NMR solution was returned to the vial and  $[\text{UO}_2\text{Cl}_2(\text{THF})_2]$  (0.5 equiv., 2.4 mg, 0.0025 mmol) was added. The mixture was stirred vigorously until all the solids were dissolved (~20 min), resulting in a light-yellow coloured solution. After 1 h, a 500- $\mu\text{l}$  aliquot was taken from the reaction mixture and placed in an NMR tube equipped with a  $\text{MeCN-d}_3$  capillary tube. A  $^{31}\text{P}\{^1\text{H}\}$  NMR spectrum was obtained (Extended Data Fig. 5b). After the spectrum was recorded, the NMR sample was transferred back into the reaction mixture.

**Reduction.**  $\text{CoCp}_2^+$  (4.0 equiv., 6.6 mg, 0.02 mmol) in 100  $\mu\text{l}$  of benzene was added dropwise to the generated solution described above. Upon addition, the solution turned golden in colour and was stirred for 1 h at room temperature. A 500- $\mu\text{l}$  aliquot was then taken from the reaction mixture and placed in an NMR tube equipped with a  $\text{MeCN-d}_3$  capillary tube. A  $^{31}\text{P}\{^1\text{H}\}$  NMR spectrum was obtained (Extended Data Fig. 5c), and then the NMR solution was transferred back into the reaction mixture.

**Oxidation.**  $[\text{Fc}][\text{PF}_6]$  (4.0 equiv., 6.6 mg, 0.02 mmol) was added to the reduced solution described above. Upon addition, the solution turned green and then a golden colour. The solution was stirred for 1 h at room temperature, after which a 500- $\mu\text{l}$  aliquot was taken from the reaction mixture and placed in an NMR tube equipped with a  $\text{MeCN-d}_3$  capillary tube. A  $^{31}\text{P}\{^1\text{H}\}$  NMR spectrum was obtained (Extended Data Fig. 5d). After the spectrum was obtained, the NMR sample was transferred back into the reaction mixture.

### Monophasic electrochemical capture and release of $\text{UO}_2^{2+}$

**Experimental conditions.** Galvanostatic bulk electrolysis experiments were carried out in a divided glass H-cell (Extended Data Fig. 8a, b). The physical barrier between each component of the cell and the respective two Bio-Logic high-surface coiled Pt electrodes was an anion-exchange membrane (Membranes International, AMI-7001) held in place by two fluorinated ethylene propylene-encapsulated silicon o-rings with a metal clamp. The electrodes were cleaned by rinsing with distilled water and acetone and then heating until white-hot with a butane torch before use. The anion-exchange membrane was soaked in a 0.1 M  $[\text{Bu}_4\text{N}][\text{PF}_6]$  solution of PC/benzene (3:1) over 3-Å molecular sieves for 24 h before use. The left compartment, containing the counter electrode, consisted of Fc (41.9 mg, 0.225 mmol) and  $[\text{Fc}][\text{PF}_6]$  (74.5 mg, 0.225 mmol) in 7.0 ml of a 0.1 M  $[\text{Bu}_4\text{N}][\text{PF}_6]$  PC:benzene solution. The right compartment, containing the working electrode, contained **1** (5 equiv., 40.8 mg, 0.075 mmol), TPO (6 equiv., 25.0 mg, 0.09 mmol),  $[\text{UO}_2\text{Cl}_2(\text{THF})_2]$  (0.5 equiv., 7.3 mg, 0.0075 mmol of dimer (1.0 equiv. of U monomer)) and  $[\text{Ph}_3\text{PNPPh}_3][\text{PF}_6]$  (1.0 equiv., 10.2 mg, 0.015 mmol) in a 0.1 M  $[\text{Bu}_4\text{N}][\text{PF}_6]$  PC:benzene solution (7.0 ml).

**Experimental parameters.** The cell was charged/discharged over the course of six cycles. To initiate  $\text{UO}_2^{2+}$  capture, the first cycle was charged with an applied current of -201.0  $\mu\text{A}$  over the course of 6 h to a 75% SOC relative to the  $[\text{UO}_2\text{Cl}_2(\text{THF})_2]$  concentration. After the cell was charged,

a wait period of 2 h was incorporated between charge/discharge cycles (Fig. 2c, grey dashed).  $\text{UO}_2^{2+}$  release was achieved by discharging the cell galvanostatically at an applied current of 68.94  $\mu\text{A}$  over the course of 13 h, using voltage cutoffs (0.0 V), to a final SOC of approximately 15% relative to the initial  $[\text{UO}_2\text{Cl}_2(\text{THF})_2]$  concentration. After each cell discharge, a wait period of 4–5 h was incorporated (depending on when the voltage cutoffs were applied) between discharging/charging cycles. Each additional cycle thereafter was charged and discharged galvanostatically at currents of -160.87  $\mu\text{A}$  and 68.94  $\mu\text{A}$ , respectively. This resulted in charging cycles of -15–75% SOC and -75–15% SOC, respectively. Between each charge/discharge a  $^{31}\text{P}\{^1\text{H}\}$  NMR spectrum was obtained (Extended Data Fig. 6a) using a 40-s relaxation delay (see NMR details above) with  $[\text{Ph}_3\text{PNPPh}_3][\text{PF}_6]$  as the standard. We note that an excess of **1** was used to keep the applied current ( $I_{\text{app}}$ ) below the limiting current at any given time ( $I_l(t)$ ) for the presumed electrochemical–chemical mechanism involving reduction of **1** followed by uranyl ligation. This allowed the use of a galvanostatic charge/discharge procedure operating close to the mass-transfer-controlled plateau (similar to potentiostatic methods) but with the added benefit of not requiring prior knowledge of the optimal applied voltage, which is a function of both the onset of the reductive process and the total cell impedance<sup>24</sup>. Attempts at GBE with stoichiometric equivalents of **1** revealed an earlier-than-expected onset of  $I_{\text{app}} > I_l(t)$ , clearly indicating that additional and unwanted electrochemical processes were being accessed and perhaps suggesting an initial degradation of **1** within the system. Therefore, an initial ratio of 0.5:6:8 for  $[\text{UO}_2\text{Cl}_2(\text{THF})_2]$ :1:TPO reagents was used.

### Biphasic electrochemical capture and release of $\text{UO}_2^{2+}$

**Experimental conditions.** A complete, stepwise, half-cell figure of the experiments conducted in this section, along with spectroscopic data, are shown in Extended Data Fig. 7. Two-electrode galvanostatic bulk electrolysis was performed in an argon glovebox using a two-compartment H-cell with a glass-frit separator, a stir bar in each compartment, and reticulated vitreous carbon (RVC) foam electrodes for both the working and counter electrodes (Extended Data Fig. 8c, d). The RVC foam electrodes consisted of a -5-cm steel rod inserted into a 100 PPI Duocel RVC foam core (length -2.5 cm; diameter -3 mm), with a tap bore (length -5 mm; diameter -2 mm), which was filled with molten gallium to fuse the steel connector to the RVC foam. Each electrode had an end-to-tip resistance of <5  $\Omega$ . The RVC electrodes were rinsed with methanol and dried under reduced pressure overnight before use. The Ketjenblack used was dried for 48 h in a 175 °C oven and ground in a glass mortar and pestle under inert atmosphere before use.

**Reduction (charging).** The counter compartment consisted of 400 mg of Ketjenblack suspended in 6 ml of a 0.1 M solution of  $[\text{Bu}_4\text{N}][\text{PF}_6]$  in DCE. The working compartment consisted of **1** (34 mg, 0.0625 mmol, 1.0 equiv.) dissolved in 6 ml of a 0.1 M solution of  $[\text{Bu}_4\text{N}][\text{PF}_6]$  in DCE. A charging current of -107.1  $\mu\text{A}$  with a -9.25 V charge cutoff was used, resulting in a -75% SOC after 24 h assuming 100% Coulombic efficiency. Upon completion, the working compartment solution was analysed by  $^{31}\text{P}\{^1\text{H}\}$  NMR spectroscopy to reveal the formation of **2b** (Extended Data Fig. 9a). The working compartment solution was then removed from the H-cell and placed in a 20-ml vial for subsequent capture chemistry.

**$\text{UO}_2^{2+}$  capture.** A 5-ml vial was charged with excess  $\text{UO}_2(\text{NO}_3)_2(\text{THF})_2$  (42 mg, 0.078 mmol, 1.25 equiv.) and dissolved in 3 ml of a 0.1 M sodium acetate buffer adjusted to pH 5.4 (0.026 M  $\text{UO}_2^{2+}$ ). An aliquot of the resulting pale-yellow solution was used to record an initial UV-Vis spectrum (Extended Data Fig. 10a, blue). The aliquot was transferred back to the 5-ml vial and this solution was added slowly, dropwise and without stirring to the DCE solution containing the electrochemically reduced **1** (forming **2b**). After addition, the mixture was allowed to stir for 2 h, resulting in a bright-yellow organic phase and a very-pale-yellow

aqueous phase. Stirring was discontinued and the organic and aqueous phases were separated using a small separatory funnel. An aliquot of the aqueous phase was used to record a UV-Vis spectrum (Extended Data Fig. 10a, red), indicating that 0.022 mmol of  $\text{UO}_2^{2+}$  remained, which is equivalent to the capture of 0.056 mmol (-0.9 equiv.) to the organic phase. A 1-ml aliquot was taken from the pale-yellow dichloroethane layer and transferred to an NMR tube. An unlocked  $^3\text{P}\{^1\text{H}\}$  NMR spectrum was collected indicating the formation of **3N/4N** (Extended Data Fig. 9b). The NMR solution was returned to the 20-ml vial.

**Oxidation (discharging).** Two-electrode galvanostatic bulk electrolysis (discharging) of the captured DCE solution was performed using the same cell used for charging. A discharging current of 107.1  $\mu\text{A}$  was applied until 9.49 C of charge was transferred, resulting in a final SOC of -0% (assuming 100% Coulombic efficiency and no loss of material during the biphasic capture). Upon completion, the working compartment solution was removed and placed in a 20-ml vial for subsequent release chemistry.

**$\text{UO}_2^{2+}$  release.** The 20-ml vial containing the electrochemically oxidized **3N/4N** yellow DCE solution was equipped with a stirbar, and a solution of 0.1 M sodium acetate buffer adjusted to pH 5.4 (3 ml) was added dropwise. The mixture was allowed to stir for 12 h, resulting in a pale-yellow aqueous phase and a colourless organic layer. The organic and aqueous phases were separated using a small separatory funnel, and an aliquot of the aqueous layer was used to take a UV-Vis spectrum indicating the presence of released  $\text{UO}_2^{2+}$  (0.031 mmol, -0.5 equiv.) (Extended Data Fig. 10b). A 1-ml aliquot was taken from the yellow DCE layer and transferred to an NMR tube. An unlocked  $^3\text{P}\{^1\text{H}\}$  NMR spectrum was collected that indicated the clean formation of **1** and a small unknown byproduct at 20.1 ppm (Extended Data Fig. 9c).

#### Biphasic control experiments

**$\text{UO}_2^{2+}$  migration from water to DCE in the absence of carborane (**1** or **2a/b**).** A 5-ml vial was charged with  $\text{UO}_2(\text{NO}_3)_2(\text{THF})_2$  (14.0 mg, 0.026 mmol) and dissolved in 1.5 ml of a 0.1 M sodium acetate buffer adjusted to pH 5.4 (0.017 M  $\text{UO}_2^{2+}$ ). An aliquot of the resulting pale-yellow solution was used to record an initial UV-Vis spectrum (Extended Data Fig. 10c, blue). The aliquot was transferred back to the 5-ml vial. A separate 20-ml vial equipped with a stirbar was charged with  $[\text{Bu}_4\text{N}][\text{PF}_6]$  (0.2324 g, 0.1 M) dissolved in DCE (6.0 ml). To the clear DCE solution, the pale-yellow aqueous solution was added slowly dropwise over the course of 2 min without stirring. After addition, the mixture was allowed to stir for 4 h and the organic phase remained clear. Stirring was discontinued and the organic and aqueous phases were separated using a small separatory funnel. Small aliquots of the aqueous (Extended Data Fig. 10c, red) and organic (Extended Data Fig. 10d) phases were used to record UV-Vis spectra, which together clearly indicated that the  $\text{UO}_2^{2+}$  had remained in the aqueous phase.

**$\text{UO}_2^{2+}$  migration from water to DCE in the presence of **1**.** A 5-ml vial was charged with  $\text{UO}_2(\text{NO}_3)_2(\text{THF})_2$  (14.0 mg, 0.026 mmol, 1.0 equiv.) dissolved in 1.5 ml of a 0.1 M sodium acetate buffer adjusted to pH 5.4 (0.017 M  $\text{UO}_2^{2+}$ ). An aliquot of the resulting pale-yellow solution was used to record an initial UV-Vis spectrum (Extended Data Fig. 10e, blue). The aliquot was transferred back to the 5-ml vial. A separate 20-ml vial with a stirbar was charged with **1** (14.1 mg, 0.026 mmol, 1.0 equiv.),  $[\text{Bu}_4\text{N}][\text{PF}_6]$  (0.2324 g, 0.1 M) and DCE (6.0 ml). To the clear DCE solution, the pale-yellow aqueous solution was added slowly dropwise over the course of 2 min without stirring. After addition, the mixture was allowed to stir for 3 h and the organic phase remained clear. Stirring was discontinued and the organic and aqueous phases were separated using a small separatory funnel. Small aliquots of the aqueous (Extended Data Fig. 10e, red) and organic (Extended Data Fig. 10f) phases were used to record UV-Vis spectra, which together clearly indicated negligible transfer of  $\text{UO}_2^{2+}$  from the aqueous to the organic phase.

#### DFT studies

DFT calculations were performed using Gaussian 09.2<sup>36</sup>. Geometry optimizations for all molecules were performed using the B3LYP/def2-SVP<sup>37,38</sup> level of theory (see Supplementary Information for atom coordinates) in DCM using the conductor-like polarizable continuum model (CPCM) implemented in the Gaussian 09 software<sup>39–41</sup>. Electron density surfaces with electrostatic potentials were extracted from optimized **1** and **2a** (Extended Data Fig. 1d). Thermal energy corrections were extracted from the results of the frequency analyses performed at the same level of theory. Frequency analyses of all molecules and intermediates contained no imaginary frequency, showing that these are energy minima. The equilibrium constants were calculated from the Gibbs free energy values  $G$  for the proton-transfer reactions ( $K_{\text{eq}} = e^{-\Delta G/(RT)}$ ;  $R$ , molar gas constant;  $T$ , temperature). See Supplementary Information for the competition reaction results and atom coordinates.

#### Data availability

X-ray data are available free of charge from the Cambridge Crystallographic Data Centre ([https://www.ccdc.cam.ac.uk/data\\_request/cif](https://www.ccdc.cam.ac.uk/data_request/cif)) under reference numbers CCDC-1903723 (**1**), CCDC-1903724 (**2a**), CCDC-1903725 (**3**) and CCDC-1903726 (**4**). All other data generated or analysed during this study are included in the published article.

- Wilkerson, M. P., Burns, C. J., Paine, R. T. & Scott, B. L. Synthesis and crystal structure of  $\text{UO}_2\text{Cl}_2(\text{THF})_2$ : a simple preparation of an anhydrous uranyl reagent. *Inorg. Chem.* **38**, 4156–4158 (1999).
- Reynolds, J. G., Zalkin, A. & Templeton, D. H. Structure of uranyl nitrate-bis(tetrahydrofuran). *Inorg. Chem.* **16**, 3357–3359 (1977).
- Lalancette, J. M., Rollin, G. & Dumas, P. Metals intercalated in graphite. I. Reduction and oxidation. *Can. J. Chem.* **50**, 3058–3062 (1972).
- Liu, Y. et al. Mechanistic understanding of dinuclear cobalt(III) complex mediated highly enantioselective copolymerization of meso-epoxides with  $\text{CO}_2$ . *Macromolecules* **47**, 7775–7788 (2014).
- Alexander, R. P. & Schroeder, H. Chemistry of decaborane-phosphorus compounds. IV. Monomeric, oligomeric, and cyclic phosphinocarboranes. *Inorg. Chem.* **2**, 1107–1110 (1963).
- Gaussian 09 (Gaussian Inc., 2010).
- Lee, C., Yang, W. & Parr, R. G. Development of the Colle-Salvetti correlation-energy formula into a functional of the electron density. *Phys. Rev. B* **37**, 785–789 (1988).
- Weigend, F. & Ahlrichs, R. Balanced basis sets of split valence, triple zeta valence and quadruple zeta valence quality for H to Rn: design and assessment of accuracy. *Phys. Chem. Chem. Phys.* **7**, 3297–3305 (2005).
- Cossi, M., Rega, N., Scalmani, G. & Barone, V. Energies, structures, and electronic properties of molecules in solution with the C-PCM solvation model. *J. Comput. Chem.* **24**, 669–681 (2003).
- Barone, V. & Cossi, M. Quantum calculation of molecular energies and energy gradients in solution by a conductor solvent model. *J. Phys. Chem. A* **102**, 1995–2001 (1998).
- Andzelm, J., Kölmel, C. & Klamt, A. Incorporation of solvent effects into density functional calculations of molecular energies and geometries. *J. Chem. Phys.* **103**, 9312–9320 (1995).

**Acknowledgements** We thank H. Zhou and G. Wu for assistance with NMR and XRD experiments, respectively. J. Kaare-Rasmussen is thanked for experimental support. The US-Israel Binational Science Foundation (grant 2016241), the ACS Petroleum Research Fund (58693-DNI3), the US Department of Energy, Office of Basic Energy Sciences (contract DE-SC-0001861), the University of California, Santa Barbara, and Tel Aviv University are thanked for financial support.

**Author contributions** M.K. carried out the synthetic work and analytical characterization, performed the electrochemical-chemical monophasic reactions and acquired most of the NMR and XRD data. C.H. devised the electrochemical setup and the mono- and biphasic experiments. T.G.C. and M.K. devised all the biphasic capture and release experiments. T.G.C. and V.K. synthesized precursor **1**. R.D. performed all DFT studies. M.K., C.H. and G.M. wrote the manuscript with input from all authors. R.D., T.W.H. and G.M. assisted with data analysis. G.M. directed the research.

**Competing interests** The authors declare no competing interests.

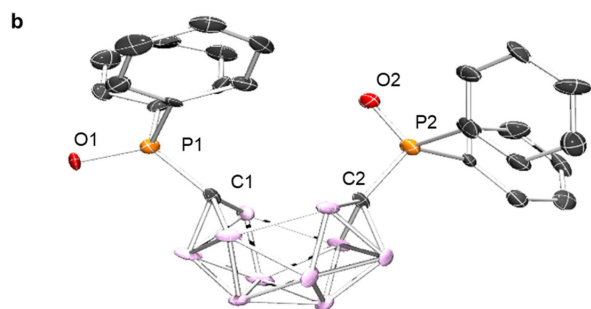
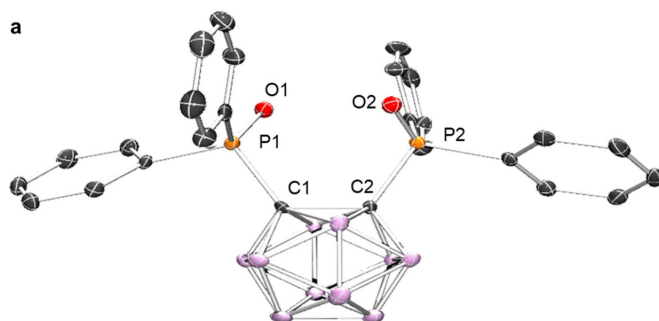
#### Additional information

**Supplementary information** is available for this paper at <https://doi.org/10.1038/s41586-019-1926-4>.

**Correspondence and requests for materials** should be addressed to G.M.

**Peer review information** Nature thanks Vincent Lavallo, Zuowei Xie and the other, anonymous, reviewer(s) for their contribution to the peer review of this work.

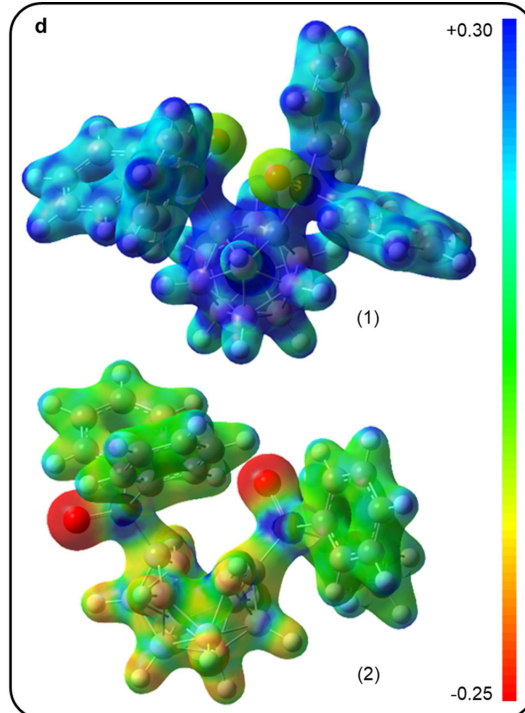
**Reprints and permissions information** is available at <http://www.nature.com/reprints>.



**c**

	1	2a	3*	4*
C...C	1.688(4) Å	2.860 Å	2.855 Å	2.857 Å
P...P	3.537 Å	5.036 Å	4.697 Å	4.806 Å
O1-U-O2			86.5(3)°	89.7(17)°

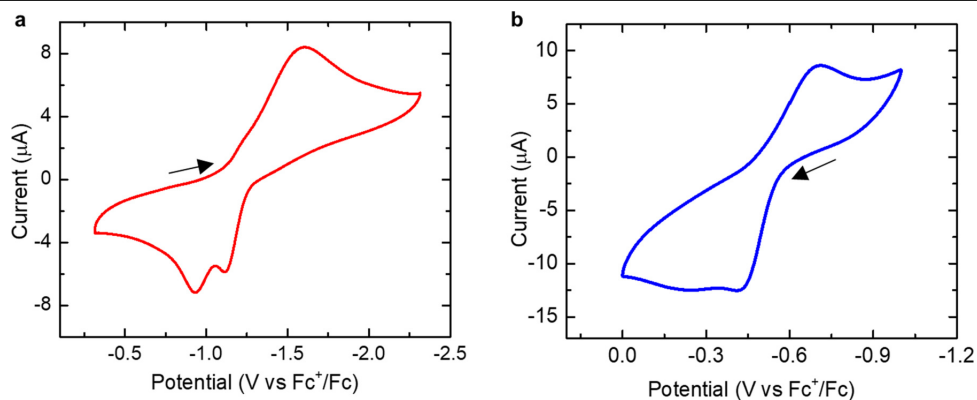
\*Solid-state molecular structures 3 and 4 are shown in Figure1.



**Extended Data Fig. 1 | Solid-state molecular structures and electron density surfaces. a, b,** Solid-state molecular structures of complexes **1** (**a**) and **2a** (**b**). H atoms,  $[\text{CoCp}_2]^+$  counter cations (**2a**) and all co-crystallized solvent molecules are omitted for clarity. **c,** Selected interatomic distances and angles

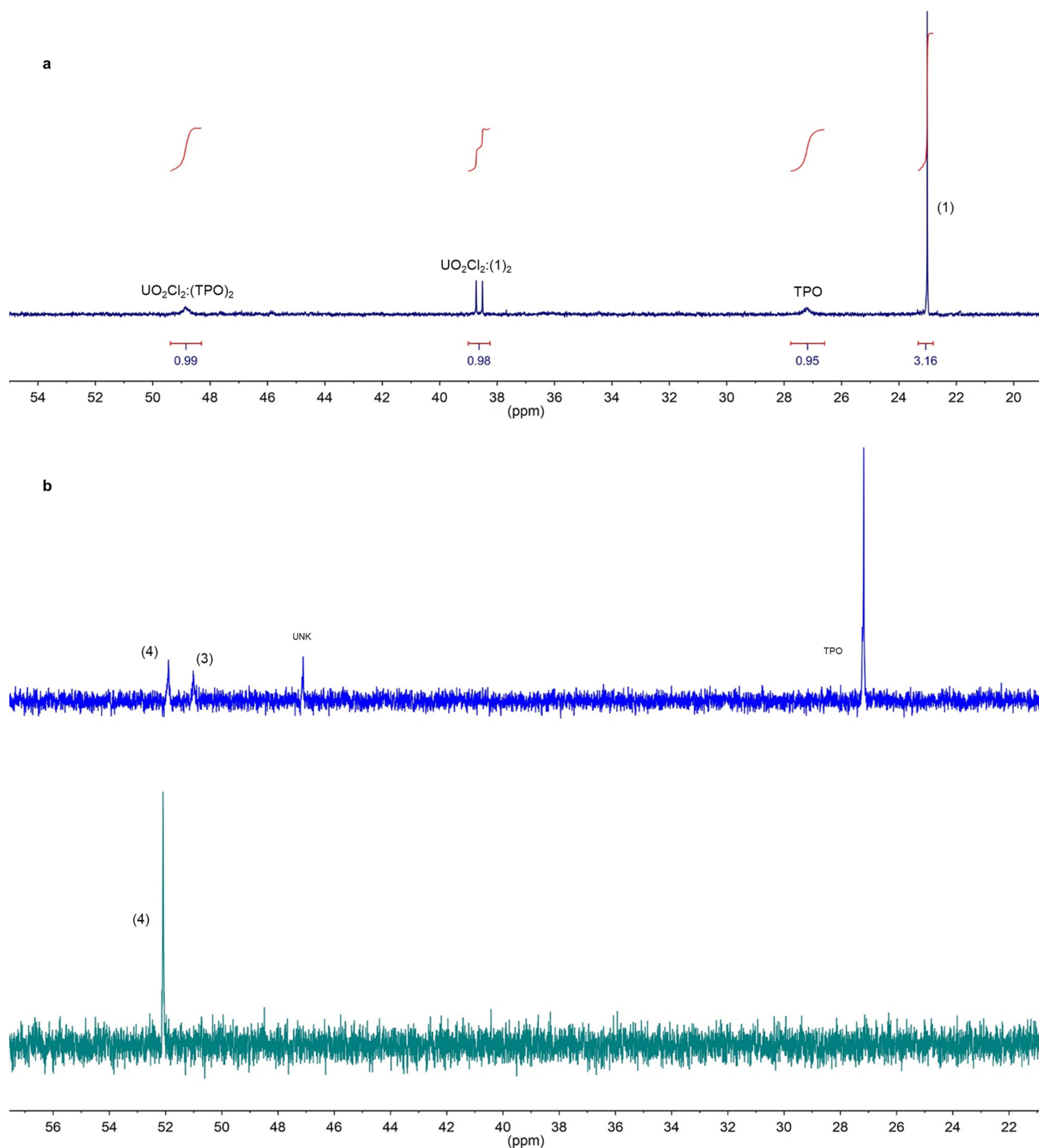
for complexes **1**, **2a**, **3** and **4**. **d,** Electron density surfaces with colour-coded electrostatic potentials obtained from DFT calculations using optimized structures of **1** and the anion of **2a**, labelled **2** (negative values (red) are indicative of higher electron density).





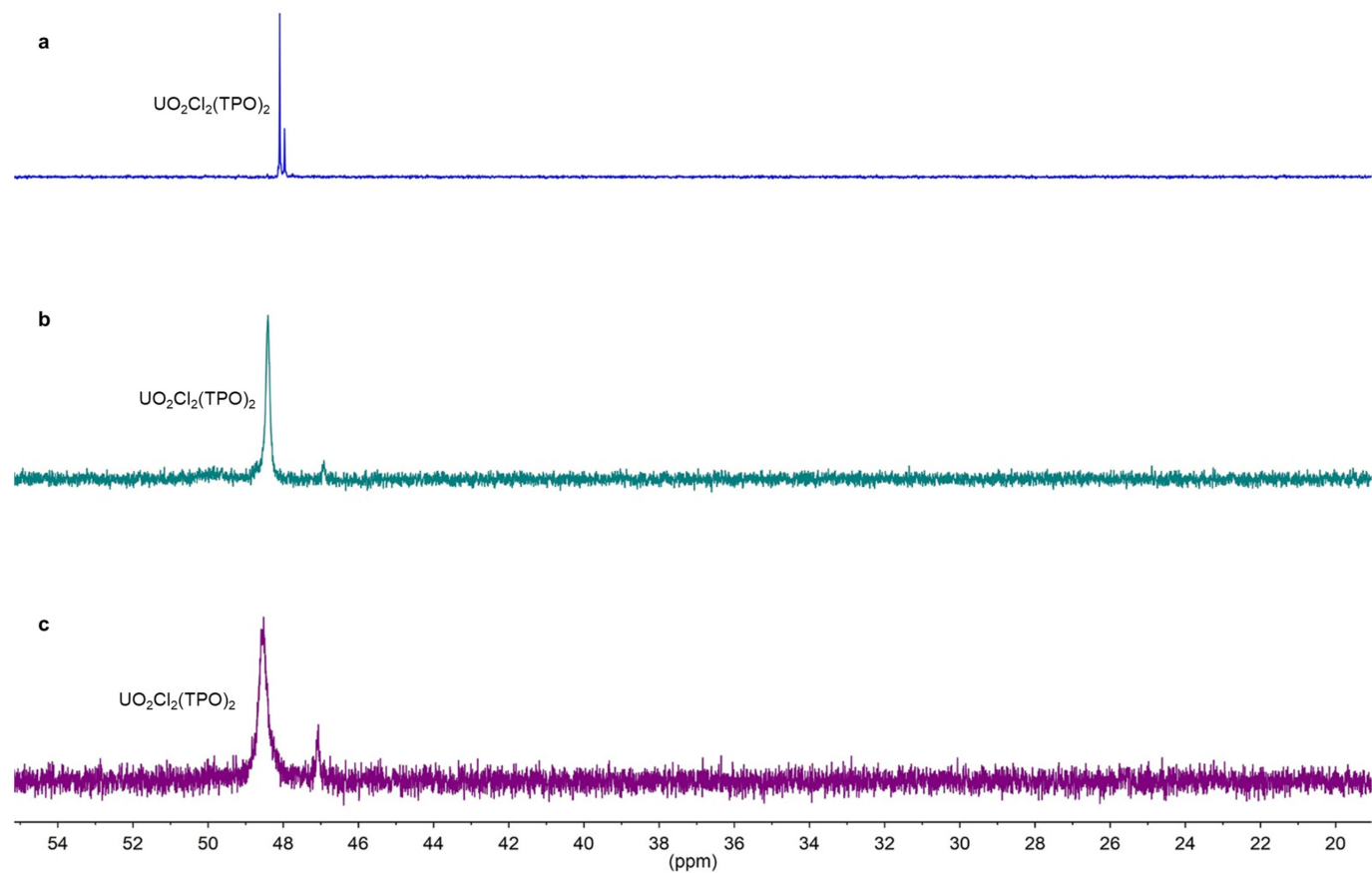
**Extended Data Fig. 2 | Cyclic voltammetry data for **1** and **4**.** **a**, Cyclic voltammogram of **1** (0.5 mM) in a 0.1 M  $[\text{Bu}_4\text{N}][\text{PF}_6]$  THF solution, measured using a 3-mm-diameter glassy carbon working electrode and a platinum-wire counter electrode, referenced to the  $\text{Fc}^+/\text{Fc}$  redox couple (scan rate,  $100 \text{ mV s}^{-1}$ ). The quasi-reversible redox event exhibits two cathodic waves at -0.93 V and

-1.11 V. **b**, Cyclic voltammogram of **4** (1.0 mM) in a 0.1 M  $[\text{Bu}_4\text{N}][\text{PF}_6]$  PC solution, obtained using a 3-mm-diameter glassy carbon working electrode and a platinum-wire counter electrode, referenced to the  $\text{Fc}^+/\text{Fc}$  couple (scan rate,  $100 \text{ mV s}^{-1}$ ). The quasi-reversible redox event exhibits one anodic wave at -0.42 V.



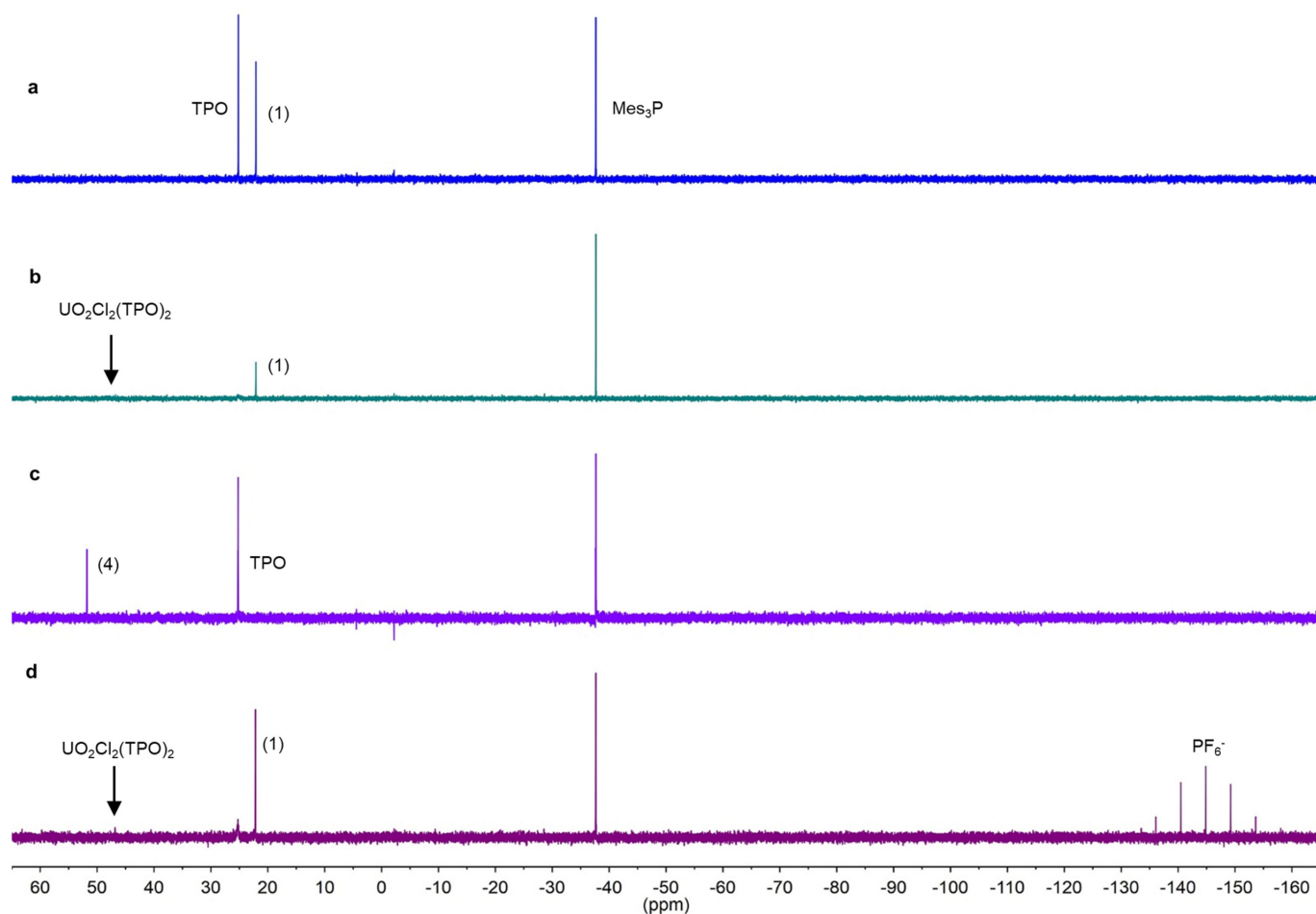
**Extended Data Fig. 3**  $^{31}\text{P}\{^1\text{H}\}$  NMR spectra from competition experiments of **1**, **2a** and TPO. **a**,  $^{31}\text{P}\{^1\text{H}\}$  NMR spectrum of 2.0 equiv. **1** with 1.0 equiv.  $\text{UO}_2\text{Cl}_2(\text{TPO})_2$  in  $\text{DCM-d}_2$ . Relative integrations are shown in red. **b**,  $^{31}\text{P}\{^1\text{H}\}$  NMR spectra of in situ reactions of 1.0 equiv. **2a** with 1.0 equiv.  $\text{UO}_2\text{Cl}_2(\text{TPO})_2$  in

$\text{DCM-d}_2$ . Rapid precipitation of a yellow solid was observed. Top,  $^{31}\text{P}\{^1\text{H}\}$  NMR spectrum of the  $\text{DCM-d}_2$  supernatant. An unknown byproduct at 47 ppm is observed. Bottom,  $^{31}\text{P}\{^1\text{H}\}$  NMR spectrum of the filtrate dissolved in PC with a  $\text{DCM-d}_2$  capillary tube.



**Extended Data Fig. 4**  $^{31}\text{P}\{^1\text{H}\}$  NMR spectra from competition experiments of PC with  $\text{UO}_2\text{Cl}_2(\text{TPO})_2$ . **a**, Initial  $^{31}\text{P}\{^1\text{H}\}$  NMR spectrum of  $\text{UO}_2\text{Cl}_2(\text{TPO})_2$  in  $\text{DCM-d}_2$ , displaying the proposed *cis:trans* isomers. **b**,  $^{31}\text{P}\{^1\text{H}\}$  NMR spectrum

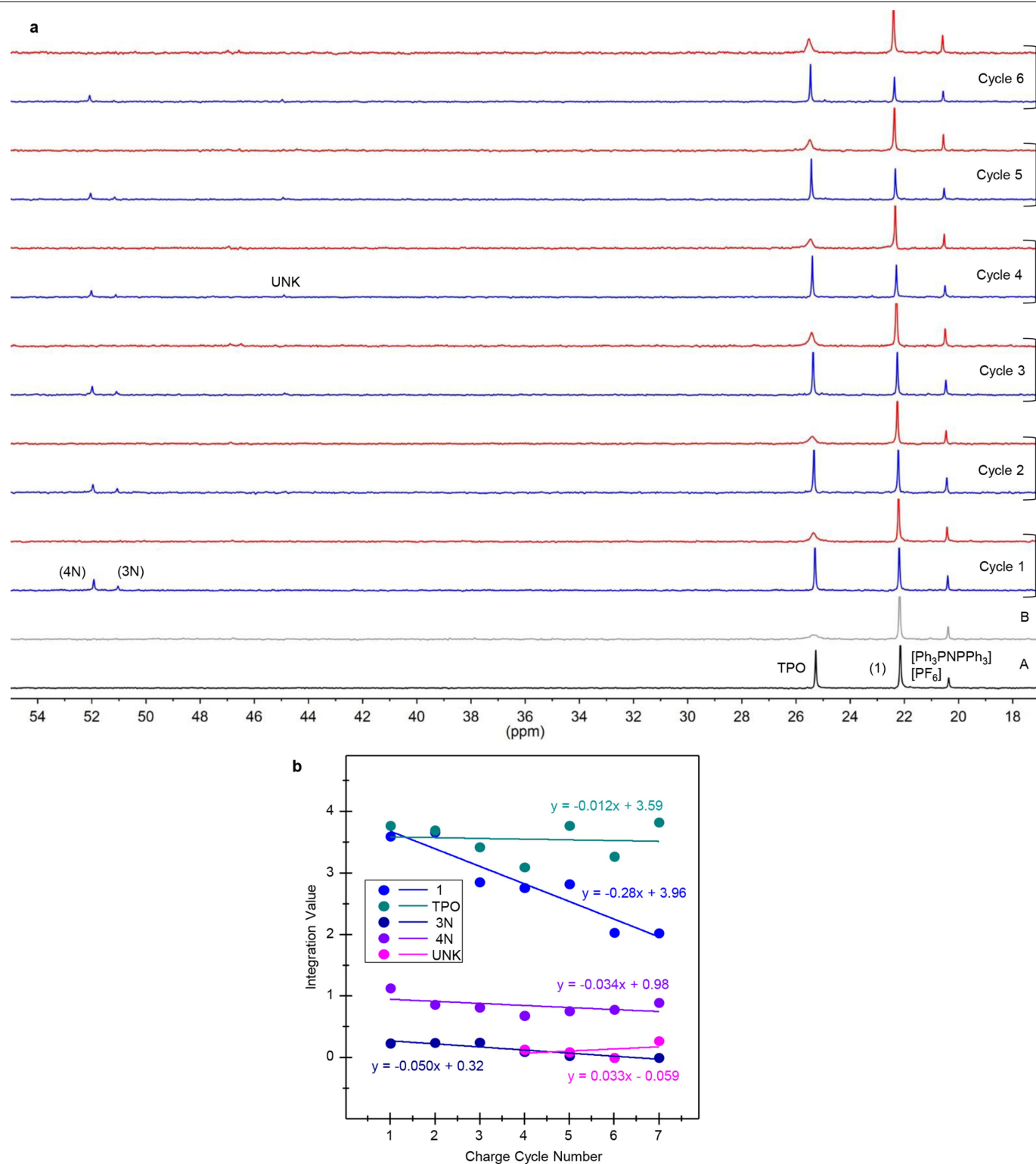
after the addition of 20.0 equiv. PC to the solution in **a**. **c**,  $^{31}\text{P}\{^1\text{H}\}$  NMR spectrum after the addition of 40.0 equiv. PC to the solution in **a**.



**Extended Data Fig. 5**  $^{31}\text{P}\{^1\text{H}\}$  NMR spectra for chemical capture and release of  $\text{UO}_2^{2+}$ . Reactions were carried out in a PC:benzene (3:1) solvent mixture with a  $\text{MeCN-d}_3$  capillary tube insert using  $\text{Mes}_3\text{P}$  as the analytical standard. A relaxation delay of 30 s was used to obtain accurate integrations of all species (see Methods). **a**,  $^{31}\text{P}\{^1\text{H}\}$  NMR spectrum of 4.0 equiv. TPO and 2.0 equiv. **1**.

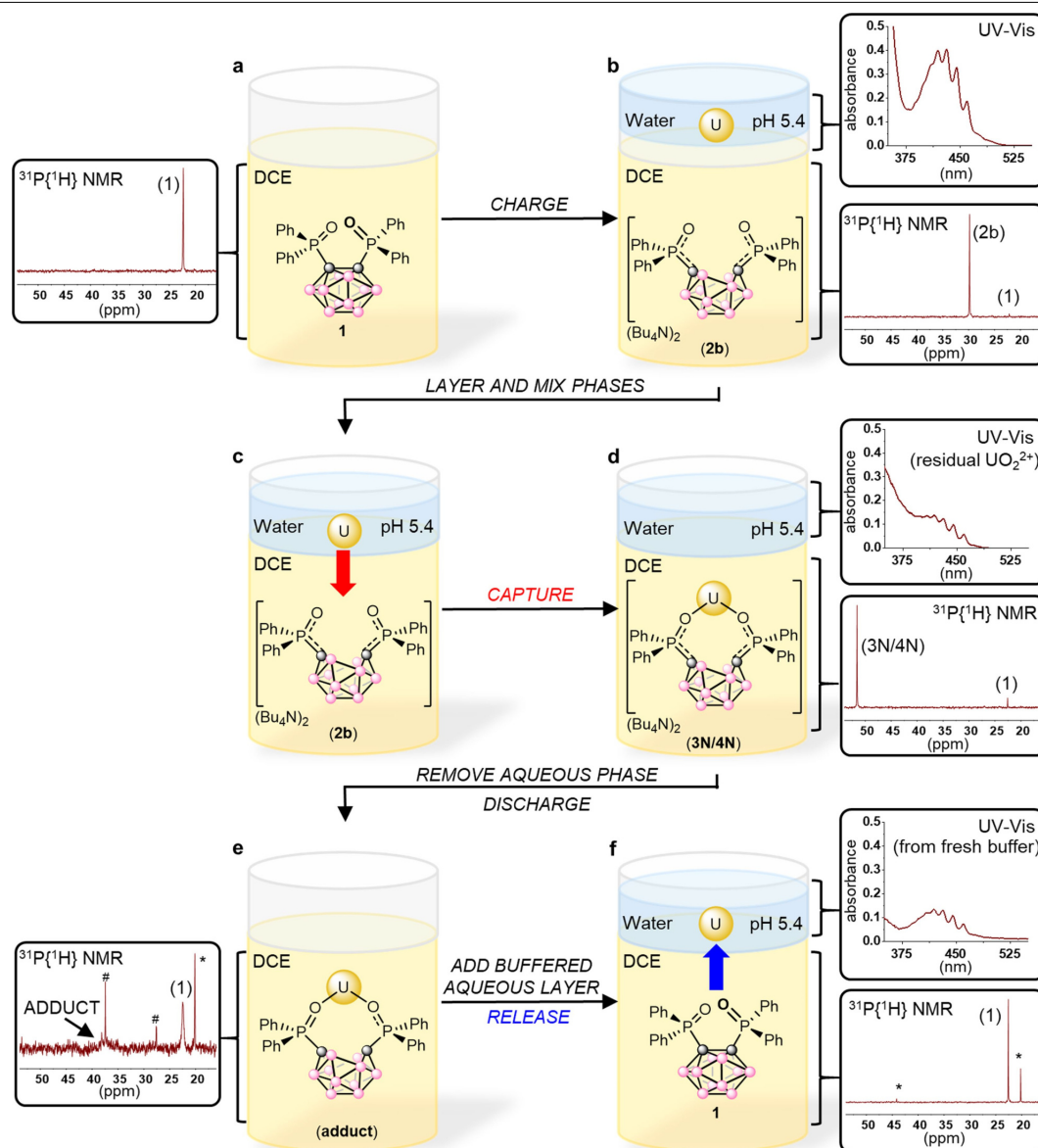
**b**,  $^{31}\text{P}\{^1\text{H}\}$  NMR spectrum of 4.0 equiv. TPO and 2.0 equiv. **1** in the presence of 0.5 equiv.  $[\text{UO}_2\text{Cl}_2(\text{THF})_2]_2$ . **c**,  $^{31}\text{P}\{^1\text{H}\}$  NMR spectrum of 4.0 equiv.  $\text{CoCp}^+$  added to the reaction in **b**. **d**,  $^{31}\text{P}\{^1\text{H}\}$  NMR spectrum after addition of 4.0 equiv.  $[\text{Fc}][\text{PF}_6]$  to the reaction in **c**. The reaction conditions are detailed in Methods.





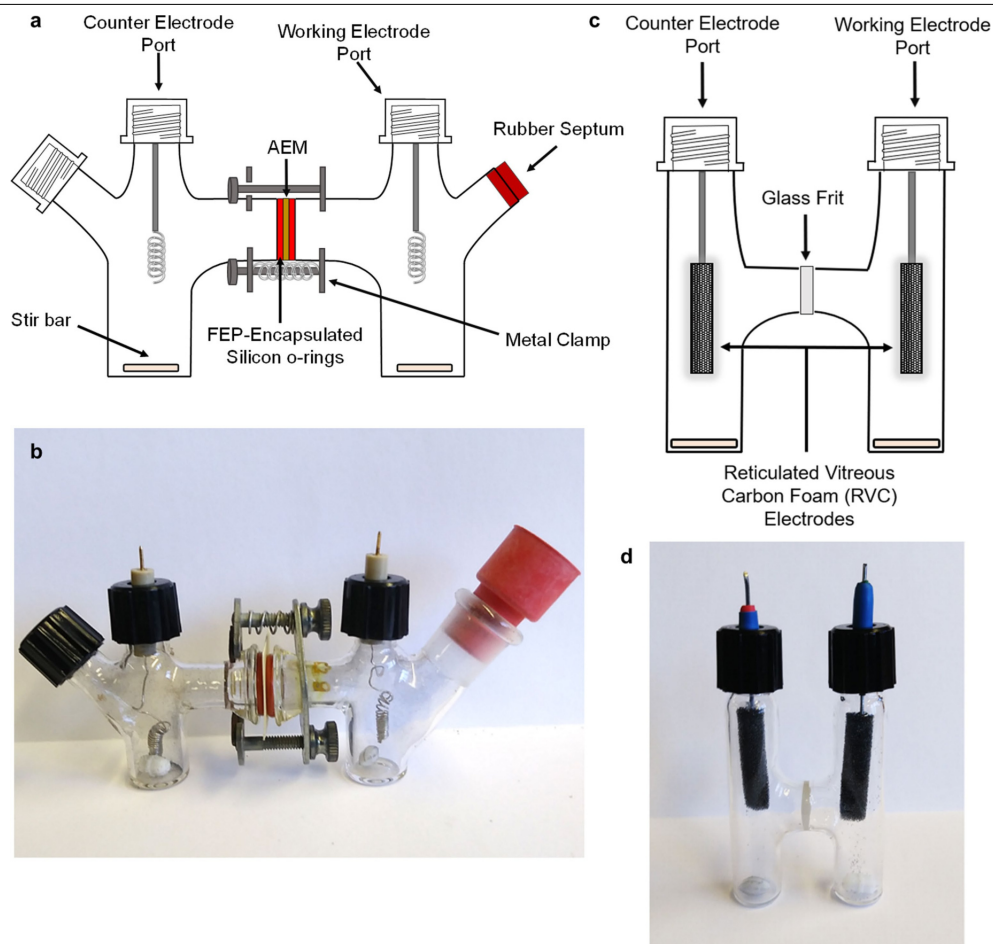
**Extended Data Fig. 6 | Monophasic electrochemical capture and release of  $\text{UO}_2^{2+}$  by GBE.** Reactions were carried out in a PC:benzene (3:1) solvent mixture with a  $\text{MeCN-d}_3$  capillary tube insert with  $[\text{Ph}_3\text{PNPPh}_3][\text{PF}_6]$  as the analytical standard. A relaxation delay of 40 s was used to obtain accurate integrations of all species (see Methods). **a**,  $^{31}\text{P}\{^1\text{H}\}$  NMR spectrum of 6.0 equiv. TPO and 5.0 equiv. **1**, with 1.0 equiv.  $[\text{Ph}_3\text{PNPPh}_3][\text{PF}_6]$  as the analytical standard. **B**:  $^{31}\text{P}\{^1\text{H}\}$  NMR spectrum of 6.0 equiv. TPO and 5.0 equiv. **1** in the presence of 0.5 equiv.  $[\text{UO}_2\text{Cl}_2(\text{THF})_2]$ . Cycles 1–6:  $^{31}\text{P}\{^1\text{H}\}$  NMR spectra of charged (blue) and discharged (red) solutions. An unknown species begins to appear at 45 ppm

after multiple cycles. Detailed experimental conditions are given in Methods. **b**, Plot of integrated values for all  $^{31}\text{P}$ -containing species, obtained from the charged spectra versus the charge cycle number. The repeated cycling resulted in loss of electrochemically generated **3N** (average loss of 15.6% per cycle) due to presumed chloride migration over the anion-exchange membrane. There was little change in the yield of TPO (average loss of 0.3% per cycle) with larger losses in **1** (average loss of 7.2% per cycle) and **4N** (average loss of 3.4% per cycle). The values of per cent loss per cycle were estimated from the calculated trendlines by taking the ratio of the slope versus the y-intercept values.



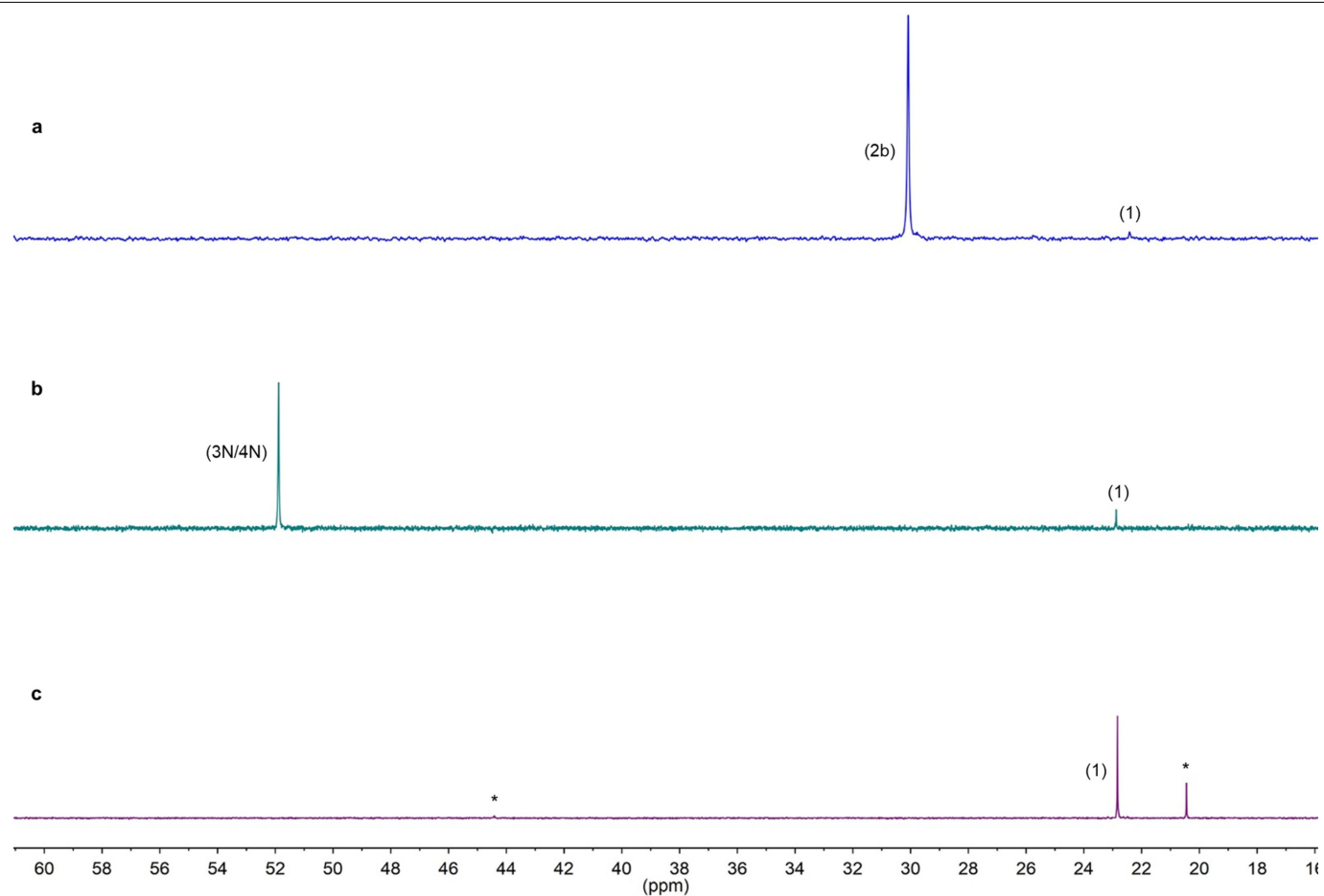
**Extended Data Fig. 7 | Stepwise procedure for the biphasic electrochemical capture and release of  $\text{UO}_2^{2+}$  (yellow U).** For simplicity, only half of the H-cell is displayed here. For the full cell design, see Extended Data Fig. 8c, d. **a**,  $^{31}\text{P}\{^1\text{H}\}$  NMR spectrum of DCE layer containing only **1** and  $[\text{Bu}_4\text{N}][\text{PF}_6]$  ( $[\text{PF}_6]^-$  resonance not shown) before charging. **b**, Top inset, UV-Vis spectrum of aqueous phase containing 1.25 equiv.  $\text{UO}_2^{2+}$  (from  $\text{UO}_2(\text{NO}_3)_2(\text{THF})_2$ ) before mixing with the DCE phase. Bottom inset,  $^{31}\text{P}\{^1\text{H}\}$  NMR spectrum of DCE layer containing **2b** (major) and **1** (minor) after charging **1** (from **a**) galvanostatically. **c**, Mixing of the phases in **b** for 2 h. **d**, Top inset, UV-Vis spectrum of aqueous phase after mixing with the DCE phase, revealing approximately 0.35 equiv.  $\text{UO}_2^{2+}$  remaining. Bottom inset,  $^{31}\text{P}\{^1\text{H}\}$  NMR spectrum of the DCE layer after mixing

with aqueous phase, showing captured products **3N/4N** (major) and **1** (minor). **e**,  $^{31}\text{P}\{^1\text{H}\}$  NMR spectrum of the DCE layer following phase separation and galvanostatic discharge. A broad peak is observed at 38 ppm, which we attribute to an adduct of  $\text{UO}_2^{2+}$  with **1**. This, together with the broadened peak of **1**, accounts for ~75% of products. The remaining unknown byproducts are marked with # or \*. **f**, Top inset, UV-Vis spectrum of aqueous phase after addition of fresh buffer to the discharged DCE solution (in **e**) and mixing for 12 h. The spectrum reveals the release of approximately 0.50 equiv.  $\text{UO}_2^{2+}$ . Bottom inset,  $^{31}\text{P}\{^1\text{H}\}$  NMR spectrum of the DCE layer after mixing with fresh buffer, showing the free carborane **1** (major), as well as unknown byproducts at 44 ppm and 20 ppm marked by \* (~20% of total).



**Extended Data Fig. 8 | Diagrams for mono- and biphasic electrochemical cells.** **a**, Schematic of the divided H-cell used for the monophasic galvanostatic bulk electrolysis cycling experiments with  $\text{UO}_2^{2+}$ . **b**, Photograph of the divided H-cell used for the monophasic galvanostatic bulk electrolysis cycling

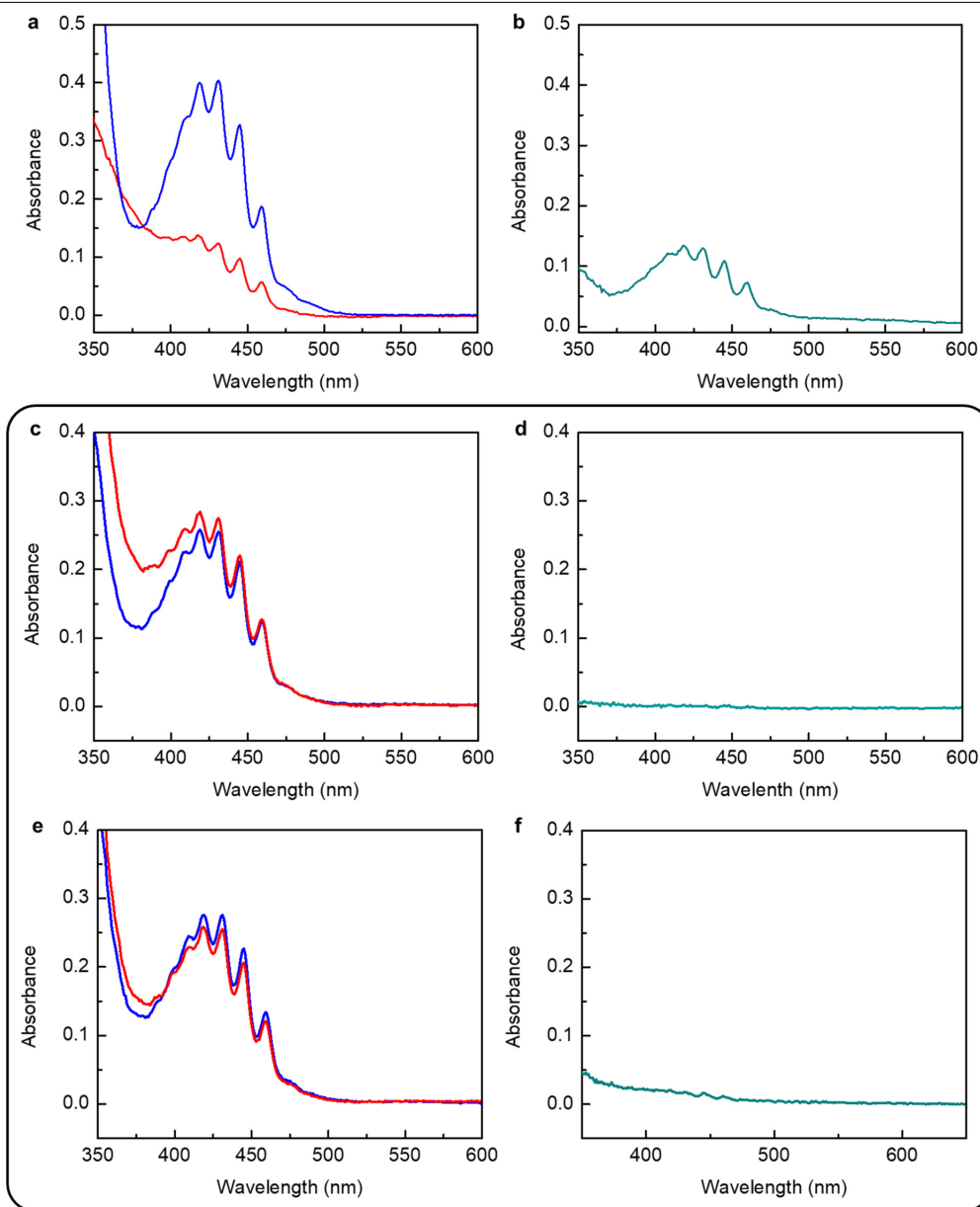
experiments with  $\text{UO}_2^{2+}$ . **c**, Schematic of the two-compartment H-cell used for the biphasic electrochemical capture and release of  $\text{UO}_2^{2+}$ . **d**, Photograph of the two-compartment H-cell used for the biphasic electrochemical capture and release of  $\text{UO}_2^{2+}$ .



**Extended Data Fig. 9 |  $^{31}\text{P}\{^1\text{H}\}$  NMR spectra for biphasic electrochemical capture and release of  $\text{UO}_2^{2+}$ .** **a.**  $^{31}\text{P}\{^1\text{H}\}$  NMR spectrum of electrochemically reduced **1** in DCE to produce **2b**. **b.**  $^{31}\text{P}\{^1\text{H}\}$  NMR spectrum of DCE layer following  $\text{UO}_2^{2+}$  capture from the aqueous layer containing  $\text{UO}_2(\text{NO}_3)_2(\text{THF})_2$  in 0.1 M

sodium acetate buffer. **c.**  $^{31}\text{P}\{^1\text{H}\}$  NMR spectrum of an electrochemically oxidized DCE layer containing **3N/4N** following extraction of  $\text{UO}_2^{2+}$  into 0.1 M sodium acetate buffer. Minor unknown byproducts (marked by asterisks) are also observed. Detailed experimental conditions are found in Methods.





**Extended Data Fig. 10 | UV-Vis spectra for the biphasic electrochemical capture and release of  $\text{UO}_2^{2+}$  and controls.** **a**, Initial UV-Vis spectrum of  $\text{UO}_2(\text{NO}_3)_2(\text{THF})_2$  (0.042 g, 0.078 mmol, 0.026 M, 1.25 equiv.) in 3 ml of 0.1 M sodium acetate buffer at pH 5.4 (blue). UV-Vis spectrum taken after mixing the aqueous layer with the DCE layer of electrochemically reduced **1** (to generate **2b**) in a 0.1 M  $[\text{Bu}_4\text{N}][\text{PF}_6]$  DCE solution for 2 h, indicating a residual concentration of 0.0073 M, consistent with a total quantity of captured  $\text{UO}_2^{2+}$  to the DCE layer of 0.056 mmol (red). **b**, UV-Vis spectrum of 0.1 M aqueous sodium acetate buffer layer at pH 5.4 after mixing for 12 h with electrochemically oxidized **3N/4N** in DCE. The concentration of  $\text{UO}_2^{2+}$  was calculated to be 0.010 M, consistent with a total quantity of 0.031 mmol of released  $\text{UO}_2^{2+}$  from the DCE layer to the aqueous phase. **c**, Control for  $\text{UO}_2^{2+}$  migration from water to DCE in the absence of carborane (**1** or **2a/b**). Initial

UV-Vis spectrum of  $\text{UO}_2^{2+}$  in 0.1 M sodium acetate-buffered solution at pH 5.4 (blue). UV-Vis spectrum of aqueous layer after mixing for 4 h with DCE solution containing  $[\text{Bu}_4\text{N}][\text{PF}_6]$  (0.1 M; red). **d**, Corresponding UV-Vis spectrum of DCE layer after mixing for 4 h with the aqueous layer containing  $\text{UO}_2^{2+}$  shown in **c**. **e**, Control for  $\text{UO}_2^{2+}$  migration from water to DCE in the presence of neutral carborane (**1**). Initial UV-Vis spectrum of  $\text{UO}_2^{2+}$  (1.0 equiv.) in 0.1 M sodium acetate-buffered solution at pH 5.4 (blue). UV-Vis spectrum of aqueous layer after mixing for 3 h with DCE solution containing  $[\text{Bu}_4\text{N}][\text{PF}_6]$  (0.1 M) and **1** (1.0 equiv.; red). **f**, Corresponding UV-Vis spectrum of DCE layer containing **1** after mixing for 3 h with the aqueous layer containing  $\text{UO}_2^{2+}$  shown in **e**. The  $\text{UO}_2^{2+}$  extinction coefficient was experimentally determined to be  $7.715 \text{ L mol}^{-1} \text{ cm}^{-1}$  (460 nm) at pH 5.4. See Methods for experimental details.

# Lactonization as a general route to $\beta$ -C( $sp^3$ )-H functionalization

<https://doi.org/10.1038/s41586-019-1859-y>

Zhe Zhuang<sup>1</sup> & Jin-Quan Yu<sup>1\*</sup>

Received: 16 July 2019

Accepted: 26 November 2019

Published online: 11 December 2019

Functionalization of the  $\beta$ -C-H bonds of aliphatic acids is emerging as a valuable synthetic disconnection that complements a wide range of conjugate addition reactions<sup>1–5</sup>. Despite efforts for  $\beta$ -C-H functionalization in carbon-carbon and carbon-heteroatom bond-forming reactions, these have numerous crucial limitations, especially for industrial-scale applications, including lack of mono-selectivity, use of expensive oxidants and limited scope<sup>6–13</sup>. Notably, the majority of these reactions are incompatible with free aliphatic acids without exogenous directing groups. Considering the challenge of developing C-H activation reactions, it is not surprising that achieving different transformations requires independent catalyst design and directing group optimizations in each case. Here we report a Pd-catalysed  $\beta$ -C( $sp^3$ )-H lactonization of aliphatic acids enabled by a mono-*N*-protected  $\beta$ -amino acid ligand. The highly strained and reactive  $\beta$ -lactone products are versatile linchpins for the mono-selective installation of diverse alkyl, alkenyl, aryl, alkynyl, fluoro, hydroxyl and amino groups at the  $\beta$  position of the parent acid, thus providing a route to many carboxylic acids. The use of inexpensive *tert*-butyl hydrogen peroxide as the oxidant to promote the desired selective reductive elimination from the Pd(IV) centre, as well as the ease of product purification without column chromatography, render this reaction amenable to tonne-scale manufacturing.

Alkyl carboxylic acids are ubiquitous and inexpensive reagents in organic chemistry; as such, they are favourable substrates for C-H activation reactions<sup>4,5</sup>. The scope of such transformations is often limited by the incompatibility of certain reaction partners. Indeed, for C-C bond formations, alkylation reactions are limited to primary alkyl iodide or alkyl boron coupling partners<sup>6–8</sup>; olefination reactions are applicable only to electron-deficient olefins<sup>9,10</sup>; alkynylation reactions are limited to silyl acetylene bromide<sup>11</sup>; and arylation reactions are compatible only with aryl iodides, but not with the more practical aryl bromides and chlorides<sup>12,13</sup>, despite the design of various directing groups. Most importantly, carbon-heteroatom (C-Y) bond-forming reactions (such as fluorination, hydroxylation and amination) based on  $\beta$ -C-H activation of free aliphatic acids have not yet been realized. Considering these persistent limitations of the conventional  $\beta$ -C-H activation approach, we turned to a one-for-all  $\beta$ -lactonization strategy (Fig. 1a).  $\beta$ -Lactones are strained heterocycles that have received considerable attention as valuable synthetic intermediates in the syntheses of natural and unnatural products<sup>14,15</sup>. Owing to their inherent ring strain, they readily react with a wide range of nucleophiles by either acyl C-O or alkyl C-O bond cleavage. The lack of precedent of this reaction is probably due to the highly unfavoured four-membered lactonization transition state<sup>15</sup>. Notably, this  $\beta$ -lactonization could provide a strategy to synthesize carboxylic acids containing  $\alpha$ -quaternary centres that are inaccessible by conjugate addition chemistry, and difficult to prepare via  $\alpha$ -substitution<sup>16</sup>.

A mixture of  $K_2PtCl_4$  (17 mol%) and  $K_3PtCl_6$  (33 mol%) can promote the formation of  $\gamma$ -lactones from aliphatic acids in 16% yield, accompanied

by 2%  $\beta$ -lactone<sup>17,18</sup>.  $\gamma$ -Lactonization of benzylic C-H bonds has also been reported using Pd and Pt catalysts<sup>19,20</sup>. These observations indicate that  $\beta$ -lactonization is a highly disfavoured process. Guided by previous work using a bystander oxidant to promote C-H activation/cyclization reactions<sup>21,22</sup>, we investigated catalysts and conditions to achieve a  $\beta$ -C-H lactonization reaction. Compared to  $\beta$ -lactam formation, where a nucleophilic directing group can be employed to form a strong C-N bond<sup>23,24</sup>,  $\beta$ -C-H lactonization poses an additional challenge because of the low nucleophilicity of the carboxylic acid, the strain generated in forming a four-membered ring and the facile ring opening under C-H activation conditions. Most problematically, Pd(IV) intermediates could readily undergo conventionally favoured reductive elimination to produce non-cyclic C-O bond-formation products, such as the most common competing pathways acetoxylation and alkoxylation (Fig. 1b). We selected 2,2-dimethylbutyric acid **1a** as a model substrate in our search for reactivity with a wide range of oxidants and catalysts. Exploratory studies using various common oxidants for Pd(II)/Pd(IV) chemistry—such as  $PhI(OAc)_2$ ,  $K_2S_2O_8$  and  $F^+$  reagents—consistently gave undesired non-cyclic oxidation products (see Supplementary Information Table 3 and section ‘Mechanistic studies’ for details). To avoid the undesired reductive-elimination pathway, we tested the sterically bulky oxidant *tert*-butyl hydrogen peroxide (TBHP)<sup>4</sup>, as well as  $PdCl_2$ -derived catalysts, because the  $^tBuO^-$  and  $Cl^-$  anions are less prone to reductive elimination due to sterics and electronics. The desired  $\beta$ -lactone **2a** was formed in 15%  $^1H$  NMR (nuclear magnetic resonance) yield using a combination of  $Pd(CH_3CN)_2Cl_2$ , TBHP oxidant,  $CsHCO_3$  and 1,1,1,3,3,3-hexafluoro-2-propanol (HFIP) solvent. Encouragingly,

<sup>1</sup>Department of Chemistry, The Scripps Research Institute, La Jolla, CA, USA. \*e-mail: yu200@scripps.edu

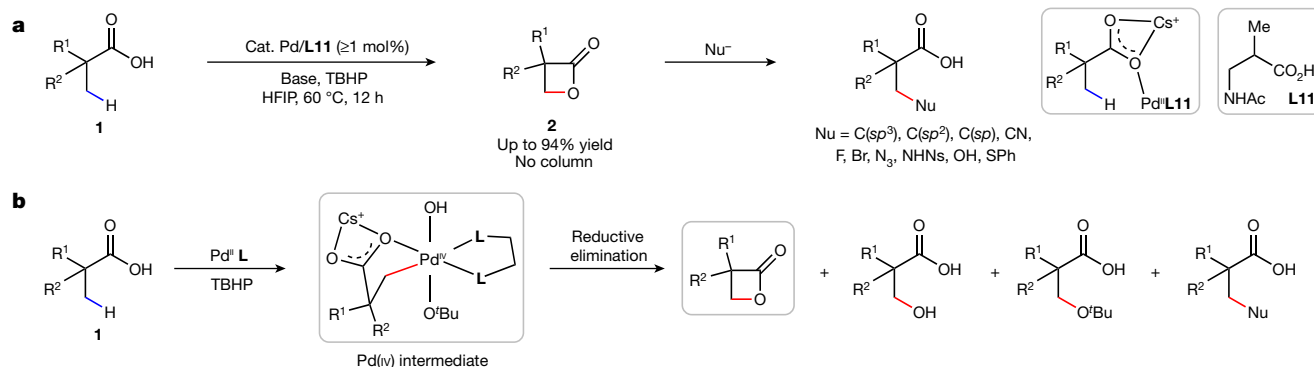


**Fig. 1** |  $\beta$ -C( $sp^3$ )-H functionalization. **a**, Lactonization as a general and scalable route to  $\beta$ -C( $sp^3$ )-H functionalization. **b**, Challenges: multiple reductive-elimination pathways of Pd(IV) centres. Nu, nucleophile (acid, solvent); L, ligand.

no  $\gamma$ -lactone or  $\beta$ ,  $\gamma$ -hydroxylated products were observed during the reaction. The unique role of TBHP in favouring  $\beta$ -lactone formation can be rationalized on the basis of studies on the oxidation of Pd(II) to Pd(IV) by benzoyl peroxide<sup>25</sup> and TBHP<sup>4</sup>. Following the oxidation of Pd(II) to Pd(IV) by TBHP, 'BuO<sup>-</sup> and HO<sup>-</sup> bound to a Pd(IV) centre are less likely to undergo rapid reductive elimination due to the strong Pd–O'Bu (OH) bond. According to the principle of organometallic chemistry, the steric hindrance of 'BuO<sup>-</sup> could also enhance the reductive elimination of the carboxylate from the substrate to generate  $\beta$ -lactone product.

In light of the recent advances in ligand-accelerated Pd(II)-catalysed C–H activation<sup>26</sup>, we next searched for ligands that could substantially improve the reactivity of the catalyst. It is also possible that an appropriate ligand could enhance the otherwise unfavoured  $\beta$ -lactonization. Using the mono-*N*-protected  $\alpha$ -amino acid (MPAA) ligand *N*-acetyl glycine **L1**, the yield was improved to 36%. Modification of the backbone of the  $\alpha$ -amino acid ligand led only to minor improvements (**L2** to **L5**). Considering the challenging reductive elimination of a strained four-membered ring from Pd(IV), we reasoned that switching the ligand

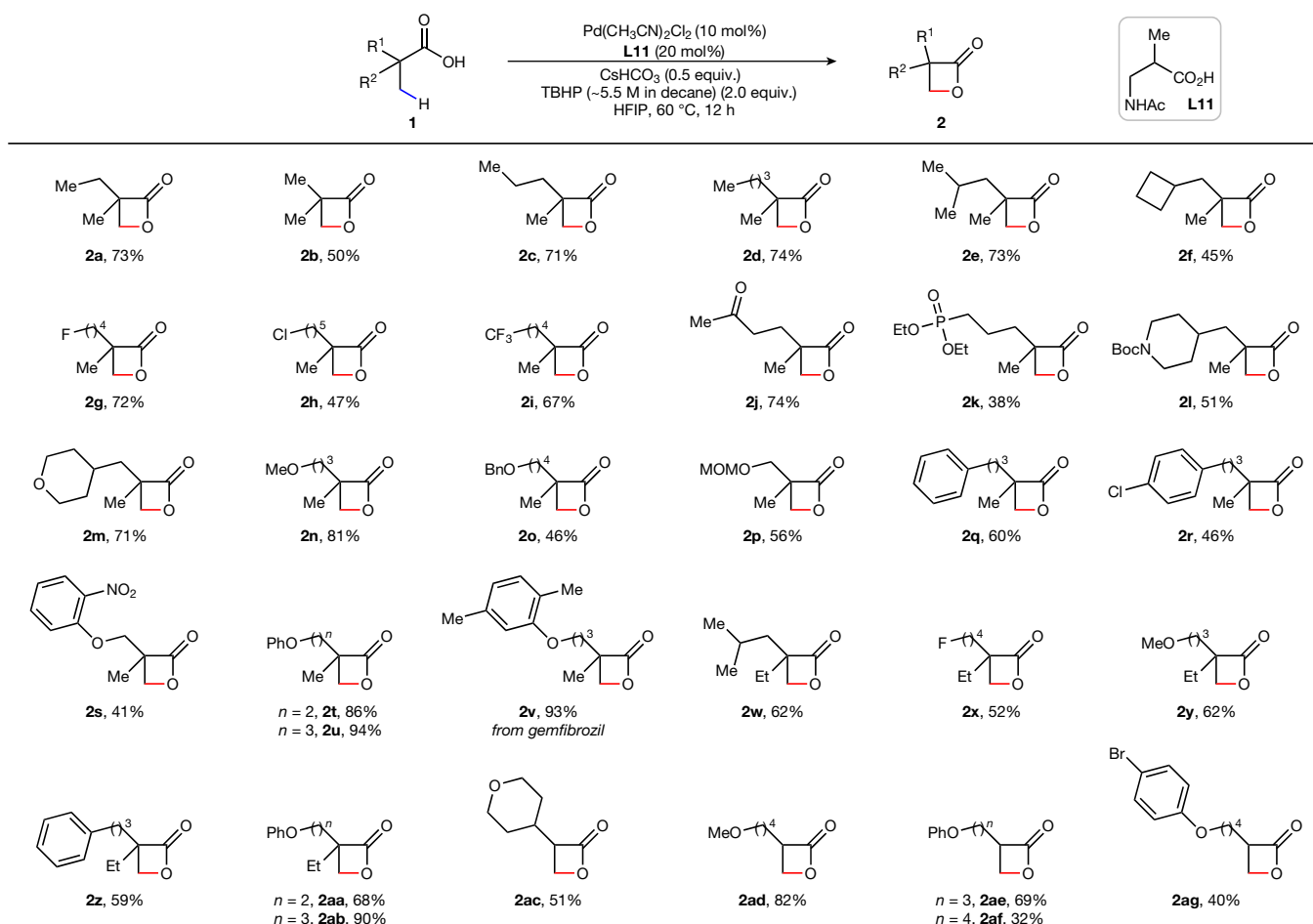


**Fig. 2** | Aliphatic acid scope for  $\beta$ -C( $sp^3$ )-H lactonization. Conditions for **2a** to **2s** and **2w** to **2z**: **1** (0.1 mmol), Pd(CH<sub>3</sub>CN)<sub>2</sub>Cl<sub>2</sub> (10 mol%), **L11** (20 mol%), CsHCO<sub>3</sub> (0.5 equiv.), TBHP (about 5.5 M in decane) (2.0 equiv.), HFIP (1.0 mL), 60 °C, 12 h.

Conditions for **2t** to **2v** and **2aa** to **2ag**: **1** (0.1 mmol), Pd(OAc)<sub>2</sub> (10 mol%), **L11** (20 mol%), NaOAc (1.0 equiv.), TBHP (about 5.5 M in decane) (2.0 equiv.), HFIP (1.0 mL), 60 °C, 12 h. See Supplementary Information for details.

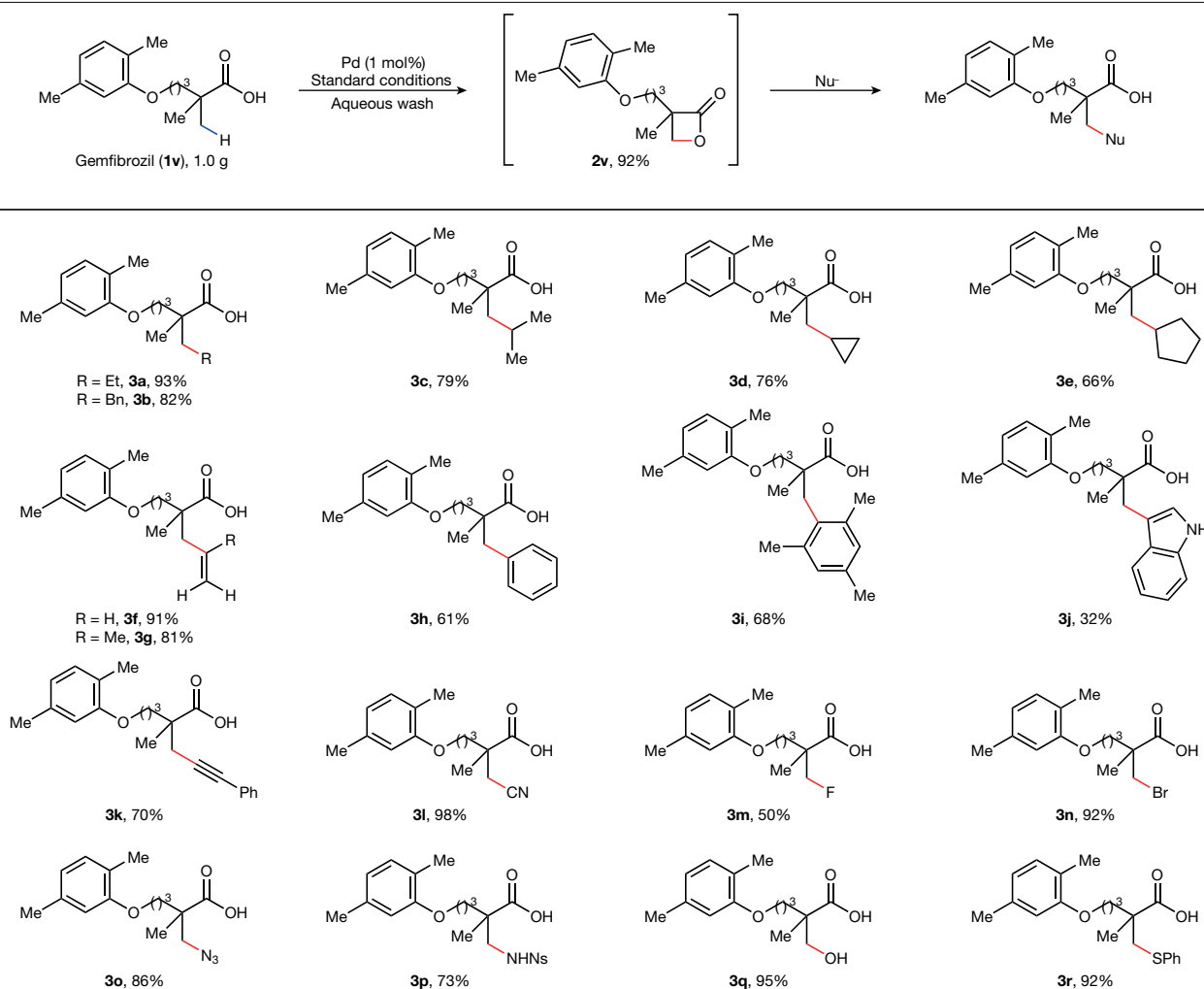


**Fig. 3 | Gram-scale  $\beta$ -C( $sp^3$ )-H lactonization of Gemfibrozil with 1 mol% Pd and diverse transformations.** Nu, Grignard reagents (**3a** to **3j**), alkynylaluminum reagent (**3k**), TBACN (**3l**), TBAF (**3m**),  $MgBr_2$  (**3n**),  $NaN_3$  (**3o**),  $NaNHNs$  (**3p**), KOH (**3q**),  $PhSNa$  (**3r**). Conditions for **3a** to **3j**: **2v** (0.1 mmol),

$CuBr \cdot SMe_2$  (20 mol%),  $Me_2S$  (1.0 equiv.), Nu (3.0 equiv.), THF (1.0 mL), 0 °C, 1 h. Conditions for **3k** to **3r**: **2v** (0.1 mmol), Nu (2.0 or 3.0 equiv.), 1–12 h. See Supplementary Information for details.

binding mode from five- to six-membered chelation will increase the bite angle, thereby favouring the desired reductive elimination. The  $\beta$ -amino acid-derived ligand *N*-acetyl  $\beta$ -alanine **L6** under the same conditions improved the yield to 48%. Building on this promising finding, we then investigated the influence of substituents on the ligand's side chain. Substituents at the  $\beta$  position slightly reduced the reactivity (**L7** to **L10**), suggesting that steric hindrance around the  $NHAc$  moiety was detrimental to reactivity. Moreover, substitution at the  $\alpha$  position proved beneficial (**L11** to **L13**), with methyl-substituted **L11** giving 65% yield. The isolated yield of  $\beta$ -lactone could be further improved to 73% when using TBHP in decane (see Supplementary Information for further optimization).

After determining the optimized ligand and conditions, we explored the scope of this methodology (Fig. 2). Aliphatic acids containing  $\alpha$ -gem-dimethyl groups with various aliphatic chains including cyclobutanes (**2f**) were all compatible, affording the  $\beta$ -lactones (**2a** to **2f**) in high yields. A range of functionalities—such as fluoro (**2g**), chloro (**2h**), trifluoromethyl (**2i**), ketone (**2j**) and phosphoric ester (**2k**)—were tolerated, with halogen (**2h**), ketone (**2j**) and phosphoric ester (**2k**) moieties serving as useful synthetic handles for subsequent derivatization. The lactone products containing a piperidine (**2l**) or a tetrahydropyran (**2m**) motif are especially valuable. Different protecting groups on the hydroxyl group including simple methyl (Me) (**2n**), benzyl (Bn)

(**2o**), and methoxymethyl (MOM) (**2p**) were also well tolerated. Phenyl (**2q** to **2r**) and phenyl ether (**2s** to **2v**) groups were compatible with the TBHP system, and remained intact despite the potentially reactive aryl or benzylic C–H bonds. A range of substituents on the aryl ring from electron-donating (Me and O-alkyl) to electron-withdrawing (chloro, bromo and nitro) groups were all well tolerated. Gemfibrozil (**1v**), an oral drug used to lower lipid levels<sup>27</sup>, was converted to the corresponding  $\beta$ -lactone **2v** in high yield. This lactone could serve as a versatile intermediate for library construction in medicinal chemistry (see below). Notably, the remaining  $\alpha$ -methyl group from the above cases could then undergo further C–H functionalizations to afford greater structural diversity. Tertiary aliphatic acids containing a single  $\alpha$ -methyl group (**2w** to **2ab**) consistently afforded useful yields, in addition to those substrates containing  $\alpha$ -hydrogens (**2ac** to **2ag**).

To demonstrate the scalability and practicality of this transformation, we conducted a gram-scale  $\beta$ -lactonization of Gemfibrozil (**1v**) with 1 mol% Pd (Fig. 3). Pure product was obtained by a simple aqueous wash without chromatography. 1.0 g gemfibrozil (**1v**) in HFIP, Pd(OAc)<sub>2</sub> (1.0 mol%), commercially available MPAA ligand **L6** (2.0 mol%) and NaOAc (1.0 equiv.) were added to a reaction tube, followed by TBHP (70% in water) (2.0 equiv.). After stirring at 60 °C for 24 h, the HFIP solvent was removed by evaporation, followed by dissolution with ethyl acetate and washing with saturated  $NaHCO_3$  solution to remove



unreacted acid, ligand and metal complex. Evaporation of solvent delivered the lactone product **2v** in 92% yield. From a practical standpoint, this reaction has several key advantages over other C–H activation protocols: (1) the inexpensive oxidant TBHP (US\$5 per mole); (2) it tolerates air and moisture; (3) it can be reliably scaled up; (4) the aqueous wash delivers the product without chromatography.

As depicted in Fig. 3, the  $\beta$ -lactone product **2v** is a stepping stone for mono-selective installation of a range of alkyl, alkenyl, aryl, alkynyl, cyano, halogen, amino, hydroxyl and thiophenyl groups<sup>28–30</sup>. Various alkyl (**3a** to **3e**), alkenyl (**3f** to **3g**) and aryl (**3h** to **3j**) Grignard reagents in the presence of catalytic copper were able to successfully open the  $\beta$ -lactone to build new C–C bonds at the  $\beta$  position of the parent aliphatic acids<sup>28,29</sup>. In particular, secondary alkyl structure motifs, such as isopropyl (**3c**), cyclopropyl (**3d**) and cyclopentyl (**3e**), could be efficiently installed; by contrast, the analogous secondary alkyl iodides are usually incompatible in Pd-catalysed C–H alkylation reactions.  $\beta$ -Vinyl aliphatic acids (**3f** to **3g**) were directly accessible through reaction with their corresponding vinyl (**3f**) and isopropenyl (**3g**) Grignard reagents, which provided a strategy complementary to the Pd-catalysed  $\beta$ -C–H olefination of free acids and their derivatives, where only electron-deficient olefins were effective.  $\beta$ -Lactone **2v** may also be expediently elaborated into the corresponding  $\beta$ -arylated aliphatic acids (**3h** to **3j**); this approach is particularly crucial in the case of **3i** and **3j**, because the corresponding iodides are often not viable coupling partners. The use of Grignard reagents prepared from readily available aryl bromides or chlorides also provides a practical advantage. Additionally,  $\beta$ -phenylacetylene aliphatic acids **3k** could be successfully synthesized from  $\beta$ -lactone **2v** on treatment with alkynyl aluminium reagent. Cyanide could also open the lactone to construct a new C–C bond, affording the corresponding  $\beta$ -cyano aliphatic acids **3l**. The electrophilicity of the  $\beta$ -lactone carbonyl was further exploited by the addition of the weak fluoride nucleophile (**3m**) to introduce a  $\text{CH}_2\text{F}$  fragment, a highly sought-after bioisostere in medicinal chemistry. By a similar  $\beta$ -lactone opening,  $\text{MgBr}_2$  delivered the formally  $\beta$ -brominated aliphatic acid **3n** in high yield, a versatile linchpin for further elaboration. Further manipulations of the  $\beta$ -lactone in the presence of the hard nucleophiles  $\text{NaN}_3$  or  $\text{NaNHNs}$  afforded coveted  $\beta$ -amino acid scaffolds (**3o** to **3p**) in consistently high yields. By making use of the  $\beta$ -lactone as a masked aldol adduct, mild hydrolysis afforded the  $\beta$ -hydroxyl acid **3q** in high yield. Finally, the formal  $\beta$ -chalcogenation product **3r** was obtained in near quantitative yield using thiophenol sodium salt as a nucleophile.

## Online content

Any methods, additional references, Nature Research reporting summaries, source data, extended data, supplementary information, acknowledgements, peer review information; details of author contributions and competing interests; and statements of data and code availability are available at <https://doi.org/10.1038/s41586-019-1859-y>.

1. Daugulis, O., Roane, J. & Tran, L. D. Bidentate, monoanionic auxiliary-directed functionalization of carbon–hydrogen bonds. *Acc. Chem. Res.* **48**, 1053–1064 (2015).
2. Lyons, T. W. & Sanford, M. S. Palladium-catalyzed ligand-directed C–H functionalization reactions. *Chem. Rev.* **110**, 1147–1169 (2010).
3. He, J., Wasa, M., Chan, K. S. L., Shao, Q. & Yu, J.-Q. Palladium-catalyzed transformations of alkyl C–H bonds. *Chem. Rev.* **117**, 8754–8786 (2017).

4. Giri, R., Guo Foxman, C. B. M. & Yu, J.-Q. et al. Pd-catalyzed stereoselective oxidation of methyl groups by inexpensive oxidants under mild conditions: a dual role for carboxylic anhydrides in catalytic C–H bond oxidation. *Angew. Chem. Int. Ed.* **44**, 7420–7424 (2005).
5. Giri, R. et al. Palladium-catalyzed methylation and arylation of  $\text{sp}^2$  and  $\text{sp}^3$  C–H bonds in simple carboxylic acids. *J. Am. Chem. Soc.* **129**, 3510–3511 (2007).
6. Wang, D.-H., Wasa, M., Giri, R. & Yu, J.-Q. Pd(II)-catalyzed cross-coupling of  $\text{sp}^3$  C–H bonds with  $\text{sp}^2$  and  $\text{sp}^3$  boronic acids using air as the oxidant. *J. Am. Chem. Soc.* **130**, 7190–7191 (2008).
7. Shabashov, D. & Daugulis, O. Auxiliary-assisted palladium-catalyzed arylation and alkylation of  $\text{sp}^2$  and  $\text{sp}^3$  carbon–hydrogen bonds. *J. Am. Chem. Soc.* **132**, 3965–3972 (2010).
8. Zhang, S.-Y., Li, Q., He, G., Nack, W. A. & Chen, G. Stereoselective synthesis of  $\beta$ -alkylated  $\alpha$ -amino acids via palladium-catalyzed alkylation of unactivated methylene  $\text{C}(\text{sp}^3)$ –H bonds with primary alkyl halides. *J. Am. Chem. Soc.* **135**, 12135–12141 (2013).
9. Zhuang, Z. et al. Ligand-enabled  $\beta$ -C( $\text{sp}^3$ )–H olefination of free carboxylic acids. *J. Am. Chem. Soc.* **140**, 10363–10367 (2018).
10. Wasa, M., Engle, K. M. & Yu, J.-Q. Pd(II)-catalyzed olefination of  $\text{sp}^3$  C–H bonds. *J. Am. Chem. Soc.* **132**, 3680–3681 (2010).
11. Ano, Y., Tobisu, M. & Chatani, N. Palladium-catalyzed direct ethynylation of  $\text{C}(\text{sp}^3)$ –H bonds in aliphatic carboxylic acid derivatives. *J. Am. Chem. Soc.* **133**, 12984–12986 (2011).
12. Zaitsev, V. G., Shabashov, D. & Daugulis, O. Highly regioselective arylation of  $\text{sp}^3$  C–H bonds catalyzed by palladium acetate. *J. Am. Chem. Soc.* **127**, 13154–13155 (2005).
13. Shen, P.-X., Hu, L., Shao, Q., Hong, K. & Yu, J.-Q. Pd(II)-catalyzed enantioselective  $\text{C}(\text{sp}^3)$ –H arylation of free carboxylic acids. *J. Am. Chem. Soc.* **140**, 6545–6549 (2018).
14. Wang, Y., Tennyson, R. L. & Romo, D.  $\beta$ -Lactones as intermediates for natural product total synthesis and new transformations. *Heterocycles* **64**, 605–658 (2004).
15. Robinson, S. L., Christenson, J. K. & Wackett, L. P. Biosynthesis and chemical diversity of  $\beta$ -lactone natural products. *Nat. Prod. Rep.* **36**, 458–475 (2019).
16. Quasdorf, K. W. & Overman, L. E. Catalytic enantioselective synthesis of quaternary carbon stereocentres. *Nature* **516**, 181–191 (2014).
17. Kao, L.-C. & Sen, A. Platinum(II) catalysed selective remote oxidation of unactivated C–H bonds in aliphatic carboxylic acids. *J. Chem. Soc. Chem. Commun.* 1242–1243 (1991).
18. Dangel, B. D., Johnson, J. A. & Sames, D. Selective functionalization of amino acids in water: a synthetic method via catalytic C–H bond activation. *J. Am. Chem. Soc.* **123**, 8149–8150 (2001).
19. Lee, J. M. & Chang, S. Pt-catalyzed  $\text{sp}^3$  C–H bond activation of  $\alpha$ -alkyl substituted aromatic carboxylic acid derivatives for the formation of aryl lactones. *Tetrahedr. Lett.* **47**, 1375–1379 (2006).
20. Novák, P., Correa, A., Gallardo-Donaire, J. & Martin, R. Synergistic palladium-catalyzed  $\text{C}(\text{sp}^3)$ –H activation/ $\text{C}(\text{sp}^3)$ –O bond formation: a direct, step-economical route to benzolactones. *Angew. Chem. Int. Ed.* **50**, 12236–12239 (2011).
21. Mei, T.-S., Wang, X. & Yu, J.-Q. Pd(II)-catalyzed amination of C–H bonds using single-electron or two-electron oxidants. *J. Am. Chem. Soc.* **131**, 10806–10807 (2009).
22. Engle, K. M., Mei, T.-S., Wang, X. & Yu, J.-Q. Bystanding  $\text{F}^\bullet$  oxidants enable selective reductive elimination from high-valent metal centers in catalysis. *Angew. Chem. Int. Ed.* **50**, 1478–1491 (2011).
23. Zhang, Q. et al. Stereoselective synthesis of chiral  $\alpha$ -amino- $\beta$ -lactams through palladium(II)-catalyzed sequential monoarylation/amidation of  $\text{C}(\text{sp}^3)$ –H bonds. *Angew. Chem. Int. Ed.* **52**, 13588–13592 (2013).
24. McNally, A., Haffemayer, B., Collins, B. S. L. & Gaunt, M. J. Palladium-catalysed C–H activation of aliphatic amines to give strained nitrogen heterocycles. *Nature* **510**, 129–133 (2014); corrigendum **512**, 338 (2014).
25. Canty, A. J., Jin, H., Skelton, B. W. & White, A. H. Oxidation of complexes by  $(\text{O}_2\text{CPh})_2$  and  $(\text{ER})_2$  ( $\text{E} = \text{S}, \text{Se}$ ), including structures of  $\text{Pd}(\text{CH}_2\text{CH}_2\text{CH}_2\text{CH}_2)(\text{SePh})_2(\text{bpy})$  ( $\text{bpy} = 2,2'$ -bipyridine) and  $\text{MMe}_2(\text{SePh})_2(\text{L}_2)$  ( $\text{M} = \text{Pd}, \text{Pt}$ ;  $\text{L}_2 = \text{bpy}, 1,10$ -phenanthroline) and  $\text{C}\cdots\text{O}$  and  $\text{C}\cdots\text{E}$  bond formation at palladium(IV). *Inorg. Chem.* **37**, 3975–3981 (1998).
26. Wang, D.-H., Engle, K. M., Shi, B.-F. & Yu, J.-Q. Ligand-enabled reactivity and selectivity in a synthetically versatile aryl C–H olefination. *Science* **327**, 315–319 (2010).
27. Todd, P. A. & Ward, A. Gemfibrozil – a review of its pharmacodynamic and pharmacokinetic properties, and therapeutic use in dyslipidaemia. *Drugs* **36**, 314–339 (1988).
28. Sato, T., Kawara, T., Kawashima, M. & Fujisawa, T. Copper-catalyzed reaction of Grignard reagents with  $\beta$ -propiolactones: a convenient method for the synthesis of  $\beta$ -substituted propionic acids. *Chem. Lett.* **9**, 571–574 (1980).
29. Smith, N. D., Wohlrab, A. M. & Goodman, M. Enantiocontrolled synthesis of  $\alpha$ -methyl amino acids via  $\text{Br}_2/\text{N}$ - $\alpha$ -methylserine- $\beta$ -lactone. *Org. Lett.* **7**, 255–258 (2005).
30. Arnold, L. D., Kalantar, T. H. & Vederas, J. C. Conversion of serine to stereochemically pure  $\beta$ -substituted  $\alpha$ -amino acids via  $\beta$ -lactones. *J. Am. Chem. Soc.* **107**, 7105–7109 (1985).

**Publisher's note** Springer Nature remains neutral with regard to jurisdictional claims in published maps and institutional affiliations.

© The Author(s), under exclusive licence to Springer Nature Limited 2019

# Article

## Methods

### General procedure for $\beta$ -C( $sp^3$ )-H lactonization

$\text{Pd}(\text{CH}_3\text{CN})_2\text{Cl}_2$  (10 mol%, 2.6 mg), ligand **L11** (20 mol%, 2.9 mg),  $\text{CsHCO}_3$  (0.5 equiv., 9.7 mg) and carboxylic acid **1** (0.1 mmol), in that order, were weighed in air and placed in a culture tube with a magnetic stir bar. Then HFIP (1.0 mL) and TBHP (about 5.5 M in decane) (2.0 equiv., 36  $\mu\text{L}$ ) were added. The reaction mixture was stirred at room temperature for 3 min and then heated to 60 °C for 12 h (600 rpm). After cooling to room temperature, the mixture was concentrated in vacuo, and the resulting mixture was purified by preparative thin-layer chromatography or diluted with ethyl acetate and washed with saturated  $\text{NaHCO}_3$  solution. The full experimental details and characterization of the new compounds can be found in Supplementary Information.

### Data availability

The data supporting the findings of this study are available within the article and its Supplementary Information files.

**Acknowledgements** We acknowledge The Scripps Research Institute and the NIH (NIGMS, R01GM084019) for financial support.

**Author contributions** J.-Q.Y. conceived the concept. Z.Z. developed the lactonization reaction. J.-Q.Y. directed the project.

**Competing interests** The authors declare no competing interests.

### Additional information

**Supplementary information** is available for this paper at <https://doi.org/10.1038/s41586-019-1859-y>.

**Correspondence and requests for materials** should be addressed to J.-Q.Y.

**Peer review information** *Nature* thanks Michael Doyle and the other, anonymous, reviewer(s) for their contribution to the peer review of this work.

**Reprints and permissions information** is available at <http://www.nature.com/reprints>.

# Oceanic forcing of penultimate deglacial and last interglacial sea-level rise

<https://doi.org/10.1038/s41586-020-1931-7>

Received: 28 December 2018

Accepted: 9 November 2019

Published online: 29 January 2020

Peter U. Clark<sup>1,2,11\*</sup>, Feng He<sup>3,11</sup>, Nicholas R. Golledge<sup>4,5</sup>, Jerry X. Mitrovica<sup>6</sup>, Andrea Dutton<sup>7,10</sup>, Jeremy S. Hoffman<sup>8</sup> & Sarah Dendy<sup>9</sup>

Sea-level histories during the two most recent deglacial–interglacial intervals show substantial differences<sup>1–3</sup> despite both periods undergoing similar changes in global mean temperature<sup>4,5</sup> and forcing from greenhouse gases<sup>6</sup>. Although the last interglaciation (LIG) experienced stronger boreal summer insolation forcing than the present interglaciation<sup>7</sup>, understanding why LIG global mean sea level may have been six to nine metres higher than today has proven particularly challenging<sup>2</sup>. Extensive areas of polar ice sheets were grounded below sea level during both glacial and interglacial periods, with grounding lines and fringing ice shelves extending onto continental shelves<sup>8</sup>. This suggests that oceanic forcing by subsurface warming may also have contributed to ice-sheet loss<sup>9–12</sup> analogous to ongoing changes in the Antarctic<sup>13,14</sup> and Greenland<sup>15</sup> ice sheets. Such forcing would have been especially effective during glacial periods, when the Atlantic Meridional Overturning Circulation (AMOC) experienced large variations on millennial timescales<sup>16</sup>, with a reduction of the AMOC causing subsurface warming throughout much of the Atlantic basin<sup>9,12,17</sup>. Here we show that greater subsurface warming induced by the longer period of reduced AMOC during the penultimate deglaciation can explain the more-rapid sea-level rise compared with the last deglaciation. This greater forcing also contributed to excess loss from the Greenland and Antarctic ice sheets during the LIG, causing global mean sea level to rise at least four metres above modern levels. When accounting for the combined influences of penultimate and LIG deglaciation on glacial isostatic adjustment, this excess loss of polar ice during the LIG can explain much of the relative sea level recorded by fossil coral reefs and speleothems at intermediate- and far-field sites.

The evolution of the climate over the last two terminations (T-II, about 136–129 ka; T-I, about 19–11.7 ka) shares a number of similarities (Extended Data Fig. 1). Proxy records of ocean circulation show that the last two terminations were accompanied by large reductions in the Atlantic Meridional Overturning Circulation (AMOC). Climate responses to these reductions show the characteristic bipolar see-saw due to reduced northerly ocean heat transport and the weakening of the Asian monsoon due to the cooling of the Northern Hemisphere. Other similarities include an increase in the rate of sea-level rise when the AMOC begins to decrease and the occurrence of a Heinrich event during the period of reduced AMOC. Similar climate changes accompanied earlier terminations over the last 640 kyr (ref. <sup>18</sup>), suggesting that a reduced AMOC is a characteristic feature of these periods of rapid deglaciation.

There are also several notable differences between the last two terminations (Extended Data Figs. 1 and 2). First, proxy data suggest that the AMOC during T-II remained in a reduced state for ~7 kyr before

recovering at the start of the LIG. By contrast, during T-I, the AMOC remained weak only for ~3.5 kyr before recovering to nearly full strength during the 1.5-kyr Bølling–Allerød warm interval. It then decreased again during the 1.2-kyr Younger Dryas cold interval, with its final recovery at the start of the present interglaciation. Second, sea level rose ~130 m during the 7-kyr sustained ‘one-step’ T-II period of reduced AMOC, whereas it rose only ~70 m during the ~6.5-kyr ‘two-step’ T-I period of reduced AMOC<sup>3</sup>, with the remaining ~60 m occurring after the start of the present interglaciation, 11.7 ka (Fig. 1). Third, ice-rafted debris (IRD) suggests that Heinrich event 11 (H11), which is nearly twice as long as Heinrich event 1 (H1), was sourced from more than just the Hudson Strait Ice Stream, which was the primary source for H1<sup>19</sup>.

A transient simulation of T-I climate used an atmosphere–ocean general circulation model (the National Center for Atmospheric Research Community Climate System Model version 3; NCAR CCSM3) forced by changes in insolation, CO<sub>2</sub>, ice sheets and freshwater (FW) fluxes that, while not in full agreement with reconstructions, were designed

<sup>1</sup>College of Earth, Ocean, and Atmospheric Sciences, Oregon State University, Corvallis, OR, USA. <sup>2</sup>School of Geography and Environmental Sciences, University of Ulster, Coleraine, UK.

<sup>3</sup>Center for Climatic Research, Nelson Institute for Environmental Studies, University of Wisconsin–Madison, Madison, WI, USA. <sup>4</sup>Antarctic Research Centre, Victoria University of Wellington, Wellington, New Zealand. <sup>5</sup>GNS Science, Lower Hutt, New Zealand. <sup>6</sup>Department of Earth and Planetary Sciences, Harvard University, Cambridge, MA, USA. <sup>7</sup>Department of Geological Sciences, University of Florida, Gainesville, FL, USA. <sup>8</sup>Science Museum of Virginia, Richmond, VA, USA. <sup>9</sup>Department of Geology, University of Illinois, Urbana-Champaign, IL, USA. <sup>10</sup>Present address: Department of Geoscience, University of Wisconsin, Madison, WI, USA. <sup>11</sup>These authors contributed equally: Peter U. Clark, Feng He. \*e-mail: [clarkp@onid.orst.edu](mailto:clarkp@onid.orst.edu)

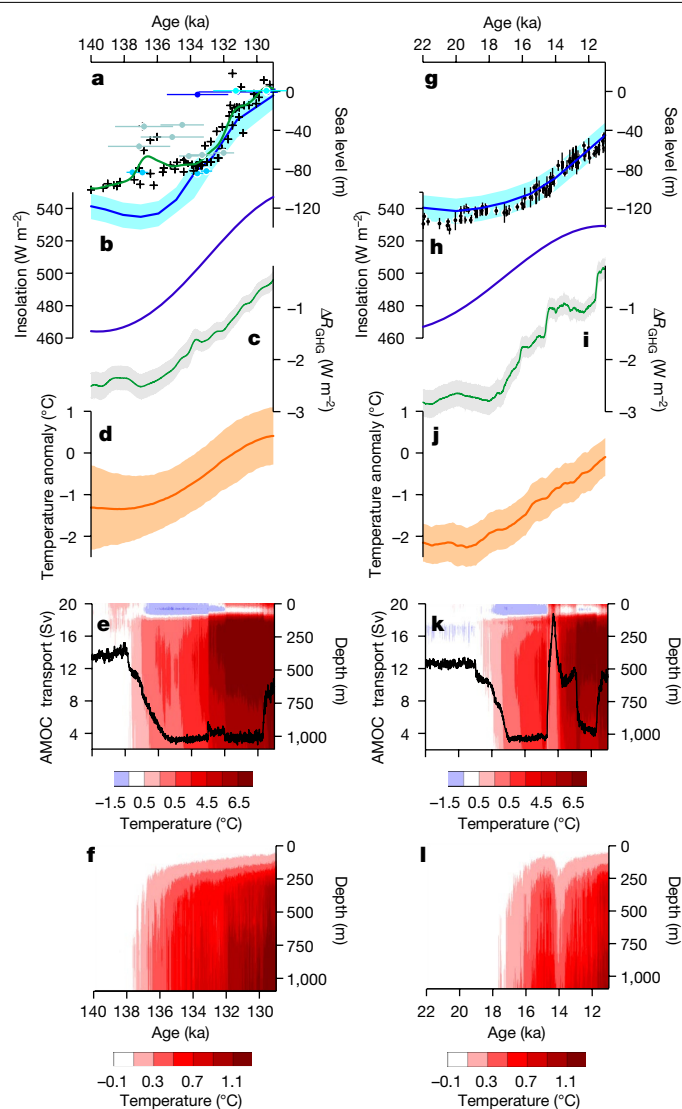


**Fig. 1 | Sea-level change and climate forcings during the penultimate (left) and last (right) deglaciations.** **a, g**, Eustatic sea-level record based on benthic foraminifera isotopic records (blue line with  $1\sigma$  uncertainty) (**a**) and in a compilation of sea-level proxies shown by black dots with depth-range uncertainties (**g**) (see Methods, Extended Data Figure 2). Also shown are RSL records based on Red Sea isotopes (grey crosses) placed on a revised age model, and U-series-dated corals in Tahiti (sky blue circles), Huon Peninsula (light blue–green circles) and western Australia (blue circles) (Methods, Extended Data Figure 2). All of the U-series ages have been recalculated and normalized with the same set of decay constants for  $^{234}\text{U}$  and  $^{230}\text{Th}$ . Error bars show  $2\sigma$  age uncertainty. **b, h**, Insolation on 21 June for  $65^\circ\text{N}$  (data from ref. <sup>7</sup>). **c, i**, Change in radiative forcing ( $R$ ) from GHGs ( $\text{CO}_2$ ,  $\text{CH}_4$ , and  $\text{N}_2\text{O}$ )<sup>6</sup>. The uncertainty (shaded envelope) is the square root of the sum of squares of the uncertainties of the individual GHGs. **d, j**, Tropical ( $23.5^\circ\text{N}$ – $23.5^\circ\text{S}$ ) mean annual SST anomalies with 2 s.d. (shaded envelope) relative to the HadISST1.1 1870–1889 data<sup>4,5</sup>. **e, k**, Changes in the model maximum AMOC transport (below 500 m; black line) and temperature (colour scale) as a function of time and depth at  $45^\circ\text{N}$ ,  $30^\circ\text{W}$  relative to 140 ka (**e**) and 22 ka (**k**)<sup>17</sup> as simulated by NCAR CCSM3 (Methods). **f, l**, Evolution of temperature (colour scale) as a function of time and depth at  $70^\circ\text{S}$ ,  $45^\circ\text{W}$  relative to 140 ka (**f**) and 22 ka (**l**)<sup>17</sup> as simulated by NCAR CCSM3 (Methods).

to cause the two-step reduction of the AMOC<sup>17</sup> (Fig. 1k). The simulation successfully captured many aspects of the climate evolution through T-I as recorded by proxy records<sup>17,20,21</sup>. Subsurface warming throughout much of the Atlantic basin was one of the responses to a reduced AMOC<sup>17</sup> (Fig. 1k, l), supported by proxy temperature records

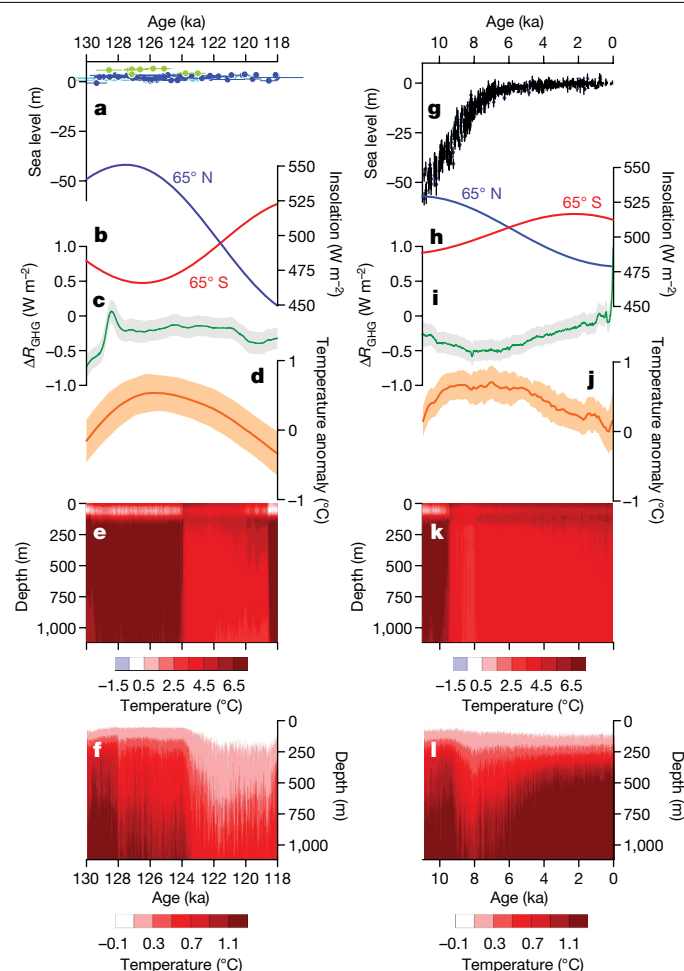


**Fig. 2 | Sea-level change and climate forcings during the last and present interglaciations.** **a, g**, Records of relative and global mean sea level (Methods, Extended Data Fig. 2). The uncertainty (bars) on the coral data (circles) is  $2\sigma$ . **b, h**, Insolation on 21 June for  $65^\circ\text{N}$  (data from ref. <sup>7</sup>). **c, i**, Radiative forcing from GHGs<sup>6</sup>. The uncertainty is the square root of the sum of squares of the uncertainties of the individual GHGs. **d, j**, Global mean annual SST anomalies with 2 s.d. relative to the HadISST1.1 1870–1889 data<sup>4,5</sup>. **e, k**, Evolution of temperature as a function of time and depth at  $45^\circ\text{N}$ ,  $30^\circ\text{W}$  relative to 140 ka (**e**) and 22 ka (**k**)<sup>17</sup> as simulated by NCAR CCSM3 (Methods). **f, l**, Evolution of temperature as a function of time and depth at  $70^\circ\text{S}$ ,  $45^\circ\text{W}$  relative to 140 ka (**f**) and 22 ka (**l**)<sup>17</sup> as simulated by NCAR CCSM3 (Methods).

from intermediate-depth (1,000–1,500 m) North Atlantic core sites<sup>12</sup>.

We used the same climate model to conduct a transient simulation that spans T-II and the LIG (140–115 ka) (Methods). We applied a FW forcing consistent with reconstructions that reproduced the 7-kyr one-step reduction in the AMOC suggested by proxy records of ocean circulation (Extended Data Figs. 1 and 3) to quantify the associated changes in subsurface temperatures during T-II and into the LIG and thus allow a direct comparison with the subsurface warming simulated for T-I.

Figure 1 compares forcing of ice-sheet surface mass balance from insolation, greenhouse gases (GHGs) and low-latitude Pacific sea surface temperatures (SSTs) for T-II and T-I to representative examples of the simulated oceanic forcing at sites in the North ( $45^\circ\text{N}$ ,  $30^\circ\text{W}$ ) (Fig. 1e, k) and South Atlantic ( $70^\circ\text{S}$ ,  $45^\circ\text{W}$ ) (Fig. 1f, l). Changes in GHG concentrations and SSTs are similar during the two terminations, with increases of  $-2\text{ W m}^{-2}$  from GHGs and  $-2^\circ\text{C}$  of warming from low-latitude Pacific SSTs, which strongly influence Northern Hemisphere ice-sheet surface mass balance<sup>10</sup>. Despite these similarities, sea level reached modern levels by the end of T-II, while it remained  $\sim 50\%$  below modern levels at



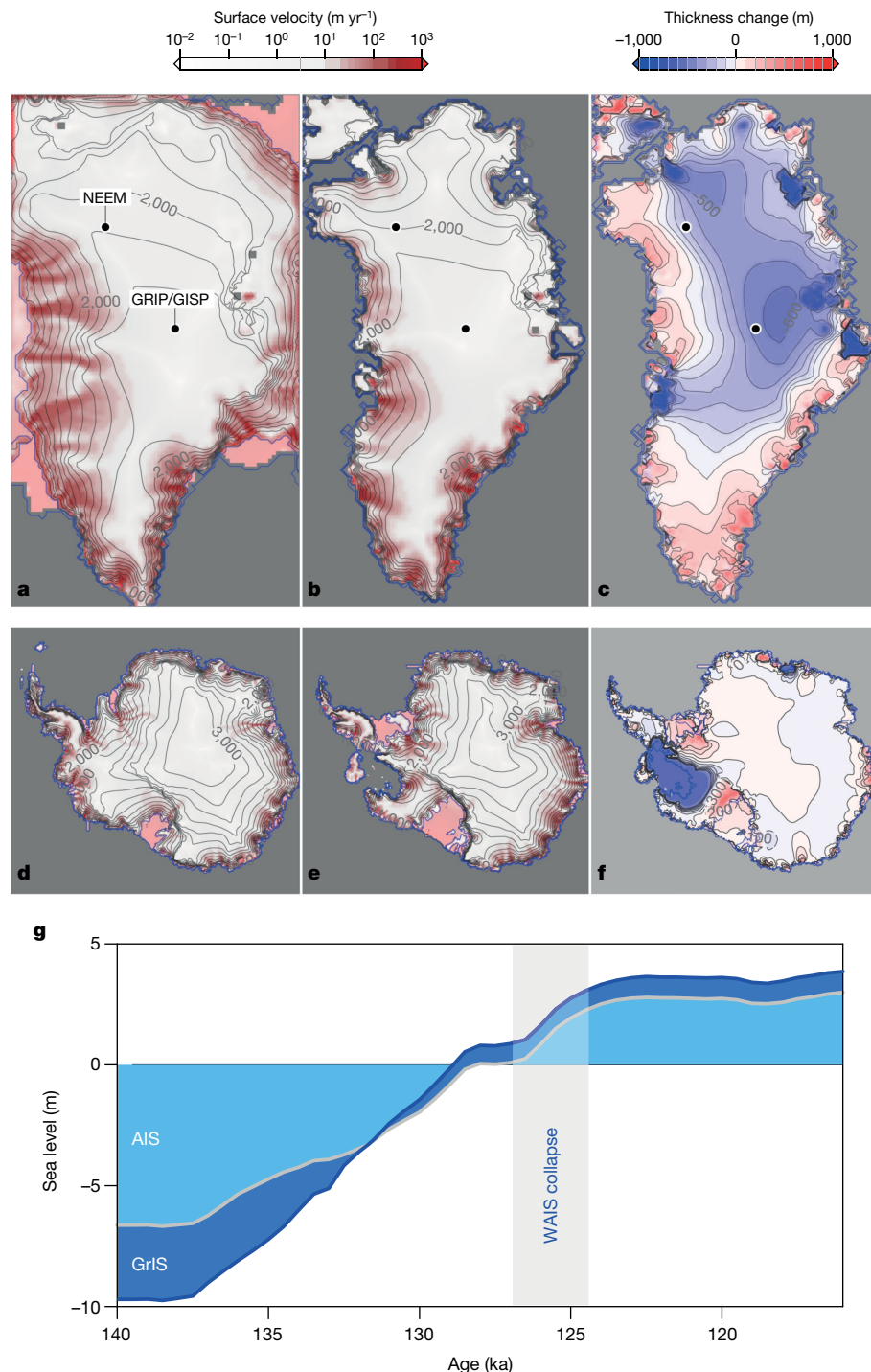


**Fig. 3 | Simulations of the Greenland and Antarctic ice sheets.** **a**, The Greenland Ice Sheet at the PGM. Shown are the Greenland ice-core sites North Greenland Eemian Ice Drilling (NEEM), Greenland Ice Core Project (GRIP) and Greenland Ice Sheet Project (GISP). **b**, The Greenland Ice Sheet at 116 ka. The logarithmic colour scale shows the velocity fields and contours on the ice sheet indicate the surface elevation (m). **c**, Change in the thickness of the Greenland Ice Sheet between 116 ka and the present day. Contours on the ice surface and the colour scale show the thickness change. **d**, The Antarctic Ice Sheet at the

PGM. **e**, The Antarctic Ice Sheet at 116 ka. The logarithmic colour scale shows the velocity fields and contours on the ice sheet indicate the surface elevation (m). **f**, Change in the thickness of the Antarctic Ice Sheet between 116 ka and the present day. Contours on the ice surface and the colour scale show the thickness change. **g**, Contributions of the Greenland Ice Sheet (GrIS) and Antarctic Ice Sheet (AIS) to global mean sea level between 140 ka and 116 ka. WAIS, West Antarctic Ice Sheet.

the end of T-I (Fig. 1a, g). Some have attributed the faster rate of sea-level rise during T-II to the greater boreal summer insolation forcing<sup>3</sup>, but that forcing only exceeds that of T-I after the majority (~80 m) of T-II sea-level rise had occurred (Fig. 1a, b, Extended Data Fig. 2). Otherwise, insolation forcing during the first 8 kyr of each termination is similar

(~55 W m<sup>-2</sup>), whereas the associated 80 m of sea-level rise during T-II is much greater than that during T-I (~35 m).

Given the similar radiative forcing and temperature changes during the last two terminations, we attribute this contrast in sea-level response to the greater subsurface warming during T-II associated with

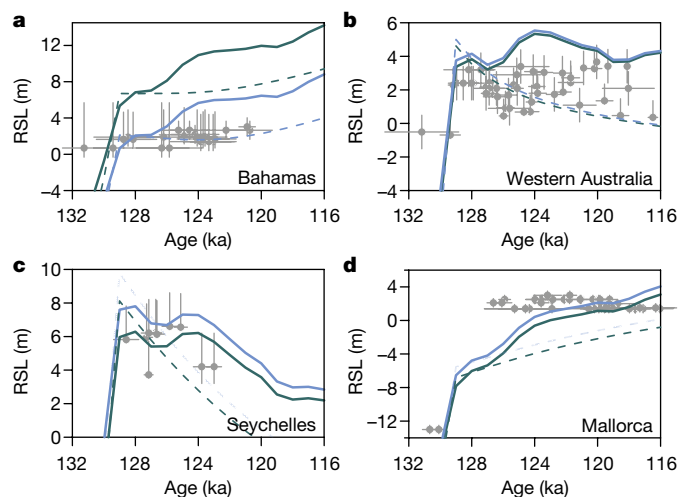


**Fig. 4 | Predictions of RSL at four far-field sites. a**, RSL data from the Bahamas based on well-dated corals compared with predicted RSL from our simulated LIG loss from the Greenland and Antarctic ice sheets and the LAM ice history<sup>22</sup> (solid green line) and the HYB ice history (solid blue line) (see Methods). Also shown are predictions of RSL using just the LAM ice history<sup>22</sup> (dashed green line) and the HYB ice history (dashed blue line). **b, c**, As in **a**, for Western Australia (**b**) and the Seychelles (**c**). Horizontal error bars are for age ( $2\sigma$ ), vertical error bars are for elevation (in metres; below data points) and coral-depth habitat (in metres, above data points). **d**, RSL data from Mallorca based on speleothem records. Horizontal error bars are for age ( $2\sigma$ ) and vertical error bars for the growth range of the speleothem. The Earth models used in the calculations are characterized by a lithospheric thickness and upper and lower mantle viscosity of: 140 km,  $0.3 \times 10^{21}$  Pa s,  $8.0 \times 10^{22}$  Pa s (**a**), 96 km,  $0.3 \times 10^{21}$  Pa s,  $5.0 \times 10^{22}$  Pa s (**b**), 30 km,  $0.5 \times 10^{21}$  Pa s,  $3.0 \times 10^{22}$  Pa s (**c**) and 120 km,  $2.0 \times 10^{21}$  Pa s,  $8.0 \times 10^{22}$  Pa s (**d**). Each of the coral records comprise data collected from multiple sites and the RSL predictions are shown for the following representative locations: 24.05° N, 285.47° E (**a**), 21.97° S, 113.93° E (**b**), 4.28° S, 55.73° E (**c**) and 39.61° N, 3.38° E (**d**). The consistency between the data and the predictions would be unaffected if we plotted RSL histories at each location that accounted for the spatial distances between individual sample collection sites.

the one-step reduction in the AMOC than the T-I two-step reduction, leading to greater oceanic forcing of marine ice-sheet margins in the North (Fig. 1e, k, Extended Data Fig. 4) and South (Fig. 1f, l, Extended Data Fig. 4) Atlantic. The Eurasian Ice Sheet during the Penultimate Glacial Maximum (PGM, -140 ka) was also larger than during the Last Glacial Maximum (LGM, -21 ka), with most of the excess mass located in low-lying areas south-southeast of the glaciated Barents and Kara seas<sup>22</sup> that was also marine-based owing to isostatic depression (Extended Data Fig. 5). We thus hypothesize that collapse of this large marine-based ice complex triggered by oceanic forcing would also have contributed to the rapid T-II sea-level rise, with the associated IRD contribution to H11 diluting the contribution from the Hudson Strait Ice Stream<sup>19</sup>. This greater FW flux from deglaciating Northern Hemisphere ice sheets during T-II provided an important positive feedback on that deglaciation through its influence on the AMOC and subsurface temperatures.

Figure 2 compares forcings during the last two interglaciations. Peak global mean SSTs were similar (Fig. 2d, j) whereas LIG radiative forcing from  $\text{CO}_2$  was only slightly higher ( $-0.25 \text{ W m}^{-2}$ ) than during the present interglaciation (Fig. 2c, i). The main difference is in the higher boreal and lower austral summer insolation forcing during the LIG (Fig. 2b, h). Modelling studies show that this forcing would cause excess mass loss from the Greenland Ice Sheet during the LIG, but the estimated 1–3 m increase in global mean sea-level equivalent (GMSLE) is too small to explain the LIG highstand, thus requiring a contribution from the Antarctic Ice Sheet<sup>2</sup>. However, lower austral summer insolation forcing during the LIG (Fig. 2b) results in surface cooling over most of Antarctica. This

suggests that oceanic forcing plays an important role, with warming hypothesized to originate from an AMOC reduction during the LIG<sup>11</sup> or from a lagged ice-sheet response to warming from a change in the strength and/or position of the Southern Ocean westerlies associated with the T-II AMOC reduction<sup>3</sup>. One ice-sheet model simulates up to 6.7 m of sea-level rise when specifying a uniform increase in Southern Ocean temperatures of  $3^\circ \text{C}$  (ref. <sup>11</sup>).

Our transient climate simulation shows that T-II oceanic forcing in the Southern Ocean, as well as the North Atlantic, continued into the early LIG (Fig. 2e, f, Extended Data Fig. 4). We use the Parallel Ice Sheet Model (PISM) to assess the response of the Antarctic and Greenland ice sheets to this oceanic and surface forcing through T-II and into the LIG as simulated by our transient climate run (Methods). The Greenland Ice Sheet starts to deglaciate from its PGM extent when adjacent ocean temperatures begin to warm at -137.5 ka (Figs. 1e, 3g). It reaches its present extent at 131.5 ka and then loses an additional 0.88 m GMSLE by 119.5 ka, largely through oceanic forcing of those sectors of the ice sheet that remain marine-based, causing draw-down of the ice-sheet interior (Fig. 3c). The majority (3.42 m) of the total sea-level rise (3.88 m) occurs between 136–129 ka (Fig. 3g), corresponding to the period of rapid rise in global mean sea level (GMSL) (Fig. 1a). Sensitivity tests in which ocean temperatures are held constant at either PGM or LIG values show that the simulated deglaciation is controlled entirely by oceanic forcing (Methods, Extended Data Fig. 6), supporting our hypothesis that oceanic forcing contributed to deglaciation of other Northern Hemisphere ice sheets (Extended Data Fig. 4).

Our simulations also show that the major deglacial phase of the Antarctic Ice Sheet from its PGM extent closely coincides with the onset of warming of adjacent ocean temperatures at -137.5 ka induced by the slowdown in AMOC (Figs. 1f and 3g). In particular, the ice sheet retreats to its present extent at -128 ka, with the majority (6.25 m) of the total (6.65 m) sea-level rise occurring during the rapid T-II rise in global sea level (Fig. 3g). Sea-level rise then begins to slow at 128 ka, followed by an acceleration starting at 126.5 ka; a total of 2.99 m of LIG sea-level rise occurred by 116 ka (Fig. 3g). The majority of this LIG deglaciation is associated with collapse of the Amundsen Sea sector of the West Antarctic Ice Sheet (Fig. 3e) largely in response to oceanic forcing (Extended Data Fig. 6), similar to what is suggested by observed recent changes and projected for future ice-sheet recession in this area<sup>13,14</sup>. This destabilization leads to ice-sheet retreat that continues after the period of peak oceanic forcing at a rate that is determined largely by the retrograde gradient of the bed beneath the West Antarctic Ice Sheet, followed by a slowing of this retreat as the Southern Ocean cools (Fig. 2f).

We next apply an ice-age sea-level model<sup>23</sup> to predict how our simulated changes in LIG ice-sheet mass would be recorded at three widely distributed sites with well-dated corals that provide minimum estimates of relative sea level (RSL) during the LIG<sup>24,25</sup>, and a speleothem record that bounds RSL during the same period<sup>26</sup> (Methods). Of the five adopted ice histories, the two that are based on studies that use a considerably larger Eurasian Ice Sheet during the PGM relative to the LGM<sup>22,27</sup> (Lambeck (LAM) and Hybrid (HYB); see Methods) predict RSL histories during the LIG that are consistent with the elevation determined from the corals from the Bahamas, Western Australia and the Seychelles (Fig. 4a–c, Extended Data Fig. 7). However, all simulations tend to underestimate the first half (before 122 ka) of the LIG RSL evolution inferred from the speleothem record in Mallorca (Fig. 4d, Extended Data Fig. 7).

In the absence of melting of polar ice during the LIG, predictions of RSL at the Bahamas and Mallorca would show a monotonic rise, while those at the Seychelles and Western Australia would tend to show a monotonic fall (Fig. 4)<sup>28</sup>. Our ice-sheet simulations, however, are characterized by excess melt from the West Antarctic Ice Sheet (relative to the present day) that increases from 0 to 3 m GMSLE between 127 ka and 124 ka (Fig. 3g). This signal is responsible for the accentuated RSL rise over the same period in the prediction for the Bahamas and

Mallorca and the reversal in the RSL trend at Western Australia and the Seychelles (Fig. 4).

Our results do not account for several other processes that may have caused LIG global mean sea level and RSL to have been even higher than modelled here. For example, our atmospheric modelling may underestimate surface melting around the lower-elevation margins of the Greenland Ice Sheet. The greater boreal summer insolation forcing during the LIG relative to the present interglaciation probably caused even greater mass loss from glaciers, which today account for 0.41 m GMSLE. Warmer-than-present LIG temperatures would have caused additional thermosteric sea-level rise<sup>5</sup>. Finally, we note that any additional melt near the start of the LIG would change the preferred Earth models identified in our analysis (Methods). LIG RSL could also be influenced by dynamic topography due to mantle convection, introducing metre-scale displacement on timescales of tens of kiloyears<sup>29</sup>.

In summary, several lines of evidence suggest that the greater oceanic forcing during T-II, as simulated by our climate modelling, contributed to the more-rapid sea-level rise during that period than T-I. First, forcing of ice-sheet surface mass balance was similar during the two terminations, indicating that an additional forcing is required to explain the differences in rates of sea-level rise. Second, our glacio-isostatic adjustment modelling demonstrates that the larger PGM Eurasian ice sheet caused a substantially larger fraction of the ice-sheet bed to be below sea level, and thus more vulnerable to oceanic forcing, than during T-I. Third, our ice-sheet modelling shows that >85% of the volume loss of the PGM Greenland and Antarctic ice sheets to their present sizes occurs in response to oceanic forcing during T-II. Although additional modelling of the deglaciation of the former Northern Hemisphere ice sheets during T-II will be required to further support this hypothesis, our ice-sheet modelling does show that oceanic forcing was the primary driver of excess ice loss from the Greenland and Antarctic ice sheets during the LIG. Our sea-level predictions demonstrate that the modelled 4 m increase in GMSLE from LIG deglaciation of the Greenland and Antarctic ice sheets may explain much of the LIG RSL at intermediate- and far-field sites when GIA from T-II deglaciation is included, although additional melt is required to fully reconcile these data.

## Online content

Any methods, additional references, Nature Research reporting summaries, source data, extended data, supplementary information, acknowledgements, peer review information; details of author contributions and competing interests; and statements of data and code availability are available at <https://doi.org/10.1038/s41586-020-1931-7>.

1. Waelbroeck, C. et al. Sea-level and deep water temperature changes derived from benthic foraminifera isotopic records. *Quat. Sci. Rev.* **21**, 295–305 (2002).
2. Dutton, A. et al. Sea-level rise due to polar ice-sheet mass loss during past warm periods. *Science* **349**, aaa4019 (2015).
3. Marino, G. et al. Bipolar seesaw control on last interglacial sea level. *Nature* **522**, 197–201 (2015); corrigendum **526**, 144 (2015).

4. Marcott, S. A., Shakun, J. D., Clark, P. U. & Mix, A. C. A reconstruction of regional and global temperature for the past 11,300 years. *Science* **339**, 1198–1201 (2013).
5. Hoffman, J. S., Clark, P. U., Parnell, A. C. & He, F. Regional and global sea-surface temperatures during the last interglaciation. *Science* **355**, 276–279 (2017).
6. Köhler, P., Nehrbass-Ahles, C., Schmitt, J., Stocker, T. F. & Fischer, H. A. 156 kyr smoothed history of the atmospheric greenhouse gases CO<sub>2</sub>, CH<sub>4</sub>, and N<sub>2</sub>O and their radiative forcing. *Earth Syst. Sci. Data* **9**, 363–387 (2017).
7. Berger, A. & Loutre, M.-F. Insolation values for the climate of the last 10 million years. *Quat. Sci. Rev.* **10**, 297–317 (1991).
8. Hughes, T., Denton, G. H. & Grosswald, M. G. Was there a late-Würm Arctic Ice Sheet? *Nature* **266**, 596–602 (1977).
9. Shaffer, G., Olsen, S. M. & Bjerrum, C. J. Ocean subsurface warming as a mechanism for coupling Dansgaard-Oeschger climate cycles and ice-rafting events. *Geophys. Res. Lett.* **31**, L24202 (2004).
10. Clark, P. U., Hostetler, S. W., Pisias, N. G., Schmittner, A. & Meisner, K. J. in *Ocean Circulation: Mechanisms and Impacts* Vol. 173 (eds Schmittner, A. et al.) 209–246 (American Geophysical Union, 2007).
11. DeConto, R. M. & Pollard, D. Contribution of Antarctica to past and future sea-level rise. *Nature* **531**, 591–597 (2016).
12. Marcott, S. A. et al. Ice-shelf collapse from subsurface warming as a trigger for Heinrich events. *Proc. Natl Acad. Sci. USA* **108**, 13415–13419 (2011).
13. Joughin, I., Smith, B. E. & Medley, B. Marine ice sheet collapse potentially under way for the Thwaites Glacier basin, West Antarctica. *Science* **344**, 735–738 (2014).
14. Rignot, E., Mouginot, J., Morlighem, M., Seroussi, H. & Scheuchl, B. Widespread, rapid grounding line retreat of Pine Island, Thwaites, Smith, and Kohler glaciers, West Antarctica, from 1992 to 2011. *Geophys. Res. Lett.* **41**, 3502–3509 (2014).
15. Wood, M. et al. Ocean-induced melt triggers glacier retreat in northwest Greenland. *Geophys. Res. Lett.* **45**, 8334–8342 (2018).
16. Böhm, E. et al. Strong and deep Atlantic meridional overturning circulation during the last glacial cycle. *Nature* **517**, 73–76 (2015).
17. Liu, Z. et al. Transient simulation of last deglaciation with a new mechanism for Bolling-Allerød warming. *Science* **325**, 310–314 (2009).
18. Cheng, H. et al. The Asian monsoon over the past 640,000 years and ice age terminations. *Nature* **534**, 640–646 (2016); corrigendum **541**, 122 (2017).
19. Obrochta, S. P. et al. Climate variability and ice-sheet dynamics during the last three glaciations. *Earth Planet. Sci. Lett.* **406**, 198–212 (2014).
20. Shakun, J. D. et al. Global warming preceded by increasing carbon dioxide concentrations during the last deglaciation. *Nature* **484**, 49–54 (2012).
21. He, F. et al. Northern Hemisphere forcing of Southern Hemisphere climate during the last deglaciation. *Nature* **494**, 81–85 (2013).
22. Lambeck, K. et al. Constraints on the Late Saalian to early Middle Weichselian ice sheet of Eurasia from field data and rebound modelling. *Boreas* **35**, 539–575 (2006).
23. Kendall, R. A., Mitrovica, J. X. & Milne, G. A. On post-glacial sea level—II. Numerical formulation and comparative results on spherically symmetric models. *Geophys. J. Int.* **161**, 679–706 (2005).
24. Dutton, A. & Lambeck, K. Ice volume and sea level during the Last Interglacial. *Science* **337**, 216–219 (2012).
25. Dutton, A., Webster, J. M., Zwart, D., Lambeck, K. & Wohlfarth, B. Tropical tales of polar ice: evidence of Last Interglacial polar ice sheet retreat recorded by fossil reefs of the granitic Seychelles islands. *Quat. Sci. Rev.* **107**, 182–196 (2015).
26. Polyak, V. J. et al. A highly resolved record of relative sea level in the western Mediterranean Sea during the Last Interglacial period. *Nat. Geosci.* **11**, 860–864 (2018).
27. Colleoni, F., Wekerle, C., Naslund, J. O., Brandefelt, J. & Masina, S. Constraint on the penultimate glacial maximum Northern Hemisphere ice topography (≈140 kyr BP). *Quat. Sci. Rev.* **137**, 97–112 (2016).
28. Dendy, S., Austermann, J., Creveling, J. R. & Mitrovica, J. X. Sensitivity of Last Interglacial sea-level high stands to ice sheet configuration during Marine Isotope Stage 6. *Quat. Sci. Rev.* **171**, 234–244 (2017).
29. Austermann, J., Mitrovica, J. X., Huybers, P. & Rovere, A. Detection of a dynamic topography signal in last interglacial sea-level records. *Sci. Adv.* **3**, e1700457 (2017).

**Publisher's note** Springer Nature remains neutral with regard to jurisdictional claims in published maps and institutional affiliations.

© The Author(s), under exclusive licence to Springer Nature Limited 2020

## Methods

### Transient climate modelling

We use the fully coupled configuration of CCSM3 with T31 model spectral resolution (approximately  $3.75^\circ$ )<sup>30</sup> for the transient simulation of the penultimate deglaciation and LIG from 140 to 120 ka. CCSM3 was used in the TraCE-21K transient simulation of the past 21 kyr spanning the last deglaciation and the current interglaciation<sup>17,21,31</sup>. The transient simulation of the penultimate deglaciation was initialized with a 600-yr equilibrium simulation of the PGM that branched off the TraCE-21K LGM simulation with an orbital configuration<sup>7</sup> and GHG contribution ( $\text{CO}_2$ ) for 140 kyr (ref. <sup>32</sup>). The transient simulation of the penultimate deglaciation with CCSM3 was integrated from 140 ka to 129 ka with varying atmospheric GHG concentrations<sup>32</sup>, Earth orbital configurations<sup>7</sup> and continental ice sheets based on ICE-5G<sup>33</sup>, but with the timing of the corresponding sea-level rise adjusted to closely follow the Waelbroeck et al.<sup>1</sup> and Grant et al.<sup>34</sup> sea-level reconstructions for the penultimate deglaciation (Extended Data Figs. 2 and 3). We note that our sea-level modelling suggests that the sizes of the PGM Northern Hemisphere ice sheets differed from those in the LGM, and thus our climate modelling does not account for these important difference between the two terminations. Further climate modelling is therefore needed to assess how these differences may have affected both atmospheric circulation over the North Atlantic Ocean and the AMOC.

To simulate the impact of FW forcing from H11 on the AMOC, fresh water is added at the surface of the North Atlantic in the area between  $50^\circ$  and  $70^\circ$  N and ramped to  $0.17 \text{ Sv}$  (sverdrup,  $1 \text{ Sv} = 10^6 \text{ m}^3 \text{ s}^{-1}$ ) from 138 ka to 135.5 ka; it then remains constant until 129.7 ka when it is shut off (Extended Data Fig. 3). The transient simulation of the LIG with CCSM3 was integrated from 129 ka to 116 ka with changing orbits and atmospheric GHG concentrations under present-day ice-sheet configurations. No additional FW fluxes were applied during the transient simulation of the LIG.

### Ice-sheet modelling

We use version 0.7.1 of PISM, in which the dynamical core superposes velocity fields from the shallow shelf and shallow ice approximations across the entire domain. Fast flow ('streaming') of grounded ice is enabled by plastic failure of subglacial sediments, which depends on a prescribed but spatially variable till friction angle that represents sediment strength and its degree of saturation. The till friction angle is based primarily on topography, so that deeper areas have lower friction angles. This mimics the effect of weaker sediments accumulating in deeper basins. The parameterization follows the form,  $\phi_{\text{min}}/\phi_{\text{max}}/\text{elevation min}/\text{elevation max}$ , in which the  $\phi_{\text{min}}$  is the friction angle applied below elevation min,  $\phi_{\text{max}}$  is the friction angle applied above elevation max, and values in between are linearly interpolated. For our Greenland simulations we prescribe values of  $10/30/-300/300$ , and for Antarctica  $6/30/-700/-100$ . These values are based on, but modified from previous work ( $5/40/-700/700$  for Greenland<sup>35</sup>;  $10/30/-1000/200$  for Antarctica<sup>36</sup>), but these values are uncertain. Our values were chosen following exploratory simulations that sought to best capture the broad-scale geometric and dynamic features of the ice sheets.

Sediment strength evolves dynamically depending on the basal ice temperature. Where ice is sufficiently thick to allow basal melting, meltwater weakens the substrate until driving stresses exceed till cohesion. Failure of the substrate that results in acceleration of the overlying ice follows a pseudo-plastic law<sup>37,38</sup>, such that a small increase in stress above the shear strength of the substrate leads to an increasing velocity response. This ultimately thins the ice, which reduces the gravitational driving stress and results in a deceleration of the ice sheet. The cyclic behaviour of ice streams that occurs as a consequence of this mechanism is described in more detail elsewhere<sup>39</sup>. PISM uses a sub-grid grounding line scheme<sup>40</sup> in which the interpolation of sub-ice shelf melt across the grounded to floating transition may

be turned on or off. When turned on, the scheme tends to accelerate ice-sheet retreat in marine basins, whereas when it is off, the scheme produces a slower response<sup>36</sup>. This difference in behaviour results in differences in retreat rates, but equilibrium states (such as ice volume) are less affected. In our experiments we investigated both approaches, and found that interpolating sub-shelf melt across the grounding line produced simulations that were more consistent with geological constraints for T-I (see below).

We also used a range of enhancement factors for the shallow ice (SIAe) and shallow shelf (SSAe) equations ( $\text{SIAe} = 1, 2, 3$ ;  $\text{SSAe} = 0.5, 1$ ), and different values for the basal sliding exponent that controls how plastic or linear the substrate deformation response to applied driving stresses ( $q = 0.25, 0.6$ ). Floating ice is controlled by two calving mechanisms: one is based on horizontal strain rates<sup>41</sup> and the other prescribes a minimum thickness criterion (50 m for Greenland, 200 m for Antarctica).

We run separate simulations for the Greenland and Antarctic ice sheets, both at 20-km resolution. To drive our ice-sheet model, we use output climatologies from the transient CCSM3 simulations described above for T-I and T-II. Atmospheric outputs are applied as anomalies to present-day air temperature and precipitation fields<sup>42,43</sup>, in the same manner previous studies<sup>44</sup>. We employ a positive-degree day (PDD) model to translate temperatures above freezing into surface melt, of which 60% remains in the snowpack as a consequence of refreezing during percolation. The proportion of refreezing that takes place even under present conditions is difficult to constrain precisely<sup>45</sup>, so we use a uniform value both for the control and perturbation experiments to minimize the effects of this parameterization. That is, differences in the simulation outputs are unlikely to arise from uncertainty in this aspect of the model parameterization.

During our model tuning process, we explored a wide range of degree-day values (from  $1 \text{ mm } ^\circ\text{C}^{-1} \text{ day}^{-1}$  up to  $64 \text{ mm } ^\circ\text{C}^{-1} \text{ day}^{-1}$ ) independently for both snow and ice. We tried the more usual melt threshold of 273 K and the lower value of 270 K following van den Broeke et al.<sup>46</sup>. The latter method yields more widespread melt, mimicking the possible melt arising from shortwave radiation under sub-freezing conditions, and thus degree-day factors are typically lower<sup>46</sup>. We also allow for stochastic variability in daily temperatures using a zero-mean white noise component with a standard deviation set at 5 K. Although the choice of PDD parameters did exert some control on the geometry of the evolving ice mass, the basic shape of the ice sheet evolved in a similar manner regardless of either the melt forcing or the glaciological parameterization, suggesting that the dominant control on ice-sheet geometry is the climate forcing from the our general circulation model. Recent work has shown that our simulations of surface mass balance (SMB) of the Greenland Ice Sheet (GrIS) under the high boreal summer insolation of the LIG may be sensitive to climate model resolution and SMB model type (that is, PDD, surface energy balance)<sup>47</sup>.

Oceanic fields for temperature and salinity at 500 m depth were used as inputs to a thermodynamic ocean model that calculates basal melt from salt and heat-flux gradients across the ice-ocean interface, according to the scheme described in ref. <sup>48</sup>. As with the atmospheric variables, we apply the oceanic fields as anomalies from a present-day ocean configuration that for Antarctica is tuned to reproduce observed melt-rate patterns<sup>49</sup>. As such constraints are not currently available for Greenland, we use a spatially uniform melt factor instead, which is iteratively refined so that both LGM and present-day ice-sheet extents are reproduced (see below). Ice thickness and bed topography for the two ice sheets are taken from the most recent compilations<sup>50,51</sup>.

With the model set-up as described above, we ran a series of time-evolving experiments that first focused on T-I, rather than T-II. The rationale for this approach is that substantial geological data exist with which to constrain the evolving ice-sheet geometry through the last deglaciation, whereas there are few constraints for the preceding T-II. Therefore, to optimize our parameter settings, we undertook >500



experiments for T-I for both ice sheets until a good fit to empirical constraints was found. For Antarctica, our guiding constraints are that the ice sheet at the LGM, immediately before T-I, should occupy the majority of the continental shelf and have an ice-volume excess above the present that is within the range of 5.6–14.5 m from previous simulations<sup>52–55</sup>. Furthermore, we required that the evolution of the simulated ice sheet must reproduce the glacial maximum thickening in West Antarctica and thinning in East Antarctica inferred from ice-core analyses<sup>55</sup>, and exhibit a pattern of mass loss that is consistent with geologically inferred deglacial changes in ice discharge<sup>56</sup>. In Greenland, geological constraints on the offshore extent of the LGM ice sheet are sparse, but the ice volume excess is thought to have been in the range of 2–5 m GMSLE<sup>57,58</sup>. We use this range as our target (Extended Data Fig. 8). Finally, both ice sheets are required to reproduce present-day grounded ice extent and volume as closely as possible at the end of the T-I simulations.

Once this phase of parameter optimization is complete, we run our experiments for T-II using the same settings, changing only the input climatology based on outputs from CCSM3. This dual approach allows the robust simulation of a period, such as T-II, for which few data exist to constrain outputs. In addition, this methodology allows for the direct comparison of model outputs for the two periods, allowing any differences to be attributed solely to the imposed climate forcing rather than to uncertainties in the modelling procedure. Finally, by tuning the model to fit relatively well-known constraints such as LGM and present-day extent and volume, we reduce the influence of any inaccuracies in the climate model representation of air or ocean temperatures during the periods of simulation. Thus, if CCSM3 under- or overestimates the magnitude of past climate anomalies with respect to the present, the internal consistency between the T-I and T-II climate simulations coupled with the data-constrained simulation of T-I mean that the reliability of the T-II simulation is unaffected.

A novelty of our ice-sheet simulations compared with previous studies<sup>59,60</sup> is that we use a fully evolving T-I experiment to constrain our model parameterizations. This includes components such as degree-day factors for the PDD scheme. For Greenland, we run an ensemble of tuning experiments that explore a range of snow and ice melt factors as well as ice-flow enhancement coefficients (Extended Data Fig. 8). By then selecting the parameterization that at the end of the T-I simulation most closely reproduces present-day ice volume and geometry we ensure that the surface melt fields we generate are realistic. We then apply this set-up to our T-II experiments. Our annual temperature range is defined by the CCSM3 outputs. However, we also experimented with duplicate simulations in which we modified our Greenland climatologies to incorporate summer temperatures from Fausto et al.<sup>42</sup>. These simulations resulted in only minor differences in mass change, suggesting that atmospheric forcing plays a lesser role than oceanic forcing in our experiments (Extended Data Figs. 6 and 9). This is supported by experiments in which we also explored alternative grounding line schemes to make the ice sheets either more or less sensitive to ocean temperature change. In the less-sensitive experiments, the ice sheet failed to advance sufficiently far offshore, and was thus incompatible with geological constraints.

## Predictions of relative sea level

Calculations of glacial isostatic adjustment described in the text are based on a pseudo-spectral sea-level theory<sup>23</sup> for the case of spherically symmetric Maxwell viscoelastic Earth models (that is, rheology varies with depth alone), with a truncation at spherical harmonic degree and order 256. The theory incorporates time-varying coastlines, changes in the perimeter of grounded, marine-based ice sheets and the impact on sea level of load-induced perturbations to the Earth's rotation axis, where these perturbations are computed using the rotational stability theory of Mitrovica et al.<sup>61</sup>. Profiles of the density and elastic structure of the Earth model are taken from the seismic Preliminary Reference Earth

Model<sup>62</sup>. The viscosity structure of the Earth models is defined by three layers: a lithospheric zone of infinite viscosity and sub-lithospheric upper and lower mantle regions, where the boundary between the latter two regions is taken to be 670 km depth. The thickness of the lithosphere and the viscosity of the upper and lower mantle are free parameters and are varied, respectively, within the following ranges: 30–140 km;  $2\text{--}20 \times 10^{20}$  Pa s; and  $2\text{--}100 \times 10^{21}$  Pa s.

The set of five ice histories adopted in this study is based, in part, on histories constructed by Dendy et al.<sup>28</sup> in their investigation of the sensitivity of LIG sea level predictions to variations in the timing and geometry of ice cover during Marine Isotope Stage 6. We begin by summarizing these ice histories.

All models in Dendy et al.<sup>28</sup> use the ICE6G ice history<sup>63</sup> for the period extending from the LGM to present day and they extend back four full glacial cycles. The models are constrained to have interglacial ice volumes and geometry identical to present-day ice cover on the Earth (that is, there is no excess ice melting during previous interglaciations, including the LIG). The so-called Waelbroeck (WAE) ice model adopts the eustatic sea-level curve estimated by Waelbroeck et al.<sup>1</sup> on the basis of benthic foraminifera isotope records. In the period before the LGM, the ice geometry is constrained to be identical to the geometry post-LGM whenever the eustatic values are identical. The LAM and Colleoni (COL) models in Dendy et al.<sup>28</sup> also adopt the pre-LGM eustatic curve of Waelbroeck et al.<sup>1</sup>, but are distinguished from WAE by their ice history during the penultimate glacial cycle. In particular, these models adopt the ice geometry during the PGM inferred by Lambeck et al.<sup>22</sup> and Colleoni et al.<sup>27</sup>, which are both characterized by more substantial ice cover over Eurasia during the PGM than the LGM. As the difference in peak Eurasian ice volume during the PGM in the LAM and COL models is large (55 m and 71 m GMSLE, respectively), we have constructed an intermediate ice history (HYB) that is essentially the average of these models (peak volume of 66 m GMSLE during the PGM). The increased ice cover of the LAM, HYB and COL models relative to the WAE model is compensated, in large part, by a reduction of the volume of the Laurentide Ice Sheet during the PGM relative to the LGM<sup>22,27</sup>. All four models, WAE, LAM, HYB and COL, converge to the same ice geometry (that is, the present-day ice geometry) at the beginning of the model LIG. We note that we have adapted the WAE, LAM and COL models described by Dendy et al.<sup>28</sup> to more closely follow the eustatic curve of Waelbroeck et al.<sup>1</sup>. Finally, the model SHA in Dendy et al.<sup>28</sup> is constructed in a manner identical to WAE, with the exception that the model adopts the eustatic curve derived by Shakun et al.<sup>64</sup> in the period before the LGM.

The ice histories considered in the present study combine the five models described above with the Antarctic Ice Sheet (AIS) and GrIS histories discussed in the main text. Specifically, the difference in ice height during the period from 140 ka to 116 ka relative to the present day in the ice-sheet simulations of the main text are applied to each of the Dendy et al.<sup>28</sup> models. The net result is that the five models constructed in this manner are characterized, in contrast to those in Dendy et al.<sup>28</sup>, by excess melting of the AIS and GrIS during the LIG relative to the present day. We ran 337 Earth models for each of the 5 ice histories (total of 1,685 simulations) in which parameters defining the Earth model were varied over plausible ranges.

In exploring the fit of the RSL predictions to the coral record, we considered three sites that have the largest datasets of well-dated corals (the Bahamas, Seychelles and Western Australia) and a relatively new speleothem data set from Mallorca<sup>26</sup> (Extended Data Fig. 7). Given that corals provide a minimum bound on sea level, our metric for fit for these data was the number of coral records that any specific RSL prediction bounded from above. By contrast, we interpret the height uncertainties associated with the published speleothem data to represent a two-way bound on peak RSL.

None of the 1,685 simulations (that is, our sampling of 337 Earth models and 5 ice histories) were successful in bounding all coral records from above. As an indication of performance, Extended Data Fig. 7

shows predictions from the full suite of simulations that satisfy the following criteria: (1) all coral data from Western Australia and the Bahamas, with the exception of the earliest datum at the latter site (at ~131 ka), fall below the prediction; and (2) the prediction at the Seychelles falls above all three coral records at an elevation of ~4 m. The various lines on the figure represent the different Earth models for each ice history that satisfy these constraints. For each ice history (that is, each column of Extended Data Fig. 7), the Earth models sampled on each frame (that is, each site) represent a discrete set that may or may not overlap with the set from a different site. As an example, in the case of the LAM and COL ice histories, no single Earth model appears on the results for all three sites. This is reflected in Fig. 4, where the simulation highlighted in each frame is the result for a distinct Earth model. This variation is justified by the fact that the Earth's mantle is subject to large amplitude variations in viscoelastic structure and so the sea-level response at each of the three sites would not be expected to favour the same Earth model.

Note that the number of simulations that satisfy our plotting criterion for the Bahamas increases as one moves to ice histories with larger Eurasian ice cover at the PGM (that is, from the WAE to the COL results), but the number of simulations that satisfy the criteria for the Seychelles decreases in the same sense. While not apparent from Extended Data Fig. 7, the predicted highstand at Seychelles increases as one considers Earth models with progressively thinner elastic lithospheres (see figure 9A of ref. <sup>28</sup>), and the simulations that predict RSL highstands above the Seychelles records are those based on a lithospheric thickness of 30 km (as in Fig. 4) or, in a couple of cases for the WAE ice history, 50 km. This raises two important issues. First, none of the simulations that yield RSL above all the coral elevations at the Seychelles also satisfy the geological constraints at the Bahamas. Second, as the predicted highstand at the Seychelles is sensitive to the adopted lithospheric thickness, there is a trade-off between the preferred value of this parameter and the level of excess melting during the LIG. That is, increasing polar ice sheet melting above the ~4 m GMSLE adopted in the simulations in Extended Data Fig. 7 would increase the range of lithospheric thickness that would satisfy the Seychelles coral record, and thus bring the inference into better accord with other GIA-based estimates of this Earth model parameter.

This issue may also be relevant to the results for Mallorca (Extended Data Fig. 7), where simulations are plotted only if the misfit between the GIA predictions and the speleothem observations is within 50% of the minimum misfit achieved in all simulations. In this case, fewer of the simulations provide a reasonable fit to the speleothem record as one considers ice histories with progressively larger volumes over Eurasia at PGM; no simulations based on the COL ice history satisfy our plotting criterion. However, regardless of the adopted ice history, none of the simulations fit the highstand constraints before 125 ka. Bringing the GIA predictions in Extended Data Fig. 7 into accord with the Mallorca observations would require additional excess melting that is limited to the earliest phase of the LIG.

As a final point, simulations based on the SHA ice history yielded misfits significantly larger than predictions shown in Extended Data Fig. 7.

The sea-level simulations described above yield changes in sea level and topography at each time slice of the ice history. As an example, Extended Data Fig. 5 shows the reconstructed topography for the area covered by the Scandinavian Ice Sheet at 131 ka, near the end of the Marine Isotope Stage 6 deglaciation, for a simulation based on the LAM ice history and a specific Earth model (see caption). The map supports the suggestion that the margin of grounded ice complexes in this region across MIS6 through 5e were marine-based.

### Evidence for warming over the GrIS during the LIG

Here we evaluate the evidence for warming over the GrIS during the LIG. This supports our climate model simulation, which showed that while the LIG atmosphere was warmer than in the pre-industrial, it

largely remained below freezing and did not lead to significant mass loss from surface melting.

Regarding the reconstructed LIG temperatures at the NEEM<sup>65</sup> and GISP2<sup>66</sup> ice-core sites, there is uncertainty in which  $d\delta^{18}O_{ice}/dT$  (where  $T$  is the temperature) relationship should be used to reconstruct LIG temperatures, and this uncertainty is exacerbated when applying the modern  $d\delta^{18}O_{ice}/dT$  relationship to past climates, where differences in orbital forcing, moisture transport pathways, ice-sheet topography and sea-ice extent can change the relationship<sup>67–72</sup>. To illustrate some of these uncertainties, we have compared our simulated temperatures for the NEEM and GISP2 ice-core sites with the temperature reconstructions for these sites based on  $\delta^{18}O_{ice}$  (Extended Data Fig. 10). These reconstructions span the interval 127–120 ka, which is the warmest interval in the ice-core records for the LIG suggested by this proxy. The published reconstructed temperatures for GISP2 (blue symbols in Extended Data Fig. 10a)<sup>66,73</sup> and NEEM (dark blue line on Extended Data Fig. 10b)<sup>65</sup> are based on the relation  $d\delta^{18}O_{ice}/dT \approx 0.5\text{‰}\text{C}^{-1}$ , which is derived from Greenland ice-core sites elsewhere<sup>74</sup>. During the LIG, the precipitation-weighted  $\delta^{18}O$  is probably biased towards summer months rather than mean annual temperature (van de Berg et al.<sup>68</sup>), so we compare this reconstruction with our simulated summer temperature (JJA) (grey line in Extended Data Fig. 10). This suggests that our simulated JJA temperatures underestimate the mean of the reconstructions by 4–5 °C. This difference is reduced when we account for our simulated ice-surface lowering of ~200 m at NEEM and ~400 m at GISP2 (see Fig. 3c) and assume the lapse rate of 7.5 °C km<sup>-1</sup> used by Dahl-Jensen et al.<sup>65</sup>, thus placing our results within the published uncertainties of the reconstructions (green line in Extended Data Fig. 10).

However, following the publication of Dahl-Jensen et al.<sup>65</sup>, Masson-Delmotte et al.<sup>75</sup> established that the  $d\delta^{18}O_{ice}/dT$  relation at the NEEM site is ~1.1‰ °C<sup>-1</sup>, suggesting that the NEEM and GISP2 LIG summer temperatures are about half of the originally published values based on the Vinther et al.<sup>74</sup>  $d\delta^{18}O_{ice}/dT$  relation (red symbols in upper panel, red line in lower panel of Extended Data Fig. 10). Masson-Delmotte et al. (page 1,500 of ref. <sup>75</sup>) conclude that “For the last interglacial period, the observed  $\delta^{18}O$  anomaly of 3.6‰ at NEEM deposition site would then translate into  $3.6 \pm 0.7$  °C warming, instead of the estimate of  $7.5 \pm 1.8$  °C (NEEM, 2013) that was obtained using the Greenland average Holocene isotope–temperature relationship (Vinther et al., 2009).”

Our simulated JJA temperatures (grey line in Extended Data Fig. 10) are thus only 1–2 °C colder than the mean reconstructions for GISP2 and NEEM based on this new calibration, but they are in excellent agreement with the mean values when accounting for our modelled ice-surface lowering (green line in Extended Data Fig. 10).

Landais et al.<sup>76</sup> used  $\delta^{15}N$  from the NEEM core to reconstruct temperatures that were  $8.5 \pm 2.5$  °C warmer during the LIG compared with pre-industrial temperatures. However, the  $\delta^{15}N$  reconstruction represents annual temperature, whereas the  $\delta^{18}O_{ice}$  temperatures are biased towards the summer (is the critical season for influencing changes in surface mass balance through melting). The two temperature reconstructions are thus not directly comparable. Moreover, Landais et al.<sup>76</sup> identify “large uncertainties” (p. 1944) in their temperature reconstruction, including in the firn model used, in the assumed accumulation rates and in the potential influence of surface melt on firn depth.

We thus conclude that when using the most suitable temperature calibration for the ice-core sites and within the uncertainties of the ice-core proxy reconstructions, our climate model successfully captures the LIG summer (JJA) temperature anomaly relative to pre-industrial temperatures at NEEM and GISP2. Consistent with this model–data agreement for warmer LIG JJA temperatures, we find that the LIG surface mass balance of the GrIS is more negative than the present day mass balance (Extended Data Fig. 9).

Dahl-Jensen et al.<sup>65</sup> stated that “during our NEEM field campaigns (2007–2012), the mean surface air temperature in July reached ~5.4 °C.” However, Box<sup>77</sup> reported the average JJA temperature for 2007–2012

at NEEM site as  $-10.9 \pm 0.3$  °C, suggesting that Dahl-Jensen et al.<sup>65</sup> are reporting a maximum July temperature value during their period of record rather than climatology. But the JJA temperature that matters for comparison with the LIG are the pre-industrial temperatures, which Box<sup>77</sup> found to be  $-12.6 \pm 0.6$  °C for 1840–1870 (the record closest to the pre-industrial period). (Dahl-Jensen et al.<sup>65</sup> compared with the average of the last millennium.) Thus, even if the Dahl-Jensen et al.<sup>65</sup> LIG temperature reconstruction is correct ( $7.5 \pm 1.8$  °C warmer than the mean of the past millennium), average LIG summer temperatures would still be well below freezing (approximately  $-5$  °C). It is more likely, however, that they are even further below freezing when using the  $\delta^{18}\text{O}_{\text{ice}}/dT$  relation established for the NEEM site<sup>75</sup>, that is,  $3.6 \pm 0.7$  °C warmer than the mean of the past millennium, with average LIG summer temperatures thus being  $-9$  °C.

The evidence for surface melt at the NEEM ice core site is based on: (1) a low-resolution record showing that 7 out of 73 samples have elevated  $\text{CH}_4$  and  $\text{N}_2\text{O}$  during the interval 127–118 ka, and (2) a high-resolution  $\text{CH}_4$  record that suggests five melt events in the 123.5–122.5 ka interval, or one every 200 years<sup>65,78</sup>. Noble gases that were measured at the times of four of the five elevated  $\text{CH}_4$  events in the high-resolution record confirm melting during these events<sup>78</sup>. This alone makes it clear that these were infrequent periods of melting rather than continuous melting throughout the LIG. According to Anais Orsi (personal communication), during a melt event, such as the 2012 event<sup>79</sup>, the melt percolates and refreezes in the top 1 m of the firn, often in many layers, so one melt event may be represented by more than one melt layer. Moreover, although the noble gas results clearly identify four periods of enhanced melting, one cannot exclude the possibility that each sample represents a single 2012-like melt event.

In summary, ice-core proxies suggest that Greenland LIG temperatures were warmer than present, but the amount of warming from these proxies remains subject to uncertainty. However, even the highest estimates of warming still suggest that average JJA temperatures remained well below freezing relative to pre-industrial temperatures, and—on the basis of the more-appropriate  $\delta^{18}\text{O}_{\text{ice}}$ -temperature calibration from Masson-Delmotte et al.<sup>75</sup>—are in good agreement with our simulated temperatures for the ice-core sites. Consistent with this model–data agreement for warmer LIG JJA temperatures, we find that the LIG surface mass balance of the GrIS is more negative than the present day mass balance. Rare episodes of melting occurred, but while their frequency may increase under higher mean temperatures and insolation (such as those recorded in the Holocene section of the GISP2 ice core<sup>80</sup>), we conclude that with a frequency of perhaps only one melt event every 200 years, they had a negligible influence on the long-term surface mass balance, and average summer temperatures at the NEEM site otherwise remained well below freezing during the LIG.

## Influence of FW forcing from modelled mass loss from the GrIS and AIS on ocean circulation during the LIG

We did not include additional FW forcing after 129.5 ka, but we show here that the FW fluxes from our modelled mass loss from the GrIS and AIS after 129.5 ka (during the LIG) were too small to have influenced the AMOC or Antarctic Bottom Water formation. As global sea level reached modern levels at 129–130 ka and our modelled AMOC resumes at 129.5 ka, we consider only the FW fluxes from the GrIS and AIS since 129.5 ka.

From 129.5 ka to 127 ka, modelled GrIS mass loss was 0.2 m of GMSLE, which is equivalent to a FW flux of 0.0009 Sv. From 127 ka to 117.5 ka, GrIS mass loss was 0.09 m, which is equivalent to 0.0001 Sv. For reference, Bakker et al.<sup>81</sup> showed that a FW flux of 0.01 Sv from Greenland for the RCP 4.5 scenario (see their figure SI3) results in a median reduction in the AMOC of  $-5\%$  (their Fig. 2, GrIS only). The FW fluxes from LIG loss of the GrIS in our model are two orders of magnitude smaller than this, and would therefore have no impact on the AMOC, or consequently on our ice-sheet model simulations.

From 129.5 ka to 123.5 ka, AIS mass loss was 4.1 m, which is equivalent to a FW flux of 0.008 Sv. Bakker et al.<sup>82</sup> found that a FW flux of 0.12 Sv from the AIS increases variability in the Antarctic Bottom Water by  $\sim 10\%$  and in AMOC by  $\sim 5\%$ . The FW fluxes from LIG loss of the AIS in our model is a factor of 15 smaller than this, and thus would have no impact on the Antarctic Bottom Water or the AMOC, or consequently on our ice-sheet model simulations.

## Data availability

Antarctic bedrock topography and ice thickness data are from the BEDMAP2 compilation, available at <https://secure.antarctica.ac.uk/data/bedmap2/>. Greenland topography and ice thickness data are from BedMachine v3, available at <https://nsidc.org/data/idbmg4>. Greenland mass balance and geothermal heat flux data are available from the seaRISE website: <http://websrv.cs.umd.edu/isis/index.php/Data>. Information on the Antarctic surface mass balance data is available at <http://www.projects.science.uu.nl/iceclimate/models/antarctica.php#racmo23>. Antarctic geothermal heat flux data are available at the Open Science Framework <https://doi.pangaea.de/10.1594/PAN-GAEA.882503>. The datasets generated and used for this study (Figs. 1–4, Extended Data Figs. 3–9) are available from the Open Science Framework (<https://doi.org/10.17605/OSF.IO/FX7WK>).

## Code availability

CCSM3 is freely available as open-source code from <http://www.cesm.ucar.edu/models/ccsm3.0/>. PISM is freely available as open-source code from <https://github.com/pism/pism.git>.

- Yeager, S. G., Shields, C. A., Large, W. G. & Hack, J. J. The low-resolution CCSM3. *J. Clim.* **19**, 2545–2566 (2006).
- He, F. *Simulating Transient Climate Evolution of the Last Deglaciation with CCSM3*. PhD thesis, Univ Wisconsin–Madison (2011).
- Lüthi, D. et al. High-resolution carbon dioxide concentration record 650,000–800,000 years before present. *Nature* **453**, 379–382 (2008).
- Peltier, W. R. Global glacial isostasy and the surface of the ice-age earth: the ice-5G (VM2) model and grace. *Annu. Rev. Earth Planet. Sci.* **32**, 111–149 (2004).
- Grant, K. M. et al. Rapid coupling between ice volume and polar temperature over the past 150,000 years. *Nature* **491**, 744–747 (2012).
- Aschwanden, A., Fahnestock, M. A. & Truffer, M. Complex Greenland outlet glacier flow captured. *Nat. Commun.* **7**, 10524 (2016).
- Golledge, N. R. et al. The multi-millennial Antarctic commitment to future sea-level rise. *Nature* **526**, 421–425 (2015).
- Schoof, C. A variational approach to ice stream flow. *J. Fluid Mech.* **556**, 227–251 (2006).
- Bueler, E. & Brown, J. Shallow shelf approximation as a “sliding law” in a thermomechanically coupled ice sheet model. *J. Geophys. Res. Earth Surf.* **114**, F03008 (2009).
- Van Pelt, W. J. J. & Oerlemans, J. Numerical simulations of cyclic behaviour in the Parallel Ice Sheet Model (PISM). *J. Glaciol.* **58**, 347–360 (2012).
- Feldmann, J., Albrecht, T., Khroulev, C., Pattyn, F. & Levermann, A. Resolution-dependent performance of grounding line motion in a shallow model compared with a full-Stokes model according to the MISIP3d intercomparison. *J. Glaciol.* **60**, 353–360 (2014).
- Levermann, A. et al. Kinematic first-order calving law implies potential for abrupt ice-shelf retreat. *Cryosphere* **6**, 273–286 (2012).
- Fausto, R. S., Ahlstrom, A. P., Van As, D., Boggild, C. E. & Johnsen, S. J. A new present-day temperature parameterization for Greenland. *J. Glaciol.* **55**, 95–105 (2009).
- Van Wessem, J. M. et al. Improved representation of East Antarctic surface mass balance in a regional atmospheric climate model. *J. Glaciol.* **60**, 761–770 (2014).
- Golledge, N. R. et al. Antarctic climate and ice-sheet configuration during the early Pliocene interglacial at 4.23 Ma. *Clim. Past* **13**, 959–975 (2017).
- Munneke, P. K. et al. A new albedo parameterization for use in climate models over the Antarctic ice sheet. *J. Geophys. Res. Atmos.* **116**, D05114 (2011).
- van den Broeke, M., Bus, C., Ettema, J. & Smeets, P. Temperature thresholds for degree-day modelling of Greenland ice sheet melt rates. *Geophys. Res. Lett.* **37**, L18501 (2010).
- Plach, A. et al. Eemian Greenland SMB strongly sensitive to model choice. *Clim. Past* **14**, 1463–1485 (2018).
- Hellmer, H. H. & Olbers, D. J. A 2-dimensional model for the thermohaline circulation under an ice shelf. *Antarct. Sci.* **1**, 325–336 (1989).
- Bernales, J., Rogozhina, I. & Thomas, M. Melting and freezing under Antarctic ice shelves from a combination of ice-sheet modelling and observations. *J. Glaciol.* **63**, 731–744 (2017).
- Morlighem, M. et al. BedMachine v3: complete bed topography and ocean bathymetry mapping of Greenland from multibeam echo sounding combined with mass conservation. *Geophys. Res. Lett.* **44**, 11051–11061 (2017).

51. Fretwell, P. et al. Bedmap2: improved ice bed, surface and thickness datasets for Antarctica. *Cryosphere* **7**, 375–393 (2013).
52. Mackintosh, A. et al. Retreat of the East Antarctic ice sheet during the last glacial termination. *Nat. Geosci.* **4**, 195–202 (2011).
53. Briggs, R., Pollard, D. & Tarasov, L. A glacial systems model configured for large ensemble analysis of Antarctic deglaciation. *Cryosphere* **7**, 1949–1970 (2013).
54. Golledge, N. R., Fogwill, C. J., Mackintosh, A. N. & Buckley, K. M. Dynamics of the last glacial maximum Antarctic ice-sheet and its response to ocean forcing. *Proc. Natl Acad. Sci. USA* **109**, 16052–16056 (2012).
55. Golledge, N. R. et al. Antarctic contribution to meltwater pulse 1A from reduced Southern Ocean overturning. *Nat. Commun.* **5**, 6107 (2014).
56. Weber, M. E. et al. Millennial-scale variability in Antarctic ice-sheet discharge during the last deglaciation. *Nature* **510**, 134–138 (2014).
57. Simpson, M. J. R., Milne, G. A., Huybrechts, P. & Long, A. J. Calibrating a glaciological model of the Greenland ice sheet from the Last Glacial Maximum to present-day using field observations of relative sea level and ice extent. *Quat. Sci. Rev.* **28**, 1631–1657 (2009).
58. Lecavalier, B. S. et al. A model of Greenland ice sheet deglaciation constrained by observations of relative sea level and ice extent. *Quat. Sci. Rev.* **102**, 54–84 (2014).
59. Stone, E. J., Lunt, D. J., Annan, J. D. & Hargreaves, J. C. Quantification of the Greenland ice sheet contribution to Last Interglacial sea level rise. *Clim. Past* **9**, 621–639 (2013).
60. Goelzer, H., Huybrechts, P., Loutre, M. F. & Fichefet, T. Last Interglacial climate and sea-level evolution from a coupled ice sheet-climate model. *Clim. Past* **12**, 2195–2213 (2016).
61. Mitrovica, J. X., Wahr, J., Matsuyama, I. & Paulson, A. The rotational stability of an ice-age earth. *Geophys. J. Int.* **161**, 491–506 (2005).
62. Dziewonski, A. M. & Anderson, D. L. Preliminary reference Earth model. *Phys. Earth Planet. Inter.* **25**, 297–356 (1981).
63. Peltier, W. R., Argus, D. F. & Drummond, R. Space geodesy constrains ice age terminal deglaciation: the global ICE-6G\_C (VM5a) model. *J. Geophys. Res. Solid Earth* **120**, 450–487 (2015).
64. Shakun, J. D., Lea, D. W., Lisiecki, L. E. & Raymo, M. E. An 800-kyr record of global surface ocean  $\delta^{18}\text{O}$  and implications for ice volume-temperature coupling. *Earth Planet. Sci. Lett.* **426**, 58–68 (2015).
65. NEEM community members Eemian interglacial reconstructed from a Greenland folded ice core. *Nature* **493**, 489–494 (2013).
66. Yau, A., Bender, M. L., Robinson, A. & Brook, E. J. Reconstructing the last interglacial at Summit, Greenland: insights from GISP2. *Proc. Natl Acad. Sci. USA* **113**, 9710–9715 (2016).
67. Liu, Z. Y. et al. Younger Dryas cooling and the Greenland climate response to  $\text{CO}_2$ . *Proc. Natl Acad. Sci. USA* **109**, 11101–11104 (2012).
68. van de Berg, W. J., van den Broeke, M. R., van Meijgaard, E. & Kaspar, F. Importance of precipitation seasonality for the interpretation of Eemian ice core isotope records from Greenland. *Clim. Past* **9**, 1589–1600 (2013).
69. Sime, L. C. et al. Warm climate isotopic simulations: what do we learn about interglacial signals in Greenland ice cores? *Quat. Sci. Rev.* **67**, 59–80 (2013).
70. Buizert, C. et al. Greenland temperature response to climate forcing during the last deglaciation. *Science* **345**, 1177–1180 (2014).
71. Rhines, A. & Huybers, P. J. Sea ice and dynamical controls on preindustrial and Last Glacial Maximum accumulation in Central Greenland. *J. Clim.* **27**, 8902–8917 (2014).
72. Pedersen, R. A., Langen, P. L. & Vinther, B. M. Greenland during the last interglacial: the relative importance of insolation and oceanic changes. *Clim. Past* **12**, 1907–1918 (2016).
73. Suwa, M., von Fischer, J. C., Bender, M. L., Landais, A. & Brook, E. J. Chronology reconstruction for the disturbed bottom section of the GISP2 and the GRIP ice cores: implications for Termination II in Greenland. *J. Geophys. Res. Atmos.* **111**, D02101 (2006).
74. Vinther, B. M. et al. Holocene thinning of the Greenland ice sheet. *Nature* **461**, 385–388 (2009).
75. Masson-Delmotte, V. et al. Recent changes in north-west Greenland climate documented by NEEM shallow ice core data and simulations, and implications for past-temperature reconstructions. *Cryosphere* **9**, 1481–1504 (2015).
76. Landais, A. et al. How warm was Greenland during the last interglacial period? *Clim. Past* **12**, 1933–1948 (2016).
77. Box, J. E. Greenland Ice Sheet mass balance reconstruction. Part II: surface mass balance (1840–2010). *J. Clim.* **26**, 6974–6989 (2013).
78. Orsi, A. J. et al. Differentiating bubble-free layers from melt layers in ice cores using noble gases. *J. Glaciol.* **61**, 585–594 (2015).
79. Tedesco, M. et al. Evidence and analysis of 2012 Greenland records from spaceborne observations, a regional climate model and reanalysis data. *Cryosphere* **7**, 615–630 (2013).
80. Alley, R. B. & Anandakrishnan, A. Variations in melt-layer frequency in the GISP2 ice core: implications for Holocene summer temperatures in central Greenland. *Ann. Glaciol.* **21**, 64–70 (1995).
81. Bakker, P. et al. Fate of the Atlantic Meridional Overturning Circulation: strong decline under continued warming and Greenland melting. *Geophys. Res. Lett.* **43**, 12252–12260 (2016).
82. Bakker, P., Clark, P. U., Golledge, N. R., Schmittner, A. & Weber, M. E. Centennial-scale Holocene climate variations amplified by Antarctic Ice Sheet discharge. *Nature* **541**, 72–76 (2017).
83. Deaney, E. L., Barker, S. & van de Flierdt, T. Timing and nature of AMOC recovery across Termination 2 and magnitude of deglacial  $\text{CO}_2$  change. *Nat. Commun.* **8**, 14595 (2017).
84. Bazin, L. et al. An optimized multi-proxy, multi-site Antarctic ice and gas orbital chronology (AICC2012): 120–800 ka. *Clim. Past* **9**, 1715–1731 (2013).
85. Oppo, D. W., McManus, J. F. & Cullen, J. L. Evolution and demise of the Last Interglacial warmth in the subpolar North Atlantic. *Quat. Sci. Rev.* **25**, 3268–3277 (2006).
86. Skinner, L. C. & Shackleton, N. J. Deconstructing Terminations I and II: revisiting the glacioeustatic paradigm based on deep-water temperature estimates. *Quat. Sci. Rev.* **25**, 3312–3321 (2006).
87. Sánchez Goni, M. F. S. et al. European climate optimum and enhanced Greenland melt during the Last Interglacial. *Geology* **40**, 627–630 (2012).
88. Roberts, N. L., Piotrowski, A. M., McManus, J. F. & Keigwin, L. D. Synchronous deglacial overturning and water mass source changes. *Science* **327**, 75–78 (2010).
89. McManus, J. F., Francois, R., Gherardi, J. M., Keigwin, L. D. & Brown-Leger, S. Collapse and rapid resumption of Atlantic meridional circulation linked to deglacial climate changes. *Nature* **428**, 834–837 (2004).
90. Stern, J. V. & Lisiecki, L. E. North Atlantic circulation and reservoir age changes over the past 41,000 years. *Geophys. Res. Lett.* **40**, 3693–3697 (2013).
91. Menviel, L. et al. The penultimate deglaciation: protocol for Paleoclimate Modeling Intercomparison Project (PMIP) phase 4 transient numerical simulations between 140 and 127 ka, version 1.0. *Geosci. Model Dev.* **12**, 3649–3685 (2019).
92. Thomas, A. L. et al. Penultimate deglacial sea-level timing from uranium/thorium dating of Tahitian corals. *Science* **324**, 1186–1189 (2009).
93. Esat, T. M., McCulloch, M. T., Chappell, J., Pillans, B. & Omura, A. Rapid fluctuations in sea level recorded at Huon Peninsula during the penultimate deglaciation. *Science* **283**, 197–201 (1999).
94. Cheng, H. et al. Improvements in  $^{230}\text{Th}$  dating,  $^{230}\text{Th}$  and  $^{234}\text{U}$  half-life values, and U–Th isotopic measurements by multi-collector inductively coupled plasma mass spectrometry. *Earth Planet. Sci. Lett.* **371–372**, 82–91 (2013).
95. Peak, B. A., Mitrovica, J. X., Latychev, K., Powell, E. & Lau, H. C. P. Complex Earth structure and glacial isostatic adjustment in the Red Sea. *AGU Fall Meeting 2018*, abstr. PP13C-1343 (American Geophysical Union, 2018).
96. Lambeck, K. et al. Sea level and shoreline reconstructions for the Red Sea: isostatic and tectonic considerations and implications for hominin migration out of Africa. *Quat. Sci. Rev.* **30**, 3542–3574 (2011).
97. Lambeck, K., Rouby, H., Purcell, A., Sun, Y. & Sambridge, M. Sea level and global ice volumes from the Last Glacial Maximum to the Holocene. *Proc. Natl Acad. Sci. USA* **111**, 15296–15303 (2014).

**Acknowledgements** This work was funded by the US National Science Foundation (NSF) through grant numbers AGS-1503032 (to P.U.C.), AGS-1502990 (to F.H.) OCE-1702684 (to J.X.M.) and 1559040 (to A.D.); the NOAA Climate and Global Change Postdoctoral Fellowship programme, administered by the University Corporation for Atmospheric Research (to F.H.); contract number VUW1501 from the Royal Society Te Aparangi with support from the Antarctic Research Centre, Victoria University of Wellington (to N.R.G.); contract number C05X1001 to GNS Science from the Ministry for Business, Innovation and Employment (to N.R.G.); and Harvard University (J.X.M.). We acknowledge high-performance computing support from Yellowstone (ark:/85065/d7wd3xhc) provided by NCAR's Computational and Information Systems Laboratory, sponsored by the NSF. This research used resources of the Oak Ridge Leadership Computing Facility at the Oak Ridge National Laboratory, which is supported by the Office of Science of the US Department of Energy under contract number DE-AC05-00OR22725. PISM is supported by NASA grant numbers NNX13AM16G and NNX13AK27G. We thank J. Box, C. Buizert and A. Orsi for discussions.

**Author contributions** F.H. performed the general circulation modelling. N.R.G. performed the ice-sheet modelling. J.X.M. performed the sea-level modelling with help from S.D. P.U.C., A.D. and J.S.H. performed the data analysis. P.U.C., F.H., N.R.G. and J.X.M. wrote the manuscript. All authors discussed the results and contributed towards improving the final manuscript.

**Competing interests** The authors declare no competing interests.

#### Additional information

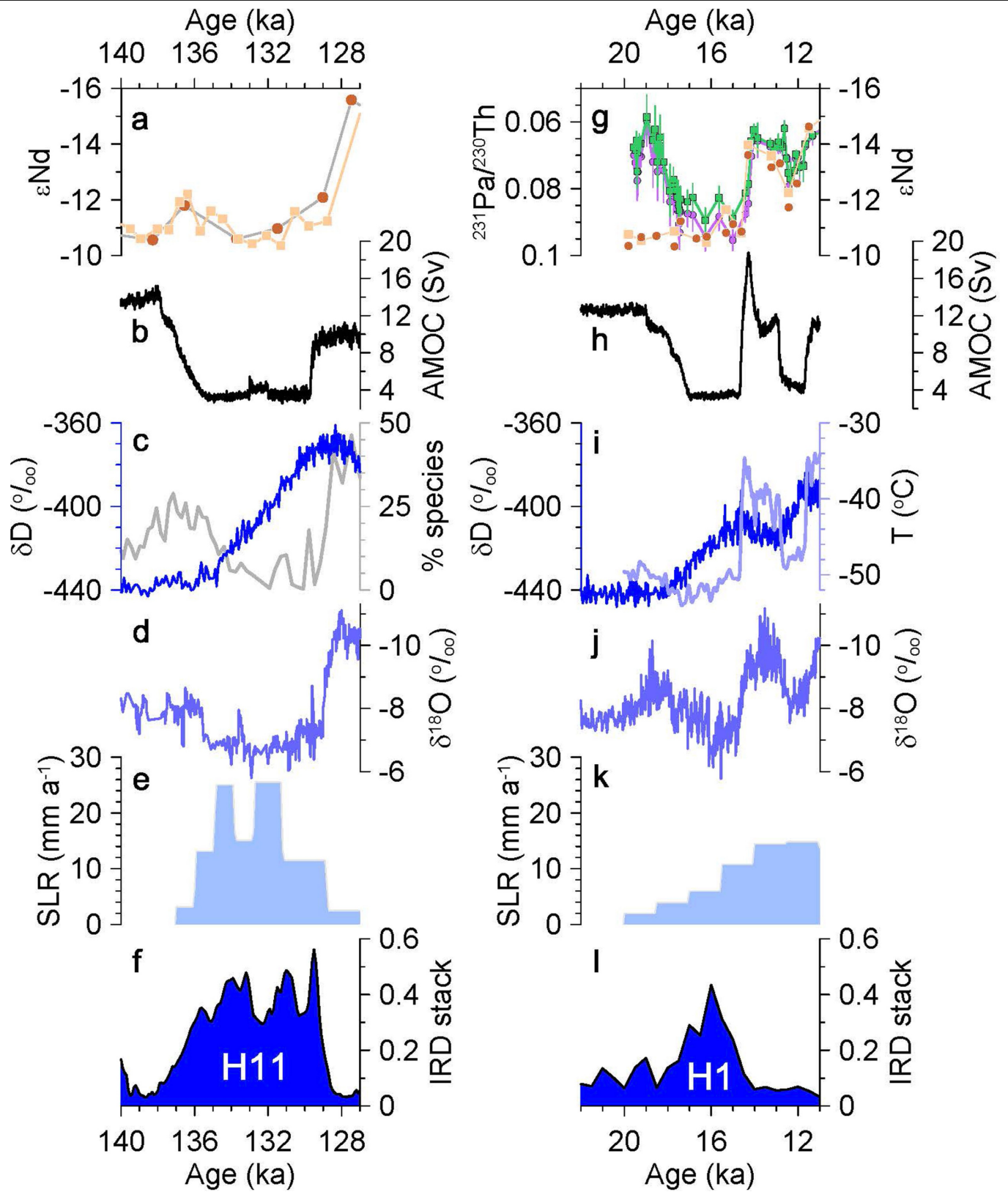
**Supplementary information** is available for this paper at <https://doi.org/10.1038/s41586-020-1931-7>.

**Correspondence and requests for materials** should be addressed to P.U.C.

**Peer review information** Nature thanks Paul Valdes and the other, anonymous, reviewer(s) for their contribution to the peer review of this work.

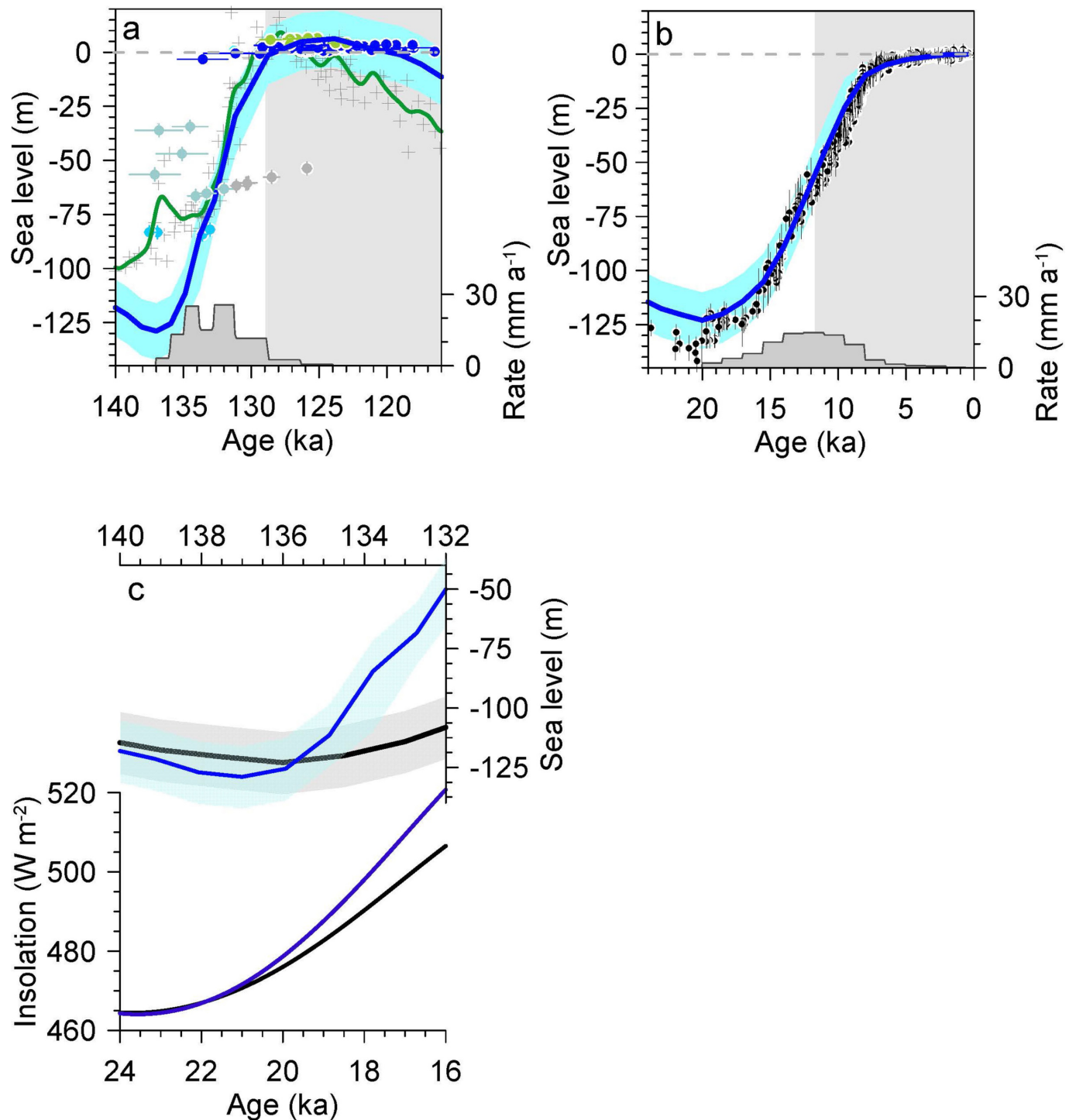
**Reprints and permissions information** is available at <http://www.nature.com/reprints>.





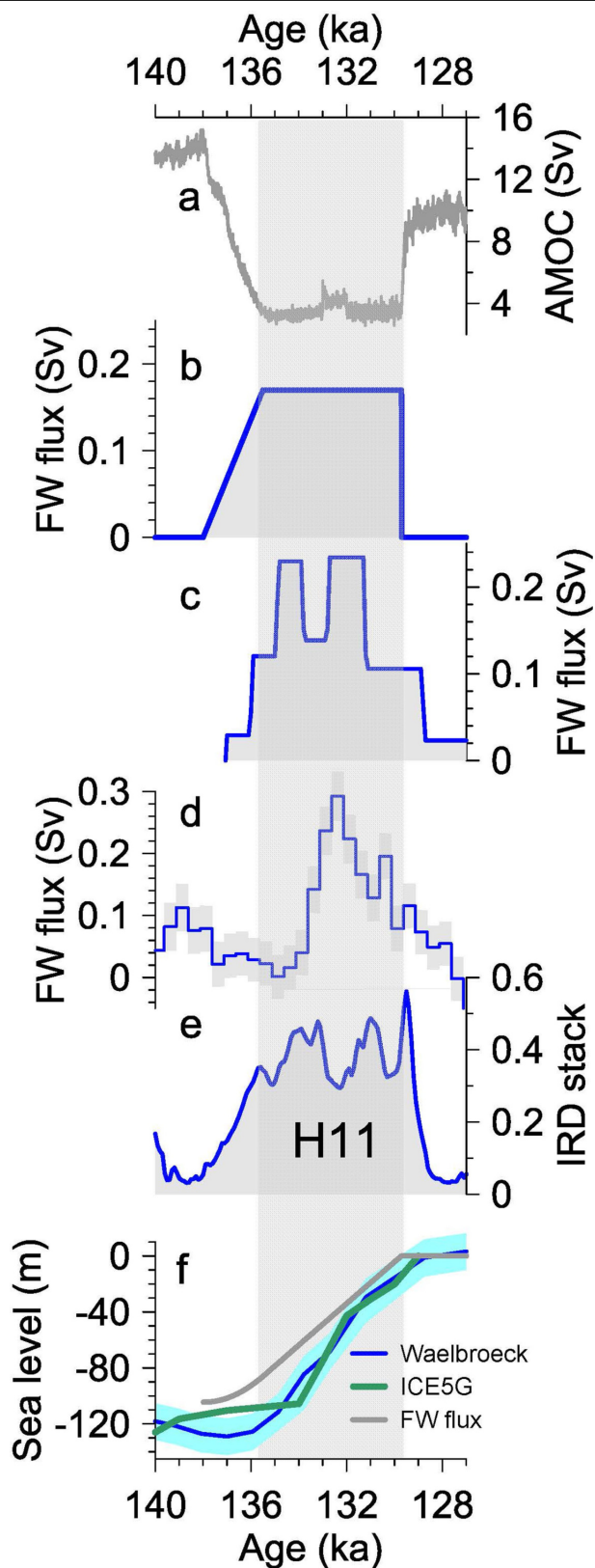
Extended Data Fig. 1 | See next page for caption.

**Extended Data Fig. 1 | Climate and sea-level records for T-II and T-I.** **a**,  $\epsilon\text{Nd}$  records from the North Atlantic Ocean as proxies of AMOC transport<sup>16,83</sup>. **b**, CCSM3 maximum AMOC transport (below 500 m) (this study). **c**, EPICA Dome C  $\delta\text{D}$  record on AICC2012 age model as proxy of Antarctic temperature<sup>84</sup> (blue line) and percentage of warm planktonic foraminiferal species as proxy of North Atlantic sea surface temperatures<sup>83</sup> (grey line). **d**,  $\delta^{18}\text{O}$  record from Chinese stalagmite as proxy of Asian monsoon strength<sup>18</sup>. **e**, Rate of sea-level change derived from an RSL reconstruction based on benthic foraminifera isotopes<sup>1</sup>. **f**, A stack of North Atlantic ice-rafted debris records recording  $\text{Hf}^{83,85-87}$ . **g**,  $\epsilon\text{Nd}$  (ref. <sup>88</sup>; brown, orange symbols) and  $\text{Pa/Th}$  (ref. <sup>89</sup>; purple, green symbols,  $1\sigma$  uncertainty) records from the North Atlantic Ocean as proxies of AMOC. **h**, CCSM3 maximum AMOC transport (below 500 m) (this study). **i**, EPICA Dome C  $\delta\text{D}$  record on the AICC2012 age model (dark blue line)<sup>84</sup> as proxy of Antarctic temperature and a temperature reconstruction from the Greenland GISP2 ice core (light blue line)<sup>70</sup>. **j**,  $\delta^{18}\text{O}$  record from a Chinese stalagmite as proxy of Asian monsoon strength<sup>18</sup>. **k**, Rate of sea-level change derived from an RSL reconstruction based on benthic foraminifera isotopes<sup>1</sup>. **l**, A stack of North Atlantic IRD records that log  $\text{Hf}^{90}$ .



**Extended Data Fig. 2 | Sea-level records for the last two terminations and interglaciations.** **a**, Sea-level reconstructions for the penultimate deglaciation and the LIG (the latter identified by the grey-shaded area). The eustatic sea-level record is based on benthic foraminifera isotopes (blue line with 1σ uncertainty)<sup>1</sup> and the RSL record is based on Red Sea isotopes (grey crosses; green line, 1-kyr moving Gaussian filter)<sup>34</sup> placed on a revised age model<sup>91</sup>. Also shown are RSL data from U-series dated corals at Tahiti (sky blue circles)<sup>92</sup>, the Huon Peninsula (light blue-green circle; altered samples shown by grey circles)<sup>93</sup>, the Seychelles (light green circles)<sup>25</sup>, western Australia (blue circles)<sup>24</sup> and the Bahamas (cyan circles)<sup>24</sup>. All of the U-series ages have been recalculated to normalize them with the same set of decay constants for <sup>234</sup>U and <sup>230</sup>Th (ref. <sup>94</sup>) and are shown with 2σ age uncertainty. We note that the offset between the Red Sea record (green line) and the benthic foraminifera record (blue line) may reflect the complex three-dimensional Earth structure in the vicinity of

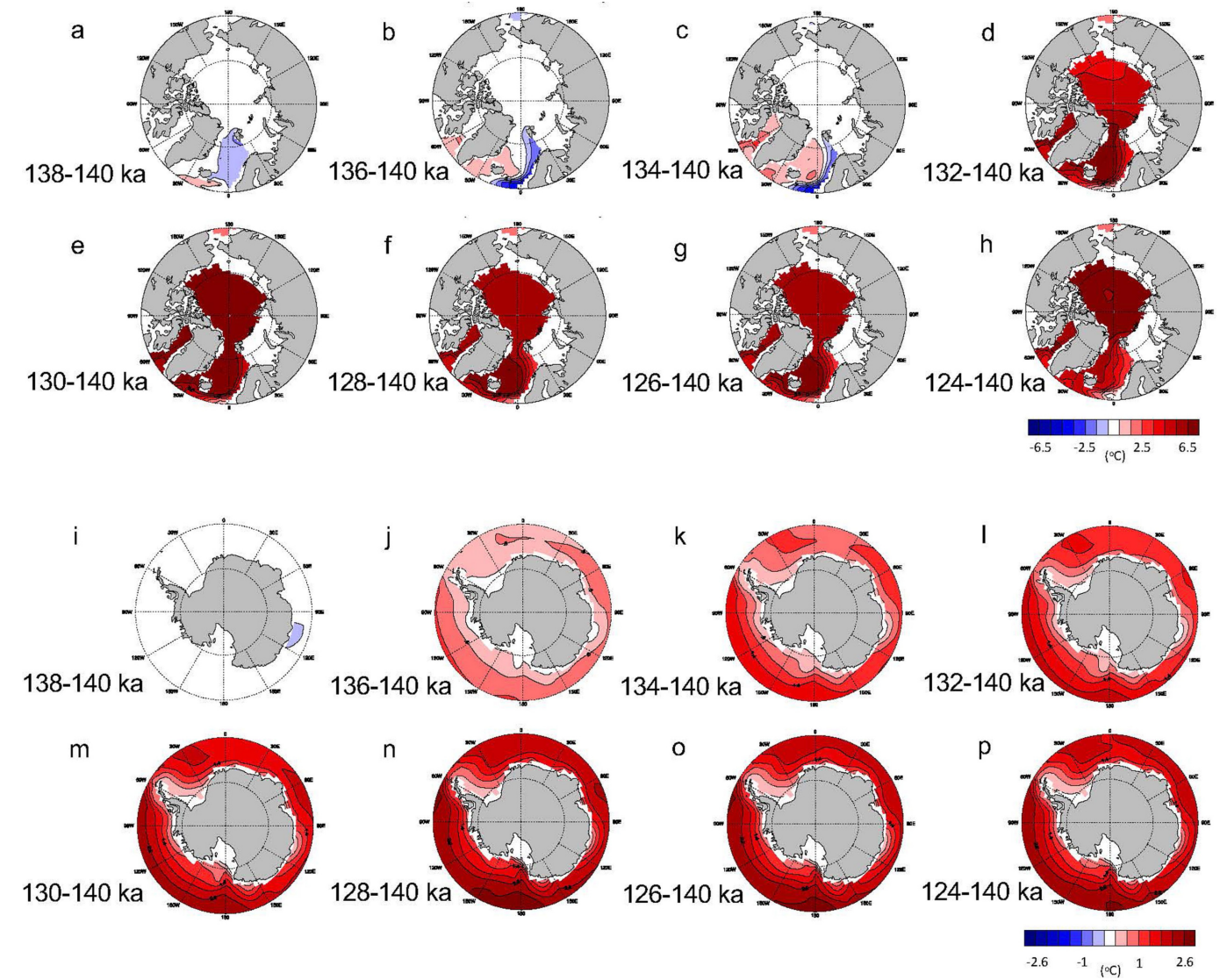
the Red Sea rift<sup>95,96</sup>. The variability in the Red Sea and Huon Peninsula RSL records may reflect a sea-level reversal at -137 ka (ref. <sup>91</sup>), which, if it existed, was too small to be recorded by the benthic foraminiferal record. The rate of sea-level change based on the benthic foraminiferal record is also shown. **b**, Sea-level reconstructions for the last deglaciation and the present interglaciation (the latter identified by the grey-shaded area). The record of global mean sea level is based on benthic foraminifera isotopes (blue line with 1σ uncertainty)<sup>1</sup>. Also shown are individual sea-level estimates (black circles, 2σ uncertainty) that have been corrected for glacial isostatic adjustment<sup>97</sup>. The rate of sea-level change based on the benthic foraminiferal record is also shown. **c**, Top, eustatic sea-level reconstructions for the penultimate deglaciation (blue line with 1σ uncertainty) and the last deglaciation (black line with 1σ uncertainty)<sup>1</sup>. Bottom, 21 June insolation for 65° N for the penultimate deglaciation (blue line) and the last deglaciation (black line)<sup>7</sup>.



**Extended Data Fig. 3 | Comparison of our FW forcing during T-II with other estimates.** **a**, Our simulated changes in AMOC. **b**, Our FW forcing. **c**, Reconstruction of the FW flux from sea-level reconstructions from Waelbroeck et al.<sup>1</sup>. **d**, Reconstruction of FW flux from sea-level reconstructions from Marino et al.<sup>3</sup>. **e**, Our stack of IRD for H11 (Extended Data Fig. 1), which shows that the H11 interval of iceberg discharge is in good agreement with the timing of our FW forcing. **f**, The sea-level change associated with our FW flux into the North Atlantic (grey line), the sea-level change associated with the ICE-5G ice sheets<sup>33</sup> used as a boundary condition in our climate model (green line) and a reconstruction of global sea-level change<sup>1</sup> (blue line with  $1\sigma$  uncertainty). The timing of sea-level change in the ICE-5G time series shown here was adjusted from its chronology for T-I by adjusting the corresponding sea-level rise to closely follow the sea-level reconstructions from Waelbroeck et al.<sup>1</sup> and Grant et al.<sup>34</sup> for the penultimate deglaciation.

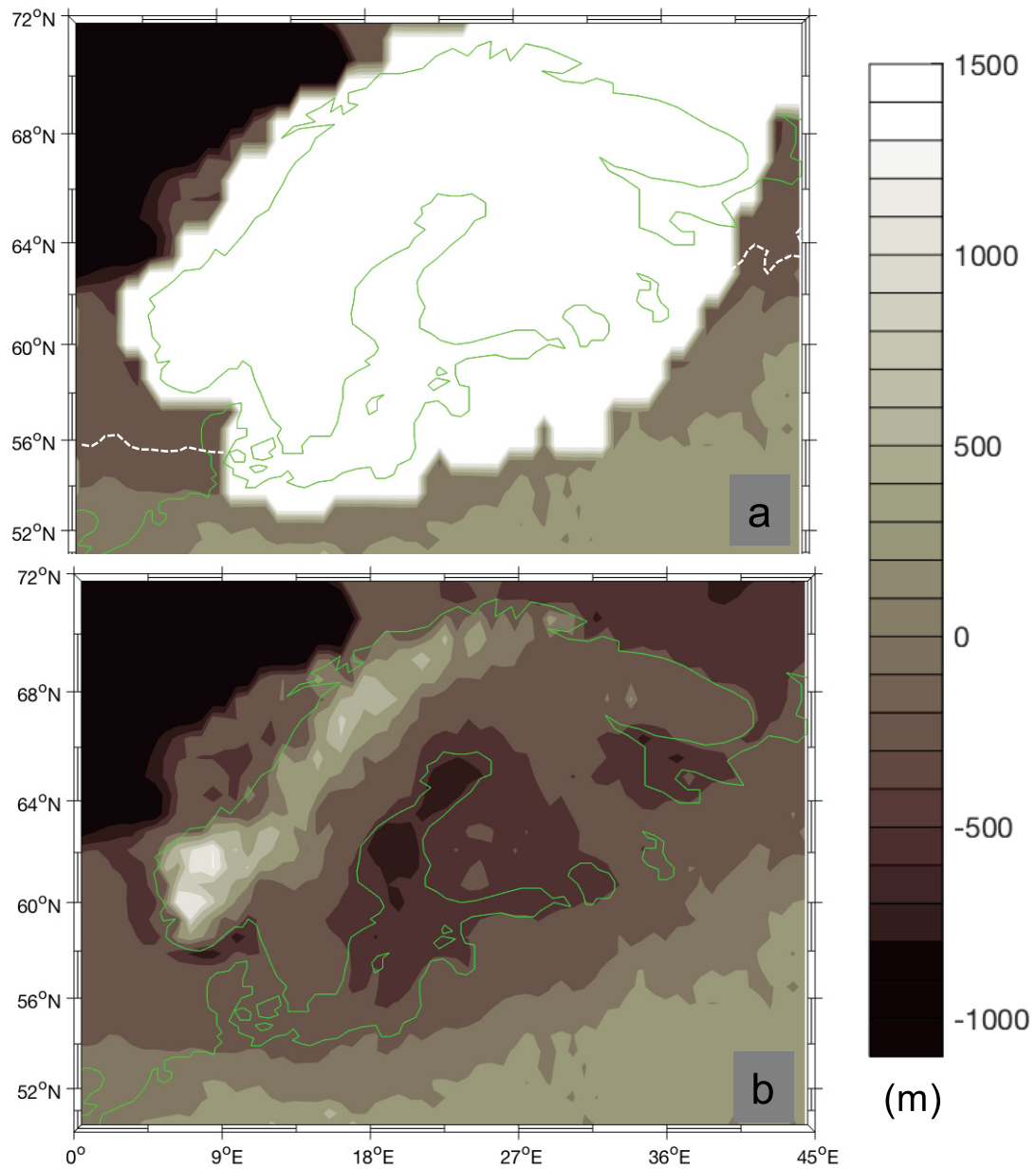
Extended Data Fig. 3 | See next page for caption.





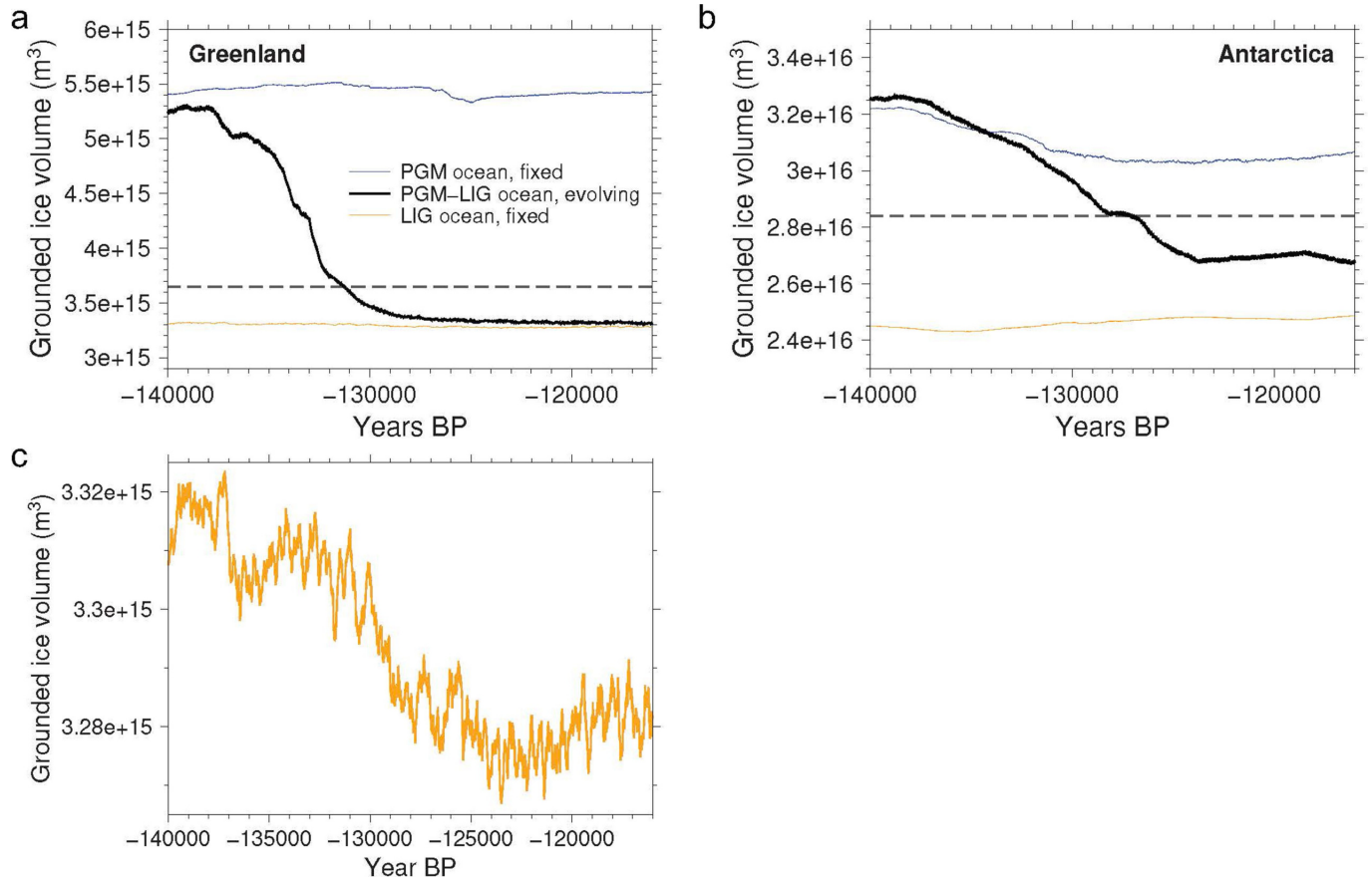
**Extended Data Fig. 4 | Maps of the evolution of temperature at 400 m water depth in the North Atlantic, Arctic and Southern oceans between 138 ka and 124 ka relative to the temperature at 140 ka. a–h, Maps of the evolution of temperature at 400 m water depth in the North Atlantic and Arctic oceans for 140–138 ka (a), 140–136 ka (b), 140–134 ka (c), 140–132 ka (d), 140–130 ka (e),**

**140–128 ka (f), 140–126 ka (g) and 140–124 ka (h). i–p, Maps of the evolution of temperature at 400 m water depth in the Southern Ocean for 140–138 ka (i), 140–136 ka (j), 140–134 ka (k), 140–132 ka (l), 140–130 ka (m), 140–128 ka (n), 140–126 ka (o) and 140–124 ka (p).**



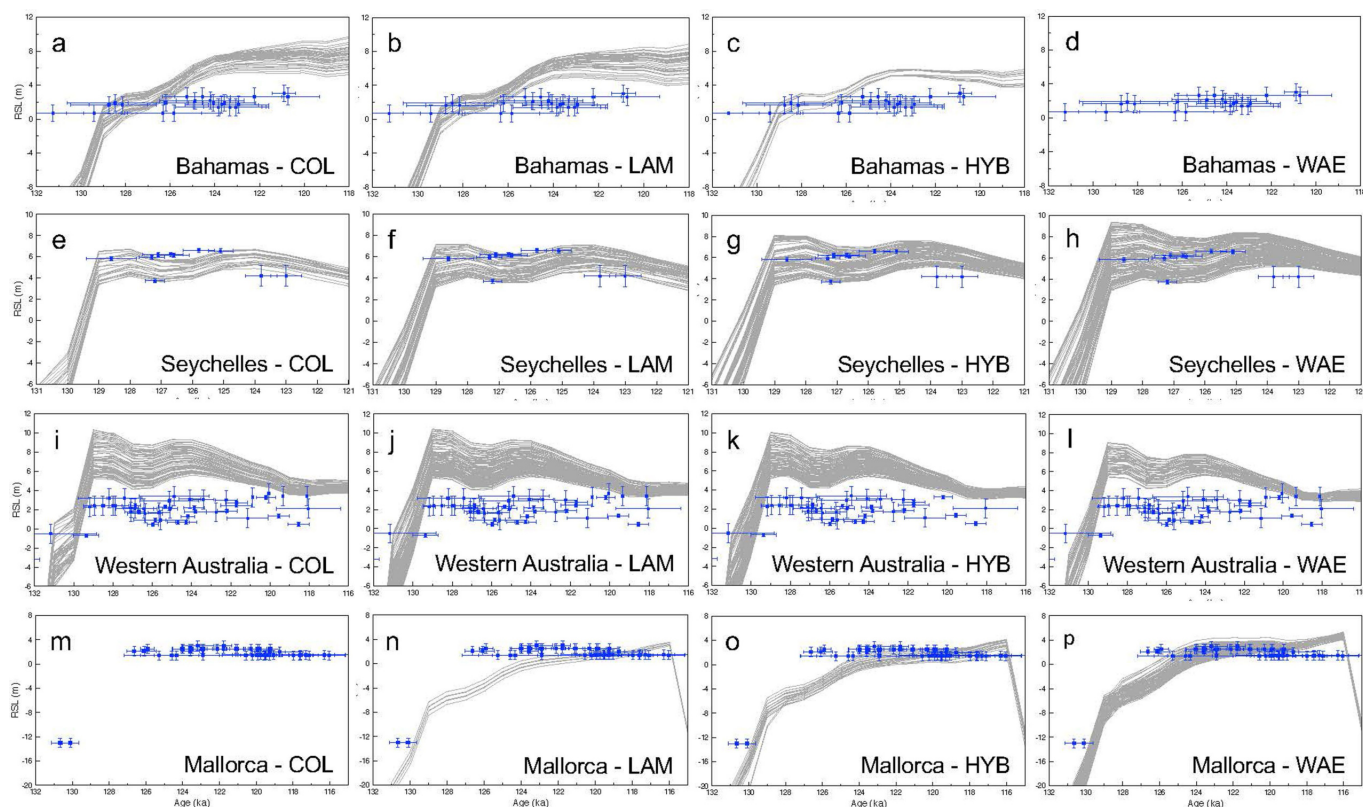
**Extended Data Fig. 5 | Predicted topography for the area covered by the Scandinavian Ice Sheet at 131 ka.** The calculation is based on the LAM ice history (see text) and an Earth model characterized by a lithosphere of 100 km thickness, an upper mantle viscosity of  $3 \times 10^{20}$  Pa s and a lower mantle viscosity of  $5 \times 10^{22}$  Pa s. The white zone in **a** represents the coverage of grounded ice

extent at this time and the dashed white line on this frame is the shoreline location. **b**, As for **a**, except the area of ice coverage is removed. It is clear from **a** that all but the southeast section of the perimeter of the Scandinavian ice sheet is predicted to be marine-based at this time, and from **b** that much of the interior of the ice sheet was also marine-based.



**Extended Data Fig. 6 | Results of sensitivity tests to oceanic forcing of the GrIS and AIS. a,** Response of the GrIS to atmospheric forcing from CCSM3 with fixed ocean temperatures for the PGM (blue line) and LIG (orange line) compared with the ice-sheet response to atmospheric and oceanic forcing (black line). The present-day interglacial ice volume shown by horizontal dashed line. **b,** Response of the AIS to atmospheric forcing from CCSM3 with fixed ocean temperatures for the PGM (blue line) and for the LIG (orange line) compared to ice-sheet response to atmospheric and oceanic forcing (black

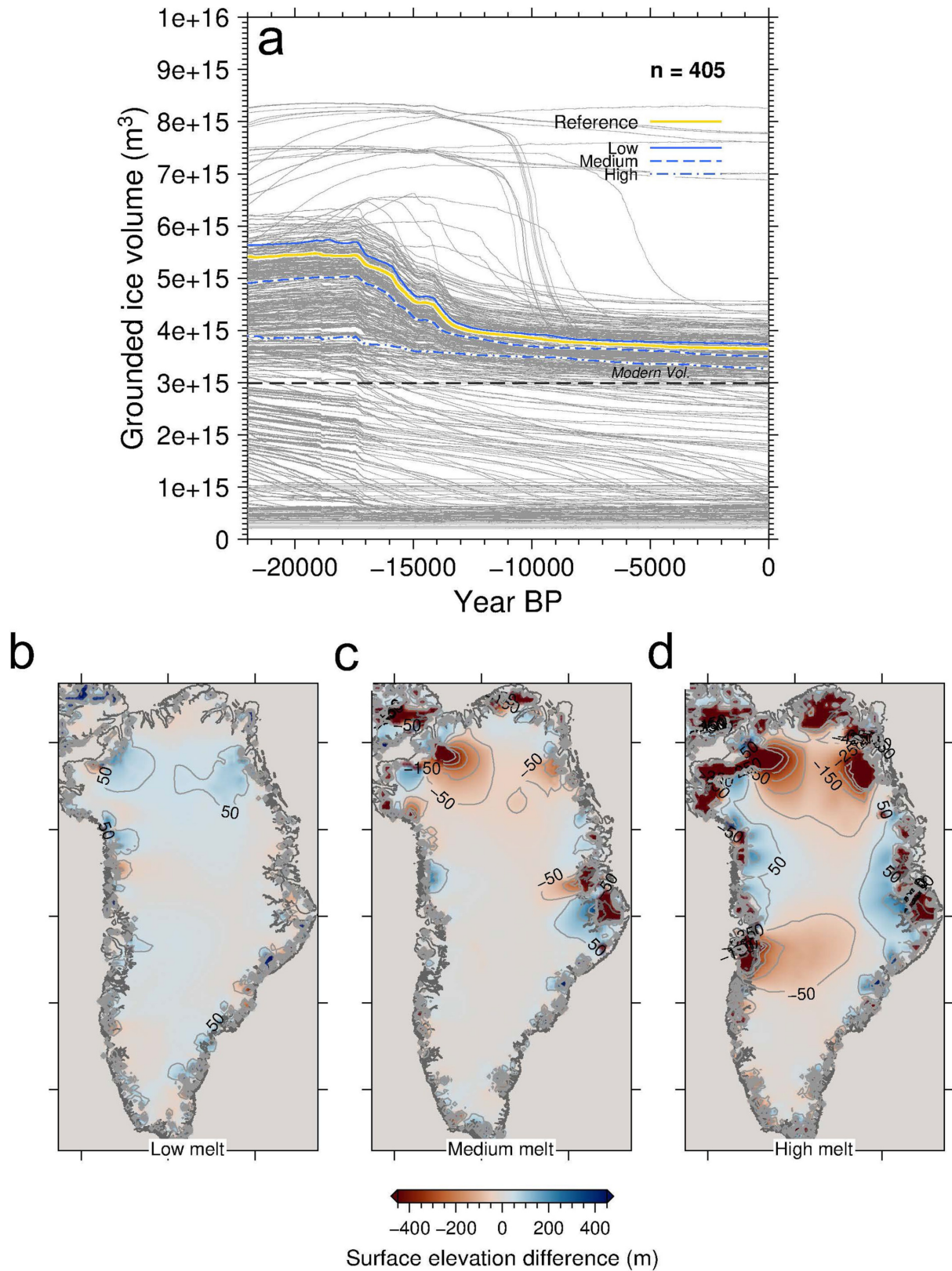
line). Present interglacial ice volume shown by the horizontal dashed line. **c,** As in **a**, but the vertical scale (grounded ice volume) has been increased to better illustrate the response. The initial ice-sheet size used in this experiment (and the comparable one for Antarctica) was the LIG ice sheet, whereas the climate forcing used was for the penultimate deglaciation and the LIG: that is, from a colder-than-present to LIG climate, resulting in a small response to the atmospheric forcing, as the LIG ice-sheet size had already adjusted to the combined atmospheric and oceanic forcing, as shown by the black line in **a**.



**Extended Data Fig. 7 | Predictions of RSL at three far-field sites (the Seychelles, Western Australia and Mallorca) and one intermediate-field site (the Bahamas).** **a–d**, RSL predictions for the Bahamas from the full suite of simulations that bound from above all of the coral data with the exception of the earliest datum (at 131 ka) for the COL ice history (**a**), the LAM ice history (**b**), the HYB ice history (**c**) and the WAE ice history (**d**). **e–h**, RSL predictions for the Seychelles from the full suite of simulations that lie above the three coral records with an elevation of  $\sim 4$  m for the COL ice history (**e**), the LAM ice history (**f**), the HYB ice history (**g**) and the WAE ice history (**h**). **i–l**, RSL predictions for

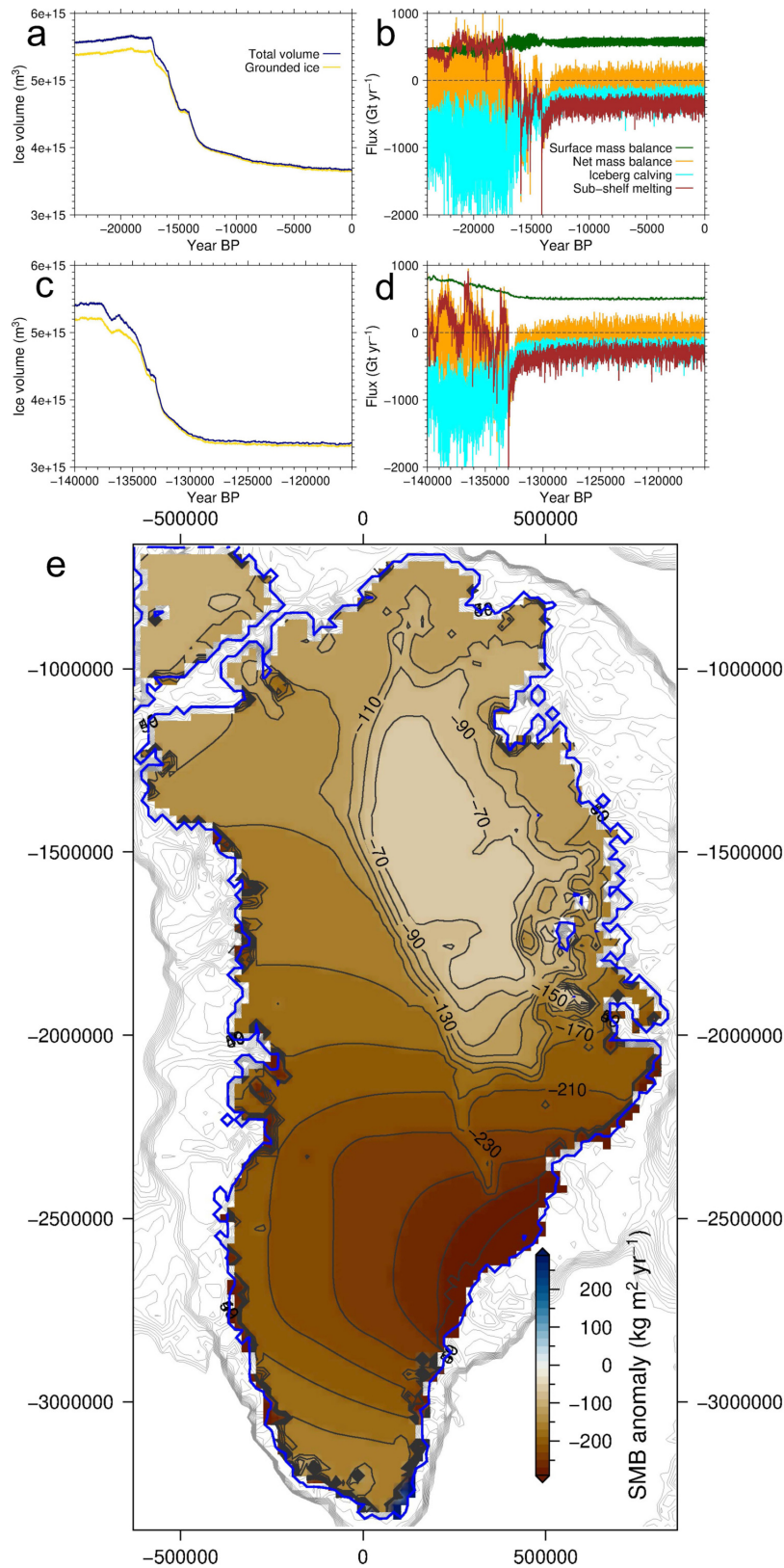
western Australia from the full suite of simulations that bound from above all of the coral data for the COL ice history (**i**), the LAM ice history (**j**), the HYB ice history (**k**) and the WAE ice history (**l**). The age uncertainty is  $2\sigma$ , and the depth uncertainty reflects the uncertainty in habitat depth. **m–p**, RSL predictions for Mallorca from the full suite of simulations that fit the data within 50% of the minimum misfit achieved for all simulations for the COL ice history (**m**), the LAM ice history (**n**), the HYB ice history (**o**) and the WAE ice history (**p**). The age uncertainty is  $2\sigma$ , and the depth uncertainty reflects the uncertainty in speleothem water depth.





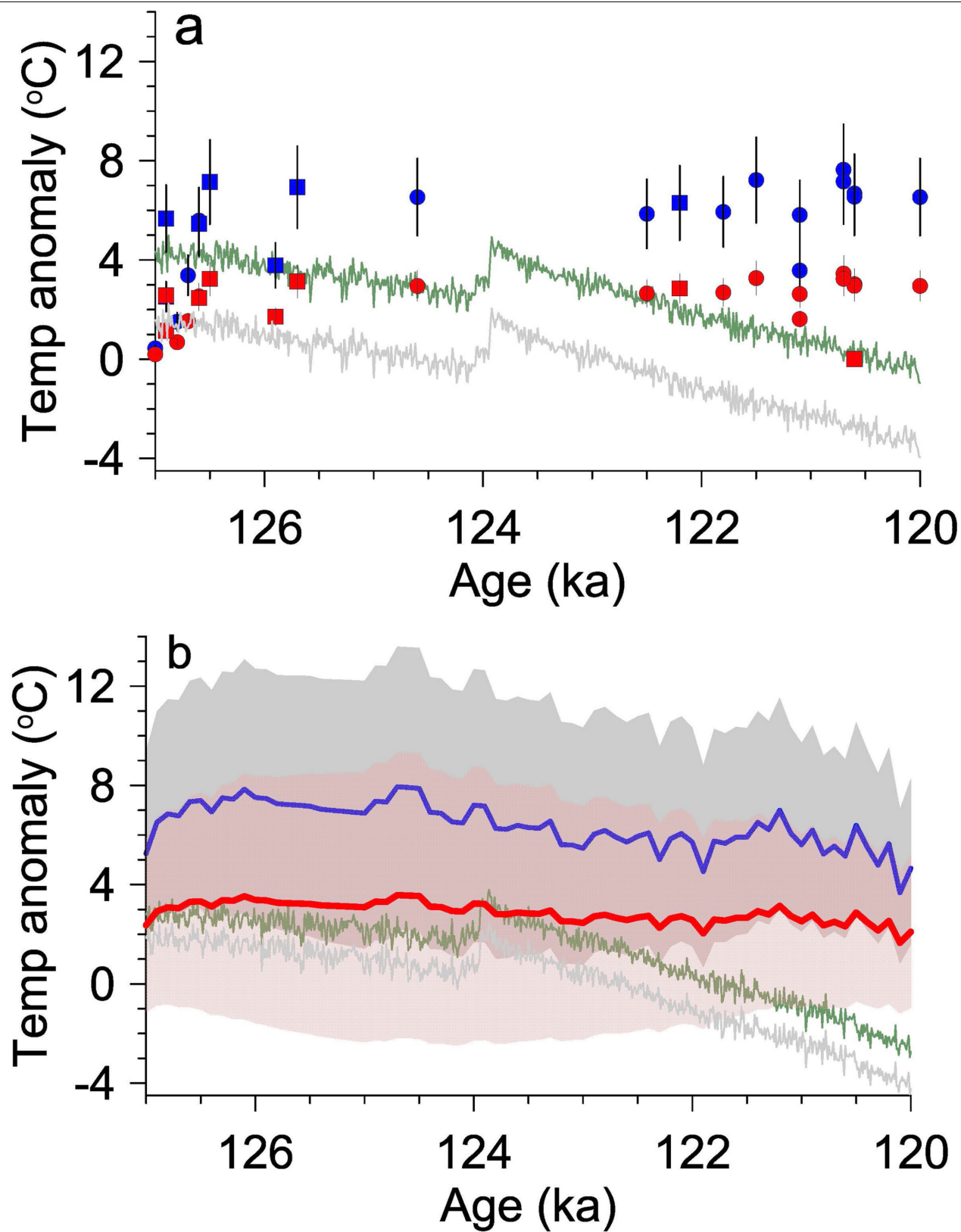
**Extended Data Fig. 8 | Sensitivity of the GrIS model to melt parameterization.** **a**, Time series of tuning experiments for the GrIS with the preferred run in blue and three runs used for **b–d** shown in green, orange, and red. **b–d**, Surface elevation differences under a present-day climatology at the end of the 40,000-yr T-I parameter tuning experiments, using degree-day factors drawn from our ensemble that give a low amount of surface melting (**b**),

a medium amount of surface melting (**c**), and a high amount of surface melting (**d**). Values shown are the differences from the reference experiment. These experiments are identical to the T-I reference experiment used to parameterize the T-II simulations (Fig. 3) except for the degree-day factors used. The results show that our ice-sheet model is sensitive to the way in which surface mass balance is parameterized by controlling the amount of surface melting.



**Extended Data Fig. 9 | Simulated ice-volume changes and components of the mass balance for the GrIS. a,** Simulated changes in ice volume for T-I. **b,** Simulated changes in mass-balance components for T-I. **c,** Simulated

changes in ice volume for T-II. **d,** Simulated changes in mass-balance components for T-II. **e,** Modelled surface mass balance anomaly during the LIG (129–120 ka) with respect to the modelled present-day mass balance.



Extended Data Fig. 10 | See next page for caption.

**Extended Data Fig. 10 | Comparison of our simulated summer temperature for Greenland ice-core sites with the temperature reconstructions for these sites based on  $\delta^{18}\text{O}_{\text{ice}}$ .** **a**, The simulated summer temperature (JJA) (grey line) and lapse-rate corrected JJA temperature (green line) compared with reconstructed temperatures for the GISP2 ice-core site (blue symbols,  $1\sigma$  uncertainty)<sup>66,73</sup> based on the relation  $d\delta^{18}\text{O}_{\text{ice}}/dT = -0.5\text{‰ C}^{-1}$ , which is derived from Greenland ice-core sites elsewhere<sup>74</sup>. Also shown are the reconstructed temperatures using the  $d\delta^{18}\text{O}_{\text{ice}}/dT$  relation established for the NEEM site ( $-1.1\text{‰ C}^{-1}$ )<sup>75</sup> (red symbols,  $1\sigma$  uncertainty), suggesting that the GISP2 LIG summer temperatures are about half of the originally published values based on the Vinther et al.<sup>74</sup>  $d\delta^{18}\text{O}_{\text{ice}}/dT$  relation and in good agreement with our

model results. **b**, The simulated JJA temperature (grey line) and lapse-rate corrected JJA temperature (green line) compared with reconstructed temperatures for the NEEM ice-core site (dark blue line, grey shading is uncertainty)<sup>65</sup> based on the relation  $d\delta^{18}\text{O}_{\text{ice}}/dT = -0.5\text{‰ C}^{-1}$  which is derived from Greenland ice-core sites elsewhere<sup>74</sup>. Also shown are the reconstructed temperatures using the  $d\delta^{18}\text{O}_{\text{ice}}/dT$  relation established for the NEEM site ( $-1.1\text{‰ C}^{-1}$ )<sup>75</sup> (red line, pink shading is uncertainty), suggesting that the NEEM LIG summer temperatures are about half of the originally published values based on the Vinther et al.<sup>74</sup>  $d\delta^{18}\text{O}_{\text{ice}}/dT$  relation and in good agreement with our model results. These reconstructions span the interval 127–120 ka, which is the warmest interval in the ice-core records for the LIG suggested by this proxy.



# Ancient West African foragers in the context of African population history

<https://doi.org/10.1038/s41586-020-1929-1>

Received: 27 November 2018

Accepted: 29 November 2019

Published online: 22 January 2020

Mark Lipson<sup>1\*</sup>, Isabelle Ribot<sup>2</sup>, Swapan Mallick<sup>1,3,4</sup>, Nadin Rohland<sup>1</sup>, Iñigo Olalde<sup>1,26</sup>, Nicole Adamski<sup>1,4</sup>, Nasreen Broomandkhoshbacht<sup>1,4,27</sup>, Ann Marie Lawson<sup>1,4</sup>, Saïoa López<sup>5</sup>, Jonas Oppenheimer<sup>1,4,28</sup>, Kristin Stewardson<sup>1,4</sup>, Raymond Neba'ane Asombang<sup>6</sup>, Hervé Bocherens<sup>7,8</sup>, Neil Bradman<sup>5,29</sup>, Brendan J. Culleton<sup>9</sup>, Els Cornelissen<sup>10</sup>, Isabelle Crevecoeur<sup>11</sup>, Pierre de Maret<sup>12</sup>, Forka Leypey Mathew Fomine<sup>13</sup>, Philippe Lavachery<sup>14</sup>, Christophe Mbida Mindzie<sup>15</sup>, Rosine Orban<sup>16</sup>, Elizabeth Sawchuk<sup>17</sup>, Patrick Semal<sup>16</sup>, Mark G. Thomas<sup>5,18</sup>, Wim Van Neer<sup>16,19</sup>, Krishna R. Veeramah<sup>20</sup>, Douglas J. Kennett<sup>21</sup>, Nick Patterson<sup>1,22</sup>, Garrett Hellenthal<sup>5,18</sup>, Carles Lalueza-Fox<sup>23</sup>, Scott MacEachern<sup>24</sup>, Mary E. Prendergast<sup>1,25,30</sup> & David Reich<sup>1,3,4,22,30</sup>

Our knowledge of ancient human population structure in sub-Saharan Africa, particularly prior to the advent of food production, remains limited. Here we report genome-wide DNA data from four children—two of whom were buried approximately 8,000 years ago and two 3,000 years ago—from Shum Laka (Cameroon), one of the earliest known archaeological sites within the probable homeland of the Bantu language group<sup>1–11</sup>. One individual carried the deeply divergent Y chromosome haplogroup A00, which today is found almost exclusively in the same region<sup>12,13</sup>. However, the genome-wide ancestry profiles of all four individuals are most similar to those of present-day hunter-gatherers from western Central Africa, which implies that populations in western Cameroon today—as well as speakers of Bantu languages from across the continent—are not descended substantially from the population represented by these four people. We infer an Africa-wide phylogeny that features widespread admixture and three prominent radiations, including one that gave rise to at least four major lineages deep in the history of modern humans.

The deposits at Shum Laka, a rockshelter located in the Grassfields region of western Cameroon, are among the most important archaeological sources for the study of Late Pleistocene and Holocene prehistory in western Central Africa<sup>1–4</sup>. The oldest human-occupied layers at the site date to about 30,000 calendar years before present (BP; taken as AD 1950 in accordance with radiocarbon calibration convention), but of special interest are artefacts and skeletons dating to between the end of the Later Stone Age (about 8,000 BP) and the beginning of the Iron Age (about 2,500 BP) (Extended Data Fig. 1, Supplementary Information section 1). This transitional period—sometimes referred to as the ‘Stone to Metal Age’—featured a gradual appearance of new stone tools, as well as pottery<sup>3–5</sup>. Subsistence evidence in the rockshelter during the Stone to Metal Age points primarily to foraging, but with an

increasing use of the fruits of *Canarium schweinfurthii* that coincided with developments in material culture and served as a foundation for later agriculture<sup>3</sup> (Supplementary Information section 1, Supplementary Table 1). These cultural changes and their early appearance at Shum Laka are particularly intriguing because during the late Holocene epoch, the area around the present-day border between Cameroon and Nigeria was probably the cradle of the Bantu language group, and of populations whose descendants would spread across much of the southern half of Africa between about 3,000 and 1,500 BP, resulting in the vast range and diversity of Bantu languages today<sup>6–11</sup>.

A total of 18 human skeletons have been discovered at Shum Laka, comprising 2 distinct burial phases<sup>1–3</sup> (Supplementary Information section 1). We attempted to retrieve DNA from six petrous-bone samples

<sup>1</sup>Department of Genetics, Harvard Medical School, Boston, MA, USA. <sup>2</sup>Département d'Anthropologie, Université de Montréal, Montreal, Quebec, Canada. <sup>3</sup>Medical and Population Genetics Program, Broad Institute of MIT and Harvard, Cambridge, MA, USA. <sup>4</sup>Howard Hughes Medical Institute, Harvard Medical School, Boston, MA, USA. <sup>5</sup>UCL Genetics Institute, University College London, London, UK. <sup>6</sup>Department of Arts and Archaeology, University of Yaoundé I, Yaoundé, Cameroon. <sup>7</sup>Department of Geosciences, Biogeology, University of Tübingen, Tübingen, Germany. <sup>8</sup>Senckenberg Research Centre for Human Evolution and Palaeoenvironment, University of Tübingen, Tübingen, Germany. <sup>9</sup>Institutes of Energy and the Environment, Pennsylvania State University, University Park, PA, USA. <sup>10</sup>Department of Cultural Anthropology and History, Royal Museum for Central Africa, Tervuren, Belgium. <sup>11</sup>CNRS, UMR 5199-PACEA, Université de Bordeaux, Bordeaux, France. <sup>12</sup>Faculté de Philosophie et Sciences Sociales, Université Libre de Bruxelles, Brussels, Belgium. <sup>13</sup>Department of History and African Civilization, University of Buea, Buea, Cameroon. <sup>14</sup>Agence Wallonne du Patrimoine, Service Public de Wallonie, Namur, Belgium. <sup>15</sup>Department of Arts and Archaeology, University of Yaoundé I, Yaoundé, Cameroon. <sup>16</sup>Royal Belgian Institute of Natural Sciences, Brussels, Belgium. <sup>17</sup>Department of Anthropology, Stony Brook University, Stony Brook, NY, USA. <sup>18</sup>Department of Genetics, Evolution and Environment, University College London, London, UK. <sup>19</sup>Department of Biology, University of Leuven, Leuven, Belgium. <sup>20</sup>Department of Ecology and Evolution, Stony Brook University, Stony Brook, NY, USA. <sup>21</sup>Department of Anthropology, University of California, Santa Barbara, CA, USA. <sup>22</sup>Department of Human Evolutionary Biology, Harvard University, Cambridge, MA, USA. <sup>23</sup>Institute of Evolutionary Biology (CSIC-UPF), Barcelona, Spain. <sup>24</sup>Division of Social Science, Duke Kunshan University, Kunshan, China. <sup>25</sup>Department of Sociology and Anthropology, Saint Louis University, Madrid, Spain. <sup>26</sup>Present address: Institute of Evolutionary Biology (CSIC-UPF), Barcelona, Spain. <sup>27</sup>Present address: Department of Anthropology, University of California, Santa Cruz, CA, USA. <sup>28</sup>Present address: Department of Biomolecular Engineering, University of California, Santa Cruz, CA, USA. <sup>29</sup>Present address: The Henry Stewart Group, London, UK. <sup>30</sup>These authors jointly supervised this work: Mary E. Prendergast, David Reich. \*e-mail: mlipson@genetics.med.harvard.edu

Table 1 | Details of the four Shum Laka individuals in the study

Identifier	Age at death	Date	Radiocarbon date	Sex	Mt haplogroup	Y haplogroup	Coverage	SNPs	Mt and X contamination (%)
2/SE I	4 ± 1	7,920–7,690	6,985 ± 30 (PSUAMS-6307)	M	L0a2a1	B	0.70	564,164	1.0 and 1.0
2/SE II	15 ± 3	7,970–7,800	7,090 ± 35 (PSUAMS-6308)	M	L0a2a1	A00	7.71	1,082,018	1.5 and 0.6
4/A	8 ± 2	3,160–2,970	2,940 ± 20 (PSUAMS-6309)	M	L1c2a1b	B2b	3.83	935,777	0.3 and 0.5
5/B	4 ± 1	3,210–3,000	2,970 ± 25 (PSUAMS-6310)	F	L1c2a1b	NA	6.41	1,014,618	0.5 and NA

Age at death is given in years (mean ± s.e.m.), and was determined from skeletal remains<sup>2</sup>. Sex was determined from genetic data. Date is given in calibrated years BP as a 95.4% confidence interval (Methods). Radiocarbon date is given in uncalibrated radiocarbon years before present (mean ± s.e.m.), with the laboratory sample code shown in parentheses. Coverage refers to the average sequencing coverage, and contamination to the estimated contamination from mtDNA (Mt) or the X chromosome (X). NA, not applicable. Y, Y chromosome. Additional information is provided in Supplementary Table 2.

and obtained working data from two individuals of the early Stone to Metal Age and two of the late Stone to Metal Age (about 8,000 and 3,000 BP, respectively) (Table 1, Supplementary Table 2). The two earlier individuals—a boy of 4 ± 1 years old at time of death (given the identifying code 2/SE I) lying on top of the lower limbs of an adolescent male of 15 ± 3 years old (denoted 2/SE II)<sup>2</sup>—were recovered from a primary double burial, and the two later individuals—a boy of 8 ± 2 years (denoted 4/A) and a girl of 4 ± 1 years (denoted 5/B)<sup>2</sup>—were in adjacent primary single burials.

We extracted DNA from bone powder and prepared 2 or 4 libraries per individual for Illumina sequencing, enriching for about 1.2 million target single-nucleotide polymorphisms (SNPs) across the genome (Methods, Supplementary Table 2). Final coverage ranged from 0.7 to 7.7× (from 0.56 to 1.08 million SNPs). The authenticity of the data was supported by the observed rate of apparent C-to-T substitutions in the final base of sequenced fragments (4–10%, within the expected range given our library preparation strategy<sup>14</sup>) and of heterozygosity for mitochondrial DNA (mtDNA) and for the X chromosome in males (estimated contamination 0.3–1.5%). We also generated whole-genome shotgun sequence data for individuals 2/SE II (about 18.5× coverage) and 4/A (about 3.9× coverage), as well as genome-wide data (about 598,000 SNPs) for 63 individuals from 5 present-day Cameroonian populations (Extended Data Table 1, Supplementary Table 3).

Uniparental markers and kinship analysis

All of the mtDNA and Y chromosome haplogroups we observe at Shum Laka are associated today with sub-Saharan Africans. The two earlier individuals carry mtDNA haplogroup L0a (specifically L0a2a1), which is widespread in Africa, and the two later individuals carry L1c (specifically L1c2a1b), which is found among both farmers and hunter-gatherers in Central and West Africa<sup>15,16</sup>. Individuals 2/SE I and 4/A have Y chromosomes from macrohaplogroup B (often found today in hunter-gatherers from Central Africa<sup>17</sup>), and 2/SE II has the rare Y chromosome haplogroup A00, which was discovered in 2013 and is present at appreciable frequencies only in Cameroon—in particular, among the Mbo and Bangwa in the western part of the country<sup>12,13</sup>. A00 is the oldest known branch of the modern human Y chromosome tree, with a split time of about 300,000–200,000 BP from all other known lineages<sup>12,18,19</sup>. At 1,666 positions (from whole-genome sequence data; Supplementary Table 4) that differ between present-day A00<sup>18</sup> and all other Y chromosomes, the sequence of the Shum Laka individual carries the non-reference allele at a total of 1,521, translating to a within-A00 split at about 37,000–25,000 BP (95% confidence interval) (Fig. 1, Methods).

Leveraging the effects of chromosomal segments that are shared identical by descent (IBD), we computed rates of allele matching for each pair of individuals to infer degrees of relatedness. Both of the contemporaneous pairs display elevated levels of matching: 2/SE I and 2/SE II share alleles at the level of fourth-degree relatives, and 4/A and 5/B at the level of second-degree relatives (either uncle and niece, aunt and nephew or half-siblings) (Extended Data Fig. 2), supporting

archaeological interpretations that—during both burial phases—the rockshelter was used as a cemetery for extended families<sup>2</sup>. We would expect more recent shared ancestry for the contemporaneous pairs even if they were not closely related, but we observe clear signatures of long IBD segments across the genome, which confirms their close family relatedness (Supplementary Information section 2). All four individuals also have evidence of intra-individual IBD, and thus of recent inbreeding.

PCA and allele-sharing statistics

We visualized the genome-wide relationships between the Shum Laka individuals and diverse present-day and ancient sub-Saharan Africans (Extended Data Table 1) using principal component analysis (PCA). Initially, we computed axes using East and West Africans and hunter-gatherers from southern Africa and eastern Central Africa (Fig. 2a). The Shum Laka individuals project to the right of present-day West African populations and speakers of Bantu languages (hereafter, Bantu-speakers) and are closest to present-day hunter-gatherers from Cameroon (Baka, Bakola and Bedzan<sup>20</sup>) and the Central African Republic (Aka, often known as Biaka). We then carried out a second PCA using only West and East Africans and Aka to compute the axes, and again the Shum Laka individuals project in the direction of hunter-gatherers from western Central Africa (Fig. 2b). By contrast, present-day groups from western Cameroon, who speak languages from the Niger–Congo family, cluster tightly with other West Africans (Fig. 2, Extended Data Fig. 3a). In both plots, the two earlier Shum Laka individuals fall slightly closer to West and East Africans, but—on the basis of their overall similarity—we grouped all four Shum Laka individuals together for most subsequent analyses.

Using *f*-statistics (Fig. 3a), we investigated components of ‘deep ancestry’ from sources that diverged earlier than the split between non-Africans and most sub-Saharan Africans (above point (2) in Fig. 4a). We began with the statistic *f*<sub>4</sub>(X, Mursi; ancient South African hunter-gatherers, Han), which is expected to be positive if deep ancestry in

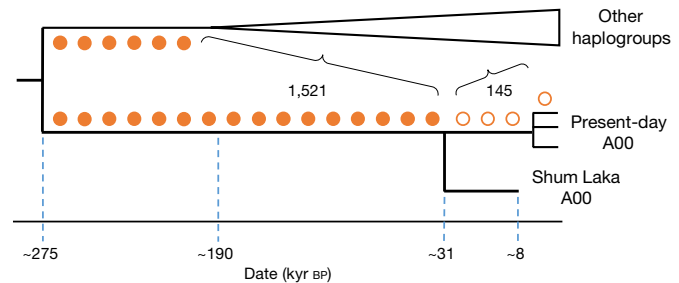
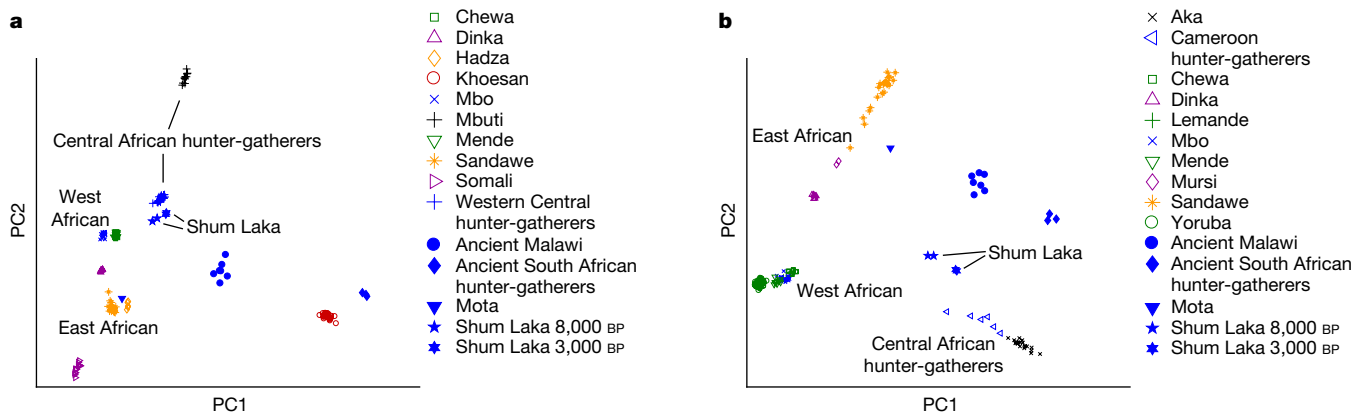


Fig. 1 | Y chromosome phylogeny. Circles represent mutations along the (unrooted) A00 lineage where we observe the alternative (filled) or reference (empty) allele in the A00 sequence carried by Shum Laka individual 2/SE II. Branch lengths are not drawn to scale. kyr, thousand years.



**Fig. 2 | PCA results. a**, Broad-scale analysis. **b**, Narrow-scale analysis. Groups in blue (including ancient individuals (filled symbols)) were projected onto axes computed using the other populations, using 593,124 SNPs (Methods). The

population *X* induces allele-sharing between *X* and ancient South African hunter-gatherers<sup>21,22</sup> (with a baseline of zero set by the Mursi, a group of pastoralists from western Ethiopia who speak a Nilotic language<sup>20</sup>). The Shum Laka individuals show a large positive statistic that is comparable to that of hunter-gatherers from western Central Africa (Fig. 3a top), whereas other West Africans (for example, Yoruba and Mende) yield smaller—but still significantly positive (Fig. 3a)—values, as do East African hunter-gatherers (the Hadza from Tanzania, as well as the ancient individual from Mota Cave in Ethiopia (hereafter, Mota individual), dating to approximately 4,500 BP<sup>23</sup>). We also obtained consistent results from analogous statistics using different reference groups (Extended Data Table 2).

Next, using chimpanzees as an outgroup that is symmetric to all human populations, we computed  $f_4(X, \text{Mursi}; \text{chimpanzee, ancient South African hunter-gatherers})$  to evaluate whether any of this deep ancestry is from sources that diverged more deeply than southern African hunter-gatherers (the modern human lineage with the oldest known average split date<sup>21,24,25</sup>). Previous work has shown that southern African hunter-gatherers are not a symmetric outgroup relative to other sub-Saharan Africans: West Africans (especially the Mende) have excess affinity towards deeper outgroups<sup>22</sup>. Indeed, our test statistic is maximized in Mende and other West Africans (Fig. 3a, bottom). The Hadza, and the Mota individual, have values close to zero, and the Shum

western Central hunter-gatherer group in **a** comprises the Aka plus Cameroon hunter-gatherers (Baka, Bakola and Bedzan).

Laka individuals and Central African hunter-gatherers are intermediate. Some populations yield positive values for both  $f_4$ -statistics (Fig. 3a), but the two sets are poorly correlated, which implies that they—at least in part—reflect separate signals.

Combining our newly genotyped individuals with published data<sup>20</sup>, we searched for differential allele-sharing between the Shum Laka individuals (compared to either East Africans (Somali) or to the Aka) and present-day Cameroonians (Fig. 3b, Extended Data Fig. 3b). We identified three distinct clusters: (1) Mada and Fulani, (2) hunter-gatherers and (3) other populations who speak languages in the Niger–Congo family (shown in close-up in Fig. 3b). Within the third cluster are the only groups—Mbo, Aghem and Bafut (all of whom live close to the site of Shum Laka today)—with significantly Shum-Laka-directed statistics in both dimensions, consistent with small proportions of Shum-Laka-related admixture (a maximum of about 7–8%) (Supplementary Information section 3).

### Admixture graph analysis

Finally, we built an admixture graph (Fig. 4a, Extended Data Fig. 4, Methods) comodelling the Shum Laka, Mota and ancient South African hunter-gatherer individuals; present-day Mbuti, Aka, Agaw (speakers of an Afroasiatic language, from Ethiopia<sup>20</sup>), Yoruba, Mende and

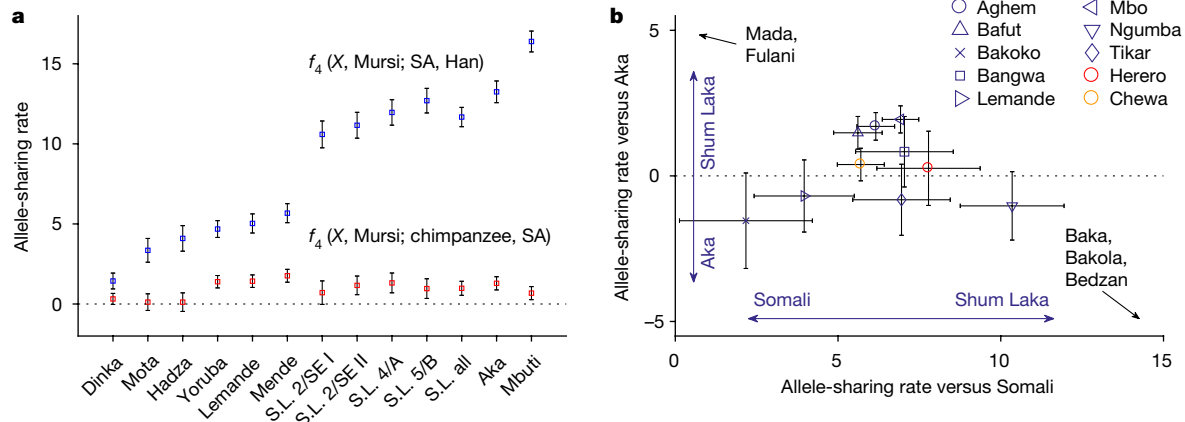


**Fig. 3 | Allele-sharing statistics. a**, Statistics sensitive to deep ancestry (mean  $\pm$  2 s.e.m., multiplied by 1,000). Blue, deeper than non-Africans; red, deeper than southern African hunter-gatherers; computed on 1,121,119 SNPs. SA, ancient South African hunter-gatherers; S.L., Shum Laka. **b**, Relative allele sharing (mean  $\pm$  s.e.m., multiplied by 10,000; computed on 538,133 SNPs) with

the Shum Laka individuals versus East Africans ( $f_4(X, \text{Yoruba}; \text{Shum Laka, Somali})$ ; x axis) and versus Aka ( $f_4(X, \text{Yoruba}; \text{Shum Laka, Aka})$ ; y axis) for present-day populations from Cameroon (blue) and southern (Herero, red) and eastern (Chewa, orange) Bantu-speakers. See also Extended Data Fig. 3b.

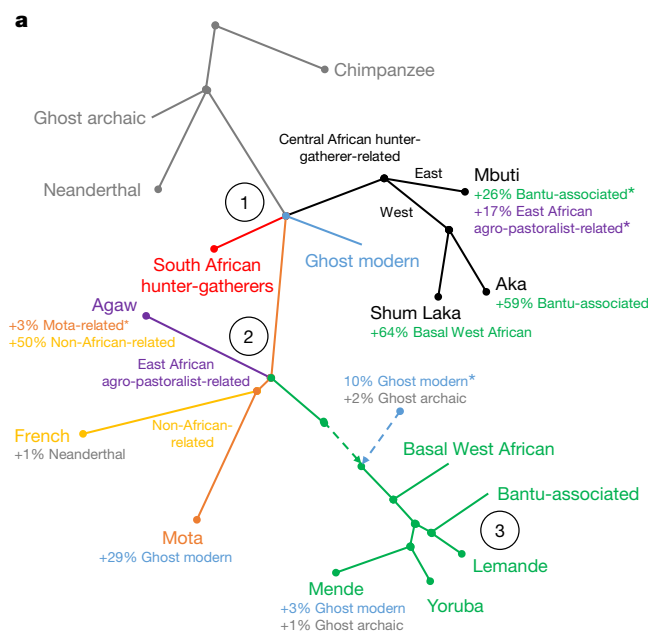


**Fig. 4 | Admixture graph results.** Points at which multiple lineages are shown diverging simultaneously indicate splits occurring in short succession (the order of which we cannot confidently assess) but do not represent exact multifurcations. Key points are (1) the early modern human split, (2) East African divergences and (3) the expansion of ancestry associated with Bantu-speakers. Branch lengths are not drawn to scale. **a**, Full model (Extended Data

Lemane; non-Africans (French); and two outgroups (Neanderthal and chimpanzees). We also fit versions of the model using alternative SNP ascertainment and additional populations (Hadza, Mbo, Herero, Chewa, Mursi, Baka, Bakola, Bedzan, Mada, Fulani and ancient individuals from Taforalt in Morocco<sup>26</sup>) and obtained similar results (Extended Data Table 3, Supplementary Information section 3).

Among modern humans, the deepest-splitting branch is inferred to be the one that leads to Central African hunter-gatherers, although four lineages diverge in a very short span: those that contribute the primary ancestry to (1) Central African hunter-gatherers, (2) southern African hunter-gatherers and (3) other modern human populations, along with (4) a 'ghost' source that contributes a minority of the ancestry in West Africans and the Mota individual. Central African hunter-gatherers separate into eastern (Mbuti) and western clades; the latter then branches into components represented in Aka and the Shum Laka individuals. Next, a second cluster of divergences involves West Africans, two East African lineages (one associated with hunter-gatherers and another with agro-pastoralists) and non-Africans (who are tentatively inferred to split closest to the Mota individual, but with no deep ghost ancestry). Within the West African clade, we identify Yoruba and Mende as sister groups (with Lemane as an outgroup), and—most basally—a separate lineage that contributed to the Shum Laka individuals (64%). A source associated with Bantu-speakers (most closely related to Lemane) contributes 59% of the ancestry in Aka and 26% in Mbuti (who also have ancestry (17%) from a source related to agro-pastoralists of East Africa). In a model separating the two pairs of Shum Laka individuals, the pair dating to 3,000 BP have about 5% more ancestry related to hunter-gatherers from Central Africa (as confirmed by the significantly positive statistic  $f_4$ (Shum Laka 8,000 BP, Shum Laka 3,000 BP; Yoruba, Aka) ( $Z = 4.2$ )) (Supplementary Information section 3).

We can also obtain a good fit for the Shum Laka individuals in a less-parsimonious alternative model using three components, replacing the basal West African source with a combination of ancestry from inside the clade defined by the other West African populations and from a source

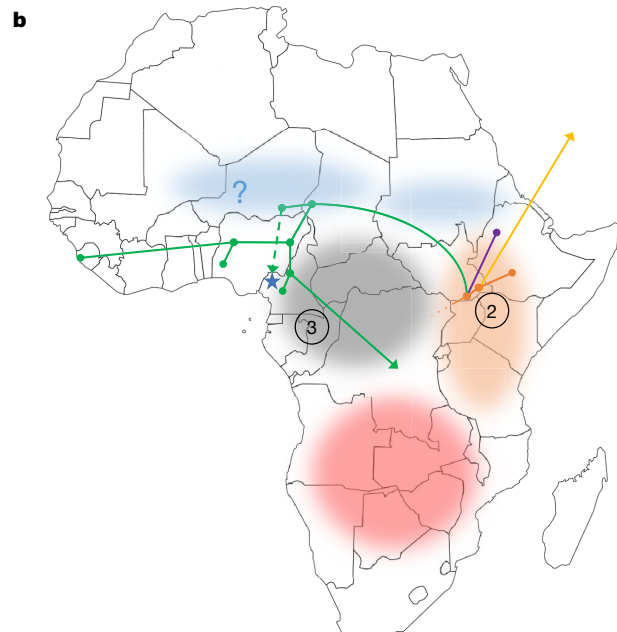


**Fig. 4). \*Proportion not well-constrained. b**, Geographical structure. Shaded areas denote the hypothesized historical locations of lineages descended from split point (1) in **a**, and branching order is shown for populations descended from split point (2) (one ancestry component per population, with leaf nodes at sampling locations). The blue star represents Shum Laka (dashed line, possible direction of gene flow).

entirely outside the West African clade (near one lineage that contributes to the Taforalt individuals) (Extended Data Fig. 5, Supplementary Information section 3). However, two-component models for the Shum Laka individuals that have the majority source splitting closer to other West or East Africans are rejected ( $Z = 7.1$  and  $Z = 3.7$ , respectively).

The West African clade is distinguished by admixture from a deep source that can be modelled as a combination of modern human and archaic ancestry. The modern human component diverges at almost the same point as Central and southern African hunter-gatherers and is tentatively related to the deep source that contributes ancestry to the Mota individual, and the archaic component diverges close to the split between Neanderthals and modern humans (Supplementary Information section 3). The signals of deep ancestry in groups related to the West African clade (Fig. 3a) can be explained by two admixture events: one along the ancestral West African lineage, and a second, smaller contribution (about 4%) to Mende from the same source (Fig. 4a). Accordingly,  $f_4$  statistics testing for ancestry basal to southern African hunter-gatherers (Fig. 3a, bottom) are well-correlated with the inferred proportions of ancestry from the West African clade (Extended Data Fig. 6). We estimate the shared admixture to introduce 10% deep modern human and 2% archaic ancestry, although the first proportion is not well-constrained (Extended Data Table 3). An alternative model with no archaic component—in which the West African clade receives deep ancestry from a single source<sup>22</sup> that splits before point (1) in Fig. 4a—also provides a reasonable fit to the data (Extended Data Fig. 7, Supplementary Information section 3), although it does not account for previous evidence of archaic ancestry in sub-Saharan Africans<sup>27–31</sup>.

## Genetics and archaeology at Shum Laka

Our analyses show that the 4 sampled children from Shum Laka can be modelled as admixed with about 35% ancestry related to hunter-gatherers from western Central Africa and about 65% from a basal West African source, or—alternatively—as a mixture of ancestry related to



hunter-gatherers plus two additional components, one from inside the clade of present-day West Africans and one that splits between East and West Africans. The first component plausibly represents ancestry that has been present in the area since at least the Later Stone Age (prior to 8,000 BP), whereas the second component (or the third in the alternative model) may have its origins farther to the north, given the geography and phylogeny of the other populations we studied (Fig. 4b). The chronology of the archaeological record at Shum Laka also suggests a possible northern influence on cultural developments during the Stone to Metal Age<sup>3,9</sup>. These developments include (1) changes in stone tools (which can be interpreted as a fusion of local tool-making traditions of the Later Stone Age with new macrolithic technologies that were introduced from the north<sup>3</sup>), and (2) the appearance of ceramics (four sherds have been found in the burial layer associated with the early Stone to Metal Age, and more abundant and distinct ceramics are found in later Stone to Metal Age deposits), which are potentially related to earlier pottery-working traditions in the Sahara and Sahel<sup>3,32</sup>. Moreover, gene flow from the north before 8,000 BP is plausible in light of a short period of Saharan and Sahelian aridification<sup>3,33</sup>, which could have contributed to population movements. Present-day groups in northern West Africa and the Sahel have substantial admixture connected to later migrations<sup>34</sup>, so identifying the exact source area may require additional ancient DNA studies.

Although the scope of our sampling is limited to two individuals at either end of the Stone to Metal Age, the observed genetic similarity across a span of almost 5,000 years—a similarity that is consistent with skeletal morphometric analyses—suggests a long-term presence of related peoples who used the rockshelter for various activities, including burying their dead (Supplementary Information section 1). However, most populations in Cameroon today are more closely related to other West Africans than to the group represented by these individuals. Present-day hunter-gatherers in Cameroon are also not descended substantially from this specific group, as they lack the signal of basal West African ancestry (Supplementary Information section 3). We do observe elevated levels of allele-sharing between the Shum Laka individuals and present-day populations of the Grassfields region, so the genetic discontinuity is not absolute. Additionally, the adolescent male 2/SE II carried an A00 Y chromosome, which suggests both that the concentration of this haplogroup in western Cameroon may have a long history and that A00 was formerly more diverse (given that the Shum Laka sequence falls outside of known present-day variation)<sup>12,13</sup>. The divergence time of A00 from other modern human haplogroups, of about 300,000–200,000 BP<sup>18,19</sup>, could support its association either with the component of the ancestry of the Shum Laka individuals that is related to Central African hunter-gatherers or with the deep modern human portion of their West-African-related ancestry.

Linguistic and genetic evidence points to western Cameroon as the most likely area for the development of Bantu languages and as the ultimate source of subsequent migrations of Bantu-speakers, and—although the regional mid-Holocene archaeological record is sparse—Shum Laka has previously been highlighted as a site that was potentially important in the early phase of this process<sup>1–4,6–11</sup>. However, the genetic profiles of our four sampled individuals—even by about 3,000 BP, when the spreads of Bantu languages and of ancestry associated with Bantu-speakers were already underway—are very different from those of most speakers of Niger–Congo languages today, which implies that these individuals are not representative of the primary source population(s) that were ancestral to present-day Bantu-speakers. These results neither support nor contradict a central role for the Grassfields area in the origins of Bantu-speakers, and it may be that multiple, highly differentiated populations formerly lived in the region—with potentially either high or low levels of linguistic diversity. It would not be surprising if the Shum Laka site itself was used (either successively or concurrently) by multiple groups with different ancestry, cultural traditions or languages<sup>1</sup>, evidence of which may not be visible from the collection of remains as preserved today.

## Implications for deep population history

By analysing data from Shum Laka and other ancient individuals in conjunction with present-day groups, we gain insights into African population structure on multiple timescales. First, we infer a series of closely spaced population splits that involve one West-African-related lineage and two East-African-related lineages, as well as non-Africans (point (2) in Fig. 4a). The geography of the populations involved suggests the centre of this radiation was plausibly in East Africa (Fig. 4b), and estimated divergences of African and non-African populations place its date at about 80,000–60,000 BP<sup>24,35</sup>. Such an expansion is also consistent with mtDNA phylogeography—specifically the diversification of haplogroup L3, which probably originated in East Africa about 70,000 BP<sup>36,37</sup>—and potentially with the origins of clade CT in the Y chromosome tree at a similar time depth<sup>18,38</sup>.

Second, we infer a phase of divergences that involved at least four lineages early in the history of modern humans (point (1) in Fig. 4a). Recent consensus has been that southern African hunter-gatherers, who split from other populations about 250,000–200,000 BP, represent the deepest sampled branch of modern human variation<sup>21,24,25</sup>. Our results suggest that Central African hunter-gatherers split at close to the same time (or perhaps slightly earlier), and thus that both clades—as well as the lineage that would later diversify at point (2) (Fig. 4a)—originated as part of a large-scale radiation.

In addition to the well-characterized deep lineages, we also detect at least one deep ghost source that contributed to West Africans and East African hunter-gatherers. This signal corroborates previous evidence for the Hadza and Sandawe<sup>39</sup> and for West Africans<sup>22</sup>, although we find that the best fit is a source that splits near the same point as southern and Central African hunter-gatherers. Our results are also consistent with previous reports of archaic ancestry in African populations<sup>27–31</sup>, specifically in West Africans. The presence of deep ancestry in the West African clade is notable in light of the Pleistocene archaeological record<sup>5,40</sup>, which is limited but includes *Homo sapiens* fossils dated to about 300,000 BP in northwestern Africa<sup>41</sup>, as well as an individual with archaic features buried about 12,000 BP in southwestern Nigeria (the oldest known human fossil from West Africa proper)<sup>42</sup>. Middle Stone Age artefacts have also been found in parts of West Africa into the terminal Pleistocene<sup>43</sup>, despite the development of Later Stone Age technologies elsewhere (as, for example, at Shum Laka). Thus, the available material and fossil evidence is concordant with our genetic results in indicating long-term African population structure and admixture<sup>44,45</sup>.

Further genetic studies may reveal additional complexities in deep human population history, although some early human groups will probably remain known only through fossils<sup>44,45</sup>. On the basis of our current understanding, the presence of at least 4 modern human lineages that diversified about 250,000–200,000 BP and are represented in people living today provides further support for archaeological evidence that suggests this era was a pivotal period for human evolution in Africa.

## Online content

Any methods, additional references, Nature Research reporting summaries, source data, extended data, supplementary information, acknowledgements, peer review information; details of author contributions and competing interests; and statements of data and code availability are available at <https://doi.org/10.1038/s41586-020-1929-1>.

1. de Maret, P. In *Aspects of African Archaeology: Papers from the 10th Congress of the Pan-African Association of Prehistory and Related Studies* (eds Pwiti, G. & Soper, R.) 274–279 (Univ. of Zimbabwe Publications, Harare, 1996).
2. Ribot, I., Orban, R. & de Maret, P. *The Prehistoric Burials of Shum Laka Rockshelter (North-West Cameroon)* (Annales du Musée Royal de l'Afrique Centrale vol. 164) (Musée Royal de l'Afrique Centrale, Tervuren, 2001).
3. Lavachery, P. The Holocene archaeological sequence of Shum Laka rock shelter (Grassfields, western Cameroon). *Afr. Archaeol. Rev.* **18**, 213–247 (2001).

4. de Maret, P. in *The Oxford Handbook of African Archaeology* (eds Mitchell, P. & Lane, P.) 627–643 (Oxford Univ. Press, 2013).
5. Cornelissen, E. in *The Oxford Handbook of African Archaeology* (eds Mitchell, P. & Lane, P.) 403–417 (Oxford Univ. Press, 2013).
6. Vansina, J. New linguistic evidence and ‘the Bantu expansion’. *J. Afr. Hist.* **36**, 173–195 (1995).
7. Tishkoff, S. A. et al. The genetic structure and history of Africans and African Americans. *Science* **324**, 1035–1044 (2009).
8. Berniell-Lee, G. et al. Genetic and demographic implications of the Bantu expansion: insights from human paternal lineages. *Mol. Biol. Evol.* **26**, 1581–1589 (2009).
9. Bostoen, K. et al. Middle to late Holocene Paleoclimatic change and the early Bantu expansion in the rain forests of Western Central Africa. *Curr. Anthropol.* **56**, 354–384 (2015).
10. Patin, E. et al. Dispersals and genetic adaptation of Bantu-speaking populations in Africa and North America. *Science* **356**, 543–546 (2017).
11. Bostoen, K. in *Oxford Research Encyclopedia of African History* (ed. Spear, T.) <https://oxfordre.com/africanhistory/view/10.1093/acrefore/9780190277734.001.0001/acrefore-9780190277734-e-191> (Oxford Univ. Press, 2018).
12. Mendez, F. L. et al. An African American paternal lineage adds an extremely ancient root to the human Y chromosome phylogenetic tree. *Am. J. Hum. Genet.* **92**, 454–459 (2013).
13. Krahn, T., Schrack, B., Fomine, F. L. M. & Krahn, A.-M. Searching for our most distant (paternal) cousins in Cameroon. *Institute for Genetic Genealogy 2016 Conference, San Diego* (2016).
14. Rohland, N., Harney, E., Mallick, S., Nordenfelt, S. & Reich, D. Partial uracil-DNA-glycosylase treatment for screening of ancient DNA. *Phil. Trans. R. Soc. Lond. B* **370**, 20130624 (2015).
15. Gonder, M. K., Mortensen, H. M., Reed, F. A., de Sousa, A. & Tishkoff, S. A. Whole-mtDNA genome sequence analysis of ancient African lineages. *Mol. Biol. Evol.* **24**, 757–768 (2007).
16. Batini, C. et al. Phylogeography of the human mitochondrial L1c haplogroup: genetic signatures of the prehistory of Central Africa. *Mol. Phylogenet. Evol.* **43**, 635–644 (2007).
17. Wood, E. T. et al. Contrasting patterns of Y chromosome and mtDNA variation in Africa: evidence for sex-biased demographic processes. *Eur. J. Hum. Genet.* **13**, 867–876 (2005).
18. Karmin, M. et al. A recent bottleneck of Y chromosome diversity coincides with a global change in culture. *Genome Res.* **25**, 459–466 (2015).
19. Mendez, F. L., Poznik, G. D., Castellano, S. & Bustamante, C. D. The divergence of Neandertal and modern human Y chromosomes. *Am. J. Hum. Genet.* **98**, 728–734 (2016).
20. Fan, S. et al. African evolutionary history inferred from whole genome sequence data of 44 indigenous African populations. *Genome Biol.* **20**, 82 (2019).
21. Schlebusch, C. M. et al. Southern African ancient genomes estimate modern human divergence to 350,000 to 260,000 years ago. *Science* **358**, 652–655 (2017).
22. Skoglund, P. et al. Reconstructing prehistoric African population structure. *Cell* **171**, 59–71 (2017).
23. Gallego Llorente, M. et al. Ancient Ethiopian genome reveals extensive Eurasian admixture in Eastern Africa. *Science* **350**, 820–822 (2015).
24. Gronau, I., Hubisz, M. J., Gulko, B., Danko, C. G. & Siepel, A. Bayesian inference of ancient human demography from individual genome sequences. *Nat. Genet.* **43**, 1031–1034 (2011).
25. Mallick, S. et al. The Simons Genome Diversity Project: 300 genomes from 142 diverse populations. *Nature* **538**, 201–206 (2016).
26. van de Loosdrecht, M. et al. Pleistocene North African genomes link Near Eastern and sub-Saharan African human populations. *Science* **360**, 548–552 (2018).
27. Plagnol, V. & Wall, J. D. Possible ancestral structure in human populations. *PLoS Genet.* **2**, e105 (2006).
28. Hammer, M. F., Woerner, A. E., Mendez, F. L., Watkins, J. C. & Wall, J. D. Genetic evidence for archaic admixture in Africa. *Proc. Natl Acad. Sci. USA* **108**, 15123–15128 (2011).
29. Durvasula, A. & Sankararaman, S. Recovering signals of ghost archaic admixture in the genomes of present-day Africans. Preprint at bioRxiv <https://doi.org/10.1101/285734> (2018).
30. Hey, J. et al. Phylogeny estimation by integration over isolation with migration models. *Mol. Biol. Evol.* **35**, 2805–2818 (2018).
31. Ragsdale, A. P. & Gravel, S. Models of archaic admixture and recent history from two-locus statistics. *PLoS Genet.* **15**, e1008204 (2019).
32. Huysecom, E. et al. The emergence of pottery in Africa during the 10th millennium calBC: new evidence from Ounjougou (Mali). *Antiquity* **83**, 905–917 (2009).
33. Gasse, F. Hydrological changes in the African tropics since the Last Glacial Maximum. *Quat. Sci. Rev.* **19**, 189–211 (2000).
34. Triska, P. et al. Extensive admixture and selective pressure across the Sahel belt. *Genome Biol. Evol.* **7**, 3484–3495 (2015).
35. Laval, G., Patin, E., Barreiro, L. B. & Quintana-Murci, L. Formulating a historical and demographic model of recent human evolution based on resequencing data from noncoding regions. *PLoS ONE* **5**, e10284 (2010).
36. Soares, P. et al. The expansion of mtDNA haplogroup L3 within and out of Africa. *Mol. Biol. Evol.* **29**, 915–927 (2012).
37. Behar, D. M. et al. A “Copernican” reassessment of the human mitochondrial DNA tree from its root. *Am. J. Hum. Genet.* **90**, 675–684 (2012).
38. Poznik, G. D. et al. Punctuated bursts in human male demography inferred from 1,244 worldwide Y-chromosome sequences. *Nat. Genet.* **48**, 593–599 (2016).
39. Pickrell, J. et al. The genetic prehistory of southern Africa. *Nat. Commun.* **3**, 1143 (2012).
40. Scerri, E. in *Oxford Research Encyclopedia of African History* (ed. Spear, T.) <https://oxfordre.com/africanhistory/view/10.1093/acrefore/9780190277734.001.0001/acrefore-9780190277734-e-137> (Oxford University Press, 2017).
41. Hublin, J.-J. et al. New fossils from Jebel Irhoud, Morocco and the pan-African origin of *Homo sapiens*. *Nature* **546**, 289–292 (2017).
42. Harvati, K. et al. The later Stone Age calvaria from Iwo Eleru, Nigeria: morphology and chronology. *PLoS ONE* **6**, e24024 (2011).
43. Scerri, E. M., Blinkhorn, J., Niang, K., Bateman, M. D. & Groucutt, H. S. Persistence of Middle Stone Age technology to the Pleistocene/Holocene transition supports a complex hominin evolutionary scenario in West Africa. *J. Archaeol. Sci. Rep.* **11**, 639–646 (2017).
44. Scerri, E. M. L. et al. Did our species evolve in subdivided populations across Africa, and why does it matter? *Trends Ecol. Evol.* **33**, 582–594 (2018).
45. Henn, B. M., Steele, T. E. & Weaver, T. D. Clarifying distinct models of modern human origins in Africa. *Curr. Opin. Genet. Dev.* **53**, 148–156 (2018).

**Publisher's note** Springer Nature remains neutral with regard to jurisdictional claims in published maps and institutional affiliations.

© The Author(s), under exclusive licence to Springer Nature Limited 2020

## Methods

No statistical methods were used to predetermine sample size. The experiments were not randomized and investigators were not blinded to allocation during experiments and outcome assessment.

### Ancient DNA sample processing

We obtained bone powder from the Shum Laka skeletons (see Supplementary Information section 1 for more information on the site and burials) by drilling cochlear portions of petrous bone samples in a clean room facility at the Royal Belgian Institute of Natural Sciences. In dedicated clean rooms at Harvard Medical School, we extracted DNA using published protocols<sup>46,47</sup>. From the extracts, we prepared barcoded double-stranded libraries treated with uracil-DNA glycosylase (UDG) to reduce the rate of characteristic ancient DNA damage<sup>14,48</sup> in a modified partial UDG preparation that included magnetic bead clean-ups<sup>14,49</sup>. For the SNP capture data, we used two rounds of in-solution target hybridization to enrich for sequences that overlap the mitochondrial genome and approximately 1.2 million genome-wide SNPs<sup>50–54</sup>. We then added 7-base-pair indexing barcodes to the adapters of each library<sup>55</sup> and sequenced on an Illumina NextSeq 500 system with 76-base-pair paired-end reads. For individuals 2/SE II and 4/A, we also generated whole-genome shotgun data from the same libraries but without the target enrichment step. Sequencing was performed at the Broad Institute on Illumina HiSeq X Ten systems, using 19 lanes for 2/SE II (yielding approximately 18.5× average coverage, including 1,216,658 sites covered from the set of target SNPs used in most analyses) and two lanes for 4/A (3.9× average coverage, 1,158,884 sites covered).

From the raw sequencing results, we retained reads with no more than one mismatch per read pair to the library-specific barcodes. Before alignment, we merged paired-end sequences on the basis of forward and reverse mate overlaps and trimmed barcodes and adapters. Pre-processed reads were then mapped to both the mitochondrial reference genome RSR3<sup>37</sup> and the human reference genome (version hg19) using the same command with default parameters in BWA (version 0.6.1)<sup>56</sup>. Duplicate molecules (with the same mapped start and end positions and strand orientation) were removed after alignment. We filtered the mapped sequences (requiring mapping quality scores of at least 10 for targeted SNP capture and 30 for whole-genome shotgun data) and trimmed 2 terminal bases to eliminate almost all damage-induced errors.

For mtDNA, we called haplogroups using HaploGrep2<sup>57</sup>. For nuclear DNA obtained from SNP capture and for the whole-genome shotgun data for individual 4/A, we selected one allele at random per site to create pseudohaploid genotypes. For the whole-genome shotgun data for individual 2/SE II, we used a previously described reference-bias-free diploid-genotype calling procedure<sup>25</sup>, converting the resulting genotypes into a fasta-like encoding that allows for extraction of data at specified sites using cascertain and cTools<sup>25</sup>. We determined the sex of each individual by examining the fractions of sequences mapping to the X and Y chromosomes<sup>58</sup>, and we determined Y chromosome haplogroups by comparing sequence-level SNP information to the tree established by the International Society of Genetic Genealogy (<http://www.isogg.org>).

To ensure authenticity, we computed the proportion of C-to-T deamination errors in terminal positions of sequenced molecules and evaluated possible contamination via heterozygosity at variable sites in haploid genome regions, using contamMix<sup>50</sup> and ANGSD<sup>59</sup> for mtDNA and the X chromosome (in males), respectively. Observed damage rates (4–10%) were relatively low but within the expected range after partial UDG treatment<sup>14</sup>, and apparent heterozygosity rates for mtDNA (0.3–1.5% estimated contamination) and the X chromosome (0.5–1.0% estimated contamination) were minimal. The molecular preservation of the samples is impressive given the long-term warm and humid climate

at Shum Laka<sup>60</sup> (which supports a mixed forest–savannah environment, at an elevation of about 1,650 m above sea level).

### Radiocarbon dates

At the Pennsylvania State University (PSU) Radiocarbon Laboratory, we generated direct radiocarbon dates via accelerator mass spectrometry (AMS) for the four analysed individuals, using fragments of the same temporal bone portions that were sampled for ancient DNA. We extracted and purified amino acids using a modified XAD process<sup>61</sup> and assessed sample quality using stable isotope analysis. C:N ratios for all 4 samples fell between 3.3 and 3.4, well within the nominal range of 2.9–3.6 that indicates good collagen preservation<sup>62</sup>. The PSU AMS dates were in good agreement with previously reported direct dates for different bones from individuals 2/SE II ( $7,150 \pm 70$  uncalibrated radiocarbon years before present, calibrated to 8,160–7,790 BP (Oxford Radiocarbon Accelerator Unit sample code OxA-5203)) and 4/A ( $3,045 \pm 60$  uncalibrated radiocarbon years before present, calibrated to 3,380–3,010 BP, OxA-5205)<sup>1,2,63,64</sup>, but on the basis of a (modestly) aberrant date<sup>65</sup> from a rib of individual 2/SE I (Supplementary Table 5), we restricted our final reported results to the temporal bones. We performed calibrations using OxCal<sup>66</sup> version 4.3.2 with a mixture of the IntCal13<sup>67</sup> and SHCal13<sup>68</sup> curves, specifying 'U(0,100)' to allow for a flexible combination<sup>66,69</sup>, and rounding final results to the nearest 10 years (Supplementary Information section 1).

### Present-day data

We generated genome-wide SNP genotype data for 63 individuals from 5 present-day Cameroonian populations on the Human Origins array: Aghem (28), Bafut (11), Bakoko (1), Bangwa (2) and Mbo (21) (Extended Data Table 1, Supplementary Table 3). Samples were collected with informed consent, with collection and analysis approved by the UCL/UCLH Committee on the Ethics of Human Research, Committee A and Alpha.

### A00 Y chromosome split time estimation

Present-day A00 Y chromosomes are classified into the subtypes A00a, A00b and A00c, the divergence times of which from each other have not been precisely estimated but are quite recent—perhaps only a few thousand years ago<sup>12,13</sup>. To estimate the split time of the Shum Laka A00 Y chromosome from present-day A00, we called genotypes for individual 2/SE II (from our whole-genome sequence data) at a set of positions at which sequences from two present-day individuals with haplogroup A00<sup>18</sup> differ from all non-A00 individuals. At every subtype-specific site for which we had coverage, the Shum Laka A00 carries the ancestral allele. To avoid needing to determine the status of mutations as ancestral or derived, we considered the entire unrooted lineage specific to A00 (Fig. 1). The total time span represented by this lineage is approximately 359,000 years, using published values of about 275,000 BP for the divergence of the A00 lineage from other modern human haplogroups<sup>19</sup> and about 191,000 BP for the next-oldest split within macrohaplogroup A<sup>70</sup>. With a requirement of at least 90% agreement among the reads at each site, we called 1,521 positions as having the alternative allele (that is, matching the present-day A00 and differing from the human reference sequence) and 145 as having the reference allele (taking the average of 143 and 147 for the 2 present-day individuals). The fraction  $145/(145 + 1,521)$  then defines the position of the split of the Shum Laka individual along the (unrooted) A00 lineage. Split times computed either from all sites (relaxing the 90% threshold and using the majority allele), or from additionally requiring at least two reads per site, differ from our primary estimate by only a few hundred years. To produce a confidence interval, we used the variance in the published estimates and assumed an independent Poisson sampling error for the number of observed reference alleles. The final point estimate was about 31,000 BP (95% confidence interval, 37,000–25,000 BP), which means that the A00 of the Shum Laka individual (with a sample date of about 8,000 BP) cannot be directly ancestral to the present-day subtypes.

## PCA and allele-sharing statistics

We performed PCA using smartpca (with the lsqproject and autoshrink options)<sup>71,72</sup> and computed  $f_4$ -statistics using ADMIXTOOLS (with standard errors estimated via block jackknife over 5 cM chromosomal segments)<sup>73</sup>. We projected all ancient individuals in PCA rather than using them to compute axes to avoid artefacts caused by missing data. In each PCA, we also projected a subset of the present-day populations to enable controlled comparisons with ancient individuals. In most cases, reported  $f_4$ -statistics are based on the approximately 1.15 million autosomal SNPs from our target capture set. For PCA and for  $f_4$ -statistics testing differential relatedness to the Shum Laka individuals, we used autosomal SNPs from the Human Origins array (a subset of the target capture set), with some populations in the analyses only genotyped on this subset (Extended Data Table 1). For these latter  $f_4$ -statistics, we excluded for all populations a set of roughly 40,000 SNPs having high missingness in the present-day Cameroon data.

## Admixture graphs

We fit admixture graphs with the ADMIXTUREGRAPH (qpGraph) program in ADMIXTOOLS (with the options 'outpop: NULL', 'lambdascale: 1', 'inbreed: YES' and 'diag: 0.0001')<sup>73–75</sup>, using the 1.15 million autosomal SNPs from our target capture set by default, and other sets of SNPs in alternative model versions as specified. The program requires as input the branching order of the populations in the graph and a list of admixture events, and it then solves for the optimal parameters of the model (branch lengths and mixture proportions) via an objective function measuring the deviation between predicted and observed values of a basis set of  $f$ -statistics. From the inferred parameters, poorly fitting topologies (including positions of admixture sources) can be corrected by changing split orders at internal nodes that appear as trifurcations under the constraints enforced by the input (Supplementary Information section 3).

To evaluate the fit quality of output models, we used two metrics: first, a list of residual  $Z$ -scores for all  $f$ -statistics relating the populations in the graph, and second, a combined approximate log-likelihood score. The first metric is useful for identifying particularly poorly fitting models and the elements that are most responsible for the poor fits, and the second provides a means for comparing the overall fits of separate models (Supplementary Information section 3). To assess the degree of constraint on individual parameter inferences, we were guided primarily by the variability across different model versions (using different populations and SNP sets) (Extended Data Table 3, Supplementary Information section 3), which reflects both statistical uncertainty and changes in model-specific assumptions. In our primary model, all  $f$ -statistics relating subsets of the populations are predicted to within 2.3 standard errors of their observed values.

Initially, we detected a slight—but significant—signal (maximum  $Z = 2.5$ ) of allele-sharing between the Shum Laka individuals and non-Africans, which we hypothesize is due to a small amount of DNA contamination. To prevent this effect from influencing our results, we included a 'dummy' admixture of non-African ancestry into the Shum Laka individuals (inferred 1.1%, consistent with mtDNA- and X chromosome-based contamination estimates), although model parameters without the dummy admixture are also very similar (Extended Data Table 3, Supplementary Information section 3).

## Reporting summary

Further information on research design is available in the Nature Research Reporting Summary linked to this paper.

## Data availability

The aligned sequences are available through the European Nucleotide Archive under accession number PRJEB32086. Genotype data used in

analysis are available at <https://reich.hms.harvard.edu/datasets>. Any other relevant data are available from the corresponding author upon reasonable request.

46. Dabney, J. et al. Complete mitochondrial genome sequence of a Middle Pleistocene cave bear reconstructed from ultrashort DNA fragments. *Proc. Natl Acad. Sci. USA* **110**, 15758–15763 (2013).
47. Korlević, P. et al. Reducing microbial and human contamination in DNA extractions from ancient bones and teeth. *Biotechniques* **59**, 87–93 (2015).
48. Briggs, A. W. et al. Removal of deaminated cytosines and detection of *in vivo* methylation in ancient DNA. *Nucleic Acids Res.* **38**, e87 (2010).
49. Lipson, M. et al. Ancient genomes document multiple waves of migration in Southeast Asian prehistory. *Science* **361**, 92–95 (2018).
50. Fu, Q. et al. DNA analysis of an early modern human from Tianyuan Cave, China. *Proc. Natl Acad. Sci. USA* **110**, 2223–2227 (2013).
51. Haak, W. et al. Massive migration from the steppe was a source for Indo-European languages in Europe. *Nature* **522**, 207–211 (2015).
52. Fu, Q. et al. An early modern human from Romania with a recent Neanderthal ancestor. *Nature* **524**, 216–219 (2015).
53. Mathieson, I. et al. Genome-wide patterns of selection in 230 ancient Eurasians. *Nature* **528**, 499–503 (2015).
54. Lazaridis, I. et al. Genomic insights into the origin of farming in the ancient Near East. *Nature* **536**, 419–424 (2016).
55. Kircher, M., Sawyer, S. & Meyer, M. Double indexing overcomes inaccuracies in multiplex sequencing on the Illumina platform. *Nucleic Acids Res.* **40**, e3 (2012).
56. Li, H. & Durbin, R. Fast and accurate long-read alignment with Burrows–Wheeler transform. *Bioinformatics* **26**, 589–595 (2010).
57. Weissensteiner, H. et al. HaploGrep 2: mitochondrial haplogroup classification in the era of high-throughput sequencing. *Nucleic Acids Res.* **44**, W58–W63 (2016).
58. Skoglund, P., Storå, J., Götherström, A. & Jakobsson, M. Accurate sex identification of ancient human remains using DNA shotgun sequencing. *J. Archaeol. Sci.* **40**, 4477–4482 (2013).
59. Korneliusson, T. S., Albrechtsen, A. & Nielsen, R. ANGSD: analysis of next generation sequencing data. *BMC Bioinformatics* **15**, 356 (2014).
60. Giresse, P., Maley, J. & Brenac, P. Late Quaternary palaeoenvironments in the Lake Barombi Mbo (West Cameroon) deduced from pollen and carbon isotopes of organic matter. *Palaeogeogr. Palaeoclimatol. Palaeoecol.* **107**, 65–78 (1994).
61. Lohse, J. C., Culleton, B. J., Black, S. L. & Kennett, D. J. A precise chronology of middle to late Holocene bison exploitation in the far southern Great Plains. *J. Texas Archeol. Hist.* **1**, 94–126 (2014).
62. van Klinken, G. J. Bone collagen quality indicators for palaeodietary and radiocarbon measurements. *J. Archaeol. Sci.* **26**, 687–695 (1999).
63. Lavachery, P. *De la Pierre au Métal: Archéologie des Dépôts Holocènes de l'Abri de Shum Laka (Cameroun)*. PhD thesis, Université Libre de Bruxelles (1997).
64. Bronk Ramsey, C., Higham, T. F., Owen, D., Pike, A. & Hedges, R. E. Radiocarbon dates from the Oxford AMS system: archaeometry datelist 31. *Archaeometry* **44**, 1–150 (2002).
65. Ward, G. K. & Wilson, S. R. Procedures for comparing and combining radiocarbon age determinations: a critique. *Archaeometry* **20**, 19–31 (1978).
66. Ramsey, C. B. & Lee, S. Recent and planned developments of the program OxCal. *Radiocarbon* **55**, 720–730 (2013).
67. Reimer, P. J. et al. IntCal13 and Marine13 radiocarbon age calibration curves 0–50,000 years cal bp. *Radiocarbon* **55**, 1869–1887 (2013).
68. Hogg, A. G. et al. SHCal13 Southern Hemisphere calibration, 0–50,000 years cal BP. *Radiocarbon* **55**, 1889–1903 (2013).
69. Marsh, E. J. et al. IntCal, SHCal, or a mixed curve? Choosing a <sup>14</sup>C calibration curve for archaeological and paleoenvironmental records from tropical South America. *Radiocarbon* **60**, 925–940 (2018).
70. Jobling, M. A. & Tyler-Smith, C. Human Y-chromosome variation in the genome-sequencing era. *Nat. Rev. Genet.* **18**, 485–497 (2017).
71. Patterson, N., Price, A. L. & Reich, D. Population structure and eigenanalysis. *PLoS Genet.* **2**, e190 (2006).
72. Liu, L. T., Dobriban, E. & Singer, A. ePCA: high dimensional exponential family PCA. Preprint at <https://arxiv.org/abs/1611.05550> (2016).
73. Patterson, N. et al. Ancient admixture in human history. *Genetics* **192**, 1065–1093 (2012).
74. Lipson, M. & Reich, D. A working model of the deep relationships of diverse modern human genetic lineages outside of Africa. *Mol. Biol. Evol.* **34**, 889–902 (2017).
75. Lipson, M. et al. Parallel palaeogenomic transects reveal complex genetic history of early European farmers. *Nature* **551**, 368–372 (2017).
76. Moeyersons, J., Cornelissen, E., Lavachery, P. & Doutrelepon, H. L'abri sous-roche de Shum Laka (Cameroun Occidental): données climatologiques et occupation humaine depuis 30.000 ans. *Geo. Eco. Trop.* **20**, 39–60 (1996).
77. Cornelissen, E. in *Field Manual for African Archaeology* (eds Smith, A. L. et al.) 168–173 (Royal Museum for Central Africa, 2017).
78. Prüfer, K. et al. The complete genome sequence of a Neanderthal from the Altai Mountains. *Nature* **505**, 43–49 (2014).

**Acknowledgements** We thank I. Lazaridis, V. Narasimhan and K. Sirak for discussions and comments; M. Karmin for help with Y chromosome data; L. Eccles for help with radiocarbon dating; B. Erkkila for help with isotopic analysis; R. Bernardos, M. Mah and Z. Zhang for other technical assistance; J.-P. Warnier for his role in locating the site of Shum Laka; and O. Graf for proofreading, photograph editing and other figure assistance for the Supplementary Information. The Shum Laka excavations were supported by the Belgian Fund for Scientific Research (FNRS), the Université Libre de Bruxelles, the Royal Museum for Central Africa and the Leakey Foundation. The collection of samples from present-day individuals in Cameroon was supported by N. Bradman and the Melford Charitable Trust. The genotyping of the



present-day individuals sampled from Cameroon was supported by the Biotechnology and Biological Sciences Research Council (grant number BB/L009382/1). I.R. was supported by a Université de Montréal exploration grant (2018-2020). M.G.T. was supported by Wellcome Trust Senior Investigator Award Grant 100719/Z/12/Z. G.H. was supported by a Sir Henry Dale Fellowship jointly funded by the Wellcome Trust and the Royal Society (grant number 098386/Z/12/Z). C.L-F. was supported by Obra Social La Caixa 328, Secretaria d'Universitats i Recerca del Departament d'Economia i Coneixement de la Generalitat de Catalunya (GRC 2017 SGR 880), and a FEDER-MINECO grant (PGC2018-095931-B-I00). Radiocarbon work was supported by the NSF Archaeometry program (grant BCS-1460369) to D.J.K. and B.J.C. M.E.P. was supported by a fellowship from the Radcliffe Institute for Advanced Study at Harvard University during the development of this project. D.R. was supported by the National Institutes of Health (NIGMS GM100233), by an Allen Discovery Center grant and by grant 61220 from the John Templeton Foundation, and is an Investigator of the Howard Hughes Medical Institute.

**Author contributions** N.R., G.H., M.E.P. and D.R. supervised the study. I.R., R.N.A., H.B., E.C., I.C., P.d.M., P.L., C.M.M., R.O., E.S., P.S., W.V.N., C.L.-F., S. MacEachern and M.E.P. provided

samples and assembled archaeological and anthropological materials and information. S.L., N. Bradman, F.L.M.F., M.G.T., K.R.V. and G.H. provided data from present-day populations. S. Mallick, N.R., N.A., N. Broomandkoshbacht, A.M.L., J.O., K.S. and D.R. performed ancient DNA laboratory and data-processing work. B.J.C. and D.J.K. performed radiocarbon analysis. M.L., S. Mallick, I.O., N.P. and D.R. analysed genetic data. M.L., I.R., H.B., E.S., C.L.-F., S. MacEachern, M.E.P. and D.R. wrote the manuscript.

**Competing interests** The authors declare no competing interests.

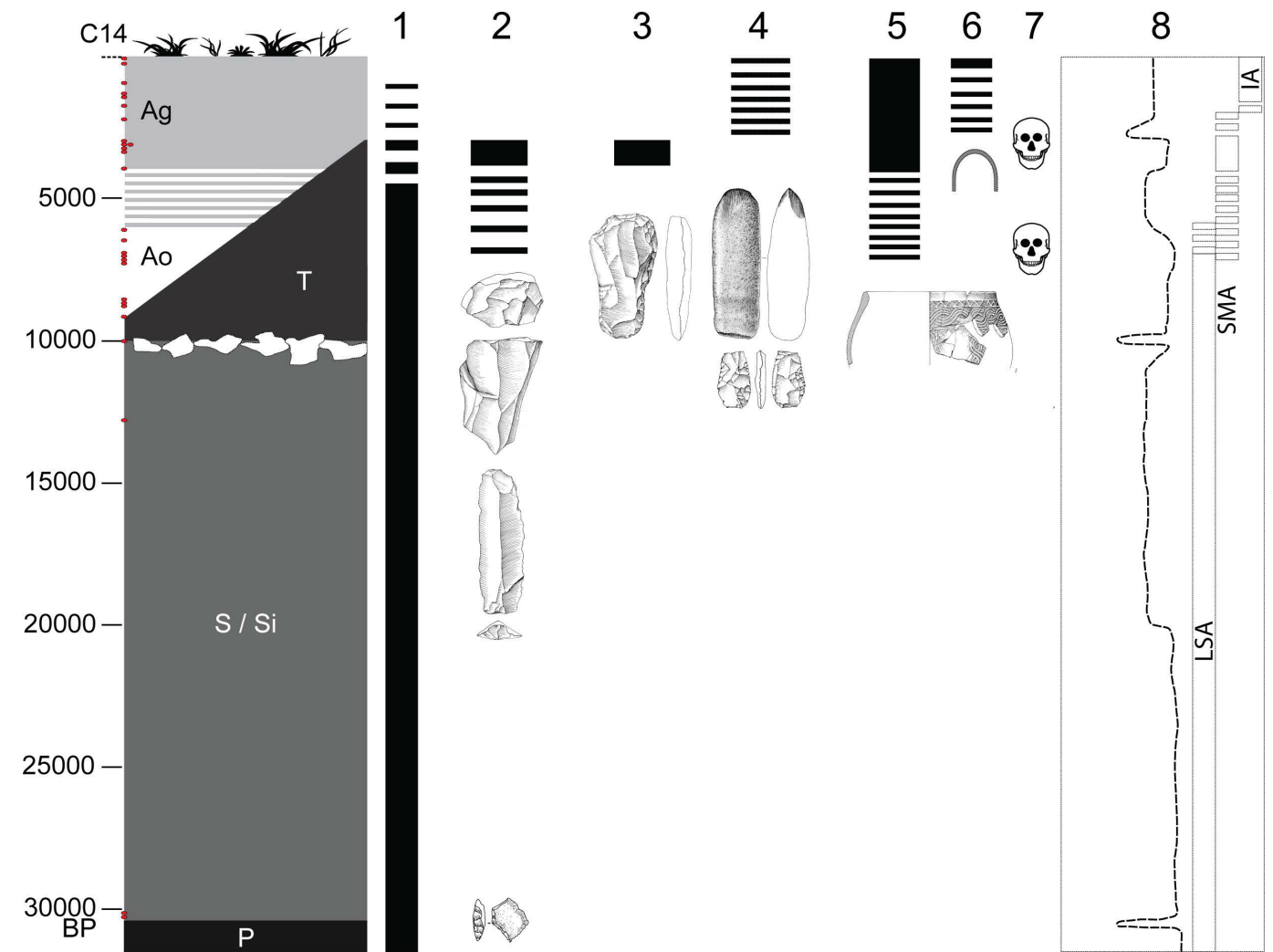
#### **Additional information**

**Supplementary information** is available for this paper at <https://doi.org/10.1038/s41586-020-1929-1>.

**Correspondence and requests for materials** should be addressed to M.L.

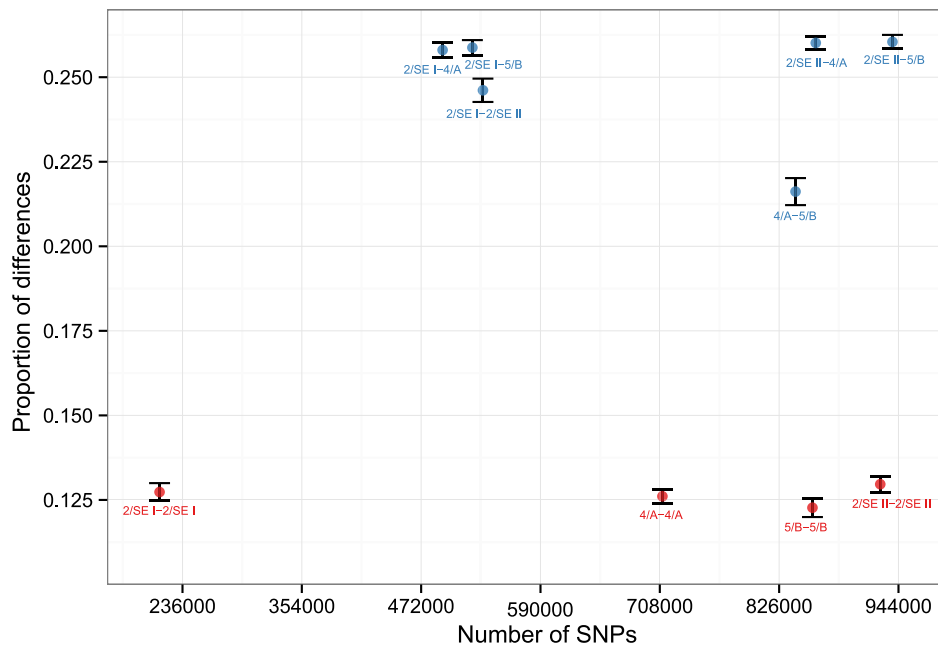
**Peer review information** *Nature* thanks George Busby, Katerina Harvati, Stephan Schiffels, Lluís Quintana-Murci and the other, anonymous, reviewer(s) for their contribution to the peer review of this work.

**Reprints and permissions information** is available at <http://www.nature.com/reprints>.



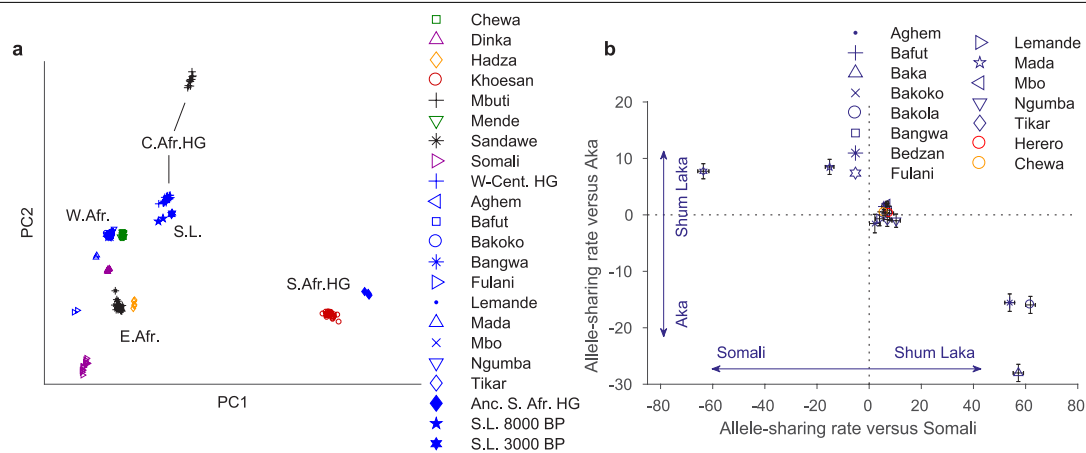
**Extended Data Fig. 1 | Overview of the site of Shum Laka.** The left column represents generalized stratigraphy, with radiocarbon dates (uncalibrated years before present) shown as red dots on the y axis, and deposits indicated by their archaeological nomenclature. P, S/Si, Pleistocene; T, A, Holocene; Ao, Holocene ochre ashy layer; Ag, Holocene grey ashy layer (after ref. <sup>76</sup>). Columns 1–6 display the chronological extents of technological traditions: 1, microlithic quartz industry; 2, macrolithic flake and blade industry on basalt; 3, bifaces of the axe-hoe type; 4, pecked grounded adze and arrow heads; 5, pottery; and 6,

iron objects. Column 7 indicates the two burial phases. Column 8 shows climatic reconstructions based on carbon stable isotopes and pollen from organic matter extracted from sediment cores at Lake Barombi Mbo in western Cameroon (more arid conditions to the left and more humid conditions to the right<sup>60,76</sup>), along with archaeological eras. IA, Iron Age; LSA, Later Stone Age; SMA, Stone to Metal Age. RMCA Collection; drawings by Y. Paquay, composition © RMCA, Tervuren; modified by E. Cornelissen<sup>77</sup>.



**Extended Data Fig. 2 | Kinship analysis.** Mean genome-wide allelic mismatch rates for each pair of individuals (blue), as well as intra-individual comparisons (red), are shown. We selected one read per individual at random at each targeted SNP (using all 1,233,013 targeted sites). Monozygotic twins (or intra-individual comparisons) are expected to have a value one-half as large as unrelated individuals; first-degree relatives, halfway between monozygotic twins and unrelated individuals; second-degree relatives, halfway between first-degree relatives and unrelated individuals; and so on. The presence of

inbreeding also serves to reduce the rate of mismatches. For 4/A and 5/B, we can eliminate a grandparent–grandchild relationship because both died as children, and the lack of long segments with IBD sharing on both homologous chromosomes implies that they are not double cousins (the few ostensible double-IBD stretches are probably a result of inbreeding (Supplementary Information section 2)). Thus, we can conclude that they were either uncle and niece (or aunt and nephew) or half-siblings. Bars show 99% confidence intervals (computed by block jackknife).

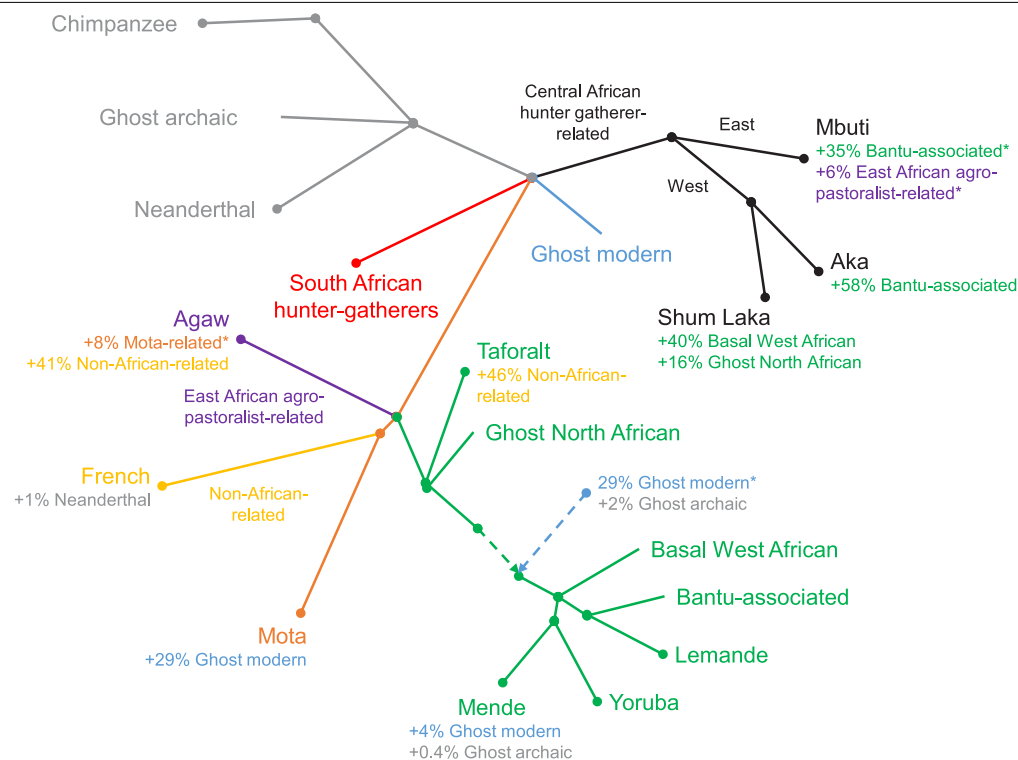


**Extended Data Fig. 3 | Alternative PCA and allele-sharing analyses. a**, Broad-scale PCA (differing from Fig. 2a by projecting all present-day Cameroon populations; again using 593,124 Human Origins SNPs). Groups shown in blue were projected onto axes computed using the other populations. HG, hunter-gatherers. The grouping marked W-Cent. HG consists of Aka and Cameroon hunter-gatherers (Baka, Bakola and Bedzan). The majority of the present-day Cameroon individuals fall in a tight cluster near other West Africans and Bantu-speakers. **b**, Relative allele sharing (mean  $\pm$  s.e.m., multiplied by 10,000, computed on 538,133 SNPs, as in Fig. 3b) with the Shum Laka individuals versus

East Africans ( $f_4(X, \text{Yoruba}; \text{Shum Laka}, \text{Somali})$ ; x axis) and versus Aka ( $f_4(X, \text{Yoruba}; \text{Shum Laka}, \text{Aka})$ ; y axis) for present-day populations from Cameroon (blue points) and southern and eastern Bantu-speakers (Herero in red and Chewa in orange). The Mada and Fulani share more alleles with the Shum Laka individuals than they do with the Aka, but this is probably a secondary consequence of admixture from East or North African sources (as reflected in greater allele sharing with Somali individuals) (Supplementary Information section 3). Bars show one s.e.m. in each direction.

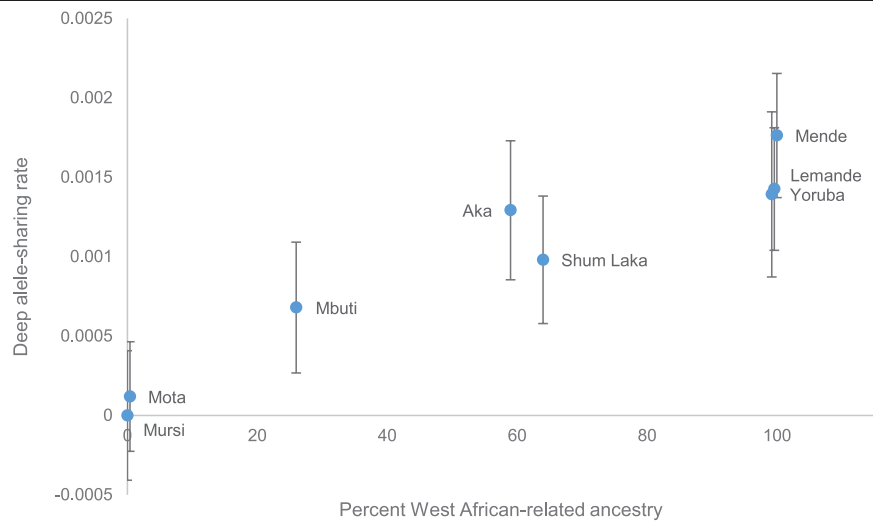






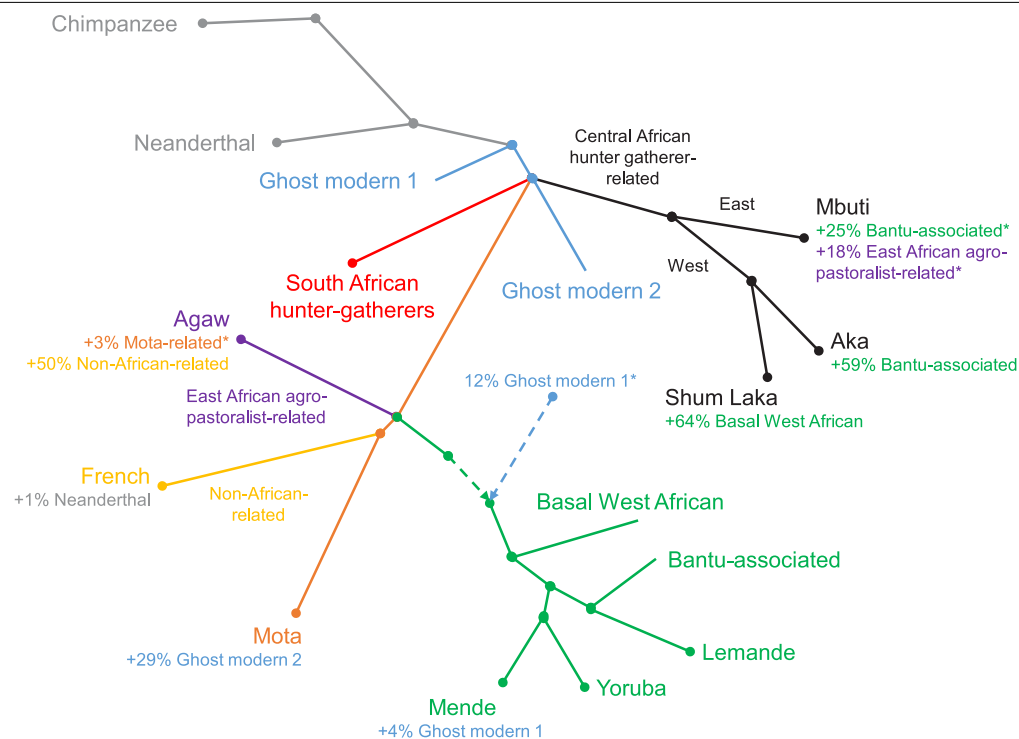
**Extended Data Fig. 5 | Schematic of first alternative admixture graph.** Results are shown including ancient individuals from Taforalt in Morocco associated with the Iberomaurusian culture, with the Shum Laka individuals modelled as having a mixture of ancestry related to western Central African hunter-gatherers plus two additional components: one from within the main portion of the West African clade, and one that splits at nearly the same point as one of the sources that contributes ancestry to the Taforalt individuals. Branch

lengths are not drawn to scale. Points at which multiple lineages are shown diverging simultaneously indicate splits that occur in short succession (the order of which we cannot confidently assess) but are not meant to represent exact multifurcations. \*Proportion not well-constrained (for Mbuti, the sum of the two indicated proportions is well-constrained but not the separate values). Supplementary Information section 3 provides the full parameters of the inferred model.



**Extended Data Fig. 6 | Deep ancestry correlation from the West African clade.** An allele-sharing statistic sensitive to ancestry that splits more deeply than southern African hunter-gatherers ( $f_4(X, \text{Mursi}; \text{chimpanzee, ancient South African hunter-gatherers})$ , mean  $\pm 2$  s.e.m. from block jackknife, computed on 1,121,119 SNPs, as in Fig. 3a) is shown as a function of ancestry

related to the West African clade (from admixture graph results; the Mota individual, Yoruba and Lemande are shifted slightly away from the boundaries for legibility). The (relative) allele-sharing rate for Mursi is zero according to the definition of the statistic.



**Extended Data Fig. 7 | Schematic of the second alternative admixture graph.** Results are shown with a single-component deep source for West Africans. Branch lengths are not drawn to scale. Points at which multiple lineages are shown diverging simultaneously indicate splits that occur in short succession (the order of which we cannot confidently assess) but are not meant to

represent exact multifurcations. \*Proportion is not well-constrained (for Mbuti, the sum of the two indicated proportions is well-constrained but not the separate values). Supplementary Information section 3 provides the full parameters of the inferred model.



**Extended Data Table 1 | Populations in the study**

Population	Country	Language family	Date	Sample size	Data type	Reference
Shum Laka	Cameroon		~8000–3000 BP	4/1/1	1240k/DG/SG	This paper
Ancient Malawi HG	Malawi		~8100–2500 BP	7*	1240k	[22]
Mota	Ethiopia		~4500 BP	1	SG	[23]
Ancient South African HG	South Africa		~2000 BP	3†	SG	[21, 22]
Taforalt	Morocco		~15,000–14,000 BP	6	1240k	[26]
Altai Neanderthal	Russia		~120,000 BP	1	DG	[78]
Aghem	Cameroon	NC	Present	28	HO	This paper
Bafut	Cameroon	NC	Present	11	HO	This paper
Baka	Cameroon	NC	Present	2	DG	[20]
Bakoko	Cameroon	NC	Present	1	HO	This paper
Bakola	Cameroon	NC	Present	2	DG	[20]
Bangwa	Cameroon	NC	Present	2	HO	This paper
Bedzan	Cameroon	NC	Present	2	DG	[20]
Fulani	Cameroon	NC	Present	2	DG	[20]
Lemande	Cameroon	NC	Present	2	DG	[25]
Mada	Cameroon	AA	Present	2	DG	[20]
Mbo	Cameroon	NC	Present	21	HO	This paper
Ngumba	Cameroon	NC	Present	2	DG	[20]
Tikar	Cameroon	NC	Present	2	DG	[20]
Agaw	Ethiopia	AA	Present	2	DG	[20]
Aka (Biaka)	Central African Republic	NC	Present	20/2	HO/DG	[22, 25]
Chewa	Malawi	NC	Present	11	HO	[22]
Dinka	Sudan	NS	Present	7/4	HO/DG	[22, 25]
French	France	IE	Present	3	DG	[25]
Hadza	Tanzania	KS	Present	5(2)/1	HO/DG	[22, 25]
Han	China	ST	Present	4	DG	[25]
Herero	Namibia	NC	Present	2	DG	[25]
Khoesan	Namibia	KS	Present	22	HO	[22]
Mbuti	DR Congo	NC, NS	Present	10/4	HO/DG	[22, 25]
Mende	Sierra Leone	NC	Present	8/2	HO/DG	[22, 25]
Mursi	Ethiopia	NS	Present	2	DG	[20]
Sandawe	Tanzania	KS	Present	22	HO	[22]
Somali	Kenya	AA	Present	13	HO	[22]
Yoruba	Nigeria	NC	Present	70/3	HO/DG	[22, 25]

List of populations in the analyses in this study. Data types are in-solution targeted SNP capture (1240k); whole-genome sequences with pseudohaploid genotype calls (SG); high-coverage whole-genome sequences with diploid genotype calls (DG); and Human Origins SNP array (HO). For some populations, we used different sets of samples for different analyses (indicated by forward slashes); individuals genotyped on the Human Origins array were used for PCA and for *f*-statistics testing differential relatedness to Shum Laka individuals (Fig. 3b, Extended Data Fig. 3b). For the Hadza, we used five individuals with Human Origins data for PCA and two of these five individuals for admixture graph modelling. Data for the Altai Neanderthal individual are from ref. 78. AA, Afroasiatic; IE, Indo-European; KS, Khoesan; NC, Niger-Congo; NS, Nilo-Saharan; ST, Sino-Tibetan.

\*Individuals from Hora, Chencherere and Fingira.

†Individuals from Ballito Bay (A and B) and St Helena Bay.

Extended Data Table 2 | Allele-sharing statistics for deep ancestry

	$f_4(X, \text{Mursi}; \text{SA}, \text{Han})$		$f_4(X, \text{Mota}; \text{SA}, \text{Han})$		$f_4(X, \text{Han}; \text{SA}, \text{Mursi})$		$f_4(X, \text{Mota}; \text{SA}, \text{Mursi})$	
Test pop	Value	Z-score	Value	Z-score	Value	Z-score	Value	Z-score
Dinka	1.4	5.8	-2.0	-5.5	0.1	0.2	-6.3	-20.2
Mota	3.4	9.0	0	0	6.3	18.1	0	0
Hadza	4.1	10.3	0.8	1.7	7.3	21.2	1.0	2.7
Yoruba	4.7	17.8	1.3	3.8	5.2	18.2	-1.1	-3.5
Lemande	5.0	16.8	1.7	4.5	5.7	18.2	-0.6	-2.1
Mende	5.7	19.1	2.3	6.3	6.3	20.0	0	0
Shum Laka	11.7	38.7	8.3	22.6	12.7	40.8	6.4	20.5
Aka	13.3	39.1	9.9	25.2	13.6	40.4	7.3	22.0
Mbuti	16.4	50.4	13.0	34.9	16.4	49.9	10.0	31.8
Mursi	0	0	-3.4	-9.0	..	..	..	..
Agaw	..	..	..	..	0.1	0.3	-6.2	-18.9
SA	..	..	..	..	..	..	..	..
	$f_4(X, \text{Mursi}; \text{SA}, \text{Mota})$		$f_4(X, \text{Han}; \text{SA}, \text{Mota})$		$f_4(X, \text{Han}; \text{SA}, \text{Yor})$		$f_4(X, \text{Mursi}; \text{Chimp}, \text{Yor})$	
Test pop	Value	Z-score	Value	Z-score	Value	Z-score	Value	Z-score
Dinka	0.8	3.3	3.7	11.9	-0.7	-2.8	-0.9	-4.7
Mota	..	..	..	..	5.7	18.1	5.2	17.7
Hadza	4.1	11.5	7.0	17.7	4.8	15.2	3.4	11.4
Yoruba	4.1	15.7	7.1	21.6	..	..	..	..
Lemande	4.1	14.5	7.1	21.0	..	..	..	..
Mende	4.8	17.3	7.8	22.5	..	..	..	..
Shum Laka	9.1	29.8	12.0	33.7	8.0	28.7	8.3	31.9
Aka	10.3	33.4	13.2	35.5	7.8	24.8	8.5	30.1
Mbuti	12.5	41.8	15.5	44.1	11.6	40.8	11.8	46.3
Mursi	0	0	3.0	8.8	0.6	2.2	0	0
Agaw	-2.4	-7.7	0.6	1.8	0	0.2	-0.2	-0.9
SA	..	..	..	..	..	..	20.3	66.0

Variations of allele-sharing statistics (multiplied by 1,000; computed on 1,121,119 SNPs) sensitive to ancestry in the test population *X* from a deeply-splitting lineage, along with Z-scores for difference from zero. The zero level has a different meaning depending on which population is in the second position in the statistic. Blank entries are statistics that are confounded by specific relationships between the test population and one of the reference populations (in the third or fourth position; either duplication of the same group, Agaw with Han owing to ancestry related to non-Africans, or Yoruba with other West Africans). From the statistics  $f_4(\text{Mursi or Agaw}, \text{Han}; \text{ancient South African hunter-gatherers}, \text{Yoruba})$ , we find minimal differences in deep ancestry proportions among Han, Mursi, and Agaw; from  $f_4(X, \text{Mursi}; \text{chimpanzee}, \text{Yoruba})$ , we obtain a value for ancient South African hunter-gatherers that is roughly twice as large as that for Central African hunter-gatherers. SA, ancient South African hunter-gatherers; Yor, Yoruba.

Extended Data Table 3 | Admixture graph parameter estimates

Model version:	1	2	3	4	5	6	7	8	9	10	11	12	13	14	15	16	17	18	19	20	21	22	23
Mixture proportions (%)																							
Shum Laka basal WA	64	66	62	71	64	58	63	61	63	61	64	64	64	64	63	63	63	..	64	61	69	63	67/62*
Aka Bantu-associated	59	59	57	63	59	56	58	57	59	58	59	59	59	59	59	58	58	59	58	62	61	59	
Mbuti Bantu-associated	26	24	33	19	28	27	26	12	28	30	32	25	24	26	29	28	35	35	25	35	23	36	27
Mbuti East African-related	17	19	10	27	14	9	16	23	15	13	11	19	20	18	13	14	6	6	18	9	23	8	16
West African clade archaic	2	2	4	4	3	3	3	2	2	2	3	2	2	2	3	3	3	2	..	..	..	..	2
West African clade deep modern human	10	9	17	8	12	29	15	24	11	18	19	9	8	9	14	13	29	29	..	..	..	..	11
Mende deep ancestry	4	4	4	3	4	3	4	6	5	5	5	4	4	4	5	5	5	5	4	4	4	3	4
Mota deep ancestry	29	29	30	29	30	31	31	30	29	31	29	29	29	28	30	31	29	29	29	30	27	26	29
Branch lengths																							
Basal WA split†	2	3	3	3	3	1	3	2	2	2	2	2	3	3	2	2	3	..	2	3	3	1	3
South African HG split‡	1	1	0	4	1	-1	1	2	1	1	1	1	1	1	1	1	1	1	1	0	4	0	1
Ghost modern human split#	1	1	1	-3	1	1	0	-2	1	0	-1	1	1	1	0	1	1	1	..	..	..	..	2

Key admixture graph parameter estimates across different model versions. Supplementary Information section 3 provides the full details. 1,Primary model; 2, no ‘dummy’ admixture; 3, African-ascertained SNPs; 4, transversion SNPs; 5, whole-genome sequence data for the Shum Laka individuals; 6, outgroup-ascertained transversions; 7, Hadza added; 8, Mbo in place of Lemande; 9, Herero added; 10, Chewa added; 11, Mursi in place of Agaw; 12, Baka added; 13, Bakola added; 14, Bedzan added; 15, Mada added; 16, Fulani added; 17, Taforalt added; 18, alternative admixture for the Shum Laka individuals; 19, alternative deep source; 20, alternative deep source with African-ascertained SNPs; 21, alternative deep source with transversion SNPs; 22, alternative deep source with outgroup-ascertained transversions; 23, pairs of Shum Laka individuals fit separately. WA, West African.

\*Earlier pair/later pair.

†Units above the main West African clade.

‡Units below the split of the Central African hunter-gather lineage (negative value indicates distance above).

#Units along the Central African hunter-gather lineage (negative values indicate distances along an adjacent edge).

## Reporting Summary

Nature Research wishes to improve the reproducibility of the work that we publish. This form provides structure for consistency and transparency in reporting. For further information on Nature Research policies, see [Authors & Referees](#) and the [Editorial Policy Checklist](#).

### Statistical parameters

When statistical analyses are reported, confirm that the following items are present in the relevant location (e.g. figure legend, table legend, main text, or Methods section).

n/a Confirmed

- ☐ ☒ The exact sample size ( $n$ ) for each experimental group/condition, given as a discrete number and unit of measurement
- ☐ ☒ An indication of whether measurements were taken from distinct samples or whether the same sample was measured repeatedly
- ☐ ☒ The statistical test(s) used AND whether they are one- or two-sided  
*Only common tests should be described solely by name; describe more complex techniques in the Methods section.*
- ☒ ☐ A description of all covariates tested
- ☐ ☒ A description of any assumptions or corrections, such as tests of normality and adjustment for multiple comparisons
- ☐ ☒ A full description of the statistics including central tendency (e.g. means) or other basic estimates (e.g. regression coefficient) AND variation (e.g. standard deviation) or associated estimates of uncertainty (e.g. confidence intervals)
- ☐ ☒ For null hypothesis testing, the test statistic (e.g.  $F$ ,  $t$ ,  $r$ ) with confidence intervals, effect sizes, degrees of freedom and  $P$  value noted  
*Give  $P$  values as exact values whenever suitable.*
- ☒ ☐ For Bayesian analysis, information on the choice of priors and Markov chain Monte Carlo settings
- ☒ ☐ For hierarchical and complex designs, identification of the appropriate level for tests and full reporting of outcomes
- ☒ ☐ Estimates of effect sizes (e.g. Cohen's  $d$ , Pearson's  $r$ ), indicating how they were calculated
- ☐ ☒ Clearly defined error bars  
*State explicitly what error bars represent (e.g. SD, SE, CI)*

Our web collection on [statistics for biologists](#) may be useful.

### Software and code

Policy information about [availability of computer code](#)

Data collection BWA v0.6.1, HaploGrep2 v2.1.19, cTools v11/2016, contamMix v1.0-10, ANGSD v0.923, OxCal v4.3.2

Data analysis ADMIXTOOLS v5.1, EIGENSOFT v7.2.1, IBM SPSS Statistics v.25, SYSTAT v.11.5

For manuscripts utilizing custom algorithms or software that are central to the research but not yet described in published literature, software must be made available to editors/reviewers upon request. We strongly encourage code deposition in a community repository (e.g. GitHub). See the Nature Research [guidelines for submitting code & software](#) for further information.

### Data

Policy information about [availability of data](#)

All manuscripts must include a [data availability statement](#). This statement should provide the following information, where applicable:

- Accession codes, unique identifiers, or web links for publicly available datasets
- A list of figures that have associated raw data
- A description of any restrictions on data availability

The aligned sequences are available through the European Nucleotide Archive under accession number PRJEB32086. Genotype data used in analysis are available at <https://reich.hms.harvard.edu/datasets>.



## Field-specific reporting

Please select the best fit for your research. If you are not sure, read the appropriate sections before making your selection.

☐ Life sciences ☐ Behavioural & social sciences ☒ Ecological, evolutionary & environmental sciences

For a reference copy of the document with all sections, see [nature.com/authors/policies/ReportingSummary-flat.pdf](https://www.nature.com/authors/policies/ReportingSummary-flat.pdf)

## Ecological, evolutionary & environmental sciences study design

All studies must disclose on these points even when the disclosure is negative.

Study description	Genetic analyses were performed on DNA data generated from ancient human skeletons. Population genetic statistics, primarily testing historical relationships by measuring allele-sharing patterns across populations, were computed using genome-wide SNP genotypes.
Research sample	Four ancient human individuals buried at Shum Laka in Cameroon; 63 newly reported present-day individuals from five populations in Cameroon (for comparative analyses); ancient African individuals from Gallego Llorente et al. 2015, Schlebusch et al. 2017, and Skoglund et al. 2017; present-day African individuals from Mallick et al. 2016 and Fan et al. 2019.
Sampling strategy	We sampled available bones from six Shum Laka individuals and obtained working data from four. We targeted approximately 1.2 million genome-wide SNPs, which effectively cover almost all independent loci (due to linkage disequilibrium) and provide good power in population history analyses (all remains in this study yielding good coverage).
Data collection	DNA from the ancient remains was extracted, sequenced, and processed into SNP genotype calls (final data overseen by D.R. and S.Mal.).
Timing and spatial scale	Ancient individuals were sampled from the Shum Laka rockshelter in western Cameroon. Newly reported present-day individuals were from western and southwestern Cameroon.
Data exclusions	Two of the sampled skeletons did not yield working data as assessed by pre-established ancient DNA quality criteria.
Reproducibility	All attempts to reproduce were successful.
Randomization	The only subgroup assignments were by date for the ancient individuals and by ethno-linguistic group for the present-day individuals.
Blinding	Analyses were performed either for all four individuals separately, all four grouped together, or for the two temporally separated pairs; other sample-specific features were not relevant to results.
Did the study involve field work?	<input type="checkbox"/> Yes <input checked="" type="checkbox"/> No

## Reporting for specific materials, systems and methods

### Materials & experimental systems

n/a	Involved in the study
<input checked="" type="checkbox"/>	<input type="checkbox"/> Unique biological materials
<input checked="" type="checkbox"/>	<input type="checkbox"/> Antibodies
<input checked="" type="checkbox"/>	<input type="checkbox"/> Eukaryotic cell lines
<input checked="" type="checkbox"/>	<input type="checkbox"/> Palaeontology
<input checked="" type="checkbox"/>	<input type="checkbox"/> Animals and other organisms
<input type="checkbox"/>	<input checked="" type="checkbox"/> Human research participants

### Methods

n/a	Involved in the study
<input checked="" type="checkbox"/>	<input type="checkbox"/> ChIP-seq
<input checked="" type="checkbox"/>	<input type="checkbox"/> Flow cytometry
<input checked="" type="checkbox"/>	<input type="checkbox"/> MRI-based neuroimaging

## Human research participants

Policy information about [studies involving human research participants](#)

Population characteristics	Samples were collected at market places or other locations of a similar nature where many individuals of the ethnic group of interest were expected to reside or assemble. Samples were only collected from males who declared themselves to be 18 years of age or older and not the sibling of another donor. The self-declared ethnic identity of the donor was recorded after the sample was taken, but samples were collected without discrimination on the basis of ethnic identity. There was no genotypic
----------------------------	--

## Recruitment

data on donors available to collectors; subsequently, for analysis, we confirmed that none of the individuals were substantial genetic outliers relative to their ethno-linguistic groups.

Participants were recruited by public announcement at the sampling location with samples taken in the order donors presented themselves. No monetary reward was offered.

# A distributional code for value in dopamine-based reinforcement learning

<https://doi.org/10.1038/s41586-019-1924-6>

Received: 3 January 2019

Accepted: 19 November 2019

Published online: 15 January 2020

Will Dabney<sup>1,5\*</sup>, Zeb Kurth-Nelson<sup>1,2,5</sup>, Naoshige Uchida<sup>3</sup>, Clara Kwon Starkweather<sup>3</sup>, Demis Hassabis<sup>1</sup>, Rémi Munos<sup>1</sup> & Matthew Botvinick<sup>1,4,5</sup>

Since its introduction, the reward prediction error theory of dopamine has explained a wealth of empirical phenomena, providing a unifying framework for understanding the representation of reward and value in the brain<sup>1–3</sup>. According to the now canonical theory, reward predictions are represented as a single scalar quantity, which supports learning about the expectation, or mean, of stochastic outcomes. Here we propose an account of dopamine-based reinforcement learning inspired by recent artificial intelligence research on distributional reinforcement learning<sup>4–6</sup>. We hypothesized that the brain represents possible future rewards not as a single mean, but instead as a probability distribution, effectively representing multiple future outcomes simultaneously and in parallel. This idea implies a set of empirical predictions, which we tested using single-unit recordings from mouse ventral tegmental area. Our findings provide strong evidence for a neural realization of distributional reinforcement learning.

The reward prediction error (RPE) theory of dopamine derives from work in the artificial intelligence (AI) field of reinforcement learning (RL)<sup>7</sup>. Since the link to neuroscience was first made, however, RL has made substantial advances<sup>8,9</sup>, revealing factors that greatly enhance the effectiveness of RL algorithms<sup>10</sup>. In some cases, the relevant mechanisms invite comparison with neural function, suggesting hypotheses concerning reward-based learning in the brain<sup>11–13</sup>. Here we examine a promising recent development in AI research and investigate its potential neural correlates. Specifically, we consider a computational framework referred to as distributional reinforcement learning<sup>4–6</sup> (Fig. 1a, b).

Similar to the traditional form of temporal-difference RL—on which the dopamine theory was based—distributional RL assumes that reward-based learning is driven by a RPE, which signals the difference between received and anticipated reward. (For simplicity, we introduce the theory in terms of a single-step transition model, but the same principles hold for the general multi-step (discounted return) case; see Supplementary Information.) The key difference in distributional RL lies in how ‘anticipated reward’ is defined. In traditional RL, the reward prediction is represented as a single quantity: the average over all potential reward outcomes, weighted by their respective probabilities. By contrast, distributional RL uses a multiplicity of predictions. These predictions vary in their degree of optimism about upcoming reward. More optimistic predictions anticipate obtaining greater future rewards; less optimistic predictions anticipate more meager outcomes. Together, the entire range of predictions captures the full probability distribution over future rewards (more details in Supplementary Information).

Compared with traditional RL procedures, distributional RL can increase performance in deep learning systems by a factor of two or more<sup>5,14,15</sup>, an effect that stems in part from an enhancement of

representation learning (see Extended Data Figs. 2, 3 and Supplementary Information). This prompts the question of whether RL in the brain might leverage the benefits of distributional coding. This question is encouraged both by the fact that the brain utilizes distributional codes in numerous other domains<sup>16</sup>, and by the fact that the mechanism of distributional RL is biologically plausible<sup>6,17</sup>. Here we tested several predictions of distributional RL using single-unit recordings in the ventral tegmental area (VTA) of mice performing tasks with probabilistic rewards.

## Value predictions vary among dopamine neurons

In contrast to classical temporal-difference (TD) learning, distributional RL posits a diverse set of RPE channels, each of which carries a different value prediction, with varying degrees of optimism across channels. (Value is formally defined in RL as the mean of future outcomes, but here we relax this definition to include predictions about future outcomes that are not necessarily the mean.) These value predictions in turn provide the reference points for different RPE signals, causing the latter to also differ in terms of optimism. As a surprising consequence, a single reward outcome can simultaneously elicit positive RPEs (within relatively pessimistic channels) and negative RPEs (within more optimistic ones).

This translates immediately into a neuroscientific prediction, which is that dopamine neurons should display such diversity in ‘optimism’. Suppose an agent has learned that a cue predicts a reward whose magnitude will be drawn from a probability distribution. In the standard RL theory, receiving a reward with magnitude below the mean of this distribution will elicit a negative RPE, whereas larger magnitudes will elicit positive RPEs. The reversal point—the magnitude at which prediction errors transition from negative to positive—in standard RL is the expectation of the magnitude’s distribution. By contrast, in

<sup>1</sup>DeepMind, London, UK. <sup>2</sup>Max Planck UCL Centre for Computational Psychiatry and Ageing Research, University College London, London, UK. <sup>3</sup>Center for Brain Science, Department of Molecular and Cellular Biology, Harvard University, Cambridge, MA, USA. <sup>4</sup>Gatsby Computational Neuroscience Unit, University College London, London, UK. <sup>5</sup>These authors contributed equally: Will Dabney, Zeb Kurth-Nelson, Matthew Botvinick. \*e-mail: wdabney@google.com

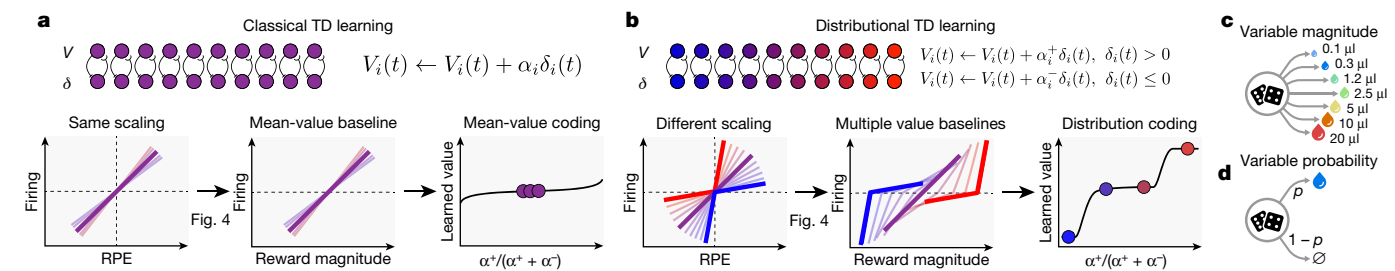


**Fig. 1 | Distributional value coding arises from a diversity of relative scaling of positive and negative prediction errors.** **a**, In the standard temporal-difference (TD) theory of the dopamine system, all value predictors learn the same value  $V$ . Each dopamine cell is assumed to have the same relative scaling for positive and negative RPEs (left). This causes each value prediction (or value baseline) to be the mean of the outcome distribution (middle). Dotted lines indicate zero RPE or pre-stimulus firing. **b**, In our proposed model, distributional TD, different channels have different relative scaling for positive

( $\alpha^+$ ) and negative ( $\alpha^-$ ) RPEs. Red shading indicates  $\alpha^+ > \alpha^-$ , and blue shading indicates  $\alpha^- > \alpha^+$ . An imbalance between  $\alpha^+$  and  $\alpha^-$  causes each channel to learn a different value prediction. This set of value predictions collectively represents the distribution over possible rewards. **c**, We analyse data from two tasks. In the variable-magnitude task, there is a single cue, followed by a reward of unpredictable magnitude. **d**, In the variable-probability task, there are three cues, which each signal a different probability of reward, and the reward magnitude is fixed.

distributional RL, the reversal point differs across dopamine neurons according to their degree of optimism.

We tested for such reversal-point diversity in optogenetically verified dopaminergic VTA neurons, focusing on responses to receipt of liquid rewards, the volume of which was drawn at random on each trial from seven possible values (Fig. 1c). As anticipated by distributional RL, but not by the standard theory, we found that dopamine neurons had substantially different reversal points, ranging from cells that reversed between the smallest two rewards to cells that reversed between the largest two rewards (Fig. 2a, b). This diversity was not owing to noise, as the reversal point estimated on a random half of the data was a robust predictor of the reversal point estimated on the other half of the data ( $R = 0.58$ ,  $P = 1.8 \times 10^{-5}$  by linear regression; Fig. 2c). In fact, in response to the 5  $\mu$ l reward, 13 out of 40 cells had significantly above-baseline responses and 10 out of 40 cells had significantly below-baseline responses. Note that while some cells appeared pessimistic and others appeared optimistic, there was also a population of cells with approximately neutral responses, as predicted by the distributional RL model (compare with Fig. 2a, right).

A stronger test of our theory is whether this diversity also exists within a single animal. Most animals had too few cells for analysis, but within the single animal with the highest number of recorded cells, reversal points estimated on half of the data were robustly predictive of reversal points estimated on the other half ( $P = 0.008$ ). Furthermore, in response to a single reward magnitude (5  $\mu$ l), 6 out of 16 cells had significantly above-baseline responses and 5 out of 16 cells had significantly below-baseline responses. Finally, Fig. 2d shows rasters of two example cells from this animal, exhibiting consistently opposite responses to the same reward.

Because the diversity we observe is reliable across trials, it cannot be explained by adding measurement noise to non-distributional TD models. As detailed in section 2 of the Supplementary Information (see also Extended Data Fig. 4), we also analysed several more elaborate alternative models, and whereas some of these can give rise to the appearance of reversal-point diversity under some analysis methods, the same models are contradicted by other aspects of the experimental data, which we report below.

Our first prediction dealt with the relationship between dopaminergic signalling and reward magnitude; dopaminergic RPE signals also scale with reward probability<sup>2,18</sup>, and distributional RL also leads to a prediction in this domain. Pursuing this, we analysed data from a second task in which sensory cues indicated the probability of an upcoming liquid reward (Fig. 1d). One cue indicated a 10% probability of reward, a different cue indicated a 50% probability, and a third a 90% probability. The standard RPE theory predicts that, considering responses at the time the cue is presented, all dopamine neurons should have the same relative spacing between 10%, 50% and 90% cue responses. (Under neutral risk

preferences, the 50% cue response should be midway between the 10% and 90% cues. Under different risk preferences, the 50% cue response might be at a different position between 10% and 90%, but it should be the same for all neurons). Distributional RL predicts, instead, that dopamine neurons should vary in their responses to the 50% cue: some neurons should respond optimistically, emitting a RPE nearly as large as to the 90% cue. Others should respond pessimistically, emitting a RPE closer to the 10% cue response (Fig. 3a). Labelling these two cases as optimistically and pessimistically biased, respectively, distributional RL predicts that as a population, dopamine neurons should show concurrent optimistic and pessimistic coding for reward probability.

To test this prediction, we analysed responses of dopaminergic VTA neurons in the cued probability task just described (see Methods for more details). As predicted by distributional RL, but not by the standard theory, dopamine neurons differed in their patterns of response across the three reward-probability cues, with both optimistic and pessimistic probability coding observed (Fig. 3b left, Extended Data Figs. 6, 7). Again, this diversity was not due to noise, as 10 out of 31 cells were significantly optimistic and 9 out of 31 cells were significantly pessimistic, at a  $P < 0.05$  threshold (see Methods). By comparison, at a 0.05 threshold, approximately 3 out of 31 cells in a non-distributional TD system are expected by chance to appear either significantly optimistic or pessimistic. At the group level, the null hypothesis of no diversity was rejected by one-way analysis of variance (ANOVA) ( $F(30, 3335) = 4.31$ ,  $P = 6 \times 10^{-14}$ ). Notably, both forms of probability coding were observed side by side in individual animals. In the animal with the largest number of recorded cells, 4 out of 17 cells were consistently optimistic and 5 out of 17 cells were consistently pessimistic. This was also significant by ANOVA ( $F(15, 1652) = 4.02$ ,  $P = 3 \times 10^{-7}$ ).

Because most cells were recorded in different sessions, it was important to examine whether global changes in reward expectations between sessions might explain the observed diversity in optimism. To this end, we analysed patterns of anticipatory licking. Here we found that, although within-session fluctuations in licking were predictive of within-session fluctuations in dopamine cell firing, there was no relationship between optimism and licking on a cell-by-cell basis (Extended Data Fig. 9). This observation makes it unlikely that the diverse responses we observed in dopamine neurons are explained by session-to-session variability in global reward expectation. That interpretation is further undermined by the fact that reversal-point diversity was observed in the one case where several cells were recorded simultaneously in one animal (Fig. 3c and Supplementary Information).

## GABAergic neurons make diverse reward predictions

In distributional RL, diversity in RPE signalling arises because different RPE channels listen to different reward predictions, which vary



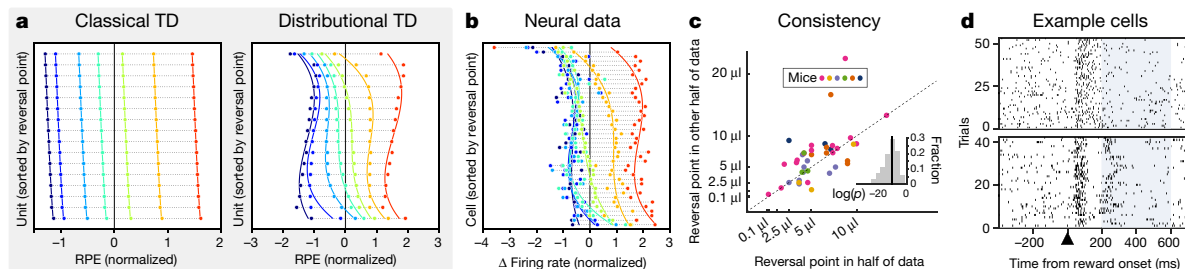


**Fig. 2 | Different dopamine neurons consistently reverse from positive to negative responses at different reward magnitudes.** Variable-magnitude task from ref. <sup>30</sup>. On each trial, the animal experiences one of seven possible reward magnitudes (0.1, 0.3, 1.2, 2.5, 5, 10 or 20  $\mu$ l), selected randomly. **a**, RPEs produced by classical and distributional TD simulations. Each horizontal bar is one simulated neuron. Each dot colour corresponds to a particular reward magnitude. The x axis is the cell's response (change in firing rate) when reward is delivered. Cells are sorted by reversal point. In classical TD, all cells carried approximately the same RPE signal. Note that the slight differences between cells arose from Gaussian noise added to the simulation; the differences between cells in the classical TD simulation were not statistically reliable. Conversely, in distributional TD, cells had reliably different degrees of optimism. Some responded positively to almost all rewards, and others

responded positively to only the very largest reward. **b**, Responses recorded from light-identified dopamine neurons in behaving mice. Neurons differed markedly in their reversal points. **c**, To assess whether this diversity was reliable, we randomly partitioned the data into two halves and estimated reversal points independently in each half. We found that the reversal point estimated in one half was correlated with that estimated in the other half ( $P = 1.8 \times 10^{-5}$  by linear regression). **d**, Spike rasters for two example dopamine neurons from the same animal, showing responses to all trials when the 5  $\mu$ l reward was delivered. We analysed data from 200 to 600 ms after reward onset (highlighted), to exclude the initial transient that was positive for all magnitudes. During this epoch, the cell on the bottom fires above its baseline rate, while the cell on the top pauses.

in their degree of optimism. From a neuroscientific perspective, it should thus be possible to track the effects we have identified at the level of VTA dopamine neurons back to upstream neurons signalling reward predictions. Previous work strongly suggests that VTA GABAergic ( $\gamma$ -aminobutyric acid) neurons have precisely this role, and that the reward prediction used to compute the RPE is reflected in their firing rates<sup>19</sup>. Therefore, we predicted that, in the same task described above, the population of VTA GABAergic neurons should also contain concurrent optimistic and pessimistic probability coding. As predicted, consistent differences in probability coding were observed across putative GABAergic neurons, again with concurrent optimism and pessimism (Fig. 3b, right). In the animal with the largest number of cells recorded, 12 out of 36 cells were consistently optimistic and 11 out of 36 cells were consistently pessimistic (example cells shown in Fig. 3d).

## Distribution coding from asymmetric RPE scaling

The results reported in the preceding sections suggest that a distribution of value predictions is coded in the neural circuits underlying RL. How might such coding arise in the first place? Recent AI work on distributional RL<sup>15</sup> has shown that distributional coding arises automatically if a single change is made to the classical TD learning mechanism.

In classical TD, positive and negative errors are given equal weight. As a result, positive and negative errors are in equilibrium when the learned prediction equals the mean of the reward distribution. Therefore, classical TD learns to predict the average over future rewards.

By contrast, in distributional TD, different RPE channels place different relative weights on positive versus negative RPEs (see Fig. 1b). In channels that overweight positive RPEs, reaching equilibrium requires these positive errors to become less frequent, so the learning dynamics converge on a

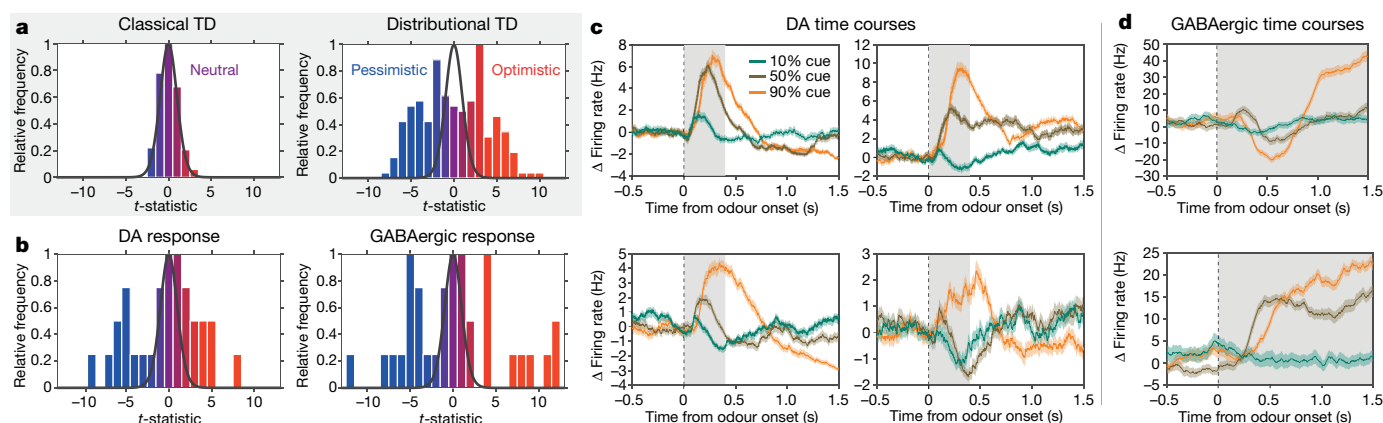


**Fig. 3 | Optimistic and pessimistic probability coding occur concurrently in dopamine and VTA GABAergic neurons.** Data from variable-probability task. **a**, Histogram (across simulated cells) of  $t$ -statistics which compare each cell's 50% cue response against the mean 50% cue response across cells. Qualitatively identical results hold when comparing the 50% cue response against the midpoint of 10% and 90% responses. The superimposed black curve shows the  $t$ -distribution with the corresponding degrees of freedom. Distributional TD predicts simultaneous optimistic and pessimistic coding of probability, whereas classical TD predicts that all cells have the same coding. Colour indicates the degree of optimism or pessimism. **b**, Same as **a**, but using data

from real dopamine and putative GABAergic neurons. The pattern of results closely matches the predictions from the distributional TD model.

**c**, Responses of four example dopamine neurons recorded simultaneously in a single animal. Each trace is the average response to one of the three cues. Shaded area shows s.e.m. Time zero is the onset of the odour cue. Some cells code the 50% cue similarly to the 90% cue, while others simultaneously code it similarly to the 10% cue. Grey areas show epoch averaged for summary analyses. **d**, Responses of two example VTA GABAergic cells from the same animal.

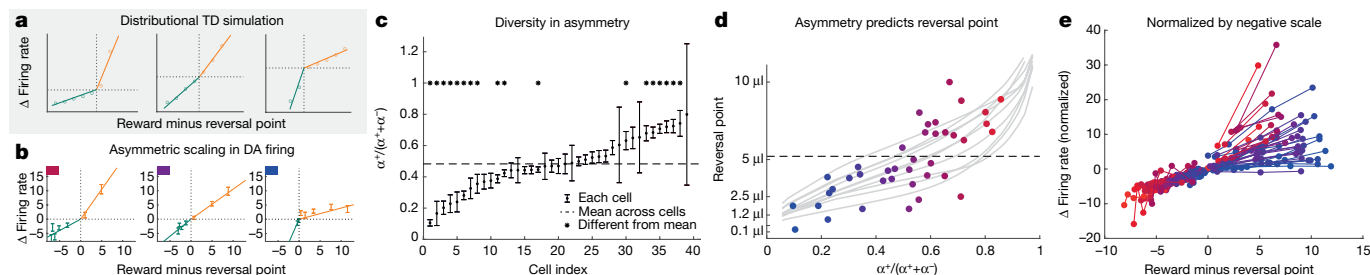


**Fig. 4 | Relative scaling of positive and negative dopamine responses predicts reversal point.** **a**, Three simulated dopamine neurons—each with a different asymmetry—in the variable-magnitude task. For each unit, we empirically estimated the reversal point where responses switch from negative to positive. The x-axis shows reward minus the per-cell reversal point, effectively aligning each cell's responses to its respective reversal point. Baseline-subtracted response to reward is plotted on the y-axis. Responses below the reversal point are shown in green and those above are shown in orange. Solid curves show linear functions fit separately to the above-reversal and below-reversal domains of each cell. **b**, Same as **a**, but showing three real example dopamine cells. **c**, The diversity in relative scaling of positive and negative responses in dopamine cells is statistically reliable (one-way ANOVA;  $F(38, 234) = 2.93$ ,  $P = 4 \times 10^{-7}$ ). The mean and 95% confidence intervals of

$\alpha^+ / (\alpha^+ + \alpha^-)$  are displayed, where  $\alpha^+$  and  $\alpha^-$  are the slopes estimated above. **d**, Relative scaling of positive and negative responses predicts that cell's reversal point ( $P = 8.1 \times 10^{-5}$  by linear regression). Each point represents one dopamine cell. Dashed line is the mean over cells. Light grey traces show reversal points measured in distributional TD simulations of the same task, and show variability over simulation runs. **e**, All 40 dopamine cells plotted in the same fashion as in **b**, except normalized by the slope estimated in the negative domain. Thus, the observed variability in slope in the positive domain corresponds to diversity in relative scaling of positive and negative responses. Cells are coloured by reversal point, to illustrate the relationship between reversal point and asymmetric scaling. In all panels, reward magnitudes are in estimated utility space (see Methods).

more optimistic reward prediction. Conversely, in channels overweighting negative RPEs, a more pessimistic prediction is needed to attain equilibrium (Fig. 4a, Extended Data Fig. 1a). Together, the set of predictions learned across all channels encodes the full shape of the reward distribution.

When distributional RL is considered as a model of the dopamine system, these points translate into two testable predictions. First, dopamine neurons should differ in their relative scaling of positive and negative RPEs. To test this prediction, we analysed activity from VTA dopamine neurons in the variable-magnitude task described above. We first estimated a reversal point for each cell as previously described. Then, for each cell, we separately estimated two slopes:  $\alpha^+$  for responses in the positive domain (that is, above the reversal point), and  $\alpha^-$  for the negative domain (Fig. 4b). This revealed reproducible differences across dopamine neurons in the relative magnitude of positive versus negative RPEs (Extended Data Fig. 5). Across all animals, the mean value of the ratio  $\alpha^+ / (\alpha^+ + \alpha^-)$  was 0.48. However, many cells had a value significantly above or below this mean (Fig. 4c; see Methods for details of statistical test). At the group level, there was significant diversity between cells by one-way ANOVA ( $F(38, 234) = 2.93$ ,  $P = 4 \times 10^{-7}$ ). In the animal with the largest number of recorded cells, 3 out of 15 cells were significantly above the mean and 3 out of 15 were significantly below the mean; ANOVA again rejected the null hypothesis of no diversity between cells ( $F(14, 90) = 4.06$ ,  $P = 2 \times 10^{-5}$ ).

Second, RPE asymmetry should correlate, across dopamine neurons, with reversal point. Dopamine neurons that scale positive RPEs more steeply relative to negative RPEs should be linked with relatively optimistic reward predictions, and so should have reversal points at relatively high reward magnitudes. Dopamine neurons that scale positive RPEs less steeply should have relatively low reversal points. Again using data from the variable-magnitude task, we found a strong correlation between RPE asymmetry and reversal point ( $P = 8.1 \times 10^{-5}$  by linear regression; Fig. 4d, e), validating this prediction. Furthermore, this effect survived when only considering data from the single animal with the largest number of recorded cells ( $P = 0.002$ ).

## Decoding reward distributions

As we have discussed, the distributional TD model correctly predicts that dopamine neurons should show diverse reversal points and response asymmetries, and that these should correlate. Finally, we consider the most detailed prediction of the model. The specific reversal points observed in any experimental situation, together with the

particular response asymmetries in the corresponding neurons, should encode an approximate representation of the anticipated probability distribution over future rewards.

If this is the case, then with sufficient data it should be possible to decode the full value distribution from the responses of dopamine neurons. As a final test of the distributional RL hypothesis, we attempted this type of decoding. The distributional TD model implies that, if dopaminergic responses are approximately linear in the positive and negative domains, then the resultant learned reward predictions will correspond to expectiles of the reward distribution<sup>20</sup> (expectiles are a statistic of distributions, which generalize the mean in the same way that quantiles generalize the median).

We therefore treated the reversal points and response asymmetries measured in the variable-magnitude task as defining a set of expectiles, and we transformed these expectiles into a probability density (see Methods). As shown in Fig. 5a–c, the resulting density captured multiple modes of the ground-truth value distribution. Decoding the RPEs produced by a distributional TD simulation, but not a classical TD simulation, produced the same pattern of results.

Parallel analyses focusing on the variable-probability task (see Methods) yielded similarly good matches to the ground-truth distributions in that task (Fig. 5d, e). In both tasks, successful decoding depended on the specific pattern of variability in the neural data, and not on the presence of variability per se (Extended Data Fig. 8).

It is worth emphasizing that none of the effects we have reported are anticipated by the standard RPE theory of dopamine, which implies that all dopamine neurons should transmit essentially the same RPE signal. Why have the present effects not been observed before? In some cases, relevant data have been hiding in plain sight. For example, a number of studies have reported marked variability in the relative magnitude of positive and negative RPEs across dopamine neurons; however, they have treated this as an incidental finding or a reflection of measurement error, or viewed it as a problem for the RPE theory<sup>17</sup>. One of the earliest studies of reward-probability coding in dopaminergic RPEs remarked on apparent diversity across dopamine neurons, but only in a footnote<sup>18</sup>. A more general issue is that the forms of variability we have reported are masked by traditional analysis techniques, which typically focus on average responses across dopamine neurons (see Supplementary Information and Extended Data Fig. 10).

Distributional RL offers a range of untested predictions. Dopamine neurons should maintain their ordering of relative optimism across task

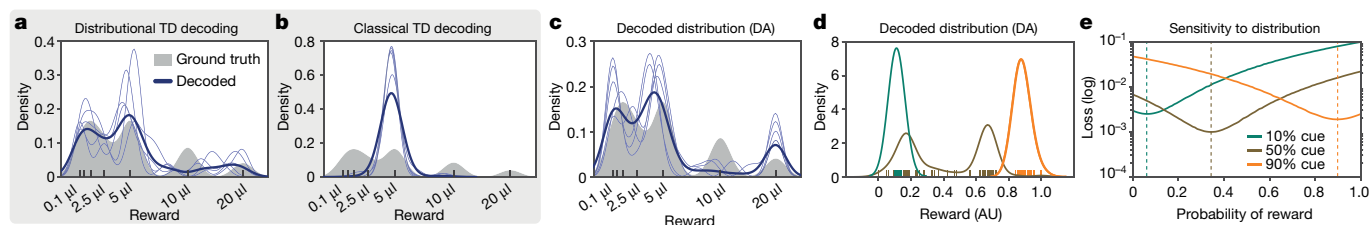


**Fig. 5 | Decoding reward distributions from neural responses.**

**a**, Distributional TD simulation trained on the variable-magnitude task, whose actual (smoothed) distribution of rewards is shown in grey. After training the model, we interpret the learned values as a set of expectiles. We then decode the set of expectiles into a probability density (blue traces). Multiple solutions are shown in light blue, and the average across solutions is shown in dark blue. (See Methods for more details.) **b**, Same as **a**, but with a classical TD simulation. **c**, Same as **a**, but using data from recorded dopamine cells. The expectiles are defined by the reversal points and the relative scaling from the slopes of

positive and negative RPEs, as shown in Fig. 4. Unlike the classical TD simulation, the real dopamine cells collectively encode the shape of the reward distribution that animals have been trained to expect. **d**, Same decoding analysis, using data from each of the cue conditions in the variable-probability task, based on cue responses of dopamine neurons (decoding for GABAergic neurons shown in Extended Data Fig. 8i, j). **e**, The neural data for both dopamine and GABAergic neurons were best fit by Bernoulli distributions closely approximating the ground-truth reward probabilities in all three cue conditions.

contexts, even as the specific distribution of rewards changes. If RPE channels with particular levels of optimism are selectively activated with optogenetics, this should sculpt the learned distribution, which should in turn be detectable with behavioural measures of sensitivity to moments of the distribution. We list further predictions in the Supplementary Information.

Distributional RL also gives rise to a number of broader questions. What are the circuit- or cellular-level mechanisms that give rise to a diversity of asymmetry in positive versus negative RPE scaling? It is also worth considering whether other mechanisms, aside from asymmetric scaling of RPEs, might contribute to distributional coding. It is well established, for example, that positive and negative RPEs differentially engage striatal D<sub>1</sub> and D<sub>2</sub> dopamine receptors<sup>21</sup>, and that the balance of these receptors varies anatomically<sup>22–24</sup>. This suggests a second potential mechanism for differential learning from positive versus negative RPEs<sup>25</sup>. Moreover, how do different RPE channels anatomically couple with their corresponding reward predictions (see Extended Data Fig. 4i–k)? Finally, what effects might distributional coding have downstream, at the level of action learning and selection? With this question in mind, it is notable that some current theories in behavioural economics centre on risk measures that can be easily read out from the kind of distributional codes that the present work has considered.

Finally, we speculate on the implications of the distributional hypothesis of dopamine for the mechanisms of mental disorders such as addiction and depression. Mood has been linked with predictions of future reward<sup>26</sup>, and it has been proposed that both depression and bipolar disorder may involve biased forecasts concerning value-laden outcomes<sup>27</sup>. It has recently been proposed that such biases may arise from asymmetries in RPE coding<sup>28,29</sup>. There are clear potential connections between these ideas and the phenomena we have reported here, presenting opportunities for further research.

## Online content

Any methods, additional references, Nature Research reporting summaries, source data, extended data, supplementary information, acknowledgements, peer review information; details of author contributions and competing interests; and statements of data and code availability are available at <https://doi.org/10.1038/s41586-019-1924-6>.

- Schultz, W., Stauffer, W. R. & Lak, A. The phasic dopamine signal maturing: from reward via behavioural activation to formal economic utility. *Curr. Opin. Neurobiol.* **43**, 139–148 (2017).
- Glimcher, P. W. Understanding dopamine and reinforcement learning: the dopamine reward prediction error hypothesis. *Proc. Natl Acad. Sci. USA* **108**, 15647–15654 (2011).
- Watabe-Uchida, M., Eshel, N. & Uchida, N. Neural circuitry of reward prediction error. *Annu. Rev. Neurosci.* **40**, 373–394 (2017).
- Morimura, T., Sugiyama, M., Kashima, H., Hachiya, H. & Tanaka, T. Parametric return density estimation for reinforcement learning. In *Proc. 26th Conference on Uncertainty in Artificial Intelligence* (eds Grunwald, P. & Spirtes, P.) <http://dl.acm.org/citation.cfm?id=3023549.3023592> (2010).

- Bellemare, M. G., Dabney, W. & Munos, R. A distributional perspective on reinforcement learning. In *International Conference on Machine Learning* (eds Precup, D. & The, Y. W.) 449–458 (2017).
- Dabney, W., Rowland, M., Bellemare, M. G. & Munos, R. Distributional reinforcement learning with quantile regression. In *AAAI Conference on Artificial Intelligence* (2018).
- Sutton, R. S. & Barto, A. G. *Reinforcement Learning: an Introduction* Vol. 1 (MIT Press, 1998).
- Mnih, V. et al. Human-level control through deep reinforcement learning. *Nature* **518**, 529–533 (2015).
- Silver, D. et al. Mastering the game of Go with deep neural networks and tree search. *Nature* **529**, 484–489 (2016).
- Hessel, M. et al. Rainbow: combining improvements in deep reinforcement learning. In *32nd AAAI Conference on Artificial Intelligence* (2018).
- Botvinick, M. M., Niv, Y. & Barto, A. G. Hierarchically organized behavior and its neural foundations: a reinforcement learning perspective. *Cognition* **113**, 262–280 (2009).
- Wang, J. X. et al. Prefrontal cortex as a meta-reinforcement learning system. *Nat. Neurosci.* **21**, 860–868 (2018).
- Song, H. F., Yang, G. R. & Wang, X. J. Reward-based training of recurrent neural networks for cognitive and value-based tasks. *eLife* **6**, e21492 (2017).
- Barth-Maron, G. et al. Distributed distributional deterministic policy gradients. In *International Conference on Learning Representations* <https://openreview.net/forum?id=SyZpzbCb> (2018).
- Dabney, W., Ostrovski, G., Silver, D. & Munos, R. Implicit quantile networks for distributional reinforcement learning. In *International Conference on Machine Learning* (2018).
- Pouget, A., Beck, J. M., Ma, W. J. & Latham, P. E. Probabilistic brains: knowns and unknowns. *Nat. Neurosci.* **16**, 1170–1178 (2013).
- Lammel, S., Lim, B. K. & Malenka, R. C. Reward and aversion in a heterogeneous midbrain dopamine system. *Neuropharmacology* **76**, 351–359 (2014).
- Fiorillo, C. D., Tobler, P. N. & Schultz, W. Discrete coding of reward probability and uncertainty by dopamine neurons. *Science* **299**, 1898–1902 (2003).
- Eshel, N. et al. Arithmetic and local circuitry underlying dopamine prediction errors. *Nature* **525**, 243–246 (2015).
- Rowland, M., et al. Statistics and samples in distributional reinforcement learning. In *International Conference on Machine Learning* (2019).
- Frank, M. J., Seeberger, L. C. & O'Reilly, R. C. By carrot or by stick: cognitive reinforcement learning in parkinsonism. *Science* **306**, 1940–1943 (2004).
- Hirvonen, J. et al. Striatal dopamine D1 and D2 receptor balance in twins at increased genetic risk for schizophrenia. *Psychiatry Res. Neuroimaging* **146**, 13–20 (2006).
- Piggott, M. A. et al. Dopaminergic activities in the human striatum: rostrocaudal gradients of uptake sites and of D1 and D2 but not of D3 receptor binding or dopamine. *Neuroscience* **90**, 433–445 (1999).
- Rosa-Neto, P., Doudet, D. J. & Cumming, P. Gradients of dopamine D1- and D2/3-binding sites in the basal ganglia of pig and monkey measured by PET. *Neuroimage* **22**, 1076–1083 (2004).
- Mikhael, J. G. & Bogacz, R. Learning reward uncertainty in the basal ganglia. *PLOS Comput. Biol.* **12**, e1005062 (2016).
- Robb, B. et al. A computational and neural model of momentary subjective well-being. *Proc. Natl Acad. Sci. USA* **111**, 12252–12257 (2014).
- Huys, Q. J., Daw, N. D. & Dayan, P. Depression: a decision-theoretic analysis. *Annu. Rev. Neurosci.* **38**, 1–23 (2015).
- Bennett, D. & Niv, Y. Opening Burton's clock: psychiatric insights from computational cognitive models. Preprint at <https://doi.org/10.31234/osf.io/y2vzu> (2018).
- Tian, J. & Uchida, N. Habenula lesions reveal that multiple mechanisms underlie dopamine prediction errors. *Neuron* **87**, 1304–1316 (2015).
- Eshel, N., Tian, J., Bukwich, M. & Uchida, N. Dopamine neurons share common response function for reward prediction error. *Nat. Neurosci.* **19**, 479–486 (2016).

**Publisher's note** Springer Nature remains neutral with regard to jurisdictional claims in published maps and institutional affiliations.

© The Author(s), under exclusive licence to Springer Nature Limited 2020

### Distributional RL model

The model for distributional RL we use throughout the work is based on the principle of asymmetric regression and extends recent results in AI<sup>5,6,15</sup>. We present a more detailed and accessible introduction to distributional RL in the Supplementary Information. Here we outline the method in brief.

Let  $f: \mathbb{R} \rightarrow \mathbb{R}$  be a response function. In each observed state  $x$ , let there be a set of value predictions  $V_i(x)$  which are updated with learning rates  $\alpha_i^+, \alpha_i^- \in \mathbb{R}^+$ . Then given a state  $x$ , next-state  $x'$ , resulting reward signal  $r$  and time discount  $\gamma \in [0, 1]$ , the distributional TD model computes distributional TD errors

$$\delta_i = r + \gamma V_j(x') - V_i(x) \quad (1)$$

where  $V_j(x')$  is a sample from the distribution  $V(x')$ . The model then updates the baselines with

$$V_i(x) \leftarrow V_i(x) + \alpha_i^+ f(\delta_i) \quad \text{for } \delta_i > 0 \quad (2)$$

$$V_i(x) \leftarrow V_i(x) + \alpha_i^- f(\delta_i) \quad \text{for } \delta_i \leq 0 \quad (3)$$

When performed with a tabular representation, asymmetry uniformly distributed, and  $f(\delta) = \text{sgn}(\delta)$ , this method converges to the  $\tau_i$  quantile,  $\tau_i = \frac{\alpha_i^+}{\alpha_i^+ + \alpha_i^-}$ , of the distribution over discounted returns at  $x$  (ref. <sup>6</sup>). Similarly, asymmetric regression with response function  $f(\delta) = \delta$  corresponds to expectile regression<sup>31</sup>. Like quantiles, expectiles fully characterize the distribution and have been shown to be particularly useful for measures of risk<sup>32,33</sup>.

Finally, we note that throughout the paper, we use the terms optimistic and pessimistic to refer to return predictions that are above or below the mean (expected) return. Importantly, these predictions are optimistic in the sense of corresponding to particularly good outcomes from the set of possible outcomes. They are not optimistic in the sense of corresponding to outcomes that are impossibly good.

### Artificial agent results

Atari results are on the Atari-57 benchmark using the publicly available Arcade Learning Environment<sup>34</sup>. This is a set of 57 Atari 2600 games and human-performance baselines. Refer to previous work for details on deep  $Q$ -networks (DQN) and computation of human-normalized scores<sup>8</sup>. The distributional TD agent uses our proposed model and a DQN with multiple ( $n = 200$ ) value predictors, each with a different asymmetry, spaced uniformly in  $[0, 1]$ . The training objective of DQN, the Huber loss, is replaced with the asymmetric quantile-Huber loss, which corresponds to the  $\kappa$ -saturating response function  $f(\delta) = \max(\min(\delta, \kappa), -\kappa)$ , with  $\kappa = 1$ .

Finally, at each update we train all channels based on the immediate reward and the predicted future returns from all next-state value predictors. Further details can be found in ref. <sup>6</sup>. The physics-based motor-control task requires control of a 28 degrees-of-freedom humanoid to complete a 3D obstacle course in minimal time<sup>35</sup>. Full details for the D3PG and distributional D3PG agents are as described<sup>14</sup>. Distributions over return shown in Extended Data Fig. 2d, f are based on the network-predicted distribution in each of the given frames.

### Tabular simulations

Tabular simulations of the classical TD and distributional TD models used a population of learning rates selected uniformly at random,  $\alpha_i^+ \sim U(0, 1)$  for each cell  $i$ . In all cases the only algorithmic difference between the classical and distributional TD models was that the distributional model used a separately varying learning rate for negative prediction errors,  $\alpha_i^- \sim U(0, 1)$  for each cell  $i$ . Both methods used a linear response function. Qualitatively similar results were also obtained

with other response functions (for example, Hill function<sup>30</sup> or  $\kappa$ -saturating), despite these leading to semantically different estimators of the distribution. The population sizes were chosen for clarity of presentation and to provide similar variability as observed in the neuronal data. Each cell was paired with a different state-dependent value estimate  $V_i(x)$ . Note that while these simulations focused on immediate rewards, the same algorithm also learns distributions over multi-step returns.

In the variable-probability task, each cue corresponded to a different value estimate and reward probability (90%, 50% or 10%). When rewarded, the agent received numerical reward of 1.0, and when omitted, it received 0.0. Both agents were trained for 100 trials of 5,000 updates, and both simulated  $n = 31$  cells (separate value estimates). The learning rates were all selected uniformly at random between  $[0.001, 0.2]$ . Cue response was taken to be the temporal difference from a constant zero baseline to the value estimate.

In the variable-magnitude task, all rewards were taken to be the water magnitude measured in microlitres (qualitatively same results obtained with utilities instead of magnitudes). For Fig. 2 we ran 10 trials of 25,000 updates each for 150 estimators with random learning rates in  $[0.001, 0.02]$ . These smaller learning rates and larger number of updates were intended to ensure the values converged fully with low error. We then report temporal difference errors for ten cells taken uniformly to span the range of value estimates for each agent. Reported errors (simulating change in firing rate) are the utility of a reward minus the value estimate and scaled by the learning rate. As with the neuronal data, these are reported averaged over trials and normalized by variance over reward magnitudes. Distributional TD RPEs are computed using asymmetric learning rates, with a small constant (floor) added to the learning rates.

### Distribution decoding

For both real neural data and TD simulations, we performed distribution decoding. The distributional and classical TD simulations used for decoding in the variable-magnitude task each used 40 value predictors, to match the 40 recorded cells in the neural data (neural analyses were pooled across the six animals). In the distributional TD simulation, each value predictor used a different asymmetric scaling factor  $\tau_i = \frac{\alpha_i^+}{\alpha_i^+ + \alpha_i^-}$ , and therefore learned a different value prediction  $V_i$ .

The decoding analyses began with a set of reversal points,  $V_i$ , and asymmetric scaling factors  $\tau_i$ . For the neural data, these were obtained as described elsewhere. For the simulations, they were read directly from the simulation. These numbers were interpreted as a set of expectiles, with the  $\tau_i$ -th expectile having value  $V_i$ . We decoded these into probability densities by solving an optimization problem to find the density most compatible with the set of expectiles<sup>20</sup>. For optimization, the density was parameterized as a set of samples. For display in Fig. 5, the samples are smoothed with kernel density estimation.

### Animals and behavioural tasks

The rodent data we re-analysed here were first reported in ref. <sup>19</sup>. Methods details can be found in that paper and in ref. <sup>30</sup>. We give a brief description of the methods below.

Five mice were trained on a 'variable-probability' task, and six different mice on a 'variable-magnitude' task. In the variable-probability task, in each trial the animal first experienced one of four odour cues for 1 s, followed by a 1-s pause, followed by a reward (3.75  $\mu$ l water), an aversive airpuff or nothing. Odour 1 signalled a 90% chance of reward, odour 2 signalled a 50% chance of reward, odour 3 signalled a 10% chance of reward and odour 4 signalled a 90% chance of airpuff. Odour meanings were randomized across animals. Inter-trial intervals were exponentially distributed.

An infrared beam was positioned in front of the water delivery spout, and each beam break was recorded as one lick event. We report the average lick rate over the entire interval between the cue and the outcome (that is, 0–2,000 ms after cue onset).



In the variable-magnitude task, in 10% of trials an odour cue was delivered that indicated that no reward would be delivered on that trial. In the remaining 90% of trials, one of the following reward magnitudes was delivered, at random: 0.1, 0.3, 1.2, 2.5, 5, 10 or 20  $\mu\text{l}$ . In half of these trials, this reward was preceded by 1,500 ms by an odour cue (which indicated that a reward was forthcoming but did not disclose its magnitude). In the other half, it was unsignalled.

In order to identify dopamine neurons while recording, neurons in the VTA were tagged with channelrhodopsin-2 (ChR2) by injecting adeno-associated virus (AAV) that expresses ChR2 in a Cre-dependent manner into the VTA of transgenic mice that express Cre recombinase under the promoter of the dopamine transporter (DAT) gene *Slc6a3* (B6.SJL-Slc6a3tm1.1(cre)Bkmn/J, The Jackson Laboratory)<sup>36</sup>. Mice were implanted with a head plate and custom-built microdrive containing 6–8 tetrodes (Sandvik) and optical fibre, as described<sup>37</sup>.

All experiments were performed in accordance with the US National Institutes of Health Guide for the Care and Use of Laboratory Animals and approved by the Harvard Institutional Animal Care and Use Committee.

### Neuronal data and analysis

Extracellular recordings were made from VTA using a data acquisition system (DigiLynx, Neuralynx). VTA recording sites were verified histologically. The identity of dopaminergic cells was confirmed by recording the electrophysiological responses of cells to a brief blue light pulse train, which stimulates only DAT-expressing cells. Spikes were sorted using SpikeSort3D (Neuralynx) or MClust-3.5 (A.D. Redish). Putative GABAergic neurons in the VTA were identified by clustering of firing patterns as described previously<sup>30,37</sup>. All confidence intervals are s.e.m. unless otherwise noted.

Data analyses were performed using NumPy 1.15 and MATLAB R2018a (Mathworks). Spike times were collected in 1-ms bins to create per-stimulus time histograms. These histograms were then smoothed by convolving with the function  $(1 - e^{-t}) \cdot e^{-t/T}$ , where  $T$  was a time constant, set to 20 ms as in ref.<sup>30</sup>. For single-cell traces, we set  $T$  to 200 ms for display purposes.

After smoothing, the data were baseline-corrected by subtracting from each trial and each neuron independently the mean over that trial's activity from –1,000 to 0 ms relative to stimulus onset (or relative to reward onset in the unexpected reward condition).

**Variable-probability task.**  $n = 31$  cells were recorded from five animals, with the following number of cells per animal: 1, 4, 16, 1 and 9. Responses to cue for dopamine neurons were defined as the average activity from 0 to 400 ms after cue onset. This interval was chosen to match ref.<sup>30</sup>. Responses to cue for putative GABAergic neurons were defined as the average activity from 0 to 1,500 ms after cue onset. This longer interval was chosen because these neurons had much slower responses, often ramping up slowly over the first 500 or 1,000 ms after cue onset<sup>37</sup> (Fig. 3d).

We were interested in whether there was between-cell diversity in responses to the 50% cue. We first normalized the responses to the 50% cue on a per-cell basis as follows:  $c_{50}^{\text{norm}} = (c_{50} - \text{mean}(c_{10})) / (\text{mean}(c_{90}) - \text{mean}(c_{10}))$ , where mean indicates the mean over trials within a cell. In order to be agnostic about the risk preferences of the animal, we then performed a two-tailed  $t$ -test of the cell's normalized responses to the 50% cue against the average of all cells' normalized responses to the 50% cue. This is the test for optimistic or pessimistic probability coding that we report in the main text. Note that these  $t$ -statistics would be  $t$ -distributed if the differences between cells were due to chance. We also report ANOVA results where we evaluate the null hypothesis that all cells' normalized 50% responses have the same mean.

The same pattern of results held when instead comparing responses to the 50% cue against the midway point between responses to the 10% cue and responses to the 90% cue.

The per-cell cue responses shown in Extended Data Fig. 7 were normalized to zero mean and unit variance, to allow direct comparison of cells with different response variability. Each cell appears in one of three panels based on the outcome of two single-tailed Mann–Whitney tests evaluating the rank order for  $c_{10} < c_{50}$  and  $c_{50} < c_{90}$  (see Supplementary Information section 3.3 for further details). The left, centre and right panels correspond to outcomes ( $P \geq 0.05, P < 0.05$ ), ( $P < 0.05, P < 0.05$  or  $P \geq 0.05, P \geq 0.05$ ) and ( $P < 0.05, P \geq 0.05$ ), respectively.

**Variable-magnitude task.**  $n = 40$  cells were recorded from five animals, with the following number of cells per animal: 3, 6, 9, 16 and 6. Responses to reward were defined as the average activity from 200 to 600 ms after reward onset. This time interval was selected to match ref.<sup>30</sup> as closely as possible, while excluding the initial response to the feeder click<sup>30,38,39</sup>, which was not selective to reward magnitude and was positive for all reward magnitudes. This enabled us to find the reward magnitudes for which the dopamine response was either boosted or suppressed relative to baseline.

The reversal point (that is, the reward magnitude that would elicit neither a positive nor a negative deflection in firing relative to baseline) for each cell was defined as the magnitude  $M_R$  that maximized the number of positive responses to rewards greater than  $M_R$  plus the number of negative responses to rewards less than  $M_R$ . To obtain statistics for reliability of cell-to-cell differences in reversal point, we partitioned the data into random halves and estimated the reversal point for each cell separately in each half. We repeated this procedure 1,000 times with different random partitions, and we report the mean  $R$  value and geometric mean  $p$  value across these 1,000 folds.

After measuring reversal points, we fit linear functions separately to the positive and negative domains of each cell. To obtain confidence intervals, we divided the data into seven random partitions (seven being the smallest number of trials in any condition for any cell), subject to the constraint that every condition for every cell contain at least one trial in each partition. In each partition, we repeated the procedure for estimating reversal points and finding slopes in the positive and negative domains. Our confidence interval on  $\tau = \alpha^+ / (\alpha^+ + \alpha^-)$  was then the s.e.m. of the values calculated across the seven partitions. ANOVAs are also reported testing the null hypothesis that means (across partitions) were not different between cells.

Fitting linear functions to dopamine responses was more logical in utility space than in reward volume space. We relied on ref.<sup>38</sup> to approximate the underlying utility function from the dopamine responses to rewards of varying magnitudes. We used these empirical utilities instead of raw reward magnitudes for the analyses shown in Fig. 4. However, none of the reported results were sensitive to this choice of utility function. We also ran the analyses using other utility functions, and these results are reported in Extended Data Fig. 5. One cell was excluded from analyses in Fig. 5: because it had no positive responses to any reward magnitude, a slope could not be fit in the positive domain.

When measuring the correlation (across cells) between reversal point and  $\tau$ , we first randomly split the data into two disjoint halves of trials. In one half, we first calculated reversal points  $RP_1$  and used these reversal points to calculate  $\alpha^+$  and  $\alpha^-$ . In the other half, we calculated reversal points  $RP_2$ . The correlation we report is between  $RP_2$  and  $\tau = \alpha^+ / (\alpha^+ + \alpha^-)$ . We did this to avoid confounds associated with using the same data to estimate both slopes and intercepts.

### Reporting summary

Further information on research design is available in the Nature Research Reporting Summary linked to this paper.

### Data availability

The neuronal data analysed in this work are available at <https://doi.org/10.17605/OSF.IO/UX5RG>.



## Code availability

The analysis code from our value-distribution decoding and code used to generate model predictions for distributional TD are available at <https://doi.org/10.17605/OSF.IO/UX5RG>.

31. Newey, W. K. & Powell, J. L. Asymmetric least squares estimation and testing. *Econometrica* **55**, 819–847 (1987).
32. Chris Jones, M. Expectiles and m-quantiles are quantiles. *Stat. Probab. Lett.* **20**, 149–153 (1994).
33. Ziegel, J. F. Coherence and elicibility. *Math. Finance* **26**, 901–918 (2016).
34. Bellemare, M. G., Naddaf, Y., Veness, J. & Bowling, M. The arcade learning environment: an evaluation platform for general agents. *J. Artif. Intell. Res.* **47**, 253–279 (2013).
35. Heess, N. et al. Emergence of locomotion behaviours in rich environments. Preprint at <https://arxiv.org/abs/1707.02286> (2017).
36. Bäckman, C. M., et al. Characterization of a mouse strain expressing cre recombinase from the 3' untranslated region of the dopamine transporter locus. *Genesis* **44**, 383–390 (2006).
37. Cohen, J. Y. et al. Neuron-type-specific signals for reward and punishment in the ventral tegmental area. *Nature* **482**, 85–88 (2012).
38. Stauffer, W. R., Lak, A. & Schultz, W. Dopamine reward prediction error responses reflect marginal utility. *Curr. Biol.* **24**, 2491–2500 (2014).
39. Fiorillo, C. D., Song, M. R. & Yun, S. R. Multiphasic temporal dynamics in responses of midbrain dopamine neurons to appetitive and aversive stimuli. *J. Neurosci.* **33**, 4710–4725 (2013).

40. Schaul, T., Quan, J., Antonoglou, I. & Silver, D. Prioritized experience replay. In *International Conference on Learning Representations* (2016).
41. Van Hasselt, H., Guez, A. & Silver, D. Deep reinforcement learning with double q-learning. In *AAAI Conference on Artificial Intelligence* (2016).
42. Krizhevsky, A. & Hinton, G. *Learning Multiple Layers of Features from Tiny Images* (Univ. of Toronto, 2009).

**Acknowledgements** We thank K. Miller, P. Dayan, T. Stepleton, J. Paton, M. Frank, C. Clopath, T. Behrens and the members of the Uchida laboratory for comments on the manuscript; and N. Eshel, J. Tian, M. Bukwich and M. Watabe-Uchida for providing data.

**Author contributions** W.D. conceived the project. W.D., Z.K.-N. and M.B. contributed ideas for experiments and analysis. W.D. and Z.K.-N. performed simulation experiments and analysis. N.U. and C.K.S. provided neuronal data for analysis. W.D., Z.K.-N. and M.B. managed the project. M.B., N.U., R.M. and D.H. advised on the project. M.B., W.D. and Z.K.-N. wrote the paper. W.D., Z.K.-N., M.B., N.U., C.K.S., D.H. and R.M. provided revisions to the paper.

**Competing interests** The authors declare no competing interests.

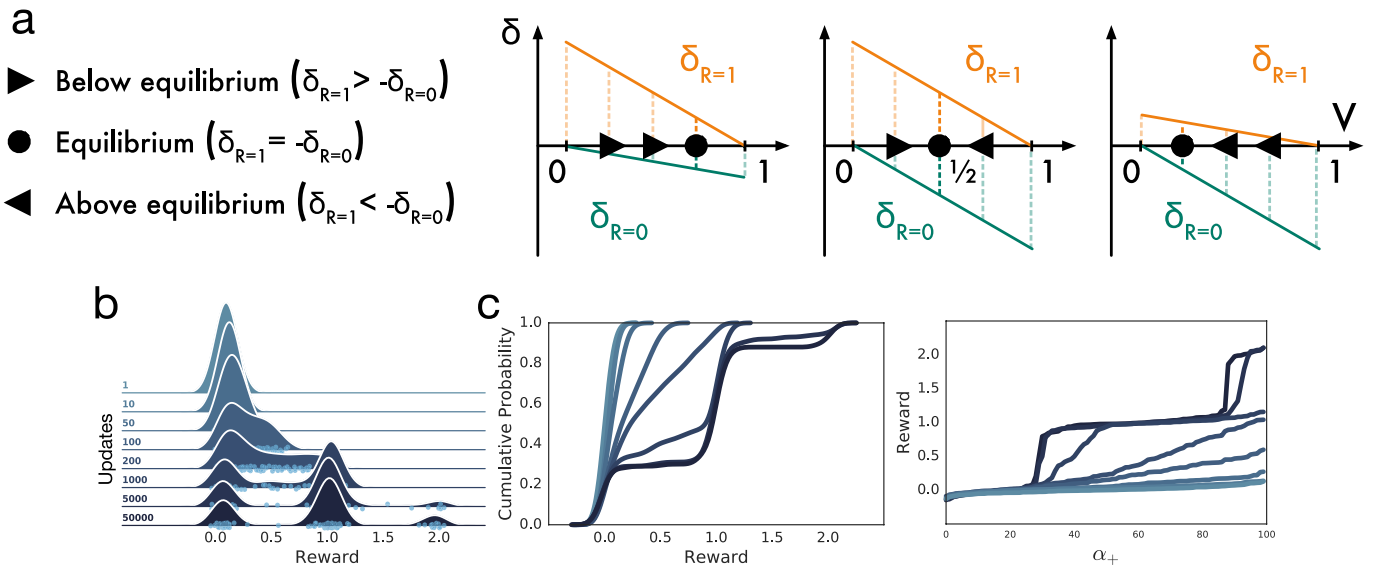
## Additional information

**Supplementary information** is available for this paper at <https://doi.org/10.1038/s41586-019-1924-6>.

**Correspondence and requests for materials** should be addressed to W.D.

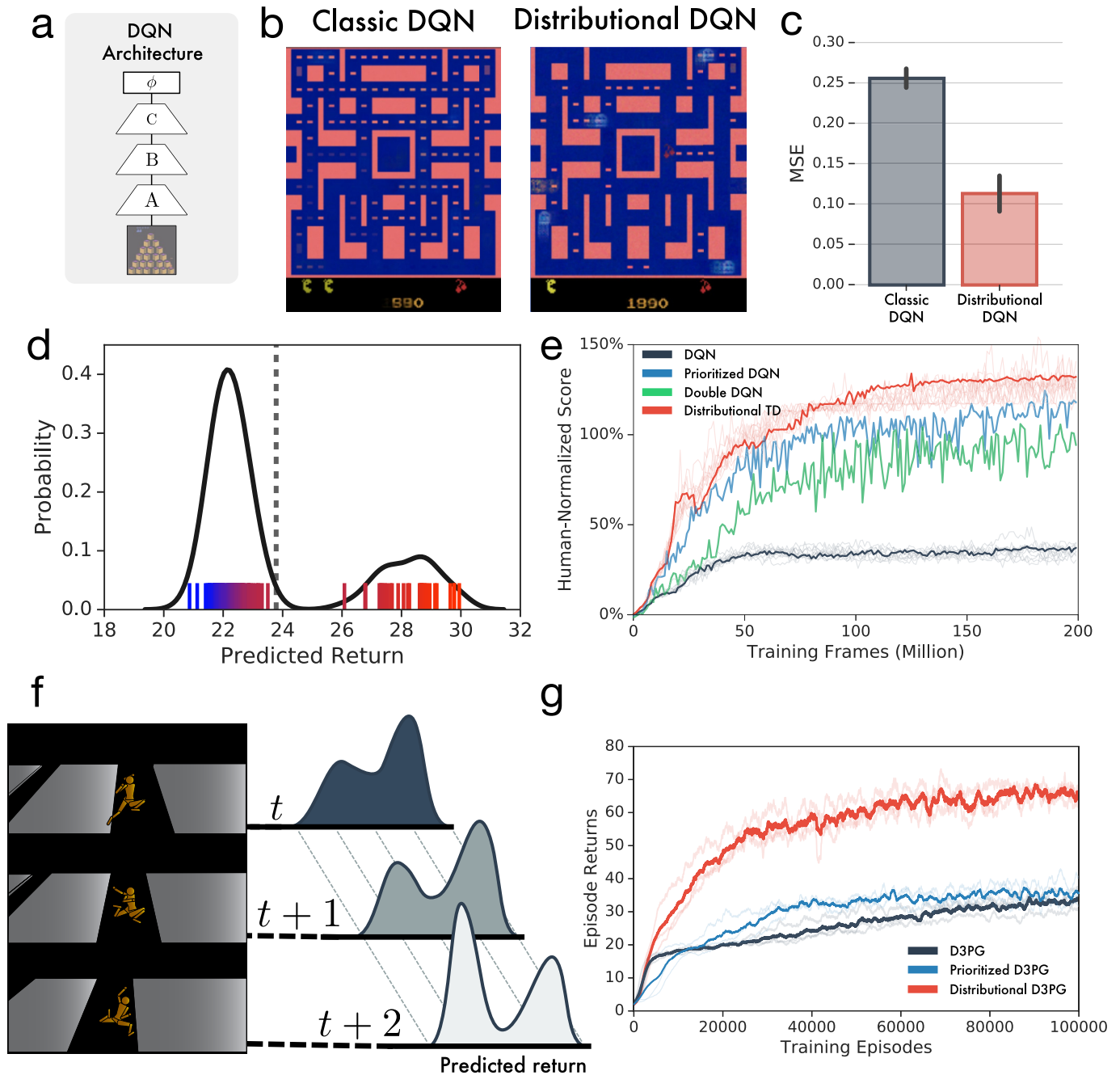
**Peer review information** *Nature* thanks Rui Costa, Michael Littman and the other, anonymous, reviewer(s) for their contribution to the peer review of this work.

**Reprints and permissions information** is available at <http://www.nature.com/reprints>.



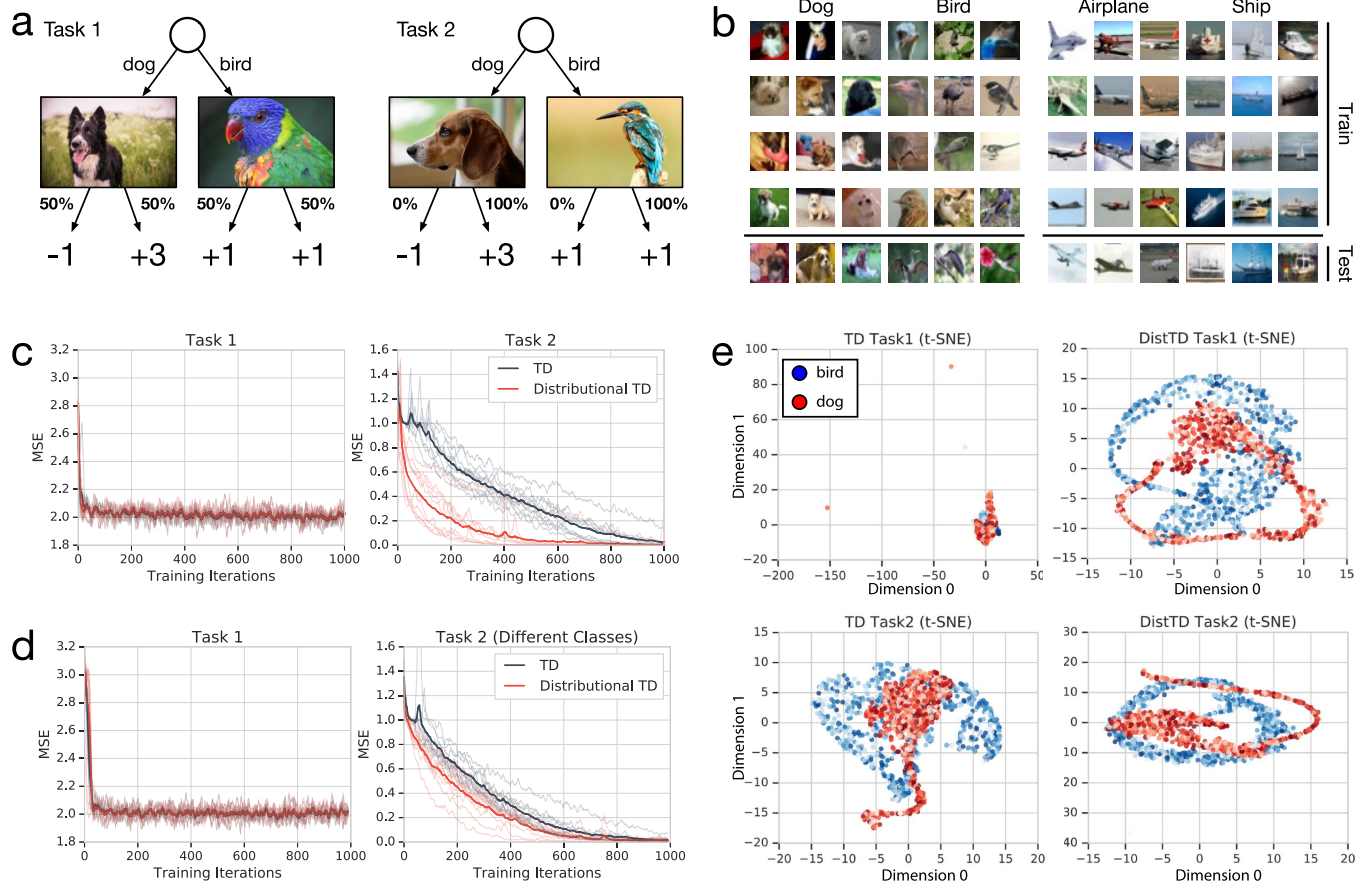
**Extended Data Fig. 1 | Mechanism of distributional TD. a**, The degree of asymmetry in positive to negative scale determines the equilibrium where positive and negative errors balance. Equal scaling equilibrates at the mean, whereas a larger positive (negative) scaling produces an equilibrium above (below) the mean. **b**, Distributional prediction emerges through experience.

Quantile (sign function) version is displayed here for clarity. Model is trained on arbitrary task with trimodal reward distribution. **c**, Same as **b**, viewed in terms of cumulative distribution (left) or learned value for each predictor (quantile function) (right).



**Extended Data Fig. 2 | Learning the distribution of returns improves performance of deep RL agents across multiple domains.** **a**, DQN and distributional TD share identical nonlinear network structures. **b, c**, After training classical or distributional DQN on MsPacman, we freeze the agent and then train a separate linear decoder to reconstruct frames from the agent's final layer representation. For each agent, reconstructions are shown. The distributional model's representation allows substantially better reconstruction. **d**, At a single frame of MsPacman (not shown), the agent's value predictions together represent a probability distribution over future rewards.

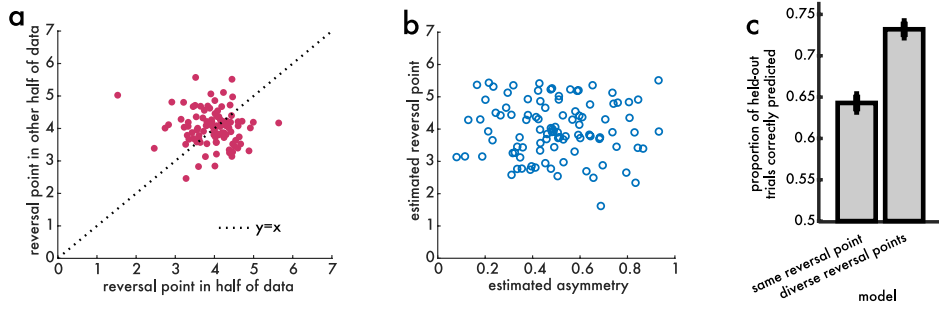
Reward predictions of individual RPE channels shown as tick marks ranging from pessimistic (blue) to optimistic (red), and kernel density estimate shown in black. **e**, Atari-57 experiments with single runs of prioritized experience replay<sup>40</sup> and double DQN<sup>41</sup> agents for reference. Benefits of distributional learning exceed other popular innovations. **f, g**, The performance pay-off of distributional RL can be seen across a wide diversity of tasks. Here we give another example, a humanoid motor-control task in the MuJoCo physics simulator. Prioritized experience replay agent is shown for reference<sup>44</sup>. Traces show individual runs; averages are in bold.



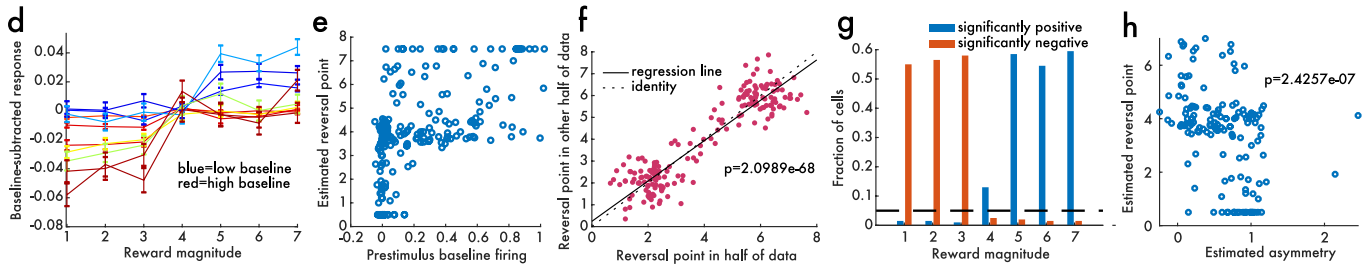
**Extended Data Fig. 3 | Simulation experiment to examine the role of representation learning in distributional RL. a,** Illustration of tasks 1 and 2. **b,** Example images for each class used in our experiment<sup>42</sup> **c,** Experimental results, where each of ten random seeds yields an individual run shown with traces; average over seeds is shown in bold. **d,** Same as **c**, but for control

experiment. **e,** Bird-dog *t*-SNE visualization of final hidden layer of network, given different input images (blue, bird; red, dog). Left, classical TD; right, distributional TD; top row, representation after training on task 1; bottom row, representation after training on task 2.

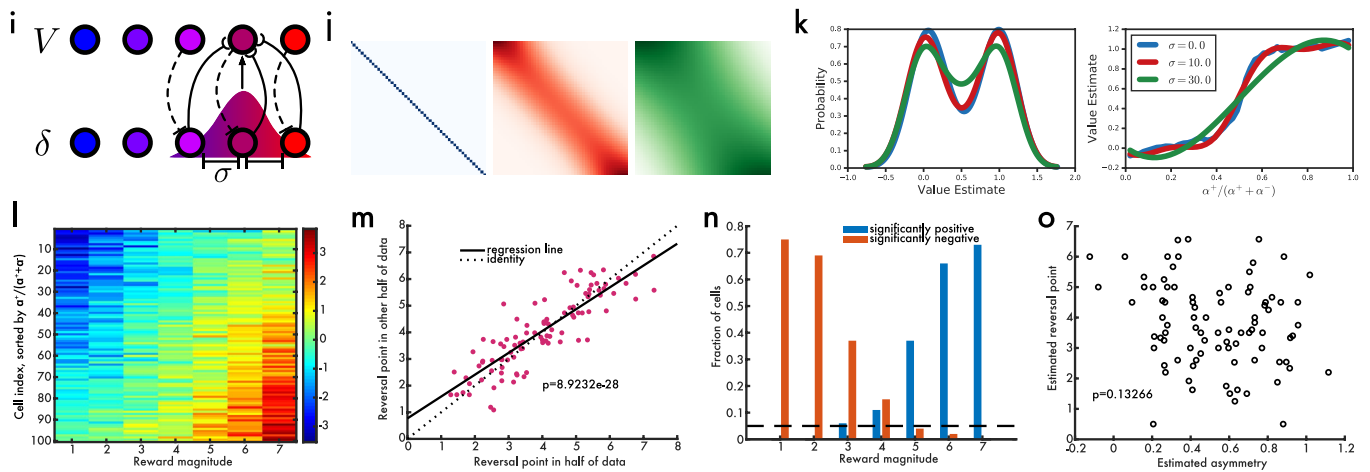
## Model 1: RPE+noise



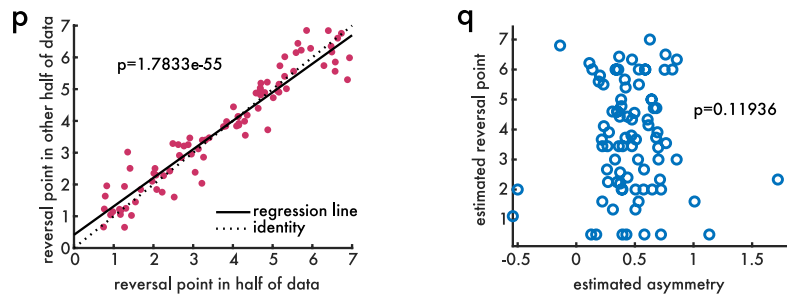
## Model 3: $\sigma$ (RPE+bias)+noise



## Model 5: "One-sided" distributional RL



## Model 6: Synaptic asymmetries

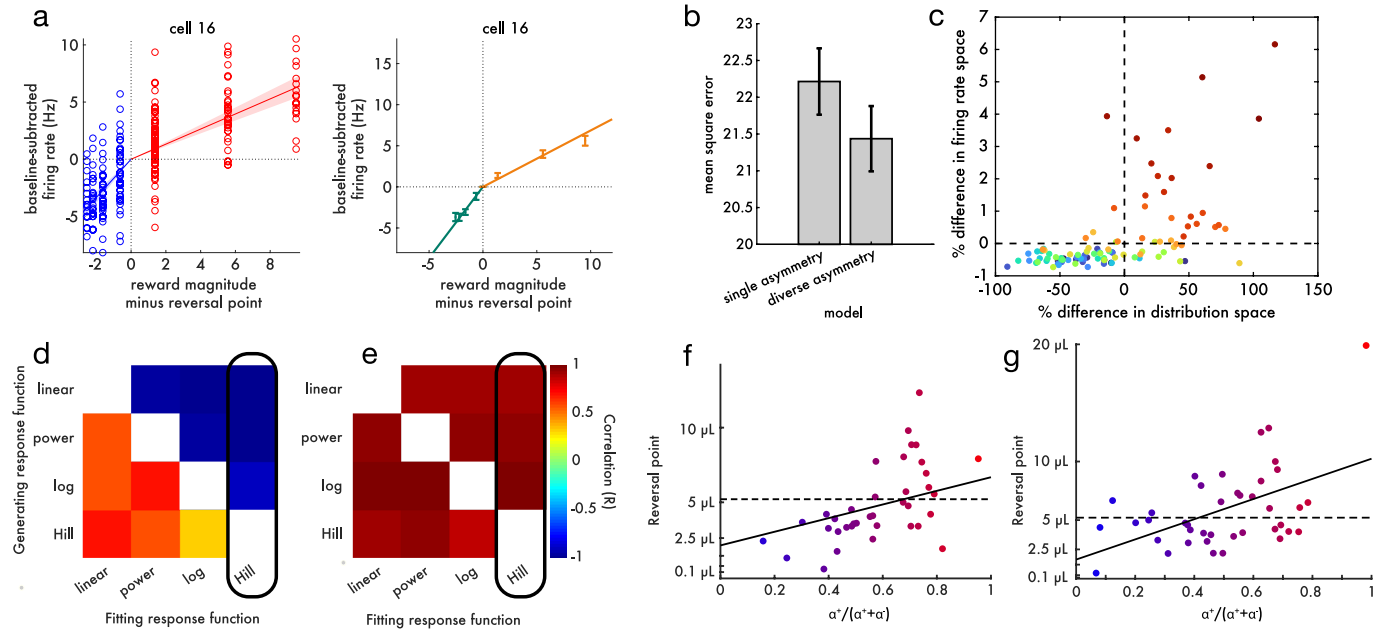


Extended Data Fig. 4 | See next page for caption.



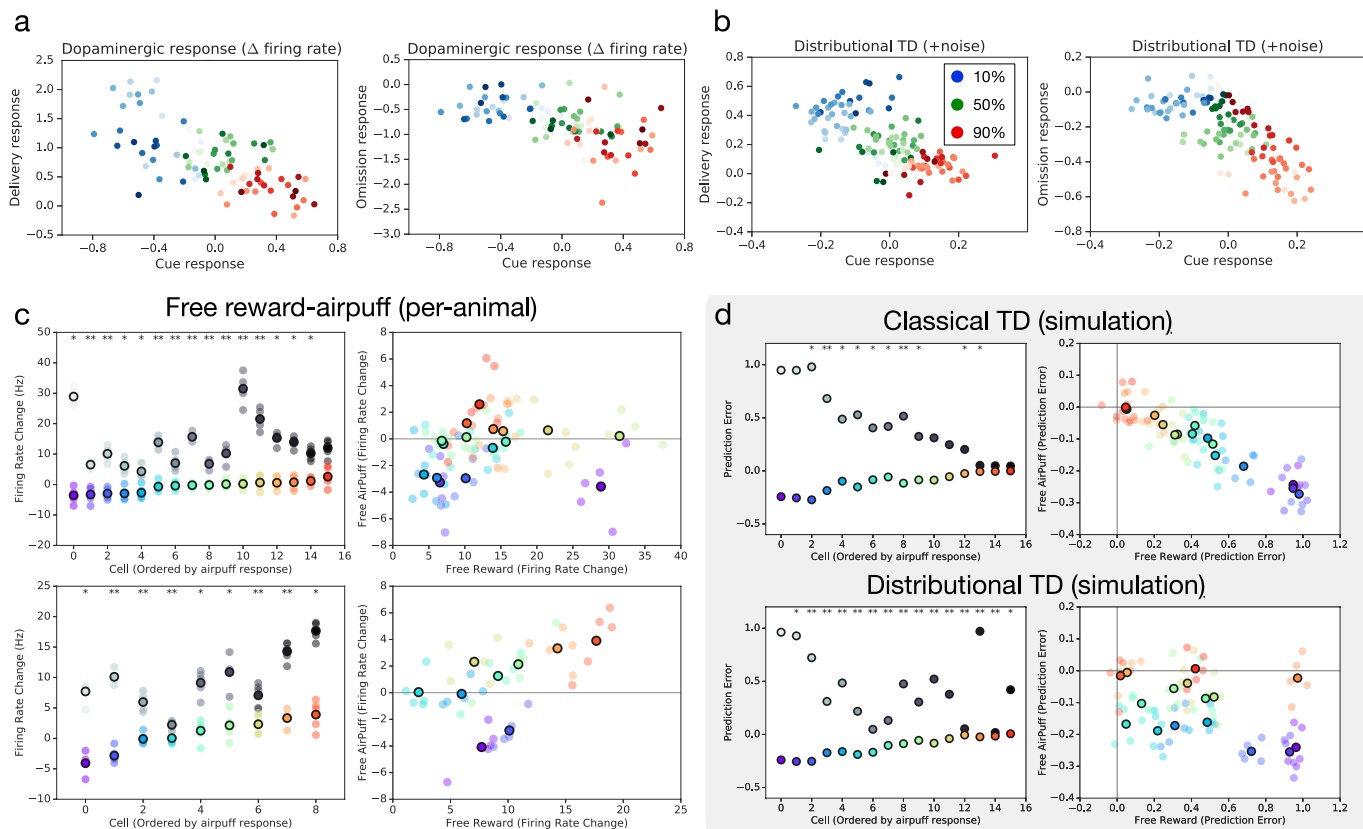
**Extended Data Fig. 4 | Null models.** **a**, Classical TD plus noise does not give rise to the pattern of results observed in real dopamine data in the variable-magnitude task. When reversal points were estimated in two independent partitions there was no correlation between the two ( $P = 0.32$  by linear regression). **b**, We then estimated asymmetric scaling of responses and found no correlation between this and reversal point ( $P = 0.78$  by linear regression). **c**, Model comparison between 'same', a single reversal point, and 'diverse', separate reversal points. In both, the model is used to predict whether a held-out trial has a positive or negative response. **d**, Simulated baseline-subtracted RPEs, colour-coded according to the ground-truth value of bias added to that cell's RPEs. **e**, Across all simulated cells, there was a strong positive relationship between pre-stimulus baseline firing and the estimated reversal point. **f**, Two independent measurements of the reversal point were strongly correlated. **g**, The proportion of simulated cells that have significantly positive (blue) or negative (red) responses showed no magnitudes with both positive and negative responses. **h**, In the simulation, there was a significant negative relationship between the estimated asymmetry of each cell and its estimated

reversal point (opposite that observed in neural data). **i**, Diagram illustrating a Gaussian-weighted topological mapping between RPEs and value predictors. **j**, Varying the standard deviation of this Gaussian modulates the degree of coupling. **k**, In a task with equal chance of a reward 1.0 or 0.0, distributional TD with different levels of coupling shows robustness to the degree of coupling. **l**, When there is no coupling, a distributional code is not learned, but asymmetric scaling can cause spurious detection of diverse reversal points. **m**, Even though every cell has the same reward prediction they appear to have different reversal points. **n**, With this model, some cells may have significantly positive responses, and others significantly negative responses, in response to the same reward. **o**, But this model is unable to explain a positive correlation between asymmetric scaling and reversal points. **p**, Simulation of 'synaptic' distributional RL, in which learning rates but not firing rates are asymmetrically scaled. This model predicts diversity in reversal points between dopamine neurons. **q**, The model predicts no correlation between asymmetric scaling of firing rates and reversal point.



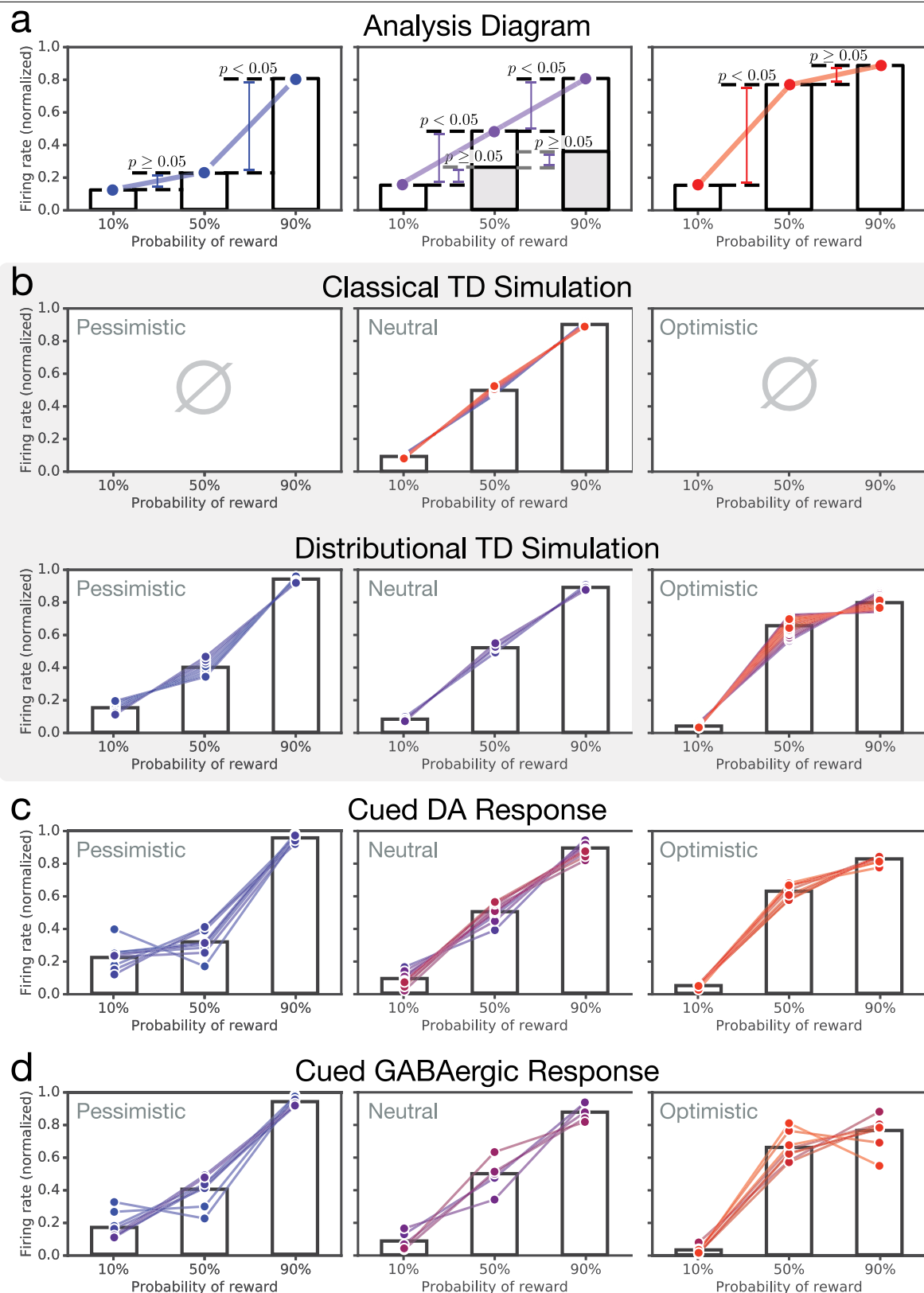
**Extended Data Fig. 5 | Asymmetry and reversal.** **a**, Left, all data points (trials) from an example cell. The solid lines are linear fits to the positive and negative domains, and the shaded areas show 95% confidence intervals calculated with Bayesian regression. Right, the same cell plotted in the format of Fig. 4b. **b**, Cross-validated model comparison on the dopamine data favours allowing each cell to have its own asymmetric scaling ( $P=1.4 \times 10^{-11}$  by paired  $t$ -test). The standard error of the mean appears large relative to the  $P$  value because the  $P$  value is computed using a paired test. **c**, Although the difference between single-asymmetry and diverse-asymmetry models was small in firing-rate space, such small differences correspond to large differences in decoded distribution space (more details in Supplementary Information). Each point is a TD simulation; colour indicates the degree of diversity in asymmetric scaling within that simulation. **d**, We were interested in whether an apparent correlation between reversal point and asymmetry could arise as an artefact, owing to a mismatch between the shape of the actual dopamine response function and the function used to fit it. Here we simulate the variable-magnitude task using a TD model without a true correlation between asymmetric scaling and reversal point. We then apply the same analysis pipeline as in the main paper, to measure the correlation (colour axis) between

asymmetric scaling and reversal point. We repeat this procedure 20 times with different dopamine response functions in the simulation, and different functions used to fit the positive and negative domains of the simulated data. The functions are sorted in increasing order of concavity. An artefact can emerge if the response function used to fit the data is less concave than the response function used to generate the data. For example, when generating data with a Hill function but fitting with a linear function, a positive correlation can be spuriously measured. **e**, When simulating data from the distributional TD model, where a true correlation exists between asymmetric scaling and reversal point, it is always possible to detect this positive correlation, even if the fitting response function is more concave than the generating response function. The black rectangle highlights the function used to fit real neural data in **c**. **f**, Here we analyse the real dopamine cell data identically to Fig. 4d, but using Hill functions instead of linear functions to fit the positive and negative domains. Because the correlation between asymmetric scaling and reversal point still appears under these adversarial conditions, we can be confident it is not driven by this artefact. **g**, Same as Fig. 4d, but using linear response function and linear utility function (instead of empirical utility).



**Extended Data Fig. 6 | Cue responses versus outcome responses, and more evidence for diversity.** **a**, In the variable-probability task: firing at cue, versus firing at reward (left) or omission (right). Colour brightness denotes asymmetry. **b**, Same as **a**, but showing RPEs from distributional TD simulation. **c**, Data from ref.<sup>30</sup> also included unpredicted rewards and unpredicted airpuffs. Top two panels show responses for all the cells recorded in one animal and bottom two panels show responses for all the cells of another animal. Left, the x axis is the baseline-subtracted response to free reward and the y axis is the

baseline-subtracted response to airpuff. Dots with black outlines are per-cell means, and un-outlined dots are means of disjoint subsets of trials indicating consistency of asymmetry. Right, the same data plotted in a different way, with cells sorted along the x axis by response to airpuff. Response to reward is shown in greyscale dots. Asterisks indicate significant difference in firing rates from one or both neighbouring cells. **d**, Simulations for distributional but not classical TD produce diversity in relative response.

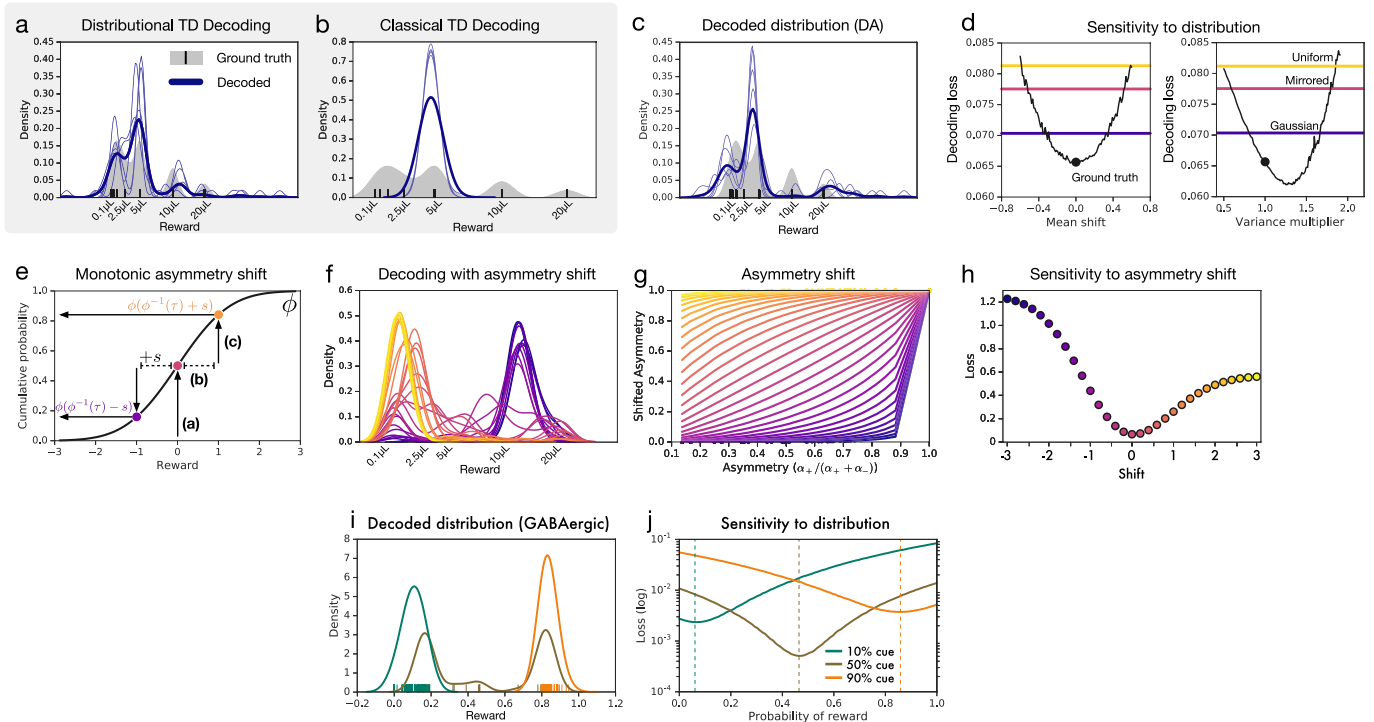


**Extended Data Fig. 7 | More details of data in variable-probability task.**

**a**, Details of analysis method. Of the four possible outcomes of the two Mann-Whitney tests (Methods), two outcomes correspond to interpolation (middle) and one each to the pessimistic (left) and optimistic (right) groups.

**b**, Simulation results for the classical TD and distributional TD models. y-axis shows the average firing-rate change, normalized to mean zero and unit variance, in response to each of the three cues. Each curve is one cell. The cells

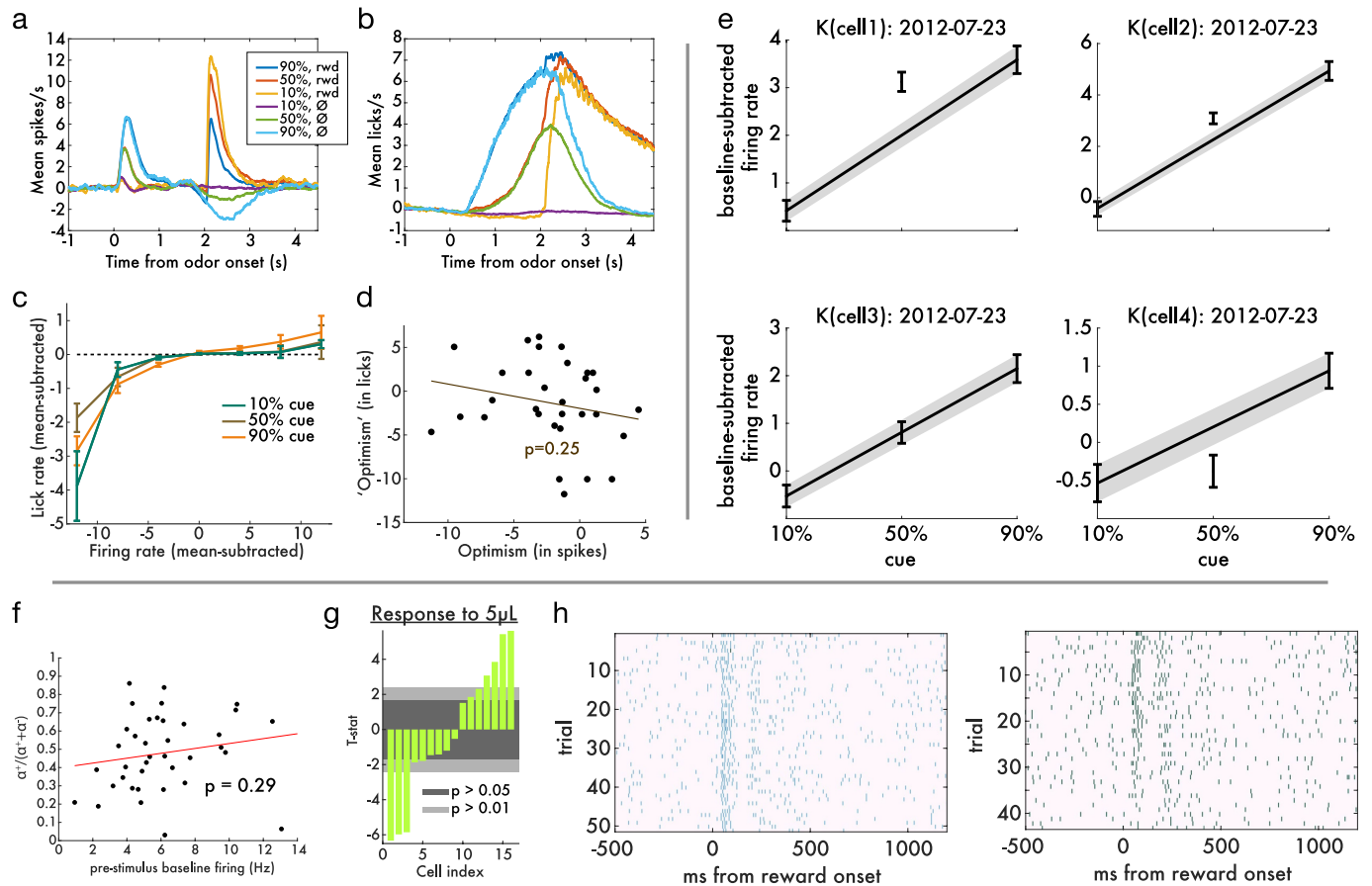
are split into panels according to a statistical test for type of probability coding (see Methods for details). Colour indicates the degree of optimism or pessimism. Distributional TD predicts simultaneous optimistic and pessimistic coding of probability, whereas classical TD predicts all cells have the same coding. **c**, Same as **b**, but using data from real dopamine neurons. The pattern of results closely matches the predictions from the distributional TD model. **d**, Same as **b**, using data from putative VTA GABAergic interneurons.



**Extended Data Fig. 8 | Further distribution decoding analysis.** This figure pertains to the variable-magnitude experiment. **a–c**, In the decoding shown in the main text, we constrained the support of the distribution to the range of the rewards in the task. Here, we applied the decoding analysis without constraining the output values. We find similar results, although with increased variance. **d**, We compare the quality of the decoded distribution against several controls. The real decoding is shown as black dots. In coloured lines are reference distributions (uniform and Gaussian with the same mean and variance as the ground truth; and the ground truth mirrored). Black traces shift or scale the ground-truth distribution by varying amounts. **e**, Nonlinear

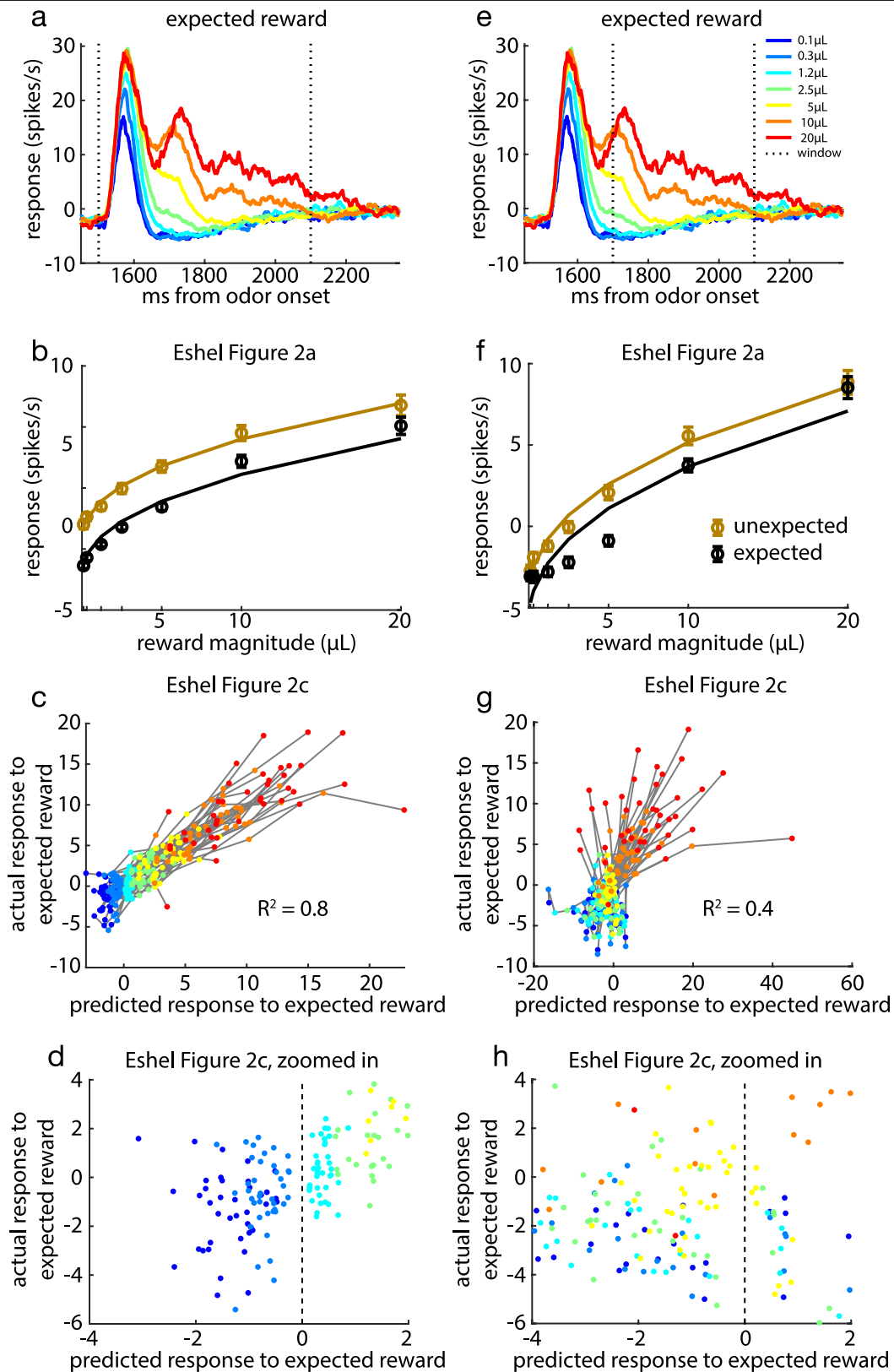
functions used to shift asymmetries, to measure degradation of decoded distribution. The normal cumulative distribution function  $\phi$  is used to transform asymmetry  $z$ . This is shifted by some value  $s$  and transformed back through the normal quantile function  $\phi^{-1}$ . Positive values  $s$  increase the value of  $z$  and negative values decrease the value of  $z$ . **f**, Decoded distributions under different shifts,  $s$ . **g**, Plot of shifted asymmetries for values of  $s$  used. **h**, Quantification of match between decoded and ground-truth distribution, for each  $s$ . **i, j**, Same as Fig. 5d, e, but for putative GABAergic cells rather than dopamine cells.





**Extended Data Fig. 9 | Simultaneous diversity. a, b**, Variable-probability task. Mean spiking (**a**) and licking (**b**) activity in response to each of the three cues (indicating 10%, 50% or 90% probability of reward) at time 0, and in response to the outcome (reward or no reward) at time 2,000 ms. **c**, Trial-to-trial variations in lick rates were strongly correlated with trial-to-trial variations in dopamine firing rates. Mean of each cell is subtracted from each axis, and the x axis is binned for ease of visualization. **d**, Dopaminergic coding of the 50% cue relative to the 10% and 90% cues (as shown in **b**) was not correlated with the same measure computed on lick rates. Therefore, between-session differences in cue preference, measured by anticipatory licking, cannot explain between-cell differences in optimism. **e**, Four simultaneously recorded dopamine neurons.

These are the same four cells whose time courses are shown in Fig. 3c. **f**, Variable-magnitude task. Across cells, there was no relationship between asymmetric scaling of positive versus negative prediction errors, and baseline firing rates ( $R = 0.18$ ,  $P = 0.29$ ). Each point is a cell. These data are from dopamine neurons at reward delivery time. **g**,  $t$ -statistics of response to 5  $\mu$ L reward compared with baseline firing rate, for all 16 cells from animal D. Some cells respond significantly above baseline and others significantly below. Cells are sorted by  $t$ -statistic. **h**, Spike rasters showing all trials in which the 5  $\mu$ L reward was delivered. The two panels are two example cells from the same animal with rasters shown in Fig. 2.



**Extended Data Fig. 10 | Relationship of results to original analysis.** Here we reproduce results for the variable-magnitude task in ref.<sup>30</sup> with two different time windows. **a**, Change in firing rate in response to cued reward delivery averaged over all cells. **b**, Comparing Hill-function fit and response averaged over all cells for expected (cued) and unexpected reward delivery.

**c**, Correlation between response predicted by scaled common response function and actual response to expected reward delivery. **d**, Zooming in on **c** shows correlation driven primarily by larger reward magnitudes. **e–h**, Repeating the above analysis for a window of 200–600 ms.

## Reporting Summary

Nature Research wishes to improve the reproducibility of the work that we publish. This form provides structure for consistency and transparency in reporting. For further information on Nature Research policies, see [Authors & Referees](#) and the [Editorial Policy Checklist](#).

### Statistics

For all statistical analyses, confirm that the following items are present in the figure legend, table legend, main text, or Methods section.

n/a Confirmed

- ☐ ☒ The exact sample size ( $n$ ) for each experimental group/condition, given as a discrete number and unit of measurement
- ☐ ☒ A statement on whether measurements were taken from distinct samples or whether the same sample was measured repeatedly
- ☐ ☒ The statistical test(s) used AND whether they are one- or two-sided  
*Only common tests should be described solely by name; describe more complex techniques in the Methods section.*
- ☐ ☒ A description of all covariates tested
- ☐ ☒ A description of any assumptions or corrections, such as tests of normality and adjustment for multiple comparisons
- ☐ ☒ A full description of the statistical parameters including central tendency (e.g. means) or other basic estimates (e.g. regression coefficient) AND variation (e.g. standard deviation) or associated estimates of uncertainty (e.g. confidence intervals)
- ☐ ☒ For null hypothesis testing, the test statistic (e.g.  $F$ ,  $t$ ,  $r$ ) with confidence intervals, effect sizes, degrees of freedom and  $P$  value noted  
*Give  $P$  values as exact values whenever suitable.*
- ☒ ☐ For Bayesian analysis, information on the choice of priors and Markov chain Monte Carlo settings
- ☒ ☐ For hierarchical and complex designs, identification of the appropriate level for tests and full reporting of outcomes
- ☐ ☒ Estimates of effect sizes (e.g. Cohen's  $d$ , Pearson's  $r$ ), indicating how they were calculated

*Our web collection on [statistics for biologists](#) contains articles on many of the points above.*

### Software and code

Policy information about [availability of computer code](#)

Data collection

Simulation experiments were built with custom code and use the following components: Python 2.7 and Tensorflow 1.13.1. Artificial agent experiments are based upon previously published methods.

Data analysis

Data analysis was performed using MATLAB R2018a, NumPy 1.15, and SciPy 1.2.1. Analysis code from our value-distribution decoding analyses, as well as code used to generate model predictions for distributional TD, are available at <https://doi.org/10.17605/OSF.IO/UX5RG>.

For manuscripts utilizing custom algorithms or software that are central to the research but not yet described in published literature, software must be made available to editors/reviewers. We strongly encourage code deposition in a community repository (e.g. GitHub). See the Nature Research [guidelines for submitting code & software](#) for further information.

### Data

Policy information about [availability of data](#)

All manuscripts must include a [data availability statement](#). This statement should provide the following information, where applicable:

- Accession codes, unique identifiers, or web links for publicly available datasets
- A list of figures that have associated raw data
- A description of any restrictions on data availability

The neuronal data analyzed in this work have been uploaded to OSF and are available at <https://doi.org/10.17605/OSF.IO/UX5RG>.

## Field-specific reporting

Please select the one below that is the best fit for your research. If you are not sure, read the appropriate sections before making your selection.

☒ Life sciences ☐ Behavioural & social sciences ☐ Ecological, evolutionary & environmental sciences

For a reference copy of the document with all sections, see [nature.com/documents/nr-reporting-summary-flat.pdf](https://www.nature.com/documents/nr-reporting-summary-flat.pdf)

## Life sciences study design

All studies must disclose on these points even when the disclosure is negative.

Sample size	All data were taken from a previously-published set of experiments (Eshel et al 2015, 2016).
Data exclusions	No data were excluded.
Replication	Cross-validation was used to avoid over-fitting.
Randomization	There were no between-animal manipulations. Trial sequences were randomized.
Blinding	There were no design factors to which blinding would be relevant.

## Reporting for specific materials, systems and methods

We require information from authors about some types of materials, experimental systems and methods used in many studies. Here, indicate whether each material, system or method listed is relevant to your study. If you are not sure if a list item applies to your research, read the appropriate section before selecting a response.

### Materials & experimental systems

n/a	Involved in the study
<input checked="" type="checkbox"/>	<input type="checkbox"/> Antibodies
<input checked="" type="checkbox"/>	<input type="checkbox"/> Eukaryotic cell lines
<input checked="" type="checkbox"/>	<input type="checkbox"/> Palaeontology
<input type="checkbox"/>	<input checked="" type="checkbox"/> Animals and other organisms
<input checked="" type="checkbox"/>	<input type="checkbox"/> Human research participants
<input checked="" type="checkbox"/>	<input type="checkbox"/> Clinical data

### Methods

n/a	Involved in the study
<input checked="" type="checkbox"/>	<input type="checkbox"/> ChIP-seq
<input checked="" type="checkbox"/>	<input type="checkbox"/> Flow cytometry
<input checked="" type="checkbox"/>	<input type="checkbox"/> MRI-based neuroimaging

## Animals and other organisms

Policy information about [studies involving animals](#); [ARRIVE guidelines](#) recommended for reporting animal research

Laboratory animals	The rodent data we re-analyzed here were first reported in Eshel et al. (2015). We used 5 adult male mice, backcrossed for more than 5 generations with C57/BL6J mice, that were heterozygous for Cre recombinase under the control of either the DAT gene or the Vgat gene.
Wild animals	The study did not involve wild animals.
Field-collected samples	The study did not involve field-collected samples.
Ethics oversight	All experiments were performed in accordance with the US National Institutes of Health Guide for the Care and Use of Laboratory Animals and approved by the Harvard Institutional Animal Care and Use Committee.

Note that full information on the approval of the study protocol must also be provided in the manuscript.

# Hyperactivation of sympathetic nerves drives depletion of melanocyte stem cells

<https://doi.org/10.1038/s41586-020-1935-3>

Received: 22 May 2019

Accepted: 13 December 2019

Published online: 22 January 2020

Bing Zhang<sup>1</sup>, Sai Ma<sup>1,2,3</sup>, Inbal Rachmin<sup>4</sup>, Megan He<sup>1,5</sup>, Pankaj Baral<sup>6</sup>, Sekyu Choi<sup>1</sup>, William A. Gonçalves<sup>7</sup>, Yulia Shwartz<sup>1</sup>, Eva M. Fast<sup>1,8</sup>, Yiqun Su<sup>4</sup>, Leonard I. Zon<sup>1,8,9</sup>, Aviv Regev<sup>2,3,9</sup>, Jason D. Buenrostro<sup>1</sup>, Thiago M. Cunha<sup>5,10</sup>, Isaac M. Chiu<sup>6</sup>, David E. Fisher<sup>4</sup> & Ya-Chieh Hsu<sup>1\*</sup>

Empirical and anecdotal evidence has associated stress with accelerated hair greying (formation of unpigmented hairs)<sup>1,2</sup>, but so far there has been little scientific validation of this link. Here we report that, in mice, acute stress leads to hair greying through the fast depletion of melanocyte stem cells. Using a combination of adrenalectomy, denervation, chemogenetics<sup>3,4</sup>, cell ablation and knockout of the adrenergic receptor specifically in melanocyte stem cells, we find that the stress-induced loss of melanocyte stem cells is independent of immune attack or adrenal stress hormones. Instead, hair greying results from activation of the sympathetic nerves that innervate the melanocyte stem-cell niche. Under conditions of stress, the activation of these sympathetic nerves leads to burst release of the neurotransmitter noradrenaline (also known as norepinephrine). This causes quiescent melanocyte stem cells to proliferate rapidly, and is followed by their differentiation, migration and permanent depletion from the niche. Transient suppression of the proliferation of melanocyte stem cells prevents stress-induced hair greying. Our study demonstrates that neuronal activity that is induced by acute stress can drive a rapid and permanent loss of somatic stem cells, and illustrates an example in which the maintenance of somatic stem cells is directly influenced by the overall physiological state of the organism.

Stress has been anecdotally associated with a variety of changes in tissues, including hair greying. However, whether external stressors are the causal factors, and whether stress-related changes occur at the level of somatic stem cells, remain poorly understood. The hair follicle cycles between growth (anagen), degeneration (catagen) and rest (telogen)<sup>5</sup>. The bulge and hair germ region of the follicle contains two populations of stem cells: hair follicle stem cells (HFSCs), which are epithelial tissues, and melanocyte stem cells (MeSCs)<sup>6</sup>, which are derived from the neural crest. HFSCs and MeSCs are normally quiescent except during early anagen, when they are activated concurrently to regenerate a pigmented hair<sup>7,8</sup>. Activation of HFSCs produces a new hair follicle. Activation of MeSCs generates differentiated melanocytes that migrate downwards, whereas MeSCs remain close to the bulge. At the hair bulb, differentiated melanocytes synthesize melanin to colour the newly regenerated hair from the root. At catagen, mature melanocytes are destroyed, leaving only the MeSCs that will initiate new rounds of melanogenesis in future cycles<sup>9,10</sup> (Extended Data Fig. 1a). The predictable behaviour of MeSCs and melanocytes, and the visible nature of hair colour, makes the melanocyte lineage an accessible model to investigate how stress influences tissue regeneration.

## Diverse stressors induce hair greying

To examine whether psychological or physical stressors promote hair greying, we used three approaches to model stress in C57BL/6J mice with black coat colour: restraint stress<sup>11,12</sup>, chronic unpredictable stress<sup>13,14</sup> and nociception-induced stress (which was achieved through an injection of resiniferatoxin (RTX), an analogue of capsaicin<sup>15,16</sup>). All three procedures led to increased numbers of unpigmented white hairs over time. Restraint stress and chronic unpredictable stress led to noticeable hair greying after three to five rounds of hair cycles. Nociception-induced stress produced the most pronounced and rapid effect—many new hairs that formed in the next hair cycle after RTX injection became unpigmented (Fig. 1a, b, Extended Data Fig. 1b, c).

Psychological or physical stressors trigger the adrenal glands to release stress hormones and catecholamines into the bloodstream<sup>17</sup>. In accordance with this, we detected an increase in both corticosterone (the primary glucocorticoid stress hormone in rodents that is equivalent to cortisol in humans) and noradrenaline (a catecholamine) in the blood of mice that were subjected to different stressors (Fig. 1c, Extended Data Fig. 1d), suggesting that our approaches induced classic stress responses.

<sup>1</sup>Department of Stem Cell and Regenerative Biology, Harvard University and Harvard Stem Cell Institute, Cambridge, MA, USA. <sup>2</sup>Klarman Cell Observatory, Broad Institute of MIT and Harvard, Cambridge, MA, USA. <sup>3</sup>Department of Biology and Koch Institute, Massachusetts Institute of Technology, Cambridge, MA, USA. <sup>4</sup>Cutaneous Biology Research Center, Department of Dermatology, Massachusetts General Hospital, Harvard Medical School, Charlestown, MA, USA. <sup>5</sup>Department of Molecular and Cellular Biology, Harvard University, Cambridge, MA, USA. <sup>6</sup>Department of Immunology, Harvard Medical School, Boston, MA, USA. <sup>7</sup>Institute of Biological Science, Federal University of Minas Gerais, Belo Horizonte, Brazil. <sup>8</sup>Stem Cell Program and Division of Hematology/Oncology, Boston Children's Hospital and Dana-Farber Cancer Institute, Harvard Medical School, Boston, MA, USA. <sup>9</sup>Howard Hughes Medical Institute, Chevy Chase, MD, USA. <sup>10</sup>Center for Research in Inflammatory Diseases (CRID), Department of Pharmacology, Ribeirão Preto Medical School, University of São Paulo, Ribeirão Preto, Brazil. \*e-mail: yachieh\_hsu@harvard.edu



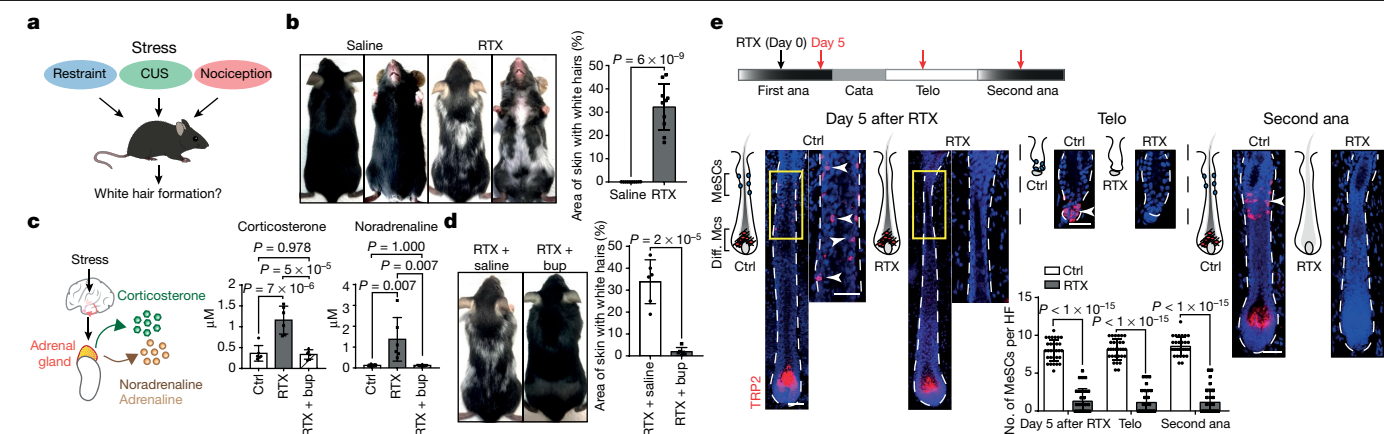


**Fig. 1 | Stress depletes MeSCs.** **a**, Black-coated C57BL/6J mice were subjected to different stress models. CUS, chronic unpredictable stress. **b**, Hair greying after injection of mice with RTX or saline. Right, quantification of the area of skin covered by white hairs ( $n = 10$  mice for each condition, two-tailed unpaired  $t$ -test). **c**, Liquid chromatography with tandem mass spectrometry (LC–MS/MS) was used to quantify the concentration of serum stress hormones (corticosterone and noradrenaline) after injection of RTX alone or in combination with buprenorphine (bup) ( $n = 6$  mice for each condition, one-way analysis of variance (ANOVA) with Tukey's multiple comparisons test). **d**, Injection of RTX with buprenorphine blocks formation of white hairs ( $n = 6$  mice for each condition, two-tailed unpaired  $t$ -test). **e**, Top, experimental

design (black arrow, RTX injection; red arrows, collection of skin samples). Bottom, immunofluorescent staining for TRP2 (a marker of the melanocyte lineage) in the hair follicle (HF) of control (ctrl, saline-injected) and RTX-injected mice ( $n = 30$  hair follicles throughout the skin from 6 mice for each condition, two-way ANOVA with Benjamini–Hochberg correction). Yellow boxes denote the upper region of the hair follicle, where MeSCs reside. Enlarged views are shown to the right, and the number of MeSCs for each condition is quantified. Arrowheads denote MeSCs. Ana, anagen; cata, catagen; telo, telogen; diff. Mcs, differentiated melanocytes. Scale bars, 50  $\mu$ m. All data are mean  $\pm$  s.d.

RTX induces nociception by activating nociceptive sensory neurons<sup>18</sup>. Blocking the ability of mice to sense pain with buprenorphine (an opioid analgesic) prevented the increase of corticosterone and noradrenaline after RTX injection, suggesting that blocking pain sensation alleviates the physiological stress responses that are induced by RTX (Fig. 1c). Moreover, buprenorphine also suppressed the formation of white hairs in mice that were injected with RTX (Fig. 1d). These data show that regardless of the stress modality, premature hair greying can occur under stress. Because the effect of nociception induction on hair greying was the strongest and fastest of all the stressors we tested, we focused on RTX injection as our primary stressor.

## Stress leads to loss of MeSCs

Loss of hair pigmentation can be due to defects in the synthesis of melanin<sup>19,20</sup>, loss of differentiated melanocytes<sup>21</sup> or problems in the maintenance of MeSCs<sup>22</sup>. To understand how stress affects the melanocyte lineage, we injected RTX into mice during anagen, a stage in which both MeSCs and differentiated melanocytes were present but located within distinct compartments—MeSCs were near to the bulge, whereas differentiated melanocytes were at the hair bulb (Fig. 1e). After injection of RTX, TRP2<sup>+</sup> MeSCs were significantly reduced in number across the entire skin (Fig. 1e). In many hair follicles, MeSCs were completely lost from the bulge within five days, whereas differentiated melanocytes in the same hair follicle remained unperturbed (Fig. 1e, Extended Data Fig. 1e). These differentiated melanocytes continued to generate pigments, and the hair coat remained black five days after RTX injection (Extended Data Fig. 1f, g). When hair follicles in the RTX-injected mice entered catagen and telogen, many had lost all MeSCs (Fig. 1e). Subsequently, when the next round of anagen started, differentiated melanocytes were not produced to colour new hair shafts, and unpigmented hairs emerged (Fig. 1e, Extended Data Fig. 1h). Although some regenerated hairs remained pigmented, the numbers of MeSCs in these pigmented hairs were also reduced compared to those in mice not treated with RTX (Extended Data Fig. 1i). RTX injection led to the same extent of hair greying in both male and female mice (Extended Data Fig. 1j). Moreover, RTX also caused the loss of MeSCs when injected

during telogen. In this case, unpigmented hairs appeared as soon as new hairs emerged in the following anagen (Extended Data Fig. 2a, b). These results suggest that MeSCs are exquisitely sensitive to RTX-induced stress, whereas differentiated melanocytes and the synthesis of melanin are not directly affected. MeSCs were also lost or reduced in mice that were subjected to restraint stress or chronic unpredictable stress (Extended Data Fig. 2c). Because stress depleted MeSCs, the loss of hair pigmentation in all three conditions was permanent (Extended Data Fig. 2d). Collectively, these data indicate that stress leads to loss of MeSCs.

## Noradrenaline drives loss of MeSCs

Next, we asked how stress transmits to the periphery to alter MeSCs (Fig. 2a). Immune attack has been postulated to cause stress-induced hair greying<sup>2,23</sup>. To test the involvement of the immune system, we injected RTX into *Rag1* mutant mice, which lack both T and B cells, and into *CD11b-DTR* mice, in which myeloid lineages had been ablated by diphtheria toxin. Injection of RTX into these immune-deficient mice still resulted in formation of white hairs, suggesting that RTX-induced hair greying is independent of T cells, B cells or myeloid cells (Extended Data Fig. 3a, b).

As all stressors led to an increase in the levels of corticosterone and noradrenaline in the blood, we asked if these stress-induced circulating factors had a role in the stress-induced loss of MeSCs. RNA sequencing (RNA-seq) data from MeSCs that were purified by fluorescence-activated cell sorting (FACS) suggested that MeSCs express the glucocorticoid receptor (*GR*, also known as *Nr3c1*, a receptor for corticosterone) and the  $\beta_2$ -adrenergic receptor (*Adrb2*, a receptor for noradrenaline) (Extended Data Fig. 3c, Methods). To determine whether the glucocorticoid receptor mediated the effects of stress on MeSCs, we depleted this protein in MeSCs using Tyr–CreERT2—a tamoxifen-inducible CreERT2 fusion protein directed by a mouse tyrosinase promoter<sup>8,24–26</sup>. RTX injection into *Tyr<sup>CreERT2</sup>;GR<sup>f/f</sup>* mice still resulted in hair greying (Extended Data Fig. 3d). Moreover, no changes in MeSCs or hair pigmentation were observed when the levels of corticosterone were increased by feeding (Extended Data Fig. 3e). These data suggest that corticosterone is not a major driver of stress-induced loss of MeSCs.

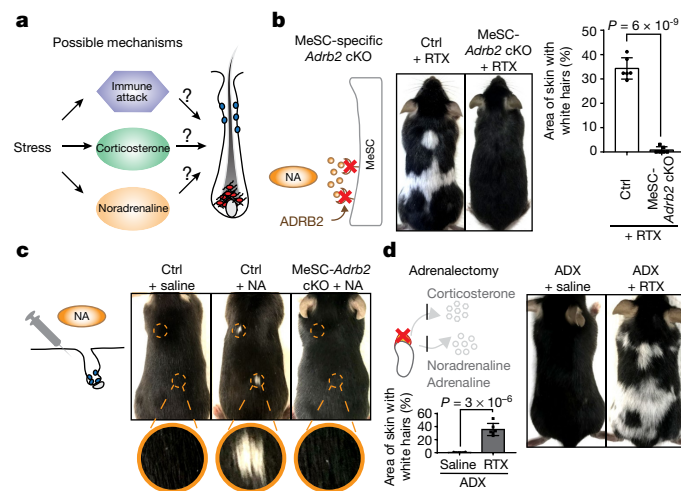


**Fig. 2 | Noradrenaline drives hair greying.** **a**, Possible mechanisms of loss of MeSCs. **b**, Injection of RTX into *Tyr<sup>creERT2</sup>; ADRB2<sup>fl/fl</sup>* (MeSC-specific *Adrb2* conditional knockout (cKO)) mice does not trigger hair greying ( $n = 6$  mice for each condition, two-tailed unpaired  $t$ -test). NA, noradrenaline. **c**, Formation of white hairs at sites of noradrenaline injection ( $n = 10$  injected sites from 8 mice for each condition). For quantifications, see Extended Data Fig. 4e. Yellow dashed circles denote intradermal injection sites. **d**, Formation of white hairs after RTX injection in adrenalectomized mice (ADX) ( $n = 6$  mice for each condition, two-tailed unpaired  $t$ -test). All data are mean  $\pm$  s.d.

We then investigated whether ADRB2 might mediate the effect of stress on MeSCs. After injection of RTX, we observed a marked induction of phosphorylated CREB (a downstream effector of ADRB2) in MeSCs, but not in mature melanocytes (Extended Data Fig. 4a). Moreover, when we depleted ADRB2 from MeSCs using *Tyr-CreERT2*, white hairs did not form after RTX injection (Fig. 2b). These data suggest that ADRB2 expressed by MeSCs is essential for stress-induced hair greying. By contrast, when ADRB2 was depleted from hair follicle stem cells that share the same niche with MeSCs, RTX injection still resulted in hair greying (Extended Data Fig. 4b). In the absence of stress, depletion of ADRB2 in MeSCs did not lead to changes in MeSCs, melanocytes or pigment production, suggesting that the noradrenaline–ADRB2 pathway is dispensable for melanogenesis during the normal hair cycle (Extended Data Fig. 4c, d). Collectively, these data suggest that noradrenaline signals through ADRB2 on MeSCs to mediate stress-induced hair greying.

To test whether an increase in noradrenaline was sufficient to cause hair greying in the absence of stress, we introduced noradrenaline locally to the skin through intradermal injections. Local injection of noradrenaline promoted hair greying at the injection sites in wild-type mice and mice with HFSC-specific knockout of *Adrb2*, but did not cause hair greying in mice with MeSC-specific knockout of *Adrb2* (Fig. 2c, Extended Data Fig. 4e–g). Together, our data demonstrate that although immune cells and corticosterone are dispensable, noradrenaline signalling appears to be necessary for stress-induced hair greying and sufficient to trigger hair greying in the absence of stress.

### Finding the source of noradrenaline

As the adrenal gland is a major source of noradrenaline under stress, to determine whether noradrenaline derived from the adrenal glands mediates stress-induced hair greying, we surgically removed both adrenal glands. Adrenalectomy significantly reduced the levels of corticosterone and noradrenaline in the bloodstream of RTX-injected mice (Extended Data Fig. 5a). However, injection of RTX into adrenalectomized mice still caused hair greying—suggesting that RTX-induced hair greying is independent of hormones or catecholamines from the adrenal glands (Fig. 2d).

An alternative source of noradrenaline is the sympathetic nervous system. Under stress, the sympathetic nervous system becomes activated to induce fight-or-flight responses through the secretion of noradrenaline from peripheral axon terminals<sup>17</sup>. In the skin, sympathetic nerves terminate close to the bulge where MeSCs reside (Fig. 3a). Furthermore, skin regions with high numbers of unpigmented hairs also have denser sympathetic innervation (Extended Data Fig. 5b).

To determine whether sympathetic nerves are indeed activated after RTX injection, we examined the levels of FOS, an immediate early transcription factor that serves as a reporter of neuronal activity<sup>27</sup>. Robust induction of FOS was detected in the cell bodies of sympathetic neurons within 1 hour of RTX injection, peaking at around 2–4 hours and diminishing after 24 hours, which suggests that RTX injection led to a burst activation of sympathetic neurons (Fig. 3b, Extended Data Fig. 5c). Moreover, when buprenorphine was injected together with RTX to block pain, FOS expression was not induced in sympathetic neurons (Fig. 3b). These data suggest that the sympathetic nervous system becomes highly activated following nociception-induced stress.

To test whether activation of sympathetic nerves is responsible for the loss of MeSCs and hair greying under stress, we used 6-hydroxy dopamine (6-OHDA)—a selective neurotoxin for sympathetic nerves<sup>28</sup>—to ablate sympathetic nerves. Sympathectomy blocked RTX-induced hair greying and loss of MeSCs (Fig. 3c, Extended Data Fig. 5d), suggesting that sympathetic nerves do mediate stress-induced hair greying. In addition, guanethidine—a chemical that blocks the release of noradrenaline from sympathetic nerve terminals<sup>29</sup>—suppressed hair greying and loss of MeSCs after RTX injection (Extended Data Fig. 5e). Collectively, these data suggest that noradrenaline secreted from sympathetic nerve terminals mediates the effect of stress on MeSCs.

To determine whether the activation of sympathetic nerves in the absence of stress is sufficient to drive the loss of MeSCs, we took a chemogenetic approach using the DREADDs (designer receptors exclusively activated by designer drugs) system<sup>3,4</sup>.  $G_q$ -DREADD is an artificial  $G_q$ -protein-coupled receptor that is activated by the inert molecule clozapine *N*-oxide (CNO), but not by endogenous ligands. Activation of  $G_q$ -DREADD leads to intracellular release of calcium and neuronal firing. We generated *TH<sup>creERT2</sup>; CAG-LSL-G<sub>q</sub>-DREADD; Rosa<sup>mT/mG</sup>* mice in which the sympathetic nerves can be activated artificially with CNO (Fig. 3d, Supplementary Discussion). Injection of CNO induced the activation of FOS in sympathetic ganglia, confirming the efficacy of this strategy (Extended Data Fig. 5f). Activation of sympathetic nerves with the DREADD system led to loss of MeSCs and hair greying at the sites where CNO was injected (Fig. 3d, Extended Data Fig. 5g). Moreover, when *TH-CreERT2* was activated mosaically by a low dose of tamoxifen, intradermal CNO injection resulted in loss of MeSCs only in hair follicles innervated by DREADD-positive nerve fibres (recognizable by their expression of GFP in the membrane; Fig. 3e, Extended Data Fig. 5h). These data suggest that activation of sympathetic nerves in the absence of stressors is sufficient to drive the loss of MeSCs. Together, our findings suggest that increased noradrenaline secreted from the sympathetic nerve terminals drives the depletion of MeSCs under stress.

### Stress drives hyperproliferation of MeSCs

Next, we aimed to identify the early changes in MeSCs under stress that might account for their loss (Fig. 4a). Immunofluorescence failed to detect active caspase-3 or TUNEL (terminal deoxynucleotidyl transferase dUTP nick end labelling) signals in MeSCs before their depletion from the niche after injection of RTX or noradrenaline. Moreover, RTX injection into *Ripk3* mutant mice, which lack a key kinase for necrosis, still caused hair greying (Extended Data Fig. 6a–c). These data suggest that stress-induced loss of MeSCs is not mediated by apoptosis or necrosis. Radiation causes DNA damage in MeSCs, and leads to their differentiation within the niche<sup>22</sup>. However, we failed to detect  $\gamma$ -H2AX



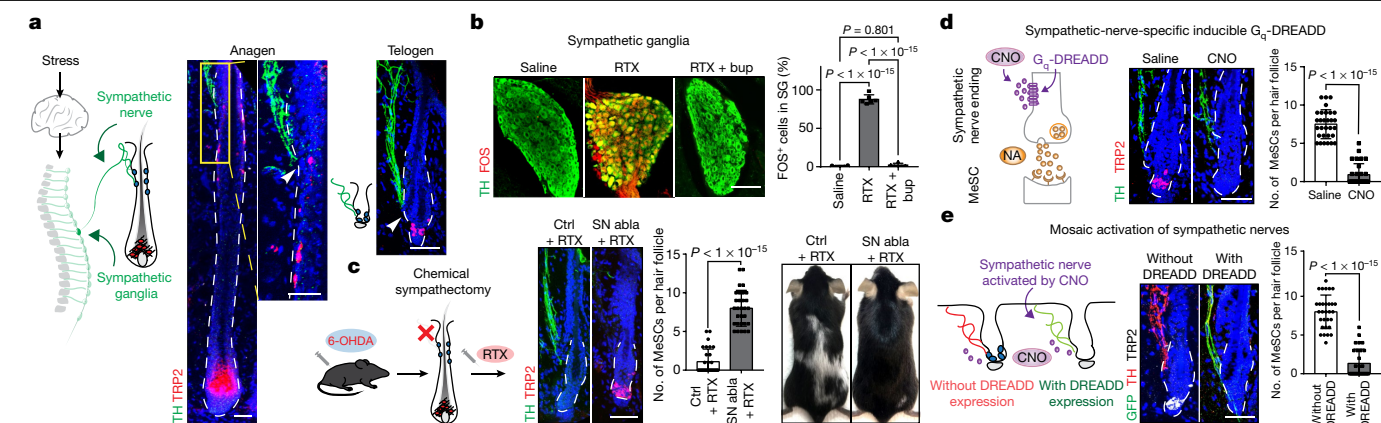


**Fig. 3 | Hyperactivation of the sympathetic nervous system depletes MeSCs.** **a**, Sympathetic nerves innervate MeSC niches. White arrowhead on the immunofluorescent staining indicates the close proximity of nerve endings to MeSCs ( $n = 6$  mice for each condition). **b**, Left, immunofluorescent staining of sympathetic ganglia for tyrosine hydroxylase (TH; green) and FOS (red) from mice injected with saline, RTX and RTX with buprenorphine. Right, quantification of FOS<sup>+</sup> cells in sympathetic ganglia (SG) ( $n = 6$  ganglia from 3 mice for each condition, one-way ANOVA with Tukey's multiple comparisons test). **c**, Injection of 6-hydroxydopamine (6-OHDA) blocks loss of MeSCs and induction of white hairs by RTX ( $n = 30$  hair follicles from 6 mice for each condition, two-tailed unpaired  $t$ -test). SN abla, sympathetic nerve ablation. See

also Extended Data Fig. 5d. **d**, Left, schematic of sympathetic nerve activation using a  $G_q$ -DREADD system. Right, immunofluorescent staining for TH (green) and TRP2 (red) from  $TH^{creERT2};CAG-LSL-G_q-DREADD$  mice treated with saline or CNO ( $n = 30$  hair follicles from 6 mice for each condition, two-tailed unpaired  $t$ -test). **e**, Mosaic activation of sympathetic nerves in  $TH^{creERT2};CAG-LSL-G_q-DREADD;Rosa^{mt/mG}$  mice. Bar graphs quantify the number of MeSCs in hair follicles innervated by DREADD-negative sympathetic nerves (without DREADD) versus DREADD-positive sympathetic nerves (with DREADD; marked by membrane GFP expression) ( $n = 30$  hair follicles for each condition from 4 mice, two-tailed unpaired  $t$ -test). Scale bars, 50  $\mu$ m. All data are mean  $\pm$  s.d.

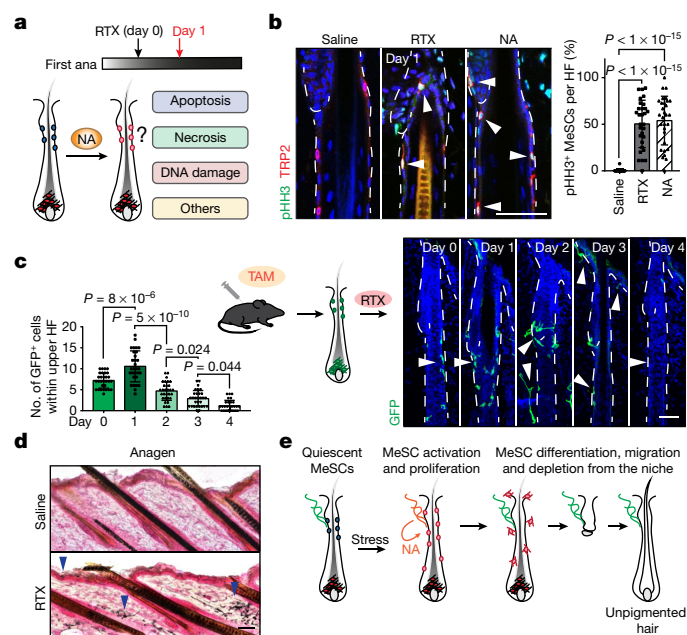


**Fig. 4 | Noradrenaline drives MeSCs out of quiescence.** **a**, Possible mechanisms by which noradrenaline depletes MeSCs. **b**, Left, immunofluorescent staining for phosphorylated histone H3 (pHH3, green) and TRP2 (red) one day after injection of RTX or noradrenaline. White arrowheads indicate the proliferative MeSCs. Right, quantification of pHH3<sup>+</sup> MeSCs ( $n = 30$  hair follicles from 5 mice for each condition, one-way ANOVA with Tukey's multiple comparisons test). **c**, Time course of MeSC behaviour after treatment with RTX in  $Tyr^{creERT2};Rosa^{mt/mG}$  mice. White arrowheads mark MeSCs ( $n = 30$  hair follicles from 3 mice for each time point, one-way ANOVA with Tukey's multiple comparisons test). TAM, tamoxifen. **d**, Fontana-Masson melanin staining five days after injection of saline or RTX ( $n = 6$  mice for each condition). Blue arrowheads indicate ectopic pigments. **e**, Model summarizing steps of stress-induced MeSC depletion. Scale bars, 50  $\mu$ m. All data are mean  $\pm$  s.d.

foci (a hallmark of DNA damage) in MeSCs after injection of RTX or noradrenaline, which suggests that stress-induced depletion of MeSCs is not mediated through DNA damage (Extended Data Fig. 6d).

Quiescence is a key feature of many somatic stem cells<sup>30–33</sup>, and loss of quiescence has been postulated to cause loss of MeSCs in *Bcl2* mutant mice<sup>10,34</sup>. To examine whether stress alters quiescence in MeSCs, we injected RTX or noradrenaline into mice that had entered full anagen (when MeSCs are normally quiescent). We saw a marked increase in the number of proliferating MeSCs within 24 hours of the injection of RTX or noradrenaline—about 50% of MeSCs became positive for phosphorylated histone H3, a marker of M phase (Fig. 4b). This number is in sharp contrast to the number of proliferating MeSCs in early anagen (about 6%), the only stage when MeSCs proliferate to self-renew<sup>9,35</sup> (Extended Data Fig. 6e). Conversely, no changes in proliferation or apoptosis were observed in mature melanocytes after injection of RTX or noradrenaline (Extended Data Fig. 6f, g). These data suggest that increased noradrenaline forces MeSCs to enter a rapid and abnormally proliferative state, but does not affect mature melanocytes.

To monitor changes in MeSCs after stress, we generated  $Tyr^{creERT2};Rosa^{mt/mG}$  mice, in which MeSCs can be traced by their membrane expression of GFP (Fig. 4c). Consistent with the observation that proliferation is an early response of MeSCs to stress, we saw a transient increase in GFP<sup>+</sup> cells shortly after RTX injection (Fig. 4c, day 1; quantified by FACS in Extended Data Fig. 6h). After this initial phase, many GFP<sup>+</sup> cells began to exhibit striking dendritic branching, which is a characteristic feature of differentiated MeSCs (Fig. 4c, day 2). They also began to move away from the bulge—some migrated downwards along the hair follicle, and some migrated out into the dermis or epidermis (Fig. 4c, days 2 and 3). By day 3, many GFP<sup>+</sup> cells had migrated out of the bulge, and by day 4, many hair follicles had lost all GFP<sup>+</sup> cells in the bulge. Moreover, ectopic pigmentation could be detected along the hair follicle, epidermis and dermis—areas that are normally devoid of pigments (Fig. 4d, Extended Data Fig. 6i). These data suggest that after stress, MeSCs undergo rapid proliferation followed by differentiation and migration, which leads to their loss from the niche (Fig. 4e, Supplementary Discussion).

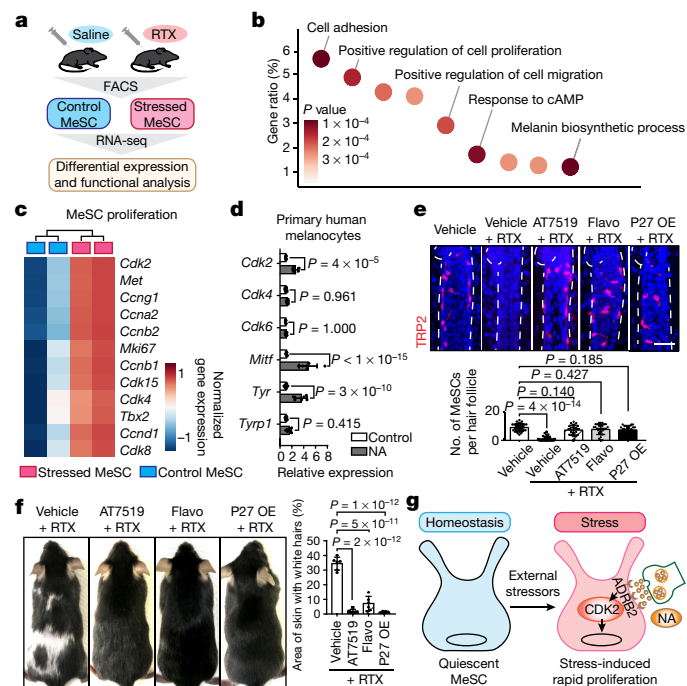


**Fig. 5 | Inhibition of aberrant MeSC proliferation prevents stress-induced hair greying.** **a**, Experimental workflow. FACS was performed in cells at telogen. **b**, GO enrichment analysis of significantly dysregulated genes in stressed MeSCs ( $n = 2$  biologically independent samples for each condition, Fisher's exact test). **c**, Heat map of signature gene expression for genes that are related to the proliferation of MeSCs ( $n = 2$  biologically independent samples for each condition). **d**, qRT-PCR of genes that are related to MeSC proliferation and differentiation in cultured primary human melanocytes treated with noradrenaline ( $n = 6$  samples from 3 independent donors, two-way ANOVA with Benjamini-Hochberg correction). **e**, Top, immunofluorescent staining for TRP2 (red) from mice five days after treatment with RTX, RTX with CDK inhibitors (AT7519 or flavopiridol (flavo)) or RTX with MeSC-specific overexpression of P27 (P27 OE). Bottom, quantification of MeSCs ( $n = 30$  hair follicles from 6 mice for each condition, one-way ANOVA with Tukey's multiple comparisons test). **f**, Topical treatment with AT7519, flavopiridol or MeSC-specific P27 overexpression inhibits RTX-induced hair greying ( $n = 6$  mice for each condition, one-way ANOVA with Tukey's multiple comparisons test). **g**, Model summarizing the main findings of the study. Under strong external stressors, activated sympathetic nerves secrete noradrenaline that binds to ADRB2 on MeSCs. Noradrenaline-ADRB2 signalling drives rapid proliferation of MeSCs, followed by their ectopic differentiation and exhaustion. Scale bars, 50  $\mu\text{m}$ . All data are mean  $\pm$  s.d.

## Transcriptome analyses of MeSCs

To discover the molecular mechanisms that drive stress-induced loss of MeSCs, we conducted RNA-seq using FACS-purified MeSCs from control and RTX-treated mice 12 hours after RTX injection, before MeSCs showed phenotypic differences (Fig. 5a, Extended Data Fig. 7a–c). Examination of the expression of marker genes for different types of skin cell confirmed that we had successfully enriched for MeSCs (Extended Data Fig. 7d). To uncover major molecular changes, we conducted Gene Ontology (GO) enrichment analysis (Fig. 5b). We also curated a list of known genes that are associated with the proliferation and differentiation of MeSCs (Fig. 5c, Extended Data Fig. 7e). Moreover, we used a list of genes that have previously been shown to be involved in entry into the cell cycle to assess whether regulators of the cell cycle are altered at the transcriptional level<sup>36</sup> (Extended Data Fig. 7f). Some of these key changes were also verified by quantitative PCR with reverse transcription (qRT-PCR) (Extended Data Fig. 7g). Collectively, we identified changes in several cell-cycle regulators in stressed MeSCs, including cyclin-dependent kinase 2 (*Cdk2*), which is

a key promoter of the G1-to-S transition. Genes encoding receptors for ligands that promote the proliferation, differentiation and migration of MeSCs, including *Kit*<sup>37</sup> and *Mc1r*<sup>38</sup>, were also upregulated. In addition, genes that are involved in melanogenesis<sup>19</sup>, including *Mitf*, *Tyrp1*, *Tyr*, *Oca2* and *Pmel*, were upregulated (Fig. 5c, Extended Data Fig. 7e, g). These data suggest that MeSCs upregulate their proliferation and differentiation programs after stress. Furthermore, treatment with noradrenaline also led to a rapid induction of proliferation-associated genes such as *Cdk2* and differentiation-associated genes such as *Mitf* and *Tyrin* in cultured human melanocyte cells (Fig. 5d). These data suggest that noradrenaline elicits similar responses in melanocyte lineages of both humans and mice.

## Blocking proliferation preserves MeSCs

Because MeSCs first lose quiescence when under stress, we asked whether transient suppression of proliferation early in the stress response might prevent their depletion. We injected RTX at full anagen and applied CDK inhibitors (AT7519 or flavopiridol) topically to suppress proliferation transiently until 48 hours after injection<sup>39,40</sup>. MeSCs in RTX-injected mice that were treated with CDK inhibitors remained quiescent and were preserved in the niche (Fig. 5e, Extended Data Fig. 8a). Proliferation of cells in the hair bulb remained largely normal, probably because the penetration of inhibitors into subcutaneous regions in full anagen was limited (Extended Data Fig. 8b). To further confirm that loss of MeSCs can be prevented by inhibiting their proliferation, we generated a genetic mouse model, *Tyr<sup>creERT2</sup>;Rosa<sup>LSL-rtTA</sup>;TetO<sup>P27</sup>*, in which the CDK inhibitor P27 can be transiently induced with doxycycline in MeSCs. Induction of P27 expression in MeSCs suppressed their aberrant proliferation and preserved MeSCs in the niche under stress (Fig. 5e, Extended Data Fig. 8a). These preserved MeSCs showed an undifferentiated morphology and retained their functionality, as newly regenerated hairs in subsequent cycles maintained pigmentation (Fig. 5f). Together, these data suggest that loss of quiescence drives the depletion of MeSCs under conditions of stress, and that suppression of the proliferation of MeSCs is sufficient to prevent their loss.

## Discussion

Acute stress is known to cause transient and beneficial fight-or-flight responses that are essential for survival. Here, we demonstrate that acute stress can also cause non-reversible depletion of somatic stem cells through activation of the sympathetic nervous system—resulting in permanent damage to tissue regeneration (Fig. 5g). Our findings support the emerging notion that the sympathetic nervous system not only regulates body physiology, but also influences a variety of processes in development and tissue maintenance<sup>13,41–43</sup>. The adrenal glands are the central regulators of stress responses. However, we show that the adrenal-gland-derived circulating stress hormones and catecholamines do not drive changes in MeSCs under stress. As sympathetic nerves innervate essentially all organs, acute stress might have a broad and rapid effect on many tissues through neuronal signals.

The reason for the existence of such an interaction between nerves and MeSCs is unknown. This said, the connection between the nervous system and pigment-producing cells is probably conserved during evolution. Cephalopods like squid, octopus and cuttlefish have sophisticated colouration systems that allow them to change colour for camouflage or communication. Neuronal activities control their pigment-producing cells (chromatophores), allowing rapid changes in colour in response to predators or threats<sup>44</sup>. Therefore, an attractive hypothesis is that sympathetic nerves might modulate MeSC activity, melanocyte migration or pigment production in situations independent of the hair cycle—for example, under bright sunlight or UV irradiation<sup>45</sup>. Under extreme stress, however, hyperactivation of neuronal activities overstimulates the pathway, which drives the depletion of MeSCs.

MeSCs also exhibit ectopic differentiation and depletion with age<sup>10,20</sup>. Of relevance, patients who have undergone partial sympathectomy develop fewer numbers of unpigmented hairs on the sympathectomized side with age<sup>46,47</sup>. In the future, it will be interesting to investigate whether the mechanisms that we have uncovered here also contribute to the loss of MeSCs that occurs during ageing, and whether stress might mimic an accelerated ageing process.

## Online content

Any methods, additional references, Nature Research reporting summaries, source data, extended data, supplementary information, acknowledgements, peer review information; details of author contributions and competing interests; and statements of data and code availability are available at <https://doi.org/10.1038/s41586-020-1935-3>.

- Ephraim, A. J. On sudden or rapid whitening of the hair. *AMA Arch. Derm.* **79**, 228–236 (1959).
- Navarini, A. A., Nobbe, S. & Trüeb, R. M. Marie Antoinette syndrome. *Arch. Dermatol.* **145**, 656 (2009).
- Alexander, G. M. et al. Remote control of neuronal activity in transgenic mice expressing evolved G protein-coupled receptors. *Neuron* **63**, 27–39 (2009).
- Zhu, H. et al. Cre-dependent DREADD (designer receptors exclusively activated by designer drugs) mice. *Genesis* **54**, 439–446 (2016).
- Müller-Röver, S. et al. A comprehensive guide for the accurate classification of murine hair follicles in distinct hair cycle stages. *J. Invest. Dermatol.* **117**, 3–15 (2001).
- Hsu, Y.-C., Li, L. & Fuchs, E. Emerging interactions between skin stem cells and their niches. *Nat. Med.* **20**, 847–856 (2014).
- Chang, C.-Y. et al. NFIB is a governor of epithelial-melanocyte stem cell behaviour in a shared niche. *Nature* **495**, 98–102 (2013).
- Rabbani, P. et al. Coordinated activation of Wnt in epithelial and melanocyte stem cells initiates pigmented hair regeneration. *Cell* **145**, 941–955 (2011).
- Nishimura, E. K. et al. Dominant role of the niche in melanocyte stem-cell fate determination. *Nature* **416**, 854–860 (2002).
- Nishimura, E. K., Granter, S. R. & Fisher, D. E. Mechanisms of hair graying: incomplete melanocyte stem cell maintenance in the niche. *Science* **307**, 720–724 (2005).
- Anthony, T. E. et al. Control of stress-induced persistent anxiety by an extra-amygdala septohypothalamic circuit. *Cell* **156**, 522–536 (2014).
- Ramirez, S. et al. Activating positive memory engrams suppresses depression-like behaviour. *Nature* **522**, 335–339 (2015).
- Heidt, T. et al. Chronic variable stress activates hematopoietic stem cells. *Nat. Med.* **20**, 754–758 (2014).
- Tye, K. M. et al. Dopamine neurons modulate neural encoding and expression of depression-related behaviour. *Nature* **493**, 537–541 (2013).
- Acs, G., Biro, T., Acs, P., Modarres, S. & Blumberg, P. M. Differential activation and desensitization of sensory neurons by resiniferatoxin. *J. Neurosci.* **17**, 5622–5628 (1997).
- Baral, P. et al. Nociceptor sensory neurons suppress neutrophil and  $\gamma\delta$  T cell responses in bacterial lung infections and lethal pneumonia. *Nat. Med.* **24**, 417–426 (2018).
- Ulrich-Lai, Y. M. & Herman, J. P. Neural regulation of endocrine and autonomic stress responses. *Nat. Rev. Neurosci.* **10**, 397–409 (2009).
- Caterina, M. J. et al. The capsaicin receptor: a heat-activated ion channel in the pain pathway. *Nature* **389**, 816–824 (1997).
- Kondo, T. & Hearing, V. J. Update on the regulation of mammalian melanocyte function and skin pigmentation. *Expert. Rev. Dermatol.* **6**, 97–108 (2011).
- Steingrimsdóttir, E., Copeland, N. G. & Jenkins, N. A. Melanocyte stem cell maintenance and hair graying. *Cell* **121**, 9–12 (2005).
- Liao, C.-P., Booker, R. C., Morrison, S. J. & Le, L. Q. Identification of hair shaft progenitors that create a niche for hair pigmentation. *Genes Dev.* **31**, 744–756 (2017).
- Inomata, K. et al. Genotoxic stress abrogates renewal of melanocyte stem cells by triggering their differentiation. *Cell* **137**, 1088–1099 (2009).
- Harris, M. L. et al. A direct link between MITF, innate immunity, and hair graying. *PLoS Biol.* **16**, e2003648 (2018).
- Bosenberg, M. et al. Characterization of melanocyte-specific inducible Cre recombinase transgenic mice. *Genesis* **44**, 262–267 (2006).
- Köhler, C. et al. Mouse cutaneous melanoma induced by mutant BRAF arises from expansion and dedifferentiation of mature pigmented melanocytes. *Cell Stem Cell* **21**, 679–693 (2017).
- Moon, H. et al. Melanocyte stem cell activation and translocation initiate cutaneous melanoma in response to UV exposure. *Cell Stem Cell* **21**, 665–678 (2017).
- Sheng, M. & Greenberg, M. E. The regulation and function of c-fos and other immediate early genes in the nervous system. *Neuron* **4**, 477–485 (1990).
- Kostrzewa, R. M. & Jacobowitz, D. M. Pharmacological actions of 6-hydroxydopamine. *Pharmacol. Rev.* **26**, 199–288 (1974).
- Boullin, D. J., Costa, E. & Brodie, B. B. Discharge of tritium-labeled guanethidine by sympathetic nerve stimulation as evidence that guanethidine is a false transmitter. *Life Sci.* **5**, 803–808 (1966).
- Acar, M. et al. Deep imaging of bone marrow shows non-dividing stem cells are mainly perisinusoidal. *Nature* **526**, 126–130 (2015).
- Lay, K., Kume, T. & Fuchs, E. FOXO1 maintains the hair follicle stem cell niche and governs stem cell quiescence to preserve long-term tissue-regenerating potential. *Proc. Natl Acad. Sci. USA* **113**, E1506–E1515 (2016).
- Wang, L., Siegenthaler, J. A., Dowell, R. D. & Yi, R. Foxc1 reinforces quiescence in self-renewing hair follicle stem cells. *Science* **351**, 613–617 (2016).
- Cho, I. J. et al. Mechanisms, hallmarks, and implications of stem cell quiescence. *Stem Cell Reports* **12**, 1190–1200 (2019).
- Nishimura, E. K. et al. Key roles for transforming growth factor  $\beta$  in melanocyte stem cell maintenance. *Cell Stem Cell* **6**, 130–140 (2010).
- Takeo, M. et al. Ednrb governs regenerative response of melanocyte stem cells by crosstalk with Wnt signaling. *Cell Rep.* **15**, 1291–1302 (2016).
- Tirosh, I. et al. Dissecting the multicellular ecosystem of metastatic melanoma by single-cell RNA-seq. *Science* **352**, 189–196 (2016).
- Peters, E. M. J., Tobin, D. J., Botchkareva, N., Maurer, M. & Paus, R. Migration of melanoblasts into the developing murine hair follicle is accompanied by transient c-Kit expression. *J. Histochem. Cytochem.* **50**, 751–766 (2002).
- Chou, W. C. et al. Direct migration of follicular melanocyte stem cells to the epidermis after wounding or UVB irradiation is dependent on Mc1r signaling. *Nat. Med.* **19**, 924–929 (2013).
- Losiewicz, M. D., Carlson, B. A., Kaur, G., Sausville, E. A. & Worland, P. J. Potent inhibition of CDC2 kinase activity by the flavonoid L86-8275. *Biochem. Biophys. Res. Commun.* **201**, 589–595 (1994).
- Wyatt, P. G. et al. Identification of N-(4-piperidinyl)-4-(2,6-dichlorobenzoylamino)-1H-pyrazole-3-carboxamide (AT7519), a novel cyclin dependent kinase inhibitor using fragment-based X-ray crystallography and structure based drug design. *J. Med. Chem.* **51**, 4986–4999 (2008).
- Borden, P., Houtz, J., Leach, S. D. & Kuruvilla, R. Sympathetic innervation during development is necessary for pancreatic islet architecture and functional maturation. *Cell Rep.* **4**, 287–301 (2013).
- Zeng, X. et al. Innervation of thermogenic adipose tissue via a calyntenin 3 $\beta$ -S100b axis. *Nature* **569**, 229–235 (2019).
- Katayama, Y. et al. Signals from the sympathetic nervous system regulate hematopoietic stem cell egress from bone marrow. *Cell* **124**, 407–421 (2006).
- Reed, C. M. The ultrastructure and innervation of muscles controlling chromatophore expansion in the squid, *Loligo vulgaris*. *Cell Tissue Res.* **282**, 503–512 (1995).
- Fan, S. M.-Y. et al. External light activates hair follicle stem cells through eyes via an ipRGC–SCN–sympathetic neural pathway. *Proc. Natl Acad. Sci. USA* **115**, E6880–E6889 (2018).
- Lerner, A. B. Gray hair and sympathectomy. Report of a case. *Arch. Dermatol.* **93**, 235–236 (1966).
- Ortonne, J. P., Thivolet, J. & Guillet, R. Graying of hair with age and sympathectomy. *Arch. Dermatol.* **118**, 876–877 (1982).

**Publisher's note** Springer Nature remains neutral with regard to jurisdictional claims in published maps and institutional affiliations.

© The Author(s), under exclusive licence to Springer Nature Limited 2020



# Article

## Methods

### Randomization

The mice were randomly assigned into different experimental groups whenever possible, except in experiments that required specific genotypes (in this case, sex-matched littermate controls were used).

### Blinding

For LC-MS/MS analysis, RNA-seq library preparation and sequencing, experimenters were blinded to experimental conditions. Blinding was not possible in mouse studies owing to the need to identify specific genotypes or treat mice with different chemicals according to experimental designs.

### Mice

C57BL/6J, *Tyr<sup>creERT2</sup>*, *K15<sup>crePGR</sup>*, *Rag1* mutant, *CD11b-DTR*, *GR<sup>fl/fl</sup>*, *CAG-LSL-G<sub>q</sub>-DREADD*, *Rosa<sup>H2B-GFP/GPI-mCherry</sup>*, *Rosa26<sup>mT/mG</sup>*, *Rosa<sup>LSL-rtTA</sup>* and *Ripk3* mutant mice were obtained from the Jackson Laboratory. *Adrb2<sup>fl/fl</sup>* mice<sup>48</sup> were originally generated by G. Karsenty (Columbia University) and provided to us by P. Frenette (Albert Einstein College of Medicine). *TH<sup>creERT2</sup>* mice<sup>49</sup> were generated and provided by D. Ginty (Harvard Medical School). *TetO<sup>P27</sup>* mice<sup>50</sup> were originally generated by G. Cady (Roswell Park Cancer Institute) and provided to us by V. Greco (Yale School of Medicine). All experiments used balanced groups of male and female mice. All experiments were conducted using mice at the same stage of the hair cycle and in a comparable age range (postnatal day (P)20–P25 for first telogen, P31–P36 for full anagen and P50–P60 for second telogen, or long-term monitoring as specified). To monitor the hair cycle, mice were shaved at weaning to monitor changes in skin colour, and these were confirmed by skin sections. The acquisition of human melanocyte cells was carried out in accordance with the Institutional Review Board policies at Massachusetts General Hospital. All mice were maintained in an animal facility approved by the Association for Assessment and Accreditation of Laboratory Animal Care at Harvard University, Harvard Medical School and Ribeirao Preto Medical School. Procedures were approved by the Institutional Animal Care and Use Committee of all institutions and complied with all relevant ethical regulations.

### Stress procedures

Restraint and chronic unpredictable stress procedures were performed as previously described<sup>11–14</sup>. In brief, for restraint stress, C57BL/6J mice were kept in a restrainer (Thermo Fisher Scientific 12972590) for four hours per day for five days starting from mid-anagen (P28–P30). Hairs were depilated to induce hair regeneration when their hair cycle reached telogen. Mice were stressed and depilated four rounds in total to monitor long-term changes. For chronic unpredictable stress, C57BL/6J mice were exposed to a combination of stressors. Two of the stressors were applied each day. The stressors included cage tilt, isolation, damp bedding, rapid light and dark changes, overnight illumination, restraint, empty cage and changing the cage three times. All stressors were randomly repeated in consecutive weeks.

### Drug treatments

For RTX treatment (see also Supplementary Discussion), mice received injections of RTX (30–100 µg kg<sup>−1</sup>) in the flank for 1–3 days, as described previously<sup>15,16,51–56</sup>. RTX was prepared in 2% DMSO with 0.15% Tween 80 in PBS. Control mice were treated with the vehicle only. RTX injection was done either in full anagen (P31–P36) or in first telogen (P21). For corticosterone feeding, 35 µg ml<sup>−1</sup> corticosterone (Millipore Sigma, C2505) was dissolved in 0.45% hydroxypropyl-β-cyclodextrin and provided in the drinking water. Mice were treated for three days (P28–P30). Control mice received the vehicle water (0.45% β-cyclodextrin). For analgesia, mice were injected with buprenorphine (0.1 mg kg<sup>−1</sup>) 4 h before RTX injection and every 6 h after RTX injection for 2 days. For tamoxifen treatment, tamoxifen was diluted in corn oil to a final concentration

of 20 mg ml<sup>−1</sup>. To induce recombination, 20 mg kg<sup>−1</sup> was injected intraperitoneally once per day for 4–7 days. For mosaic induction of Tyr-CreERT2 and TH-CreERT2, 20 mg kg<sup>−1</sup> tamoxifen was injected intraperitoneally once per day for 3 days. For intradermal noradrenaline injection, noradrenaline (Sigma-Aldrich 489350) solution was prepared freshly by dissolving in 0.1% ascorbic acid in 0.9% sterile NaCl to a final concentration of 2 mM. Fifty microlitres was injected intradermally into experimental mice together with fluorescent beads at full anagen (around P31–P36). Control mice were injected with an equivalent volume of vehicle (0.1% ascorbic acid in 0.9% sterile NaCl) with fluorescent beads. The injection sites were marked using water-resistant ink. For ablation of sympathetic nerves, 6-hydroxydopamine hydrobromide (6-OHDA, Sigma 162957) solution was prepared freshly by dissolving 6-OHDA in 0.1% ascorbic acid in 0.9% sterile NaCl. Mice were injected intraperitoneally with 6-OHDA (100 mg per kg body weight) daily from P18 to P22. Control mice were injected with an equivalent volume of vehicle (0.1% ascorbic acid in 0.9% sterile NaCl). Ablation efficiency in the skin was confirmed by immunofluorescence staining. For guanethidine treatment, mice were intraperitoneally injected with 30 mg per kg body weight of guanethidine (Sigma-Aldrich, 1301801), once a day for 3 consecutive days before RTX administration at full anagen (around P31–P36). For induction of G<sub>q</sub>-DREADD, 50 µl CNO (1 mg ml<sup>−1</sup> in 0.9% sterile saline) was injected intradermally into experimental mice, together with fluorescent beads at full anagen (around P31–P36). Control mice were injected with an equivalent volume of vehicle (0.9% sterile saline) together with fluorescent beads. For administration of diphtheria toxin, diphtheria toxin (Sigma-Aldrich) was dissolved in 0.9% saline (0.1 mg ml<sup>−1</sup>). For ablation, *CD11b-DTR* transgenic mice were intraperitoneally injected with diphtheria toxin (25 ng per g body weight) daily 3 days before RTX injection at full anagen (around P31–P36). Diphtheria toxin (20 ng per g body weight) was injected every 3 days after RTX injection until collection of skin samples. For inhibitor treatment, mice were shaved and pre-treated with AT7519 (Cayman Chemical 16231) or flavopiridol (Cayman Chemical 10009197) (both 5 mg per kg body weight) in ethanol topically 48 h and 24 h before RTX injection, at the time of RTX injection and 24 h and 48 h after injection. For induction of P27 expression, mice were fed with the doxycycline rodent diet (VWR 89067-462) for three days before RTX treatment and three days after. RTX was given at Anagen VI (around P31–P36).

### Quantification of unpigmented hairs

For restraint and chronic unpredictable stress, unpigmented hairs were quantified by plucking around 100 hairs from 3 or 4 regions of the skin across the anterior to posterior end, and the percentage of white hairs was calculated by dividing the number of white hairs by the total number of hairs plucked. For RTX injection experiments, the percentage of regions with white hairs was calculated by dividing the size of areas with white hairs by the size of the whole skin (both areas were measured using ImageJ). For intradermal injection experiments (noradrenaline or CNO), unpigmented hairs were quantified by plucking around 100 hairs from each injection site (marked by water-resistant ink at the time of injection), and the percentage of white hairs was calculated by dividing the number of white hairs by the total number of hairs plucked.

### Histology and immunohistochemistry

Mouse skin samples were fixed using 4% paraformaldehyde (PFA) for 15 min at room temperature, washed 6 times with PBS and immersed in 30% sucrose overnight at 4 °C. Samples were then embedded in optimal cutting temperature (OCT) compound (Sakura Finetek). Sections of approximately 35–50 µm were fixed in 4% paraformaldehyde (PFA) for 2 min and washed with PBS and 0.1% Triton X-100 in PBS. Slides were then blocked using blocking buffer (5% donkey serum; 1% BSA, 2% cold water fish gelatin in 0.3% Triton X-100 in PBS) for 1 h at room temperature, followed by staining with primary antibodies overnight at 4 °C and secondary antibody for 4 h at room temperature. For quantification

of the density of sympathetic nerves, 90- $\mu$ m sections were used. The TUNEL assay was performed according to the manufacturer's instructions (Roche). Fontana-Masson staining was performed according to the manufacturer's instructions (Market Lab ML7255). Antibodies used: TRP2 (Santa Cruz 10451, 1:800), tyrosine hydroxylase (rabbit, Millipore AB152, 1:1,000 or sheep, Millipore AB1542, 1:150–1:300), FOS (Abcam, 190289, 1:1,000),  $\gamma$ -H2AX (Cell Signaling, 9718, 1:400), phosphorylated histone H3 (rabbit, Cell Signaling Technology 3377S, 1:500), cleaved caspase 3 (rabbit, Cell Signaling Technology 9664S, 1:400), GFP (rabbit, Abcam ab290, 1:1,000 or chicken, Aves labs GFP-1010, 1:200), CD3 (eBioscience 14-0032-81, 1:800), CD11B (eBioscience 14-0112-81, 1:800), phosphorylated CREB (Cell Signaling 9198, 1:800) and MITF (Abcam ab12039, 1:400).

### Measurement of stress hormones

A sample of 50  $\mu$ l of blood plasma was collected from each mouse and transferred into a 1.5-ml microcentrifuge tube. Ten microlitres of internal solution was added to each sample followed by 100  $\mu$ l water and 640  $\mu$ l methanol. Samples were incubated at  $-20^{\circ}\text{C}$  for 1 h, then centrifuged for 30 min at maximum speed at  $-9^{\circ}\text{C}$ . The supernatant was transferred to a new tube and dried under N<sub>2</sub> flow, then resuspended in 50  $\mu$ l methanol and transferred to micro-inserts. All samples were run on an Agilent 6460 Triple Quad LC/MS with an Agilent 1290 Infinity HPLC. For corticosterone-treated mice, plasma corticosterone levels were determined by ELISA according to the manufacturer's instructions (Arbor Assays, K014-H1).

### Radiation

Ten-week-old C57BL/6J mice were gamma-irradiated (<sup>137</sup>Cs source) with a dose of 10.5 Gy. Mice were transplanted with 300,000 whole bone marrow cells to ensure survival after lethal irradiation.

### FACS

Mouse dorsal skin was collected, and the fat layer was removed by gentle scraping from the dermal side. The skin was incubated in 0.25% collagenase in Hank's balanced salt solution (HBSS) at  $37^{\circ}\text{C}$  for 35–45 min on an orbital shaker. Single-cell suspension was collected by gentle scraping of the dermal side and filtering through 70- $\mu$ m and 40- $\mu$ m filters. The epidermal layer was incubated in trypsin-EDTA at  $37^{\circ}\text{C}$  for 35–45 min on an orbital shaker. Single-cell suspension was collected by gentle scraping of the epidermal side and filtering through 70- $\mu$ m and 40- $\mu$ m filters. The single-cell suspension was centrifuged for 5 min at  $4^{\circ}\text{C}$ , resuspended in 0.25% FBS in PBS and stained with fluorescent-dye-conjugated antibodies for 30 min. For late anagen skin samples, the bottom parts of the hair follicles, containing mature melanocytes, were removed by gentle scraping under a dissection microscope. The MeSCs located close to the bulge remained and were verified by immunostaining. Antibodies used: CD140A (Invitrogen 13-1401-82, 1:200), CD45 (Invitrogen 13-0451-82, 1:400), SCA1 (Invitrogen 13-5981-82, 1:1,000), CD34 (Invitrogen 13-0341-82, 1:100), CD117 (Biolegend 135136, 1:400). See a published protocol for detailed instructions<sup>57</sup>.

### RNA isolation

RNA was isolated using a RNeasy Micro Kit (Qiagen) with QIAcube according to the manufacturer's instructions. RNA concentration and RNA integrity were determined by Bioanalyzer (Agilent) using the RNA 6000 Nano chip. High-quality RNA samples with an RNA integrity number of 8 or higher were used as input for RT-PCR and RNA-seq.

### Cell culture

Primary human melanocytes were derived from neonatal foreskin as previously described<sup>58</sup> and cultured in Medium 254 (Invitrogen, Thermo Fisher Scientific). Melanocytes (passages 2 and 4) were starved for 24 h in Ham's F-10 nutrient mixture with 1% penicillin–streptomycin–glutamine before the addition of noradrenaline (10  $\mu$ M).

### qRT-PCR

The cDNA libraries were synthesized using Superscript IV VILO master mix with ezDNase (Thermo Fisher Scientific). qPCR was performed using power SYBR green (Thermo Fisher Scientific) on an ABI QuantStudio6 Flex qPCR instrument.  $C_t$  values were normalized to an internal control of  $\beta$ -actin (Actb).

### Imaging and image analysis

All images were acquired using a Zeiss LSM 880 confocal microscope or Keyence microscope with  $\times 20$  or  $\times 40$  magnification lenses. Images are presented as maximum intensity projection images. For colocalization analysis, images are presented as a single z-stack. For quantification of the density of sympathetic nerves, tyrosine hydroxylase staining of sympathetic nerves was performed on samples of skin sections (90- $\mu$ m thickness) to ensure the capture of all fibres innervating each hair follicle. Sympathetic nerves innervating individual hair follicles were selected and imaged using a Zeiss LSM 880 confocal microscope. Three-dimensional (3D) surfaces of tyrosine hydroxylase staining were created using Imaris x64 9.3.0 software and the volume was measured and compared. To quantify cell numbers (MeSC numbers, cell death events, proliferation events) within a hair follicle, immunofluorescence staining images of skin sections from multiple regions across the body were used. The number of cells was counted manually or by using ImageJ.

### Statistical analysis

Statistical analyses were performed with GraphPad Prism 7.00, using unpaired two-tailed Student's *t*-tests, one-way or two-way ANOVA. All of the statistical tests performed are indicated in the figure legends. The data are presented as mean  $\pm$  s.d. No statistical methods were used to predetermine sample size.

### RNA-seq and computational analysis

MeSCs were purified from skin samples from control and stressed mice at telogen using FACS, based on their expression of CD117<sup>7</sup> and starting from a population that is negative for CD140A, CD45, SCA1 and CD34<sup>57</sup>. A total of 2 ng of RNA from each sample was used to generate RNA-seq libraries using a SMART-Seq v4 Ultra Low Input RNA kit (Takara, 634888) and Nextera XT DNA Library Preparation Kit (Illumina, FC-131-1024). Single-end sequencing reads were obtained using the Illumina NextSeq 500 platform. Sequencing reads from RNA-seq libraries were trimmed using Trim Galore! ([https://www.bioinformatics.babraham.ac.uk/projects/trim\\_galore/](https://www.bioinformatics.babraham.ac.uk/projects/trim_galore/)) and aligned to the mouse reference genome (mm10) using STAR aligner<sup>59</sup>. Reads with alignment quality < Q30 were discarded. Gene expression levels were normalized and differential expression of genes was calculated using the DESeq2 package in R<sup>60</sup>. Gene set functional enrichment analysis was performed using DAVID<sup>61,62</sup>. Transcripts per million (TPM) calculated from count tables of control MeSC samples were used to determine the expression levels of adrenergic receptors and glucocorticoid receptor shown in Extended Data Fig. 3c.

### Reporting summary

Further information on research design is available in the Nature Research Reporting Summary linked to this paper.

### Data availability

The sequencing data that support the findings of this study have been deposited in the Gene Expression Omnibus (GEO) with the accession code GSE131566. Source data for all main figures and Extended Data figures are provided with the paper.

48. Hinoi, E. et al. The sympathetic tone mediates leptin's inhibition of insulin secretion by modulating osteocalcin bioactivity. *J. Cell Biol.* **183**, 1235–1242 (2008).

49. Abaira, V. E. et al. The cellular and synaptic architecture of the mechanosensory dorsal horn. *Cell* **168**, 295–310 (2017).
50. Pruitt, S. C., Freeland, A., Rusiniak, M. E., Kunnev, D. & Cady, G. K. Cdkn1b overexpression in adult mice alters the balance between genome and tissue ageing. *Nat. Commun.* **4**, 2626 (2013).
51. Szallasi, A. & Blumberg, P. M. Resiniferatoxin, a phorbol-related diterpene, acts as an ultrapotent analog of capsaicin, the irritant constituent in red pepper. *Neuroscience* **30**, 515–520 (1989).
52. Riol-Blanco, L. et al. Nociceptive sensory neurons drive interleukin-23-mediated psoriasiform skin inflammation. *Nature* **510**, 157–161 (2014).
53. Kashem, S. W. et al. Nociceptive sensory fibers drive interleukin-23 production from CD301b<sup>+</sup> dermal dendritic cells and drive protective cutaneous immunity. *Immunity* **43**, 515–526 (2015).
54. Marshall, I. C. B. et al. Activation of vanilloid receptor 1 by resiniferatoxin mobilizes calcium from inositol 1,4,5-trisphosphate-sensitive stores. *Br. J. Pharmacol.* **138**, 172–176 (2003).
55. Neubert, J. K. et al. Peripherally induced resiniferatoxin analgesia. *Pain* **104**, 219–228 (2003).
56. Watanabe, T., Sakurada, N. & Kobata, K. Capsaicin-, resiniferatoxin-, and olvanil-induced adrenaline secretions in rats via the vanilloid receptor. *Biosci. Biotechnol. Biochem.* **65**, 2443–2447 (2001).
57. Zhang, B., He, M. & Hsu, Y.-C. FACS isolation of melanocyte stem cells from mouse skin. *Protoc. Exch.* <https://doi.org/10.21203/rs.2.17987/v1> (2019).
58. Gilchrist, B. A., Vrabel, M. A., Flynn, E. & Szabo, G. Selective cultivation of human melanocytes from newborn and adult epidermis. *J. Invest. Dermatol.* **83**, 370–376 (1984).
59. Dobin, A. et al. STAR: ultrafast universal RNA-seq aligner. *Bioinformatics* **29**, 15–21 (2013).
60. Love, M. I., Huber, W. & Anders, S. Moderated estimation of fold change and dispersion for RNA-seq data with DESeq2. *Genome Biol.* **15**, 550 (2014).
61. Huang, W., Sherman, B. T. & Lempicki, R. A. Bioinformatics enrichment tools: paths toward the comprehensive functional analysis of large gene lists. *Nucleic Acids Res.* **37**, 1–13 (2009).
62. Huang, W., Sherman, B. T. & Lempicki, R. A. Systematic and integrative analysis of large gene lists using DAVID bioinformatics resources. *Nat. Protocols* **4**, 44–57 (2009).

**Acknowledgements** We thank G. Karsenty for *Adrb2<sup>fl/fl</sup>* mice, D. Ginty for *TH<sup>CreERT2</sup>* mice and many colleagues who donated mice to the Jackson Laboratory; A. Wagers, W. Anderson, C.-Y. Chang, Y. Fong, Q. Ma, M. Nahrendorf, A. Sahay and members of the Y.-C.H. laboratory, in particular M. Gonzalez-Celeiro, for discussions and comments on the manuscript; S. Kim, Y.-L. Kang and O. Chung for technical assistance; and HCBI, the HSCRB FACS core and histology core, FAS Small Molecule Mass Spectrometry Facility, Office of Animal Resources and the Bauer Core Facility at Harvard University for technical support. This work was supported in part by the Harvard Stem Cell Institute; Harvard NeuroDiscovery Center; Harvard Medical School Dean's Innovation Grant; Smith Family Foundation Odyssey Award; American Cancer Society (RSG-18-152-01-DDC); NIH (R01AR070825 to Y.-C.H., R01AR043369-23, R01CA222871, R01AR072304 and P01CA163222 to D.E.F., R01CA103846 and P01CA163222 to L.I.Z. and DP2AT009499 and R01AI130019 to I.M.C.); and grants from the Dr. Miriam and

Sheldon G. Adelson Medical Research Foundation to D.E.F. and from Klarman Cell Observatory to A.R. Y.-C.H. is a Pew Scholar and a NYSCF – Robertson Investigator; A.R. and L.I.Z. are HHMI investigators; B.Z. is a recipient of the Charles A. King Trust Postdoctoral Research Fellowship; M.H. is a recipient of the NSF Graduate Research Fellowships Program (DGE1745303) and was supported by the Joint Program in Molecules, Cells, and Organisms (5T32GM007598-40); Y. Schwartz is a Helen Hay Whitney postdoctoral fellow and a recipient of the Woman in Science Weizmann Institute of Science Award; T.M.C. had a CAPES/HARVARD fellowship for visiting professor from CAPES (Process no. 88881.162285/2017-01) and is supported by a FAPESP grant (2013/08216-2); E.M.F. was supported by a Leukemia & Lymphoma Society Scholar grant (5372-15); and J.D.B. and S.M. acknowledge support from the Broad Institute Fellows Program.

**Author contributions** B.Z. and Y.-C.H. conceived the project. B.Z. performed most of the experiments. S.M. performed bioinformatic analysis. I.R. and Y. Su performed the human melanocyte experiments. M.H. performed the immunostaining of sympathetic ganglia and quantifications of sympathetic nerve density. P.B. and I.M.C. made the initial observations of hair greying in RTX-injected mice. S.C. performed experiments related to chronic unpredictable stress and corticosterone feeding. Y. Schwartz performed the sympathetic nerve ablation experiments. W.A.G. and T.M.C. performed the guanethidine experiments. E.M.F. performed the radiation experiments. Y.-C.H., D.E.F., I.M.C., T.M.C., J.D.B., A.R. and L.I.Z. provided intellectual input and helped shape the research. B.Z. and Y.-C.H. wrote the manuscript, with discussions and feedback from all co-authors.

**Competing interests** L.I.Z. is a founder and stockholder of Fate Therapeutics, Scholar Rock and CAMP4 Therapeutics. D.E.F. has a financial interest in Soltego, a company developing salt-inducible kinase inhibitors for topical skin-darkening treatments that might be used for a broad set of human applications. The interests of D.E.F. were reviewed and are managed by Massachusetts General Hospital and Partners HealthCare in accordance with their conflict of interest policies. A.R. is a member of the Scientific Advisory Board (SAB) of Thermo Fisher Scientific, Neogene Therapeutics, Asimov and Syros Pharmaceuticals; an equity holder of Immunitas; and a founder and an equity holder of Celsius Therapeutics. I.M.C. is an SAB member of GSK Pharmaceuticals and Kintai Therapeutics. A provisional patent application has been filed based on this work (applicants: President and Fellows of Harvard College and The General Hospital Corporation; inventors: Y.-C.H., B.Z., D.E.F. and I.R.); application number: 62/903,517; status: pending/provisional; aspect covered: methods and compositions for controlling hair greying). All of the other authors declare no competing interests.

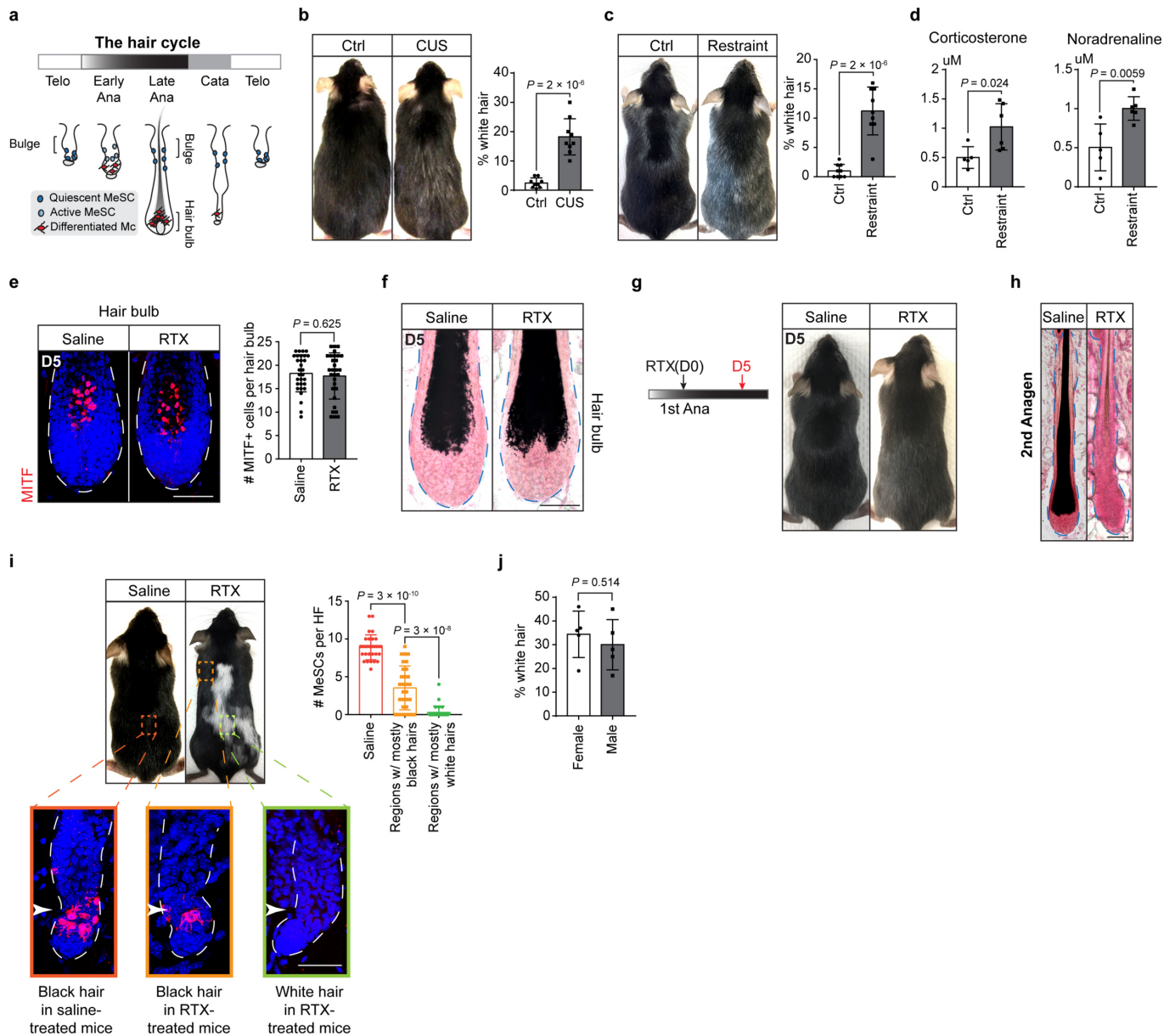
## Additional information

**Supplementary information** is available for this paper at <https://doi.org/10.1038/s41586-020-1935-3>.

**Correspondence and requests for materials** should be addressed to Y.-C.H.

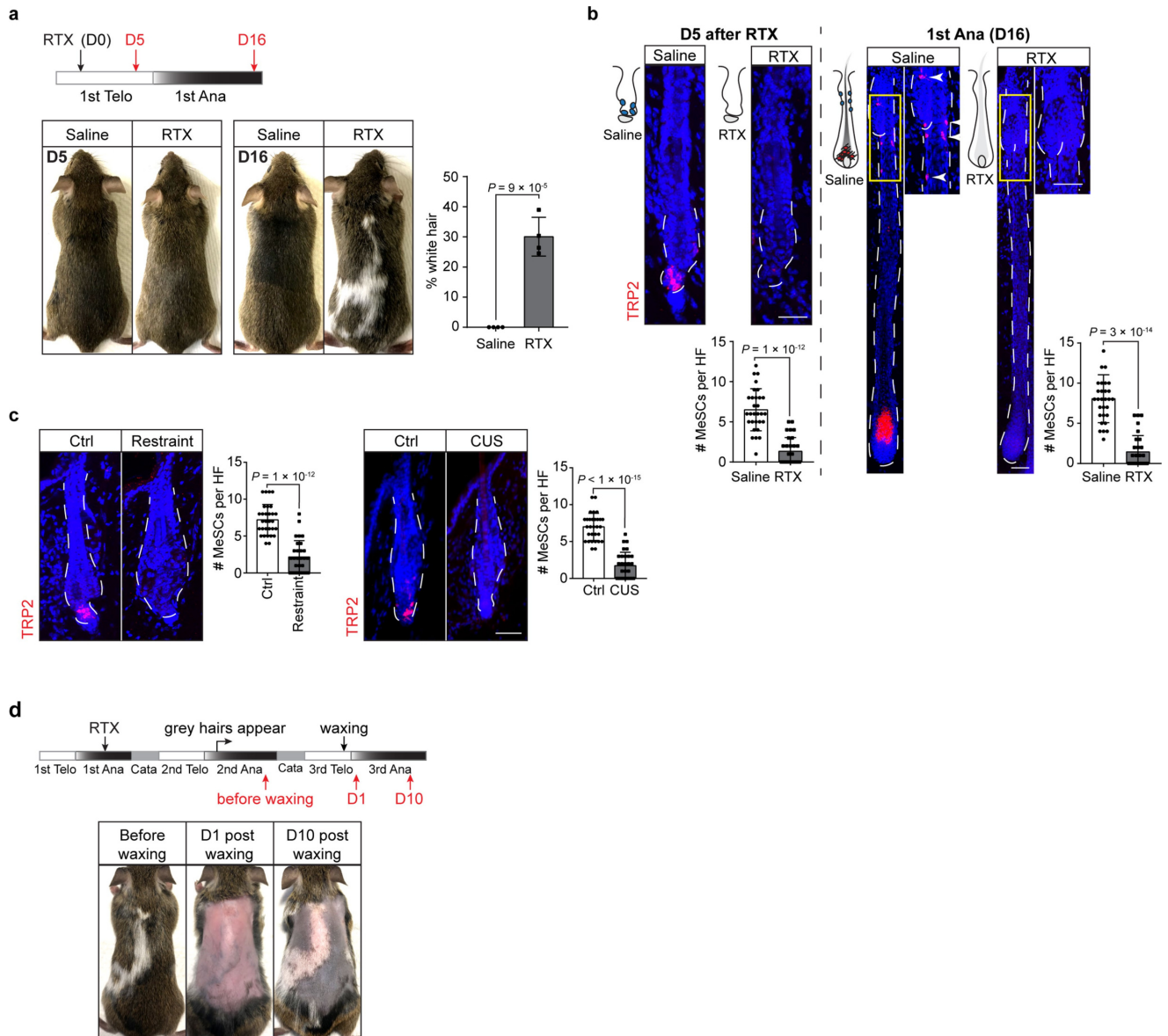
**Peer review information** *Nature* thanks Salvador Aznar Benitah, Christopher Deppmann, William Lowry and the other, anonymous, reviewer(s) for their contribution to the peer review of this work.

**Reprints and permissions information** is available at <http://www.nature.com/reprints>.



**Extended Data Fig. 1 | Effects of stress on the hair pigmentation.** **a**, Schematic of MeSC behaviour during the hair cycle. **b**, Hair greying after mice were subjected to chronic unpredictable stress. Quantifications were done by plucking around 100 hairs from different regions across the skin and counting the number of white hairs ( $n = 9$  plucked regions from 3 mice for each condition, two-tailed unpaired  $t$ -test). **c**, Hair greying after mice were subjected to restraint stress. Quantifications as described in **b**. **d**, LC-MS/MS quantification of corticosterone and noradrenaline after restraint stress ( $n = 5$  mice for control and  $n = 6$  mice for restraint, two-tailed unpaired  $t$ -test). **e**, Left, immunofluorescent staining of hair bulbs for melanocyte-inducing transcription factor (MITF, red) from mice five days after treatment with saline or RTX. Right, quantification of MITF<sup>+</sup> cells ( $n = 30$  hair follicles from 3 mice for each condition, two-tailed unpaired  $t$ -test). **f**, Fontana-Masson staining of hair bulbs for melanin from mice five days after treatment with saline or RTX ( $n = 6$  mice for each condition). **g**, Coat colour in mice five days after RTX injection in anagen. RTX was injected in full anagen and the mice were examined five days

later, at late anagen. The coat colour remained black ( $n = 6$  mice for each condition). **h**, Fontana-Masson staining of hair follicles for melanin from mice that were treated with saline or RTX at first anagen and examined at second anagen (see Fig. 1e for corresponding fluorescent images) ( $n = 6$  mice for each condition). **i**, Quantification of the number of MeSCs in the skin of mice injected with saline or RTX. For the RTX-injected mice, the numbers of MeSCs in regions with predominantly black hairs and regions with many white hairs are quantified separately. Orange and green dashed boxes denote representative black and white hair regions, respectively, in RTX-injected mice. Enlarged boxes show representative immunofluorescent images of hair follicles from each region. White arrowheads indicate regions where MeSCs reside ( $n = 30$  hair follicles from 3 mice for each condition, one-way ANOVA with Tukey's multiple comparisons test). **j**, Quantification of the body area covered by white hairs in female versus male mice ( $n = 5$  mice for each sex, two-tailed unpaired  $t$ -test). All data are mean  $\pm$  s.d.



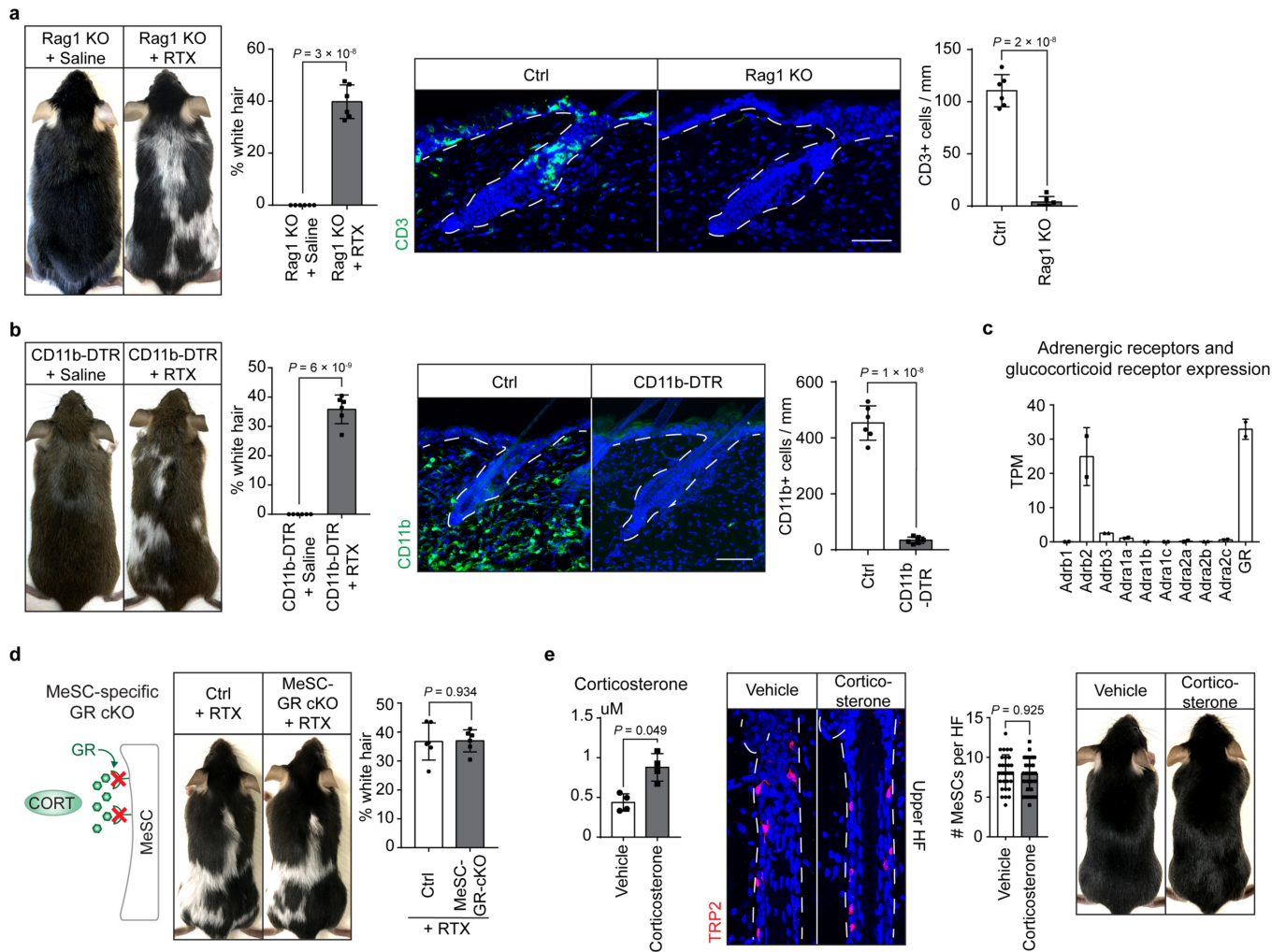
### Extended Data Fig. 2 | Loss of MeSCs in three different models of stress.

**a**, Top, schematic of experimental design for RTX injection in first telogen (red arrows indicate collection of skin samples). Bottom left, representative mouse images 5 days and 16 days after RTX injection in first telogen. Bottom right, quantification of the body area covered by white hairs 16 days after RTX injection ( $n = 4$  mice for each condition, two-tailed unpaired  $t$ -test).

**b**, Immunofluorescent staining for TRP2 from mice injected with saline or RTX in first telogen ( $n = 30$  hair follicles from 4 mice for each condition, two-tailed unpaired  $t$ -test). Yellow boxes denote the upper region of the hair follicle,

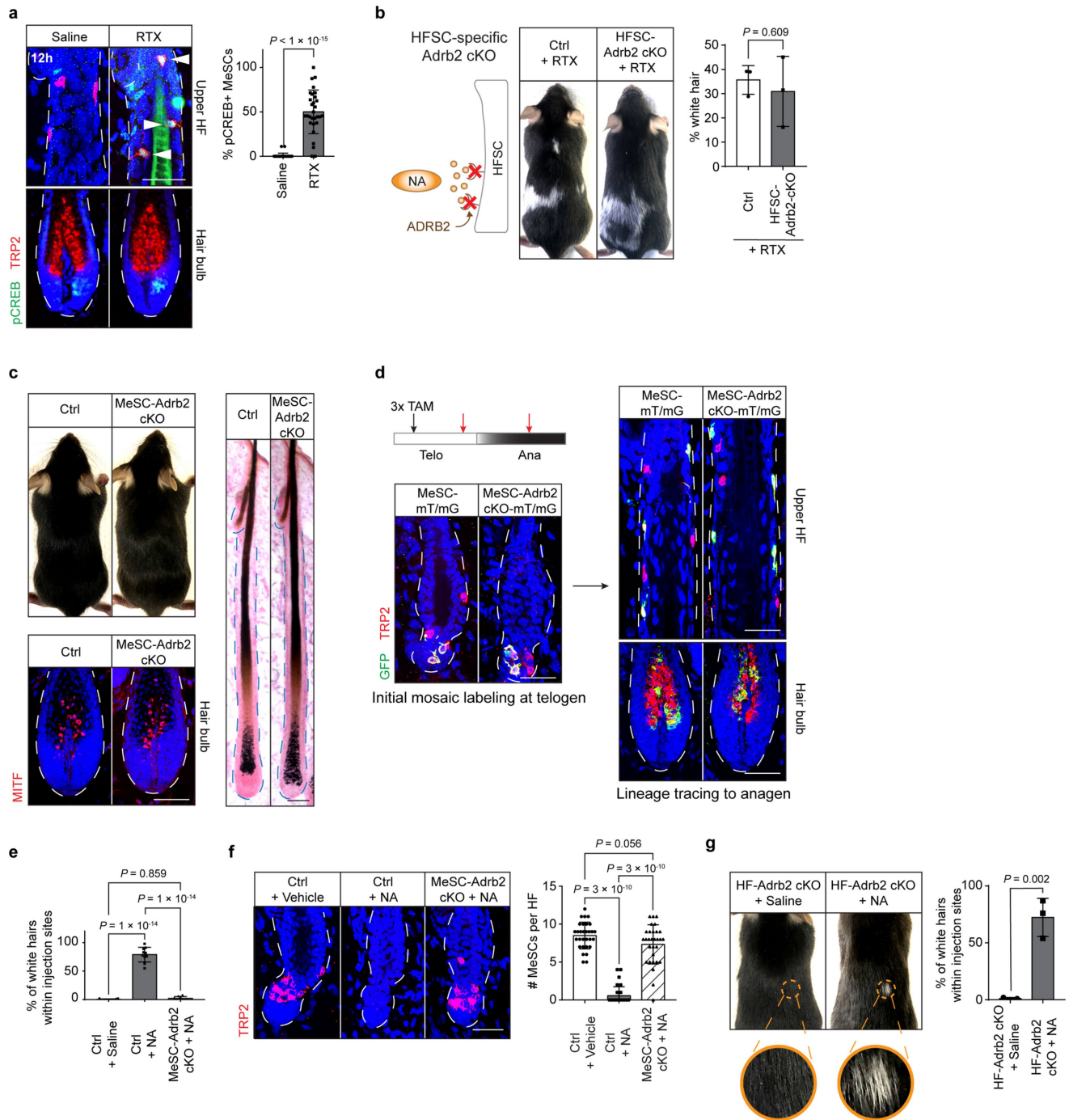
where MeSCs reside. Enlarged views of the yellow-boxed regions are shown to the right. White arrowheads indicate MeSCs. Quantifications of MeSCs are also shown (bottom). **c**, Immunofluorescent staining for TRP2 (red) (left) and quantification of MeSCs (right) from mice subjected to chronic unpredictable stress or restraint stress ( $n = 30$  hair follicles from 5 mice for each condition, two-tailed unpaired  $t$ -test). **d**, Hair coat colour was monitored in RTX-injected mice for multiple rounds of hair-follicle regeneration (waxing was used to initiate new rounds of anagen) ( $n = 3$  mice for each condition). Schematic denotes the experimental design. Scale bars, 50  $\mu$ m. All data are mean  $\pm$  s.d.





**Extended Data Fig. 3 | Stress-induced hair greying is not mediated by corticosterone or immune attack. a**, Left, formation of white hairs after RTX injection in *Rag1* mutant mice that are devoid of T and B cells (*Rag1* KO) ( $n = 6$  for each condition, two-tailed unpaired *t*-test). Right, immunofluorescent staining for the T cell marker CD3 (green) in control and *Rag1* KO skin ( $n = 6$  mice for each condition, two-tailed unpaired *t*-test). **b**, Left, hair greying occurs when RTX is injected into *CD11b-DTR* mice that were treated with diphtheria toxin to deplete myeloid cells ( $n = 6$  mice for each condition). Right, immunofluorescent staining for CD11b (green) in skin from control and *CD11b-DTR* mice that were treated with diphtheria toxin ( $n = 6$  mice for each condition). **c**, Expression of adrenergic receptors and glucocorticoid receptor (GR) in MeSCs ( $n = 2$

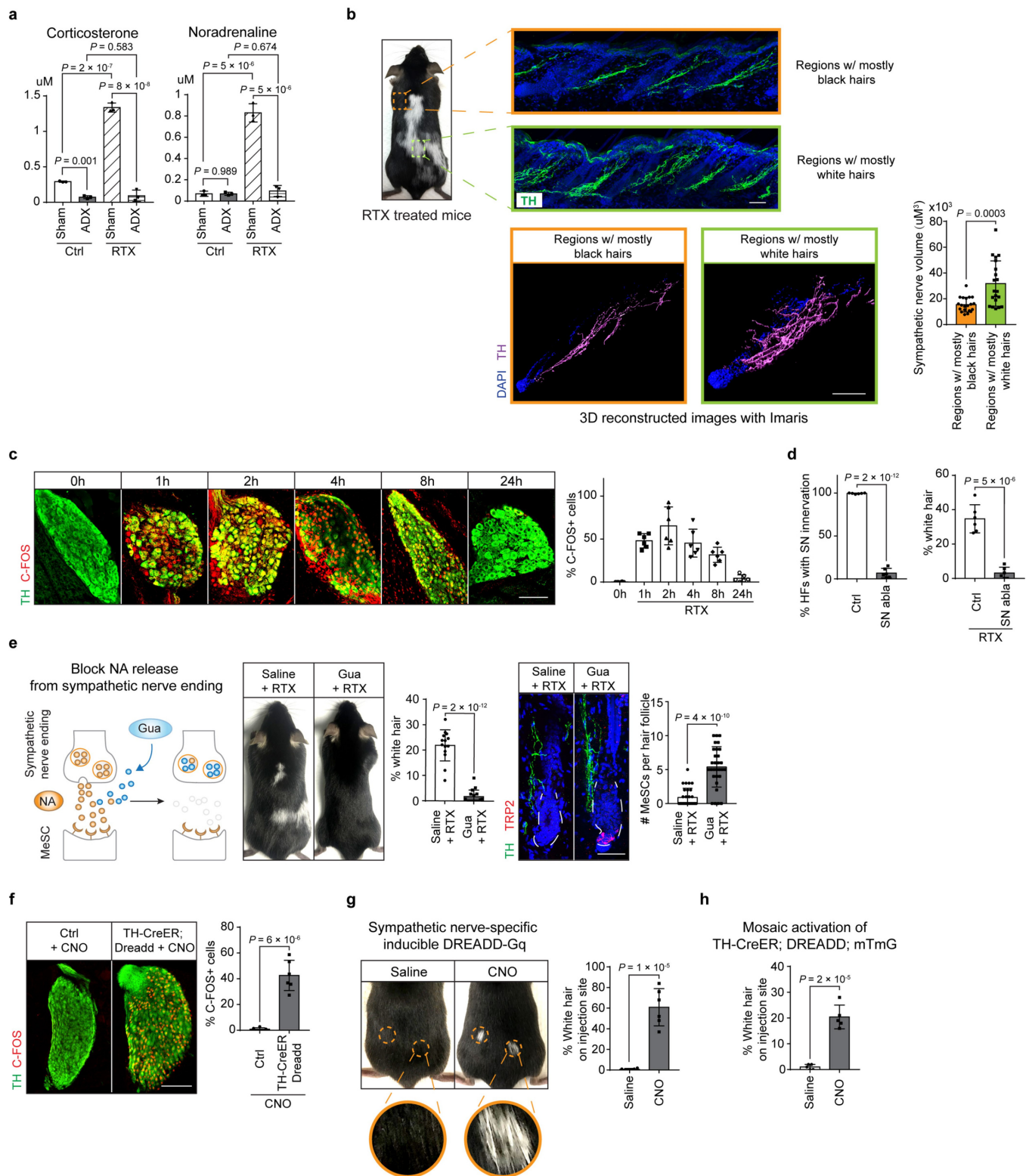
biologically independent samples). **d**, Formation of white hairs after RTX injection into *Tyr<sup>creERT2</sup>;GR<sup>fl/fl</sup>* mice (MeSC-GR cKO) ( $n = 6$  mice for each condition, two-tailed unpaired *t*-test). **e**, Left, enzyme-linked immunosorbent assay (ELISA) measurement of the level of corticosterone in the blood three days after supplying corticosterone in the drinking water ( $n = 4$  mice for each condition). Middle, immunofluorescent staining of hair follicles for TRP2 (red) from mice five days after treatment with corticosterone ( $n = 30$  hair follicles from 3 mice for each condition, two-tailed unpaired *t*-test). Right, coat colour after hair follicles in corticosterone-treated mice enter another round of anagen to regenerate new hairs. Scale bars, 50  $\mu$ m. All data are mean  $\pm$  s.d.



**Extended Data Fig. 4 | Perturbations of the noradrenaline-ADRB2 pathway.**

**a**, Left, immunofluorescent staining of hair follicles for phosphorylated CREB (pCREB; green) and TRP2 (red) 12 h after RTX injection. Right, quantification of the percentage of pCREB<sup>+</sup> MeSCs ( $n = 30$  hair follicles from 3 mice for each condition, two-tailed unpaired  $t$ -test). White arrowheads indicate pCREB<sup>+</sup> MeSCs in upper hair follicles after RTX injection. **b**, Formation of white hairs after RTX injection into  $K15^{crePGR}; Adrb2^{fl/fl}$  mice (HFSC-Adr2 cKO) ( $n = 3$  mice for each condition, two-tailed unpaired  $t$ -test). **c**, Top left, coat colour in un stressed  $Tyr^{creERT2}; Adrb2^{fl/fl}$  mice (MeSC-Adr2 cKO) in the second telogen after treatment with tamoxifen (seven times) at the first telogen. Bottom left, immunofluorescent staining of hair bulbs for MITF (red) in  $Tyr^{creERT2}; Adrb2^{fl/fl}$  mice in anagen. Right, Fontana-Masson melanin staining of anagen hair follicles from  $Tyr^{creERT2}; Adrb2^{fl/fl}$  mice ( $n = 3$  mice for each condition). **d**, Top left, schematic of experimental design for mosaic labelling in un stressed control and  $Adrb2$  knockout mice (red arrows indicate collection of skin samples). Bottom left, immunofluorescent staining for GFP (green) and TRP2 (red) from

$Tyr^{creERT2}; Rosa^{mT/mG}$  mice (MeSC-mT/mG) and  $Tyr^{creERT2}; Adrb2^{fl/fl}; Rosa^{mT/mG}$  mice (MeSC-Adr2 cKO-mT/mG) after treatment with tamoxifen (three times) at first telogen. Right, immunofluorescent staining of hair follicles for GFP (green) and TRP2 (red) after the mice enter anagen ( $n = 3$  mice for each condition). **e**, Quantification of the percentage of white hairs after intradermal injection of saline or noradrenaline ( $n = 10$  injected sites from 6–8 mice for each condition, one-way ANOVA with Tukey's multiple comparisons test). **f**, Left, immunofluorescent staining of hair follicles for TRP2 (red) from the skins of mice that were intradermally injected with noradrenaline ( $n = 30$  hair follicles from 10 injection sites for each condition, one-way ANOVA with Tukey's multiple comparisons test). Right, quantification of MeSCs. **g**, White hairs are formed after intradermal injection of noradrenaline in  $K15^{crePGR}; Adrb2^{fl/fl}$  mice (HF-Adr2 cKO) ( $n = 3$  injection sites for each condition, two-tailed unpaired  $t$ -test). Yellow dashed circles denote intradermal injection sites. Scale bars, 50  $\mu$ m. All data are mean  $\pm$  s.d.

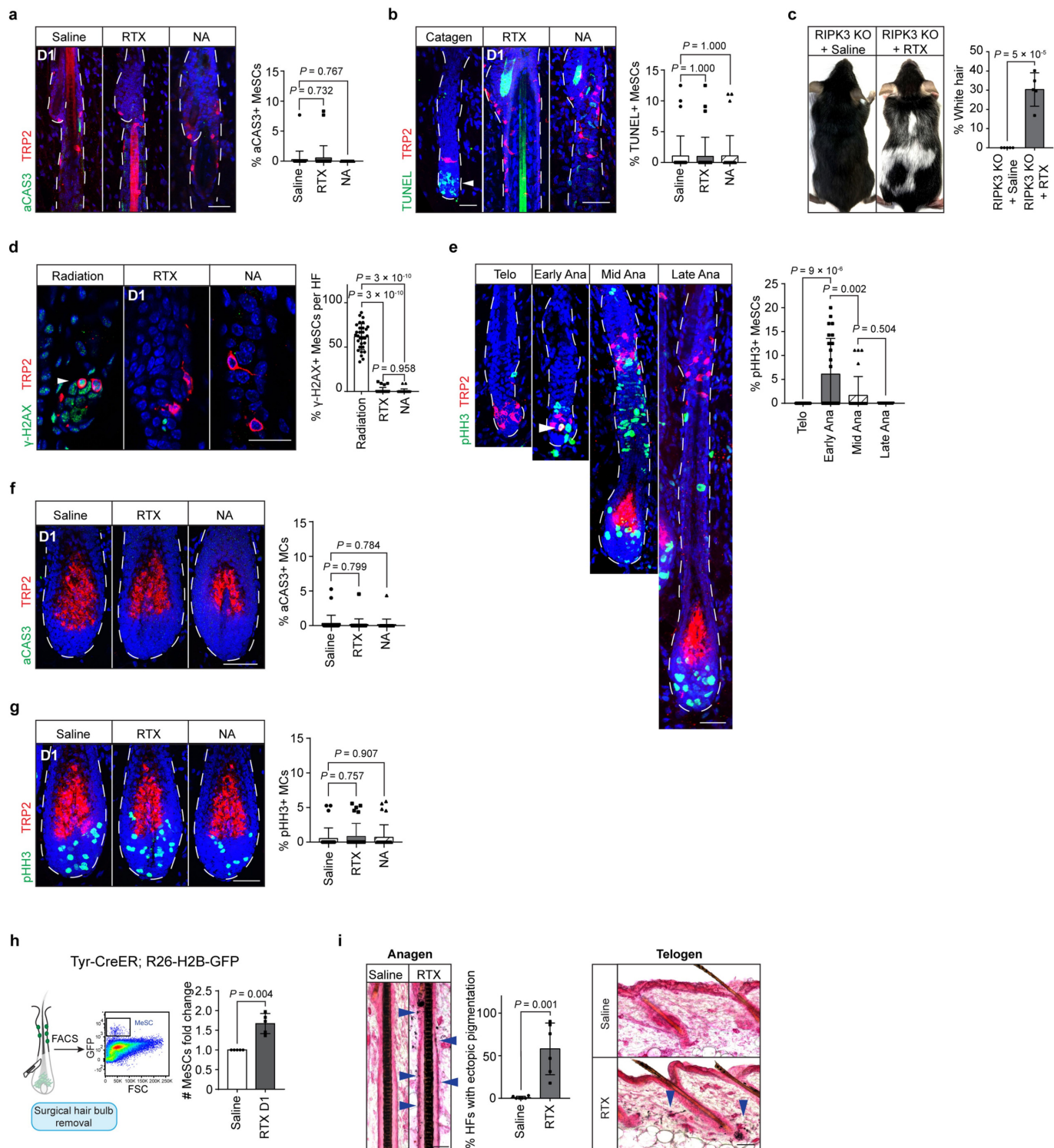


**Extended Data Fig. 5** | See next page for caption.

**Extended Data Fig. 5 | Activation of the sympathetic nervous system by nociception-induced stress or sympathetic-nerve-specific inducible  $G_q$ -DREADD.** **a**, LC-MS/MS quantification of stress hormones in sham-operated and adrenalectomized mice ( $n = 3$  mice for each condition, two-way ANOVA with Benjamini–Hochberg correction). **b**, Top, immunofluorescent staining of sympathetic nerves in the skin regions with predominantly black hairs (orange box) and with mostly white hairs (green box) ( $n = 3$  mice for each condition). Bottom, 3D surfaces of tyrosine hydroxylase (TH) staining, created using Imaris software, and quantification of the sympathetic nerve volume from regions with different numbers of unpigmented hairs ( $n = 20$  hair follicles for each region from 3 mice, two-tailed unpaired  $t$ -test). **c**, Left, immunofluorescent staining of sympathetic ganglia for tyrosine hydroxylase (green) and FOS (red) from mice injected with RTX. Cells were collected at different time points between 0 and 24 h. Right, quantification of FOS<sup>+</sup> cells ( $n = 6$  sympathetic ganglia from 3 mice for each time point). **d**, Quantification of the efficiency of chemical sympathectomy ( $n = 6$  mice for each condition, two-tailed unpaired  $t$ -test), and percentage of white hairs in RTX-injected mice

treated with vehicle (ctrl) or 6-OHDA (SN abla) ( $n = 6$  mice for each condition, two-tailed unpaired  $t$ -test). **e**, Guanethidine (gua) injection blocks the formation of white hairs that is induced by RTX injection (quantification for percentage of white hairs:  $n = 14$  mice for each condition, two-tailed unpaired  $t$ -test; quantification for numbers of MeSCs:  $n = 30$  hair follicles from 6 mice for each condition, two-tailed unpaired  $t$ -test). **f**, Left, immunofluorescent staining of sympathetic ganglia for tyrosine hydroxylase (green) and FOS (red) from  $TH^{creERT2};CAG-LSL-G_q-DREADD$  mice that were injected with CNO; cells were collected 6 h later. Right, quantification of FOS<sup>+</sup> cells ( $n = 6$  sympathetic ganglia from 2 mice for each condition, two-tailed unpaired  $t$ -test). **g**, Formation of white hairs after intradermal injection of CNO into  $TH^{creERT2};CAG-LSL-G_q-DREADD$  mice ( $n = 6$  injection sites from 5 mice for each condition, two-tailed unpaired  $t$ -test). Yellow dashed circles denote intradermal CNO injection sites. **h**, Quantification of the percentage of white hairs at CNO injection sites in mosaically induced  $TH^{creERT2};CAG-LSL-G_q-DREADD;Rosa^{mT/mG}$  mice ( $n = 5$  injection sites from 4 mice for each condition, two-tailed unpaired  $t$ -test). Scale bars, 50  $\mu$ m. All data are mean  $\pm$  s.d.





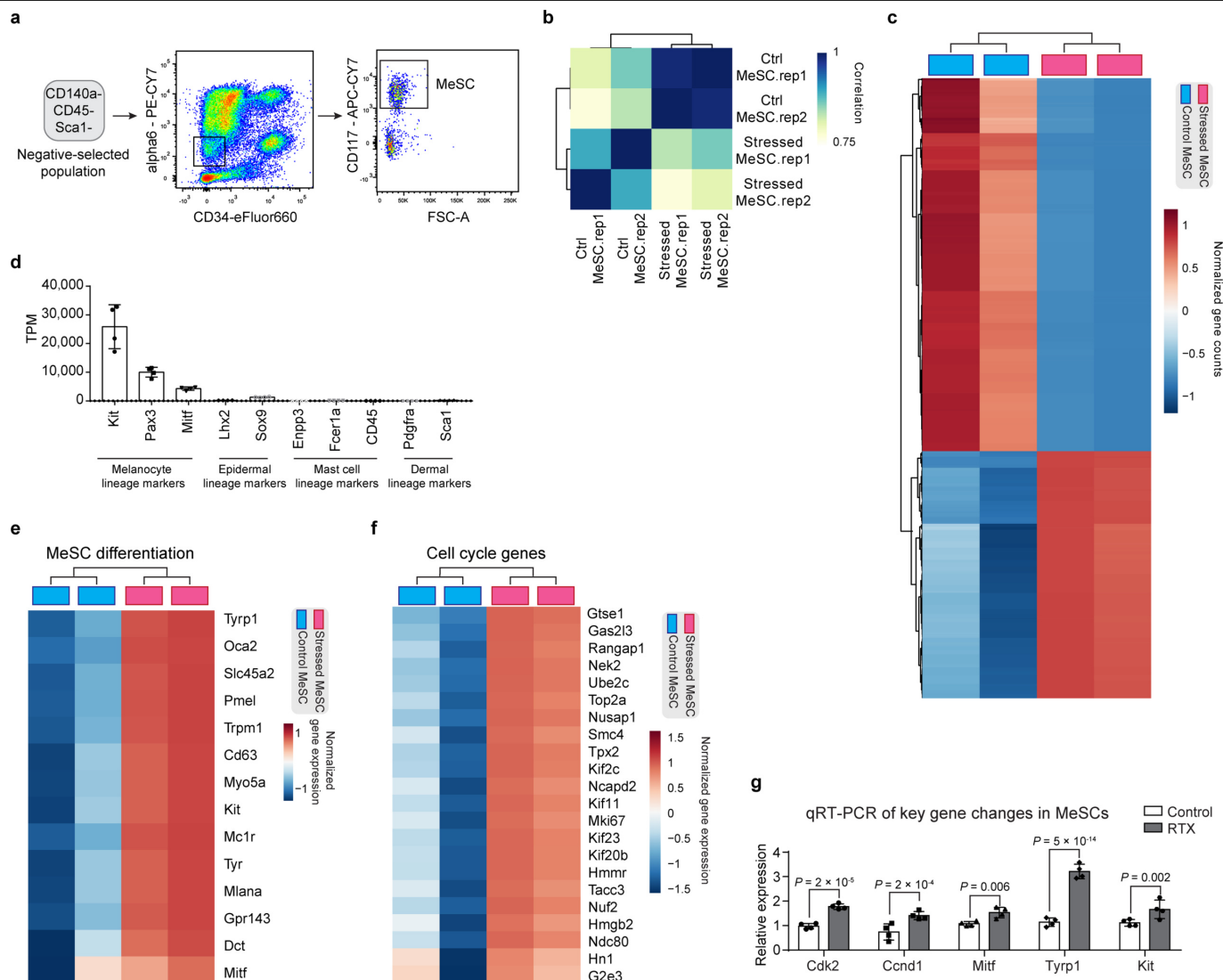
**Extended Data Fig. 6** | See next page for caption.



# Article

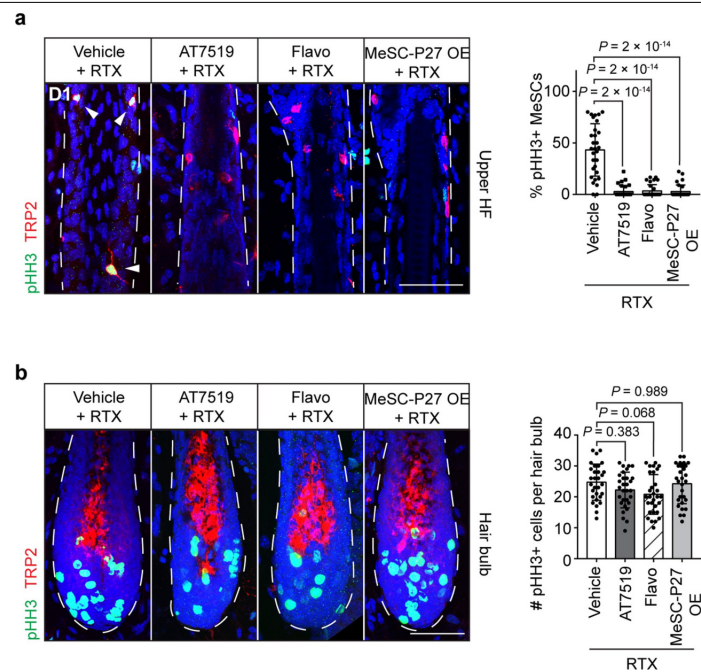
**Extended Data Fig. 6 | Analysis of apoptosis and proliferation of MeSCs and the effect of RTX or noradrenaline on mature melanocytes.** **a**, Left, immunofluorescent staining of active caspase-3 (aCAS3; green) and TRP2 (red) from mice one day after injection with RTX or noradrenaline. Right, quantification of aCAS3<sup>+</sup> MeSCs ( $n = 30$  hair follicles from 6 mice for each condition, one-way ANOVA with Tukey's multiple comparisons test). **b**, TUNEL assay of hair follicles from mice one day after treatment with RTX or noradrenaline. Catagen hair follicles were used as positive controls for TUNEL. White arrowhead points to apoptotic hair follicle cells ( $n = 30$  hair follicles from 6 mice for each condition, one-way ANOVA with Tukey's multiple comparisons test). **c**, Formation of white hairs in *Ripk3* mutant mice (RIPK3 KO) injected with RTX ( $n = 5$  mice for each condition, two-tailed unpaired *t*-test). **d**, Left, immunofluorescent staining of hair follicles for the DNA damage marker  $\gamma$ -H2AX (green) and TRP2 (red) from mice one day after treatment with RTX or noradrenaline. Hair follicles from irradiated mice were used as positive controls. White arrowhead indicates the MeSCs with DNA damage. Right, quantification of  $\gamma$ -H2AX<sup>+</sup> MeSCs ( $n = 30$  hair follicles from 6 mice for each condition, one-way ANOVA with Tukey's multiple comparisons test). **e**, Left,

immunofluorescent staining for phosphorylated histone H3 (pHH3; green) and TRP2 (red) of control hair follicles at different stages of the hair cycle. Right, quantification of pHH3<sup>+</sup> MeSCs ( $n = 25$  hair follicles from 3 mice for each condition, one-way ANOVA with Tukey's multiple comparisons test). **f**, Left, immunofluorescent staining of hair bulbs for aCAS3 (green) and TRP2 (red) from mice one day after injection with RTX or noradrenaline. Right, quantification of aCAS3<sup>+</sup> mature melanocytes (MCs) ( $n = 30$  hair follicles from 3 mice for each condition, one-way ANOVA with Tukey's multiple comparisons test). **g**, Left, immunofluorescent staining of hair bulbs for pHH3 (green) and TRP2 (red) from mice one day after injection with RTX or noradrenaline. Right, quantification of pHH3<sup>+</sup> mature melanocytes ( $n = 30$  hair follicles from 3 mice for each condition, one-way ANOVA with Tukey's multiple comparisons test). **h**, Left, schematic of the strategy for isolation of MeSCs. Right, FACS analysis of the numbers of MeSCs one day after RTX injection ( $n = 5$  mice for each condition, two-tailed unpaired *t*-test). **i**, Fontana-Masson melanin staining of anagen or telogen samples five days after injection of saline or RTX ( $n = 6$  mice for each condition, two-tailed unpaired *t*-test). Blue arrowheads indicate ectopic pigments. Scale bars, 50  $\mu$ m. All data are mean  $\pm$  s.d.



**Extended Data Fig. 7 | Differential gene expression in normal and stressed MeSCs.** **a**, FACS strategy for the purification of MeSCs. MeSCs were selected on the basis of their expression of CD117, from a population that is negative for CD140A, CD45, SCA1 and CD34 and that shows modest expression for integrin  $\alpha 6$ . **b**, Sample clustering based on Pearson's correlation of transcriptomes between control and stressed MeSCs ( $n = 2$  biologically independent samples for each condition). **c**, Heat map of all differentially expressed genes ( $n = 2$  biologically independent samples for each condition;  $P$  values were calculated using the Wald test implemented in DESeq2, and adjusted using the Benjamini-Hochberg method. Differentially expressed genes were those that had the

absolute value of  $\log_2$ (gene expression in stressed versus control MeSCs)  $\geq 0.58$  and adjusted  $P$  value  $< 0.05$ . **d**, Expression levels of marker genes for different cell types in the skin, confirming the purity of MeSCs that were used for RNA-seq ( $n = 4$  biologically independent samples). TPM, transcripts per million. **e**, Heat maps showing expression of signature genes that are related to the differentiation of MeSCs. **f**, Heat maps showing expression of cell-cycle signature genes. *Hn1* is also known as *ptl*. **g**, qRT-PCR validation of selected differentially expressed genes in FACS-purified mouse MeSCs from skins of control and RTX-injected mice ( $n = 4$  biological replicates for each condition, two-way ANOVA with Benjamini-Hochberg correction). All data are mean  $\pm$  s.d.



**Extended Data Fig. 8 | Proliferation analysis of RTX-injected mice that were treated with CDK inhibitors chemically or genetically. a, b, Left, immunofluorescent staining of upper hair follicles (a) and hair bulbs (b) for pHH3 (green) and TRP2 (red) from mice one day after RTX injection, RTX injection with topical application of CDK inhibitors (AT7519 or flavopiridol) or**

RTX injection with MeSC-specific overexpression of P27 (MeSC-P27 OE). Right, quantification of pHH3<sup>+</sup> cells ( $n = 30$  hair follicles from 3 mice for each condition, one-way ANOVA with Tukey's multiple comparisons test). Scale bars, 50  $\mu\text{m}$ . All data are mean  $\pm$  s.d.

## Reporting Summary

Nature Research wishes to improve the reproducibility of the work that we publish. This form provides structure for consistency and transparency in reporting. For further information on Nature Research policies, see [Authors & Referees](#) and the [Editorial Policy Checklist](#).

### Statistics

For all statistical analyses, confirm that the following items are present in the figure legend, table legend, main text, or Methods section.

n/a Confirmed

- ☐ ☒ The exact sample size ( $n$ ) for each experimental group/condition, given as a discrete number and unit of measurement
- ☐ ☒ A statement on whether measurements were taken from distinct samples or whether the same sample was measured repeatedly
- ☐ ☒ The statistical test(s) used AND whether they are one- or two-sided  
*Only common tests should be described solely by name; describe more complex techniques in the Methods section.*
- ☐ ☒ A description of all covariates tested
- ☐ ☒ A description of any assumptions or corrections, such as tests of normality and adjustment for multiple comparisons
- ☐ ☒ A full description of the statistical parameters including central tendency (e.g. means) or other basic estimates (e.g. regression coefficient) AND variation (e.g. standard deviation) or associated estimates of uncertainty (e.g. confidence intervals)
- ☐ ☒ For null hypothesis testing, the test statistic (e.g.  $F$ ,  $t$ ,  $r$ ) with confidence intervals, effect sizes, degrees of freedom and  $P$  value noted  
*Give  $P$  values as exact values whenever suitable.*
- ☒ ☐ For Bayesian analysis, information on the choice of priors and Markov chain Monte Carlo settings
- ☒ ☐ For hierarchical and complex designs, identification of the appropriate level for tests and full reporting of outcomes
- ☒ ☐ Estimates of effect sizes (e.g. Cohen's  $d$ , Pearson's  $r$ ), indicating how they were calculated

*Our web collection on [statistics for biologists](#) contains articles on many of the points above.*

### Software and code

Policy information about [availability of computer code](#)

Data collection BD FACSDiva (8.0.2), ZEN 2.3 SP1 (black 64 bit)

Data analysis ImageJ (1.52h), Imaris (x64 9.3.0), Prism (7.00), Trim Galore! (0.4.1), STAR (2.5.3), DESeq2 (1.22.2), FlowJo (v10.0.7), DAVID (6.8), RStudio (Version 1.1.453), R (3.5.1)

For manuscripts utilizing custom algorithms or software that are central to the research but not yet described in published literature, software must be made available to editors/reviewers. We strongly encourage code deposition in a community repository (e.g. GitHub). See the Nature Research [guidelines for submitting code & software](#) for further information.

### Data

Policy information about [availability of data](#)

All manuscripts must include a [data availability statement](#). This statement should provide the following information, where applicable:

- Accession codes, unique identifiers, or web links for publicly available datasets
- A list of figures that have associated raw data
- A description of any restrictions on data availability

Sequence data that support the findings of this study have been deposited in GEO with the accession codes GSE131566 (<https://www.ncbi.nlm.nih.gov/geo/query/acc.cgi?acc=GSE131566>).

Source data for all figures are provided with the paper.

## Field-specific reporting

Please select the one below that is the best fit for your research. If you are not sure, read the appropriate sections before making your selection.

☒ Life sciences ☐ Behavioural & social sciences ☐ Ecological, evolutionary & environmental sciences

For a reference copy of the document with all sections, see [nature.com/documents/nr-reporting-summary-flat.pdf](https://www.nature.com/documents/nr-reporting-summary-flat.pdf)

## Life sciences study design

All studies must disclose on these points even when the disclosure is negative.

Sample size	Sample sizes were determined based on prior studies and literatures of the field using similar experimental paradigms.
Data exclusions	No data were excluded from analysis
Replication	For in vivo experiments using rodent, biological replicates and independent cohorts of mice were used; for in vitro experiments, biological replicates as well as technical triplicates were used to ensure reproducibility. All attempts at replication were successful.
Randomization	The mice were randomly assigned into different experimental groups whenever possible, except in experiments required specific genotypes.
Blinding	For LC-MS-MS analysis, RNA-seq library preparation, and sequencing, experimenters were blinded to experimental conditions. Blinding was not possible in mouse studies due to the need to identify specific genotypes or treat mice with different chemicals according to experimental designs.

## Reporting for specific materials, systems and methods

We require information from authors about some types of materials, experimental systems and methods used in many studies. Here, indicate whether each material, system or method listed is relevant to your study. If you are not sure if a list item applies to your research, read the appropriate section before selecting a response.

### Materials & experimental systems

n/a	Involved in the study
<input type="checkbox"/>	<input checked="" type="checkbox"/> Antibodies
<input checked="" type="checkbox"/>	<input type="checkbox"/> Eukaryotic cell lines
<input checked="" type="checkbox"/>	<input type="checkbox"/> Palaeontology
<input type="checkbox"/>	<input checked="" type="checkbox"/> Animals and other organisms
<input checked="" type="checkbox"/>	<input type="checkbox"/> Human research participants
<input checked="" type="checkbox"/>	<input type="checkbox"/> Clinical data

### Methods

n/a	Involved in the study
<input checked="" type="checkbox"/>	<input type="checkbox"/> ChIP-seq
<input type="checkbox"/>	<input checked="" type="checkbox"/> Flow cytometry
<input checked="" type="checkbox"/>	<input type="checkbox"/> MRI-based neuroimaging

## Antibodies

### Antibodies used

TRP2 (Santa Cruz, CAT 10451, Clone D18, Lot k2114, Dilution 1:400)  
 Tyrosine hydroxylase (Millipore, CAT AB152, Clone N/A, Lot 3072361, Dilution 1:1000)  
 Tyrosine hydroxylase (Millipore, CAT AB1542, Clone N/A, Lot 3168710, Dilution 1:150-1:300)  
 c-Fos (Abcam, CAT 190289, Clone N/A, Lot GR3253255-1, Dilution 1:400)  
 γ-H2AX (Cell Signaling Technology, CAT 9718, Clone 20E3, Lot 17, Dilution 1:400)  
 Phospho-Histone H3 (Cell Signaling Technology, CAT 3377S, Clone D2C8, Lot 7, Dilution 1:250)  
 Cleaved Caspase-3 (Cell Signaling Technology, CAT 9664S, Clone 5A1E, Lot 45, Dilution 1:300)  
 GFP (Abcam, CAT ab290, Clone N/A, Lot N/A, Dilution 1:800)  
 CD3 (eBioscience, CAT 14-0032-81, Clone 17A2, Lot 4342633, Dilution 1:800)  
 CD11b (eBioscience, CAT 14-0112-81, Clone M1/70, Lot E03529-1632, Dilution 1:400)  
 Phospho-CREB (Cell Signaling Technology, CAT 9198, Clone 87G3, Lot 14, Dilution 1:800)  
 MITF (Abcam, CAT ab12039, Clone C5, Lot GR3206967-1, Dilution 1:400)  
 CD140a (Invitrogen, CAT 13-1401-82, Clone APA5, Lot 1993111, Dilution 1:200)  
 CD45 (Invitrogen, CAT 13-0451-82, Clone 30-F11, Lot 1989134, Dilution 1:400)  
 Sca1 (Invitrogen, CAT 13-5981-82, Clone D7, Lot 4346548, Dilution 1:1000)  
 CD34 (Invitrogen, CAT 13-0341-82, Clone RAM34, Lot 1993111, Dilution 1:100)  
 CD117 (Biolegend, CAT 135136, Clone ACK2, Lot B251908, Dilution 1:400)

### Validation

TRP2 (Santa Cruz, CAT 10451): Mouse, Immunohistochemistry, validated on manufactures's website: [http://www.emdmillipore.com/US/en/product/Anti-Tyrosine-Hydroxylase-Antibody,MM\\_NF-AB152#overview](http://www.emdmillipore.com/US/en/product/Anti-Tyrosine-Hydroxylase-Antibody,MM_NF-AB152#overview)

Tyrosine hydroxylase (Millipore, CAT AB152): Mouse, Immunohistochemistry, validated on manufactures's website: [http://www.emdmillipore.com/US/en/product/Anti-Tyrosine-Hydroxylase-Antibody,MM\\_NF-AB152#overview](http://www.emdmillipore.com/US/en/product/Anti-Tyrosine-Hydroxylase-Antibody,MM_NF-AB152#overview)



[www.emdmillipore.com/US/en/product/Anti-Tyrosine-Hydroxylase-Antibody,MM\\_NF-AB152#overview](http://www.emdmillipore.com/US/en/product/Anti-Tyrosine-Hydroxylase-Antibody,MM_NF-AB152#overview)

Tyrosine hydroxylase (Millipore, CAT AB1542): Mouse, Immunohistochemistry, validated on manufactures's website: [http://www.emdmillipore.com/US/en/product/Anti-Tyrosine-Hydroxylase-Antibody,MM\\_NF-AB1542#overview](http://www.emdmillipore.com/US/en/product/Anti-Tyrosine-Hydroxylase-Antibody,MM_NF-AB1542#overview)

c-Fos (Abcam, CAT 190289, Clone N/A): Mouse, Immunohistochemistry, validated on manufactures's website: <https://www.abcam.com/c-fos-antibody-ab190289.html#top-500>

$\gamma$ -H2AX (Cell Signaling Technology, CAT 9718): Mouse, Immunohistochemistry, validated on manufactures's website: <https://www.cellsignal.com/products/primary-antibodies/phospho-histone-h2a-x-ser139-20e3-rabbit-mab/9718>

Phospho-Histone H3 (Cell Signaling Technology, CAT 3377S): Mouse, Immunohistochemistry, validated on manufactures's website: <https://www.cellsignal.com/products/primary-antibodies/phospho-histone-h3-ser10-d2c8-xp-rabbit-mab/3377>

Cleaved Caspase-3 (Cell Signaling Technology, CAT 9664S): Mouse, Immunohistochemistry, validated on manufactures's website: <https://www.cellsignal.com/products/primary-antibodies/cleaved-caspase-3-asp175-5a1e-rabbit-mab/9664>

GFP (Abcam, CAT ab290, Clone N/A): Mouse, Immunohistochemistry, validated on manufactures's website: <https://www.abcam.com/gfp-antibody-chip-grade-ab290.html?productWallTab=ShowAll>

CD3 (eBioscience, CAT 14-0032-81, Clone 17A2): Mouse, Immunohistochemistry, validated on manufactures's website: <https://www.thermofisher.com/antibody/product/CD3-Antibody-clone-17A2-Monoclonal/14-0032-82>

CD11b (eBioscience, CAT 14-0112-81, Clone M1/70): Mouse, Immunohistochemistry, validated on manufactures's website: <https://www.thermofisher.com/antibody/product/CD11b-Antibody-clone-M1-70-Monoclonal/14-0112-82>

Phospho-CREB (Cell Signaling Technology, CAT 9198): Mouse, Immunohistochemistry, validated on manufactures's website: <https://www.cellsignal.com/products/primary-antibodies/phospho-creb-ser133-87g3-rabbit-mab/9198>

MITF (Abcam, CAT ab12039, Clone C5): Mouse, Immunohistochemistry, validated on manufactures's website: <https://www.abcam.com/mitf-antibody-c5-chip-grade-ab12039.html>

CD140a (Invitrogen, CAT 13-1401-82, Clone APA5): Mouse, FACS, validated on manufactures's website: <https://www.thermofisher.com/antibody/product/CD140a-PDGFR-Alpha-Antibody-clone-APA5-Monoclonal/13-1401-82>

CD45 (Invitrogen, CAT 13-0451-82, Clone 30-F11): Mouse, FACS, validated on manufactures's website: <https://www.thermofisher.com/antibody/product/CD45-Antibody-clone-30-F11-Monoclonal/13-0451-82>

Sca1 (Invitrogen, CAT 13-5981-82, Clone D7): Mouse, FACS, validated on manufactures's website: <https://www.thermofisher.com/antibody/product/Ly-6A-E-Sca-1-Antibody-clone-D7-Monoclonal/13-5981-82>

CD34 (Invitrogen, CAT 13-0341-82, Clone RAM34): Mouse, FACS, validated on manufactures's website: <https://www.thermofisher.com/antibody/product/CD34-Antibody-clone-RAM34-Monoclonal/13-0341-82>

CD117 (Biolegend, CAT 135136, Clone ACK2): Mouse, FACS, validated on manufactures's website: <https://www.biolegend.com/en-us/products/apccyanine7-anti-mouse-cd117-c-kit-antibody-13795>

## Animals and other organisms

Policy information about [studies involving animals](#); [ARRIVE guidelines](#) recommended for reporting animal research

### Laboratory animals

C57BL/6J, Tyr-CreER, K15-CrePGR, Rag1 KO, CD11b-DTR, GR flox, Dreadd flox, Rosa-H2BGFP/mCherry, Rosa26-rtTA, Rosa-mTmG, RIPK3 knockout, Adrb2 flox, TH-CreER, pTRE-P27. All experiments used balanced groups of male and female mice. All experiments are conducted and compared using mice of the same hair cycle stage in comparable age range (P20-P25 for 1st telogen, P31-P36 for full anagen, and P50-P60 for 2nd telogen, or long-term monitoring as specified).

### Wild animals

This study did not involve wild animals.

### Field-collected samples

This study did not involve field-collected samples.

### Ethics oversight

All animals were maintained in an Association for Assessment and Accreditation of Laboratory Animal Care-approved animal facility at Harvard University, Harvard Medical School, and Ribeirao Preto Medical School. Procedures were approved by the Institutional Animal Care and Use Committee of all institutions and were in compliance with all relevant ethical regulations.

Note that full information on the approval of the study protocol must also be provided in the manuscript.

## Flow Cytometry

### Plots

Confirm that:

- ☒ The axis labels state the marker and fluorochrome used (e.g. CD4-FITC).
- ☒ The axis scales are clearly visible. Include numbers along axes only for bottom left plot of group (a 'group' is an analysis of identical markers).
- ☒ All plots are contour plots with outliers or pseudocolor plots.
- ☒ A numerical value for number of cells or percentage (with statistics) is provided.

### Methodology

Sample preparation

Mouse dorsal skin was collected, and the fat layer was removed by gentle scrapping from the dermal side. The skin was incubated in 0.25% collagenase in HBSS at 37 °C for 35-45 minutes on an orbital shaker. Single cell suspension was collected by gentle scraping of the dermal side and filtering through 70 µm and 40 µm filters. The epidermal layer was incubated in trypsin-EDTA at 37 °C for 35-45 minutes on an orbital shaker. Single cell suspension was collected by gentle scraping of the epidermal side and filtering through 70 µm and 40 µm filters. The single cell suspension was centrifuged for 5 minutes at 4°C, resuspended in 0.25% FBS in PBS, and stained with fluorescent dye-conjugated antibodies for 30 minutes. For late anagen skin samples, the bottom parts of the hair follicles containing mature melanocytes were removed by gentle scrapping under dissection microscope. The MeSCs located close to the bulge remained and were verified by immunostaining.

Instrument

FACS: BD FACSAria III

Software

BD FACSDiva (8.0.2), FlowJo (v10.0.7)

Cell population abundance

For sorting for RNA-seq, at least 10,000 MeSCs were collected. The purity was verified by expression of GFP driven by lineage specific CreER.

Gating strategy

Positive and negative gates were set using fluorescence minus one (FMO) background intensity controls. Fluorophores were chosen to minimize spectral overlap.

- ☒ Tick this box to confirm that a figure exemplifying the gating strategy is provided in the Supplementary Information.

# Host-mediated ubiquitination of a mycobacterial protein suppresses immunity

<https://doi.org/10.1038/s41586-019-1915-7>

Received: 8 October 2018

Accepted: 21 November 2019

Published online: 15 January 2020

Lin Wang<sup>1,8</sup>, Juehui Wu<sup>1,2,8</sup>, Jun Li<sup>3,8</sup>, Hua Yang<sup>1</sup>, Tianqi Tang<sup>2</sup>, Haijiao Liang<sup>1,2</sup>, Mianrong Zuo<sup>2</sup>, Jie Wang<sup>1</sup>, Haipeng Liu<sup>1,4</sup>, Feng Liu<sup>1</sup>, Jianxia Chen<sup>1,4</sup>, Zhonghua Liu<sup>1</sup>, Yang Wang<sup>2</sup>, Cheng Peng<sup>2</sup>, Xiangyang Wu<sup>2</sup>, Ruijuan Zheng<sup>1</sup>, Xiaochen Huang<sup>1</sup>, Yajun Ran<sup>3</sup>, Zihao Rao<sup>3,5,6,7\*</sup> & Baoxue Ge<sup>1,2,4\*</sup>

*Mycobacterium tuberculosis* is an intracellular pathogen that uses several strategies to interfere with the signalling functions of host immune molecules. Many other bacterial pathogens exploit the host ubiquitination system to promote pathogenesis<sup>1,2</sup>, but whether this same system modulates the ubiquitination of *M. tuberculosis* proteins is unknown. Here we report that the host E3 ubiquitin ligase ANAPC2—a core subunit of the anaphase-promoting complex/cyclosome—interacts with the mycobacterial protein Rv0222 and promotes the attachment of lysine-11-linked ubiquitin chains to lysine 76 of Rv0222 in order to suppress the expression of proinflammatory cytokines. Inhibition of ANAPC2 by specific short hairpin RNA abolishes the inhibitory effect of Rv0222 on proinflammatory responses. Moreover, mutation of the ubiquitination site on Rv0222 impairs the inhibition of proinflammatory cytokines by Rv0222 and reduces virulence during infection in mice. Mechanistically, lysine-11-linked ubiquitination of Rv0222 by ANAPC2 facilitates the recruitment of the protein tyrosine phosphatase SHP1 to the adaptor protein TRAF6, preventing the lysine-63-linked ubiquitination and activation of TRAF6. Our findings identify a previously unrecognized mechanism that *M. tuberculosis* uses to suppress host immunity, and provide insights relevant to the development of effective immunomodulators that target *M. tuberculosis*.

To identify *M. tuberculosis* proteins that inhibit host inflammatory responses, we examined the effects of 208 mycobacterial secreted proteins and lipoproteins on the activation of NF- $\kappa$ B<sup>3</sup>, a transcription factor that is involved in numerous cellular processes, including inflammation. Of these mycobacterial proteins, Rv0222—a serodiagnostic target for tuberculosis<sup>4</sup>—inhibited NF- $\kappa$ B activation. Consistent with this, transient expression of Rv0222 in HEK293T cells markedly inhibited the activation of both NF- $\kappa$ B and AP-1, another transcription factor (Extended Data Fig. 1a, b). Transfection with Rv0222 also resulted in reduced activation of NF- $\kappa$ B signalling in immortalized bone-marrow-derived macrophages (iBMDMs) infected with *M. tuberculosis*, again suggesting that Rv0222 inhibits NF- $\kappa$ B activation (Extended Data Fig. 1c).

## Rv0222 inhibits host immunity

To further investigate the effect of Rv0222 on host immune responses, we generated a Rv0222-deletion mutant of the *M. tuberculosis* strain H37Rv (H37Rv $\Delta$ Rv0222) (Extended Data Fig. 1d). Primary peritoneal macrophages—which serve as both a habitat for, and first line of defence against, *M. tuberculosis*—were infected with H37Rv or H37Rv $\Delta$ Rv0222 before gene-expression profiling. Macrophages infected with the

H37Rv $\Delta$ Rv0222 strain had much higher mRNA levels of proinflammatory cytokines, including interleukin (IL)-1b, IL-6 and IL-12, than those infected with wild-type H37Rv (Fig. 1a and Extended Data Fig. 1e–g), but there was no significant difference in cell death ( $P=0.76$  when infected for 12 h and  $P=0.91$  when infected for 24 h) and bacterial entry ( $P=0.67$ ) (Extended Data Fig. 1h, i). Consistent with this finding, the lung tissue of mice infected with H37Rv $\Delta$ Rv0222 had much higher levels of mRNAs encoding IL-1b, IL-6 and the IL-12 p40 subunit than did the lung tissue of mice infected with H37Rv (Fig. 1b–d). Furthermore, complementation of H37Rv $\Delta$ Rv0222 with Rv0222, but not with green-fluorescent protein (GFP), restored the inhibition of *Il1b*, *Il6* and *Il12 p40* expression upon infection with H37Rv (Fig. 1e–g and Extended Data Fig. 1d). Together, these results provide further evidence that Rv0222 inhibits *M. tuberculosis*-triggered inflammatory responses.

We next investigated the functional relevance of Rv0222 in the pathogenesis of *M. tuberculosis* infection. The lung tissues of C57BL/6 mice infected with H37Rv( $\Delta$ Rv0222 + GFP) had less immune-cell infiltration and fewer inflammatory lesions than those infected with H37Rv (Fig. 1h). As shown above, H37Rv $\Delta$ Rv0222 induced a higher level of *Il12 p40* expression than did wild-type H37Rv (Fig. 1d). IL-12 p40 has been reported to increase the differentiation of T-helper-1 ( $T_H1$ )

<sup>1</sup>Shanghai Key Laboratory of Tuberculosis, Shanghai Pulmonary Hospital, Tongji University School of Medicine, Shanghai, China. <sup>2</sup>Department of Microbiology and Immunology, Tongji University School of Medicine, Shanghai, China. <sup>3</sup>Shanghai Institute for Advanced Immunochemical Studies and School of Life Science and Technology, ShanghaiTech University, Shanghai, China. <sup>4</sup>Clinical Translation Research Center, Shanghai Pulmonary Hospital, Tongji University School of Medicine, Shanghai, China. <sup>5</sup>Laboratory of Structural Biology, Tsinghua University, Beijing, China. <sup>6</sup>State Key Laboratory of Medicinal Chemical Biology, College of Life Sciences and College of Pharmacy, Nankai University, Tianjin, China. <sup>7</sup>National Laboratory of Biomacromolecules, CAS Center for Excellence in Biomacromolecules, Institute of Biophysics, Beijing, China. <sup>8</sup>These authors contributed equally: Lin Wang, Juehui Wu, Jun Li. \*e-mail: raozh@mail.tsinghua.edu.cn; baoxue\_ge@tongji.edu.cn

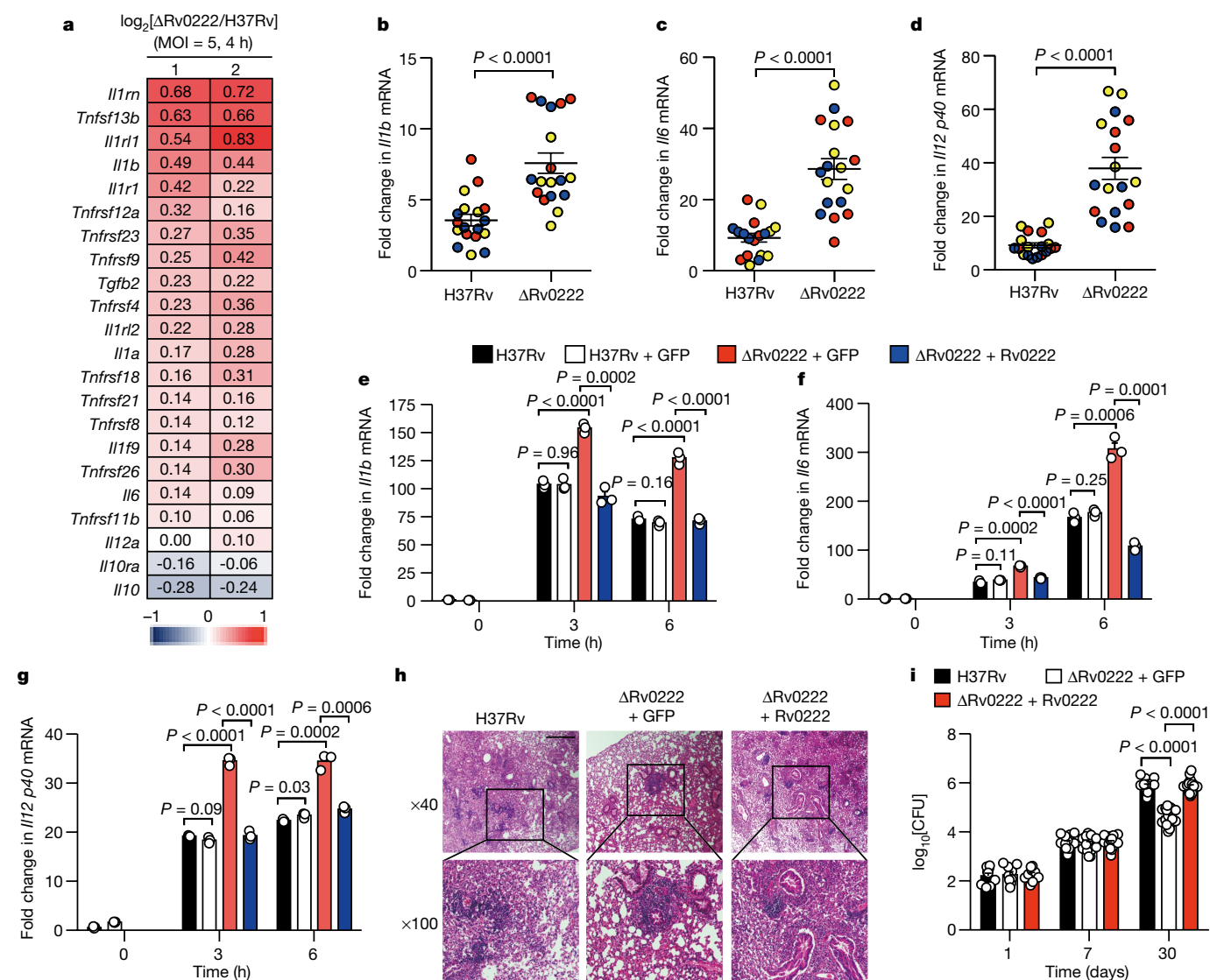


**Fig. 1 | Rv0222 inhibits host inflammatory responses.** **a**, Heat map of downregulated (blue) and upregulated (red) mRNAs from peritoneal macrophages infected with H37Rv ( $n = 2$ ) versus  $\Delta Rv0222$  ( $n = 2$ ) (multiplicity of infection (MOI) = 5) for 4 h. Numbers 1 and 2 refer to two independent experimental analyses of  $\log_2(\Delta Rv0222/H37Rv)$ . **b–d**, Quantitative polymerase chain reaction (qPCR) analysis of *Il1b* (**b**), *Il6* (**c**) and *Il12p40* (**d**) mRNA from the lungs of C57BL/6 mice aerosol-infected with roughly 200 colony-forming units (CFUs) per mouse of H37Rv or  $\Delta Rv0222$  for 7 days. The graphs show cumulative data from three independent experiments (mean  $\pm$  s.e.m. of  $n = 18$ ), with red, blue and yellow circles denoting separate experiments. **e–g**, qPCR analysis of *Il1b* (**e**), *Il6* (**f**) and *Il12p40* (**g**) mRNA from peritoneal macrophages infected with H37Rv, H37Rv + GFP, H37Rv( $\Delta Rv0222$  + GFP) or H37Rv( $\Delta Rv0222$  + Rv0222) for 3 h or 6 h (MOI = 5)

(mean  $\pm$  s.e.m.). Data are representative of one experiment with at least three independent biological replicates; each circle represents one technical repeat. Bar charts show means. **h, i**, C57BL/6 mice were aerosol-infected with roughly 200 CFUs per mouse of H37Rv, H37Rv( $\Delta Rv0222$  + GFP) or H37Rv( $\Delta Rv0222$  + Rv0222). Histopathology was assessed in lung sections stained with haematoxylin and eosin from mice infected for 30 days (**h**; representative of one experiment with at least three independent replicates; scale bars, 1,000  $\mu$ m (top) and 200  $\mu$ m (bottom)), and bacterial titres were assessed in lungs from mice infected for 1, 7 or 30 days (**i**; cumulative data from three independent experiments; mean  $\pm$  s.e.m. of  $n = 9$  mice infected for 1 day and  $n = 18$  mice infected for 7 or 30 days). Two-tailed unpaired Student's *t*-test (**b–g**) and two-sided Mann–Whitney *U*-test (**i**) were used for statistical analysis. For gel source data, see Supplementary Fig. 1.

cells during *M. tuberculosis* infection<sup>5</sup>;  $T_H1$  cells produce interferon (IFN) $\gamma$ ; and IFN $\gamma$  inhibits the accumulation of pathogenic neutrophils in infected lungs during *M. tuberculosis* infection<sup>6,7</sup>. Hence, the reduced immune-cell infiltration that we observed in the lungs of H37Rv( $\Delta Rv0222$ )-infected mice could be due to a higher level of IFN $\gamma$ -producing  $T_H1$  cells. The bacterial burden in the lung tissue of mice infected with H37Rv( $\Delta Rv0222$  + Rv0222) was much higher than in mice infected with H37Rv( $\Delta Rv0222$  + GFP) (Fig. 1i and Extended Data Fig. 1j). Together, these results suggest that Rv0222 is an essential virulence factor for *M. tuberculosis*.

## Rv0222 inhibits TRAF6

Various pattern-recognition receptors (PRRs) in hosts regulate *M. tuberculosis*-induced cytokine expression by activating mitogen-activated protein (MAP) kinase and NF- $\kappa$ B pathways. We found that, in the absence of Rv0222, macrophages infected with H37Rv exhibited much stronger activation of MAP kinase and NF- $\kappa$ B (Extended Data Fig. 2a), suggesting that Rv0222 may inhibit the activation of pathways that comprise the p38 MAP kinases, the c-Jun amino-terminal kinases (JNKs, which are downstream of MAP kinases) or NF- $\kappa$ B in response to *M. tuberculosis* infection. Inhibition of p38, JNK or NF- $\kappa$ B attenuated the enhanced expression levels

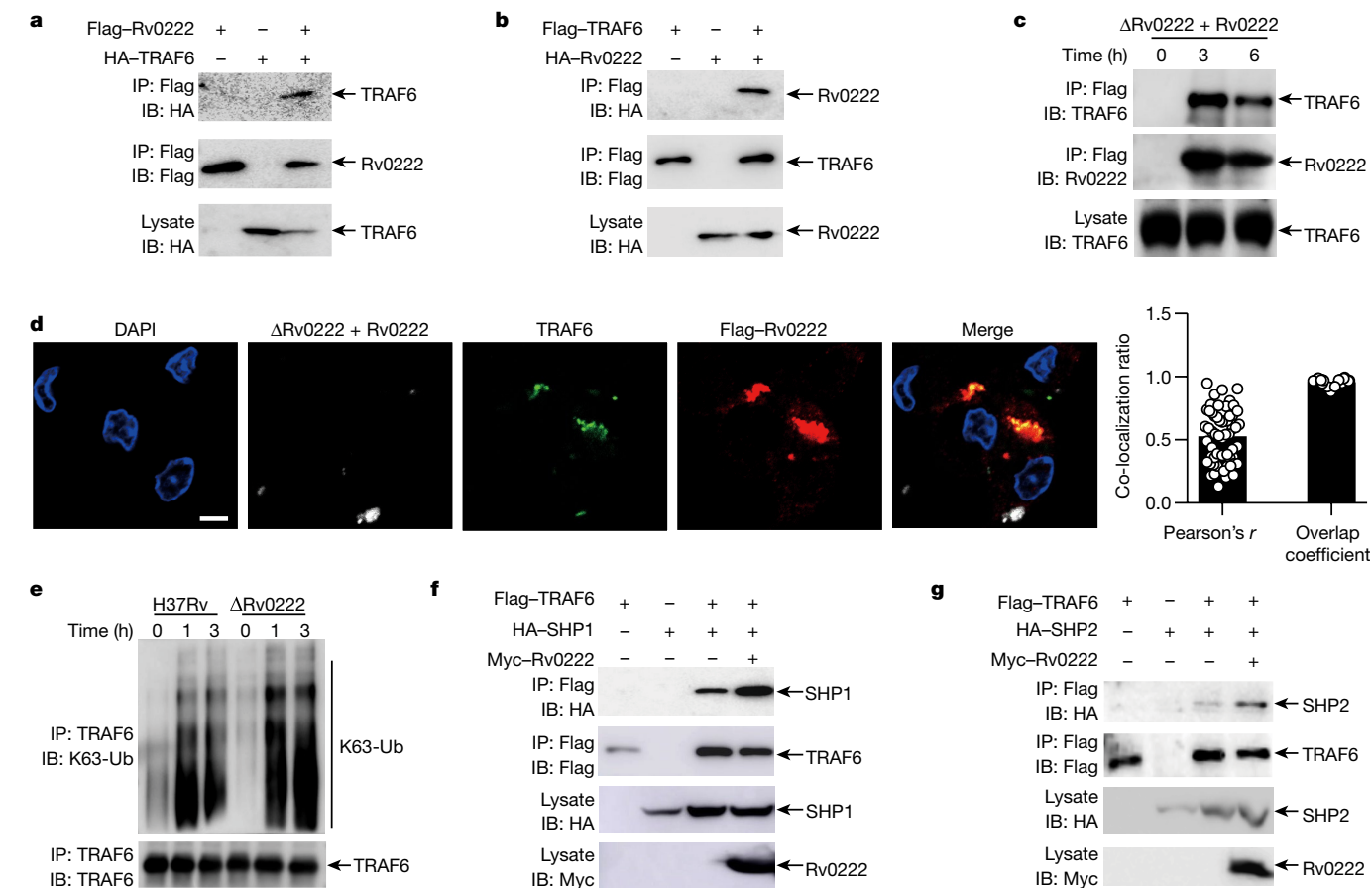


**Fig. 2 | Rv0222 interacts with and inhibits TRAF6 signalling.**

**a, b**, Immunoblot (IB) and immunoprecipitation (IP) of lysates of HEK293T cells transfected with various plasmids as indicated. **c**, Endogenous interaction of Rv0222 with TRAF6 in H37Rv(ΔRv0222 + Rv0222)-infected peritoneal macrophages (MOI = 5). **d**, Left, images show confocal microscopy of peritoneal macrophages infected with H37Rv(ΔRv0222 + Rv0222) for 3 h (MOI = 5). Scale bar, 5 μm. Right, the co-localization ratio from 60 macrophages (mean ± s.e.m.). **e**, Peritoneal macrophages were infected with H37Rv or ΔRv0222 for the

indicated times (MOI = 5); cell lysates were immunoprecipitated with an anti-TRAF6 antibody; and immunoprecipitates were analysed with an anti-K63-Ub antibody. **f, g**, Immunoblot and immunoprecipitation of lysates from HEK293T cells transfected with plasmids as indicated. Data in **a–g** represent one experiment with at least three independent biological replicates. For gel source data, see Supplementary Fig. 1.

of *Il1b* and *Il6* in macrophages infected with H37RvΔRv0222 (Extended Data Fig. 2b, c), suggesting that Rv0222 may inhibit the *M. tuberculosis*-induced expression of proinflammatory cytokines by downregulating the activation of the p38, JNK and NF-κB pathways.

*M. tuberculosis* infection induces the expression of proinflammatory cytokines via the Toll-like receptor (TLR) signalling pathway<sup>8,9</sup>, which is composed of several adaptor proteins, namely tumour necrosis factor (TNF)-receptor-associated factor 6 (TRAF6), transforming growth factor-β (TGFβ)-activated kinase 1 (TAK1) and TAK1-binding protein 1 (TAB1)<sup>10</sup>. We found that TRAF6 interacts with Rv0222 (Fig. 2a, b and Extended Data Fig. 2d). Moreover, through co-immunoprecipitation and confocal microscopy analysis of macrophages infected with H37Rv(ΔRv0222 + Rv0222), we observed an endogenous interaction between Rv0222 and TRAF6 (Fig. 2c, d). Among TRAF-family proteins, Rv0222 associates with TRAF1 and TRAF6 (Extended Data Fig. 2d). Rv0222 efficiently blocked the TRAF6-triggered, but not the TAK1-plus-TAB1-triggered, activation of NF-κB and AP-1 (Extended Data Fig. 2e–h). Knockdown of TRAF6 by specific shRNA markedly attenuated the inhibitory effect of Rv0222 on the expression of *Il1b*, *Il6* and *Il12 p40* (Extended Data Fig. 2i–k). Consistent with this, knockdown of TAK1 in iBMDMs by specific shRNA also markedly reduced the Rv0222-mediated inhibitory effect on the expression of *Il1b*, *Il6* and *Il12 p40* (Extended Data Fig. 2l–n). However, TRAF1 had no marked effect on the activation of the NF-κB or MAP kinase signalling pathways, or on

cytokine expression in *M. tuberculosis*-infected macrophages (Extended Data Fig. 2o–r). Together, these data suggest that Rv0222 may inhibit the activation of host MAP kinase and NF-κB signalling by targeting the TRAF6 pathway.

Activation of TRAF6 is a ubiquitination-dependent process<sup>10</sup>. We found that overexpression of Rv0222 markedly inhibited both total ubiquitination and K63-linked ubiquitination of TRAF6 in HEK293T cells (Extended Data Fig. 2s, t), whereas deletion of Rv0222 markedly enhanced K63-linked ubiquitination of TRAF6 in macrophages infected with H37Rv (Fig. 2e). The protein tyrosine phosphatases SHP1 and SHP2 (hereafter SHP1/2) have been reported to interact with TRAF6 and inhibit its ubiquitination<sup>11</sup>. Therefore, we next examined the effect of Rv0222 on the interaction between SHP1/2 and TRAF6. In HEK293T cells, Rv0222 promoted the binding of SHP1/2 with TRAF6 (Fig. 2f, g). We generated iBMDMs in which *Shp1* and *Shp2* were stably knocked down (Extended Data Fig. 2u), and found that silencing of *Shp1/2* by specific shRNA eliminated the inhibitory effect of Rv0222 on cytokine expression (Extended Data Fig. 2v–y). Together, these data suggest that Rv0222 facilitates the association of SHP1/2 with TRAF6, thus inhibiting TRAF6 activation.

### K11-linked Rv0222 ubiquitination by ANAPC2

Given that TRAF6 serves as a classical E3 ligase for the K63-linked polyubiquitination of multiple signalling molecules<sup>12</sup>, and that Rv0222



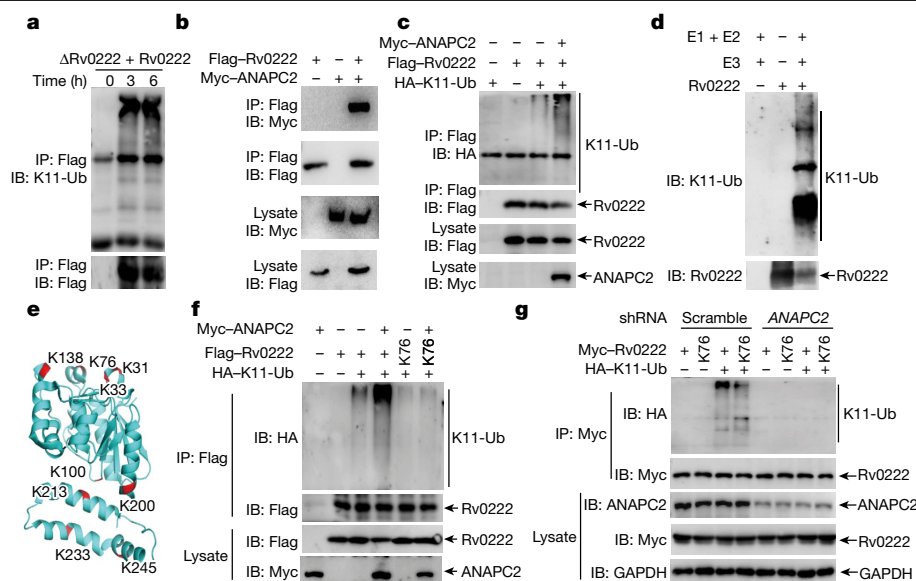


**Fig. 3 | Rv0222 is K11-ubiquitinated at K76 by host ANAPC2.** **a**, Immunoblot and immunoprecipitation of lysates from peritoneal macrophages infected with H37Rv(ΔRv0222 + Rv0222) for the indicated times (MOI = 5). **b**, Immunoblot and immunoprecipitation of lysates of HEK293T cells transfected with plasmids encoding Flag-Rv0222 and Myc-ANAPC2. **c**, Immunoblot and immunoprecipitation of lysates of HEK293T cells transfected with plasmids encoding HA-tagged K11-linked ubiquitin (K11-Ub), Flag-tagged Rv0222 and Myc-tagged ANAPC2. **d**, The E3 ligase APC/C produces K11-linked ubiquitin chains on Rv0222 in vitro. **e**, Locations of lysine residues (red) on the Rv0222 structure

(Protein Data Bank code 5KJP or 6LDZ; structure generated with PyMOL, version 2.0). **f**, Immunoblot and immunoprecipitation of lysates of HEK293T cells transfected with plasmids encoding HA-tagged K11-Ub, Myc-tagged ANAPC2 and Flag-tagged Rv0222 or Flag-tagged Rv0222(K76A). **g**, Immunoblot and immunoprecipitation of lysates of control (scramble) or ANAPC2-knockdown HEK293T cells transfected with plasmids encoding HA-tagged K11-Ub and Myc-tagged Rv0222 or Myc-tagged Rv0222(K76A). Data in **a–d**, **f**, **g** are representative of one experiment with at least three independent biological replicates. For gel source data, see Supplementary Fig. 1.

interacts with TRAF6, we next examined whether Rv0222 is ubiquitinated in host cells. We first detected the possible polyubiquitination of Rv0222 in HEK293T cells (Extended Data Fig. 3a). Seven lysine residues in ubiquitin—K6, K11, K27, K29, K33, K48 and K63—have been reported to form polyubiquitin chains<sup>13–17</sup>. We therefore co-transfected haemagglutinin (HA)-tagged wild-type ubiquitin (containing all seven lysine residues) or sequential ubiquitin substitution mutants (with only one of the seven lysine residues retained as lysine, and the other six replaced with arginine) with Flag-tagged Rv0222 into HEK293T cells. A co-immunoprecipitation assay showed that the K11 ubiquitin mutant markedly increased the polyubiquitination of Rv0222 (Extended Data Fig. 3b). In addition, we detected endogenous K11-linked polyubiquitin conjugates on Rv0222 in macrophages infected with H37Rv(ΔRv0222 + Rv0222) (Fig. 3a and Extended Data Fig. 3c). Thus, Rv0222 may undergo K11-linked polyubiquitination in host cells.

We therefore hypothesized that a host factor is likely to be involved in its polyubiquitination. ANAPC2, BIRC2 and RNF7 are three known host E3 ligases with K11-linked polyubiquitination activity<sup>16</sup>. Co-immunoprecipitation showed that ANAPC2 interacted with Rv0222 (Fig. 3b and Extended Data Fig. 3d), and markedly increased the K11-linked polyubiquitination of Rv0222 (Fig. 3c). We further performed biochemical confirmation of ANAPC2-mediated ubiquitination of Rv0222 in vitro (as described previously<sup>13,17</sup>), and found that K11-linked polyubiquitination conjugates of Rv0222 were formed only in the presence of ANAPC2 (Fig. 3d), suggesting an essential role of this ligase in mediating K11-linked polyubiquitination of Rv0222 directly. It has been reported that the anaphase-promoting complex/cyclosome (APC/C) assembles K11/K48-branched chains<sup>14</sup>. Using a K11/K48-bispecific antibody, we did not observe notable amounts of K11/K48-branched chains on Rv0222 (Extended Data Fig. 3c, e), suggesting that Rv0222 is mainly ubiquitinated with K11-linked polyubiquitin.

## Ubiquitination of Rv0222 inhibits immunity

To determine the location of the lysine residue on Rv0222 responsible for the attachment of K11-linked polyubiquitin, we examined the structure of Rv0222 (Protein Data Bank code 5KJP or 6LDZ) and identified nine lysine residues (Fig. 3e). Substitution of Rv0222 K76 with alanine nearly abrogated K11-linked ubiquitination, suggesting that K76 is essential for such ubiquitination (Fig. 3f). Furthermore, overexpression of ANAPC2 markedly enhanced the K11-linked ubiquitination of Rv0222 but not of Rv0222(K76A) in HEK293T cells (Fig. 3f). In addition, shRNA-mediated silencing of ANAPC2 markedly inhibited K11-linked polyubiquitination of Rv0222 in HEK293T cells (Fig. 3g). Thus, host ANAPC2 may enhance the K11-linked polyubiquitin of *M. tuberculosis* Rv0222 at K76.

We next investigated the role of K11-linked Rv0222 polyubiquitination in inhibition of TRAF6 signalling. In HEK293T cells, TRAF6-induced activation of the NF-κB and AP-1 reporter genes was markedly inhibited by Rv0222, but not by mutant Rv0222(K76A) (Extended Data Fig. 4a, b). Moreover, Rv0222(K76A) lost its inhibitory effect on K63-linked polyubiquitination of TRAF6 in HEK293T cells (Extended Data Fig. 4c). Levels of proinflammatory cytokine mRNAs were much lower in primary peritoneal macrophages infected with the H37Rv(ΔRv0222 + Rv0222) strain than in those infected with H37Rv(ΔRv0222 + GFP), but were much higher in macrophages infected with H37Rv(ΔRv0222 + Rv0222(K76A)) than in those infected with H37Rv(ΔRv0222 + Rv0222) (Fig. 4a–c). The cytokine levels were not completely restored when the mutant strain was complemented with the K76A mutant, suggesting that Rv0222 may regulate the expression of *Il1b* and *Il6* through an additional K76-independent mechanism. Furthermore, the expression of proinflammatory cytokines in lung tissue from both H37RvΔRv0222-infected C57BL/6 and severe combined immunodeficient (SCID) mice<sup>18</sup> was substantially higher than in H37Rv-infected mice, confirming the inhibitory effect of Rv0222 on cytokine expression in vivo. However, infection with H37RvΔRv0222

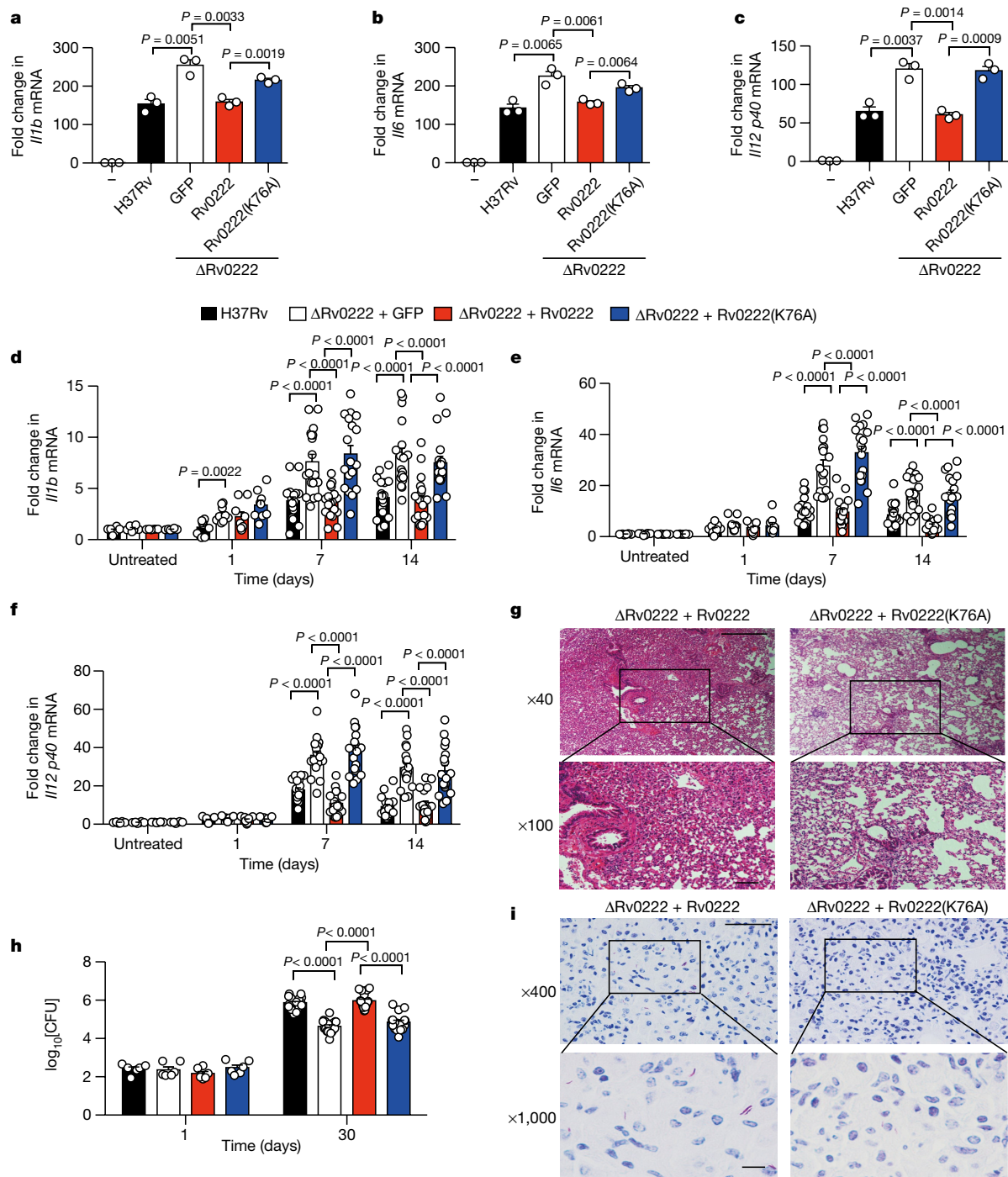


**Fig. 4 | K11-linked ubiquitination of Rv0222 by ANAPC2 suppresses anti-tuberculosis immunity.** **a–c**, qPCR analysis of *Il1b* (**a**), *Il6* (**b**) and *Il12 p40* (**c**) mRNA from peritoneal macrophages infected with H37Rv, H37Rv( $\Delta$ Rv0222 + GFP), H37Rv( $\Delta$ Rv0222 + Rv0222) or H37Rv( $\Delta$ Rv0222 + Rv0222(K76A)) for the indicated times (MOI = 5) (mean  $\pm$  s.e.m.). Data are representative of one experiment with at least three independent biological replicates; each circle represents one technical repeat. **d–f**, Six-week-old female C57BL/6 mice were aerosol-infected with roughly 200 CFUs per mouse of H37Rv, H37Rv( $\Delta$ Rv0222 + GFP), H37Rv( $\Delta$ Rv0222 + Rv0222) or H37Rv( $\Delta$ Rv0222 + Rv0222(K76A)). **d–f**, qPCR analysis of *Il1b* (**d**), *Il6* (**e**) and *Il12 p40* (**f**) mRNA in lungs from mice infected for 0, 1, 7 and 14 days. Cumulative data from three independent experiments (mean  $\pm$  s.e.m. of  $n = 6$  mice

untreated,  $n = 9$  mice infected for 1 day and  $n = 18$  mice infected for 7 and 14 days). **g–i**, For lungs of mice infected for 30 days (**g**, **i**) or 1 and 30 days (**h**), we assessed: histopathology in sections stained with haematoxylin and eosin (**g**; scale bars, 1,000  $\mu$ m (top) and 200  $\mu$ m (bottom)); bacterial titres (**h**; cumulative data from three independent experiments, mean  $\pm$  s.e.m. of  $n = 6$  mice infected for 1 day and  $n = 18$  mice infected for 30 days); and acid-fast staining (**i**; scale bars, 100  $\mu$ m (top) and 20  $\mu$ m (bottom)). The outlined areas in the top images are enlarged in the bottom images. Two-tailed unpaired Student's *t*-test (**a–f**) and two-sided Mann–Whitney *U*-test (**h**) were used for statistical analysis. **g**, **i**, Data are representative of one experiment with at least three independent biological replicates.

complemented with Rv0222, but not with Rv0222(K76A), induced much lower expression of proinflammatory cytokines in the lungs of *M. tuberculosis*-infected mice (Fig. 4d–f and Extended Data Fig. 4d, e). Together, these results suggest that K76 is essential for Rv0222 to inhibit host proinflammatory cytokines.

We also found that Rv0222(K76A) did not bind as efficiently as wild-type Rv0222 to either TRAF6 or SHP1 (Extended Data Fig. 4f, g). Consistent with this, overexpression of Rv0222 rather than Rv0222(K76A) in HEK293T cells markedly enhanced the association between SHP1 and TRAF6 (Extended Data Fig. 4h). Thus, the increased Rv0222-induced binding of SHP1 to TRAF6 may require K11-linked polyubiquitination on K76 of Rv0222. Although further functional studies are required to elucidate the mechanism by which K11-linked polyubiquitination of Rv0222 leads to an enhanced interaction between SHP1 and TRAF6 and hence to the inhibitory effect of Rv0222, one possible explanation is that the polyubiquitin chains are required directly to form a Rv0222–SHP1–TRAF6 complex. Alternatively, K11-linked polyubiquitination might cause a conformational change in Rv0222 that renders it more accessible for the binding of TRAF6 and SHP1, enhancing their interaction and inhibiting the K63-linked polyubiquitin of TRAF6.

Given that ANAPC2 promotes the K11-linked polyubiquitination of Rv0222 at K76, we next investigated whether ANAPC2 is involved in suppressing TRAF6 signalling by Rv0222. In ANAPC2-knockdown HEK293T cells, TRAF6-induced NF- $\kappa$ B luciferase reporter activity was not substantially inhibited by Rv0222 (Extended Data Fig. 4i). Moreover, silencing of ANAPC2 with specific shRNA markedly reduced the binding of Rv0222 with TRAF6 in HEK293T cells (Extended Data Fig. 4j). ANAPC2 knockdown also impaired the inhibitory effect of Rv0222 on K63-linked polyubiquitination of TRAF6 in HEK293T cells (Extended Data Fig. 4k). Furthermore, in ANAPC2-knockdown HEK293T cells, Rv0222 was considerably less able to enhance the association of SHP1 with TRAF6 (Extended Data Fig. 4l). Finally, we found that infection with H37Rv $\Delta$ Rv0222 induced much higher proinflammatory cytokine expression than did infection with H37Rv in THP1 cells, but ANAPC2-knockdown THP1 cells infected with H37Rv $\Delta$ Rv0222 showed an even lower level of proinflammatory cytokine expression than did those cells infected with H37Rv (Extended Data Fig. 4m–o). Silencing of ANAPC2 by specific shRNA led to a marked reduction in cytokine levels in both H37Rv- and H37Rv $\Delta$ Rv0222-infected cells, suggesting that ANAPC2 may also regulate the expression of cytokines in a Rv0222-independent manner. We also observed that knockdown of ANAPC2 by specific shRNA in iBMDMs almost eliminated the H37Rv-induced activation of MAP kinases and NF- $\kappa$ B (Extended Data Fig. 4p). ANAPC2 is an important host E3 ligase, but it remains to be seen whether ANAPC2 is involved in activating the inflammatory signalling pathway through other mechanisms. Together, our results suggest that the host ubiquitin ligase ANAPC2 regulates the inhibitory effect of Rv0222 on cytokine expression by promoting its K11-linked polyubiquitination.

## Virulence of Rv0222 requires ubiquitination

To investigate the pathological relevance of the K11-linked polyubiquitination of Rv0222 in *M. tuberculosis* infection, we challenged C57BL/6 and SCID<sup>18</sup> mice with wild-type H37Rv, H37Rv( $\Delta$ Rv0222 + GFP), H37Rv( $\Delta$ Rv0222 + Rv0222) or H37Rv( $\Delta$ Rv0222 + Rv0222(K76A)), and examined histopathology and bacterial burden in the lungs. For C57BL/6 mice, infection with H37Rv $\Delta$ Rv0222 complemented with wild-type Rv0222 (rather than with the K76A mutant) led to more-severe histological damage and more immune-cell infiltration into the lungs (Fig. 4g). For SCID mice, at eight weeks after infection, almost all mice infected with H37Rv or H37Rv( $\Delta$ Rv0222 + Rv0222) died, but those infected with H37Rv( $\Delta$ Rv0222 + GFP) or H37Rv( $\Delta$ Rv0222 + Rv0222(K76A)) lived for much longer (Extended Data

Fig. 5a). Similarly, the growth defects of H37Rv( $\Delta$ Rv0222 + GFP) in the lung tissue of infected C57BL/6 mice or SCID mice were rescued when the strain was complemented with wild-type Rv0222 but not with the K76A mutant (Fig. 4h, i and Extended Data Fig. 5b), suggesting that the virulence of H37Rv bacteria requires the K11-linked ubiquitination of Rv0222 at K76.

Our findings identify Rv0222 as a previously unrecognized component of the immunological signature of *M. tuberculosis*. Previous studies have shown the accumulation of ubiquitin on host membranous structures containing *M. tuberculosis*<sup>19–23</sup>, and the interaction of a bacterial ubiquitin-binding protein with a host signalling molecule<sup>8</sup>; however, mycobacteria possess only a pupylation system for protein post-translational modification<sup>24</sup>, rather than an endogenous ubiquitination system. Our results reveal a mechanism for subverting host immunity that depends on the ubiquitination of *M. tuberculosis* Rv0222 by a host E3 ligase, ANAPC2, highlighting the versatility of host–*M. tuberculosis* interactions (Extended Data Fig. 6). Future research will expand to the role of ubiquitination mediated by other host E3 ligases<sup>16,25</sup>. Notably, the K11-linked ubiquitination of Rv0222 by ANAPC2 seems to have a different cellular effect to the APC/C-triggered degradation of many cell-cycle regulators<sup>26</sup>: the Rv0222 ubiquitination promotes the binding of phosphatases to immune signalling molecules, rather than substrate recognition by the proteasome<sup>14</sup>. Our findings could pave the way to the development of effective anti-tuberculosis treatments that target the Rv0222–ANAPC2 interface.

## Online content

Any methods, additional references, Nature Research reporting summaries, source data, extended data, supplementary information, acknowledgements, peer review information; details of author contributions and competing interests; and statements of data and code availability are available at <https://doi.org/10.1038/s41586-019-1915-7>.

- Kubori, T., Kitao, T. & Nagai, H. Emerging insights into bacterial deubiquitinases. *Curr. Opin. Microbiol.* **47**, 14–19 (2019).
- Herhaus, L. & Dikic, I. Regulation of *Salmonella*–host cell interactions via the ubiquitin system. *Int. J. Med. Microbiol.* **308**, 176–184 (2018).
- Wang, L. et al. Oxidization of TGF $\beta$ -activated kinase by MPT53 is required for immunity to *Mycobacterium tuberculosis*. *Nat. Microbiol.* **4**, 1378–1388 (2019).
- Song, L. et al. Identification of antibody targets for tuberculosis serology using high-density nucleic acid programmable protein arrays. *Mol. Cell. Proteomics* **16**, S277–S289 (2017).
- Khader, S. A. et al. Interleukin 12p40 is required for dendritic cell migration and T cell priming after *Mycobacterium tuberculosis* infection. *J. Exp. Med.* **203**, 1805–1815 (2006).
- Mazmanian, S. K., Liu, C. H., Tzianabos, A. O. & Kasper, D. L. An immunomodulatory molecule of symbiotic bacteria directs maturation of the host immune system. *Cell* **122**, 107–118 (2005).
- Nandi, B. & Behar, S. M. Regulation of neutrophils by interferon- $\gamma$  limits lung inflammation during tuberculosis infection. *J. Exp. Med.* **208**, 2251–2262 (2011).
- Wang, J. et al. *Mycobacterium tuberculosis* suppresses innate immunity by coopting the host ubiquitin system. *Nat. Immunol.* **16**, 237–245 (2015).
- Underhill, D. M., Ozinsky, A., Smith, K. D. & Aderem, A. Toll-like receptor-2 mediates mycobacteria-induced proinflammatory signaling in macrophages. *Proc. Natl Acad. Sci. USA* **96**, 14459–14463 (1999).
- Chen, Z. J. Ubiquitination in signaling to and activation of IKK. *Immunol. Rev.* **246**, 95–106 (2012).
- Yan, D., Wang, X., Luo, L., Cao, X. & Ge, B. Inhibition of TLR signaling by a bacterial protein containing immunoreceptor tyrosine-based inhibitory motifs. *Nat. Immunol.* **13**, 1063–1071 (2012).
- Walsh, M. C., Lee, J. & Choi, Y. Tumor necrosis factor receptor-associated factor 6 (TRAF6) regulation of development, function, and homeostasis of the immune system. *Immunol. Rev.* **266**, 72–92 (2015).
- Swatek, K. N. & Komander, D. Ubiquitin modifications. *Cell Res.* **26**, 399–422 (2016).
- Yau, R. G. et al. Assembly and function of heterotypic ubiquitin chains in cell-cycle and protein quality control. *Cell* **171**, 918–933 (2017).
- Oh, E., Akopian, D. & Rape, M. Principles of ubiquitin-dependent signaling. *Annu. Rev. Cell Dev. Biol.* **34**, 137–162 (2018).
- Deshaies, R. J. & Joazeiro, C. A. RING domain E3 ubiquitin ligases. *Annu. Rev. Biochem.* **78**, 399–434 (2009).
- Wu, T. et al. UBE2S drives elongation of K11-linked ubiquitin chains by the anaphase-promoting complex. *Proc. Natl Acad. Sci. USA* **107**, 1355–1360 (2010).
- Köster, S. et al. *Mycobacterium tuberculosis* is protected from NADPH oxidase and LC3-associated phagocytosis by the LCP protein CpsA. *Proc. Natl Acad. Sci. USA* **114**, E8711–E8720 (2017); correction **114**, E9752 (2017).

19. Alonso, S., Pethe, K., Russell, D. G. & Purdy, G. E. Lysosomal killing of *Mycobacterium* mediated by ubiquitin-derived peptides is enhanced by autophagy. *Proc. Natl Acad. Sci. USA* **104**, 6031–6036 (2007).
20. Franco, L. H. et al. The ubiquitin ligase Smurf1 functions in selective autophagy of *Mycobacterium tuberculosis* and anti-tuberculous host defense. *Cell Host Microbe* **21**, 59–72 (2017); correction **22**, 421–423 (2017).
21. Houben, D. et al. ESX-1-mediated translocation to the cytosol controls virulence of mycobacteria. *Cell. Microbiol.* **14**, 1287–1298 (2012).
22. Manzanillo, P. S. et al. The ubiquitin ligase parkin mediates resistance to intracellular pathogens. *Nature* **501**, 512–516 (2013).
23. Watson, R. O., Manzanillo, P. S. & Cox, J. S. Extracellular *M. tuberculosis* DNA targets bacteria for autophagy by activating the host DNA-sensing pathway. *Cell* **150**, 803–815 (2012).
24. Barandun, J., Delley, C. L. & Weber-Ban, E. The pupylation pathway and its role in mycobacteria. *BMC Biol.* **10**, 95 (2012).
25. Ribet, D. & Cossart, P. Ubiquitin, SUMO, and NEDD8: key targets of bacterial pathogens. *Trends Cell Biol.* **28**, 926–940 (2018).
26. Davey, N. E. & Morgan, D. O. Building a regulatory network with short linear sequence motifs: lessons from the degrons of the anaphase-promoting complex. *Mol. Cell* **64**, 12–23 (2016).

**Publisher's note** Springer Nature remains neutral with regard to jurisdictional claims in published maps and institutional affiliations.

© The Author(s), under exclusive licence to Springer Nature Limited 2020

## Methods

### Bacterial strains and cells

Bacterial strains are described in Supplementary Table 1. Mycobacterial strains were grown in Middlebrook 7H9 broth supplemented with 10% oleic acid–albumin–dextrose–catalase (OADC) and 0.05% Tween-80 (Sigma) or Middlebrook 7H10 agar (BD) supplemented with 10% OADC. When required, the antibiotic kanamycin or hygromycin was added at a concentration of 100 µg ml<sup>-1</sup> for mycobacterial strain selection. Mycobacteria cultures were grown up to mid-log phase (an optical density at 600 nm of approximately 0.6). Aliquots of bacterial cultures were prepared in 20% glycerol and Middlebrook 7H9 medium and preserved at -80 °C. The CFU per ml of the stocks was titred by plating serial dilutions on Middlebrook 7H10 agar plates plus 10% OADC. These stocks were used for all subsequent infections of macrophages and mice.

HEK293T cells (ATCC CRL-3216) and iBMDMs (provided by F. Shao, National Institute of Biological Sciences, Beijing) were maintained in Dulbecco's modified Eagle's medium (DMEM; HyClone) supplemented with 10% (v/v) heat-inactivated fetal bovine serum (FBS, Gibco) and 100 U ml<sup>-1</sup> penicillin and streptomycin. Macrophages and THP1 cells (ATCC TIB-202) were cultured in RPMI-1640 medium supplemented with 10% (v/v) FBS. Peritoneal macrophages were obtained from mice three days after injection of thioglycollate (BD). We routinely tested all cells for mycoplasma contamination, and used only those cells that tested negative for further study.

### Plasmids, reagents and antibodies

Plasmids are described in Supplementary Table 1. The following antibodies were used for western blot or immunoprecipitation: from Sigma-Aldrich, monoclonal mouse anti-Flag M2 affinity gel (catalogue number/clone: A2220/M2), rabbit anti-HA antibody (H6908/polyclonal), rabbit anti-GAPDH antibody (SAB2701826/polyclonal), rabbit anti-Flag antibody (F7425/polyclonal), rabbit anti-Myc antibody (C3956/polyclonal) and rabbit anti-K11 antibody (MABS107-I/2A3/2E6); from Cell Signaling Technology, rabbit anti-APC2 antibody (12301/polyclonal), rabbit anti-phosphorylated (p)-p65 antibody (3033/93H1), rabbit anti-p-p38 antibody (9215/3D7), rabbit anti-p-Jnk antibody (9251/polyclonal), rabbit anti-K63-polyubiquitin antibody (5621/polyclonal), anti-rabbit IgG horseradish peroxidase (HRP)-linked antibody (7074) and anti-mouse IgG HRP-linked antibody (7076); from Santa Cruz Biotechnology, rabbit anti-TRAF6 antibody (sc-7221/polyclonal). Antibody against K11/K48-branched ubiquitin chains was provided by M. Rape (Howard Hughes Medical Institute) and M. Matsumoto (Genentech)<sup>14</sup>. The rabbit polyclonal antibody against Rv0222 was generated by immunization of rabbits with purified histidine-tagged Rv0222 fusion protein, in collaboration with ABclonal Biotech. For western blot, all primary antibodies were diluted 1/1,000 and secondary antibodies were diluted 1/2,000. For immunofluorescence, monoclonal mouse anti-Flag M2 antibody was used at 1/500 dilution and rabbit anti-TRAF6 at 1/100 dilution. Corresponding Alexa Fluor 633- or Alexa Fluor 555-labelled anti-rabbit or anti-mouse antibodies (Invitrogen) were used as secondary antibodies (1/1,000 dilution). Fluorescein isothiocyanate (FITC) for strain dyeing was from Sangon Biotech (catalogue number 3326-32-7).

### Construction of *Mycobacteria* strains

We used the pYUB854 system<sup>27</sup> to generate the H37Rv strain with deletion of the gene encoding Rv0222 (H37RvΔRv0222). In brief, upstream flanking sequence (UFS) and downstream flanking sequence (DFS) either side of the Rv0222 gene were amplified from H37Rv genomic DNA. Following purification, the PCR products of UFS and DFS were ligated into the pGEM-Tamp vector (Promega), and the resulting plasmid was transformed into competent *E. coli* DH5α cells, which were plated on LB agar plus 100 µg ml<sup>-1</sup> ampicillin. Following overnight incubation of isolated white colonies in LB broth plus ampicillin,

PCR analysis was used as above to identify successful ligations. The cloned UFS or DFS fragment was then subcloned into pYUB854 digested with the appropriate restriction enzyme. The temperature-sensitive phage pHA159 and the pYUB854 vector, containing both UFS and DFS fragments for a particular Rv0222 gene disruption, were digested with PacI; following gel extraction, these fragments were ligated using T4 DNA ligase to create a shuttle plasmid, which was then in vitro packaged using the Lambda DNA Packaging System (Promega) and transformed into *E. coli* HB101 cells. Successful plasmids were identified by PacI digestion, followed by antibiotic selection on LB plus hygromycin (100 µg ml<sup>-1</sup>) plates. The plasmid was then transduced into *M. smegmatis* (mc<sup>2</sup>155) at the permissive temperature of 30 °C, which allows replication and lysis, and a high-titre lysate was produced (more than 10<sup>10</sup> ml<sup>-1</sup>). Transduction into H37Rv was then carried out with the high-titre lysate at an MOI of 10 at the nonpermissive temperature of 37 °C, which results in the delivery of the substrate. Cells-only and phage-only controls were included. Following incubation for two to three weeks on 7H10 plus OADC, glycerol and hygromycin, colonies were picked and grown in liquid medium (7H9 plus OADC, glycerol, Tween-80 and hygromycin) for two weeks; then, gene deletion was confirmed as above via PCR using primers outside the upstream and downstream flanking regions, with a shift in size indicating a mutant. Immunoblot analysis was also used to confirm the deletion of Rv0222 in the H37Rv strain. The shuttle vector pMV261 (provided by K. Mi, Institute of Microbiology, Beijing, China) was used to complement the strain H37RvΔRv0222 with wild-type Rv0222 (with a carboxy-terminal Flag-tag) or to create the strain H37Rv Rv0222(K76A) (with a C-terminal Flag-tag). Expression of Rv0222 or its mutants (with a C-terminal Flag-tag) in mycobacteria was examined by immunoblot analysis.

### Transfection and confocal microscopy

HEK293T cells were transiently transfected using Lipofectamine 2000 (catalogue number 11668; Invitrogen). Confocal microscopy was performed as described<sup>11</sup>.

### Luciferase assay

The dual-luciferase reporter assay system (Promega) was used for luciferase assays. HEK293T cells were transiently transfected with pNF-kB-luc, p-AP-1-luc, pRL-TK and indicated plasmids for 24 h.

### Reverse transcription-PCR analysis

RNA preparation and qPCR analysis were performed as described using gene-specific primers (Supplementary Table 1).

### Immunoprecipitation and immunoblotting

For immunoprecipitation, HEK293T cells were transiently transfected using Lipofectamine 2000. After 48 h, cells were washed with phosphate-buffered saline (PBS) and then lysed in cell-lysis buffer for western blotting and immunoprecipitation (Beyotime), supplemented with 1% protease-inhibitor cocktail (catalogue number P8340, Sigma). After 30 min on ice, the lysates were centrifuged at 13,523g for 10 min at 4 °C to remove debris. The cell lysates were incubated with anti-Flag M2 affinity gel overnight at 4 °C. For endogenous immunoprecipitation, primary peritoneal macrophages were stimulated with mycobacteria for the indicated time periods. The cells were lysed, and the lysates were incubated with anti-TRAF6 antibody and protein A/G (sepharose) overnight at 4 °C. The sepharose samples were centrifuged, washed five times with cell-lysis buffer and boiled with SDS loading buffer for 10 min. After separation by SDS-PAGE, equivalent amounts of protein were electroblotted onto nitrocellulose membranes. The membrane was blocked, incubated with primary antibodies, and washed three times before incubation with secondary antibody. After a final wash, analysis was conducted using enhanced chemiluminescence reagent (Thermo Scientific).



## Mice and infection

All animal experiments were reviewed and approved by the Animal Experiment Administration Committee of Tongji University School of Medicine and were conducted in accordance with the National Institutes of Health (NIH) Guidelines for the Care and Use of Laboratory Animals. Female SPF C57BL/6 and SCID mice were purchased from Slaccas. Six- to eight-week-old female C57BL/6 mice were used for macrophage separation. Six-week-old C57BL/6 and SCID female mice were divided randomly into cages and infected by an aerosol method with approximately 100–200 CFUs of different H37Rv strains for four weeks (using an inhalation exposure system from Glas-col)<sup>28,29</sup> at the Biosafety Level-3 (BSL-3) Laboratory. Mice were killed at 1, 7, 14 or 30 days after infection. Lungs were collected and homogenized in 1 ml of PBS. Mycobacterial burden was determined by plating tenfold serial dilutions of each tissue homogenate on Middlebrook 7H10 agar plates. Colonies were counted after three to four weeks of incubation at 37 °C in 5% CO<sub>2</sub>. For histology, lungs were removed, fixed in 4% paraformaldehyde in PBS and embedded in paraffin. Sections were cut and stained with haematoxylin and eosin (H&E) or Ziehl–Neelsen stain (acid-fast bacillus) according to standard protocols. Imaging was performed by microscopy (TCS CP5II, Leica). All mice were age- and sex-matched in each experiment. Sample size was based on empirical data from pilot experiments. For in vitro *M. tuberculosis* infections, macrophages were infected with a single-cell suspension of bacteria at an MOI of 5.

## shRNA-mediated gene interference

Short hairpin RNA in the pLKO.1 vector was introduced into target cells via lentiviral transduction. pLKO.1-TRAF6-1 and pLKO.1-TRAF6-2 were gifts from G. Meng<sup>30</sup>. The targeting sequences were: human *ANAPC2* shRNA, 5'-GCAGATTAAAGCAAGTCAGAT-3'; mouse *Anapc2* shRNA, 5'-GCGACGTTCTTCAGACATCAT-3'; mouse *Tak1* shRNA, 5'-GCGCC TGAAGTATTTGAAGGT-3'; mouse *Shp1* shRNA, 5'-GCTAGACTGTG ACATTGATAT-3'; mouse *Shp2* shRNA, 5'-CGTGTTAGGAACGTCAA AGAA-3'; mouse *Traf1* shRNA, 5'-GCATCCTTTGATGGTACTTTC-3'. HEK293T cells were transfected with pSPAX2, pMD2.G and pLKO.1 containing shRNAs targeting different genes. Lentiviruses were collected 48 h later and were used to infect iBMDMs (for ANAPC2, TRAF6, TRAF1, TAK1, SHP1 and SHP2 knockdown) or HEK293T cells and THP1 cells (for ANAPC2 knockdown). Subsequently, selection with puromycin (2 µg ml<sup>-1</sup>) was carried out.

## Ubiquitination assay

HA-tagged ubiquitin plasmids were gifts from X. Cao<sup>31</sup>. HEK293T cells were transiently transfected with the indicated plasmids for 48 h. Rv0222 or TRAF6 was immunoprecipitated with anti-Flag M2 affinity gel or protein A/G plus anti-TRAF6 antibody, and the obtained complexes were washed three times with urea (8 M, in PBS) to separate proteins bound by noncovalent bonds. Ubiquitinated Rv0222 or ubiquitinated TRAF6 was detected by immunoblot analysis using HA-specific antibodies or specific ubiquitin antibody. For in vitro experiments, His-Rv0222 was purified from *E. coli* BL21 and APC/C was purified from G1 HEK293T cells by anti-CDC27 antibody (Santa Cruz) and protein A/G (Santa Cruz) at 4 °C. The beads were washed three times with SB (25 mM HEPES pH 7.5, 1.5 mM MgCl<sub>2</sub>, 5 mM KCl, 1 mM dithiothreitol (DTT), 1× protease inhibitor, 15 mM creatine phosphate, 2 mM ATP) plus 0.05% Tween-20, and twice with SB before being resuspended in 40 ml SB. Beads were incubated with 100 nM E1 (Boston Biochem), 125 nM UbcH10 (Boston Biochem), 1.5 mg ml<sup>-1</sup> ubiquitin, 20 mM ATP, 15 mM creatine phosphate, creatine phosphokinase, 1 mM DTT in UBAB buffer (25 mM Tris/HCl pH 7.5, 50 mM NaCl, 10 mM MgCl<sub>2</sub>). The reaction was

started when Rv0222 was added, incubated at 30 °C for 1 h, stopped when loading buffer was added and analysed by western blot with anti-ubiquitin antibody.

## Statistical analysis

Statistical significance between groups was determined by two-tailed Student's *t*-test, two-tailed analysis of variance followed by Bonferroni post hoc test or two-sided Mann–Whitney *U*-test. Differences were significant at *P* < 0.05. The experiments were not randomized, and the investigators were not blinded to allocation during experiments and outcome assessment.

## Reporting summary

Further information on research design is available in the Nature Research Reporting Summary linked to this paper.

## Data availability

RNA-sequencing data have been deposited in Gene Expression Omnibus (GEO) under accession codes GSM4005162, GSM4005163, GSM4005164, GSM4005165, GSM4005166 and GSM4005167. Other data that support the findings of this study are available within the Source Data and Supplementary Information. Source Data for Figs. 1, 2, 4 and Extended Data Figs. 1, 2, 4, 5 are provided with the paper.

27. Bardarov, S. et al. Specialized transduction: an efficient method for generating marked and unmarked targeted gene disruptions in *Mycobacterium tuberculosis*, *M. bovis* BCG and *M. smegmatis*. *Microbiology* **148**, 3007–3017 (2002).
28. Cai, Y. et al. xCT increases tuberculosis susceptibility by regulating antimicrobial function and inflammation. *Oncotarget* **7**, 31001–31013 (2016).
29. Zheng, R. J. et al. Notch4 negatively regulates the inflammatory response to *Mycobacterium tuberculosis* infection by inhibiting TAK1 activation. *J. Infect. Dis.* **218**, 312–323 (2018).
30. Xing, Y. et al. Cutting edge: TRAF6 mediates TLR/IL-1R signaling-induced nontranscriptional priming of the NLRP3 inflammasome. *J. Immunol.* **199**, 1561–1566 (2017).
31. Liu, J. et al. Rbhd3 controls autoimmunity by suppressing the production of IL-6 by dendritic cells via K27-linked ubiquitination of the regulator NEMO. *Nat. Immunol.* **15**, 612–622 (2014).

**Acknowledgements** We thank M. Rape (Howard Hughes Medical Institute) and M. Matsumoto (Genentech) for providing antibody against K11/K48-branched ubiquitin chains; L.-D. Lyu (CAS Key Laboratory of Synthetic Biology) for technical assistance in constructing the Rv0222-knockout strain; K. Mi (CAS Key Laboratory of Pathogenic Microbiology and Immunology) for the pMV261 plasmid; X. Cao (Second Military Medical University) for ubiquitin plasmids; G. Meng (Institute Pasteur of Shanghai) for pLKO.1-TRAF6 plasmids; F. Shao (National Institute of Biological Sciences) and C. G. Feng (Sydney Medical School, University of Sydney) for critical reading of the manuscript; and members of the B.G. laboratory for discussions and technical assistance. This project was supported by grants from the Chinese National Program on Key Basic Research Project (2017YFA0505900 to B.G.; 2017YFC0840300 to Z.R.), the Strategic Priority Research Program of the Chinese Academy of Sciences (XDB08020200 to Z.R.), the National Natural Science Foundation of China (91842303, 31730025, 91542111, 81330069, 31030028 and 30525012 to B.G.; 81800004 to L.W.; and 81520108019 and 813300237 to Z.R.), Fundamental Research Funds for the Central Universities (22120180024 to L.W.), the clinical key discipline construction project from the Shanghai Municipal Health Commission (2017ZZ02003 to B.G.) and Shanghai Pulmonary Hospital (fkyq1909 to L.W.).

**Author contributions** L.W. and B.G. designed the study. L.W. and J. Wu performed most experiments and analysed data. T.T., H. Liang, M.Z. and C.P. performed the qPCR and co-immunoprecipitation experiments and analysed data. H. Liu and F.L. provided technical help and assisted with manuscript preparation. J.C., Z.L., Y.W., X.W. and R.Z. performed mouse infection experiments and analysed data. J. Wang and H.Y. constructed the knockout H37Rv strain. The Rv0222 structure (Protein Data Bank code 6LDZ) was solved and analysed by J.L., Y.R. and Z.R. The H37Rv strain was stored by X.H. All authors discussed the results and commented on the manuscript.

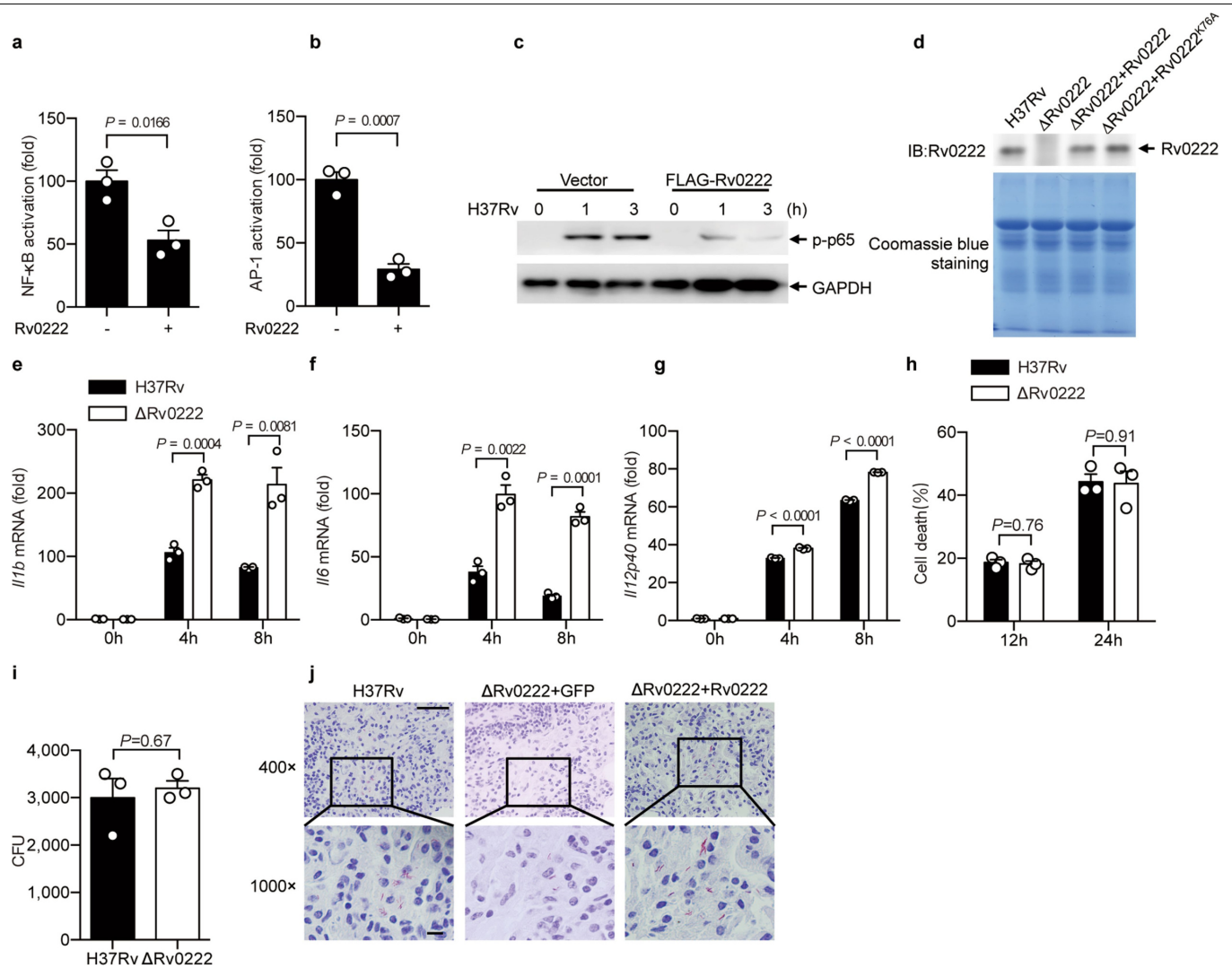
**Competing interests** The authors declare no competing interests.

## Additional information

**Supplementary information** is available for this paper at <https://doi.org/10.1038/s41586-019-1915-7>.

**Correspondence and requests for materials** should be addressed to Z.R. or B.G.

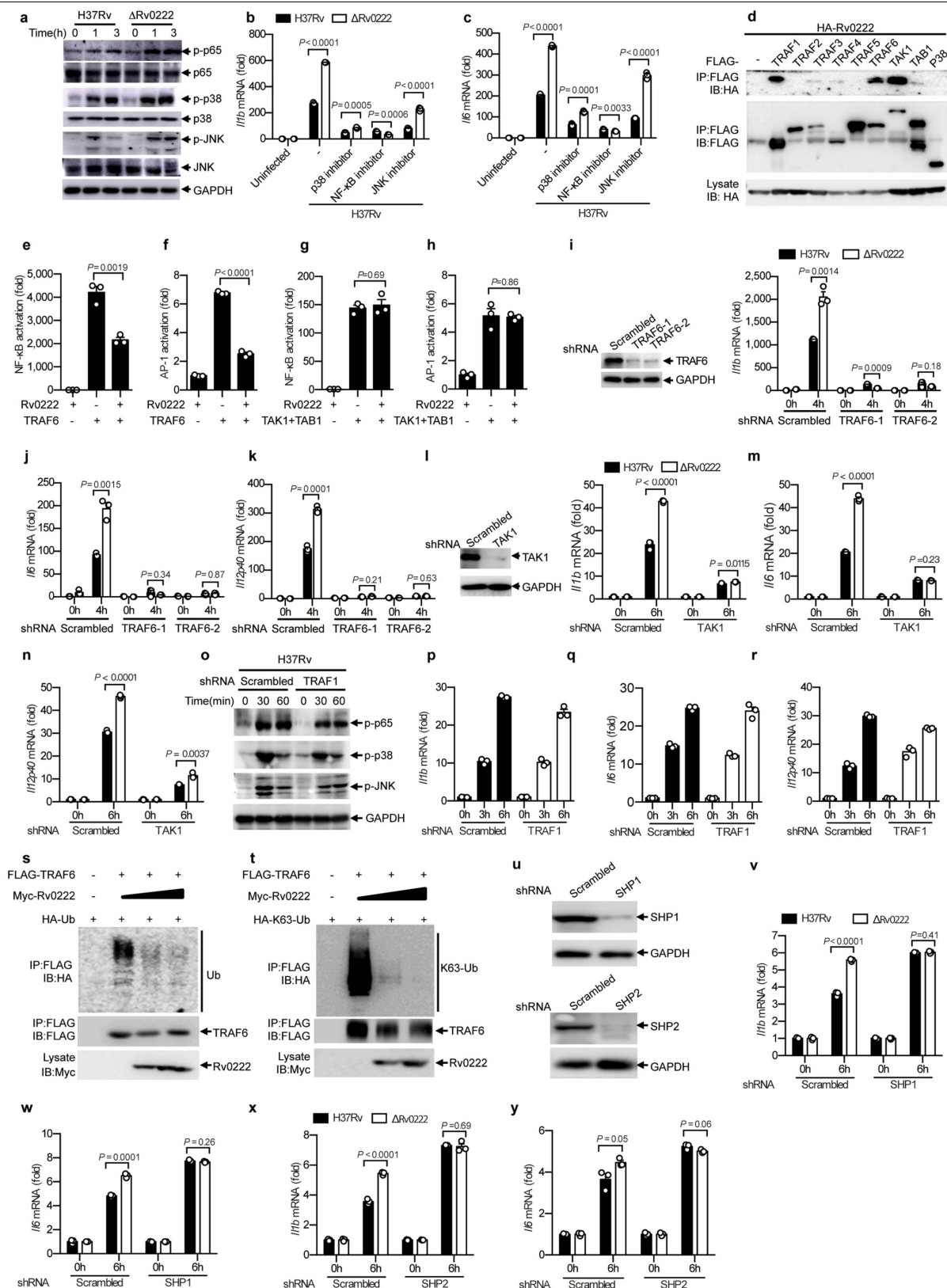
**Reprints and permissions information** is available at <http://www.nature.com/reprints>.



#### Extended Data Fig. 1 | Rv0222 inhibits host inflammatory responses.

**a, b**, Luciferase assay of HEK293T cells transfected with the NF-κB (**a**) or AP-1 (**b**) reporter gene with Rv0222 plasmid (+) or vector plasmid (-). **c**, Immunoblot of lysates from iBMDMs transfected with a plasmid encoding Flag-tagged Rv0222 for 48 h, following infection with H37Rv for the indicated times (MOI = 5). p-p65, phosphorylated p65, an indicator of NF-κB activation; GAPDH, glyceraldehyde-3-phosphate dehydrogenase, a loading control. **d**, Immunoblot of Rv0222 protein in H37Rv, ΔRv0222, H37Rv(ΔRv0222 + Rv0222) and H37Rv(ΔRv0222 + Rv0222(K76A)) cells with anti-Rv0222 antibody. Coomassie blue staining was used as a control. **e–g**, qPCR analysis of *Il1b* (**e**), *Il6* (**f**) and *Il12 p40* (**g**) mRNA from peritoneal macrophages infected with H37Rv or ΔRv0222

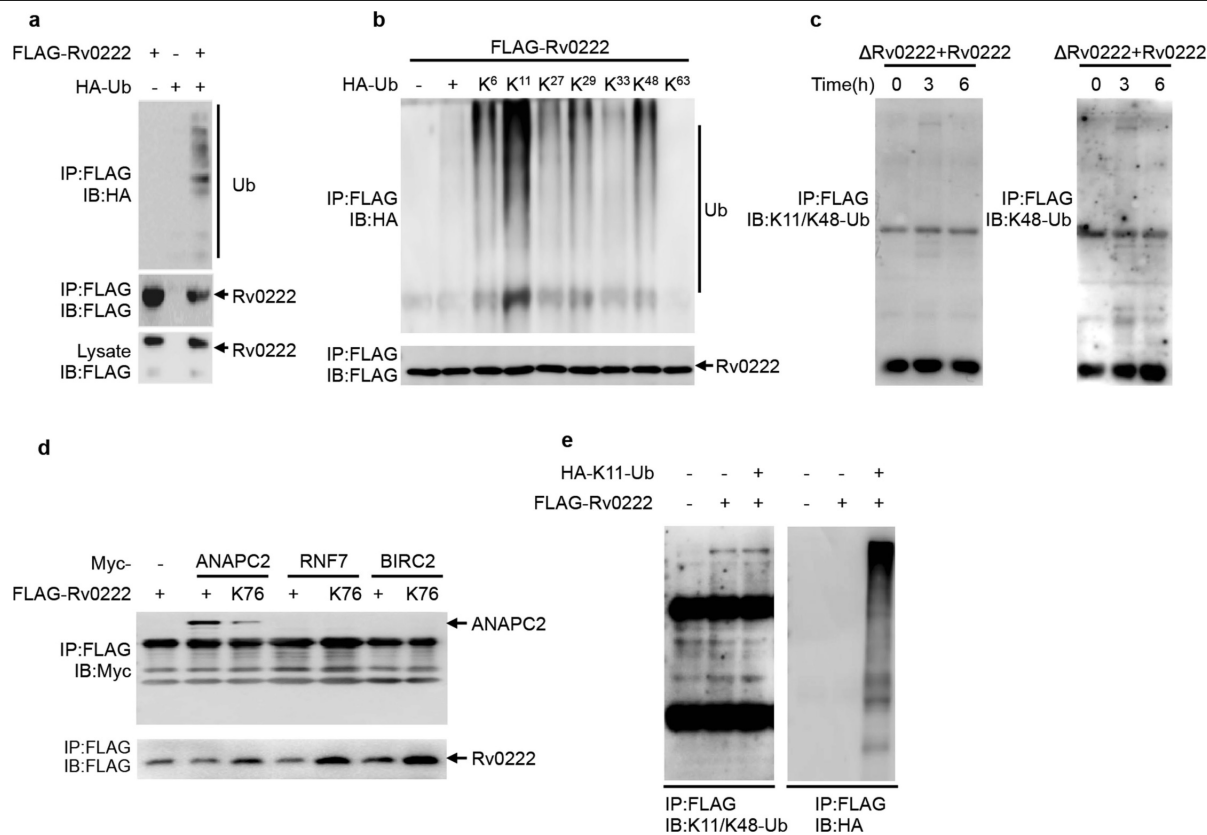
for the indicated times (MOI = 5). **h, i**, Lactate dehydrogenase assay for cell death (**h**) and CFU assay (**i**) in mice peritoneal macrophages infected with H37Rv or ΔRv0222 for 3 h (**i**), 12 h or 24 h (MOI = 5). **j**, C57BL/6 mice were aerosol-infected with roughly 200 CFUs per mouse of H37Rv, H37Rv(ΔRv0222 + GFP) or H37Rv(ΔRv0222 + Rv0222) for 30 days. Histopathology was assessed in lung sections stained with acid-fast (scale bars, 100 μm (top) and 20 μm (bottom)). Two-tailed unpaired Student's *t*-test (**a, b, e–i**) was used for statistical analysis. Data are representative of one experiment with at least three independent biological replicates in **c, d, j**; and show mean ± s.e.m. of  $n = 3$  cultures in **a, b, e–i**. For gel source data, see Supplementary Fig. 1.



Extended Data Fig. 2 | See next page for caption.

**Extended Data Fig. 2 | Rv0222 interacts with and inhibits TRAF6 signalling.** **a**, Immunoblot of lysates from peritoneal macrophages infected with H37Rv or  $\Delta$ Rv0222 for the indicated times (MOI = 5). **b, c**, qPCR analysis of *Il1b* (**b**) and *Il6* (**c**) mRNA from peritoneal macrophages treated with the p38 inhibitor SB203580, JNK inhibitor SP600125 or NF- $\kappa$ B inhibitor PDTC for 1 h following H37Rv or  $\Delta$ Rv0222 infection for 8 h (MOI = 5). **d**, Immunoblots and immunoprecipitates of lysates from HEK293T cells transfected with the indicated plasmids. **e–h**, Luciferase assay of the effect of Rv0222 on the activation of TRAF6/TAK1 in HEK293T cells transfected with a plasmid encoding NF- $\kappa$ B (**e, g**) or AP-1 (**f, h**) luciferase reporter or indicated plasmids for 24 h. **i–k**, qPCR analysis of *Il1b* (**i**, right), *Il6* (**j**) and *Il12p40* (**k**) mRNA from control or TRAF6-knockdown iBMDMs infected with H37Rv or  $\Delta$ Rv0222 for 4 h (MOI = 5). **i**, Left, immunoblots of TRAF6 in lysates from control ('Scrambled') or TRAF6-knockdown (TRAF6-1, TRAF6-2) iBMDMs. **l–n**, qPCR analysis of *Il1b* (**l**, right), *Il6* (**m**) and *Il12p40* (**n**) mRNA from control or TAK1-knockdown

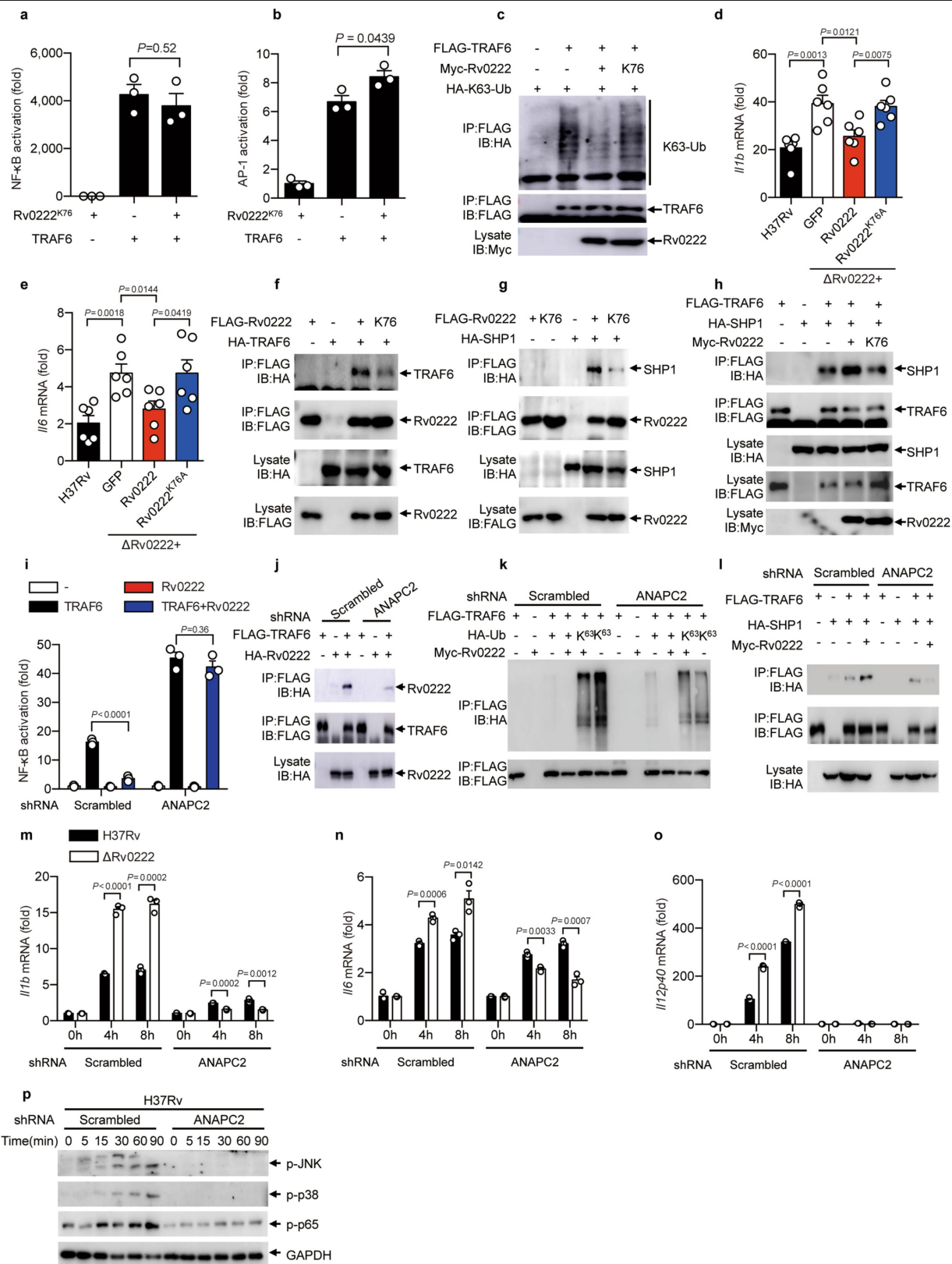
iBMDMs infected with H37Rv or  $\Delta$ Rv0222 for 6 h (MOI = 5). **l**, Left, immunoblots of TAK1 in lysates from control or TAK1-knockdown iBMDMs. **o**, Immunoblots of lysates from control or TRAF1-knockdown iBMDMs infected with H37Rv for the indicated times (MOI = 5). **p–r**, qPCR analysis of *Il1b* (**p**), *Il6* (**q**) and *Il12p40* (**r**) mRNA from control or TRAF1-knockdown iBMDMs infected with H37Rv for the indicated times (MOI = 5). **s, t**, Immunoblots and immunoprecipitation of lysates from HEK293T cells transfected with a plasmid encoding HA-tagged Ub (**s**) or K63-Ub (**t**), Flag-tagged TRAF6 and increasing amounts of Myc-tagged Rv0222 (0  $\mu$ g, 1  $\mu$ g and 2  $\mu$ g). **u**, Immunoblots of lysates from control or SHP1- or SHP2-knockdown iBMDMs. **v–y**, qPCR analysis of *Il1b* and *Il6* mRNA from control or SHP1/2-knockdown iBMDMs infected with H37Rv or  $\Delta$ Rv0222 for 6 h (MOI = 5). Two-tailed unpaired Student's *t*-tests (**b, c, e–n, v–y**) were used for statistical analysis. Data are representative of one experiment with at least three independent biological replicates (**a, d, o, s–u**) and are mean  $\pm$  s.e.m in **b, c, e–n, p–r, v–y**. For gel source data, see Supplementary Fig. 1.



**Extended Data Fig. 3 | Rv0222 is K11-ubiquitinated at K76 by host ANAPC2.**  
**a, b**, Immunoblots and immunoprecipitates of HEK293T cell lysates transfected with a plasmid encoding Flag-tagged Rv0222 and HA-tagged wild-type ubiquitin (Ub) or HA-tagged Ub with a single lysine residue left unmutated among K6, K11, K27, K29, K33, K48 and K63. **c**, Immunoblots and immunoprecipitates of lysates from peritoneal macrophages infected with H37Rv( $\Delta$ Rv0222 + Rv0222) for the indicated times (MOI = 5). **d**, Immunoblots

and immunoprecipitates of HEK293T cell lysates transfected with a plasmid encoding Flag-tagged Rv0222 and Myc-tagged ANAPC2, RNF7 and BIRC2. **e**, Immunoblots and immunoprecipitates of HEK293T cell lysates transfected with the indicated plasmids. Data are representative of one experiments with at least three independent biological replicates. For gel source data, see Supplementary Fig. 1.

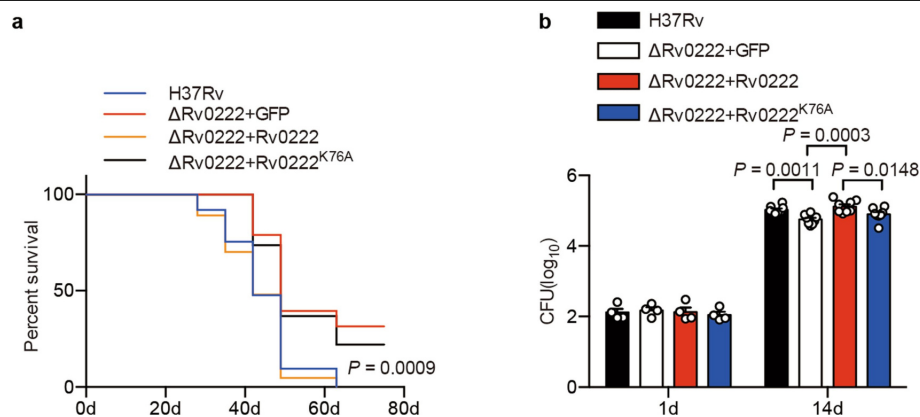




**Extended Data Fig. 4** | See next page for caption.

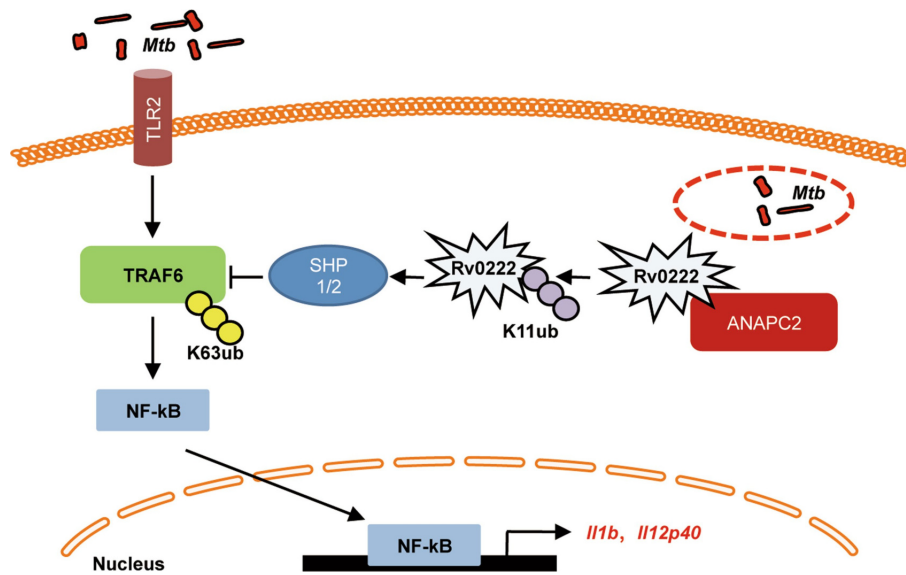
**Extended Data Fig. 4 | K11-linked ubiquitination of Rv0222 by ANAPC2 suppresses TRAF6 signalling.** **a, b**, Luciferase assay of HEK293T cells transfected with a plasmid encoding NF- $\kappa$ B (**a**) or AP-1 (**b**) luciferase reporter or the indicated plasmids for 24 h. **c**, Immunoblots and immunoprecipitates of HEK293T cell lysates transfected with the indicated plasmids. Six-week-old female SCID mice were aerosol-infected with roughly 100 CFUs per mouse of H37Rv, H37Rv( $\Delta$ Rv0222 + GFP), H37Rv( $\Delta$ Rv0222 + Rv0222) or H37Rv( $\Delta$ Rv0222 + Rv0222(K76A)). **d, e**, qPCR analysis of *Il1b* (**d**) and *Il6* (**e**) mRNA in lung tissues from mice infected for 7 days. **f–h**, Immunoblots and immunoprecipitates of HEK293T cell lysates transfected with indicated plasmids. **i**, Luciferase assay of control or ANAPC2-knockdown HEK293T cells transfected with a plasmid encoding NF- $\kappa$ B luciferase reporter or the indicated

plasmids for 24 h. **j–l**, Immunoblots and immunoprecipitates of lysates from control or ANAPC2-knockdown HEK293T cells transfected with the indicated plasmids. **m–o**, qPCR analysis of *Il1b* (**m**), *Il6* (**n**) and *Il12 p40* (**o**) mRNA from control or ANAPC2-knockdown THP1 cells infected with H37Rv or  $\Delta$ Rv0222 for the indicated times (MOI = 5). **p**, Immunoblot of lysates from control or ANAPC2-knockdown iBMDMs infected with H37Rv for the indicated times (MOI = 5). Two-tailed unpaired Student's *t*-test (**a, b, d, e, i, m–o**) were used for statistical analysis. Data are representative of one experiment with at least three independent biological replicates (**c, f–h, j–l, p**) and are mean  $\pm$  s.e.m. in **a, b, i, m–o, d, e**. Cumulative data from two independent experiments ( $n = 6$  mice). For gel source data, see Supplementary Fig. 1.



**Extended Data Fig. 5 | K11-linked ubiquitination of Rv0222 by ANAPC2 suppresses anti-tuberculosis immunity. a**, Survival of six-week-old female SCID mice aerosol-infected with roughly 100 CFUs per mouse of H37Rv, H37Rv(ΔRv0222 + GFP), H37Rv(ΔRv0222 + Rv0222) or H37Rv(ΔRv0222 + Rv0222(K76A)). **b**, Bacterial titres in lungs from mice

infected for 1 day or 14 days. Gehan–Breslow–Wilcoxon test (**a**) and two-sided Mann–Whitney *U*-test (**b**) were used for statistical analysis. Cumulative data from two independent experiments ( $n = 37$  mice in **a**;  $n = 4$  mice infected for 1 day and  $n = 8$  mice infected for 14 days in **b**).



**Extended Data Fig. 6 | Summary diagram.** The K11-linked ubiquitination (K11ub) of *M. tuberculosis*-secreted protein Rv0222 by host ANAPC2 suppresses the TLR2/TRAFF6/NF-κB-mediated expression of proinflammatory cytokine

mRNAs (*Il1b* and *Il12p40*), part of innate immunity, by facilitating the recruitment of SHP1/2 to polyubiquitinated (K63ub) TRAF6. Mtb, *M. tuberculosis*.

## Reporting Summary

Nature Research wishes to improve the reproducibility of the work that we publish. This form provides structure for consistency and transparency in reporting. For further information on Nature Research policies, see [Authors & Referees](#) and the [Editorial Policy Checklist](#).

### Statistics

For all statistical analyses, confirm that the following items are present in the figure legend, table legend, main text, or Methods section.

- |                                     |  |
|-------------------------------------|--|
| n/a                                 | Confirmed  |
| <input type="checkbox"/>            | <input checked="" type="checkbox"/> The exact sample size ( <i>n</i> ) for each experimental group/condition, given as a discrete number and unit of measurement   |
| <input type="checkbox"/>            | <input checked="" type="checkbox"/> A statement on whether measurements were taken from distinct samples or whether the same sample was measured repeatedly  |
| <input type="checkbox"/>            | <input checked="" type="checkbox"/> The statistical test(s) used AND whether they are one- or two-sided<br><i>Only common tests should be described solely by name; describe more complex techniques in the Methods section.</i>   |
| <input checked="" type="checkbox"/> | <input type="checkbox"/> A description of all covariates tested  |
| <input checked="" type="checkbox"/> | <input type="checkbox"/> A description of any assumptions or corrections, such as tests of normality and adjustment for multiple comparisons   |
| <input type="checkbox"/>            | <input checked="" type="checkbox"/> A full description of the statistical parameters including central tendency (e.g. means) or other basic estimates (e.g. regression coefficient) AND variation (e.g. standard deviation) or associated estimates of uncertainty (e.g. confidence intervals) |
| <input type="checkbox"/>            | <input checked="" type="checkbox"/> For null hypothesis testing, the test statistic (e.g. <i>F</i> , <i>t</i> , <i>r</i> ) with confidence intervals, effect sizes, degrees of freedom and <i>P</i> value noted<br><i>Give P values as exact values whenever suitable.</i>                     |
| <input checked="" type="checkbox"/> | <input type="checkbox"/> For Bayesian analysis, information on the choice of priors and Markov chain Monte Carlo settings  |
| <input checked="" type="checkbox"/> | <input type="checkbox"/> For hierarchical and complex designs, identification of the appropriate level for tests and full reporting of outcomes  |
| <input checked="" type="checkbox"/> | <input type="checkbox"/> Estimates of effect sizes (e.g. Cohen's <i>d</i> , Pearson's <i>r</i> ), indicating how they were calculated  |

Our web collection on [statistics for biologists](#) contains articles on many of the points above.

### Software and code

Policy information about [availability of computer code](#)

#### Data collection

The qRT-PCR data: ViiA 7 Software v1.2.4 on ViiA 7DX.  
The western blot data: ImageQuant LAS 4000mini and Amersham Imager 600.  
The confocal data: Leica Microsystems on Leica TCS SP8 confocal laser microscopy system.

#### Data analysis

GraphPad Prism software 5.0 was used for all analyses.  
Image J software 1.51 was used for calculating co-localization ratio of confocal data.

For manuscripts utilizing custom algorithms or software that are central to the research but not yet described in published literature, software must be made available to editors/reviewers. We strongly encourage code deposition in a community repository (e.g. GitHub). See the Nature Research [guidelines for submitting code & software](#) for further information.

### Data

Policy information about [availability of data](#)

All manuscripts must include a [data availability statement](#). This statement should provide the following information, where applicable:

- Accession codes, unique identifiers, or web links for publicly available datasets
- A list of figures that have associated raw data
- A description of any restrictions on data availability

RNA-seq data have been deposited in the Gene Expression Omnibus under accession code GSM4005162, GSM4005163, GSM4005164, GSM4005165, GSM4005166 and GSM4005167. Other data that support the findings of this study are available within the source data and Supplementary Information.



## Field-specific reporting

Please select the one below that is the best fit for your research. If you are not sure, read the appropriate sections before making your selection.

☒ Life sciences ☐ Behavioural & social sciences ☐ Ecological, evolutionary & environmental sciences

For a reference copy of the document with all sections, see [nature.com/documents/nr-reporting-summary-flat.pdf](https://www.nature.com/documents/nr-reporting-summary-flat.pdf)

## Life sciences study design

All studies must disclose on these points even when the disclosure is negative.

Sample size	No statistical methods were used to predetermine sample sizes. Sample size was based on empirical data from pilot experiments. Reported in Materials and Methods section (Mice and infection).
Data exclusions	No exclusion of data points or images were used.
Replication	All attempts at replication were successful as indicated in the figure legends. All animal experiments were repeated and the data pooled for statistical analyses.
Randomization	For mice infection experiment, Six -week-old C57BL/6 and SCID female mice were divided randomly into cages and infected with approximately 100-200 CFUs of different H37Rv strains. H37Rv strains were allocated into groups according to genotype of interest.
Blinding	The investigators were blinded during data collection and analysis where possible. This included Q-PCR data collection in cell and mice tissue cytokines assay.

## Reporting for specific materials, systems and methods

We require information from authors about some types of materials, experimental systems and methods used in many studies. Here, indicate whether each material, system or method listed is relevant to your study. If you are not sure if a list item applies to your research, read the appropriate section before selecting a response.

### Materials & experimental systems

n/a	Involved in the study
<input type="checkbox"/>	<input checked="" type="checkbox"/> Antibodies
<input type="checkbox"/>	<input checked="" type="checkbox"/> Eukaryotic cell lines
<input checked="" type="checkbox"/>	<input type="checkbox"/> Palaeontology
<input type="checkbox"/>	<input checked="" type="checkbox"/> Animals and other organisms
<input checked="" type="checkbox"/>	<input type="checkbox"/> Human research participants
<input checked="" type="checkbox"/>	<input type="checkbox"/> Clinical data

### Methods

n/a	Involved in the study
<input checked="" type="checkbox"/>	<input type="checkbox"/> ChIP-seq
<input checked="" type="checkbox"/>	<input type="checkbox"/> Flow cytometry
<input checked="" type="checkbox"/>	<input type="checkbox"/> MRI-based neuroimaging

## Antibodies

### Antibodies used

The following antibodies were used for western blot or immunoprecipitation: Monoclonal mouse anti-FLAG M2 affinity gel (Catalog#/Clone: A2220/M2), rabbit anti-HA antibody (Catalog#/Clone:H6908/polyclonal), rabbit anti-GAPDH antibody (Catalog#/Clone:SAB2701826/polyclonal), rabbit anti-FLAG antibody (Catalog#/Clone:F7425/polyclonal), and rabbit anti-K11 antibody (Catalog#/Clone: MABS107-I/2A3/2E6) antibodies were purchased from Sigma-Aldrich, St. Louis, MO. Rabbit anti-APC2 antibody (Catalog#/Clone: 12301/polyclonal), rabbit anti-phospho p65 antibody (Catalog#/Clone:3033/93H1), rabbit anti-phospho p38 antibody (Catalog#/Clone:9215/3D7), rabbit anti-phospho Jnk antibody (Catalog#/Clone:9251/polyclonal) antibody, anti-rabbit IgG HRP-linked antibody (Catalog#/Clone:7074) and anti-mouse IgG HRP-linked antibody(Catalog#/Clone:7076) were from Cell Signaling Technology, Danvers, MA; rabbit anti-TRAF6 (Catalog#/Clone:sc-7221/polyclonal) and monoclonal mouse anti-Myc (Catalog#/Clone:sc-40/9E10) antibodies were from Santa Cruz Biotechnology, USA. The K11/K48-branched ubiquitin chains antibody was provided by Prof. Michael Rape (Howard Hughes Medical Institute) and Dr. Marissa Matsumoto (Genentech Inc.). The rabbit polyclonal antibody to Rv0222 was generated by immunization of rabbits with the purified His-Rv0222 fusion protein, in collaboration with ABclonal Biotech, Shanghai, China. For western blot, all the primary antibodies were 1/1000 diluted and secondary antibodies were 1/2000 diluted.

For immunofluorescence assay, monoclonal mouse anti-FLAG M2 antibody (Catalog#/Clone: F1804/M2, 1/200 dilution) were purchased from Sigma-Aldrich, St. Louis, MO and rabbit anti-TRAF6 (Catalog#/Clone:sc-7221/polyclonal, 1/100 dilution) was from Santa Cruz Biotechnology, USA. Corresponding Alexa Fluor 633- or Alexa Fluor 555-labeled anti-rabbit or anti-mouse antibodies (Invitrogen) were used as secondary antibody (1/1000 dilution). FITC, Fluorescein isothiocyanate (Catalog# 3326-32-7) was from Sangon Biotech, Shanghai, China for strains dyeing.

### Validation

The Monoclonal mouse anti-FLAG M2 affinity gel, rabbit anti-HA antibody, rabbit anti-GAPDH antibody, rabbit anti-FLAG

antibody, rabbit anti-phospho p65 antibody, rabbit anti-phospho p38 antibody, rabbit anti-phospho Jnk antibody, rabbit anti-TRAF6 antibody rabbit anti-Myc antibody and rabbit anti-K63-linkage specific polyubiquitin antibody was validated for western blots of mouse samples or HEK293T cells overexpression system by many our previous publications (PMID: 26928339; 23001144; 31110366). The rabbit anti-K11 antibody was validated for western blots of K11 recombinant protein on the manufacturer's website(<https://www.sigmaaldrich.com/catalog/product/mm/mabs107i?lang=zh&region=CN>). Rabbit anti-APC2 antibody was validated for western blots of human samples by previous publication (PMID: 29987118). The K11/K48-branched ubiquitin chains antibody was validated for western blots of Hela cell lysate by previous publication (PMID: 29033132). The rabbit polyclonal antibody to Rv0222 was validated in this study. Rv0222 was detected in H37Rv (wild-type Mtb) with western blot using anti-Rv0222 antibody, while none was detected in Rv0222 bacteria (knockout Rv0222 in H37Rv)(Extended data Figure 1b).

For immunofluorescence assay, monoclonal mouse anti-FLAG M2 antibody was validated for IF in U2OS cells expressing exogenous FLAG-tagged protein by previous publication (PMID: ZBTB48 is both a vertebrate telomere-binding protein and a transcriptional activator). The rabbit anti-TRAF6 antibody was validated for IF in mice BMDCs by previous publication (PMID:21460221).

## Eukaryotic cell lines

Policy information about [cell lines](#)

Cell line source(s)	HEK293T cells (ATCC CRL-3216) and THP1 (ATCC TIB-202) were obtained from the American Type Culture Collection (ATCC).
Authentication	Cell lines purchased from commercial vendors, ATCC have been authenticated by the commercial vendor using short tandem repeat (STR) analysis. Generated knockout or knockdown cells were validated by specific antibodies as shown in extended figure.
Mycoplasma contamination	All the cells were routinely tested for contamination by mycoplasma and tested negative cells were used in the study.
Commonly misidentified lines (See <a href="#">ICLAC</a> register)	No commonly misidentified cell lines were used in this study.

## Animals and other organisms

Policy information about [studies involving animals](#); [ARRIVE guidelines](#) recommended for reporting animal research

Laboratory animals	All animal experiments were reviewed and approved by the Animal Experiment Administration Committee of Tongji University School of Medicine and were conducted in accordance with the National Institutes of Health (NIH) Guidelines for the Care and Use of Laboratory Animals. Female SPF C57BL/6 and SCID mice were purchased from Slaccas (Shanghai). Six- to eight-week-old female C57BL/6 mice were used for macrophage separation. Six -week-old C57BL/6 and SCID female mice were divided randomly into cages and infected by an aerosol method with approximately 100-200 CFUs of different H37Rv strains for 4 weeks (using a Glas-Col inhalation exposure system (Glas-col, Terre Haute, IN)) at the Biosafety Level-3 (BSL-3) Laboratory.
Wild animals	The study did not involve wild animals.
Field-collected samples	The study did not involve samples collected from the field.
Ethics oversight	All animal experiments were reviewed and approved by the Animal Experiment Administration Committee of Tongji University School of Medicine and were conducted in accordance with the National Institutes of Health (NIH) Guidelines for the Care and Use of Laboratory Animals. Reported in Materials and Methods section (Mice and infection).

Note that full information on the approval of the study protocol must also be provided in the manuscript.

# VEGF-C-driven lymphatic drainage enables immunosurveillance of brain tumours

<https://doi.org/10.1038/s41586-019-1912-x>

Received: 16 January 2019

Accepted: 21 November 2019

Published online: 15 January 2020

Eric Song<sup>1</sup>, Tianyang Mao<sup>1</sup>, Huiping Dong<sup>1</sup>, Ligia Simoes Braga Boisserand<sup>2</sup>, Salli Antila<sup>3</sup>, Marcus Bosenberg<sup>1,4,5</sup>, Kari Alitalo<sup>3</sup>, Jean-Leon Thomas<sup>2,6,8\*</sup> & Akiko Iwasaki<sup>1,3,7,8\*</sup>

Immune surveillance against pathogens and tumours in the central nervous system is thought to be limited owing to the lack of lymphatic drainage. However, the characterization of the meningeal lymphatic network has shed light on previously unappreciated ways that an immune response can be elicited to antigens that are expressed in the brain<sup>1–3</sup>. Despite progress in our understanding of the development and structure of the meningeal lymphatic system, the contribution of this network in evoking a protective antigen-specific immune response in the brain remains unclear. Here, using a mouse model of glioblastoma, we show that the meningeal lymphatic vasculature can be manipulated to mount better immune responses against brain tumours. The immunity that is mediated by CD8 T cells to the glioblastoma antigen is very limited when the tumour is confined to the central nervous system, resulting in uncontrolled tumour growth. However, ectopic expression of vascular endothelial growth factor C (VEGF-C) promotes enhanced priming of CD8 T cells in the draining deep cervical lymph nodes, migration of CD8 T cells into the tumour, rapid clearance of the glioblastoma and a long-lasting antitumour memory response. Furthermore, transfection of an mRNA construct that expresses VEGF-C works synergistically with checkpoint blockade therapy to eradicate existing glioblastoma. These results reveal the capacity of VEGF-C to promote immune surveillance of tumours, and suggest a new therapeutic approach to treat brain tumours.

We used the C57BL/6 syngeneic cell line GL261 to model glioblastoma in mice. Mice injected orthotopically with luciferase-expressing GL261 cells (GL261-Luc) showed cell-number-dependent growth kinetics and lethality (Extended Data Fig. 1a–c), demonstrating that intracranial injection of GL261-Luc is not sufficient to promote tumour rejection in the central nervous system (CNS). To evaluate the effects of enhanced lymphangiogenesis, we used two modes of delivery to express the lymphangiogenesis-promoting factor VEGF-C in mice: an adeno-associated viral vector (AAV9) and an mRNA delivery vector. Consistent with previous reports<sup>1,4,5</sup>, injection of AAV-VEGF-C into the cerebrospinal fluid (CSF) of mice through the cisterna magna remodelled meningeal lymphatic vessels in the dural confluence of sinuses (Fig. 1a, b) and in the sagittal sinuses (Extended Data Fig. 1h, i), and did not affect the integrity of the blood–brain barrier<sup>4</sup> (Extended Data Fig. 1d, e). In mice that were prophylactically treated with AAV-VEGF-C, we observed a near-complete rejection of tumours (Fig. 1c, Extended Data Fig. 1j).

## VEGF-C-mediated protection requires T cells

Previous studies have shown that deep cervical lymph nodes are the primary draining lymph nodes of the CNS, and that mandibular and superficial cervical lymph nodes contribute to antigen sampling

in the CNS<sup>1,3,6,7</sup>. Thus, we surgically ligated the afferent lymphatic vessels that drain to both deep cervical lymph nodes in mice treated with AAV-VEGF-C. Although AAV-VEGF-C-treated mice showed prolonged survival compared to control mice (Fig. 1d), after ligation of the deep cervical lymph nodes the majority of the AAV-VEGF-C-treated mice succumbed to the tumour. This indicates that VEGF-C-mediated protection against glioblastoma requires lymph drainage to the deep cervical lymph nodes.

The requirement for the deep cervical lymph nodes suggests that the immune system has a role in VEGF-C-mediated protection. Depletion of CD4 or CD8 T cells negated the protection that was conferred by VEGF-C (Fig. 1e, Extended Data Fig. 1k). By contrast, B-cell-deficient ( $\mu$ MT) mice that were treated with VEGF-C were protected from glioblastoma (Extended Data Fig. 1l). We examined the durability of this immune response against glioblastoma in mice that were treated with VEGF-C, and found that mice that rejected the intracranial tumour showed long-term systemic memory responses; rechallenge with GL261-Luc in the flank resulted in no detectable tumours (Fig. 1f, Extended Data Fig. 1m). Together, these data demonstrate that by increasing lymphangiogenesis in the meninges, prophylactic treatment with VEGF-C can evoke a robust and long-lasting T-cell-dependent immune response against brain neoplasms.

<sup>1</sup>Department of Immunobiology, Yale University School of Medicine, New Haven, CT, USA. <sup>2</sup>Department of Neurology, Yale University School of Medicine, New Haven, CT, USA. <sup>3</sup>Translational Cancer Medicine Program and Wihuri Research Institute, Biomedicum Helsinki, University of Helsinki, Helsinki, Finland. <sup>4</sup>Department of Dermatology, Yale University School of Medicine, New Haven, CT, USA. <sup>5</sup>Department of Pathology, Yale University School of Medicine, New Haven, CT, USA. <sup>6</sup>Institut du Cerveau et de la Moelle Épinrière, INSERM U1127, CNRS UMR 7225, GH Pitié-Salpêtrière, Sorbonne Université, Paris, France. <sup>7</sup>Howard Hughes Medical Institute, Chevy Chase, MD, USA. <sup>8</sup>These authors jointly supervised this work: Jean-Leon Thomas, Akiko Iwasaki. \*e-mail: jean-leon.thomas@yale.edu; akiko.iwasaki@yale.edu

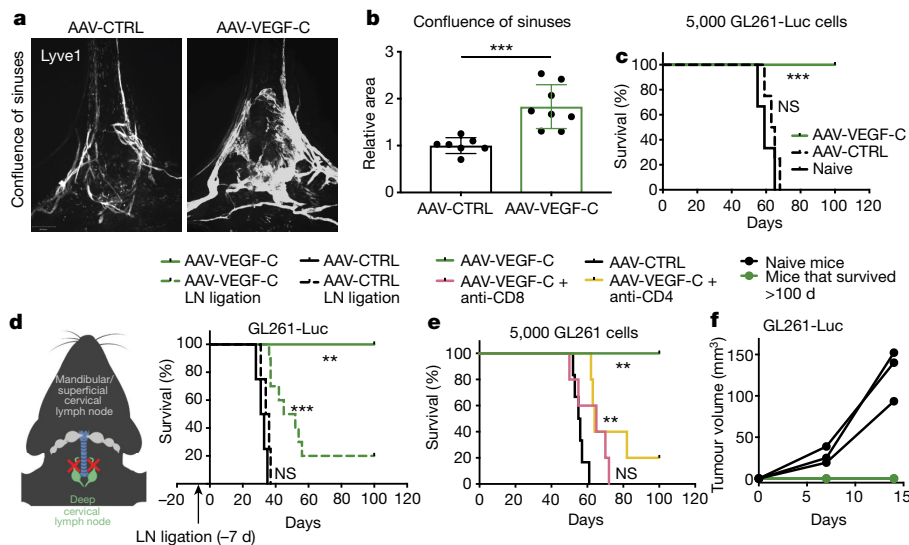


**Fig. 1 | VEGF-C-mediated protection against glioblastoma depends on the draining lymph nodes and on T cells.** **a, b**, C57BL/6 mice were injected with AAV-CTRL or AAV-VEGF-C intracisternally through the cisterna magna. Six to eight weeks later, mice were euthanized and the dura was collected to image the lymphatic vasculature (LYVE1<sup>+</sup>) in the confluence of sinuses (AAV-CTRL,  $n = 7$ ; AAV-VEGF-C,  $n = 8$ ). \*\*\* $P = 0.0007$ . **c**, C57BL/6 mice that had been injected with AAV-CTRL or AAV-VEGF-C two months previously were implanted with 5,000 GL261-Luc cells in the striatum and monitored for survival (naive,  $n = 3$ ; AAV-CTRL,  $n = 4$ ; AAV-VEGF-C,  $n = 8$ ). \*\*\* $P = 0.0004$  for naive versus AAV-VEGF-C;  $P = 0.33$  (NS, not significant) for naive versus AAV-CTRL. **d**, Six to eight weeks after injection of AAV vectors, the deep cervical lymph nodes of mice were ligated using a cauterizer. Seven days later, mice were challenged with 50,000 GL261-Luc cells in the striatum and monitored for survival (AAV-CTRL,  $n = 4$ ; AAV-CTRL with lymph node (LN) ligation,  $n = 4$ ; AAV-VEGF-C,  $n = 4$ ; AAV-VEGF-C with lymph node ligation,  $n = 10$ ). \*\* $P = 0.007$  for AAV-CTRL

versus AAV-VEGF-C; \*\*\* $P < 0.0001$  for AAV-CTRL versus AAV-VEGF-C LN ligation;  $P = 0.15$  (NS) for AAV-CTRL versus AAV-CTRL LN ligation. **e**, Similar to **c**, but mice that had previously been injected with AAV-VEGF-C were treated with anti-CD4 or anti-CD8 antibodies (AAV-CTRL,  $n = 6$ ; AAV-VEGF-C,  $n = 5$ ; AAV-VEGF-C + anti-CD8,  $n = 5$ ; AAV-VEGF-C + anti-CD4,  $n = 5$ ). \*\* $P = 0.0014$  for AAV-CTRL versus AAV-VEGF-C;  $P = 0.34$  (NS) for AAV-CTRL versus AAV-VEGF-C with anti-CD8; \*\* $P = 0.0014$  for AAV-CTRL versus AAV-VEGF-C with anti-CD4. **f**, Mice injected with AAV-CTRL or AAV-VEGF-C that survived over 100 days after challenge with 5,000 GL261-Luc cells were rechallenged with 500,000 GL261-Luc cells in the flank. Tumours were measured after flank rechallenge at days 7 and 15 ( $n = 3$  per group, all 3 mice from the GL261 100 d group had no measurable tumours). Data are pooled from two independent experiments (**b–f**) and are mean  $\pm$  s.d.  $P$  values were calculated by two-tailed unpaired Student's  $t$ -test or two-sided log-rank Mantel–Cox test.

## Glioblastoma is devoid of lymphangiogenic signals

Previous studies have shown that tumour-intrinsic overexpression of VEGF-C in mice or humans results in poorer prognosis for malignancies that occur in areas outside of the CNS<sup>8,9</sup>. We compared the transcriptomes of brain tissue from healthy control individuals and patients with glioblastoma using data from the Genotype-Tissue Expression project (GTEx) and The Cancer Genome Atlas (TCGA), respectively. Tumour tissue showed higher expression of *VEGFA* and *CD31* (also known as *PECAM1*) than control tissue, as previously shown<sup>10</sup>, but a decrease in the expression of *VEGFC* (Fig. 2a–c, Extended Data Fig. 2a, b)—which was also seen in mice that bear glioblastoma tumours (Extended Data Fig. 2c). When we stratified the patients with glioblastoma into two groups on the basis of their *VEGFC* expression levels (high versus low), we observed no differences in survival (Extended Data Fig. 2d, e), as the expression levels of *VEGFC* in patients with glioblastoma were lower than those in healthy brain tissue even in the group with high *VEGFC* expression. However, in a recently published dataset<sup>11</sup> of patients with glioblastoma who were treated with neoadjuvant anti-PD-1, the expression of *VEGFC* was highly correlated with an increase in the infiltration of T cells (as measured by the expression of the T cell marker genes *CD3E*, *CD4* and *CD8B*) after treatment (Fig. 2d–f). Collectively, these results suggest that the glioblastoma microenvironment is deprived of lymphangiogenic signals both in patients with glioblastoma and in experimental mice, and that ectopic expression of VEGF-C confers protection against glioblastoma in a mouse model.

## VEGF-C potentiates immune checkpoint blockade

Although treating mice with AAV-VEGF-C led to survival benefits with no long-term side effects (Extended Data Fig. 1d, e, g), this vector

is—owing to the immunogenicity of AAV<sup>12</sup>—less effective when given subsequently to the same host. By contrast, an mRNA delivery vector does not elicit an immune response against the vector<sup>13</sup>. Therefore, we designed an mRNA construct to express *VEGFC*, with stabilizing base substitutions (Extended Data Fig. 3a, b). Transfection of HEK293T cells with the *VEGFC* mRNA construct produced both the full-length and the processed form of VEGF-C<sup>14</sup> (Extended Data Fig. 3c). Administration of the *VEGFC* mRNA construct into the cisterna magna of mice resulted in high levels of VEGF-C in the CSF (Extended Data Fig. 3d). We used Cy5-labelled mRNA to confirm the wide distribution of *VEGFC* mRNA within the dura mater (Extended Data Fig. 3f), and saw its uptake by immune cells (CD45<sup>+</sup>), endothelial cells (CD45<sup>−</sup>CD31<sup>+</sup>) and other cells (CD45<sup>−</sup>CD31<sup>−</sup>) in the brain, meninges and deep cervical lymph nodes (Extended Data Fig. 3g, h). Furthermore, we observed an increase in the levels of secreted VEGF-C protein that was specific to the CSF and meninges, with no changes in the brain or serum (Extended Data Fig. 3i). Using AKT phosphorylation to measure vascular endothelial growth factor receptor (VEGFR) signalling in endothelial cells after treatment with VEGF-C, we observed an increase in VEGFR signalling that was specific to the lymphatic endothelial cell (LEC) population; by contrast, no changes were observed in the blood endothelial cells (BECs) in the meninges or deep cervical lymph nodes (Extended Data Fig. 4a–c). This increase in VEGFR signalling was not accompanied by structural deformities in either the LECs or the BECs, even within an angiogenic tumour environment (Extended Data Fig. 4b–e). These data indicate that whereas *VEGFC* mRNA is taken up by various cells of the brain, meninges and deep cervical lymph nodes, VEGF-C protein is mostly confined to the CSF and meninges, and activates LECs.

In addition to the difference in immunogenicity, the expression kinetics of the *VEGFC* mRNA construct and the AAV-VEGF-C vector differ; the



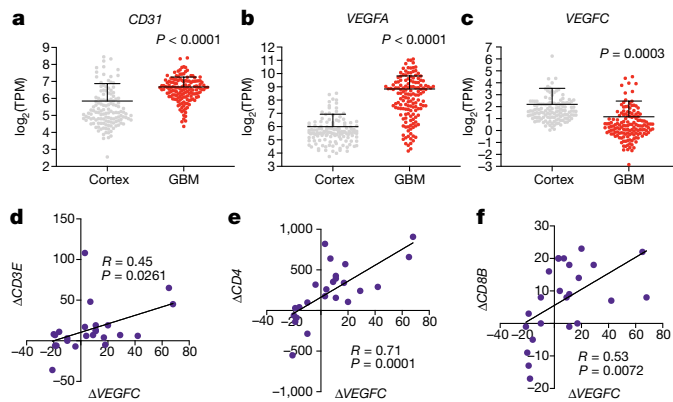


**Fig. 2 | Human glioblastoma is deprived of lymphangiogenic signals at steady state, and VEGF-C levels correlate with T cell infiltration with anti-PD-1 therapy.** RNA sequencing (RNA-seq) data of tumour tissue (TCGA, study accession phs000178.v10.p8) and healthy brain cortex (GTEx, study accession phs000424.v7.p2). **a–c**, Expression profiles of *VEGFA* (**b**), *CD31* (angiogenic) (**a**) and *VEGFC* (lymphangiogenic) (**c**) genes in samples of healthy cortex versus glioblastoma (cortex,  $n = 133$  samples; glioblastoma,  $n = 147$  samples). **d–f**, Correlation (from RNA-seq) of changes in the expression of *VEGFC* and of the T cell markers *CD3E* (**d**), *CD4* (**e**) and *CD8B* (**f**) after PD-1 therapy (data from GSE121810;  $n = 24$ ). Data are mean  $\pm$  s.d.  $P$  values were calculated by two-tailed unpaired Student's  $t$ -test or Pearson's correlation.

*VEGFC* mRNA construct shows peak expression after 24 h, whereas the expression of AAV-VEGF-C does not reach maximal levels for several weeks<sup>15</sup>. We evaluated the therapeutic efficacy of both modalities by administering mice with each vector on different days, and found that only prophylactic (day 60) treatment with AAV-VEGF-C resulted in long-term survival (Extended Data Fig. 4f–h). By contrast, when monotherapy with the *VEGFC* mRNA construct was administered at days 0, 3 or 7, survival benefits were still observed—although none of these treated mice survived in the face of rapid glioblastoma development (Extended Data Fig. 4f).

Similarly, anti-PD-1 and other checkpoint blockade therapies show little benefit against glioblastoma when used as monotherapies in preclinical models<sup>16,17</sup>, and have not shown favourable responses in clinical trials<sup>18</sup>. However, strategies that promote T cell responses—such as activation of dendritic cells<sup>19</sup>, or radiation<sup>16</sup>—potentiate anti-PD-1 therapy against glioblastoma, suggesting that the hurdles in the treatment of cancers of the CNS may be during T cell priming. Hypothesizing that VEGF-C increases immune surveillance of the brain, we reasoned that therapy using VEGF-C would have synergistic antitumour effects with checkpoint inhibitor therapy. Whereas anti-PD-1 alone had marginal effects on survival, a combination of treatment with *VEGFC* mRNA and anti-PD-1 antibody resulted in regression of tumours and survival benefits in mice bearing established GL261 tumours (Fig. 3a, b), in a T-cell-dependent manner (Extended Data Fig. 5d). When mice that survived in the long term were rechallenged with tumours in the contralateral hemisphere, they exhibited resistance to the secondary challenge (Extended Data Fig. 5b), and T cells transferred from the draining lymph nodes and spleen of mice that rejected tumours conferred protection against a primary challenge (Extended Data Fig. 5c). A survival benefit was also observed in mice bearing tumours derived from a more proliferative and invasive syngeneic glioblastoma cell line (CT-2A) after treatment with a combination of *VEGFC* mRNA and anti-PD-1 together with the T-cell-activating agent anti-4-1BB<sup>20</sup> (Extended Data Fig. 5e–g). In addition, other checkpoint inhibitors that are known to be ineffective<sup>16,17,21</sup> were potentiated with *VEGFC* mRNA (Extended Data Fig. 5h–j). Even when mice were treated after the tumour mass had increased substantially (day 20), the combination therapy showed survival benefits (Extended Data Fig. 5k, l).

To assess whether T cell priming against glioblastoma in the deep cervical lymph nodes was increased after mice were treated with VEGF-C, we used an endogenous tumour antigen that is present in many mouse cancers<sup>22</sup>. Endogenous retroviruses are integrated remnants of retrovirus in the host genome that are silenced epigenetically, but which often become aberrantly expressed in the dysregulated transcriptional states that are found in cancers<sup>23</sup>. We identified endogenous retrovirus sequences based on the gene *Emv2* that were overexpressed in GL261 cells (Extended Data Fig. 6a, b). We therefore constructed tetramers against *emv2-env* (an envelope protein coded by *Emv2*)<sup>22</sup> and found that after administration of GL261 cells in the flank of mice, tetramer-positive CD8 T cells were enriched in the draining inguinal lymph nodes (Extended Data Fig. 6d)—demonstrating that endogenous tumour-specific T cell priming occurs in an antigen-dependent manner in response to GL261.

Intracranial inoculation of mice with GL261-Luc resulted in small tetramer-positive populations of T cells in the deep cervical lymph nodes (1.54%) (Fig. 3c, d). However, treatment with the *VEGFC* mRNA construct resulted in significant increases in the tumour-specific T cell population in the deep cervical lymph nodes (3.65%) (Fig. 3c, d). In addition, increases in both the percentage (Fig. 3d) and the absolute numbers (Extended Data Fig. 5a) of tumour-specific T cells were detected in the brain after treatment with the *VEGFC* mRNA construct. These data reveal that intracranial tumours elicit minimal CD8 T cell responses in the deep cervical lymph nodes, but that *VEGFC* mRNA enhances the priming of CD8 T cells against tumours in the brain.

We then examined the specificity of VEGF-C in potentiating checkpoint inhibitor therapy. First, to confirm the requirement of meningeal lymphatic vessels, a soluble version of VEGFR-3 (VEGFR-3<sub>1-3</sub>-Ig) was administered, using an AAV construct, to sequester VEGF-C; this resulted in atrophy of lymphatic vasculature in the dura<sup>4,24</sup> (Extended Data Fig. 7a, b). Treatment with VEGFR-3<sub>1-3</sub>-Ig abrogated the efficacy of *VEGFC* mRNA and anti-PD-1 therapy (Extended Data Fig. 7c). VEGF-C also uniquely provided therapeutic benefits in combination with anti-PD-1 when compared to other recombinant proteins of the VEGF family (VEGF-A, VEGF-B, VEGF-Cs and VEGF-D; Cs is Cys156Ser, a VEGFR-3-selective agonist) (Extended Data Fig. 7d–f). These experiments demonstrate the specificity of the antitumour capacity of VEGF-C and the requirement for the meningeal lymphatic vessels in providing therapeutic benefits against glioblastoma.

Tumour-intrinsic VEGF-C has also previously been reported to mediate increased metastases in melanoma and breast cancer<sup>9,24,25</sup>. To assess whether this was a possibility in the CNS, cells expressing blue fluorescence protein (BFP) were tracked to determine the distribution of tumour cells *in vivo*. We collected the brain and deep cervical lymph nodes to measure tumour cells (CD45<sup>+</sup>BFP<sup>+</sup>), as well as immune cells that may have phagocytosed tumour cells (CD45<sup>+</sup>BFP<sup>+</sup>). No CD45<sup>+</sup>BFP<sup>+</sup> cells were found in the deep cervical lymph nodes after treatment with VEGF-C, suggesting that VEGF-C does not promote metastasis of glioblastoma to the lymph nodes (Extended Data Fig. 7g–k). In addition, direct effects of VEGF-C on tumour cells are unlikely, as glioblastoma cells showed no expression of VEGFR-3, and VEGF-C had no effect on cell proliferation in culture (Extended Data Fig. 7l, m). Of note, both VEGF-C delivery vectors (AAV and mRNA) resulted in an increase in the number of CD45<sup>+</sup>BFP<sup>+</sup> cells in the deep cervical lymph nodes (Extended Data Fig. 7i)—consistent with reports that antigen drainage is increased by exogenous VEGF-C<sup>1,2</sup>.

To examine how VEGF-C modifies the immune landscape of tumours before anti-PD-1 therapy, we performed flow cytometry in the brain, meninges and deep cervical lymph nodes of mice after treatment with the *VEGFC* mRNA construct. Myeloid populations of cells showed minimal changes, with no differences in their levels of activation (CD80) or antigen-presentation capabilities (major histocompatibility complex (MHC) II) (Extended Data Fig. 8a–g). The largest changes induced by treatment with the *VEGFC* mRNA construct were in the number and



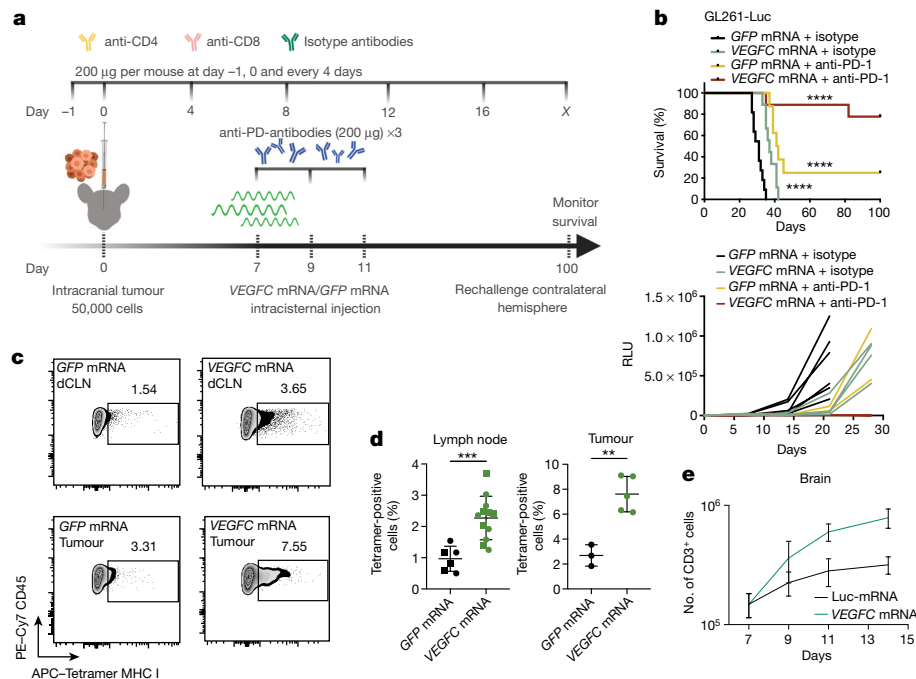


**Fig. 3 | Therapeutic delivery of VEGF-C potentiates checkpoint inhibitor therapy by enhancing T cell priming and recruitment. a**, Schematic of treatment plans. **b**, Mice inoculated with 50,000 GL261-Luc cells were treated with *VEGFC* mRNA or *GFP* mRNA constructs (day 7) and with either anti-PD-1 (RMP1-14) antibodies or isotype control antibodies (days 7, 9 and 11), and monitored for survival (top; Kaplan–Meier curve; *GFP* mRNA + isotype, *n* = 11; *VEGFC* mRNA + isotype, *n* = 9; *GFP* mRNA + anti-PD-1, *n* = 8; *VEGFC* mRNA + anti-PD-1, *n* = 10) and tumour burden (bottom; *GFP* mRNA + isotype, *n* = 7; *VEGFC* mRNA + isotype, *n* = 5; *GFP* mRNA + anti-PD-1, *n* = 4; *VEGFC* mRNA + anti-PD-1, *n* = 5). Data are pooled from 2 independent experiments. \*\*\*\**P* < 0.0001. RLU, relative luminescence units. **c, d**, Mice were inoculated with 50,000 GL261-Luc cells and treated with *GFP* mRNA or *VEGFC* mRNA at day 7. Seven days after mRNA treatment, the deep cervical lymph nodes (dCLN) and tumour-bearing brain hemispheres were collected to detect tetramer-positive

CD8 T cells. **c**, Concatenated fluorescence-activated cell sorting (FACS) plots of CD45<sup>+</sup>CD3<sup>+</sup>CD8<sup>+</sup>CD44<sup>+</sup> T cells in tumour-bearing brain and deep cervical lymph nodes after treatment with *GFP* mRNA or *VEGFC* mRNA. **d**, Quantification of deep cervical lymph nodes (left; circle, ipsilateral; square, contralateral (*GFP* mRNA, *n* = 6; *VEGFC* mRNA, *n* = 12) or tumour-infiltrating tetramer-positive CD8 T cells (right) (*GFP* mRNA, *n* = 3; *VEGFC* mRNA, *n* = 5). The experiment was repeated independently with similar results. \*\*\**P* = 0.007 (lymph nodes); \*\**P* = 0.002 (tumour). **e**, Mice were inoculated with 50,000 GL261-Luc cells and treated with Luc mRNA or *VEGFC* mRNA at day 7. Tumour-inoculated brain hemisphere tissue was collected and analysed using FACS, and the number of CD3-positive cells was assessed (*n* = 3; 3 mice were pooled for each sample). Data are mean ± s.d. *P* values were calculated by two-tailed unpaired Student's *t*-test or two-sided log-rank Mantel–Cox test.

the phenotypes of T cells that infiltrate the brain (Fig. 3e, Extended Data Fig. 9a). This result, combined with the increase in CD45<sup>+</sup>BFP<sup>+</sup> cells in the deep cervical lymph nodes (Extended Data Fig. 7i), suggests that the increased priming and subsequent infiltration of T cells is a result of increased antigen drainage. Mice that were treated with the *VEGFC* mRNA construct also showed a stable number of TCF1<sup>+</sup> CD8 T cells—a population that is important for eliciting antitumour effector responses<sup>26,27</sup> (Extended Data Fig. 9c–f)—in the three compartments (brain, meninges and deep cervical lymph nodes), along with increased FOXP3<sup>+</sup> CD4 T cells (Extended Data Fig. 9f). Notably, a higher proportion of FOXP3<sup>+</sup> cells expressed T-bet, which is a critical regulator of the differentiation of T helper 1 cells (Extended Data Fig. 9f) and is associated with increased levels of IFN $\gamma$  in regulatory (CD4<sup>+</sup>CD25<sup>+</sup>) T cells and reduced suppression of CD4 effector cells<sup>28</sup>. These data indicate that there is a shift towards an antitumour immune response in mice that are treated with VEGF-C. Consistent with this, CD8 T cells in the brain of VEGF-C treated mice were also capable of producing multiple cytokines after ex vivo stimulation (Extended Data Fig. 9e–i)—a positive prognostic factor for immunotherapy<sup>29</sup>. All of these changes seemed to occur independently of a direct effect on T cells, as no VEGFR-3 expression was detectable in CD4 and CD8 T cells (Extended Data Fig. 7n), and VEGF-C did not affect the proliferation of T cells in vitro (Extended Data Fig. 7p). We did not observe expression of VEGFR-3 in other immune compartments, and stimulation of bone-marrow-derived dendritic cells with VEGF-C induced no change in the expression levels of MHC II or costimulatory molecules (Extended Data Fig. 7o). Together, these

results show that VEGF-C provides a potent antitumour environment, which—in association with increased lymphatic drainage and antigen presentation—promotes multifunctional and durable T cell immunity against glioblastoma.

### VEGF-C restores CNS-restricted T cell priming

In contrast to what is seen in patients with glioblastoma, reports have shown that combined therapy with nivolumab and ipilimumab had intracranial efficacy, concordant with extracranial activity, in patients with melanoma that had metastasized to the brain<sup>30</sup>. Consistent with clinical observations, mice with both a flank and an intracranial tumour responded better to immunotherapy than did those with just an intracranial melanoma<sup>31</sup>. To examine whether *VEGFC* mRNA is effective in treating other (non-glioblastoma) types of cancer in the CNS, we used the melanoma cell lines YUMMER1.7 and B16 (Extended Data Fig. 10a). Mice bearing only intracranial YUMMER1.7 tumours showed significant survival benefits when treated with *VEGFC* mRNA and checkpoint inhibitor therapy (Fig. 4a). By contrast, mice with both intracranial and flank tumours benefited from checkpoint inhibitor therapy regardless of *VEGFC* mRNA treatment (Fig. 4b). In fact, the survival benefits to mice with only intracranial tumours that received combination therapy were similar to mice with both intracranial and flank tumours that were treated with checkpoint inhibitor therapy alone (Fig. 4c). In addition, ligation of the deep cervical lymph nodes only affected mice with intracranial tumours, not mice with both intracranial and flank

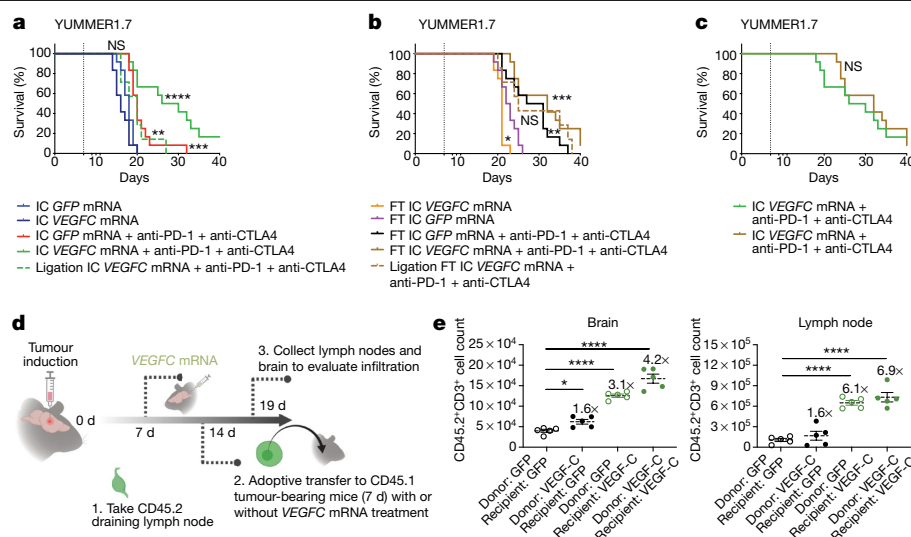


**Fig. 4 | Therapeutic delivery of VEGF-C mediates protection against intracranial melanoma when combined with checkpoint inhibitor blockade and is equivalent to peripheral priming. a–c,** Mice were given either only YUMMER1.7 intracranial tumours (IC) (a) or both a YUMMER1.7 intracranial tumour and a YUMMER1.7 flank tumour (FT) (b), and treated with GFP mRNA or VEGFC mRNA on day 7, and anti-PD-1 (RMP1-14) and anti-CTLA4 (9H10) on days 7, 9 and 11. Two groups (ligation IC VEGFC mRNA + anti-PD-1 + anti-CTLA4 and ligation FT IC VEGFC mRNA + anti-PD-1 + anti-CTLA4) had lymph nodes ligated 7 days before tumour implantation (a,  $n=12$  for all groups except ligation IC VEGFC mRNA + anti-PD-1 + anti-CTLA4,  $n=7$ ; b,  $n=12$  for all groups except ligation FT IC VEGFC mRNA + anti-PD-1 + anti-CTLA4,  $n=7$ ). P-values: a,  $P=0.13$  (NS) for IC VEGFC mRNA; \*\*\* $P=0.001$  for IC GFP mRNA + anti-PD-1 + anti-CTLA4; \*\*\*\* $P<0.0001$  for IC VEGFC mRNA + anti-PD-1 + anti-CTLA4; \*\* $P=0.069$  for ligation IC VEGFC mRNA + anti-PD-1 + anti-CTLA4 (all versus IC GFP mRNA); b, \* $P=0.013$  for FT IC VEGFC mRNA; \*\* $P=0.0029$  for FT IC GFP mRNA + anti-

PD-1 + anti-CTLA4; \*\*\* $P=0.0003$  for FT IC VEGFC mRNA + anti-PD-1 + anti-CTLA4;  $P=0.051$  (NS) for ligation FT IC VEGFC mRNA + anti-PD-1 + anti-CTLA4 (all versus FT IC GFP mRNA); c,  $P=0.72$  (NS) for IC VEGFC mRNA + anti-PD-1 + anti-CTLA4 versus FT IC VEGFC mRNA + anti-PD-1 + anti-CTLA4. d, Schematic of experimental design for the results shown in e. Congenic CD45.2 mice were injected with GL261 tumours. Seven days later, mice were treated with GFP mRNA or VEGFC mRNA. Seven days after the mRNA treatment (14 days after tumour inoculation) leukocytes from deep cervical lymph nodes were transferred into congenic CD45.1 mice bearing 7-day tumours. Five days after transfer, the deep cervical lymph nodes and brain tissues were collected to analyse T cell infiltration. e, Quantification of brain-infiltrating T cells and T cells in lymph nodes; numbers denote the fold change in the number of cells over donor GFP and recipient GFP groups ( $n=5$  mice per group). Data are mean  $\pm$  s.e.m. For P-values in e, \* $P<0.05$ ; \*\*\*\* $P<0.0001$ . P-values were calculated by two-tailed unpaired Student's  $t$ -test or two-sided log-rank Mantel–Cox test.

tumours (Fig. 4a, b). Similar results were observed with the B16 cell line (Extended Data Fig. 10c–e). These results are consistent with the idea that T cell priming—either through expression of VEGF-C in the CSF or through a flank tumour—enables efficient checkpoint inhibitor responses in the CNS. However, in the case of a tumour that is confined to the CNS at steady state, immune checkpoint inhibitors alone do not confer notable benefits, regardless of tumour type.

Finally, we sought to understand whether the antitumour effects of VEGF-C are due to (i) the expansion and differentiation of T cells that are capable of trafficking to the brain (that is, T-cell-intrinsic); or (ii) changes in the brain environment that cause an increase in the recruitment of T cells (that is, T-cell-extrinsic). We performed adoptive transfer of leukocytes from the draining lymph nodes of tumour-bearing mice into recipient mice that also had tumours (Fig. 4d, e). The infiltration of T cells into the brain was slightly increased (T-cell-intrinsic; 1.6-fold increase) if the T cells were from mice treated with VEGFC mRNA. However, T cells from tumour-bearing control mice were able to migrate into glioblastoma-affected brains to a greater extent if the recipient was treated with the VEGFC mRNA construct (T-cell-extrinsic; 3.1-fold increase) (Fig. 4e). Moreover, donor T cells from mice that were treated with VEGFC mRNA, transferred into a host that was also treated with VEGFC mRNA, were able to infiltrate the tumour most efficiently (combinatorial; 4.2-fold increase). Increases in the numbers of T cells in the lymph nodes were dependent on the recipient mice having been treated with VEGFC mRNA—consistent with the notion that antigen-specific T cells proliferate only after increased drainage of tumour antigens from the CNS. These results show that VEGF-C provides an antitumour environment through a combination of its effect on the meningeal lymphatic vasculature and the changes that it induces in T-cell-intrinsic properties.

## Discussion

We have demonstrated that ectopic expression of VEGF-C has the potential to manipulate meningeal lymphatics, and thereby enables immune surveillance and T-cell-mediated immunity against brain tumours (Extended Data Fig. 10g). These results support a growing body of work that highlights the importance of the meningeal lymphatic network in controlling immune responses in the CNS<sup>3–5</sup>. The lack of immune responses against tissue grafts<sup>32</sup> in the CNS has led to the idea that the brain has an immune-privileged status, and a similar phenomenon of immune privilege may allow primary brain tumours such as glioblastoma to grow unhindered in the CNS<sup>33</sup>. Together with these previous reports, our study suggests that tumours confined within the CNS may be inaccessible for immune priming, and that exogenous expression of VEGF-C potentiates endogenous immune responses. We considered the possibility that immune-cell- or tumour-cell-intrinsic VEGF-C signalling causes this phenomenon, but found that immune and tumour cells showed no changes after direct stimulation with VEGF-C. Instead, our data suggest that VEGF-C (and its relationship with its main receptor partner VEGFR-3) leads to an increase in lymphatic drainage<sup>34</sup>, which is necessary for immunosurveillance against glioblastoma—similar to the way in which melanoma-intrinsic overexpression of VEGF-C enhances antitumour T cell responses<sup>8</sup>. It is worth noting that the immune-privileged status of the CNS does not apply to all brain antigens<sup>6</sup>, and future studies are needed to define the rules of CNS antigen sampling. In summary, our study shows that increasing lymphatic drainage can overcome the immune ignorance of glioblastoma. This lays the foundation for a new strategy in which modulation of the lymphatic vasculature is used to increase the effects of checkpoint inhibitor therapy against tumours in immune-privileged sites.

## Online content

Any methods, additional references, Nature Research reporting summaries, source data, extended data, supplementary information, acknowledgements, peer review information; details of author contributions and competing interests; and statements of data and code availability are available at <https://doi.org/10.1038/s41586-019-1912-x>.

- Aspelund, A. et al. A dural lymphatic vascular system that drains brain interstitial fluid and macromolecules. *J. Exp. Med.* **212**, 991–999 (2015).
- Louveau, A. et al. Structural and functional features of central nervous system lymphatic vessels. *Nature* **523**, 337–341 (2015).
- Louveau, A. et al. CNS lymphatic drainage and neuroinflammation are regulated by meningeal lymphatic vasculature. *Nat. Neurosci.* **21**, 1380–1391 (2018).
- Antila, S. et al. Development and plasticity of meningeal lymphatic vessels. *J. Exp. Med.* **214**, 3645–3667 (2017).
- Da Mesquita, S. et al. Functional aspects of meningeal lymphatics in ageing and Alzheimer's disease. *Nature* **560**, 185–191 (2018).
- Harris, M. G. et al. Immune privilege of the CNS is not the consequence of limited antigen sampling. *Sci. Rep.* **4**, 4422 (2014).
- Mathieu, E., Gupta, N., Macdonald, R. L., Ai, J. & Yücel, Y. H. In vivo imaging of lymphatic drainage of cerebrospinal fluid in mouse. *Fluids Barriers CNS* **10**, 35 (2013).
- Fankhauser, M. et al. Tumor lymphangiogenesis promotes T cell infiltration and potentiates immunotherapy in melanoma. *Sci. Transl. Med.* **9**, eaal4712 (2017).
- Skobe, M. et al. Induction of tumor lymphangiogenesis by VEGF-C promotes breast cancer metastasis. *Nat. Med.* **7**, 192–198 (2001).
- Gilbert, M. R. et al. A randomized trial of bevacizumab for newly diagnosed glioblastoma. *N. Engl. J. Med.* **370**, 699–708 (2014).
- Cloughesy, T. F. et al. Neoadjuvant anti-PD-1 immunotherapy promotes a survival benefit with intratumoral and systemic immune responses in recurrent glioblastoma. *Nat. Med.* **25**, 477–486 (2019).
- Mingozzi, F. & High, K. A. Immune responses to AAV vectors: overcoming barriers to successful gene therapy. *Blood* **122**, 23–36 (2013).
- Sabnis, S. et al. A novel amino lipid series for mRNA delivery: improved endosomal escape and sustained pharmacology and safety in non-human primates. *Mol. Ther.* **26**, 1509–1519 (2018).
- Joukov, V. et al. Proteolytic processing regulates receptor specificity and activity of VEGF-C. *EMBO J.* **16**, 3898–3911 (1997).
- Zincarelli, C., Soltys, S., Rengo, G. & Rabinowitz, J. E. Analysis of AAV serotypes 1–9 mediated gene expression and tropism in mice after systemic injection. *Mol. Ther.* **16**, 1073–1080 (2008).
- Zeng, J. et al. Anti-PD-1 blockade and stereotactic radiation produce long-term survival in mice with intracranial gliomas. *Int. J. Radiat. Oncol. Biol. Phys.* **86**, 343–349 (2013).
- Kim, J. E. et al. Combination therapy with anti-PD-1, anti-TIM-3, and focal radiation results in regression of murine gliomas. *Clin. Cancer Res.* **23**, 124–136 (2017).
- Filley, A. C., Henriquez, M. & Dey, M. Recurrent glioma clinical trial, CheckMate-143: the game is not over yet. *Oncotarget* **8**, 91779–91794 (2017).
- Garzon-Muvdi, T. et al. Dendritic cell activation enhances anti-PD-1 mediated immunotherapy against glioblastoma. *Oncotarget* **9**, 20681–20697 (2018).
- Chongsathidkiet, P. et al. Sequestration of T cells in bone marrow in the setting of glioblastoma and other intracranial tumors. *Nat. Med.* **24**, 1459–1468 (2018).
- Belcaid, Z. et al. Focal radiation therapy combined with 4-1BB activation and CTLA-4 blockade yields long-term survival and a protective antigen-specific memory response in a murine glioma model. *PLoS ONE* **9**, e101764 (2014).
- Bronte, V. et al. Effective genetic vaccination with a widely shared endogenous retroviral tumor antigen requires CD40 stimulation during tumor rejection phase. *J. Immunol.* **171**, 6396–6405 (2003).
- Rooney, M. S., Shukla, S. A., Wu, C. J., Getz, G. & Hacohen, N. Molecular and genetic properties of tumors associated with local immune cytolytic activity. *Cell* **160**, 48–61 (2015).
- He, Y. et al. Vascular endothelial cell growth factor receptor 3-mediated activation of lymphatic endothelium is crucial for tumor cell entry and spread via lymphatic vessels. *Cancer Res.* **65**, 4739–4746 (2005).
- Hirakawa, S. et al. VEGF-C-induced lymphangiogenesis in sentinel lymph nodes promotes tumor metastasis to distant sites. *Blood* **109**, 1010–1017 (2007).
- Im, S. J. et al. Defining CD8<sup>+</sup> T cells that provide the proliferative burst after PD-1 therapy. *Nature* **537**, 417–421 (2016).
- Siddiqui, I. et al. Intratumoral Tcf1<sup>+</sup>PD-1<sup>+</sup>CD8<sup>+</sup> T cells with stem-like properties promote tumor control in response to vaccination and checkpoint blockade immunotherapy. *Immunity* **50**, 195–211 (2019).
- Lucca, L. E. et al. TIGIT signaling restores suppressor function of Th1 Tregs. *JCI Insight* **4**, 124427 (2019).
- Huang, A. C. et al. T-cell invigoration to tumour burden ratio associated with anti-PD-1 response. *Nature* **545**, 60–65 (2017).
- Tawbi, H. A. et al. Combined nivolumab and ipilimumab in melanoma metastatic to the brain. *N. Engl. J. Med.* **379**, 722–730 (2018).
- Taggart, D. et al. Anti-PD-1/anti-CTLA-4 efficacy in melanoma brain metastases depends on extracranial disease and augmentation of CD8<sup>+</sup> T cell trafficking. *Proc. Natl Acad. Sci. USA* **115**, E1540–E1549 (2018).
- Medawar, P. B. Immunity to homologous grafted skin. III. The fate of skin homografts transplanted to the brain, to subcutaneous tissue, and to the anterior chamber of the eye. *Br. J. Exp. Pathol.* **29**, 58–69 (1948).
- Volovitz, I. et al. Split immunity: immune inhibition of rat gliomas by subcutaneous exposure to unmodified live tumor cells. *J. Immunol.* **187**, 5452–5462 (2011).
- Breslin, J. W. et al. Vascular endothelial growth factor-C stimulates the lymphatic pump by a VEGF receptor-3-dependent mechanism. *Am. J. Physiol. Heart Circ. Physiol.* **293**, H709–H718 (2007).

**Publisher's note** Springer Nature remains neutral with regard to jurisdictional claims in published maps and institutional affiliations.

© The Author(s), under exclusive licence to Springer Nature Limited 2020

## Methods

### Mice

Four- to-eight-week-old mixed sex C57BL/6 mice, B6.129S2-*Igh<sup>tm1Cgn</sup>*/J ( $\mu$ Mt) mice and B6.SJL-*Ptpcr<sup>d</sup>Pepr<sup>b</sup>*/BoyCrl mice were purchased from the National Cancer Institute, Jackson Laboratory and Charles River, respectively, and subsequently bred and housed at Yale University. All procedures used in this study (sex-matched, age-matched) complied with federal guidelines and the institutional policies of the Yale School of Medicine Animal Care and Use Committee.

### Cells

GL261 parental cells were obtained from the NIH cancer cell repository. GL261-Luc cells were a gift from J. Zhou (Yale Neurosurgery) and C. Rothlin (Yale Immunobiology). YUMMER1.7 cell lines have previously been reported<sup>35</sup>. CT-2A and CT-2A-BFP cells were a gift from T. Mathivet (Paris Centre de Recherche Cardiovasculaire). B16 cells were a gift from N. Palm (Yale Immunobiology). HEK293T cells were purchased from ATCC. HEK293T, CT-2A, CT-2A-BFP and B16 cells were cultured in complete DMEM (4.5g l<sup>-1</sup> glucose, 10% FBS, 1% penicillin/streptomycin). YUMMER1.7 cells were cultured in DMEM/F-12 medium (10% FBS, 1% non-essential amino acids, 1% penicillin/streptomycin). GL261 and GL261-Luc cells were cultured in RPMI (10% FBS, 1% penicillin/streptomycin). All cells tested negative for mycoplasma contamination.

### Viral vectors

We used AAV9 encoding either human VEGF-C, mouse VEGF-C or soluble mouse VEGFR-3. AAV-VEGF-C (mouse) was generated using the psubCMV WPRE plasmid as previously reported for human VEGF-C<sup>4</sup>. Control AAV-VEGFR-3<sub>4-7</sub>-lg encodes domains 4–7 of mouse VEGFR-3 (that do not bind VEGF-C or VEGF-D) fused to the mouse IgG1Fc domain. VEGFR-3<sub>1-3</sub>-lg, which encodes domains 1–3 of mouse VEGFR-3, was used to sequester VEGF-C in vivo. Young mice (2–4 weeks old, AAV-VEGFR-3; 4–6 weeks old, AAV-VEGF-C) received an injection of a single dose of AAVs ( $3 \times 10^{12}$  viral particles per mouse per 3  $\mu$ l) into the cisterna magna. After 6–8 weeks, they were engrafted with intracerebral GL261 or CT-2A glioblastoma cells.

### Antibodies and tetramer

Anti-CD45 (30-F11, APC-Cy7, B266564; 104, BUV737, 9051755; 104, PE-Cy7, B268066; A20, APC, B254042; 30-F11, BV605, B278000), anti-CD3 (17A2, BV605, B264993; 145-2C11, APC-Cy7; 17A2, BUV737, 9042537; 17A2, biotin, B259691), anti-CD4 (GK1.5, Pacific Blue, B199050; GK1.5, BUV496, 8080653), anti-CD8 (53-6.7, BV711, B259953; 53-6.7, BUV395, 8306672), anti-IFN $\gamma$  (XMG1.2, BV711, B236526), anti-GZMB (GB11, FITC, B275568), anti-TNF (MP6-XT22, PE-Cy7, B251190), anti-IL-2 (JES6-5H4, APC, B248053), anti-CD44 (IM7, A700, B244378), anti-TBET (4B10, BV711, B268785), anti-TIM3 (RMT3-23, BV605, B262042), anti-FOXP3 (FJK-16 s, BV421, B266620), anti-TCF7 (C63D9, A488, 8, Cell Signaling Technology), anti-PD-1 (29F.1A12, APC-Cy7, B260172), anti-ROR $\gamma$ T (B2D, APC, E16663-102), anti-CD40 (PE, E028955), anti-CD80 (16-10A1, BUV395; 16-10A1, FITC, E029730), anti-CD86 (APC, B175381), anti-CX3CR1 (SA011F11, BV421, B231871), anti-Ly6C (AL21, FITC, 33380), anti-CD11c (N418, PE-Cy7, B264758; BV421, B264454), anti-CD11b (MI/70, PE, B228654), anti-Ly6G (IA8, APC-Cy7, B153128), anti-MHCII (M5/114.15.2, A700, B264454), anti-CD64 (X54-5/7.1, APC, B254424), anti-B220 (RA3-6B2, BUV496, 8096734), anti-NK1.1 (PK136, biotin, B255213), anti-CD19 (6D5, biotin, B250292), anti-F4/80 (BM8, biotin, B253458), anti-podoplanin (eBio8.1.1, PE, E11344-399, eBioscience), anti-CD31 (390, A647, 8187629) and anti-AKT (pS473) (M89-61, BV421, 7198801) antibodies other than anti-TCF7 and anti-podoplanin were purchased from BioLegend or BD Biosciences. Anti-VEGFR-3 and anti-FLT-4 (FAB743P, PE, ACBF0117091) antibodies were purchased from R&D Biosciences. The emv2-env tetramer (K<sup>b</sup>-restricted peptides

aa 604–611 of p15E protein (KSPWFTTL)) was made through the NIH tetramer core facility. KSPWFTTL peptide was made by Biomatik Corporation. The depletion antibodies anti-CD4 (GK1.5), anti-CD8 (YTS169.4), anti-PD-1 (RMP1-14), anti-CTLA4 (9H10), anti-TIM3 (RMT3-23) and anti-4-1BB (LOB12.3) were purchased from Bio X Cell.

### VEGFC mRNA construct

The *VEGFC* mRNA construct (Extended Data Fig. 2) was made by TriLink BioTechnologies (with full substitution of pseudouridine and 5-methylcytosine bases), capped using CleanCap Reagent AG and polyadenylated (120A). mRNA was mixed at a ratio of 1  $\mu$ g per 0.1  $\mu$ l of in vivo-JETPEI (Polyplus Transfection) and vortexed for 30 s and incubated in room temperature for 15 min before use. Control mRNA (Cy5-labelled GFP, *GFP* mRNA; luciferase, Luc mRNA) was also purchased from TriLink Biotechnologies. Recombinant proteins (VEGF-A, VEGF-B, VEGF-Cs and VEGF-D) were purchased from R&D Systems.

### Tissue processing and microscopy

Meningeal lymphatic vessels were detected on whole-mount preparations of the dura matter. Skull-cap samples were dissected, fixed in 2% PFA for one hour and immediately processed in a blocking solution (10% normal donkey serum, 1% bovine serum albumin, 0.3% PBS-Triton X-100) for overnight incubation at 4 °C. For detection of lymphatic vessels, samples were incubated with the primary antibody anti-LYVE-1 (AngioBio, 11-034, 1:400), overnight at 4 °C, then washed five times at room temperature in PBS and 0.5% Triton X-100, before incubation with a fluoro-conjugated secondary antibody (Alexa Fluor anti-rabbit 647, Thermo Fisher Scientific, 1:500) diluted in PBS and 5% normal donkey serum. Meningeal lymphatic vessel images were acquired using a spinning-disk confocal (Nikon Eclipse Ti). Quantitative analysis of meningeal lymphatic coverage was performed using either Fiji or ImageJ image-processing software (NIH or Bethesda). LYVE-1<sup>+</sup> macrophages that are less intensely labelled than lymphatic vessels were eliminated by adjusting image contrast. Otsu's thresholding method was then used to convert captured images into binary images. The fluorescence-labelled area covered by meningeal lymphatic vessels was measured in the confluence of sinuses and the sagittal sinus regions, and was normalized to the average fluorescence of the same regions of meningeal lymphatic vasculature in AAV-CTRL-treated mice. For brain sections, anti-CD3 (17A2, biotin), anti-CD31 (2H8, GeneTex) and anti-LYVE1 (AF2125, R&D Systems) antibodies were used with anti-streptavidin (FITC, BD Biosciences, 4031801), anti-hamster (127-165-160, Cy3, Jackson ImmunoResearch, 128827) and anti-goat (705-175-147, Cy5, Jackson ImmunoResearch, 138513) secondary antibodies, respectively. Confocal images were taken on a Leica SP8 microscope. Three-dimensional (3D) rendering was completed using Imaris 8 software (Oxford Instruments).

### Western blot

HEK293T cells were transfected with the *VEGFC* mRNA construct combined with lipofectamine. Samples were lysed in RIPA buffer and boiled for 5 min with sample buffer. For in vivo delivery, *VEGFC* mRNA with JETPEI was used. The CSF was pooled from 10 mice and spun down to remove cells; the CSF was then filtered using a 100k Amicon filter and the wash-through was boiled with sample buffer for western blotting. Western blotting was performed in a similar manner to that previously reported<sup>2</sup>. In brief, 15% gels were used and run at 10 mA per gel for 30 min and 40 mA per gel until separation of ladder. Wet transfer was performed at 120 mA per gel for 90 min on ice. Anti-VEGF-C antibody was used at a concentration of 1:1,000 (R&D Systems, AF752) and incubated overnight in the cold room. After washing, HRP-conjugated anti-goat secondary antibodies were used at a concentration of 1:5,000 at room temperature for 2 h and imaged using the ChemiDoc MP imaging system (Bio-Rad).

## Tumour inoculation

Mice were anaesthetized using a mixture of ketamine (50 mg kg<sup>-1</sup>) and xylazine (5 mg kg<sup>-1</sup>), injected intraperitoneally. Mice heads were shaved and then placed in a stereotaxic frame. After sterilization of the scalp with alcohol and betadine, a midline scalp incision was made to expose the coronal and sagittal sutures, and a burr hole was drilled 2 mm lateral to the sagittal suture and 0.5 mm posterior to the bregma. A 10- $\mu$ l Hamilton syringe loaded with tumour cells was inserted into the burr hole at a depth of 2.5 mm from the surface of the brain and left to equilibrate for 1 min before infusion. A micro-infusion pump (World Precision Instruments) was used to infuse 3  $\mu$ l of tumour cells at 1  $\mu$ l min<sup>-1</sup>. Once the infusion was finished, the syringe was left in place for another minute before removal of the syringe. Bone wax was used to fill the burr hole and the skin was stapled and cleaned. Following intramuscular administration of analgesic (meloxicam and buprenorphine, 1 mg kg<sup>-1</sup>), mice were placed in a heated cage until full recovery.

## Intracisterna-magna injection and collection of CSF

For intracisterna-magna injections, mice were anaesthetized using ketamine and xylazine, and the dorsal neck was shaved and cleaned with alcohol. A 2-cm incision was made at the base of the skull, and the dorsal neck muscles were separated using forceps. After visualization of the cisterna magna, a Hamilton syringe with a 15-degree, 33-gauge needle was used to puncture the dura. Three microlitres of AAV9 (3  $\times$  10<sup>12</sup> viral particles per mouse) or mRNA vector (4–5  $\mu$ g) was administered per mouse at a rate of 1  $\mu$ l min<sup>-1</sup>. After completion of the injection, the needle was left in to prevent backflow for an additional 3 min. For CSF collection, a custom-pulled micropipette (0.75/1 lbrl GF; Stoelting) was used to penetrate the dura and ensure no blood was collected. The skin was stapled and cleaned and the same postoperative procedures were performed as for the tumour inoculations.

## Ligation of deep cervical lymph nodes

For ligation of lymph nodes, mice were anaesthetized using ketamine and xylazine, and the rostral neck was shaved and disinfected. A 2-cm incision was made and the salivary glands containing the superficial cervical lymph nodes were retracted and the deep cervical lymph nodes were visualized. The afferent lymph vessels were tied off with a 4-0 Vicryl suture, and then cauterized. The incision was closed with a 4-0 Vicryl suture and mice were subjected to the same postoperative procedures as above.

## Flank tumour inoculation

Mice were anaesthetized using ketamine and xylazine, and the flank was shaved and disinfected. A 1-ml syringe with a 30G needle was used to deliver 100  $\mu$ l of 500,000 cells subcutaneously. For GL261-Luc cells, cells were mixed in a 1:1 volume with Matrigel (Corning) before delivering.

## Adoptive transfer

To evaluate memory against tumour using adoptive transfer, T cells from deep cervical lymph nodes and spleens of mice that rejected tumours after treatment with *VEGFC* mRNA and anti-PD-1 were isolated using the EasySep Mouse T cell Isolation Kit (StemCell Technologies) and transferred into naive mice 24 h before tumour inoculation (all the T cells from one donor were transferred to one recipient).

To study leukocyte trafficking after treatment with VEGF-C, CD45.2 mice were inoculated with GL261 tumours. At day 7, mice were treated with *GFP* mRNA or *VEGFC* mRNA. Seven days after treatment, deep cervical lymph nodes were collected and filtered through 70- $\mu$ m filter paper, and whole-leukocyte suspensions (30 million cells per mouse; approximately 3–5 deep cervical lymph nodes transferred into one mouse) were adoptively transferred in to CD45.1 mice bearing 7-day tumours. After transfer, mice were treated with *GFP* mRNA or *VEGFC*

mRNA intracisternally. Five days later, deep cervical lymph nodes and brain tissue were collected to evaluate immune cell trafficking. Five minutes before euthanizing the mouse, 25  $\mu$ g of anti-CD45 PE (30-F11, PE, Biolegend) antibodies were administered intravenously to stain circulating immune cells.

## IVIS imaging

Mice were anaesthetized using isoflurane and injected intraperitoneally with RediJect D-Luciferin Ultra (PerkinElmer) (200  $\mu$ l, 30 mg ml<sup>-1</sup>). After 10 min, mice were imaged using the IVIS Spectrum In Vivo Imaging System (PerkinElmer).

## RNA-seq

RNA-seq data were aligned using STAR (STAR/2.5.3a-foss-2016b, mm10 assembly) with parameters: –runThreadN 20 –outSAMtype BAM SortedByCoordinate –limitBAMsortRAM 35129075129 –outFilterMultimapNmax 1 –outFilterMismatchNmax 999 –outFilterMismatchNoverLmax 0.02 –alignIntronMin 20 –alignIntronMax 1000000 –alignMatesGapMax 1000000 for mapping of repetitive elements. Counts were counted using BEDTools (BEDTools/2.27.1-foss-2016b) (coverageBed function), normalized using DESeq2 and graphed using the Morpheus web tool from the Broad Institute. Human RNA-seq data were obtained from TCGA and GTEx databases and analysed using the above parameters (hg38 assembly) (Extended Data Fig. 2a–c), and survival stratified by VEGF-C expression was analysed using OncoLnc (www.OncoLnc.org) (Extended Data Fig. 2e, f).

## Isolation of mononuclear cells and flow cytometry

Tissue was collected and incubated in a digestion cocktail containing 1 mg ml<sup>-1</sup> collagenase D (Roche), 1 mg ml<sup>-1</sup> collagenase A (Roche) and 30  $\mu$ g ml<sup>-1</sup> DNase I (Sigma-Aldrich) in complete RPMI (10% FBS) at 37 °C for 30 min. Tissue was then filtered through a 70- $\mu$ m filter. For brain tissues, cells were mixed in 4 ml of 25% Percoll (Sigma-Aldrich) solution and centrifuged at 530g for 15 min without a brake. The Percoll layer was removed and cells were diluted in 5 ml of 1% BSA. Cells were treated with ACK buffer and resuspended in 1% BSA. At this point, cells were counted using an automated cell counter (Thermo Fisher Scientific).

For tetramer experiments, staining was performed with antibodies (1:200) and tetramer (1:50) for 60 min at room temperature. Cells were washed to remove excess antibodies and resuspended in 1% BSA with 10  $\mu$ l of CountBright absolute counting beads (Life Technologies) for multiparameter analyses on the LSR II flow cytometer (Becton Dickinson), and then analysed using FlowJo software (10.5.3, Tree Star). For calculation of tetramer-positive T cells in each organ the following formula was used: number of tetramer-positive T cells  $\times$  (no. of input beads/no. of counted beads)  $\times$  (no. of cells from automated counter/no. of total events in flow cytometry).

For cytokine stimulation, surface markers were first stained on ice for 30 min. After washing, cells were stimulated in complete RPMI with 200  $\mu$ l of 1 $\times$  eBioscience Cell Stimulation Cocktail (Thermo Fisher Scientific) without protein transporter inhibitor for 1 h at 37 °C. Fifty microlitres of 5 $\times$  eBioscience Cell Stimulation Cocktail with protein transporter (Thermo Fisher Scientific) was added and incubated for an additional 4 h. Cells were then fixed with 100  $\mu$ l 2% formaldehyde on ice for 45 min. Cells were washed with 1 $\times$  Perm/Wash Buffer (BD Cytofix/Cytoperm, BD Biosciences), and then permeabilized with 1 $\times$  Perm/Wash Buffer (BD Cytofix/Cytoperm, BD Biosciences) for 10 min on ice. Intracellular antigens were stained on ice for 30 min.

For transcription factor staining, surface markers were first stained on ice for 30 min. Cells were then fixed with 100  $\mu$ l 2% formaldehyde on ice for 45 min. Cells were washed with 1 $\times$  Perm/Wash Buffer (eBioscience FOXP3/Transcription Factor Staining Buffer Set, Thermo Fisher Scientific), and then permeabilized with 1 $\times$  FOXP3 Perm/Wash Buffer for 10 min on ice. Intracellular antigens were stained on ice for 30 min.



For AKT phosphorylation staining, surface markers were first stained on ice for 30 min. Cells were then fixed and washed following the directions of the BD Phosflow kit. Samples were run on an Attune NxT flow cytometer.

#### Enzyme-linked immunosorbent assay

Enzyme-linked immunosorbent assay (ELISA) was performed using a mouse VEGF-C ELISA Kit (Cusabio LLC, E07361m-96) following the manufacturer's instructions.

#### mRNA tropism

Mice were injected in the cisterna magna with Cy5-labelled *GFP* mRNA with JETPEI. A day (24 h) after injection, brains, meninges and lymph nodes were collected for flow cytometry. Samples were run on an Attune NxT flow cytometer.

#### Blood–brain barrier permeability

Mice were injected intravenously with fluorescein-labelled dextran (molecular weight, 70,000 kDa) (Thermo Fisher Scientific) or 0.5% Evans Blue. For microscopy, brains were collected 2 h later and flash-frozen for sectioning. For Evans Blue quantification, mice were perfused with ice-cold PBS intraventricularly (heart) and Evans Blue was extracted using dimethylformamide. The relative absorbance was measured using a SpectraMax i3 platform (Molecular Devices) at 620-nm wavelength.

#### T cell proliferation

T cells were isolated using the EasySep Mouse T cell Isolation Kit (StemCell Technologies). T cells were stained using CellTrace Violet, and stimulated with CD3/CD28 antibodies from Bio X Cell for 24 h in complete RPMI. After 24 h, cells were resuspended in medium containing IL-2 and VEGF-C for 4 days and FACS was performed at the end of the 4 days.

#### Culture and stimulation of bone-marrow-derived dendritic cells

Bone marrow was collected from wild-type mice and cultured in complete RPMI supplemented with granulocyte–macrophage colony-stimulating factor for six days. After 6 days, cells were stimulated with LPS and VEGF-C for 24 h and FACS was performed.

#### Statistical analysis

For revision experiments, power analysis was completed to estimate sample size. A summary of key phenotypes that we observed throughout multiple experiments were graphed. These experiments showed response rates of around 70%, and the sample size calculation required for an  $\alpha$  value of 0.05 was  $n = 6$  (power 95%) and  $n = 5$  (power 90%).

For all tumour-related experiments with luciferase constructs, mice were measured for tumour size at day 4–6, and randomized into groups to ensure similar tumour size. For experiments in which mice were pooled, those mice within each pool were also ensured to have tumours of a similar size to minimize variation in downstream analysis.

Mice that underwent treatment were randomized after the measurement of tumour size at day seven. Investigators were not blinded for the majority of the study; however, all survival studies were monitored with the help of veterinarians from the Yale animal facility who were blinded to the studies and reported endpoints accordingly. In addition,

animals were in mixed cages and labelled with numbers that blinded all involved with scoring mice health.

Survival curves were analysed using a log-rank (Mantel–Cox) test. For other data, normally distributed continuous variable comparisons used a two-tailed unpaired Student's *t*-test or paired Student's *t*-test with Prism software.

#### Graphical illustrations

Graphical illustrations were made using BioRender (<https://biorender.com/>).

#### Reporting summary

Further information on research design is available in the Nature Research Reporting Summary linked to this paper.

#### Data availability

No new sequencing data were generated for this study. All datasets generated and/or analysed during the current study are available in the Article, the Source Data files that accompany Figs. 1–4 and Extended Data Fig. 1–10, or the Supplementary Information.

#### Code availability

All of the code used for analysis is described in the methods. Detailed files will be made available from the corresponding authors on request.

35. Wang, J. et al. UV-induced somatic mutations elicit a functional T cell response in the YUMMER1.7 mouse melanoma model. *Pigment Cell Melanoma Res.* **30**, 428–435 (2017).

**Acknowledgements** We thank members of the A.I. laboratory for insightful discussions and help with protocols; M. Saltzman (Yale Biomedical Engineering) for allowing us to use mice stereotaxic equipment and for help with materials; S. Lee from the J.-L.T. laboratory for initial help in breeding mice; and the ICM Vectorology platform for production of AAV material. This study was supported by National Institutes of Health grants T32GM007205 (MSTP training grant) and F30CA239444 (to E.S.); AI054359 and AI127429 (to A.I.); R01EB016629-01 and R01 EY025979-01 (to J.-L.T.); and CA196660, CA128814 and CA121974 (to M.B.). A.I. is an investigator of the Howard Hughes Medical Institute. L.S.B.B. and J.-L.T. were supported by the Yale School of Medicine. Work in the K.A. laboratory was funded by the iCAN Digital Precision Cancer Medicine Flagship, Academy of Finland (grants 292816, 273817 and 307366), the Centre of Excellence Program 2014–2019, the Cancer Foundation in Finland, the Sigrid Juselius Foundation, the Hospital District of Helsinki, Uusimaa Research Grants, Helsinki Institute of Life Sciences (HiLIFE) and Biocenter Finland.

**Author contributions** E.S., J.-L.T. and A.I. planned the project. E.S. and A.I. designed, analysed and interpreted data and wrote the manuscript. E.S., L.S.B.B. and T.M. performed experiments and analysed data. H.D. bred and cared for mice. J.-L.T. provided AAV material. S.A., M.B. and K.A. provided expertise, materials and analysis of data.

**Competing interests** A.I., E.S. and J.-L.T. have filed a patent related to the manuscript as inventors (application number, US 62/768,390; status of application, provisional; specific aspect of manuscript covered in patent application, manipulation of meningeal lymphatic vasculature for brain and CNS tumour therapy. K.A. is an inventor on several patents that relate to VEGF-C. He and his wife currently have no income, stock or other benefits from companies that are related to the manuscript. Helsinki University is a shareholder in companies that are related to the use of VEGF-C. M.B. is a consultant for Eli Lilly and Company.

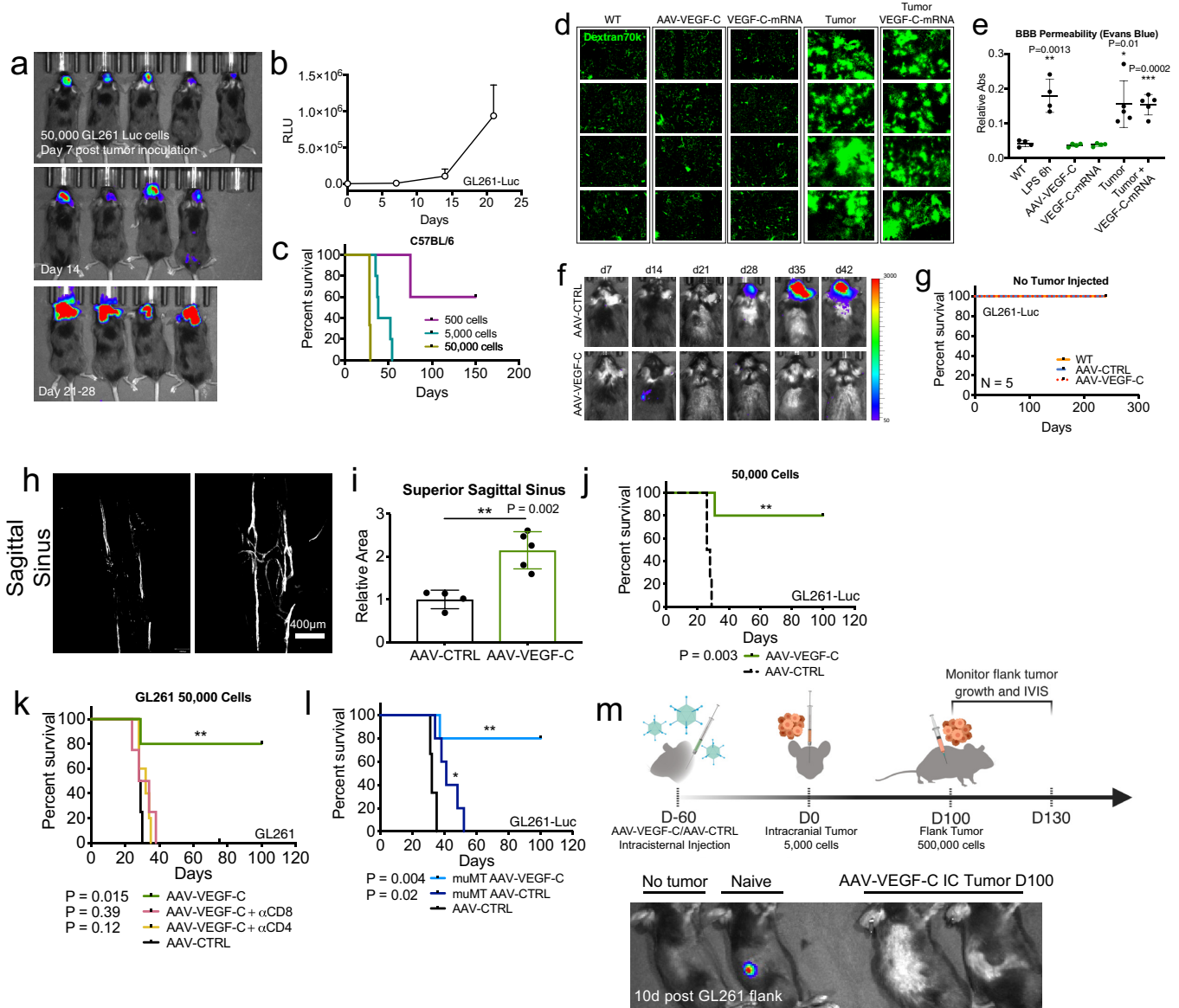
#### Additional information

**Supplementary information** is available for this paper at <https://doi.org/10.1038/s41586-019-1912-x>.

**Correspondence** and requests for materials should be addressed to J.-L.T. or A.I.

**Peer review information** Nature thanks Jonathan Kipnis, Ingo K. Mellingerhoff, Michelle Monje-Deisseroth, Christine Moussion and Shannon Turley for their contribution to the peer review of this work.

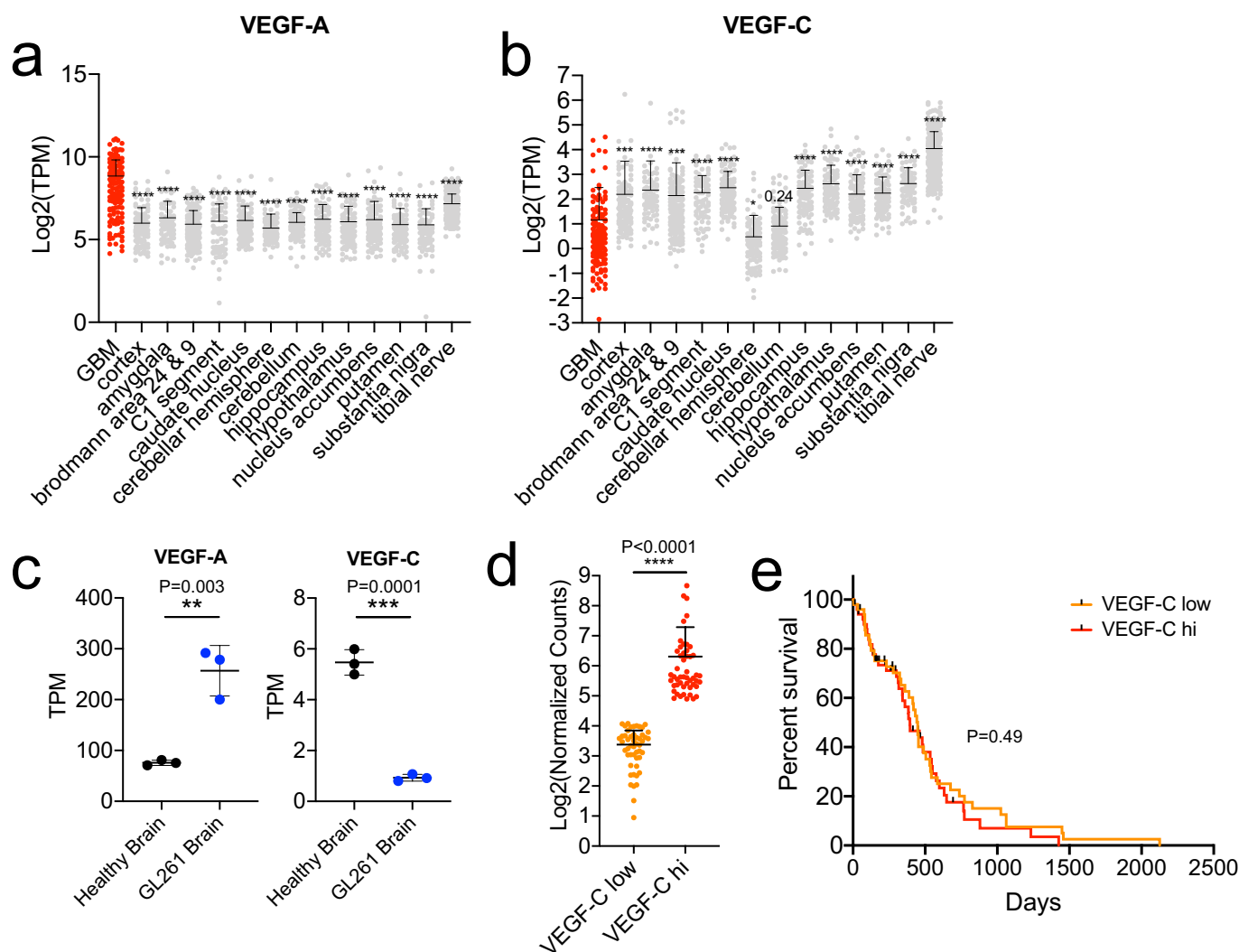
**Reprints and permissions information** is available at <http://www.nature.com/reprints>.



**Extended Data Fig. 1 | Increased meningeal lymphatic vasculature confers protection against intracranial glioblastoma challenge and provides long-term immunity without perturbation of the blood-brain barrier.**

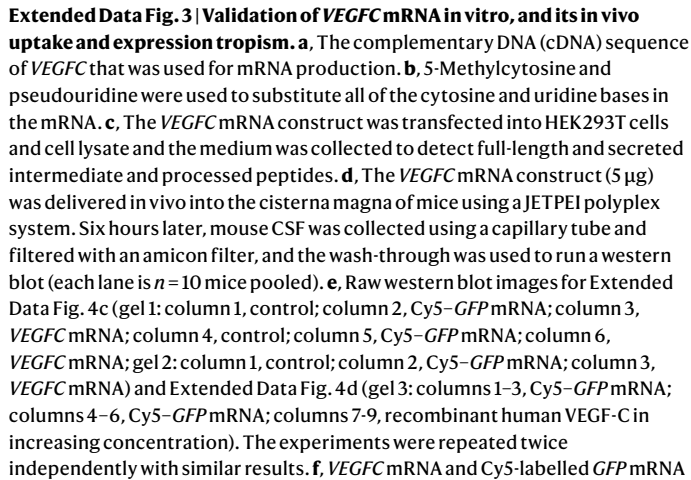
**a, b**, Mice inoculated with 50,000 GL261-Luc cells were imaged every 7 days and showed consistent and reliable tumour growth ( $n=4$ ). **c**, GL261-Luc cells result in lethality in mice in a cell-number-dependent manner (500 cells,  $n=5$  mice; 5,000 cells,  $n=5$  mice; 50,000 cells,  $n=9$  mice). **d**, Mice were injected intravenously with dextran-fluorescein (molecular weight, 70,000 kDa) and euthanized after 2 h. Brains were collected and cryosectioned ( $n=4$ ). The experiment was repeated independently with similar results. **e**, Mice were injected intravenously with 0.5% Evans Blue. After 2 h mice were perfused intraventricularly and Evans Blue was extracted from brain tissue using dimethylformamide (wild type, LPS, AAV-VEGF-C, VEGF-C-mRNA,  $n=4$ ; tumour, tumour + VEGF-C-mRNA,  $n=5$ ). BBB, blood-brain barrier. **f**, Representative images of AAV-CTRL and AAV-VEGF-C-treated mice after implantation of 5,000 cells. The experiment was repeated independently with similar results. **g**, Monitoring of the long-term survival of mice after AAV-VEGF-C and AAV-CTRL injections into the cisterna magna ( $n=5$ ). **h, i**, C57BL/6 mice received an injection of AAV-CTRL or AAV-VEGF-C through the cisterna magna. Six to eight weeks later, mice were euthanized and the dura was collected to image the

lymphatic vasculature (LYVE1\*) in the superior sagittal sinus (AAV-CTRL,  $n=4$ ; AAV-VEGF-C,  $n=5$ ). **j**, C57BL/6 mice that had been injected with CTRL-AAV or AAV-VEGF-C two months previously were implanted with 50,000 GL261-Luc cells in the striatum and monitored for survival (AAV-CTRL,  $n=4$ ; AAV-VEGF-C,  $n=5$ ). **k**, AAV-CTRL- or AAV-VEGF-C-treated mice were depleted of CD4 or CD8 T cells using anti-CD4 (GK1.5) or anti-CD8 (YTS169.4) antibodies starting one day before tumour inoculation (GL261) and redosed every four days afterwards (AAV-CTRL,  $n=4$ ; AAV-VEGF-C,  $n=5$ ; AAV-VEGF-C + anti-CD8,  $n=4$ ; AAV-VEGF-C + anti-CD4,  $n=5$ ). **l**,  $\mu$ MT B-cell-deficient mice were injected with AAV-CTRL or AAV-VEGF-C and challenged with 50,000 GL261-Luc cells two months afterwards (AAV-CTRL,  $n=5$ ;  $\mu$ MT AAV-CTRL,  $n=3$ ;  $\mu$ MT AAV-VEGF-C,  $n=5$ ). **m**, Top, schematic of the schedule of procedures for the experiments below (bottom panel) and in Fig. 1f. Mice injected with AAV-CTRL or AAV-VEGF-C that survived over 100 days after challenge with 5,000 GL261-Luc cells were rechallenged with 500,000 GL261-Luc cells in the flank. Bottom, IVIS imaging of mice ten days after flank rechallenge. Data are pooled from two independent experiments (**h-m**) and are mean  $\pm$  s.d. \* $P < 0.05$ ; \*\* $P < 0.01$ ; \*\*\* $P < 0.001$ ; \*\*\*\* $P < 0.0001$  (two-tailed unpaired Student's  $t$ -test or two-sided log-rank Mantel-Cox test).

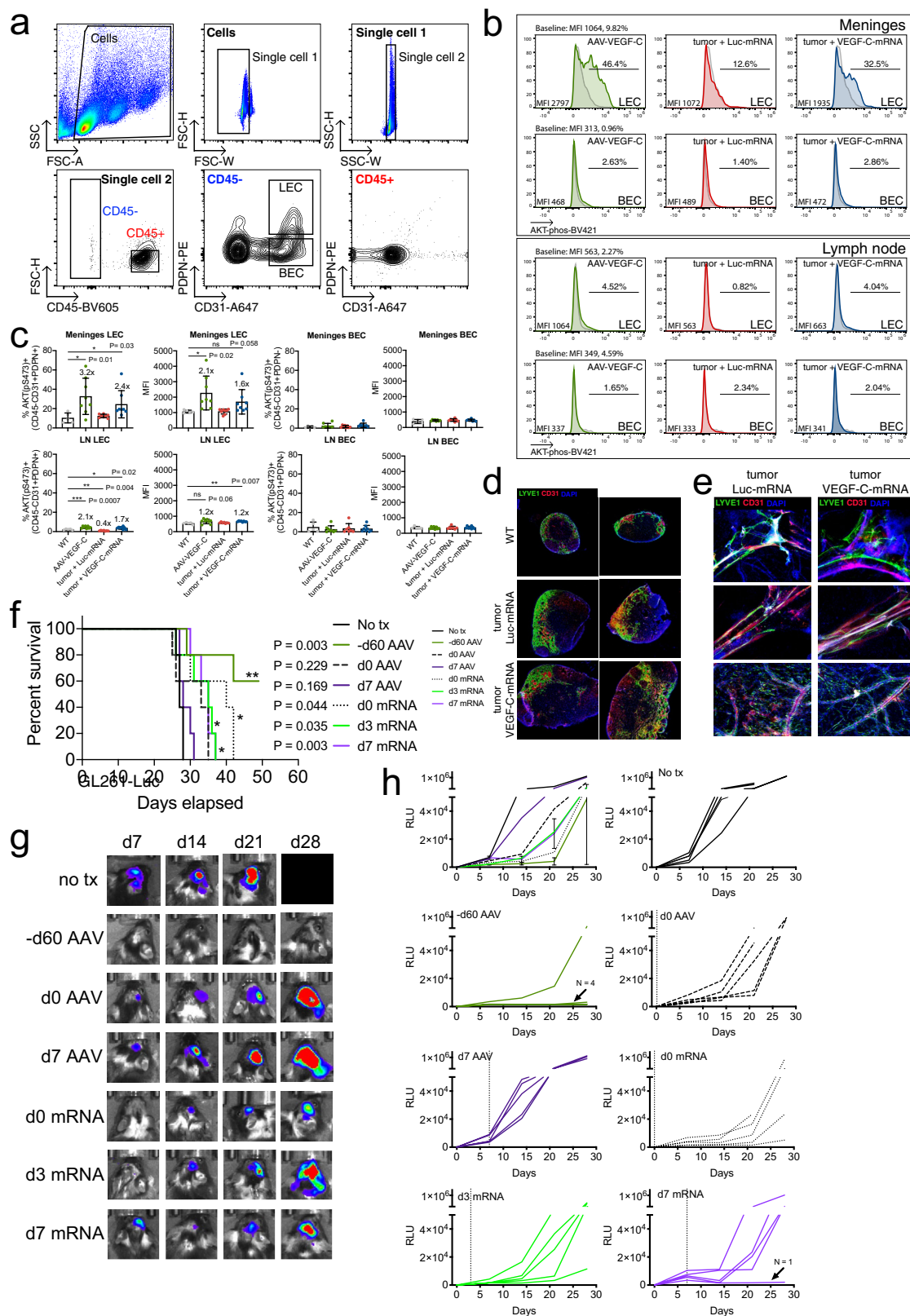


**Extended Data Fig. 2 | Correlation of VEGF-C expression profiles between human and mouse glioblastoma.** **a–c**, RNA-seq data of tumour tissue and healthy brain tissue from different regions (TCGA, study accession phs000178, v10.p8, and GTEx, study accession phs000424.v7.p2, respectively). **a, b**, Expression profiles of VEGF-A (**a**) and VEGF-C (**b**) (glioblastoma (GBM),  $n=147$ ; cortex,  $n=133$ ; amygdala,  $n=81$ ; Brodmann areas 24 and 9,  $n=215$ ; C1 segment,  $n=75$ ; caudate nucleus,  $n=135$ ; cerebellar hemisphere,  $n=115$ ; cerebellum,  $n=146$ ; hippocampus,  $n=103$ ; hypothalamus,  $n=101$ ; nucleus

accumbens,  $n=125$ ; putamen,  $n=103$ ; substantia nigra,  $n=72$ ; tibial nerve,  $n=329$ ). **c**, RNA-seq data of mouse healthy brain and GL261 tumours were analysed ( $n=3$  biologically independent samples). **d**, ONCLNC (www.oncolnc.org) data of patients with glioblastoma stratified into two groups (VEGF-C low, lower 33%; VEGF-C high, upper 33%;  $n=50$ ). **e**, Kaplan–Meier survival curves of patients from **d** ( $n=50$ ). Data are mean  $\pm$  s.d. \* $P<0.05$ ; \*\* $P<0.01$ ; \*\*\* $P<0.001$ ; \*\*\*\* $P<0.0001$  (two-tailed unpaired Student's  $t$ -test, two-sided log-rank Mantel–Cox test or Pearson's correlation).



were mixed at a 1:1 ratio and delivered to mice in vivo using JETPEI. Fifteen minutes later, mice were euthanized and the whole skull cap was imaged to observe the distribution of mRNA particles. The experiments were repeated independently twice with similar results. **g, h**, *VEGFC* mRNA and Cy5-labelled *GFP* mRNA were mixed at a 1:1 ratio and delivered to mice in vivo using JETPEI. After 24 h, the brains, meninges and lymph nodes of treated mice were collected for flow cytometry to measure the percentage of Cy5-positive cells in each compartment (control,  $n = 6$ ; Cy5-labelled mRNA,  $n = 9$ ; data are pooled from two independent experiments). **i**, The CSF, meninges, brain and serum were collected after two months (AAV-CTRL, AAV-VEGF-C), after 24 h (*GFP* mRNA, *VEGFC* mRNA) or at days 7 and 28 after tumour inoculation, and an ELISA was performed to detect VEGF-C (CSF: AAV-VEGF-C,  $n = 6$ ; other groups,  $n = 3$ ; 5 mice were pooled for each sample; meninges: AAV-VEGF-C,  $n = 6$ ; 7-day tumour,  $n = 3$ ; other groups,  $n = 5$ ; brain: AAV-CTRL, *GFP* mRNA,  $n = 6$ ; AAV-VEGF-C, *VEGFC* mRNA,  $n = 5$ ; 7-day tumour,  $n = 3$ ; 28-day tumour,  $n = 7$ ; serum:  $n = 3$ ). Data are mean  $\pm$  s.d. \* $P < 0.05$ ; \*\* $P < 0.01$ ; \*\*\* $P < 0.001$ ; \*\*\*\* $P < 0.0001$  (two-tailed unpaired Student's *t*-test).



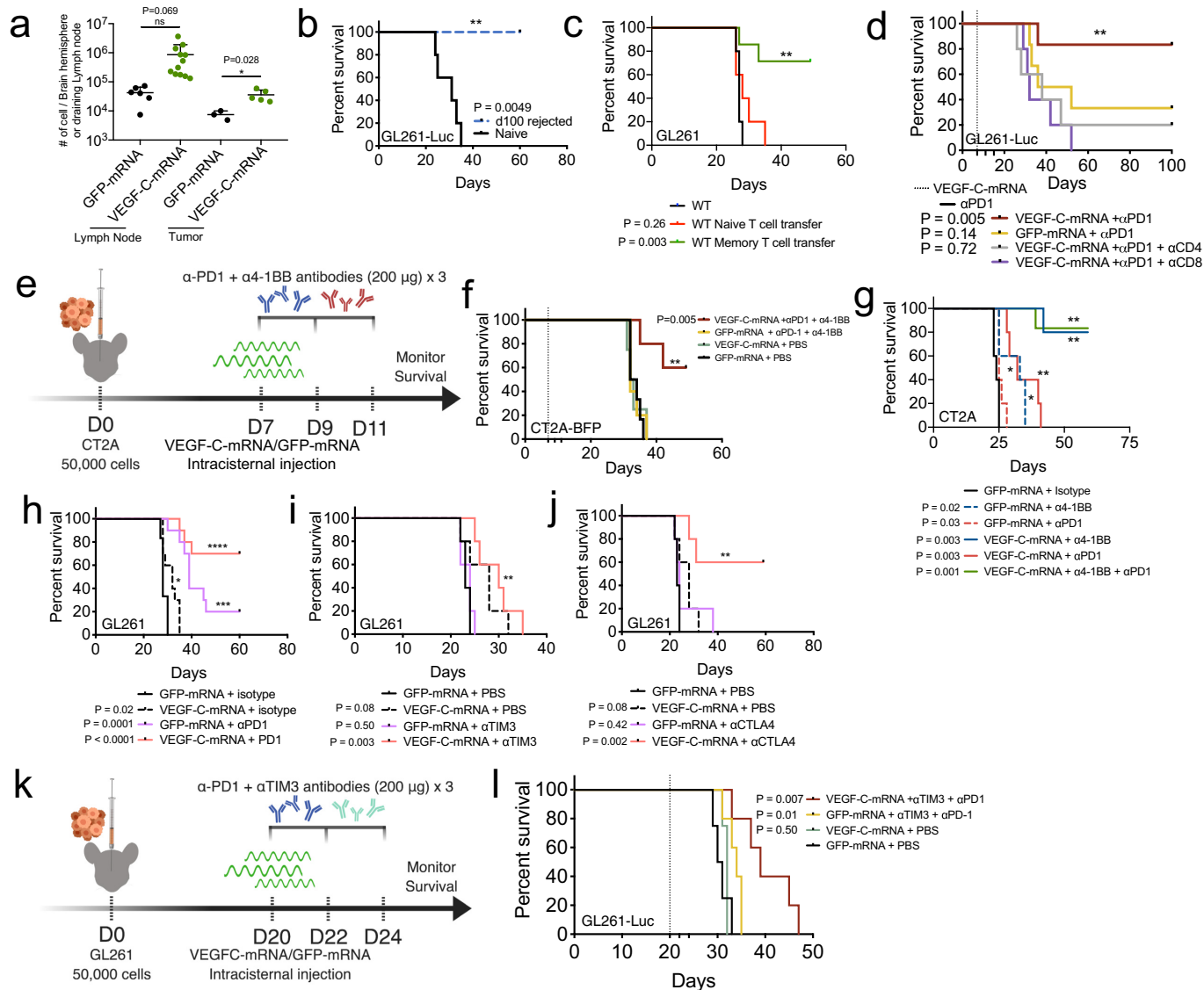
**Extended Data Fig. 4** | See next page for caption.



**Extended Data Fig. 4 | VEGF-C signals specifically in lymphatic endothelial cells in the meninges and deep cervical lymph nodes and provides survival benefits in a manner that depends on the administration time point.**

**a**, Gating strategy for LECs and BECs. **b**, Concatenated FACS plots of LECs and BECs from meninges and lymph nodes, depicting AKT phosphorylation intensity. The experiment was repeated independently with similar results. **c**, Quantification of the AKT(pS473)-positive population and mean fluorescence intensity (MFI) within LECs and BECs in the meninges and deep cervical lymph nodes (meninges: wild type,  $n = 5$ ; AAV-VEGF-C, tumour + Luc mRNA, tumour + *VEGFC* mRNA,  $n = 8$ ; lymph nodes: wild type,  $n = 5$ ; AAV-VEGF-C,  $n = 8$ ; tumour + Luc mRNA,  $n = 7$ ; tumour + *VEGFC* mRNA,

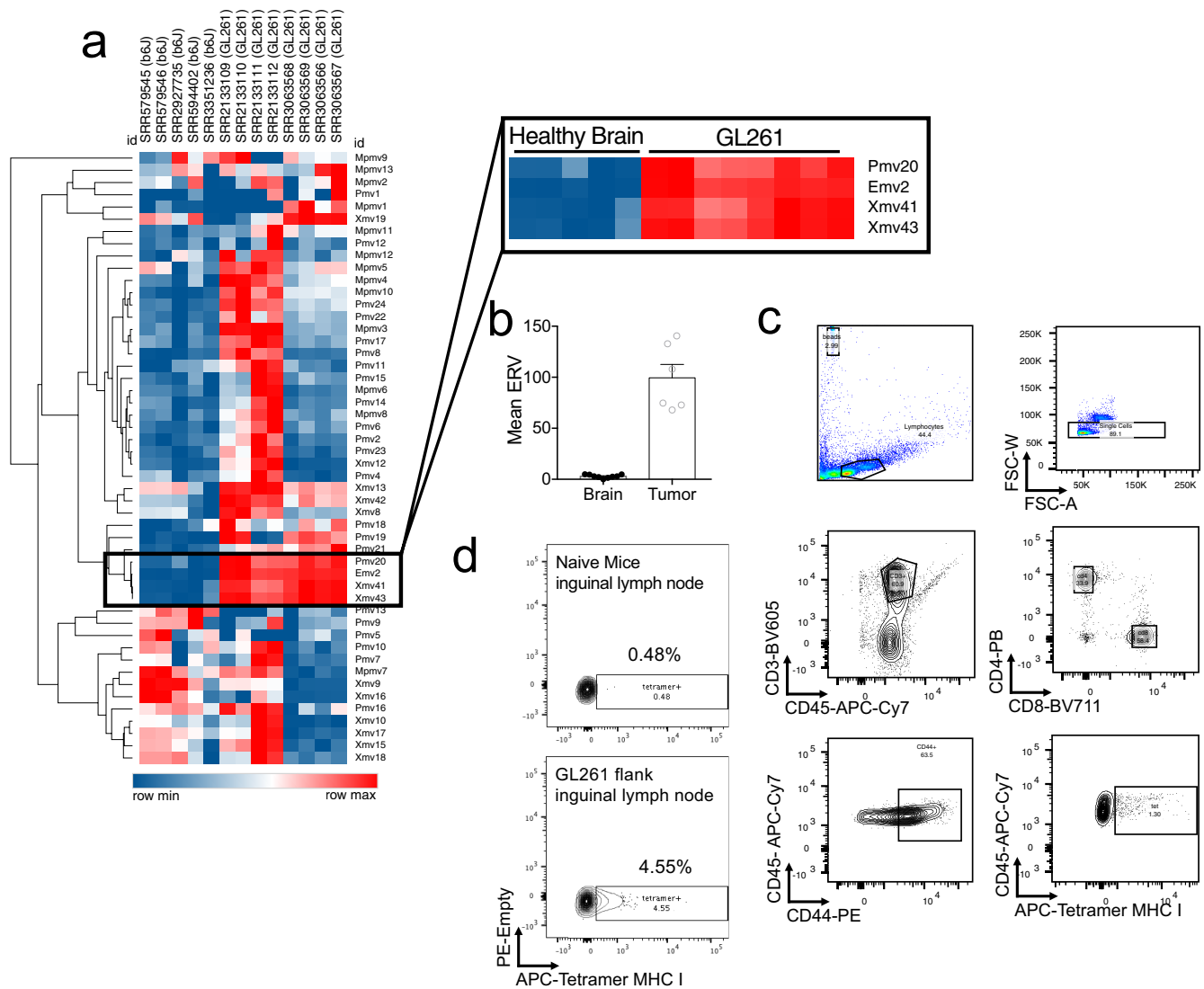
$n = 8$ ). **d**, Fluorescence microscopy images of deep cervical lymph nodes after treatment with *VEGFC* mRNA in tumour-bearing mice (CD31, red; LYVE1, green; DAPI, blue). **e**, Fluorescence microscopy images of meninges after treatment with *VEGFC* mRNA in tumour-bearing mice (CD31, red; LYVE1, green; DAPI, blue). The experiment was repeated independently with similar results. **f–h**, Mice were treated with AAV-VEGF-C or *VEGFC* mRNA at different time points relative to GL261-Luc tumour inoculation (day 0). Tumour growth kinetics (**g**, **h**) and survival (**f**) were monitored ( $n = 5$  for all groups, no tx refers to mice receiving no treatment). Data are mean  $\pm$  s.d. \* $P < 0.05$ ; \*\* $P < 0.01$ ; \*\*\* $P < 0.001$ ; \*\*\*\* $P < 0.0001$  (two-tailed unpaired Student's *t*-test or two-sided log-rank Mantel–Cox test).



**Extended Data Fig. 5 | Therapeutic delivery of VEGF-C potentiates checkpoint inhibitor therapy even at late stages of tumour development.**

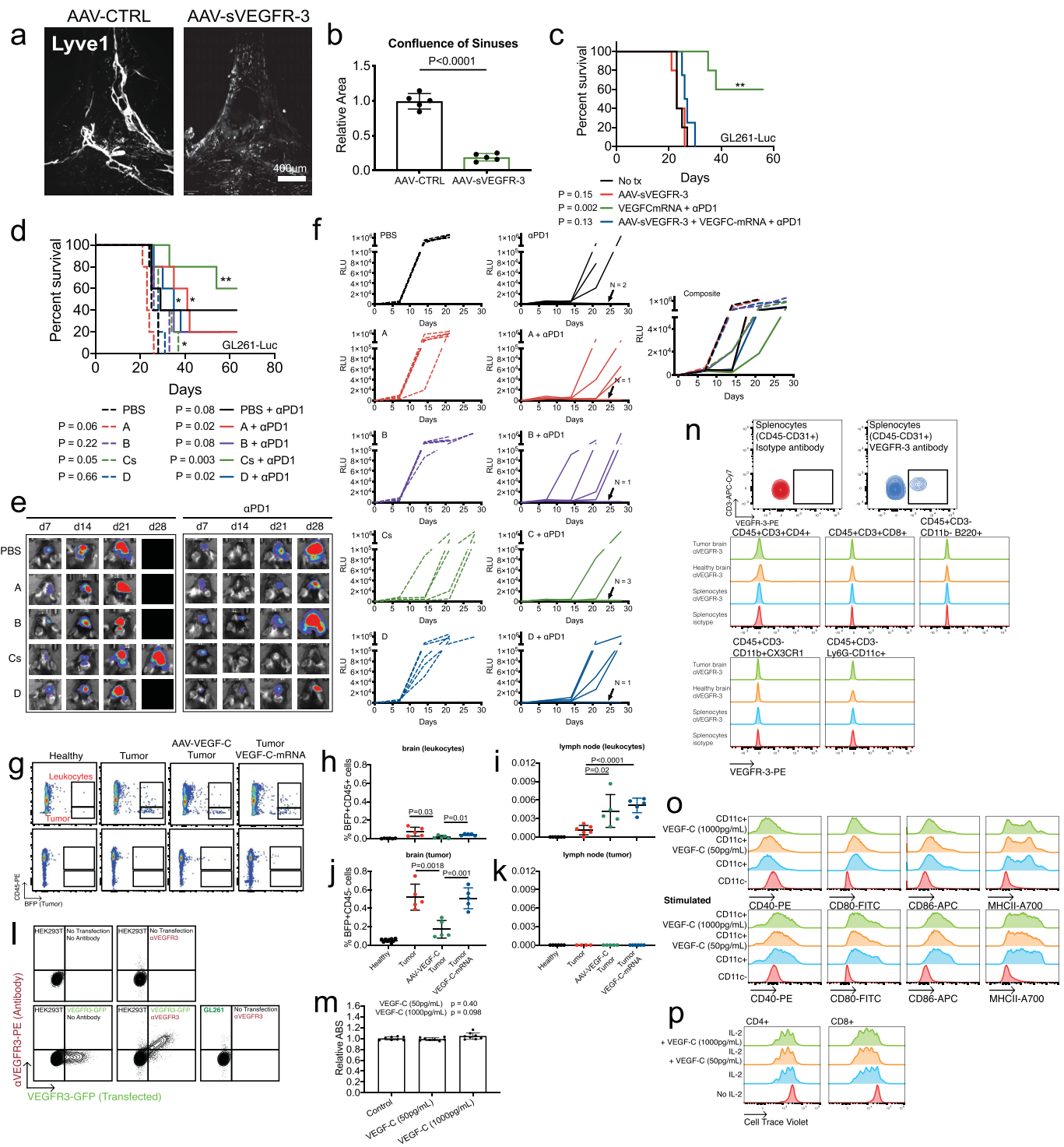
**a**, Related to Fig. 3c, d. Quantification of the number of cells per tumour-bearing brain hemisphere or lymph node using CountBright absolute counting beads and autocounter (see Methods for details) (lymph nodes: *GFP* mRNA,  $n=6$ ; *VEGFC* mRNA,  $n=12$ ; tumour: *GFP* mRNA,  $n=3$ ; *VEGFC* mRNA,  $n=5$ ). **b**, Mice that rejected tumours after combination therapy with *VEGFC* mRNA and anti-PD-1 (RMP1-14) were rechallenged in the contralateral hemisphere and observed for survival (naive,  $n=5$ ; day 100 rejected,  $n=4$ ). **c**, T cells from lymph nodes and spleens from mice that rejected tumours after combination therapy with *VEGFC* mRNA and anti-PD-1 (RMP1-14) or naive wild-type mice were isolated and transferred into naive wild-type mice intravenously. After 24 h, GL261 tumours were inoculated intracranially and the mice were observed for survival (wild type,  $n=5$ ; wild type with transfer of naive T cells,  $n=5$ ; wild type with transfer of memory T cells,  $n=7$ ). **d**, Mice inoculated with 50,000 GL261-Luc cells were treated with *VEGFC* mRNA or *GFP* mRNA (day 7) and with either anti-PD-1 (RMP1-14) antibodies or isotype antibodies (days 7, 9 and 11), and monitored for survival. Mice were depleted of CD4 or CD8 T cells using anti-CD4 (GK1.5) or anti-CD8 (YTS169.4) antibodies starting one day before tumour inoculation and redosed every four days afterwards (*VEGFC* mRNA + anti-PD-1,

$n=6$ ; *GFP* mRNA + anti-PD-1,  $n=6$ ; *VEGFC* mRNA + anti-PD-1 + anti-CD4,  $n=5$ ; *VEGFC* mRNA + anti-PD-1 + anti-CD8,  $n=5$ ). **e**, Schematic of experimental design for the results shown in **f** and **g**. **f**, Mice inoculated with 50,000 CT-2A-BFP cells (**f**) or CT-2A cells (**g**) were treated with *VEGFC* mRNA or *GFP* mRNA (day 7) and either with PBS or with anti-PD-1 (RMP1-14) and/or anti-4-1BB (LOB12.3) antibodies (days 7, 9 and 11), and monitored for survival (**f**, *VEGFC* mRNA + anti-PD-1 + anti-4-1BB,  $n=5$ ; *GFP* mRNA + anti-PD-1 + anti-4-1BB,  $n=5$ ; *VEGFC* mRNA + PBS,  $n=4$ ; *GFP* mRNA + PBS,  $n=6$ ; **g**,  $n=5$  for all groups except *VEGFC* mRNA + anti-4-1BB + anti-PD-1,  $n=7$ ). **h**–**j**, Mice inoculated with 50,000 GL261 cells were treated with *VEGFC* mRNA or *GFP* mRNA (day 7) and either with PBS or with anti-PD-1 (RMP1-14) (**h**), anti-TIM3 (RMT3-23) (**i**) or anti-CTLA4 (9H10) antibodies (**j**) (days 7, 9 and 11), and monitored for survival ( $n=5$ ). For **i** and **j**, the same control mice were used for the *GFP* mRNA + PBS and *VEGFC* mRNA + PBS groups. **k**, Schematic of experimental design for the results shown in **l**. **l**, Mice inoculated with 50,000 GL261-Luc cells were treated with *VEGFC* mRNA or *GFP* mRNA (day 20) and either with PBS or with anti-PD-1 (RMP1-14) and anti-TIM3 (RMT3-23) antibodies (days 20, 22 and 24), and monitored for survival ( $n=5$ ).  $*P<0.05$ ;  $**P<0.01$ ;  $***P<0.001$ ;  $****P<0.0001$  (two-tailed unpaired Student's *t*-test or two-sided log-rank Mantel–Cox test).



**Extended Data Fig. 6 | Validation of endogenous retrovirus EMV2 as a tumour antigen for GL261.** **a**, RNA-seq analysis of mouse endogenous retrovirus elements in publicly available datasets on C57BL/6J mice brains and GL261 cell lines from various sources. **b**, Quantification of endogenous retrovirus elements in healthy brain and tumour tissue, from RNA-seq (brain,  $n = 9$ ; tumour,  $n = 6$ ). **c**, Gating strategies for tetramer staining.

**d**, Mice were injected with 500,000 GL261 cells or PBS in the flank. Seven days after tumour inoculation, draining inguinal lymph nodes were collected and emv2-env ( $K^b$ -restricted peptides aa 604–611 of p15E protein (KSPWFTTL)) tetramers were used to validate tumour-specific T cell proliferation. The experiments were repeated twice independently with similar results. Data are mean  $\pm$  s.e.m.

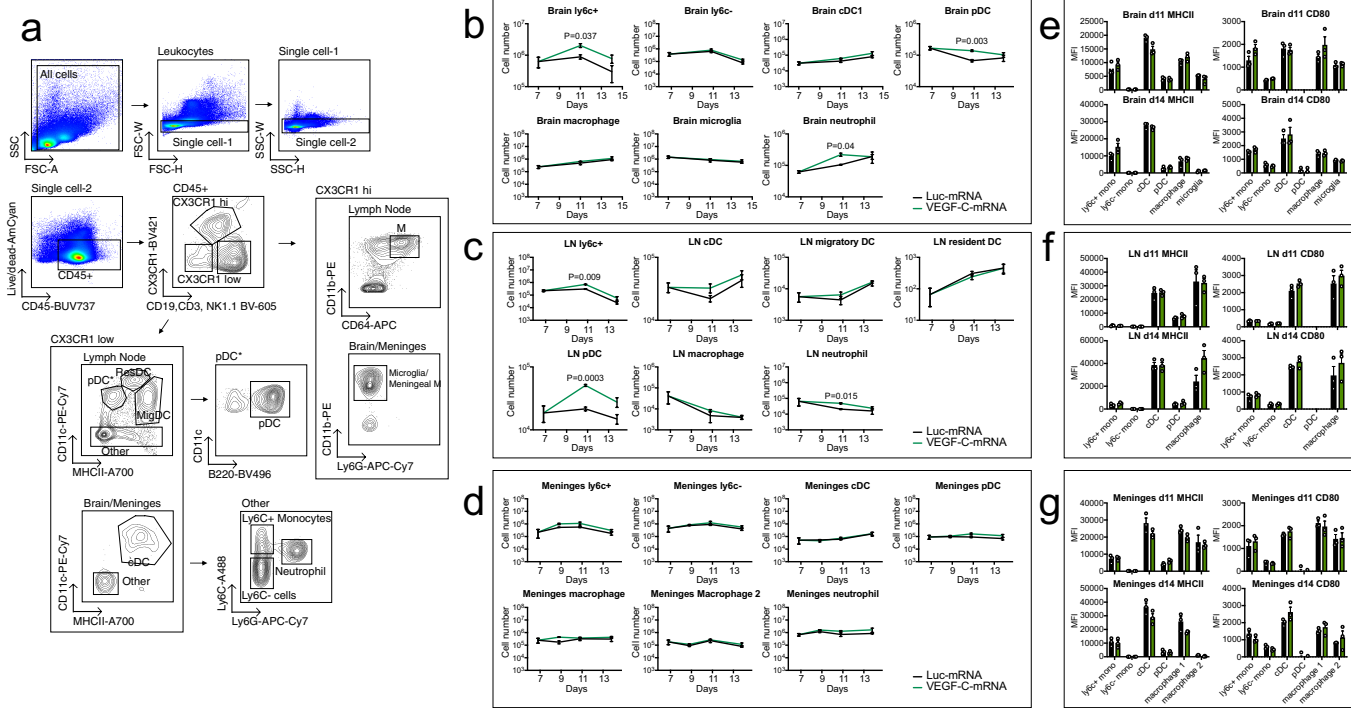


**Extended Data Fig. 7** | See next page for caption.

**Extended Data Fig. 7 | VEGF-C-dependent anti-PD-1 potentiation is specific to VEGF-C among proteins of the VEGF family, and is not caused by a direct effect on tumour or immune cells.** **a, b**, C57BL/6 mice received an injection of AAV-CTRL or AAV-s(oluble)VEGFR-3 intracisternally through the cisterna magna. After four weeks, mice were euthanized and the dura mater was collected to image the lymphatic vasculature (LYVE1) in the confluence of sinuses (**a**). The relative area of lymphatic vasculature in the confluence of sinuses was quantified (**b**) ( $n = 5$ ). **c**, Mice were pretreated with AAV-sVEGFR-3 four to six weeks before tumour inoculation. Seven days after tumour inoculation, mice were treated with *VEGFC* mRNA and anti-PD-1 (RMP1-14) antibodies (days 7, 9 and 11) ( $n = 5$ ). **d–f**, Mice were treated with 5  $\mu$ g of recombinant protein (VEGF-A, VEGF-B, VEGF-Cs or VEGF-D) in combination with anti-PD-1 (RMP1-14) antibodies (days 7, 9 and 11) and monitored for survival and tumour growth ( $n = 5$ ). **g–k** Mice were injected with CT-2A-BFP tumours and were treated with *VEGFC* mRNA at day 7. On day 8, brains and lymph nodes from all mice were collected and analysed using flow cytometry.

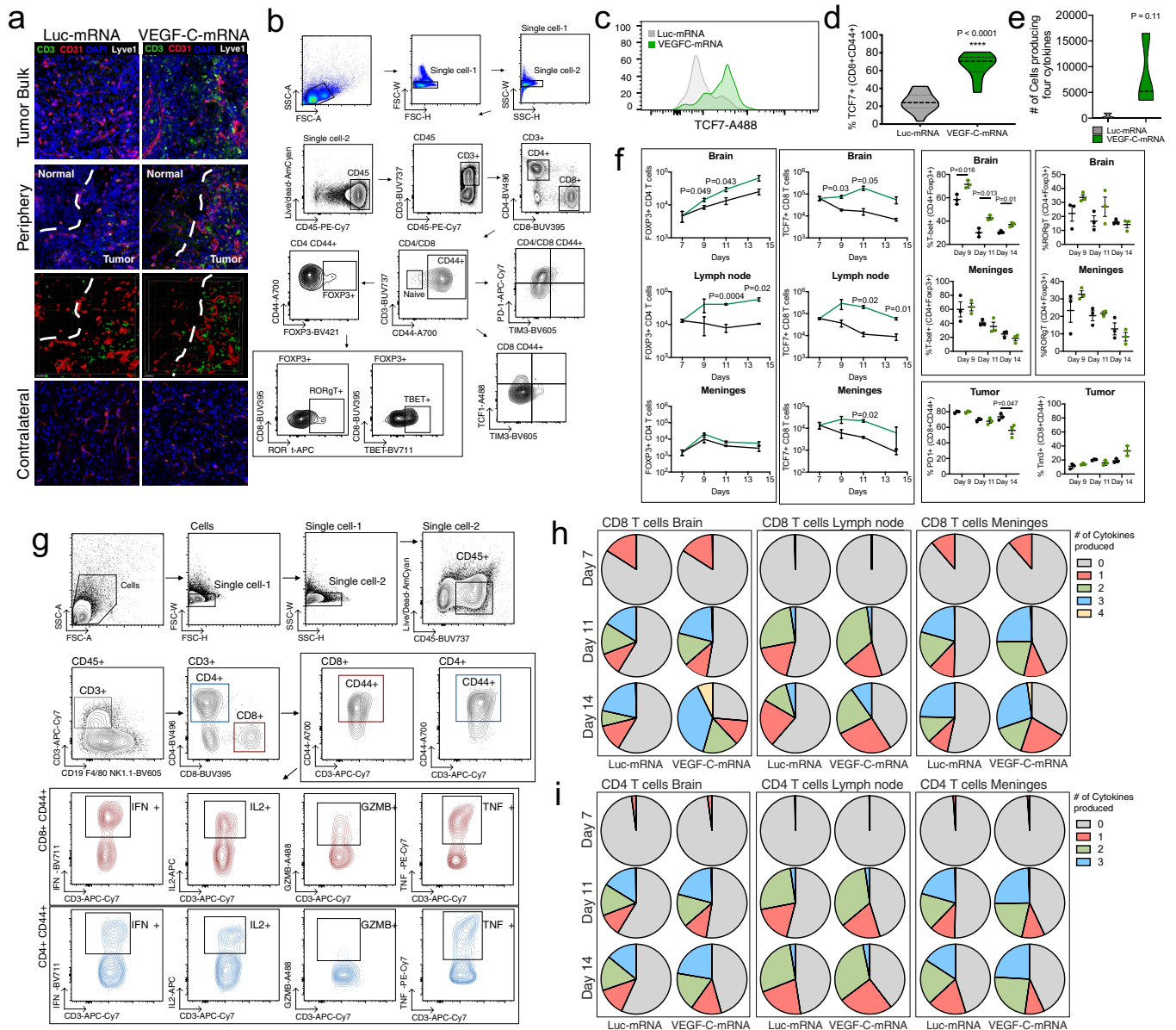
The experiment was repeated independently with similar results. **g**, Sample flow cytometry plots of experiments. **h–k**, Quantification of experiments ( $n = 5$ ). **l**, Flow cytometry was used to evaluate the expression of VEGFR-3 in GL261 cells. A VEGFR3–GFP plasmid was transfected into HEK293T cells as a positive control. The experiment was repeated independently with similar results. **m**, MTT assay to measure the proliferation of GL261 cancer cells in the presence of VEGF-C after 48 h ( $n = 8$  per group). **n**, Flow cytometry was used to evaluate the expression of VEGFR-3 in leukocyte compartments in the tumour. The experiment was repeated independently with similar results. **o**, Bone-marrow-derived dendritic cells were cultured with VEGF-C and evaluated for the expression of costimulatory molecules in the naive state (top row) or with LPS stimulation (bottom row). **p**, Isolated T cells were activated in vitro with CD3 or CD28 and IL-2 in the presence of VEGF-C. Data are mean  $\pm$  s.d. \* $P < 0.05$ ; \*\* $P < 0.01$ ; \*\*\* $P < 0.001$ ; \*\*\*\* $P < 0.0001$  (two-tailed unpaired Student's *t*-test or two-sided log-rank Mantel–Cox test).





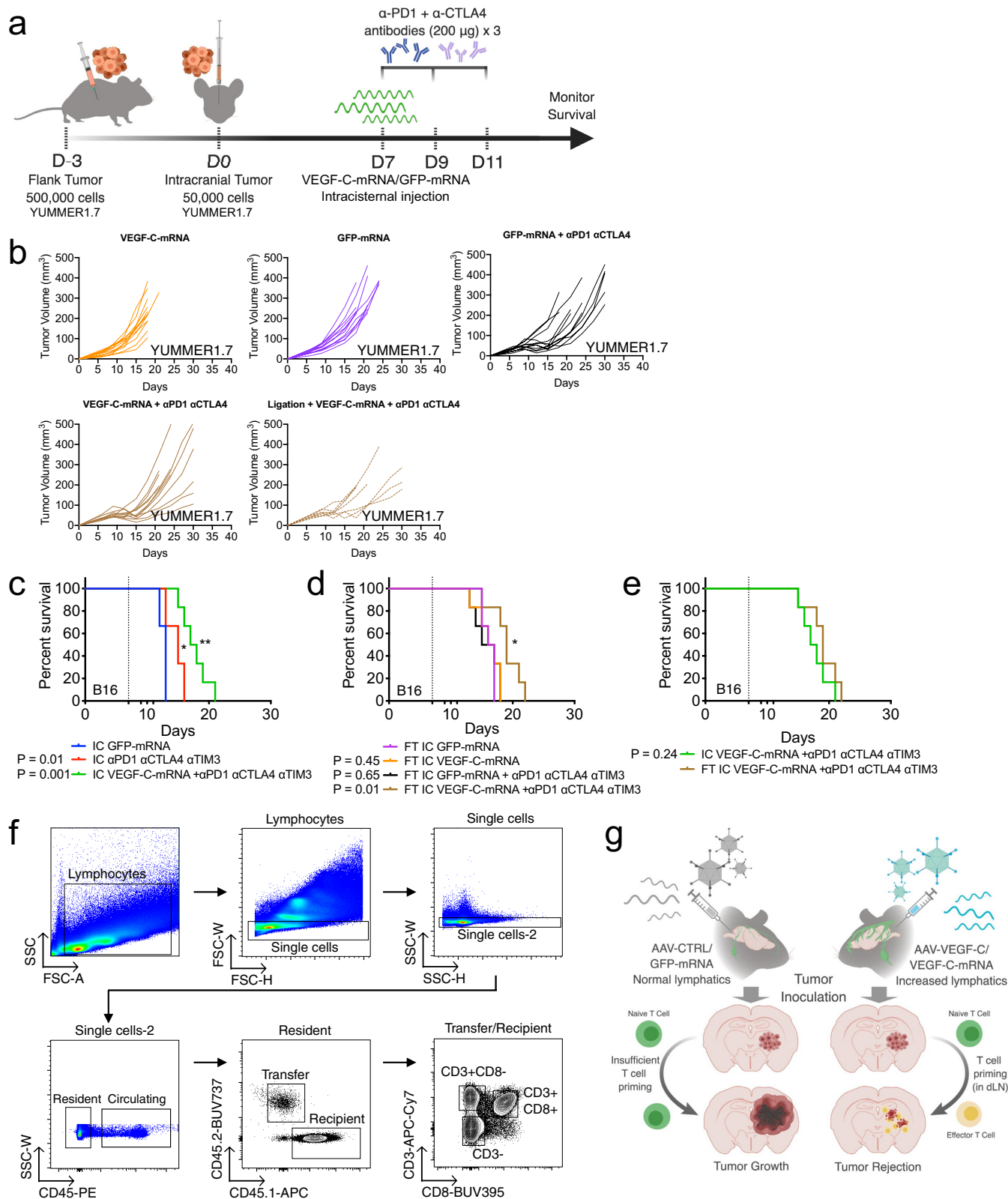
**Extended Data Fig. 8 | Flow cytometry analysis of myeloid cell populations after treatment with VEGF-C.** Mice bearing 7-day tumours were treated with Luc mRNA or VEGF-C mRNA and evaluated for changes in the populations of myeloid cells. **a**, Gating strategy for different myeloid cells. **b–d**, Cell counts of different cell types were measured at different time points after VEGF-C mRNA treatment. cDC, classical dendritic cell; DC, dendritic cell; pDC, plasmacytoid

dendritic cell. **e–g**, MHCII and CD80 MFI levels were quantified and showed no significant alteration after treatment with VEGF-C mRNA. **b** and **e** are leukocytes from brain tissue; **c** and **f** are leukocytes from draining cervical lymph nodes; **d** and **g** are leukocytes from meninges ( $n = 3$ , mice were pooled for each replicate). Data are mean  $\pm$  s.e.m. \* $P < 0.05$ ; \*\* $P < 0.01$ ; \*\*\* $P < 0.001$ ; \*\*\*\* $P < 0.0001$  (two-tailed unpaired Student's  $t$ -test).



**Extended Data Fig. 9 | VEGF-C treatment changes T cell phenotypes and functionality.** Mice bearing 7-day-tumours were treated with Luc mRNA or VEGF-C mRNA and evaluated for changes. **a**, Mouse brains were collected two days after treatment with VEGF-C mRNA, cryosectioned and analysed by immunofluorescence microscopy. **b**, Gating strategy for flow cytometry analysis of T cells. **c**, Example of TCF7 staining in CD3<sup>+</sup>CD8<sup>+</sup>CD44<sup>+</sup> cell populations after VEGF-C mRNA treatment. The experiment was repeated twice independently with similar results. **d**, Percentage of TCF7<sup>+</sup> T cells in the CD3<sup>+</sup>CD8<sup>+</sup>CD44<sup>+</sup> population in the brain (Luc mRNA,  $n=14$ ; VEGF-C mRNA,  $n=9$ ; data pooled from 3 independent experiments). **e**, Number of CD3<sup>+</sup>CD8<sup>+</sup>CD44<sup>+</sup>

cells producing IFN $\gamma$ , TNF, IL-2 and GZMB in the brain ( $n=3$ ; 3 mice were pooled for each sample). Violin plots display quartiles (dotted horizontal lines), median (dashed line) and minimum and maximum values (solid lines). **f**, Quantification of cell counts in different compartments after treatment with VEGF-C mRNA. Percentage of cells expressing specific transcription factors or immune checkpoint inhibitors after treatment with VEGF-C mRNA. **g**, Gating strategy for cytokine production in T cells. **h**, **i**, Quantification of T cells expressing multiple cytokines ( $n=3$ , 3 mice were pooled for each replicate). Data are mean  $\pm$  s.e.m. \* $P < 0.05$ ; \*\* $P < 0.01$ ; \*\*\* $P < 0.001$ ; \*\*\*\* $P < 0.0001$  (two-tailed unpaired Student's  $t$ -test).



**Extended Data Fig. 10 | Therapeutic application of VEGF-C mediates protection against intracranial melanoma cell lines when combined with various checkpoint inhibitors.** **a**, Schematic of experimental design for Fig. 4a–c and **b–e**. **b**, Growth kinetics of flank tumours from Fig. 4a–c were measured using a caliper ( $n = 12$  for all groups except the ligation group,  $n = 7$ ). **c–e**, Mice were given either only B16 intracranial tumours (IC) (**c**) or both a B16

intracranial tumour and a B16 flank tumour (FT) (**d**) and treated with *GFP* mRNA or *VEGF-C* mRNA on day 7, and anti-PD-1 (RMP1-14), anti-CTLA4 (9H10) and anti-TIM3 (RMT3-23) on days 7, 9 and 11. **f**, Flow cytometry gating strategy for Fig. 4e, **g**, Schematic of VEGF-C-induced tumour rejection. \* $P < 0.05$ ; \*\* $P < 0.01$ ; \*\*\* $P < 0.001$ ; \*\*\*\* $P < 0.0001$  (two-sided log-rank Mantel–Cox test).

## Reporting Summary

Nature Research wishes to improve the reproducibility of the work that we publish. This form provides structure for consistency and transparency in reporting. For further information on Nature Research policies, see [Authors & Referees](#) and the [Editorial Policy Checklist](#).

### Statistics

For all statistical analyses, confirm that the following items are present in the figure legend, table legend, main text, or Methods section.

- |                                     |   |
|-------------------------------------|---|
| n/a                                 | Confirmed   |
| <input type="checkbox"/>            | <input checked="" type="checkbox"/> The exact sample size ( $n$ ) for each experimental group/condition, given as a discrete number and unit of measurement   |
| <input type="checkbox"/>            | <input checked="" type="checkbox"/> A statement on whether measurements were taken from distinct samples or whether the same sample was measured repeatedly   |
| <input type="checkbox"/>            | <input checked="" type="checkbox"/> The statistical test(s) used AND whether they are one- or two-sided<br><i>Only common tests should be described solely by name; describe more complex techniques in the Methods section.</i>  |
| <input checked="" type="checkbox"/> | <input type="checkbox"/> A description of all covariates tested   |
| <input checked="" type="checkbox"/> | <input type="checkbox"/> A description of any assumptions or corrections, such as tests of normality and adjustment for multiple comparisons  |
| <input checked="" type="checkbox"/> | <input type="checkbox"/> A full description of the statistical parameters including central tendency (e.g. means) or other basic estimates (e.g. regression coefficient) AND variation (e.g. standard deviation) or associated estimates of uncertainty (e.g. confidence intervals) |
| <input type="checkbox"/>            | <input checked="" type="checkbox"/> For null hypothesis testing, the test statistic (e.g. $F$ , $t$ , $r$ ) with confidence intervals, effect sizes, degrees of freedom and $P$ value noted<br><i>Give <math>P</math> values as exact values whenever suitable.</i>                 |
| <input checked="" type="checkbox"/> | <input type="checkbox"/> For Bayesian analysis, information on the choice of priors and Markov chain Monte Carlo settings   |
| <input checked="" type="checkbox"/> | <input type="checkbox"/> For hierarchical and complex designs, identification of the appropriate level for tests and full reporting of outcomes   |
| <input checked="" type="checkbox"/> | <input type="checkbox"/> Estimates of effect sizes (e.g. Cohen's $d$ , Pearson's $r$ ), indicating how they were calculated   |

Our web collection on [statistics for biologists](#) contains articles on many of the points above.

### Software and code

Policy information about [availability of computer code](#)

Data collection	Nikon Eclipse Ti image software Leica SP8 imaging software Imaris 8
Data analysis	STAR/2.5.3a-foss-2016b, mm10 assembly, hg38 assembly, BEDTools/2.27.1-foss-2016b, DESEQ2, www.OncoLnc.org, PRISM 8.1.2, excel 16.16.6, Fiji (ImageJ) 2.0.0, Morpheus Webtool ( <a href="https://software.broadinstitute.org/morpheus/">https://software.broadinstitute.org/morpheus/</a> )

For manuscripts utilizing custom algorithms or software that are central to the research but not yet described in published literature, software must be made available to editors/reviewers. We strongly encourage code deposition in a community repository (e.g. GitHub). See the Nature Research [guidelines for submitting code & software](#) for further information.

### Data

Policy information about [availability of data](#)

All manuscripts must include a [data availability statement](#). This statement should provide the following information, where applicable:

- Accession codes, unique identifiers, or web links for publicly available datasets
- A list of figures that have associated raw data
- A description of any restrictions on data availability

Fig 2d-f; GSE121810

Fig 2a-c, Extended Data Fig 3; TCGA (phs000178.v10.p8), GTEx (phs000424.v7.p2)

Extended Data Fig 9; SRR579545 (b6J) SRR579546 (b6J) SRR2927735 (b6J) SRR594402 (b6J) SRR3351236 (b6J) SRR2133109 (GL261) SRR2133110 (GL261) SRR2133111 (GL261) SRR2133112 (GL261) SRR3063568 (GL261) SRR3063569 (GL261) SRR3063566 (GL261) SRR3063567 (GL261)

## Field-specific reporting

Please select the one below that is the best fit for your research. If you are not sure, read the appropriate sections before making your selection.

☒ Life sciences ☐ Behavioural & social sciences ☐ Ecological, evolutionary & environmental sciences

For a reference copy of the document with all sections, see [nature.com/documents/nr-reporting-summary-flat.pdf](https://www.nature.com/documents/nr-reporting-summary-flat.pdf)

## Life sciences study design

All studies must disclose on these points even when the disclosure is negative.

Sample size	We graphed a summary of key phenotypes we observed throughout multiple experiments. With these two experiments showing ~70% response rates, the sample size calculation required for an alpha of 0.05 is N = 6 (power 95%) and N = 5 (power 90%).
Data exclusions	Data was only excluded when experiment collection machine failed and no data points were collected. as were not able to produce readable result files.
Replication	All experiments were repeated as a variation (changes in time points) or in smaller n numbers, and showed similar trends and experimental conclusions. For most experiments depicted, they are concatenated examples of all experiments performed (not true for experiments where variation between different days are higher, ie. MFI measurements). All experiments were reproducible.
Randomization	For all tumor-related experiments with luciferase constructs, mice were measured for tumor size at day 4-6, and randomized into groups to ensure similar tumor size. For experiments where animals were pooled, animals within each pool were also ensured to have similar size tumors to minimize variation in downstream analysis.
Blinding	Investigators were not blinded for majority of the study; however all survival studies were monitored with the help of Yale animal facility Vets who were blinded to the studies. In addition, animals were mixed and labeled with numbers that blinded all involved with scoring mice health.

## Reporting for specific materials, systems and methods

We require information from authors about some types of materials, experimental systems and methods used in many studies. Here, indicate whether each material, system or method listed is relevant to your study. If you are not sure if a list item applies to your research, read the appropriate section before selecting a response.

### Materials & experimental systems

n/a	Involved in the study
<input type="checkbox"/>	<input checked="" type="checkbox"/> Antibodies
<input type="checkbox"/>	<input checked="" type="checkbox"/> Eukaryotic cell lines
<input checked="" type="checkbox"/>	<input type="checkbox"/> Palaeontology
<input type="checkbox"/>	<input checked="" type="checkbox"/> Animals and other organisms
<input checked="" type="checkbox"/>	<input type="checkbox"/> Human research participants
<input type="checkbox"/>	<input checked="" type="checkbox"/> Clinical data

### Methods

n/a	Involved in the study
<input checked="" type="checkbox"/>	<input type="checkbox"/> ChIP-seq
<input type="checkbox"/>	<input checked="" type="checkbox"/> Flow cytometry
<input checked="" type="checkbox"/>	<input type="checkbox"/> MRI-based neuroimaging

## Antibodies

### Antibodies used

Anti-CD45 (30-F11, APC-Cy7, B266564, 1:100; 104, BUV737, 9051755, 1:100; 104, PE-Cy7, B268066, 1:100; A20, APC, B254042, 1:100; 30-F11, BV605, B278000, 1:100), anti-CD3 (17A2, BV605, B264993, 1:100; 145-2C11, APC-Cy7, 1:100; 17A2, BUV737, 9042537, 1:100; 17A2, Biotin, B259691, 1:100), anti-CD4 (GK1.5, Pacific Blue, B199050, 1:100; GK1.5, BUV496, 8080653, 1:100), anti-CD8 (53-6.7, BV711, B259953, 1:100; 53-6.7, BUV395, 8306672, 1:100), anti-IFN $\gamma$  (XMG1.2, BV711, B236526, 1:100), anti-GZMB (GB11, FITC, B275568, 1:100), anti-TNF $\alpha$  (MP6-XT22, PE-Cy7, B251190, 1:100), anti-IL2 (JES6-5H4, APC, B248053, 1:100), anti-CD44 (IM7, A700, B244378, 1:100), anti-TBET (4B10, BV711, B268785, 1:100), anti-TIM3 (RMT3-23, BV605, B262042, 1:100), anti-FOXP3 (FJK-16s, BV421, B266620, 1:100), anti-TCF7 (C63D9, A488, 8, Cell Signaling Technology, 1:100), anti-PD-1 (29F.1A12, APC-Cy7, B260172, 1:100), anti-ROR $\gamma$ T (B2D, APC, E16663-102, 1:100), anti-CD40 (PE, E028955, 1:100), anti-CD80 (16-10A1, BUV395, 1:100; 16-10A1, FITC, E029730, 1:100), anti-CD86 (APC, B175381, 1:100), anti-CX3CR1 (SA011F11, BV421, B231871, 1:100), anti-Ly6C (AL21, FITC, 33380, 1:100), anti-CD11c (N418, PE-Cy7, B264758, 1:100; BV421, B264454, 1:100), anti-CD11b (M1/70, PE, B228654, 1:100), anti-Ly6G (IA8, APC-Cy7, B153128, 1:100), anti-MHCII (M5/114.15.2, A700, B264454, 1:200), anti-CD64 (X54-5/7.1, APC, B254424, 1:100), anti-B220 (RA3-6B2, BUV496, 8096734, 1:100), anti-NK1.1 (PK136, biotin, B255213, 1:100), anti-CD19 (6D5, biotin, B250292, 1:100), anti-F4/80 (BM8, biotin, B253458, 1:100), anti-Podoplanin (eBio8.1.1, PE, E11344-399, eBioscience, 1:100), anti-CD31 (390, A647, 8187629, 1:100), anti-AKT (pS473) (M89-61, BV421, 7198801, 1:100) antibodies were purchased from BioLegend (Bxxxxxx) or BD Biosciences (xxxxxxx). anti-VEGFR-3/FLT-4 (FAB743P, PE, ACBF0117091, 1:100) antibodies were purchased from R&D Biosciences. Kb-restricted peptides aa 604–611 of p15E protein (KSPWFTTL) tetramer was made through the NIH tetramer core facility. KSPWFTTL peptide was made by Biomatik Corporation (Ontario, CA). Depletion antibodies anti-CD4 (GK1.5), anti-CD8 (YTS169.4), anti-PD1 (RMP1-14), anti-CTLA4 (9H10), anti-TIM3 (RMT3-23), anti-4-1BB (LOB12.3) antibodies were purchased from BioXCell (West Lebanon, NH). For brain sections, anti-CD3



(17A2, biotin, 1:500), anti-CD31 (2H8, GeneTex, 1:500) and anti-LYVE1 (AF2125, R&D systems, 1:250) antibodies were used with anti-streptavidin (FITC, BD biosciences, 4031801, 1:1000), anti-hamster (127-165-160, Cy3, Jackson ImmunoResearch, 128827, 1:500), and anti-goat (705-175-147, Cy5, Jackson ImmunoResearch, 138513, 1:500) secondary antibodies respectively.

#### Validation

antibodies were all validated on their respective websites, and all are antibodies regularly used in our lab for other purposes.

## Eukaryotic cell lines

### Policy information about [cell lines](#)

#### Cell line source(s)

GL261 parental cells were obtained from the NIH cancer cell repository. GL261-Luciferase cells were kind gifts from Dr. Jiangbing Zhou (Yale Neurosurgery) and Dr. Carla Rothlin (Yale Immunobiology). YUMMER 1.7 cell lines are previously reported<sup>50</sup>. CT2A and CT2A-BFP cells were a kind gift from Dr. Thomas Mathivet (PARCC, Paris). B16 cells were a kind gift from Dr. Noah Palm (Yale Immunobiology). HEK293T cells were purchased from ATCC. HEK293T, CT2A, CT2A-BFP and B16 cells were cultured in complete DMEM (4.5g/L glucose, 10% FBS, 1% penicillin/streptomycin). YUMMER 1.7 cells were cultured in DMEM/F12 media (10% FBS, 1% nonessential amino acids, 1% penicillin/streptomycin). GL261 and GL261-Luc cells were cultured in RPMI (10% FBS, 1% penicillin/streptomycin).

#### Authentication

No authentication was performed.

#### Mycoplasma contamination

All cells were mycoplasma negative

#### Commonly misidentified lines (See [ICLAC](#) register)

No commonly misidentified lines were used, and all cells were obtained from trusted sources (in material methods).

## Animals and other organisms

### Policy information about [studies involving animals](#); [ARRIVE guidelines](#) recommended for reporting animal research

#### Laboratory animals

Four- to eight-week-old mixed sex C57BL/6 mice, B6.129S2-Ightm1Cgn/J ( $\mu$ MT) mice, B6.SJL-PtprcaPepcb/BoyCrl mice, were purchased from the National Cancer Institute, Jackson Laboratory and Charles River respectively and subsequently bred and housed at Yale University. All procedures used in this study (sex-matched, age-matched) complied with federal guidelines and institutional policies by the Yale School of Medicine Animal Care and Use Committee.

#### Wild animals

no wild animals were used

#### Field-collected samples

No field-collected samples were used.

#### Ethics oversight

All procedures used in this study (sex-matched, age-matched) complied with federal guidelines and institutional policies by the Yale School of Medicine Animal Care and Use Committee.

Note that full information on the approval of the study protocol must also be provided in the manuscript.

## Clinical data

### Policy information about [clinical studies](#)

All manuscripts should comply with the ICMJE [guidelines for publication of clinical research](#) and a completed [CONSORT checklist](#) must be included with all submissions.

#### Clinical trial registration

No clinical studies were performed

#### Study protocol

*Note where the full trial protocol can be accessed OR if not available, explain why.*

#### Data collection

*Describe the settings and locales of data collection, noting the time periods of recruitment and data collection.*

#### Outcomes

*Describe how you pre-defined primary and secondary outcome measures and how you assessed these measures.*

## Flow Cytometry

### Plots

Confirm that:

- ☒ The axis labels state the marker and fluorochrome used (e.g. CD4-FITC).
- ☒ The axis scales are clearly visible. Include numbers along axes only for bottom left plot of group (a 'group' is an analysis of identical markers).
- ☒ All plots are contour plots with outliers or pseudocolor plots.
- ☒ A numerical value for number of cells or percentage (with statistics) is provided.

## Methodology

### Sample preparation

Isolation of mononuclear cells and flow cytometry. Tissue was harvested and incubated in a digestion cocktail containing 1 mg ml<sup>-1</sup> collagenase D (Roche), 1 mg ml<sup>-1</sup> collagenase A (Roche) and 30 µg ml<sup>-1</sup> DNase I (Sigma-Aldrich) in complete RPMI (10% FBS) at 37 °C for 30 min. Tissue was then filtered through a 70 µm filter. For brain tissues, cells were mixed in 4 mL of 25% Percoll (Sigma-Aldrich) solution and centrifuged at 530g for 15 minutes without a brake. The Percoll layer was removed and cells were diluted in 5 mL of 1% BSA. Cells were treated with ACK buffer, and resuspended in 1% BSA. At this point cells were counted using an automated cell counter (Thermo fisher).

For tetramer experiments, staining was performed with antibodies (1:200) and tetramer (1:50) for 60 minutes at room temperature. Cells were washed to remove excess antibodies and resuspended in 1% BSA with 10 µL of CountBright absolute counting beads (Life technologies, OR) for multiparameter analyses on the LSR II flow cytometer (Becton Dickinson), and subsequently analyzed using FlowJo software (10.5.3, Tree Star). For calculation of tetramer positive T cells in each organ this calculation was used:

number of tetramer positive T cells \* (# of input beads / # of counted beads) \* (# of cells from automated counter / # of total events in flow cytometry).

For cytokine stimulation, surface markers were first stained on ice for 30 minutes. After washing, cells were stimulated in complete RPMI with 200µL of 1x Cell stimulation cocktail without protein transporter inhibitor (eBioscience Cell Stimulation Cocktail, ThermoFisher) for 1 hour at 37C. 50 µL of 5x Cell stimulation cocktail with protein transporter (eBioscience Cell Stimulation Cocktail, ThermoFisher) was added and incubated for an additional 4 hours. Cells were then fixed with 100µL 2% formaldehyde on ice for 45 minutes. Cells were washed with 1x Perm/Wash Buffer (BD Cytofix/Cytoperm, BD Biosciences), and then permeabilized with 1x Perm/Wash Buffer (BD Cytofix/Cytoperm, BD Biosciences) for 10 minutes on ice. Intracellular antigens were stained on ice for 30 minutes.

For transcription factor staining, surface markers were first stained on ice for 30 minutes. Cells were then fixed with 100µL 2% formaldehyde on ice for 45 minutes. Cells were washed with 1x Perm/Wash Buffer (eBioscience Foxp3/Transcription Factor Staining Buffer Set, ThermoFisher), and then permeabilized with 1x FOXP3Perm/Wash Buffer for 10 minutes on ice. Intracellular antigens were stained on ice for 30 minutes.

For AKT phosphorylation staining, surface markers were first stained on ice for 30 minutes. Cells were then fixed and washed following BD Phosflow kit directions.

### Instrument

LSRII  
Attune NxT Flow Cytometer

### Software

FlowJo 10.6.0

### Cell population abundance

n/a

### Gating strategy

All gates are shown in the supplementary information.

☒ Tick this box to confirm that a figure exemplifying the gating strategy is provided in the Supplementary Information.

# Mechanism of adrenergic Ca<sub>v</sub>1.2 stimulation revealed by proximity proteomics

<https://doi.org/10.1038/s41586-020-1947-z>

Received: 10 July 2019

Accepted: 9 December 2019

Published online: 22 January 2020

Guoxia Liu<sup>1,7</sup>, Arianne Papa<sup>2,7</sup>, Alexander N. Katchman<sup>1,7</sup>, Sergey I. Zakharov<sup>1,7</sup>, Daniel Roybal<sup>3</sup>, Jessica A. Hennessey<sup>1</sup>, Jared Kushner<sup>1</sup>, Lin Yang<sup>1</sup>, Bi-Xing Chen<sup>1</sup>, Alexander Kushnir<sup>1</sup>, Katerina Dangas<sup>1</sup>, Steven P. Gygi<sup>4</sup>, Geoffrey S. Pitt<sup>5</sup>, Henry M. Colecraft<sup>2,3</sup>, Manu Ben-Johny<sup>2</sup>, Marian Kalocsay<sup>6\*</sup> & Steven O. Marx<sup>1,3\*</sup>

Increased cardiac contractility during the fight-or-flight response is caused by  $\beta$ -adrenergic augmentation of Ca<sub>v</sub>1.2 voltage-gated calcium channels<sup>1–4</sup>. However, this augmentation persists in transgenic murine hearts expressing mutant Ca<sub>v</sub>1.2  $\alpha_{1C}$  and  $\beta$  subunits that can no longer be phosphorylated by protein kinase A—an essential downstream mediator of  $\beta$ -adrenergic signalling—suggesting that non-channel factors are also required. Here we identify the mechanism by which  $\beta$ -adrenergic agonists stimulate voltage-gated calcium channels. We express  $\alpha_{1C}$  or  $\beta_{2B}$  subunits conjugated to ascorbate peroxidase<sup>5</sup> in mouse hearts, and use multiplexed quantitative proteomics<sup>6,7</sup> to track hundreds of proteins in the proximity of Ca<sub>v</sub>1.2. We observe that the calcium-channel inhibitor Rad<sup>8,9</sup>, a monomeric G protein, is enriched in the Ca<sub>v</sub>1.2 microenvironment but is depleted during  $\beta$ -adrenergic stimulation. Phosphorylation by protein kinase A of specific serine residues on Rad decreases its affinity for  $\beta$  subunits and relieves constitutive inhibition of Ca<sub>v</sub>1.2, observed as an increase in channel open probability. Expression of Rad or its homologue Rem in HEK293T cells also imparts stimulation of Ca<sub>v</sub>1.3 and Ca<sub>v</sub>2.2 by protein kinase A, revealing an evolutionarily conserved mechanism that confers adrenergic modulation upon voltage-gated calcium channels.

The positive inotropic effect of  $\beta$ -adrenergic agonists on the heart is a classical physiological phenomenon that is universally experienced during excitement, exercise and the fight-or-flight response. The effect is mediated by  $\beta$ -adrenergic activation of protein kinase A (PKA), which in turn leads to increased Ca<sup>2+</sup> influx through L-type Ca<sub>v</sub>1.2 channels in cardiomyocytes<sup>1–4</sup>. The commonly accepted model is that PKA increases the Ca<sup>2+</sup> current through Ca<sub>v</sub>1.2 channels by phosphorylating Ca<sub>v</sub>1.2  $\alpha_{1C}$  and/or  $\beta_{2B}$  subunits (Fig. 1a). However, previously proposed putative regulatory residues on the carboxyl termini of  $\alpha_{1C}$  (Ser1928, Ser1700 and Thr1704)<sup>10,11</sup> and  $\beta_{2B}$  (Ser512 and Ser570)<sup>12</sup> have been shown to be dispensable for  $\beta$ -adrenergic stimulation of Ca<sup>2+</sup> currents in the heart<sup>13–16</sup>. Nevertheless, given the numerous other serine and threonine residues of  $\alpha_{1C}$  and  $\beta_{2B}$ , it remained possible that PKA-mediated phosphorylation of some combination of these was responsible for  $\beta$ -adrenergic modulation of Ca<sub>v</sub>1.2 channels in cardiomyocytes. As shown below, this also is not the case.

## No role for core Ca<sub>v</sub>1.2 phosphorylation

We developed a transgenic approach that enables doxycycline-inducible expression of Flag-tagged, dihydropyridine (DHP)-resistant Ca<sub>v</sub>1.2 channels in mice (Fig. 1b)<sup>16</sup>. The transgenic and endogenous Ca<sub>v</sub>1.2

currents are distinguishable by application of nisoldipine, a Ca<sup>2+</sup>-channel DHP antagonist<sup>16</sup>. We mutated all 51 conserved and nonconserved serine and threonine residues within the 35 intracellular PKA consensus phosphorylation sites of rabbit  $\alpha_{1C}$  to alanine ('35-mutant  $\alpha_{1C}$ '; Extended Data Fig. 1a). In cardiomyocytes, the nisoldipine-insensitive 35-mutant Ca<sup>2+</sup> currents were both activated at more negative potentials and increased in response to isoproterenol (a  $\beta$ -adrenoreceptor agonist) or forskolin (which stimulates adenylyl cyclase to produce cyclic AMP, thereby activating PKA), to the same extent as were nisoldipine-insensitive wild-type channels ('pseudo-wild-type (pWT)'  $\alpha_{1C}$  channels) (Fig. 1c, d and Extended Data Fig. 1b, c).

Similarly, we mutated to alanine all 37 conserved and nonconserved serine and threonine residues within 28 PKA-consensus phosphorylation sites of human  $\beta_{2B}$  ('28-mutant  $\beta_{2B}$ '; Extended Data Fig. 1d). Cardiomyocytes expressing green fluorescent protein (GFP)-tagged 28-mutant  $\beta_{2B}$  (Extended Data Fig. 1e, f) displayed isoproterenol- or forskolin-induced stimulation of Ca<sub>v</sub>1.2 current amplitude (Fig. 1e, g) and a hyperpolarizing shift in the voltage dependence of activation (Extended Data Fig. 1b), similar to cardiomyocytes isolated from transgenic mice expressing GFP-tagged wild-type  $\beta_{2B}$  (ref. <sup>17</sup>).

Finally, we crossed 35-mutant  $\alpha_{1C}$  with 28-mutant  $\beta_{2B}$  transgenic mice. Immunoprecipitation with anti-Flag antibody indicated that

<sup>1</sup>Division of Cardiology, Department of Medicine, Columbia University, Vagelos College of Physicians and Surgeons, New York, NY, USA. <sup>2</sup>Department of Physiology and Cellular Biophysics, Columbia University, Vagelos College of Physicians and Surgeons, New York, NY, USA. <sup>3</sup>Department of Pharmacology, Columbia University, Vagelos College of Physicians and Surgeons, New York, NY, USA. <sup>4</sup>Department of Cell Biology, Harvard Medical School, Boston, MA, USA. <sup>5</sup>Cardiovascular Research Institute, Weill Cornell Medical College, New York, NY, USA. <sup>6</sup>Department of Systems Biology, Laboratory of Systems Pharmacology, Harvard Medical School, Boston, MA, USA. <sup>7</sup>These authors contributed equally: Guoxia Liu, Arianne Papa, Alexander N. Katchman, Sergey I. Zakharov. \*e-mail: Marian\_Kalocsay@hms.harvard.edu; sm460@cumc.columbia.edu

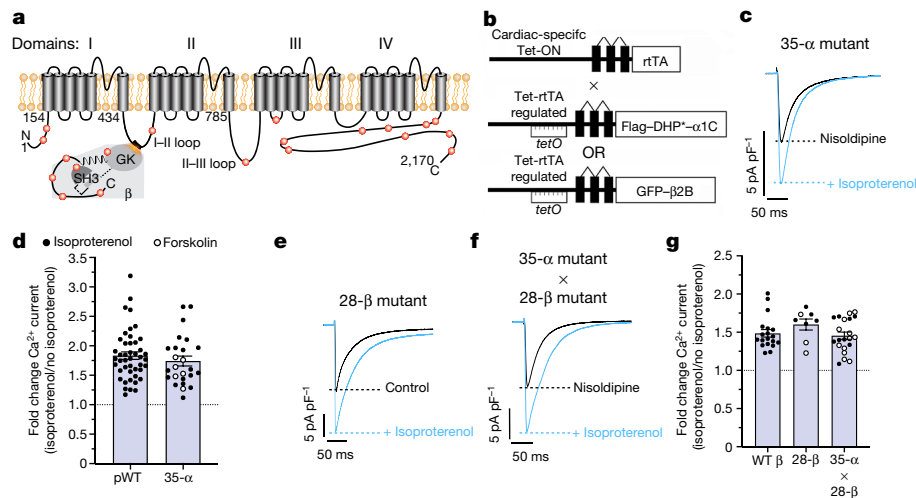


**Fig. 1 | Phosphorylation of  $\alpha_{1C}$  and  $\beta$  subunits by PKA is not required for  $\beta$ -adrenergic regulation of  $\text{Ca}_v1.2$ .** **a**, Diagram showing rabbit cardiac  $\alpha_{1C}$  (top) and  $\beta$  (bottom) subunits. Red dots indicate putative sites of phosphorylation by PKA. GK, guanylate kinase domain; SH3, Src homology 3 domain.

**b**, Diagrams showing the binary transgene system that permits robust expression of Flag-tagged DHP-resistant (DHP<sup>r</sup>)  $\alpha_{1C}$  or GFP-tagged  $\beta_{2B}$  only in the presence of both a reverse tetracycline-controlled transactivator (rtTA) and doxycycline (Tet-ON). The top diagram shows expression of the rtTA driven by the cardiac-specific  $\alpha$ -myosin heavy chain ( $\alpha$ -MHC) promoter. The three non-coding exons that make up the 5'-untranslated region of the  $\alpha$ -MHC gene are depicted as black boxes, and the introns as lines. The lower two diagrams show cDNAs for Flag-DHP<sup>r</sup>- $\alpha_{1C}$  or GFP- $\beta_{2B}$  ligated behind seven tandem *tetO* sequences, which impart tetracycline inducibility. **c**, Exemplar whole-cell  $\text{Ca}_v1.2$  currents of 35-mutant  $\alpha_{1C}$  cardiomyocytes (from transgenic mice) in nisoldipine

before (black trace) and after (blue trace) treatment with isoproterenol. Representative of 25 experiments; pA pF<sup>-1</sup>, picoamperes per picofarad.

**d**, Fold change in peak DHP-resistant  $\text{Ca}^{2+}$  current at 0 mV caused by isoproterenol or forskolin. Dots show data points. Data are mean  $\pm$  s.e.m.;  $P=0.39$  by unpaired two-tailed *t*-test;  $n=45$  cardiomyocytes from 5 mice (isoproterenol);  $n=25$  cardiomyocytes from 5 mice (forskolin). **e**, **f**, Exemplar whole-cell  $\text{Ca}_v1.2$  currents of cardiomyocytes from GFP-tagged 28-mutant  $\beta_{2B}$  transgenic mice (**e**), and from 35-mutant  $\alpha_{1C}$  crossed with 28-mutant  $\beta_{2B}$  transgenic mice (**f**). Representative of 8 and 22 independent experiments respectively.

**g**, Fold change in peak  $\text{Ca}^{2+}$  current caused by isoproterenol or forskolin for cardiomyocytes isolated from transgenic mice expressing GFP-tagged wild-type (WT)  $\beta_{2B}$  subunit<sup>17</sup>, GFP-tagged 28-mutant  $\beta_{2B}$ , or both 35-mutant  $\alpha_{1C}$  and GFP-tagged 28-mutant  $\beta_{2B}$ . Data are mean  $\pm$  s.e.m.;  $P=0.27$  by one-way ANOVA;  $n=19$ , 8 and 21 cardiomyocytes from 4, 4 and 3 mice, from left to right.

GFP-tagged 28-mutant  $\beta_{2B}$  subunits dominate in the 35-mutant  $\alpha_{1C}$  complex (Extended Data Fig. 1g) in cardiomyocytes isolated from these mice. These mutant channels also displayed a normal isoproterenol- or forskolin-induced increase in peak  $\text{Ca}^{2+}$  current (Fig. 1f, g) and a hyperpolarizing shift in the  $V_{50}$  of activation (Extended Data Fig. 1b). These results indicate that  $\beta$ -adrenergic stimulation of  $\text{Ca}_v1.2$  does not involve direct phosphorylation of  $\alpha_{1C}$  or  $\beta_2$  subunits.

## Identifying the $\text{Ca}_v1.2$ subdomain proteome

Given the foregoing results, we adapted for application to cardiomyocytes an enzyme-catalysed proximity labelling method<sup>5,6</sup> in order to comprehensively identify components of the  $\text{Ca}_v1.2$  macromolecular complex. We generated transgenic mice with doxycycline-inducible, cardiomyocyte-specific expression of DHP-resistant  $\alpha_{1C}$  or  $\beta_{2B}$  proteins with ascorbate peroxidase (APEX2) and a V5 epitope conjugated to the amino termini, enabling biotin labelling of proteins within around 20 nm (ref. 18) of the  $\text{Ca}^{2+}$  channels. Fusing APEX2 to  $\alpha_{1C}$  and  $\beta_{2B}$  did not affect  $\text{Ca}_v1.2$  subcellular localization and function in cardiomyocytes, as assessed using cellular electrophysiology, fractional shortening and immunofluorescence (Extended Data Fig. 2a–d). Incubating isolated ventricular cardiomyocytes or perfusing whole hearts with a solution containing biotin phenol, followed by exposure to hydrogen peroxide, induced robust biotinylation of proteins in a striated z-disk pattern, coinciding with the pattern of transgenic  $\alpha_{1C}$  and  $\beta_{2B}$  subunits (Fig. 2a, b and Extended Data Fig. 2d, e).

Western blots confirmed the biotinylation of proteins known to be localized near  $\text{Ca}_v1.2$  at dyadic junctions in cardiomyocytes (Fig. 2c). By contrast,  $\text{K}_v1.5$  channels were not biotinylated and enriched (Fig. 2c), implying that these channels may not be as closely localized to  $\text{Ca}_v1.2$ . Triple-stage mass spectrometry (TMT SPS MS<sup>3</sup>) identified and quantified hundreds of other biotinylated proteins (Supplementary Table 1),

although many probably constitute bystanders rather than physically interacting proteins. Of these, the 150 proteins with the highest peptide counts were remarkably similar in  $\alpha_{1C}$ -APEX2 and  $\beta_{2B}$ -APEX2 transgenic mice (Extended Data Fig. 3a). These were primarily classified as being membrane, cytoskeletal or sarcomeric proteins (Extended Data Fig. 3b, c and Supplementary Table 2). Some of these proteins, however, were associated with other compartments, probably reflecting the labelling of proteins encountered during  $\text{Ca}_v1.2$ -APEX2 synthesis, maturation and trafficking.

## Adrenergic modulation of $\text{Ca}_v1.2$ neighbourhood

It seemed likely that PKA-dependent stimulation of  $\text{Ca}^{2+}$  currents in the heart involves recruitment of a distinct activator protein to, or loss of an inhibitory protein from, the  $\text{Ca}_v1.2$  macromolecular complex. Recently, APEX2 labelling, combined with either multiplexed quantitative mass spectrometry<sup>7</sup> or quantitative proteomics using a system of spatial references and bystander ratio calculations<sup>19</sup>, was used to analyse ligand-induced changes in the local environment of G-protein-coupled receptors. Notably, we found that conjugation of peroxidase to either of the  $\text{Ca}_v1.2$  subunits did not interfere with  $\beta$ -adrenergic stimulation of  $\text{Ca}^{2+}$  currents (Extended Data Fig. 2f, g), and that the  $\beta$ -adrenergic agonist signalling pathways were preserved in the presence of biotin phenol and during hydrogen-peroxide-induced labelling, assessed by phospholamban phosphorylation (Extended Data Fig. 2h–k).

We preincubated isolated cardiomyocytes from  $\alpha_{1C}$ -APEX2 and  $\beta_{2B}$ -APEX2 mice with biotin phenol for 30 minutes; during the final 10 minutes, the cells were also exposed to either isoproterenol or vehicle (Fig. 2d). We purified and quantified biotinylated proteins using TMT SPS MS<sup>3</sup>. The relative summed peptide TMT signal-to-noise ratio—indicating relative protein quantification—changed for several proteins (Fig. 2e, f). We also probed the effect of isoproterenol

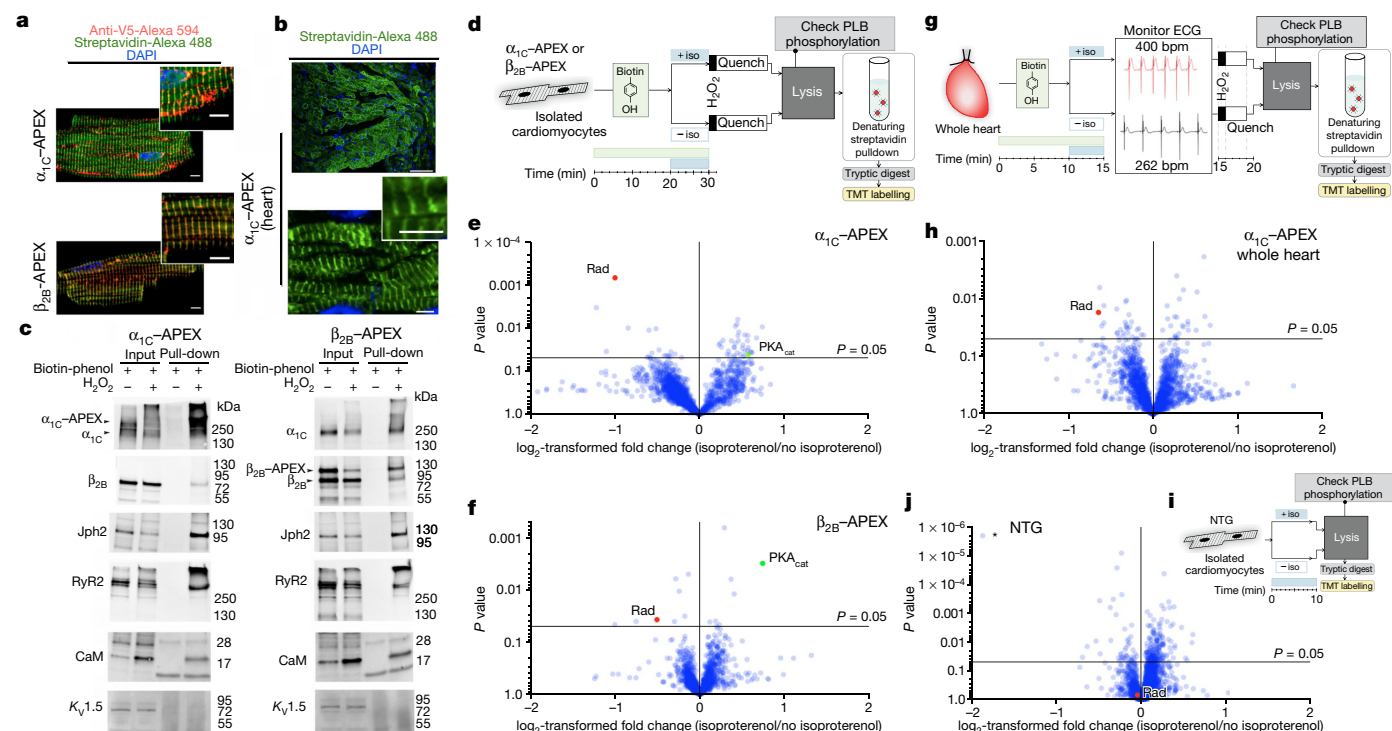


**Fig. 2 | Changes in the  $\text{Ca}_v1.2$  subdomain proteome upon  $\beta$ -adrenergic agonist activation of PKA signalling in the heart.** **a**, Immunofluorescence of isolated  $\alpha_{IC}$ -APEX2 and  $\beta_{2B}$ -APEX2 cardiomyocytes exposed to biotin-phenol and hydrogen peroxide. Representative of 13 and 8 cardiomyocytes from 2 and 3 mice respectively. Staining is with anti-V5 and Alexa594-conjugated secondary antibodies and streptavidin-conjugated Alexa488; nuclear labelling is with 4',6-diamidino-2-phenylindole (DAPI). Scale bars, 5  $\mu\text{m}$ . **b**, Immunofluorescence of tissue sections of Langendorff-perfused  $\alpha_{IC}$ -APEX2 heart. Scale bars, upper panel, 100  $\mu\text{m}$ ; lower panel, 5  $\mu\text{m}$ ; lower inset, 5  $\mu\text{m}$ . Representative of ten sections from two mice. **c**, Immunoblots of biotin-labelled proteins from cardiomyocytes of  $\alpha_{IC}$ -APEX2 and  $\beta_{2B}$ -APEX2 mice.  $\text{Ca}_v1.2$  subunits, RyR2, Jph2 and CaM are detected, whereas  $\text{K}_v1.5$  channels are not detected, in streptavidin pull-down. Blots representative of three independent experiments. **d**, Workflow for processing of isolated cardiomyocytes.  $\text{H}_2\text{O}_2$ , hydrogen peroxide; iso, isoproterenol; PLB, phospholamban. **e**, Volcano plot of fold change for relative protein quantification by TMT mass spectrometry of  $\alpha_{IC}$ -APEX2 samples. Data are means from five pairs of biologically independent samples; non-adjusted unpaired two-tailed  $t$ -test. Levels of Rad in the neighbourhood of  $\text{Ca}_v1.2$  (red

dot) are reduced by 50%, and levels of the PKA catalytic subunit (green dot) are increased by 50%, upon application of isoproterenol. **f**, As in **e**, except for cardiomyocytes from  $\beta_{2B}$ -APEX2 mice. Data are means from three pairs of biologically independent samples. Levels of Rad are reduced by 30% and of the PKA catalytic subunit are increased by 68% in the neighbourhood of  $\text{Ca}_v1.2$  following application of isoproterenol. **g**, Workflow showing protein labelling and analysis of Langendorff-perfused  $\alpha_{IC}$ -APEX2 mouse hearts. Bpm, beats per minute. **h**, As in **e**, but for proteins from  $\alpha_{IC}$ -APEX2 whole-heart samples. Data are means for five hearts: five without and five with isoproterenol. Levels of Rad in the neighbourhood of  $\text{Ca}_v1.2$  are reduced by 36% following application of isoproterenol. **i**, Workflow for analysis of isolated cardiomyocytes from non-transgenic (NTG) mice. **j**, As in **e**, but for proteins isolated from NTG cardiomyocytes without biotinylation or pull-down. The asterisk indicates the single peptide ESFDSQSLNNQSK, mapping to Uniprot D3Z0N2 (Sorbs2), with its apparent abundance reduced by isoproterenol treatment in non-transgenic cardiomyocytes to about 27%, probably because of post-translational modification. Data are means for four pairs of biologically independent samples. Levels of Rad in whole heart are unchanged by isoproterenol. For source gel data, see Supplementary Fig. 1.

on the  $\text{Ca}_v1.2$  proteome signature in Langendorff-perfused whole hearts (Fig. 2g, h). We detected isoproterenol-induced recruitment of the PKA catalytic subunit ( $\text{PKA}_{cat}$ ) to  $\text{Ca}_v1.2$  channels in cardiomyocytes isolated from both  $\alpha_{IC}$ -APEX2 and  $\beta_{2B}$ -APEX2 mice (Fig. 2e, f). All three approaches (using isolated cardiomyocytes from  $\alpha_{IC}$ -APEX2 and  $\beta_{2B}$ -APEX2 mice, and  $\alpha_{IC}$ -APEX2 whole hearts) indicated a 30–50% decrease in the amount of the small Ras-like G protein Rad in the neighbourhood of  $\text{Ca}_v1.2$  following application of isoproterenol (Fig. 2e, f, h, Extended Data Figs. 4a–c, 5a, b and Supplementary Tables 3–5). By analysing the overlap of proteins displaying isoproterenol-induced changes in  $\alpha_{IC}$ -APEX2 and  $\beta_{2B}$ -APEX2 experiments, we found Rad to be the only candidate protein displaying this behaviour (Extended Data Fig. 5b, c). By contrast, a 10-minute exposure of cardiomyocytes isolated from nontransgenic mice to isoproterenol (Fig. 2i) had a minimal effect on proteins relatively quantified by TMT SPS MS<sup>3</sup>, and specifically no substantial effect on the amount of Rad by comparison with untreated paired cardiomyocytes (Fig. 2j, Extended Data Fig. 4d and Supplementary Table 6). In this control experiment, proteins were not proximity labelled. Thus,  $\beta$ -adrenergic

stimulation depletes Rad from the neighbourhood of  $\text{Ca}_v1.2$ , but not from the cell as a whole.

Rad is a member of the Rad, Rem, Rem2 and Gem/Kir (RGK) family of Ras-like GTP-binding proteins—known for their capacity to inhibit all high-voltage-activated  $\text{Ca}^{2+}$  channels<sup>8,9</sup>—and is a potential PKA target<sup>20</sup>. Rad-knockout mice display an increased basal  $\text{Ca}^{2+}$  current with activation at lower voltages and reduced  $\beta$ -adrenergic stimulation of their  $\text{Ca}^{2+}$  channels<sup>21,22</sup>. Other studies, however, led to expectations that Rad is not directly involved in adrenergic regulation of  $\text{Ca}_v1.2$ , because overexpression of Rad<sup>23</sup> or Rem<sup>24</sup> in cultured cardiomyocytes markedly attenuated the basal  $\text{Ca}_v1.2$  current, which was also not increased by  $\beta$ -adrenergic stimulation. Nevertheless, our proximity labelling results elevated Rad as the leading candidate for the critical missing link that enables PKA regulation of  $\text{Ca}_v1.2$ .

## PKA regulates $\text{Ca}_v1.2$ via Rad phosphorylation

The robust heterologous reconstitution of PKA regulation of  $\text{Ca}_v1.2$  currents has long been pursued as a crucial step in identifying and



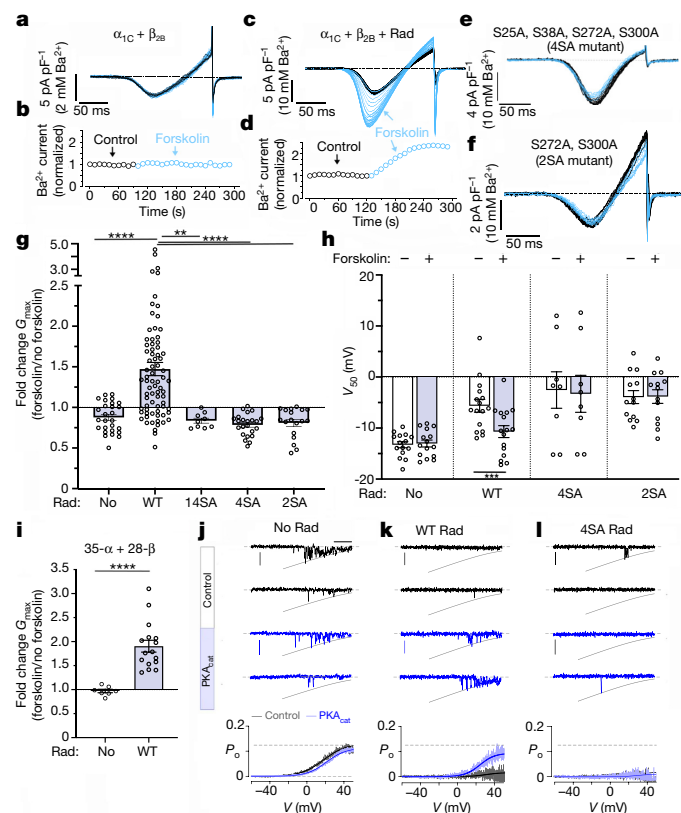


**Fig. 3 | Phosphorylation of Rad is required for cAMP-PKA-mediated activation of  $\text{Ca}_v1.2$ .** **a, c, e, f,**  $\text{Ba}^{2+}$  current elicited by voltage ramp every 10 s, with black traces obtained before and blue traces obtained after forskolin treatment. Representative of 15, 16, 8 and 13 cells, from left to right. **b, d,** Diary plot of normalized  $\text{Ba}^{2+}$  current amplitude at 0 mV. Representative of 15 and 16 cells. **g,** Fold change in maximum conductance ( $G_{\text{max}}$ ) induced by forskolin. Data are mean  $\pm$  s.e.m.;  $P < 0.0001$  by one-way ANOVA;  $**P < 0.01$ ,  $****P < 0.0001$  by Tukey's test.  $n = 27, 76, 9, 23$  and 18 cells, from left to right. Specific  $P$  values can be found in the associated Source Data (see Supplementary Information). **h,** Boltzmann function parameter  $V_{50}$ . Data are mean  $\pm$  s.e.m.;  $***P < 0.001$  by two-tailed paired  $t$ -test.  $n = 15, 16, 8$  and 13, from left to right. **i,** Fold change in  $G_{\text{max}}$  induced by forskolin in the absence and presence of Rad. Data are mean  $\pm$  s.e.m.;  $****P < 0.0001$  by unpaired two-tailed  $t$ -test.  $n = 7$  and 16, from left to right. **j–l,** The top rows display stochastic records, where channel closures are zero-current portions of the trace (horizontal grey lines) and openings are downward deflections to the open level (slanted grey lines). In the bottom row, pale blue and grey lines are average  $P_0$ -V relationships from multiple cells. Blue and black lines are Boltzmann fits. In all experiments,  $\alpha_{1C}$  and  $\beta_{2B}$  were expressed in HEK cells with no Rad (**j**), with wild-type Rad (**k**), or with 4 SA-mutant Rad (**l**), in the absence or presence of exogenous PKA catalytic subunit. The upper dashed lines show maximal  $P_0$  for control of  $\alpha_{1C}$  plus  $\beta_{2B}$  without Rad. Scale bars, 1 pA and 25 ms. Control,  $n = 10$ ; control plus PKA,  $n = 5$ ; Rad,  $n = 5$ ; Rad plus PKA,  $n = 8$ ; 4SA mutant Rad,  $n = 6$ ; 4SA mutant Rad plus PKA,  $n = 5$ .

validating the mechanism. We now find that Rad was the missing ingredient. To prove this experimentally, we coexpressed Rad with  $\alpha_{1C}$  and  $\beta_{2B}$  subunits in HEK293T cells, limiting Rad expression by using a 1/3 to 1/6 ratio of Rad/ $\text{Ca}_v1.2$  complementary DNA to avoid complete inhibition of the  $\text{Ca}^{2+}$  current. We used a perforated, whole-cell patch clamp technique to preserve the normal intracellular milieu and signalling cascades, and to minimize current run-down.  $\text{Ba}^{2+}$  was used as a charge carrier to eliminate  $\text{Ca}^{2+}$ -dependent inactivation. In HEK293T cells transfected with only  $\alpha_{1C}$  plus  $\beta_{2B}$ , superfusion of forskolin over 1–3 minutes had no impact on a  $\text{Ba}^{2+}$  current (Fig. 3a, b, g, h). By contrast, applying forskolin to cells expressing  $\alpha_{1C}$ ,  $\beta_{2B}$  and Rad increased the

maximal conductance ( $G_{\text{max}}$ ) by as much as 4.5-fold and by a mean of 1.5-fold, and shifted the  $V_{50}$  for activation (Fig. 3c, d, g, h and Extended Data Fig. 6a, b). The forskolin-induced increase in current was inversely proportional to the basal current density, as observed in cardiomyocytes (Extended Data Figs. 1c, 6c). In HEK293T cells expressing 35-mutant  $\alpha_{1C}$  plus 28-mutant  $\beta_{2B}$  plus Rad, applying forskolin increased  $G_{\text{max}}$  by as much as 3.1-fold and by a mean of 1.9-fold, and caused a hyperpolarizing shift in the  $V_{50}$  for activation (Fig. 3i and Extended Data Fig. 6d, e). For both wild-type and phosphorylation-site-mutant  $\alpha_{1C}$  and  $\beta_{2B}$  subunits, the forskolin-induced enhancement of  $\text{Ba}^{2+}$  current in Rad-transfected cells was greatest at hyperpolarized potentials and fell as the test potential approached the reversal potential (Extended Data Fig. 6f, g), consistent with observations in cardiomyocytes<sup>25</sup>.

We used single-channel recordings to determine the mechanism of PKA/Rad modulation of  $\text{Ca}_v1.2$ . In the absence of Rad, sweeps with no openings or blank sweeps are rare, while most sweeps exhibit either intermediate or high levels of openings (Fig. 3j and Extended Data Fig. 6h, k). In HEK293T cells transfected with  $\alpha_{1C}$  plus  $\beta_{2B}$ , coexpression of PKA<sub>cat</sub> subunit has no effect on open probability ( $P_0$ ) (Fig. 3j). When Rad is expressed, the fraction of blank sweeps is increased, the low-activity mode predominates, and the  $P_0$  is reduced (Fig. 3k and Extended Data Fig. 6i). By comparison, if the PKA<sub>cat</sub> subunit is coexpressed with Rad, the fraction of blank sweeps is reduced, the high-activity mode resurges, and the  $P_0$  is increased by  $10.6 \pm 2.9$ -fold compared with transfection without PKA (Fig. 3k and Extended Data Fig. 6j, l). These results suggest that Rad potentially dampens the  $\text{Ca}_v1.2$  current, while phosphorylation of Rad allows channels to operate as though they were devoid of Rad.

We identified 14 consensus PKA phosphorylation sites in Rad (Extended Data Fig. 7a), and we mutated these sites to alanine. The mutant Rad effectively inhibited  $\text{Ca}_v1.2$  currents; however, the cAMP/PKA-mediated upregulation of  $\text{Ca}_v1.2$  current was lost (Fig. 3g). In lysates from forskolin-stimulated HEK293T cells transfected with GFP-Rad, we observed phosphorylation of Ser25, Ser38 and Ser300 by mass spectrometry (Extended Data Fig. 7b). These residues were previously identified in mouse hearts as phosphorylation targets<sup>26</sup> (Extended Data Fig. 7c). We were unable to detect either unphosphorylated or phosphorylated peptides containing Ser272, notwithstanding prior biochemical studies identifying this residue as a PKA target<sup>20</sup>. Alanine substitutions of Ser25, Ser38, Ser272 and Ser300 in Rad (4-SA mutant; Extended Data Fig. 7d) prevented the forskolin-induced increase in  $G_{\text{max}}$  and hyperpolarizing shift in the current–voltage curve (Fig. 3e, g, h). By contrast with transfection with wild-type Rad, cotransfection of PKA with 4-SA mutant Rad failed to increase  $P_0$  (PKA to no PKA,  $1.15 \pm 0.56$ -fold; Fig. 3l).

A C-terminal polybasic region of 32 amino acids in Rad is involved in plasma-membrane targeting via binding to negatively charged phospholipids such as phosphatidylinositol 4,5-bisphosphate ( $\text{PtdIns}(4,5)\text{P}_2$ , also known as  $\text{PIP}_2$ )<sup>27</sup>. Deletion of the C terminus of RGK GTPases prevents their inhibition of  $\text{Ca}^{2+}$ -channel function<sup>9</sup>. We found that alanine substitutions at Ser272 and Ser300 (2-SA mutant) within the C-terminal polybasic membrane region prevented both the forskolin-induced increase in current amplitude and the hyperpolarizing shift in the current–voltage curve (Fig. 3f, h and Extended Data Fig. 6c).

## Role of Rad binding to $\text{Ca}_v1.2$ $\beta$ subunits

Rad can inhibit  $\text{Ca}_v1.2$  via  $\beta$ -dependent and  $\beta$ -independent ( $\alpha_{1C}$ -dependent) mechanisms<sup>28</sup>. Substituting Rad residues Arg208 and Leu235, or  $\beta_{2B}$  residues Asp244, Asp320 and Asp322, with alanine (Extended Data Fig. 8a, b) attenuates Rad binding to  $\beta$  subunits<sup>28,29</sup>. These mutations prevented the forskolin-induced increase in  $G_{\text{max}}$  and the hyperpolarizing shift in the current–voltage curve (Fig. 4a and Extended Data Fig. 8c, d). Thus, the interaction between Rad and  $\beta$  subunits is essential for cAMP–PKA regulation of  $\text{Ca}_v1.2$ .

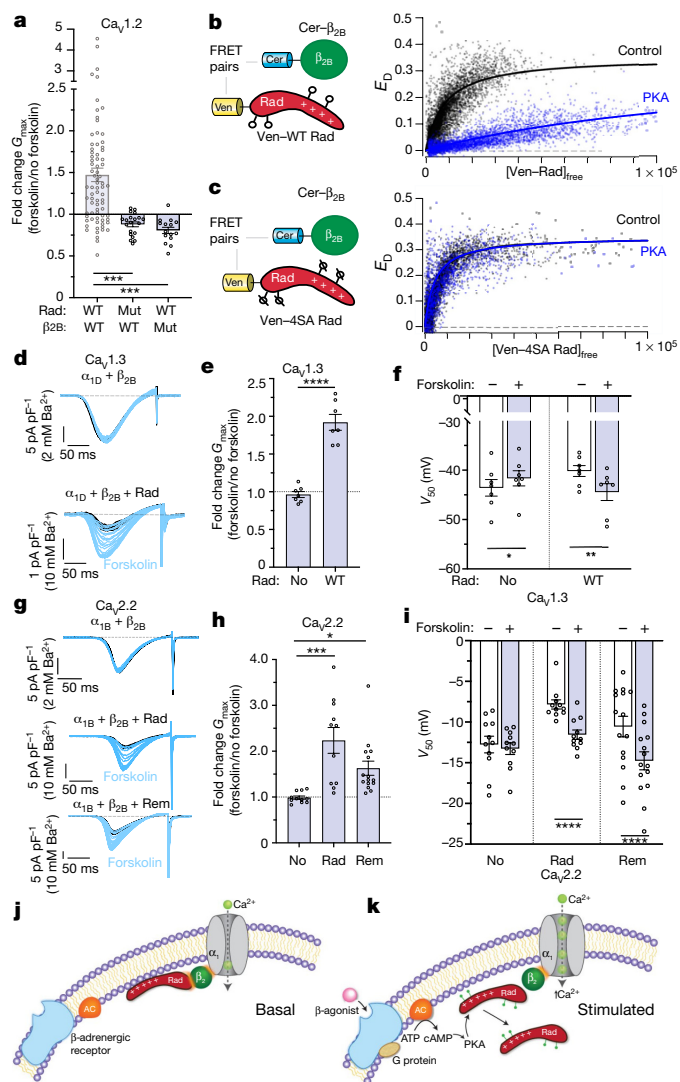


**Fig. 4 | RGK GTPases confer adrenergic regulation to  $\text{Ca}_v1.2$ ,  $\text{Ca}_v1.3$  and  $\text{Ca}_v2.2$  channels via binding to  $\beta$ .** **a**, Fold change in  $G_{\text{max}}$  for different combinations of wild-type and mutant Rad and  $\beta_{2B}$  subunit. Data are mean  $\pm$  s.e.m.;  $P < 0.0001$  by one-way ANOVA;  $***P < 0.001$  by Dunnett's test. The data for WT Rad and WT  $\beta_{2B}$  are as in Fig. 3g.  $n = 76, 20$  and  $15$ , left to right. Specific  $P$  values can be found in the associated Source Data (see Supplementary Information). **b, c**, At the left are shown schematics of the FRET pairs, Cer- $\beta_{2B}$  with Ven-WT-Rad (**b**) or Ven-4SA-mutant Rad (**c**) (where Ven is the venus tag and Cer is the cerulean tag). At the right, FRET efficiency ( $E_D$ ) is plotted against the free concentration of Ven-WT (**b**) or Ven-4SA-mutant Rad (**c**). The solid line fits a 1/1 binding isotherm. **d**,  $\text{Ba}^{2+}$  current of  $\text{Ca}_v1.3$  channels, without or with expression of Rad, elicited by voltage ramp every 10 s. Black traces indicate before and blue traces after forskolin treatment. No Rad, Rad: seven cells each. **e**, Fold change in  $G_{\text{max}}$ . Data are mean  $\pm$  s.e.m.;  $****P < 0.0001$  by unpaired two-tailed  $t$ -test;  $n = 7$  in both cases. **f**, Boltzmann function parameter  $V_{50}$ . Data are mean  $\pm$  s.e.m.;  $*P < 0.05$ ;  $**P < 0.01$  by paired two-tailed  $t$ -test;  $n = 7$  in all cases. **g**,  $\text{Ba}^{2+}$  current of  $\text{Ca}_v2.2$  channels, without or with expression of Rad or Rem, elicited by voltage ramp every 10 s. Black traces were obtained before, and blue traces after, treatment with forskolin. Representative of 11, 11 and 15 cells, from top to bottom. **h**, Fold change in  $G_{\text{max}}$ . Data are mean  $\pm$  s.e.m.  $P < 0.001$  by one-way ANOVA;  $****P < 0.001$ ,  $*P < 0.05$  by Dunnett's test.  $n = 11, 11$  and  $15$ , from left to right. **i**, Boltzmann function parameter  $V_{50}$ . Data are mean  $\pm$  s.e.m.;  $****P < 0.001$  by paired two-tailed  $t$ -test;  $n = 11, 11$  and  $15$ , from left to right. **j, k**, Proposed model of  $\beta$ -adrenergic regulation of  $\text{Ca}_v1.2$  channels. **j**, Basal state (**j**), and after  $\beta$ -agonist-induced activation of adenylyl cyclase (AC) (**k**) leads to activation of PKA and hence to PKA-mediated phosphorylation of Rad, causing dissociation of Rad from the  $\text{Ca}_v1.2$  complex and therefore increased  $\text{Ca}^{2+}$  influx.

We used a flow-cytometry Förster resonance energy transfer (FRET) two-hybrid assay<sup>30</sup> to probe potential PKA-mediated changes in the binding of  $\beta_{2B}$  subunits and wild-type Rad. At baseline, we detected robust binding between cerulean-tagged  $\beta_{2B}$  subunit and venus-tagged wild-type Rad, consistent with previous studies<sup>31</sup> (with an effective dissociation constant ( $K_{d,\text{EFF}}$ ) of  $7,957 \pm 418$ ; Fig. 4b and Extended Data Fig. 9c). Coexpression of the PKA<sub>cat</sub> subunit, however, markedly weakened this interaction ( $K_{d,\text{EFF}} = 145,231 \pm 3,084$ ). By contrast, coexpression of the PKA<sub>cat</sub> subunit in cells expressing fluorophore-tagged  $\beta_{2B}$  and 4-SA mutant Rad had no effect on FRET binding ( $K_{d,\text{EFF}} = 4,349 \pm 138$  versus  $K_{d,\text{EFF}} = 4,346 \pm 197$  with and without, respectively, the PKA catalytic domain; Fig. 4c and Extended Data Fig. 9c). These results suggest that phosphorylation of Rad is required for dissociation of the Rad- $\beta_{2B}$  interaction. In a similar manner, PKA phosphorylation of Rad also reduced FRET binding to both  $\beta_3$  and  $\beta_4$  (Extended Data Fig. 9a–c).

## Unified mechanism for PKA regulation

In adrenal chromaffin cells and the sinus node cells of the heart, L-type  $\text{Ca}_v1.3$  channels are robustly stimulated by PKA<sup>32,33</sup>. We found that, in HEK293T cells transfected with only  $\text{Ca}_v1.3 \alpha_{1D}$  plus  $\beta_{2B}$ , superfusion of forskolin over 1–3 minutes had no impact on the  $\text{Ba}^{2+}$  current (Fig. 4d–f). By contrast, in cells expressing  $\alpha_{1D}$ ,  $\beta_{2B}$  and Rad, applying forskolin increased  $G_{\text{max}}$  by as much as 2.3-fold and by a mean of 1.9-fold, and shifted the  $V_{50}$  for activation (Fig. 4d–f). We also expressed the N-type  $\text{Ca}_v2.2 \alpha_{1B}$  subunit, which is widely expressed in neurons, with  $\beta_{2B}$  and Rad in HEK293T cells. Forskolin increased  $G_{\text{max}}$  through  $\text{Ca}_v2.2$  when coexpressed with Rad by a mean of 2.2-fold and shifted the  $V_{50}$  for activation (Fig. 4g–i). For both  $\text{Ca}_v1.3$  and  $\text{Ca}_v2.2$ , attenuating binding of Rad to  $\beta$  subunits prevented the forskolin-induced modulation of  $\text{Ca}_v$  current (Extended Data Fig. 8e, f). We also expressed in HEK293T cells the  $\text{Ca}_v2.2 \alpha_{1B}$  subunit with  $\beta_{2B}$  and Rem, another member of the RGK GTPase family. Forskolin increased  $G_{\text{max}}$  through  $\text{Ca}_v2.2$  when coexpressed with Rem by 1.6-fold and shifted the  $V_{50}$  for activation (Fig. 4g–i). Thus, PKA-mediated modulation of  $\text{Ca}_v$  channels is not idiosyncratic, as currently believed; rather, it is emerging to be a universal mechanism transferable to all  $\text{Ca}_v$  channels that bind  $\beta$  subunits.

## Discussion

The core  $\alpha_{1C}$  and  $\beta_{2B}$  subunits, previously hypothesized to contain the PKA target sites required for  $\beta$ -adrenergic agonist-induced stimulation of  $\text{Ca}_v1.2$ , do not. Rather, successful reconstitution of regulation in a heterologous expression system requires an additional component, which we now identify as Rad. The cAMP–PKA-mediated regulation of  $\text{Ca}_v1.2$  requires both phosphorylation by PKA on the C terminus of Rad and the interaction of Rad with the  $\beta$  subunit. Multiple-alignment analysis of Rad from mice and other species shows that the four phosphorylation sites are conserved (Extended Data Fig. 10a). The required interaction with the  $\beta$  subunit is consistent with our recent finding that disrupting the  $\alpha_{1C}$ – $\beta$  interaction prevents the regulation of  $\text{Ca}_v1.2$  by PKA in the heart<sup>17</sup>.

Analysis of Rad and other members of the RGK GTPase family indicates that their C-terminal phosphorylation sites are highly similar (Extended Data Fig. 10b). Short stretches of basic and hydrophobic amino acids are known to interact with the membrane<sup>27</sup> and phosphorylation of residues within these stretches alters their electrostatic character, thereby reducing membrane affinity<sup>34</sup>. We found that phosphorylation of two serine residues within the C-terminal polybasic region of Rad releases  $\text{Ca}^{2+}$  channels from Rad-mediated inhibition, probably by means of reducing the affinity of Rad with the membrane and with the  $\text{Ca}_v \beta$  subunit (Fig. 4j, k). This mechanism of regulation is modular and transferable, as  $\text{Ca}_v1.3$  channels and neuronal  $\text{Ca}_v2.2$  channels are also imparted with forskolin/PKA-mediated upregulation via Rad and Rem. The activation of  $\text{Ca}^{2+}$  channels via release of inhibition

by PKA phosphorylation is reminiscent of PKA phosphorylation of phospholamban, an inhibitor of the sarco/endoplasmic reticulum  $\text{Ca}^{2+}$ -ATPase<sup>35</sup>.

Whereas phosphorylation of Ser1928 is definitively not required for  $\beta$ -adrenergic regulation of  $\text{Ca}_v1.2$  in the heart, substitution of this residue with alanine prevents  $\beta$ -adrenergic stimulation of  $\text{Ca}^{2+}$  channels in hippocampal neurons and hyperglycaemia-induced stimulation of  $\text{Ca}^{2+}$  currents in arterial smooth muscle cells<sup>36,37</sup>. Perhaps there are tissue-specific differences in  $\text{Ca}_v1.2$  regulation. Phosphorylation of the  $\alpha_{1C}$  subunit may also affect the trafficking and clustering of channels in neurons and cardiomyocytes<sup>38,39</sup>.

Our results demonstrate that proximity labelling using APEX2 is feasible in the heart and, combined with multiplexed TMT proteomics, can identify a dynamically evolving network of interactions induced by  $\beta$ -adrenergic stimulation. This study establishes the utility of proximity labelling in animals and provides an important foundation for future studies that will investigate how diseases, such as heart failure, change the proteomic subdomain of the excitation–contraction coupling machinery.

Augmented  $\text{Ca}^{2+}$  entry enhances the opening of ryanodine receptors via  $\text{Ca}^{2+}$ -induced  $\text{Ca}^{2+}$  release and increases cardiac contractility. Dysregulation of  $\text{Ca}_v1.2$  activity can result in cardiac arrhythmias, heart failure and sudden death. Supporting an important role of RGK GTPases in humans, a Rem2 variant has been identified as a genetic modifier in long QT syndrome 2 (ref. 40), and a Rad variant was recently linked to Brugada syndrome<sup>41</sup>. Our results identify potential targets and interaction sites for the therapeutic modulation of  $\beta$ -adrenergic regulation of  $\text{Ca}^{2+}$  currents in the heart and other tissues. For instance, disrupting the interaction between Rad and  $\beta$  subunits can be inotropic by increasing  $\text{Ca}^{2+}$  entry in the heart. Conversely, interfering with the  $\alpha_{1C}$ – $\beta$  interaction<sup>17</sup>, blocking PKA phosphorylation of Rad or potentially enhancing the interaction of Rad with the plasma membrane could attenuate the sympathetic nervous system activation of cardiac  $\text{Ca}^{2+}$  entry and inotropy more specifically than do  $\beta$ -blockers.

## Online content

Any methods, additional references, Nature Research reporting summaries, source data, extended data, supplementary information, acknowledgements, peer review information; details of author contributions and competing interests; and statements of data and code availability are available at <https://doi.org/10.1038/s41586-020-1947-z>.

- Cachelin, A. B., de Peyer, J. E., Kokubun, S. & Reuter, H.  $\text{Ca}^{2+}$  channel modulation by 8-bromocyclic AMP in cultured heart cells. *Nature* **304**, 462–464 (1983).
- Reuter, H. & Scholz, H. The regulation of the calcium conductance of cardiac muscle by adrenaline. *J. Physiol.* **264**, 49–62 (1977).
- Hartzell, H. C., Méry, P. F., Fischmeister, R. & Szabo, G. Sympathetic regulation of cardiac calcium current is due exclusively to cAMP-dependent phosphorylation. *Nature* **351**, 573–576 (1991).
- Tsien, R. W., Giles, W. & Greengard, P. Cyclic AMP mediates the effects of adrenaline on cardiac purkinje fibres. *Nat. New Biol.* **240**, 181–183 (1972).
- Hung, V. et al. Spatially resolved proteomic mapping in living cells with the engineered peroxidase APEX2. *Nat. Protocols* **11**, 456–475 (2016).
- Rhee, H. W. et al. Proteomic mapping of mitochondria in living cells via spatially restricted enzymatic tagging. *Science* **339**, 1328–1331 (2013).
- Paek, J. et al. Multidimensional tracking of GPCR signaling via peroxidase-catalyzed proximity labeling. *Cell* **169**, 338–349 (2017).
- Béguin, P. et al. Regulation of  $\text{Ca}^{2+}$  channel expression at the cell surface by the small G-protein kir/Gem. *Nature* **411**, 701–706 (2001).
- Finlin, B. S., Crump, S. M., Satin, J. & Andres, D. A. Regulation of voltage-gated calcium channel activity by the Rem and Rad GTPases. *Proc. Natl Acad. Sci. USA* **100**, 14469–14474 (2003).
- De Jongh, K. S. et al. Specific phosphorylation of a site in the full-length form of the  $\alpha_1$  subunit of the cardiac L-type calcium channel by adenosine 3',5'-cyclic monophosphate-dependent protein kinase. *Biochemistry* **35**, 10392–10402 (1996).

- Fuller, M. D., Emrick, M. A., Sadilek, M., Scheuer, T. & Catterall, W. A. Molecular mechanism of calcium channel regulation in the fight-or-flight response. *Sci. Signal.* **3**, ra70 (2010).
- Gerhardtstein, B. L., Puri, T. S., Chien, A. J. & Hosey, M. M. Identification of the sites phosphorylated by cyclic AMP-dependent protein kinase on the  $\beta_2$  subunit of L-type voltage-dependent calcium channels. *Biochemistry* **38**, 10361–10370 (1999).
- Ganesan, A. N., Maack, C., Johns, D. C., Sidor, A. & O'Rourke, B.  $\beta$ -adrenergic stimulation of L-type  $\text{Ca}^{2+}$  channels in cardiac myocytes requires the distal carboxyl terminus of  $\alpha_1C$  but not serine 1928. *Circ. Res.* **98**, e11–e18 (2006).
- Lemke, T. et al. Unchanged  $\beta$ -adrenergic stimulation of cardiac L-type calcium channels in  $\text{Ca}_v1.2$  phosphorylation site S1928A mutant mice. *J. Biol. Chem.* **283**, 34738–34744 (2008).
- Brandmayr, J. et al. Deletion of the C-terminal phosphorylation sites in the cardiac  $\beta$ -subunit does not affect the basic  $\beta$ -adrenergic response of the heart and the  $\text{Ca}_v1.2$  channel. *J. Biol. Chem.* **287**, 22584–22592 (2012).
- Yang, L. et al.  $\beta$ -adrenergic regulation of the L-type  $\text{Ca}^{2+}$  channel does not require phosphorylation of  $\alpha_1C$  Ser1700. *Circ. Res.* **113**, 871–880 (2013).
- Yang, L. et al. Cardiac  $\text{Ca}_v1.2$  channels require  $\beta$  subunits for  $\beta$ -adrenergic-mediated modulation but not trafficking. *J. Clin. Invest.* **129**, 647–658 (2019).
- Martell, J. D. et al. Engineered ascorbate peroxidase as a genetically encoded reporter for electron microscopy. *Nat. Biotechnol.* **30**, 1143–1148 (2012).
- Lobingier, B. T. et al. An approach to spatiotemporally resolve protein interaction networks in living cells. *Cell* **169**, 350–360 (2017).
- Moyers, J. S., Zhu, J. & Kahn, C. R. Effects of phosphorylation on function of the Rad GTPase. *Biochem. J.* **333**, 609–614 (1998).
- Manning, J. R. et al. Rad GTPase deletion increases L-type calcium channel current leading to increased cardiac contraction. *J. Am. Heart Assoc.* **2**, e000459 (2013).
- Levitani, B. M. et al. Rad-deletion phenocopies tonic sympathetic stimulation of the heart. *J. Cardiovasc. Transl. Res.* **9**, 432–444 (2016).
- Wang, G. et al. Rad as a novel regulator of excitation-contraction coupling and  $\beta$ -adrenergic signaling in heart. *Circ. Res.* **106**, 317–327 (2010).
- Xu, X., Marx, S. O. & Colecraft, H. M. Molecular mechanisms, and selective pharmacological rescue, of Rem-inhibited  $\text{Ca}_v1.2$  channels in heart. *Circ. Res.* **107**, 620–630 (2010).
- Bean, B. P., Nowicky, M. C. & Tsien, R. W.  $\beta$ -adrenergic modulation of calcium channels in frog ventricular heart cells. *Nature* **307**, 371–375 (1984).
- Huttlin, E. L. et al. A tissue-specific atlas of mouse protein phosphorylation and expression. *Cell* **143**, 1174–1189 (2010).
- Heo, W. D. et al.  $\text{PI}(3,4,5)\text{P}_3$  and  $\text{PI}(4,5)\text{P}_2$  lipids target proteins with polybasic clusters to the plasma membrane. *Science* **314**, 1458–1461 (2006).
- Yang, T., Puckerin, A. & Colecraft, H. M. Distinct RGK GTPases differentially use  $\alpha_1$ - and auxiliary  $\beta$ -binding-dependent mechanisms to inhibit  $\text{Ca}_v1.2/\text{Ca}_v2.2$  channels. *PLoS One* **7**, e37079 (2012).
- Béguin, P. et al. RGK small GTP-binding proteins interact with the nucleotide kinase domain of  $\text{Ca}^{2+}$ -channel  $\beta$ -subunits via an uncommon effector binding domain. *J. Biol. Chem.* **282**, 11509–11520 (2007).
- Lee, S. R., Sang, L. & Yue, D. T. Uncovering aberrant mutant PKA function with flow cytometric FRET. *Cell Rep.* **14**, 3019–3029 (2016).
- Chang, D. D. & Colecraft, H. M. Rad and Rem are non-canonical G-proteins with respect to the regulatory role of guanine nucleotide binding in  $\text{Ca}_v1.2$  channel regulation. *J. Physiol.* **593**, 5075–5090 (2015).
- Mahapatra, S., Marcantoni, A., Zuccotti, A., Carabelli, V. & Carbone, E. Equal sensitivity of  $\text{Ca}_v1.2$  and  $\text{Ca}_v1.3$  channels to the opposing modulations of PKA and PKG in mouse chromaffin cells. *J. Physiol.* **590**, 5053–5073 (2012).
- Mangoni, M. E. et al. Functional role of L-type  $\text{Ca}_v1.3$   $\text{Ca}^{2+}$  channels in cardiac pacemaker activity. *Proc. Natl Acad. Sci. USA* **100**, 5543–5548 (2003).
- Bailey, M. J. & Prehoda, K. E. Establishment of Par-polarized cortical domains via phosphoregulated membrane motifs. *Dev. Cell* **35**, 199–210 (2015).
- Kranias, E. G. Regulation of  $\text{Ca}^{2+}$  transport by cyclic 3',5'-AMP-dependent and calcium-calmodulin-dependent phosphorylation of cardiac sarcoplasmic reticulum. *Biochim. Biophys. Acta* **844**, 193–199 (1985).
- Qian, H. et al. Phosphorylation of Ser<sup>1928</sup> mediates the enhanced activity of the L-type  $\text{Ca}^{2+}$  channel  $\text{Ca}_v1.2$  by the  $\beta_2$ -adrenergic receptor in neurons. *Sci. Signal.* **10**, eaaf9659 (2017).
- Nystoriak, M. A. et al. Ser<sup>1928</sup> phosphorylation by PKA stimulates the L-type  $\text{Ca}^{2+}$  channel  $\text{Ca}_v1.2$  and vasoconstriction during acute hyperglycemia and diabetes. *Sci. Signal.* **10**, eaaf9647 (2017).
- Folci, A. et al. Molecular mimicking of C-terminal phosphorylation tunes the surface dynamics of  $\text{Ca}_v1.2$  calcium channels in hippocampal neurons. *J. Biol. Chem.* **293**, 1040–1053 (2018).
- Ito, D. W. et al.  $\beta$ -adrenergic-mediated dynamic augmentation of sarcolemmal  $\text{Ca}_v1.2$  clustering and co-operativity in ventricular myocytes. *J. Physiol.* **597**, 2139–2162 (2019).
- Chai, S. et al. Physiological genomics identifies genetic modifiers of long QT syndrome type 2 severity. *J. Clin. Invest.* **128**, 1043–1056 (2018).
- Belbachi, N. et al. RRAD mutation causes electrical and cytoskeletal defects in cardiomyocytes derived from a familial case of Brugada syndrome. *Eur. Heart J.* **40**, 3081–3094 (2019).

**Publisher's note** Springer Nature remains neutral with regard to jurisdictional claims in published maps and institutional affiliations.

© The Author(s), under exclusive licence to Springer Nature Limited 2020

## Methods

### Clone construction and cell culture

All mouse N-terminally GFP-tagged Rad (GenBank accession number XM\_006531206) constructs in a pEGFP-C1 vector were generated by gene synthesis (Gene Universal). Human  $\text{Ca}_v2.2$  (pSAD442-1) was a gift from D. Lipscombe (Addgene plasmid 62,574; <http://n2t.net/addgene:62574>; Resource Identification (RRID) number Addgene\_62574). All cDNA clones were authenticated by sequencing.

HEK293T cells (American Type Culture Collection (ATCC), CRL-3216) were cultured in Dulbecco's modified Eagle's medium (DMEM) with 10% fetal bovine serum (FBS) and 1% penicillin/streptomycin, and were transfected with 3  $\mu\text{g}$  rabbit  $\alpha_{1C}$  (accession number X15539), human  $\alpha_{1B}$  (for  $\text{Ca}_v2.2$  experiments) or rat  $\alpha_{1D}$  (for  $\text{Ca}_v1.3$  experiments, accession number AF3070009), 3  $\mu\text{g}$  human  $\beta_{2B}$  (NM-201590.3) and 0.5  $\mu\text{g}$  N-terminal-GFP-tagged mouse Rad using Lipofectamine 2000 (Thermo Fisher Scientific). For the FRET experiments, rat  $\beta_3$  (accession number NM\_012828) and rat  $\beta_4$  (accession number L02315) were used. The media was changed 4–6 h after transfection. The cells were split onto coverslips coated with attachment factor protein (Gibco). Electrophysiological recordings were carried out at room temperature 24–48 h after transfection. The cells were authenticated by ATCC and tested for mycoplasma contamination.

### Generation of transgenic mice

The Institutional Animal Care and Use Committee at Columbia University approved all animal experiments. We used male and female mixed-strain mice at 6 weeks to 4 months of age. Sample sizes exceeded the number of samples determined by power calculations, which were based on effect sizes reported previously<sup>16,17,42,43</sup>. The number of mice was always greater than three per genotype. The investigators were blinded to group allocation during data acquisition and analysis.

Transgenic constructs were generated by fusing rabbit  $\alpha_{1C}$  cDNA or human  $\beta_{2B}$  cDNA to the modified murine  $\alpha$ -myosin heavy chain (MHC) tetracycline-inducible-promoter vector (a gift from J. Robbins and J. Molkentin, University of Cincinnati, Cincinnati, OH)<sup>44,45</sup>. A 3 $\times$  Flag epitope was ligated in-frame to the N terminus of  $\alpha_{1C}$ . The  $\alpha_{1C}$  subunit was engineered to be dihydropyridine (DHP)-insensitive with the substitutions T1066Y and Q1070M (refs. <sup>46,47</sup>). GFP was ligated to the N terminus of  $\beta_{2B}$ . The creation of GFP-WT- $\beta_{2B}$  transgenic mice was described previously<sup>17</sup>. The V5 epitope and APEX2 cDNA<sup>5,48</sup>, created by gene synthesis, were conjugated to the N terminus of DHP-resistant  $\alpha_{1C}$  and WT  $\beta_{2B}$ .

The 35- $\alpha$  mutant and the 28- $\beta$  mutant cDNA were generated by site-directed mutagenesis. The optimal PKA phosphorylation motif is a tetrapeptide with arginine at the second and third positions (termed -2 and -3) before the phosphorylated serine or threonine, and a large hydrophobic residue immediately thereafter (R-R-X-S/T- $\Phi$ )<sup>49–51</sup>. The requirement for a positive charge is highest for residues at -2 and -3, but can be found for residues as far as position -6 in PKA target sites<sup>52</sup>. Sites with arginine in positions between -4 and -1 are strongly preferred, and histidine or lysine to a lesser extent<sup>50,53</sup>. We identified all potential intracellular PKA phosphorylation sites (Extended Data Fig. 1a, d) in rabbit  $\alpha_{1C}$  and human  $\beta_{2B}$  using both manual sequence analysis and several web-based PKA phosphorylation prediction tools, including pkaPS<sup>54</sup>, DISPHOS<sup>55</sup>, GPS<sup>56</sup>, NETPHOS<sup>57</sup> and SCANSITE<sup>58</sup>. Each predicted serine or threonine was mutated to alanine. We also mutated additional serines and threonines within several amino-acid residues C-terminal to the arginine or lysine, in order to ensure that we fully captured each phospho-regulatory site. We replaced 51 residues in rabbit  $\alpha_{1C}$  with alanine at 35 potential phospho-regulatory domains in the 35-mutant  $\alpha_{1C}$  construct, and replaced 37 residues with alanine at 28 putative phospho-regulatory domains of  $\beta_{2B}$ . We excluded those sites that were predicted to be extracellular or within the plasma membrane.

Transgenic mice with non-targeted insertion of these tetracycline-regulated cDNAs (Fig. 1b) were bred with cardiac-specific ( $\alpha$ -MHC), doxycycline-regulated, codon-optimized reverse transcriptional transactivator (rtTA) mice<sup>59</sup> (obtained via the Mutant Mouse Resource and Research Center) to generate double-transgenic mice. For the  $\alpha_{1C}$ -APEX2 and  $\beta_{2B}$ -APEX2 mice, transgene expression did not require doxycycline owing to a low basal binding of rtTA protein to the *Tet* operator sequences (so called 'leak')<sup>59</sup>. These expression levels result in  $\text{Ca}^{2+}$  current levels similar to those found under native conditions in the heart. The results presented here were consistent across all founder lines and gender, and therefore were pooled.

### Isolation of adult cardiac myocytes

Mice ventricular myocytes were isolated by enzymatic digestion using a Langendorff perfusion apparatus as described<sup>16,17,42,43,60</sup>. Cardiomyocytes were isolated from 8–12-week-old non-transgenic and transgenic mice. Only non-contracting rod-shaped cells with clear striations were used for functional studies (electrophysiology and excitation–contraction coupling).

### Proximity labelling biotinylation

Proximity labelling was performed as described<sup>48</sup> with minor modifications. Isolated ventricular cardiomyocytes were incubated in labelling solution with 0.5 mM biotin-phenol (Iris-biotech) for 30 min. For some experiments, during the final 10 min of incubation, 1  $\mu\text{M}$  isoproterenol (Sigma I5627) was added. To initiate labelling,  $\text{H}_2\text{O}_2$  (Sigma H1009) was added to a final concentration of 1 mM for 1 min. Exactly 1 min after  $\text{H}_2\text{O}_2$  treatment, the cells were washed three times with cold quenching solution containing 10 mM sodium ascorbate (VWR 95035-692), 5 mM Trolox (Sigma 238813) and 10 mM sodium azide (Sigma S2002). After cells were harvested by centrifugation, the quenching solution was aspirated and the pellet was flash-frozen and stored at  $-80^\circ\text{C}$  until streptavidin pull-down.

For biotinylation in Langendorff-perfused hearts, mice were injected with 5  $\text{mg kg}^{-1}$  propranolol (Sigma PHR1308) in order to suppress adrenergic stimulation during isoflurane anaesthesia and cardiectomy. Hearts were retrograde perfused with Krebs solution for 10 min before addition of biotin-phenol for 15 min. During the final 5 min, 1  $\mu\text{M}$  isoproterenol or vehicle was added to the perfusate. Electrocardiograms were monitored throughout the experiment to ensure viability of the preparation and an isoproterenol-induced increase in heart rate.

The cells or whole heart tissue were lysed with a hand-held tip homogenizer in a solution containing 50 mM Tris (tris(hydroxymethyl)aminomethane), 150 mM NaCl, 10 mM EGTA, 10 mM EDTA, 1% Triton X-100 (v/v), 0.1% SDS (w/v), 10 mM sodium ascorbate, 5 mM Trolox and 10 mM sodium azide, phosphatase inhibitors (Sigma 4906845001), protease inhibitors (Sigma 4693159001), calpain inhibitor I (Sigma A6185) and calpain inhibitor II (Sigma A6060). Biotin labelling of the samples was confirmed after size fractionation of proteins on SDS–polyacrylamide gel electrophoresis (PAGE), transfer to nitrocellulose membranes, and probing with streptavidin-conjugated horseradish peroxidase (HRP) (ThermoFisher, S911, lot number 1711896, 0.6  $\text{mg ml}^{-1}$ ). The response to isoproterenol was assessed by immunoblotting with an anti-phospholamban (Ser16/Thr17) antibody (Cell Signaling, number 8496, lot number 1; 1/1,000 dilution).

Biotinylated proteins were bound to streptavidin magnetic beads (Thermo Fisher Scientific 88817), and the beads were washed three times with a solution containing 4 M urea, 0.5% SDS (w/v) and 100 mM sodium phosphate pH 8. Proteins were size-separated on SDS–PAGE, transferred to nitrocellulose membranes, and probed with anti-V5 antibody (ThermoFisher, R960-25; 1/5,000 dilution), a custom-made polyclonal anti- $\alpha_{1C}$  antibody (Yenzy, 1/1,000 dilution)<sup>61,62</sup>, a custom-made polyclonal anti- $\beta$ -antibody (epitope: mouse residues 120–138, DSYTSRPSDSDVSLEEDRE; Yenzy; 1/1,000 dilution), an anti-JPH2 antibody (Pierce, PA5-20642, lot number NG1583142; 1/1,000 dilution),



# Article

an anti-calmodulin antibody (Millipore Sigma 05-173; 1/1,000 dilution), a custom-made anti-RyR2 antibody (1/5,000 dilution)<sup>63</sup>, and an anti-K<sub>v</sub>1.5 antibody (Alomone, APC-150, lot number APC004AN0850; 1/1,000 dilution).

## Immunoprecipitations

Cardiomyocytes were lysed with a hand-held tip homogenizer in a 1% (v/v) Triton X-100 buffer containing 50 mM Tris-HCl (pH 7.4) 150 mM NaCl, 10 mM EDTA, 10 mM EGTA and 0.01 mM calpain inhibitor I, 0.01 mM calpain inhibitor II, and complete protease inhibitors (1 per 7 ml, Roche). The lysates were incubated on ice for 30 min and centrifuged at 14,000 r.p.m at 4 °C for 10 min; supernatants were then collected. Anti-Flag antibody (Sigma, F7425, lot number 078M4886V) immunoprecipitations were performed, as described<sup>17</sup>, overnight in a lysis buffer consisting of 50 mM Tris-HCl pH 7.4, 150 mM NaCl, 0.25%-1% Triton X-100 (v/v), 10 mM EDTA, 10 mM EGTA, 0.01 mM calpain inhibitor I, 0.01 mM calpain inhibitor II, and complete protease inhibitors (1 per 7 ml). Antibody-protein complexes were collected using protein-A-conjugated agarose (Amersham) for 2 h, followed by three washes in lysis buffer. Proteins were size-separated by SDS, transferred to nitrocellulose membranes and probed with HRP-conjugated anti-Flag antibody (Sigma, A8592), a custom-made anti-β-antibody and HRP-conjugated secondary goat anti-rabbit antibody. Detection of luminescence was performed with a charge-coupled-device (CCD) camera (Carestream Imaging). The uncut gels are shown in Supplementary Fig. 1.

## Immunofluorescence

Isolated cardiomyocytes were first exposed to biotin-phenol and H<sub>2</sub>O<sub>2</sub> as described above. After quenching, the cells were fixed for 15 min in 4% paraformaldehyde, washed with glycine/phosphate-buffered saline (PBS) twice, treated with 0.1% Triton X-100 (v/v) in PBS (PBST) for 5 min, and blocked with 3% bovine serum albumin (BSA; w/v) in PBS for 1 h. Indirect immunofluorescence was performed using 1/500 dilutions of anti-V5 antibody (Thermo Fisher, R960-25), 1/200 dilutions of Alexa594-labelled goat anti-mouse antibody (Thermo Fisher, A11032, lot 2069816) and 1/800 dilutions of streptavidin-Alexa Fluor 488 conjugate (Thermo Fisher, S32354, lot 1719656). Images were acquired using a confocal microscope.

## Processing biotinylated proteins for mass spectrometry

Proteins were prepared as described<sup>7,64</sup> with some modifications. Proteins were precipitated with trichloroacetic acid (TCA; Sigma T9159) and then centrifuged at 21,130g at 4 °C for 10 min. The pellet was washed with -20 °C cold acetone (Sigma 650501), vortexed, and centrifuged at 21,130g at 4 °C for 10 min. Following centrifugation, acetone was aspirated and the pellet was washed with acetone three more times. After the last washing step, the pellet was resuspended in 8 M urea, 100 mM sodium phosphate pH 8, 100 mM ammonium bicarbonate and 1% SDS (w/v), and then rotated at room temperature until fully dissolved. Resuspended proteins were centrifuged at 21,130g at room temperature for 10 min and the cleared supernatant was transferred to a new microcentrifuge tube. To reduce disulphides, we added 10 mM Tris (2-carboxyethyl)phosphine hydrochloride (TCEP-HCl; Thermo Fisher Scientific PG82089) in Milli-Q water titrated to pH 7.5 with sodium hydroxide. To alkylate free cysteine, we added freshly prepared 400 mM iodoacetamide (Thermo Fisher Scientific 90034) stock solution in 50 mM ammonium bicarbonate to the supernatant to a final concentration of 20 mM, then immediately vortexed and incubated the solution in the dark for 25 min at room temperature. After alkylation, freshly prepared dithiothreitol (DTT) stock solution was added to a final concentration of 50 mM in order to quench alkylation. Water was added to each sample to reach a final concentration of 4 M urea and 0.5% (w/v) SDS.

A 100 µl suspension equivalent per sample of streptavidin magnetic beads was washed twice with a solution containing 4 M urea,

0.5% SDS (w/v) and 100 mM sodium phosphate pH 8, and was added to each 1 mg of protein sample, diluting each sample with an equal amount of water to reach a final concentration of 2 M urea, 0.25% SDS (w/v), 50 mM sodium phosphate pH 8 during pull-down. The tubes were rotated overnight at 4 °C. Following streptavidin pull-down, the magnetic beads were washed three times with a solution containing 4 M urea, 0.5% SDS (w/v), 100 mM sodium phosphate pH 8, and three times with the same buffer without SDS. The beads were transferred to new tubes for the last wash step. Before final pulldown of the beads for mass-spectrometry analysis, streptavidin-HRP blotting was performed on 5% of the resuspended beads.

## On-bead digestion and TMT labelling

Samples were prepared as described<sup>7</sup>. Liquid reagents used were of high-performance liquid chromatography (HPLC) quality grade. Washed beads were resuspended in 50 µl of 200 mM 3-[4-(2-hydroxyethyl)-piperazin-1-yl]propane-1-sulfonic acid (EPPS) buffer pH 8.5, 2% acetonitrile (v/v) with 1 µl of LysC stock solution (2 mg ml<sup>-1</sup>, Wako), vortexed briefly and incubated at 37 °C for 3 h. Then, 50 µl of trypsin stock (Promega V5111) diluted 1/100 (v/v) in 200 mM EPPS pH 8.5 was added. After mixing, digests were incubated at 37 °C overnight and beads were magnetically removed. Peptides were directly labelled after digest. For this, acetonitrile was added to a concentration of 30% (v/v) and peptides were labelled with TMT 10-plex or 11-plex reagents (Thermo Fisher Scientific 90406 and A34807) for 1 h. Reactions were quenched with hydroxylamine at a final concentration of 0.3% (v/v) for 15 min, and 1% of labelled peptides were analysed for efficiency of label incorporation and relative ratios by mass spectrometry. After quenching, peptide solutions were acidified with formic acid, trifluoroacetic acid (TFA) was added to a concentration of 0.1%, and peptides were desalted and fractionated by high pH reversed phase chromatography (Thermo Fisher Scientific 84868). After loading of labelled peptides onto preconditioned columns and a single wash with water, excess unincorporated TMT label was removed by washing reversed phase columns once with 0.1% trimethylamine (TEA) buffer containing 5% acetonitrile. Samples were fractionated under alkaline conditions into 12 fractions with increasing concentrations of acetonitrile: 10%, 12.5%, 15%, 17.5%, 20%, 25%, 30%, 35%, 40%, 50%, 65% and 80%. Fractions 1 and 7, 2 and 8, 3 and 9, 4 and 10, 5 and 11, and 6 and 12 were pooled to obtain 6 final pooled fractions for subsequent analysis. Pooled fractions were dried to completion and further purified and desalted by acidic C<sub>18</sub> solid phase extraction (StageTip). Labelled peptides were finally resuspended in 1% formic acid (v/v) and 3% acetonitrile (v/v).

## Whole-cell proteomics

Isolated nontransgenic cardiomyocytes were lysed by homogenization (QIAshredder cartridges, Qiagen) in lysis buffer (2% SDS, 150 mM NaCl, 50 mM Tris pH 7.4). Lysates were reduced with 5 mM DTT and alkylated with 15 mM iodoacetamide for 30 min in the dark; alkylation reactions were quenched with freshly prepared DTT added to a concentration of 50 mM, and proteins were precipitated by methanol/chloroform precipitation. Digests were carried out in 1 M urea freshly prepared in 200 mM EPPS pH 8.5 in the presence of 2% acetonitrile (v/v) with LysC (Wako, 2 mg ml<sup>-1</sup>, 1/75 (w/w) protease/substrates during digest) for 3 h at room temperature and after subsequent addition of trypsin (Promega V5111, stock 1/100 w/w protease/substrates) overnight at 37 °C. The missed cleavage rate was assayed from a small aliquot by mass spectrometry. For whole-proteome analysis, digests containing approximately 60 µg of peptide material were directly labelled with TMT reagents (Thermo Fisher Scientific). Labelling efficiency and TMT ratios were assayed by mass spectrometry, while labelling reactions were stored at -80 °C. After quenching of TMT labelling reactions with hydroxylamine, TMT labelling reactions were mixed, solvent evaporated to near completion, and TMT-labelled peptides purified and desalted by acidic reversed phase C<sub>18</sub> chromatography. Peptides



were then fractionated by alkaline reversed phase chromatography into 96 fractions and combined into 24 samples.

### Mass-spectrometry analysis

Data collection followed a MultiNotch MS<sup>3</sup> TMT method<sup>65</sup> using an Orbitrap Lumos mass spectrometer coupled to a Proxeon EASY-nLC 1200 liquid chromatography system (both Thermo Fisher Scientific). The capillary column used was packed with C<sub>18</sub> resin (length 35 cm, inner diameter 75 µm, matrix 2.6 µm Accucore (Thermo Fisher Scientific)). Peptides of each fraction were separated for 4 h over acidic acetonitrile gradients by liquid chromatography before mass-spectrometry analysis. The scan sequence started with an MS<sup>1</sup> scan (Orbitrap analysis; resolution 120,000; mass range 400–1,400 Th). MS<sup>2</sup> analysis followed collision-induced dissociation (CID; CID energy = 35) with a maximum ion-injection time of 150–300 ms and an isolation window of 0.4 *m/z*. In order to obtain quantitative information, we fragmented MS<sup>3</sup> precursors by high-energy collision-induced dissociation (HCD) and analysed the fragments in the Orbitrap at a resolution of 50,000 at 200 Th. Further details on liquid-chromatography and mass-spectrometry parameters and settings were described recently<sup>66</sup>.

Peptides were searched with a SEQUEST (v.28, rev. 12)-based software against a size-sorted forward and reverse database of the *Mus musculus* proteome (Uniprot 07/2014) with added common contaminant proteins. For this, spectra were first converted to mzXML. Searches were performed using a mass tolerance of 20 p.p.m. for precursors and a fragment-ion tolerance of 0.9 Da. For the searches, a maximum of two missed cleavages per peptide was allowed. We searched dynamically for oxidized methionine residues (+15.9949 Da) and, where indicated, for phospho-modification of serine, threonine and tyrosine residues (+79.9663 Da). We applied a target decoy database strategy, and set a false discovery rate (FDR) of 1% for peptide–spectrum matches following filtering by linear discriminant analysis (LDA)<sup>26,66</sup>. The FDR for final collapsed proteins was 1%. We calibrated MS<sup>1</sup> data post-search and performed searches again. We used a modified version of the Ascore algorithm to quantify the confidence assignment of phosphorylation sites. Phosphorylation localized to particular residues required Ascore values of more than 13 ( $P \leq 0.05$ ) for confident localization<sup>26</sup>. Quantitative information on peptides was derived from MS<sup>3</sup> scans. Quantitative tables were generated requiring an MS<sup>2</sup> isolation specificity of more than 70% for each peptide and a sum of TMT signal-to-noise (*s/n*) ratios of more than 200 over all channels for any given peptide; the tables were exported to Excel and processed further therein. Details of the TMT intensity quantification method and further search parameters were described previously<sup>67</sup>. Proteomics raw data and search results were deposited in the PRIDE archive<sup>68,69</sup> and can be accessed under ProteomeXchange accession numbers PXD014499, PXD014500 and PXD014501.

The relative summed TMT *s/n* ratios for proteins between two experimental conditions (referred to as ‘enriched’) were calculated from the sum of TMT *s/n* ratios for all peptides quantified of a given protein. For enrichment of Gene Ontology (GO) terms, the BINGO package in Cytoscape was used<sup>70</sup>. Scaled quantification data were subjected to two-way clustering (JMP software package) and changes in enrichment were analysed using Graphpad Prism 8 (Graphpad Software). Statistical significance was determined by multiple *t*-tests without correction for multiple comparisons and  $\alpha = 0.05$ . Data for relative protein quantification can be found in Supplementary Tables 1, 3–6.

### Phosphoproteomic analysis of Rad

HEK293T cells were cultured in DMEM with 10% FBS and 1% penicillin/streptomycin. Cells were transfected with GFP-labelled Rad using Lipofectamine 2000 as above. The medium was changed 4–6 h after transfection. After 24 h, cells were treated with trypsin and spun down for 5 min at 1,000 r.p.m. Cells were then resuspended in PBS with 10 µM forskolin for 5 min. After washing cell pellets three times with PBS, cells

were frozen at –80 °C. Cold cell pellets were lysed in PBS with 0.1% triton X-100 (v/v, Sigma) and a phosphatase-inhibitor mixture (Complete and PhosSTOP, both from Roche) by pipetting up and down several times. Lysates were homogenized by passing them through QIAshredder cartridges (Qiagen) and incubated with GFP–trap agarose beads (Chromotek, Germany) for 4 h at 4 °C with constant rotation. Beads were washed three times with PBS with 0.1% (v/v) Triton and three times with detergent-free PBS and subjected to on-bead digest with trypsin (Promega V5111), LysC (Wako) or ArgC (Promega V1881, ArgC digestion buffer 50 mM Tris-HCl pH 7.8, 5 mM CaCl<sub>2</sub>, 2 mM EDTA, 2% acetonitrile (v/v)) separately as described above overnight at 37 °C. After acidification, peptides were purified by reversed phase C<sub>18</sub> chromatography and subjected to MS/MS analysis. For this, the same parameters as above for MS<sup>1</sup> and MS<sup>2</sup> scans were used with an isolation window of 1.2 Da and taking a neutral loss of 97.9763 Da into account, with multi-stage activation (MSA) set for MS<sup>2</sup> scans. Analysis of phospho-site localization was performed as above.

### Fractional shortening

Freshly isolated myocytes were perfused with a Tyrode’s solution containing 1.8 mM CaCl<sub>2</sub>. Myocytes were field stimulated at 1 Hz. Nisoldipine (300 nM) dissolved in Tyrode’s solution was then superfused. Fractional shortening of sarcomere length was measured using the SarcLen module of Ionoptix.

### Whole-cell patch-clamp electrophysiology

Isolated cardiomyocytes or HEK cells attached on glass 8 × 8 mm coverslips were placed in Biopetechs Delta T dishes filled with solution containing 112 mM NaCl, 5.4 mM KCl, 1.7 mM NaH<sub>2</sub>PO<sub>4</sub>, 1.6 mM MgCl<sub>2</sub>, 20.4 mM HEPES pH 7.2, 30 mM taurine, 2 mM D/L-carnitine, 2.3 mM creatine and 5.4 mM glucose. The Petri dishes were mounted on the stage of an inverted microscope and served as a perfusion chamber. After establishing a seal and achieving whole-cell configuration, external solutions were changed by the fast local perfusion method.

For cardiomyocytes, pipette resistance was between 1 and 3 MΩ. Membrane currents were measured by the conventional (ruptured) whole-cell patch-clamp method using a MultiClamp 700B or Axopatch200B amplifier and pCLAMP 10.7 software (Molecular Devices). Capacitance transients and series resistance were compensated. Voltage was corrected for liquid junction potential (–10 mV) during analysis. Leak currents were subtracted by a P/4 protocol. The parameters of voltage-dependent activation were obtained using a modified Boltzmann distribution:  $I(V) = G_{\max} \times (V - E_{\text{rev}}) / [1 + \exp((V - V_{50})/V_c)]$ , where  $I(V)$  is the peak current,  $G_{\max}$  is the maximal conductance,  $E_{\text{rev}}$  is the reversal potential,  $V_{50}$  is the midpoint, and  $V_c$  is the slope factor.

The pipette solution contained 40 mM CsCl, 80 mM caesium gluconate, 10 mM 1,2-bis(*o*-aminophenoxy)ethane-*N,N,N',N'*-tetraacetic acid (BAPTA), 1 mM MgCl<sub>2</sub>, 4 mM Mg-ATP, 2 mM CaCl<sub>2</sub> and 10 mM 4-(2-hydroxyethyl)-1-piperazineethanesulfonic acid (HEPES), adjusted to pH 7.2 with CsOH. After the isolated cardiomyocytes were dialysed and adequately buffered with 10 mM BAPTA in the internal solution, cells were superfused with 140 mM tetraethylammonium chloride (TEA-Cl), 1.8 mM CaCl<sub>2</sub>, 1 mM MgCl<sub>2</sub>, 10 mM glucose and 10 mM HEPES, adjusted to pH 7.4 with CsOH. To measure peak currents, we held the cell membrane potential at –50 mV and stepped it to +0 mV for 350 ms every 10 s. To evaluate the current–voltage (*I*–*V*) relationship in cardiomyocytes, we repeated the same protocol with steps between –40 mV and +60 mV in 10-mV increments. Nisoldipine (Santa Cruz) was stored protected from light at –20 °C as 3 mM stock in ethanol. The final dilution of nisoldipine to 300 nM was in the extracellular recording solution immediately before the experiment. Isoproterenol (Sigma I5627) and forskolin (Santa Cruz) were prepared daily and diluted in extracellular solution.

For HEK293T cell experiments involving the forskolin-induced stimulation of Ca<sub>v</sub>1.2, Ca<sub>v</sub>1.3 and Ca<sub>v</sub>2.2 currents, we implemented

# Article

the perforated whole-cell patch-clamp technique in order to minimize current run-down and preserve the intracellular milieu. Amphotericin B (Sigma A9528) was initially dissolved in DMSO (20 mg ml<sup>-1</sup>) and used in the pipette solution at a final concentration of 200 µg ml<sup>-1</sup>. The tip of the pipette was filled with amphotericin-free solution containing 80 mM caesium gluconate, 40 mM CsCl, 10 mM HEPES, 10 mM BAPTA, 1 mM MgCl<sub>2</sub> and 1 mM Mg-ATP, pH adjusted to 7.2 with CsOH. The pipette was backfilled with 125 mM CsCl, 10 mM HEPES, 4 mM CaCl<sub>2</sub>, 1 mM MgCl<sub>2</sub> pH 7.2 and CsOH containing amphotericin at 200 µg ml<sup>-1</sup>. CaCl<sub>2</sub> (4 mM) was added to the patch electrode solution to enable the detection of conversion from perforated to ruptured configuration. The external solution contained 130 mM tetraethylammonium methanesulfonate, 10 mM HEPES, 1 mM MgCl<sub>2</sub>, 10 mM (with Rad expression) or 2 mM (without Rad expression) BaCl<sub>2</sub>, 5 mM glucose. For experiments with HEK293T cells, in addition to step protocols, we used a ramp protocol with a 200-ms voltage ramp from -60 mV to +60 mV (0.6 V s<sup>-1</sup>) applied every 10 s to monitor the *I*-*V* relationship. All experiments were performed at room temperature, 22 ± 1 °C. Cells were selected on the basis of co-transfection of a vector containing GFP in the absence of Rad, or of a vector containing GFP-conjugated Rad. For both cardiomyocytes and HEK293T cells, cells without a stable baseline (possibly due to run-down or run-up) were not studied.

The voltage-steps protocol used in cardiomyocytes studies evaluated  $I_{\text{peak}} = I_{\text{peak}}(V)$ , which was recalculated in CLAMPFIT to  $G = G(V)$  as  $G = I/(V - E_{\text{rev}})$ . For HEK cell experiments, we used a ramp protocol (Extended Data Fig. 8b). The experimental records were  $I = I(t)$ , where  $t$  = time. We transformed these records to  $I = I(V)$ , which was then further transformed to  $G = G(V)$  in CLAMPFIT (Extended Data Fig. 8b). The parameters of voltage-dependent activation were obtained using a modified Boltzmann distribution. A nonlinear fit with Boltzmann sigmoidal function was carried out in Prism (GraphPad), with a goodness of fit ( $R^2$ ) of more than 0.99.

## Single-channel patch-clamp electrophysiology

Cell-attached single-channel recordings were performed at room temperature as described<sup>71,72</sup>. Patch pipettes (5–10 MΩ) were pulled from ultra-thick-walled borosilicate glass (BF200-116-10, Sutter Instruments), and coated with Sylgard. Currents were filtered at 2 kHz. The pipette solution contained 140 mM tetraethylammonium methanesulfonate; 10 mM HEPES; 40 mM BaCl<sub>2</sub>; at 300 mOsm l<sup>-1</sup>, adjusted with tetraethylammonium methanesulfonate; and pH 7.4, adjusted with tetraethylammonium hydroxide. To maintain the membrane potential at 0 mV, the bath contained 132 mM potassium glutamate, 5 mM KCl, 5 mM NaCl, 3 mM MgCl<sub>2</sub>, 2 mM EGTA, 10 mM glucose, 20 mM HEPES; at 300 mOsm l<sup>-1</sup>, adjusted with glucose; and pH 7.4, adjusted with sodium hydroxide. Cell-attached single-channel currents were measured during 200-ms voltage ramps between -80 mV and +70 mV (portions between -50 mV and +40 mV are displayed and analysed). For each patch, we recorded 80–120 sweeps with a repetition interval of 10 s.

The sample size for the  $P_o$ -*V* relationships are as follows: α<sub>1C</sub>,  $n = 10$  (3 transfections), 933 sweeps; α<sub>1C</sub> plus PKA,  $n = 5$  (2 transfections), 450 sweeps; Rad,  $n = 5$  (3 transfections), 372 sweeps; Rad plus PKA,  $n = 8$  (3 transfections), 527 sweeps; 4SA mutant Rad,  $n = 6$  (4 transfections), 388 sweeps; and 4SA mutant Rad plus PKA,  $n = 5$  (3 transfections), 439 sweeps.

The modal analyses are histograms of single-trial average  $P_o$  values obtained from one-channel patches. For  $P_o$ -*V* analysis, we conservatively corrected for shifts in voltage. The numbers of sweeps are as follows: α<sub>1C</sub> alone: 281 sweeps (from three one-channel patches); Rad, 372 sweeps (from five one-channel patches); and Rad plus PKA, 311 sweeps (from three one-channel patches).

## Flow-cytometric FRET two-hybrid assay

For flow-cytometric FRET assays, HEK293 cells (ATCC CRL1573) were cultured in 12-well plates and transfected with polyethylenimine (PEI)

25 kDa linear polymer (Polysciences number 2396602). Briefly, 1.5 µg of cerulean (Cer)- and venus (Ven)-tagged cDNA pairs were mixed together in 100 µl of serum-free DMEM media and 6 µl of PEI was added to each sterile tube. FRET experiments were performed one day post-transfection. The protein-synthesis inhibitor cycloheximide (100 µM) was added to cells 2 h before experimentation to halt synthesis of new fluorophores, in order to allow existing fluorophores to fully mature.

For FRET measurements, we used an LSR II (BD Biosciences) flow cytometer, equipped with 405-nm, 488-nm and 633-nm lasers for excitation and 18 different emission channels. Forward- and side-scatter signals were detected and used to gate for single and healthy cells. To determine FRET efficiency, we measured three distinct fluorescence signals: first,  $S_{\text{Cer}}$  (corresponding to emission from the cerulean tag) is measured through the BV421 channel (excitation, 405 nm; emission, 450/50); second,  $S_{\text{Ven}}$  (corresponding to emission from the venus tag) is measured via the FITC channel (excitation, 405 nm; dichroic, 505LP; emission, 525/50); and third,  $S_{\text{FRET}}$  (corresponding to FRET emission) is measured via the BV510 channel (excitation, 405 nm; dichroic, 505LP; emission, 525/50). These raw fluorescence measurements are subsequently used to obtain  $\text{Ven}_{\text{direct}}$  (venus emission due to direct excitation),  $\text{Cer}_{\text{direct}}$  (cerulean emission due to direct excitation), and  $\text{Ven}_{\text{FRET}}$  (venus emission due to FRET excitation). Flow-cytometric signals were collected at a medium flow rate (2,000 to 8,000 events per second). Fluorescence data were exported as FCS 3.0 files for further processing and analysis using custom MATLAB functions (MathWorks).

For each experimental run on the flow cytometer, we performed several control experiments. First, the background fluorescence level for each fluorescent channel ( $\text{BG}_{\text{Cer}}$ ,  $\text{BG}_{\text{Ven}}$  and  $\text{BG}_{\text{FRET}}$ ) was obtained by measuring fluorescence from cells exposed to PEI without any fluorophore-containing plasmids. Second, cells expressing the Ven fluorophore alone were used to measure the spectral crosstalk parameter  $R_{\text{A1}}$ , corresponding to bleed-through of Ven fluorescence into the FRET channel. Third, cells expressing the Cer fluorophore alone were used to measure spectral crosstalk parameters  $R_{\text{D1}}$  and  $R_{\text{D2}}$ , corresponding to bleed-through of Cer fluorescence into the FRET and Ven channels respectively. Fourth, FRET measurements also require determination of instrument-specific calibration parameters  $g_{\text{Ven}}/g_{\text{Cer}}$  and  $f_{\text{Ven}}/f_{\text{Cer}}$ , which are respectively ratios of fluorescence excitation and emission for Ven to Cer fluorophores. These parameters also incorporate fluorophore-dependent aspects, including molar extinction (for  $g$ ) and quantum yield (for  $f$ ), as well as instrument-specific parameters, including laser power, attenuation by optical components, and photodetection, amplification and digitization of fluorescence. To determine these parameters, we used Cer-Ven dimers with four different linker lengths (5, 32, 40 and 228). Fifth, coexpression of Cer and Ven fluorophores provided estimates for concentration-dependent collisional FRET.

In our experiments,  $R_{\text{A1}}$  was approximately 0.11,  $R_{\text{D1}}$  approximately 2.8, and  $R_{\text{D2}}$  approximately 0.006. We observed only minor day-to-day variation in these measurements. For each cell, spectral cross-talk was subtracted as follows:  $\text{Cer}_{\text{direct}} = R_{\text{D1}} \times S_{\text{Cer}}$ ;  $\text{Ven}_{\text{direct}} = R_{\text{A1}} \times (S_{\text{Ven}} - R_{\text{D2}} \times S_{\text{Cer}})$ ; and  $\text{Ven}_{\text{FRET}} = S_{\text{FRET}} - R_{\text{A1}} \times (S_{\text{Ven}} - R_{\text{D2}} \times S_{\text{Cer}}) - R_{\text{D1}} \times S_{\text{Cer}}$ .

Following spectral unmixing, we obtained  $g_{\text{Ven}}/g_{\text{Cer}}$  and  $f_{\text{Ven}}/f_{\text{Cer}}$  from data for Cer-Ven dimers by determining the slope and intercept for the following linear relationship:

$$\frac{\text{Ven}_{\text{FRET}}}{\text{Cer}_{\text{direct}}} = \frac{g_{\text{Cer}}}{g_{\text{Ven}}} \times \frac{\text{Ven}_{\text{direct}}}{\text{Cer}_{\text{direct}}} - \frac{f_{\text{Ven}}}{f_{\text{Cer}}}$$

For typical experiments,  $g_{\text{Ven}}/g_{\text{Cer}} = 0.0194$  and  $f_{\text{Ven}}/f_{\text{Cer}} = 2.3441$ . Having obtained these calibration values, we computed donor-centric FRET efficiencies as:

$$E_D = \frac{\text{Ven}_{\text{FRET}}}{\text{Ven}_{\text{FRET}} + \frac{f_{\text{Ven}}}{f_{\text{Cer}}} \times \text{Cer}_{\text{direct}}}$$

For Cer–Ven dimers, we obtained FRET efficiencies of roughly 0.55, 0.38, and 0.05 for linker lengths 5, 32, and 228 respectively, matching previous work<sup>30</sup>. The relative proportion of Cer and Ven fluorophores in each cell was determined as  $N_{\text{Cer}} = \text{Cer}_{\text{direct}} / (1 - E_D)$  and  $N_{\text{Ven}} = \text{Ven}_{\text{direct}} / (g_{\text{Ven}}/g_{\text{Cer}} \times f_{\text{Ven}}/f_{\text{Cer}})$ . To construct FRET two-hybrid-binding curves, we imposed a 1:1 binding isotherm as in previous studies<sup>30</sup>. For each FRET pair, we obtained effective dissociation constant ( $K_{\text{d,EFF}}$ ),  $E_{\text{D,max}}$  and 95% confidence intervals by constrained least-squares fit.

For Fig. 4b, c and Extended Data Fig. 9a, b, we show all individual cells from two different transfections. We fit these data with the equation  $E_D = E_{\text{max}} \times [\text{Ven} - \text{Rad}]_{\text{free}} / ([\text{Ven} - \text{Rad}]_{\text{free}} + K_{\text{d,EFF}})$  using the least-squares algorithm (<https://www.mathworks.com/help/stats/nlinfit.html>). The  $K_{\text{d,EFF}}$  fit value based on all of the data points is shown as the bar in Extended Data Fig. 9c. The error is calculated by the fitting algorithm as a 95% confidence interval on the fit parameter (<https://www.mathworks.com/help/stats/nlparci.html>).

## Statistical analysis

Experiments were not randomized. Results are presented as mean  $\pm$  s.e.m. For comparisons between two groups, we used Student's *t*-test. Statistical analyses were performed using Prism 8 (Graphpad Software). For multiple group comparisons, we performed a one-way ANOVA followed by either Dunnett's or Tukey's post-hoc test using Prism 8. Differences were considered statistically significant at values of  $P < 0.05$ .

## Reporting summary

Further information on research design is available in the Nature Research Reporting Summary linked to this paper.

## Data and material availability

All transgenic mice are available from S.O.M. under a material agreement with Columbia University. All data are available in the main text, the Extended Data or the Supplementary Information. Proteomics raw data and search results were deposited in the PRIDE archive and can be accessed via the ProteomeXchange under accession numbers PXD014499, PXD014500 and PXD014501. The FRET software is accessible on github at [https://github.com/manubenjohny/FACS\\_FRET](https://github.com/manubenjohny/FACS_FRET). Source data for Figs. 1–4 and Extended Data Figs. 1, 2, 6, 8 are provided with the paper.

42. Katchman, A. et al. Proteolytic cleavage and PKA phosphorylation of  $\alpha_1\text{C}$  subunit are not required for adrenergic regulation of  $\text{Ca}_v1.2$  in the heart. *Proc. Natl Acad. Sci. USA* **114**, 9194–9199 (2017).
43. Yang, L. et al. The PDZ motif of the  $\alpha_1\text{C}$  subunit is not required for surface trafficking and adrenergic modulation of  $\text{Ca}_v1.2$  channel in the heart. *J. Biol. Chem.* **290**, 2166–2174 (2015).
44. Sanbe, A. et al. Reengineering inducible cardiac-specific transgenesis with an attenuated myosin heavy chain promoter. *Circ. Res.* **92**, 609–616 (2003).
45. Hambleton, M. et al. Inducible and myocyte-specific inhibition of PKC $\alpha$  enhances cardiac contractility and protects against infarction-induced heart failure. *Am. J. Physiol. Heart Circ. Physiol.* **293**, H3768–H3771 (2007).
46. He, M., Bodi, I., Mikala, G. & Schwartz, A. Motif III S5 of L-type calcium channels is involved in the dihydropyridine binding site. A combined radioligand binding and electrophysiological study. *J. Biol. Chem.* **272**, 2629–2633 (1997).
47. Hockerman, G. H. et al. Construction of a high-affinity receptor site for dihydropyridine agonists and antagonists by single amino acid substitutions in a non-L-type  $\text{Ca}^{2+}$  channel. *Proc. Natl Acad. Sci. USA* **94**, 14906–14911 (1997).
48. Lam, S. S. et al. Directed evolution of APEX2 for electron microscopy and proximity labeling. *Nat. Methods* **12**, 51–54 (2015).
49. Bramson, H. N., Kaiser, E. T. & Mildvan, A. S. Mechanistic studies of cAMP-dependent protein kinase action. *CRC Crit. Rev. Biochem.* **15**, 93–124 (1984).
50. Kemp, B. E., Graves, D. J., Benjamini, E. & Krebs, E. G. Role of multiple basic residues in determining the substrate specificity of cyclic AMP-dependent protein kinase. *J. Biol. Chem.* **252**, 4888–4894 (1977).
51. Moore, M. J., Adams, J. A. & Taylor, S. S. Structural basis for peptide binding in protein kinase A. Role of glutamic acid 203 and tyrosine 204 in the peptide-positioning loop. *J. Biol. Chem.* **278**, 10613–10618 (2003).
52. Feramisco, J. R., Glass, D. B. & Krebs, E. G. Optimal spatial requirements for the location of basic residues in peptide substrates for the cyclic AMP-dependent protein kinase. *J. Biol. Chem.* **255**, 4240–4245 (1980).

53. Songyang, Z. et al. Use of an oriented peptide library to determine the optimal substrates of protein kinases. *Curr. Biol.* **4**, 973–982 (1994).
54. Neuberger, G., Schneider, G. & Eisenhaber, F. pKaPS: prediction of protein kinase A phosphorylation sites with the simplified kinase-substrate binding model. *Biol. Direct* **2**, 1 (2007).
55. Iakouchcheva, L. M. et al. The importance of intrinsic disorder for protein phosphorylation. *Nucleic Acids Res.* **32**, 1037–1049 (2004).
56. Zhou, F. F., Xue, Y., Chen, G. L. & Yao, X. GPS: a novel group-based phosphorylation predicting and scoring method. *Biochem. Biophys. Res. Commun.* **325**, 1443–1448 (2004).
57. Blom, N., Gammeltoft, S. & Brunak, S. Sequence and structure-based prediction of eukaryotic protein phosphorylation sites. *J. Mol. Biol.* **294**, 1351–1362 (1999).
58. Obenaus, J. C., Cantley, L. C. & Yaffe, M. B. Scansite 2.0: proteome-wide prediction of cell signaling interactions using short sequence motifs. *Nucleic Acids Res.* **31**, 3635–3641 (2003).
59. Valencik, M. L. & McDonald, J. A. Codon optimization markedly improves doxycycline regulated gene expression in the mouse heart. *Transgenic Res.* **10**, 269–275 (2001).
60. Wan, E. et al. Aberrant sodium influx causes cardiomyopathy and atrial fibrillation in mice. *J. Clin. Invest.* **126**, 112–122 (2016).
61. Yang, L., Katchman, A., Morrow, J. P., Doshi, D. & Marx, S. O. Cardiac L-type calcium channel ( $\text{Ca}_v1.2$ ) associates with gamma subunits. *FASEB J.* **25**, 928–936 (2011).
62. Yang, L. et al. Protein kinase C isoforms differentially phosphorylate  $\text{Ca}_v1.2 \alpha_1\text{C}$ . *Biochemistry* **48**, 6674–6683 (2009).
63. Marx, S. O. et al. PKA phosphorylation dissociates FKBP12.6 from the calcium release channel (ryanodine receptor): defective regulation in failing hearts. *Cell* **101**, 365–376 (2000).
64. Kalocsay, M. APEX peroxidase-catalyzed proximity labeling and multiplexed quantitative proteomics. *Methods Mol. Biol.* **2008**, 41–55 (2019).
65. McAlister, G. C. et al. MultiNotch MS3 enables accurate, sensitive, and multiplexed detection of differential expression across cancer cell line proteomes. *Anal. Chem.* **86**, 7150–7158 (2014).
66. Beausoleil, S. A., Villén, J., Gerber, S. A., Rush, J. & Gygi, S. P. A probability-based approach for high-throughput protein phosphorylation analysis and site localization. *Nat. Biotechnol.* **24**, 1285–1292 (2006).
67. Paulo, J. A. et al. Quantitative mass spectrometry-based multiplexing compares the abundance of 5000 *S. cerevisiae* proteins across 10 carbon sources. *J. Proteomics* **148**, 85–93 (2016).
68. Perez-Riverol, Y. et al. The PRIDE database and related tools and resources in 2019: improving support for quantification data. *Nucleic Acids Res.* **47** (D1), D442–D450 (2019).
69. Deutsch, E. W. et al. The ProteomeXchange consortium in 2017: supporting the cultural change in proteomics public data deposition. *Nucleic Acids Res.* **45** (D1), D1100–D1106 (2017).
70. Maere, S., Heymans, K. & Kuiper, M. BiNGO: a Cytoscape plugin to assess overrepresentation of gene ontology categories in biological networks. *Bioinformatics* **21**, 3448–3449 (2005).
71. Tay, L. H. et al. Nanodomain  $\text{Ca}^{2+}$  of  $\text{Ca}^{2+}$  channels detected by a tethered genetically encoded  $\text{Ca}^{2+}$  sensor. *Nat. Commun.* **3**, 778 (2012).
72. Adams, P. J., Ben-Johny, M., Dick, I. E., Inoue, T. & Yue, D. T. Apocalmodulin itself promotes ion channel opening and  $\text{Ca}^{2+}$  regulation. *Cell* **159**, 608–622 (2014).

**Acknowledgements** We thank A. Karlin for helpful discussions and editing the manuscript; B. Soda for creating the cell-model illustration; and G. A. Bradshaw for technical assistance. This publication was supported by the National Institutes of Health (NIH; grants R01 HL113136, R01 HL121253 and R01 HL146149) and by the National Center for Advancing Translational Sciences (grant UL1TR001873). These studies used the resources of the Herbert Irving Comprehensive Cancer Center Flow Cytometry Shared Resources, funded in part through Center Grant P30CA013696. Images were collected (and analysed) in the Confocal and Specialized Microscopy Shared Resource of the Herbert Irving Comprehensive Cancer Center at Columbia University, supported by NIH grant P30 CA013696 (National Cancer Institute). A.P. was supported by NIH grant T32 HL120826 and National Science Foundation (NSF) Division of Graduate Education (DGE) grant 1644869. D.R. was supported by grants T32 HL120826 and F31 HL142178. J.K. was supported by grant T32 HL007343 and the Glorney–Raisbeck Fellowship from the New York Academy of Medicine, and J.A.H. was supported by grant T32 HL007854. The content is solely the responsibility of the authors and does not necessarily represent the official views of the NIH.

**Author contributions** The following authors designed research and analysed data: G.L., A.P., A.N.K., S.I.Z., D.R., J.A.H., J.K., L.Y., B.-X.C., A.K., S.P.G., G.S.P., H.M.C., M.B.-J., M.K. and S.O.M. The following authors performed research and analysed data: G.L., A.P., A.N.K., S.I.Z., D.R., J.A.H., J.K., L.Y., B.-X.C., A.K., K.D., G.S.P., H.M.C., M.B.J., M.K. and S.O.M. The following authors wrote the paper with input from all authors: S.O.M., M.K., H.M.C., G.S.P. and M.B.J. All authors provided feedback and agreed on the final manuscript.

**Competing interests** The authors declare no competing interests.

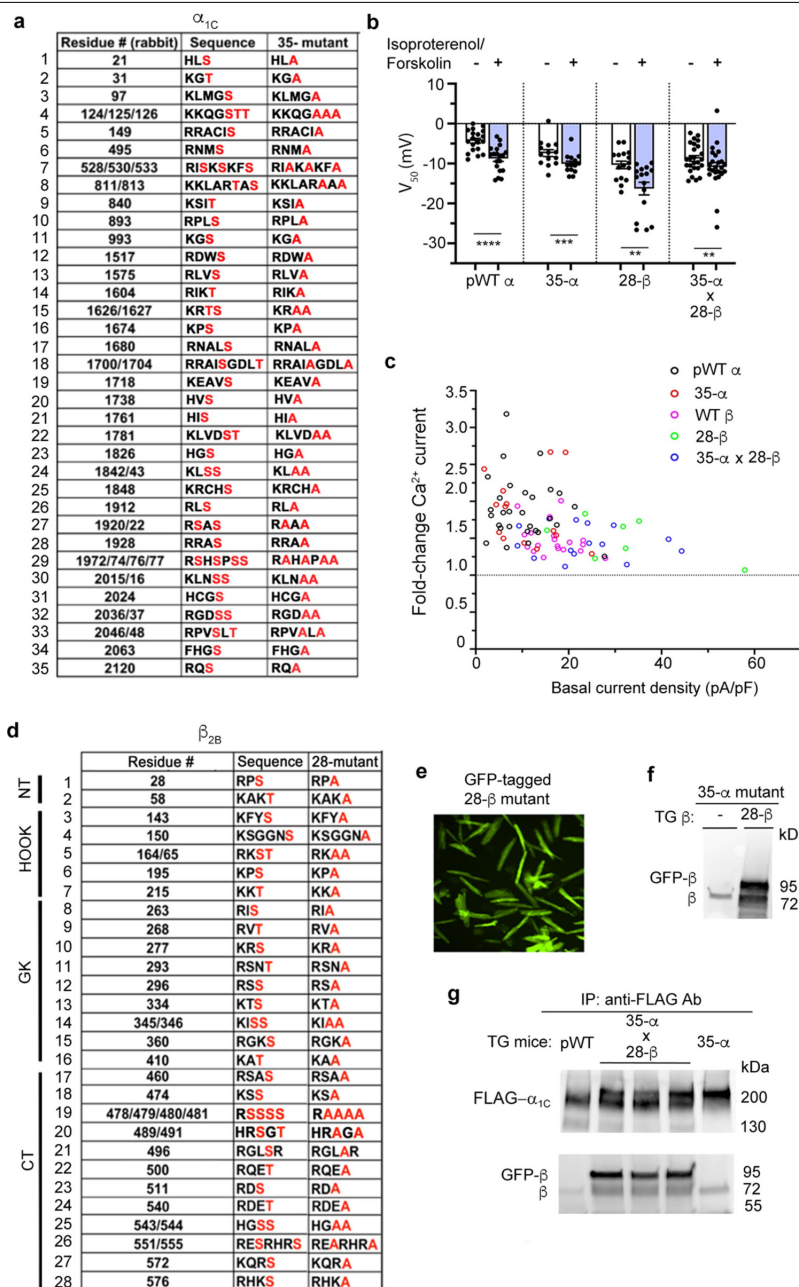
## Additional information

**Supplementary information** is available for this paper at <https://doi.org/10.1038/s41586-020-1947-z>.

**Correspondence and requests for materials** should be addressed to M.K. or S.O.M.

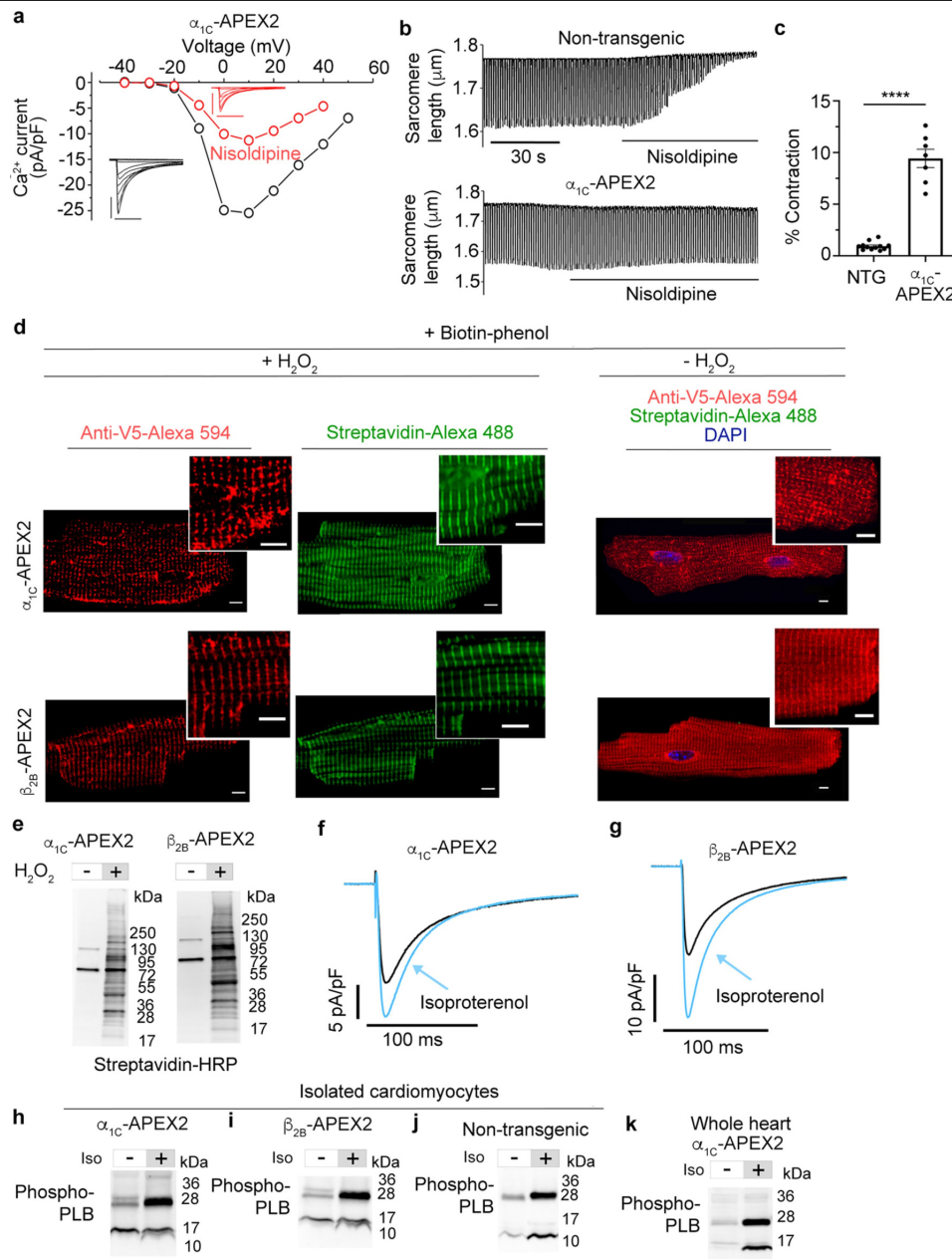
**Peer review information** Nature thanks Donald Bers, Alice Ting and the other, anonymous, reviewer(s) for their contribution to the peer review of this work.

**Reprints and permissions information** is available at <http://www.nature.com/reprints>.



**Extended Data Fig. 1 | Putative PKA phosphorylation sites in  $\alpha_{1C}$  and  $\beta_{2B}$  subunits. a**, Left column, the 35 putative PKA phosphorylation sites in rabbit  $\alpha_{1C}$ . Centre, the 51 residues in red are either predicted phosphorylation sites or within the immediate region of the predicted phosphorylation sites. Right, all 51 residues were replaced with alanine in 35-mutant  $\alpha_{1C}$  transgenic mice. **b**, Combined bar and column scatter plot of Boltzmann function parameters,  $V_{50}$ . Data are mean  $\pm$  s.e.m.  $**P < 0.01$ ;  $***P < 0.001$ ;  $****P < 0.0001$  by paired two-tailed  $t$ -test. pWT  $\alpha$ ,  $n = 19$ ; 35- $\alpha$  mutant,  $n = 14$ ; 28- $\beta$  mutant,  $n = 16$ ; 35- $\alpha$  mutant  $\times$  28- $\beta$  mutant,  $n = 24$ . Specific  $P$  values can be found in the associated Source Data (see Supplementary Information). **c**, Graph showing isoproterenol- and forskolin-induced increases in nisoldipine-resistant current, stratified by total basal current density before nisoldipine treatment. **d**, Left, the 28 putative PKA phosphorylation sites in the N-terminal (NT), Hook, GK and C-terminal (CT) domains of  $\beta_{2B}$ . Centre, the 37 residues in red are either

predicted phosphorylation sites or within the immediate vicinity of predicted phosphorylation sites, and were mutated to alanine in the 28-mutant GFP-tagged  $\beta_{2B}$  transgenic mice (right). **e**, Fluorescence imaging of isolated cardiomyocytes expressing the GFP-tagged 28- $\beta$  mutant. Representative of images from more than five biologically independent mice. **f**, Anti- $\beta$ -subunit immunoblot of cleared lysates from doxycycline-fed 35-mutant  $\alpha_{1C}$  transgenic (TG) mice or 35-mutant  $\alpha_{1C} \times$  GFP-tagged 28-mutant  $\beta_{2B}$  expressing mice hearts. Representative of immunoblots obtained from at least three biologically independent mice. **g**, Anti-Flag antibody (upper) and anti- $\beta$  antibody (lower) immunoblots of anti-Flag antibody immunoprecipitations from cleared lysates of hearts from pWT, 35- $\alpha$  and three mice expressing 35- $\alpha \times$  GFP-tagged-28- $\beta$ . Representative images from two independent experiments. For source gel data, see Supplementary Fig. 1.

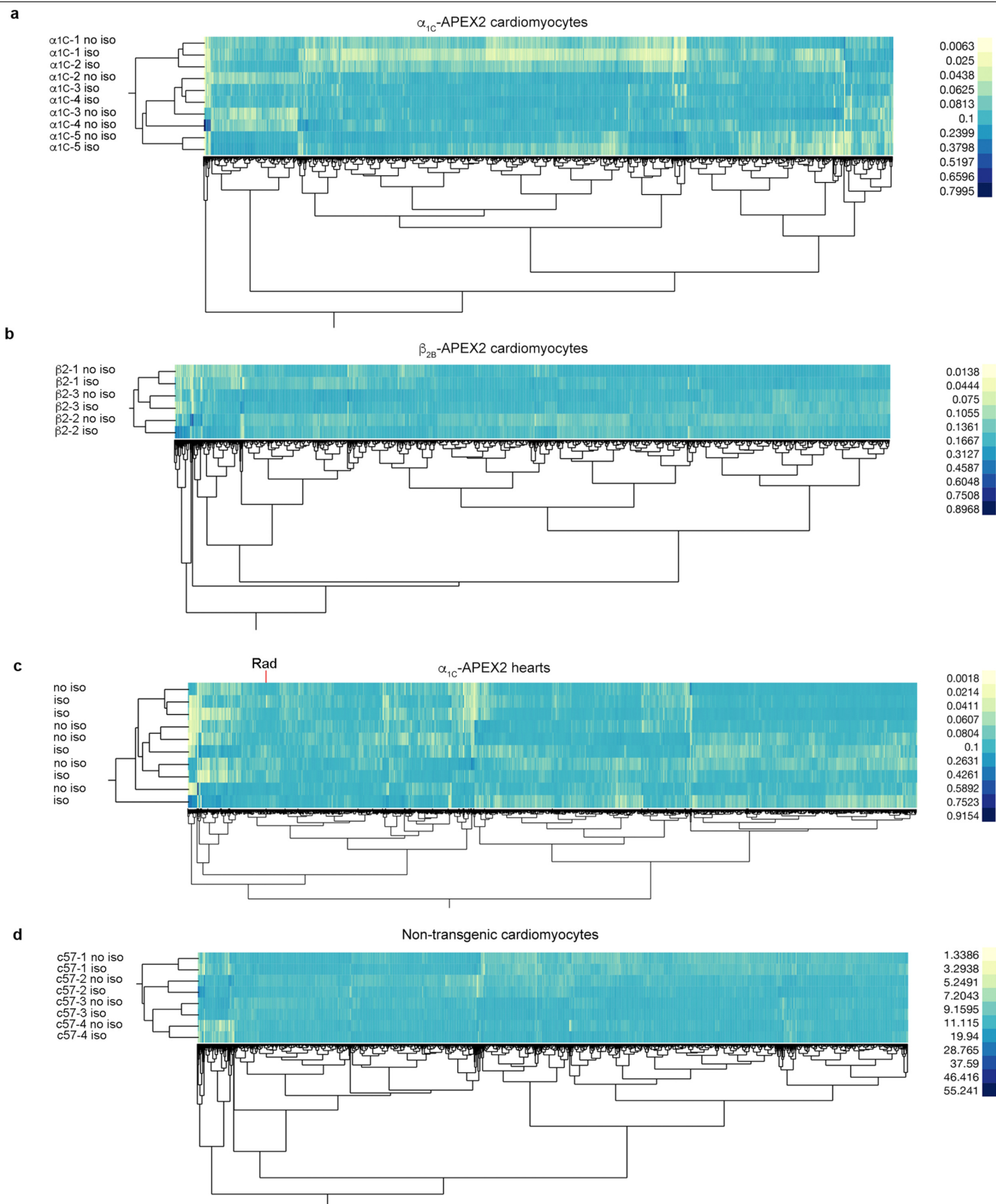


**Extended Data Fig. 2 | Trafficking and function of APEX2-conjugated  $\text{Ca}_v1.2$  subunits in heart.** **a**, Exemplar current-voltage relationship of  $\text{Ca}^{2+}$  currents from cardiomyocytes of  $\alpha_{1C}$ -APEX2 mice, acquired in the absence (black trace) and presence (red trace) of nisoldipine. Insets show series of whole-cell  $\text{Ca}_v1.2$  currents recorded from a series of voltage steps between  $-40$  mV and  $+60$  mV from a holding potential of  $-50$  mV. Scale bars, horizontal 100 ms, vertical 10 pA/pF. Representative of five experiments. **b**, Time course of changes in sarcomere length after superfusion of nisoldipine-containing solution. Representative of seven experiments. **c**, Percentage sarcomere shortening in the presence of nisoldipine. Data are mean  $\pm$  s.e.m. \*\*\*\* $P < 0.0001$  by unpaired two-tailed  $t$ -test.  $n = 12$  and 7 cardiomyocytes from left to right: NTG, nontransgenic. **d**, Immunofluorescence of cardiomyocytes isolated from mice expressing  $\alpha_{1C}$ -APEX2 and  $\beta_{2B}$ -APEX2, exposed to biotin-phenol and  $\text{H}_2\text{O}_2$  or no  $\text{H}_2\text{O}_2$ . Staining is with anti-V5 and Alexa594-conjugated secondary antibodies and streptavidin-conjugated Alexa488, and nuclear labelling is with DAPI. Scale bar, 5  $\mu\text{m}$ . Representative of 13 and 8 cardiomyocytes from 2 and 3 mice respectively. **e**, Streptavidin-HRP blot of lysates from isolated ventricular cardiomyocytes, representative of five similar experiments. **f**, Exemplar whole-

cell  $\text{Ca}_v1.2$  currents recorded from cardiomyocytes of  $\alpha_{1C}$ -APEX2 transgenic mice. Black trace, 300 nM nisoldipine; blue trace, 200 nM isoproterenol plus nisoldipine. Representative of nine cells from two biologically independent mice. **g**, As in **f**, except from  $\beta_{2B}$ -APEX2 mice. Black trace, control; blue trace, 200 nM isoproterenol. Representative of seven experiments from two biologically independent mice. **h, i**, Anti-phospho-phospholamban immunoblot of proteins from cardiomyocytes isolated from  $\alpha_{1C}$ -APEX2 and  $\beta_{2B}$ -APEX2 mice. Cardiomyocytes were exposed to either vehicle or 1  $\mu\text{M}$  isoproterenol after incubation with biotin-phenol. Blots are representative of three independent experiments from at least five biologically independent mice for each genotype. **j**, As in **h** and **i**, except that cardiomyocytes were isolated from non-transgenic mice without incubation with biotin-phenol. Blot is representative of three independent experiments from three biologically independent mice. **k**, As **h** and **i**, except that whole heart was exposed to 1  $\mu\text{M}$  isoproterenol for 5 min after infusion of biotin-phenol. This blot is representative of at least five biologically independent mice for no isoproterenol and at least five biologically independent mice for isoproterenol. For source gel data, see Supplementary Fig. 1.



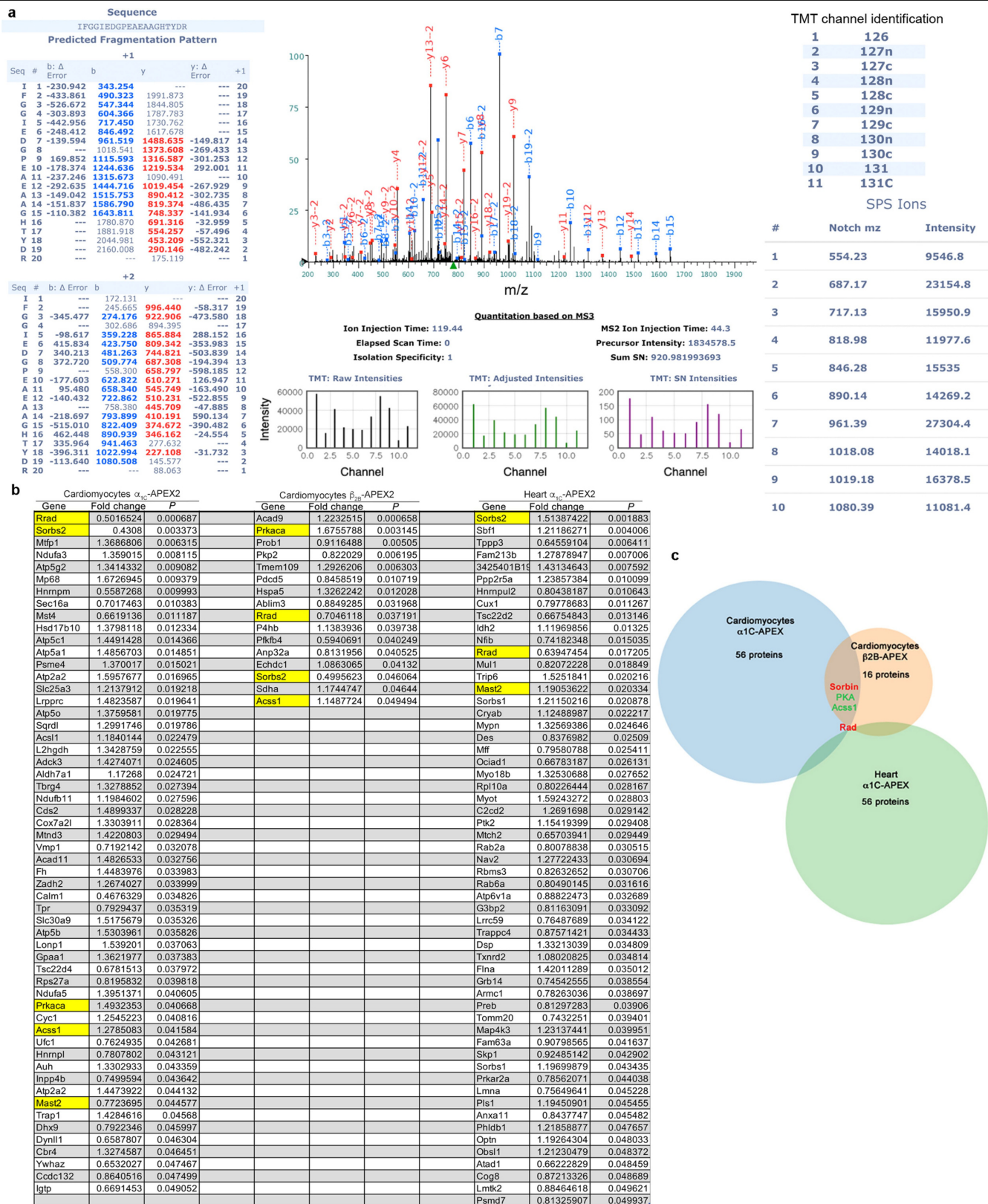




**Extended Data Fig. 4** | See next page for caption.

**Extended Data Fig. 4 | Two-way hierarchical clustering of scaled data from Fig. 2. a,** Dendrogram showing two-way hierarchical clustering of scaled TMT *s/n* data for streptavidin-purified proteins from  $\alpha_{1C}$ -APEX2 cardiomyocytes after stimulation with vehicle or isoproterenol. Shown are scaled relative TMT protein quantification data for 1,951 proteins from biological quintuplicate  $\alpha_{1C}$ -APEX2 mice. Clustering used Ward's minimum-variance method. **b,** Dendrogram showing two-way hierarchical clustering of scaled relative quantification data for 1,936 proteins from biological triplicate  $\beta_{2B}$ -APEX2 experiments. Heterogeneity between cardiomyocyte preparations from different mice is apparent. **c,** Dendrogram showing two-way hierarchical

clustering of scaled relative quantification data for 2,610 proteins from whole-organ  $\alpha_{1C}$ -APEX without or with perfusion of isoproterenol. Prominent heterogeneity in relative protein quantification between hearts is apparent. The position of Rad is indicated by a red line. In this experiment, the individual hearts were not paired. **d,** Dendrogram showing two-way hierarchical clustering of scaled TMT *s/n* data from non-transgenic mouse cardiomyocytes stimulated with isoproterenol or with vehicle. Scaled data for 4,622 quantified proteins from a biological quadruplicate experiment are displayed. Pairing of samples is apparent.

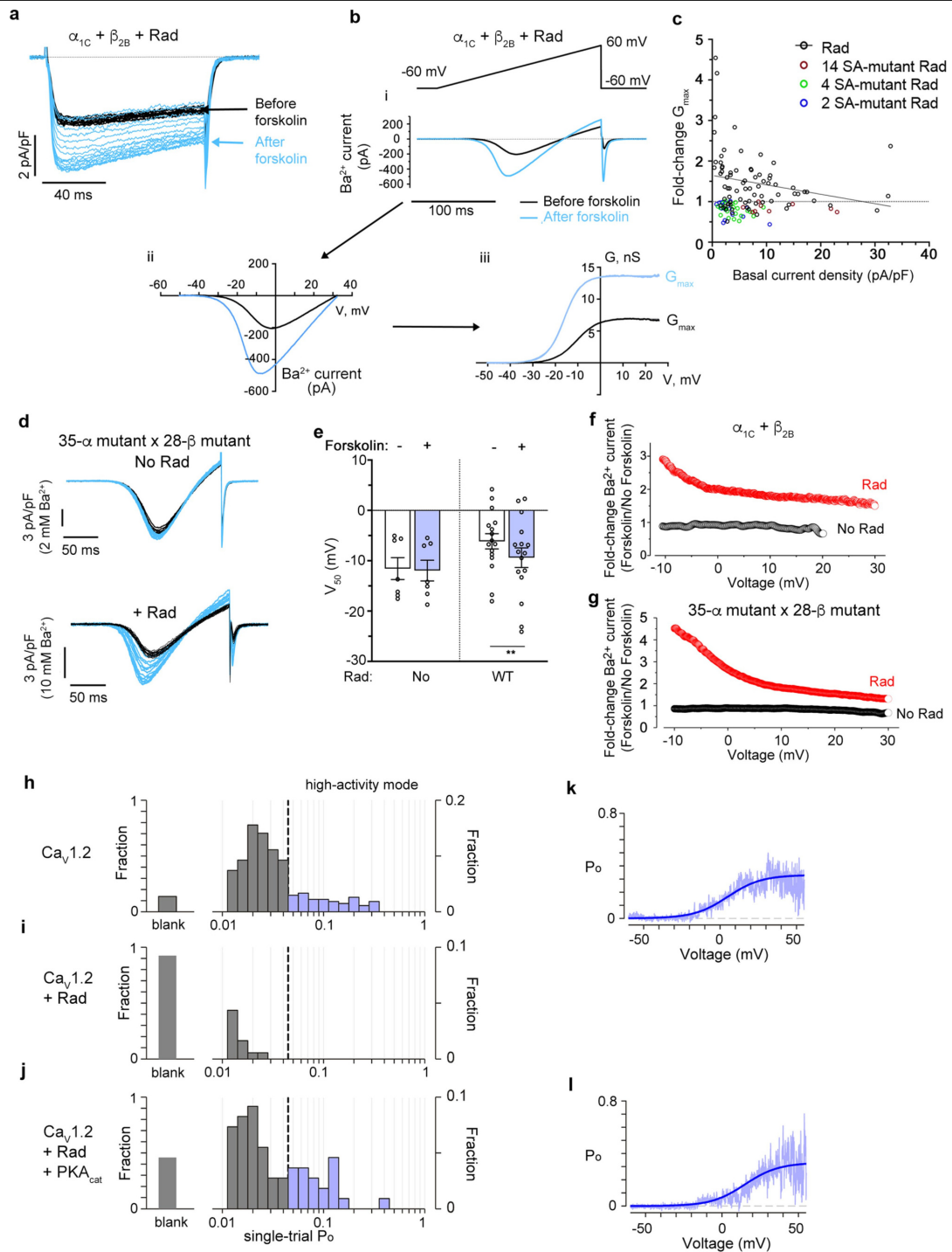


Extended Data Fig. 5 | See next page for caption.

**Extended Data Fig. 5 | Isoproterenol-induced change in Rad detected by mass spectrometry.** **a.** Right, the MS<sup>2</sup> spectrum (top) and TMT quantification parameters (bottom) for a Rad peptide changed upon treatment of murine hearts with isoproterenol. Shown is the MS<sup>2</sup> spectrum that was used to identify the Rad peptide IFGGIEDGPEAEAAGHTYDR. Left, *m/z* ratios for b and y ions identified in the spectrum and their deviation from theoretical *m/z* ratios. We measured the precursor mass as 778.71 Da with a charge of +3. Peptide modifications were +229.16 Da for TMT on the peptide N terminus and lysine residues, +57.02 Da for cysteine alkylation and +15.99 for methionine oxidation. Shown are ion injection times, isolation specificity, sum of signal-to-noise (SN) over all TMT channels, TMT raw intensities, adjusted intensities and final SN intensities used for relative quantification, as well as synchronous precursor selection (SPS) ion *m/z* ratios (isolated in the ion trap with Notch filtering;

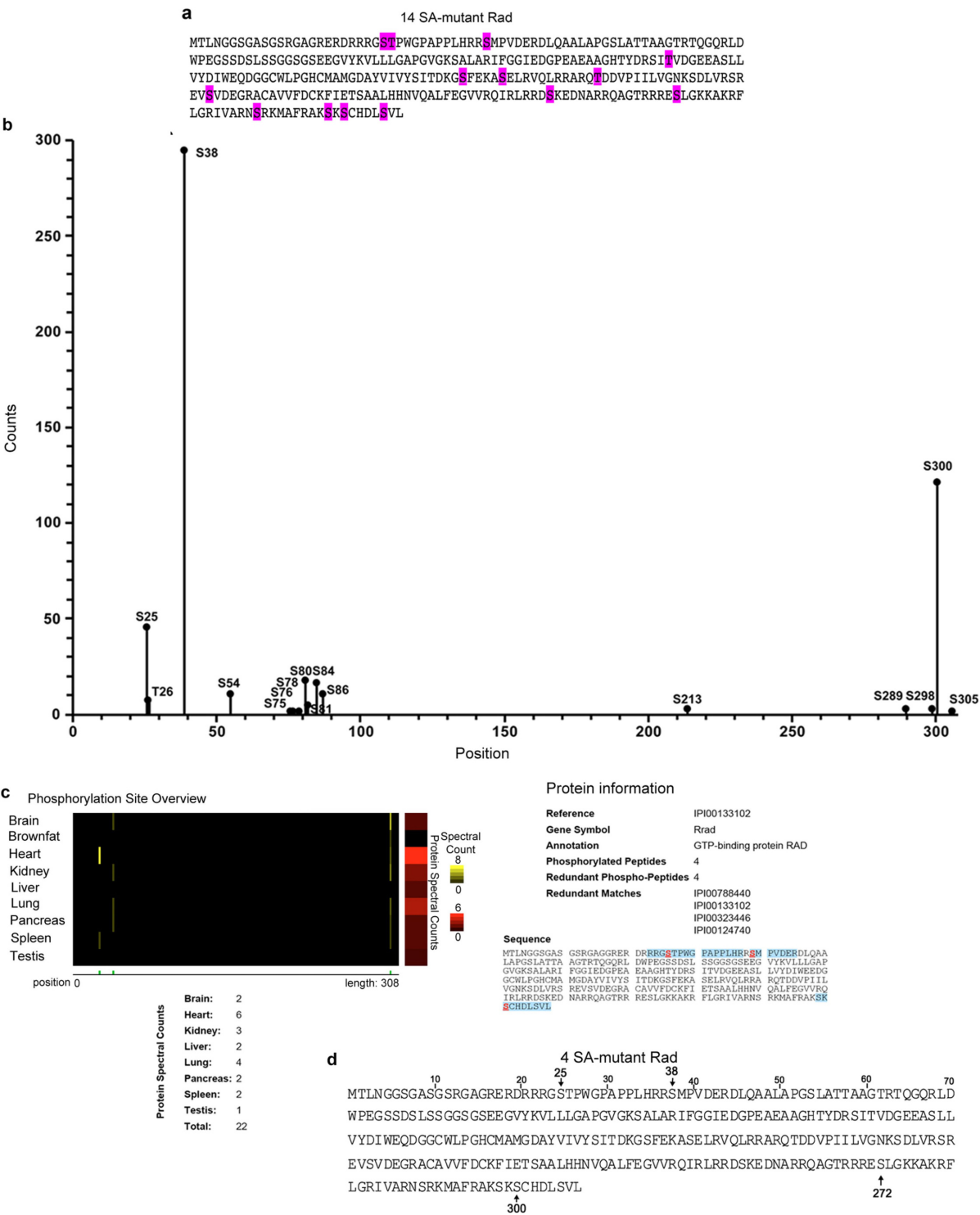
'Notch *mz*' denotes the ion *m/z* ratio of individual isolated SPS ions prior to HCD fragmentation and MS<sup>3</sup>). **b.** Table showing gene names of proteins with *P* < 0.05 for the three approaches: cardiomyocytes isolated from α<sub>1C</sub>-APEX and β<sub>2B</sub>-APEX mice, and α<sub>1C</sub>-APEX hearts. Genes in yellow are common to all groups, but note that for Mast2, the fold change is not consistent. Data are mean fold changes for five pairs of biologically independent pairs of α<sub>1C</sub>-APEX2 cardiomyocyte samples, three pairs of biologically independent pairs of β<sub>2B</sub>-APEX cardiomyocyte samples, and ten α<sub>1C</sub>-APEX2 hearts, five without isoproterenol and five with isoproterenol. Non-adjusted unpaired two-tailed *t*-test. **c.** Venn diagram showing the data from **b.** Rrad, Rad; Prkaca, PKA catalytic subunit; Acss1, acyl-CoA synthetase short-chain family member 1. Rad is the only protein that is consistently changed amongst the three approaches.





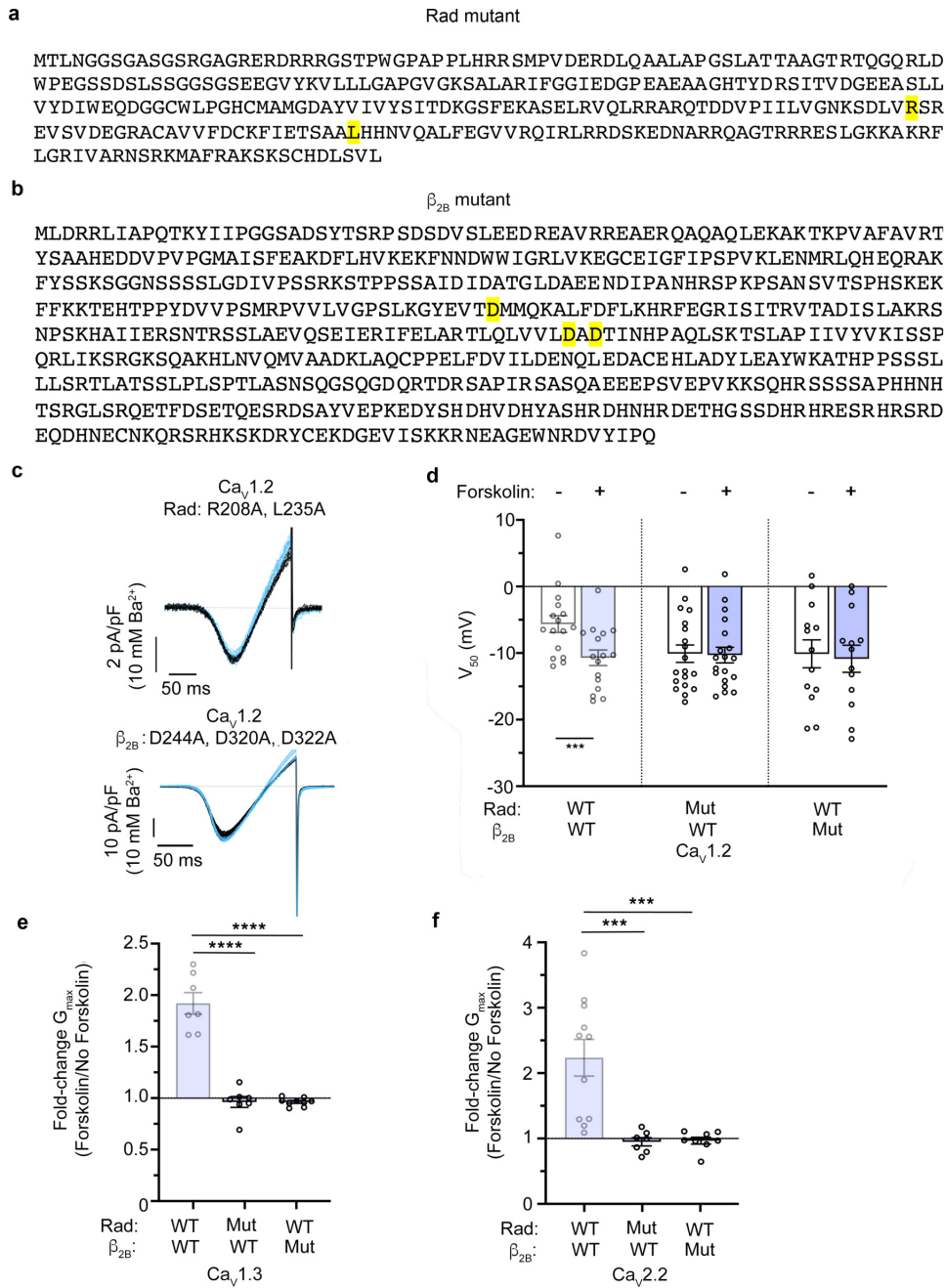
**Extended Data Fig. 6 | Rad is required for forskolin-induced activation of heterologously expressed  $\text{Ca}_v1.2$  channels.** **a**, Exemplar whole-cell  $\text{Ca}_v1.2$  currents elicited from step depolarizations recorded from HEK293T cells expressing Rad. Voltage command steps were applied every 10 s before (black traces) and during (blue traces) forskolin treatment. Representative of at least ten cells. **b**, Methodology used for generating  $G/V$  curves. **i**, Upper, a 200-ms voltage ramp from  $-60$  mV to  $+60$  mV was applied every 10 s. Lower, current traces, each an average of three traces before (black) and three traces after (blue) forskolin treatment. **ii**, Conversion of time scale to applied voltage. **iii**, Conversion to  $G-V$  relationship. Fold change was calculated at  $G_{\text{max}}$ . **c**, Graph showing forskolin-induced fold change in current, stratified by basal current density. **d**, Exemplar traces of  $\text{Ba}^{2+}$  currents in the absence and presence of Rad elicited by voltage ramp every 10 s. Black traces, before forskolin treatment; blue traces after treatment; no Rad, 7 cells; Rad, 16 cells. **e**, Boltzmann function

parameter  $V_{50}$ . Data are mean  $\pm$  s.e.m.  $**P < 0.01$  by paired two-tailed  $t$ -test.  $n = 7$  and 16, from left to right. **f, g**, Ratio of  $\text{Ba}^{2+}$  current after forskolin treatment to  $\text{Ba}^{2+}$  current before treatment for cells transfected without and with Rad. Representative of analyses for three cells for each condition. **h–l**, Distribution of sweep-by-sweep average  $P_o$  (single-trial  $P_o$ ) for different conditions. **h**, In the absence of Rad, sweeps with no openings or blank sweeps are rare (10%); most sweeps exhibit either intermediate or high levels of openings. **i**, The fraction of blank sweeps is increased with expression of Rad. **j**, If the PKA catalytic domain is also coexpressed with Rad, the fraction of blank sweeps is reduced and there is a resurgence of the high-activity mode. **k**, Pale blue lines show conditional  $P_o$ -voltage relationships obtained for sweeps exhibiting high activity in the absence of Rad and PKA. The dark blue line is the Boltzmann fit. **l**, As in **k**, but with Rad and PKA expression.



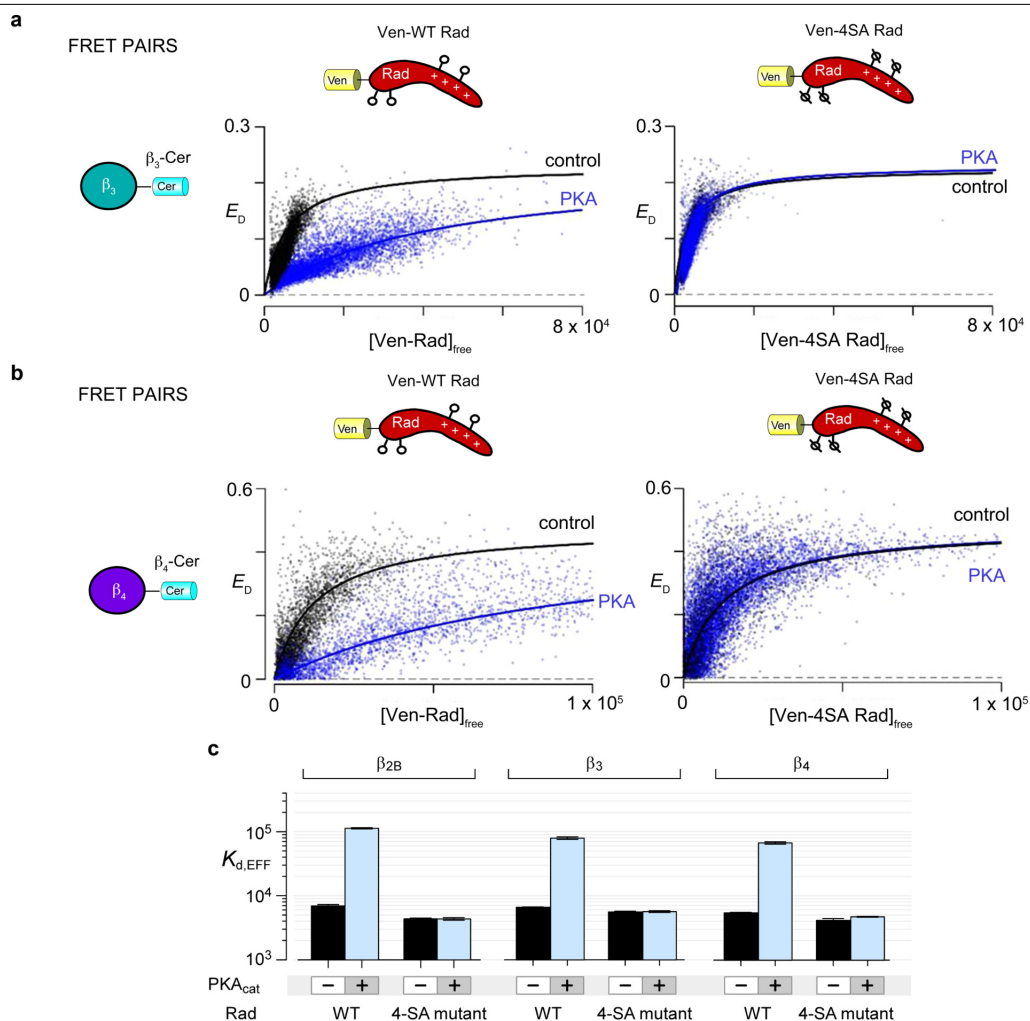
**Extended Data Fig. 7 | PKA phosphorylation sites in mouse Rad. a**, Serine/threonine residues (in purple) that are mutated to alanine in the 14-SA mutant. **b**, Mass-spectrometry identification of phosphorylated residues on Rad enriched with an anti-GFP nanobody matrix, from HEK cells expressing GFP-Rad and treated with forskolin. The number of spectral counts is plotted against the position of the phosphorylated amino acids in Rad. We detected 534 aggregated phosphopeptides in two independent experiments. **c**, Database entry for phosphorylation sites identified previously in Rad

([https://phosphomouse.hms.harvard.edu/site\\_view.php?ref=IPI00133102](https://phosphomouse.hms.harvard.edu/site_view.php?ref=IPI00133102)). The highest level of Rad phosphorylation was detected in the heart (left panel). The lower right panel shows peptides detected with phosphorylated serine residues on positions 25, 38 and 300 (in bold red; mapped to the Rad expression constructs used here; blue highlighting indicates sequence covered by peptides). **d**, Serine residues mutated to alanine in the 4-SA mutant (arrows).



**Extended Data Fig. 8 | Binding of Rad and  $\beta_{2B}$  is required for regulation of forskolin-induced stimulation of voltage-gated Ca<sup>2+</sup> channels.** **a**, The Rad protein sequence shown here indicates the residues Arg208 and Leu235 that were substituted with alanine (yellow). **b**, The  $\beta_{2B}$  protein sequence indicates the residues Asp244, Asp320 and Asp322 that were substituted with alanine (yellow), resulting in attenuation of Rad binding to the  $\beta$  subunit, as described previously<sup>28,29</sup>. **c**, Ba<sup>2+</sup> currents from Ca<sub>v</sub>1.2 channels, elicited by voltage ramp every 10 s from -60 mV to +60 mV over 200 ms, before (black) and after (blue) treatment with forskolin. Representative of 20 (top) and 15 (bottom) cells. **d**, Boltzmann function parameter V<sub>50</sub>. Data are mean ± s.e.m. \*\*\**P* < 0.001 by

paired two-tailed *t*-test. The data for wild-type Rad are the same as in Fig. 3h. Specific *P* values can be found in the associated Source Data. *n* = 16, 19 and 13, from left to right. **e**, Fold change in G<sub>max</sub> in Ca<sub>v</sub>1.3 channels. Data are mean ± s.e.m. *P* < 0.0001 by one-way ANOVA; \*\*\*\**P* < 0.0001 by Dunnett's test. The data for wild-type Rad and wild-type  $\beta_{2B}$  are the same as in Fig. 4e. *n* = 7, 7 and 9 cells, from left to right. **f**, Fold change in G<sub>max</sub> in Ca<sub>v</sub>2.2 channels. Data are mean ± s.e.m. *P* < 0.001 by one-way ANOVA; \*\*\**P* < 0.001 by Dunnett's test. Data for wild-type Rad and wild-type  $\beta_{2B}$  are as in Fig. 4h. *n* = 11, 7 and 8 cells, from left to right.



**Extended Data Fig. 9 | Phosphorylation-dependent dissociation of Rad,  $\beta_3$  and  $\beta_4$  subunits. a, b,** FRET two-hybrid binding isotherms were determined for Cer-tagged  $\beta_3$  (a) and  $\beta_4$  (b) subunits, and N-terminal Ven-tagged wild-type (left) or 4-SA mutant (right) Rad. FRET efficiency ( $E_D$ ) is plotted against the free concentration Ven-WT or Ven-4SA-mutant Rad. The solid line fits a 1/1 binding isotherm. Coexpression of the PKA catalytic subunit weakened binding in cells expressing wild-type Rad, but not in cells expressing 4-SA mutant Rad. c, Bar

graph summarizing mean  $K_{d,EFF}$  for  $\beta_{2B}$ ,  $\beta_3$  and  $\beta_4$ , and wild-type and 4-SA mutant Rad, expressed without and with the PKA catalytic subunit. Data are mean  $\pm$  95% confidence intervals; error bars show 95% confidence intervals for the pooled nonlinear fits based on the Jacobians computed. The sample size for each condition is 1,580–10,364 cells, acquired via two independent transfections and then pooled. The distribution of data in this graph is reflected in Fig. 4b, c, and in a, b.







## Reporting Summary

Nature Research wishes to improve the reproducibility of the work that we publish. This form provides structure for consistency and transparency in reporting. For further information on Nature Research policies, see [Authors & Referees](#) and the [Editorial Policy Checklist](#).

### Statistics

For all statistical analyses, confirm that the following items are present in the figure legend, table legend, main text, or Methods section.

n/a Confirmed

- ☒ The exact sample size ( $n$ ) for each experimental group/condition, given as a discrete number and unit of measurement
- ☒ A statement on whether measurements were taken from distinct samples or whether the same sample was measured repeatedly
- ☒ The statistical test(s) used AND whether they are one- or two-sided  
*Only common tests should be described solely by name; describe more complex techniques in the Methods section.*
- ☒ A description of all covariates tested
- ☒ A description of any assumptions or corrections, such as tests of normality and adjustment for multiple comparisons
- ☒ A full description of the statistical parameters including central tendency (e.g. means) or other basic estimates (e.g. regression coefficient) AND variation (e.g. standard deviation) or associated estimates of uncertainty (e.g. confidence intervals)
- ☒ For null hypothesis testing, the test statistic (e.g.  $F$ ,  $t$ ,  $r$ ) with confidence intervals, effect sizes, degrees of freedom and  $P$  value noted  
*Give  $P$  values as exact values whenever suitable.*
- ☒ For Bayesian analysis, information on the choice of priors and Markov chain Monte Carlo settings
- ☒ For hierarchical and complex designs, identification of the appropriate level for tests and full reporting of outcomes
- ☒ Estimates of effect sizes (e.g. Cohen's  $d$ , Pearson's  $r$ ), indicating how they were calculated

*Our web collection on [statistics for biologists](#) contains articles on many of the points above.*

### Software and code

Policy information about [availability of computer code](#)

Data collection pClamp 10.7 software (Molecular Devices), Sequest (V.28, rev. 12)

Data analysis Graphpad Prism 8, Origin 7.5, JMP 14 Pro, The FRET software is on github: [https://github.com/manubenjohny/FACS\\_FRET](https://github.com/manubenjohny/FACS_FRET)

For manuscripts utilizing custom algorithms or software that are central to the research but not yet described in published literature, software must be made available to editors/reviewers. We strongly encourage code deposition in a community repository (e.g. GitHub). See the Nature Research [guidelines for submitting code & software](#) for further information.

### Data

Policy information about [availability of data](#)

All manuscripts must include a [data availability statement](#). This statement should provide the following information, where applicable:

- Accession codes, unique identifiers, or web links for publicly available datasets
- A list of figures that have associated raw data
- A description of any restrictions on data availability

The authors declare that the data supporting the findings of this study are available within the paper, its supplemental figures and tables, and all raw mass spectrometry data have been deposited.

## Field-specific reporting

Please select the one below that is the best fit for your research. If you are not sure, read the appropriate sections before making your selection.

x

# Life sciences study design

All studies must disclose on these points even when the disclosure is negative.

Sample size	Sample sizes exceeded the number of samples determined by power calculations, which were based on effect sizes previously reported in the literature. Number of animals was always greater than 3 per genotype. Sample size was determined to be adequate based on the magnitude and consistency of measurable differences between groups and low observed variability between samples.
Data exclusions	No data were excluded from analyses. For electrophysiological studies, cells were not studied if baseline electrophysiological determinations demonstrated current run-down. These cells were excluded before any experiment was initiated (a predetermined criteria). Once nisoldipine, isoproterenol or forskolin was added, the cells were included in all analyses. See Methods for details.
Replication	All experiments were replicated and all attempts at replication were successful and consistent.
Randomization	No randomization of mice. Mice were litter-mates when possible.
Blinding	The investigators were blinded to group allocation during data acquisition and analysis.

## Reporting for specific materials, systems and methods

We require information from authors about some types of materials, experimental systems and methods used in many studies. Here, indicate whether each material, system or method listed is relevant to your study. If you are not sure if a list item applies to your research, read the appropriate section before selecting a response.

### Materials & experimental systems

n/a	Involved in the study
<input type="checkbox"/>	<input checked="" type="checkbox"/> Antibodies
<input type="checkbox"/>	<input checked="" type="checkbox"/> Eukaryotic cell lines
<input checked="" type="checkbox"/>	<input type="checkbox"/> Palaeontology
<input type="checkbox"/>	<input checked="" type="checkbox"/> Animals and other organisms
<input checked="" type="checkbox"/>	<input type="checkbox"/> Human research participants
<input checked="" type="checkbox"/>	<input type="checkbox"/> Clinical data

### Methods

n/a	Involved in the study
<input checked="" type="checkbox"/>	<input type="checkbox"/> ChIP-seq
<input checked="" type="checkbox"/>	<input type="checkbox"/> Flow cytometry
<input checked="" type="checkbox"/>	<input type="checkbox"/> MRI-based neuroimaging

## Antibodies

Antibodies used	<p>Additional information for all antibodies are provided in the Methods section.</p> <p>Anti-V5 Tag Monoclonal Antibody(Thermofisher, R960-25) 1:5000 dilution,            Anti-Jph2 Antibody(Pierce, PA5-20642, lot# NG1583142) 1:1000 dilution,            Anti-Calmodulin Antibody(Millipore Sigma, 05-173),1:1000 dilution,            Anti-RyR2 Antibody(5029) dilute 1:5000,            Anti-Kv1.5 Antibody(Alomone Labs, APC-004.Lot# APC004AN0850), 1:1000 dilution,            Anti-phospho-phospholamban(Ser16/Thur17) Antibody(Cell signaling, #8496, Lot#1) 1:1000 dilution,            Goat anti-Mouse IgG (H+L) Highly Cross-Adsorbed Secondary Antibody, Alexa Fluor 594 (Thermofisher, A11032, Lot#2069816) 1:200 dilution,            Streptavidin, Alexa FluorTM 488 Conjugate(Thermofisher, S32354, Lot# 1719656), 1:800 dilution,            Streptavidin, horseradish peroxidase conjugate(Thermofisher, s911, Lot# 1711896), 0.6mg/ml,            Anti-Alpha1C antibody (custom-made by YenZym) 1:1000 dilution            Anti-CaVbeta antibody (custom-made by YenZym) 1:500 dilution            Anti- FLAG antibody (Sigma, F7425, Lot#078M4886V) 1:1000 dilution</p>
Validation	<p>These antibodies were used for both heterologous expression studies and mouse cardiomyocytes.</p> <p>The alpha1C antibody was custom-made by YenZym and has been used for more than a decade in the laboratory. It has been validated using heterologous expression studies.</p> <p>The anti-beta antibody was also custom-made by YenZym and has been used for more than a decade in my laboratory. We have validated this antibody using heterologous expression studies. Antibodies were also validated in our previous work (Yang et al 2019).</p> <p>The anti-jutophilin antibody and anti-FLAG antibody were validated using heterologous expression studies, by their manufacturer and in the case of anti-FLAG antibody using transgenic mice created in the laboratory.</p> <p>Anti-V5 Tag Monoclonal Antibody- validated by 310 published papers for WB and 70 published papers for Immunofluorescence.</p> <p>Anti-Jph2 Antibody- validated by Invitrogen and published paper.</p> <p>Anti-Calmodulin Antibody- validated by Millipore Sigma and also multiple published papers.</p> <p>Anti-RyR2 Antibody - validated by multiple published papers and heterologous expression studies.</p> <p>Anti-Kv1.5 Antibody- validated by Alomone Laboratory and multiple published paper</p>

Anti-phospho-phospholamban(Ser16/Thur17) Antibody validated by Cell Signaling and multiple published papers  
 Goat anti-Mouse IgG (H+L) Highly Cross-Adsorbed Secondary Antibody, Alexa Fluor 594 validated by Invitrogen.  
 Streptavidin, Alexa Fluor™ 488 Conjugate validated by Invitrogen and published papers.  
 Streptavidin, horseradish peroxidase conjugate validated by Invitrogen and published papers

## Eukaryotic cell lines

Policy information about [cell lines](#)

Cell line source(s)	HEK293T cells (human, ATCC, CRL-3216) for electrophysiology; HEK293 (human, ATCC, CRL-1573) for FRET were purchased directly from ATCC.
Authentication	Cell lines are authenticated by ATCC.
Mycoplasma contamination	All cell lines were tested negative for mycoplasma
Commonly misidentified lines (See <a href="#">ICLAC</a> register)	No commonly misidentified cell lines were used.

## Animals and other organisms

Policy information about [studies involving animals](#); [ARRIVE guidelines](#) recommended for reporting animal research

Laboratory animals	Mice, mixed strain, ages 6 weeks - 4 months, male and female. Description of research mice used for experiments can be found in the relevant figure legends and Methods.
Wild animals	The study did not involve wild animals
Field-collected samples	The study did not involve samples collected from the field
Ethics oversight	Columbia University IACUC

Note that full information on the approval of the study protocol must also be provided in the manuscript.

# Negative supercoil at gene boundaries modulates gene topology

<https://doi.org/10.1038/s41586-020-1934-4>

Received: 30 April 2019

Accepted: 25 November 2019

Published online: 22 January 2020

Yathish Jagadheesh Achar<sup>1\*</sup>, Mohamood Adhil<sup>1</sup>, Ramveer Choudhary<sup>1</sup>, Nick Gilbert<sup>2</sup> & Marco Foiani<sup>1,3\*</sup>

Transcription challenges the integrity of replicating chromosomes by generating topological stress and conflicts with forks<sup>1,2</sup>. The DNA topoisomerases Top1 and Top2 and the HMGB family protein Hmo1 assist DNA replication and transcription<sup>3–6</sup>. Here we describe the topological architecture of genes in *Saccharomyces cerevisiae* during the G1 and S phases of the cell cycle. We found under-wound DNA at gene boundaries and over-wound DNA within coding regions. This arrangement does not depend on Pol II or S phase. Top2 and Hmo1 preserve negative supercoil at gene boundaries, while Top1 acts at coding regions. Transcription generates RNA–DNA hybrids within coding regions, independently of fork orientation. During S phase, Hmo1 protects under-wound DNA from Top2, while Top2 confines Pol II and Top1 at coding units, counteracting transcription leakage and aberrant hybrids at gene boundaries. Negative supercoil at gene boundaries prevents supercoil diffusion and nucleosome repositioning at coding regions. DNA looping occurs at Top2 clusters. We propose that Hmo1 locks gene boundaries in a cruciform conformation and, with Top2, modulates the architecture of genes that retain the memory of the topological arrangements even when transcription is repressed.

RNA polymerases generate positive and negative supercoils ahead and behind transcription bubbles, respectively<sup>7</sup>. Positive supercoiling accumulates in front of replication forks and precatenanes are generated behind forks<sup>8,9</sup>. TMP (4,5',8-trimethylpsoralen) has been used to map DNA supercoiling<sup>10–13</sup>, as intercalation of psoralen is proportional to negative superhelical tension<sup>14</sup>. Using biotinylated TMP (bTMP)<sup>12</sup>, we investigated the topology of transcribed genes and the contributions of Top1, Top2 and Hmo1 to maintenance of the topological architecture of transcription units.

## Topological context of Pol II genes

We analysed the distributions of Rpb3 (a Pol II subunit), Top2, Top1 and Hmo1 in S phase and performed a meta-analysis on Pol II-transcribed genes (Fig. 1a). Rpb3 accumulated at open reading frames (ORFs), peaking at transcription start sites (TSSs) and transcription termination sites (TTSs); this probably reflects slow transcription modes where transcription begins, and where transcription-coupled transactions occur at termination<sup>15</sup>. Top2 and Hmo1 accumulated upstream and downstream of ORFs. Top1 was confined within the ORFs, accumulating close to TTSs.

Using bTMP, we mapped negative and positive supercoil and stable regions<sup>12</sup> (Extended Data Fig. 1a, b). The three topological clusters were distributed near-equally (Extended Data Fig. 1c). Negative supercoiled regions were mainly found at intergenic regions (49%), whereas transcribed units exhibited a positive supercoiled context (40%; Fig. 1b, c). Nucleosome-occupied regions were distributed near-equally within the

three topological territories (Extended Data Fig. 1c). Negative supercoil mirrored Top2 clusters (Fisher's exact test  $P < 1 \times 10^{-5}$ ) and positive supercoil reflected Top1 distribution (Fisher's exact test  $P < 1 \times 10^{-20}$ ). Gene topology was comparable in cells during G1 and S phase (Fig. 1b, c, Extended Data Fig. 1d, e).

We analysed the topological profiles of conditionally expressed genes such as *ASF2* (transcribed in S phase) and the galactose-inducible gene cluster (Extended Data Fig. 1f, g). We found comparable bTMP profiles at *ASF2* in G1 (repressing conditions) and S, and at the Gal genes in cells cultured with glucose (repressing conditions) and galactose. We analysed the locus containing the highly expressed *LEU2* gene and the two moderately expressed *NFS1* and *DCC1* genes (Extended Data Fig. 1h). Rpb3 accumulated at *LEU2* but was undetectable at *NFS1* and *DCC1*. However, Top1 accumulated at *LEU2*, as well as at *NFS1* and *DCC1*. Top2 and Hmo1 were present at gene boundaries. Hence, the topological context of Pol II-transcribed genes does not depend on Pol II and the negative supercoil context at gene boundaries does not depend on Top2, as Top2 is recruited after G1 phase<sup>16</sup>.

We compared supercoil distribution among genes that showed high, medium or low expression (Extended Data Fig. 2a). Highly expressed genes accumulated more Top2 and negative supercoil, compared to the other two classes (Fig. 1d, e). Conversely, highly expressed genes exhibited less positive supercoil (Extended Data Fig. 2b). Accumulation of Pol II and Top1 mirrored the levels of expression (Fig. 1d), whereas distribution of Hmo1 was comparable in genes of all three levels of expression (Fig. 1d). Hence, distribution of under-wound DNA at Pol II gene boundaries is enhanced in highly expressed genes.

<sup>1</sup>IFOM (Fondazione Istituto FIRC di Oncologia Molecolare), Milan, Italy. <sup>2</sup>Medical Research Council Human Genetics Unit, Institute of Genetics and Molecular Medicine, University of Edinburgh, Edinburgh, UK. <sup>3</sup>Università degli Studi di Milano, Milan, Italy. \*e-mail: yathish.achar@ifom.eu; marco.foiani@ifom.eu

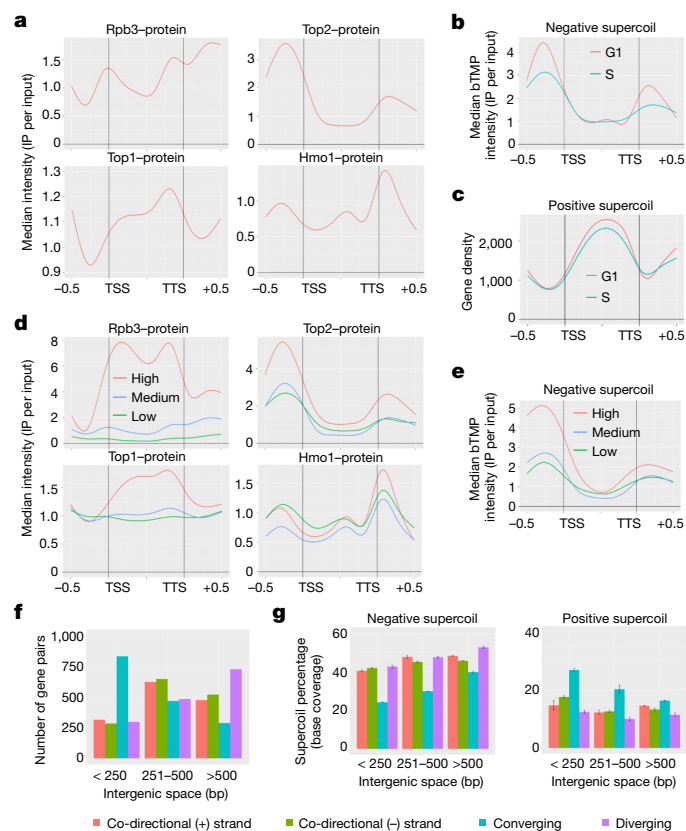


**Fig. 1 | Topological context of Pol II genes.** Chromatin immunoprecipitation (ChIP)-on-chip was carried out in cells released from G1 into S phase. Pol II-coding regions (replicates  $n = 2$ ; meta-gene analysis  $n = 6,706$  genes) were scaled to 1 kb and the flanking 0.5 kb from TSSs and TTSs were plotted against median intensity on the y-axis. **a**, Meta-gene plot showing accumulation of Pol II (Rpb3-10× Flag), Top2 (Top2-10× Flag), Top1 (Top1-10× Flag) and Hmo1 (Hmo1-10× Flag). **b**, Meta-gene plot for negative supercoil in G1 and S, plotted against median bTMP intensity. **c**, Positive supercoil distribution in Pol II genes plotted against average gene density on the y-axis. **d**, Pol II genes were grouped into three categories; high, medium and low expression based on the fragments per million kilobases (FPKM) value from RNA sequencing carried out in S phase at 28 °C. Meta-gene plots for three categories of gene expression for Pol II, Top2, Top1 and Hmo1. **e**, Negative supercoil distribution in high-, medium- and low-expression genes. **f**, Pol II genes were grouped according to their orientation with respect to neighbouring genes as: co-directional (+ strand;  $n = 1,453$  gene pairs), co-directional (- strand;  $n = 1,415$  gene pairs), converging ( $n = 1,590$  gene pairs) and diverging ( $n = 1,512$  gene pairs). The numbers of gene pairs at different intergenic spaces (<250 bp = 1,729 gene pairs, 251–500 bp = 2,224 gene pairs and >500 bp = 2,010 gene pairs) were plotted with respect to their orientation. **g**, Base coverage percentage of supercoil accumulation at different intergenic spaces with respect to gene pairs grouped according to orientation (two replicates, mean  $\pm$  s.d.).

We compared the supercoil context at intergenic spaces with respect to gene orientation by grouping Pol II genes into co-directional (plus and minus strands), converging and diverging classes (Fig. 1f). Intergenic spaces between converging genes were smaller than in the other directional classes. Diverging genes exhibited larger intergenic spaces. Converging genes accumulated more positive supercoil at intergenic spaces, at the expense of negative supercoil (Fig. 1g). Accordingly, converging intergenic regions exhibited lower Top2 binding, whereas Top1 binding was not affected (Extended Data Fig. 2c). Hence, convergent and divergent transcription have imposed specific topological contexts at intergenic spaces.

## Top2 and Hmo1 contribute to gene topology

Temperature sensitive *top2-1* mutants exhibited a reduction in negative supercoil at gene boundaries and an increase in positive supercoil at the same regions (Fig. 2a, Extended Data Fig. 2d, h). In G1 phase, *top2-1* mutants did not show a reduction in negative supercoil (Extended Data Fig. 2e). *top1Δ* cells did not show changes in the topological context of gene boundaries or transcribed regions (Fig. 2a, Extended Data Fig. 2f, h). Like *top2-1* mutants, *top1Δtop2-1* mutants exhibited a decrease in negative supercoil at gene boundaries (Fig. 2a), although the accumulation of positive supercoil at the same regions was lower than in *top2-1* cells (Extended Data Fig. 2g); *top1Δtop2-1* mutants accumulated less positive supercoil at transcribed regions than did wild-type cells, suggesting that, during transcription, the two topoisomerases can substitute for each other in maintaining a positive supercoiled context. Localization of Top1 in wild-type cells was restricted to coding regions, but in *top2-1* mutants it accumulated at gene boundaries (Fig. 2b, Extended Data Fig. 2i). Thus, Top2 restricts Top1 at transcribed regions and *top2* mutants exhibit the unscheduled relocation of Top1 at gene boundaries, which can account for the local increase in positive supercoil. Moreover, in *top2-1* mutants, Pol II accumulated more at gene boundaries than in wild-type cells (Fig. 2c, Extended Data Fig. 2i). Hence, Top2 confines the transcription apparatus within the coding regions.

*hmo1Δ* cells exhibited a reduction in negative supercoil and accumulation of positive supercoil at gene boundaries, resembling *top2-1* mutants (Fig. 2d, Extended Data Fig. 3a, d). Ablation of Hmo1 in *top2-1* mutants restored a wild-type-like topological context at transcribed genes (Fig. 2d, Extended Data Fig. 3b, d). The distribution of Top1 in *hmo1Δ* and *hmo1Δtop2-1* mutants was similar to that in wild-type cells (Extended Data Fig. 3c, e). Thus, the gene topological profiles of *hmo1Δ* and *top2-1* are comparable, but *hmo1Δ*, unlike *top2-1* mutation, does not cause accumulation of Top1 at gene boundaries. It is possible that, in *top2-1* mutants, accumulation of Top1 at gene boundaries depends on DNA substrates generated by Hmo1.

## Top2 restricts RNA–DNA hybrids within ORFs

Using the SF9 antibody<sup>17,18</sup>, we investigated whether accumulation of RNA–DNA hybrids reflected a specific topological context. In wild-type cells, hybrids were distributed within ORFs and peaked at TTSS (Extended Data Fig. 4a). Their accumulation did not correlate with gene expression levels (Extended Data Fig. 4b). RNaseH and the Rrm3 and Sen1 helicases counteract hybrid accumulation<sup>19</sup>. In *rrh1Δ* mutant cells, hybrids accumulated throughout Pol II gene units, whereas in *rrm3Δ* and *sen1<sup>CT</sup>* mutants hybrids accumulated at TTS sites (Extended Data Fig. 4c); this is consistent with the function of Rrm3 in dismantling RNA transcripts while travelling on the lagging strand<sup>20</sup> and with the role of Sen1 in facilitating transcription termination<sup>21</sup>. These observations suggest that RNA–DNA hybrids represent a physiological intermediate during transcription and are confined within coding regions, and that their accumulation close to TTSS may reflect the slow-down of Pol II elongation at termination<sup>22</sup>.

In *top2* mutants, specifically in S phase, hybrids accumulated at gene boundaries, where there is a reduction in negative supercoil (Fig. 2e). *top1top2* double mutants resembled *top2* mutants (Extended Data Fig. 4e). *top1Δ* cells accumulated hybrids throughout the gene bodies (Fig. 2e), perhaps owing to frequent Pol II pausing and back-tracking; because the viability of *top1Δ* cells depends on Top2, it is possible that *top1Δ* cells phenocopy a Top2 defect, leading to Pol II leakage and accumulation of hybrids at gene boundaries. Previous findings implicated Top1 in preventing hybrid accumulation<sup>23</sup>. Hence, Top2 counteracts hybrid accumulation and, in *top2* mutants, the accumulation of hybrids at flanking regions reflects the local decrease in negative supercoil and aberrant Pol II transcription. *hmo1Δ* cells exhibited a marked reduction in hybrid accumulation compared to wild-type cells, and *hmo1Δtop2-1*



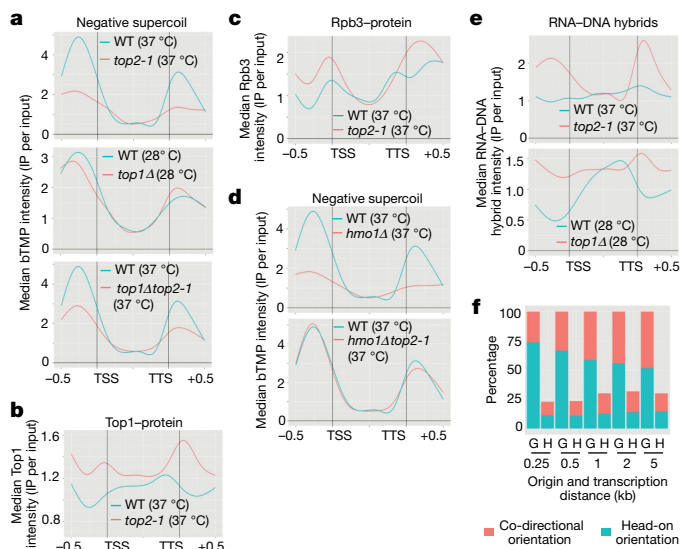


**Fig. 2 | Top2 and Hmo1 contribute to gene topology.** G1 cells were released at 28 °C into S phase and temperature shifted to 37 °C for *top2-1* mutants (replicates  $n = 2$ ; meta-gene analysis  $n = 6,706$  genes). **a**, Meta-gene profiles for negative supercoil comparison in wild-type (WT), *top2-1*, *top1Δ* and *top1Δtop2-1* cells. **b**, **c**, Meta-gene profiles comparing wild-type and *top2-1* cells for accumulation of Top1 protein (Top1-10× Flag) (**b**) or Pol II (Rpb3-10× Flag) (**c**). **d**, Meta-gene profile comparison for negative supercoil in wild-type, *hmo1Δ* and *hmo1Δtop2-1* cells. **e**, Meta-gene profiles for RNA-DNA hybrid comparison in wild-type, *top2-1* and *top1Δ* cells. **f**, Percentage of genes (G) and RNA-DNA hybrid (H) in either head-on or co-directional orientation with respect to replication forks. Genes were grouped with respect to their distance (0.25 kb,  $n = 140$  genes; 0.5 kb,  $n = 235$  genes; 1 kb,  $n = 347$  genes; 2 kb,  $n = 539$  genes; 5 kb,  $n = 1,121$  genes) and direction (head-on or co-directional) from replication origin.

mutants behaved similarly to *hmo1Δ* cells (Extended Data Fig. 4f, g). Hence, ablation of *HMO1* also rescued the aberrant accumulation of hybrids at flanking regions in *top2* mutants.

We investigated whether a clash between forks and transcribed genes might influence the accumulation of hybrids, by analysing 173 efficient replication origins<sup>24</sup>. Transcription units in a head-on or co-directional orientation with replication forks within 0.25, 0.5, 1, 2 or 5 kb of the origin point were selected. There was a significant enrichment of transcribed genes oriented head-on with replication forks (Fig. 2f); this reflects the overlap between the signals that specify transcription termination and those that promote replication initiation<sup>25</sup>. However, the relative accumulation of hybrids in the head-on and the co-directional classes of genes were comparable (Fig. 2f, Extended Data Fig. 4h). Notably, the intergenic regions of converging genes were prone to accumulate hybrids, while this was not the case for the intergenic regions of diverging genes (Extended Data Fig. 4i).

## Negative supercoil affects gene architecture

To validate the previous observations, we expressed *Escherichia coli* DNA topoisomerase I (TopA). TopA expression in *top1top2* mutants depletes negative supercoil in plasmids<sup>26</sup>. Wild-type and *top1Δtop2-1* cells harbouring either control vector or TopA-expressing plasmids were analysed after 60 and 120 min at the restrictive temperature for *top2-1* mutation (Fig. 3a, b). TopA expression in wild-type cells showed a reduction in negative supercoil at ORF-flanking regions and, in *top1Δtop2-1* cells, nearly abolished the negative supercoil at flanking regions (Fig. 3a, Extended Data Fig. 5a). Hence, the presence of Hmo1 at gene boundaries in *top1Δtop2-1* double mutants does not prevent TopA from resolving negative supercoil. TopA acts on negative supercoil to

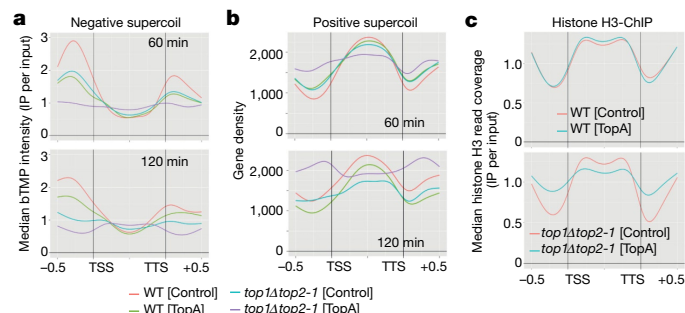


**Fig. 3 | Negative supercoil disruption causes disarray in nucleosome occupancy.** Wild-type and *top1Δtop2-1* mutants either harbouring control plasmid or expressing *E. coli* DNA TopA plasmid were grown at 28 °C and shifted to 37 °C for 60 or 120 min to inactivate Top2 (replicates  $n = 2$ ; meta-gene analysis  $n = 6,706$  genes). **a**, Meta-gene profiles for negative supercoil comparison in wild-type [Control plasmid], wild-type [TopA], *top1Δtop2-1* [Control] and *top1Δtop2-1* [TopA] at 60 min and 120 min at restrictive temperature. **b**, Meta-gene profile for positive supercoil accumulation. **c**, Meta-gene profiles of histone H3 in wild-type and *top1Δtop2-1* mutants with control or TopA plasmids plotted against median read coverage on the y-axis.

convert it into positive supercoil<sup>26</sup>. Accordingly, the disappearance of negative supercoil at flanking regions paralleled the progressive accumulation of over-wound DNA at the same location (Fig. 3b). Expression of TopA caused a reduction in positive supercoil at transcribed regions in wild-type cells, whereas it had the opposite effect in *top1Δtop2-1* mutants (Fig. 3b). This could result from the diffusion of supercoil waves across the entire gene bodies, perhaps owing to the destruction of topological or architectural confinements. Binding of Hmo1 was reduced in *top1Δtop2-1* mutants compared to wild-type cells and was nearly abolished in *top1Δtop2-1* cells expressing TopA (Extended Data Fig. 5b), indicating that association of Hmo1 with gene boundaries depends on negative supercoil.

In wild-type cells, histone H3 was distributed at transcribed units but was less abundant at gene boundaries (Fig. 3c). *top1top2* mutants resembled wild-type cells, suggesting that the aberrant topological context in the double mutants did not affect the nucleosome context. Expression of TopA did not alter nucleosome positioning and distribution in wild-type cells, but in *top1top2* mutants it caused reduction of H3 distribution (Extended Data Fig. 5c). Moreover, H3 redistributed as its levels increased at flanking regions and, concomitantly, decreased at transcribed units, starting from position +2 (Fig. 3c, Extended Data Fig. 5d). Hence, expression of TopA caused an increase in positive supercoil followed by diffusion of supercoil waves across the entire gene body and massive nucleosome repositioning.

## Top2 mediates chromatin loop formation

Using the chromatin interaction analysis by paired-end tag sequencing (ChIA-PET)<sup>27</sup> method, we investigated whether Top2 mediates the formation of chromatin loops. We used Top2 as bait in S phase cells. Following DNA sequencing, we acquired one million independently mapped paired end tags (PETs) (Extended Data Fig. 6a, b) and, by keeping a 1-kb minimum distance, we obtained 1,887 inter-ligation PET clusters (Extended Data Fig. 6b, c). The lengths of the Top2-mediated loops varied; some were larger than 10 kb (~100 interactions), while the majority of loops were between 1,500 and 2,000 bp in size with a median of 1,900 bp (Fig. 4a, b, Extended Data Fig. 6d). Sixty-four per cent of the interactions corresponded to previously described Top2-binding sites<sup>3</sup> and, for the majority of the interactions (66%), Top2 was found only at one end of the loop (Extended Data Fig. 6e). Overall, 45% of the Pol II genes were located within loops. Several loops were organized

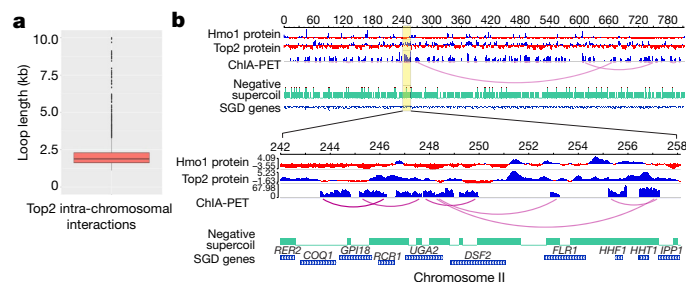


**Fig. 4 | Top2 mediates chromatin loop formation.** **a**, Box plot showing loop size distribution ( $n = 1,505$  loops; min = 1.1 kb; max = 662 kb; median = 1.9 kb; 25th percentile = 1.6 kb; 75th percentile = 2.4 kb). **b**, Genome browser view of how Top2 mediates chromatin interactions on chromosome II, along with Top2 and Hmo1 protein chip data. Highlighted area (chr. II: 242000 to 258000) is enlarged below.

in clusters, with 31% of loops containing more than one gene and 51% of loops containing a single gene (Fig. 4b, Extended Data Fig. 6e, f).

## Discussion

We have shown that Top1 localizes at coding regions. Top2 instead acts at negatively supercoiled gene boundaries and engages genes in loop-like structures, bringing promoters and terminators into proximity<sup>28</sup>. Multiple twin topological domains are likely to be generated within the gene loops by waves of Pol II complexes<sup>29</sup>. Whereas in prokaryotes negative supercoil behind the first transcription bubble might adsorb the positive supercoil generated by the next approaching Pol II complex<sup>30</sup>, in eukaryotes, it may enable nucleosome assembly following Pol II passage<sup>31</sup>. Hence, eukaryotic RNA polymerase progression might depend strongly on Top1 in resolving topological stress in front of Pol II. Accordingly, accumulation of Top1 at coding regions depends on transcription levels. Coding regions exhibit a positive supercoiled context, even when transcription is repressed, implying that genes retain a 'memory' of a topological architecture that does not reflect the dynamics of elongating Pol II<sup>7,32</sup>.

The negatively supercoiled regions that flank ORFs are refractory to nucleosome formation; TopA depletes negative supercoil specifically at these regions. Hence, gene boundaries exhibit an ideal topological context to 'breathe out' and undergo alternative structural transitions<sup>33</sup>. Nucleosome-free negatively supercoiled regions can form pseudo-cruciform structures<sup>34</sup>, characterized by two B-DNA duplex arms and two intra-strand plectonemic arms in a non-B-DNA conformation (Extended Data Fig. 7a). Such structures can branch-migrate, thereby modulating the extension of the intra-strand plectonemic duplexes<sup>35</sup>. Like other HMG box proteins<sup>36</sup>, Hmo1 binds four-way junctions with high affinity. Moreover, it stabilizes nucleosome-free regions, and dimerizes to promote DNA bridging<sup>37</sup>. We propose that Hmo1 locks cruciform DNA and thereby counteracts branch migration and nucleosome formation. Stable negatively supercoiled gene boundaries in a cruciform conformation might help to insulate the topological architecture of gene loops to facilitate elongation of the multiple Pol II complexes, allowing efficient recycling of Pol II from TTS to TSS. Dimerization of Hmo1<sup>37</sup> may promote gene looping, even in G1, without the mediation of Top2. Pol II movement and transcription-coupled processes, such as gene gating and/or splicing, might also contribute to gene looping by extruding portions of the transcribed DNA<sup>38</sup>. In S phase, Top2 would act at the loop base, probably to counteract the disruptive potential of incoming forks and/or to reset gene topology after fork passage (Extended Data Fig. 7b). Notably, Top2-dependent DNA loops can contain more than one transcription unit, and can be organized in clusters, thus generating complex topological structures.

S phase cells accumulate RNA–DNA hybrids at ORFs in about 45% of genes, independent of gene expression levels and of the direction of

transcription–replication. However, the intergenic regions of converging genes exhibit a bias for hybrid accumulation. Pol II back-tracking during elongation, and a slow-down of Pol II during termination<sup>39,40</sup>, could account for the formation of hybrids at ORFs under physiological conditions. The under-wound DNA behind Pol II can easily accommodate RNA–DNA pairing<sup>41</sup>, and might even muffle the negative supercoil generated by Pol II movement. Our data suggest that hybrid formation is a physiological event, intrinsic to the topological dynamics generated by transcription and co-transcriptional processes. However, converging genes might generate the context for unscheduled genotoxic events, as in the case of CSR-activated B cells<sup>42</sup>.

Our model (Extended Data Fig. 7b) leads to the following predictions. (i) Recruitment of Hmo1 at gene boundaries would depend on their negative supercoil state; Hmo1 would then generate stable negative supercoiled cruciforms at gene boundaries (Extended Data Fig. 7a). Hmo1 is always found at negative supercoiled and nucleosome-free regions flanking ORFs, whereas Top2 is recruited in S phase. Counteracting negative supercoil at gene boundaries prevents recruitment of Hmo1. Without Hmo1, cruciforms would be unstable but remain in a negative supercoiled state, becoming an ideal substrate for Top2 (Extended Data Fig. 7c). Accordingly, inactivation of Top2 in *hmo1* cells rescues negative supercoil at gene boundaries. (ii) In *top2* mutants, negative supercoil decreases at ORF-flanking regions, probably owing to the unscheduled and massive recruitment of Top1 at gene boundaries. Notably, non-B-DNA structures can be a substrate for Top1<sup>43</sup>, and Top1 can efficiently relax both positive and negative supercoil<sup>44</sup>. Hence, Hmo1 cannot protect cruciforms from Top1 activity when *top2* is mutated, implying that, in *top2* mutants, Top1 might cause genotoxic events at Hmo1-locked cruciforms, such as extensive nicking and/or knotting<sup>45</sup> (Extended Data Fig. 7c). Notably, deletion of *HMO1* in *top2* mutants, besides alleviating *top2* temperature sensitivity<sup>3</sup>, prevents relocation of Top1 at flanking regions, and *hmo1top2* double mutants exhibit a wild-type-like topological context. (iii) In S phase *top2* mutants, Pol II leaks outside the canonical transcribed regions. This aberrant Pol II distribution is likely to reflect the inability of *top2* mutants to recycle Pol II from TTSs to TSSs, owing to the loss of proximity between promoters and terminators. In this view, Top2 might protect the gene loop structure from incoming forks. (iv) The aberrant Pol II distribution in *top2* mutants may also account for hybrid accumulation at gene boundaries. In *top2* mutants, hybrid accumulation downstream of ORFs may result from aberrant transcription termination, while upstream of ORFs it might be facilitated by the Top1-mediated processing of cruciform DNA. In fact, *top2top1* mutants exhibit fewer hybrids than single *top2* mutants. Another possibility is that Top2 defects promote aberrant antisense transcription initiation events close to TSSs.

The hybrids that accumulate at gene boundaries in *top2* mutants may generate genotoxic events and the unscheduled synthesis of small RNA species, and might contribute to absorbance of the negative supercoil, thus implying that negative supercoil reduction at flanking regions may represent an indirect consequence of Top1 relocation.

Our observations suggest that Top1, Top2 and Hmo1 contribute to the topological architecture of transcribed genes, particularly in S phase when forks reset the topological states of chromosomes and their chromatin context. Interfering with the topological context of gene-flanking regions may cause a variety of pathological consequences, such as the generation of aberrant RNA species, the accumulation of RNA–DNA hybrids and alterations at the level of chromatin architecture.

## Online content

Any methods, additional references, Nature Research reporting summaries, source data, extended data, supplementary information, acknowledgements, peer review information; details of author contributions and competing interests; and statements of data and code availability are available at <https://doi.org/10.1038/s41586-020-1934-4>.

1. Bermejo, R., Lai, M. S. & Foiani, M. Preventing replication stress to maintain genome stability: resolving conflicts between replication and transcription. *Mol. Cell* **45**, 710–718 (2012).
2. García-Muse, T. & Aguilera, A. Transcription-replication conflicts: how they occur and how they are resolved. *Nat. Rev. Mol. Cell Biol.* **17**, 553–563 (2016).
3. Bermejo, R. et al. Genome-organizing factors Top2 and Hmo1 prevent chromosome fragility at sites of S phase transcription. *Cell* **138**, 870–884 (2009).
4. Sperling, A. S., Jeong, K. S., Kitada, T. & Grunstein, M. Topoisomerase II binds nucleosome-free DNA and acts redundantly with topoisomerase I to enhance recruitment of RNA Pol II in budding yeast. *Proc. Natl Acad. Sci. USA* **108**, 12693–12698 (2011).
5. Wang, J. C. Cellular roles of DNA topoisomerases: a molecular perspective. *Nat. Rev. Mol. Cell Biol.* **3**, 430–440 (2002).
6. Pedersen, J. M. et al. DNA topoisomerases maintain promoters in a state competent for transcriptional activation in *Saccharomyces cerevisiae*. *PLoS Genetics* **8**, e1003128 (2012).
7. Liu, L. F. & Wang, J. C. Supercoiling of the DNA template during transcription. *Proc. Natl Acad. Sci. USA* **84**, 7024–7027 (1987).
8. Postow, L., Crisona, N. J., Peter, B. J., Hardy, C. D. & Cozzarelli, N. R. Topological challenges to DNA replication: conformations at the fork. *Proc. Natl Acad. Sci. USA* **98**, 8219–8226 (2001).
9. Schwartzman, J. B. & Stasiak, A. A topological view of the replicon. *EMBO Rep.* **5**, 256–261 (2004).
10. Lal, A. et al. Genome scale patterns of supercoiling in a bacterial chromosome. *Nat. Commun.* **7**, 11055 (2016).
11. Bermúdez, I., García-Martínez, J., Pérez-Ortín, J. E. & Roca, J. A method for genome-wide analysis of DNA helical tension by means of psoralen-DNA photobinding. *Nucleic Acids Res.* **38**, e182 (2010).
12. Naughton, C. et al. Transcription forms and remodels supercoiling domains unfolding large-scale chromatin structures. *Nat. Struct. Mol. Biol.* **20**, 387–395 (2013).
13. Kouzine, F. et al. Transcription-dependent dynamic supercoiling is a short-range genomic force. *Nat. Struct. Mol. Biol.* **20**, 396–403 (2013).
14. Sinden, R. R., Carlson, J. O. & Pettijohn, D. E. Torsional tension in the DNA double helix measured with trimethylpsoralen in living *E. coli* cells: analogous measurements in insect and human cells. *Cell* **21**, 773–783 (1980).
15. Perales, R. & Bentley, D. “Cotranscriptionality”: the transcription elongation complex as a nexus for nuclear transactions. *Mol. Cell* **36**, 178–191 (2009).
16. Bermejo, R. et al. Top1- and Top2-mediated topological transitions at replication forks ensure fork progression and stability and prevent DNA damage checkpoint activation. *Genes Dev.* **21**, 1921–1936 (2007).
17. Boguslawski, S. J. et al. Characterization of monoclonal antibody to DNA, RNA and its application to immunodetection of hybrids. *J. Immunol. Methods* **89**, 123–130 (1986).
18. Chan, Y. A. et al. Genome-wide profiling of yeast DNA:RNA hybrid prone sites with DRIP-chip. *PLoS Genet.* **10**, e1004288 (2014).
19. Hamperl, S. & Cimprich, K. A. The contribution of co-transcriptional RNA:DNA hybrid structures to DNA damage and genome instability. *DNA Repair* **19**, 84–94 (2014).
20. Rossi, S. E., Ajazi, A., Carotenuto, W., Foiani, M. & Giannattasio, M. Rad53-mediated regulation of Rrm3 and Pif1 DNA helicases contributes to prevention of aberrant fork transitions under replication stress. *Cell Rep.* **13**, 80–92 (2015).
21. Hazelbaker, D. Z., Marquardt, S., Wlotzka, W. & Buratowski, S. Kinetic competition between RNA Polymerase II and Sen1-dependent transcription termination. *Mol. Cell* **49**, 55–66 (2013).
22. Skourti-Stathaki, K., Kamieniarz-Gdula, K. & Proudfoot, N. J. R-loops induce repressive chromatin marks over mammalian gene terminators. *Nature* **516**, 436–439 (2014).
23. Tuduri, S. et al. Topoisomerase I suppresses genomic instability by preventing interference between replication and transcription. *Nat. Cell Biol.* **11**, 1315–1324 (2009).
24. Fachinetti, D. et al. Replication termination at eukaryotic chromosomes is mediated by Top2 and occurs at genomic loci containing pausing elements. *Mol. Cell* **39**, 595–605 (2010).
25. Chen, S., Reger, R., Miller, C. & Hyman, L. E. Transcriptional terminators of RNA polymerase II are associated with yeast replication origins. *Nucleic Acids Res.* **24**, 2885–2893 (1996).
26. Gartenberg, M. R. & Wang, J. C. Positive supercoiling of DNA greatly diminishes mRNA synthesis in yeast. *Proc. Natl Acad. Sci. USA* **89**, 11461–11465 (1992).
27. Li, X. et al. Long-read ChIA-PET for base-pair-resolution mapping of haplotype-specific chromatin interactions. *Nat. Protocols* **12**, 899–915 (2017).
28. O’Sullivan, J. M. et al. Gene loops juxtapose promoters and terminators in yeast. *Nat. Genet.* **36**, 1014–1018 (2004).
29. Levens, D., Baranello, L. & Kouzine, F. Controlling gene expression by DNA mechanics: emerging insights and challenges. *Biophys. Rev.* **8**, 259–268 (2016).
30. Rovinskiy, N., Agbleke, A. A., Chesnokova, O., Pang, Z. & Higgins, N. P. Rates of gyrase supercoiling and transcription elongation control supercoil density in a bacterial chromosome. *PLoS Genet.* **8**, e1002845 (2012).
31. Patterson, H. G. & von Holt, C. Negative supercoiling and nucleosome cores. I. The effect of negative supercoiling on the efficiency of nucleosome core formation *in vitro*. *J. Mol. Biol.* **229**, 623–636 (1993).
32. Ma, J., Bai, L. & Wang, M. D. Transcription under torsion. *Science* **340**, 1580–1583 (2013).
33. Kouzine, F. et al. Permanganate/S1 nuclease footprinting reveals non-B DNA structures with regulatory potential across a mammalian genome. *Cell Syst.* **4**, 344–356 (2017).
34. Lilley, D. M. DNA opens up—supercoiling and heavy breathing. *Trends Genet.* **4**, 111–114 (1988).
35. Murchie, A. I. & Lilley, D. M. Supercoiled DNA and cruciform structures. *Methods Enzymol.* **211**, 158–180 (1992).
36. Pöhler, J. R. G., Norman, D. G., Bramham, J., Bianchi, M. E. & Lilley, D. M. HMG box proteins bind to four-way DNA junctions in their open conformation. *EMBO J.* **17**, 817–826 (1998).
37. Murugesapillai, D. et al. DNA bridging and looping by HMO1 provides a mechanism for stabilizing nucleosome-free chromatin. *Nucleic Acids Res.* **42**, 8996–9004 (2014).
38. Tan-Wong, S. M., Wijayatilake, H. D. & Proudfoot, N. J. Gene loops function to maintain transcriptional memory through interaction with the nuclear pore complex. *Genes Dev.* **23**, 2610–2624 (2009).
39. Saponaro, M. et al. RECQL5 controls transcript elongation and suppresses genome instability associated with transcription stress. *Cell* **157**, 1037–1049 (2014).
40. Cheung, A. C. & Cramer, P. Structural basis of RNA polymerase II backtracking, arrest and reactivation. *Nature* **471**, 249–253 (2011).
41. Drolet, M. et al. Overexpression of RNase H partially complements the growth defect of an *Escherichia coli* delta topA mutant: R-loop formation is a major problem in the absence of DNA topoisomerase I. *Proc. Natl Acad. Sci. USA* **92**, 3526–3530 (1995).
42. Meng, F. L. et al. Convergent transcription at intragenic super-enhancers targets AID-initiated genomic instability. *Cell* **159**, 1538–1548 (2014).
43. Husain, A. et al. Chromatin remodeller SMARCA4 recruits topoisomerase 1 and suppresses transcription-associated genomic instability. *Nat. Commun.* **7**, 10549 (2016).
44. Fernández, X., Díaz-Ingelmo, O., Martínez-García, B. & Roca, J. Chromatin regulates DNA torsional energy via topoisomerase II-mediated relaxation of positive supercoils. *EMBO J.* **33**, 1492–1501 (2014).
45. Brown, P. O. & Cozzarelli, N. R. Catenation and knotting of duplex DNA by type 1 topoisomerases: a mechanistic parallel with type 2 topoisomerases. *Proc. Natl Acad. Sci. USA* **78**, 843–847 (1981).

**Publisher’s note** Springer Nature remains neutral with regard to jurisdictional claims in published maps and institutional affiliations.

© The Author(s), under exclusive licence to Springer Nature Limited 2020

### Strains and growing conditions

All *S. cerevisiae* strains are W303 derivatives<sup>46</sup>. The relevant genotypes are shown in Extended Data Table 1. Strains were grown at 28 °C in YPD medium. G1 synchronization was carried out using 3–5 µg/ml of α factor. For S-phase samples, G1 cells were washed twice in YP medium and allowed to grow for 15 min in fresh medium. For temperature-sensitive strains, cells were allowed to grow for 10 min in fresh medium after G1 release, centrifuged and then dissolved in pre-warmed medium at 37 °C and allowed to grow for 15 min. Cell cycle progression into S phase was monitored by fluorescence-activated cell sorting (FACS) and budding profiles. For *E. coli* TopA expression, wild-type cells and *top1Δtop2-1* mutants harbouring either control or TopA expression plasmids were grown at 25 °C in synthetic medium lacking leucine. Cells were shifted to 37 °C for inactivation of Top2 after reaching  $8 \times 10^6$  cells/ml concentration.

### bTMP-ChIP

We adapted the previously described method to yeast<sup>12</sup>. Sodium azide (0.1%) was used to block cells and to ensure the preservation of the most prevalent topological context present at any given genomic position. We note that this method does not aim to study dynamic topological transitions. Permeabilized yeast cells were incubated with bTMP (400 µg per  $2 \times 10^9$  cells) in the dark for 90 min and then cross-linked by 365 nm UV (800 mJ/cm<sup>2</sup>) light to form adducts between two DNA strands. Cells were washed twice with ice-cold PBS and lysed in 1 ml of lysis buffer (50 mM HEPES-KOH pH 7.5, 140 mM NaCl, 1 mM EDTA, 1% Triton X-100, 0.1% Na-deoxycholate) using Zirconia beads. The cross-linked chromatin was sheared to an average size of 500 bp by 6 × 15-s pulses using a Biorupter sonicator and DNA was purified. Purified DNA was incubated with Dynabeads MyOne streptavidin (Invitrogen cat. no. 65001) overnight at 4 °C. The beads were washed twice with each of the following buffers; wash buffer-I (20 mM Tris-HCL pH 8, 2 mM EDTA, 150 mM NaCl, 1% Triton X, 0.1% SDS), wash buffer-II (20 mM Tris-HCL pH 8, 2 mM EDTA, 500 mM NaCl, 1% Triton X, 0.1% SDS), wash buffer III (250 mM LiCl, 10 mM Tris pH 8.0, 0.5% Na-deoxycholate, 0.5% NP-40, 1 mM EDTA) and 1× TE (20 mM Tris pH 8.0, 2 mM EDTA). The bTMP–DNA complexes were eluted from the beads in 250 µl elution buffer (95% formamide, 10 mM EDTA) at 90 °C for 20 min and eluted samples were cleaned with a Qiagen PCR clean up kit. Input DNA was isolated from sheared chromatin input (1/100 of the material used for ChIP). For bTMP-ChIP with naked DNA, genomic DNA was isolated from Qiagen Genomic-tip 100/G (cat. no. 13343) and Genomic DNA Buffer Set (cat. no. 19060). Purified DNA was sheared to an average size of 500 bp by 6 × 15-s pulses using a Biorupter sonicator. bTMP was added to purified DNA and incubated in the dark for 90 min and cross-linked with UV at 365 nm (800 mJ/cm<sup>2</sup>). DNA was precipitated using isopropanol and washed with 70% ethanol. The dried pellet was dissolved in buffer (50 mM Tris pH 8.0, 10 mM EDTA, 0.1% SDS) and incubated with Dynabeads MyOne streptavidin (Invitrogen cat. no. 65001) overnight at 4 °C. Washing and elution was as described above. Both IP and input samples were processed as described in the in microarray section.

The procedure for bTMP titration is presented in Extended Data Fig. 8. bTMP binding normalization and the dispersion profile for bTMP are presented in Extended Data Fig. 9.

### Protein ChIP

ChIP analysis for proteins was carried out as described<sup>47</sup> with few modifications. Cells were cross-linked with 1% formaldehyde in culture medium for 30 min at room temperature followed by quenching with 0.125 M glycine for 5 min. Cells were washed twice with ice-cold PBS and lysed in 1 ml of lysis buffer (50 mM HEPES-KOH pH 7.5, 140 mM NaCl, 1 mM EDTA, 1% Triton X-100, 0.1% Na-deoxycholate) using Zirconia beads. Cross-linked chromatin was sheared to an average

size of 500 bp by 6 × 15-s pulses using a Biorupter sonicator. The lysate was then centrifuged to remove cell debris. The chromatin fraction was incubated with Dynabeads protein G beads (Invitrogen, cat. no. 10003D) coated with anti-Flag antibody (M2-antiflag, Sigma) overnight at 4 °C. The immune complexes were washed with the following buffers 2×; Chip-lysis buffer, high-salt lysis buffer (Chip-lysis buffer + 360 mM NaCl), Chip-wash buffer (250 mM LiCl, 10 mM Tris pH 8.0, 0.5% Na-deoxycholate, 0.5% NP-40, 1 mM EDTA) and 1× TE (20 mM Tris pH 8.0, 2 mM EDTA). The protein–DNA complexes were eluted from the beads in 250 µl elution buffer (1% SDS, 50 mM Tris pH 8.0, 10 mM EDTA) at 65 °C for 20 min followed by the addition of proteinase K to 500 µg/ml and overnight incubation at 65 °C. Input DNA was isolated from sheared chromatin input (1/100 of the material used for ChIP). Both IP and input samples were processed as mentioned in the section 'Microarray and data processing'.

### DRIP-ChIP

DRIP-ChIP was performed using anti-DNA:RNA hybrid monoclonal mouse antibody S9.6 as previously described<sup>18</sup>. In brief, cells were cross-linked with 1% formaldehyde in culture medium for 20 min at room temperature followed by quenching with 0.125 M glycine for 5 min. Cells were washed twice with ice-cold PBS and lysed in 1 ml of lysis buffer (50 mM HEPES-KOH pH 7.5, 140 mM NaCl, 1 mM EDTA, 1% Triton X-100, 0.1% Na-deoxycholate) using Zirconia beads. Cross-linked chromatin was sheared to an average size of 500 bp by 6 × 15-s pulses using a Biorupter sonicator. The lysate was then centrifuged to remove cell debris. The chromatin fraction was incubated with Protein-A magnetic beads (Invitrogen, cat. no. 10001D) coated with anti-DNA:RNA hybrid S9.6 antibody<sup>17</sup> overnight at 4 °C. The immune complexes were washed with the following buffers 2×; Chip-lysis buffer, high-salt lysis buffer (Chip-lysis buffer + 360 mM NaCl), Chip-wash buffer (250 mM LiCl, 10 mM Tris pH 8.0, 0.5% Na-deoxycholate, 0.5% NP-40, 1 mM EDTA) and 1× TE (20 mM Tris pH 8.0, 2 mM EDTA). The RNA:DNA hybrid complexes were eluted from the beads in 250 µl elution buffer (1% SDS, 50 mM Tris pH 8.0, 10 mM EDTA) at 65 °C for 20 min followed by the addition of proteinase K to 500 µg/ml and overnight incubation at 65 °C. Input DNA was isolated from sheared chromatin input (1/100 of the material used for ChIP). Both IP and input samples were processed as mentioned in the section 'Microarray and data processing'.

### Histone H3 ChIP sequencing

ChIP analysis for proteins was carried out as described previously<sup>48</sup>. In brief, cells were cross-linked with 1% formaldehyde in culture medium for 15 min at room temperature followed by quenching with 0.125 M glycine for 5 min. Cells were washed twice with ice-cold PBS and lysed in 1 ml of lysis buffer (50 mM HEPES-KOH pH 7.5, 140 mM NaCl, 1 mM EDTA, 1% Triton X-100, 0.1% Na-deoxycholate) using Zirconia beads. Cross-linked chromatin was sheared to an average size of 200 bp in Covaris S220 Focused Ultrasonicators. The lysate was then centrifuged to remove cell debris. The chromatin fraction was incubated with Protein-G magnetic beads (Invitrogen, cat. no. 10003D) coated with anti-histone H3 antibody (Abcam, cat. no. ab1791) overnight at 4 °C. The immune complexes were washed twice with the following buffers; Chip-lysis buffer, high-salt lysis buffer (CHIP-lysis buffer + 360 mM NaCl), CHIP-wash buffer (250 mM LiCl, 10 mM Tris pH 8.0, 0.5% Na-deoxycholate, 0.5% NP-40, 1 mM EDTA) and 1× TE (20 mM Tris pH 8.0, 2 mM EDTA). The protein–DNA complexes were eluted from the beads in 250 µl elution buffer (1% SDS, 50 mM Tris pH 8.0, 10 mM EDTA) at 65 °C for 20 min followed by the addition of proteinase K to 500 µg/ml and overnight incubation at 65 °C. Input DNA was isolated from sheared chromatin input (1/100 of the material used for ChIP).

For sequencing, IP and input ChIP sequencing (ChIP–seq) libraries were prepared according to the manufacturer's protocols for the Ion Proton sequencer (Thermo Fisher Scientific/Life Technologies). In brief, 10 ng of ChIP DNA was end repaired and adaptor ligated using the KAPA



Library Preparation Kit for Ion Torrent (KAPA Biosystems) and adaptor barcode Kapa Barcode Adaptors 9-24. After adaptor ligation, each sample was size selected using AMPure XP Bead (Beckman Coulter). An amplification reaction was set up in a final volume of 50 µl. A SPRI cleanup with a 1.5× bead:DNA ratio was performed after amplification and final libraries were eluted in 35 µl. Libraries were quantified on a Qubit fluorometer with HS DNA (Thermo Fisher Scientific/Life Technologies) and checked for size on an Agilent Bioanalyzer with an HS DNA kit (Agilent). Each size-selected library was diluted to a final concentration of 11 pM and clonally amplified using the Ion Proton Hi-Q Template Kit (Thermo Fisher Scientific/Life Technologies) with IonOneTouch 2 instrument (Thermo Fisher Scientific/Life Technologies). After emulsion PCR, DNA-positive ion sphere particles (ISPs) were recovered and enriched according to standard protocols with the IonOneTouch ES Instrument (Thermo Fisher Scientific/Life Technologies). A sequencing primer was annealed to DNA-positive ISPs and the sequencing polymerase bound, before loading of ISPs into Ion P1 sequencing chips. Sequencing of the samples was conducted according to the Ion Proton Hi-Q Sequencing Kit protocol. One P1 sequencing chip with six libraries was loaded and run on an Ion Proton sequencer.

### RNA sequencing

Total RNA was isolated from  $5 \times 10^7$  cells with the RNeasy Mini Kit (50) (Qiagen cat. no. 74104). Prior to library preparation, cytoplasmic and mitochondrial ribosomal RNA was removed using the Ribo-Zero Gold rRNA Removal Kit (Yeast) (Illumina, cat. no. MRZY1324). Libraries for RNA sequencing were prepared according to the manufacturer's protocols for transcriptome sequencing with the Ion Proton sequencer (Thermo Fisher Scientific/Life Technologies). In brief, 1 µg total RNA was poly-A-selected using the Dynabeads mRNA Direct Micro Purification kit (Thermo Fisher Scientific, cat. no. 61021) according to the manufacturer's protocol. About 50 ng of poly-A RNA was used to prepare strand-specific barcoded RNA libraries with the Ion Total RNA-Seq kit v.2.0 (Thermo Fisher Scientific, cat. no. 4475936). In brief, poly-A RNA was fragmented with RNase III and purified with Nucleic Acid Binding Beads. After purification, the poly-A RNA fragments were hybridized and ligated with Ion Adaptor and subsequently reverse transcribed for cDNA preparation. cDNAs were amplified with Ion Torrent barcoded primers and purified with Nucleic Acid Binding Beads. Final libraries were quantified on a Qubit fluorometer with HS DNA (Thermo Fisher Scientific) and checked for size on an Agilent Bioanalyzer with an HS DNA kit (Agilent). Four barcoded libraries were pooled together on an equimolar basis at a final concentration of 11 pM and clonally amplified using the Ion Proton Hi-Q Template Kit (Thermo Fisher Scientific, cat. no. A26434) with IonOneTouch 2 instrument (Thermo Fisher Scientific/Life Technologies). After emulsion PCR, DNA-positive ISPs were recovered and enriched by standard protocols with the IonOneTouch ES Instrument (Thermo Fisher Scientific/Life Technologies). A sequencing primer was annealed to DNA-positive ISPs and the sequencing polymerase bound, before loading of ISPs into Ion P1 sequencing chips. Sequencing of the samples was conducted according to the Ion Proton Hi-Q Sequencing Kit (Thermo Fisher Scientific, cat. no. A26433) Protocol on Ion Proton instrument.

### ChIA-PET

We adopted the previously described method<sup>27</sup>. Cells were cross-linked with 1% formaldehyde in culture medium for 30 min at room temperature followed by quenching with 0.125 M glycine for 5 min. Cells were washed twice with ice-cold PBS and lysed in 1 ml of lysis buffer (50 mM HEPES-KOH pH 7.5, 140 mM NaCl, 1 mM EDTA, 1% Triton X-100, 0.1% Na-deoxycholate) using Zirconia beads. Cross-linked chromatin was sheared to an average size of 500 bp by 6×15-s pulses using a Biorupter sonicator. The lysate was then centrifuged to remove cell debris. The chromatin fraction was incubated with Dynabeads protein G beads (Invitrogen, cat no 10003D) coated with anti-Flag antibody

(M2-antiflag, Sigma) overnight at 4 °C. The immune complexes were washed twice with the following buffers: ChIP-lysis buffer, high-salt lysis buffer (ChIP-lysis buffer + 360 mM NaCl), ChIP-wash buffer (250 mM LiCl, 10 mM Tris pH 8.0, 0.5% Na-deoxycholate, 0.5% NP-40, 1 mM EDTA) and 1× TE (20 mM Tris pH 8.0, 2 mM EDTA). Beads were pooled and end-repair was carried out using T4 DNA polymerase (NEB, cat. no. M0203L) by rotating on a Intelli-Mixer at 37 °C for 40 min. Beads were washed 3× with ice-cold ChIA-PET wash buffer (10 mM Tris pH 7.4, 1 mM EDTA, 500 mM NaCl). A-tailing was carried out using Kleenow fragment (3'-5' exo-) (NEB, cat. no. M0212M) in the presence of 100 µM dATP by rotating on a Intelli-Mixer at 37 °C for 50 min. Beads were washed 3× with ice cold ChIA-PET wash buffer (10 mM Tris pH 7.4, 1 mM EDTA, 500 mM NaCl). For proximity ligation, a bridge linker was prepared by annealing Linker-F and Linker-R (HPLC purified (250 nmole) from IDT (Integrated DNA Technologies): bridge linker-F: 5'-/5Phos/CGCGATATC/IBIOdT/TATCTGACT-3'; bridge linker-R: 5'-/5Phos/GTCA-GATAAGATATCGCGT-3'.

Proximity ligation was carried out using T4 DNA ligase (NEB cat. no. M0202M), in the presence of bridge linker at a concentration of 0.57 ng/µl by rotating at 16 °C overnight. Beads were washed once in ChIA-PET wash buffer and eluted in elution buffer (10 mM Tris pH 8.0, 1 mM EDTA, 1% SDS) at 65 °C for 15 min. Reverse cross-linking was carried out at 65 °C in the presence of proteinase K. DNA was purified using phenol-chloroform-isoamyl alcohol (pH 7.9) and MaXtract High Density-2ml (QIAGEN, cat. no. 129056) and precipitated with isopropanol. Tagmentation of proximity-ligated DNA was carried out by Tn5 transposome using the Nextera DNA Sample Preparation Kit (24) (Illumina FC-121-1030). Tagmented DNA was purified using the Zymo Genomic DNA Clean & Concentrator kit (Zymo Research, cat. no. D4014) and fragments containing linker DNA were enriched with Dynabeads M-280 Streptavidin (Invitrogen, cat. no. 11205D). Beads were washed with 2× SSC/0.5% (wt/vol) SDS five times and twice in 1× B&W buffer (10 mM Tris pH 8.0, 1 mM EDTA, 1 M NaCl). The sequencing library was amplified using beads and the purified library was used for paired-end sequencing using MiSeq Reagent Kit v3 (600 cycle) on an Illumina MiSeq instrument.

### Microarray and data processing

Both IP and input DNA were amplified using the GenomePlex complete whole-genome amplification kit (Sigma, cat. no. WGA1-50RXN), biotin-labelled and hybridized to Affymetrix GeneChip *S. cerevisiae* Tiling 1.0R Array (Sc03b\_MR) according to the Affymetrix standard protocol. The CEL files were processed using rMAT<sup>49</sup> R package to identify enriched regions across the genome. At first, systematic biases such as probe effect were corrected by normalization. Then probe intensities were smoothed and a score was calculated for each probe using IP and input. To detect enriched regions based on the probe score, the following parameters were used; dMax = 300 (sliding window size), nProbesMin = 8 (minimum number of probes to average), method = Score (calling enriched regions based on sliding window scores), log<sub>2</sub> threshold = 1.5 (equal and greater than 1.5 are labelled as enriched regions). For bTMP experiments, bTMP binding 'in cells' (IP/input) was subtracted from the 'naked genomic DNA' score (IP/input) to correct for false positive binding of bTMP.

### Meta-gene analysis

Meta-gene analysis was used to study the averaged enriched peak profile across all protein-coding genes (6,706 genes from SacCer 2011 annotation) or a specific set of genes upstream (−500 bases from TSS) and downstream (+500 bases from TTS) in the yeast genome. The peak scores were mapped using bedtools<sup>50</sup>, for every base of the gene including upstream (−500 b) and downstream (+500b). The length of the gene was scaled to 1,000 bases. For scaling the ORF region to 1,000 bases, the following equation was iterated for every base across all the genes  $(Z - x_i)/(y_i - x_i) \times 1,000$  where  $x_i$  is the start position of the  $i$ th gene,



# Article

$i = (1, 2, 3 \dots \text{total genes})$ ,  $y_i$  is the end position of the  $i$ th gene,  $i = (1, 2, 3 \dots \text{total genes})$ ,  $Z$  is base position  $(1, 2, 3 \dots y_i - x_i)$ . For the average intensity plot, the IP/input values of the normalized position  $(1,000 \text{ ORF}, -500 \text{ upstream and } +500 \text{ downstream})$  of each gene were aggregated using median. For average gene density, the IP/input score was converted into a categorical value of either 1 or 0 based on the threshold of 1.5 ( $\geq 1.5$  is 1 and  $< 1.5$  is 0) of all the normalized positions  $(1,000 \text{ ORF}, -500 \text{ upstream and } +500 \text{ downstream})$  of each gene and aggregated using the sum function. For visualization, average intensity and average gene density were plotted with respect to normalized ORF position. The points were smoothed using the generalized additive model (GAM) to obtain a curve using ggplot2 R package.

## RNA-seq data processing

The RNA-seq data from the IonTorrent proton instrument contains approximately 25 million reads for each sample. The raw reads were filtered on the basis of quality value ( $-q 20$  and  $-p 30$ ) using the FASTX Toolkit. The filtered reads were aligned to the reference genome (SacCer 2011) using STAR aligner<sup>51</sup>. Aligned BAM files were used for transcript quantification (FPKM) using RSEM<sup>52</sup>. The gene sets were divided into three equal categories (low, medium and high expression) according to FPKM values and used to plot the supercoiling, protein and RNA-DNA hybrid profile using the meta-gene calculation mentioned above.

## Histone H3 ChIP-seq data processing

The ChIP-seq data from the IonTorrent proton instrument contain approximately 15 million reads for each sample. The raw reads were filtered on the basis of quality value ( $-q 20$  and  $-p 30$ ) using the FASTX Toolkit. The filtered reads were aligned to the reference genome (SacCer 2011) using TMAP aligner. The PCR duplicates were removed from the aligned BAM files using PICARD tools. The BAM files were sorted and indexed for the peak calling using SAMtools. The bedgraph files were generated by comparing bam files of IP and input (IP read coverage/input read coverage) resulting in a ratio for every base across the whole genome using deepTools (bamCompare)<sup>53</sup>. Finally, peak calling was performed using the DANPOS (dpos) toolkit<sup>54</sup> with the IP/input threshold 1.4 ( $-q 1.4$ ) where the output peaks corresponds to the individual nucleosome. The DANPOS was preferred over the MACS toolkit for the dynamic nucleosome analysis at single-nucleotide resolution.

## ChIA-PET data processing

ChIA-PET data contain approximately 10 million reads with a median length of approximately 105 nucleotides. Raw reads were filtered on the basis of quality value ( $-q 20$  and  $-p 30$ ) using the FASTX Toolkit. The filtered reads were scanned for bridge linker (ACGCGATATCT-TATCTGACT, AGTCAGATAAGATATCGCGT) with a maximum of two mismatches using cutadapt. The reads containing the bridge linker were aligned to the reference genome (SacCer 2011) using the bwa mem module. PCR duplicates were removed using Picard MarkDuplicates module. The aligned bam file was converted to a bed pair end interaction file (bedpe) for cluster generation using bedtools (bamtobed) module. PETs with less than 1 kb distance (self-ligation loops) were not considered for the PET clustering. Individual PET interactions were clustered by extending each PET by 500 bp and PETs that overlapped at both ends were clustered together as a single PET cluster<sup>27</sup>. PET clusters with more than or equal to 2 were considered for meta-analysis. WashU Epigenome Browser was used to visualize chromatin-chromatin interactions<sup>55</sup>.

## Tool kits

FASTX Toolkit: [http://hannonlab.cshl.edu/fastx\\_toolkit/](http://hannonlab.cshl.edu/fastx_toolkit/)  
TMAP Toolkit: <https://github.com/iontorrent/TMAP>  
PICARD Toolkit: <https://broadinstitute.github.io/picard/>  
BWA Toolkit: <http://bio-bwa.sourceforge.net/>

## Statistics and reproducibility

All experiments were carried out with two biological replicates. To test the significance of the overlap between two replicates (supercoiling, protein and hybrid peak calls), intersect and Fisher's exact test from bedtools were used. For bedtools intersect, a minimum of 80% overlap was expected for further downstream analysis such as meta-gene plotting. The number of overlap peaks and sum of overlap bases between two sets of intervals from bedtools were visualized using VennDiagram library from R. Protein-coding genes ( $n = 6,706$ ) from SacCer 2011 were used for meta-gene plotting.

## Reporting summary

Further information on research design is available in the Nature Research Reporting Summary linked to this paper.

## Data availability

All raw and processed data are available at the Gene Expression Omnibus (GEO) under the following accession numbers: GSE114410 (bTMP, RNA-DNA hybrids, Top1 protein ChIP-on-chip and RPB3 protein ChIP-on-chip); GSE114444 (RNA-seq, H3 ChIP-seq and ChIA-PET); GSE16258<sup>47</sup> (Top2 protein ChIP-chip, Hmo1 protein ChIP-chip and RPB3 protein ChIP-chip).

## Code availability

All the custom-made scripts used for this study are available in the GitHub repository at <https://github.com/adhilmd/TopologyCustomAnalysis>.

46. Thomas, B. J. & Rothstein, R. Elevated recombination rates in transcriptionally active DNA. *Cell* **56**, 619–630 (1989).
47. Bermejo, R., Katou, Y. M., Shirahige, K. & Foiani, M. ChIP-on-chip analysis of DNA topoisomerases. *Methods Mol. Biol.* **582**, 103–118 (2009).
48. Rodriguez, J., McKnight, J. N. & Tsukiyama, T. Genome-wide analysis of nucleosome positions, occupancy, and accessibility in yeast: nucleosome mapping, high-resolution histone ChIP, and NCAM. *Curr. Protoc. Mol. Biol.* **108**, 21.28.1–21.28.16 (2014).
49. Droit, A., Cheung, C. & Gottardo, R. rMAT—an R/Bioconductor package for analyzing ChIP-chip experiments. *Bioinformatics* **26**, 678–679 (2010).
50. Quinlan, A. R. & Hall, I. M. BEDTools: a flexible suite of utilities for comparing genomic features. *Bioinformatics* **26**, 841–842 (2010).
51. Dobin, A. et al. STAR: ultrafast universal RNA-seq aligner. *Bioinformatics* **29**, 15–21 (2013).
52. Li, B. & Dewey, C. N. RSEM: accurate transcript quantification from RNA-seq data with or without a reference genome. *BMC Bioinformatics* **12**, 323 (2011).
53. Ramirez, F., Dündar, F., Diehl, S., Grünig, B. A. & Manke, T. deepTools: a flexible platform for exploring deep-sequencing data. *Nucleic Acids Res.* **42**, W187–W191 (2014).
54. Chen, K. et al. DANPOS: dynamic analysis of nucleosome position and occupancy by sequencing. *Genome Res.* **23**, 341–351 (2013).
55. Zhou, X. et al. The human epigenome browser at Washington University. *Nat. Methods* **8**, 989–990 (2011).

**Acknowledgements** We thank J. Roca for sharing TopA-expressing plasmids, and M. Bianchi, G. Liberi and all our laboratory members for discussions. We thank Cogentech and C. Valli, M. Riboni and S. Minardi for microarray and DNA sequencing. Research was supported by grants from the Associazione Italiana per la Ricerca sul Cancro (AIRC), the European Union, MIUR, Worldwide Cancer Research, and Telethon-Italy to M.F. Y.J.A. is supported by the European Community's Seventh Framework Programme under grant agreement no. 246549 – Train 2009. N.G. is funded by the UK Medical Research Council (MR/J00913X/1; MC\_UU\_00007/13).

**Author contributions** Y.J.A. and M.F. designed the experiments, interpreted results and prepared the manuscript. Y.J.A. and M.A. performed the experiments. M.A. performed statistical and computational analysis. R.C. provided technical input and N.G. provided bTMP and technical input for supercoil analysis.

**Competing interests** The authors declare no competing interests.

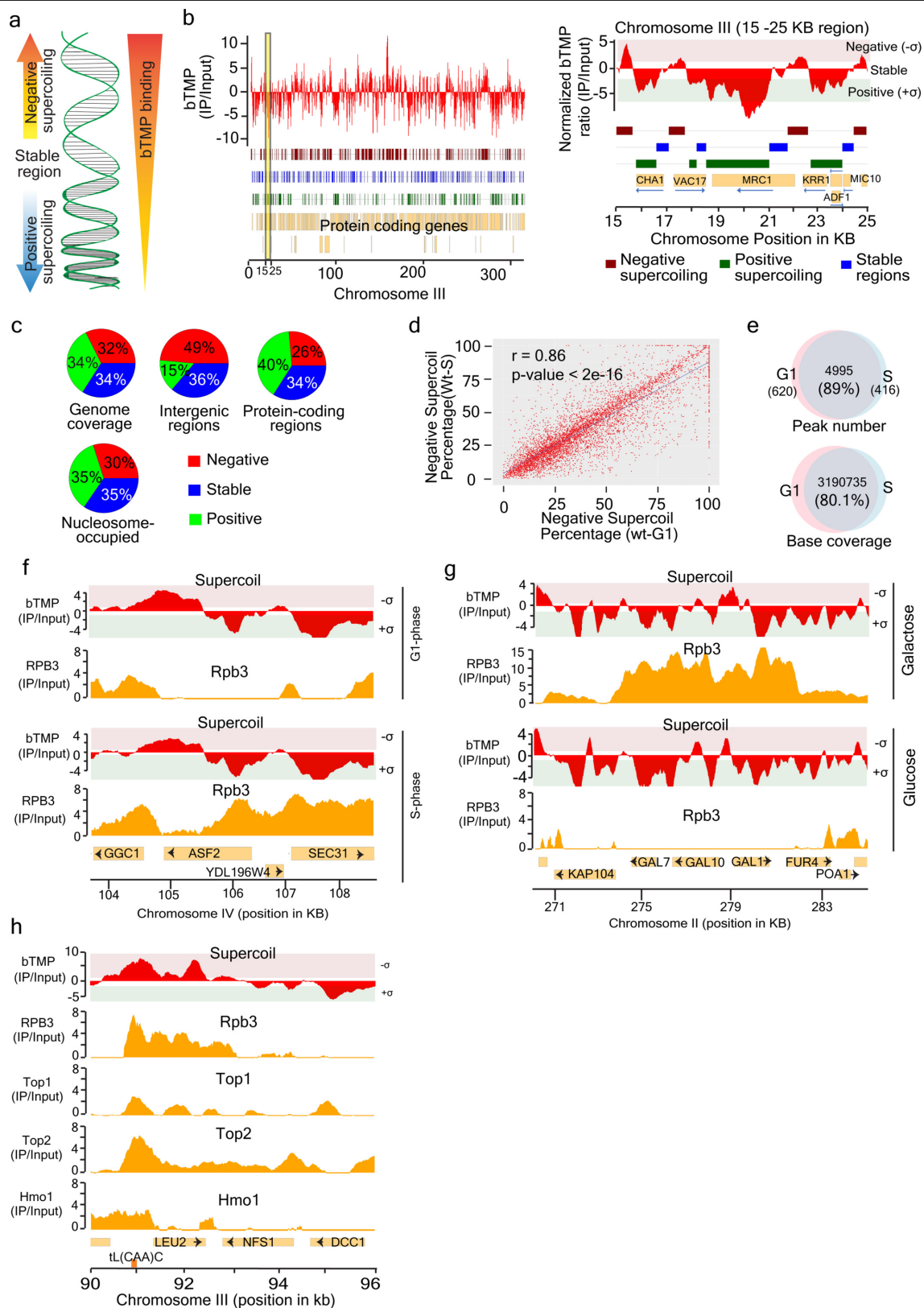
## Additional information

**Supplementary information** is available for this paper at <https://doi.org/10.1038/s41586-020-1934-4>.

**Correspondence and requests for materials** should be addressed to Y.J.A. or M.F.

**Peer review information** Nature thanks Duncan Clarke, Anne Grove and the other, anonymous, reviewer(s) for their contribution to the peer review of this work.

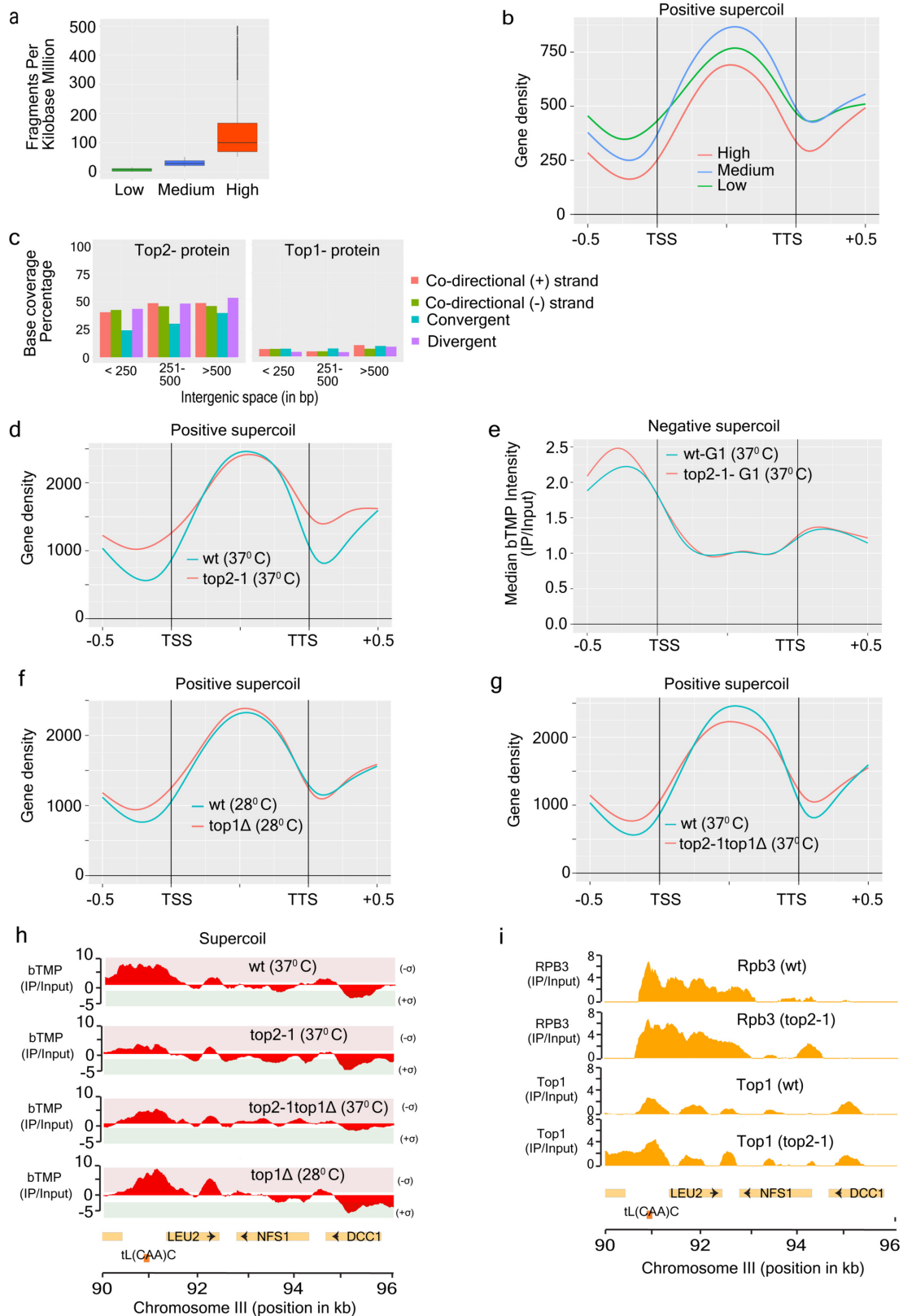
**Reprints and permissions information** is available at <http://www.nature.com/reprints>.



**Extended Data Fig. 1** | See next page for caption.

**Extended Data Fig. 1 | DNA supercoil accumulation across the genome in wild-type conditions.** **a**, Schematic representation of bTMP binding to DNA in a supercoil-dependent manner. Based on normalized bTMP (IP/input) values, the genomic region is categorized into negative, positive and stable regions. **b**, Genome browser profile for bTMP binding on chromosome III. On the basis of peak intensities, bTMP peaks were called for negative (red), stable (blue) and positive (green) regions. Right, expanded view of chromosome III from 15 to 25 kb. For the bTMP profile, positive value peaks (normalized IP/input) that were above the threshold (+1.5) were designated as 'negative supercoil' ( $-\sigma$ ), and negative value peaks (normalized IP/input) that were below the threshold ( $-1.5$ ) were designated as 'positive supercoil' ( $+\sigma$ ). Peaks in between the thresholds (from  $-1.5$  to  $+1.5$ ) were considered stable regions. **c**, Pie charts showing the coverage of negative, positive and stable regions based on bTMP-ChIP values plotted as percentage coverage for whole genome, intergenic

regions, protein-coding regions and nucleosome-occupied regions. **d**, Gene correlation plot for negative supercoil (percentage) accumulation for wild-type cells in G1 and S phase ( $n = 6,706$  genes; two-sided paired  $t$ -test,  $P < 2 \times 10^{-16}$ ; Pearson correlation  $r = 0.86$ ). **e**, Venn diagram comparison of G1 and S phase for bTMP binding with respect to peak number and base coverage. **f**, Genome browser view of the *ASF2* locus on chromosome IV, showing bTMP peaks and accumulation of Pol II (Rpb3-ChIP) in G1 and S phase. **g**, Gal genes in chromosome II (from 270 to 285 kb), depicting bTMP and Pol II (Rpb3-ChIP) binding profiles under glucose and galactose conditions in S phase. **h**, Expanded view of chromosome III from 90 to 96 kb, containing a highly active gene (*LEU2*) close to tRNA (tL(CAA)C) and two moderately expressed genes (*NFS1* and *DCCI*). Positive and negative supercoil and accumulation of Pol II (Rpb3-ChIP), Top1, Top2 and Hmo1 are shown.

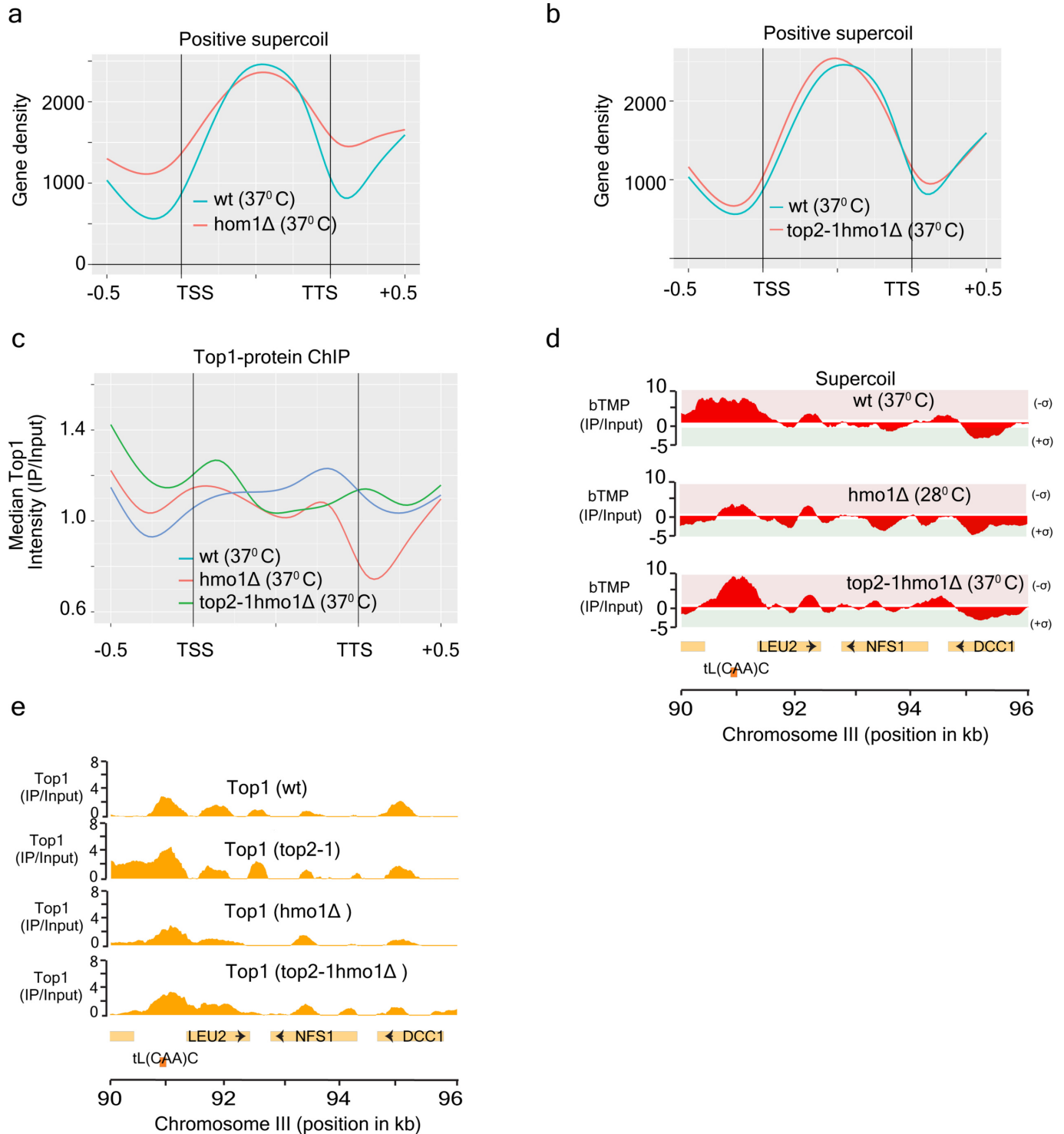


**Extended Data Fig. 2** | See next page for caption.

**Extended Data Fig. 2 | Negative and positive supercoil distribution in DNA topoisomerase mutants.** **a**, Pol II-coding genes were grouped into three categories; high, medium and low expression based on FPKM values from RNA-seq data ( $n = 6,706$  genes; low = medium = high = 2,235 genes). **b**, Positive supercoil distribution in high-, medium- and low-expression genes. **c**, Base coverage percentage of accumulation of Top2 and Top1 accumulation at different intergenic spaces (<250 bp = 1,729 gene pairs, 251–500 bp = 2,224 gene pairs and >500 bp = 2,010 gene pairs) with respect to gene pairs grouped according to orientation. **d**, Accumulation of positive supercoil in wild-type

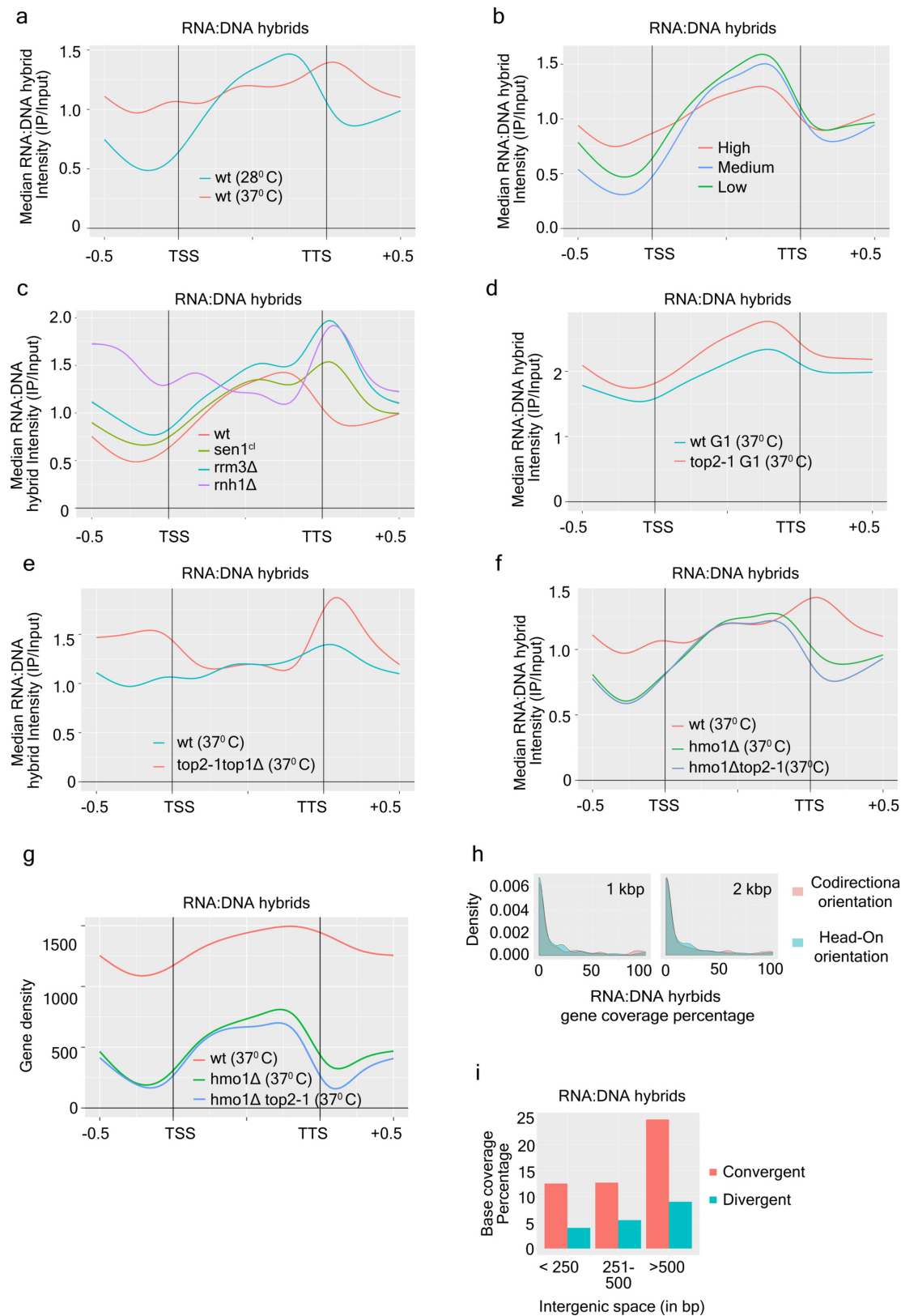
and *top2-1* cells in S phase. Pol II genes are plotted against average gene density on the y-axis. **e**, Meta-gene plot for negative supercoil in G1 synchronized wild-type and *top2-1* cells. **f**, Accumulation of positive supercoil in wild-type and *top1Δ* cells in S phase. **g**, Accumulation of positive supercoil in wild-type and *top1Δtop2-1* cells in S phase. **h**, Genome browser profile of chromosome III from 90 to 96 kb, showing comparative bTMP binding in wild-type cells and topoisomerase mutants. **i**, Genome browser profile of chromosome III from 90 to 96 kb, showing Pol II (Rpb3-ChIP) and Top1 protein accumulation in wild-type cells and *top2-1* mutants.





**Extended Data Fig. 3 | Negative and positive supercoil accumulation in *hmo1* mutants.** **a**, Positive supercoil accumulation in wild-type and *hmo1Δ* cells in S phase. Pol II genes are plotted against average gene density on the y-axis. **b**, Positive supercoil accumulation in wild-type and *hmo1Δtop2-1* cells in S phase. **c**, Comparison of the accumulation of Top1 protein (Top1-10× Flag) in

wild-type, *hmo1Δ* and *hmo1Δtop2-1* cells. **d**, Genome browser profile of chromosome III from 90 to 96 kb, showing comparative bTMP binding in wild-type, *hmo1Δ* and *hmo1Δtop2-1* cells in S phase. **e**, Genome browser profile of chromosome III from 90 to 96 kb, showing accumulation of Top1 in wild-type, *hmo1Δ*, *top2-1* and *hmo1Δtop2-1* mutants.

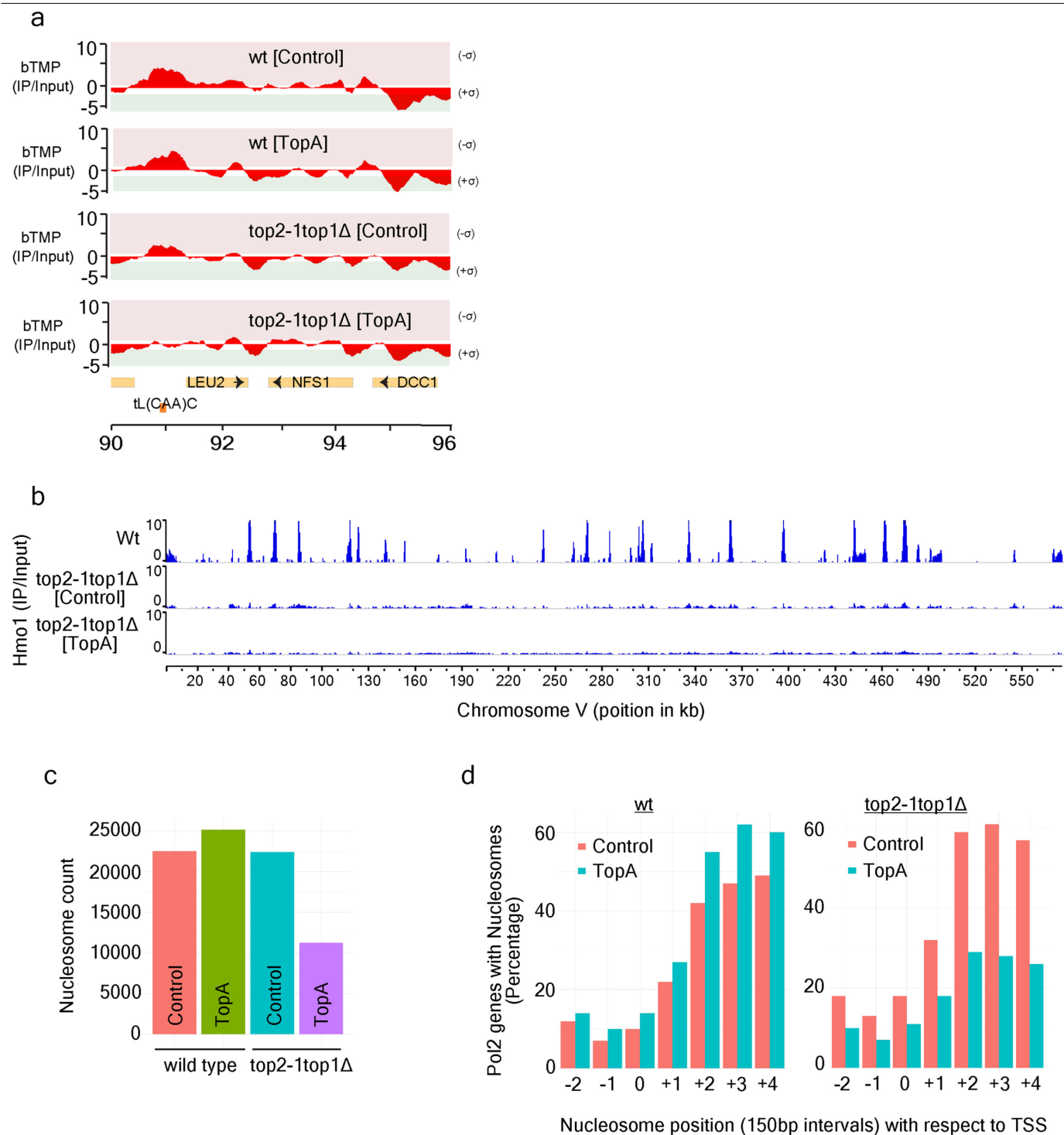


Extended Data Fig. 4 | See next page for caption.

**Extended Data Fig. 4 | RNA–DNA hybrid accumulation in wild-type and mutant cells.**

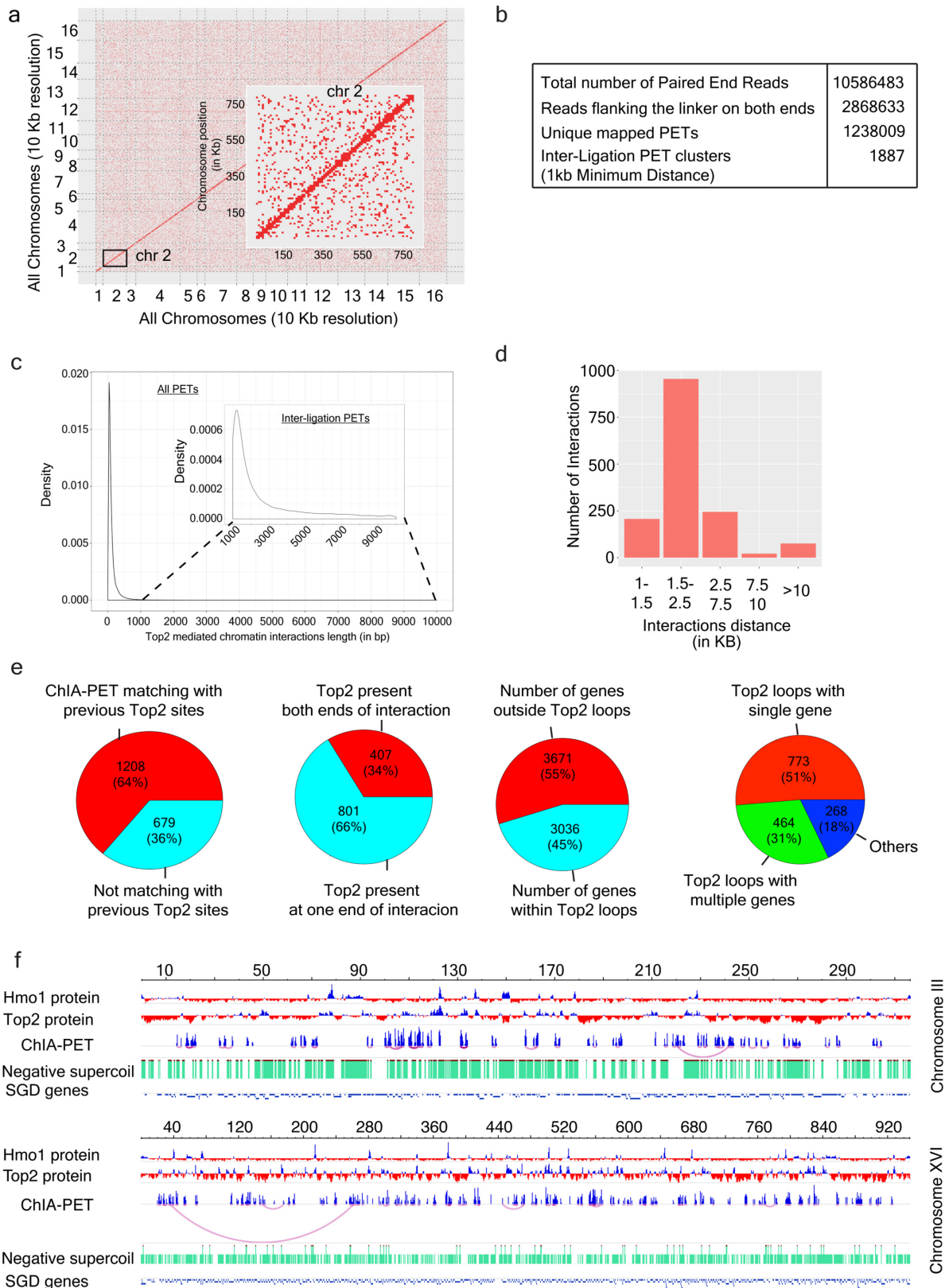
**a**, Meta-gene profiles for RNA–DNA hybrid comparison in wild-type cells (at 28 °C and 37 °C). **b**, Accumulation of RNA–DNA hybrids in different expression classes. Pol II genes were grouped into three categories: high-, medium- and low-expression genes based on FPKM values from RNA-seq (Extended Data Fig. 2a). **c**, Meta-gene profiles for RNA–DNA hybrids in S phase in wild-type, *rnh1Δ*, *rrm3Δ* and *sen1<sup>cl</sup>* cells (a conditional lethal strain GAL::URL-HA-Sen1, which shows lethality in glucose). **d**, Meta-gene profiles for RNA–DNA hybrids in G1 synchronized wild-type and *top2-1* cells. **e**, Meta-gene profile for RNA–DNA hybrid comparison in wild-type cells and *top1Δtop2-1* double-

mutant cells. **f**, Meta-gene profiles for RNA–DNA hybrid comparison in wild-type, *hmo1Δ*, and *hmo1Δtop2-1* cells. **g**, Gene density plot comparison of RNA–DNA hybrids in wild-type, *hmo1Δ* and *hmo1Δtop2-1* cells. **h**, Density plot showing the base coverage of RNA–DNA hybrids in genes with head-on or co-directional orientation with respect to replication fork. Genes within 1 kb (top, *n* = 347 genes) or 2 kb (bottom, *n* = 539 genes) of the replication origins were considered. **i**, Base coverage percentage of accumulation of RNA–DNA hybrids at different intergenic spaces (<250 bp = 1,729 gene pairs, 251–500 bp = 2,224 gene pairs and >500 bp = 2,010 gene pairs) with respect to gene pairs grouped according to orientation.



**Extended Data Fig. 5 | Ablation of negative supercoil at boundaries causes topological alterations and nucleosome repositioning.** **a**, Genome browser profile of chromosome III from 90 to 96 kb, showing comparative bTMP binding in wild-type[Control], wild type[TopA], *top1Δtop2-1* [Control] and *top1Δtop2-1* [TopA] cells after 120 min at restrictive temperature. **b**, Genome browser profile of chromosome V showing Hmo1 accumulation in wild-type, *top1Δtop2-1* [Control], and *top1Δtop2-1* [TopA] cells after 120 min at restrictive

temperature. **c**, Absolute nucleosome count was derived from histone H3 ChIP-seq analysis of wild-type [Control], wild type [TopA], *top1Δtop2-1* [Control] and *top1Δtop2-1* [TopA] cells after 120 min at restrictive temperature. **d**, Nucleosome positions (150-bp intervals) in wild-type cells and *top1Δtop2-1* double mutants harbouring either control or TopA-expressing plasmids mapped with respect to TSS against Pol II gene percentage on the y-axis.

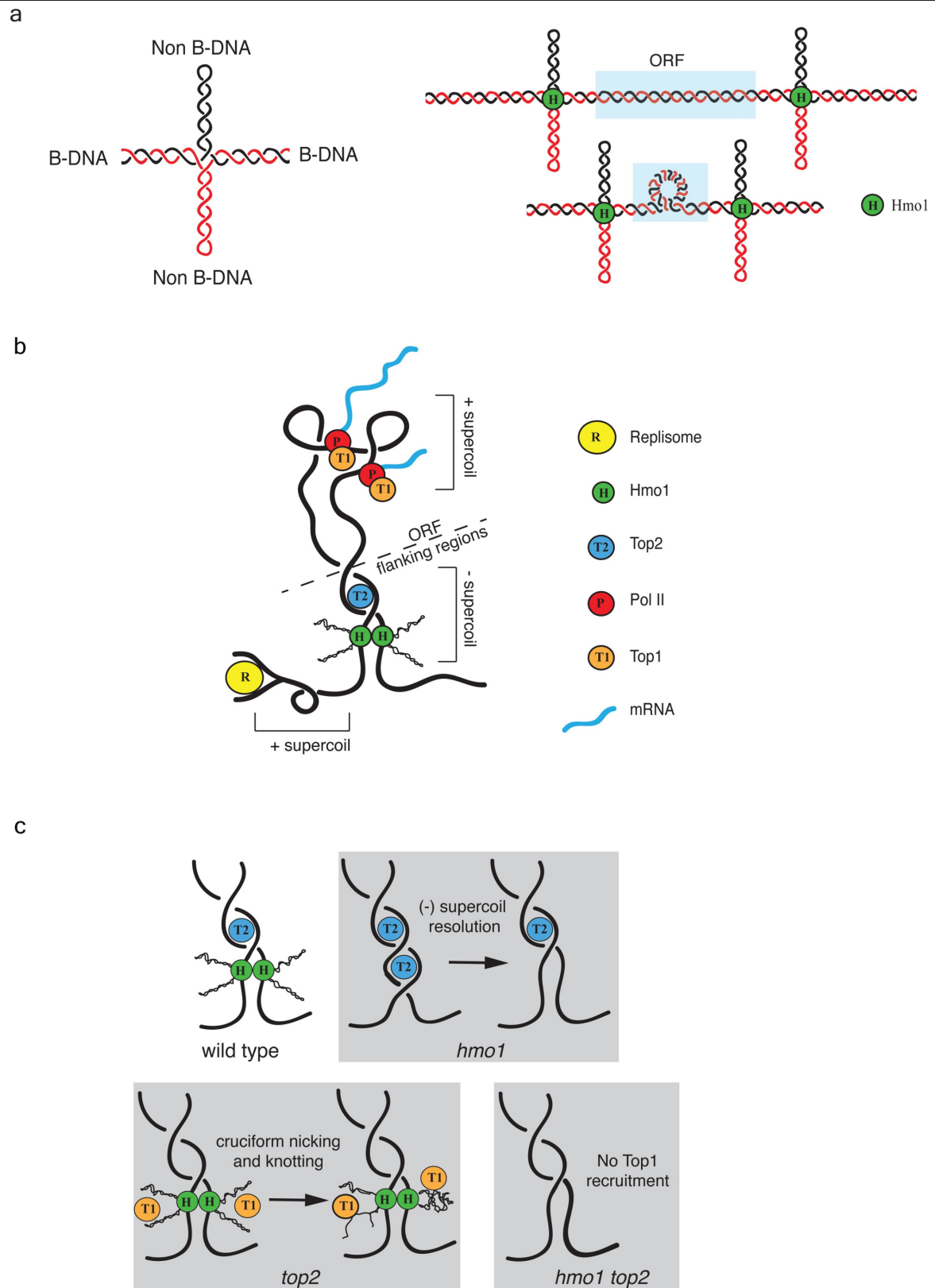


#### Extended Data Fig. 6 | Top2 mediates chromatin–chromatin interactions.

**a**, Heat map showing PET clusters in all of the chromosomes at 10-kb resolution. Inset, enlarged view of chromosome II. **b**, Table showing the number of paired-end reads, reads with linker on both ends, unique mapped PETs and inter-ligation clusters obtained after Top2 ChIA-PET analysis. **c**, Density map showing PET density at different interaction lengths. Inset shows enlarged view of the region from 1,000 to 10,000 bp that was considered for analysis. **d**, Bar plot showing size-wise distribution of chromatin loops. **e**, Pie chart showing

number of interactions matching with previous Top2-binding sites, number of interactions containing Top2 sites on either single or both sides of the interaction, number of genes within and outside the Top2-mediated chromatin loops and number of loops containing a single gene or multiple genes. Other categories include genes partially overlapping with the loops and all other elements. **f**, Genome browser view of ChIA-PET interactions along with Top2- and Hmo1-binding sites in chromosomes III and XVI.



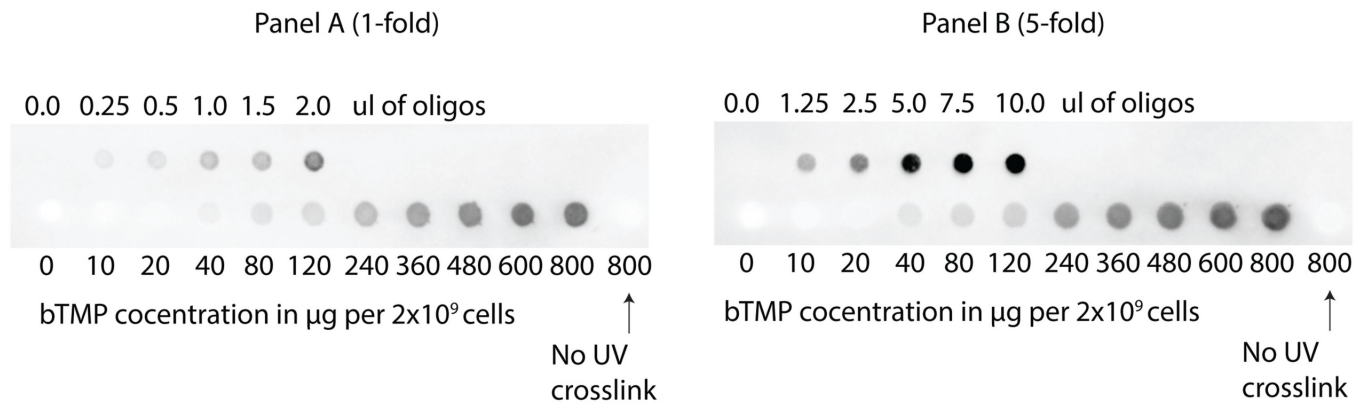


**Extended Data Fig. 7** | See next page for caption.

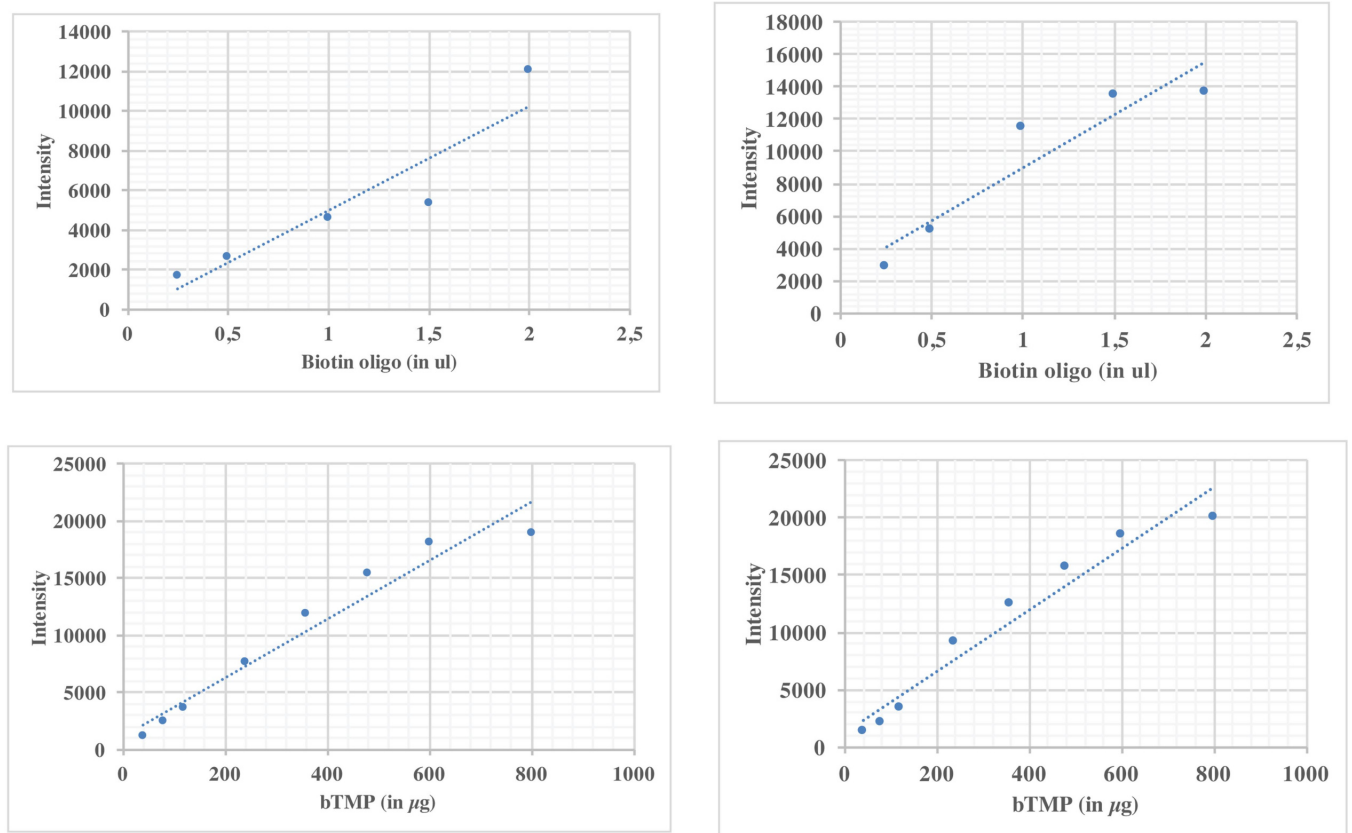
**Extended Data Fig. 7 | A model for Hmo1, Top2 and Top1-mediated topological dynamics at Pol II genes.** **a**, Schematic representation of cruciform DNA structures arising at negatively supercoiled DNA formed by two branches in a B-DNA duplex structure (red and black) and two branches in a non-B-DNA duplex conformation (red or black). Cruciform DNA structures could form at gene boundaries and be stabilized by Hmo1. Gene looping is described in the blue area. **b**, Schematic representation of gene loop structures in S phase. Top2 associates with gene boundaries to harmonize topological transactions when transcribed genes are approached by incoming replication

forks. We note that the topological dynamics described in the twin topological domain model<sup>7</sup> are not represented in our scheme. **c**, In the absence of Hmo1, negative supercoil would lose the cruciform conformation and become a substrate for Top2. Top2 defects would delocalize Top1 at gene boundaries. The cruciform structures stabilized by Hmo1 would then become substrates for unscheduled Top1 activity that would convert them into aberrant intermediates such as single-stranded DNA, nicks and knots. In *hmo1top2* double mutants, Top1 is not recruited at the gene boundaries, which remain in a negative supercoil context.

a

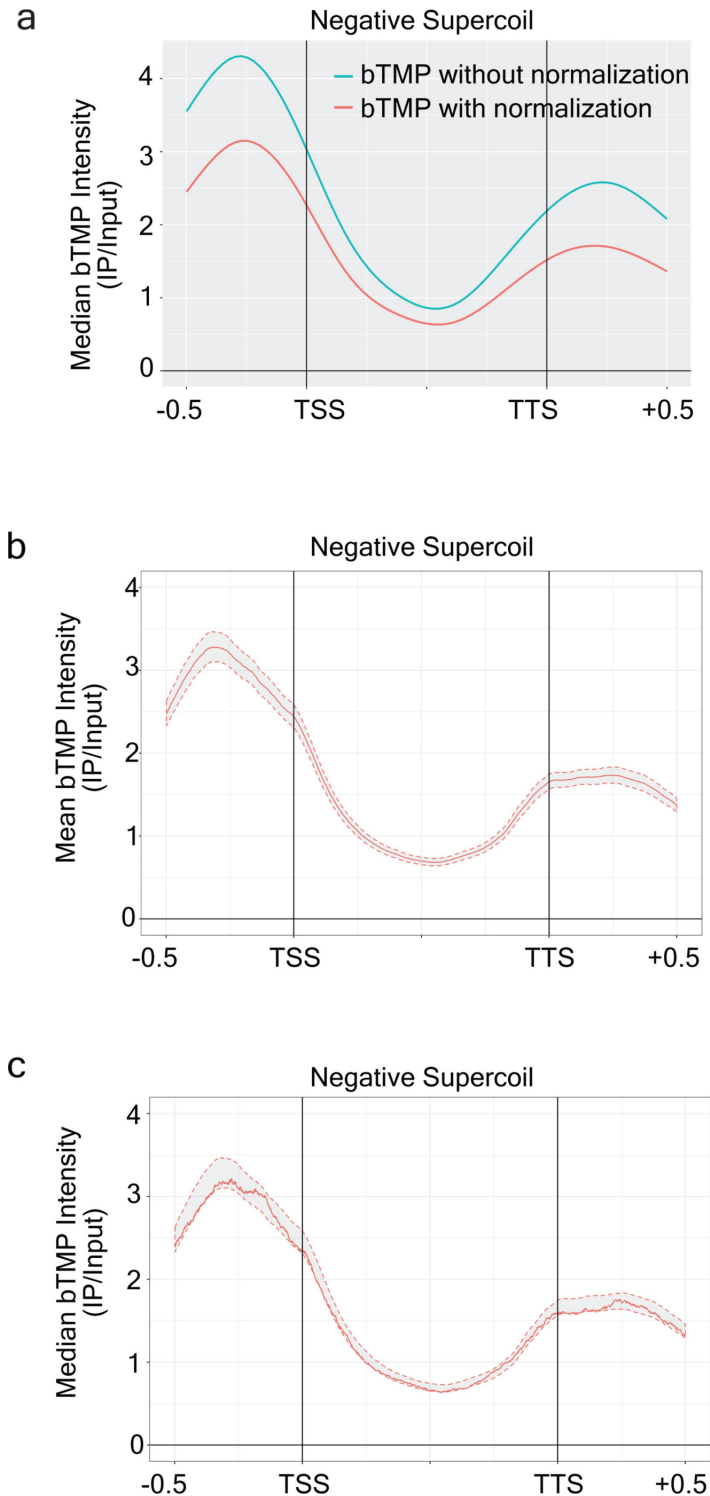


b



**Extended Data Fig. 8 | bTMP titration. a, b,** By using a biotin-labelled oligo as a reference point, we titrated in vivo binding of bTMP in yeast at different concentrations (from 0 to 800 ng). We diluted 4.16 pmol of biotin-labelled oligos into 200 µl of TE. The shown volumes of oligos were spotted onto a hybond membrane after equilibration with  $1 \times$  maleic acid. Genomic DNA was isolated after UV (365 nm) cross-linking with the respective amount of

bTMP and about 300 ng (a) or 1,500 ng (b) was spotted on the blot. The last sample was kept as a negative control for UV cross-linking. In Panel B, fivefold more oligo and genomic DNA was spotted compared to Panel A. Dot blot was developed with ExtrAvidin-Peroxidase antibody (Sigma-Aldrich, cat no: E2886). **b,** By measuring dot blot intensities, we estimated that 400 µg of bTMP was needed for  $2 \times 10^9$  yeast cells.



**Extended Data Fig. 9 | bTMP binding normalization and dispersion profile for bTMP. a,** To avoid bias, normalization was performed to filter potential sequence-specific psoralen DNA binding<sup>23</sup>. To normalize the data, we first purified and sonicated genomic DNA and then performed the bTMP-ChIP procedure on purified DNA fragments. The correction for microarray readings was done by subtracting bTMP binding in vivo from bTMP binding on purified/sonicated genomic DNA as follows: (bTMP cells – IP/input) – (bTMP purified DNA – IP/input), which gives the normalized ratio of bTMP (bTMP – IP/input)

binding. The meta ORF plot shows bTMP profiles with or without control DNA normalization of bTMP in wild-type S phase cells. **b, c,** Meta-gene plot showing the normalized mean bTMP ratio (**b**) and median bTMP (**c**) ratio in wild-type S phase cells. For both the plots, bTMP binding ratios for all protein-coding genes were plotted without smoothing, along with upper and lower confidence intervals ( $\alpha = 0.05$  or 95% limit). Dotted lines represent upper and lower confidence intervals ( $\alpha = 0.05$  or 95% limit). The confidence interval does not deviate significantly from the mean and median values.

Extended Data Table 1 | List of *S. cerevisiae* strains

	Strain	Stock Number	Genotype	Reference
1	Wt	SY2080	Mata, ade2-1, ura3-1, trp1-1, leu2-3, leu2-112, his3-11, his3-15, can1-100, GAL, PSI+, RAD5+	Lab collection
2	<i>top2-1</i>	CY8423	MATa ADE2+ CAN1+, ura3-1, his3-11,15 leu2-3, 12 trp1-1, RAD5+, top2-1	Lab collection
3	<i>hmo1</i> $\Delta$	CY8476	MATa, ADE2+ CAN1+, ura3-1, his3-11,15 leu2-3, 112 trp1-1, RAD5+, hmo1::HIS	Lab collection
4	<i>top2-1hmo1</i> $\Delta$	CY8475	MATa, ADE2+ CAN1+, ura3-1, his3-11,15 leu2-3, 112 trp1-1, RAD5+, hmo1::HIS, top2-1	Lab collection
5	<i>top1</i> $\Delta$	CY9950	MATa ADE2+ CAN1+, ura3-1, his3-11,15 leu2-3, 12 trp1-1, RAD5+, top1::HIS	Lab collection
6	Top1-6XHis-10xFlag	CY7178	Mata, ade2-1, ura3-1, trp1-1, leu2-3, leu2-112, his3-11, his3-15, can1-100, GAL, PSI+, RAD5+, ura3::URA3/GPD-TK(7X), top1-6His10Flag (KANr)	Lab collection
7	<i>top2-1</i> ,Top1-6XHis-10xFlag	CY7411	Mata, ade2-1, ura3-1, trp1-1, leu2-3, leu2-112, his3-11, his3-15, can1-100, GAL, PSI+, RAD5+, ura3::URA3/GPD-TK(7X), top1-6His10Flag (KANr), top2-1	Lab collection
8	<i>top2-1top1</i> $\Delta$	CY10344	MATa ADE2+ CAN1+, ura3-1, his3-11,15 leu2-3, 12 trp1-1, RAD5+, top2-1, top1::HIS	Lab collection
9	<i>hmo1</i> $\Delta$ ,Top1-6XHis-10xFlag	CY15215	Mata, ade2-1, ura3-1, trp1-1, leu2-3, leu2-112, his3-11, his3-15, can1-100, GAL, PSI+, RAD5+, hmo1::Hygromycin, top1-6His10Flag (KANr)	This Study
10	<i>hmo1</i> $\Delta$ <i>top2-1</i> ,Top1-6XHis-10x Flag	CY15216	Mata, ade2-1, ura3-1, trp1-1, leu2-3, leu2-112, his3-11, his3-15, can1-100, GAL, PSI+, RAD5+, top1-6His10Flag (KANr), top2-1, hmo1::Hygromycin	This Study
11	Rpb3-10X-Flag	CY15214	Mata, ade2-1, ura3-1, trp1-1, leu2-3, leu2-112, his3-11, his3-15, can1-100, GAL, PSI+, RAD5+, HIS3::BrdU-Inc, rpb3::RPB3-10X Flag-KanMX6	This Study
12	Wt [control]	CY15421	Mata, ade2-1, ura3-1, trp1-1, leu2-3, leu2-112, his3-11, his3-15, can1-100, GAL, PSI+, RAD5+ [pYEpl3-LEU empty]	This Study
13	Wt [TopA]	CY15422	Mata, ade2-1, ura3-1, trp1-1, leu2-3, leu2-112, his3-11, his3-15, can1-100, GAL, PSI+, RAD5+ [pJRW13-YEptopA-pGPD-LEU]	This Study
14	<i>top2-1top1</i> $\Delta$ [control]	CY15423	MATa ADE2+ CAN1+, ura3-1, his3-11,15 leu2-3, 12 trp1-1, RAD5+, top2-1, top1::HIS [pYEpl3-LEU empty]	This Study
15	<i>top2-1top1</i> $\Delta$ [TopA]	CY15424	MATa ADE2+ CAN1+, ura3-1, his3-11,15 leu2-3, 12 trp1-1, RAD5+, top2-1, top1::HIS [pJRW13-YEptopA-pGPD-LEU]	This Study
16	<i>top2-1top1</i> $\Delta$ ,Hmo1-10X Flag, [Control]	CY15427	MATa ADE2+ CAN1+, ura3-1, his3-11,15 leu2-3, 12 trp1-1, RAD5+, top2-1, top1::HIS, HMO1::HMO1-10X Flag [pYEpl3-LEU empty]	This Study
17	<i>top2-1top1</i> $\Delta$ ,Hmo1-10X Flag, [TopA]	CY15428	MATa ADE2+ CAN1+, ura3-1, his3-11,15 leu2-3, 12 trp1-1, RAD5+, top2-1, top1::HIS, HMO1::HMO1-10X Flag [pJRW13-YEptopA-pGPD-LEU]	This Study



## Reporting Summary

Nature Research wishes to improve the reproducibility of the work that we publish. This form provides structure for consistency and transparency in reporting. For further information on Nature Research policies, see [Authors & Referees](#) and the [Editorial Policy Checklist](#).

### Statistics

For all statistical analyses, confirm that the following items are present in the figure legend, table legend, main text, or Methods section.

- |                                     |  |
|-------------------------------------|--|
| n/a                                 | Confirmed  |
| <input type="checkbox"/>            | <input checked="" type="checkbox"/> The exact sample size ( $n$ ) for each experimental group/condition, given as a discrete number and unit of measurement  |
| <input type="checkbox"/>            | <input checked="" type="checkbox"/> A statement on whether measurements were taken from distinct samples or whether the same sample was measured repeatedly  |
| <input type="checkbox"/>            | <input checked="" type="checkbox"/> The statistical test(s) used AND whether they are one- or two-sided<br><i>Only common tests should be described solely by name; describe more complex techniques in the Methods section.</i>   |
| <input checked="" type="checkbox"/> | <input type="checkbox"/> A description of all covariates tested  |
| <input checked="" type="checkbox"/> | <input type="checkbox"/> A description of any assumptions or corrections, such as tests of normality and adjustment for multiple comparisons   |
| <input type="checkbox"/>            | <input checked="" type="checkbox"/> A full description of the statistical parameters including central tendency (e.g. means) or other basic estimates (e.g. regression coefficient) AND variation (e.g. standard deviation) or associated estimates of uncertainty (e.g. confidence intervals) |
| <input type="checkbox"/>            | <input checked="" type="checkbox"/> For null hypothesis testing, the test statistic (e.g. $F$ , $t$ , $r$ ) with confidence intervals, effect sizes, degrees of freedom and $P$ value noted<br><i>Give <math>P</math> values as exact values whenever suitable.</i>                            |
| <input checked="" type="checkbox"/> | <input type="checkbox"/> For Bayesian analysis, information on the choice of priors and Markov chain Monte Carlo settings  |
| <input checked="" type="checkbox"/> | <input type="checkbox"/> For hierarchical and complex designs, identification of the appropriate level for tests and full reporting of outcomes  |
| <input type="checkbox"/>            | <input checked="" type="checkbox"/> Estimates of effect sizes (e.g. Cohen's $d$ , Pearson's $r$ ), indicating how they were calculated   |

Our web collection on [statistics for biologists](#) contains articles on many of the points above.

### Software and code

Policy information about [availability of computer code](#)

Data collection	No software was used
Data analysis	<p>rMAT (Droit A, 2010) (v3.33.0)            STAR aligner (Dobin A, 2013)            RSEM (Dewey, 2011) (v1.2.31)            SAMTOOLS (v 1.9)            DEEPTOOLS (Ramirez et al., 2014) (v3.2.0)            DANPOS toolkit (Chen et al., 2013) (v2.2.2)            BEDTOOLS (v2.29.0)            FASTX Toolkit: <a href="http://hannonlab.cshl.edu/fastx_toolkit/">http://hannonlab.cshl.edu/fastx_toolkit/</a> (v0.0.14)            TMAP Toolkit: <a href="https://github.com/iontorrent/TMAP">https://github.com/iontorrent/TMAP</a> (v3.4.0)            PICARD Toolkit: <a href="https://broadinstitute.github.io/picard/">https://broadinstitute.github.io/picard/</a> (v2.14.1)            MACS2 Toolkit (v2.1.2)            BWA Toolkit: <a href="http://bio-bwa.sourceforge.net/">http://bio-bwa.sourceforge.net/</a> (v0.7.17-r1188)            ggplot2 R package (v 3.2.1)</p> <p>All the custom-made scripts used for this study are made available in the GitHub repository  <a href="https://github.com/adhilmd/TopologyCustomAnalysis">https://github.com/adhilmd/TopologyCustomAnalysis</a></p>

For manuscripts utilizing custom algorithms or software that are central to the research but not yet described in published literature, software must be made available to editors/reviewers. We strongly encourage code deposition in a community repository (e.g. GitHub). See the Nature Research [guidelines for submitting code & software](#) for further information.

## Data

Policy information about [availability of data](#)

All manuscripts must include a [data availability statement](#). This statement should provide the following information, where applicable:

- Accession codes, unique identifiers, or web links for publicly available datasets
- A list of figures that have associated raw data
- A description of any restrictions on data availability

NCBI GEO accession ID: GSE114410 (This study) Contains bTMP, RNA:DNA hybrids, Protein ChIP-chip RAW & processed data

NCBI GEO accession ID: GSE114444 (This study) Contains RNA-seq, H3 ChIP-seq RAW, ChIA-PET RAW & processed data

NCBI GEO accession ID: GSE16258 (Bermejo et al., 2009) Contains Top2, Hmo1, RPB3 protein ChIP-chip data

## Field-specific reporting

Please select the one below that is the best fit for your research. If you are not sure, read the appropriate sections before making your selection.

☒ Life sciences ☐ Behavioural & social sciences ☐ Ecological, evolutionary & environmental sciences

For a reference copy of the document with all sections, see [nature.com/documents/nr-reporting-summary-flat.pdf](https://www.nature.com/documents/nr-reporting-summary-flat.pdf)

## Life sciences study design

All studies must disclose on these points even when the disclosure is negative.

Sample size 6706 RNA pol II transcribed genes  
173 replication origins

Data exclusions No data excluded

Replication All experiments were performed with biological replicates

Randomization Not relevant to this study, as samples were yeast strain specific

Blinding Not relevant to this study, as samples were yeast strain specific

## Reporting for specific materials, systems and methods

We require information from authors about some types of materials, experimental systems and methods used in many studies. Here, indicate whether each material, system or method listed is relevant to your study. If you are not sure if a list item applies to your research, read the appropriate section before selecting a response.

### Materials & experimental systems

n/a	Involved in the study
<input type="checkbox"/>	<input checked="" type="checkbox"/> Antibodies
<input checked="" type="checkbox"/>	<input type="checkbox"/> Eukaryotic cell lines
<input checked="" type="checkbox"/>	<input type="checkbox"/> Palaeontology
<input checked="" type="checkbox"/>	<input type="checkbox"/> Animals and other organisms
<input checked="" type="checkbox"/>	<input type="checkbox"/> Human research participants
<input checked="" type="checkbox"/>	<input type="checkbox"/> Clinical data

### Methods

n/a	Involved in the study
<input type="checkbox"/>	<input checked="" type="checkbox"/> ChIP-seq
<input checked="" type="checkbox"/>	<input type="checkbox"/> Flow cytometry
<input checked="" type="checkbox"/>	<input type="checkbox"/> MRI-based neuroimaging

## Antibodies

Antibodies used anti-Flag (M2-antiflag) Antibody (Sigma-Aldrich cat no F3165, clone: M2, Lot#: SLBQ6349V)  
S9.6 Monoclonal RNA:DNA Antibody (Boguslawski et al.,1986)  
anti-Hstone H3 antibody (Abcam cat no 1791, Lot#:GR3236305-1)  
ExtrAvidin-Peroxidase antibody (Sigma-Aldrich cat no: E2886, Lot#:015M4844V, For dot blot 1:4000 dilution is used )

Validation S9.6 Monoclonal RNA:DNA Antibody (Boguslawski et al.,1986) is validated and used in several publications including: El Hage, A., et al. (2010), Chan, Y. A., et al. (2014), Wahba, L., et al. (2016), Vanoosthuyse, V. (2018), El Hage, A. and D. Tollervey (2018)

## ChIP-seq

### Data deposition

- ☒ Confirm that both raw and final processed data have been deposited in a public database such as [GEO](#).
- ☒ Confirm that you have deposited or provided access to graph files (e.g. BED files) for the called peaks.

#### Data access links

*May remain private before publication.*

NCBI GEO accession ID: GSE114444 (This study) Contains H3 ChIP-seq, Hmo1tag protein ChIP-seq, ChIA-PET RAW & processed data

#### Files in database submission

GSM3664900 ChIP-seq: WT-Controlplasmid-nucleosome-Input  
 GSM3664901 ChIP-seq: WT-Controlplasmid-nucleosome-IP  
 GSM3664902 ChIP-seq: Top2-1-Top1-Controlplasmid-nucleosome-Input  
 GSM3664903 ChIP-seq: Top2-1-Top1-Controlplasmid-nucleosome-IP  
 GSM3664904 ChIP-seq: WT-TopAplasmid-nucleosome-Input  
 GSM3664905 ChIP-seq: WT-TopAplasmid-nucleosome-IP  
 GSM3664906 ChIP-seq: Top2-1-Top1-TopAplasmid-nucleosome-Input  
 GSM3664907 ChIP-seq: Top2-1-Top1-TopAplasmid-nucleosome-IP  
 GSM3664908 ChIP-seq: Hmo1tag-Top2-1-Top1-Controlplasmid-protein-Input  
 GSM3664909 ChIP-seq: Hmo1tag-Top2-1-Top1-Controlplasmid-protein-IP  
 GSM3664910 ChIP-seq: Hmo1tag-Top2-1-Top1-TopAplasmid-protein-Input  
 GSM3664911 ChIP-seq: Hmo1tag-Top2-1-Top1-TopAplasmid-protein-IP  
 GSM4094803 ChIA-PET: Top2-ChIA-PET

#### Genome browser session

(e.g. [UCSC](#))

(i) H3 ChIP-seq (Nucleosome):  
<http://epigenomegateway.wustl.edu/legacy/?genome=sacCer3&session=2IU7XHkwi&statusId=1279418941>  
 (Note: Use the Nucleosome\_TopA Session: First and second track is WT-control plasmid (bed density and bedgraph), third and fourth track is WT-TopA plasmid (bed density and bedgraph), fifth and sixth track is Top2-1-Top1-Control plasmid (bed density and bedgraph), seventh and eighth track is Top2-1-Top1-TopA plasmid (bed density and bedgraph)

(ii) Protein ChIP-seq:  
<http://epigenomegateway.wustl.edu/legacy/?genome=sacCer3&session=4FQoSLC1lk&statusId=1043438118>  
 (Note: Use the TopA\_Hmo1 Session: First track is Hmo1tag-Top2-1-Top1-Controlplasmid and Second track is Hmo1tag-Top2-1-Top1-TopAplasmid)

(iii) ChIA-PET:  
<http://epigenomegateway.wustl.edu/legacy/?genome=sacCer3&session=arHkgZiCZP&statusId=302725081>  
 (Note: Use the ChIA-PET-Data Session: First track is Hmo1 protein binding regions, Second track is Top2 protein binding regions, Third track is ChIA-PET data for Top2-10X Flag and Fourth track is the interaction points for ChIA-PET Top2-10X Flag)

No longer applicable for final submission.

## Methodology

#### Replicates

One biological replicate for each sample is generated and analyzed for consistency. (Replicates were not yet deposited in the GEO)

#### Sequencing depth

(i) H3 ChIP-seq (Nucleosome): Average Reads: ~15 Million Reads, Average Read length: ~180bp, Average Mapped Reads: ~8 Million Reads and single end reads (Ion Torrent Platform)  
 (ii) Protein ChIP-seq: Average Reads: ~15 Million Reads, Average Read length: ~180bp, Average Mapped Reads: ~8 Million Reads and single end reads (Ion Torrent Platform)

#### Antibodies

(i) H3 ChIP-seq (Nucleosome): anti-Hstone H3 antibody (Abcam cat no 1791)  
 (ii) Protein ChIP-seq: anti-Flag (M2-antiflag) Antibody (Sigma-Aldrich cat no F3165)  
 (iii) ChIA-PET: anti-Flag (M2-antiflag) Antibody (Sigma-Aldrich cat no F3165)

#### Peak calling parameters

(i) H3 ChIP-seq: The raw reads were filtered based on the quality value (-q 20 and -p 30) using FASTX Toolkit. The filtered reads were aligned to the reference genome (SacCer 2011) using TMAP aligner. The PCR duplicates were removed from the aligned BAM files using PICARD tools. The BAM files were sorted and indexed for the peak calling using SAMTOOLS. The bedgraph files were generated by comparing bam files of IP and Input (IP read coverage/Input read coverage) result in the ratio for every base across the whole genome using DEEPTOOLS (bamCompare) (Ramirez et al., 2014). Finally, peak calling was performed using DANPOS (dpos) toolkit (Chen et al., 2013) with the IP/Input threshold 1.4 (-q 1.4) where the output peaks corresponds to the individual nucleosome. The DANPOS was preferred over MACS toolkit for the dynamic nucleosome analysis at single nucleotide resolution.  
 (ii) Protein ChIP-seq: The raw reads were filtered based on the quality value (-q 20 and -p 30) using FASTX Toolkit. The filtered reads were aligned to the reference genome (SacCer 2011) using TMAP aligner. The PCR duplicates were removed from the aligned BAM files using PICARD tools. Finally, MACS2 tool is used for peak calling with the following parameters (-f BAM -gsize=1.21e+7 -n ctrl-A -B -p 0.01 --nomodel --extsize 200 --broad).

#### Data quality

The peak fold enrichment were in the range of 1.5 to 3.0

SAMTOOLS (v 1.9)  
DEEPTOOLS (Ramirez et al., 2014) (v3.2.0)  
DANPOS toolkit (Chen et al., 2013) (v2.2.2)  
BEDTOOLS (v2.29.0)  
FASTX Toolkit: [http://hannonlab.cshl.edu/fastx\\_toolkit/](http://hannonlab.cshl.edu/fastx_toolkit/) (v0.0.14)  
TMAP Toolkit: <https://github.com/iontorrent/TMAP> (v3.4.0)  
PICARD Toolkit: <https://broadinstitute.github.io/picard/> (v2.14.1)  
MACS2 Toolkit (v2.1.2)  
BWA Toolkit: <http://bio-bwa.sourceforge.net/> (v0.7.17-r1188)

# Improved protein structure prediction using potentials from deep learning

<https://doi.org/10.1038/s41586-019-1923-7>

Received: 2 April 2019

Accepted: 10 December 2019

Published online: 15 January 2020

Andrew W. Senior<sup>1,4\*</sup>, Richard Evans<sup>1,4</sup>, John Jumper<sup>1,4</sup>, James Kirkpatrick<sup>1,4</sup>, Laurent Sifre<sup>1,4</sup>, Tim Green<sup>1</sup>, Chongli Qin<sup>1</sup>, Augustin Židek<sup>1</sup>, Alexander W. R. Nelson<sup>1</sup>, Alex Bridgland<sup>1</sup>, Hugo Penedones<sup>1</sup>, Stig Petersen<sup>1</sup>, Karen Simonyan<sup>1</sup>, Steve Crossan<sup>1</sup>, Pushmeet Kohli<sup>1</sup>, David T. Jones<sup>2,3</sup>, David Silver<sup>1</sup>, Koray Kavukcuoglu<sup>1</sup> & Demis Hassabis<sup>1</sup>

Protein structure prediction can be used to determine the three-dimensional shape of a protein from its amino acid sequence<sup>1</sup>. This problem is of fundamental importance as the structure of a protein largely determines its function<sup>2</sup>; however, protein structures can be difficult to determine experimentally. Considerable progress has recently been made by leveraging genetic information. It is possible to infer which amino acid residues are in contact by analysing covariation in homologous sequences, which aids in the prediction of protein structures<sup>3</sup>. Here we show that we can train a neural network to make accurate predictions of the distances between pairs of residues, which convey more information about the structure than contact predictions. Using this information, we construct a potential of mean force<sup>4</sup> that can accurately describe the shape of a protein. We find that the resulting potential can be optimized by a simple gradient descent algorithm to generate structures without complex sampling procedures. The resulting system, named AlphaFold, achieves high accuracy, even for sequences with fewer homologous sequences. In the recent Critical Assessment of Protein Structure Prediction<sup>5</sup> (CASP13)—a blind assessment of the state of the field—AlphaFold created high-accuracy structures (with template modelling (TM) scores<sup>6</sup> of 0.7 or higher) for 24 out of 43 free modelling domains, whereas the next best method, which used sampling and contact information, achieved such accuracy for only 14 out of 43 domains. AlphaFold represents a considerable advance in protein-structure prediction. We expect this increased accuracy to enable insights into the function and malfunction of proteins, especially in cases for which no structures for homologous proteins have been experimentally determined<sup>7</sup>.

Proteins are at the core of most biological processes. As the function of a protein is dependent on its structure, understanding protein structures has been a grand challenge in biology for decades. Although several experimental structure determination techniques have been developed and improved in accuracy, they remain difficult and time-consuming<sup>2</sup>. As a result, decades of theoretical work has attempted to predict protein structures from amino acid sequences.

CASP<sup>5</sup> is a biennial blind protein structure prediction assessment run by the structure prediction community to benchmark progress in accuracy. In 2018, AlphaFold joined 97 groups from around the world in entering CASP13<sup>8</sup>. Each group submitted up to 5 structure predictions for each of 84 protein sequences for which experimentally determined structures were sequestered. Assessors divided the proteins into 104 domains for scoring and classified each as being amenable to template-based modelling (TBM, in which a protein with a similar sequence has a known structure, and that homologous structure is modified in accordance with the sequence differences) or requiring free modelling (FM, in cases in which no homologous structure is available), with

an intermediate (FM/TBM) category. Figure 1a shows that AlphaFold predicts more FM domains with high accuracy than any other system, particularly in the 0.6–0.7 TM-score range. The TM score—ranging between 0 and 1—measures the degree of match of the overall (backbone) shape of a proposed structure to a native structure. The assessors ranked the 98 participating groups by the summed, capped z-scores of the structures, separated according to category. AlphaFold achieved a summed z-score of 52.8 in the FM category (best-of-five) compared with 36.6 for the next closest group (322). Combining FM and TBM/FM categories, AlphaFold scored 68.3 compared with 48.2. AlphaFold is able to predict previously unknown folds to high accuracy (Fig. 1b). Despite using only FM techniques and not using templates, AlphaFold also scored well in the TBM category according to the assessors' formula 0-capped z-score, ranking fourth for the top-one model or first for the best-of-five models. Much of the accuracy of AlphaFold is due to the accuracy of the distance predictions, which is evident from the high precision of the corresponding contact predictions (Fig. 1c and Extended Data Fig. 2a).

<sup>1</sup>DeepMind, London, UK. <sup>2</sup>The Francis Crick Institute, London, UK. <sup>3</sup>University College London, London, UK. <sup>4</sup>These authors contributed equally: Andrew W. Senior, Richard Evans, John Jumper, James Kirkpatrick, Laurent Sifre. \*e-mail: andrewsenior@google.com



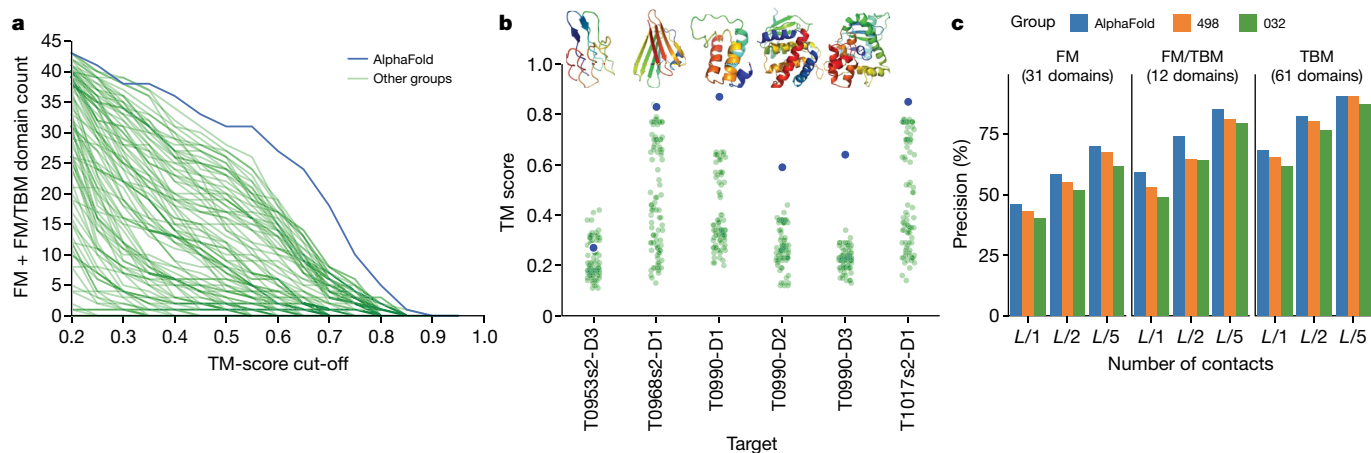


**Fig. 1 | The performance of AlphaFold in the CASP13 assessment.** **a**, Number of FM (FM + FM/TBM) domains predicted for a given TM-score threshold for AlphaFold and the other 97 groups. **b**, For the six new folds identified by the CASP13 assessors, the TM score of AlphaFold was compared with the other groups, together with the native structures. The structure of T1017s2-D1 is not available for publication. **c**, Precisions for long-range contact prediction in

CASP13 for the most probable  $L$ ,  $L/2$  or  $L/5$  contacts, where  $L$  is the length of the domain. The distance distributions used by AlphaFold in CASP13, thresholded to contact predictions, are compared with the submissions by the two best-ranked contact prediction methods in CASP13: 498 (RaptorX-Contact<sup>26</sup>) and 032 (TripletRes<sup>32</sup>) on 'all groups' targets, with updated domain definitions for T0953s2.

The most-successful FM approaches thus far<sup>9–11</sup> have relied on fragment assembly. In these approaches, a structure is created through a stochastic sampling process—such as simulated annealing<sup>12</sup>—that minimizes a statistical potential that is derived from summary statistics extracted from structures in the Protein Data Bank (PDB)<sup>13</sup>. In fragment assembly, a structure hypothesis is repeatedly modified, typically by changing the shape of a short section while retaining changes that lower the potential, ultimately leading to low potential structures. Simulated annealing requires many thousands of such moves and must be repeated many times to have good coverage of low-potential structures.

In recent years, the accuracy of structure predictions has improved through the use of evolutionary covariation data<sup>14</sup> that are found in sets of related sequences. Sequences that are similar to the target sequence are found by searching large datasets of protein sequences derived from DNA sequencing and aligned to the target sequence to generate a multiple sequence alignment (MSA). Correlated changes in the positions of two amino acid residues across the sequences of the MSA can be used to infer which residues might be in contact. Contacts are typically defined to occur when the  $\beta$ -carbon atoms of 2 residues are within 8 Å of one another. Several methods<sup>15–18</sup>, including neural networks<sup>19–22</sup>, have been used to predict the probability that a pair of residues is in contact based on features computed from MSAs. Contact predictions are incorporated in structure predictions by modifying the statistical potential to guide the folding process to structures that satisfy more of the predicted contacts<sup>11,23</sup>. Other studies<sup>24,25</sup> have used predictions of the distance between residues, particularly for distance geometry approaches<sup>26–28</sup>. Neural network distance predictions without covariation features were used to make the evolutionary pairwise distance-dependent statistical potential<sup>25</sup>, which was used to rank structure hypotheses. In addition, the QUARK pipeline<sup>11</sup> used a template-based distance-profile restraint for TBM.

In this study, we present a deep-learning approach to protein structure prediction, the stages of which are illustrated in Fig. 2a. We show that it is possible to construct a learned, protein-specific potential by training a neural network (Fig. 2b) to make accurate predictions about the structure of the protein given its sequence, and to predict the structure itself accurately by minimizing the potential by gradient descent (Fig. 2c). The neural network predictions include backbone torsion angles and pairwise distances between residues. Distance predictions provide more specific information about the structure than contact predictions and provide a richer training signal for the

neural network. By jointly predicting many distances, the network can propagate distance information that respects covariation, local structure and residue identities of nearby residues. The predicted probability distributions can be combined to form a simple, principled protein-specific potential. We show that with gradient descent, it is simple to find a set of torsion angles that minimizes this protein-specific potential using only limited sampling. We also show that whole chains can be optimized simultaneously, avoiding the need to segment long proteins into hypothesized domains that are modelled independently as is common practice (see Methods).

The central component of AlphaFold is a convolutional neural network that is trained on PDB structures to predict the distances  $d_{ij}$  between the  $C_\beta$  atoms of pairs,  $ij$ , of residues of a protein. On the basis of a representation of the amino acid sequence,  $S$ , of a protein and features derived from the MSA( $S$ ) of that sequence, the network, which is similar in structure to those used for image-recognition tasks<sup>29</sup>, predicts a discrete probability distribution  $P(d_{ij}|S, \text{MSA}(S))$  for every  $ij$  pair in any  $64 \times 64$  region of the  $L \times L$  distance matrix, as shown in Fig. 2b. The full set of distance distribution predictions constructed by combining such predictions that covers the entire distance map is termed a distogram (from distance histogram). Example distogram predictions for one CASP protein, T0955, are shown in Fig. 3c, d. The modes of the distribution (Fig. 3c) can be seen to closely match the true distances (Fig. 3b). Example distributions for all distances to one residue (residue 29) are shown in Fig. 3d. We found that the predictions of the distance correlate well with the true distance between residues (Fig. 3e). Furthermore, the network also models the uncertainty in its predictions (Fig. 3f). When the s.d. of the predicted distribution is low, the predictions are more accurate. This is also evident in Fig. 3d, in which more confident predictions of the distance distribution (higher peak and lower s.d. of the distribution) tend to be more accurate, with the true distance close to the peak. Broader, less-confidently predicted distributions still assign probability to the correct value even when it is not close to the peak. The high accuracy of the distance predictions and consequently the contact predictions (Fig. 1c) comes from a combination of factors in the design of the neural network and its training, data augmentation, feature representation, auxiliary losses, cropping and data curation (see Methods).

To generate structures that conform to the distance predictions, we constructed a smooth potential  $V_{\text{distance}}$  by fitting a spline to the negative log probabilities, and summing across all of the residue pairs

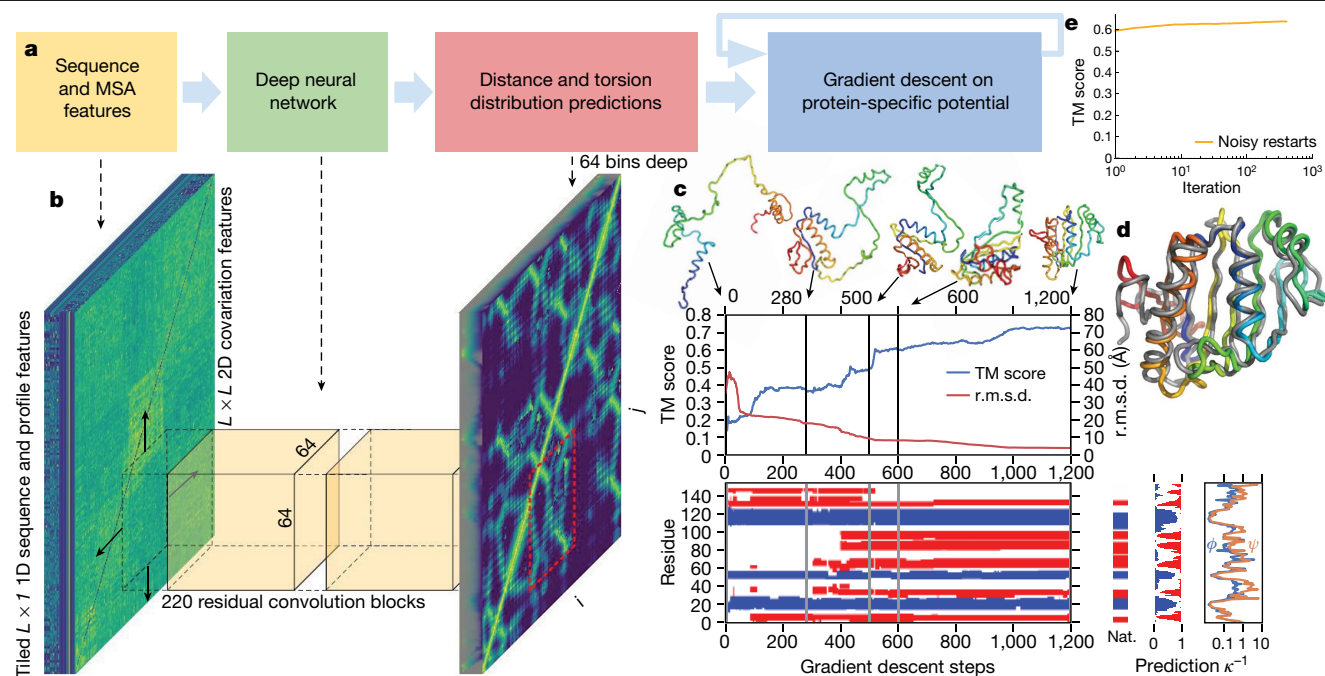


**Fig. 2 | The folding process illustrated for CASP13 target T0986s2.** CASP target T0986s2,  $L = 155$ , PDB: 6N9V. **a**, Steps of structure prediction. **b**, The neural network predicts the entire  $L \times L$  distogram based on MSA features, accumulating separate predictions for  $64 \times 64$ -residue regions. **c**, One iteration of gradient descent (1,200 steps) is shown, with the TM score and root mean square deviation (r.m.s.d.) plotted against step number with five snapshots of the structure. The secondary structure (from SST<sup>33</sup>) is also shown (helix in blue, strand in red) along with the native secondary structure (Nat.), the secondary

structure prediction probabilities of the network and the uncertainty in torsion angle predictions (as  $\kappa^{-1}$  of the von Mises distributions fitted to the predictions for  $\varphi$  and  $\psi$ ). While each step of gradient descent greedily lowers the potential, large global conformation changes are effected, resulting in a well-packed chain. **d**, The final first submission overlaid on the native structure (in grey). **e**, The average (across the test set,  $n = 377$ ) TM score of the lowest-potential structure against the number of repeats of gradient descent per target (log scale).

(see Methods). We parameterized protein structures by the backbone torsion angles ( $\varphi, \psi$ ) of all residues and build a differentiable model of protein geometry  $\mathbf{x} = G(\varphi, \psi)$  to compute the  $C_\beta$  coordinates,  $\mathbf{x}_i$  for all residues  $i$  and thus the inter-residue distances,  $d_{ij} = \|\mathbf{x}_i - \mathbf{x}_j\|$ , for each structure, and express  $V_{\text{distance}}$  as a function of  $\varphi$  and  $\psi$ . For a protein with  $L$  residues, this potential accumulates  $L^2$  terms from marginal distribution predictions. To correct for the overrepresentation of the prior, we subtract a reference distribution<sup>30</sup> from the distance potential in the log domain. The reference distribution models the distance distributions  $P(d_{ij}|\text{length})$  independent of the protein sequence and is computed by training a small version of the distance prediction neural network on the same structures, without sequence or MSA input features. A separate output head of the contact prediction network is trained to predict discrete probability distributions of backbone torsion angles  $P(\varphi_i, \psi_i | S, \text{MSA}(S))$ . After fitting a von Mises distribution, this is used to add a smooth torsion modelling term,  $V_{\text{torsion}}$ , to the potential. Finally, to prevent steric clashes, we add the  $V_{\text{score2\_smooth}}$  score of Rosetta<sup>9</sup> to the potential, as this incorporates a van der Waals term. We used multiplicative weights for each of the three terms in the potential; however, no combination of weights noticeably outperformed equal weighting.

As all of the terms in the combined potential  $V_{\text{total}}(\varphi, \psi)$  are differentiable functions of  $(\varphi, \psi)$ , it can be optimized with respect to these variables by gradient descent. Here we use L-BFGS<sup>31</sup>. Structures are initialized by sampling torsion values from  $P(\varphi_i, \psi_i | S, \text{MSA}(S))$ . Figure 2c illustrates a single gradient descent trajectory that minimizes the potential, showing how this greedy optimization process leads to increasing accuracy and large-scale conformation changes. The secondary structure is partly set by the initialization from the predicted torsion angle distributions. The overall accuracy (TM score) improves quickly and after a few hundred steps of gradient descent the accuracy of the structure has converged to a local optimum of the potential.

We repeated the optimization from sampled initializations, leading to a pool of low-potential structures from which further structure initializations are sampled, with added backbone torsion noise ('noisy restarts'), leading to more structures to be added to the pool. After only a few hundred cycles, the optimization converges and the lowest potential structure is chosen as the best candidate structure. Figure 2e shows the progress in the accuracy of the best-scoring structures over multiple restarts of the gradient descent process, showing that after a few iterations the optimization has converged. Noisy restarts enable structures with a slightly higher TM score to be found than when continuing to sample from the predicted torsion distributions (average of 0.641 versus 0.636 on our test set, shown in Extended Data Fig. 4).

Figure 4a shows that the distogram accuracy (measured using the local distance difference test (IDDT<sub>12</sub>) of the distogram; see Methods) correlates well with the TM score of the final realized structures. Figure 4b shows the effect of changing the construction of the potential. Removing the distance potential entirely gives a TM score of 0.266. Reducing the resolution of the distogram representation below six bins by averaging adjacent bins causes the TM score to degrade. Removing the torsion potential, reference correction or  $V_{\text{score2\_smooth}}$  degrades the accuracy only slightly. A final 'relaxation' (side-chain packing interleaved with gradient descent) with Rosetta<sup>9</sup>, using a combination of the Talaris2014 potential and a spline fit of our reference-corrected distance potential adds side-chain atom coordinates, and yields a small average improvement of 0.007 TM score.

We show that a carefully designed deep-learning system can provide accurate predictions of inter-residue distances and can be used to construct a protein-specific potential that represents the protein structure. Furthermore, we show that this potential can be optimized with gradient descent to achieve accurate structure predictions.

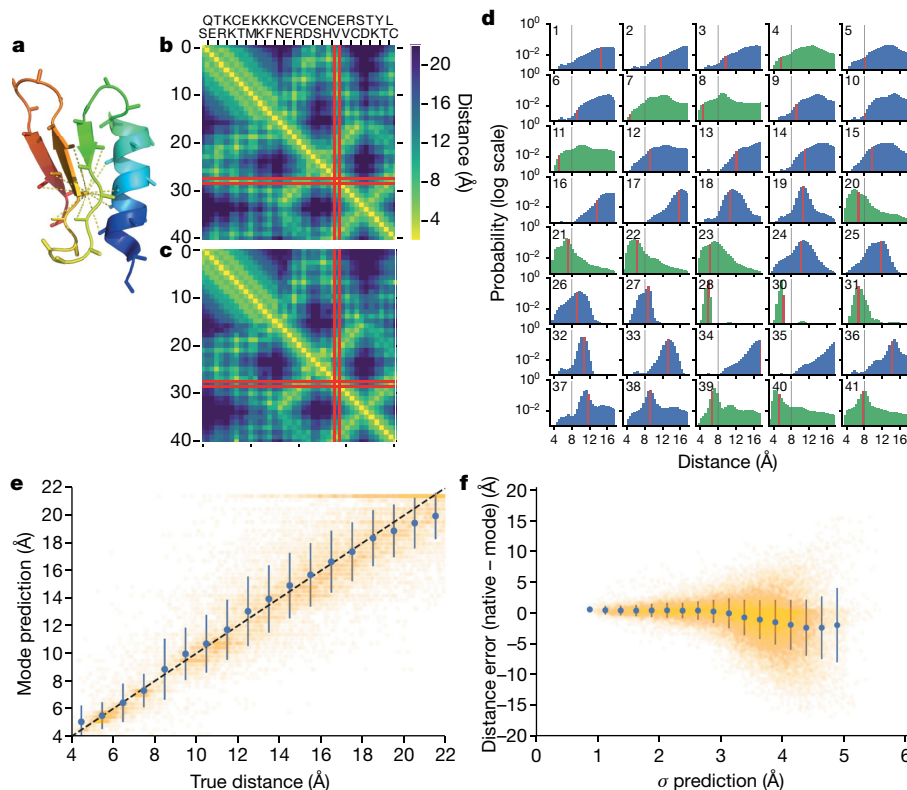


**Fig. 3 | Predicted distance distributions compared with true distances.** **a–d**, CASP target T0955,  $L = 41$ , PDB 5W9F. **a**, Native structure showing distances under 8 Å from the  $C_\beta$  of residue 29. **b**, **c**, Native inter-residue distances (**b**) and the mode of the distance predictions (**c**), highlighting residue 29. **d**, The predicted probability distributions for distances of residue 29 to all other residues. The bin corresponding to the native distance is highlighted in red, 8 Å is drawn in black. The distributions of the true contacts are plotted in green, non-contacts in blue. **e**, **f**, CASP target T0990,  $L = 552$ , PDB 6N9V.

**e**, The mode of the predicted distance plotted against the true distance for all residue pairs with distances  $\leq 22$  Å, excluding distributions with s.d.  $> 3.5$  Å ( $n = 28,678$ ). Data are mean  $\pm$  s.d. calculated for 1 Å bins. **f**, The error of the mode distance prediction versus the s.d. of the distance distributions, excluding pairs with native distances  $> 22$  Å ( $n = 61,872$ ). Data are mean  $\pm$  s.d. are shown for 0.25 Å bins. The true distance matrix and distogram for T0990 are shown in Extended Data Fig. 2b, c.

Whereas FM predictions only rarely approach the accuracy of experimental structures, the CASP13 assessment shows that the AlphaFold system achieves unprecedented FM accuracy and that this FM method

can match the performance of template-modelling approaches without using templates and is starting to reach the accuracy needed to provide biological insights (see Methods). We hope that the methods we have

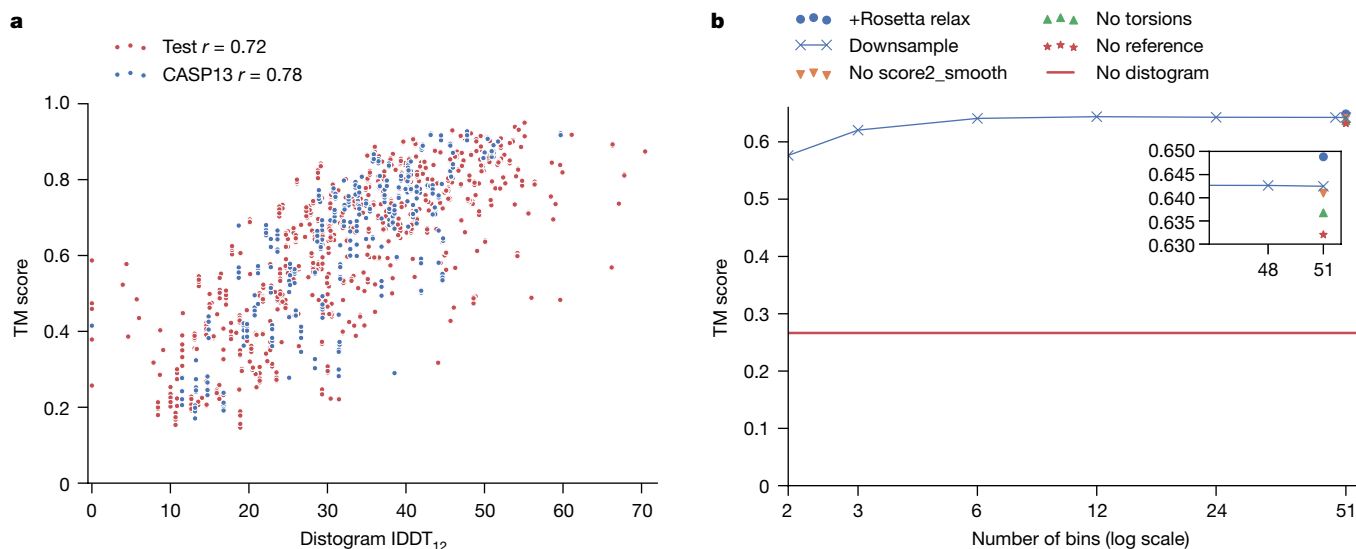


**Fig. 4 | TM scores versus the accuracy of the distogram, and the dependency of the TM score on different components of the potential.** **a**, TM score versus distogram IDDT<sub>12</sub> with Pearson's correlation coefficients, for both CASP13 ( $n = 500$ ; 5 decoys for all domains, excluding T0999) and test ( $n = 377$ ) datasets.

**b**, Average TM score over the test set ( $n = 377$ ) versus the number of histogram bins used when downsampling the distogram, compared with removing different components of the potential, or adding Rosetta relaxation.

described can be developed further and applied to benefit all areas of protein science with more accurate predictions for sequences of unknown structure.

## Online content

Any methods, additional references, Nature Research reporting summaries, source data, extended data, supplementary information, acknowledgements, peer review information; details of author contributions and competing interests; and statements of data and code availability are available at <https://doi.org/10.1038/s41586-019-1923-7>.

- Dill, K. A., Ozkan, S. B., Shell, M. S. & Weikl, T. R. The protein folding problem. *Annu. Rev. Biophys.* **37**, 289–316 (2008).
- Dill, K. A. & MacCallum, J. L. The protein-folding problem, 50 years on. *Science* **338**, 1042–1046 (2012).
- Schaarschmidt, J., Monastyrsky, B., Kryshchuk, A. & Bonvin, A. M. J. J. Assessment of contact predictions in CASP12: co-evolution and deep learning coming of age. *Proteins* **86**, 51–66 (2018).
- Kirkwood, J. Statistical mechanics of fluid mixtures. *J. Chem. Phys.* **3**, 300–313 (1935).
- Kryshchuk, A., Schwede, T., Topf, M., Fidelis, K. & Mout, J. Critical assessment of methods of protein structure prediction (CASP)—Round XIII. *Proteins* **87**, 1011–1020 (2019).
- Zhang, Y. & Skolnick, J. Scoring function for automated assessment of protein structure template quality. *Proteins* **57**, 702–710 (2004).
- Zhang, Y. Protein structure prediction: when is it useful? *Curr. Opin. Struct. Biol.* **19**, 145–155 (2009).
- Senior, A. W. et al. Protein structure prediction using multiple deep neural networks in the 13th Critical Assessment of Protein Structure Prediction (CASP13). *Proteins* **87**, 1141–1148 (2019).
- Das, R. & Baker, D. Macromolecular modeling with Rosetta. *Annu. Rev. Biochem.* **77**, 363–382 (2008).
- Jones, D. T. Predicting novel protein folds by using FRAGFOLD. *Proteins* **45**, 127–132 (2001).
- Zhang, C., Mortuza, S. M., He, B., Wang, Y. & Zhang, Y. Template-based and free modeling of I-TASSER and QUARK pipelines using predicted contact maps in CASP12. *Proteins* **86**, 136–151 (2018).
- Kirkpatrick, S., Gelatt, C. D. Jr & Vecchi, M. P. Optimization by simulated annealing. *Science* **220**, 671–680 (1983).
- Berman, H. M. et al. The Protein Data Bank. *Nucleic Acids Res.* **28**, 235–242 (2000).
- Altschuh, D., Lesk, A. M., Bloomer, A. C. & Klug, A. Correlation of co-ordinated amino acid substitutions with function in viruses related to tobacco mosaic virus. *J. Mol. Biol.* **193**, 693–707 (1987).
- Ovchinnikov, S., Kamisetty, H. & Baker, D. Robust and accurate prediction of residue–residue interactions across protein interfaces using evolutionary information. *eLife* **3**, e02030 (2014).
- Seemayer, S., Gruber, M. & Söding, J. CCMpred—fast and precise prediction of protein residue–residue contacts from correlated mutations. *Bioinformatics* **30**, 3128–3130 (2014).
- Morcos, F. et al. Direct-coupling analysis of residue coevolution captures native contacts across many protein families. *Proc. Natl Acad. Sci. USA* **108**, E1293–E1301 (2011).
- Jones, D. T., Buchan, D. W., Cozzetto, D. & Pontil, M. PSICOV: precise structural contact prediction using sparse inverse covariance estimation on large multiple sequence alignments. *Bioinformatics* **28**, 184–190 (2012).
- Skwark, M. J., Raimondi, D., Michel, M. & Elofsson, A. Improved contact predictions using the recognition of protein like contact patterns. *PLOS Comput. Biol.* **10**, e1003889 (2014).
- Jones, D. T., Singh, T., Kosciulek, T. & Tetchner, S. MetaPSICOV: combining coevolution methods for accurate prediction of contacts and long range hydrogen bonding in proteins. *Bioinformatics* **31**, 999–1006 (2015).
- Wang, S., Sun, S., Li, Z., Zhang, R. & Xu, J. Accurate de novo prediction of protein contact map by ultra-deep learning model. *PLOS Comput. Biol.* **13**, e1005324 (2017).
- Jones, D. T. & Kandathil, S. M. High precision in protein contact prediction using fully convolutional neural networks and minimal sequence features. *Bioinformatics* **34**, 3308–3315 (2018).
- Ovchinnikov, S. et al. Improved de novo structure prediction in CASP11 by incorporating coevolution information into Rosetta. *Proteins* **84**, 67–75 (2016).
- Aszodi, A. & Taylor, W. R. Estimating polypeptide  $\alpha$ -carbon distances from multiple sequence alignments. *J. Math. Chem.* **17**, 167–184 (1995).
- Zhao, F. & Xu, J. A position-specific distance-dependent statistical potential for protein structure and functional study. *Structure* **20**, 1118–1126 (2012).
- Xu, J. & Wang, S. Analysis of distance-based protein structure prediction by deep learning in CASP13. *Proteins* **87**, 1069–1081 (2019).
- Aszodi, A., Gradwell, M. J. & Taylor, W. R. Global fold determination from a small number of distance restraints. *J. Mol. Biol.* **251**, 308–326 (1995).
- Kandathil, S. M., Greener, J. G. & Jones, D. T. Prediction of interresidue contacts with DeepMetaPSICOV in CASP13. *Proteins* **87**, 1092–1099 (2019).
- He, K., Zhang, X., Ren, S. & Sun, J. Deep residual learning for image recognition. In *Proc. IEEE Conference on Computer Vision and Pattern Recognition* 770–778 (2016).
- Simons, K. T., Kooperberg, C., Huang, E. & Baker, D. Assembly of protein tertiary structures from fragments with similar local sequences using simulated annealing and Bayesian scoring functions. *J. Mol. Biol.* **268**, 209–225 (1997).
- Liu, D. C. & Nocedal, J. On the limited memory BFGS method for large scale optimization. *Math. Program.* **45**, 503–528 (1989).
- Li, Y., Zhang, C., Bell, E. W., Yu, D.-J. & Zhang, Y. Ensembling multiple raw coevolutionary features with deep residual neural networks for contact-map prediction in CASP13. *Proteins* **87**, 1082–1091 (2019).
- Konagurthu, A. S., Lesk, A. M. & Allison, L. Minimum message length inference of secondary structure from protein coordinate data. *Bioinformatics* **28**, i97–i105 (2012).

**Publisher's note** Springer Nature remains neutral with regard to jurisdictional claims in published maps and institutional affiliations.

© The Author(s), under exclusive licence to Springer Nature Limited 2020



## Methods

Extended Data Figure 1a shows the steps involved in MSA construction, feature extraction, distance prediction, potential construction and structure realization.

### Tools

The following tools and dataset versions were used for the CASP system and for subsequent experiments: PDB 15 March 2018; CATH 16 March 2018; HHblits based on v.3.0-beta.3 (three iterations,  $E=1\times 10^{-3}$ ); HHpred web server; Uniclust30 2017-10; PSI-BLAST v.2.6.0 nr dataset (as of 15 December 2017) (three iterations,  $E=1\times 10^{-3}$ ); SST web server (March 2019); BioPython v.1.65; Rosetta v.3.5; PyMol 2.2.0 for structure visualization; TM-align 20160521.

### Data

Our models are trained on structures extracted from the PDB<sup>13</sup>. We extract non-redundant domains by utilizing the CATH<sup>34</sup> 35% sequence similarity cluster representatives. This generated 31,247 domains, which were split into train and test sets (29,427 and 1,820 proteins, respectively), keeping all domains from the same homologous superfamily (H-level in the CATH classification) in the same partition. The CATH superfamilies of FM domains from CASP11 and CASP12 were also excluded from the training set. From the test set, we took—at random—a single domain per homologous superfamily to create the 377 domain subset used for the results presented here. We note that accuracies for this set are higher than for the CASP13 test domains.

CASP13 submission results are drawn from the CASP13 results pages with additional results shown for the CASP13 dataset for ‘all groups’ chains, scored on CASP13 PDB files, by CASP domain definitions. Contact prediction accuracies were recomputed from the group 032 and 498 submissions (as RR files), compared with the distogram predictions used by AlphaFold for CASP13 submissions. Contact prediction probabilities were obtained from the distograms by summing the probability mass in each distribution below 8 Å.

For each training sequence, we searched for and aligned to the training sequence similar protein sequences in the Uniclust30<sup>35</sup> dataset with HHblits<sup>36</sup> and used the returned MSA to generate profile features with the position-specific substitution probabilities for each residue as well as covariation features—the parameters of a regularized pseudolikelihood-trained Potts model similar to CCMpred<sup>16</sup>. CCMpred uses the Frobenius norm of the parameters, but we feed both this norm (1 feature) and the raw parameters (484 features) into the network for each residue pair  $ij$ . In addition, we provide the network with features that explicitly represent gaps and deletions in the MSA. To make the network better able to make predictions for shallow MSAs, and as a form of data augmentation, we take a sample of half the sequences from the HHblits MSA before computing the MSA-based features. Our training set contains 10 such samples for each domain. We extract additional profile features using PSI-BLAST<sup>37</sup>.

The distance prediction neural network was trained with the following input features (with the number of features indicated in brackets).

- Number of HHblits alignments (scalar).
- Sequence-length features: 1-hot amino acid type (21 features); profiles: PSI-BLAST (21 features), HHblits profile (22 features), non-gapped profile (21 features), HHblits bias, HMM profile (30 features), Potts model bias (22 features); deletion probability (1 feature); residue index (integer index of residue number, consecutive except for multi-segment domains, encoded as 5 least-significant bits and a scalar).
- Sequence-length-squared features: Potts model parameters (484 features, fitted with 500 iterations of gradient descent using Nesterov momentum 0.99, without sequence reweighting); Frobenius norm (1 feature); gap matrix (1 feature).

The z-scores were taken from the results CASP13 assessors ([http://predictioncenter.org/casp13/zscores\\_final.cgi?formula=assessors](http://predictioncenter.org/casp13/zscores_final.cgi?formula=assessors)).

**Distogram prediction.** The inter-residue distances are predicted by a deep neural network. The architecture is a deep two-dimensional dilated convolutional residual network. Previously, a two-dimensional residual network was used that was preceded by one-dimensional embedding layers for contact prediction<sup>21</sup>. Our network is two-dimensional throughout and uses 220 residual blocks<sup>29</sup> with dilated convolutions<sup>38</sup>. Each residual block, illustrated in Extended Data Fig. 1b, consists of a sequence of neural network layers<sup>39</sup> that interleave three batchnorm layers; two  $1\times 1$  projection layers; a  $3\times 3$  dilated convolution layer and exponential linear unit (ELU)<sup>40</sup> nonlinearities. Successive layers cycle through dilations of 1, 2, 4, 8 pixels to allow propagation of information quickly across the cropped region. For the final layer, a position-specific bias was used, such that the biases were indexed by residue-offset (capped at 32) and bin number.

The network is trained with stochastic gradient descent using a cross-entropy loss. The target is a quantification of the distance between the  $C_\beta$  atoms of the residues (or  $C_\alpha$  for glycine). We divide the range 2–22 Å into 64 equal bins. The input to the network consists of a two-dimensional array of features in which each  $ij$  feature is the concatenation of the one-dimensional features for both  $i$  and  $j$  as well as the two-dimensional features for  $ij$ .

Individual training runs were cross-validated with early stopping using 27 CASP11 FM domains as a validation set. Models were selected by cross-validation on 27 CASP12 FM domains.

### Neural network hyperparameters

- 7 groups of 4 blocks with 256 channels, cycling through dilations 1, 2, 4, 8.
- 48 groups of 4 blocks with 128 channels, cycling through dilations 1, 2, 4, 8.
- Optimization: synchronized stochastic gradient descent
- Batch size: batch of 4 crops on each of 8 GPU workers.
- 0.85 dropout keep probability.
- Nonlinearity: ELU.
- Learning rate: 0.06.
- Auxiliary loss weights: secondary structure: 0.005; accessible surface area: 0.001. These auxiliary losses were cut by a factor 10 after 100 000 steps.
- Learning rate decayed by 50% at 150,000, 200,000, 250,000 and 350,000 steps.
- Training time: about 5 days for 600,000 steps.

**Cropped distograms.** To constrain memory usage and avoid overfitting, the network was always trained and tested on  $64\times 64$  regions of the distance matrix, that is, the pairwise distances between 64 consecutive residues and another group of 64 consecutive residues. For each training domain, the entire distance matrix was split into non-overlapping  $64\times 64$  crops. By training off-diagonal crops, the interaction between residues that are further apart than 64 residues could be modelled. Each crop consisted of the distance matrix that represented the juxtaposition of two 64-residue fragments. It has previously been shown<sup>22</sup> that contact prediction needs only a limited context window. We note that the distance predictions close to the diagonal  $i=j$ , encode predictions of the local structure of the protein, and for any cropped region the distances are governed by the local structure of the two fragments represented by the  $i$  and  $j$  ranges of the crop. Augmenting the inputs with the on-diagonal two-dimensional input features that correspond to both the  $i$  and  $j$  ranges provides additional information to predict the structure of each fragment and thus the distances between them. It can be seen that if the fragment structures can be well predicted (for instance, if they are confidently predicted as helices or sheets), then the prediction of a single contact



between the fragments will strongly constrain the distances between all other pairs.

Randomizing the offset of the crops each time a domain is used in training leads to a form of data augmentation in which a single protein can generate many thousands of different training examples. This is further enhanced by adding noise proportional to the ground-truth resolution to the atom coordinates, leading to variation in the target distances. Data augmentation (MSA subsampling and coordinate noise), together with dropout<sup>41</sup>, prevents the network from overfitting to the training data.

To predict the distance distribution for all  $L \times L$  residue pairs, many  $64 \times 64$  crops are combined. To avoid edge effects, several such tilings are produced with different offsets and averaged together, with a heavier weighting for the predictions near the centre of the crop. To improve accuracy further, predictions from an ensemble of four separate models, trained independently with slightly different hyperparameters, are averaged together. Extended Data Figure 2b, c shows examples of the true distances and the mode of the distogram predictions for a three-domain CASP13 target, T0990.

As the network has a rich representation capable of incorporating both profile and covariation features of the MSA, we argue that the network can be used to predict the secondary structure directly. By mean- and max- pooling the two-dimensional activations of the penultimate layer of the network separately in both  $i$  and  $j$ , we add an additional one-dimensional output head to the network that predicts eight-class secondary structure labels as computed by DSSP<sup>42</sup> for each residue in  $j$  and  $i$ . The resulting accuracy of the Q3 (distinguishing the three helix/sheet/coil classes) predictions is 84%, which is comparable to the state-of-the-art predictions<sup>43</sup>. The relative accessible surface area (ASA) of each residue can also be predicted.

The one-dimensional pooled activations are also used to predict the marginal Ramachandran distributions,  $P(\phi_i, \psi_i | S, \text{MSA}(S))$ , independently for each residue, as a discrete probability distribution approximated to  $10^\circ$  (1,296 bins). In practice during CASP13 we used distograms from a network that was trained to predict distograms, secondary structure and ASA. Torsion predictions were taken from a second similar network trained to predict distograms, secondary structure, ASA and torsions, as the former had been more thoroughly validated.

Extended Data Figure 3b shows that an important factor in the accuracy of the distograms (as has previously been found with contact prediction systems) is  $N_{\text{eff}}$ , the effective number of sequences in the MSA<sup>20</sup>. This is the number of sequences found in the MSA, discounting redundancy at the 62% sequence identity level, which we then divide by the number of residues in the target, and is an indication of the amount of covariation information in the MSA.

**Distance potential.** The distogram probabilities are estimated for discrete distance bins; therefore, to construct a differentiable potential, the distribution is interpolated with a cubic spline. Because the final bin accumulates probability mass from all distances beyond 22 Å, and as greater distances are harder to predict accurately, the potential was only fitted up to 18 Å (determined by cross-validation), with a constant extrapolation thereafter. Extended Data Figure 3c (bottom) shows the effect of varying the resolution of the distance histograms on structure accuracy.

To predict a reference distribution, a similar model is trained on the same dataset. The reference distribution is not conditioned on the sequence, but to account for the atoms between which we are predicting distances, we do provide a binary feature  $\delta_{\alpha\beta}$  to indicate whether the residue is a glycine ( $C_\alpha$  atom) or not ( $C_\beta$ ) and the overall length of the protein.

A distance potential is created from the negative log likelihood of the distances, summed over all pairs of residues  $i, j$  (Supplementary equation (1)). With a reference state, this becomes the log-likelihood

ratio of the distances under the full conditional model and under the background model (Supplementary equation (2)).

Torsions are modelled as a negative log likelihood under the predicted torsion distributions. As we have marginal distribution predictions, each of which can be multimodal, it can be difficult to jointly optimize the torsions. To unify all of the probability mass, at the cost of modelling fidelity of multimodal distributions, we fitted a unimodal von Mises distribution to the marginal predictions. This potential was summed over all residues  $i$  (Supplementary equation (3)).

Finally, to prevent steric clashes, a van der Waals term was introduced through the use of Rosetta's  $V_{\text{score2\_smooth}}$ . Extended Data Figure 3c (top) shows the effect on the accuracy of the structure prediction of different terms in the potential.

**Structure realization by gradient descent.** To realize structures that minimize the constructed potential, we created a differentiable model of ideal protein backbone geometry, giving backbone atom coordinates as a function of the torsion angles  $(\phi, \psi)$ :  $\mathbf{x} = G(\phi, \psi)$ . The complete potential to be minimized is then the sum of the distance, torsion and score2\_smooth (Supplementary equation (4)). Although there is no guarantee that these potentials have equivalent scale, scaling parameters on the terms were introduced and chosen by cross-validation on CASP12 FM domains. In practice, equal weighting for all terms was found to lead to the best results.

As every term in  $V_{\text{total}}$  is differentiable with respect to the torsion angles, given an initial set of torsions  $\phi, \psi$ , which can be sampled from the predicted torsion marginals, we can minimize  $V_{\text{total}}$  using a gradient descent algorithm, such as L-BFGS<sup>31</sup>. The optimized structure is dependent on the initial conditions, so we repeat the optimization multiple times with different initializations. A pool of the 20 lowest-potential structures is maintained and once full, we initialize 90% of trajectories from those with 30° noise added to the backbone torsions (the remaining 10% still being sampled from the predicted torsion distributions). In CASP13, we obtained 5,000 optimization runs for each chain. Figure 2c shows the change in TM score against the number of restarts per protein. As longer chains take longer to optimize, this work load was balanced across  $(50 + L)/2$  parallel workers. Extended Data Figure 4 shows similar curves against computation time, always comparing sampling starting torsions from the predicted marginal distributions with restarting from the pool of previous structures.

**Accuracy.** We compare the final structures to the experimentally determined structures to measure their accuracy using metrics such as TM score, GDT\_TS (global distance test, total score<sup>44</sup>) and r.m.s.d. All of these accuracy measures require geometric alignment between the candidate structure and the experimental structure. An alternative accuracy measure that requires no alignment is the IDDT<sup>45</sup>, which measures the percentage of native pairwise distances  $D_{ij}$  under 15 Å, with sequence offsets  $\geq r$  residues, that are realized in a candidate structure (as  $d_{ij}$ ) within a tolerance of the true value, averaging across tolerances of 0.5, 1, 2 and 4 Å (without stereochemical checks), as shown in Supplementary equation (5)).

As the distogram predicts pairwise distances, we can introduce distogram IDDT (DLDDT), a measure similar to IDDT that is computed directly from the probabilities of the distograms, as shown in Supplementary equation (6)). As distances between residues nearby in the sequence are often short, easier to predict and are not critical in determining the overall fold topology, we set  $r = 12$ , considering only those distances for residues with a sequence separation  $\geq 12$ . Because we predict  $C_\beta$  distances, for this study we computed both IDDT and DLDDT using the  $C_\beta$  distances. Extended Data Figure 3a shows that DLDDT<sub>12</sub> has high correlation (Pearson's  $r = 0.92$  for CASP13) with the IDDT<sub>12</sub> of the realized structures.

**Full chains without domain segmentation.** Parameterizing proteins of length  $L$  by two torsion angles per residue, the dimension of the space of structures grows as  $2L$ ; thus, searching for structures of large proteins becomes much more difficult. Traditionally this problem was addressed by splitting longer protein chains into pieces—termed domains—that fold independently. However, domain segmentation from the sequence alone is itself difficult and error-prone. For this study, we avoided domain segmentation and folded entire chains. Typically, MSAs are based on a given domain segmentation; however, we used a sliding window approach, computing a full-chain MSA to predict a baseline full-sequence distogram. We then computed MSAs for subsequences of the chain, trying windows of size 64, 128, 256 with offsets at multiples of 64. Each of these MSAs gave rise to an individual distogram that corresponded to an on-diagonal square of the full-chain distogram. We averaged all of these distograms together, weighted by the number of sequences in the MSA to produce an average full-chain distogram that is more accurate in regions in which many alignments can be found. For the CASP13 assessment, full chains were relaxed with Rosetta relax with a potential of  $V_{\text{Talaris2014}} + 0.2 V_{\text{distance}}$  (weighting determined by cross-validation) and submissions from all of the systems were ranked based on this potential.

**CASP13 results.** For CASP13, the five AlphaFold submissions were from three different systems, all of which used potentials based on the neural network distance predictions. The systems that are not described here are described in a separate paper<sup>8</sup>. Before T0975, two systems based on simulated annealing and fragment assembly (and using 40-bin distance distributions) were used. From T0975 onward, newly trained 64-bin distogram predictions were used and structures were generated by the gradient descent system described here (three independent runs) as well as one of the fragment assembly systems (five independent runs). The five submissions were chosen from these eight structures (the lowest potential structure generated by each independent run) with the first submission (top-one) being the lowest-potential structure generated by gradient descent. The remaining four submissions were the four best other structures, with the fifth being a gradient descent structure if none had been chosen for position 2, 3 or 4. All submissions for T0999 were generated by gradient descent. Extended Data Figure 5a shows the methods used for each submission, comparing with ‘back-fill’ structures generated by a single run of gradient descent for targets before T0975. Extended Data Figure 5b shows that the gradient descent method that was used later in CASP performed better than the fragment assembly method, in each category. Extended Data Figure 5c compares the accuracy of the AlphaFold submissions for FM and FM/TBM domains with the next best group 322. The assessors of CASP13 FM used expert visual inspection<sup>46</sup> to choose the best submissions for each target and found that AlphaFold had nearly twice as many best models as the next best group.

**Biological relevance of AlphaFold predictions.** There is a wide range of uses of predicted structures, all with different accuracy requirements, from generally understanding the fold shape to understanding detailed side-chain configurations in binding regions. Contact predictions alone can guide biological insights<sup>47</sup>, for instance, to target mutations to destabilize the protein. Figure 1c and Extended Data Fig. 2a show that the accuracy of the contact predictions from AlphaFold exceeds that of the state-of-the-art predictions. In Extended Data Figs. 6–8, we present further results that show that the accuracy improvements of AlphaFold lead to more accurate interpretations of function (Extended Data Fig. 6); better interface prediction for protein–protein interactions (Extended Data Fig. 7); better binding pocket prediction (Extended Data Fig. 8) and improved molecular replacement in crystallography.

Thus far only template-based predictions have been able to deliver the most accurate predictions. Although AlphaFold is able to match TBM without using templates, and in some cases outperform other methods (for example, T0981-D5, 72.8 GDT\_TS, and T0957s1-D2, 88.0 GDT\_TS, two TBM-hard domains for which the top-one model of AlphaFold is 12 GDT\_TS better than any other top-one submission), the accuracy for FM targets still lags behind that for TBM targets and can still not be relied on for the detailed understanding of hard structures. In an analysis of the performance of CASP13 TBM predictions for molecular replacement, another study<sup>48</sup> reported that the AlphaFold predictions (raw coordinates, without B-factors) led to a marginally greater log-likelihood gain than those of any other group, indicating that these improved structures can assist in phasing for X-ray crystallography.

**Interpretation of distogram neural network.** We have shown that the deep distance prediction neural network achieves high accuracy, but we would like to understand how the network arrives at its distance predictions and—in particular—to understand how the inputs to the model affect the final prediction. This might improve our understanding of the folding mechanisms or suggest improvements to the model. However, deep neural networks are complex nonlinear functions of their inputs, and so this attribution problem is difficult, under-specified and an on-going topic of research. Even so, there are a number of methods for such analysis: here we apply Integrated Gradients<sup>49</sup> to our trained distogram network to indicate the location of input features that affect the network’s predictions of a particular distance.

In Extended Data Fig. 9, plots of summed absolute Integrated Gradient,  $\sum_c |S_{ij,c}^U|$ , (defined in Supplementary equations (7)–(9)) are shown for selected  $I/J$  output pairs in T0986s2; and in Extended Data Fig. 10, the top-10 highest attribution input pairs for each output pair are shown on top of the top-one predicted structure of AlphaFold. The attribution maps are sparse and highly structured, closely reflecting the predicted geometry of the protein. For the four in-contact pairs presented (1, 2, 3, 5), all of the highest attribution pairs are pairs within or between the secondary structure that one or both of the output pair(s) are members of. In 1, the helix residues are important as well as connections between the strands that follow either end of the helix, which might indicate strain on the helix. In 2, all of the most important residue pairs connect the same two strands, whereas in 3, a mixture of inter-strand pairs and strand residues is most salient. In 5, the most important pairs involve the packing of nearby secondary structure elements to the strand and helix. For the non-contacting pair, 4, the most important input pairs are the residues that are geometrically between  $I$  and  $J$  in the predicted protein structure. Furthermore, most of the high-attribution input pairs are themselves in contact.

As the network is tasked with predicting the spatial geometry, with no structure available at the input, these patterns of interaction indicate that the network is using intermediate predictions to discover important interactions and channelling information from related residues to refine the final prediction.

## Reporting summary

Further information on research design is available in the Nature Research Reporting Summary linked to this paper.

## Data availability

Our training, validation and test data splits (CATH domain codes) are available from [https://github.com/deepmind/deepmind-research/tree/master/alphafold\\_casp13](https://github.com/deepmind/deepmind-research/tree/master/alphafold_casp13). The following versions of public datasets were used in this study: PDB 2018-03-15; CATH 2018-03-16; Uniclust30 2017-10; and PSI-BLAST nr dataset (as of 15 December 2017).

## Code availability

Source code for the distogram, reference distogram and torsion prediction neural networks, together with the neural network weights and input data for the CASP13 targets are available for research and non-commercial use at [https://github.com/deepmind/deepmind-research/tree/master/alphafold\\_casp13](https://github.com/deepmind/deepmind-research/tree/master/alphafold_casp13). We make use of several open-source libraries to conduct our experiments, particularly HHblits<sup>36</sup>, PSI-BLAST<sup>37</sup> and the machine-learning framework TensorFlow (<https://github.com/tensorflow/tensorflow>) along with the TensorFlow library Sonnet (<https://github.com/deepmind/sonnet>), which provides implementations of individual model components<sup>50</sup>. We also used Rosetta<sup>9</sup> under license.

34. Dawson, N. L. et al. CATH: an expanded resource to predict protein function through structure and sequence. *Nucleic Acids Res.* **45**, D289–D295 (2017).
35. Mirdita, M. et al. Uniclust databases of clustered and deeply annotated protein sequences and alignments. *Nucleic Acids Res.* **45**, D170–D176 (2017).
36. Remmert, M., Biegert, A., Hauser, A. & Söding, J. HHblits: lightning-fast iterative protein sequence searching by HMM–HMM alignment. *Nat. Methods* **9**, 173–175 (2012).
37. Altschul, S. F. et al. Gapped BLAST and PSI-BLAST: a new generation of protein database search programs. *Nucleic Acids Res.* **25**, 3389–3402 (1997).
38. Yu, F. & Koltun, V. Multi-scale context aggregation by dilated convolutions. Preprint at *arXiv* <https://arxiv.org/abs/1511.07122> (2015).
39. Oord, A. d. et al. Wavenet: a generative model for raw audio. Preprint at *arXiv* <https://arxiv.org/abs/1609.03499> (2016).
40. Clevert, D.-A., Unterthiner, T. & Hochreiter, S. Fast and accurate deep network learning by exponential linear units (ELUs). Preprint at *arXiv* <https://arxiv.org/abs/1511.07289> (2015).
41. Srivastava, N., Hinton, G., Krizhevsky, A., Sutskever, I. & Salakhutdinov, R. Dropout: a simple way to prevent neural networks from overfitting. *J. Mach. Learn. Res.* **15**, 1929–1958 (2014).
42. Kabsch, W. & Sander, C. Dictionary of protein secondary structure: pattern recognition of hydrogen-bonded and geometrical features. *Biopolymers* **22**, 2577–2637 (1983).
43. Yang, Y. et al. Sixty-five years of the long march in protein secondary structure prediction: the final stretch? *Briefings Bioinf.* **19**, 482–494 (2018).
44. Zemla, A., Venclovas, C., Moul, J. & Fidelis, K. Processing and analysis of CASP3 protein structure predictions. *Proteins* **37**, 22–29 (1999).
45. Mariani, V., Biasini, M., Barbato, A. & Schwede, T. IDDT: a local superposition-free score for comparing protein structures and models using distance difference tests. *Bioinformatics* **29**, 2722–2728 (2013).

46. Abriata, L. A., Tamo, G. E. & Dal Peraro, M. A further leap of improvement in tertiary structure prediction in CASP13 prompts new routes for future assessments. *Proteins* **87**, 1100–1112 (2019).
47. Kayikci, M. et al. Visualization and analysis of non-covalent contacts using the Protein Contacts Atlas. *Nat. Struct. Mol. Biol.* **25**, 185–194 (2018).
48. Croll, T. I. et al. Evaluation of template-based modeling in CASP13. *Proteins* **87**, 1113–1127 (2019).
49. Sundararajan, M., Taly, A. & Yan, Q. Axiomatic attribution for deep networks. In *Proc. 34th International Conference on Machine Learning* Vol. **70**, 3319–3328 (2017).
50. Abadi, M. et al. Tensorflow: a system for large-scale machine learning. In *Proc. 12th USENIX Symposium on Operating Systems Design and Implementation (OSDI 16)* 265–283 (2016).
51. Söding, J., Biegert, A. & Lupas, A. N. The HHpred interactive server for protein homology detection and structure prediction. *Nucleic Acids Res.* **33**, W244–W248 (2005).
52. Cong, Q. et al. An automatic method for CASP9 free modeling structure prediction assessment. *Bioinformatics* **27**, 3371–3378 (2011).
53. Zhang, Y. & Skolnick, J. TM-align: a protein structure alignment algorithm based on the TM-score. *Nucleic Acids Res.* **33**, 2302–2309 (2005).
54. Tovchigrechko, A., Wells, C. A. & Vakser, I. A. Docking of protein models. *Protein Sci.* **11**, 1888–1896 (2002).
55. Audet, M. et al. Crystal structure of misoprostol bound to the labor inducer prostaglandin E<sub>2</sub> receptor. *Nat. Chem. Biol.* **15**, 11–17 (2019).

**Acknowledgements** We thank C. Meyer for assistance in preparing the paper; B. Coppin, O. Vinyals, M. Barwinski, R. Sun, C. Elkin, P. Dolan, M. Lai and Y. Li for their contributions and support; O. Ronneberger for reading the paper; the rest of the DeepMind team for their support; the CASP13 organisers and the experimentalists whose structures enabled the assessment.

**Author contributions** R.E., J.J., J.K., L.S., A.W.S., C.Q., T.G., A.Ž., A.B., H.P. and K.S. designed and built the AlphaFold system with advice from D.S., K.K. and D.H. D.T.J. provided advice and guidance on protein structure prediction methodology. S.P. contributed to software engineering. S.C., A.W.R.N., K.K. and D.H. managed the project. J.K., A.W.S., T.G., A.Ž., A.B., R.E., P.K. and J.J. analysed the CASP results for the paper. A.W.S. and J.K. wrote the paper with contributions from J.J., R.E., L.S., T.G., A.B., A.Ž., D.T.J., P.K., K.K. and D.H. A.W.S. led the team.

**Competing interests** A.W.S., J.K., T.G., J.J., L.S., R.E., H.P., C.Q., K.S., A.Ž. and A.B. have filed provisional patent applications relating to machine learning for predicting protein structures. The remaining authors declare no competing interests.

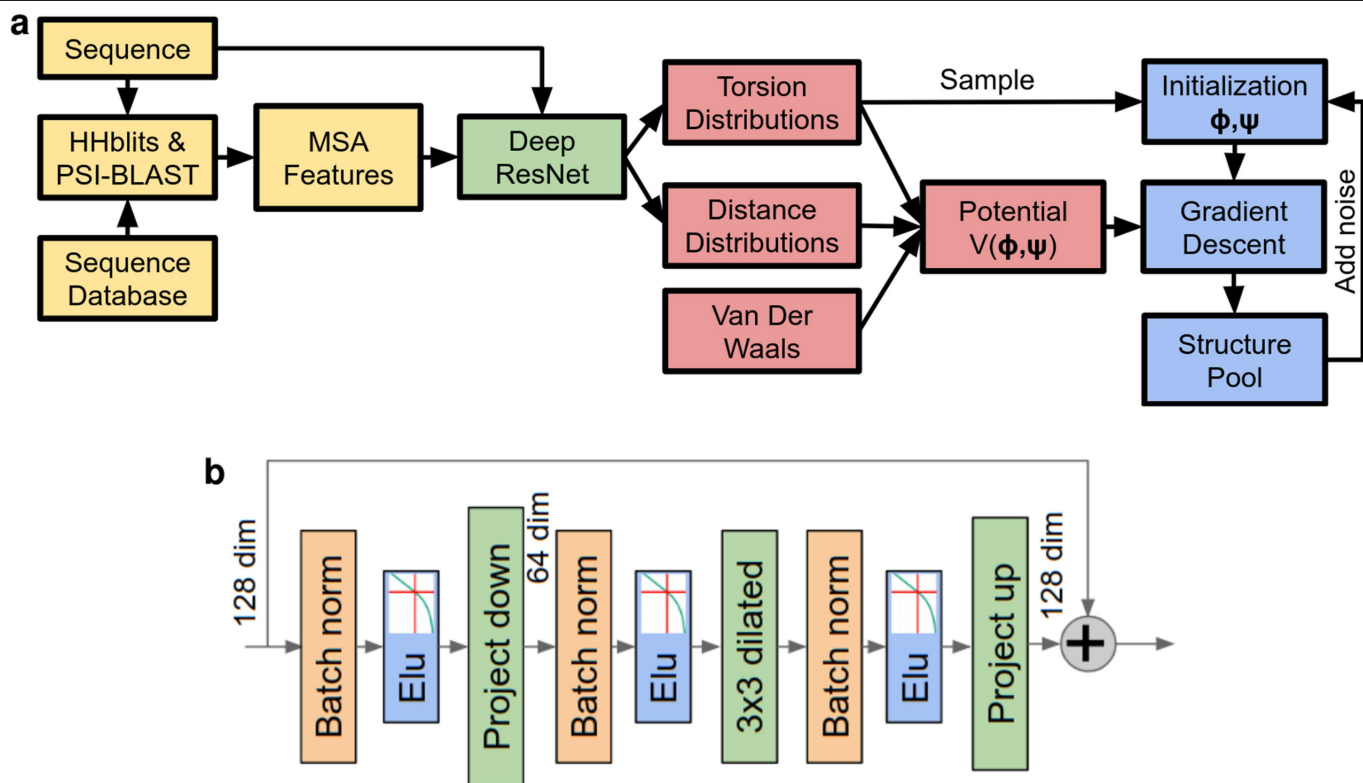
## Additional information

**Supplementary information** is available for this paper at <https://doi.org/10.1038/s41586-019-1923-7>.

**Correspondence and requests for materials** should be addressed to A.W.S.

**Peer review information** *Nature* thanks Mohammed AlQuraishi and the other, anonymous, reviewer(s) for their contribution to the peer review of this work.

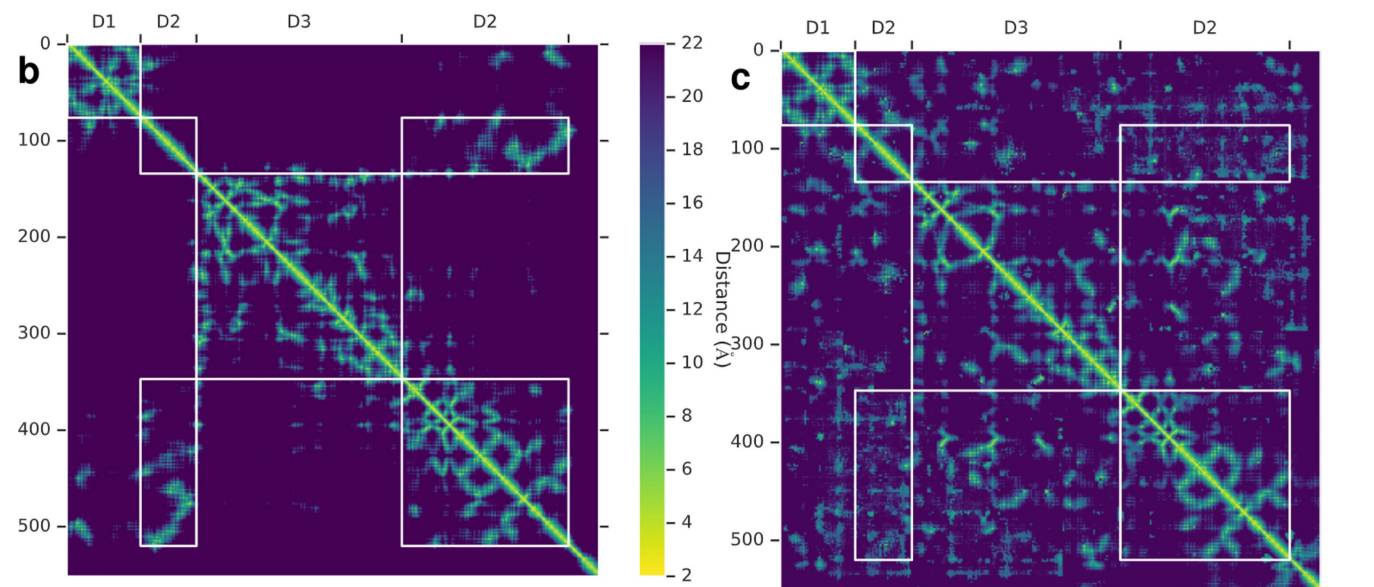
**Reprints and permissions information** is available at <http://www.nature.com/reprints>.



**Extended Data Fig. 1 | Schematics of the folding system and neural network.**  
**a**, The overall folding system. Feature extraction stages (constructing the MSA using sequence database search and computing MSA-based features) are shown in yellow; the structure-prediction neural network in green; potential construction in red; and structure realization in blue. **b**, The layers used in one

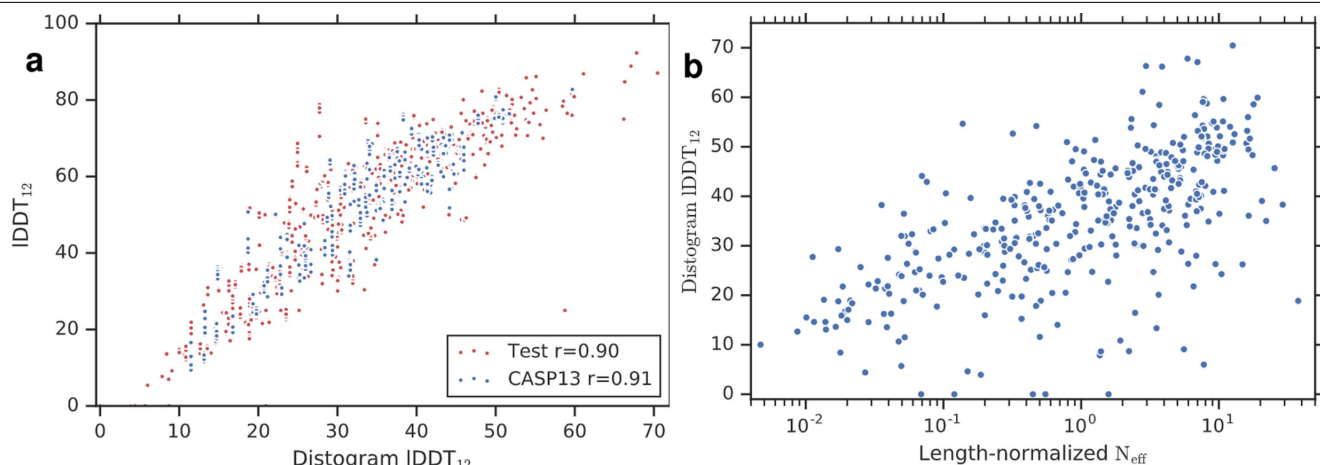
block of the deep residual convolutional network. The dilated convolution is applied to activations of reduced dimension. The output of the block is added to the representation from the previous layer. The bypass connections of the residual network enable gradients to pass back through the network undiminished, permitting the training of very deep networks.

a	Contact precisions		L long			L/2 long			L/5 long		
	Set	<i>N</i>	AF	498	032	AF	498	032	AF	498	032
	FM	31	<b>46.1</b>	43.1	40.1	<b>58.5</b>	54.9	51.6	<b>69.9</b>	67.3	61.9
	FM/TBM	12	<b>59.1</b>	53.0	48.9	<b>74.2</b>	64.5	64.2	<b>85.3</b>	81.0	79.6
	TBM	61	<b>68.3</b>	65.5	61.9	<b>82.4</b>	80.3	76.4	<b>90.6</b>	90.5	87.1



**Extended Data Fig. 2 | CASP13 contact precisions.** **a**, Precisions (as shown in Fig. 1c) for long-range contact prediction in CASP13 for the most probable  $L$ ,  $L/2$  or  $L/5$  contacts, where  $L$  is the length of the domain. The distance distributions used by AlphaFold (AF) in CASP13, thresholded to contact predictions, are compared with submissions by the two best-ranked contact prediction methods in CASP13: 498 (RaptorX-Contact<sup>26</sup>) and 032 (TripletRes<sup>32</sup>), on 'all groups' targets, with updated domain definitions for T0953s2. **b, c**, True distances (**b**) and modes of the predicted distogram (**c**) for CASP13 target T0990. CASP divides this chain into three domains as shown (D3 is inserted in D2) for which there are 39, 36 and 42 HHblits alignments, respectively (from the CASP website).

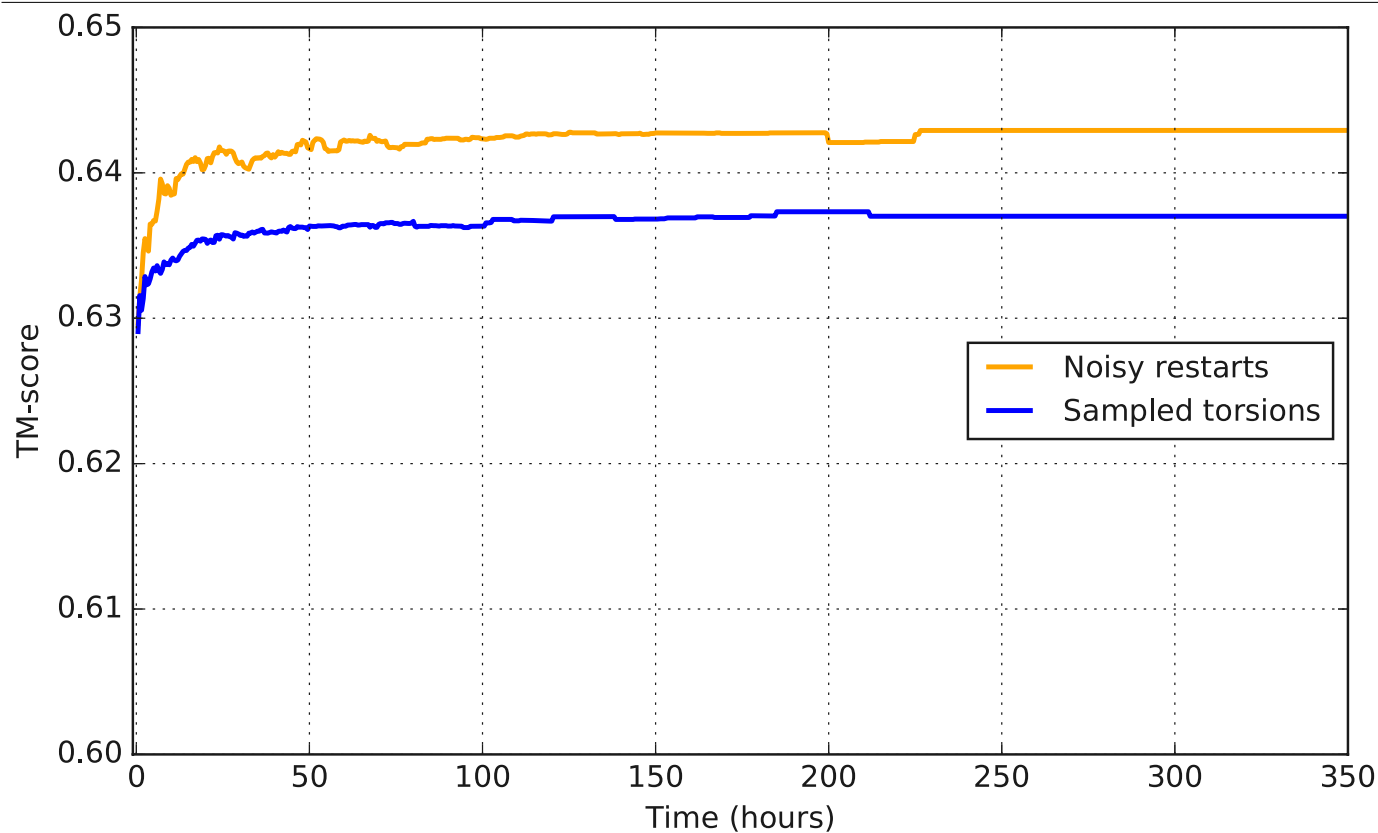




Potential	Bins	TM-score	GDT_TS	IDDT	RMSD (Å)	$-\log_{10} P$
Full + relax	51/64	0.649	65.8	54.2	5.94	7.3
Full	51/64	0.642	65.0	53.9	5.91	–
W/o reference	51/64	0.632	64.3	50.0	6.64	4.0
W/o score2_smooth	51/64	0.641	64.8	53.7	5.93	1.2
W/o torsions	51/64	0.637	64.3	53.6	6.04	8.2
W/o distogram	51/64	0.266	29.1	19.1	14.88	130
Full	48/64	0.643	65.0	54.1	5.90	
Full	24/32	0.643	65.0	53.8	5.89	
Full	12/16	0.644	65.1	53.9	5.85	
Full	6/8	0.641	64.6	53.7	5.94	
Full	3/4	0.620	62.4	52.8	6.22	
Full	2/3	0.576	58.2	49.3	8.38	

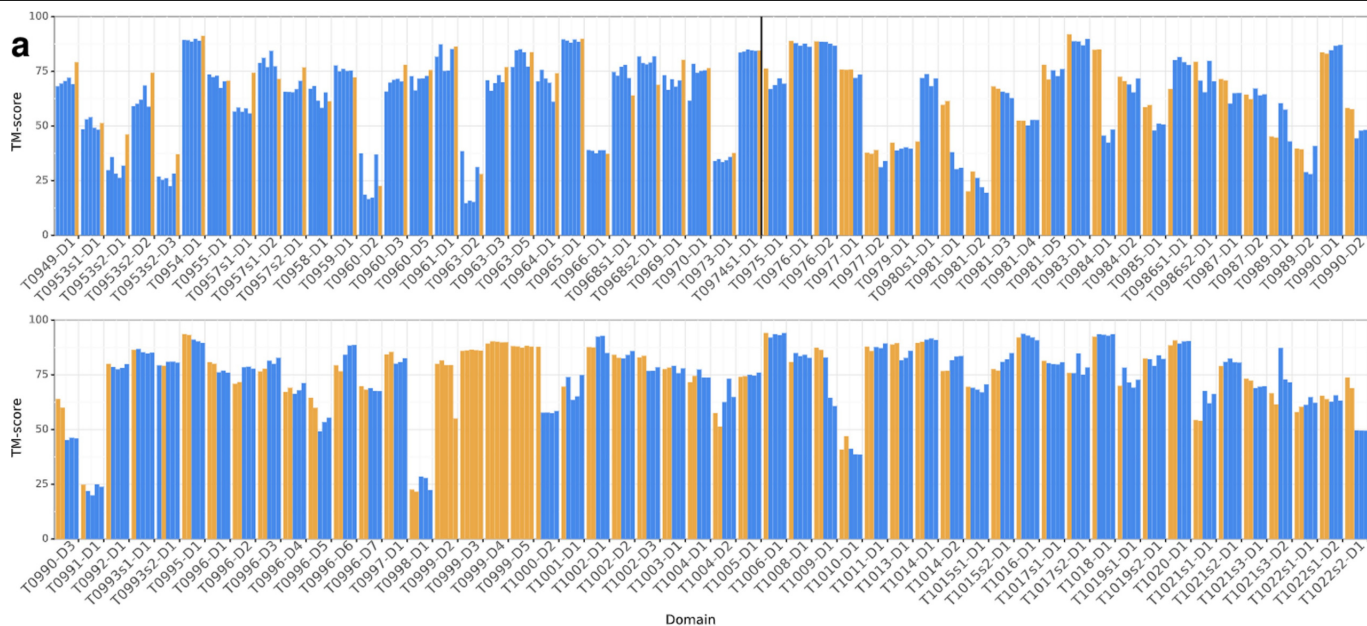
**Extended Data Fig. 3 | Analysis of structure accuracies.** **a**, IDDT<sub>12</sub> versus distogram IDDT<sub>12</sub> (see Methods, ‘Accuracy’). The distogram accuracy predicts the IDDT of the realized structure well (particularly for medium- and long-range residue pairs, as well as the TM score as shown in Fig. 4a) for both CASP13 ( $n = 500$ ; 5 decoys for domains excluding T0999) and test ( $n = 377$ ) datasets. Data are shown with Pearson’s correlation coefficients. **b**, DLDDT<sub>12</sub> against the effective number of sequences in the MSA ( $N_{\text{eff}}$ ) normalized by sequence length ( $n = 377$ ). The number of effective sequences correlates with this measure of distogram accuracy ( $r = 0.634$ ). **c**, Structure accuracy measures, computed on the test set ( $n = 377$ ), for gradient descent optimization of different forms of the potential. Top, removing terms in the potential, and showing the effect of following optimization with Rosetta relax. ‘P’ shows the significance of the

potential giving different results from ‘Full’, for a two-tailed paired data  $t$ -test. ‘Bins’ shows the number of bins fitted by the spline before extrapolation and the number in the full distribution. In CASP13, splines were fitted to the first 51 of 64 bins. Bottom, reducing the resolution of the distogram distributions. The original 64-bin distogram predictions are repeatedly downsampled by a factor of 2 by summing adjacent bins, in each case with constant extrapolation beyond 18 Å (the last quarter of the bins). The two-level potential in the final row, which was designed to compare with contact predictions, is constructed by summing the probability mass below 8 Å and between 8 and 14 Å, with constant extrapolation beyond 14 Å. The TM scores in this table are plotted in Fig. 4b.

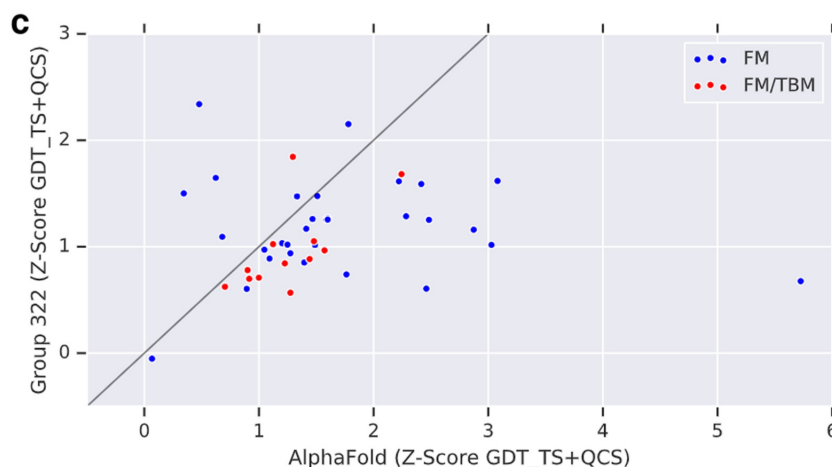


**Extended Data Fig. 4 | TM score versus per-target computation time computed as an average over the test set.** Structure realization requires a modest computation budget, which can be parallelized over multiple machines. Full optimization with noisy restarts (orange) is compared with initialization from sampled torsions (blue). Computation is measured as the

product of the number of (CPU-based) machines and time elapsed and can be largely parallelized. Longer targets take longer to optimize. Figure 2e shows how the TM score increases with the number of repeats of gradient descent.  $n = 377$ .

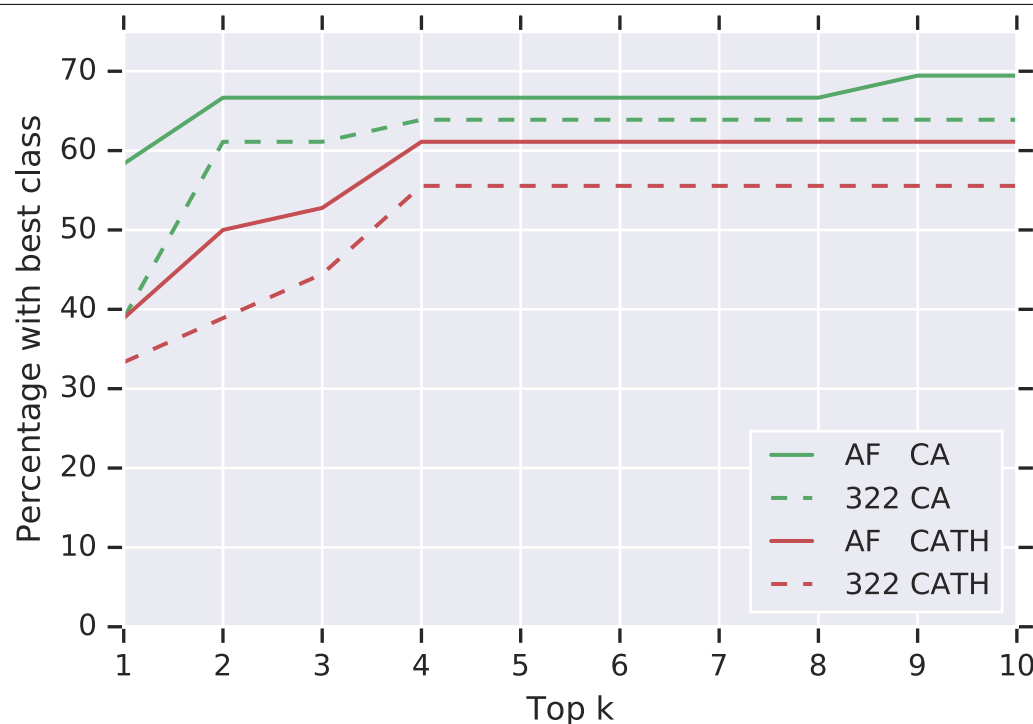


Method	FM	TBM/FM	TBM	All
Top-1	58.0	68.1	76.2	69.9
Best-of-5	62.6	73.6	78.6	73.2
1× gradient descent	58.4	71.6	76.3	70.4
1× fragment assembly	54.3	69.9	74.5	68.0



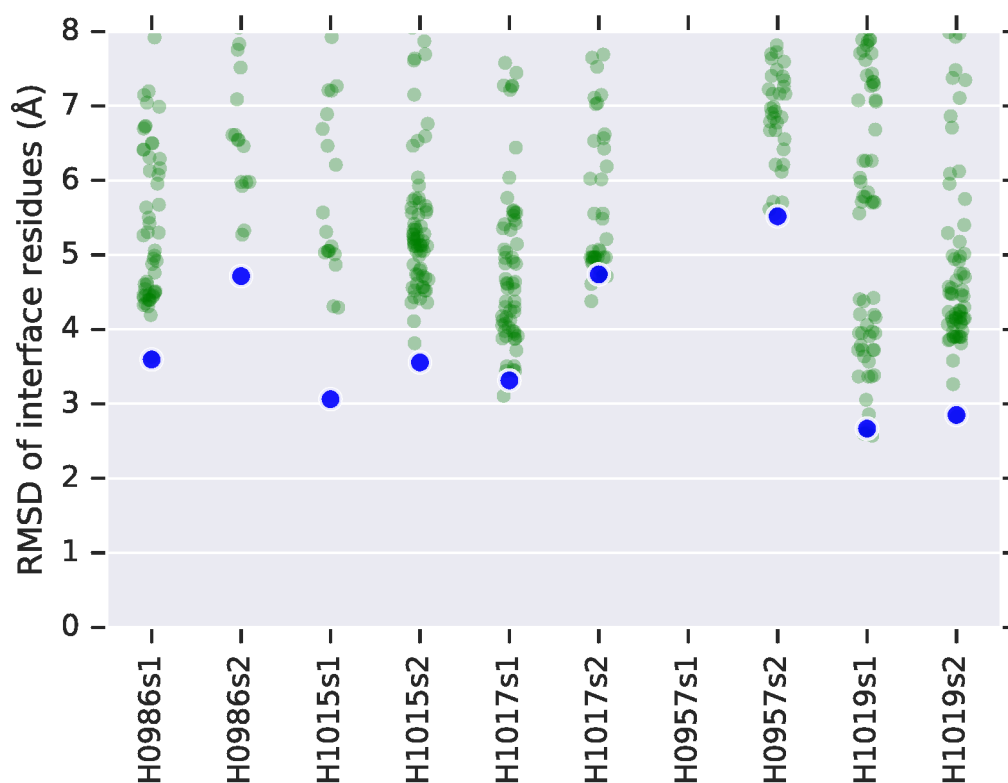
**Extended Data Fig. 5 | AlphaFold CASP13 results.** **a**, The TM score for each of the five AlphaFold CASP13 submissions is shown. Simulated annealing with fragment assembly entries are shown in blue. Gradient-descent entries are shown in yellow. Gradient descent was only used for targets T0975 and later, so to the left of the black line we also show the results for a single 'back-fill' run of gradient descent for each earlier target using the deployed system. T0999 (1,589 residues) was manually segmented based on HHpred<sup>51</sup> homology matching. **b**, Average TM scores of the AlphaFold CASP13 submissions ( $n = 104$  domains), comparing the first model submitted, the best-of-five model

(submission with highest GDT\_TS), a single run of full-chain gradient descent (a CASP13 run for T0975 and later, back-fill for earlier targets) and a single CASP13 run of fragment assembly with domain segmentation (using a gradient descent submission for T0999). **c**, The formula-standardized (z) scores of the assessors for GDT\_TS + QCS<sup>52</sup>, best-of-five for CASPFM ( $n = 31$ ) and FM/TBM ( $n = 12$ ) domains comparing AlphaFold with the closest competitor (group 322), coloured by domain category. AlphaFold performs better ( $P = 0.0032$ , one-tailed paired statistic  $t$ -test).



**Extended Data Fig. 6 | Correct fold identification by structural search in CATH.** Often protein function can be inferred by finding homologous proteins of known function. Here we show that the FM predictions of AlphaFold give greater accuracy in a structure-based search for homologous domains in the CATH database. For each of the FM or TBM/FM domains, the top-one submission and ground truth are compared to all 30,744 CATH S40 non-redundant domains with TM-align<sup>53</sup>. For the 36 domains for which there is a

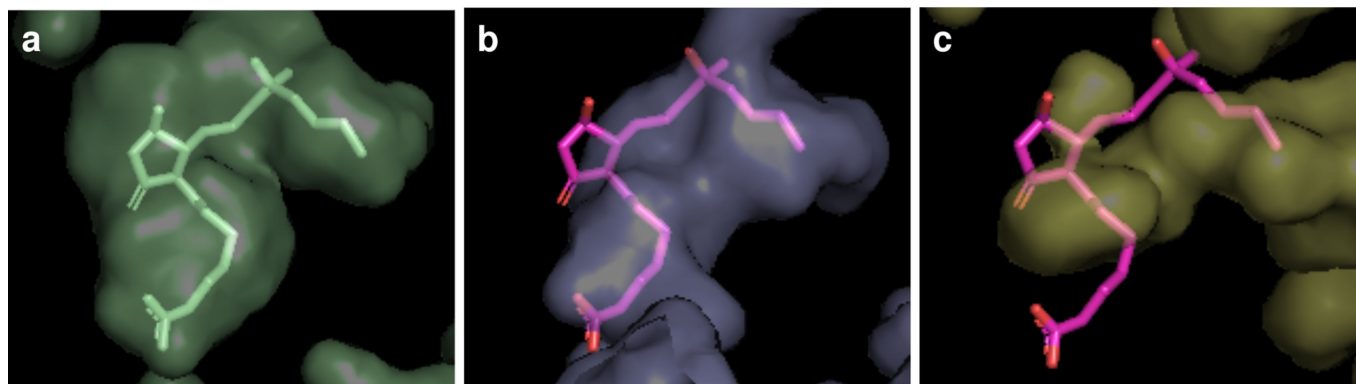
good ground-truth match (score > 0.5), we show the percentage of decoys for which a domain with the same CATH code (CATH in red, CA in green; CAT results are close to CATH results) as the top ground-truth match is in the top-*k* matches with score > 0.5. Curves are shown for AlphaFold and the next-best group (322). AlphaFold predictions determine the matching fold more accurately. Determination of the matching CATH domain can provide insights into the function of a new protein.



**Extended Data Fig. 7 | Accuracy of predictions for interfaces.** Protein–protein interaction is an important domain for understanding protein function that has hitherto largely been limited to template-based models because of the need for high-accuracy predictions, although there has been moderate success<sup>54</sup> in docking with predicted structures up to 6 Å r.m.s.d. This figure shows that the predictions by AlphaFold improve accuracy in the interface regions of chains in hetero-dimer structures and are probably better candidates for docking, although docking did not form part of the AlphaFold

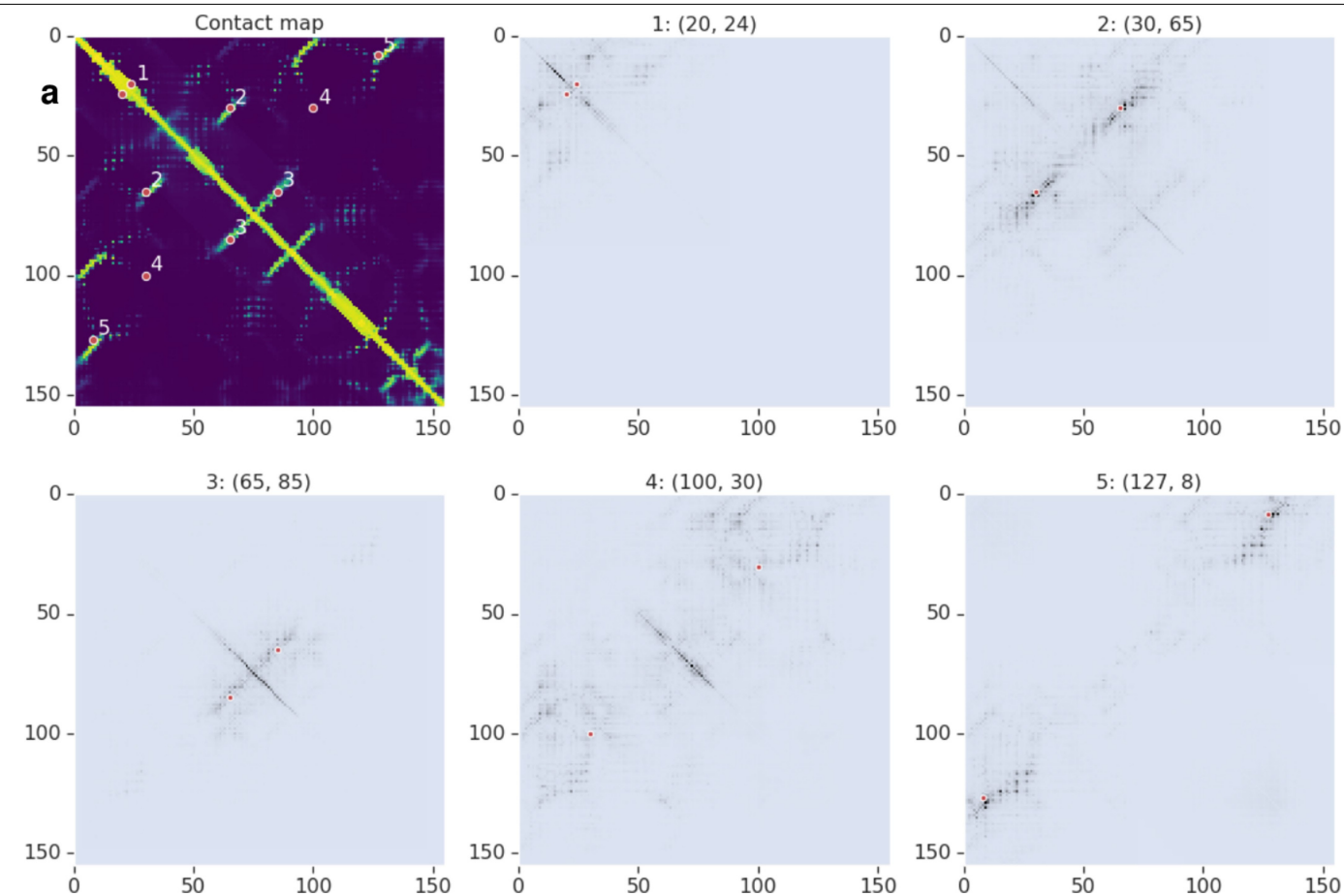
system and all submissions were for isolated chains rather than complexes. For the five all-groups heterodimer CASP13 targets, the full-atom r.m.s.d. values of the interface residues (residues with a ground-truth inter-chain heavy-atom distance <10 Å) are computed for the chain submissions of all groups (green), relative to the target complex. Results >8 Å are not shown. AlphaFold (blue) achieves consistently high accuracy interface regions and, for 4 out of 5 targets, predicts interfaces below <5 Å for both chains.





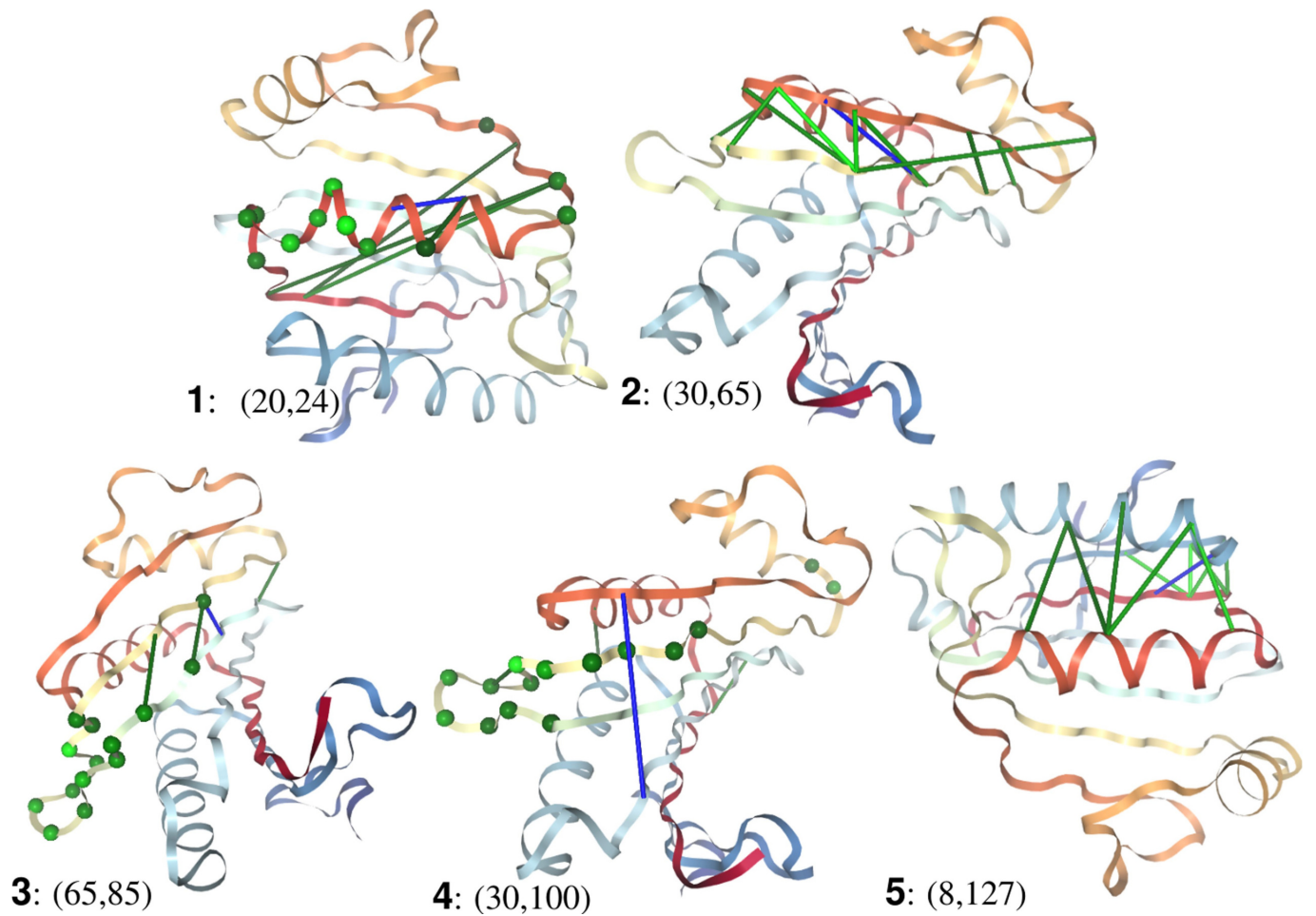
**Extended Data Fig. 8 | Ligand pocket visualizations for T1011.** T1011 (PDB 6M9T) is the EP3 receptor bound to misoprostol-FA<sup>35</sup>. **a**, The native structure showing the ligand in a pocket. **b, c**, Submission 5 (78.0 GDT TS) by AlphaFold (**b**), made without knowledge of the ligand, shows a pocket more similar to the

true pocket than that of the best other submission (322, model 3, 68.7 GDT TS) (**c**). Both submissions are aligned to the native protein using the same subset of residues from the helices close to the ligand pocket and visualized with the interior pocket together with the native ligand position.



**Extended Data Fig. 9 | Attribution map of distogram network.** The contact probability map of T0986s2, and the summed absolute value of the Integrated Gradient,  $\sum_c |S_{i,j,c}^{IJ}|$ , of the input two-dimensional features with respect to the expected distance between five different pairs of residues ( $I, J$ ): (1) a helix self-

contact, (2) a long-range strand-strand contact, (3) a medium-range strand-strand contact, (4) a non-contact and (5) a very long-range strand-strand contact. Each pair is shown as two red dots on the diagrams. Darker colours indicate a higher attribution weight.



**Extended Data Fig. 10 | Attribution shown on predicted structure.** For T0986s2 (TM score 0.8), the top 10 input pairs, including self-pairs, with the highest attribution weight for each of the five output pairs shown in Extended Data Fig. 9, are shown as lines (or spheres for self-pairs) coloured by sensitivity,

lighter green colours indicate more sensitive, and the output pair is shown as a blue line.

## Reporting Summary

Nature Research wishes to improve the reproducibility of the work that we publish. This form provides structure for consistency and transparency in reporting. For further information on Nature Research policies, see [Authors & Referees](#) and the [Editorial Policy Checklist](#).

### Statistical parameters

When statistical analyses are reported, confirm that the following items are present in the relevant location (e.g. figure legend, table legend, main text, or Methods section).

n/a Confirmed

- ☐ ☒ The exact sample size ( $n$ ) for each experimental group/condition, given as a discrete number and unit of measurement
- ☐ ☒ An indication of whether measurements were taken from distinct samples or whether the same sample was measured repeatedly
- ☐ ☒ The statistical test(s) used AND whether they are one- or two-sided  
*Only common tests should be described solely by name; describe more complex techniques in the Methods section.*
- ☐ ☒ A description of all covariates tested
- ☐ ☒ A description of any assumptions or corrections, such as tests of normality and adjustment for multiple comparisons
- ☐ ☒ A full description of the statistics including central tendency (e.g. means) or other basic estimates (e.g. regression coefficient) AND variation (e.g. standard deviation) or associated estimates of uncertainty (e.g. confidence intervals)
- ☒ ☐ For null hypothesis testing, the test statistic (e.g.  $F$ ,  $t$ ,  $r$ ) with confidence intervals, effect sizes, degrees of freedom and  $P$  value noted  
*Give  $P$  values as exact values whenever suitable.*
- ☒ ☐ For Bayesian analysis, information on the choice of priors and Markov chain Monte Carlo settings
- ☒ ☐ For hierarchical and complex designs, identification of the appropriate level for tests and full reporting of outcomes
- ☐ ☒ Estimates of effect sizes (e.g. Cohen's  $d$ , Pearson's  $r$ ), indicating how they were calculated
- ☐ ☒ Clearly defined error bars  
*State explicitly what error bars represent (e.g. SD, SE, CI)*

Our web collection on [statistics for biologists](#) may be useful.

### Software and code

Policy information about [availability of computer code](#)

#### Data collection

To ingest and pre-process the data, we used the following tools: PDB 2018-03-15 ; CATH 2018-03-16; HHblits based on version 3.0-beta.3; HHpred web server; Uniclust30 2017-10; PSI-BLAST version 2.6.0; SST web server (March 2019); BioPython v1.65; Rosetta v3.5; TM-align 20160521, as well as custom code written using Python 2.7. See the methods section for more details.

#### Data analysis

The networks used the TensorFlow library with custom extensions. Inference code for distance prediction networks used in CASP13 will be open-sourced. Analysis was performed with custom code written in Python 2.7. Visualizations were made with PyMol 2.2.0 software. Please see methods section for more detail.

For manuscripts utilizing custom algorithms or software that are central to the research but not yet described in published literature, software must be made available to editors/reviewers upon request. We strongly encourage code deposition in a community repository (e.g. GitHub). See the Nature Research [guidelines for submitting code & software](#) for further information.

## Data

Policy information about [availability of data](#)

All manuscripts must include a [data availability statement](#). This statement should provide the following information, where applicable:

- Accession codes, unique identifiers, or web links for publicly available datasets
- A list of figures that have associated raw data
- A description of any restrictions on data availability

The following public datasets were used in this work:

- PDB 2018-03-15
- CATH 2018-03-16
- Uniclust30 2017-10
- PSI-BLAST nr dataset (as of 2017-12-15)

We will make available our train/test split (CATH domain codes).

## Field-specific reporting

Please select the best fit for your research. If you are not sure, read the appropriate sections before making your selection.

☒ Life sciences ☐ Behavioural & social sciences ☐ Ecological, evolutionary & environmental sciences

For a reference copy of the document with all sections, see [nature.com/authors/policies/ReportingSummary-flat.pdf](https://www.nature.com/authors/policies/ReportingSummary-flat.pdf)

## Life sciences study design

All studies must disclose on these points even when the disclosure is negative.

### Sample size

Tests were carried out on two sets of domains generated by predetermined methods.

The principal set consisted of 104 CASP13 domains as segmented by the CASP13 assessors. (In some figures 100 domains are used, excluding the domains of T0999 where slightly different methods were used; or 41 considering FM + TBM/FM targets)

For the CASP13 datasets, accuracy measures are reported using structures & distance distributions computed during CASP (except for the "back-fill" gradient descent structures where specified). With n=41 domains, we show (Extended Data Figure 5) that (with p=0.0032) AlphaFold's results were better than the next best group.

The other test set of 377 domains was extracted from PDB, chosen to be from separate homologous superfamilies (CATH code) none of which were represented in the training set. For each superfamily the exemplar was chosen at random from the s35 cluster representatives.

Extended Data Table 3c shows that this sample size is sufficient to show that certain terms in the potential (but not score2) make a difference in the final GDT\_TS score.

### Data exclusions

The training set used one example per s35 cluster, using the representative chosen by CATH.

We further balance (and reduce the size of) the test set by keeping one example per superfamily.

CASP13 domains are only those "all groups" targets which were scored as part of CASP13.

Some CASP13 targets were excluded by the assessors e.g. because of publications or failure to solve a structure.

### Replication

Actual competition entries were used and were not replicated, but we show comparisons for top-5 decoys.

Multiple networks were trained independently and were found to give consistent results (on CASP11/12 validation sets). 4 such networks, yielding similar results, were used in CASP and are made available with the source code.

Structure generation is stochastic, but we show (Extended Data Fig 4) that it converges with relatively few attempts, so results are reproducible.

### Randomization

Superfamilies were randomly assigned to PDB train or PDB test set.

For each superfamily in the test set, a random s35 cluster representative was picked for the 377 example test set.

CASP13 assessors used a manual process (blind to the investigators) to determine evaluation units and to determine whether each domain should be treated as FM, TBM or TBM/FM.

### Blinding

Investigators were blind to the CASP13 targets which were sequestered during the assessment.

Investigators were not blind to the PDB train/test split, but cross-validation used CASP11 & 12 domains and the main results are on the blind CASP13. Models were not retrained after defining the 377 domain set.

## Reporting for specific materials, systems and methods



Materials & experimental systems

n/a	Involved in the study
<input checked="" type="checkbox"/>	<input type="checkbox"/> Unique biological materials
<input checked="" type="checkbox"/>	<input type="checkbox"/> Antibodies
<input checked="" type="checkbox"/>	<input type="checkbox"/> Eukaryotic cell lines
<input checked="" type="checkbox"/>	<input type="checkbox"/> Palaeontology
<input checked="" type="checkbox"/>	<input type="checkbox"/> Animals and other organisms
<input checked="" type="checkbox"/>	<input type="checkbox"/> Human research participants

Methods

n/a	Involved in the study
<input checked="" type="checkbox"/>	<input type="checkbox"/> ChIP-seq
<input checked="" type="checkbox"/>	<input type="checkbox"/> Flow cytometry
<input checked="" type="checkbox"/>	<input type="checkbox"/> MRI-based neuroimaging

# Structure of SAGA and mechanism of TBP deposition on gene promoters

<https://doi.org/10.1038/s41586-020-1944-2>

Received: 20 June 2019

Accepted: 19 November 2019

Published online: 22 January 2020

Gabor Papai<sup>1,2,3,4</sup>, Alexandre Frechard<sup>1,2,3,4</sup>, Olga Kolesnikova<sup>1,2,3,4</sup>, Corinne Crucifix<sup>1,2,3,4</sup>, Patrick Schultz<sup>1,2,3,4\*</sup> & Adam Ben-Shem<sup>1,2,3,4\*</sup>

SAGA (Spt–Ada–Gcn5–acetyltransferase) is a 19-subunit complex that stimulates transcription via two chromatin-modifying enzymatic modules and by delivering the TATA box binding protein (TBP) to nucleate the pre-initiation complex on DNA, a pivotal event in the expression of protein-encoding genes<sup>1</sup>. Here we present the structure of yeast SAGA with bound TBP. The core of the complex is resolved at 3.5 Å resolution (0.143 Fourier shell correlation). The structure reveals the intricate network of interactions that coordinate the different functional domains of SAGA and resolves an octamer of histone-fold domains at the core of SAGA. This deformed octamer deviates considerably from the symmetrical analogue in the nucleosome and is precisely tuned to establish a peripheral site for TBP, where steric hindrance represses binding of spurious DNA. Complementary biochemical analysis points to a mechanism for TBP delivery and release from SAGA that requires transcription factor IIA and whose efficiency correlates with the affinity of DNA to TBP. We provide the foundations for understanding the specific delivery of TBP to gene promoters and the multiple roles of SAGA in regulating gene expression.

Transcription of protein-encoding genes begins with the formation of a pre-initiation complex (PIC) comprising RNA polymerase II and several general transcription factors<sup>2</sup>. PIC assembly is nucleated by loading TBP onto promoter DNA<sup>3</sup>, a focal point for regulated gene expression<sup>4</sup>. Two multiprotein complexes, transcription factor IID (TFIID) and SAGA, can deliver TBP to gene promoters<sup>5,6</sup> and are required for global gene expression in yeast<sup>7,8</sup>.

The 1.6-MDa SAGA complex also stimulates transcription via its two chromatin-modifying enzymatic activities. The complex comprises 19 subunits organized in four modules with distinct functions<sup>2,9</sup>: a histone acetyltransferase (HAT) module, a histone deubiquitinase (DUB) module, the 430-kDa Tra1 subunit that serves as a docking platform for transcription factors that recruit SAGA to activating DNA sequences upstream of the promoter, and a 10-subunit central module that is physically connected to all other modules and is responsible for recruiting TBP to SAGA (Extended Data Fig. 1a).

Structures of several individual isolated components of SAGA, notably the DUB module<sup>10,11</sup>, the catalytic subunit of the HAT module (Gcn5)<sup>12</sup> and Tra1<sup>13,14</sup> have been obtained. Previous electron microscopy studies positioned Tra1 in one lobe of the SAGA complex, but all other subunits appeared together as a main lobe that could only be described at low resolution<sup>15,16</sup>.

The central module of yeast SAGA shares five TBP-associated factors (TAFs) with TFIID. Both complexes also contain multiple histone-fold domains that associate into heterodimers and higher-order oligomers<sup>17,18</sup> (Extended Data Fig. 1a, b). The central module is therefore expected to be structurally related to TFIID, suggesting that TBP binding in both complexes shares some common features. Progress in defining the

architecture of TFIID was reported recently; however, the machinery responsible for TBP binding and delivery remained poorly resolved<sup>19,20</sup>.

Here we report the 3.5 Å-resolution structure of the full SAGA complex bound to TBP, determined from cryo-electron microscopy (cryo-EM) maps that show clear density for the majority of the protein side chains. Our structure describes in atomic detail the network of interactions that coordinate the functional domains of SAGA as well as a machinery precisely geared to binding TBP and preventing aberrant transcription initiation. With complementary experimental findings, our structure points to a mechanism of TBP delivery and release from SAGA that depends on TFIIA and the affinity of promoter DNA to TBP, providing new insights into regulation of PIC assembly.

## Overall architecture of SAGA

We reconstituted the complex with SAGA purified from the yeast *Komagataella phaffii* (also known as *Pichia pastoris*), full length TBP and ubiquitin aldehyde and collected a dataset of more than one million particles. Image analysis resulted in a map of the full SAGA complex at 3.8 Å resolution, calculated from 338,850 selected particles (Fig. 1a, Extended Data Figs. 1c, d, 2, Supplementary Video 1, Extended Data Table 1). Focused refinement of the main lobe and of Tra1 further improved their average resolution to 3.5 Å, with many regions reaching as high as 3 Å. Hence, Tra1 and the central module, as well as the domains of Sgf73 that anchor the DUB to the central module, show clear densities for the majority of side chains (Fig. 1b, Extended Data Fig. 2b, c).

At the periphery of SAGA, exposed next to Spt3, we identified the distinctive saddle-shaped density of the conserved core of TBP (cTBP),

<sup>1</sup>Institut de Génétique et de Biologie Moléculaire et Cellulaire, Integrated Structural Biology Department, Equipe labellisée Ligue Contre le Cancer, Illkirch, France. <sup>2</sup>Centre National de la Recherche Scientifique, UMR7104, Illkirch, France. <sup>3</sup>Institut National de la Santé et de la Recherche Médicale, U1258, Illkirch, France. <sup>4</sup>Université de Strasbourg, Illkirch, France. \*e-mail: patrick.schultz@igbmc.fr; adam@igbmc.fr

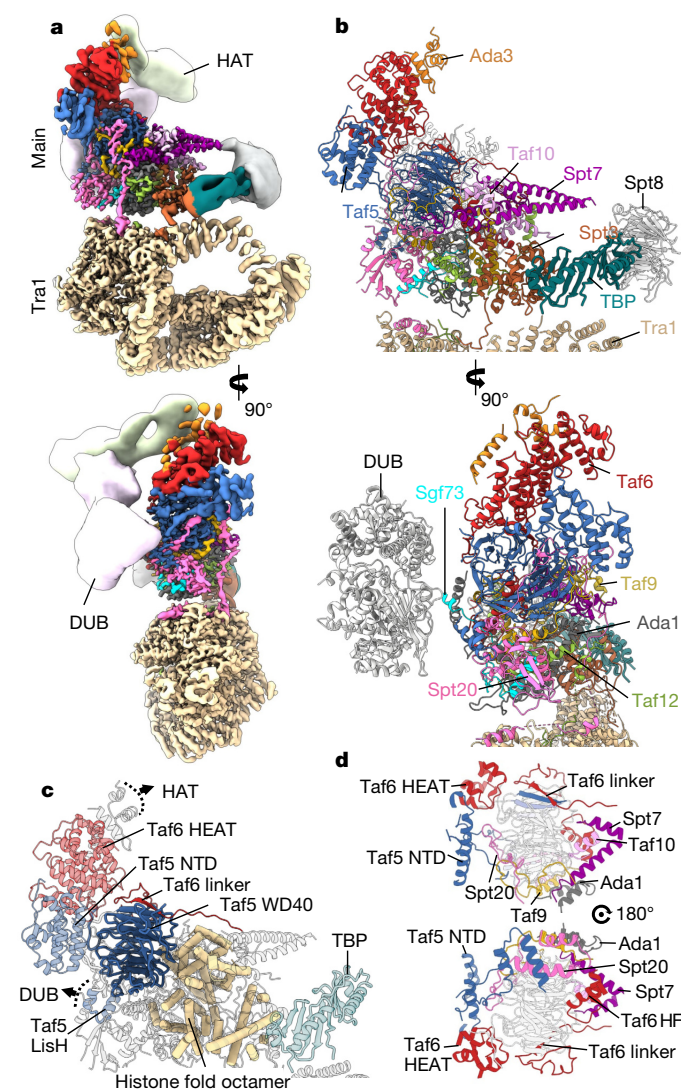


**Fig. 1 | Structure of the yeast SAGA-TBP complex.** **a**, Front (top) and side (bottom) views of a composite cryo-EM reconstruction of the yeast SAGA-TBP complex. Maps from focused refinements of Tra1 (tan), DUB (light pink), Spt8 (white), the main lobe and TBP (blue-green) were combined. HAT density (light green) is taken from the low-pass-filtered map of the full complex. **b**, Corresponding views of the atomic model of the SAGA-TBP complex focusing on the main lobe. **c**, The Taf5 WD40 domain structurally orchestrates the main lobe. Orientation as in **a** (top). **d**, Intricate network of protein contacts with the Taf5 WD40 domain (white).

which was absent in a separate map of SAGA lacking TBP (Extended Data Fig. 3a–d). Local classification revealed sufficient secondary structural features to guide the precise positioning of cTBP. Site-specific cross-linking and documented mutations resolved any ambiguity in orientation arising from the pseudosymmetric fold of cTBP<sup>21,22</sup>. A disc-shaped density neighbouring TBP was assigned to the WD40 protein Spt8, which was shown to interact with TBP<sup>23</sup> (Extended Data Fig. 3e, f). At the opposite pole of the main lobe, the DUB crystal structure fits into and occupies a large but not well-resolved density that is nearly completely detached from and independent of SAGA. The DUB module is connected to the main lobe by a narrow, elongated density that contacts the surface of SAGA proximal to the Spt20 SEP domain and the LisH domain of Taf5 (Fig. 1a, b, Extended Data Fig. 1). The HAT enzymatic module adopts multiple conformations and orientations. Accordingly, the bulk of this module is visible only as an elongated featureless density at the tip of our map. Nevertheless, we could identify its docking site

on SAGA, where two helical domains—attributable to Ada3—lie at the surface of the Taf6 HEAT-repeats domain.

### Taf5 orchestrates the main lobe

The main lobe is dominated by the seven-blade WD40 propeller of Taf5 (Fig. 1c). This domain occupies a central position, serving as a structural hub that connects all major SAGA functions. The flat top face of the propeller disc clamps together the Taf5 N-terminal domain (NTD) and the Taf6 HEAT repeats that bind the HAT module. The opposite bottom face of WD40 holds the histone-fold machinery that ultimately binds TBP and connects to the DUB module and Tra1.

The positions of the Taf5 NTD and Taf6 HEAT repeats are markedly different in SAGA compared with TFIID<sup>19</sup>, as these domains assume different roles in establishing connections to the enzymatic DUB (the LisH extension of Taf5 NTD) and HAT (Taf6) modules (Fig. 1c, Extended Data Fig. 4). Compared with TFIID, the Taf5 NTD in SAGA makes a rotation of almost 180 degrees around the WD40 domain, and the Taf6 HEAT repeats, which are remote in TFIID, are relocated to the vicinity of the top face of WD40 in SAGA. Notably, unlike SAGA, TFIID harbours two copies of Taf5 and Taf6 that are held together by homodimerization of Taf5 NTDs and Taf6 HEAT repeats. As a result of all these variations and additional interactions with SAGA-specific subunits, the Taf5 WD40 environment is very different in SAGA compared with TFIID.

The ability of Taf6 HEAT repeats to occupy three different positions in SAGA and TFIID relative to the histone fold is afforded by a 136-residue linker between these two domains. The Taf6 linker partially encircles the Taf5 WD40 domain (Fig. 1c), and its position is stabilized by several interactions along its trajectory. Most notably, the Taf6 linker residues T135–L141 add a  $\beta$ -strand to the last blade of the WD40 propeller, forming an inter-protein  $\beta$ -sheet.

WD40 domains are recognized as potential hubs that mediate protein–protein interactions. The Taf5 WD40 in SAGA is a noteworthy demonstration of this capacity, as it associates with at least 11 different protein domains (Fig. 1c, d). Taf5 is thus a centrally located master hub that orchestrates the architecture of the entire main lobe.

### A deformed histone-fold octamer

An octamer consisting of four histone-fold pairs arranged in a disc-shaped spiral, similar to the nucleosomal histone octamer, has been proposed to reside in TFIID and SAGA<sup>24,25</sup>. Our structure presents an atomic model of the full histone-fold octamer that resides at the core of SAGA and, most probably with minor variations, in the TBP-binding lobe of TFIID (Fig. 2a). It reveals a disparity between histone-fold interactions in SAGA compared with the nucleosome, particularly regarding the incorporation into SAGA of the TBP-binding subunit Spt3, a homologue of the TFIID Taf11–Taf13 histone-fold pair<sup>24</sup> (Supplementary Video 2).

In the nucleosome, the interaction between neighbouring histone pairs is mediated by a tightly packed four-helix bundle composed of helices  $\alpha$ 2 and  $\alpha$ 3 of one histone from each pair<sup>26</sup>. The SAGA histone-fold pairs are organized along the spiral in the following order: Taf6–Taf9, Taf12–Ada1, Spt7–Taf10 and Spt3, which contains two histone folds, one at each of its ends: nSpt3-HF and cSpt3-HF. Whereas all other histone-fold pairs are oriented as in the nucleosome, the Spt3 pair is tilted by 20 degrees compared with its analogous nucleosome H2A–H2B histone pair (Fig. 2b). This tilt prevents participation of the Taf10  $\alpha$ 3-helix in the interaction, shears the four-helix bundle and therefore nearly completely frees Spt3 from its association with the histone-fold octamer. The remaining contact is facilitated by a slight tilt in Taf10 and maintained by only very few bonds between Spt3 and Taf10 residues (Fig. 2c). To secure incorporation of Spt3 into SAGA, the C-terminal tail of Spt3 inserts into the centre of the spiral disc (a void volume in the nucleosome), makes a near complete circle and forms single bonds with each of the other histone folds in SAGA (Fig. 2d).

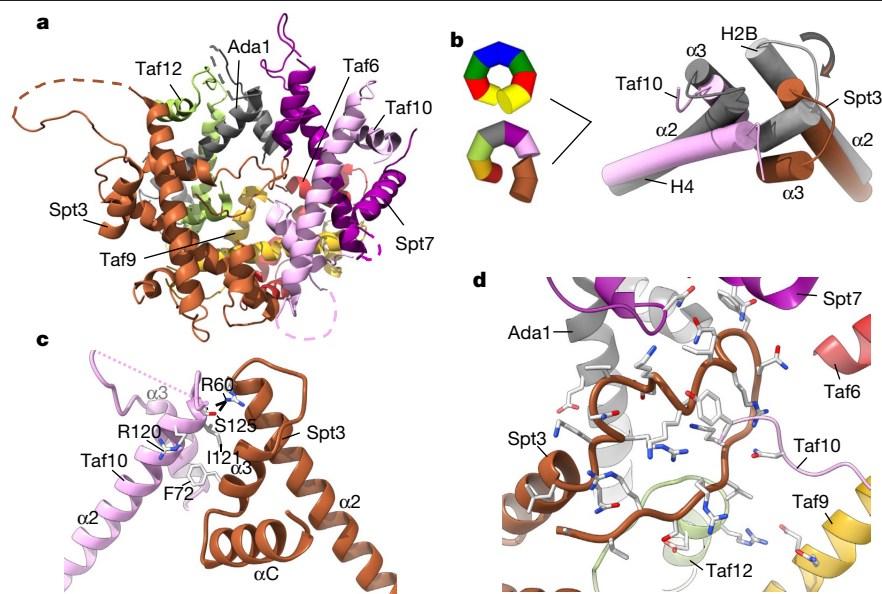


**Fig. 2 | The octamer of histone folds.** **a**, Structural organization of the four pairs of histone folds forming an octamer analogous to the nucleosomal histones. **b**, Left, schematic representation of the histone-fold octamer in the nucleosome (top) and in SAGA (bottom). Right, the four-helix bundle connecting the Spt7–Taf10 histone-fold pair (pink) to the partially dislodged

nSpt3–cSpt3 histone-fold pair (brown) compared with the analogous nucleosome interaction (grey). **c**, Detailed view of the interaction between the Spt7–Taf10 histone-fold pair and the nSpt3–cSpt3 histone-fold pair. **d**, The C-terminal tail of Spt3 inserts into the centre of the histone-fold octamer.

The Spt3 deviation from the canonical octamer does not originate from a single structural determinant. The atypical sequences of the histone folds (in particular Taf10 and Spt3), the long Taf10 loop between its  $\alpha 2$ - and  $\alpha 3$ -helices and the inherent asymmetry arising from the eight different histone-fold proteins involved all contribute. In this respect, it is noteworthy that the deviation from the nucleosome pattern is already apparent at the preceding four-helix bundle where the association almost entirely lacks hydrophobic packing (Extended Data Fig. 5). We propose that this assembly of histone folds, which deviates considerably from the symmetric arrangement in the nucleosome, is geared specifically towards a delicate balance between a rigid Spt3 that is firmly embedded into the octamer and an overly flexible Spt3 that associates with SAGA through loops alone. Below we examine these ideas in the context of TBP binding and release from SAGA.

### TBP binding and release machinery

SAGA presents TBP at the extremity of the main lobe embracing it by binding to two opposite ends of its surface and orienting the DNA-binding cleft of TBP towards the main body of SAGA (Fig. 3a). The principal component in coupling TBP to SAGA and determining its position is Spt3. The C-terminal stirrup of TBP is the primary binding site for Spt3, similar to the interaction between TBP and TFIIB<sup>27</sup>. In SAGA, the stirrup is nearly completely buried and forms multiple contacts in a large pocket created by helices  $\alpha N$  and  $\alpha 2$  from cSpt3–HF and by helix  $\alpha C$ , which is joined to nSpt3–HF via a conserved two-amino-acid rigid turn (Figs. 2c, 3b). The association of the C-terminal half of the pseudosymmetric cTBP with Spt3 is in line with previous biochemical and genetic data<sup>21,22</sup> (Extended Data Fig. 6). Indeed, accommodation of the cTBP N-terminal half by Spt3 is unfavourable, as this would involve the negatively charged D81 facing a negatively charged patch on Spt3 and place the bulky charged R98 where the C-terminal stirrup L189 is tightly packed against a hydrophobic crevice (Fig. 3b).

In contrast to Spt3, we find that Spt8 is not part of the central module (Fig. 3a). It is flexibly tethered via a fuzzy density to the outward tips of two long helices, extensions of each end of the Spt7 histone fold. The fuzzy density corresponds, at least in part, to a 30-residue-long

unstructured region in the C terminus of Spt7, the deletion of which results in loss of Spt8<sup>28</sup>. The connection of Spt8 to the N-terminal half of cTBP is flexible and appears to have a secondary role in positioning TBP. This finding is consistent with deletion mutants of Spt3 in yeast showing a sharp decline in global levels of newly synthesized mRNA, whereas impairment of Spt8 had almost no effect<sup>7</sup>. We suggest that Spt8 has an auxiliary role in tuning the orientation of TBP and in competing with other TBP-associated proteins<sup>29–31</sup>. The flexible tethering of Spt8 to the SAGA core contributes to small movements of TBP that are reflected in a lower local resolution. This ‘breathing’ of TBP might be important in transiently enabling initial access to DNA or regulatory factors.

The space between TBP and the main lobe of SAGA is just wide enough to accommodate a double-stranded DNA bent by TBP (Fig. 4a). However, the path of DNA is obstructed by structural elements located distally to the TBP DNA-binding cleft, notably the peripheral ring of the Tra1 HEAT repeats, as well as the nSpt3–HF helix  $\alpha C$ , a major component of the pocket that envelops the C-terminal TBP stirrup. Gel-shift assays (Fig. 4b, Extended Data Fig. 7b) and pull-down assays (Fig. 4c, d,

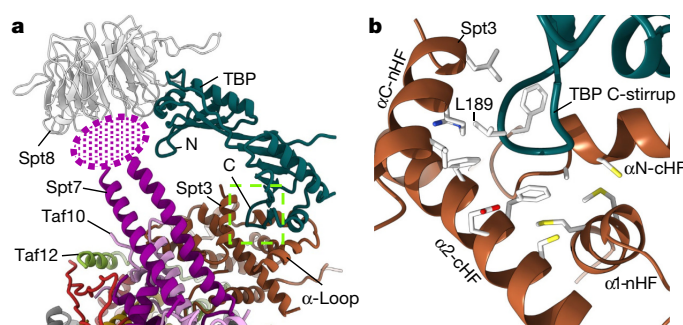


**Fig. 3 | Architecture of the TBP-docking site.** **a**, cTBP interacts with Spt3 mainly through the stirrup of its C-terminal half (labelled C), whereas its N-terminal half (N) binds to the Spt8 WD40 domain. A poorly resolved Spt7 domain (pink ellipse) connects Spt8 to the central module. **b**, Enlargement of the boxed area in **a**, depicting the interaction between the C-terminal stirrup of TBP and a pocket created by Spt3 helices.



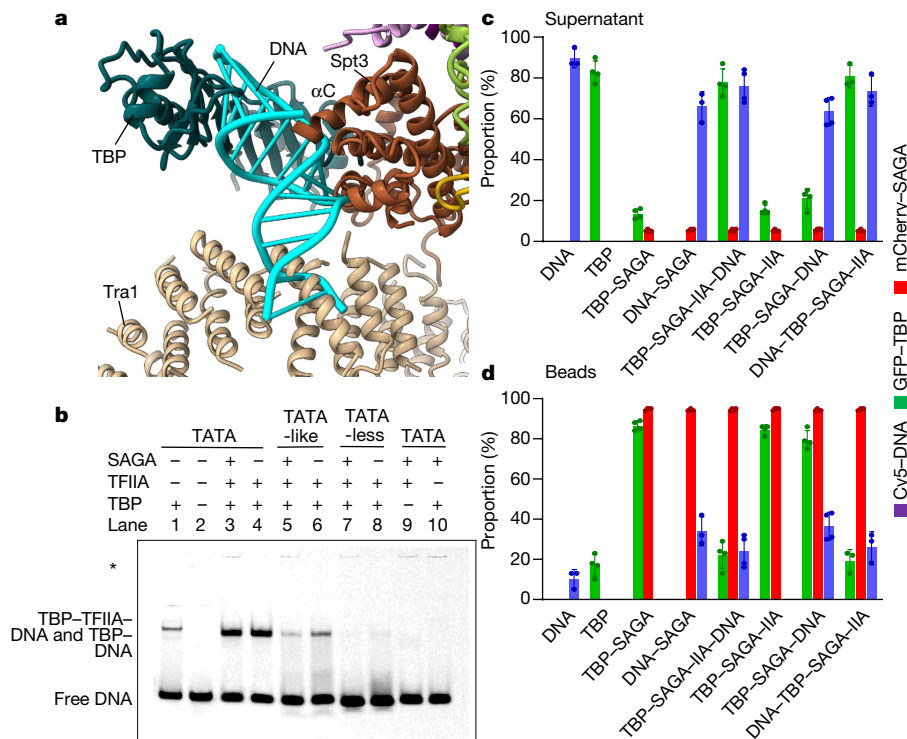


**Fig. 4 | Steric hindrance for TBP binding to DNA and TFIIA-dependent TBP delivery.** **a**, DNA (light blue) was modelled into the DNA-binding cleft of TBP by superposing the structure of cTBP-DNA (PDB: 1YTF) on SAGA-bound cTBP. DNA clashes with Tra1 HEAT repeats and with Spt3 helix  $\alpha C$ . **b**, Gel-shift assay using a Cy5-labelled TATA-containing DNA (TATA), a TATA-like DNA and a non-specific DNA (TATA-less). DNA probes and TFIIA (as indicated) were added to a preformed SAGA-TBP complex. The asterisk indicates minor non-specific DNA

association with SAGA. **c**, **d**, Pull-down assays with beads that capture SAGA. Components were labelled with different fluorophores and incubated as for gel-shift experiments. The proportion of fluorescent signal that is due to the unbound (**c**) and bound (**d**) complexes is presented. The rightmost bars represent experiments in which TBP was first incubated with DNA and TFIIA before the addition of SAGA. Experiments were repeated three to four times. Data are shown as dots for individual experiments and mean  $\pm$  s.d.

Extended Data Fig. 7a) of DNA binding to SAGA-TBP demonstrate that this mild steric hindrance is nonetheless sufficient to impede binding of even high-affinity DNA containing a consensus TATA box (Fig. 4b, lane 10, Fig. 4c, d).

The general transcription factor TFIIA enhances DNA binding to TBP, competes with Spt8 for occupation of the N-terminal half of cTBP and is found in PICs nucleated by SAGA<sup>32–34</sup>. When a consensus TATA-box-containing DNA was incubated with the SAGA-TBP complex together with TFIIA, TBP was released from SAGA as a ternary DNA-TBP-TFIIA complex (Fig. 4b, lane 3, Extended Data Fig. 7d). The binding of DNA to TBP is coupled with the release of TBP, as we did not observe any DNA associated with SAGA-bound TBP. Indeed, the release of TBP from SAGA can now be understood as being essential for the subsequent steps in assembling the PIC because the clasping of the TBP C-terminal stirrup by Spt3 and TFIIIB are mutually exclusive. TBP was also detached from SAGA, although less efficiently, when DNA bearing the TATA element containing two mismatches was used (Fig. 4b, lanes 5 and 6), whereas no release of TBP was observed when the DNA did not contain any TATA or TATA-like elements (Fig. 4b, lanes 7, 8). These experiments show that the detachment of TBP from SAGA correlates with the affinity of TBP for its DNA substrate.

Our structure suggests that the TFIIA-stimulated mechanism for the concerted DNA binding and TBP release from SAGA includes the following steps: TFIIA first displaces Spt8 from TBP; it then promotes an initial binding of DNA to TBP, thus shifting helix  $\alpha C$  of Spt3, which obstructs the path of DNA. Notably, as helix  $\alpha C$  is firmly joined to helix  $\alpha 3$  in nSpt3-HF, this crucial step is made possible because the deformed octamer does not immobilize this histone fold via a tight four-helix bundle. Shifting helix  $\alpha C$  breaks the pocket that clasps the C-terminal stirrup; TBP can then tilt, allowing DNA to pass in the gap between

Tra1 and the main body of SAGA, completing the binding to DNA. Final release of TBP from SAGA might still require a further conformational change in Spt3. Spt3 alone is unable to bind TBP<sup>23</sup>, and it is tempting to speculate that by shifting helices  $\alpha C$ – $\alpha 3$  of nSpt3-HF, partially loosening Spt3 ties with SAGA, a conformation similar to isolated Spt3 ensues. Following the release of TBP and DNA, helix  $\alpha C$  can regain its position, enabling Spt3 to restore its TBP-binding conformation.

It has been suggested that in TFIID, the association of TBP with spurious DNA is prevented by a helical protein domain that mimics TATA DNA and binds at the DNA cleft of TBP<sup>35</sup>. Remarkably, our maps do not show any substantial density attached at the DNA-binding cleft of TBP. Instead, our structure reveals a mechanism for preventing association of non-specific DNA based on limited steric hindrance, distal to the DNA cleft in TBP. Only the synergy of a cognate TATA or TATA-like DNA with TFIIA can overcome this hindrance.

### Firmly tethered flexible enzymatic modules

The DUB and HAT modules are highly dynamic (Fig. 1a, b, Extended Data Fig. 8a, b), permitting the exploration of a large conformational space in search of their chromatin substrates. The structure shows how these modules maintain a robust binding to SAGA despite this flexibility. The DUB module consists of three subunits and the Sgf73 N-terminal end. The C-terminal part of Sgf73 was implicated in attaching DUB to SAGA, and deletion analysis narrowed down the anchoring region to residues 350–400 in *Saccharomyces cerevisiae* (227–277 in *K. phaffii*), as removal of this region leads to dissociation of an intact DUB module from SAGA<sup>36,37</sup>. We found that these residues form an elongated domain comprising two helices, Sgf73-H1 and Sgf73-H2, connected by a stretched loop and embedded in the central module (Fig. 5a). This



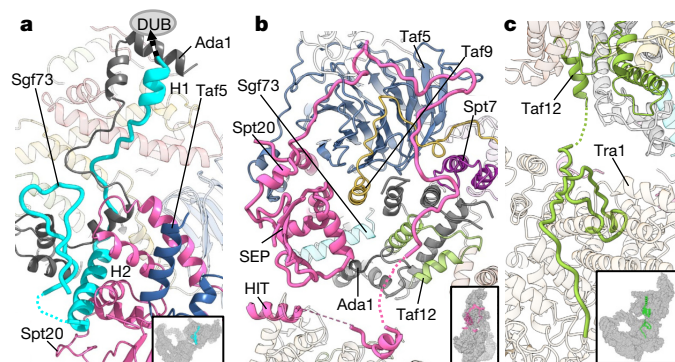


**Fig. 5 | Connecting the DUB module and Tra1 to the central module.** **a**, The Sgf73 domain that contains helices Sgf73-H1 and Sgf73-H2 (cyan) anchors the DUB module within the central module. Sgf73-H2 is embedded in a chamber formed by Spt20 (pink) and Ada1 (dark grey). The insert highlights the depicted region within the overall structure of SAGA. **b**, **c**, Bridges between the central module and Tra1 (tan) established by Spt20 (pink) (**b**) and Taf12 (green) (**c**).

DUB-anchoring domain traverses the core, entering proximal to the Taf9 histone fold and exiting next to the Spt20 SEP domain. Sgf73-H2 lies in a chamber-like structure composed of several helices from the Spt20 SEP domain and from an elongated domain of Ada1. The chamber consists exclusively of SAGA-specific elements with no contribution from subunits shared with TFIID. Thus, a dedicated environment is created at the core of SAGA, partially occupied in TFIID by the Taf5 NTD, to house the helix that anchors the DUB module into SAGA. The DUB module is tethered to the SAGA core through a 164-residue poorly resolved linker that connects the anchoring domain to the N-terminal end of Sgf73 (Extended Data Fig. 8c, d).

In contrast to the DUB, no parts of the HAT module are embedded in the SAGA core (Fig. 1b). The HAT densities emerge, harbouring two Ada3 helical domains, at the surface of the Taf6 HEAT repeats that are used for homodimerization in TFIID (Extended Data Fig. 8e, f).

Thus, the two enzymatic modules of SAGA adopt very different strategies to remain bound to SAGA while maintaining their freedom of movement. The DUB module is a stably folded structure<sup>10,11</sup> that gains independence through an unstructured long linker that has little contact with the SAGA surface until it connects to an extension firmly embedded in the SAGA core. The HAT module, on the other hand, is itself a flexible structure<sup>12</sup>, with several submodules as well as a large proportion of intrinsically unfolded sequences, and it binds only to the surface of the SAGA core, using two helical domains of Ada3.

### Network of unstructured protein elements

Three distinct bridges serve to physically and possibly functionally couple Tra1 to the central module. The first bridge is established by a highly dispersed domain of Spt20 that originates as a strand joining the Spt20 SEP  $\beta$ -sheet, followed by a helix-turn-helix that also interacts extensively with the Spt20 SEP domain (Fig. 5b). It continues as a loop of around 70 residues, touching several subunits as it traverses the surface of the SAGA core on its 160 Å-long way to Tra1. There, it forms a helix that associates with the surface of the FAT (FRAP, ATM and TRRAP) domain and is followed by a second helix, which is clamped within a concave structure in Tra1. This second helix corresponds to the Spt20 region that is denoted as the HIT domain and the deletion of which prevents assembly of Tra1 into SAGA<sup>38</sup>. An exceptionally long loop that precedes the histone fold of Taf12 is responsible for establishing the second bridge (Fig. 5c). Residues 430–474 from this loop trace a lasso-shaped thread at the surface of the Tra1 FAT domain within the deep groove formed between two tetratricopeptide repeat-containing domains (TRDs). The third bridge is formed by the loop connecting the

second and third helices of cSpt3-HF as it infiltrates between two HEAT repeats of the Tra1 ring (Extended Data Fig. 9a, b).

We also observe several protein stretches that lack secondary structure elements but contact multiple subunits and contribute considerably to an intricate intertwined network of interactions within the main lobe of SAGA. For example, the C-terminal tail in Taf9 and the short loop preceding it contact four histone folds and six other domains (Extended Data Fig. 9c). This network of interactions is necessary for stabilizing an octamer that could not be reconstituted *in vitro* from its constituent histone folds and underlies the effects of some mutations on functions that do not directly involve the altered proteins<sup>39</sup>.

### Conclusion

The high-resolution description of SAGA unravels how the central module acts as a scaffold that coordinates an activator-interaction platform and two enzymatic modules, as well as TBP binding and release. Our structure reveals that a deformed histone-fold octamer, aided by components of Spt7 and Spt8, is finely tuned to define a TBP-docking site in which distal steric hindrance represses DNA binding, thus preventing unwanted transcription initiation. However, with the assistance of TFIIA, TBP can productively bind DNA to form a ternary TBP–TFIIA–DNA complex that is released from SAGA. The efficiency and probability of TBP detachment is commensurate with the affinity of TBP for the DNA sequence.

These findings imply a short residency time for SAGA on the minimal promoter, in accordance with genome-wide analyses that locate SAGA mainly at upstream activating sequences (UASs)<sup>7,40</sup>. The peripheral position of TBP and its binding mode in SAGA also suggest that transcription regulatory factors such as negative cofactor 2 (NC2) or Mot1 could gain access to TBP with relative ease. These results are consistent with a highly dynamic scenario for the control of TBP turnover<sup>41</sup>.

Sequence homology strongly suggests that the histone-fold machinery in TFIID assumes a similar function, which implies that the mechanics of depositing TBP on DNA by the two complexes share common features. However, several crucial aspects of TBP binding and delivery vary between the two complexes, including the capacity of the TFIID subunits Taf2 and Taf4 to bind promoter DNA, the ability of the Taf1 NTD to interact with the DNA-binding interface of TBP and the stronger affinity of Taf11–13, compared with Spt3, for TBP<sup>42</sup>. Thus, access of transcription regulatory factors to TBP and residency time at the minimal promoter are expected to be significantly different between TFIID and SAGA.

### Online content

Any methods, additional references, Nature Research reporting summaries, source data, extended data, supplementary information, acknowledgements, peer review information; details of author contributions and competing interests; and statements of data and code availability are available at <https://doi.org/10.1038/s41586-020-1944-2>.

- Helmlinger, D. & Tora, L. Sharing the SAGA. *Trends Biochem. Sci.* **42**, 850–861 (2017).
- Roeder, R. G. The role of general initiation factors in transcription by RNA polymerase II. *Trends Biochem. Sci.* **21**, 327–335 (1996).
- Sainsbury, S., Bernecky, C. & Cramer, P. Structural basis of transcription initiation by RNA polymerase II. *Nat. Rev. Mol. Cell Biol.* **16**, 129–143 (2015).
- Hahn, S. & Young, E. T. Transcriptional regulation in *Saccharomyces cerevisiae*: transcription factor regulation and function, mechanisms of initiation, and roles of activators and coactivators. *Genetics* **189**, 705–736 (2011).
- Larschan, E. & Winston, F. The *S. cerevisiae* SAGA complex functions *in vivo* as a coactivator for transcriptional activation by Gal4. *Genes Dev.* **15**, 1946–1956 (2001).
- Bhaumik, S. R. & Green, M. R. Differential requirement of SAGA components for recruitment of TATA-box-binding protein to promoters *in vivo*. *Mol. Cell Biol.* **22**, 7365–7371 (2002).
- Baptista, T. et al. SAGA is a general cofactor for RNA polymerase II transcription. *Mol. Cell* **68**, 130–143 (2017).
- Warfield, L. et al. Transcription of nearly all yeast RNA polymerase II-transcribed genes is dependent on transcription factor TFIID. *Mol. Cell* **68**, 118–129 (2017).

9. Lee, K. K. et al. Combinatorial depletion analysis to assemble the network architecture of the SAGA and ADA chromatin remodeling complexes. *Mol. Syst. Biol.* **7**, 503 (2011).
10. Köhler, A., Zimmerman, E., Schneider, M., Hurt, E. & Zheng, N. Structural basis for assembly and activation of the heterotetrameric SAGA histone H2B deubiquitinase module. *Cell* **141**, 606–617 (2010).
11. Samara, N. L. et al. Structural insights into the assembly and function of the SAGA deubiquitinating module. *Science* **328**, 1025–1029 (2010).
12. Sun, J. et al. Structural basis for activation of SAGA histone acetyltransferase Gcn5 by partner subunit Ada2. *Proc. Natl Acad. Sci. USA* **115**, 10010–10015 (2018).
13. Díaz-Santín, L. M., Lukyanova, N., Aciyan, E. & Cheung, A. C. Cryo-EM structure of the SAGA and NuA4 coactivator subunit Tra1 at 3.7 angstrom resolution. *eLife* **6**, e28384 (2017).
14. Sharov, G. et al. Structure of the transcription activator target Tra1 within the chromatin modifying complex SAGA. *Nat. Commun.* **8**, 1556 (2017).
15. Setiawati, D. et al. Conformational flexibility and subunit arrangement of the modular yeast Spt-Ada-Gcn5 acetyltransferase complex. *J. Biol. Chem.* **290**, 10057–10070 (2015).
16. Wu, P. Y., Ruhlmann, C., Winston, F. & Schultz, P. Molecular architecture of the *S. cerevisiae* SAGA complex. *Mol. Cell* **15**, 199–208 (2004).
17. Gangloff, Y. G., Romier, C., Thuault, S., Werten, S. & Davidson, I. The histone fold is a key structural motif of transcription factor TFIID. *Trends Biochem. Sci.* **26**, 250–257 (2001).
18. Grant, P. A. et al. A subset of TAF(II)s are integral components of the SAGA complex required for nucleosome acetylation and transcriptional stimulation. *Cell* **94**, 45–53 (1998).
19. Kolesnikova, O. et al. Molecular structure of promoter-bound yeast TFIID. *Nat. Commun.* **9**, 4666 (2018).
20. Patel, A. B. et al. Structure of human TFIID and mechanism of TBP loading onto promoter DNA. *Science* **362**, eaau8872 (2018).
21. Eisenmann, D. M., Arndt, K. M., Ricupero, S. L., Rooney, J. W. & Winston, F. SPT3 interacts with TFIID to allow normal transcription in *Saccharomyces cerevisiae*. *Genes Dev.* **6**, 1319–1331 (1992).
22. Mohibullah, N. & Hahn, S. Site-specific cross-linking of TBP in vivo and in vitro reveals a direct functional interaction with the SAGA subunit Spt3. *Genes Dev.* **22**, 2994–3006 (2008).
23. Sermwittayawong, D. & Tan, S. SAGA binds TBP via its Spt8 subunit in competition with DNA: implications for TBP recruitment. *EMBO J.* **25**, 3791–3800 (2006).
24. Birck, C. et al. Human TAF<sub>II</sub>28 and TAF<sub>II</sub>18 interact through a histone fold encoded by atypical evolutionary conserved motifs also found in the SPT3 family. *Cell* **94**, 239–249 (1998).
25. Hoffmann, A. et al. A histone octamer-like structure within TFIID. *Nature* **380**, 356–359 (1996).
26. Luger, K., Mäder, A. W., Richmond, R. K., Sargent, D. F. & Richmond, T. J. Crystal structure of the nucleosome core particle at 2.8 Å resolution. *Nature* **389**, 251–260 (1997).
27. Nikolov, D. B. et al. Crystal structure of a TFIIB–TBP–TATA-element ternary complex. *Nature* **377**, 119–128 (1995).
28. Wu, P. Y. & Winston, F. Analysis of Spt7 function in the *Saccharomyces cerevisiae* SAGA coactivator complex. *Mol. Cell. Biol.* **22**, 5367–5379 (2002).
29. Geiger, J. H., Hahn, S., Lee, S. & Sigler, P. B. Crystal structure of the yeast TFIIB/TBP/DNA complex. *Science* **272**, 830–836 (1996).
30. Tan, S., Hunziker, Y., Sargent, D. F. & Richmond, T. J. Crystal structure of a yeast TFIIB/TBP/DNA complex. *Nature* **381**, 127–134 (1996).
31. Wollmann, P. et al. Structure and mechanism of the Swi2/Snf2 remodeller Mot1 in complex with its substrate TBP. *Nature* **475**, 403–407 (2011).
32. Imbalzano, A. N., Zaret, K. S. & Kingston, R. E. Transcription factor (TF) IIB and TFIIB can independently increase the affinity of the TATA-binding protein for DNA. *J. Biol. Chem.* **269**, 8280–8286 (1994).
33. Warfield, L., Ranish, J. A. & Hahn, S. Positive and negative functions of the SAGA complex mediated through interaction of Spt8 with TBP and the N-terminal domain of TFIIB. *Genes Dev.* **18**, 1022–1034 (2004).
34. Petrenko, N., Jin, Y., Dong, L., Wong, K. H. & Struhl, K. Requirements for RNA polymerase II preinitiation complex formation in vivo. *eLife* **8**, e43654 (2019).
35. Anandapadamanaban, M. et al. High-resolution structure of TBP with TAF1 reveals anchoring patterns in transcriptional regulation. *Nat. Struct. Mol. Biol.* **20**, 1008–1014 (2013).
36. Han, Y., Luo, J., Ranish, J. & Hahn, S. Architecture of the *Saccharomyces cerevisiae* SAGA transcription coactivator complex. *EMBO J.* **33**, 2534–2546 (2014).
37. Kamata, K. et al. C-terminus of the Sgf73 subunit of SAGA and SLIK is important for retention in the larger complex and for heterochromatin boundary function. *Genes Cells* **18**, 823–837 (2013).
38. Elias-Villalobos, E., Toullec, D., Faux, C., Séveno, M. & Helmlinger, D. Chaperone-mediated ordered assembly of the SAGA and NuA4 transcription co-activator complexes. *Nat. Commun.* **10**, 5237 (2019).
39. Saint, M. et al. The TAF9 C-terminal conserved region domain is required for SAGA and TFIID promoter occupancy to promote transcriptional activation. *Mol. Cell. Biol.* **34**, 1547–1563 (2014).
40. Huisinga, K. L. & Pugh, B. F. A genome-wide housekeeping role for TFIID and a highly regulated stress-related role for SAGA in *Saccharomyces cerevisiae*. *Mol. Cell* **13**, 573–585 (2004).
41. Ravarani, C. N., Chalancon, G., Breker, M., de Groot, N. S. & Babu, M. M. Affinity and competition for TBP are molecular determinants of gene expression noise. *Nat. Commun.* **7**, 10417 (2016).
42. Gupta, K. et al. Architecture of TAF11/TAF13/TBP complex suggests novel regulation properties of general transcription factor TFIID. *eLife* **6**, e30395 (2017).

**Publisher's note** Springer Nature remains neutral with regard to jurisdictional claims in published maps and institutional affiliations.

© The Author(s), under exclusive licence to Springer Nature Limited 2020

## Methods

No statistical methods were used to predetermine sample size.

### Purification of SAGA

The SAGA complex was purified from nuclear extracts of the budding yeast *K. phaffii* (also known as *P. pastoris*) using the 38-amino-acid streptavidin-binding peptide (SBP) affinity tag that was fused to the C terminus of the endogenous Sgf73 subunit (Extended Data Figs. 1, 7e). We introduced several modifications into our original procedure<sup>14</sup>, with the combined effect of increasing the yield by three times. These improvements enabled us to reduce the harmful effects of proteases and to keep SAGA more concentrated along the different steps of the procedure.

Two litres of yeast cells (four flat-bottom flasks with 0.5 l in each) were grown at 24 °C with glycerol as carbon source and collected when optical density at 600 nm ( $OD_{600\text{nm}}$ ) reached 16–18. Cells were washed in ice-cold water and then treated with 10 mM DTT. The cell wall was digested by addition of lyticase and spheroplasts were pelleted at 5,500g for 20 min. All further steps were performed at 0 to 4 °C. Protease inhibitors were added to all buffers. Spheroplasts were washed twice in 1.1 M sorbitol and were then disrupted by suspension in a hypotonic buffer (15–18% Ficoll 400, 0.6 mM  $MgCl_2$ , 20 mM K-phosphate buffer pH 6.6) using a ULTRA-TURRAX disperser. Sucrose (0.1 M) and  $MgCl_2$  (5 mM) were then added. Nuclei (and some debris) were pelleted at 33,000g for 37 min, resuspended in a wash buffer (0.6 M sucrose, 8% polyvinylpyrrolidone, 1 mM  $MgCl_2$ , 20 mM phosphate buffer pH 6.6) and pelleted again at 34,000g for 50 min. Nuclei were resuspended in low ionic extraction buffer (40 mM HEPES pH 8.0, 20% sucrose, 8 mM  $MgCl_2$ , 5–6 mM DTT) with 30 strokes using a tight pestle in a dounce homogenizer. Very few molecules of SAGA are liberated under the low ionic conditions, leaving time for protease inhibitors to bind their targets before SAGA is extracted.

After 20 min of incubation, 300 mM NaCl, 2 mM  $CaCl_2$  and 150  $\mu$ l of  $\alpha$ -amylase solution (MegaZyme) were added. Following another 30 min of incubation, debris was precipitated at 33,000g for 38 min. The supernatant was collected and 1–2% PEG 20,000 as well as additional 5 mM  $MgCl_2$  were added to precipitate some remaining organelles and membrane parts by a short centrifugation step at 33,000g for 10 min. The increase in magnesium concentration (final 13 mM) proved crucial to prevent precipitation of SAGA at this step. The PEG 20,000 concentration was then increased to 5.8% and SAGA precipitated in a second short centrifugation step. The pellet was solubilized in a minimal volume and avidin was added to block endogenously biotinylated proteins. The suspension was incubated with streptavidin beads for 4 h in buffer A (40 mM HEPES pH 8.0, 250 mM sodium chloride, 10% sucrose, 2 mM  $MgCl_2$ , 2 mM DTT) washed 5 times and eluted with buffer A containing 10 mM biotin. The eluate was concentrated with Millipore Amicon-Ultra (50 kDa cut-off) and spun in a 10–30% sucrose gradient with buffer B (20 mM HEPES pH 8.0, 150 mM potassium acetate, 2 mM DTT, 6 mM  $MgCl_2$ ) in rotor SW60 (38,300 rpm for 13.5 h). SAGA was fractionated at approximately 25% sucrose and concentrated with Amicon-Ultra to ~2 mg  $ml^{-1}$ . It is important to note that mass spectrometry (Extended Data Fig. 7) and SDS–PAGE analysis<sup>14</sup> show no cleavage of the Spt7 subunit or sub-stoichiometric amounts of Spt8. It is also noteworthy that very little endogenous TBP is present in our final SAGA sample.

### Purification of TBP and TFIIA

Full-length yeast *S. cerevisiae* TBP was expressed as N-terminal 6 $\times$ His–GFP fusion protein in *Escherichia coli* strain BL21(DE3)RIL. Cells were grown in LB medium with ampicillin until an  $OD_{600\text{nm}}$  of 0.7 was reached. Expression was induced with 1 mM IPTG for 3 h at 37 °C. The cells were collected by centrifugation and resuspended in lysis buffer (20 mM HEPES–KOH (pH 7.5), 0.5 M NaCl, 10% glycerol). Cells were treated with 1 mg  $ml^{-1}$  lysozyme (Sigma) for 30 min on ice, and then

lysed by sonication after the addition of cComplete, EDTA-free Protease Inhibitor Cocktail (Roche) and PMSF to a final concentration of 1 mM. The resulting lysate was clarified by centrifugation and incubated with equilibrated cComplete His-Tag Purification Resin (Roche) for 1 h at 4 °C. After the beads were collected, they were washed three times with lysis buffer supplemented with 5 mM imidazole, and the bound protein was eluted with 20 mM HEPES–KOH (pH 7.5), 0.2 M NaCl, 10% glycerol supplemented with 250 mM imidazole. The recombinant protein was further purified on a Heparine HiTrap 1 ml column (GE Healthcare) equilibrated with 20 mM HEPES–KOH (pH 7.5), 0.2 M NaCl, 20% glycerol and eluted with a gradient from 200 mM to 1 M NaCl. Fractions were analysed by Coomassie blue staining, pooled and concentrated in Amicon-Ultra with a 10,000 (10K)-molecular-weight cut-off (Millipore) to a final concentration of 3 mg  $ml^{-1}$ . DTT (5 mM) was added to all buffers immediately before use. The yeast *S. cerevisiae* TFIIA was expressed in *E. coli*, purified from inclusion bodies and reconstituted as described earlier<sup>43</sup>.

### Gel-shift DNA-binding assays

DNA probes were obtained by annealing of equimolar amounts of complementary oligonucleotides (Eurofins Genomics for short DNA, SIGMA for long DNA) at a final concentration of 25  $\mu$ M in 20 mM HEPES–KOH, 50 mM NaCl by heating the mixture to 100 °C for 5 min and cooling slowly down to room temperature. To estimate the quality of annealing, the obtained DNA fragments were loaded on a 12% polyacrylamide gel and analysed using a Typhoon FLA9500 Imager (GE Healthcare) to follow Cy5 fluorescence signal. No Cy5-labelled single-stranded DNA was detected (Extended Data Fig. 7c). To further ascertain that we removed all effects of single-stranded DNA, all DNA samples were treated with Exonuclease I (NEB). Binding assays (10  $\mu$ l) contained 3 mM Tris–HCl (pH 8.0), 6 mM HEPES–KOH (pH 8.0), 45 mM KAc, 20–42 mM KCl, 5 mM  $MgCl_2$ , 3% glycerol, 6% sucrose, DNA probe (Cy5-labelled), 0.01% NP40, 25  $\mu$ g  $ml^{-1}$  bovine serum albumin (BSA) (NEB), 1 mM DTT and proteins as indicated. TBP was incubated first with a fourfold excess of SAGA complex for 1 h at 4 °C. Under these conditions almost all TBP was bound to SAGA. Then DNA and TFIIA were added, and the reaction mixtures were incubated for 20 min at room temperature before they were loaded onto agarose-polyacrylamide native gels (1% agarose, 1.3% acrylamide with 1 $\times$  Tris-glycine buffer, 5 mM  $MgCl_2$  in the gel and running buffer). The final reaction mix contained 0.075  $\mu$ M GFP–TBP, 0.3  $\mu$ M SAGA, 0.075  $\mu$ M DNA and 0.15  $\mu$ M TFIIA complex. Binding assays with long (100-bp) DNA fragments were done under similar conditions except that a threefold excess (with respect to SAGA) of long non-labelled TATA-less DNA was also added because SAGA was shown to bind long DNA non-specifically<sup>44</sup>.

The gel-shift experiments were repeated several times, all showing consistent results. Gels were analysed using a Typhoon FLA9500 Imager to follow Cy5 fluorescence signal. TBP–DNA and TBP–TFIIA–DNA migrate similarly in native agarose-polyacrylamide gels due to the limited resolving power of these gels for relatively low-molecular-weight complexes. We ascertained the composition of the shifted bands by mass spectrometry (Extended Data Fig. 7d). Sequences of DNA molecules used: ‘TATA’ (yeast *CYC1* TATA), 5′-Cy5–TGCTCTG-TATGTATATAAACTCTTG-3′; ‘TATA-like’ (*CYC1* TATA with two mutations decreasing the affinity to TBP), 5′-Cy5–TGCTCTGTATGTAGAGAAACTCTTG-3′; ‘TATA-less’ (non-specific DNA, *CYC1* UAS), 5′-Cy5–GGCCGGGGTTTACGGACGATGGCAG-3′; ‘TATA<sub>L</sub>’ (*Pichia pastoris* pGAP promoter fragment), TGTCATGAGATTATTGGAAACCACAGAATCGAATATAAAAGGCGAACACCTTTCCCAATTTGGTTTCTCCTGACCCAAAGACTTTAAATTTAATTTA; ‘TATA-like<sub>L</sub>’ (TATA<sub>L</sub> with two mutations decreasing the affinity to TBP), TGTCATGAGATTATTGGAAACCACAGAAATCGAAGAGAGAAAGGCGAACACCTTTCCCAATTTGGTTTCTCCTGACCCAAAGACTTTAAATTTAATTTA; ‘TATA-less<sub>L</sub>’ (non-specific DNA), GACTCATGTATGATGATCATTGGACACCACAGAATCGCGTATCGAAGGCGAACACCTGTCTACGTCTGGTGTCTCTGACGCACAGACTTCGAA

CGTA. The position of the TATA sequence is indicated by bold letters and the two mismatches in the TATA-less sequences are underlined.

## Pull-down DNA-binding assays

Binding assays (20  $\mu$ l) contained 3 mM Tris-HCl (pH 8.0), 5 mM HEPES-KOH (pH 8.0), 35 mM KAc, 46 mM KCl, 5 mM MgCl<sub>2</sub>, 3% glycerol, 6% sucrose, 0.01% NP40, 25  $\mu$ g ml<sup>-1</sup> BSA (NEB), 1 mM DTT, proteins and DNA probe (Cy5-labelled 'TATA' DNA) as indicated. TBP was incubated first with a fourfold excess of SAGA complex for 1 h at 4 °C. Then DNA and TFIIA were added (as indicated), and the reaction mixtures were incubated for 20 min at room temperature. The final reaction mix contained 0.075  $\mu$ M GFP-TBP, 0.3  $\mu$ M SAGA (with Sgf11 subunit fused to mCherry), 0.075  $\mu$ M Cy5-DNA and 0.15  $\mu$ M TFIIA complex. Ten microlitres of streptavidin-sepharose beads (equilibrated with the binding buffer) were added to each reaction mix and tubes were incubated for 2 h at 4 °C with shaking using ThermoMixerC (Eppendorf, shaking frequency 1,220 rpm). Each reaction mix containing beads was transferred into an Ultrafree-MC centrifugal filter unit and centrifuged for 5 min at 12,000g at 4 °C. Beads with retained protein or DNA-protein complexes and the flowthrough with unbound material were analysed using a PHERAstar Plus microplate reader (BMG LABTECH) to quantify the fluorescence signal of GFP (corresponding to TBP), mCherry (corresponding to SAGA complex) and Cy5 (corresponding to DNA). A complementary experiment with the reverse order of incubations was also carried out. Hence, TBP was first incubated with Cy5-labelled DNA and TFIIA for 20 min at room temperature, then a fourfold excess of SAGA complex was added and reactions were incubated for 1 h at 4 °C. Experiments were repeated three to four times.

## Cryo-EM sample preparation and data acquisition

Concentrated SAGA was incubated overnight on ice with an excess of ubiquitin aldehyde (UbAl) at a molar ratio of 1:4. Complete binding and inhibition was ascertained by following the activity of SAGA using Ubiquitin-AMC (Enzo). SAGA-UbAl complexes were precipitated with PEG to remove sucrose<sup>14</sup>, suspended at a concentration of 1 mg ml<sup>-1</sup> and incubated overnight on ice with a 5:1 molar excess of full-length *S. cerevisiae* TBP. SAGA-TBP was then diluted to 0.2 mg ml<sup>-1</sup> and cross-linked with 0.1% glutaraldehyde for 30 min on ice. About 3  $\mu$ l of sample was applied onto a holey carbon grid (Quantifoil R2/2 300 mesh) rendered hydrophilic by a 90-s treatment in a Fischione 1070 plasma cleaner operating at 30% power with a gas mixture of 80% argon:20% oxygen. The grid was blotted for 1 s (blot force 8) and flash-frozen in liquid ethane using a Vitrobot Mark IV (FEI) at 4 °C and 95–100% humidity. To verify that the occupancy of GFP-TBP on SAGA was approaching 100%, we loaded the cross-linked complex on a superose 6 10/300 GL column (GE Healthcare) and compared the fluorescent signal at the peak fraction with that of cross-linked GFP-TBP of known concentrations. The concentrations of SAGA were estimated by UV absorbance. Images were acquired on a Cs-corrected Titan Krios (Thermo Fisher) microscope operating at 300 kV in nanoprobe mode using the serialEM software for automated data collection<sup>45</sup>. Movie frames were recorded on a 4k  $\times$  4k Gatan K2 summit direct electron detector after a Quantum LS 967 energy filter using a 20-eV slit width in zero-loss mode. Images were acquired in super-resolution mode at a nominal magnification of 105,000, which yielded a pixel size of 0.55 Å. Forty movie frames were recorded at a dose of 1.32 e<sup>-</sup> Å<sup>-2</sup> per frame, corresponding to a total dose of 52.8 e<sup>-</sup> Å<sup>-2</sup>, but only the last 38 frames were kept for further processing.

## Image processing

Movie frames were aligned, dose-weighted, binned by 2 and averaged using Motioncor2<sup>46</sup> to correct for beam-induced specimen motion and to account for radiation damage by applying an exposure-dependent filter. Non-weighted movie sums were used for contrast transfer function (CTF) estimation with the Gctf<sup>47</sup> program, while dose-weighted sums

were used for all subsequent steps of image processing. After manual screening, images with poor CTF, particle aggregation or ice contamination were discarded. Particles were picked using crYOLO (<https://doi.org/10.1101/356584>). These datasets were analysed in RELION 3.0<sup>48</sup>, cryoSPARC<sup>49</sup> and cisTEM<sup>50</sup> according to standard protocols. In brief, three rounds of reference-free 2D classification of the individual particle images were performed in RELION to remove images, like ice contaminations or deformed particles, that failed to enter into high-resolution class averages. The selected images were aligned against a low-pass-filtered starting model<sup>14</sup>. Three rounds of 3D classification with increasing regularization parameter  $\gamma$  were performed and classes showing high-resolution features were selected for the subsequent steps. These images were imported, and refined in cryoSPARC v.2. Three-dimensional classification of the entire dataset could not clearly separate distinct conformations of the SAGA complex. Therefore, we carried out a focused refinement of the separate lobes using the masked lobes as references. The Tra1 lobe was refined with a mask covering the Tra1 densities using the 'Local refinement' module. The structure of the main lobe was obtained by using signal subtraction, in which the densities corresponding to the Tra1 lobe were subtracted from the images. This operation was followed by local refinement with a mask covering the main lobe densities. Global resolution estimates were determined using the Fourier shell correlation (FSC) = 0.143 criterion after a gold-standard refinement. Local resolutions were estimated with ResMap<sup>51</sup> and cryoSPARC. Maps to fit TBP, Spt8 and the DUB module were obtained after 3D classifications using RELION 3 by applying masks covering the region of interest.

To describe the flexibility of the DUB and HAT modules, the selected SAGA images were analysed using the IMAGIC software package<sup>52</sup>. The selected images were aligned against 75 equidistant projections of the 3D model and clustered to form 1,000 2D classes. Images from classes corresponding to two different views were grouped and aligned separately against their corresponding reference. Local classification into 50 classes was performed for each group by using an adapted mask and the best class averages were selected to show the extent of protein density variation within each view.

## Model building

Pairwise alignment was performed with Needle<sup>53</sup>. Homology models for Tra1, TBP, Spt8, DUB module, all eight histone folds, Taf6 HEAT repeats, Taf5 WD40, Spt20 SEP domain and Taf5 NTD domains were generated using I-TASSER<sup>54</sup> or Swiss-Model and docked into the maps manually. The rigid-body-docking of DUB and Spt8 was guided by the overall shape of the local density, which lacked clear secondary structure features, probably owing to the peripheral position and flexible nature of their connection to the SAGA core. The position of the DUB is consistent with previous studies, notably XL/MS<sup>36</sup> and negatively stained particles with GFP-labelled subunits of the module<sup>15</sup>. As the DUB is composed of two lobes with similar overall shape we cannot exclude at the current resolution an inverted (upside-down) orientation for the DUB. The location and orientation of Spt8 is validated by cross-linking mass spectrometry<sup>36</sup>, specific single-site photo-activated cross-linking<sup>23,33</sup> and biochemical data<sup>16</sup>.

The other homology models, with the notable exception of TBP, for which only a minor tilt of the C-terminal stirrup was applied, were rebuilt according to density using Coot<sup>55</sup> and then extended from their N' and C' termini until a significant discontinuity in the map was encountered. Such discontinuities normally corresponded to sites where RaptorX<sup>56</sup> and PSIPRED<sup>57</sup> predictions indicated a large disordered region. To assign densities that were not clearly connected to any of these extended starting models, we considered the local map properties including secondary structure features, proteins in the vicinity, biochemical data, cross-linking information for surrounding domains and, most importantly, the fit between protein side chains and the density. These parts of the structure were then built de novo.

For a large proportion of the side chains, density was clear and practically all densities in the core of SAGA and Tra1 could be assigned with confidence. The single exception to this procedure is the Ada3 domain at the docking site of the HAT module, where density showed secondary structure elements but could not resolve individual side chains. We cannot therefore exclude errors in amino-acids register for this domain. Tra1 and the main lobe were separately geometry-optimized in PHENIX<sup>58</sup> followed by real-space refinement with secondary structure restraints against the corresponding post-processed maps. This procedure was repeated after a round of final manual corrections to the structure in Coot. All display images were generated using UCSF Chimera<sup>59</sup> and ChimeraX<sup>60</sup>.

## Reporting summary

Further information on research design is available in the Nature Research Reporting Summary linked to this paper.

## Data availability

The cryo-EM maps have been deposited in the Electron Microscopy Data Bank (EMDB) under accession codes EMD-10438 (SAGA-TBP), EMD-10440 (SAGA-TBP, refined for Tra1 lobe), EMD-10441 (SAGA-TBP, refined for main lobe), EMD-10446 (SAGA-TBP, low-pass-filtered), EMD-10448 (SAGA-TBP, focused classification on TBP), EMD-10447 (SAGA without TBP). The model coordinates for SAGA-TBP were deposited in the Protein Data Bank (PDB) under the accession codes 6TB4 and 6TBM (including Spt8 and DUB).

43. Ranish, J. A., Lane, W. S. & Hahn, S. Isolation of two genes that encode subunits of the yeast transcription factor IIA. *Science* **255**, 1127–1129 (1992).
44. Mittal, C., Culbertson, S. J. & Shogren-Knaak, M. A. Distinct requirements of linker DNA and transcriptional activators in promoting SAGA-mediated nucleosome acetylation. *J. Biol. Chem.* **293**, 13736–13749 (2018).
45. Mastrorade, D. N. Automated electron microscope tomography using robust prediction of specimen movements. *J. Struct. Biol.* **152**, 36–51 (2005).
46. Zheng, S. Q. et al. MotionCor2: anisotropic correction of beam-induced motion for improved cryo-electron microscopy. *Nat. Methods* **14**, 331–332 (2017).
47. Zhang, K. Gctf: Real-time CTF determination and correction. *J. Struct. Biol.* **193**, 1–12 (2016).
48. Zivanov, J. et al. New tools for automated high-resolution cryo-EM structure determination in RELION-3. *eLife* **7**, e42166 (2018).
49. Punjani, A., Rubinstein, J. L., Fleet, D. J. & Brubaker, M. A. cryoSPARC: algorithms for rapid unsupervised cryo-EM structure determination. *Nat. Methods* **14**, 290–296 (2017).
50. Grant, T., Rohou, A. & Grigorieff, N. cisTEM, user-friendly software for single-particle image processing. *eLife* **7**, e35383 (2018).
51. Kucukelbir, A., Sigworth, F. J. & Tagare, H. D. Quantifying the local resolution of cryo-EM density maps. *Nat. Methods* **11**, 63–65 (2014).
52. van Heel, M., Harauz, G., Orlova, E. V., Schmidt, R. & Schatz, M. A new generation of the IMAGIC image processing system. *J. Struct. Biol.* **116**, 17–24 (1996).

53. Madeira, F. et al. The EMBL-EBI search and sequence analysis tools APIs in 2019. *Nucleic Acids Res.* **47**, W636–W641 (2019).
54. Yang, J. & Zhang, Y. I-TASSER server: new development for protein structure and function predictions. *Nucleic Acids Res.* **43**, W174–81 (2015).
55. Emsley, P., Lohkamp, B., Scott, W. G. & Cowtan, K. Features and development of Coot. *Acta Crystallogr. D* **66**, 486–501 (2010).
56. Källberg, M. et al. Template-based protein structure modeling using the RaptorX web server. *Nat. Protoc.* **7**, 1511–1522 (2012).
57. Buchan, D. W., Minneci, F., Nugent, T. C., Bryson, K. & Jones, D. T. Scalable web services for the PSIPRED Protein Analysis Workbench. *Nucleic Acids Res.* **41**, W349–57 (2013).
58. Terwilliger, T. C. Rapid model building of alpha-helices in electron-density maps. *Acta Crystallogr. D* **66**, 268–275 (2010).
59. Goddard, T. D., Huang, C. C. & Ferrin, T. E. Visualizing density maps with UCSF Chimera. *J. Struct. Biol.* **157**, 281–287 (2007).
60. Goddard, T. D. et al. UCSF ChimeraX: Meeting modern challenges in visualization and analysis. *Protein Sci.* **27**, 14–25 (2018).
61. Zhou, Q. & Berk, A. J. The yeast TATA-binding protein (TBP) core domain assembles with human TBP-associated factors into a functional TFIID complex. *Mol. Cell. Biol.* **15**, 534–539 (1995).
62. Kelleher, R. J., III et al. Yeast and human TFIIDs are interchangeable for the response to acidic transcriptional activators in vitro. *Genes Dev.* **6**, 296–303 (1992).
63. Ozer, J., Lezina, L. E., Ewing, J., Audi, S. & Lieberman, P. M. Association of transcription factor IIA with TATA binding protein is required for transcriptional activation of a subset of promoters and cell cycle progression in *Saccharomyces cerevisiae*. *Mol. Cell. Biol.* **18**, 2559–2570 (1998).
64. Laprade, L., Rose, D. & Winston, F. Characterization of new Spt3 and TATA-binding protein mutants of *Saccharomyces cerevisiae*: Spt3 TBP allele-specific interactions and bypass of Spt8. *Genetics* **177**, 2007–2017 (2007).

**Acknowledgements** We thank D. Devys and L. Tora for carefully reading the manuscript and for advice; R. Wagner and B. Séraphin for advice during the initial stages of this project; and R. Ben-Shem for graphics expertise. We acknowledge support from the Institut National de la Santé et de la Recherche Médicale (INSERM), the Centre National pour la Recherche Scientifique (CNRS), the Association pour la Recherche sur le Cancer (ARC), the Ligue contre le Cancer, ANR-15-CE11-0022-01 and ANR-10-LABX-0030-INRT, a French State fund managed by the Agence Nationale de la Recherche under the frame program Investissements d’Avenir ANR-10-IDEX-0002-02. We acknowledge the use of resources of the French Infrastructure for Integrated Structural Biology FRISBI ANR-10-INBS-05 and of Instruct-ERIC.

**Author contributions** P.S. and A.B.-S. designed the study; A.B.-S. designed the SAGA purification method and reconstituted the SAGA-TBP complex; A.B.-S. and C.C. defined conditions for grid preparation and freezing; C.C. and G.P. froze grids; G.P. collected and analysed cryo-EM data; A.F., G.P. and A.B.-S. interpreted the maps by fitting crystal coordinates and model building; O.K. purified TBP, TFIIA and SAGA and used them to perform pull-down and gel-shift assays; P.S. and A.B.-S. supervised the work; G.P. and O.K. prepared figures; and A.B.-S. and P.S. wrote the manuscript with input from all authors.

**Competing interests** The authors declare no competing interests.

## Additional information

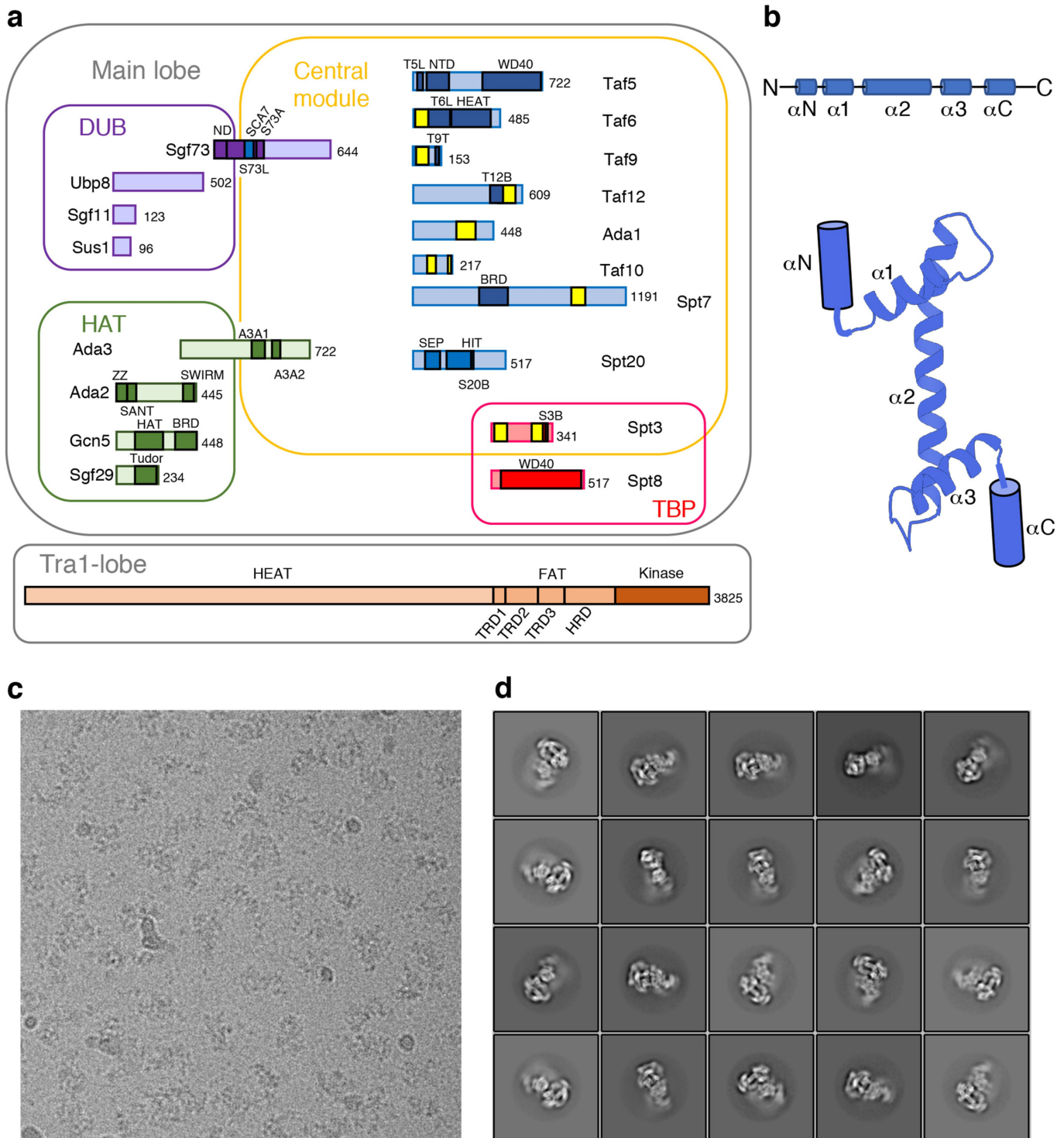
**Supplementary information** is available for this paper at <https://doi.org/10.1038/s41586-020-1944-2>.

**Correspondence and requests for materials** should be addressed to P.S. or A.B.-S.

**Peer review information** Nature thanks Steve Hahn and the other, anonymous, reviewer(s) for their contribution to the peer review of this work.

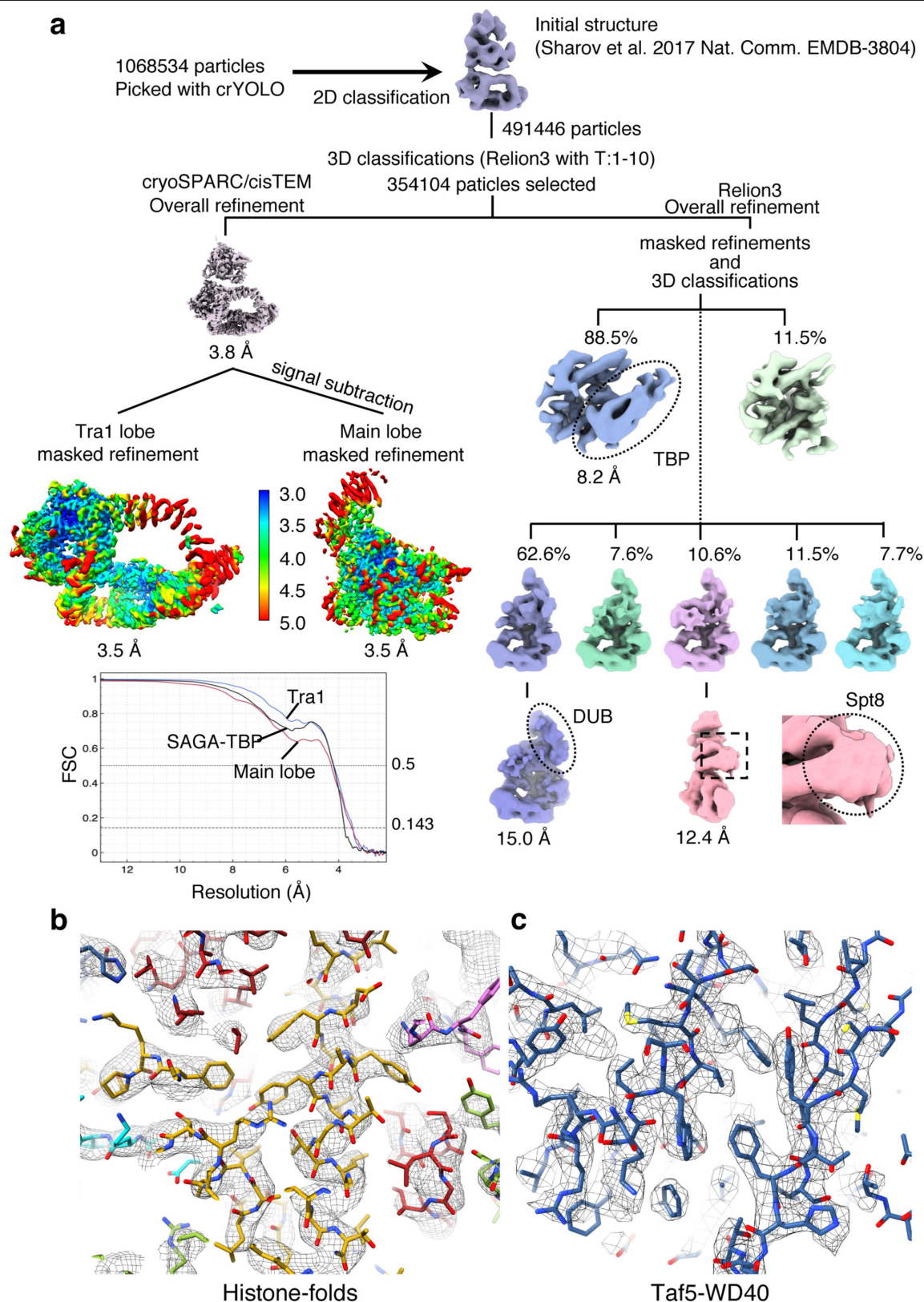
**Reprints and permissions information** is available at <http://www.nature.com/reprints>.





**Extended Data Fig. 1 | Subunit and domain organization of the yeast SAGA complex.** **a**, SAGA subunits are organized into the Tra1 lobe and the main lobe. The main lobe is divided into enzymatic HAT and DUB modules, a central module and a TBP-binding module. Overlaps appear as the central module is a scaffold for the assembly of all other modules. Abbreviations used owing to space limitations: Taf5 lissencephaly homology (LisH) domain (T5L), Taf6 linker domain (N83–S218, T6L), Taf9 C tail (N110–L139, T9T), Sgf73 NTD (M1–K69, ND), Sgf73 linker region (I70–H234, S73L), Sgf73 anchoring domain (E235–L277, S73A), Spt20 HIT domain interacting with Tra1 (M325–L340, HIT), Ada3 anchoring domains (K398–L471, A3A1) and (Y509–E557, A3A2) and bromodomain (BRD). The SEP domain found in Spt20 is named after

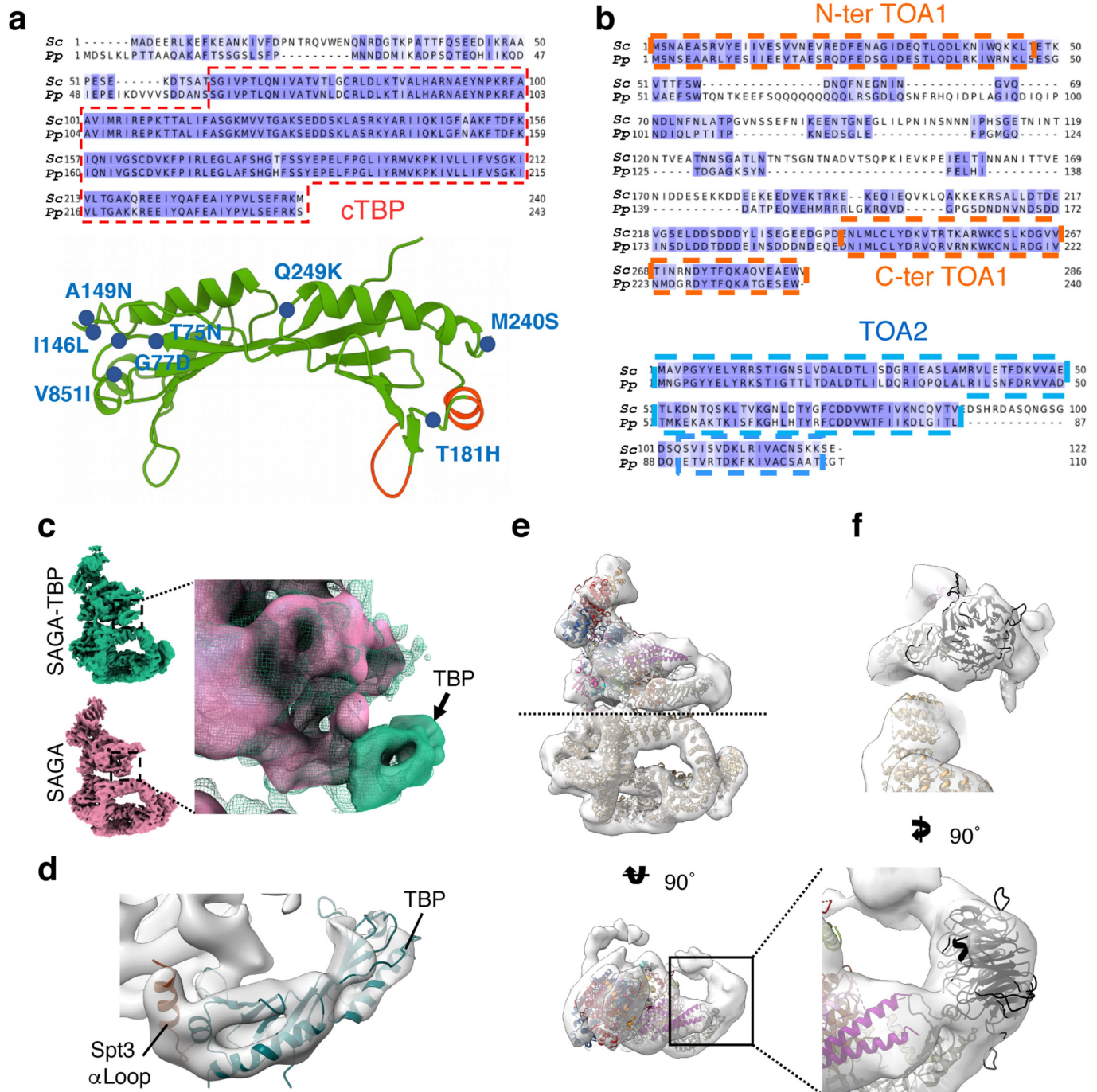
*S. cerevisiae* Shp1, *Drosophila melanogaster* eyes closed gene (Eyc) and vertebrate P47. The FAT repeats are divided into three TRD domains and one HEAT-repeats domain (HRD). We defined three bridge-forming domains involved in connecting Tra1 to the central module: the Spt20 bridge (K184–K336, S20B), the Taf12 bridge (T430–K502, T12B) and the Spt3 bridge (E268–I304, S3B). The histone-fold domains, present in seven subunits, are highlighted as yellow boxes. **b**, Schematic representation and helix nomenclature for histone-fold domains. **c**, Original micrograph of frozen-hydrated *P. pastoris* SAGA-TBP complex. **d**, Two-dimensional class averages showing high-resolution structural features.



**Extended Data Fig. 2 | Cryo-EM data-analysis strategy and resolution assessment of the cryo-EM structures.** **a**, Image-processing strategy used to obtain the 3.5 Å resolution maps of the SAGA-TBP complex. Maps coloured in rainbow represent the local resolution of the reconstructions. FSC curves are depicted as a function of resolution in angstrom for the entire SAGA-TBP complex (black), the Tra1 lobe (blue) and the main lobe (red). cryoSPARC v.2 and cisTEM were used to generate the 3.5 Å resolution maps of the Tra1 and main lobes. RELION 3 was used for masked refinements and classifications of

flexible regions, corresponding to TBP, the DUB module and Spt8. Dotted circles show the regions that were used to dock the crystal structures of TBP (PDB: 1TBP), Spt8 (homology model by Swiss-Model using PDB 4J87 as template) and the DUB module (PDB: 6AQR). **b**, **c**, Representative regions illustrating the quality of the cryo-EM map and the high-resolution structural features. Cryo-EM map and atomic model showing that side chains are clearly identified. **b**, Histone-fold domain of Taf9. **c**, Part of the Taf5 WD40 domain.

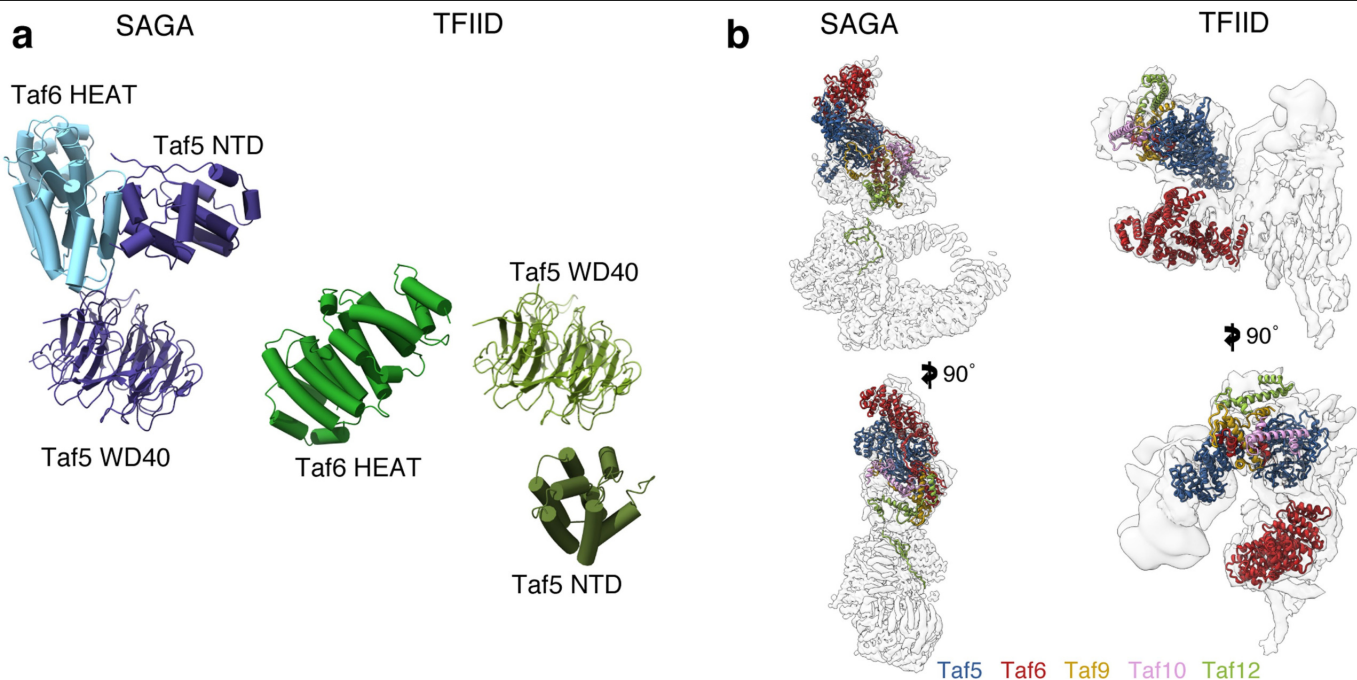




### Extended Data Fig. 3 | Fitting of TBP and Spt8 into the cryo-EM map.

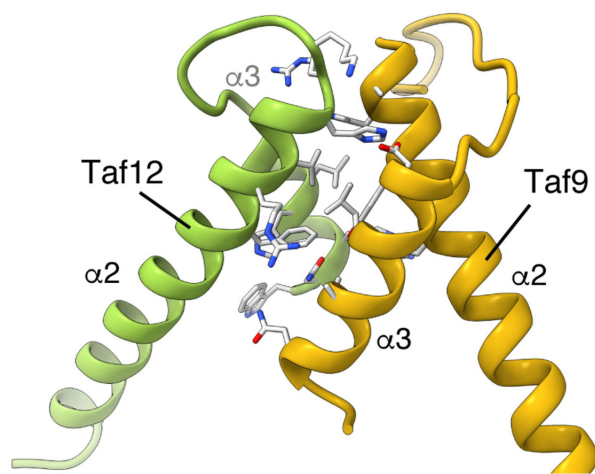
**a**, Pairwise alignment of TBP from *P. pastoris* and *S. cerevisiae*. Eight residues (out of 180) differ between the two organisms within the conserved C-terminal part of TBP (marked by a dotted line). These residues are mapped on the structure of cTBP (PDB: 1YTF). None of these residues occur in regions that contact SAGA (highlighted in red). **b**, Pairwise alignment of TFIIA subunits, Toa1 and Toa2, from *P. pastoris* and *S. cerevisiae*. The evolutionary conserved and structured domains of TFIIA (marked by dotted lines) show 60% identity and 80% similarity between the two organisms. It is worth noting that TBP and TFIIA have both been shown to be highly similar even across large evolutionary distances. For example, TBP, as well as Toa2, from yeast and human are functionally interchangeable in Pol II transcription<sup>61–63</sup> and yeast TFIIA

complements a mammalian in vitro transcription system depleted of TFIIA<sup>43</sup>. Hence, TBP and TFIIA from *S. cerevisiae*, which are easier to overproduce in *E. coli*, are valid substitutes in our experimental system for their homologues from the closely related budding yeast *P. pastoris*. **c**, Cryo-EM reconstructions determined in the presence (green) and in the absence (pink) of TBP. The enlarged panel shows the superimposition of both maps and highlights the additional density corresponding to TBP. **d**, Fitting of the cTBP crystal structure into the additional density observed in the SAGA-TBP complex. The  $\alpha$ -loop denotes an  $\alpha$ -helix from the linker connecting the two histone folds in Spt3. **e, f**, Fitting of the WD40 repeat of subunit Spt8 into the cryo-EM map of the SAGA-TBP complex next to TBP.

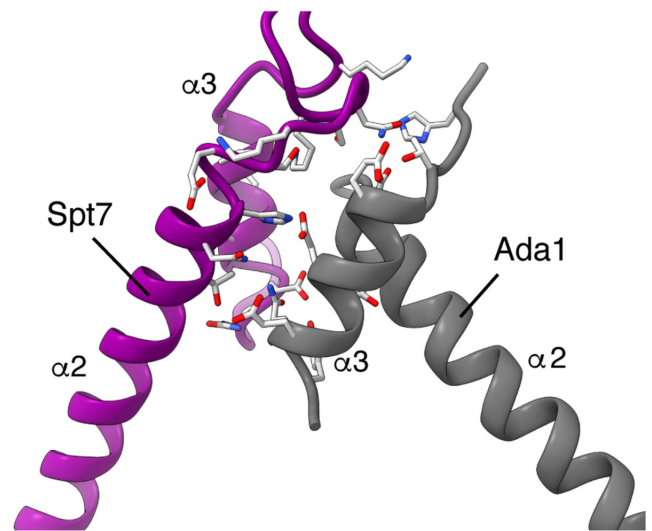


**Extended Data Fig. 4 | Comparing the arrangement of common SAGA and TFIID subunits.** **a**, The Taf5 NTD and Taf6 HEAT repeats have different positions in SAGA and in TFIID. The structures of Taf5 NTD, Taf6 HEAT repeats and Taf5 WD40 domain in SAGA (left) and in the twin lobe of TFIID<sup>19</sup> (right) are depicted. For the sake of clarity, all other parts of SAGA and TFIID were removed. To compare the position of the Taf5 NTD and Taf6 HEAT repeats between SAGA and TFIID, both complexes were aligned to have the same orientation of the Taf5 WD40 domain. The top face of the WD40 repeat, which is to a large extent free in TFIID, is nearly completely engaged in SAGA. The

positions of the Taf5 NTD and Taf6 HEAT repeats are defined by direct interactions of the two domains between themselves, with the WD40 surface, and with the  $\alpha$ -helix A352–D364 of Taf5. **b**, SAGA and TFIID share five subunits (Taf5 and the four histone fold-containing subunits Taf6, Taf9, Taf10 and Taf12). These subunits are present as one and two copies in SAGA and TFIID, respectively. The relative positions of these subunits are depicted in both complexes. Note that in TFIID, the TBP-binding lobe was poorly resolved<sup>19,20</sup> and therefore the second copy of only the Taf6 HEAT repeats and Taf5 NTD is shown.

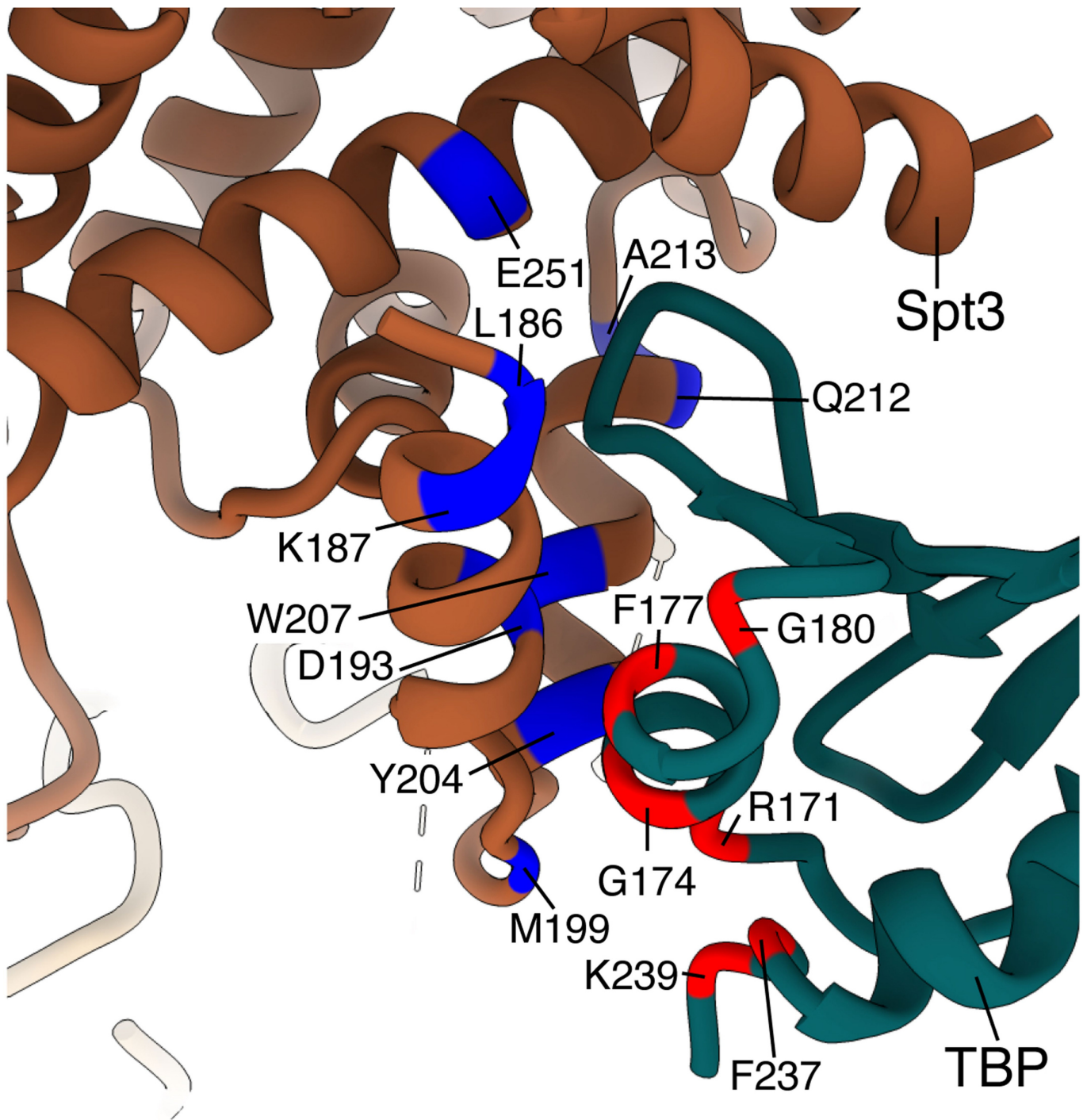


**Extended Data Fig. 5 | Interactions between histone-fold pairs in SAGA deviate from the nucleosome pattern already at the four-helix bundle preceding the weak association between Spt3 and Taf10.** The binding between the first two histone-fold pairs along the spiral (left), Taf6–Taf9 with Taf12–Ada1, shows little difference from the nucleosome, possibly reflecting the fact that these histone folds have the highest sequence similarity to



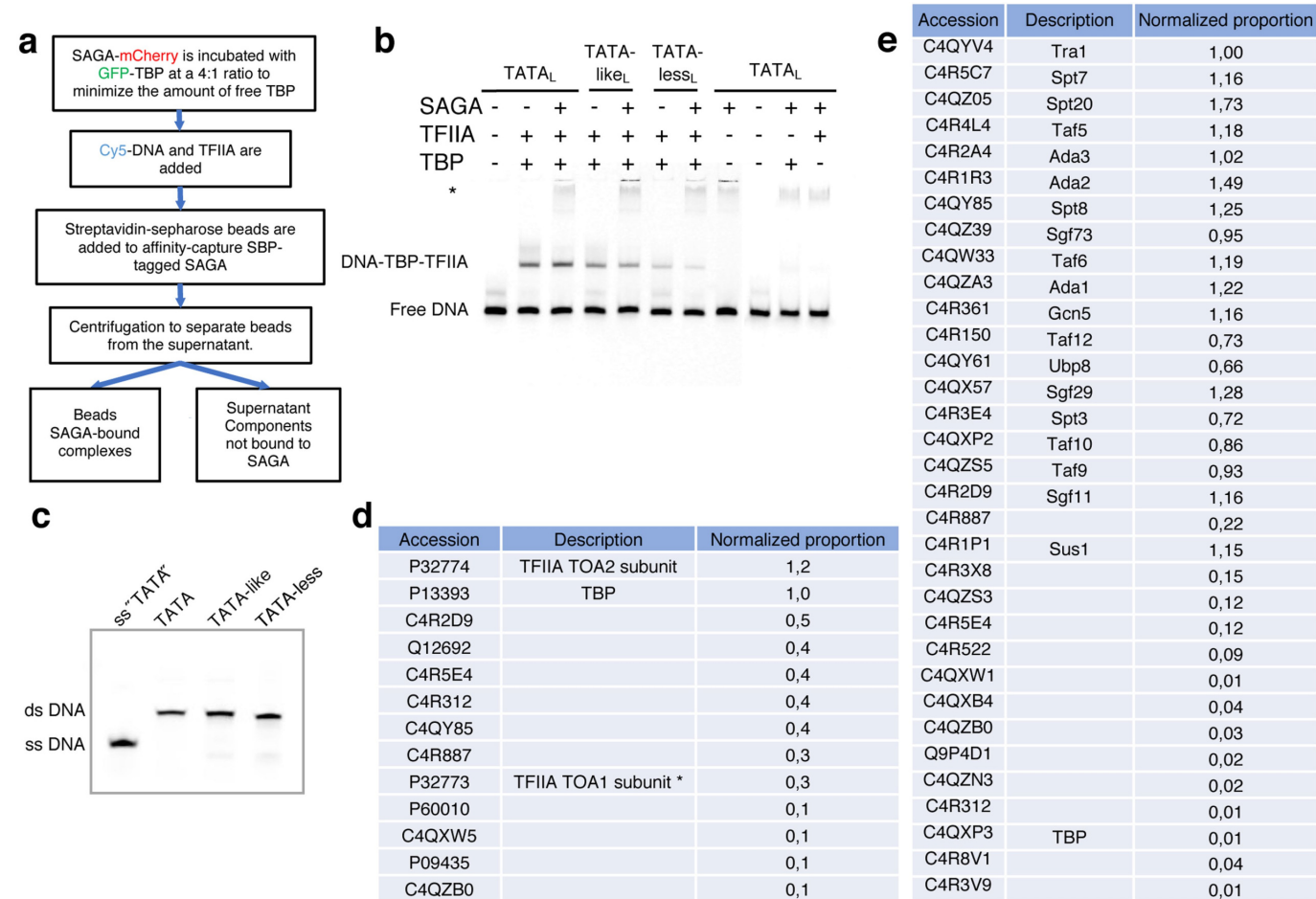
histones. As in the nucleosome analogue, hydrophobic interactions have a very important role in this binding. By contrast, the four-helix bundle preceding the association between Spt3 and the Spt7–Taf10 pair, linking Taf12–Ada1 to Spt7–Taf10, is maintained almost solely by hydrogen and electrostatic bonds. Only side chains of residues that participate in the interactions are shown.





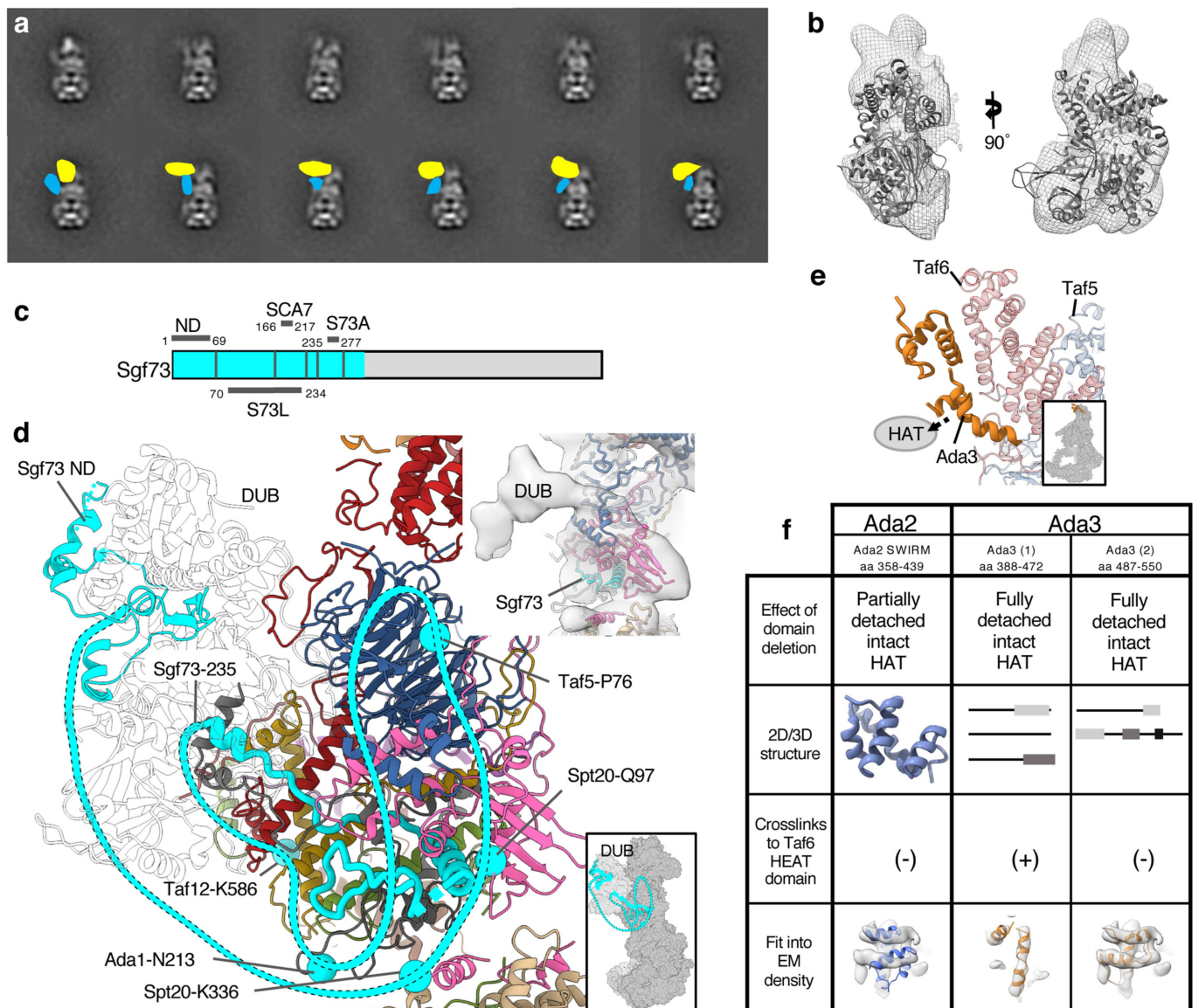
**Extended Data Fig. 6 | Mapping previously isolated mutations in Spt3 and TBP.** Several classes of Spt3 and TBP mutations were shown to interact genetically with respect to transcription. Mutations from two major studies<sup>21,64</sup>

are mapped on the structure of Spt3 and TBP in the SAGA-TBP complex. The mutations appear to cluster at the contact sites between TBP and Spt3.



**Extended Data Fig. 7 | TFIIA-dependent TBP release from SAGA.**  
**a**, Experimental set-up for pull-down assays that investigate TBP and DNA interactions with SBP-tagged SAGA. **b**, Gel-shift assay as presented in Fig. 4b but using a longer (100-bp) Cy5-labelled DNA: TATA-containing promoter (TATA<sub>L</sub>), a TATA-like DNA probe (TATA-like<sub>L</sub>) and a non-specific DNA probe (TATA-less<sub>L</sub>). The asterisk indicates non-specific DNA association with SAGA. **c**, Cy5-labelled DNA was almost exclusively double-stranded. Annealed Cy5-labelled DNA used in gel-shift and pull-down assays was loaded on a polyacrylamide 12% gel. Single stranded Cy5-labelled TATA DNA was loaded for

comparison. **d**, Summary of mass-spectrometry data for the major shifted DNA band (Fig. 4, lane 3) showing that it contains both TBP and TFIIA as its major constituents. The spectral count divided by the length in amino acids (PSM/AA) of each protein was normalized with respect to PSM/AA of TBP (raw data are provided in Supplementary Table 1). **e**, Summary of mass-spectrometry data of purified SAGA. To estimate stoichiometry, PSM/AA was calculated for each protein and normalized with respect to PSM/AA of subunit Tra1 (raw data are provided in Supplementary Table 2). Experiments were repeated three to four times.

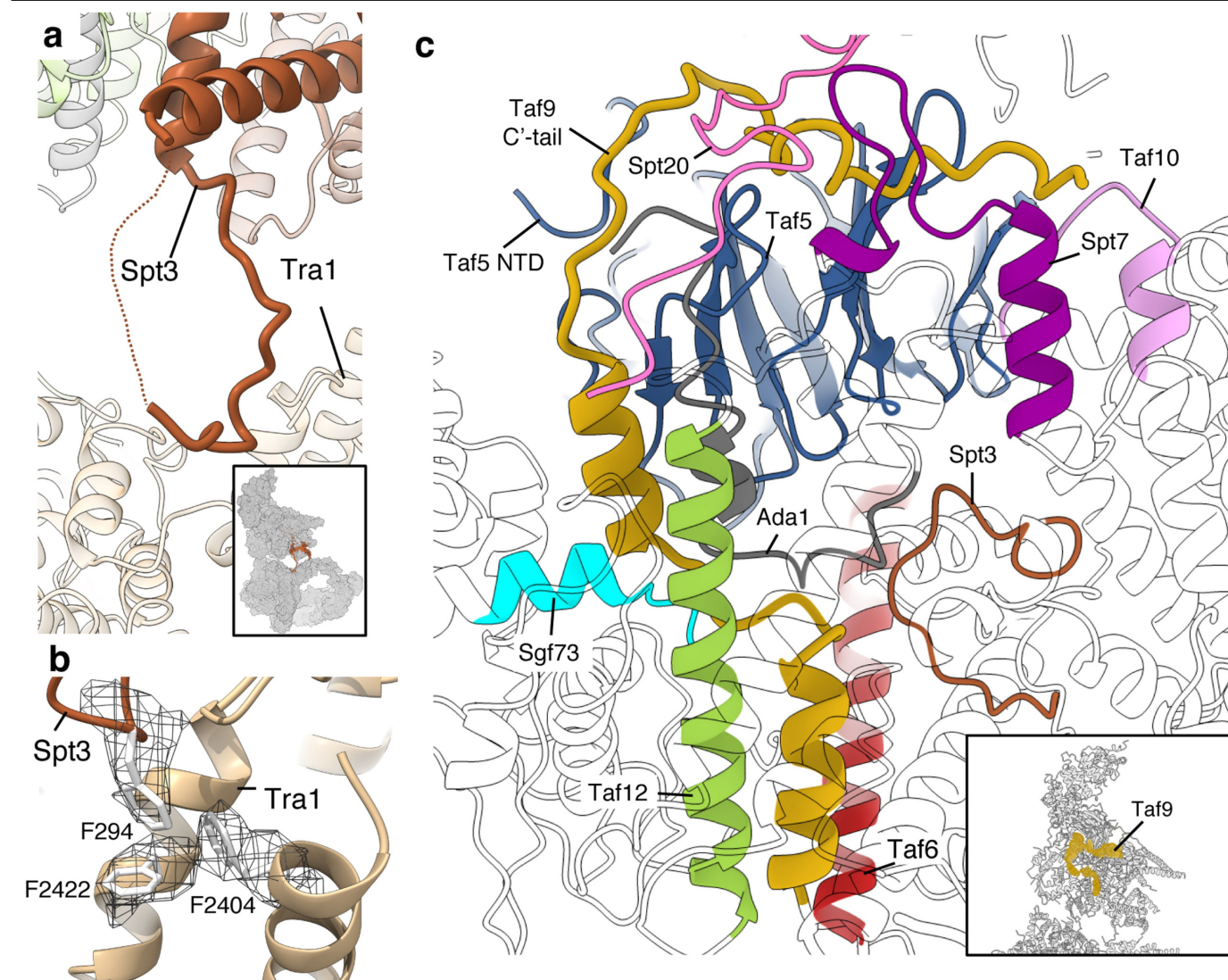


#### Extended Data Fig. 8 | Flexibility and anchoring of the enzymatic modules.

**a**, Two-dimensional classes of SAGA side views revealing different positions of the enzymatic HAT and DUB modules. Bottom, approximate positions of the modules are highlighted in yellow for the HAT module and in blue for the DUB module. The HAT module seems more diffuse and flexible than the DUB module, whose position fluctuates less. **b**, Docking of the DUB crystal structure (PDB: 6AQR) into the 15 Å resolution cryo-EM map reconstructed from a small class of particles that probably share a similar position for the DUB. **c**, Domain organization of the Sgf73 subunit. **d**, The Sgf73 linker tethers DUB to the central module. The linker (S73L) connecting the N-terminal end (ND), which is part of the DUB, and the anchoring domain (S73A) embedded in the central module, includes a SCA7 domain but additionally includes roughly 90 amino acids predicted to be unstructured. All residues that cross-link<sup>36</sup> to the Sgf73 linker can be mapped on the surface of SAGA. These residues are depicted with

light-blue spheres. A putative path for the 164-residue-long linker is delineated (dashed) according to the cross-linking sites and scarce traces of the linker found in the cryo-EM map. The top insert shows the density that forms contact between DUB and the central module. This contact point is located next to the Spt20 SEP and Taf5 LisH domains and is the only trace of the flexible Sgf73 linker in our maps. **e**, Two helical domains (ochre) anchor the HAT module at the surface of the Taf6 HEAT repeats (red). **f**, These helical domains are assigned to Ada3. Domain-deletion analysis identified two domains in Ada3 and one in Ada2 that serve to dock HAT on SAGA and whose deletion results in the release of intact HAT from SAGA<sup>36</sup>. Fit between the maps and secondary structure predictions (PSIPRED 3.3) or 3D structure of the Ada3 and Ada2 domains is presented in addition to available cross-linking data between these domains and the Taf6 HEAT repeats.





**Extended Data Fig. 9 | Protein loops and tails contribute to an intricate network of interactions and to bridges between the central module and Tra1.** **a**, Bridge established by the loop connecting the second and third helices of the cSpt3 histone fold (brown). **b**, The loop between helices  $\alpha 2$  and  $\alpha 3$  of the cSpt3 histone fold inserts between two helices of Tra1. Aromatic stacking interactions are formed between Spt3 F294 of this loop and F2404 and F2422 of Tra1. The map density for these three phenylalanine residues is depicted. **c**, The

C-terminal tail of Taf9 (R101–L139) and the short preceding loop illustrate the importance of regions lacking secondary structure elements in SAGA. These parts of Taf9 interact with many subunits and domains, including the Spt3 C' tail, Spt20 bridge domain, Taf12 histone fold, Ada1, Sgf73 anchoring domain, Taf6 histone fold, Spt7 histone fold, Taf5 WD40, Taf5 NTD and Taf10 histone fold.

Extended Data Table 1 | Cryo-EM data collection, refinement and validation statistics

	SAGA EMD-10447	SAGA-TBP EMD-10438 (overall) EMD-10440 (Tra1) EMD-10441 (main lobe)	Modelled coordinates PDB 6TB4 *
<b>Data collection and processing</b>			
Magnification	105000	105000	
Voltage (kV)	300	300	
Electron exposure (e <sup>-</sup> /Å <sup>2</sup> )	52.8	52.8	
Defocus range (μm)	0.6-4.6	0.5-4.9	
Pixel size (Å)	1.09	1.09	
Symmetry imposed	C1	C1	
Initial particle images (no.)	426839	1068534	
Final particle images (no.)	218114	338850	
Map resolution (Å)			
Overall	5.92	3.80	
Main Lobe	4.87	3.52	
Tra1 Lobe	4.52	3.50	
FSC threshold	0.143	0.143	
Map resolution range (Å)			
<b>Refinement</b>			
Model composition			
Non-hydrogen atoms			39144
Protein residues			5144
Ligands			
R.m.s. deviations			
Bond lengths (Å)			0.008
Bond angles (°)			1.38
Validation			
MolProbity score			1.86
Clashscore			5.53
Poor rotamers (%)			0.46
Ramachandran plot			
Favored (%)			89.5
Allowed (%)			10.4
Disallowed (%)			0.16

\*In addition a model including Spt8 and DUB fitted into lower-resolution maps was deposited under PDB accession code 6TBM.



## Reporting Summary

Nature Research wishes to improve the reproducibility of the work that we publish. This form provides structure for consistency and transparency in reporting. For further information on Nature Research policies, see [Authors & Referees](#) and the [Editorial Policy Checklist](#).

### Statistics

For all statistical analyses, confirm that the following items are present in the figure legend, table legend, main text, or Methods section.

n/a Confirmed

- ☒ ☐ The exact sample size ( $n$ ) for each experimental group/condition, given as a discrete number and unit of measurement
- ☒ ☐ A statement on whether measurements were taken from distinct samples or whether the same sample was measured repeatedly
- ☒ ☐ The statistical test(s) used AND whether they are one- or two-sided  
*Only common tests should be described solely by name; describe more complex techniques in the Methods section.*
- ☒ ☐ A description of all covariates tested
- ☒ ☐ A description of any assumptions or corrections, such as tests of normality and adjustment for multiple comparisons
- ☒ ☐ A full description of the statistical parameters including central tendency (e.g. means) or other basic estimates (e.g. regression coefficient) AND variation (e.g. standard deviation) or associated estimates of uncertainty (e.g. confidence intervals)
- ☒ ☐ For null hypothesis testing, the test statistic (e.g.  $F$ ,  $t$ ,  $r$ ) with confidence intervals, effect sizes, degrees of freedom and  $P$  value noted  
*Give  $P$  values as exact values whenever suitable.*
- ☒ ☐ For Bayesian analysis, information on the choice of priors and Markov chain Monte Carlo settings
- ☒ ☐ For hierarchical and complex designs, identification of the appropriate level for tests and full reporting of outcomes
- ☒ ☐ Estimates of effect sizes (e.g. Cohen's  $d$ , Pearson's  $r$ ), indicating how they were calculated

*Our web collection on [statistics for biologists](#) contains articles on many of the points above.*

### Software and code

Policy information about [availability of computer code](#)

Data collection

serialEM 3.7

Data analysis

Motioncor2, Gctf 1.06, crYOLO 1.5, Relion 3.0, cisTEM 1.0, CryoSparc 2, Imagic 4, Needle as part Emboss 6.6, iTASSER 5.1, Swiss-model 2019, Coot 0.87, RaptorX 1.02, PSIPRED 3.3 and 4, Chimera 1.14

For manuscripts utilizing custom algorithms or software that are central to the research but not yet described in published literature, software must be made available to editors/reviewers. We strongly encourage code deposition in a community repository (e.g. GitHub). See the Nature Research [guidelines for submitting code & software](#) for further information.

### Data

Policy information about [availability of data](#)

All manuscripts must include a [data availability statement](#). This statement should provide the following information, where applicable:

- Accession codes, unique identifiers, or web links for publicly available datasets
- A list of figures that have associated raw data
- A description of any restrictions on data availability

The pdb and emdb accession codes are now provided

## Field-specific reporting

Please select the one below that is the best fit for your research. If you are not sure, read the appropriate sections before making your selection.

- ☒ Life sciences ☐ Behavioural & social sciences ☐ Ecological, evolutionary & environmental sciences

## Life sciences study design

All studies must disclose on these points even when the disclosure is negative.

Sample size	For image analysis sample size (n=1068534) was chosen to assure the possibility to reach highest resolution
Data exclusions	After 2-D classification, images corresponding to false particles or to damages particles were excluded
Replication	Gel shift and pull-down experiments were performed in triplicates and all attempts were successfull
Randomization	All particles in the raw images were selected and analysed to ensure a unbiased initial particle population
Blinding	Image collection was performed automatically without human supervision or selection

## Reporting for specific materials, systems and methods

We require information from authors about some types of materials, experimental systems and methods used in many studies. Here, indicate whether each material, system or method listed is relevant to your study. If you are not sure if a list item applies to your research, read the appropriate section before selecting a response.

Materials & experimental systems		Methods	
n/a	Involved in the study	n/a	Involved in the study
<input checked="" type="checkbox"/>	<input type="checkbox"/> Antibodies	<input checked="" type="checkbox"/>	<input type="checkbox"/> ChIP-seq
<input type="checkbox"/>	<input checked="" type="checkbox"/> Eukaryotic cell lines	<input checked="" type="checkbox"/>	<input type="checkbox"/> Flow cytometry
<input checked="" type="checkbox"/>	<input type="checkbox"/> Palaeontology	<input checked="" type="checkbox"/>	<input type="checkbox"/> MRI-based neuroimaging
<input checked="" type="checkbox"/>	<input type="checkbox"/> Animals and other organisms		
<input checked="" type="checkbox"/>	<input type="checkbox"/> Human research participants		
<input checked="" type="checkbox"/>	<input type="checkbox"/> Clinical data		

## Eukaryotic cell lines

Policy information about [cell lines](#)

Cell line source(s)	Pichia Pastoris X33 edited to add a SBP affinity tag on the endogenous Sgf73 subunit
Authentication	sequencing
Mycoplasma contamination	Light microscopy control showed no contaminating organism
Commonly misidentified lines (See <a href="#">ICLAC</a> register)	No commonly misidentified cell lines were used

# Structure of the transcription coactivator SAGA

<https://doi.org/10.1038/s41586-020-1933-5>

Received: 23 August 2019

Accepted: 27 November 2019

Published online: 22 January 2020

Haibo Wang<sup>1</sup>, Christian Dienemann<sup>1</sup>, Alexandra Stützer<sup>2</sup>, Henning Urlaub<sup>2,3</sup>, Alan C. M. Cheung<sup>4,5</sup> & Patrick Cramer<sup>1\*</sup>

Gene transcription by RNA polymerase II is regulated by activator proteins that recruit the coactivator complexes SAGA (Spt–Ada–Gcn5–acetyltransferase)<sup>1,2</sup> and transcription factor IID (TFIID)<sup>2–4</sup>. SAGA is required for all regulated transcription<sup>5</sup> and is conserved among eukaryotes<sup>6</sup>. SAGA contains four modules<sup>7–9</sup>: the activator-binding Tra1 module, the core module, the histone acetyltransferase (HAT) module and the histone deubiquitination (DUB) module. Previous studies provided partial structures<sup>10–14</sup>, but the structure of the central core module is unknown. Here we present the cryo-electron microscopy structure of SAGA from the yeast *Saccharomyces cerevisiae* and resolve the core module at 3.3 Å resolution. The core module consists of subunits Taf5, Sgf73 and Spt20, and a histone octamer-like fold. The octamer-like fold comprises the heterodimers Taf6–Taf9, Taf10–Spt7 and Taf12–Ada1, and two histone-fold domains in Spt3. Spt3 and the adjacent subunit Spt8 interact with the TATA box-binding protein (TBP)<sup>2,7,15–17</sup>. The octamer-like fold and its TBP-interacting region are similar in TFIID, whereas Taf5 and the Taf6 HEAT domain adopt distinct conformations. Taf12 and Spt20 form flexible connections to the Tra1 module, whereas Sgf73 tethers the DUB module. Binding of a nucleosome to SAGA displaces the HAT and DUB modules from the core-module surface, allowing the DUB module to bind one face of an ubiquitinated nucleosome.

SAGA contains 19 subunits, distributed over four modules<sup>18</sup>. The Tra1 module binds activators<sup>19,20</sup>, the core module recruits TBP<sup>21</sup>, the HAT module contains the histone H3 acetyltransferase Gcn5<sup>1</sup> and the DUB module comprises a histone H2B deubiquitinase<sup>22,23</sup>. To determine the structure of SAGA, we purified the endogenous complex from *S. cerevisiae* using a strain with a C-terminal TAP-tag on subunit Spt20 (Methods). Purified SAGA contained all 19 subunits in apparently stoichiometric amounts (Extended Data Fig. 1a); we analysed this complex using cryo-electron microscopy (cryo-EM) and protein cross-linking analysis (Methods). We obtained a reconstruction of SAGA at an overall resolution of 3.9 Å (Extended Data Fig. 1, Supplementary Video 1).

The two large SAGA modules—the Tra1 and the core module—were resolved at 3.4 Å and 3.3 Å resolution, respectively (Extended Data Figs. 1d, e, 2a). We fitted the Tra1 structure<sup>13</sup>, built the core module and the protein regions connecting the two modules and refined the structure in real space (Extended Data Tables 1, 2, Extended Data Fig. 2b). The HAT and DUB modules were more flexible and were resolved at 9 Å and 12 Å resolution, respectively. The structure of the DUB module<sup>12</sup> could be fitted, but density for the HAT module could not be interpreted (Supplementary Video 1). Our protein–protein cross-linking analysis and previous cross-linking data<sup>7</sup> validated our modelling and assigned subunit Spt8 to a remaining density located between the core and Tra1 modules (Supplementary Table 1, Extended Data Fig. 2c, d).

The structure confirms the overall topology of SAGA with four flexibly connected modules<sup>8,24</sup> and reveals the intricate subunit architecture of the coactivator complex (Fig. 1). The SAGA structure contains only one copy of each subunit, in contrast to TFIID, which contains two copies of several subunits<sup>3,4</sup>. The SAGA core module occupies a central position and comprises the subunits Taf5, Taf6, Taf9, Taf10, Taf12, Spt3, Spt7, Spt20 and Ada1. The TBP-interacting subunit Spt8 is flexibly connected to the core module, as are the HAT and DUB modules (Fig. 1a). These three functional SAGA regions are lined up on one side of the complex that is predicted to face promoter DNA (Fig. 1a).

The core module contains a histone octamer-like fold and an adjacent submodule formed by subunits Taf5, Taf6 and Spt20 (Fig. 2). The octamer-like fold comprises three pairs of subunits that each contribute one histone fold, namely Taf6–Taf9, Taf10–Spt7 and Taf12–Ada1, and Spt3, which contributes two histone folds. The presence of an octamer-like fold explains early observations of histone-like subunit pairs in SAGA<sup>25,26</sup>. In contrast to a canonical histone octamer, which shows twofold symmetry, the SAGA octamer-like fold is fully asymmetric (Extended Data Fig. 3a).

Taf5 connects the octamer-like fold to the remainder of the core module and is thus important for core-module architecture (Fig. 2b). The N-terminal helical domain of Taf5 binds the C-terminal HEAT repeat region of Taf6. The C-terminal WD40 β-propeller of Taf5 docks to the histone fold pairs Taf6–Taf9 and Taf10–Spt7, and binds Spt20, which

<sup>1</sup>Max Planck Institute for Biophysical Chemistry, Department of Molecular Biology, Göttingen, Germany. <sup>2</sup>Max Planck Institute for Biophysical Chemistry, Bioanalytical Mass Spectrometry, Göttingen, Germany. <sup>3</sup>University Medical Center Göttingen, Institute of Clinical Chemistry, Bioanalytics Group, Göttingen, Germany. <sup>4</sup>Department of Structural and Molecular Biology, Institute of Structural and Molecular Biology, University College London, London, UK. <sup>5</sup>Institute of Structural and Molecular Biology, Biological Sciences, Birkbeck College, London, UK.

\*e-mail: pcramer@mpi-bpc.de

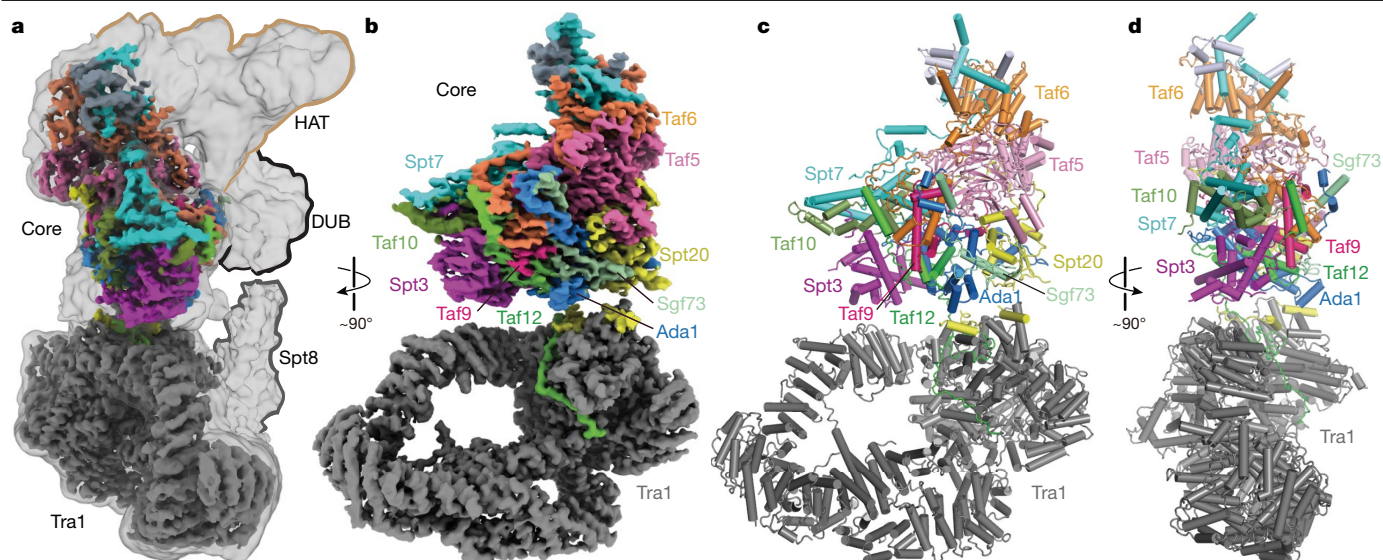


**Fig. 1 | Overall structure of SAGA. a**, Overview of SAGA structure. Low-pass-filtered and high-resolution composite cryo-EM maps of SAGA. The four SAGA modules Tra1, core, HAT and DUB are indicated. **b**, High-resolution composite

cryo-EM map reveals Tra1 and core modules. The subunit colour code is used throughout. **c, d**, Two views of the SAGA structure displayed as a ribbon model.

contains a SEP (shp1–eyc–p47) domain (Fig. 2c). Spt20 also contains an extended loop that forms a wedge between the two Taf5 domains, thereby stabilizing them in a defined orientation (Fig. 2b, Extended Data Fig. 3b). The Lis1 homology motif (LisH) helices of Taf5 interact with the SEP domain of Spt20 (Extended Data Fig. 3c). Taf6 contributes one  $\beta$ -strand to the Taf5 propeller, suggesting that Taf5 and Taf6 form an obligate heterodimer (Fig. 2c). The Taf5 propeller and the Taf6 HEAT region both interact with a stretch of Spt7 that extends from the octamer-like fold and continues into a bromodomain that is mobile.

SAGA has long been known to bind TBP<sup>15–17,27</sup>, implying a role in recruiting TBP to promoters. According to cross-linking<sup>7</sup> and genetic data<sup>2</sup>, SAGA interacts with TBP via the Spt3 and Spt8 subunits. Spt3 and Spt8 occupy adjacent locations at the edge of the octamer-like fold (Figs. 1, 3a). SAGA and TFIID share the subunits Taf5, Taf6, Taf9, Taf10 and Taf12<sup>18</sup>. TFIID consists of three lobes—A, B and C—and has been structurally defined<sup>3,4</sup>. Lobe A contains an octamer-like fold that resembles the fold observed in SAGA. However, Spt7 and Ada1 are replaced by TFIID subunits Taf3 and Taf4, respectively, and the two histone-fold domains of Spt3 are replaced by the histone fold pair Taf11–Taf13 in

TFIID (Fig. 3b). Despite these differences, the octamer-like folds in SAGA and TFIID bind TBP at the same relative position (Fig. 3a, b).

We generated a model of the SAGA–TBP complex by superposing the TBP-containing TFIID structure lobe A onto the SAGA core structure (Extended Data Fig. 3d). The model is consistent with TBP bridging between SAGA subunits Spt3 and Spt8. In TFIID, the TFIID-specific subunit Taf1 also contributes to TBP binding, and this may explain an apparently higher affinity of TFIID for TBP compared with SAGA<sup>2</sup>. TFIID lobe B contains a hexamer of histone-fold domains that lacks the Taf11–Taf13 pair and does not bind TBP, but otherwise resembles its counterpart in SAGA (Fig. 3c).

Structural comparisons also show how SAGA and TFIID form distinct structures despite sharing five subunits (Fig. 3). The shared subunits Taf5 and Taf6 have different structures in the two complexes. In TFIID, the Taf5 N-terminal domain docks to the octamer-like fold and is stabilized by the TFIID-specific subunit Taf4. In SAGA, Taf4 is absent and subunit Ada1 occupies its position. The Taf5 N-terminal domain occupies a position that is distant from the octamer-like fold, is stabilized by the SAGA-specific subunit Spt20 and contacts the Taf6 HEAT repeat

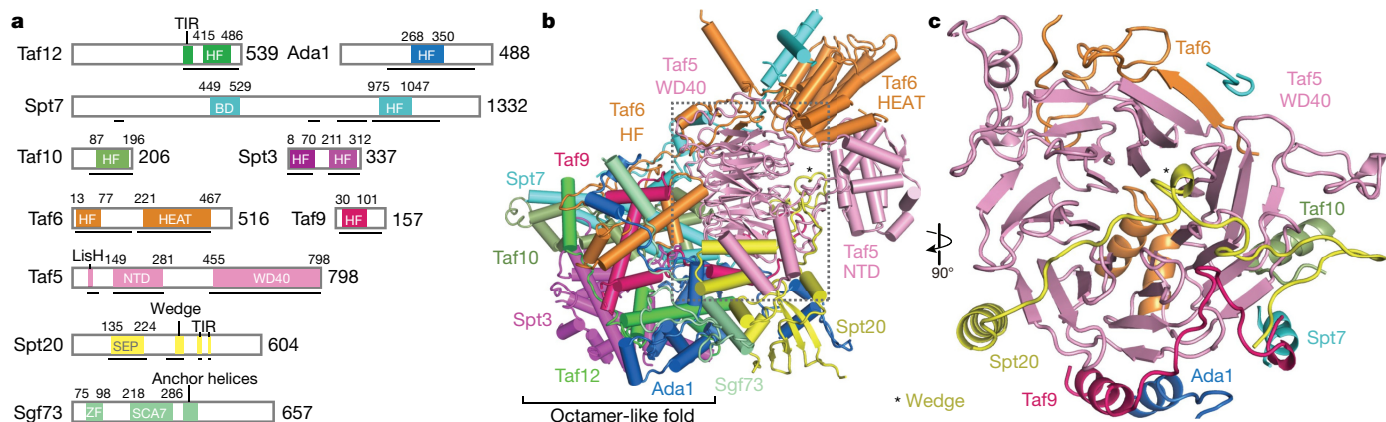


**Fig. 2 | SAGA core-module structure. a**, Subunit domain architecture. Residues at domain boundaries are indicated. BD, bromodomain; HF, histone fold; HEAT, HEAT repeat domain; NTD, N-terminal domain; WD40, WD40  $\beta$ -propeller domain; SEP, shp1–eyc–p47 domain; ZF, zinc finger domain; SCA7, SCA7

domain. Underlines indicate regions included in the structure. **b**, Ribbon model showing subunit arrangement and interactions. View and colour code as in Fig. 1. **c**, The Taf5 WD40 propeller domain interacts with six other SAGA subunits.



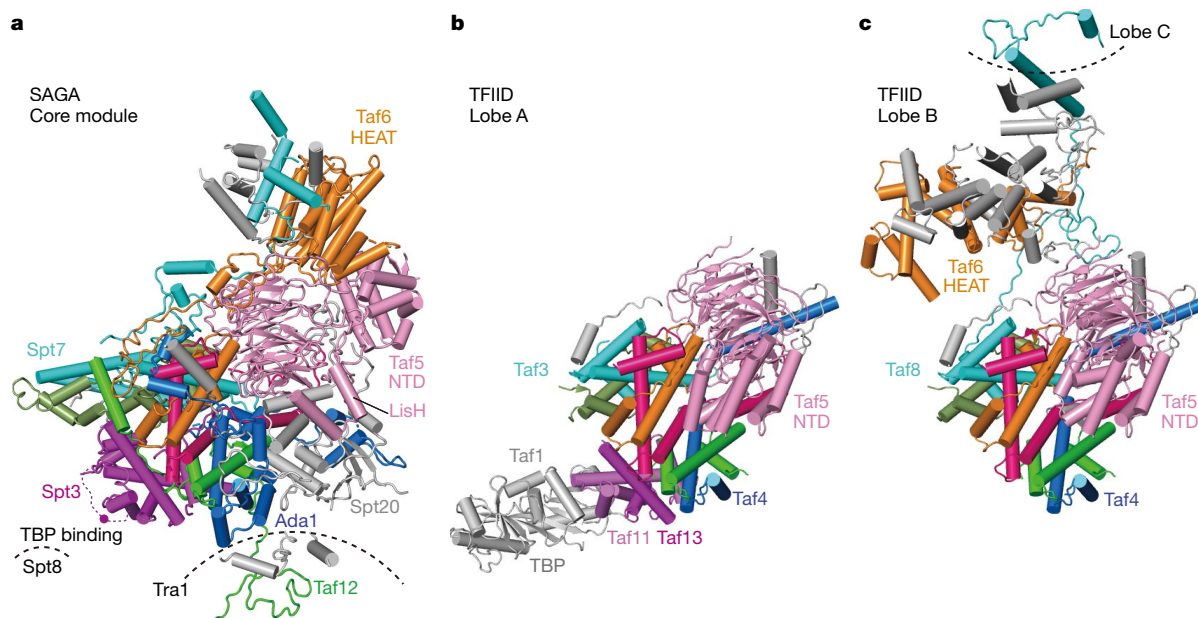


**Fig. 3 | Comparison of the SAGA core module with TFIID. a**, SAGA core module with subunits that are shared with TFIID in colour. A magenta dot depicts lysine residue K190 of Spt3 that was cross-linked to TBP<sup>18</sup> and is located in the loop between the two histone folds of Spt3 (dashed magenta line). **b**, Comparison with TBP-bound TFIID lobe A<sup>3</sup> shows that TBP binds to the same relative

position with respect to the histone-like fold in SAGA and TFIID. The histone-like folds are similar but differ in their subunit composition. **c**, Comparison with TFIID lobe B<sup>3</sup> reveals different structures of Taf5 and Taf6 that are due to complex-specific subunits.

domain, which also adopts a different position and structure compared to TFIID. Thus, incorporation of Ada1 or Taf4 into the octamer-like fold may trigger assembly of either SAGA or TFIID, respectively.

Our results also show that the core module forms flexible connections to the other modules of SAGA. The core subunits Taf12 and Spt20 contain Tra1-interacting regions (TIRs) that tether the Tra1 module. The Taf12 TIR (residues 353–410) meanders through a narrow surface groove formed by the TPR repeats of the FAT domain in Tra1, whereas Spt20 contains two TIRs (Extended Data Fig. 4a, b, d). TIR1 (residues 398–416) forms a latch that retains the Taf12 TIR, and TIR2 (residues 474–488) forms a helix that binds Tra1 (Extended Data Fig. 4a, b, d). These interactions are consistent with the known dissociation of Tra1 on Spt20 deletion<sup>28</sup>. Furthermore, subunit Sgf73 connects the core to the DUB module (Extended Data Fig. 4c, d). Whereas the central Sgf73 residues 353–437 are part of the core module (and designated ‘anchor helices’) and form interactions with Spt20, Ada1, Taf12, Taf6 and Taf9, approximately 100 N-terminal residues are part of the DUB module<sup>10–12</sup>. Consistent with this, a Sgf73 region overlapping with the anchor helices is required to retain Sgf73 in SAGA<sup>7,29</sup>.

We next investigated how SAGA binds its nucleosome substrate. Modelling a nucleosome onto the DUB module with the use of the DUB-nucleosome structure<sup>12</sup> resulted in a clash of the nucleosome with the core module. Therefore, SAGA needs to change conformation to bind the nucleosome. To investigate this, we prepared nucleosomes that were ubiquitinated at histone H2B residue K120 (corresponding to K123 of yeast H2B) and trimethylated at histone H3 residue K4 (Methods). We then formed a SAGA–nucleosome complex, and subjected this to cryo-EM analysis (Extended Data Fig. 5).

The cryo-EM data revealed the DUB module bound to the modified nucleosome at 3.7 Å resolution (Fig. 4a, Extended Data Fig. 5d–f). The obtained structure of the DUB module is virtually identical to the known structure of the isolated DUB module<sup>10,11</sup>. The DUB module binds to one face of the nucleosome in a way that is identical to that observed in the isolated DUB–nucleosome complex, although DUB modules bound to both faces of the nucleosome in this structure<sup>12</sup> (Extended Data Fig. 5g). Further data processing resolved the Tra1 module at 4.2 Å resolution, whereas the core module showed low resolution, and the HAT module

was invisible, suggesting that it became flexible on nucleosome binding (Extended Data Fig. 4d).

Comparison of low-pass-filtered maps shows that nucleosome binding displaces the HAT and DUB modules from the SAGA core module (Extended Data Fig. 5h). This is probably important for SAGA to fulfil its different functions during transcription activation when it is recruited by an activator to the promoter (Fig. 4b). Whereas the HAT and DUB modules would deubiquitinate and acetylate a promoter-bound nucleosome around or downstream of the transcription start site (TSS), the core module and Spt8 recruit TBP to the promoter upstream of the TSS. Flexibility between the modules would allow SAGA to bridge between promoter regions and to accommodate changes in their distance at different promoters.

Finally, our results have implications for understanding the structure and function of related coactivators. The yeast complex SLIK is identical to SAGA but contains a C-terminally truncated version of Spt7 and lacks Spt8<sup>30,31</sup>. In our SAGA structure, the Spt7 C-terminal region protrudes towards Spt8, suggesting that it contacts Spt8 and explaining why SLIK lacks Spt8. SAGA is highly conserved in human cells and contains

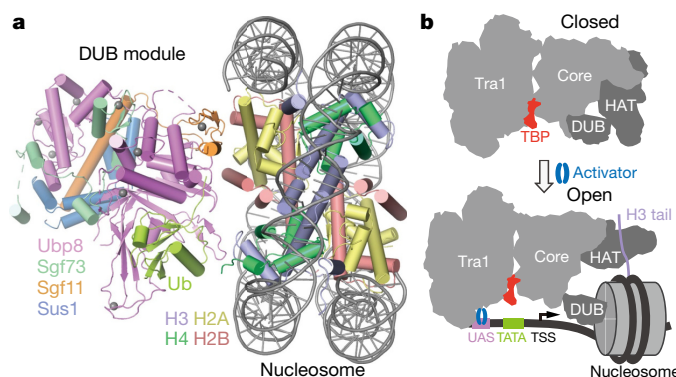


**Fig. 4 | Nucleosome binding induces changes in SAGA. a**, Structure of DUB–nucleosome complex within SAGA. **b**, Model showing changes in SAGA module orientation on nucleosome and promoter binding.



counterparts of all yeast SAGA subunits except Spt8<sup>18</sup> (Extended Data Table 3). Thus, our yeast SAGA structure is a good model for yeast SLIK and human SAGA. In conclusion, the structure of SAGA integrates available data, reveals differences to TFIID and provides a framework for studying the mechanisms used by this multifunctional coactivator to regulate transcription.

## Online content

Any methods, additional references, Nature Research reporting summaries, source data, extended data, supplementary information, acknowledgements, peer review information; details of author contributions and competing interests; and statements of data and code availability are available at <https://doi.org/10.1038/s41586-020-1933-5>.

- Grant, P. A. et al. Yeast Gcn5 functions in two multisubunit complexes to acetylate nucleosomal histones: characterization of an Ada complex and the SAGA (Spt/Ada) complex. *Genes Dev.* **11**, 1640–1650 (1997).
- Hahn, S. & Young, E. T. Transcriptional regulation in *Saccharomyces cerevisiae*: transcription factor regulation and function, mechanisms of initiation, and roles of activators and coactivators. *Genetics* **189**, 705–736 (2011).
- Patel, A. B. et al. Structure of human TFIID and mechanism of TBP loading onto promoter DNA. *Science* **362**, eaau8872 (2018).
- Kolesnikova, O. et al. Molecular structure of promoter-bound yeast TFIID. *Nat. Commun.* **9**, 4666 (2018).
- Baptista, T. et al. SAGA is a general cofactor for RNA polymerase II transcription. *Mol. Cell* **70**, 1163–1164 (2018).
- Spedale, G., Timmers, H. T. & Pijnappel, W. W. ATAC-king the complexity of SAGA during evolution. *Genes Dev.* **26**, 527–541 (2012).
- Han, Y., Luo, J., Ranish, J. & Hahn, S. Architecture of the *Saccharomyces cerevisiae* SAGA transcription coactivator complex. *EMBO J.* **33**, 2534–2546 (2014).
- Sharov, G. et al. Structure of the transcription activator target Tra1 within the chromatin modifying complex SAGA. *Nat. Commun.* **8**, 1556 (2017).
- Liu, G. et al. Architecture of *Saccharomyces cerevisiae* SAGA complex. *Cell Discov.* **5**, 25 (2019).
- Köhler, A., Zimmerman, E., Schneider, M., Hurt, E. & Zheng, N. Structural basis for assembly and activation of the heterotetrameric SAGA histone H2B deubiquitinase module. *Cell* **141**, 606–617 (2010).
- Samara, N. L. et al. Structural insights into the assembly and function of the SAGA deubiquitinating module. *Science* **328**, 1025–1029 (2010).
- Morgan, M. T. et al. Structural basis for histone H2B deubiquitination by the SAGA DUB module. *Science* **351**, 725–728 (2016).
- Díaz-Santín, L. M., Lukyanova, N., Aciyan, E. & Cheung, A. C. Cryo-EM structure of the SAGA and NuA4 coactivator subunit Tra1 at 3.7 angstrom resolution. *eLife* **6**, e28384 (2017).
- Sun, J. et al. Structural basis for activation of SAGA histone acetyltransferase Gcn5 by partner subunit Ada2. *Proc. Natl Acad. Sci. USA* **115**, 10010–10015 (2018).
- Belotserkovskaya, R. et al. Inhibition of TATA-binding protein function by SAGA subunits Spt3 and Spt8 at Gcn4-activated promoters. *Mol. Cell. Biol.* **20**, 634–647 (2000).
- Warfield, L., Ranish, J. A. & Hahn, S. Positive and negative functions of the SAGA complex mediated through interaction of Spt8 with TBP and the N-terminal domain of TFIIA. *Genes Dev.* **18**, 1022–1034 (2004).
- Sermwittayawong, D. & Tan, S. SAGA binds TBP via its Spt8 subunit in competition with DNA: implications for TBP recruitment. *EMBO J.* **25**, 3791–3800 (2006).
- Helmlinger, D. & Tora, L. Sharing the SAGA. *Trends Biochem. Sci.* **42**, 850–861 (2017).
- Larschan, E. & Winston, F. The *S. cerevisiae* SAGA complex functions in vivo as a coactivator for transcriptional activation by Gal4. *Genes Dev.* **15**, 1946–1956 (2001).
- Brown, C. E. et al. Recruitment of HAT complexes by direct activator interactions with the ATM-related Tra1 subunit. *Science* **292**, 2333–2337 (2001).
- Dudley, A. M., Rougeulle, C. & Winston, F. The Spt components of SAGA facilitate TBP binding to a promoter at a post-activator-binding step in vivo. *Genes Dev.* **13**, 2940–2945 (1999).
- Daniel, J. A. et al. Deubiquitination of histone H2B by a yeast acetyltransferase complex regulates transcription. *J. Biol. Chem.* **279**, 1867–1871 (2004).
- Henry, K. W. et al. Transcriptional activation via sequential histone H2B ubiquitylation and deubiquitylation, mediated by SAGA-associated Ubp8. *Genes Dev.* **17**, 2648–2663 (2003).
- Wu, P. Y., Ruhlmann, C., Winston, F. & Schultz, P. Molecular architecture of the *S. cerevisiae* SAGA complex. *Mol. Cell* **15**, 199–208 (2004).
- Gangloff, Y. G. et al. The human TFIID components TAF<sub>II</sub>135 and TAF<sub>II</sub>20 and the yeast SAGA components ADA1 and TAF<sub>II</sub>68 heterodimerize to form histone-like pairs. *Mol. Cell. Biol.* **20**, 340–351 (2000).
- Birck, C. et al. Human TAF<sub>II</sub>28 and TAF<sub>II</sub>18 interact through a histone fold encoded by atypical evolutionary conserved motifs also found in the SPT3 family. *Cell* **94**, 239–249 (1998).
- Eisenmann, D. M., Arndt, K. M., Ricupero, S. L., Rooney, J. W. & Winston, F. SPT3 interacts with TFIID to allow normal transcription in *Saccharomyces cerevisiae*. *Genes Dev.* **6**, 1319–1331 (1992).
- Wu, P. Y. & Winston, F. Analysis of Spt7 function in the *Saccharomyces cerevisiae* SAGA coactivator complex. *Mol. Cell. Biol.* **22**, 5367–5379 (2002).
- Kamata, K. et al. C-terminus of the Sgf73 subunit of SAGA and SLIK is important for retention in the larger complex and for heterochromatin boundary function. *Genes Cells* **18**, 823–837 (2013).
- Sternier, D. E., Belotserkovskaya, R. & Berger, S. L. SALSA, a variant of yeast SAGA, contains truncated Spt7, which correlates with activated transcription. *Proc. Natl Acad. Sci. USA* **99**, 11622–11627 (2002).
- Pray-Grant, M. G. et al. The novel SLIK histone acetyltransferase complex functions in the yeast retrograde response pathway. *Mol. Cell. Biol.* **22**, 8774–8786 (2002).

**Publisher's note** Springer Nature remains neutral with regard to jurisdictional claims in published maps and institutional affiliations.

© The Author(s), under exclusive licence to Springer Nature Limited 2020

## Methods

### Purification of endogenous SAGA

*S. cerevisiae* strain CB010 (MATa pep4::HIS3, prb1::LEU2, prc1::HISG, can1, ade2, trp1, ura3, his3, leu2-3,112) with a C-terminal TAP tag at Spt20 was grown in a 200-l fermenter (INFORS-HT) with 100 l YPD medium overnight and collected at  $OD_{600} \approx 5$ . Cell pellets were resuspended in lysis buffer (30 mM HEPES pH 7.5, 300 mM NaCl, 1.5 mM  $MgCl_2$ , 0.05% NP40, 1 mM DTT, 0.284  $\mu g\ ml^{-1}$  leupeptin, 1.37  $\mu g\ ml^{-1}$  pepstatin A, 0.17 mg  $ml^{-1}$  PMSF, 0.33 mg  $ml^{-1}$  benzamidine) and frozen in liquid nitrogen. Frozen yeast cell beads were milled to powder using a cryogenic grinder (Spex sample prep 6875D). The lysed yeast powder was thawed and mixed with half the volume of lysis buffer. Lysates were cleared by centrifugation (4,000g, 4 °C, 20 min and 235,000g, 4 °C, 60 min). The purification was performed as described<sup>28</sup>, with several modifications. In brief, the supernatant was incubated with IgG Sepharose-6 Fast Flow resin (GE Healthcare) at 4 °C for 3 h, the resin was washed with 5 column volumes of lysis buffer followed by 5 column volumes of TEV cleavage buffer (30 mM HEPES pH 7.5, 150 mM NaCl, 1.5 mM  $MgCl_2$ , 0.05% NP40, 1 mM DTT and 0.5 mM EDTA) and then resuspended in 5 ml of the TEV cleavage buffer. TEV cleavage was performed by incubating with His<sub>6</sub>-TEV protease for 16 h at 4 °C. The eluate was loaded onto a 1-ml HiTrap Q column (GE Healthcare) and eluted with a gradient using as high salt buffer 30 mM HEPES pH 7.5, 1 M NaCl, 1.5 mM  $MgCl_2$ , 1 mM DTT. Peak fractions were concentrated to approximately 1 mg  $ml^{-1}$ .

### Preparation of modified nucleosomes

To generate the K120-ubiquitinated histone H2B, we introduced a lysine-to-cysteine mutation (K120C) into the *Xenopus* H2B sequence and a glycine-to-cysteine mutation (G76C) to ubiquitin by site-directed mutagenesis. The dichloroacetone cross-link was formed between ubiquitin and H2B-K120 as described<sup>12</sup>, with minor changes. In brief, 100  $\mu M$  H2B-K120C and 100  $\mu M$  His<sub>6</sub>-Ub(G76C) proteins were incubated at 50 °C in reaction buffer (50 mM borate pH 8.1, 1 mM tris(2-carboxyethyl) phosphine (TCEP)) for 1 h to reduce cysteines, and were then cooled on ice for 1 h. Dimethyl formamide (DMF) dissolved in dichloroacetone was added to the solution to a final concentration of 100  $\mu M$  and incubated on ice for 1 h. The reaction was quenched with 50 mM  $\beta$ -mercaptoethanol, frozen and lyophilized. The resulting product mixture was resuspended in Ni-U buffer (20 mM HEPES pH 7.5, 500 mM NaCl, 6 M urea, 2 mM  $\beta$ -mercaptoethanol, 20 mM imidazole) and applied to a HisTrap HP 5 ml column (GE Healthcare). The bound proteins were eluted with Ni buffer supplemented with 150 mM imidazole, and dialysed into TEV cleavage buffer. After TEV cleavage for 16 h at 4 °C, the product was dialysed into Ni-U buffer and reappplied to a HisTrap HP 5 ml column to remove uncleaved products. The flow-through from the column was applied to a HiTrap SP 5 ml column (GE Healthcare) and eluted with a gradient of Ni-U buffer with 1M NaCl. Peak fractions were pooled and dialysed to water containing 5 mM  $\beta$ -mercaptoethanol, frozen and lyophilized.

H3K4me3 binding by the Sgf29 Tudor domain is required for chromatin targeting and histone H3 acetylation of SAGA<sup>32</sup>. To generate the K4-trimethylated histone H3 variant, a single lysine-to-cysteine mutation (K4C) was introduced into the H3 sequence by site-directed mutagenesis. Cysteine-engineered histone H3 K4C protein was alkylated as described<sup>33</sup>. In brief, purified protein was reduced with DTT before addition of a 50-fold molar excess of trimethylammonium bromide (Sigma 117196–25G). The reaction mixture was incubated for 4 h at 50 °C before quenching with 5 mM  $\beta$ -mercaptoethanol. The modified protein was desalted using a PD-10 desalting column (GE Healthcare) pre-equilibrated in water supplemented with 2 mM  $\beta$ -mercaptoethanol and lyophilized. Successful alkylation was confirmed by MALDI-TOF mass spectrometry. The Widom 601145 bp DNA was purified as described from the pUC19 8 × 145 bp 601-sequence plasmid using the restriction enzyme EcoRV to digest the DNA into

fragments<sup>34</sup>. Nucleosomes were reconstituted with modified histones and the Widom 601 DNA as described<sup>34</sup>.

### Cryo-EM sample preparation

Purified SAGA (or SAGA mixed with the modified nucleosome at a molar ratio of 1:2) was incubated with 3 mM BS3 for 1 h on ice, and quenched for 10 min using 10 mM Tris-HCl pH 7.5, 2 mM lysine and 8 mM aspartate. Quenched samples were applied to a 15–40% sucrose gradient in dialysis buffer (20 mM HEPES pH 7.5, 150 mM NaCl, 1.5 mM  $MgCl_2$ , 1 mM TCEP, 2% glycerol), and ultracentrifuged at 32,000 rpm (SW60 rotor) for 16 h at 4 °C. Gradients were fractionated in 200  $\mu l$  and analysed with native PAGE. The gels were stained with Syber Gold (Invitrogen) and Coomassie brilliant blue. Peak fractions containing SAGA or the SAGA–nucleosome complex were dialysed overnight, concentrated to approximately 0.2 mg  $ml^{-1}$  and used for grid preparation. Two microlitres of sample was applied to glow-discharged UltrAuFoil 2/2 grids (Quantifoil) on each side of the grid. After incubation for 10 s, the sample was blotted for 4 s and vitrified by plunging into liquid ethane using a Vitrobot Mark IV (FEI Company) operated at 4 °C and 100% humidity.

### Cryo-EM data collection and image processing

Cryo-EM data of the SAGA and SAGA–NCP were acquired on a FEI Titan Krios transmission electron microscope operated at 300 keV, equipped with a K2 summit direct detector and a GIF quantum energy filter (Gatan). Automated data acquisition was carried out using EPU software (FEI) at a nominal magnification of 130,000× or 105,000×, resulting in calibrated pixel sizes of 1.05 Å and 1.35 Å for SAGA and the SAGA–nucleosome complex, respectively. Movies of 40 frames were collected in counting mode over 9 s with a defocus range of 1.25–2.75  $\mu m$ . The dose rate was 4.7  $e^- \text{Å}^{-2} s^{-1}$  resulting in 1.06  $e^- \text{Å}^{-2}$  per frame for SAGA, and 4.9  $e^- \text{Å}^{-2} s^{-1}$  resulting in 1.10  $e^- \text{Å}^{-2}$  per frame for the SAGA–nucleosome complex, respectively. A total of 4,697 and 4,866 movies were collected for SAGA and the SAGA–nucleosome complex, respectively. Movie stacks were motion-corrected, CTF-estimated and dose-weighted using Warp<sup>35</sup>.

Particles of the SAGA data were auto-picked by Warp, yielding 250,368 particle images. Image processing was performed with RELION 3.0.5<sup>36</sup>. Particles were extracted using a box size of 400<sup>2</sup> pixels, and normalized. Reference-free 2D classification was performed to screen for good particles in the dataset. An ab initio model generated from cryoSPARC<sup>37</sup> was used as an initial reference for subsequent 3D classification. All classes containing intact SAGA density were combined (107,759 particles) and used for a global 3D refinement resulting in a map at 4.7 Å resolution. To improve the map for the core module of SAGA, focused 3D classification without image alignment was performed using a mask around the core module. The class that showed the best density for the core module was subjected to another round of 3D refinement resulting in an overall resolution of 4.1 Å. Focused refinement further improved the resolution to 3.4 Å and 3.3 Å for Tra1 and the core module, respectively. Post-processing of refined reconstructions was performed using automatic B-factor determination in RELION and reported resolutions are based on the gold-standard Fourier shell correlation (FSC) 0.143 criterion (B-factors of 107 Å<sup>2</sup> and 91 Å<sup>2</sup> for the Tra1 and the core module, respectively). Local resolution estimates were obtained using the built-in local resolution estimation tool of RELION using the estimated B-factors.

For the SAGA–nucleosome complex sample, 579,759 particles were auto-picked by Warp. As the DUB–nucleosome and the remaining parts of SAGA were not present together during the classification steps, particles of SAGA in the nucleosome-bound state and the DUB–nucleosome were processed separately. Otherwise, the processing procedure was the same as that for SAGA. However, focused 3D classification without alignment did not yield good core-module particles from the SAGA–nucleosome dataset. A reconstruction at 6.1 Å overall resolution was obtained from 86,910 particles of SAGA in the nucleosome-bound state.

# Article

Focused refinement further improved the resolution to 4.2 Å for the Tra1 lobe. For the DUB–nucleosome complex, a reconstruction at 3.7 Å overall resolution was obtained from 113,856 particles. Post-processing of the refined reconstructions was performed using automated B-factor determination in RELION and reported resolutions are based on the gold-standard FSC 0.143 criterion (B-factors of –149 Å<sup>2</sup> and –115 Å<sup>2</sup> for the Tra1 lobe and the DUB–nucleosome, respectively). Local resolution estimates were obtained using the built-in local resolution estimation tool of RELION using the previously estimated B-factors.

## Cross-linking and mass spectrometry

Samples for cross-linking mass spectrometry were performed essentially in the same way as those for cryo-EM. Cross-linked samples were purified by sucrose gradient centrifugation and fractions containing fully assembled complexes were pooled for mass spectrometry sample preparation. For in-solution digest, urea buffer (8 M urea, 50 mM NH<sub>4</sub>HCO<sub>3</sub>, pH 8) was added to pooled fractions to a final concentration of 1 M urea. Samples were reduced with 5 mM DTT (in 50 mM NH<sub>4</sub>HCO<sub>3</sub>, pH 8) for 30 min at 37 °C, 300 rpm followed by alkylation with 20 mM iodoacetamide (in 50 mM NH<sub>4</sub>HCO<sub>3</sub>, pH 8) for 30 min at 37 °C, 300 rpm, in the dark. The reaction was quenched by addition of 5 mM DTT (in 50 mM NH<sub>4</sub>HCO<sub>3</sub>, pH 8). Trypsin digest (Promega, V5111) was performed overnight at 37 °C with 1:20 mass ratio (trypsin:complex). Tryptic peptides were desalted using C18 spin columns (Harvard Apparatus 74-4601), lyophilized and dissolved in 30% (v/v) acetonitrile, 0.1% (v/v) trifluoroacetic acid. The peptide mixture was separated on a Superdex Peptide 3.2/300 (GE Healthcare) column run at 50 µl min<sup>-1</sup> with 30% (v/v) acetonitrile, 0.1% (v/v) trifluoroacetic acid. Cross-linked species are enriched by size-exclusion chromatography based on their higher molecular weight compared to linear peptides. Therefore, 50-µl fractions were collected from 1.0 ml post-injection. Fractions from 1.0–1.6 ml post-injection were dried in a speedvac and dissolved in 5% (v/v) acetonitrile, 0.05% (v/v) trifluoroacetic acid and analysed by liquid chromatography–tandem mass spectrometry (LC–MS/MS).

LC–MS/MS analyses were performed on a Q Exactive HF-X hybrid quadrupole-orbitrap mass spectrometer (Thermo Scientific) coupled to a Dionex Ultimate 3000 RSLCnano system. Peptides were loaded on a Pepmap 300 C18 column (Thermo Fisher) at a flow rate of 10 µl min<sup>-1</sup> in buffer A (0.1% (v/v) formic acid) and washed for 3 min with buffer A. The sample was separated on an in-house packed C18 column (30 cm; ReproSil–Pur 120 Å, 1.9 µm, C18-AQ; inner diameter, 75 µm) at a flow rate of 300 nl min<sup>-1</sup>. Sample separation was performed over 60 min (in-solution digest) or 120 min (in-gel digest) using a buffer system consisting of 0.1% (v/v) formic acid (buffer A) and 80% (v/v) acetonitrile, 0.08% (v/v) formic acid (buffer B). The main column was equilibrated with 5% B, followed by sample application and a wash with 5% B. Peptides were eluted by a linear gradient from 15–48% B or 20–50% B. The gradient was followed by a wash step at 95% B and re-equilibration at 5% B. Eluting peptides were analysed in positive mode using a data-dependent top-30 acquisition methods. MS1 and MS2 resolution were set to 120,000 and 30,000 full width at half maximum, respectively. Precursors selected for MS2 were fragmented using 30% normalized, higher-energy collision-induced dissociation (HCD) fragmentation. Allowed charge states of selected precursors were +3 to +7. Further MS/MS parameters were set as follows: isolation width, 1.4 *m/z*; dynamic exclusion, 10 s; max. injection time (MS1/MS2), 60 ms/200 ms. The lock mass option (*m/z* 445.12002) was used for internal calibration. All measurements were performed in duplicates. The .raw files of all replicates were searched by the software pLink 1, v.2.3.1<sup>38</sup> and pLink 2<sup>39</sup> against a customized protein database containing the expressed proteins. Protein–protein cross-links were filtered with 1% FDR and plotted using xVis<sup>40</sup>.

## Model building

The structure of the core module was built by first placing the known structure of the Taf5–Taf6–Taf9 trimer (PDB ID: 6F3T) into the density

by rigid-body fitting in Chimera. Adjustments were made to the protein sequence in Coot<sup>41</sup>; insertions and deletions were manually built according to the density. The histone-fold domains of Taf10, Spt7, Taf12, Adal and Spt3 and extensions from them were manually built. The structure of the Taf5 NTD (PDB ID: 2J49) and Taf6 HEAT domain (PDB ID: 4ATG) were placed into the density and adjusted in Coot. The remaining parts were built manually. Secondary structure predictions from PSIPRED were used to assist de novo modelling.  $\alpha$ -helices were generated using Coot and manually fitted into the density. Linkers between the helices were modelled where clear density was visible. Cross-linking restraints and densities from bulky residues such as Lys, Arg, Phe, Tyr and Trp were used to guide modelling. The SEP domain of Spt20 shares structural homology with human p47 (PDB: ISS6), and this structure guided Spt20 modelling. The structure of the Tra1 module was built by placing the structure of Tra1 (PDB ID: 5OJS) into the density by rigid-body-fitting in Chimera, and the TIRs of Taf12 and Spt20 were manually built in Coot based on the density and cross-linking restraints. The DUB–nucleosome structure (PDB ID: 4ZUX) was placed into the corresponding densities by rigid-body-fitting the DUB module and nucleosome in Chimera. All models were subjected to alternating manual adjustment and real-space refinement using Coot and PHENIX<sup>42</sup>, resulting in good stereochemistry as assessed by Molprobity<sup>43</sup>. Figures were generated in PyMOL (Schrödinger, v.2.2.2) and UCSF Chimera (v.1.13).

## Reporting summary

Further information on research design is available in the Nature Research Reporting Summary linked to this paper.

## Data availability

The electron density reconstructions and models of the complete SAGA complex, the Tra1 module, the core module, the DUB module–nucleosome complex and the nucleosome-bound state of SAGA were deposited with the Electron Microscopy Data Bank (accession codes EMD-10412, EMD-10413, EMD-10414, EMD-10415 and EMD-10416 respectively) and with the Protein Data Bank (accession codes 6T9I, 6T9J, 6T9K, and 6T9L). All the other relevant data are included in the Supplementary Information or are available from the authors upon request.

- Bian, C. et al. Sgf29 binds histone H3K4me2/3 and is required for SAGA complex recruitment and histone H3 acetylation. *EMBO J.* **30**, 2829–2842 (2011).
- Simon, M. D. et al. The site-specific installation of methyl-lysine analogs into recombinant histones. *Cell* **128**, 1003–1012 (2007).
- Dyer, P. N. et al. Reconstitution of nucleosome core particles from recombinant histones and DNA. *Methods Enzymol.* **375**, 23–44 (2004).
- Tegunov, D. & Cramer, P. Real-time cryo-electron microscopy data preprocessing with Warp. *Nat. Methods* **16**, 1146–1152 (2019).
- Zivanov, J. et al. New tools for automated high-resolution cryo-EM structure determination in RELION-3. *eLife* **7**, e42166 (2018).
- Punjani, A., Rubinstein, J. L., Fleet, D. J. & Brubaker, M. A. cryoSPARC: algorithms for rapid unsupervised cryo-EM structure determination. *Nat. Methods* **14**, 290–296 (2017).
- Yang, B. et al. Identification of cross-linked peptides from complex samples. *Nat. Methods* **9**, 904–906 (2012).
- Chen, Z. L. et al. A high-speed search engine pLink 2 with systematic evaluation for proteome-scale identification of cross-linked peptides. *Nat. Commun.* **10**, 3404 (2019).
- Combe, C. W., Fischer, L. & Rappsilber, J. xiNET: cross-link network maps with residue resolution. *Mol. Cell. Proteomics* **14**, 1137–1147 (2015).
- Emsley, P., Lohkamp, B., Scott, W. G. & Cowtan, K. Features and development of Coot. *Acta Crystallogr. D* **66**, 486–501 (2010).
- Afonine, P. V. et al. Real-space refinement in PHENIX for cryo-EM and crystallography. *Acta Crystallogr. D* **74**, 531–544 (2018).
- Chen, V. B. et al. MolProbity: all-atom structure validation for macromolecular crystallography. *Acta Crystallogr. D* **66**, 12–21 (2010).
- Yang, J. et al. The I-TASSER suite: protein structure and function prediction. *Nat. Methods* **12**, 7–8 (2015).
- Elias-Villalobos, A. et al. Chaperone-mediated ordered assembly of the SAGA and NuA4 transcription co-activator complexes in yeast. *Nat. Commun.* **10**, 5237 (2019).

**Acknowledgements** We thank M. Ninov for help with mass spectrometry and T. Schulz for yeast fermentation. H.W. was supported by an EMBO long-term fellowship (ALTF 650-2017). H.U. was supported by the Deutsche Forschungsgemeinschaft (SFB860). A.C.M.C. was

supported by Wellcome (102535/Z/13/Z). P.C. was supported by the Deutsche Forschungsgemeinschaft (SFB860, SPP1935, EXC 2067/1-390729940), the European Research Council (advanced investigator grant TRANSREGULON, grant agreement no. 693023) and the Volkswagen Foundation.

**Author contributions** H.W. carried out all experiments and data analysis except mass spectrometry analysis. C.D. assisted with cryo-EM data collection. A.C.M.C. contributed to developing the purification protocol and assisted with model building. A.S. and H.U. carried out mass spectrometry analysis. P.C. supervised research. H.W. and P.C. interpreted the data and wrote the manuscript, with input from all authors.

**Competing interests** The authors declare no competing interests.

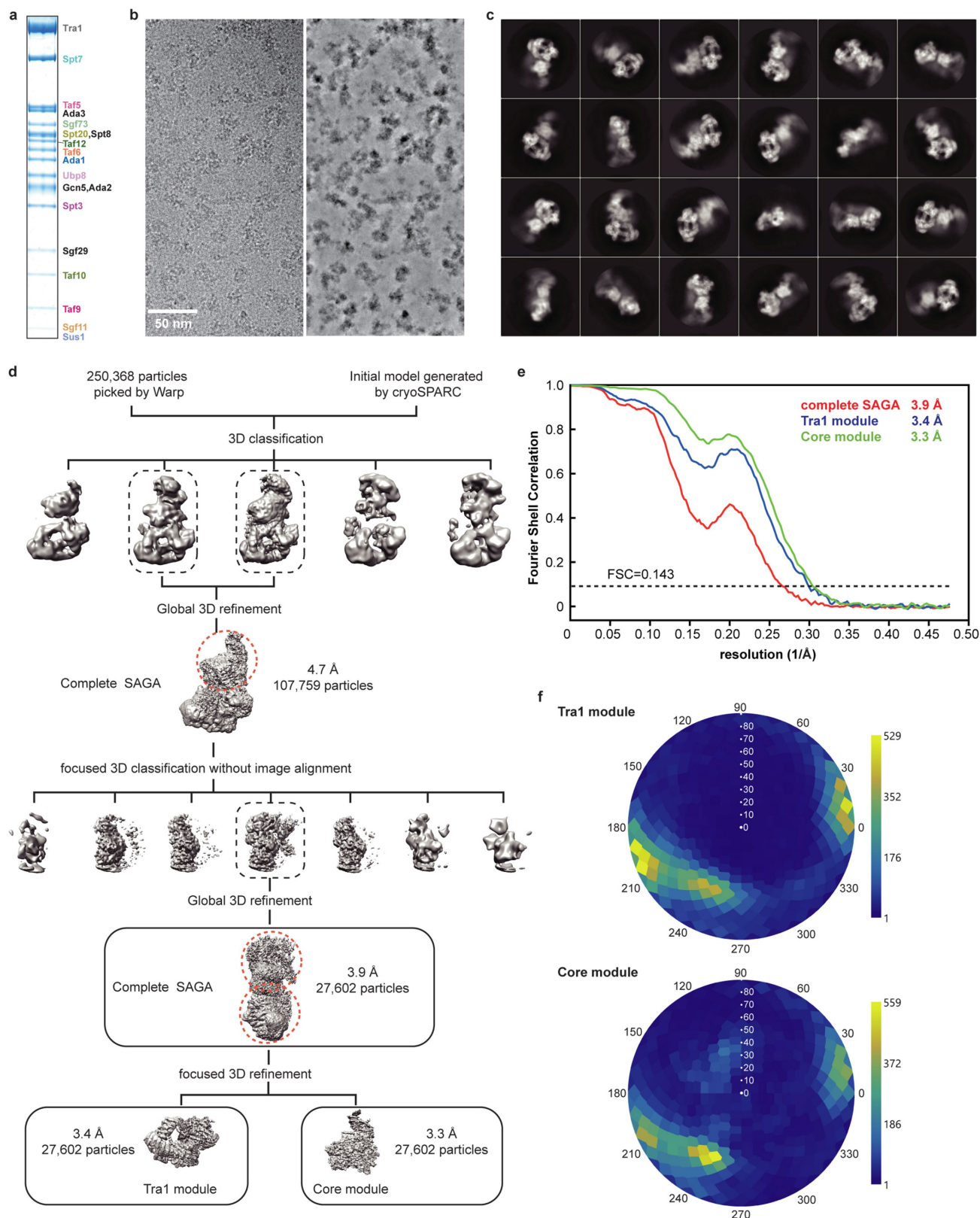
**Additional information**

**Supplementary information** is available for this paper at <https://doi.org/10.1038/s41586-020-1933-5>.

**Correspondence and requests for materials** should be addressed to P.C.

**Peer review information** *Nature* thanks Steve Hahn and the other, anonymous, reviewer(s) for their contribution to the peer review of this work.

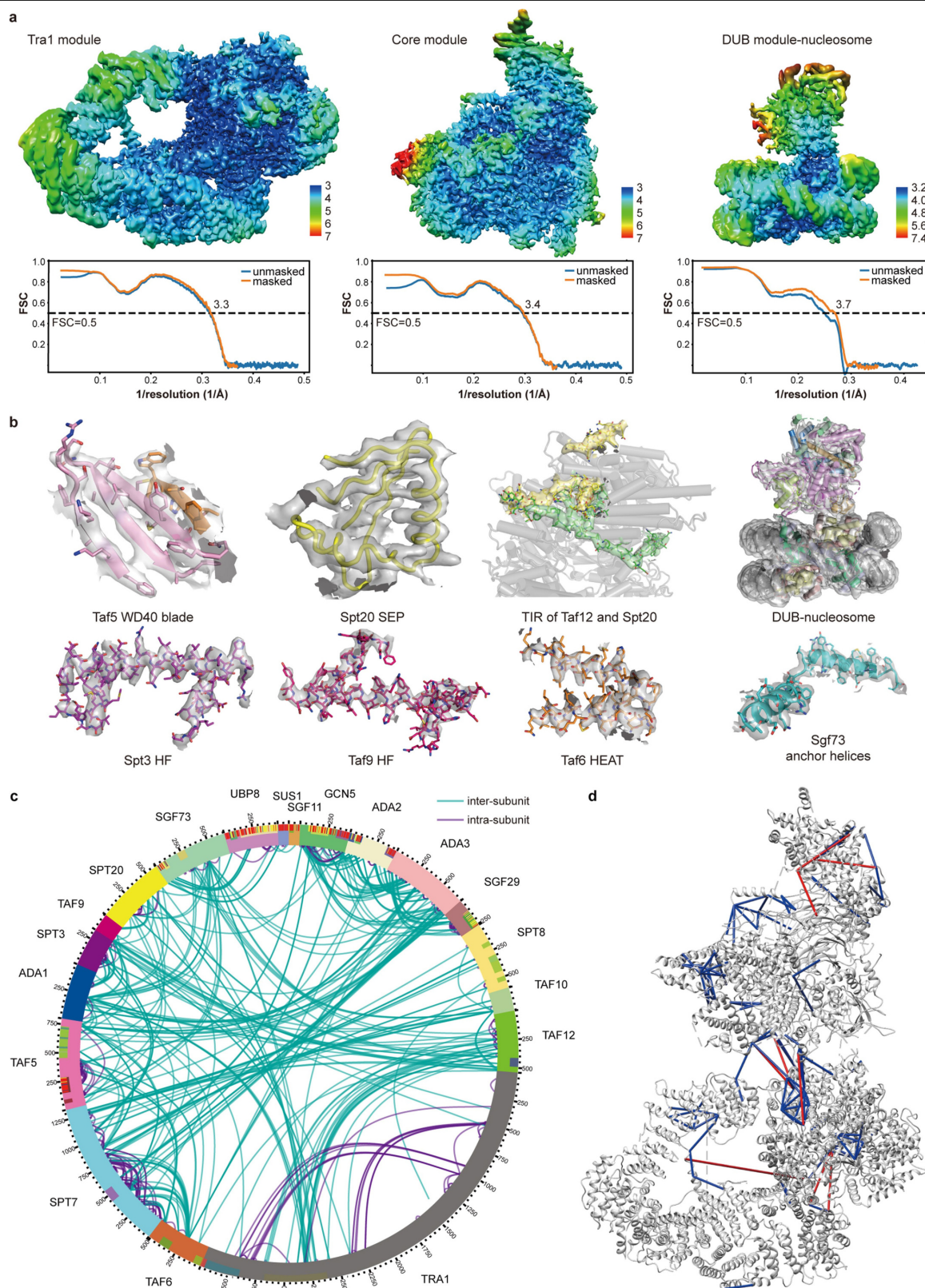
**Reprints and permissions information** is available at <http://www.nature.com/reprints>.



**Extended Data Fig. 1 | Cryo-EM structure determination and analysis of SAGA.** Related to data shown in Fig. 1. **a**, Purification of endogenous SAGA from *S. cerevisiae*. SDS-PAGE of peak fraction used for cryo-EM grid preparation. Identity of the bands was confirmed by mass spectrometry. For gel source data, see Supplementary Fig. 1. **b**, Exemplary cryo-EM micrograph of data collection. The micrograph is shown before (left) and after (right) denoising using Warp<sup>35</sup>. **c**, The 2D class averages. **d**, Sorting and classification tree used to reconstruct

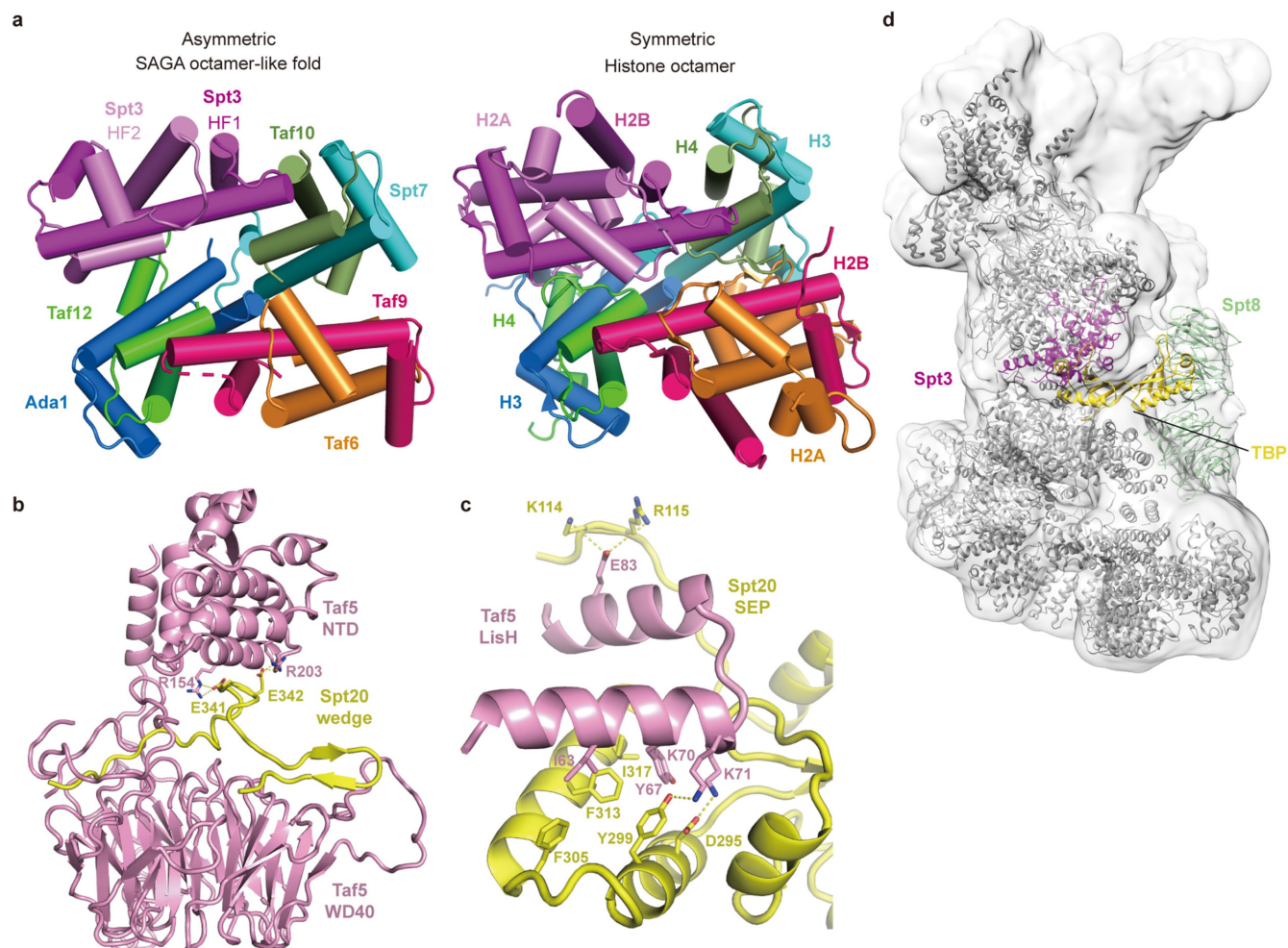
SAGA. **e**, FSC between half maps of the final reconstructions of the complete SAGA complex and the SAGA modules Tra1 and core. Resolutions for the gold-standard FSC 0.143 criterion are listed. **f**, Angular distribution plot for all particles in the final reconstructions of the SAGA core (top) and Tra1 (bottom) modules. Colour shading from blue to yellow correlates with the number of particles at a specific orientation as indicated.





**Extended Data Fig. 2 | Quality of the SAGA structure.** Relates to data in Figs. 1, 2. **a**, SAGA reconstruction coloured according to local resolution<sup>43</sup>. Model-map FSC curves calculated between the refined atomic models and maps are shown below. **b**, Electron density (grey transparent surface) for various SAGA regions as indicated. **c**, Overview of the cross-linking data. Circular plot of high-confidence lysine-lysine intersubunit (green) and intrasubunit (purple) cross-links obtained by mass spectrometry for the SAGA complex. The mass spectrometry measurement was repeated twice independently with similar

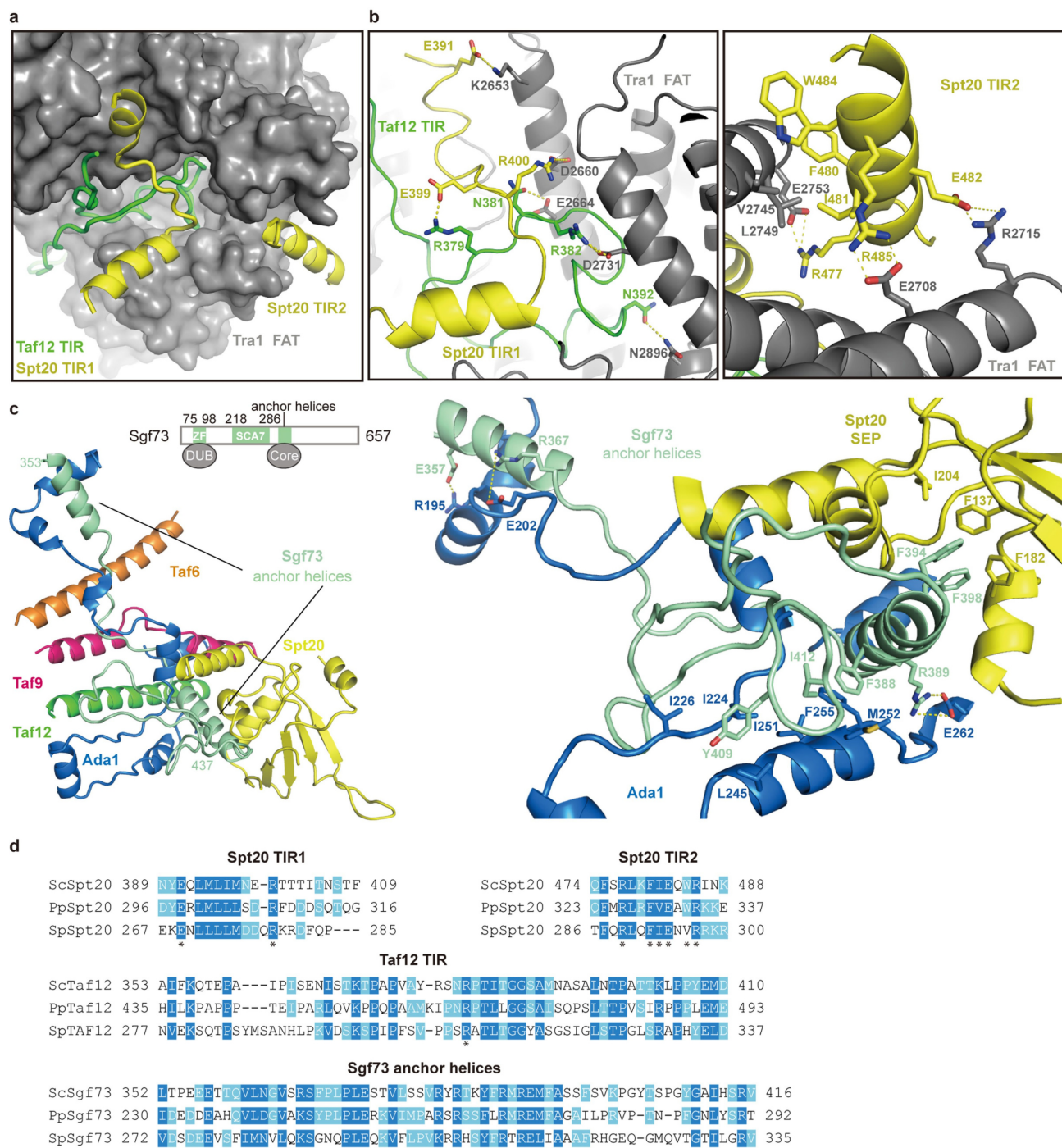
results. Totals of 396 unique intersubunit cross-links and 514 intrasubunit cross-links were obtained. **d**, Validated cross-links mapped onto the SAGA structure. Out of 396 unique intersubunit cross-links, 120 could be mapped onto the core-module structure, and 109 were located within the 30 Å distance limit for the BS3 cross-linker. Blue lines depict the cross-links with cross-linked sites within the 30 Å distance permitted by BS3, whereas red lines depict cross-links over more than 30 Å.



**Extended Data Fig. 3 | Comparison of the histone-like fold in SAGA with the histone octamer, details of Taf5-Spt20 interactions, and model of the SAGA-TBP complex.** Relates to data in Figs. 1–3. **a**, Comparison of the SAGA core module histone octamer-like structure with the canonical histone octamer core (PDB: 1AOI). The canonical octamer core is rendered as the colour for the SAGA octamer-like fold. **b**, Details of Taf5-Spt20 wedge interactions.

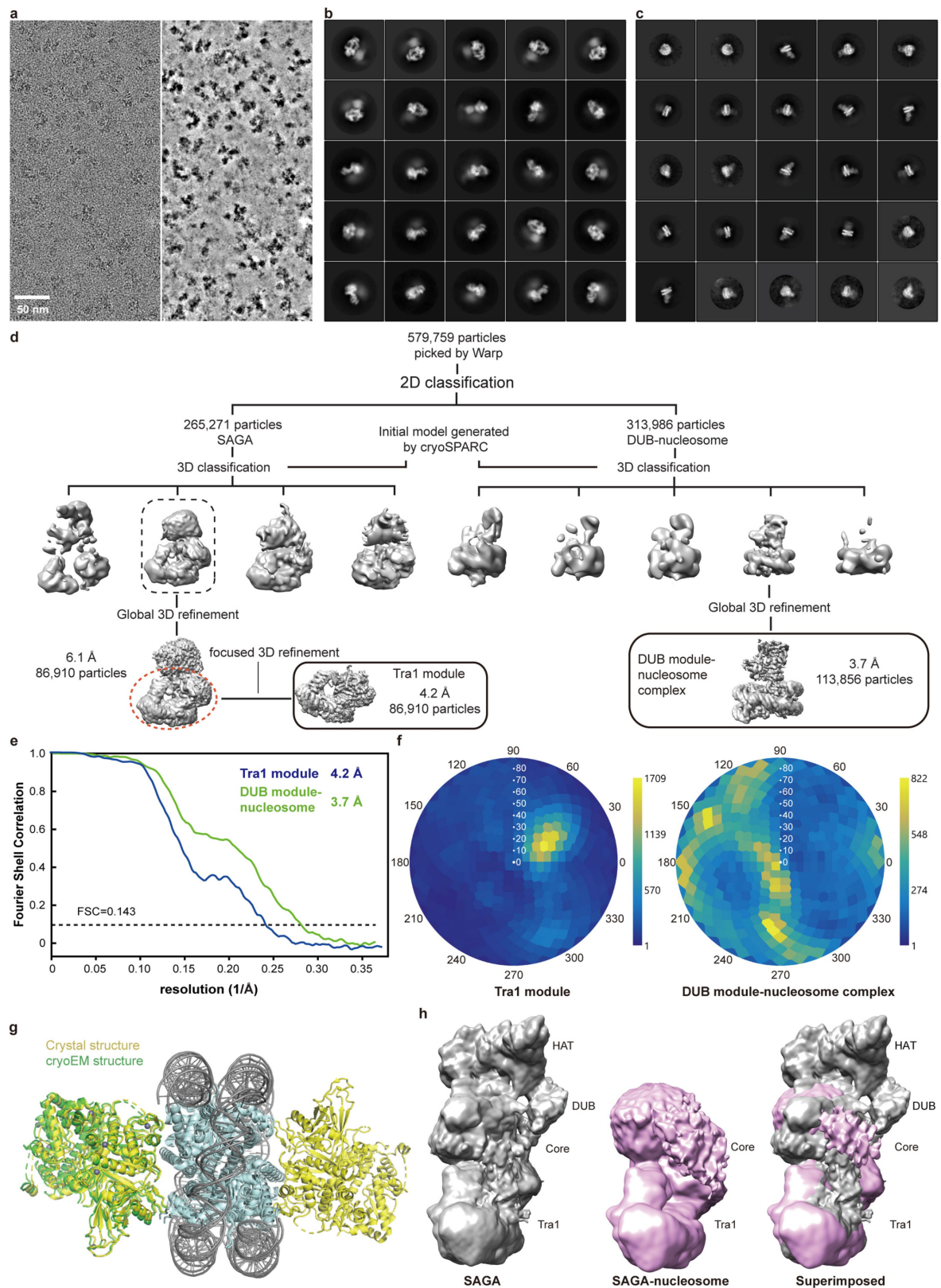
Residues involved in the interactions are shown in sticks and coloured as indicated. **c**, Details of interactions between the Taf5 LisH domain and Spt20 SEP domain. Residues involved in the interactions are shown in sticks and coloured as indicated. **d**, Model of the SAGA-TBP complex. The model was generated by superposing the TBP-containing TFIID lobe A onto the SAGA core structure. A homology model for Spt8 was generated by the I-TASSER server<sup>44</sup>.





**Extended Data Fig. 4 | Details of intermodule interactions.** Relates to data in Figs. 1, 2. **a**, Binding interface between core and Tra1 modules. The Tra1 FAT domain (grey) is shown as a surface representation. The TIRs of Taf12 (green) and Spt20 (yellow) are shown in cartoon representation. **b**, Details of the interactions depicted in **a**. **c**, Sgf73 (turquoise) tethers the DUB module to the

core module. Residues involved in the interactions are shown in sticks and coloured as indicated. **d**, Sequence alignment of SAGA subunit regions involved in intermodule interactions. Conserved residues are highlighted in blue. Key residues are labelled with asterisks<sup>45</sup>. Sc, *S. cerevisiae*; Pp, *Pichia pastoris*; Sp, *Schizosaccharomyces pombe*.



Extended Data Fig. 5 | See next page for caption.

**Extended Data Fig. 5 | Cryo-EM structure determination and analysis of the SAGA–nucleosome complex.** Relates to data in Fig. 4. **a**, Exemplary cryo-EM micrograph of data collection. The micrograph is shown before (left) and after (right) denoising using Warp<sup>35</sup>. **b**, The 2D class averages for the SAGA–nucleosome complex. **c**, The 2D class averages for the DUB module–nucleosome subcomplex. **d**, Sorting and classification tree used to reconstruct the DUB module–nucleosome complex at 3.7 Å resolution. **e**, FSC between half maps of the final reconstructions of the SAGA module, Tra1 and the DUB module–nucleosome complex from SAGA–nucleosome complex data.

Resolutions for the gold-standard FSC 0.143 criterion are listed. **f**, Angular distribution plot for all particles in the final reconstruction of the SAGA DUB module–nucleosome complex. Colour shading from blue to yellow correlates with the number of particles at a specific orientation as indicated. **g**, Superposition of the crystal structure of DUB-ubiquitinated nucleosome (4ZUX)<sup>12</sup> onto the cryo-EM structure presented here. Structures are shown in cartoon and coloured as indicated. **h**, Comparison of the low-pass-filtered overall cryo-EM maps of SAGA and the SAGA–nucleosome complex. Densities for the HAT and DUB modules are lost on nucleosome binding to SAGA.



Extended Data Table 1 | Cryo-EM data collection, refinement and validation statistics

	SAGA (EMD-10412) (PDB 6T9I)	SAGA TraI module (EMD-10413) (PDB 6T9J)	SAGA core module (EMD-10414) (PDB 6T9K)	SAGA DUB module- nucleosome (EMD-10415) (PDB 6T9L)	SAGA in nucleosome- bound state (EMD-10416)
<b>Data collection and processing</b>					
Magnification	130,000	130,000	130,000	105,000	105,000
Voltage (kV)	300	300	300	300	300
Electron exposure (e-/Å <sup>2</sup> )	42.45	42.45	42.45	44.17	44.17
Defocus range (µm)	1.25 to 2.75	1.25 to 2.75	1.25 to 2.75	1.25 to 2.75	1.25 to 2.75
Pixel size (Å)	1.05	1.05	1.05	1.37	1.37
Symmetry imposed	C1	C1	C1	C1	C1
Initial particle images (no.)	250,368	250,368	250,368	579,759	579,759
Final particle images (no.)	27,602	27,602	27,602	113,856	86,910
Map resolution (Å)	3.9	3.4	3.3	3.7	6.1
FSC threshold	0.143	0.143	0.143	0.143	0.143
Map resolution range (Å)	3.2 – 8.1	3.0 – 5.8	3.1 – 8.0	3.2 – 7.3	–
<b>Refinement</b>					
Initial models used (PDB code)	5OJS, 6MZD, 6F3T, 2J49, 4ATG, 1SS6	5OJS	6MZD, 6F3T, 2J49, 4ATG, 1SS6	4ZUX	
Model resolution (Å)	3.3	3.2	3.3	3.6	
FSC threshold	0.5	0.5	0.5	0.5	
Model resolution range (Å)	2.6 – 3.2	2.7 – 3.2	2.8 – 3.4	3.4 – 3.8	
Map sharpening <i>B</i> factor (Å <sup>2</sup> )	-137.1	-107.119	-90.9	-114.6	
Model composition					
Non-hydrogen atoms	48822	29551	19241	18157	
Protein residues	6047	3617	2426	1532	
Nucleotide	0	0	0	290	
Ligands	0	0	0	8	
<i>B</i> factor					
Protein	58.5	66.3	46.6	20.6	
Nucleic acid	-	-	-	13.6	
Ligand	-	-	-	523.51	
R.m.s. deviations	0.007	0.008	0.006	0.002	
Bond lengths (Å)	1.295	1.353	1.211	0.455	
Bond angles (°)					
Validation					
MolProbity score	1.84	1.79	1.78	1.39	
Clashscore	6.70	5.51	5.85	7.11	
Poor rotamers (%)	0.9	0.9	0.43	0.07	
Ramachandran plot					
Favored (%)	92.48	91.97	92.81	98.93	
Allowed (%)	7.45	8.00	7.10	1.07	
Disallowed (%)	0.07	0.03	0.08	0	

**Extended Data Table 2 | Modelling of yeast SAGA subunits, domains and regions**

Subunit / Chain ID	Domain	Residue range	Modelling method	Notes
Spt20 / B	SEP	112-134	<i>de novo</i> modelling	153-168 missing
		135-224	homology-modelling: 1SS6	
	Wedge	277-322	<i>de novo</i> modelling	
		323-360	<i>de novo</i> modelling	
		389-416	<i>de novo</i> modelling	
Spt3 / C	TIR	474-488	<i>de novo</i> modelling	266-297 missing
	HF1	3-86	homology-modelling: 6MZD	
	HF2	140-154	<i>de novo</i> modelling	
		191-209	<i>de novo</i> modelling	
		210-312	homology-modelling: 6MZD	
Taf5 / D	C-term	313-337	<i>de novo</i> modelling	737-742 missing
	LisH	56-88	<i>de novo</i> modelling	
	NTD	89-125	homology-modelling: 6MZD	
		149-281	Crystal structure: 2J49	
		430-454	<i>de novo</i> modelling	
Taf6 / E	WD40	455-798	homology-modelling: 6F3T & <i>de novo</i> modelling	235-242 missing 435-442 missing
	HF	8-77	homology-modelling: 6F3T	
		78-176	<i>de novo</i> modelling	
		188-220	<i>de novo</i> modelling	
	HEAT	221-467	homology-modelling: 4ATG & <i>de novo</i> modelling	
Taf9 / F	HF	30-101	homology-modelling: 6F3T	79-87 missing
	C-term	102-149	<i>de novo</i> modelling	
Taf10 / G	HF	67-86	<i>de novo</i> modelling	insertion 136-178
		87-196	homology-modelling: 6MZD & <i>de novo</i> modelling	
	C-term	197-206	<i>de novo</i> modelling	
Ada1 / H	N-term.	181-267	<i>de novo</i> modelling	327-331 missing 388-393 missing
	HF	268-350	homology-modelling: 6MZD	
		351-418	<i>de novo</i> modelling	
Taf12 / I	TIR	353-413	<i>de novo</i> modelling	
	HF	415-486	homology-modelling: 6MZD	
	C-term	487-525	<i>de novo</i> modelling	
Spt7 / K	HF	152-187	<i>de novo</i> modelling	
		728-754	<i>de novo</i> modelling	
		849-930	<i>de novo</i> modelling	
		952-974	<i>de novo</i> modelling	
		975-1047	homology-modelling: 6MZD	
Sfg73 / Q	anchor helices	1048-1085	<i>de novo</i> modelling	
		353-398 399-436	<i>de novo</i> modelling <i>de novo</i> modelling	
Tra1 / T	Finger	1-950	homology-modelling: 5OJS	160-213, 259-278, 523-557, 652-672 missing
	N-Clasp	951-1142	homology-modelling: 5OJS	
	Ring	1143-2445	homology-modelling: 5OJS	2017-2021, 2044-2088, 2108-2114, 2131-2137, 2147-2153 missing
	C-Clasp	2446-2598	homology-modelling: 5OJS	
	FAT	2599-3219	homology-modelling: 5OJS	2925-2935, 3183-3201 missing
	Kinase	3220-3744	homology-modelling: 5OJS	
Chain U	poly-alanine		<i>de novo</i> modelling	Unassigned regions

Extended Data Table 3 | Conservation of SAGA between yeast and human

	<i>S.c.</i> SAGA Subunits	<i>H.s.</i> SAGA Subunits	HHpred similarity*
HAT module	Ada2	TADA2B	0.569
	Ada3	TADA3	0.278
	Gcn5	GCN5/PCAF	0.851/0.864
	Sgf29	SGF29	0.249
DUB module	Sgf11	ATXN7L3	0.356
	Sgf73	ATXN7	0.205
	Sus1	ENY2	0.518
	Ubp8	USP22	0.576
Core module	Taf5	TAF5L	0.578
	Taf6	TAF6L	0.344
	Taf9	TAF9	0.657
	Taf10	TAF10	0.688
	Taf12	TAF12	0.677
	Ada1	TADA1	0.190
	Spt3	SUPT3H	0.378
	Spt7	SUPT7L	0.167
	Spt8	--	
	Spt20	SUPT20H	0.295
Tra1	Tra1	TRRAP	0.464

\*The HHpred similarity scores are calculated between homologous regions only.

## Reporting Summary

Nature Research wishes to improve the reproducibility of the work that we publish. This form provides structure for consistency and transparency in reporting. For further information on Nature Research policies, see [Authors & Referees](#) and the [Editorial Policy Checklist](#).

### Statistics

For all statistical analyses, confirm that the following items are present in the figure legend, table legend, main text, or Methods section.

n/a Confirmed

- ☒ ☐ The exact sample size ( $n$ ) for each experimental group/condition, given as a discrete number and unit of measurement
- ☒ ☐ A statement on whether measurements were taken from distinct samples or whether the same sample was measured repeatedly
- ☒ ☐ The statistical test(s) used AND whether they are one- or two-sided  
*Only common tests should be described solely by name; describe more complex techniques in the Methods section.*
- ☒ ☐ A description of all covariates tested
- ☒ ☐ A description of any assumptions or corrections, such as tests of normality and adjustment for multiple comparisons
- ☒ ☐ A full description of the statistical parameters including central tendency (e.g. means) or other basic estimates (e.g. regression coefficient) AND variation (e.g. standard deviation) or associated estimates of uncertainty (e.g. confidence intervals)
- ☒ ☐ For null hypothesis testing, the test statistic (e.g.  $F$ ,  $t$ ,  $r$ ) with confidence intervals, effect sizes, degrees of freedom and  $P$  value noted  
*Give  $P$  values as exact values whenever suitable.*
- ☒ ☐ For Bayesian analysis, information on the choice of priors and Markov chain Monte Carlo settings
- ☒ ☐ For hierarchical and complex designs, identification of the appropriate level for tests and full reporting of outcomes
- ☒ ☐ Estimates of effect sizes (e.g. Cohen's  $d$ , Pearson's  $r$ ), indicating how they were calculated

*Our web collection on [statistics for biologists](#) contains articles on many of the points above.*

### Software and code

Policy information about [availability of computer code](#)

Data collection EPU, pLink 1 (version 2.3.1), pLink 2

Data analysis Warp 1.0.6, RELION 3.0.5, PHENIX 1.16, COOT 0.8.9, PyMOL version 2.2.2, Chimera 1.13, XiNet webserver, xVis webserver, XlinkAnalyzer version 1.1

For manuscripts utilizing custom algorithms or software that are central to the research but not yet described in published literature, software must be made available to editors/reviewers. We strongly encourage code deposition in a community repository (e.g. GitHub). See the Nature Research [guidelines for submitting code & software](#) for further information.

### Data

Policy information about [availability of data](#)

All manuscripts must include a [data availability statement](#). This statement should provide the following information, where applicable:

- Accession codes, unique identifiers, or web links for publicly available datasets
- A list of figures that have associated raw data
- A description of any restrictions on data availability

The electron density reconstructions of the complete SAGA complex, the Tra1 module, the core modules, and the DUB module-nucleosome complex were deposited with the EM Data Base (accession codes EMD-10412, EMD-10413, EMD-10414, EMD-10415, and EMD-10416 respectively) and with the Protein Data Bank (accession codes 6T9I, 6T9J, 6T9K, and 6T9L, respectively).

## Field-specific reporting

Please select the one below that is the best fit for your research. If you are not sure, read the appropriate sections before making your selection.

x

# Life sciences study design

All studies must disclose on these points even when the disclosure is negative.

Sample size	No statistical methods were used to predetermine sample size. All biochemical experiments were replicated two or more times. The crosslinking mass spectrometry measurement was replicated twice as a standard procedure for the method.
Data exclusions	No data were excluded from the analyses.
Replication	All attempts at replication were successful by comparing the result of each replicate.
Randomization	Samples were not allocated to groups.
Blinding	Investigators were not blinded during data acquisition and analysis because it is not a common procedure for the methods employed.

# Reporting for specific materials, systems and methods

We require information from authors about some types of materials, experimental systems and methods used in many studies. Here, indicate whether each material, system or method listed is relevant to your study. If you are not sure if a list item applies to your research, read the appropriate section before selecting a response.

## Materials & experimental systems

n/a	Involved in the study
<input checked="" type="checkbox"/>	<input type="checkbox"/> Antibodies
<input type="checkbox"/>	<input checked="" type="checkbox"/> Eukaryotic cell lines
<input checked="" type="checkbox"/>	<input type="checkbox"/> Palaeontology
<input checked="" type="checkbox"/>	<input type="checkbox"/> Animals and other organisms
<input checked="" type="checkbox"/>	<input type="checkbox"/> Human research participants
<input checked="" type="checkbox"/>	<input type="checkbox"/> Clinical data

## Methods

n/a	Involved in the study
<input checked="" type="checkbox"/>	<input type="checkbox"/> ChIP-seq
<input checked="" type="checkbox"/>	<input type="checkbox"/> Flow cytometry
<input checked="" type="checkbox"/>	<input type="checkbox"/> MRI-based neuroimaging

# Eukaryotic cell lines

Policy information about [cell lines](#)

Cell line source(s)	Saccharomyces cerevisiae strain CB010 (MATa pep4::HIS3, prb1::LEU2, prc1::HISG, can1, ade2, trp1, ura3, his3, leu2-3,112)
Authentication	None of the cell lines used were authenticated.
Mycoplasma contamination	Cell lines were not tested for mycoplasma contamination.
Commonly misidentified lines (See <a href="#">ICLAC</a> register)	No commonly misidentified cell lines were used.



# Author Correction: Super-Mendelian inheritance mediated by CRISPR–Cas9 in the female mouse germline

---

<https://doi.org/10.1038/s41586-019-1861-4>

---

Correction to: *Nature* <https://doi.org/10.1038/s41586-019-0875-2>

---

Published online 23 January 2019

---

Hannah A. Grunwald, Valentino M. Gantz, Gunnar Poplawski,  
Xiang-Ru S. Xu, Ethan Bier & Kimberly L. Cooper

---

In Extended Data Fig. 2 of this Letter, the tyrosinase guide RNA sequence in the top panel was incorrectly annotated such that it was shifted 8 nucleotides to the left to align with a neighbouring protospacer adjacent motif (PAM) site. The error had no consequence for the purpose of communicating the genotypes of offspring of *Rosa26-cas9* and *H11-cas9* breeding strategies. The guide RNA sequence was correctly presented in the Supplementary Methods and in Supplementary Fig. 2. Extended Data Fig. 2 has been corrected online. We would like to thank the reader who brought this to our attention.

---

# Author Correction: Global glacier mass changes and their contributions to sea-level rise from 1961 to 2016

<https://doi.org/10.1038/s41586-019-1889-5>

Correction to: *Nature* <https://doi.org/10.1038/s41586-019-1071-0>

Published online 08 April 2019

M. Zemp, M. Huss, E. Thibert, N. Eckert, R. McNabb, J. Huber,  
M. Barandun, H. Machguth, S. U. Nussbaumer, I. Gärtner-Roer,  
L. Thomson, F. Paul, F. Maussion, S. Kutuzov & J. G. Cogley

In this Letter, the regional mass changes for Iceland were erroneously computed from the temporal variability of the glaciological sample from the Low Latitudes (instead of Iceland). Nevertheless, long-term mass changes were correctly derived from geodetic values from Iceland. Recalculation based on the correct data results in a larger inter-annual variability for Iceland (with a minimum mass balance in the hydrological year 2009/10 instead of 2015/16), a larger mass loss over the full observation period from 1961 to 2016 ( $-3.7$  gigatonnes (Gt)  $\text{yr}^{-1}$  instead of  $-2.4$  Gt  $\text{yr}^{-1}$ ), and a smaller ice loss over the last decade from 2006 to 2016 ( $-5.3$  Gt  $\text{yr}^{-1}$  instead of  $-7.5$  Gt  $\text{yr}^{-1}$ ). At global levels, however, these corrections result in changes of less than 1% and are well within the error bars. As a consequence, this error did not affect any of the conclusions in the Letter. In Table 1, in the '06 Iceland (ISL)' row, the specific mass change (m water equivalent (w.e.)  $\text{yr}^{-1}$ ) should have been  $-0.50 \pm 0.37$  (instead of  $-0.71 \pm 0.43$ ), and the mass change (Gt  $\text{yr}^{-1}$ ) should have been  $-5 \pm 4$  (instead of  $-8 \pm 5$ ); in the 'Total, excl. GRL and ANT' row, the specific mass change should have been  $-0.55 \pm 0.04$  (instead of  $-0.56 \pm 0.04$ ), and the mass change should have been  $-267 \pm 19$  (instead of  $-270 \pm 19$ ); and in the 'Global total' row, the specific mass change should have been  $-0.47 \pm 0.20$  (instead of  $-0.48 \pm 0.20$ ), and the mass change should have been  $-332 \pm 144$  (instead of  $-335 \pm 144$ ). These errors have all been corrected online. For regional comparisons with other studies, we provide a new version with corrected data files in the Zenodo repository (<https://doi.org/10.5281/zenodo.3557199>).

# Publisher Correction: Progenitors from the central nervous system drive neurogenesis in cancer

---

<https://doi.org/10.1038/s41586-019-1837-4>

---

Correction to: *Nature* <https://doi.org/10.1038/s41586-019-1219-y>

---

Published online 15 May 2019

---

**Philippe Mauffrey, Nicolas Tchitchek, Vilma Barroca,  
Alexis-Pierre Bemelmans, Virginie Firlej, Yves Allory,  
Paul-Henri Roméo & Claire Magnon**

---

In this Article, owing to an error during the production process, in Fig. 2c, 'MASHI' was inadvertently shown as 'MASTI'. In the main text, '(Fig. 2f, right)' and '(Fig. 2f, left)' should have been '(Fig. 2e, right)' and '(Fig. 2e, left)'. In addition, in Fig. 3h, the black lines indicating the *P*-value comparisons were located incorrectly, and should have been touching the tops of the blue and red bars. These errors have been corrected online.

Author Virginie Firlej should have been associated with the affiliation 'U955 (INSERM), Hôpital Henri Mondor-Université Paris-Est, Paris, France' instead of 'Department of Pathology, Hôpital Henri-Mondor-Université Paris-Est, Paris, France', and author Yves Allory should have been associated with only the affiliation 'Department of Pathology, Institut Curie, Paris, France', and not with 'Department of Pathology, Hôpital Henri-Mondor-Université Paris-Est, Paris, France'. Finally, the first name of author Alexis-Pierre Bemelmans was incorrectly shown as 'Alexis'. The original Article has been corrected online.



GETTY

Leading a diverse team requires effective communication and organization.

## FIVE 'POWER SKILLS' FOR BECOMING A TEAM LEADER

Volunteering with an organization can improve communication and help you adapt to the unexpected. **By Sarah Groover and Ruth Gotian**

**M**any scientists will oversee a team at some point in their careers, whether it is one or two undergraduates doing a summer internship, an entire research group, or a department with students, technicians and postdoctoral researchers. Scientists are trained in their discipline, but are rarely, if ever, trained in how to manage and mentor trainees. All too often, this results in a series of trials and errors that are frustrating to both mentor and protégé.

Based on our respective experiences, we have come to recognize how a skilled leader

can motivate and help trainees to reach their full potential. One of us (S.G.) is an immunology PhD student at Oklahoma State University in Tulsa and volunteers as vice-president of the American Physician Scientists Association

**“Identifying and developing ‘power skills’ can help you to succeed in a supervisory role.”**

(APSA) in Westford, Massachusetts. The other (R.G.) has nearly three decades of experience in directing leadership and mentoring development programmes in higher education and academic medical centres.

Identifying and developing ‘power skills’ – the crucial abilities that enable a manager to connect with people, communicate effectively, adapt to the unexpected and be open-minded – can help you to succeed in a supervisory role. It is never too early or too late to develop these competencies. Taking on a leadership role in a national

## Work / Careers

organization as a student or an early-career scientist can be a great way to cultivate your leadership abilities. We've compiled a list of five power skills that we feel are integral to the success of a team leader.

**Teamwork.** It is essential that you and your team have mutual trust and respect. You need to motivate and utilize the individual strengths of team members. When assigning tasks or providing feedback, it is important that your members know that their contributions are valued and that their time is appreciated. Serving on a planning committee for an organization's annual conference can be a great way to practise good teamwork. Multiple components are required to create a successful event, from branding and advertising to fundraising and accounting. Capitalize on your colleagues' strengths and passions, and align tasks accordingly.

**Communication.** This is a key component to team success. When working with people based around the country or internationally, it is important to communicate effectively so that everyone is on the same page. We've experienced the negative impacts of poor communication when organizing a national meeting, ranging from insufficient advertising of the event to forgetting to keep records of travel-grant winners. The former caused the event to have a low turnout, despite the excessive amount of time and effort that went into the planning. The latter led to confusion and embarrassment when the award recipient wanted to use funding that the organizers were unable to provide. The ability to listen to the different needs and viewpoints of your team is essential. Always ask your co-workers for their perspectives, even if they're not initially offered.

**Commitment and reliability.** To develop a strong reputation as a team leader, it's better to under-promise and over-deliver. Leadership can include finding responsible people to staff committees, which is always a struggle. And spreading many responsibilities among a few people is challenging, particularly when deadlines are looming. It is important to recognize that as part of a team, your actions can impede the mission of an organization, leading to the late completion of certain initiatives or making the group appear unprofessional to outside members or partner societies. Your disorganization should not be someone else's emergency. I (S.G.) had planned to run for president of APSA after my term as vice-president ends. However, the prerequisite president-elect and president positions will coincide with my first and second years of medical school (I start in the autumn). Instead of taking on too much, which might sacrifice quality in either commitment,



ASHLEY JONES

Ruth Gotian runs US leadership programmes in higher education.

I made the difficult decision to take on a more manageable role in the organization.

**Adaptability.** Being flexible and innovative are key to a leader's success. When resources are lacking or a committee is understaffed, emergencies occur. Being able to bounce back exemplifies how to stay optimistic and

**"Being flexible and innovative are key to a leader's success."**

focus on the solution. These opportunities can also be used to learn new skills and take on assignments. I (S.G.) have always considered myself technologically challenged, but when I needed to make some changes to the APSA website, I worked it out. Don't be afraid to step out of your comfort zone and learn something new in the process.

**Open-mindedness and empathy.** The most productive scientific groups are diverse and capitalize on their group's ability to bring different, creative or unconventional solutions to difficult questions. Volunteering with a national organization such as APSA has allowed me (S.G.) to work with a diverse group of individuals who bring a range of cultures, ages, backgrounds and perspectives to the table. Post-conference surveys highlighted that APSA members have varied interests and concerns that were not being addressed. We took strides to correct these points by creating groups and assigning them various initiatives, from mentoring to diversity. In turn, the teams created diversity summits and virtual mentoring programmes. In your own

discussions, be sure to include and amplify the voices of people who are usually overlooked; they have unique insights and opinions, and it is the responsibility of the team leader to ensure that their voices are heard. At APSA meetings, the most junior person at the table speaks first.

Being proficient in power skills such as the ones we have mentioned will equip you to effectively manage groups, projects, space and money so that everyone is motivated to give their best and maintain a healthy mindset throughout. Being a leader requires you to be reliable, self-aware, open to feedback and trust your team.

Opportunities to develop your leadership skills exist. Find an organization (preferably one you are already involved in) with a mission that aligns with yours. Spend some time working in various areas of the organization, becoming familiar with its structure, function and culture, and don't be afraid to take on a project outside your comfort zone. Use this as an opportunity to develop your leadership abilities, as well as to network in your area of expertise. Being talented in your field is important, but your impact can be much greater if you also know how to lead and motivate the next generation.

**Sarah Groover** is a PhD candidate studying cancer epidemiology and immunology at Oklahoma State University Center for Health Sciences in Tulsa, Oklahoma, and vice-president of the American Physician Scientists Association in Westford, Massachusetts. **Ruth Gotian** is the assistant dean for mentoring and executive director of the Mentoring Academy at Weill Cornell Medicine in New York City, and chief learning officer in its department of anaesthesiology.





## Where I work Mary-Anne Lea

Photographed by  
Oli Sansom.

**T**his is part of the Kerguelen Islands in the southern Indian Ocean, one of the most remote archipelagos in the world. It's more than 3,000 kilometres from Madagascar, the nearest populated place. When I did my PhD work there studying the Antarctic fur seal (*Arctocephalus gazella*), I travelled with two other researchers to our field site, Cap Noir, by helicopter. None of us, including the pilot, had ever been there.

It was very foggy, but the seal colony that we were looking for finally appeared out of the mist. As the helicopter hovered, we three researchers jumped out with our jackets and computers. We were standing in the mist and wind, hearing seals' barks and pups' bleats, smelling the fresh and wild ocean air.

It was one of those times when I've felt what it's like to live nearly alone among marine animals, and have sensed just how little we know about these species. It was like living in a David Attenborough wildlife documentary.

I've spent my career working in remote places, mostly near the Antarctic. By tracking marine predators – birds, seals, whales – we

now understand much better than we did 25 years ago how all these species and their habitats are connected, from temperate waters to polar oceans. We document the behaviour of the animals at sea – how far they travel and dive, what they eat and how they respond to extreme weather events such as marine heatwaves.

On Kerguelen, I walked through the seal colony twice a day to do a roll call; watched how the pups behaved when their mothers were out at sea; and placed satellite tags and time-depth recorders on the mums.

But there's nothing more special than a wild animal coming to investigate you, such as when a juvenile New Zealand sea lion (*Phocartos hookeri*) took my notebook out of my hand. Those moments bolster my resolve to conserve these wildernesses. Watching a wild animal's behaviour in its natural habitat is what makes me tick.

**Mary-Anne Lea** is a behavioural ecologist at the Institute for Marine and Antarctic Studies, University of Tasmania, in Hobart, Australia.

**Interview by Kendall Powell.**



nature

# outlook

## The gut microbiome



Exploring the microbes  
that affect human health

Produced with support from:



## The gut microbiome



For more on the microbiome visit [nature.com/collections/gut-microbiome-outlook](https://www.nature.com/collections/gut-microbiome-outlook)

**Editorial**

Herb Brody, Richard Hodson,  
Jenny Rooke

**Art & Design**

Mohamed Ashour, Ffion Cleverley

**Production**

Nick Bruni, Karl Smart, Ian Pope,  
Kay Lewis

**Sponsorship**

Stephen Brown, Nada Nabil,  
Claudia Danci

**Marketing**

Nicole Jackson

**Project Manager**

Rebecca Jones

**Creative Director**

Wojtek Urbanek

**Publisher**

Richard Hughes

**VP, Editorial**

Stephen Pincock

**Managing Editor**

David Payne

**Magazine Editor**

Helen Pearson

**Editor-in-Chief**

Magdalena Skipper

**W**e are not alone in our bodies. Living inside every person are trillions of microorganisms – bacteria, viruses, fungi and other life forms that are collectively known as the microbiome. Various organs have distinct microbial inhabitants, but the group that has attracted the most attention in biomedical research is the one in the gut.

To better grasp the part that gut microbes play in health and disease, researchers from around the globe are investigating what makes a ‘good’ gut microbiome (see page S6). There are, after all, hundreds of distinct bacterial species in the gut – some pathogenic and some beneficial. Computational biologist Eran Segal argues that collecting microbiome data would allow a ‘deep phenotyping’ approach that could transform drug discovery (S19). And the study of some health-promoting probiotic species is yielding biological insights that might promote drug development (S9).

Several diseases are now thought to be influenced by processes in the gut microbiome. Those include cancer (S16), autoimmune disorders such as multiple sclerosis (S12) and autism spectrum disorder (S14). The gut microbiome also strongly interacts with certain drugs, including some mental-health therapeutics, and influences their effects (S10).

With evidence mounting of the gut microbiome’s health significance, synthetic biologists are looking to engineer the microbiome – both at the individual-species level and as an ecosystem – to thwart the development of disease (S20). There is also growing public interest in how the gut microbiome can be influenced – often focused on personal dietary choices. Microbiologist Peter Turnbaugh reframes this as a question not of which foods will benefit our health, but rather what medical insights might be gleaned from the interactions between our gut microbes and what we eat (S23).

Much more research is under way on the gut microbiome than can be covered in this Outlook, but this supplement gives a taste of the breadth of this robust field (S24).

We are pleased to acknowledge the financial support of Danone Nutricia Research in producing this Outlook. As always, *Nature* retains sole responsibility for all editorial content.

**Herb Brody**

Chief supplements editor

**Contents****S6 ECOSYSTEMS**

**The hunt for a healthy microbiome**

Understanding the ecosystem

**S9 Q&A**

**Homing in on the molecules from microbes**

Michael Fischbach studies short-chain fatty acids

**S10 DRUGS**

**Gut reaction**

The link with pharmaceuticals

**S12 AUTOIMMUNE DISEASE**

**When immunity goes wrong**

The microbiome and disease

**S14 DEVELOPMENTAL DISORDERS**

**Autism and the gut**

Could there be a link?

**S16 CANCER**

**Fighting cancer with microbes**

Boosting response to therapies

**S19 PERSPECTIVE**

**Another dimension for drug discovery**

Microbiota data could transform therapy, says Eran Segal

**S20 SYNTHETIC BIOLOGY**

**Engineering the microbiome**

Modifying microbes for therapy

**S23 PERSPECTIVE**

**Use diet as a tool, not a treatment**

Scientists can’t tell you what to eat, says Peter J. Turnbaugh

**S24 CLINICAL TRIALS**

**Research round-up**

Study highlights

**On the cover**

Scientists study the microbiome to work out its role in health and disease. Credit: Antoine Doré

**About Nature Outlooks**

*Nature Outlooks* are supplements to *Nature* supported by external funding. They aim to stimulate interest and debate around a subject of particularly strong current interest to the scientific community, in a form that is also accessible to policymakers and the broader public. *Nature* has sole responsibility for all editorial content – sponsoring organizations are consulted on the topic of the supplement, but have no influence on reporting thereafter (see [go.nature.com/2NqAZ1d](https://go.nature.com/2NqAZ1d)). All *Nature Outlook* supplements are

available free online at [go.nature.com/outlook](https://go.nature.com/outlook)

**How to cite our supplements**

Articles should be cited as part of a supplement to *Nature*. For example: *Nature* Vol. XXX, No. XXXX Suppl., Sxx–Sxx (2020).

**Contact us**

[feedback@nature.com](mailto:feedback@nature.com)

For information about supporting a future *Nature Outlook* supplement, visit [go.nature.com/partner](https://go.nature.com/partner)

Copyright © 2020 Springer Nature Ltd. All rights reserved.





ILLUSTRATION BY ANTOINE DORÉ

# The hunt for a healthy microbiome

Despite evidence of the gut microbiome's role in human health, researchers are still working out what shapes the community of microbes. **By Michael Eisenstein**

**W**hat does a healthy forest look like? A seemingly thriving, verdant wilderness can conceal signs of pollution, disease or invasive species. Only an ecologist can spot problems that could jeopardize the long-term well-being of the entire ecosystem.

Microbiome researchers grapple with the same problem. Disruptions to the community of microbes living in the human gut can contribute to the risk and severity of a host of medical conditions. Accordingly, many scientists have become accomplished bacterial naturalists, labouring to catalogue the startling diversity of these commensal communities. Some 500–1,000 bacterial species reside in each person's intestinal tract, alongside an undetermined number of viruses, fungi and other microbes.

Rapid advances in DNA sequencing technology have accelerated the identification of

these bacteria, allowing researchers to create 'field guides' to the species in the human gut. "We're starting to get a feeling of who the players are," says Jeroen Raes, a bioinformatician at VIB, a life-sciences institute in Ghent, Belgium. "But there is still considerable 'dark matter'."

Currently, these field guides are of limited use in distinguishing a healthy microbiome from an unhealthy one. Part of the problem is the potentially vast differences between the microbiomes of apparently healthy people. These differences arise through a complex combination of environmental, genetic and lifestyle factors. This means that relatively subtle differences can have a disproportionate role in determining whether an individual is relatively healthy or at increased risk of developing disorders such as diabetes. Understanding the clinical implications of those differences is also a challenge, given the extensive interactions between these

microbes, and with their host, as well as the conditions in which that individual lives. "One person's healthy microbiome might not be healthy in another context – it's a tricky concept," says Ruth Ley, a microbial ecologist at the Max Planck Institute for Developmental Biology in Tübingen, Germany.

Researchers such as Ley are trying to better understand the forces that shape the human gut microbiome – both in the modern era, and across evolutionary history. The emerging picture indicates that even if there is no one healthy microbiome, there are ample opportunities for our lifestyle to interfere with the proper function of these complex commensal communities. And to understand how the breakdown of these ecosystems drives disease, researchers will need to move beyond microbial field guides and begin dissecting how these species interact with their hosts and with each other.



A mother's first gift to her newborn is a healthy smattering of microbes. Some are passed along through breastfeeding and skin-to-skin contact, but many microbes are acquired during passage through the birth canal. This means that if the baby is delivered by caesarean section, they might miss out on a valuable bacterial starter kit. Because a child's earliest years generally establish the composition of a gut community that will persist throughout adulthood, the resulting disruptions can have serious long-term health consequences. "As these infants grow, they have higher risk of obesity, and of modern plagues like diabetes, allergies and asthma," says Maria Gloria Dominguez-Bello, a microbiologist at Rutgers University in New Brunswick, New Jersey. In a small clinical study, her team found that swabbing newborns delivered by c-section with fluids from their mother's birth canal could help to mitigate some of the lost microbial diversity<sup>1</sup>. Several larger trials are under way to assess the longer-term health benefits.

Environmental exposures early in life also strongly affect a child's microbiome. Susan Lynch, a microbiome researcher at the University of California, San Francisco, has been exploring links between environmental factors during childhood and the subsequent risk of developing allergies and asthma. Her findings indicate that new parents shouldn't be afraid of a little dirt – or fur. After monitoring a cohort of nearly 1,200 infants, Lynch and her colleagues found that a dog might be a baby's best friend when it comes to avoiding respiratory disorders<sup>2</sup>. "The only factor that discriminated high- from low-risk groups was dog ownership," says Lynch. She says that dogs (and, to a lesser extent, cats) "increase the diversity of bacteria and lower the diversity of fungi in the houses where these babies are raised". This finding aligns with other research showing that a rural upbringing or growing up on a farm might yield a richer gut microbiome that reduces the risk of inflammatory respiratory diseases relative to children raised in more urban environments.

At a certain point during childhood, the composition of the gut microbiome generally stops changing – although precisely when is unclear. A study in 2012 surveyed gut microbes from individuals in Malawi, Venezuela and the United States, and found a striking pattern<sup>3</sup>. "By three, you can no longer tell the babies from the adults," says Dominguez-Bello, who was a co-author on the paper. However, she notes that there is also evidence that the microbiome remains somewhat mutable beyond this point. What is clear is that by adulthood, this ecosystem reaches a state of equilibrium. "It's very stable," says Eran Segal,

a computational biologist at the Weizmann Institute of Science in Rehovot, Israel. "We see changes, but you will still look mostly similar, even over many years."

Some of the changes seen in adulthood are driven by environment and lifestyle. In a 2018 study of 1,046 ethnically diverse adults living in Israel, Segal demonstrated microbial differences that had little to do with ethnicity<sup>4</sup>. "Environmental inputs could account for 20–25% of the variability in the microbiome," says Segal. Drugs are an obvious source of disruption, and antibiotics – taken either deliberately to fight infection or unwittingly in processed foods – can profoundly affect the microbiota. Even drugs with no clear role in controlling bacteria can cause perturbations. Raes notes that one major European microbiome study was confounded by unexpected effects from the diabetes drug metformin<sup>5</sup>.

Diet is also a powerful external influence, even if the precise mechanisms by which it exerts its effects remain unclear. One study in 2018 found that immigrants to the United States from Thailand experienced a striking 'westernization' of their gut flora – a transformation that could be, at least in part, attributed to adopting a US diet<sup>6</sup>.

### Mismatched to modernity

The changes observed in immigrants from Thailand were accompanied by increased risk of obesity. The study did not establish a causal link, but the results are consistent with an increasingly popular hypothesis that urbanization – and modern life in general – might be highly disruptive to the tight-knit relationship that has evolved between humans and their microbes. "We have made the assumption that the Western microbiome of a healthy person is a healthy microbiome," says microbiologist Justin Sonnenburg at Stanford University in California. Instead, he and others think that the intersection of diet, antimicrobial precautions and general hygiene leads to a culling of the gut community, and that this disruption might contribute to the elevated risk of chronic disease in industrialized societies. "This combination of Western diet and depleted microbiome has likely led to a simmering inflammatory state," Sonnenburg says.

Several studies have identified a stark difference between the microbiota of urban populations and those of Indigenous populations that lead traditional agrarian or hunter-gatherer lifestyles, which more closely resemble those of our early ancestors. These differences seem to be attributable mainly to loss of bacterial diversity, which might be linked to the lack of fibre in Western diets. The Hadza, a population of hunter-gatherers living in Tanzania,

eat 100–150 grams of dietary fibre per day, Sonnenburg says – ten times as much as a typical person in the United States. As a result, fibre-digesting bacteria such as those belonging to the genus *Prevotella*, which can form up to 60% of the gut microbiome in non-Western populations, are much less abundant in the United States. Sonnenburg's team has demonstrated how these changes can become firmly entrenched in a population over the course of just a few generations<sup>7</sup>. Mice colonized with human microbiota and fed a low-fibre diet lost microbial species that remained in mice eating a high-fibre diet. When the offspring of the low-fibre-diet mice were given a high-fibre diet, the species loss was reversible, but after four generations, the missing bacteria were gone for good.

Katherine Amato, an anthropologist at Northwestern University in Evanston, Illinois, has been trying to get to the evolutionary root of a healthy human microbiome by studying non-human primates and tracing the effects of changes in human lifestyle and physiology. In general, Amato says, similarities in microbiome composition among primate species are closely mapped to their evolutionary relatedness. But in a 2019 comparative analysis, Amato found that components of the human microbiota (in particular, microbes from people living in non-industrialized societies) did not map as closely as expected to those of our nearest relatives – the great apes, chimpanzees and bonobos<sup>8</sup>. Instead, the microbiota bore a striking resemblance to those of baboons – a more distant relation,

**"One person's healthy microbiome might not be healthy in another context."**

but one that has a lifestyle more similar to that of early humans. "Most great apes are living in rainforests and eating fruit diets," says Amato, "but we tend to think of our ancestors as living in open woodlands or savannah habitats, and eating an omnivorous diet – like baboons". This suggests that dietary and environmental factors have played a prominent part in shaping the human microbiome.

Ley thinks that the microbiome offers a powerful mechanism for adapting quickly to lifestyle changes – at least, relative to the normal glacial pace of evolution. Indeed, her group has found evidence of microbiome adaptation in response to the evolution of lactose tolerance<sup>9</sup> and digestion of high-starch diets – genetic adaptations that have emerged only in certain populations over the





Growing up with a dog in the house increases the diversity of bacteria children are exposed to.

past 10,000 years or so. But if changes happen quickly, as demonstrated by the rapid industrialization that occurred over the past few centuries, the historically healthy relationship between host and microbiome could become maladaptive as species that the body might have evolved to rely on are lost. “Antibiotics and sanitation have been key in controlling infectious diseases,” says Dominguez-Bello, “but have the collateral, unintended consequences of harming our good microbes.”

### Seeing the forest

Although researchers have gained a better understanding of what human gut microbiomes look like, they are still struggling to pin down which components are essential to our well-being. One problem is that there are far too few data sets to allow researchers to draw statistically robust connections between the microbiome and health or disease. Segal draws a comparison with the human genome – only when many high-quality sequences were available did it begin to offer clinical value. “There are probably 30 million people that have been genome sequenced up until today, while in the microbiome there are around 10,000 samples publicly available,” he says.

This issue is compounded by the geographic bias in microbiome data. Beyond a handful of studies of selected groups such as the Hadza, most data are from the United States, Europe and China. “We know very little about microbiome variation in Africa, southeast Asia and South America,” says Raes. That information gap will be especially relevant for understanding the extent of the suggested ‘missing microbes’ problem in the industrialized world.

A larger, more global data set would give a better-informed starting point for broadly

understanding what a normal microbiome in a healthy individual can look like – and thus make it easier to recognize disease-linked perturbations. But researchers also need to move beyond studies that simply assess correlation on the basis of presence or absence of a specific microbe in a healthy individual or a person with a disease at a particular point in time.

There are now a number of multi-year, longitudinal studies that monitor both the health and the microbiome composition of many individuals over extended periods. The Canadian Healthy Infant Longitudinal Development study, for example, is monitoring more than 3,400 children over the course of 5 years in an effort to identify factors that contribute to conditions such as asthma and allergies. “If we can see that a microbiome change precedes a clinical change, then maybe we can establish causality,” says Segal. Such patterns would give clinicians more confidence in the potential value of a diagnostic result or intervention, and would be invaluable for studying the contribution of the microbiome to chronic conditions that manifest gradually, such as diabetes.

Researchers are also making their bacterial censuses more detailed. Early microbiome investigations were limited by the narrow range of intestinal species that scientists could grow in the lab. But the plummeting cost of sequencing has made it possible to capture detailed snapshots of the DNA extracted from faecal microbes. Researchers can now go beyond species level to identify strains of bacteria, and even genomic variants in those strains. Sonnenburg, for example, is using this approach to look for mutations that might affect the metabolic activity or dietary preferences of different gut microbes.

Many microbes still slip through the net, however. Standard methods of microbiome analysis favour identification of bacteria, and are not as good at identifying other common gut microorganisms. “We rarely see signatures of fungi in our data, but we know they’re there,” says Lynch. “And we know that they’re contributing to the overall interaction between microbiome and host.” Alternative microbiome-analysis techniques offer a workaround. Harvesting and analysing RNA rather than DNA, for example, allows investigators to capture changes in gene expression that can reveal dysfunction in ostensibly normal gut species. “A perfectly nice-looking microbiome might be doing things that aren’t healthy,” says Ley. Other researchers are turning to metabolomic techniques – comprehensive chemical analysis of the various biomolecules produced in a microbiome sample. This is allowing researchers to eavesdrop on how microbes are communicating with each other and with their host’s cells. “These molecules are the end products,” says Lynch. “That’s where the meat is in trying to define biomarkers of a healthy microbiome.” Her lab has made important strides with such approaches, including homing in on a microbial lipid known as 12,13-diHOME, which seems to be a driver of inflammation in infants at high risk of asthma<sup>10</sup>.

Such data might offer the best readout yet of how well our internal ecosystem is thriving – essentially, inspecting the soil, water and leaves of the forest, rather than simply counting the trees. “There won’t be ‘the’ healthy microbiome, just like there’s no perfect genome,” says Segal. “There could be multiple healthy configurations.” These profiles of microbial activity might prove the fastest route to validating hypotheses on microbiome function and dysfunction, and accelerate the translation of discoveries into clinical trials. “The time of observation hasn’t come to an end, but I think it’s really time to move to interventions,” says Raes. “You can only understand a system if you give it a good kick and see what happens.”

**Michael Eisenstein** is a science journalist in Philadelphia, Pennsylvania.

1. Dominguez-Bello, M. G. et al. *Nature Med.* **22**, 250–253 (2016).
2. Havstad, S. et al. *J. Allergy Clin. Immunol.* **128**, 880–885 (2011).
3. Yatsunenko, T. et al. *Nature* **486**, 222–227 (2012).
4. Rothschild, D. et al. *Nature* **555**, 210–215 (2018).
5. Forslund, K. et al. *Nature* **528**, 262–266 (2015).
6. Vangay, P. et al. *Cell* **175**, 962–972 (2018).
7. Sonnenburg, E. D. et al. *Nature* **529**, 212–215 (2016).
8. Amato, K. R. et al. *Genome Biol.* **20**, 201 (2019).
9. Goodrich, J. K. et al. *Cell Host Microbe* **19**, 731–743 (2016).
10. Levan, S. R. et al. *Nature Microbiol.* **4**, 1851–1861 (2019).

## Michael Fischbach: Homing in on the molecules from microbes

**Michael Fischbach, a bioengineer at Stanford University in California, describes the small molecules produced by microbes in the gut as a surprisingly unexamined field. To explore it, his team has developed a way to 'toggle' the molecules on and off to find out exactly what they do.**

**How is your work helping you to investigate the molecules made by gut microbes?**

It gives us a way to study the effects of molecules produced by the gut microbiome, one molecule at a time. We developed our genetic system for a commensal strain of *Clostridium* that produces a lot of molecules that are characteristic of the microbiome. They are made in very high numbers and they show up in the host's bloodstream, but there was no good way of working out what they do. Our genetic system can stop the production of specific molecules; when we colonize mice with a mutant bacterial strain, the mice are deficient in those molecules. We then compare them with mice colonized by the wild-type bacterial strain and that do have the molecules, and look for differences.

**What type of molecules are you studying?**

We are focusing on branched, short-chain fatty acids. These are chemically similar to acetate, propionate and butyrate – well-studied short-chain fatty acids from commensal bacteria. But the ones we are looking at are produced by a different metabolic route – they come from branched-chain amino acids and not much is known about them.

**Why did you focus on these fatty acids?**

We are trying to look at molecules that are produced in great abundance. They are naturally present in the body at concentrations similar to those of therapeutic drugs. So there is no question about whether these molecules end up permeating the host – they do. There are dozens of them, and we feel it is warranted to take the time to treat these molecules almost like a classic pharmacology problem: you have a molecule and you want to know everything about what it does. So we try to find out what tissues it acts in, what receptors it interacts with and how that brings about an effect on host biology. It's really fundamental stuff that I think is going to end up in textbooks one day.



Michael Fischbach investigates the effects of molecules produced by gut microbes.

**What have you caught the molecules doing?**

We are finding a range of immunological differences that can be attributed to the presence or absence of individual molecules produced by microbes. For example, the branched, short-chain fatty acids seem to modulate the activity of cells that produce the protein immunoglobulin A, which is involved in barrier protection in mucous membranes. We don't have the complete story yet, but we are starting to work out the mechanism of that effect. My guess is that, in addition to modulating the immune system, the molecules do other things too. We just haven't had time to explore it all yet.

**Could microbial molecules lead to drugs that will replace whole microbe probiotics?**

Both options are on the table. If we can identify the receptors that microbial molecules bind to, we might be able to design drugs that interact with those receptors. We could mimic the effects microbial molecules have on the receptors, or we might want to block their effects. Equally, we could also use the microbes themselves. The use of whole microbes could mean delivering the effects of several molecules at a time, and could ensure more lasting effects.

There is little precedent for using microbes as drugs, and doing so will bring regulatory challenges. But we will probably see both approaches moving forward. And both could be very powerful.

**Where do you see this kind of work heading?**

We have used bacterial genetics to create a clean system for comparing two groups of mice that differ only in the presence or absence of a microbiome-derived molecule. But we did this in a rather unnatural setting: a mouse with only one bacterial species in its gut. Now, the biggest need is to create a model system for experiments such as these: bacterial communities that are completely defined, but complex enough to be similar to the native gut community. Using a community that complex, we could carry out experiments in which we remove one bacterial species – or even one gene from one bacterial species. Those are more likely to stand the test of time.

**Interview by Andrew Scott**

This interview has been edited for length and clarity.



# Gut reaction

Drugs and the microbiome can change each other in complex and little-understood ways. **By Neil Savage**

If cholesterol-lowering drugs are being impeded by the bacteria in some people's guts, Sony Tuteja is hoping to work out how.

Statins sometimes do a great job at reducing the amount of low-density lipoprotein (LDL), the 'bad' cholesterol that raises the risk of heart attacks and stroke, in the blood. But a lot of people see less of a benefit, and some none at all. In a 2016 study, 46% of those treated with the drug rosuvastatin saw their LDL drop by 50% or more<sup>1</sup>. But 43% saw a less than 50% decrease, and 11% had no reduction, or even had an increase in LDL.

The reason for the variation isn't clear, but Tuteja, a pharmacogeneticist at the University of Pennsylvania in Philadelphia, thinks the hundreds of species of bacteria in the intestinal tract might be involved. It could be that the drug throws the microbes out of balance in a way that alters cholesterol metabolism, or that certain strains of bacteria render the drugs less effective. Or, Tuteja suggests, "it could be bidirectional – the microbiome is affecting the drug and the drug is affecting the microbiome".

Her hypothesis, which she is testing in a clinical trial, is that statins reduce circulating LDL by promoting the growth of gut bacteria that produce bile salt hydrolases – enzymes that break down the bile acids used to digest fatty foods. The liver makes bile salts out of cholesterol, so as bile acids are broken down, the organ pulls more cholesterol out of the blood to replace them – lowering the levels of LDL in the blood. If some strains of bacteria don't produce as many hydrolases, that could explain why statins are less effective in some people. Or perhaps, as statins lower LDL levels, the gut is made more congenial for some bacteria and less so for others. In Tuteja's trial, about 50 volunteers will take rosuvastatin for 8 weeks; she will then compare the count of difference species of bacteria in their guts with that in people taking a placebo, to see whether the drug changes the make-up of the microbiome. Tuteja and her team will also compare the distribution of bacteria with levels of bile acid in blood and faeces and the amount of LDL in the blood, to see whether the species present in the microbiome at the beginning of treatment can predict statin effectiveness.

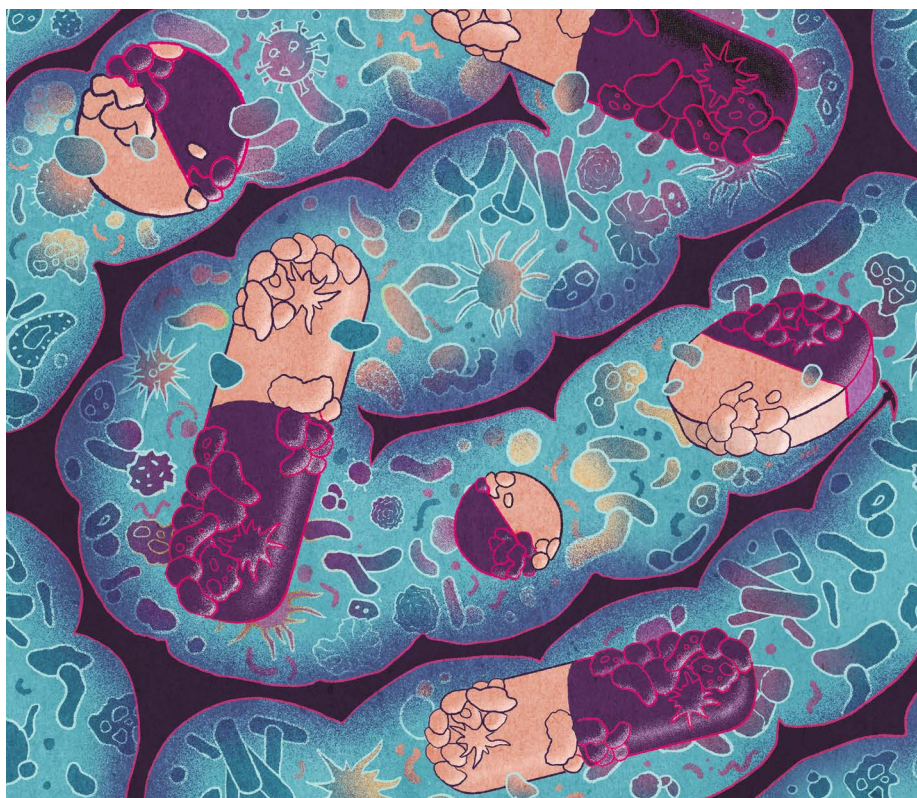


ILLUSTRATION BY ANTOINE DORE

Tuteja is one of a growing number of researchers looking into the gut microbiome's role in drug metabolism, and whether it accounts for variations in how people respond to pharmaceuticals. A whole variety of drugs could be altering the balance of bacterial species, disrupting the digestive system or causing other problems. And gut bacteria produce a range of enzymes and metabolites that might chemically alter drugs as varied as psychotropics and cancer treatments, rendering them less useful or leading to more side effects.

Understanding the interplay between microbes and medicine could lead to new therapies, or to changes in how existing drugs are prescribed. For example, physicians might be able to predict how a person will respond to a particular drug on the basis of their gut bacteria, and change a person's prescription accordingly. Dietary changes or antibiotics might also be recommended to make a person's gut microbiome more receptive to a drug.

The gut microbiome should be seen as a virtual organ in its own right, argues Ted Dinan, a psychiatrist at APC Microbiome Ireland, a research centre at University College Cork. Such is its importance to drug metabolism, he says, "in a few years neither the US Food and Drug Administration nor the European Medicines Agency will license any drug unless its impact on that virtual organ has been studied". (Another researcher at Microbiome Ireland, Niall Hyland, has received a €100,000 (US\$110,000) Global Grant for Gut Health, which is supported by Nature Research – part of *Nature's* publisher, Springer Nature – and probiotic company Yakult, based in Tokyo.)

## Back and forth

Pharmaceuticals and bacteria have an undeniable effect on each other. In 2018, researchers screened more than 1,000 drugs, marketed for various conditions, against 40 strains of human gut bacteria. They found that nearly one-quarter of those drugs had antibiotic

effects, even though none of them were being sold as antibiotics<sup>2</sup>. And in 2019, another team found that of 271 drugs incubated with gut microbes, 176 were metabolized to such an extent that the level of the drug dropped by more than 20%<sup>3</sup>.

Dinan and his colleagues are examining what part the microbiome plays in mental health, including whether it interacts with psychotropic drugs. Evidence suggests that low diversity of gut microbes is associated with mental-health conditions such as schizophrenia. Researchers at Microbiome Ireland showed that it was possible to essentially transplant a mood disorder into rats by wiping out their native microbes with antibiotics and then giving the rats a dose of gut bacteria from people whom Dinan was treating for depression<sup>4</sup>. “When they got a transplant from depressed patients, their behaviour was significantly altered,” Dinan says. That’s a strong sign that the microbiome can affect mental health, he says.

This finding might have implications for the practice of faecal microbiota transplantation, an emerging treatment for gastrointestinal illnesses such as irritable bowel syndrome. Currently, donated faecal matter is tested for infections that could be passed on, such as hepatitis C. “Because of our study,” Dinan says, “I’m convinced they should be looking at the psychiatric profile of the donor as well.”

Researchers have also found that some bacteria can synthesize neurotransmitters, such as dopamine or acetylcholine, as well as precursor chemicals such as tryptophan, which is used to make the mood-regulating chemical serotonin. “We now know that certain good bacteria – bifidobacteria – are capable of synthesizing tryptophan,” Dinan says. But the molecule is also found in foods such as turkey, and it is not known how much of the tryptophan that makes it to the brain comes from diet and how much is produced by bacteria.

## Hearts and minds

As they learn more, physicians might want to take into account a person’s particular mix of microbes when prescribing psychotropic drugs. Two species of gut bacteria, *Enterococcus faecalis* and *Eggerthella lenta*, metabolize the drug L-DOPA, which is used to treat Parkinson’s disease<sup>5</sup>. Scientists have long known about an enzyme in the body that breaks down the drug and decreases the amount that makes it to the brain. Usually, physicians prescribe a second drug alongside L-DOPA to partially counteract the breakdown, but breakdown of the drug by bacteria is not currently factored in. Researchers have, however, identified a

molecule that inhibits *E. faecalis*’s activity. “There is some potential for translating this data if a company or someone was interested,” says Peter Turnbaugh, a microbiologist at the University of California, San Francisco, who collaborated on the discovery.

The idea that bacterial metabolism affects how well drugs work is not new, Turnbaugh says. Back in 2013, he and his colleagues found a pair of genes in *E. lenta* that give it the ability to digest the heart-disease drug digoxin<sup>6</sup>. When they fed mice the amino acid arginine, however, digoxin levels stayed high. The researchers are not sure why that’s so, but it means that giving arginine along with digoxin could protect the drug. And there are signs that the bacterium might be responsible for the variation in how people respond to the rheumatoid-arthritis drug methotrexate. “We’ve known for almost a century now that the microbiome matters for drugs, but people have sort of ignored it,” Turnbaugh says. “Most development of drugs, as well as their use in the clinic, is microbiome-naïve.”

## “I’m convinced they should be looking at the psychiatric profile of the donor as well.”

A detailed understanding of which microbiota interact with which drugs, and the mechanisms behind those interactions, could suggest ways to either inhibit or enhance the interaction between drugs and the microbiome. Some mechanisms are known. For instance, the colon-cancer drug camptothecin-11 is metabolized by the liver into an inactive molecule; enzymes produced by gut bacteria, however, can reactivate it into a toxic form, causing severe diarrhoea. Researchers at the University of North Carolina at Chapel Hill have come up with a compound that could target the enzymes without disrupting the microbiome – a potential treatment for the diarrhoea. And their spin-off company, Symberix, is developing treatments to reduce side effects caused by gut bacteria.

## Complicated undertaking

But untangling the complex interaction between drugs and the microbiome won’t be an easy task. For one thing, the various species of bacteria in the human gut have 150 times more genes than the human genome. And the selection of microbes present in the gut can vary a great deal from person to person. “My microbiome is really different from yours,” says Anukriti Sharma, a microbiologist at

the University of California, San Diego. “That means we might also have very different genes that are involved in metabolism.” In fact, one of the limitations of microbiome studies is that they have mainly taken place in the United States, Europe and China, but microbiomes are known to vary widely from region to region. That can have consequences for medicine, says Turnbaugh. “If you test a drug in America, it could behave completely differently in Africa or in South America,” he says.

Another issue is that there doesn’t seem to be one common mechanism for how bacteria and drugs affect each other. “Each drug seems to have its own unique way of interacting with the microbiome,” says Filipe Cabreiro, a biochemist at Imperial College London. That, he says, makes it difficult to draw any general conclusions.

Still, Cabreiro says, there are broad similarities in how certain classes of drugs work with the microbiome. Antipsychotics often change the balance of gut bacteria. Some cancer drugs are degraded or modified by chemistry in the gut that either enhances or reduces their effects (see page S16). Metformin, a common diabetes drug that Cabreiro is studying for its anti-ageing potential, seems to trigger certain signalling pathways in bacteria that changes the production of metabolites, which then have their own effects on the body. “We have to take it a drug at a time, a microbe at a time, and a disease at a time,” Sharma says.

If that complexity can be worked out, the next step will be to look at altering the microbiome to enhance drugs’ effectiveness or decrease their side effects. As with the heart medication digoxin, that could mean supplementing a drug with another compound that influences its mechanism of interaction. It could also mean trying to change the make-up of the bacterial community, whether through strategic use of antibiotics, dietary changes to promote or discourage particular microbes, or even faecal transplants to replace ‘bad’ gut bacteria with ‘good’ ones.

And it could make precision medicine more precise, with physicians sequencing not only the genes of patients but also of their microbes to predict response to a treatment. “For the future of personalized medicine,” Cabreiro says, “you have to take into account not just the host, but the microbiome too.”

**Neil Savage** is a science journalist in Lowell, Massachusetts.

1. Ridker, P. M. et al. *Eur. Heart J.* **37**, 1373–1379 (2016).
2. Maier, L. et al. *Nature* **555**, 623–628 (2018).
3. Zimmermann, M. et al. *Nature* **570**, 462–467 (2019).
4. Kelly, J. R. et al. *J. Psych. Res.* **82**, 109–118 (2016).
5. Rekdal, V. M. et al. *Science* **364**, eaau6323 (2019).
6. Haider, H. J. et al. *Science* **341**, 295–298 (2013).





SUSAN MERRELL/UCSF

Neuroscientist Egle Cekanaviciute found that people with multiple sclerosis have different gut microbiomes from those without the disease.

## When immunity goes wrong

If the gut microbiome can trigger autoimmune diseases, can it also help to cure them? **By Eric Bender**

**F**or Gregg Silverman, a rheumatologist at New York University, the day a woman he was treating for lupus was visited by her identical twin sister was a watershed moment. The sister was a picture of health, with a one-year-old child in her arms. Silverman's patient, meanwhile, was receiving kidney dialysis and, despite his best efforts, her condition was getting worse. "Genetics was not going to explain this difference," says Silverman. The revelation launched him on a decades-long quest to seek out other factors that drive the puzzling autoimmune disease.

Researchers investigating other autoimmune diseases have also been looking beyond genetics. In the case of type 1 diabetes, the epidemiological evidence for doing so is overwhelming, says Jayne Danska, a geneticist at the Hospital for Sick Children in Toronto, Canada. Genetics "doesn't explain why the incidence of the disease has been rising over

the last 50 years in many different countries – and it doesn't explain why the age of onset is becoming progressively earlier", she says.

Many events, including viral infections and certain foods, have long been suspected of helping to trigger autoimmune diseases, in which the body attacks its own cells. But over the past decade, new suspects have emerged – the trillions of microbes inhabiting the digestive tract. Scientists have now implicated the gut microbiome in numerous autoimmune conditions, including lupus, type 1 diabetes, rheumatoid arthritis and multiple sclerosis.

For example, in 2017, researchers at the University of California, San Francisco, compared the gut microbiomes of people with multiple sclerosis with those of healthy volunteers. This study, led by geneticist Sergio Baranzini and neuroscientist Egle Cekanaviciute, found that many bacterial species were present in very different quantities in the two groups<sup>1</sup>. This

research "not only identified differences in microbial communities, but actually showed that they had physiological significance in a human immune-cell experimental system", says Cekanaviciute, who now studies microbiome health effects at NASA's Ames Research Center in Moffett Field, California.

When two species that were more abundant in people with multiple sclerosis were incubated in human blood cells *in vitro*, the cells' inflammatory responses climbed. Another bacterial species, whose levels were depressed in people with multiple sclerosis, stimulated anti-inflammatory cells. And when the investigators transferred a microbiome from a person with multiple sclerosis into germ-free mice (those reared to be devoid of microorganisms), "these mice got a lot sicker than mice receiving a healthy human microbiome", says Baranzini.

Scientists are trying to understand the mechanisms behind the apparent ability of the gut microbiota to trigger or to sustain autoimmune conditions. They hope to turn that knowledge into better therapies for conditions that are currently difficult to treat – perhaps even in the form of simple probiotic pills.

### Molecular mimicry

Autoimmune diseases are often traced, in part, to alterations in the human leukocyte antigen (HLA) gene complex, a cornerstone of the adaptive immune system, which recognizes and remembers specific pathogens. HLA genes express proteins that present antigens to our



immune system's T and B cells. The immune cells then spot and attack dangerous intruders carrying those antigen flags. T cells and B cells are selected out to ignore the body's own cells but in autoimmune diseases this doesn't happen.

Although most T cells are trained in the thymus to ignore 'self' proteins, some are trained in the gut. "Given all the different environmental factors that come in contact with the gut, you need a lot of immune tolerance there," explains Marika Falcone, an immunologist at IRCCS Ospedale San Raffaele in Milan, Italy.

Experiments in colonizing germ-free mice with specific microbes in the gut have shown that the effects are broadcast throughout the immune system, Danska says. In turn, the immune system in the gut affects the microbes there. Biologists are exploring various routes by which the gut microbiome might help to stimulate or stop immune pro-inflammatory responses – driven either by the bacteria themselves, or by the metabolites they produce, the immune cells they train, or another mechanism.

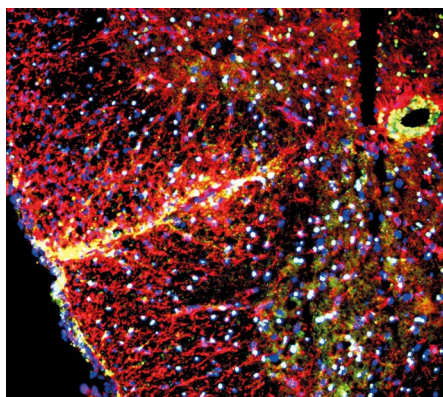
One line of enquiry is whether the enormous genetic variation between microbes leads to immune cells becoming confused as to what is foreign and what is self. A meta-analysis that examined 3,665 human samples identified more than 22 million gut microbiome genes<sup>2</sup>. The proteins produced by these genes are scrutinized by the immune system, and, overwhelmingly, found to be harmless or easily handled.

But sometimes microbial proteins that alarm immune cells contain fragments that closely resemble those of normal human proteins. With roughly a hundred times as many genes in our individual microbiomes as in our own genomes, there's a high likelihood of

## "We want to understand the rules that regulate the bacterial society in the gut."

similarities, says Martin Kriegel, an immunobiologist at Yale University in New Haven, Connecticut. The result, so the theory goes, is that this starts to teach the immune system to recognize human proteins as signs of a threat. In such cases of molecular mimicry, "the immune system gets confused", says Baranzini. "It starts reacting against the bacteria. And then it ends up reacting against our own self proteins."

Kriegel and his colleagues demonstrated a molecular mimicry response in cells from people with lupus using a bacterial protein very similar to the human protein Ro60 (ref. 3). Molecular mimicry could also be at work in rheumatoid arthritis – peptides produced



Micrograph of a spinal cord affected by multiple sclerosis.

by gut bacteria such as *Prevotella* closely resemble human peptides presented to the immune system in the joints of people with the condition. In a 2017 study<sup>4</sup>, immune reactions to the microbial peptides corresponded with those of the matching host peptides, "which was a pretty strong signal", says Allen Steere, a rheumatologist at Massachusetts General Hospital in Boston and an author of the study.

## Gut to go

If gut microbiota do confuse the immune system, the question remains of how such autoimmune effects spread from the gut. In some cases, specific cells are affected, such as nerve cells in multiple sclerosis, and pancreatic  $\beta$ -cells in type 1 diabetes. In lupus and rheumatoid arthritis, autoimmunity occurs across multiple organs.

Steere and his colleagues found evidence of *Prevotella* DNA in the joints of some people with rheumatoid arthritis<sup>4</sup>. That finding, Steere says, suggests that either the bacteria themselves, or bacterial remnants carried by immune cells, can get into joints.

In the case of multiple sclerosis, "I don't think the bacteria move, but their metabolites do," says Patrizia Casaccia, a neuroscientist at the City University of New York. She notes that the metabolites might signal through the vagus nerve, which transmits messages from the gut to the brain. In some cases, bacteria themselves have been found in affected organs – such as in the pancreas in type 1 diabetes.

Kriegel and his team showed that in mice predisposed to a lupus-like condition, *Enterococcus gallinarum* bacteria move out of the gut to other organs, including the liver, where they set off an immune cascade that leads to lupus<sup>5</sup>. The investigators also identified similar biological pathways in human liver cells. Most importantly, Kriegel says, the bacteria were found in most liver biopsies from people with lupus – but not in those from healthy people.

His team also showed that either antibiotic treatment or a vaccine against *E. gallinarum* prevented autoimmunity developing in mice. "One could already envision a potential future therapy targeted against these bugs that cross the gut barrier," Kriegel says.

## Microbes in the clinic

Reports about faecal matter transplants (FMTs) or probiotic pills have given people with immune conditions hope that there could be an easy way to prevent or treat their disease. Scientists share this desire, but warn that clinical research has barely begun.

For multiple sclerosis, for example, treatment might eventually "be as simple as a targeted dietary intervention that will shift the community from pro-inflammatory bacteria to more anti-inflammatory types", says Baranzini. In one possible step towards this goal, his team is running a small phase I clinical trial of FMT to assess safety and side effects.

Casaccia emphasizes the importance of proceeding with caution. "We want to understand the rules that regulate the bacterial society in the gut," she says. "Maybe we can develop a combination of healthy probiotics and prebiotics to support the growth of the beneficial bacteria, and perhaps dietary manipulation might contribute to that," she says. "But I'm not sure we are there yet."

Researchers do see major progress. "The enormous effort that's been spent over the last 20 years using different kinds of tools in the box is really beginning to bear fruit," says Danska. Her team has built a platform to identify antibacterial antibodies in blood. Analysing samples from children at high risk of type 1 diabetes, the platform revealed important clues about who would develop the disease<sup>6</sup>.

Danska hopes that better knowledge about the gut microbiome, especially during the first 3 years of life, will lead to disease-preventing interventions. Those might include giving babies well-defined compositions of microbes, so that a child's immune system "develops with optimal tolerance to self without sacrificing their ability to fight infection", she says. "That's the kind of therapy that could have global impact because bugs are cheap. If we can come up with defined compositions of microbes in a gummy bear – now we're talking!"

**Eric Bender** is a science writer in Newton, Massachusetts.

1. Cekanaviciute, E. et al. *Proc. Natl Acad. Sci.* **114**, 10713–10718 (2017).
2. Tierney, B. T. et al. *Cell Host Microbe* **26**, 283–295 (2019).
3. Greiling, T. M. et al. *Sci. Transl. Med.* **10**, eaan2306 (2018).
4. Pianta, A. et al. *J. Clin. Invest.* **127**, 2946–2956 (2017).
5. Manfredo Vieira, S. et al. *Science* **359**, 1156–1161 (2018).
6. Paun, A. et al. *Sci. Immunol.* **4**, eaau8125 (2019).

# Autism and the gut

The gut microbiome might have an integral role in autism spectrum disorder. But the link remains uncertain. **By Elizabeth Svoboda**



A child with autism spectrum disorder communicates using symbols during lunch.

**B**efore Ethan Loyola reached his first birthday, it was clear that something was wrong with his gut. As a baby, he had been given several courses of antibiotics to treat severe ear infections, after which he experienced foul-smelling, acidic diarrhoea that left him convulsed with pain. Around the age of one, Ethan lost the words he'd started to say and stopped making eye contact. Soon after that, he received a diagnosis: autism spectrum disorder (ASD).

As Ethan grew older, his digestive issues continued, and he struggled around other people and in unusual situations. "He had his hands over his ears, didn't want to be in crowds," says his mother, Dana Woods. "It was just too overwhelming." Then Ethan's dad saw a flyer tacked up at an autism therapy clinic. Scientists at Arizona State University in Tempe, near the family's Phoenix home, were looking for children with autism to try an experimental treatment called microbiota transfer therapy, which would be used to recolonize the children's guts with bacteria from donors who were not on the autistic spectrum. Ethan's parents enrolled him in the study.

ASD can cause various language and social

difficulties. And, for the 1 in 160 children it affects worldwide, treatments have been frustratingly slow in coming. Some parents have long claimed that changing a child's diet or giving them probiotics improves not just digestive problems, but also behavioural symptoms. Now, researchers are revealing that in addition to aiding digestion, gut bacteria also manufacture bioactive compounds that help to orchestrate brain function and social development. Studies show that children with ASD often have a mix of gut microbes that is distinct from that in children without the condition. And in lab animals, autism-like symptoms arise when normal species of gut bacteria are absent.

Although far from conclusive, these findings are driving researchers to probe the links between gut microbes and autism symptoms – and to begin testing ASD treatments that repopulate the gut microbiome from scratch.

## Laying gut groundwork

John Cryan, a biochemist at University College Cork in Ireland, was among the first researchers to investigate how gut microbes affect social behaviour. In 2014, he reported that germ-free mice – those lacking the typical

mix of gut microbes – avoided other mice, shunned new social situations and groomed themselves excessively<sup>1</sup>. "It started to crystallize that the microbiome was involved in many aspects of behaviour," Cryan says. "There seems to be something about the social brain in particular that makes it sensitive to signals from the microbiome." He and other scientists proposed the existence of a gut–brain axis, in which gut microbes produce bioactive compounds that influence brain function.

Other studies have bolstered this theory, showing that when gut bacteria help to digest food, they generate a host of by-products that can affect thinking and behaviour. *Clostridia* bacterial pathogens, for instance, generate propionic acid in the gut – a short-chain fatty acid known to disrupt the production of neurotransmitters. Propionic acid also causes autism-like symptoms in rats, such as repetitive interests, unusual motor movements and atypical social interactions<sup>2</sup>.

Deficits in beneficial gut bacteria might also affect social brain function. In 2017, Cryan reported that when mice with an autism-like condition had lower levels of *Bifidobacterium* and *Blautia* gut bacteria, their guts made less tryptophan and bile acid – compounds needed to produce serotonin<sup>3</sup>. And children with autism have been consistently found to have lower levels of *Veillonellaceae*, *Coprococcus* and *Prevotella* gut bacteria than those without the condition<sup>4</sup>. Researchers have also observed that some people with ASD could have an abnormally porous blood–brain barrier, which allows some toxic bacterial by-products to enter the bloodstream and reach the brain<sup>5</sup>.

## Behavioural change

Such findings prompted researchers at the California Institute of Technology in Pasadena to transfer the microbes of people with ASD into mice. Microbiologist Sarkis Mazmanian and his colleagues gave germ-free mice gut microbes from people with ASD; at six weeks old, offspring of these mice socialized less, produced fewer vocal sounds and engaged in more repetitive behaviour, compared with mice descended from animals that received gut microbes from donors who did not have ASD<sup>6</sup>.

BSIP/UG VIA GETTY



The differences between the two groups also proved striking on a biological level. “We uncovered several differences in faecal and serum metabolites,” says Gil Sharon, a co-author of the research. In particular, mice with gut microbes from donors with ASD had lower levels of compounds produced by gut bacteria that are thought to affect brain function. In particular, the amino acids 5-aminovaleric acid (SAV) and taurine were depleted – both metabolites increase the activity of the brain’s  $\gamma$ -aminobutyric acid (GABA) receptors. GABA is a neurotransmitter involved in sensory processing and motor control, and abnormalities in the GABA system have been noted in children with ASD.

When the team gave the two missing metabolites to mice with autism-like symptoms, Sharon says, “they improved core deficits in social interaction and repetitive behaviour”. The study has received some criticism regarding its data analysis and small sample size. The finding that mice with microbes from donors with ASD vocalized less, one critic argued (see [go.nature.com/2qbqw1](https://go.nature.com/2qbqw1)), involved gut bacteria from only five donors with autism and three without, and the researchers ran many analyses on the data to find a difference between the two groups of mice – the more analyses run on a data set, the more likely it is that a false effect could be found. The team declined to comment on these criticisms, but stands by its results.

The growing focus on the role of gut microbes in social brain function prompted the team at Arizona State University to up the ante by testing microbes in children with ASD. Microbial ecologist Rosa Krajmalnik-Brown and her colleagues recruited a group of 18 children with ASD aged between 7 and 16, including Ethan Loyola. Like Ethan, all of the children had a history of gastrointestinal problems, including chronic diarrhoea, pain and constipation.

The children in the study took the antibiotic vancomycin for two weeks to remove existing bacteria. Then, each of them received a high dose of gut microbes from donors without autism – some children received this as an enema, whereas others took a bacteria-fortified drink. The children continued to take a daily dose of microbes for seven or eight weeks (Ethan took his in a shot glass, mixed with cranberry juice), along with an antacid to neutralize stomach acid and improve the chance of the new microbes surviving.

At the end of the 18-week study period, the children’s gastrointestinal symptoms had reduced by 80%, and most of the improvement remained two years after the original study. By the two-year mark, the children’s scores on a test to measure how much they were affected by their autism were an average of 47% lower

than they had been at the beginning of the trial. Also at the two-year follow-up, the children had increased gut-bacterial diversity and greater numbers of gut bacteria that are often found in lower numbers in children with ASD, such as *Bifidobacteria* and *Prevotella*. This suggests that the treatment had succeeded in changing their microbiomes long term, Krajmalnik-Brown says.

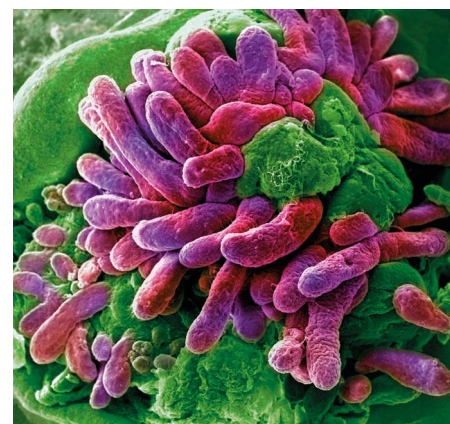
## A muddled outlook

Although these early results look promising, the authors stress that little will be known for sure until they complete a larger trial that includes a control group. “The fact that we have exciting results doesn’t mean that this will work for everyone,” Krajmalnik-Brown says. Her team is now carrying out a phase II trial of microbiota transfer therapy with 84 adults with ASD, some of whom will receive a placebo. The team is also looking for funding to start a similar trial in children. And even if these trials are successful, even bigger phase III trials will be needed a few years down the line before the treatment can be used in the clinic. Along the way, Krajmalnik-Brown’s team is hoping to work out the biological mechanisms behind the improvement in symptoms.

There is currently no approved medication specifically for the core symptoms of autism – communication difficulties, social challenges and repetitive behaviour. Krajmalnik-Brown hopes that her research will lead to one, but this is by no means assured. Although studies report that people with ASD have a gut-bacterial profile distinct from that of people without the condition, no study has yet shown that gut microbes cause autism in people. One leading hypothesis is that some microbes could cause autistic symptoms to be worse in people who are prone to the condition, but this too remains unproven. People with ASD might harbour different gut microbes from those without the condition because they tend to have very specific dietary preferences.

Likewise, evidence that gut microbial therapies can help people with ASD is mixed. Krajmalnik-Brown strikes an optimistic note, but a review of four other studies did not reach a clear conclusion about the benefits of gut bacterial supplementation in children with ASD – although these earlier studies used ordinary probiotics and not bacteria directly from the human gut<sup>7</sup>. “The human data is very heterogeneous,” Cryan says. “If we target the microbes, it will be interesting to see if we have behavioural effects, but we need more evidence overall.”

As Krajmalnik-Brown’s trials progress, she warns children and families to steer clear of do-it-yourself faecal transplants. Instead, she says they should discuss options for altering



The surface of the small intestine has projections called villi.

the balance of gut microbes, such as conventional probiotics, with their physician. She also wants to temper people’s expectations for the treatment. “This might help alleviate the symptoms. I don’t believe that we have a cure on our hands,” she says.

For Ethan, however, the Arizona State study resulted in a striking turnaround. After the microbiome transfer, his diarrhoea and cramping disappeared in months. But most dramatic was his new interest in people. He began waking up with a smile, crowing, “Good morning!” He also started asking questions, such as ‘why is the sky blue and the clouds white?’ something he had not done before, his family says. In social-skills tests, Ethan, who is now 12, scores in the same range as children who are not on the autistic spectrum.

Did Ethan make these strides because his crippling stomach pain went away? Or have the new microbes truly changed the way his brain works? No one knows for sure. But Ethan’s family welcomes the research. “The study was the tipping point,” his mother says. “It was completely life altering.”

Looking forward, Cryan says, it’s crucial for scientists to keep decoding the biological pathways that connect the gut to the brain. “We’re optimistic that a healthy gut will mean a healthy brain, but we need the data.” Those data should help to determine just what fuelled Ethan’s improvements – and whether thousands of other children could follow a similar course.

**Elizabeth Svoboda** is a science writer in San Jose, California.

1. Desbonnet, L. et al. *Mol. Psychiatry* **19**, 146–148 (2014).
2. MacFabe, D. F. et al. *Microb. Ecol. Health Dis.* **23**, 19260 (2012).
3. Golubeva, A. V. et al. *EBioMedicine* **24**, 166–178 (2017).
4. Kang, D.-W. et al. *PLoS ONE* **8**, e68322 (2013).
5. Fiorentino, M. et al. *Mol. Autism* **7**, 49 (2016).
6. Sharon, G. et al. *Cell* **177**, 1600–1618 (2019).
7. Srinivasjos, R. et al. *Arch. Dis. Child.* **100**, 505–506 (2015).



# Fighting cancer with microbes

Targeting the microbiome could hold the key to combating a range of malignant diseases. **By Elie Dolgin**

In July 1984, a young Australian gastroenterologist drank a beef broth spiked with the pathogenic bacterium *Helicobacter pylori*. Within a week, he started vomiting. His breath began to stink. And he couldn't have been happier.

Barry Marshall wanted to prove that *H. pylori* could trigger inflammation of the stomach lining, a first sign of stomach cancer. By taking a biopsy of his own stomach tissue, Marshall demonstrated unequivocally that the hardy, spiral-shaped microorganism could cause gastric disease. Twenty-one years later, Marshall and his mentor Robin Warren won the Nobel Prize in Physiology or Medicine for their discovery linking the bacterium to chronic inflammation, peptic ulcers and stomach ailments such as cancer.

Yet *H. pylori* was long considered to belong to a special club of infectious agents, together with viruses such as human papillomavirus, that could provoke tumour formation. In oncology circles, the trillions of microbes that inhabit our guts, skin and other tissues were seen mostly as benign bystanders.

Cancer researchers now realize that many of those seemingly harmless microbes are anything but. Over the past decade, it's become clear that gut microbes can produce DNA-damaging toxins and carcinogenic metabolites, induce cancer-promoting inflammation, make tumours more resistant to chemotherapy drugs, and suppress the body's anticancer immune responses. "Every day now there seems to be some new microbe associated with cancer," says Susan Bullman, a microbiologist at the Fred Hutchinson Cancer Research Center in Seattle, Washington.

While researchers such as Bullman are now racing to unravel the molecular mechanisms behind tumour-promoting bacteria – and in so doing, identify targets for risk assessment, early detection, prevention and treatment – many cancer researchers are already testing whether microbiome-based therapeutics can improve the efficacy or safety of existing anti-cancer interventions. Borrowing a

page from the gastroenterology playbook, oncologists around the world have begun giving their patients faecal transplants and bacteria-filled capsules.

These living medicines have already revolutionized the treatment of antibiotic-resistant gut infections. A few studies have also shown the potential of faecal transplants for people with blood cancers receiving a stem-cell transplant. (These patients must take broad-spectrum antibiotics to prevent infections, but in so doing they lose the bacteria that are needed to prevent donated cells attacking the host.) Now, researchers are beginning to find that a dose of beneficial microbes enhances the efficacy of immune-modulating drugs known as checkpoint inhibitors and mitigates toxicity.

"Modulating the microbiome makes complete sense," says Jennifer Wargo, a surgical oncologist at the University of Texas MD Anderson Cancer Center in Houston. "People are really embracing the idea and we're beginning to see the early fruits of that labour."

## Not the only bad guy

Microbiologist Jun Yu of the Chinese University of Hong Kong has begun to take a close look at the role that bacteria have in driving stomach cancer. Yu's team identified a handful of microbes that were consistently enriched in samples from people with gastric cancer<sup>1</sup> or precancerous stomach lesions. "*H. pylori* is not the only bad guy," she says.

Yu suspects that the focus on *H. pylori* was an accident of history. This microbe happened to grow in laboratory cultures – the standard technique for bacterial identification during the 1980s. Yu's team relied on DNA analyses instead. "Gene sequencing provides a good opportunity to identify other microbes in the stomach that also play some role but weren't discovered before," she says. Her team is now evaluating the tumour-causing potential of these bacteria in mouse models.

Gut microbes have also been linked to bowel cancer, the third most common type of cancer worldwide. A toxin produced by a strain of gut



Scanning electron micrograph of *Helicobacter pylori* on the surface of the intestine.





bacterium called *Bacteroides fragilis*, a cause of diarrhoeal disease in young children, was implicated in the development of bowel cancer in 2009. Cynthia Sears, an infectious-disease specialist at Johns Hopkins University in Baltimore, Maryland, who made the original discovery in mice, has since shown that the toxin recruits immune cells to the intestinal lining and promotes an inflammatory cascade that can lead to cancer<sup>2</sup>.

And a team led by Christian Jobin, an immunomicrobiologist at the University of Florida in Gainesville, made a similar discovery: a strain of *Escherichia coli* that induces bowel cancer through the production of a toxin that damages DNA<sup>3</sup>. None of these pathogens necessarily work in isolation, however. “It’s an assembly of microorganisms that can collectively impact genome stability and immune function,” Jobin says.

Evidence for the idea that both *B. fragilis* and *E. coli* work together to fuel tumour growth comes from Sears, who showed that people who are genetically predisposed to bowel cancer frequently have patchy bacterial biofilms in their colons composed predominantly of these two microbes<sup>4</sup>.

### Menace of microbes

Although it did not crop up in Sears’s study, there are multiple lines of evidence that the bacterium *Fusobacterium nucleatum* – a spindle-shaped microbe found in most people’s mouths – is also a major driver of bowel cancer. It seems to promote proliferation of cancer cells through direct interactions with intestinal cells, rather than through a toxin intermediary.

The association between *F. nucleatum* and cancer first emerged through sequencing-based studies of tumour samples. Immunogeneticist Robert Holt at the British Columbia Cancer Agency in Vancouver, Canada, compared RNA from 11 bowel tumours with sequences from adjacent normal tissues<sup>5</sup>. When he and his colleagues looked for microbial genes expressed at elevated levels in the tumours, “the *Fusobacterium* signal really jumped out”, Holt says. Around the same time, a team led by immunologist Wendy Garrett and cancer geneticist Matthew Meyerson at Dana-Farber Cancer Institute in Boston, Massachusetts – stumbled on the same microbe after analysing the DNA of bowel tumours<sup>6</sup>.

In the years since, research teams from the Czech Republic, China, Japan and South Korea have all found that people with higher levels of *F. nucleatum* in their bowel tumours tend to have worse survival outcomes. The biological explanation, however, remains elusive. “If you have *Fusobacterium* and advanced

colorectal cancer, that sucks because your time to progression is going to be shorter,” Garrett says. “But why is that?”

Research in mice by scientists including Garret suggests that the presence of *F. nucleatum* increases cancer growth, possibly through the modulation of immune responses or through the direct activation of cancer signalling pathways. The microbe also seems to promote resistance to chemotherapy through the induction of a cellular recycling process that enhances tumour survival in the face of drugs. Other tumour-resident bacteria can metabolize chemotherapeutics, which further contributes to drug resistance.

Last year, an international team led by Garrett and Meyerson secured a £20-million (US\$26-million) grant from Cancer Research UK to discover exactly how microbes in the body lead to bowel cancer. Part of the funding is earmarked for finding new ways to eliminate the prime suspects – *F. nucleatum*, *B. fragilis* and *E. coli* – without disturbing the entire microbial ecosystem inside the gut.

In 2017, Bullman, who was working in Meyerson’s lab at the time, showed that the antibiotic metronidazole could slow cancer growth in mice with *Fusobacterium*-positive tumours<sup>7</sup>. But the antibiotic also targets a range of beneficial microbes in the intestines. “What we really need,” says Bullman, “are more targeted approaches.” A drug specific to *Fusobacterium* could do the trick. Or a vaccine. Or perhaps a phage therapy that takes advantage of bacteria-infecting viruses to precisely eliminate the nefarious microbe.

### Targeted attack

At the 2019 International Cancer Immunotherapy Conference in Paris, scientists from microbiome therapeutic company BiomX in Ness Ziona, Israel, reported the discovery of several *Fusobacterium*-targeted phages that, when injected into the bloodstream of mice, could successfully invade bacteria nestled inside implanted tumours. According to chief executive Jonathan Solomon, BiomX is harnessing synthetic biology to turn the phages into programmable bacterial assassins that could also deliver a therapeutic payload that helps to recruit tumour-fighting immune cells to the site of attack.

Alternatively, predatory bacteria called *Bdellovibrio* could be deployed in the fight against cancer-causing microbes – and microbiologist Emma Allen-Vercoe from the University of Guelph, Canada, didn’t need to look far to discover one that could destroy *Fusobacterium*. Her team dug up a patch of clover from the lawn in front of the university’s clock tower. Among the germ-eating microbes

they found, “some are real champions at killing fusobacteria”, she says.

Despite these efforts, most specialists acknowledge that it remains to be shown definitively whether the human microbiome has a causal role in cancer. It could be that some bacteria are merely opportunistic invaders of tumours once cancer has already taken hold.

“We’re lacking solid direct evidence in the form of longitudinal cohort studies that the microbiome causes cancer,” says Alasdair Scott, a colorectal surgeon at Imperial College London. He is one of the architects of the International Cancer Microbiome Consortium, a global body that aims to establish expert consensus on the role of the microbiome in oncology. Last year, the group wrote a policy paper calling on researchers to address the question of causation versus association<sup>8</sup>.

**“Every day now there seems to be some new microbe associated with cancer.”**

Prospective cohort studies take years, however, and new treatment options for cancer are needed now. “You can’t wait until everything is completely known,” Holt says. Clinicians are therefore moving ahead with testing microbiome modulation, especially in patients receiving checkpoint-inhibitor drugs designed to rev up the body’s antitumour immune response.

At the 2019 meeting of the American Association for Cancer Research, two research groups described promising work in people receiving immunotherapy for melanoma. In both cases, the tumours of people who initially did not benefit from the treatment shrank after receiving faecal matter from someone who did respond to the drugs.

Elsewhere, researchers have been administering poo-stuffed pills from healthy donors alongside immunotherapy, with similarly favourable results. And, given that the procedure is generally considered to be low risk, some clinicians are beginning to think about a future in which stool swaps become a standard add-on to immunotherapy for all patients, not just those who fare poorly on the immune-targeted drugs to begin with. “Everybody might be doing it right off the bat,” says John Lenehan, an oncologist at the London Regional Cancer Program in Canada.

The safety of faecal transplants was called into question, however, when researchers last year described how contaminated stool left one man dead and another severely ill in experimental trials investigating the procedure for other applications<sup>9</sup>.





People with cancer might benefit from receiving microbial therapies alongside cancer drugs.

Physicians now test donated samples for the drug-resistant strain of *E. coli* that caused the infections. But fearing that a newly virulent microbe could slip through the screening process, some researchers are turning to defined, well-characterized and lab-grown formulations of microbes.

These blends of cultured strains are typically selected on the basis of observational human studies and mouse experiments that test which organisms most influence the response to immunotherapy. Wargo, for example, led one of a number of groups that described correlations between clinical responses to checkpoint inhibitors and the composition of the gut microbiome. Microbiomics company Seres Therapeutics in Cambridge, Massachusetts, took those findings, incorporated extra in-house data, and created a mix of strains from dozens of bacterial species, all in spore form. Researchers, including Wargo, have begun testing the Seres product in people with advanced-stage melanoma.

Microbial therapeutics company Vedanta Biosciences, also in Cambridge, picked 11 strains for its bacterial cocktail by looking for microbes in human faeces that most potently elicited the desired immune responses in mice. A team including Vedanta's scientists showed how each strain in isolation could enhance antimicrobial or antitumour immunity in mouse models<sup>10</sup>. "However, assembled in certain consortia, they had a much larger effect," says study co-author and Vedanta chief executive Bernat Olle.

Some firms, including pharmaceutical company 4D Pharma in Leeds, UK, are paring down the therapeutic approach even further and

administering single microbial strains with immune-stimulating effects. The company's scientists have described a strain of *Enterococcus gallinarum*, isolated from a healthy human gut, and its structural protein flagellin, which rouses the immune system by interacting with a receptor found on intestinal cells. The firm is now testing that strain in the clinic in people with lung, kidney, bladder and skin cancers, both as a therapy ahead of surgical removal of the tumours and in combination with a checkpoint inhibitor.

### Poo versus pills

Bryan Coburn, an infectious-disease specialist at the Toronto General Hospital Research Institute in Canada, points to several benefits of using rationally designed consortia of bacteria rather than relying on donor faecal material. "There are specific safety advantages, because we know exactly what's going in," says Coburn, who is clinically evaluating a multi-strain pill for cancer from NuBiyota, which is based in Pearl River, New York, and co-founded by Guelph's Allen-Vercoe. Prepared formulations are scalable and modifiable, Coburn says. Moreover, "we can assess things like potency, which you can't do easily with faecal transplants", he adds.

Microbial therapies might also need to be

**"People are really embracing the idea and we're beginning to see the early fruits of that labour."**

tailored to certain tumour types. For example, men with metastatic prostate tumours who responded to checkpoint inhibition have been found to have lower levels of a microbe called *Akkermansia muciniphila* in their stool than did men who did not respond. But the opposite is true of people with lung and kidney cancers – those with more *A. muciniphila* in their guts tended to fare better on the therapy.

Amy Moran, an immunologist at Oregon Health and Science University in Portland, thinks that the different treatments that people with different cancers receive might explain the discrepancy. "So many other types of drugs that these patients take might be impacting the composition of the microbiome," she says. She suspects that, for prostate cancer, the hormone therapies commonly used as first-line treatments might be to blame. Uncertain of which bacteria will be best in this context, Moran and her colleagues are starting by trying to boost immunotherapy response with complete faecal transplants.

Elsewhere in the oncology clinic, researchers are turning to microbiome therapeutics to manage some of the immune-related toxicity associated with checkpoint-blocking drugs. At the University of Texas MD Anderson Cancer Center, gastroenterologist Yinghong Wang is using faecal transplants to manage cases of immunotherapy-induced colitis. In 2018, she described how a woman with bladder cancer and a man with prostate cancer, both of whom developed side effects including bloody diarrhoea after receiving checkpoint inhibitors, saw their symptoms resolve after one or two transplants of stool from a healthy donor<sup>11</sup>. Wang has since treated another dozen or so people. "All of them seem to benefit from this treatment," she says.

None of Wang's patients had previously received faecal transplants to improve therapeutic responses. If they had, she suspects they would not have developed the side effects in the first place. Microbiome modulation might, therefore, offer a double benefit for people with cancer – enhancing response rates to other drugs while also guarding against the worst of their ill effects.

**Elie Dolgin** is a science journalist in Somerville, Massachusetts.

1. Coker, O. O. *et al.* *Gut* **67**, 1024–1032 (2018).
2. Chung, L. *et al.* *Cell Host Microbe* **23**, 203–214 (2018).
3. Arthur, J. C. *et al.* *Science* **338**, 120–123 (2012).
4. Dejea, C. M. *et al.* *Science* **359**, 592–597 (2018).
5. Castellarin, M. *et al.* *Genome Res.* **22**, 299–306 (2012).
6. Kostic, A. D. *et al.* *Genome Res.* **22**, 292–298 (2012).
7. Bullman, S. *et al.* *Science* **358**, 1443–1448 (2017).
8. Scott, A. J. *et al.* *Gut* **68**, 1624–1632 (2019).
9. DeFilipp, Z. *et al.* *N. Engl. J. Med.* **381**, 2043–2050 (2019).
10. Tanoue, T. *et al.* *Nature* **565**, 600–605 (2019).
11. Wang, Y. *et al.* *Nature Med.* **24**, 1804–1808 (2018).

## Perspective: Another dimension for drug discovery

**‘Deep phenotyping’ of human cohorts, including the collection of microbiome data, could transform therapy development, says Eran Segal.**

**L**ast year, drug company Novartis began charging US\$2.1 million per patient for its new spinal muscular atrophy treatment – breaking the record for the world’s most expensive drug. With so many compounds failing to reach the clinic, and the cost of turning a molecular entity into a therapy reaching billions, it’s no wonder that drugs have become so expensive. But we can do better.

One way to reduce costs is to use genetic data to inform drug design. Genetic information helps researchers to demonstrate that drug targets are relevant to the disease from the start, and drugs with this evidence are twice as likely to be approved as those without (M. R. Nelson *et al. Nature Genetics* 47, 856–860; 2015). But we can further optimize drug discovery. If we start with a ‘deep’ molecular profile that includes data about the microbiome and genome, as well as information about metabolites and proteins (the metabolome and proteome), coupled with physiological measurements, we might be able, in some cases, to skip animal testing and move straight to human trials.

The ability to start drug discovery with this in-depth information is particularly useful for finding microbiome-related therapies. Rather than focus on microbial targets with therapeutic value in animal models that might turn out to be rare in the human microbiome, or that act through different mechanisms in people, we can start with microbes associated with human disease. Interventions to modify bacteria can also start directly in people. The idea is to collect dietary and microbiome data from many individuals, derive models of how diet affects composition of the microbiome, and then validate the models with controlled dietary interventions. With more than 5 million bacterial genes, the microbiome represents a prolific reservoir of modifiable targets with potentially therapeutic effects.

The gut microbiome has been implicated in numerous conditions, including autoinflammatory disease, autism, cardiovascular disease and cancer. Growing evidence from animal and human studies suggests that it has causal effects in disease, such as by regulating host gene expression or by producing metabolites that circulate in the blood. And because the microbiome is predominantly shaped not by genetics but by modifiable environmental factors such as diet, this presents an opportunity to intervene.



**“Deep profiling allows the disease state or treatment response to be modelled as a continuum.”**

**Eran Segal** is a computational biologist at the Weizmann Institute of Science in Rehovot, Israel.  
e-mail: [eran.segal@weizmann.ac.il](mailto:eran.segal@weizmann.ac.il)

For example, dietary interventions are being targeted towards gut bacteria that synthesize the metabolite trimethylamine N-oxide (TMAO). It has been suggested that elevated plasma levels of TMAO cause cardiovascular disease; reducing TMAO production could, therefore, help to lower disease risk. And in neurological diseases, microbiome-derived metabolites that reach intestinal neurons could provide a means of getting metabolites through the barrier that separates the brain from circulating blood.

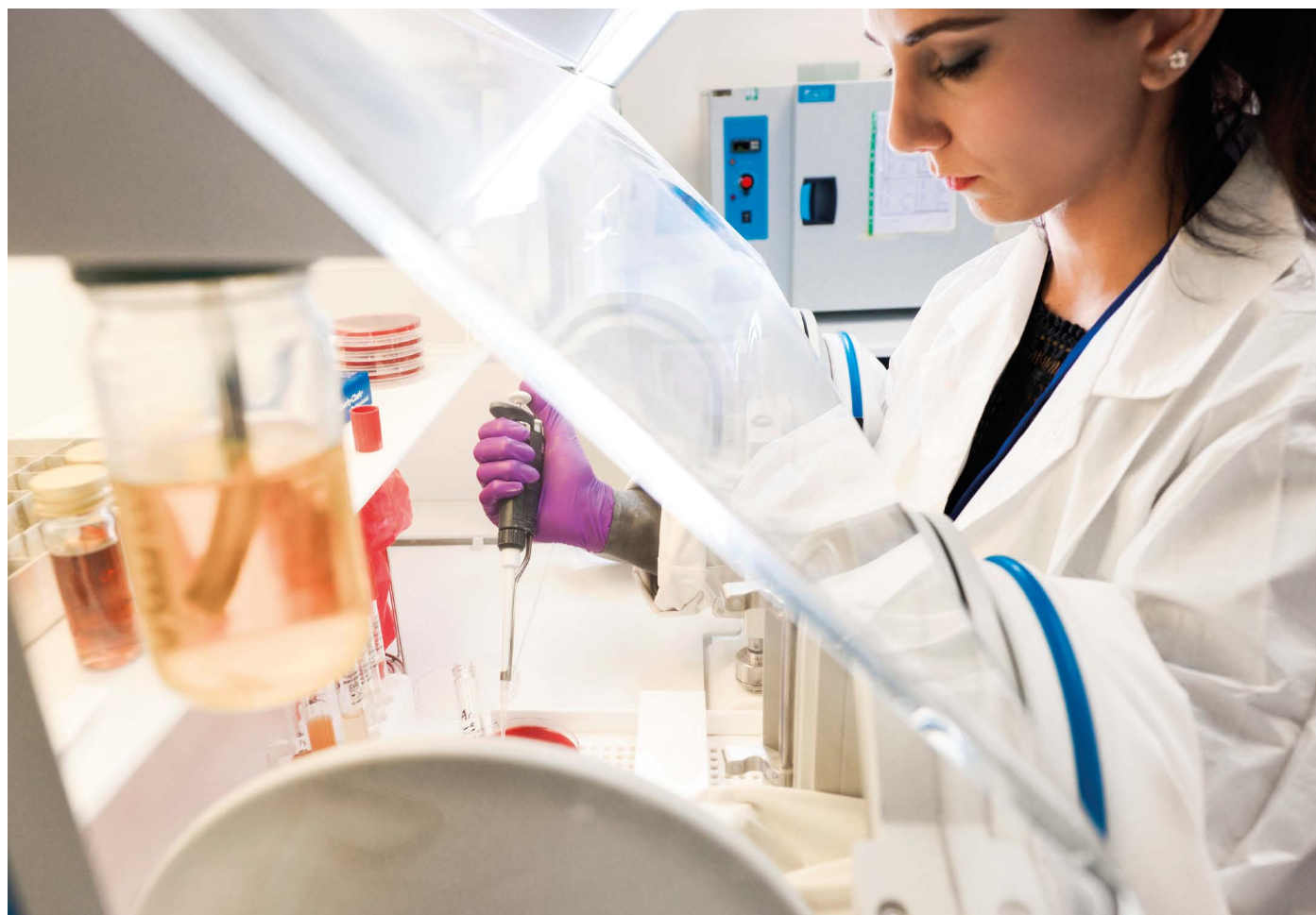
The microbiome can also affect the efficacy of pharmaceutical drugs. Bacterial enzymes, for example, can metabolize the Parkinson’s disease drug L-DOPA, and gut bacteria can affect a person’s response to cancer immunotherapy. Dietary changes targeting bacteria that interfere with drug metabolism could, therefore, be effective supplements to existing treatments. The regulatory path for approving such microbiome-nutrition interventions is much easier than for conventional pharmaceutical products.

The development of microbiome-related therapeutics faces many challenges, including the need to establish causal mechanisms. However, even if these are unknown, we might still be able to use human microbiome data to devise therapies. For example, our team has targeted post-meal blood glucose levels, which are important in obesity and diabetes. We tracked blood glucose levels in 900 people, and collected data about their microbiome, genetics, metabolomics, diet and lifestyle (D. Zeevi *et al. Cell* 163, 1079–1094; 2015). We found that people respond differently to the same meal, and devised a machine-learning algorithm that accurately predicted these personalized responses from clinical and microbiome data. In short-term and 12-month randomized controlled trials, we showed that personalized dietary interventions based on the algorithm successfully balanced glucose levels in people with higher than normal blood sugar – outperforming the standard-of-care diet.

We need new approaches to drug development. Cohorts made up of rich molecular and physiological profiles from many volunteers offer one way to prioritize human-relevant targets for development. These cohorts must be constructed carefully – the type and depth of the data collected should be relevant to the disease being studied. Having multiple types of data on the same people can be powerful for defining more exact targets and for discovering novel disease biomarkers and drug targets. Deep profiling also allows the disease state or treatment response to be modelled as a continuum, avoiding the need for arbitrary thresholds that categorize people as responders or non-responders, for example. This might lead to better estimates of disease risk and better prioritization of people to treatments and randomized controlled trials.

Longitudinal measurements of the same people are also crucial. Such studies bypass confounding factors of inter-personal variability because the volunteers serve as their own control. Finally, because resources are always limited, cohort size is an important consideration. A study of thousands or tens of thousands of participants still allows longitudinal, deep molecular profiling, but keeps costs realistic. Now is the time to use deep cohorts to end the era of laborious, costly, risky and time-consuming drug discovery. We can’t afford another world record.





LEWIS HOUGHTON/SPL

A researcher tests donor stool before it is used for faecal microbiota transplantation.

## Engineering the microbiome

Modified bacteria and carefully formulated microbial communities could form the basis of new living treatments. **By Claire Ainsworth**

**A**lthough it happened almost a decade ago, Willem de Vos still vividly remembers his colleagues being told to halt the clinical trial they had been running. De Vos was part of the team conducting the first randomized clinical trial of faecal microbiota transplantation (FMT) – faeces from healthy donors were used as a last-resort treatment for people with a devastating, recurrent gut infection caused by the bacterium *Clostridium difficile*. About a year in, the data and safety monitoring board overseeing the trial had seen enough: the trial needed to end. But it wasn't because the therapy didn't work – quite the opposite. The

transplants were proving so successful that it was no longer ethical to continue to give people in the control group the conventional antibiotic treatment with which the transplants were being compared. "That showed us that it worked and why it worked," says de Vos, a microbiologist at the University of Wageningen in the Netherlands and the University of Helsinki in Finland. The antibiotic-treated patients who relapsed were given the transplant, which cured them.

The *C. difficile* story is one of a growing list of examples of how the gut microbiome shapes our biology. The community of microbes that lives in the gut has been associated with many

aspects of our physiology – from conditions such as obesity to how the immune system functions and even mental health. The success of FMT in treating *C. difficile* also shows that, in principle, the ecology of the gut can be manipulated to treat disease. Now, scientists are attempting to engineer gut microbiota that will allow them to do just that.

Synthetic biologists are working at the level of individual species, engineering gut bacteria not only to deliver therapeutic payloads but also to monitor and respond to conditions inside the body. Meanwhile, synthetic ecologists are looking at the gut as an ecosystem and assembling communities of microbes that

interact to produce substances or behaviours for medical benefit. Both approaches are in their infancy, and there are challenges to getting them into the clinic. Yet the technologies are already proving to be powerful tools, allowing scientists to explore the complex microbial interactions in our internal ecosystem.

## Bespoke bacteria

Engineering individual microbes has an impressive array of potential applications. Gut bacteria have been altered to produce therapeutic molecules to treat metabolic conditions, kill pathogens and trigger immune responses to cancers. A strain of *Escherichia coli* engineered to produce the proteins needed to correct rare metabolic deficiencies is now in clinical trials. And in 2018, a team in Singapore revealed gut bacteria that it had engineered to stick to colon cancer cells and secrete an enzyme that converts a substance naturally found in vegetables such as broccoli into a molecule that inhibits tumour growth. When given to mice with colon cancer, the treatment shrank tumours and reduced recurrence<sup>1</sup>. Bacteria can even be engineered to sense signs of disease and respond by producing therapeutic molecules. For example, in 2017, researchers took a gut bacterium commonly used as a probiotic and gave it the ability to detect communication signals produced by pathogenic bacteria. The probiotic bacterium then produces an antimicrobial molecule in response. The researchers showed that it helped clear infections in worms and mice<sup>2</sup>.

Studies such as this show the potential of live therapeutics, but so far the engineered bacteria are comparatively straightforward systems – they produce a therapeutic molecule either at a constant rate or in response to an environmental signal. Now, researchers are looking to broaden the scope of engineered microbes and engineer bacteria with DNA containing more complex elements designed to work like electronic circuits. This is the realm of synthetic biology, a discipline that aims to apply engineering principles – such as standardized, modular components – to biological systems.

These complex feats of engineering are allowing bacteria to do simple computational tasks, such as remembering a one-off stimulus long after it has passed. For example, a team of synthetic biologists led by Pamela Silver at the Wyss Institute for Biologically Inspired Engineering at Harvard University in Boston, Massachusetts, engineered a bacterium to detect a chemical produced by inflamed gut cells. In response, the bacteria secrete a molecular signal, and continue to secrete it even if the gut inflammation dies down. The

signal can be detected in stool samples, raising the possibility of using the bacterium as a living diagnostic test for inflammatory bowel disease – which is often transient in nature and, therefore, hard to detect in the clinic. The bacteria formed a stable colony in the guts of mice for six months and responded to experimentally induced gut inflammation<sup>3</sup>. Importantly, engineered bacteria that can remember other kinds of environmental signal would allow researchers to explore conditions in different regions of the gut – something that is hard to do with conventional stool samples. “What we really would like is the bacteria to be like detectives and tell us what’s going on as they pass through,” says Silver.

Getting a genetic circuit to work in the lab is hard enough. Translating that to the messy, competitive environment of the gut microbiome presents an even greater challenge. Any modification that imposes an extra burden – say, extra protein production – on a bacterium puts it at a disadvantage, resulting in that organism either being out-competed or ditching its engineered function to survive. Partly for this reason, researchers have struggled to get many engineered bacteria to make the leap from test tube to animal models. Scientists are now working on ways around this; Silver, for example, is using genetic elements that naturally place a minimal burden on the cell.

The final hurdle will be showing that engineered bacteria are effective and safe. What’s more, unlike conventional drugs, engineered bacteria could spread into the environment and share their DNA with other bacteria. Although the chances of them surviving in the wild are thought to be low, the possibility of unforeseen consequences (not to mention the need to secure public acceptance and regulatory approval) has led researchers to explore a number of options to contain engineered bacteria, including kill switches that force bacteria to kill themselves with a toxin if their engineered circuits turn faulty or if they leave the body.

## Constructing communities

While some researchers engineer individual bacteria, others are turning their attention to groups of microbes. Just as a city functions as a result of many people doing different jobs, the gut is a hive of interactions between myriad microbes carrying out different functions. Some interactions are metabolic – one bacterium might produce something that another consumes, for instance. Others are ecological, such as when one microbe inhibits the growth of another. By working together, communities of microbes produce molecules or behaviours that would not arise

from organisms acting alone.

These emerging properties of the gut microbiome have a profound effect on our biology, such as by producing vitamins or molecules that modulate our immune responses. To understand these interactions and to devise new therapies, researchers are building combinations of different bacteria known as synthetic ecosystems. For the most part, these ecosystems are made up of naturally occurring bacterial strains, although some scientists are experimenting with ecosystems containing genetically engineered microbes.

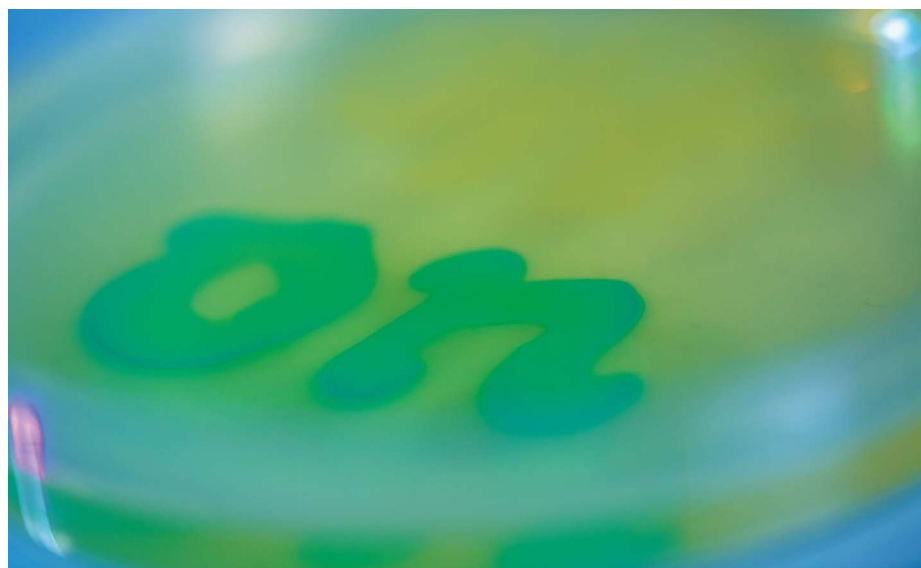
From a therapeutic point of view, synthetic ecosystems have a number of potential advantages. FMT currently relies on faecal matter provided by donors. Stool samples contain

**“What we really would like is the bacteria to be like detectives and tell us what’s going on.”**

highly complex mixtures of microbes that vary from donor to donor, and each must be screened for pathogenic microbes. If FMTs could be stripped down to just the key species needed to treat people, simplified pathogen-free mixtures of these selected microbes could be grown in the lab. Synthetic communities would offer a standardized therapeutic with a known composition, and would lift the reliance on finding suitable donors.

Research, including a few studies in people, suggest that this approach could work. Mixtures of selected bacteria isolated from stool samples have shown promise in treating people with *C. difficile*. And it’s not just infections that could be tackled, but also conditions such as inflammatory bowel disease. In 2013, a team led by scientists in Japan identified a community of human gut microbes that could promote the activity of inflammation-damping immune cells called regulatory T cells, and showed that this could ameliorate inflammatory bowel disease in mice<sup>4</sup>. As well as developing therapies, stripping down conventional FMTs is allowing scientists to work out which bacteria in stool transplants are exerting a therapeutic effect – something that de Vos and his colleagues are exploring in conditions such as inflammatory bowel disease and metabolic syndrome.

One drawback of this stripping-down approach is that it limits the applications of the synthetic community to functions that already exist. There might be situations in which you would want to create a community with a new function, such as producing a vitamin



**Synthetic biologists have engineered bacteria that remember the presence of a chemical and secrete a molecular signal that allows them to be identified.**

or degrading a toxin. Creating new functions requires designing from the bottom up – testing different combinations of microbes, including those that don't normally co-exist in nature, until one gives the desired outcome. Doing this by trial and error in lab experiments soon becomes unwieldy, so instead researchers have turned to computer modelling.

The aim here is to predict the emergent properties of a microbial community, based on expected interactions between the microbes present. A team led by Elhanan Borenstein at Tel Aviv University in Israel created computer models of the metabolic reactions inside individual microbes, and then modelled how these would behave in the presence of another microbe's metabolism<sup>5</sup>. By simulating interactions between pairs of microbes, they showed how new metabolic products emerged that wouldn't be seen if the microbes acted alone. Models can simulate ecological interactions too, such as how the abundance of one microbe affects the abundances of others. This can help scientists to design microbial communities that are stable and therefore persist over time.

### It's the ecology

Computer modelling and lab-grown communities allow researchers to gain a better understanding of how microbes in natural communities in the gut interact – both with each other, and with their human hosts. De Vos's team grew four different bacteria that usually live together in the mucus layer lining the gut<sup>6</sup>. One species, *Akkermansia muciniphila*, breaks the mucus down into compounds that other bacteria consume. The team showed that the other bacteria were not

only consuming these compounds, but were also feeding molecules they had made back to *A. muciniphila* and, in the case of butyrate, a fatty acid needed by the cells of the gut lining, to their host.

Researchers are also gaining new insights into the relationships between microbes and between microbes and their host from the creation of minimal microbiomes – constructed microbial communities containing the smallest number of species needed to create a stable ecosystem. A 2016 study showed how combining a minimal microbiome with comparative

**“We're making progress and learning a lot of interesting biology on the way.”**

genomics can lead to the design of a microbial community with a desired property. Bärbel Stecher at the Ludwig-Maximilians University of Munich in Germany and her team developed the Oligo-MM<sup>12</sup> minimal microbiome – a collection of 12 gut microbes that helps to prevent *Salmonella enterica* from colonizing the guts of mice lacking any bacteria of their own<sup>7</sup>. The 12 bacterial species excluded *Salmonella* almost, but not quite, as well as a conventional microbiome. By using genomics to compare their minimal microbiome with a complex one, the researchers singled out the ecosystem functions that were missing from their community, added three more bacterial species that could fill the gap, and produced a community that was as good as the conventional one at keeping *Salmonella* out. Ultimately,

researchers hope that studies such as this will allow them to design minimal microbiomes with defined therapeutic properties, such as producing butyrate or vitamins.

Perhaps the eventual application of microbiome engineering would be to combine synthetic biology and synthetic ecology. Scientists would create communities containing genetically-engineered microbes, the collective behaviour of which would deliver a therapeutic benefit. One advantage of this approach is that it would let engineers distribute different metabolic tasks between different bacteria. This means all the physiological stress of making a drug or a vitamin would not be placed on just one bacterium. A number of teams have made progress in this area, including exploiting a system that bacteria use to detect the presence of other bacteria and to modify their gene activity in response. Researchers are using this feature, known as quorum sensing, to control the behaviour of mixed populations of bacteria, to, for example, allow bacteria that compete with each other to co-exist and form a stable population.

The potential paybacks of engineering the gut microbiome are immense, but so are the challenges to reaching this goal. Of all the human microbiomes to take on, the gut microbiome is by far the largest and most complex. Much remains to be learnt about its denizens, their genes and their interactions. And that's before you get started on what the human host brings to the party. Indeed, there is so much variation between individuals that it's still not clear what a 'healthy' gut microbiome looks like (see page S6).

Even so, the potential payoffs are motivating the scientists to aim high. Borenstein hopes one day to take information about an individual – the microbes in their gut, their physiology, their diet and their genome – and use it to build a full-scale computer model of their gut microbiome. Such an advance might make it possible to design personalized interventions to treat or prevent disease.

“This is not something we'll get to in a year, or two or five,” Borenstein admits. “But we're making progress and learning a lot of interesting biology on the way.”

**Claire Ainsworth** is a freelance science journalist in Hampshire, UK.

1. Ho, C. L. et al. *Nature Biomed. Eng.* **2**, 27–37 (2018).
2. Hwang, I. Y. et al. *Nature Commun.* **8**, 15028 (2017).
3. Riglar, D. T. et al. *Nature Biotech.* **35**, 653–658 (2017).
4. Atarashi, K. et al. *Nature* **500**, 232–236 (2013).
5. Chiu, H.-C., Levy, R. & Borenstein, E. *PLoS Comput. Biol.* **10**, e1003695 (2014).
6. Belzer, C. et al. *mBio* **8**, e00770-17 (2017).
7. Brugiroux, S. et al. *Nature Microbiol.* **2**, 16215 (2016).



## Perspective: Use diet as a tool, not a treatment

Scientists can sequence your microbiome, but they still can't tell you what to eat to prevent or treat disease, says Peter J. Turnbaugh.

**A** recent report<sup>1</sup> about the health consequences of eating red and processed meat renewed long-standing debates about what evidence should be required before the public are told what foods they should avoid. For me, this subject hits especially close to home – my lab's research shows that meat consumption alters the human and mouse gut microbiomes, and I am frequently asked if meat is “bad for gut microbes”.

Our results indicate that meat consumption promotes the growth of bacteria that exacerbate mouse models of inflammatory bowel disease and decreases the levels of bacteria that metabolize fibre<sup>2</sup>. But our studies in both people and mice have been short, controlled and extreme in terms of the level of meat consumption. Does this really reflect what happens in people on more typical diets?

Basing dietary advice on microbiome studies also assumes that it is possible to predict the health effects of different microbial communities – a goal that is far from being realized. Even well-studied mechanisms have unclear consequences for human health. Take, for example, the production of short-chain fatty acids (SCFAs) from the bacterial digestion of fibre. SCFAs act on multiple tissues and targets of interest in both bacterial and host cells. Furthermore, not all SCFAs are the same, and they have not been considered in the context of products of carbohydrate and amino-acid fermentation – let alone the diversity of other microbial metabolites that could enhance or counteract the effects of these specific compounds. Therefore, although it is tempting to recommend diets that boost SCFAs to prevent metabolic and other diseases, the broader effects on the microbiome and its complex interactions with the host are hard to predict.

Another massive gap in our knowledge is the degree to which the microbiome is affected by, or mediates, the health consequences of our diet beyond macronutrients (fats, proteins and carbohydrates). Results from our lab have shown that the effect of raw potatoes on the gut microbiome is markedly different from that of cooked ones<sup>3</sup>. Although cooking-induced changes to carbohydrates explained much of this effect, our data also suggest the broader chemical diversity of plants should be considered. Other research has highlighted the ability of



**“The research questions pertaining to diet and the gut microbiome are wide open.”**

**Peter J. Turnbaugh is a microbiologist at the Benioff Center for Microbiome Medicine at University of California, San Francisco.**

e-mail: peter.turnbaugh@ucsf.edu

gut bacteria to inactivate potentially harmful chemicals formed during cooking<sup>4</sup>. These results make clear that researchers studying the interaction between diet and the microbiome need to consider not just the composition of foods, but also how they are prepared.

The research questions pertaining to diet and the gut microbiome are wide open. It is all the more important, therefore, that we identify reliable ways to use the data that emerge as we improve our understanding of how the microbiome works.

Two clear strategies for using microbiome data can be borrowed from more conventional drug development: biomarker discovery and target-driven screening. The use of gut microbes as biomarkers was pioneered by Eran Segal at the Weizmann Institute of Science in Rehovot, Israel, (see page S19) whose group used microbiome profiles alongside other data to predict blood glucose levels following a meal. Although the added value of microbiome data for that particular application remains debated, the general limitation of these approaches is that they provide little information about the mechanisms involved. That makes it difficult to infer causal relationships, to develop mechanistic hypotheses, or to expand these predictors to incorporate future discoveries about the host or microbiome.

The other approach, selecting specific bacterial targets for modulation by diet, has been applied to the design of diets to treat undernourished children<sup>5</sup>. Prototype diets were designed with the goal of promoting the growth of bacteria that are under-represented in children with severe acute malnutrition. Following extensive preclinical characterization of these microbes in mice and pigs, the researchers ran a randomized, double-blind controlled feeding study that provides preliminary support for efficacy in people. This target-driven approach offers a clear advantage over biomarker discovery – it is easy to see how future mechanistic insights into the components of the microbiome with compelling links to disease can be incorporated into the development of therapeutic diets.

As the amount of research into the interactions between diet and the microorganisms that populate our gut grows, it is worth considering whether dietary recommendations are the best way to use our growing knowledge about the role of the microbiome in nutrition. Adjusting the type or quantity of food eaten is an attractive intervention, given its simplicity, but a restrictive diet can be difficult to maintain over long periods of time – especially for people with severe disease. In the future, researchers might instead use diet as a discovery platform in humans and animal models to uncover specific species, genes or enzymes that could be targeted using conventional small molecule drugs, biologics or cell-based therapies. If so, rather than ‘what should people eat?’ maybe the question should be ‘how can we design the microbiome-based medicines of the future?’.

1. Johnston, B. C. et al. *Ann. Intern. Med.* **171**, 756–764 (2019).
2. David, L. A. et al. *Nature* **505**, 559–563 (2014).
3. Carmody, R. N. et al. *Nature Microbiol.* **4**, 2052–2063 (2019).
4. Wolf, A. R. et al. *Cell Host Microbe* **26**, 463–477 (2019).
5. Gehrig, J. L. et al. *Science* **365**, eaau4732 (2019).

The author declares competing interests; see [go.nature/2t0e9m8](https://go.nature/2t0e9m8) for details.

# Research round-up

## Highlights from microbe studies. By Liam Drew

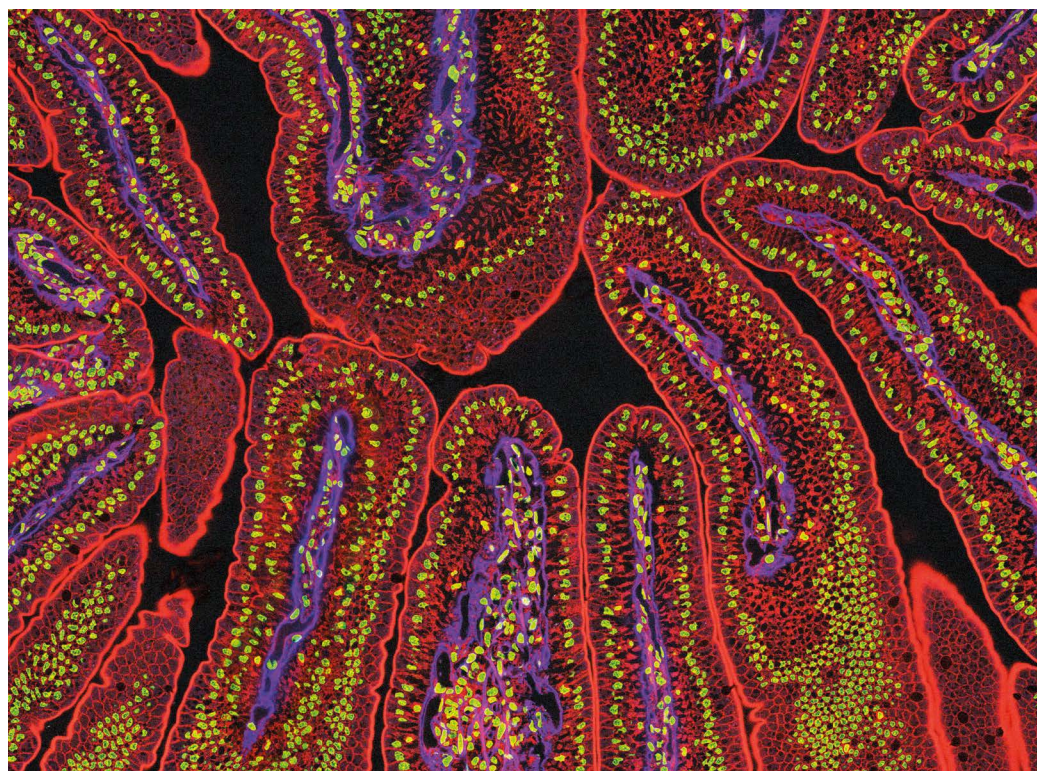
### The gut's link to mental health

A study of a pair of 1,000-strong cohorts has strengthened the link between the community of microorganisms that live in the gut and mental health.

Jeroen Raes at the Catholic University of Leuven, Belgium, and his team initially looked for links between the microbiome and depression and quality of life in participants in the Belgian Flemish Gut Flora Project. In this cohort, the team showed that two bacterial species were positively correlated with self-reported high quality of life, whereas a third was most abundant in people reporting low quality of life. A subsequent analysis that categorized people as having one of four types of microbiome found that people with depression more often had a type associated with low overall bacterial abundance. Using published genetic characterizations of gut-bacterial metabolic pathways, the team also showed around 50 routes by which various intestinal microbes can produce neuroactive metabolites. Among the pathways, it found an association between higher quality of life and the presence of bacteria that produce a metabolite of the neurotransmitter dopamine.

The study frames hypotheses for future work to investigate whether the microbiome can affect mental health – and, if so, whether this happens through altered dopamine signalling.

*Nature Microbiol.* **4**, 623–632 (2019)



THOMAS DEERINCK, NCMI/SPL

Villi of the small intestine are home to gut microbes.

### The key to faecal transplantation

A follow-up analysis of a landmark clinical trial of faecal microbiota transplantation (FMT) for ulcerative colitis might have identified bacterial species that could help to treat this form of inflammatory bowel disease. In a 2017 trial, 27% of people with ulcerative colitis entered full remission after receiving FMT – a success, but a partial one.

Now, Nadeem Kaakoush at the University of New South Wales in Sydney, Australia, and his colleagues report on detailed analyses that link remission to features of the recipients' intestinal microbiomes before and after treatment, and also to the bacterial composition of donor stool.

People whose disease went

into remission had greater overall microbiota diversity both pre- and post-FMT. But following treatment, remission was associated with the enrichment of two species of bacteria: *Eubacterium hallii* and *Roseburia inulinivorans*. These microbes are thought to boost production of short-chain fatty acids (SCFAs) and the breakdown of starch. Indeed, the guts of people in remission showed an increase in SCFA production.

The likelihood of successful treatment also correlated with the bacterial content of donated stool. Remission was more likely if the stool had high levels of *Bacteroides* species, whereas *Streptococcus* species were more common in samples that did not induce remission.

The results could allow rational selection of both donors and recipients of FMT

for ulcerative colitis, and might make it possible for physicians to use particular bacterial strains to enhance responses or treat ulcerative colitis.

*Gastroenterology* **156**, 1440–1454 (2019)

### Microbe boosts metabolic health

According to a clinical trial, a daily dose of the bacterium *Akkermansia muciniphila* might treat metabolic syndrome – a condition that predisposes individuals to type 2 diabetes and serious cardiovascular disease, and that is marked by obesity, high blood pressure, and raised levels of blood sugar, fats and cholesterol. *A. muciniphila* is abundant in the guts of lean people and



its prevalence decreases with obesity. In a proof-of-principle study, Belgian researchers gave people who were insulin-resistant and overweight or obese a preparation of either live or pasteurized *A. muciniphila*, or a placebo, daily for three months.

Both the live and pasteurized bacteria had beneficial effects. Pasteurized *A. muciniphila* in particular lowered circulating insulin and total cholesterol levels and decreased insulin resistance. The microbes also reduced white blood cell counts, an indication that there was less overall inflammation. It is unclear why dead bacteria were more effective, but the results suggest that the bacteria's metabolites or cell-wall fragments might be therapeutically active.

Patrice Cani at the Catholic University of Louvain, Louvain-la-Neuve, Belgium, and his team note the study was small, with only about ten people per group, and neither abdominal fat nor body mass index were reduced. They are now looking at the effects of individual molecules in mice and are planning a larger trial of pasteurized *A. muciniphila* in humans.

*Nature Med.* **25**, 1096–1103 (2019)

## Bacterial effect on disease pathways

Investigations of links between the gut microbiome and specific diseases tend to have a causality problem: it's unclear whether an altered microbiome contributes to the disease or whether the disease alters the collection of microbes. But a team of researchers led by Serena Sanna and Cisca Wijmenga at the University of Groningen in the Netherlands and Mark McCarthy at the University of Oxford, UK, have addressed this issue using an analytical approach called Mendelian randomization – in which genetic variants are treated as manipulations that

define experimental groups – to show that the microbiome can cause metabolic dysfunction. The team also suggested a mechanism by which this occurs: changes in microbial production of short-chain fatty acids (SCFAs).

The metabolic health of nearly 1,000 people in the Netherlands was found to correlate with the presence of certain bacteria and bacterial metabolic pathways. Most notably, higher faecal levels of butyrate – an SCFA produced by gut microbes – predicted better insulin responses. The study also showed that participants' genes partially predict the level of butyrate production in people's guts, and microbiome structure more broadly – a finding confirmed in a different group of more than 4,000 individuals.

Then came the test of causality. If altered insulin sensitivity changes the microbiome (rather than the microbiome disrupting insulin physiology), all genetic factors known to influence insulin sensitivity should also predict a person's butyrate production. But they did not. This suggests that genes associated with both microbiome structure and insulin responses influence gut microbiomes, which in turn disrupt insulin signalling.

The team also found that genetic variants elevating faecal levels of another bacteria-derived SCFA, propionate, increase the risk of type 2 diabetes. These findings pave the way for more personalized treatments of metabolic disease.

*Nature Genet.* **51**, 600–605 (2019)

## Childbirth and the microbiome

A person's gut microbiome is seeded in early life according to the bacteria they are exposed to and how successfully these microbes colonize the intestines. Research, led by Trevor Lawley

at the Wellcome Sanger Centre in Hinxton, UK, and Nigel Field at University College London, shows that a caesarean-section birth radically affects newborns' microbiomes, and that infants born this way are often host to opportunistic hospital bacteria.

Looking at 596 healthy babies shortly after birth and again at 8–10 months old, the researchers showed that when babies were 4 days old, the microbiomes of those delivered by c-section were markedly different from those of babies born vaginally. And although the microbiomes of c-section infants gradually shifted closer to those of vaginally born babies over the first three weeks of life, significant differences persisted into infancy.

One of the most pronounced differences in the microbiomes of c-section babies was a low abundance of *Bacteroides*. Levels of bacteria commonly found in hospitals in the microbiomes of c-section newborns did decrease sharply in the months after birth, but those organisms were still slightly more common than in vaginally born babies at around eight months. The authors attributed the differences to infants born by c-section having less exposure to the maternal microbiome during birth. But the study also found that when mothers who gave birth vaginally were given prenatal, prophylactic antibiotics – which are also given to nearly all women who have c-sections – their babies' microbiomes were also low in *Bacteroides* bacteria.

Both c-section delivery and antibiotic exposure have been implicated in the development of childhood allergies. Although the study does not provide direct evidence that an altered microbiome is the mechanistic link between these events and illness, it does raise the question of whether a drastically different initial gut microbiome has long-term consequences.

*Nature* **574**, 117–121 (2019)

## Weight loss without microbial gains

French scientists have examined the microbiomes of people with severe obesity, and how the communities of microbes changed after bariatric surgery. The research, by Karine Clément at Sorbonne University, Paris, and her co-workers, showed that most people who are severely obese have impoverished gut microbiomes – and that post-surgical weight loss and improved metabolic health were not accompanied by a full recovery of microbial diversity.

Microbiomes were analysed by quantifying the overall genomic diversity and measuring the serum levels of microbiome-associated metabolites before and after surgery. Three-quarters of participants had low microbial gene richness – compared with 20–40% of people who were moderately obese. When the authors looked for correlations between metabolites and microbiome structure, they found nine metabolites were affected by changes to the microbiome.

Bariatric surgery – either a gastric band or a bypass – increased microbial diversity by 25–40%, but, on average, levels remained lower than those of people of a healthy weight. This held true one year after surgery, when weight loss was maximal. In some people, the comparative lack of diversity persisted five years after surgery.

The study suggests that applying strategies to correct the gut dysbiosis associated with severe obesity, alongside surgery, could further improve metabolic function.

*Gut* **68**, 70–82 (2019)



For the latest research published by *Nature* visit: [go.nature.com/2slhci9](https://go.nature.com/2slhci9)

# Multi-omics of the gut microbial ecosystem in inflammatory bowel diseases

Jason Lloyd-Price<sup>1,2</sup>, Cesar Arze<sup>2</sup>, Ashwin N. Ananthakrishnan<sup>3</sup>, Melanie Schirmer<sup>1,3</sup>, Julian Avila-Pacheco<sup>4</sup>, Tiffany W. Poon<sup>1</sup>, Elizabeth Andrews<sup>3</sup>, Nadim J. Ajami<sup>5</sup>, Kevin S. Bonham<sup>1,2</sup>, Colin J. Brislawn<sup>6</sup>, David Casero<sup>7</sup>, Holly Courtney<sup>3</sup>, Antonio Gonzalez<sup>8</sup>, Thomas G. Graeber<sup>9</sup>, A. Brantley Hall<sup>1</sup>, Kathleen Lake<sup>10</sup>, Carol J. Landers<sup>11</sup>, Himel Mallick<sup>1,2</sup>, Damian R. Plichta<sup>1</sup>, Mahadev Prasad<sup>12</sup>, Gholamali Rahnnavard<sup>1,2</sup>, Jenny Sauk<sup>13</sup>, Dmitry Shungin<sup>1,14</sup>, Yoshiki Vázquez-Baeza<sup>15,16</sup>, Richard A. White III<sup>6</sup>, IBDMDB Investigators<sup>17</sup>, Jonathan Braun<sup>7</sup>, Lee A. Denson<sup>10,18</sup>, Janet K. Jansson<sup>6</sup>, Rob Knight<sup>8,16,19</sup>, Subra Kugathasan<sup>12</sup>, Dermot P. B. McGovern<sup>11</sup>, Joseph F. Petrosino<sup>5</sup>, Thaddeus S. Stappenbeck<sup>20</sup>, Harland S. Winter<sup>21,22</sup>, Clary B. Clish<sup>4</sup>, Eric A. Franzosa<sup>2</sup>, Hera Vlamakis<sup>1</sup>, Ramnik J. Xavier<sup>1,3,23,24</sup> & Curtis Huttenhower<sup>1,2,24\*</sup>

**Inflammatory bowel diseases, which include Crohn's disease and ulcerative colitis, affect several million individuals worldwide. Crohn's disease and ulcerative colitis are complex diseases that are heterogeneous at the clinical, immunological, molecular, genetic, and microbial levels. Individual contributing factors have been the focus of extensive research. As part of the Integrative Human Microbiome Project (HMP2 or iHMP), we followed 132 subjects for one year each to generate integrated longitudinal molecular profiles of host and microbial activity during disease (up to 24 time points each; in total 2,965 stool, biopsy, and blood specimens). Here we present the results, which provide a comprehensive view of functional dysbiosis in the gut microbiome during inflammatory bowel disease activity. We demonstrate a characteristic increase in facultative anaerobes at the expense of obligate anaerobes, as well as molecular disruptions in microbial transcription (for example, among clostridia), metabolite pools (acylcarnitines, bile acids, and short-chain fatty acids), and levels of antibodies in host serum. Periods of disease activity were also marked by increases in temporal variability, with characteristic taxonomic, functional, and biochemical shifts. Finally, integrative analysis identified microbial, biochemical, and host factors central to this dysregulation. The study's infrastructure resources, results, and data, which are available through the Inflammatory Bowel Disease Multi-omics Database (<http://ibdmdb.org>), provide the most comprehensive description to date of host and microbial activities in inflammatory bowel diseases.**

Inflammatory bowel diseases (IBD) affect more than 3.5 million people, and their incidence is increasing worldwide<sup>1</sup>. These diseases, the most prevalent forms of which are Crohn's disease (CD) and ulcerative colitis (UC), are characterized by debilitating and chronic relapsing and remitting inflammation of the gastrointestinal tract (for CD) or the colon (in UC). These conditions result from a complex interplay among host<sup>2,3</sup>, microbial<sup>4–6</sup>, and environmental<sup>7</sup> factors. Drivers of IBD in the human genome include more than 200 risk variants, many of which are responsible for host–microbe interactions<sup>3</sup>. Common changes in the gut microbiome in individuals with IBD include an increase in facultative anaerobes, including *Escherichia coli*<sup>8</sup>, and a decrease in obligately anaerobic producers of short-chain fatty acids (SCFAs)<sup>4</sup>. Here, to support a systems-level understanding of the aetiology of the IBD-associated gut microbiome that goes beyond previously reported metagenomic profiles, we introduce the IBDMDB, as part of the Integrative Human Microbiome Project.

We recruited 132 participants from five academic medical centres (three paediatric sub-cohorts: Cincinnati Children's Hospital,

Massachusetts General Hospital (MGH) Pediatrics, and Emory University Hospital; and two adult cohorts: MGH and Cedars-Sinai Medical Center; Fig. 1a, Extended Data Table 1, see Methods). Individuals not diagnosed with IBD on the basis of initial endoscopic and histopathologic findings were classified as 'non-IBD' controls. We analysed 651 biopsies (baseline) and 529 blood samples (approximately quarterly), which were collected in the clinic, and 1,785 stool samples, which were collected every two weeks using a home shipment protocol for one year (Fig. 1b). The latter yielded primarily microbially focused profiles: metagenomes (MGX), metatranscriptomes (MTX), proteomes (MPX), metabolomes (MBX), and viromes (VX) at several 'global' time points across all subjects (Fig. 1b), as well as denser, more intensive sampling from individuals with more variable disease activity (see Methods, Extended Data Fig. 1a–d). We generated multiple measurement types from many individual stool specimens, including 305 samples that yielded all stool-derived measurements, and 791 MGX–MTX pairs (Fig. 1c, Extended Data Fig. 1b). Biopsies yielded host- and microbe-targeted human RNA sequencing (RNA-seq (HTX)),

<sup>1</sup>Infectious Disease and Microbiome Program, Broad Institute of MIT and Harvard, Cambridge, MA, USA. <sup>2</sup>Department of Biostatistics, Harvard T. H. Chan School of Public Health, Boston, MA, USA. <sup>3</sup>Gastroenterology, Massachusetts General Hospital, Boston, MA, USA. <sup>4</sup>Metabolomics Platform, Broad Institute of MIT and Harvard, Cambridge, MA, USA. <sup>5</sup>Molecular Virology and Microbiology, Baylor College of Medicine, Houston, TX, USA. <sup>6</sup>Earth and Biological Sciences Directorate, Pacific Northwest National Lab, Richland, WA, USA. <sup>7</sup>Department of Pathology and Laboratory Medicine, David Geffen School of Medicine, University of California Los Angeles, Los Angeles, CA, USA. <sup>8</sup>Department of Pediatrics, University of California San Diego, La Jolla, CA, USA. <sup>9</sup>Molecular and Medical Pharmacology, University of California Los Angeles, Los Angeles, CA, USA. <sup>10</sup>Department of Pediatrics, Cincinnati Children's Hospital Medical Center, Cincinnati, OH, USA. <sup>11</sup>F. Widjaja Foundation Inflammatory Bowel and Immunobiology Research Institute, Cedars-Sinai Medical Center, Los Angeles, CA, USA. <sup>12</sup>Department of Pediatrics, Emory University, Atlanta, GA, USA. <sup>13</sup>Vatche and Tamar Manoukian Division of Digestive Diseases, University of California Los Angeles, Los Angeles, CA, USA. <sup>14</sup>Department of Odontology, Umeå University, Umeå, Sweden. <sup>15</sup>Jacobs School of Engineering, University of California San Diego, La Jolla, CA, USA. <sup>16</sup>Center for Microbiome Innovation, University of California San Diego, La Jolla, CA, USA. <sup>17</sup>A list of participants and their affiliations appears at the end of the paper. <sup>18</sup>Department of Pediatrics, University of Cincinnati College of Medicine, Cincinnati, OH, USA. <sup>19</sup>Department of Computer Science and Engineering, University of California San Diego, La Jolla, CA, USA. <sup>20</sup>Department of Pathology & Immunology, Washington University, St. Louis, MO, USA. <sup>21</sup>Department of Pediatrics, MassGeneral Hospital for Children, Boston, MA, USA. <sup>22</sup>Department of Pediatrics, Harvard Medical School, Boston, MA, USA. <sup>23</sup>Center for Microbiome Informatics and Therapeutics, Massachusetts Institute of Technology, Cambridge, MA, USA. <sup>24</sup>These authors jointly supervised this work: Ramnik J. Xavier & Curtis Huttenhower. \*e-mail: [chuttenh@hsph.harvard.edu](mailto:chuttenh@hsph.harvard.edu)

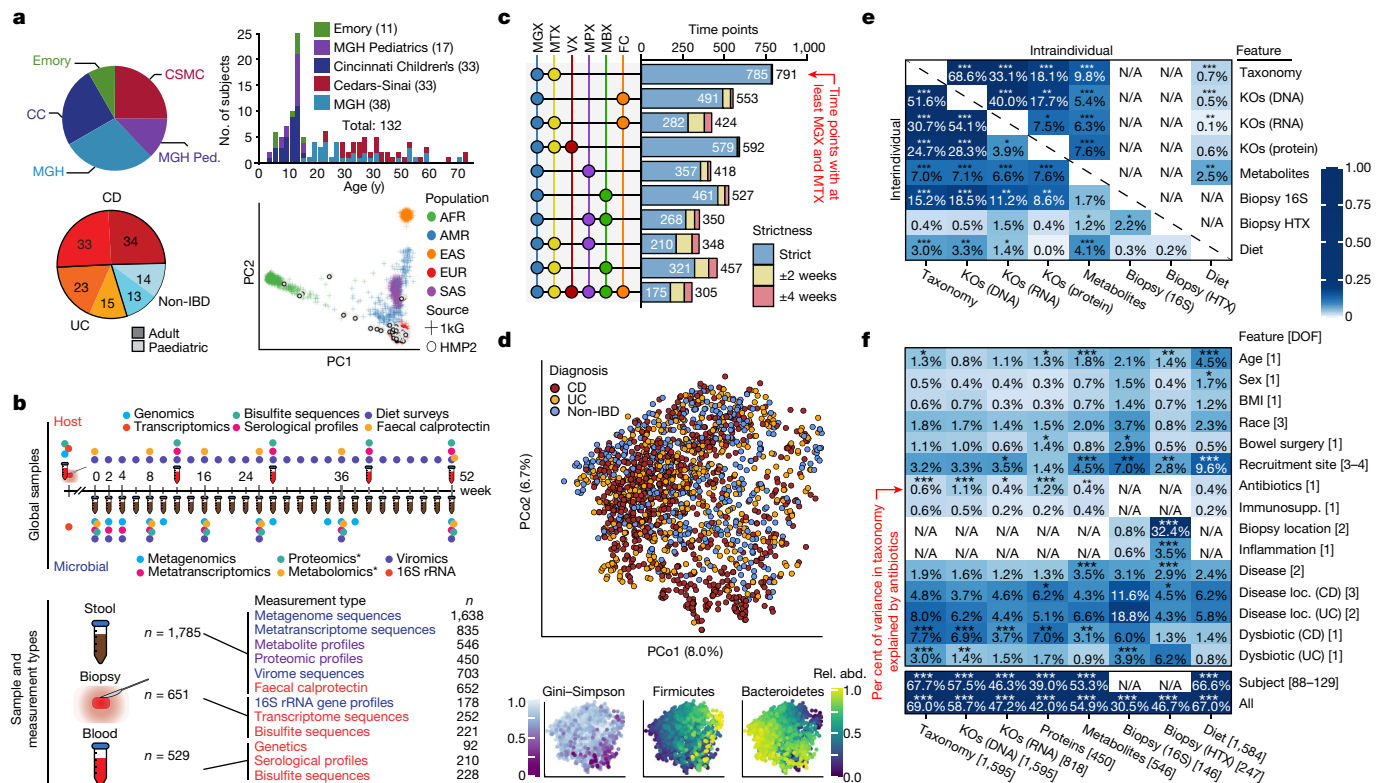


**Fig. 1 | Multi-omics of the IBD microbiome in the IBDMDb study.**

**a**, Overview of cohort characteristics. We followed 132 participants (with CD, with UC, or without IBD (control)) for one year each. Principal component analysis (PCA) of SNP profiles shows that the resulting IBDMDb cohort is mostly of European ancestry as compared to the 1000 Genomes (1kG) reference (see Methods). **b**, Sampling strategy. The study yielded host and microbial data from colon biopsy (baseline), blood (approximately quarterly), and stool (every two weeks), assessing global time points for all subjects and dense time courses for a subset. Raw, non-quality-controlled sample counts are shown. **c**, Overlap of multi-omic measurements from the same sample (strict) or from near-concordant time points (with differences of up to 2 or 4 weeks; see Methods). **d**, Principal coordinates analysis (PCoA) based on species-level Bray-Curtis dissimilarity; most variation is driven by a tradeoff between phylum Bacteroidetes versus Firmicutes. Samples from individuals with IBD (CD in particular) had weakly lower Gini-Simpson alpha diversity

epigenetic reduced representation bisulfite sequencing (RRBS), and 16S rRNA gene amplicon sequencing (16S), which were matched with human exome sequencing, serological profiles, and RRBS from blood. All data are available at <https://ibdmdb.org/>.

### Multi-omic gut microbiome changes in IBD

Consistent with prior studies<sup>4,5</sup>, although subsets of IBD (CD in particular) contributed to the second axis of taxonomy-based principal coordinates (Fig. 1d, Extended Data Fig. 2a), inter-individual variation accounted for the majority of variance for all measurement types<sup>5,9,10</sup> (Fig. 1e, f, Extended Data Fig. 2a). Even relatively large effects, such as disease status or physiological and technical factors, explained a smaller proportion of variation (Fig. 1f); this was true across measurement types, although these captured distinct aspects of IBD dysbiosis (see below).

Most measurement types captured correlated changes among and within subjects, cross-sectionally and longitudinally (Fig. 1e). Functional profiles, measured from MGX, MTX, and MPX, were the most tightly coupled (Fig. 1e), although some individual feature-wise correlations were weak (Spearman's correlation MGX-MTX  $0.44 \pm 0.10$  (mean  $\pm$  s.d.), MGX-MPX  $0.14 \pm 0.083$ , and MTX-MPX  $0.18 \pm 0.096$ ; Extended Data Fig. 2b). Unexpectedly, characterized enzymes tended to be only weakly correlated with their known

(Wald test  $P = 0.26$  and  $0.014$  for UC and CD compared with non-IBD, respectively). **e**, Mantel tests quantifying variance explained (square of Mantel statistic) between measurement type pairs, with differences across subjects (inter-individual) or within subjects over time (intra-individual; see Methods); results show tight coupling across measurement types. Sample sizes in **f**, **f**, PERMANOVA shows that inter-individual variation is largest for all measurement types, with even relatively large effects (for example, antibiotics or IBD phenotype) capturing less variation (see Methods). Stratified tests (CD/UC) consider only samples within the indicated phenotype (note that sample counts decrease for these, resulting in larger expected covariation by chance). Stars show FDR-corrected statistical significance (FDR  $*P \leq 0.05$ ,  $**P \leq 0.01$ ,  $***P \leq 0.001$ ). Variance is estimated for each feature independently (Methods). 'All' refers to a model with all metadata. Total  $n$  for each measurement type is shown in square brackets, distributed across up to 132 subjects (Extended Data Fig. 1a, see Methods).

substrates or products (Supplementary Fig. 1). Although our dietary characterization was obtained through a very broad-level food frequency questionnaire, it provides an initial characterization of longitudinal diet-microbiome coupling in a substantial population over many months; diet accounted for a small but significant 3% (false discovery rate (FDR)  $P = 7.4 \times 10^{-4}$ ) of taxonomic variation between subjects, and 0.7% (FDR  $P = 4.3 \times 10^{-4}$ ) of variation longitudinally.

Simple cross-sectional differences between individuals with IBD and those without (Supplementary Tables 1–14) were most apparent in the metabolome (Figs. 1f, 2a, Extended Data Fig. 2a, c, d, see Methods). Overall, metabolite pools were less diverse in individuals with IBD, paralleling previous observations for microbial diversity (Supplementary Table 2); this might be caused by poor nutrient absorption, greater water or blood content in the bowels, and shorter bowel transit times in individuals with active IBD<sup>11</sup>. The smaller number of compounds that were more abundant in patients with IBD included polyunsaturated fatty acids such as adrenate and arachidonate. Pantothenate and nicotinate (vitamins B5 and B3, respectively) were particularly depleted in the gut during IBD; this is notable because these are not typically among the B vitamins that are deficient in the serum of patients with IBD<sup>12</sup>, although low nicotinate levels have been detected during active CD<sup>13</sup>. Both vitamins are required to produce cofactors used in lipid metabolism<sup>14</sup>, and nicotinate has anti-inflammatory and anti-apoptotic



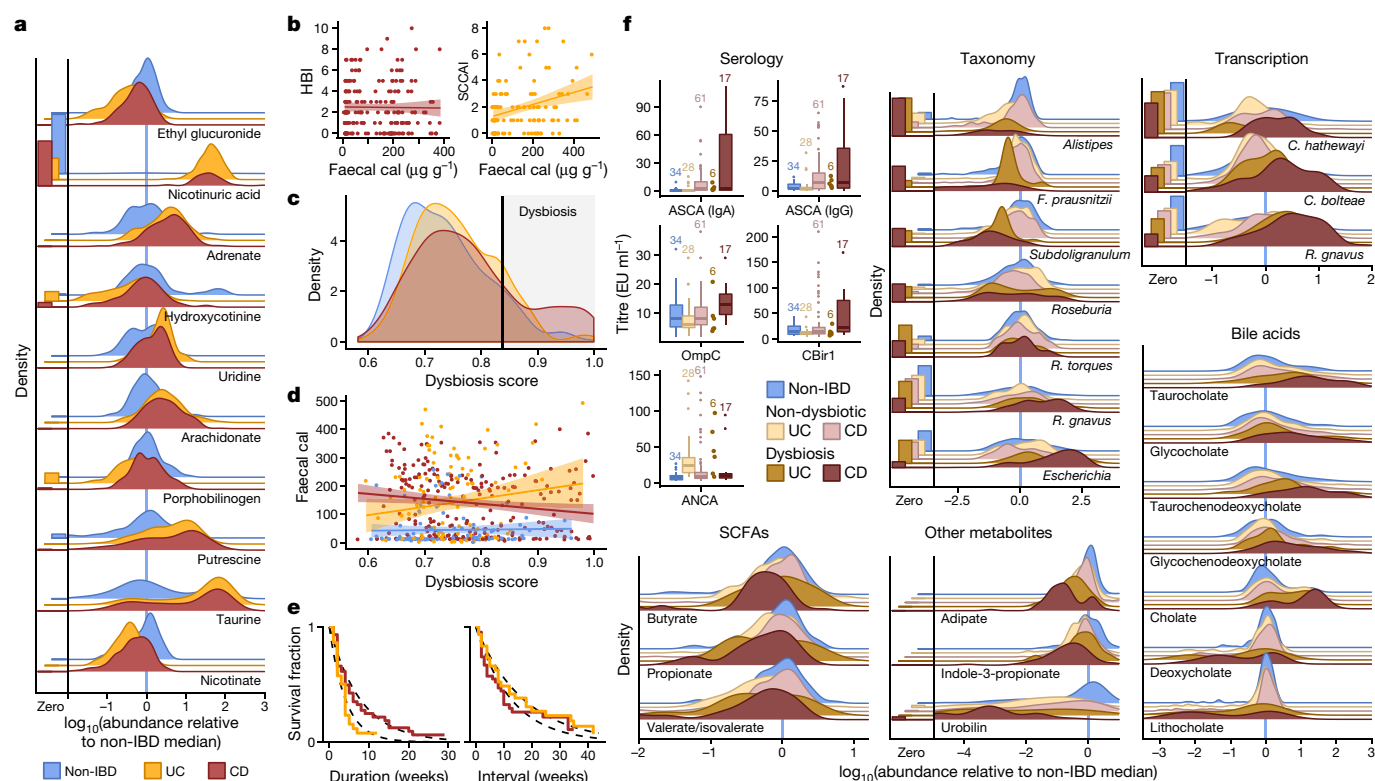


**Fig. 2 | Metagenomic, metatranscriptomic, and stool metabolomic profiles are disrupted during IBD activity.** **a**, Relative abundance distributions for ten of the most cross-sectionally significantly differentially abundant metabolites in samples from individuals with IBD, as a ratio to the median relative abundance in individuals without IBD (Wald test; all FDR  $P < 0.003$ ; see Methods; Supplementary Tables 1–14). Left, fraction of samples below detection limit (see Methods).  $n = 546$  samples from 106 subjects. **b**, Relationships between two measures of disease activity: patient-reported (Harvey–Bradshaw index (HBI) in CD,  $n = 680$  samples from 65 subjects; simple clinical colitis activity index (SCCAI) in UC,  $n = 429$  samples from 38 subjects) and host molecular (faecal calprotectin (cal))<sup>43</sup>,  $n = 652$  samples from 98 subjects). Linear regression shown with 95% confidence bound. **c**, **d**, Distribution of microbial dysbiosis scores as a measure of disease activity (**c**, median Bray–Curtis dissimilarity between a sample and non-IBD samples;

see Methods) and its relationship with calprotectin (**d**,  $n = 652$  samples from 98 subjects). Linear regression with 95% confidence. **e**, Kaplan–Meier curves for the distributions of the durations of (left) and intervals between (right) dysbiotic episodes in UC and CD. Both are approximately exponential (fits in dashed lines), with means of 4.1 and 17.2 weeks, respectively, for UC, and 7.8 and 12.8 weeks for CD (see Methods). **f**, Relative abundance distributions of significantly different metagenomic species ( $n = 1,595$  samples from 130 subjects), metabolites ( $n = 546$  samples from 106 subjects), and microbial transcribers ( $n = 818$  samples from 106 subjects) in dysbiotic samples compared to non-dysbiotic samples from the same disease group (Wald test; all FDR  $P < 0.05$ ; full results in Supplementary Tables 15–28). Also shown are antibody titres for ANCA, ASCA (IgG or IgA), anti-OmpC, and anti-CBir1 antibodies ( $n = 146$  samples from 61 subjects). Boxplots show median and lower/upper quartiles; whiskers show inner fences; sample sizes above boxes.

functions in the gut<sup>15</sup>. Notably, nicotinuric acid, a metabolite of nicotinate<sup>16</sup>, was found almost exclusively in the stool of patients with IBD. Faecal calprotectin and the Harvey–Bradshaw Index (HBI), two measures of disease severity in CD, showed no significant correlation, whereas the Simple Clinical Colitis Activity Index<sup>17</sup> (SCCAI) in UC did correlate weakly with faecal calprotectin levels (Fig. 2b).

Notably, no metagenomic species were significantly different between samples from individuals with IBD and those from control individuals after correction for multiple hypothesis testing (Supplementary Table 1), in contrast with previous work<sup>4,5,18</sup>. We hypothesized this was due to the differentiation of study participants into two subsets, one with relatively inactive IBD (due to remission or recent onset) and the other with greater activity. This differentiation has been observed in several cohorts of patients with IBD<sup>5,18</sup>, but it is more pronounced here because we did not take samples specifically from subjects selected for active disease. We therefore classified samples with taxonomic compositions highly unlike those of non-IBD control samples as ‘dysbiotic’ (Fig. 2c, Extended Data Fig. 3a–e, see Methods). Dysbiotic excursions in this cohort did not correspond with disease location (for example, ileal CD;  $F$ -test  $P = 0.11$ , see Methods), and occurred longitudinally within subjects; they were weakly correlated with patient-reported and molecular measures of disease activity (Fig. 2d, Extended Data Fig. 3a). In total, 272 dysbiotic samples were taken during 78 full periods of dysbiosis and 9 censored periods (that is, subjects who were dysbiotic at

the end of the time series, see Methods), or 17.1% of all samples ( $n = 178$  (24.3%) in CD and  $n = 51$  (11.6%) in UC). Plots of the durations of and times between dysbiotic periods were approximately exponential, suggesting that transitions are triggered, at least in part, by events with constant probability over time (and are thus potentially stochastic; Fig. 2e).

Using the resulting definition of dysbiosis, dysbiotic periods corresponded to a larger fraction of variation in all measurement types than did overall IBD phenotype (Fig. 1f, Supplementary Tables 15–28); this is likely to reflect a clearer delineation between active and less active disease states within extremely heterogeneous subjects over time. Though it is unclear which aspects of dysbiosis are causes or consequences of IBD, characterization of these changes will lead to greater understanding of microbial dynamics in disease. As in previous cross-sectional studies of established disease<sup>4</sup>, differences between dysbiotic and non-dysbiotic samples from individuals with CD were more pronounced than in those from individuals with UC (Fig. 1f). Notably, dysbiosis also distinguished between independent host measures, such as individuals with high and low ASCA (anti-*Saccharomyces cerevisiae* antibodies), ANCA (anti-neutrophil cytoplasm antibodies), OmpC (outer membrane protein C), and CBir1 (anti-flagellin) antibody titres in serological profiles (Fig. 2f; Fisher’s combined probability test  $P = 0.00044$  from Wilcoxon tests between dysbiotic and non-dysbiotic CD). Dysbiosis was not significantly associated

with demographics or medication (logistic regression with subject as random effect, all FDR  $P > 0.05$ ). Dysbiosis recapitulated a known decrease in alpha diversity in active disease, but we also identified numerous communities with normal complexity as dysbiotic (Extended Data Fig. 4a). Notably, taxonomic perturbations during dysbiosis mirrored those previously observed cross-sectionally in IBD<sup>6</sup>, such as the depletion of obligate anaerobes including *Faecalibacterium prausnitzii* and *Roseburia hominis* in CD and the enrichment of facultative anaerobes such as *E. coli* (Fig. 2f, Extended Data Fig. 4b). *Ruminococcus torques* and *Ruminococcus gnavus*, two prominent species in IBD<sup>19</sup>, were also differentially abundant in dysbiotic CD and UC, respectively (FDR  $P = 0.041$  and  $0.0087$ ). A smaller subset of species also increased significantly in transcriptional activity (mean total transcript relative abundance relative to genomic abundance; see Methods) as well as showing differences in abundance, including *Clostridium hathewayi*, *Clostridium bolteae*, and *R. gnavus* (Fig. 2f). All had significantly increased expression during dysbiosis (all FDR  $P < 0.07$ ), and thus their roles in IBD may be more pronounced than suggested solely by their differences in genomic abundance.

In the metabolome, SCFAs were generally reduced in dysbiosis (Fig. 2f). The reduction in butyrate in particular is consistent with the previously observed depletion of butyrate producers<sup>6</sup> such as *F. prausnitzii* and *R. hominis*, which was also observed here (Fig. 2f). We also detected enrichment of the primary bile acid cholate and its glycine and taurine conjugates (glycocholate  $q = 5.2 \times 10^{-5}$ , taurocholate  $q = 1.3 \times 10^{-5}$ ) in dysbiotic samples from participants with CD, when compared with non-dysbiotic samples. Similarly, glycochenodeoxycholate ( $q = 1.1 \times 10^{-4}$ ) was also enriched. By contrast, the secondary bile acids lithocholate and deoxycholate ( $q = 5 \times 10^{-7}$  and  $q = 1.8 \times 10^{-4}$ , respectively) were reduced in dysbiosis, suggesting that secondary bile-acid producing bacteria are depleted in IBD-related dysbiosis, or that transit time through the colon is too short for these compounds to be metabolized<sup>20,21</sup>. These significant metabolomic differences during microbial dysbiosis, which were concordant with changes expected during disease, provide further evidence that the dysbiosis measure is specifically relevant in IBD.

We also observed several previously undescribed biochemical differences during dysbiosis, such as large changes in acylcarnitine levels. Many acylcarnitines were significantly enriched in dysbiosis (all FDR  $P < 0.05$ ; see Extended Data Fig. 4c), whereas levels of base metabolites were typically reduced (Fig. 2f, Extended Data Fig. 4d). Of note, however, arachidonoyl carnitine (C20:4 carnitine) was reduced, and free arachidonate, a precursor of prostaglandins involved in inflammation, was increased (Fig. 2a). Like bile acids, carnitines are microbially modified compounds that can have competing phenotypic effects depending on the precise modifications: L-carnitine, for example, tends to be anti-inflammatory, whereas fatty acid-conjugated carnitine does not act uniformly on gut inflammation<sup>22</sup>. These opposing changes in biochemically related metabolites further suggest that the differences seen during dysbiosis do not stem simply from the wholesale dilution of stool. Numerous other metabolites were also significantly altered in individuals with dysbiotic IBD (117 of 548 tested known metabolites with FDR  $P < 0.05$ ; Extended Data Fig. 4d, Supplementary Table 16), showing large-scale dysregulation of metabolite pools in tandem with host- and microbiome-specific taxonomic and molecular features (Fig. 2f). Finally, although we found only a single, poorly characterized bacteriophage to be differentially prevalent in both IBD and dysbiosis (notably with reduced prevalence in IBD; Supplementary Tables 3, 17), we note that several participants showed a spike in viral load before a dysbiotic period (Supplementary Fig. 2).

### Decreased gut microbiome stability in IBD

Our dense time series for stool-derived multi-omics from many subjects enabled us to carry out in-depth longitudinal analysis, integrating multiple measurements of the microbiome. Each subject's microbiome tended to diverge more from the baseline over time for metagenomic, metatranscriptomic, and metabolomic profiles (Fig. 3a;  $F$ -test power

law fit  $P < 10^{-24}$ ; see Methods). These changes were most pronounced for the taxonomic profiles of individuals with CD and UC ( $F$ -test difference in power law fits  $P < 10^{-9}$ ), where a the microbiome of an individual may have almost no species in common with itself at an earlier time point (dissimilarity of 1; Fig. 3a), consistent with previous observations<sup>9</sup>. Transcripts summarized within species (Extended Data Fig. 5a) showed similar trends (all  $F$ -test  $P < 8 \times 10^{-4}$ ) to metagenomic species abundances. Meanwhile, gene family transcripts (Kyoto Encyclopedia of Genes and Genomes (KEGG) Orthologues (KOs)), metabolites (Fig. 3a), and proteins (KOs, Extended Data Fig. 5a) varied much more rapidly, with essentially as much change after around two weeks as over longer time periods (increasing trends less or not significant: non-IBD, UC and CD  $F$ -test  $P = 0.0006$ ,  $0.001$ , and  $0.04$ , respectively for transcripts;  $0.02$ ,  $0.06$ , and  $0.003$  for metabolites; and  $0.5$ ,  $0.15$ , and  $0.06$  for proteomics). This indicates that these features vary rapidly in the guts of individuals with and without IBD and lack additional, more extreme excursions during disease.

We further characterized large-scale temporal differences by searching for 'shifts' in the microbiome between consecutive time points, defined as Bray–Curtis dissimilarities more similar to those between different people than within one person (Fig. 3a, Extended Data Fig. 5b, see Methods). First, considering only metagenomic taxonomic profiles, we found 166 such shifts, with 39 in individuals without IBD (of 382 total possible), 44 in individuals with UC (of 381), and 83 in individuals with CD (of 650) (Supplementary Table 29). Owing to differences in total observation times, the rate of shifts was only marginally higher in individuals with CD or UC than in non-IBD participants (2.09 and 1.83 shifts per year, respectively, compared with 1.79), and these were generally confined to a subpopulation of dysbiotic individuals (Fig. 3a). However, the species with the greatest changes in relative abundance differed markedly (Fig. 3b). Shifts in individuals without IBD occurred primarily in individuals with high abundances of *Prevotella copri*, which underwent repeated expansion and relaxation cycles over the course of weeks to months (Fig. 3c). This organism is of particular interest owing to its behaviour as a population-scale outgroup and its enrichment during new-onset rheumatoid arthritis<sup>23</sup>. The lack of shifts due to *P. copri* in participants with IBD was not due to an absence of *P. copri* in these individuals or an overabundance in those without IBD (6 of 27 non-IBD subjects had at least one time point with more than 10% *P. copri*, consistent with healthy populations<sup>10,24</sup>). Instead, the relative abundances that were present remained more stable in the population with IBD (Fig. 3c). Taxonomic shifts in participants with IBD mirrored earlier observations of relative reductions in obligate anaerobes and overgrowth of facultative anaerobes (Fig. 3b, Extended Data Fig. 5c), and frequently corresponded with entry into and exit from dysbiosis (28 and 23 shifts marked entries and exits in IBD, respectively, accounting for 40% of shifts in IBD). *E. coli* in particular contributed to a large number of shifts in IBD, although there was no clear pattern in which species it traded abundance with (Extended Data Fig. 5c, d).

When we define shifts in a similar manner for metabolomics profiles (Extended Data Fig. 5e), the rate of shifts is approximately half that seen for the metagenome (1.05 shifts per year in participants without IBD, 0.99 shifts per year in UC and 1.36 shifts per year in CD), although these data were strongly affected by the availability of fewer metabolomics samples (Extended Data Fig. 5e). We examined differences in metabolite profiles between adjacent samples from the same subjects and found significant separation by diagnosis (Fig. 3d; PERMANOVA  $P < 10^{-4}$ ). These differences were largely driven by unknown compounds, emphasizing the need for further compound annotation efforts and follow up to determine the significance of these compounds in IBD. Features with the greatest differences included urobilin (which showed larger differences in individuals without IBD), urate (largely in patients with CD), and a feature with an  $m/z$  of 152.0354 and retention time (RT) of 4.16 min (potentially the formic acid adduct of pyridinaldehyde), which accounted for differences largely specific to UC. The primary contributors to shifts were largely unidentified compounds (Extended Data Fig. 5f, Supplementary Table 30). HILP\_QI22918,

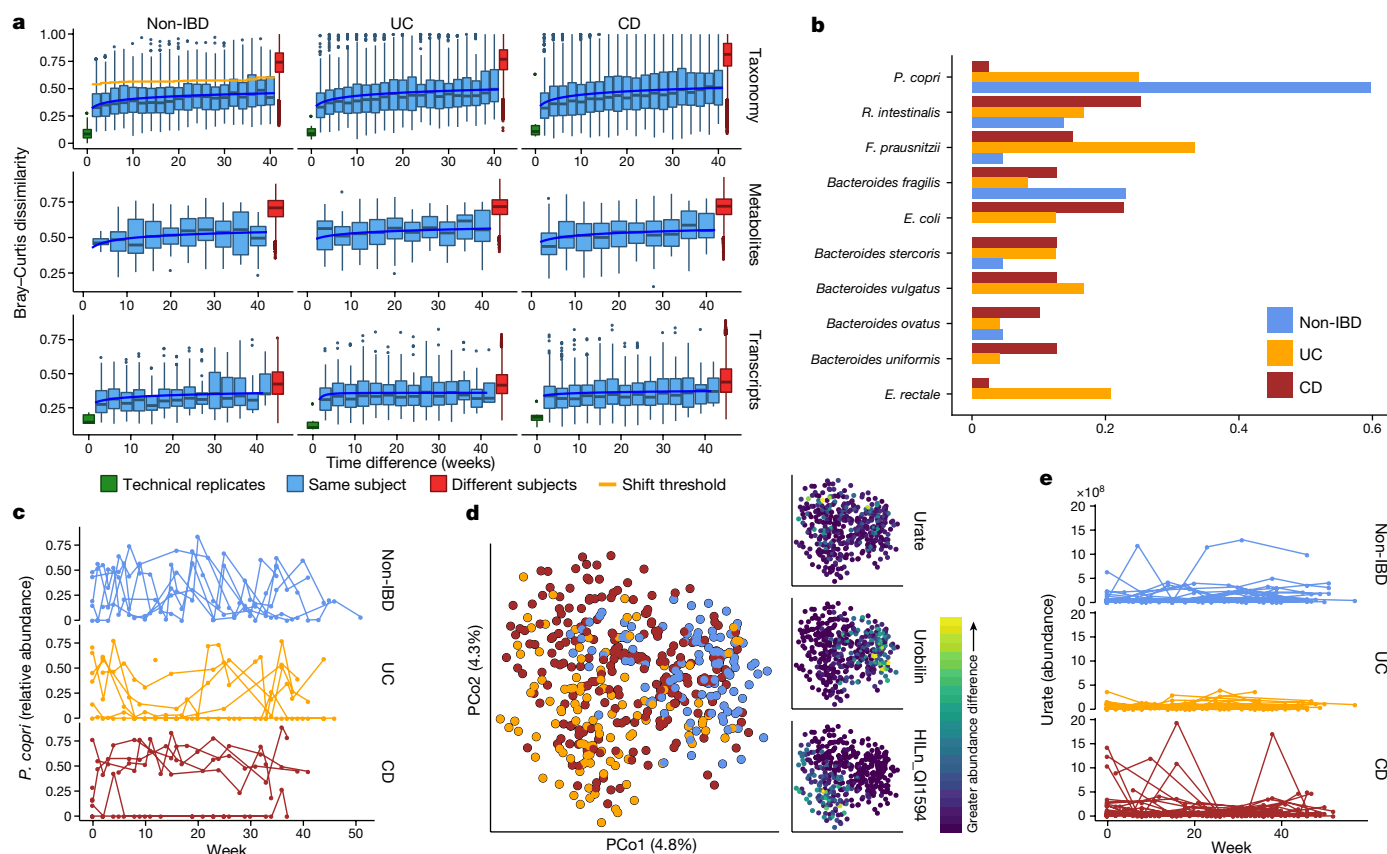


**Fig. 3 | Temporal shifts in the microbiome are more frequent and more extreme in IBD.** **a**, Bray-Curtis dissimilarities within subjects as a function of intervening time difference, as compared to different people or technical replicates; calculated for metagenomic taxonomic profiles (species;  $n = 1,595$  samples from 130 subjects), metabolomics ( $n = 546$  samples from 106 subjects), and functional profiles (KO<sup>30</sup> gene families;  $n = 818$  samples from 106 subjects). Boxplots show median and lower/upper quartiles; whiskers show inner fences. Blue, least-squares power-law fits; orange, thresholds for microbiome shifts (see Methods). Proteomics and species-level transcripts in Extended Data Fig. 5a. Within-subject changes are significantly more extreme in UC and CD than in non-IBD for taxonomic profiles ( $F$ -test  $P = 3.9 \times 10^{-10}$  and  $1.2 \times 10^{-18}$ , respectively) and transcripts ( $P = 0.00016$  and  $1.7 \times 10^{-5}$ ), with mixed differences for metabolites ( $P = 0.012$  and  $0.23$ ). Technical replicates shown (when possible) at 0 weeks. **b**, Shift frequencies for the top 10 species with greatest change during shifts, ranked by number of shifts as primary contributor,

stratified by disease phenotype(s) (full table Supplementary Table 29). **c**, *P. copri* is of interest in arthritis<sup>23</sup> and international populations<sup>44</sup>, and it alone retained stable abundances in CD but bloom-relaxation dynamics in controls (two-tailed Wilcoxon test of absolute differences between consecutive time points  $P = 4.2 \times 10^{-6}$  between non-IBD and UC, and  $1.1 \times 10^{-4}$  between non-IBD and CD). Plot shows 22 subjects with at least one time point with more than 10% differential abundance ( $n = 267$  samples). **d**, Ordination of temporally adjacent samples within individual, based on metabolomics (Bray-Curtis principal coordinates on normalized absolute abundance differences). Disease groups separate significantly ( $n = 440$  sample pairs from 106 subjects; PERMANOVA  $R^2 = 2.8\%$ ,  $P < 10^{-4}$ ). Urobilin, urate, and an unidentified untargeted feature that segregates with disease groups in the PCoA are shown (right); HILn\_Q11594 (HILIC-neg method  $m/z = 152.0354$ ,  $RT = 4.16$  min). **e**, As in **c**, but for urate (two-tailed Wilcoxon test  $P = 0.0012$  non-IBD-UC,  $P = 0.044$  non-IBD-CD;  $n = 546$  samples from 106 subjects).

an unknown feature with  $m/z$  of 648.43067 and  $RT$  of 5.03 min, contributed the most (ten) shifts exclusively in individuals with IBD. Among known compounds, methylimidazole acetic acid and urate were the primary contributors to the most shifts (four shifts each; Fig. 3e).

### Microbiome-associated host factors

When we incorporated host molecular measurements, primarily from intestinal biopsies taken colonoscopically at baseline, into our analysis of the microbiome in IBD, the main influences on population variability were strikingly different from those that affected the microbiota alone. In particular, tissue location was a major driver of intestinal epithelial gene expression (Extended Data Fig. 2c) even in the face of microbial variation<sup>25</sup> (Extended Data Fig. 2d). We therefore performed microbiome and phenotypic association analyses independently for each standardized biopsy location (see Methods).

We identified genes that were significantly differentially expressed (DEGs) in patient biopsies taken in inflamed locations of the ileum (from individuals with CD) and rectum (both CD and UC) compared to individuals without IBD (Extended Data Fig. 6a). This analysis identified 305 and 920 genes, genes that were differentially expressed

(primarily overexpressed) in the ileum and rectum, respectively, for further analysis (together representing 1,008 unique genes, negative binomial model FDR  $P < 0.05$  and fold-change  $> 1.5$ ; Fig. 4a, Supplementary Table 31). These included genes that can affect commensal microorganisms directly, such as the antimicrobial *CXCL6* (a cell membrane disruptor<sup>26</sup>) and *SAA2* (which inhibits growth of Gram-negative bacteria<sup>27</sup>), as well as indirect microbial modulators such as *DUOX2* (which produces reactive oxygen species<sup>28</sup>) and *LCN2* (which induces microbial iron starvation through sequestration<sup>29</sup>; Fig. 4b). Enrichment analysis testing for overrepresentation of KEGG<sup>30</sup> pathways among DEGs also confirmed strong representation of immune-related pathways (one-sided hypergeometric test, FDR  $P < 0.05$ ). In particular, the IL-17 signalling pathway, components of which have been previously identified in gene expression studies of ileal biopsies from patients with CD<sup>31,32</sup>, was enriched in upregulated DEGs in both ileum and rectum (FDR  $P = 2.8 \times 10^{-14}$ ; Fig. 4a, Supplementary Table 32). Among upregulated DEGs in rectal biopsies from patients with UC, we found further enrichment of the complement cascade (FDR  $P = 4.4 \times 10^{-10}$ ), a component of innate immunity<sup>33</sup> that has been implicated in IBD<sup>25,34,35</sup>.



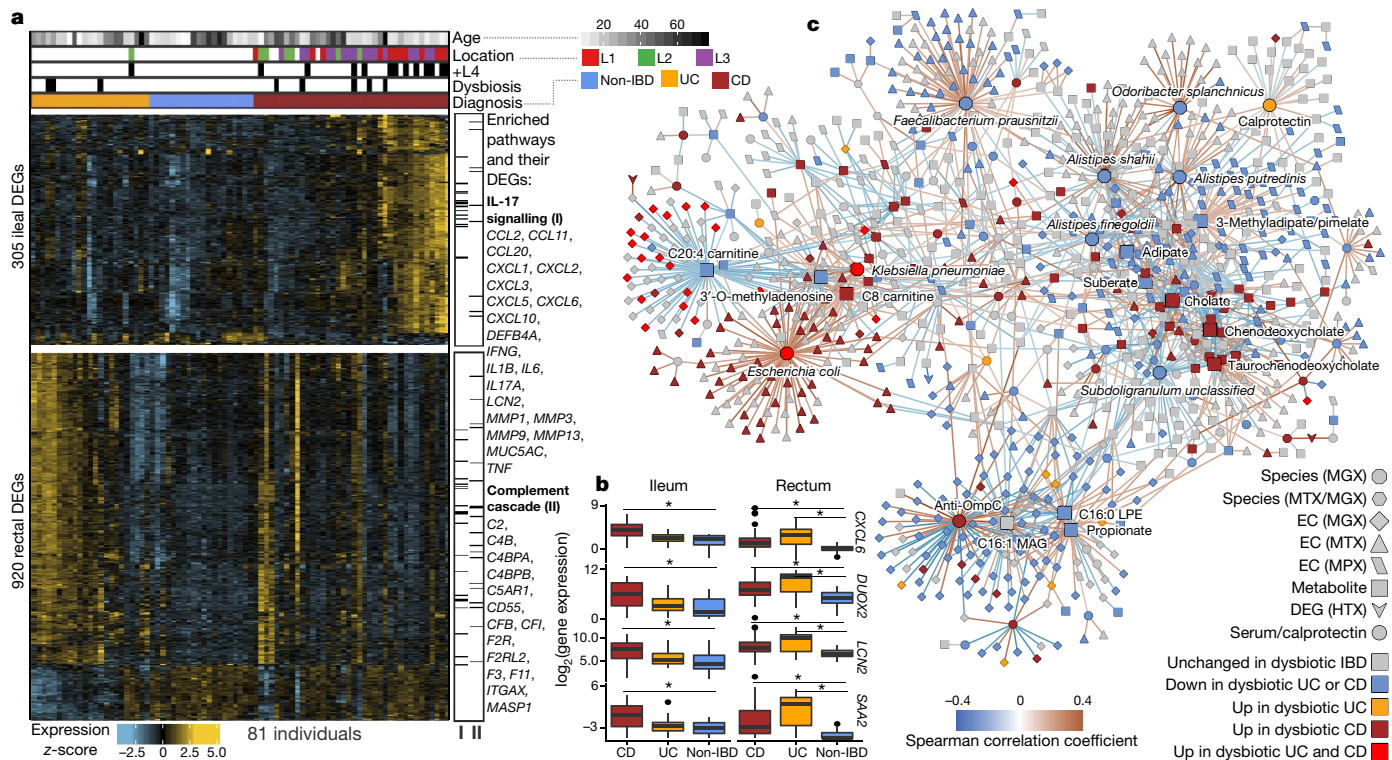


**Fig. 4 | Colonic epithelial molecular processes perturbed during IBD and in tandem with multi-omic host-microbe interactions.**

**a**, Human DEGs (negative binomial FDR  $P < 0.05$ , minimum fold change 1.5; Supplementary Table 31) from 81 subjects with paired ileal and rectal biopsies. Ordering by diagnosis, clustering within diagnosis. IL-17 signalling (I) showed strongest enrichment in ileal DEGs (FDR  $P = 8.2 \times 10^{-12}$ )<sup>31</sup>, while the complement cascade (II) was enriched in rectal DEGs from patients with UC (FDR  $P = 5.2 \times 10^{-8}$ ; KEGG<sup>30</sup> gene sets, Supplementary Table 32). Example DEGs shown with I and II. **b**, Expression of four genes involved in host-microbe interactions<sup>26–29</sup>. Inflamed biopsy samples are shown for CD from ileum (left,  $n = 20$ , 23, 39 independent samples for non-IBD, UC, CD respectively); for CD and UC in rectum (right column;  $n = 22$ , 25, 41 independent samples for non-IBD, UC, CD); non-IBD samples were non-inflamed. Asterisks indicate significant differential expression compared to non-IBD (Fisher's exact test, FDR  $P < 0.05$ ;  $P$  values in Supplementary Table 31).

To identify the components of the microbiome that were most associated with these changes, we tested for transcripts that covaried with the relative abundance of microorganisms measured directly from the same specimens using 16S amplicon sequencing. We identified 31 and 106 significant gene-operational taxonomic unit (OTU) pairs in the ileum and rectum, respectively, with no overlap between the two sites, consistent with the different overall gene expression patterns that separate them (partial Spearman correlation FDR  $P < 0.05$ ; see Methods, Extended Data Fig. 6b, Supplementary Table 33). The genes involved included known IBD-associated host-microbial interaction factors, including *DUOX2* and its maturation factor *DUOX2*<sup>31,36</sup>, both of which were negatively associated with the abundance of Ruminococcaceae UCG 005 (OTU 89) in the ileum. The expression of several chemokine genes, some of which have reported antimicrobial properties<sup>37</sup> (*CXCL6*, *CCL20*), were negatively correlated with the relative abundance of *Eubacterium rectale* (OTU 120) in the ileum, and *Streptococcus* (OTU 37) and *Eikenella* (OTU 39) in the rectum, suggesting that these species are the most susceptible to the activity of these chemokines. Finally, although this cohort was not designed for genetic association discovery (Supplementary Discussion, Extended Data Fig. 6c, d, Supplementary Table 34), we also provide exome sequencing for 92 subjects, which may be integrated with larger populations in the future.

Boxplots show median and lower/upper quartiles; whiskers show inner fences. **c**, Significant associations among 10 aspects of host-microbiome interactions: metagenomic species, species-level transcription ratios, functional profiles captured as EC gene families (MGX, MTX and MPX), metabolites, host transcription (rectum and ileum), serology, and calprotectin (sample counts in Fig. 1b, c). Network shows top 300 significant correlations (FDR  $P < 0.05$ ) between each pair of measurement types (for serology, FDR  $P < 0.25$ ). Nodes coloured by disease group in which they are 'high', edges by sign and strength of association. Spearman correlations use residuals of a mixed-effects model with subjects as random effects (or a simple linear model when only baseline samples were used (biopsies)) after covariate adjustment (see Methods). Time points approximately matched with maximum separation 4 weeks (see Methods). Singletons pruned for visualization (Extended Data Fig. 8). Hubs (nodes with at least 20 connections) emphasized.

### Dynamic, multi-omic microbiome interactions

We next searched for host and microbial molecular interactions that might underlie disease activity in IBD by constructing a large-scale cross-measurement type association network that incorporated ten microbiome measurements: metagenomic species, species-level transcription ratios, functional profiles captured as Enzyme Commission (EC) gene families (MGX, MTX and MPX), metabolites, host transcription (rectum and ileum separately), serology, and faecal calprotectin. To identify co-variation between components of the microbiome above and beyond those linked strictly to inflammation and disease state, each measurement type was first residualized using the same mixed-effects model (or linear model when appropriate) used to determine differential abundance ('adjusted' network; see Methods). This residualization uses longitudinal measurements to minimize any inter-individual variation (including IBD status), as well as dysbiotic excursions as drivers of the detected associations, and thus highlights within-person associations over time. The resulting network contained 53,161 total significant edges (FDR  $P < 0.05$ ) and 2,916 nodes spanning features from all measurement types (Supplementary Table 35). We constructed a filtered subnetwork for visualization from the top 300 edges (by  $P$  value) per measurement type in which at least one connected node was dysbiosis-associated (Fig. 4c).

Representatives from the five stool-derived measurements occurred as hubs (defined as nodes with at least 20 connections) in this network, all of which were identified as differentially abundant in dysbiosis. Particularly connected taxonomic features (from metagenomes and metatranscriptomes) included the abundances of *F. prausnitzii* and unclassified clades related to *Subdoligranulum*<sup>38</sup>, which are closely phylogenetically related, although the only molecular features common to both organisms covaried with the abundances of cholesterol and inosine (Extended Data Fig. 7a). *F. prausnitzii* accounted for some of the strongest associations overall, including the expression of numerous ECs that were downregulated in dysbiosis. On the other hand, *E. coli* (and to lesser extent *Haemophilus parainfluenzae*) accounted for a large fraction of upregulated ECs. Members of the *Roseburia* genus were also associated, metatranscriptionally as well as metagenomically, with bile acids and a number of acylcarnitines, suggesting that *Roseburia* (together with *Subdoligranulum*) are involved in the carnitine and bile acid dysregulation observed in IBD.

Acylcarnitines and bile acids as overall chemical classes featured prominently in the network, related in part to their changes during dysbiosis. Acylcarnitines were associated with numerous dysbiosis-associated species including *R. hominis* (nine acylcarnitines, FDR  $P < 0.05$ ; Supplementary Table 35), *Klebsiella pneumoniae* (three), and *H. parainfluenzae* (three), as well as expression of *C. bolteae* (three), suggesting that multiple scales of regulation, including long-term growth-based and short-term transcriptional, are involved. Particularly notable biochemical hubs in the network included C8 carnitine, another acylcarnitine that was significantly increased in dysbiotic CD, cholate, chenodeoxycholate, and taurochenodeoxycholate, which together accounted for 107 edges (6%; Fig. 4c). Other prominent metabolite associations included several long-chain lipid hubs and the SCFA propionate; antibodies against OmpC were strongly associated with these, as well as with the metagenomic abundances of the numerous ECs involved in the system's biosynthesis or as interactors. Calprotectin, as the sole feature in its own measurement type, was weakly associated with a number of metabolites that were not differentially abundant in dysbiosis, as well as with the metagenomic abundance of several dysbiosis-associated ECs. Three host genes appeared in this high-significance subnetwork: ileal expression of *GIP*, *NXPE4*, and *ANXA10*. Expression of RNA polymerase was also a prominent node in the network, though not a hub, that was upregulated in dysbiosis (Extended Data Fig. 8). The regulation of this essential enzyme class is growth-rate-dependent<sup>39</sup>, suggesting that microbial communities as a whole are more often in higher growth conditions in dysbiotic IBD.

Finally, we also identified associations among features in the microbiome that took dysbiosis into account, resulting in a second network using the same methodology but without adjusting for dysbiosis ('unadjusted'; Supplementary Discussion, Extended Data Figs. 7b, 9, Supplementary Table 36). Together, these networks contextualize the multiple types of microbiome disruption that are observed in IBD, with associations among many molecular feature types that represent potential targets for follow-up studies on the mechanisms that underlie IBD and gastrointestinal inflammation.

## Conclusions

As part of the HMP2, we have developed the IBDMDb, one of the first integrated studies of multiple molecular features of the gut microbiome that have been implicated in IBD dynamics. While overall population structure was comparable among measurements of the microbiome—metagenomic, metatranscriptomic, metabolomic, and others—each measurement identified complementary molecular components of longitudinal dysbioses in CD and UC. Some, such as taxonomic shifts in favour of aerotolerant, pro-inflammatory clades, have been captured by previous studies; others, such as greater gene expression by clostridia during disease, were discovered by the use of new measurements (metatranscriptomes). The temporal stability of multiple microbiome measurements likewise differed across IBD phenotypes and disease activity, with distinct effects on molecular components of

the microbiome (including unexpected stability of the relative abundance of *P. copri* in individuals with IBD). Our data provide a catalogue of new relationships between multi-omic features identified as potentially central during IBD, in addition to data, protocols, and relevant bioinformatic approaches to enable future research.

By leveraging a multi-omic view on the microbiome, our results single out a number of host and microbial features for follow-up characterization. An unclassified *Subdoligranulum* species, recently shown to form a complex of new species-level clades<sup>38</sup>, was both markedly reduced in IBD and central to the functional network, associating with a wide range of IBD-linked metabolites both identifiable (for example, bile acids and polyunsaturated fatty acids) and unidentifiable. The clade is likely to contain at least seven species that are closely related to the *Subdoligranulum*, *Gemmiger*, and *Faecalibacterium* genera, typically butyrate producers that are considered to be beneficial, particularly in IBD<sup>40</sup>. Therefore, the isolation and characterization of additional species—especially in tandem with these associated metabolites—is likely to reveal these clades' physiological and immunological interactions and the consequences of their depletion in IBD. More generally, strain-level profiling of implicated microorganisms remains to be carried out, particularly in direct association with host epithelium and corresponding molecular changes. This profiling is feasible with existing data from this study, and will serve to pinpoint the specific organisms responsible for IBD-associated accumulation of primary unconjugated bile acids and depletion of secondary bile acids<sup>41</sup>. Only very few, low-abundance species are currently known to be capable of secondary bile acid metabolism<sup>42</sup>, and expanding the range of strains known to carry appropriate metabolic cassettes will indicate potential new targets for therapeutic restoration. Beyond short-chain fatty acids and bile acids, the large-scale acylcarnitine dysbiosis observed here may also provide a promising new target for IBD, particularly after determining whether this shift in metabolite pools is host- or microbiome-driven.

We stress that it has not yet been determined whether these multi-omic features of the microbiome can predict disease events before their occurrence and that the disease-relevant time scales of distinct molecular events have not been identified (for example, static host genetics, relatively slow epigenetics or microbial growth, rapid host and microbial transcriptional changes). It may also be fruitful to seek out the earliest departures from a subject-specific baseline state that, while themselves still 'eubiotic', may predict the subsequent onset of dysbiosis or disease symptoms. Some such characterization may be possible in data from this study, although other causal analysis may be better carried out at finer-grained time scales or using interventional study designs. It will be most important to take these molecular results back to the clinic, in the form of better predictive biomarkers of IBD progression and outcome, and as a set of new host–microbe interaction targets for which treatments to ameliorate the disease may be developed.

## Online content

Any methods, additional references, Nature Research reporting summaries, source data, statements of data availability and associated accession codes are available at <https://doi.org/10.1038/s41586-019-1237-9>.

Received: 6 February 2018; Accepted: 16 April 2019;

Published online 29 May 2019.

- Kaplan, G. G. The global burden of IBD: from 2015 to 2025. *Nat. Rev. Gastroenterol. Hepatol.* **12**, 720–727 (2015).
- Hugot, J. P. et al. Association of NOD2 leucine-rich repeat variants with susceptibility to Crohn's disease. *Nature* **411**, 599–603 (2001).
- Huang, H. et al. Fine-mapping inflammatory bowel disease loci to single-variant resolution. *Nature* **547**, 173–178 (2017).
- Morgan, X. C. et al. Dysfunction of the intestinal microbiome in inflammatory bowel disease and treatment. *Genome Biol.* **13**, R79 (2012).
- Gevers, D. et al. The treatment-naïve microbiome in new-onset Crohn's disease. *Cell Host Microbe* **15**, 382–392 (2014).
- Kostic, A. D., Xavier, R. J. & Gevers, D. The microbiome in inflammatory bowel disease: current status and the future ahead. *Gastroenterology* **146**, 1489–1499 (2014).



7. Ananthakrishnan, A. N. Environmental risk factors for inflammatory bowel diseases: a review. *Dig. Dis. Sci.* **60**, 290–298 (2015).
8. Knights, D. et al. Complex host genetics influence the microbiome in inflammatory bowel disease. *Genome Med.* **6**, 107 (2014).
9. Halfvarson, J. et al. Dynamics of the human gut microbiome in inflammatory bowel disease. *Nat. Microbiol.* **2**, 17004 (2017).
10. Lloyd-Price, J. et al. Strains, functions and dynamics in the expanded Human Microbiome Project. *Nature* **550**, 61–66 (2017).
11. Vandeputte, D. et al. Stool consistency is strongly associated with gut microbiota richness and composition, enterotypes and bacterial growth rates. *Gut* **65**, 57–62 (2016).
12. Weisshof, R. & Chermesh, I. Micronutrient deficiencies in inflammatory bowel disease. *Curr. Opin. Clin. Nutr. Metab. Care* **18**, 576–581 (2015).
13. Kuroki, F. et al. Multiple vitamin status in Crohn's disease. Correlation with disease activity. *Dig. Dis. Sci.* **38**, 1614–1618 (1993).
14. Depeint, F., Bruce, W. R., Shangari, N., Mehta, R. & O'Brien, P. J. Mitochondrial function and toxicity: role of the B vitamin family on mitochondrial energy metabolism. *Chem. Biol. Interact.* **163**, 94–112 (2006).
15. Li, J. et al. Niacin ameliorates ulcerative colitis via prostaglandin D<sub>2</sub>-mediated D prostanoid receptor 1 activation. *EMBO Mol. Med.* **9**, 571–588 (2017).
16. Figge, H. L. et al. Comparison of excretion of nicotinic acid after ingestion of two controlled release nicotinic acid preparations in man. *J. Clin. Pharmacol.* **28**, 1136–1140 (1988).
17. Walmsley, R. S., Ayres, R. C., Pounder, R. E. & Allan, R. N. A simple clinical colitis activity index. *Gut* **43**, 29–32 (1998).
18. Frank, D. N. et al. Molecular-phylogenetic characterization of microbial community imbalances in human inflammatory bowel diseases. *Proc. Natl Acad. Sci. USA* **104**, 13780–13785 (2007).
19. Hall, A. B. et al. A novel *Ruminococcus gnavus* clade enriched in inflammatory bowel disease patients. *Genome Med.* **9**, 103 (2017).
20. Kruis, W., Kalek, H. D., Stellaard, F. & Paumgartner, G. Altered fecal bile acid pattern in patients with inflammatory bowel disease. *Digestion* **35**, 189–198 (1986).
21. Duboc, H. et al. Connecting dysbiosis, bile-acid dysmetabolism and gut inflammation in inflammatory bowel diseases. *Gut* **62**, 531–539 (2013).
22. Meadows, J. A. & Wargo, M. J. Carnitine in bacterial physiology and metabolism. *Microbiology* **161**, 1161–1174 (2015).
23. Scher, J. U. et al. Expansion of intestinal *Prevotella copri* correlates with enhanced susceptibility to arthritis. *eLife* **2**, e01202 (2013).
24. Abu-Ali, G. S. et al. Metatranscriptome of human faecal microbial communities in a cohort of adult men. *Nat. Microbiol.* **3**, 356–366 (2018).
25. Morgan, X. C. et al. Associations between host gene expression, the mucosal microbiome, and clinical outcome in the pelvic pouch of patients with inflammatory bowel disease. *Genome Biol.* **16**, 67 (2015).
26. Linge, H. M. et al. The human CXC chemokine granulocyte chemotactic protein 2 (GCP-2)/CXCL6 possesses membrane-disrupting properties and is antibacterial. *Antimicrob. Agents Chemother.* **52**, 2599–2607 (2008).
27. Eckhardt, E. R. et al. Intestinal epithelial serum amyloid A modulates bacterial growth *in vitro* and pro-inflammatory responses in mouse experimental colitis. *BMC Gastroenterol.* **10**, 133 (2010).
28. El Hassani, R. A. et al. Dual oxidase 2 is expressed all along the digestive tract. *Am. J. Physiol. Gastrointest. Liver Physiol.* **288**, G933–G942 (2005).
29. Bachman, M. A., Miller, V. L. & Weiser, J. N. Mucosal lipocalin 2 has pro-inflammatory and iron-sequestering effects in response to bacterial enterobactin. *PLoS Pathog.* **5**, e1000622 (2009).
30. Kanehisa, M. et al. Data, information, knowledge and principle: back to metabolism in KEGG. *Nucleic Acids Res.* **42**, D199–D205 (2014).
31. Haberman, Y. et al. Pediatric Crohn disease patients exhibit specific ileal transcriptome and microbiome signature. *J. Clin. Invest.* **124**, 3617–3633 (2014).
32. Kugathasan, S. et al. Prediction of complicated disease course for children newly diagnosed with Crohn's disease: a multicentre inception cohort study. *Lancet* **389**, 1710–1718 (2017).
33. Hajishengallis, G., Reis, E. S., Mastellos, D. C., Ricklin, D. & Lambris, J. D. Novel mechanisms and functions of complement. *Nat. Immunol.* **18**, 1288–1298 (2017).
34. Ross, I. N., Thompson, R. A., Montgomery, R. D. & Asquith, P. Significance of serum complement levels in patients with gastrointestinal disease. *J. Clin. Pathol.* **32**, 798–801 (1979).
35. Jain, U., Otley, A. R., Van Limbergen, J. & Stadnyk, A. W. The complement system in inflammatory bowel disease. *Inflamm. Bowel Dis.* **20**, 1628–1637 (2014).
36. Lipinski, S. et al. DUOX2-derived reactive oxygen species are effectors of NOD2-mediated antibacterial responses. *J. Cell Sci.* **122**, 3522–3530 (2009).
37. Yung, S. C. & Murphy, P. M. Antimicrobial chemokines. *Front. Immunol.* **3**, 276 (2012).
38. Pasolli, E. et al. Extensive unexplored human microbiome diversity revealed by over 150,000 genomes from metagenomes spanning age, geography, and lifestyle. *Cell* **176**, 649–662e620 (2019).
39. Ralling, G., Bodrug, S. & Linn, T. Growth rate-dependent regulation of RNA polymerase synthesis in *Escherichia coli*. *Mol. Gen. Genet.* **201**, 379–386 (1985).
40. Sokol, H. et al. *Faecalibacterium prausnitzii* is an anti-inflammatory commensal bacterium identified by gut microbiota analysis of Crohn disease patients. *Proc. Natl Acad. Sci. USA* **105**, 16731–16736 (2008).
41. Vitek, L. Bile acid malabsorption in inflammatory bowel disease. *Inflamm. Bowel Dis.* **21**, 476–483 (2015).
42. Dawson, P. A. & Karpen, S. J. Intestinal transport and metabolism of bile acids. *J. Lipid Res.* **56**, 1085–1099 (2015).
43. Walsham, N. E. & Sherwood, R. A. Fecal calprotectin in inflammatory bowel disease. *Clin. Exp. Gastroenterol.* **9**, 21–29 (2016).
44. Truong, D. T., Tett, A., Pasolli, E., Huttenhower, C. & Segata, N. Microbial strain-level population structure and genetic diversity from metagenomes. *Genome Res.* **27**, 626–638 (2017). <https://doi.org/10.1101/gr.216242.116>.
45. Ricklin, D., Reis, E. S. & Lambris, J. D. Complement in disease: a defence system turning offensive. *Nat. Rev. Nephrol.* **12**, 383–401 (2016).

**Acknowledgements** We thank G. Ackermann, E. X. Li, J. Livny, D. McDonald, C. Moran, A. Robbins-Pianka, and S. Sun for their contributions during this project; the Broad Institute of MIT and Harvard Microbial 'Omics Core, Genomics Platform, and the Harvard T. H. Chan School of Public Health Microbiome Analysis Core for data generation and management; and T. Reimels for editorial assistance. This work was supported by National Institutes of Health grants P01DK046763 (D.P.B.M.), U01DK062413 (D.P.B.M.), U54DK102557 (D.P.B.M.), UL1TR001881 (J.B.), P30DK043351 (R.J.X.), R24DK110499 (C.H.), R01HG005969 (C.H.), U54DE023798 (C.H. and R.J.X.), National Science Foundation grant DBI-1053486 (C.H.), and Army Research Office grant W911NF-11-1-0473 (C.H.). D.S. was supported by the Swedish Research Council International Career Fellowship (4.1-2016-00416). A.B.H. is a Merck Fellow of the Helen Hay Whitney Foundation. A.N.A. was supported by the Crohn's and Colitis Foundation. D.P.B.M. was supported by the Leona M. and Harry B. Helmsley Charitable Trust. Pacific Northwest National Laboratory is a multi-program laboratory operated by Battelle for the US Department of Energy under contract DE-AC05-76RL01830.

**Reviewer information** Nature thanks Jeroen Raes, Philippe Schmitt-Kopplin, Eran Segal and the other anonymous reviewer(s) for their contribution to the peer review of this work.

**Author contributions** Study design: H.C., J.S., J. Braun, J.K.J., D.P.B.M., C.B.C., R.J.X., and C.H. Clinical coordination: A.N.A., E.A., H.C., K.L., M.P., J.S., J.L.K., H.K., C.J.M., B.W.S., W.T., R.G.W., V.Y., J. Braun, L.A.D., S.K., D.P.B.M., and H.S.W. Project managers: J.A.-P., T.W.P., E.A., H.C., T.G.G., E.A.F., and H.V. Data generation: J.L.-P., M.S., J.A.-P., T.W.P., E.A., N.J.A., D.C., T.G.G., C.J.L., M.P., J.S., R.A.W., K.B., A.D., C.D., J.L.K., C.J.M., K.A.P., W.T., J.J.T.H., R.G.W., J. Braun, D.P.B.M., J.F.P., T.S.S., C.B.C., and H.V. Bioinformatics: J.L.-P., C.A., M.S., J.A.-P., N.J.A., K.S.B., C.J.B., A.G., H.M., D.R.P., G.R., D.S., Y.V.-B., R.A.W., J. Bishai, L.J.M., R.S., A.S.-M., G.W., J. Braun, J.F.P., and C.H. Manuscript: J.L.-P., C.A., M.S., J.A.-P., K.S.B., C.J.B., A.B.H., H.M., D.R.P., G.R., D.S., L.N., C.B.C., E.A.F., H.V., and C.H. Principal Investigators: J. Braun, L.A.D., J.K.J., R.K., S.K., D.P.B.M., J.F.P., H.S.W., C.B.C., H.V., R.J.X., and C.H.

**Competing interests** J. Braun is on the Scientific Advisory Board for Janssen Research & Development, LLC. C.H. is on the Scientific Advisory Board for Seres Therapeutics. J.F.P. and N.J.A. own shares at Diversigen Inc. R.J.X. is a consultant to Novartis and Nestle.

#### Additional information

**Supplementary information** is available for this paper at <https://doi.org/10.1038/s41586-019-1237-9>.

**Reprints and permissions information** is available at <http://www.nature.com/reprints>.

**Correspondence and requests for materials** regarding clinical aspects including data generation and interpretation should be addressed to R.J.X. ([xavier@molbio.mgh.harvard.edu](mailto:xavier@molbio.mgh.harvard.edu)). Correspondence regarding data generation, interpretation, and analysis should be addressed to C.H.

**Publisher's note**: Springer Nature remains neutral with regard to jurisdictional claims in published maps and institutional affiliations.



**Open Access** This article is licensed under a Creative Commons Attribution 4.0 International License, which permits use, sharing, adaptation, distribution and reproduction in any medium or format, as long as you give appropriate credit to the original author(s) and the source, provide a link to the Creative Commons license, and indicate if changes were made. The images or other third party material in this article are included in the article's Creative Commons license, unless indicated otherwise in a credit line to the material. If material is not included in the article's Creative Commons license and your intended use is not permitted by statutory regulation or exceeds the permitted use, you will need to obtain permission directly from the copyright holder. To view a copy of this license, visit <http://creativecommons.org/licenses/by/4.0/>.

© The Author(s) 2019

#### IBDMDB Investigators

Jason Bishai<sup>1</sup>, Kevin Bullock<sup>4</sup>, Amy Deik<sup>4</sup>, Courtney Dennis<sup>4</sup>, Jess L. Kaplan<sup>21</sup>, Hamed Khalili<sup>3</sup>, Lauren J. McIver<sup>2</sup>, Christopher J. Moran<sup>21</sup>, Long Nguyen<sup>3</sup>, Kerry A. Pierce<sup>4</sup>, Randall Schwager<sup>2</sup>, Alexandra Sirota-Madi<sup>1</sup>, Betsy W. Stevens<sup>3</sup>, William Tan<sup>3</sup>, Johanna J. ten Hoeve<sup>9</sup>, George Weingart<sup>2</sup>, Robin G. Wilson<sup>3</sup> & Vijay Yajnik<sup>3</sup>

## METHODS

**Recruitment and specimen collection.** *Recruitment.* Five medical centres participated in the IBDMDb: Cincinnati Children's Hospital, Emory University Hospital, Massachusetts General Hospital, Massachusetts General Hospital for Children, and Cedars-Sinai Medical Center. Patients were approached for potential recruitment upon presentation for routine age-related colorectal cancer screening, work up of other gastrointestinal (GI) symptoms, or suspected IBD, either with positive imaging (for example, colonic wall thickening or ileal inflammation) or symptoms of chronic diarrhoea or rectal bleeding. Participants could not have had a prior screening or diagnostic colonoscopy. Potential participants were excluded if they were unable to or did not consent to provide tissue, blood, or stool, were pregnant, had a known bleeding disorder or an acute gastrointestinal infection, were actively being treated for a malignancy with chemotherapy, were diagnosed with indeterminate colitis, or had undergone a prior, major gastrointestinal surgery such as an ileal/colonic diversion or j-pouch. Upon enrolment, an initial colonoscopy was performed to determine study strata. Subjects not diagnosed with IBD based on endoscopic and histopathologic findings were classified as 'non-IBD' controls, including the aforementioned healthy individuals presenting for routine screening, and those with more benign or non-specific symptoms. This creates a control group that, while not completely 'healthy', differs from the IBD cohorts specifically by clinical IBD status. Differences observed between these groups are therefore more likely to constitute differences specific to IBD, and not differences attributable to general GI distress. In total, 132 subjects took part in the study (Extended Data Table 1).

*Regulatory compliance.* The study was reviewed by the Institutional Review Boards at each sampling site: overall Partners Data Coordination (IRB #2013P002215); MGH Adult cohort (IRB #2004P001067); MGH Paediatrics (IRB #2014P001115); Emory (IRB #IRB00071468); Cincinnati Children's Hospital Medical Center (2013-7586); and Cedars-Sinai Medical Center (3358/CR00011696). All study participants gave written informed consent before providing samples. Each IRB has a federal wide assurance and follows the regulations established at 45 CFR Part 46. The study was conducted in accordance with the ethical principles expressed in the Declaration of Helsinki and the requirements of applicable federal regulations. *Specimen collection and storage.* Specimens for research (biopsies, blood draws, and stool samples) were collected during the screening colonoscopy, at up to five quarterly follow-up visits at the clinic (termed 'baseline', visit 2, and so on, occurring at months 0, 3, 6, 9, and 12), and every two weeks by mail.

*Biopsies.* Biopsies were primarily gathered during the initial screening colonoscopy, where approximately four to fourteen biopsies were collected for each subject. For each location sampled (at least ileum and 10 cm from rectum, plus discretionary sites of inflammation), one biopsy was collected for standard histopathology at the sampling institution, two biopsies were collected and stored in RNAlater for molecular data generation (host and microbial, stored at  $-20^{\circ}\text{C}$ ), and one biopsy was collected and placed in a sterile tube with 5% glycerol (stored at  $-80^{\circ}\text{C}$ ). If possible, additional biopsies from inflamed tissue and nearby non-inflamed tissue were taken from participants with CD or UC. For adults, a second set of biopsies was also collected from each location (rectum and ileum) for epithelial cell culture (for detailed protocols see <http://ibdmdb.org/protocols>). All biopsies were stored for up to two months at the collection site, and shipped overnight on dry ice to Washington University for epithelial cell culture or to the Broad Institute for molecular profiling.

*Blood samples.* Blood samples (whole blood and serum) were taken at the quarterly clinical visits. For whole blood, 1 ml of blood was collected and stored at  $-80^{\circ}\text{C}$ . For serum, blood was drawn into a 5-ml SST tube, and left at room temperature for 40 min. This was centrifuged for 15 min at 3,000 r.p.m. and 0.5-ml portions were immediately aliquoted into 2-ml microtubes. Tubes were stored at  $-80^{\circ}\text{C}$ .

*Stool samples.* Stool specimens were collected both at the clinical visits and every two weeks by mail using a home collection kit developed for the project (<http://ibdmdb.org/protocols>) and previously validated<sup>46</sup>. Participants first deposited stool into a collection bowl suspended over a commode. They then collected two aliquots using a scoop to transfer stool into two Sarstedt 80.623 tubes: one with approximately 5 ml molecular biology grade 100% ethanol, and one with no preservative. Stool samples were then sent from each participant by FedEx to the Broad Institute where they were processed immediately before storage at  $-80^{\circ}\text{C}$ . The ethanol tube was centrifuged to pellet stool, which was subaliquoted, and the supernatant was transferred to a new tube for metabolomic analysis. Stool from ethanol was aliquoted into 2-ml cryovials in ~100–200-mg aliquots, prioritizing specimens for metatranscriptomic sequencing, metabolomics, and viromics in that order. Any remaining stool was stored in additional aliquot tubes. One hundred milligrams of the non-ethanol stool was stored for assaying faecal calprotectin and the remainder was saved in a second tube. All samples were stored at  $-80^{\circ}\text{C}$  after receipt before processing. This home-collection method was shown previously to produce reproducible results compared to flash-frozen samples<sup>46</sup>, consistent with previous observations across data types<sup>47–49</sup>. Note that an accurate estimate of the

stool water content could not be obtained, as samples were collected by subjects and preserved in ethanol at room temperature until aliquots were generated for the different data generation platforms.

*Participant and sample metadata.* Descriptions of each participant and specimen were captured at baseline and accompanying each specimen collection, respectively. At baseline (that is, during or before the screening colonoscopy), subjects completed a Reported Symptoms Questionnaire, the Short Inflammatory Bowel Disease Questionnaire<sup>50</sup>, a Food Frequency Questionnaire, and an Environmental Questionnaire, and the Simple Endoscopic Score<sup>51</sup> for CD subjects or Baron's Score<sup>52</sup> for UC subjects was assessed.

During both follow-up visits and paired with mailed stool samples, subjects completed an Activity Index and Dietary Recall Questionnaire to assess their disease activity index (HBI for CD or SCCAI for UC) and provide a retrospective recall of their recent diet. All questionnaires, as well as detailed protocols (including product numbers), can be found on the IBDMDb data portal at <http://ibdmdb.org/protocols>. Responses and metadata are available at <http://ibdmdb.org/results>, and summaries of phenotypes for samples and subjects are provided (Supplementary Fig. 3) along with summaries of the final time series for each subject (Supplementary Fig. 2).

**Stool specimen processing.** *Sample selection.* Sample selection proceeded in two phases, with an initial round of data generation producing a pilot metagenomics and metatranscriptomics data set, which was analysed separately<sup>53</sup>. This pilot sample selection included at least one sample per participant that was enrolled in the study at that time, two long time courses per disease group (CD, UC, non-IBD), and multiple shorter time courses, resulting in 300 samples. For a subset of 78 samples, metatranscriptomic data were generated. Samples were chosen on the basis of sample mass, preferentially selecting samples that could be re-sequenced if needed during the later data generation.

For the second, larger phase of data generation, stool samples were selected for different assays with the goal of generating data covering as many aspects of the cohort as possible, including per-subject time courses, cross-subject global time points, and samples from all patients, phenotypes, age ranges, clinical centres, and so forth (Fig. 1b). The subset of measurements performed for each sample was determined in large part by aliquot requirements (in particular, mass requirements for the assay relative to how much the patient provided) and cost.

For proteomics and metabolomics, six global time points were equally distributed over the year-long time series for as many subjects as possible. Restrictions such as available sample mass and missing samples were incorporated by selecting the nearest suitable sample in time, resulting in slight irregularities in the sampling pattern. In total, 546 metabolite profiles and 450 proteomics profiles were generated. From among these samples, 768 were selected for metagenomics, metatranscriptomics, and viromics, corresponding to 8 plates of 96 samples each. Samples already selected for proteomics or metabolomics were prioritised to facilitate integrated data analysis (316 samples had sufficient mass), resulting in six global time points for all subjects. In cases where the respective sample was not available for a subject, the nearest suitable sample in time was selected. Subjects with greater fluctuations in their HBI or SCCAI scores were then prioritized for denser sampling, resulting in 12 long time courses for 5 participants with CD, 4 with UC, and 3 without IBD. The selection also included 23 technical replicates for metagenomics, metatranscriptomics and viromics.

Finally, 576 additional samples were selected specifically for metagenomic sequencing (6 plates) resulting in a total of 1,344 metagenomic samples. Samples at previously selected global time points and long time courses that had been restricted by available mass for other measurement types were prioritized. An additional four global time points were added by this process, as well as 15 long time courses (representing 10 participants with CD, 10 with UC, and 7 without IBD), and 22 samples that had been previously sequenced for the pilot data and represented additional technical replicates. Lastly, 522 samples were selected for faecal calprotectin measurements, prioritizing samples that were selected for any other multi-omics data generation and representing a broad overview of the cohort. Of a total of 2,653 collected stool samples, 1,785 generated at least one measurement type (Fig. 1b).

Sample selection for RNA-seq and 16S sequencing from biopsies, and host genotyping from blood draws, aimed to cover the 95 subjects who contributed at least 14 stool samples, as permitted by the availability of biopsies and blood draws for each assay. Sample selection from biopsies additionally aimed to cover biopsies from inflamed and non-inflamed sites. In total, 254 biopsies were selected for RNA-seq, covering 43 participants with CD, 25 with UC, and 22 without IBD, and distributed across biopsy sites and inflammation statuses (Extended Data Fig. 6A); and 161 biopsies were selected for 16S sequencing, covering 36 participants with CD, 21 with UC, and 22 without IBD. Exome sequencing was performed for 46 participants with CD, 24 with UC, and 22 without IBD.

Sample selection for remaining sample types (RRBS, blood serology) included all samples with a suitable sample available.



**Sequencing assays. DNA and RNA isolation for metagenomics and metatranscriptomics.** Total nucleic acid was extracted from one aliquot of each assayed stool sample via the Chemagic MSM I with the Chemagic DNA Blood Kit-96 from Perkin Elmer. This kit combines chemical and mechanical lysis with magnetic bead-based purification. Prior to extraction on the MSM-I, TE buffer, lysozyme, proteinase K, and RLT buffer with beta-mercaptoethanol were added to each stool sample. The stool lysate solution was vortexed to mix.

Samples were then placed on the MSM I unit to automate the following steps: M-PVA magnetic beads were added to the stool lysate solution and vortexed to mix. The bead-bound total nucleic acid was then removed from solution using a 96-rod magnetic head and washed in three ethanol-based wash buffers. The beads were then washed in a final water wash buffer. Finally, the beads were dipped in elution buffer to resuspend the DNA sample in solution. The beads were then removed from solution, leaving purified total nucleic acid eluate. The eluate was then split into two equal volumes: one for DNA and the other for RNA. SUPERase-IN solution was added to the DNA samples, and the reaction was cleaned up using AMPure XP SPRI beads. DNase was added to the RNA samples, and the reaction was cleaned up using AMPure XP SPRI beads.

DNA samples were quantified using a fluorescence-based PicoGreen assay. RNA samples were quantified using a fluorescence-based RiboGreen assay. RNA quality was assessed via smear analysis on the Caliper LabChip GX.

**Metagenome sequencing.** Metagenomes were generated from the resulting DNA for 1,638 stool samples, selected to obtain both a broad overview of targeted, aligned time points for all subjects (Fig. 1b), complemented by a dense sampling of subjects which tended to have greater disease activity, as determined by their HBI or SCCAI scores.

Whole-genome fragment libraries were prepared as follows. Metagenomic DNA samples were quantified by Quant-iT PicoGreen dsDNA Assay (Life Technologies) and normalized to a concentration of 50 pg/μl. Illumina sequencing libraries were prepared from 100–250 pg DNA using the Nextera XT DNA Library Preparation kit (Illumina) according to the manufacturer's recommended protocol, with reaction volumes scaled accordingly. Prior to sequencing, libraries were pooled by collecting equal volumes (200 nl) of each library from batches of 96 samples. Insert sizes and concentrations for each pooled library were determined using an Agilent Bioanalyzer DNA 1000 kit (Agilent Technologies). Libraries were sequenced on HiSeq2000 or 2500 2x101 to yield ~10 million paired end reads. Post-sequencing de-multiplexing and generation of BAM and FASTQ files were generated using the Picard suite (<https://broadinstitute.github.io/picard>).

**Metatranscriptome sequencing.** Metatranscriptomes were generated for 855 stool samples, subsampled from metagenomic selections as above. Illumina cDNA libraries were generated using a modified version of the RNAtag-seq protocol<sup>54</sup>. In brief, 500 ng–1 μg of total RNA was fragmented, depleted of genomic DNA, dephosphorylated, and ligated to DNA adapters carrying 5'-AN8-3' barcodes of known sequence with a 5' phosphate and a 3' blocking group. Barcoded RNAs were pooled and depleted of rRNA using the RiboZero rRNA depletion kit (Epicentre). Pools of barcoded RNAs were converted to Illumina cDNA libraries in two main steps: (i) reverse transcription of the RNA using a primer designed to the constant region of the barcoded adaptor with addition of an adaptor to the 3' end of the cDNA by template switching using SMARTScribe (Clontech) as described<sup>55</sup>; (ii) PCR amplification using primers whose 5' ends target the constant regions of the 3' or 5' adaptors and whose 3' ends contain the full Illumina P5 or P7 sequences. cDNA libraries were sequenced on the Illumina HiSeq2500 platform to generate ~13 million paired end reads.

**Viromics.** We selected 703 stool samples for viral profiling, following the sample selection used for metatranscriptomics and adjusted slightly only when aliquots were unavailable (Fig. 1c). Viral nucleic acids were extracted using the MagMax Viral RNA Isolation Kit (AM1939, Thermo Fisher Scientific). Viral RNA was reverse transcribed using SuperScript II RT (18064014, Thermo Fisher) and random hexamers. After short molecule and random hexamer removal using ChargeSwitch (CS12000, Thermo Fisher), molecules were amplified and tagged with a BC12-V8A2 construct<sup>56</sup> using AccuPrime™ Taq polymerase and cleaned with ChargeSwitch kit.

The resulting viral amplicons were normalized, pooled, and made into an Illumina library without shearing. The library (150–600 bp) was loaded into an Illumina HiSeq 2000 (Illumina, Carlsbad, CA) and sequenced using the 2 × 100 bp chemistry. Reads were demultiplexed into a sample bin using the barcode prefixing read-1 and read-2, allowing zero mismatches. Demultiplexed reads were further processed by trimming off barcodes, semi-random primer sequences, and Illumina adapters. This process used a custom demultiplexer and the BBduk algorithm included in BBMap (<http://sourceforge.net/projects/bbmap>). The resulting trimmed data set was analysed using a pipeline created at the Alkek Center for Metagenomics and Microbiome Research at Baylor College of Medicine<sup>57</sup>. In brief, the viral analysis pipeline uses a clustering algorithm creates putative viral genomes using a mapping assembly strategy that leverages nucleotide and translated

nucleotide alignment information. Viral taxonomies were assigned using a scoring system that incorporates nucleotide and translated nucleotide alignment results in a per-base fashion and optimizes for the highest resolution taxonomic rank.

**Metabolomics. Sample selection, receipt, and storage.** Sample selection for metabolomics aimed to obtain only a broad sampling of many subjects. In total, 546 stool samples were selected for profiling (Fig. 1b). A portion of each selected stool sample (40–100 mg) and the entire volume of originating ethanol preservative were stored in 15-ml centrifuge tubes at –80 °C until all samples were collected.

**Sample processing.** Samples were thawed on ice and then centrifuged (4 °C, 5,000g) for 5 min. Ethanol was evaporated using a gentle stream of nitrogen gas using a nitrogen evaporator (TurboVap LV; Biotage) and stored at –80 °C until all samples in the study had been dried. Aqueous homogenates were generated by sonicating each sample in 900 μl H<sub>2</sub>O using an ultrasonic probe homogenizer (Branson Sonifier 250) set to a duty cycle of 25% and output control of 2 for 3 min. Samples were kept on ice during the homogenization process. The homogenate for each sample was aliquoted into two 10-μl and two 30-μl samples in 1.5-ml centrifuge tubes for LC–MS sample preparation and 30 μl of homogenate from each sample was transferred into a 50-ml conical tube on ice to create a pooled reference sample. The pooled reference mixture was mixed by vortexing and then aliquoted (100 μl per aliquot) into 1.5-ml centrifuge tubes. Aliquots and reference sample aliquots were stored at –80 °C until LC–MS analyses were conducted.

**LC–MS analyses.** A combination of four LC–MS methods were used to profile metabolites in the faecal homogenates, as previously published<sup>58</sup>; two methods that measure polar metabolites, a method that measures metabolites of intermediate polarity (for example, fatty acids and bile acids), and a lipid profiling method. For the analysis queue in each method, subjects were randomized and longitudinal samples from each subject were randomized and analysed as a group. Additionally, pairs of pooled reference samples were inserted into the queue at intervals of approximately 20 samples for quality control and data standardization. Samples were prepared for each method using extraction procedures that are matched for use with the chromatography conditions. Data were acquired using LC–MS systems comprised of Nexera X2 U-HPLC systems (Shimadzu Scientific Instruments) coupled to Q Exactive/Exactive Plus orbitrap mass spectrometers (Thermo Fisher Scientific). The method details are summarized below.

**LC–MS Method 1: HILIC-pos (positive ion mode MS analyses of polar metabolites).** LC–MS samples were prepared from stool homogenates (10 μl) by protein precipitation with the addition of nine volumes of 74.9:24.9:0.2 v/v/v acetonitrile/methanol/formic acid containing stable isotope-labelled internal standards (valine-d8, Isotec; and phenylalanine-d8, Cambridge Isotope Laboratories). The samples were centrifuged (10 min, 9,000g, 4 °C), and the supernatants injected directly onto a 150 × 2-mm Atlantis HILIC column (Waters). The column was eluted isocratically at a flow rate of 250 μl/min with 5% mobile phase A (10 mM ammonium formate and 0.1% formic acid in water) for 1 min followed by a linear gradient to 40% mobile phase B (acetonitrile with 0.1% formic acid) over 10 min. MS analyses were carried out using electrospray ionization in the positive ion mode using full scan analysis over *m/z* 70–800 at 70,000 resolution and 3-Hz data acquisition rate. Additional MS settings are: ion spray voltage, 3.5 kV; capillary temperature, 350 °C; probe heater temperature, 300 °C; sheath gas, 40; auxiliary gas, 15; and S-lens RF level 40.

**LC–MS Method 2: HILIC-neg (negative ion mode MS analysis of polar metabolites).** LC–MS samples were prepared from stool homogenates (30 μl) by protein precipitation with the addition of four volumes of 80% methanol containing inosine-15N4, thymine-d4 and glycocholate-d4 internal standards (Cambridge Isotope Laboratories). The samples were centrifuged (10 min, 9,000g, 4 °C) and the supernatants were injected directly onto a 150 × 2.0-mm Luna NH2 column (Phenomenex). The column was eluted at a flow rate of 400 μl/min with initial conditions of 10% mobile phase A (20 mM ammonium acetate and 20 mM ammonium hydroxide in water) and 90% mobile phase B (10 mM ammonium hydroxide in 75:25 v/v acetonitrile/methanol) followed by a 10-min linear gradient to 100% mobile phase A. MS analyses were carried out using electrospray ionization in the negative ion mode using full scan analysis over *m/z* 60–750 at 70,000 resolution and 3 Hz data acquisition rate. Additional MS settings are: ion spray voltage, –3.0 kV; capillary temperature, 350 °C; probe heater temperature, 325 °C; sheath gas, 55; auxiliary gas, 10; and S-lens RF level 40.

**LC–MS Method 3: C18-neg (negative ion mode analysis of metabolites of intermediate polarity; for example, bile acids and free fatty acids).** Stool homogenates (30 μl) were extracted using 90 μl methanol containing PGE2-d4 as an internal standard (Cayman Chemical Co.) and centrifuged (10 min, 9,000g, 4 °C). The supernatants (10 μl) were injected onto a 150 × 2.1-mm ACQUITY BEH C18 column (Waters). The column was eluted isocratically at a flow rate of 450 μl/min with 20% mobile phase A (0.01% formic acid in water) for 3 min followed by a linear gradient to 100% mobile phase B (0.01% acetic acid in acetonitrile) over 12 min. MS analyses were carried out using electrospray ionization in the negative ion mode using full scan analysis over *m/z* 70–850 at 70,000 resolution and 3 Hz data

acquisition rate. Additional MS settings are: ion spray voltage,  $-3.5$  kV; capillary temperature,  $320^{\circ}\text{C}$ ; probe heater temperature,  $300^{\circ}\text{C}$ ; sheath gas, 45; auxiliary gas, 10; and S-lens RF level 60.

**LC-MS Method 4: C8-pos.** Lipids (polar and nonpolar) were extracted from stool homogenates ( $10\ \mu\text{l}$ ) using  $190\ \mu\text{l}$  isopropanol containing 1-dodecanoyl-2-tridecanoyl-*sn*-glycero-3-phosphocholine as an internal standard (Avanti Polar Lipids; Alabaster, AL). After centrifugation ( $10\ \text{min}$ ,  $9,000g$ , ambient temperature), supernatants ( $10\ \mu\text{l}$ ) were injected directly onto a  $100 \times 2.1\text{-mm}$  ACQUITY BEH C8 column ( $1.7\ \mu\text{m}$ ; Waters). The column was eluted at a flow rate of  $450\ \mu\text{l}/\text{min}$  isocratically for  $1\ \text{min}$  at 80% mobile phase A ( $95:5:0.1\ \text{v/v/v}$  10 mM ammonium acetate/methanol/acetic acid), followed by a linear gradient to 80% mobile phase B ( $99.9:0.1\ \text{v/v}$  methanol/acetic acid) over  $2\ \text{min}$ , a linear gradient to 100% mobile phase B over  $7\ \text{min}$ , and then  $3\ \text{min}$  at 100% mobile phase B. MS analyses were carried out using electrospray ionization in the positive ion mode using full scan analysis over  $m/z$   $200\text{--}1,100$  at  $70,000$  resolution and  $3\ \text{Hz}$  data acquisition rate. Additional MS settings are: ion spray voltage,  $3.0\ \text{kV}$ ; capillary temperature,  $300^{\circ}\text{C}$ ; probe heater temperature,  $300^{\circ}\text{C}$ ; sheath gas, 50; auxiliary gas, 15; and S-lens RF level 60.

**Metabolomics data processing.** Raw LC-MS data were acquired to the data acquisition computer interfaced to each LC-MS system and then stored on a robust and redundant file storage system (Isilon Systems) accessed via the internal network at the Broad Institute. Nontargeted data were processed using Progenesis Q1 software (v 2.0, Nonlinear Dynamics) to detect and de-isotope peaks, perform chromatographic retention time alignment, and integrate peak areas. Peaks of unknown ID were tracked by method,  $m/z$  and retention time. Identification of nontargeted metabolite LC-MS peaks was conducted by: i) matching measured retention times and masses to mixtures of reference metabolites analysed in each batch; and ii) matching an internal database of  $>600$  compounds that have been characterized using the Broad Institute methods. Temporal drift was monitored and normalized with the intensities of features measured in the pooled reference samples.

**Proteomics. Sample selection and LC-MS/MS.** Sample selection for proteomics largely followed sample selection for metabolomics (Fig. 1b, c), with slight adjustments when aliquots were unavailable. In total, 447 stool samples were targeted for profiling. From the selected samples, proteins were proteolytically digested using trypsin, and each digest was subjected to automated offline high-pH reversed-phase fractionation with fraction concatenation. LC-MS/MS analysis for each fraction was performed using a Thermo Scientific Q-Exactive Orbitrap mass spectrometer at UCLA, outfitted with a custom-built nano-ESI interface. Samples were loaded onto an in-house packed capillary LC column ( $70\ \text{cm} \times 75\ \mu\text{m}$ ,  $3\text{-}\mu\text{m}$  particle size), and data were acquired for  $120\ \text{min}$ . Precursor MS spectra were collected over  $400\text{--}2,000\ m/z$ , followed by data-dependent MS/MS spectra of the twelve most abundant ions, using a collision energy of  $30\%$ . A dynamic exclusion time of  $30\ \text{s}$  was used to discriminate against previously analysed ions.

**Peptide identification and protein data roll-up.** Mass spectra from the resulting analyses were evaluated using the MSGF<sup>+</sup> software<sup>59</sup> v10072 using the HMP 1 gut reference genomes (HMP\_Refgenome-gut\_2015-06-18). In brief, after conversion of the metagenomic assemblies into predicted open reading frames (for example, predicted proteins), libraries were created using the forward and reverse direction to allow determination of FDR. The reverse decoy database allows measurement of the rate of detection of false hits, which in turn allows calculation of FDR and appropriate filtering of the data to maximize real peptide identifications while minimizing spurious ones. MSGF<sup>+</sup> was then used to search the experimental mass spectra data against both the forward and reverse decoy databases. Cut-offs for data included: MSGF<sup>+</sup> spectra probability ( $>1 \times 10^{10}$ , equivalent to a BLAST  $e$  value), mass accuracy ( $\pm 20\ \text{p.p.m.}$ ), protein level FDR of  $1\%$  and one unique peptide per protein identification.

**Faecal calprotectin.** Faecal calprotectin was quantified for 652 stool samples, which were stored at  $-80^{\circ}\text{C}$  without preservative before processing. Sample selection focused on obtaining a broad survey of all subjects rather than detailed time series (Fig. 1b). Calprotectin was quantified using QUANTA Lite Calprotectin ELISA (Inova Diagnostics 704770) following the manufacturer's protocol. Between  $80$  and  $120\ \text{mg}$  of stool was used for input. Incubation time before stopping the reaction was adjusted to obtain OD<sub>405</sub> values in the suggested range for assay.

**Biopsy specimen processing. Co-isolation of DNA and RNA from frozen tissue.** DNA and RNA were extracted from RNA-later-preserved biopsies using the AllPrep DNA/RNA Universal Kit from Qiagen. Biological samples were cut into  $20\text{--}25\text{-mg}$  pieces on a dry ice batch, then placed in tubes with a steel bead for mechanical homogenization and a highly denaturing guanidine isothiocyanate-containing buffer, which immediately inactivates DNases and RNases to ensure isolation of intact DNA and RNA. After homogenization, the lysate was passed through an AllPrep DNA Mini spin column. This column, in combination with the high-salt buffer, allows selective and efficient binding of genomic DNA. On-column proteinase K digestion in optimized buffer conditions allows purification of high DNA yields from all sample types. The column was then washed

and DNA was eluted in TE buffer. Flow-through from the AllPrep DNA Mini spin column was digested by proteinase K in the presence of ethanol. This optimized digestion, together with the subsequent addition of further ethanol, allowed for appropriate binding of total RNA, including miRNA, to the RNeasy Mini spin column. Samples were then digested with DNase I to ensure high-yields of DNA-free RNA. Contaminants were efficiently washed away and RNA was eluted in water.

**16S rRNA gene profiling.** We selected 178 biopsies for 16S amplicon-based taxonomic profiling. The 16S rRNA gene-sequencing protocol was adapted from the Earth Microbiome Project<sup>60</sup> and the Human Microbiome Project<sup>61–63</sup>. In brief, bacterial genomic DNA was extracted from the total mass of the biopsied specimens using the MoBio PowerLyzer Tissue and Cells DNA isolation kit and sterile spatulas for tissue transfer. The 16S rDNA V4 region was amplified from the extracted DNA by PCR and sequenced in the MiSeq platform (Illumina) using the  $2 \times 250\ \text{bp}$  paired-end protocol, yielding pair-end reads that overlapped almost completely. The primers used contained adapters for MiSeq sequencing and single-index barcodes such that PCR products may be pooled and sequenced directly<sup>61</sup>, targeting at least  $10,000$  reads per sample.

Read pairs were demultiplexed and merged using USEARCH v7.0.1090<sup>64</sup>. Sequences were clustered into OTUs at a similarity threshold of  $97\%$  using the UPPARSE algorithm<sup>65</sup>. OTUs were subsequently mapped to a subset of the SILVA database<sup>66</sup> containing only sequences from the V4 region of the 16S rRNA gene to determine taxonomies. Abundances were then recovered by mapping the demultiplexed reads to the UPPARSE OTUs, producing the final taxonomic profiles. The 150 samples with  $\geq 1,000$  mapped reads were used in downstream analyses.

**Host RNA-seq. cDNA library construction.** In total, 252 biopsies were selected for transcriptional profiling. Total RNA was quantified using the Quant-iT RiboZero RNA Assay Kit and normalized to  $5\ \text{ng}/\mu\text{l}$ . Following plating,  $2\ \mu\text{l}$  of ERCC controls (using a  $1:1,000$  dilution) were spiked into each sample. An aliquot of  $200\ \text{ng}$  for each sample was transferred into library preparation, which was an automated variant of the Illumina TruSeq Stranded mRNA Sample Preparation Kit. This method preserves strand orientation of the RNA transcript. It uses oligo dT beads to select mRNA from the total RNA sample. It is followed by heat fragmentation and cDNA synthesis from the RNA template. The resultant  $500\text{-bp}$  cDNA then goes through library preparation (end repair, base 'A' addition, adaptor ligation, and enrichment) using Broad Institute designed indexed adapters substituted in for multiplexing. After enrichment the libraries were quantified using Quant-iT PicoGreen ( $1:200$  dilution). After normalizing samples to  $5\ \text{ng}/\mu\text{l}$ , the set was pooled and quantified using the KAPA Library Quantification Kit for Illumina Sequencing Platforms. The entire process is in  $96\text{-well}$  format and all pipetting is done by either Agilent Bravo or Hamilton Starlet.

**Illumina sequencing.** Pooled libraries were normalized to  $2\ \text{nM}$  and denatured using  $0.1\ \text{N}$  NaOH before sequencing. Flowcell cluster amplification and sequencing were performed according to the manufacturer's protocols using either the HiSeq 2000 or HiSeq 2500. Each run was a  $101\text{-bp}$  paired-end with an eight-base index barcode read. Data were organized using the Broad Institute Picard Pipeline which includes de-multiplexing and lane aggregation.

**Blood specimen processing. Serological analysis.** We analysed 210 serum samples for expression of ANCA, ASCA, anti-OmpC, and anti-CBir1 by ELISA as previously described<sup>67,68</sup>. Antibody levels were determined and the results expressed as ELISA units (EU/ml), which are relative to laboratory standards consisting of pooled, antigen-reactive sera from patients with well-characterized disease.

**DNA isolation from whole blood.** DNA was extracted using Chemagic MSM I with the Chemagic DNA Blood Kit-96 from Perkin Elmer. The kit combines chemical and mechanical lysis with magnetic bead-based purification. Whole blood samples were incubated at  $37^{\circ}\text{C}$  for  $5\text{--}10\ \text{min}$  to thaw. The blood was then transferred to a deep well plate with protease and placed on the Chemagic MSM I. The following steps were automated on the MSM I.

M-PVA magnetic beads were added to the blood and protease solution. Lysis buffer was added to the solution and vortexed to mix. The bead-bound DNA was then removed from solution using a  $96\text{-rod}$  magnetic head and washed in three ethanol-based wash buffers to eliminate cell debris and protein residue. The beads were then washed in a final water wash buffer. Finally, the beads were dipped in elution buffer to resuspend the DNA. The beads were then removed from solution, leaving purified DNA eluate. The resulting DNA samples were quantified using a fluorescence-based PicoGreen assay.

**Host exome sequencing.** Ninety-two host exomes were sequenced from DNA extracts using previously published methods<sup>69</sup>. Whole-exome libraries were constructed and sequenced on an Illumina HiSeq 4000 sequencer with  $151\text{-bp}$  paired-end reads. Output from Illumina software was processed by the Picard pipeline to yield BAM files containing calibrated, aligned reads.

**Library construction.** Library construction was performed as described<sup>69</sup> with some slight modifications. Initial genomic DNA input into shearing was reduced from  $3\ \mu\text{g}$  to  $50\ \text{ng}$  in  $10\ \mu\text{l}$  solution and enzymatically sheared. In addition, for adaptor ligation, dual-indexed Illumina paired end adapters were replaced with



palindromic forked adapters with unique 8-base index sequences embedded within the adaptor and added to each end.

**In-solution hybrid selection for exome enrichment.** In-solution hybrid selection was performed using the Illumina Rapid Capture Exome enrichment kit with 38 Mb target territory (29 Mb baited). The targeted region includes 98.3% of the intervals in the Refseq exome database. Dual-indexed libraries were pooled into groups of up to 96 samples before hybridization. The liquid handling was automated on a Hamilton Starlet. The enriched library pools were quantified using PicoGreen after elution from streptavidin beads and then normalized to a range compatible with sequencing template denature protocols.

**Preparation of libraries for cluster amplification and sequencing.** Following sample preparation, the libraries prepared using forked, indexed adapters were quantified using quantitative PCR (purchased from KAPA biosystems), normalized to 2 nM using the Hamilton Starlet Liquid Handling system, and pooled by equal volume using the Hamilton Starlet Liquid Handling system. Pools were then denatured using 0.1 N NaOH. Denatured samples were diluted into strip tubes using the Hamilton Starlet Liquid Handling system.

**Cluster amplification and sequencing.** Cluster amplification of the templates was performed according to the manufacturer's protocol (Illumina) using the Illumina cBot. Flow cells were sequenced on HiSeq 4000 Sequencing-by-Synthesis Kits, then analysed using RTA2.7.3.

**Host genetic data processing.** Host genetic exome sequence data were processed using the Broad Institute sequencing pipeline by the Data Sciences Platform (Broad Institute). This was done in three steps: pre-processing (including reads mapping, alignment to a reference genome and data cleanup), variant discovery (including per-sample variant calling and joint genotyping), and variant filtering to produce callset ready for downstream genetic analysis, using Genome Analysis Toolkit (GATK) (detailed documentation at <https://software.broadinstitute.org/gatk/documentation/>).

**Reduced representation bisulfite sequencing.** Reduced representation bisulfite sequencing (RRBS) libraries were prepared for 221 biopsies and 228 blood samples as described previously<sup>70</sup> with modifications detailed below. In brief, genomic DNA samples were quantified using a Quant-It dsDNA high sensitivity kit (ThermoFisher, Q33120) and normalized to a concentration of 10 ng/μl. A total of 100 ng of normalized genomic DNA was digested with MspI in a 20-μl reaction containing 1 μl MspI (20 U/μl) (NEB, R0106L) and 2 μl of 10× CutSmart Buffer (NEB, B7204S). MspI digestion reactions were then incubated at 37°C for 2 h followed by a 15 min incubation at 65°C.

Next, A-tailing reactions were performed by adding 1 μl dNTP mix (containing 10 mM dATP, 1 mM dCTP and 1 mM dGTP) (NEB, N0446S), 1 μl Klenow 3'-5' exo<sup>-</sup> (NEB, M0212L) and 1 μl 10× CutSmart Buffer in a total reaction volume of 30 μl. A-tailing reactions were then incubated at 30°C for 20 min, followed by 37°C for 20 min, followed by 65°C for 15 min.

Methylated Illumina sequencing adapters<sup>70</sup> were then ligated to the A-tailed material (30 μl) by adding 1 μl 10× CutSmart Buffer, 5 μl 10 mM ATP (NEB, P0756S), 1 μl T4 DNA Ligase (2,000,000 U/ml) (NEB, M0202M) and 2 μl methylated adapters in a total reaction volume of 40 μl. Adaptor ligation reactions were then incubated at 16°C overnight (16–20 h) followed by incubation at 65°C for 15 min. Adaptor ligated material was purified using 1.2× volumes of Ampure XP according to the manufacturer's recommended protocol (Beckman Coulter, A63881).

Following adaptor ligation, bisulfite conversion and subsequent sample purification were performed using the QIAGEN EpiTect kit according to the manufacturer's recommended protocol designated for DNA extracted from FFPE tissues (QIAGEN, 59104). Two rounds of bisulfite conversion were performed yielding a total of 40 μl bisulfite-converted DNA.

In order to determine the minimum number of PCR cycles required for final library amplification, 50 μl PCR reactions containing 3 μl bisulfite-converted DNA, 5 μl 10× PfuTurbo Cx hotstart DNA polymerase buffer, 0.5 μl 100 mM dNTP (25 mM each dNTP) (Agilent, 200415), 0.5 μl Illumina TruSeq PCR primers (25 μM each primer)<sup>70</sup> and 1 μl PfuTurbo Cx hotstart DNA polymerase (Agilent, 600412) were prepared. Reactions were then split equally into four separate tubes and thermocycled using the following conditions: denature at 95°C for 2 min followed by *X* cycles of 95°C for 30 s, 65°C for 30 s, 72°C for 45 s (where *X* number of cycles = 11, 13, 15 and 17), followed by a final extension at 72°C for 7 min. PCR products were purified using 1.2× volumes of Ampure XP and analysed on an Agilent Bioanalyzer using a High Sensitivity DNA kit (Agilent, 5067-4626). Once the optimal number of PCR cycles was determined, 200-μl PCR reactions were prepared using 24 μl bisulfite-converted DNA, 20 μl 10× PfuTurbo Cx hotstart DNA polymerase buffer, 2 μl 100 mM dNTPs (25 mM each), 2 μl Illumina TruSeq PCR primers (25 μM each) and 4 μl PfuTurbo Cx hotstart DNA polymerase with the thermal cycling conditions listed above. PCR reactions were purified using 1.2× volumes of Ampure XP according to the manufacturer's recommended protocol and analysed on an Agilent Bioanalyzer using a High Sensitivity DNA kit.

RRBS sequencing produced an average of 15.0M reads (s.d. 4.0M reads) over all 504 samples, with 448 (88.9%) samples exceeding 10M reads. Samples were analysed with Picard 2.9.4 using default parameters, resulting in a mean alignment rate to the human genome hg19 of 95.1%. Mean CpG coverage was 8.9× (s.d. 2.1%). As expected, 99.9% (s.d. 0.02%) of non-CpG bases and 49.8% (s.d. 2.8%) of CpG bases were converted.

**Data handling.** *Informatics for microbial community sequencing data.* For metagenomes and metatranscriptomes, sequencing reads from each sample in a pool were demultiplexed based on their associated barcode sequence using custom scripts. Up to one mismatch in the barcode was allowed provided it did not make assignment of the read to a different barcode possible. Barcode sequences were removed from the first read as were terminal Gs from the second read that may have been added by SMARTScribe during template switching.

Taxonomic and functional profiles were generated with the bioBakery metaomics workflow<sup>71</sup> v0.9.0 ([http://huttenhower.sph.harvard.edu/biobakery\\_workflows](http://huttenhower.sph.harvard.edu/biobakery_workflows)). In brief, reads mapping to the human genome were first filtered out using KneadData 0.7.0. Taxonomic profiles of shotgun metagenomes were generated using MetaPhlAn2<sup>72</sup> v2.6.0, which uses a library of clade-specific markers to provide pan-microbial (bacterial, archaeal, viral, and eukaryotic) profiling (<http://huttenhower.sph.harvard.edu/metaphlan2>). Functional profiling was performed by HUMAnN2<sup>73</sup> v0.11.0 (<http://huttenhower.sph.harvard.edu/humann2>). HUMAnN2 constructs a sample-specific reference database from the pangenomes of the subset of species detected in the sample by MetaPhlAn2 (pangenomes are precomputed representations of the open reading frames of a given species<sup>74</sup>). Sample reads are mapped against this database to quantify gene presence and abundance on a per-species basis. A translated search is then performed against a UniRef-based protein sequence catalogue<sup>75</sup> (UniRef release 2014\_07) for all reads that fail to map at the nucleotide level. The result are abundance profiles of gene families (UniRef90s), for both metagenomics and metatranscriptomics, stratified by each species contributing those genes, and which can then be summarized to higher-level gene groupings such as ECs or KOs.

Sample counts in Fig. 1b represent the numbers of raw products available. To ensure a reasonable read depth in each sample, only samples (metagenomes and metatranscriptomes) with at least 1 million reads (after human filtering) and at least one non-zero microbial abundance detected by MetaPhlAn2 were used in downstream analyses (Fig. 1c and later). In total, this was 1,595 metagenomic and 818 metatranscriptomic samples. Principal coordinates plots were generated with the *cmdscale* function in the R package *stats*. Visualizations were principally generated using *ggplot2*<sup>76</sup>.

**Species-level metaomic functional profile summaries.** Functional profiles per clade (typically species) were further quantified by summing the total sum-normalized stratified abundance attributed to each organism in the HUMAnN2 functional profiles from both metatranscriptomics and metagenomics. For metatranscriptomic analyses, the expression ratio for the species was then also defined as the ratio between these sums.

**Metaproteomic gene family functional profiles.** Gene family profiles were generated from metaproteomic peptides using UniRef90 identifiers by mapping peptide sequences to the Diamond-annotated reference in HUMAnN2 v0.11.0 with v0.8.22.84<sup>77</sup>. Each peptide was mapped to the UniRef90 with the highest per cent identity (minimum 90% match).

**Statistical methods and association testing.** *PERMANOVA and Mantel tests.* Omnibus testing was performed on Bray–Curtis dissimilarity matrices from MGX, MTX, MPX, and biopsy measurements. Functional profiles (MGX, MTX, and MPX) were first summarized to the KO level using HUMAnN2. Profiles were first normalized before calculation of dissimilarities. Dietary distance matrices were calculated by ordering the dietary intake frequencies from less to more frequent, assigning integers to these levels, and calculating the Manhattan distance.

Quantifications of covariation between measurement types in Fig. 1e were done using Mantel tests. To quantify cross-sectional ('inter-individual') covariation, we first produced an average profile for each subject by taking the feature-wise mean over all samples from the subject. Subject–subject dissimilarity matrices were then generated and compared using the *mantel.rtest* function in the R package *ape4*. To quantify longitudinal covariation, we first generated the complete sample–sample dissimilarity matrix, but only calculate the Mantel test statistic (the Pearson correlation between distances) from distances between samples from the same subject. Significance in this case was assessed using a permutation test with permutations limited within-subject.

Quantifications of variance explained in Fig. 1f were calculated using PERMANOVA with the *adonis* function in the R package *Vegan*<sup>78</sup>. Apart from the All row in Fig. 1f, the total variance explained by each variable was calculated independently of other variables (that is, as the sole variable in the model) to avoid issues related to variable ordering, and should thus be considered the total variance explainable by that variable. To account for the repeated measures present for all measurement types tested, relevant permutations were performed blocked within



subject for variables that change over time (medication, biopsy location, inflammation status, and dysbiosis). Meanwhile, variables that were constant (or change slowly enough to be considered constant) across samples from the same subject (age, sex, body mass index (BMI), race, recruitment site, diagnosis, and disease location) were first permuted across subjects and samples were relabelled with the variable from their permuted subject. To determine the significance of models including inter-individual variance (the Subject and All rows), permutations were performed freely. For subjects with incomplete records for BMI, we imputed the mean BMI of the remaining population. The All row is the total variance explained when including all other variables in the model.

**Differential microbiome feature abundance.** Differential abundance (DA) analysis of all microbial measurement types (except for viruses, which were modelled as presence/absence binary features) were tested as follows. First, an appropriate transformation/normalization method was applied: arcsine square-root transformation for microbial taxonomic and functional relative abundances, log transformation (with pseudo count 1 for zero values) for metabolite profiles and protein abundances, and log transform with no pseudocount for expression ratios (non-finite values removed). Transformed abundances were then fit with the following per-feature linear mixed-effects model:

$$\text{feature} \sim (\text{intercept}) + \text{diagnosis} + \text{diagnosis/dysbiosis} + \text{antibiotic use} \\ + \text{consent age} + (1|\text{recruitment site}) + (1|\text{subject})$$

That is, in each per-feature multivariable model, recruitment sites and subjects were included as random effects to account for the correlations in the repeated measures (denoted by  $(1|\text{recruitment site})$  and  $(1|\text{subject})$ , respectively) and the transformed abundance of each feature was modelled as a function of diagnosis (a categorical variable with non-IBD as the reference group) and dysbiosis state as a nested binary variable (with non-dysbiotic as reference) within each IBD phenotype (UC, CD, and non-IBD), while adjusting for consent age as a continuous covariate, and antibiotics as binary covariate. Pearson's residual values from the above linear mixed effects models were retained for use in subsequent analyses (see 'Cross-measurement type interaction testing').

Fitting was performed with the nlme package in R<sup>79</sup> (using the lme function), where significance of the association was assessed using Wald's test (except for viruses, where a logistic random effects model was considered with the glmer function from the lmer R package). Nominal *P* values were adjusted for multiple hypothesis testing with a target FDR of 0.25. In order to reduce the effect of zero-inflation in microbiome data, features with no variance or with >90% zeros were removed before fitting linear models. In addition, a variance filtering step was applied to remove features with very low variance. To further remove the effect of redundancy in KO gene family abundances (explainable by at most a single taxon), only features (both DNA and RNA) with low correlation with individual microbial abundances (Spearman correlation coefficient <0.6) were retained.

**Differential host gene expression.** Differentially expressed human genes between disease groups were quantified using a quasi-likelihood negative binomial generalized log-linear model (glmQLFit), implemented in the edgeR package in R<sup>80,81</sup>. Analysis was performed separately for each section of the intestine on genes with at least 2 CPM (counts per million) in 10 or more samples, with significance threshold FDR  $P < 0.05$  and >1.5 log-fold change. Gene enrichment analysis was performed on differentially expressed genes against the KEGG database<sup>82</sup> using a one-sided hypergeometric test in the package limma<sup>83</sup>.

**Associations with host gene expression.** Associations between host gene expression and biopsy taxonomic profiles were assessed using partial Spearman correlation, accounting for BMI, age at consent, sex and diagnosis. Association testing was performed for each biopsy location independently, as biopsy location was shown to heavily influence expression profiles (Figs. 1f, 4a, b). This simpler method was used rather than the more complex procedure outlined above for microbial measurement types since host gene expression, once filtered by biopsy location, do not have the same repeat measures problem as the microbial measurement types, allowing a simpler test.

**Genetic associations.** Genetic principal components for IBDMDB subjects as well as 1,000 Genomes subjects<sup>84</sup> were calculated for a set of independent SNPs overlapping between the two data sets and pruned on the basis of linkage disequilibrium (LD). Pruning was first performed in HMP2 using the `-indep-pairwise 1500 150 0.1` command in PLINK<sup>85</sup> by calculating LD ( $r^2$ ) for each pair of SNPs within a window of 1,500 SNPs, removing one of a pair of SNPs if  $r^2 > 0.1$  and repeating this procedure by shifting the window 150 SNPs forward. We then used the 1,000 Genomes reference phase 3 version 5a data for 2,504 participants ([http://bochet.gcc.biostat.washington.edu/beagle/1000\\_Genomes\\_phase3\\_v5a](http://bochet.gcc.biostat.washington.edu/beagle/1000_Genomes_phase3_v5a)) to merge with the HMP2 pruned data, resulting in 7,227 overlapping independent SNPs. Using these, we performed genome-wide estimation of identity-by-descent allele sharing on the combined data set using the `-genome` function in PLINK, followed by calculation of genetic principal

components using the `-cluster-mds-plot` function for the first two principal components (Fig. 1a).

For association analyses, we used first 20 genetic principal components as covariates, obtained from the same identity-by-descent sharing matrix using the `-cluster-pca 20` function. We targeted associations in five loci that had strong previously reported associations with IBD and/or have been implicated in microbial interactions<sup>86–88</sup>. To avoid confounding by ancestry, we restricted the analysis to subjects of European ancestry, excluding eight subjects with exomes available from other ancestral backgrounds. When available, we used reported SNPs that had minor allele frequency of at least 5% and Hardy-Weinberg equilibrium  $P < 5 \times 10^{-5}$ . If not, we used close proxies ( $LD\ r^2 < 0.8$  in CEU population using 1,000 genomes phase 3 version 5 reference via <http://analysisstools.nci.nih.gov/LDlink> (*MST1*, *FUT2*, *IRGM*, *NKX2-3*) or SNPs from the gnomAD browser at <http://gnomad.broadinstitute.org> (*PTGER4*)).

We used the following linear mixed effect model with the SNP as a predictor variable, coded with an additive genetic model with the outcome as the arcsine-square root transformed microbial relative abundance measured from stool metagenomes. Age, sex, antibiotic and immunosuppressant use, and the first 20 genetic principal components (PCs) were fitted as covariates with subjects as the random effect:

$$\text{taxon} \sim \text{intercept} + \text{SNP} + \text{antibiotic use} + \text{sex} + \text{age} \\ + \text{recruitment site} + \text{PC1-PC20} + (1|\text{subject})$$

Optimization was performed using the lme function (from the nlme R package), with *P* values calculated using the Wald test.

Associations between the rs1042712 SNP of the *LCT* locus<sup>89</sup> and self-reported milk intake from dietary recall forms were tested using the same mixed effect model. Reported dairy intake options were assigned the following numeric values for regression: 1 ('yesterday, 3 or more times'), 2 ('yesterday, 1 to 2 times'); 3 ('within the past 2 to 3 days'), 4 ('within the past 4 to 7 days'), and 5 ('did not consume in last 7 days').

**Density ridgeline plots of differentially abundant features.** To visualize the abundances of features that showed significantly different abundances by one of the tests above (Fig. 2, Extended Data Fig. 4), the bandwidth for kernel density estimation was selected independently for the portion of each feature above the detection limit (non-'zero') using the Sheather and Jones method<sup>90</sup>. Density estimates were scaled such that the maximum density for the plot spanned the distance between baselines for a given disease group. Samples below the detection limit are represented as barplots on the left, where a bar that spans the distance between baselines for a disease group represents 100% zeros. Density estimates were then additionally scaled by the fraction of non-zero samples such that relative differences in densities between groups with differing fractions of zeros are accurately represented. For both density estimates and fraction of zeros, samples were weighted by the inverse of the number of samples obtained from that subject, to avoid biasing estimates towards subjects with more densely sampled time series.

**Dysbiosis analyses.** *Dysbiosis score.* To identify samples with highly divergent (dysbiotic) metagenomic microbial compositions, as a complement to baseline disease diagnosis, we defined a dysbiosis score based on Bray-Curtis dissimilarities to non-IBD metagenomes. First, a 'reference set' of samples was constructed from non-IBD subjects by taking all samples after the 20th week after the subject's first stool sample. This was chosen because a subset of the non-IBD subjects at the start of their respective time series may not yet have overcome any gastrointestinal symptoms that triggered the initial visit to a doctor, though these were ultimately not caused by IBD. The dysbiosis score of a given sample was then defined as the median Bray-Curtis dissimilarity to this reference sample set, excluding samples that came from the same subject (Fig. 2c).

To identify samples that were highly divergent from the reference set, we thresholded the dysbiosis score at the 90th percentile of this score for non-IBD samples. This therefore identifies samples with a feature configuration that has a less than 10% probability of occurring in a participant without IBD. By this measure, 272 metagenomes were classified as dysbiotic. Samples from participants with CD or UC were overrepresented in the dysbiotic set, with 24.3% and 11.6% of their samples classified as dysbiotic, respectively. As expected, these samples also tended to locate in the extremes of the taxonomic ordination based on metagenomes (Extended Data Fig. 3b, c). Dysbiosis was unevenly distributed among subjects (Extended Data Fig. 3d), with some subjects remaining dysbiotic for all or most of their time series, while others remained non-dysbiotic for their entire time series.

To lend additional support to the definition of dysbiosis (that is, as outliers by one type of microbiome profile), we tested the concordance between dysbiosis classifications made using the same statistical definition, but applied to metabolomic rather than taxonomic profiles. That is, we defined a metabolomic dysbiosis score as the median Bray-Curtis dissimilarity of one metabolomic profile to the non-IBD metabolomic profiles (after the 20th week), and defined the dysbiosis threshold as the 90th percentile of this distribution among non-IBD metabolomic profiles.

We then compared these dysbiosis classifications with those from the nearest metagenomic sample (up to two weeks, see ‘Cross-measurement type temporal matching’) and found that dysbiotic samples identified by metagenomics were 4.6 times more likely to be dysbiotic by metabolomics (Fisher’s exact  $P = 5.9 \times 10^{-9}$ ), showing that dysbiosis measurements are highly consistent across measurement types.

To test the sensitivity of the dysbiosis classification to the choice of reference data set, we also performed the dysbiosis classification using the HMP1-II stool samples<sup>10</sup> as the reference sample set instead of the non-IBD samples. The resulting dysbiosis scores (Extended Data Fig. 3e) were highly concordant (Spearman  $\rho = 0.86$ ;  $P < 2.2 \times 10^{-16}$ ), as were the dysbiosis classifications (odds ratio of 56; Fisher’s exact  $P < 2.2 \times 10^{-16}$ ). This shows that, despite the inclusion of subjects with other conditions in the non-IBD group here, as well as large differences in measurement technologies between the data sets, the dysbiosis classification is highly robust. Furthermore, 43 out of 426 (10.1%) of non-IBD samples were classified as dysbiotic using the HMP1-II samples as reference, falling remarkably close to the 10% expected by the definition and showing that the enrichment of IBD samples in the dysbiotic set is not simply a consequence of the definition.

**Dysbiosis durations and intervals.** Samples of the dysbiosis durations and intervals were obtained by taking the difference in time between stool metagenomes in which the dysbiosis state changes, that is, the time from the first dysbiotic sample in an excursion into dysbiosis until the next non-dysbiotic sample was taken as one sample of the dysbiosis duration distribution. If the subject’s time series ended before this transition occurred, this resulted in a ‘censored’ duration or interval (Fig. 2e). Estimates of the durations of and time between dysbioses were then obtained from a censored maximum likelihood estimator for the mean of an exponential distribution. This incorporates the censored durations and intervals into the estimate to avoid underestimating these durations owing to limited observation times.

**Association of dysbiosis with disease location.** We tested for a relationship between the Montreal disease location classification in CD and periods of dysbiosis to ensure that dysbiosis was not simply detecting different disease locations. For this, an  $F$ -test of no significance was used with a Kenward–Roger approximation of degrees of freedom<sup>91</sup> in a logistic random effects regression that models dysbiosis as the binary outcome with subjects as a random effect and disease location as covariate, as implemented in the function `glmer` in the R package `lme4`. Only individuals with CD were considered.

**Temporal analyses. Power-law fits to Bray–Curtis dissimilarities.** Power-law fits to species-level metagenomic, metatranscriptomic, and metabolite Bray–Curtis dissimilarities (Fig. 3a, Extended Data Fig. 5a) were performed by fitting a power-law curve with free intercept by least-squares using the `nlmer` function from the R package `nlptr`. Significance was assessed using an  $F$ -test to compare the fit model with a flat line. Significance of the difference of the fit between disease groups was also assessed using an  $F$ -test, comparing a model jointly fit to both disease groups with separate fits to each group.

**Microbiome shifts.** A microbiome ‘shift’ was defined as having occurred between two consecutive time points from the same person if the Bray–Curtis dissimilarity between their profiles was more likely to have come from a comparison between samples from different people rather than from the same person (Extended Data Fig. 5b). As an individual’s microbial profile naturally changes over time<sup>10,92</sup>, the Bray–Curtis threshold at which this occurs will increase with the time difference between samples. To determine these thresholds, kernel density estimates were generated for the distribution of Bray–Curtis dissimilarities between profiles from different individuals without IBD and between samples from the individuals without IBD at a range of time differences, using the density function in R. The point at which the inter-individual density estimate exceeded the intra-individual density estimate was then taken as the threshold to define a ‘shift’, with the additional constraint that this must be a monotonically increasing function of the time difference between samples (Fig. 3a). Metabolomic shifts were defined similarly, although owing to the more sparse temporal sampling of the metabolomics data (Extended Data Fig. 1) and lack of a strong upward trend in Bray–Curtis dissimilarities with time difference (Fig. 3a), only a single threshold was used based on the distribution of Bray–Curtis dissimilarities from comparisons within-subject over time in participants without IBD. Heatmaps of shift differences were generated using the R package `phetmap` 1.0.10<sup>93</sup>.

**Longitudinal multi-omic study design.** Owing to the large variation in microbial profiles between people (Supplementary Fig. 2), with relatively smaller variation within subjects over time (Fig. 3a), longitudinal study designs have the potential to be higher-powered than purely cross-sectional studies, particularly in their ability to self-control individuals and to capture transitions between phenotypes (or after interventions) of interest<sup>94</sup>. Here, although some subjects remained in a dysbiotic state far longer than others (Extended Data Fig. 3d), the heterogeneity observed was enough to discover differences in measurement types other than where dysbiosis was defined. For example, subjects who had unusual, disease-associated

microbiome taxonomic profiles also proved to have generally shifted serological and/or metabolomic profiles at corresponding time points. Noting these dysbiotic time points offered a complementary set of differences to what was visible cross-sectionally (Fig. 2).

Among microbially related measurements, metabolomics provided the most robust separation between disease and dysbiosis groups, possibly because it integrated a combination of host, microbial, and dietary differences (Fig. 1e, f). Thus, despite the challenges presented by untargeted metabolomics, such as unknown compound identification, the presence of redundant and background signals, and the complexity of the stool matrix, this measurement type often provides a robust characterization of subjects, their disease state, and individual small molecules that interface between host and microbiome. Conversely, the current state of viromics assays and reference databases makes this more challenging to work with, although the importance of the virome in microbial community dynamics<sup>95</sup> will make this an extremely interesting feature space going forward.

All longitudinal microbial measurement types showed significant variation within two weeks (Fig. 3a, Extended Data Fig. 5a). This suggests that even higher sampling rates may be needed to catch relevant microbial variation, particularly before the onset of more severe clinical symptoms. Our sampling protocol also did not account for other potential sources of within-subject variation, such as transit time or the precise portion of each whole stool that was sampled. In this data set, we thus cannot distinguish between temporal and technical variation within subjects. To mitigate the higher costs associated with processing additional samples, a future study aiming to achieve higher temporal resolution might proceed in two phases, thanks to the coupling between data types (Fig. 1e): first, collect samples at a higher frequency, and process these with metagenomic or 16S sequencing. Then proceed with more expensive and detailed data generation only for samples taken specifically around periods of interest, such as periods of dysbiosis identified during the first stage. To this end, the sampling rate can also be tuned to target a particular probability of missing a dysbiosis period.

**Integrative analyses. Lenient cross-measurement type temporal matching.** For comparison between multiple measurement types, we first constructed sets of samples corresponding to the same biosample across data sets. However, exact matches were not always possible, for example, owing to specimen limitations during sample selection (see ‘Sample selection’) or to samples that failed quality control. In these cases, matching sample sets across data sets were created using nearby samples. During this process, a degree of leniency was allowed in the matching, allowing samples up to a given time difference (two or four weeks) apart to be ‘matched’. To perform this matching (sample numbers in Fig. 1c and Extended Data Fig. 1b), we used the following algorithm.

For a given set of measurement types to be matched for a particular subject, find the first time window in which all measurement types have at least one produced sample. Next, within this window, find the time point with the most measurement types produced; in the event of a tie, select earlier time points. Finally, for each data set, select the nearest sample to this target time point that is within the time window, breaking ties towards earlier time points. This set of selected samples comprises one ‘matched’ sample. For each data set, all samples up to and including the later of the selected sample or the target time point are then disregarded from future consideration (and thus any sample will be included in at most only one matched time point). This process is repeated for each subject until no such window exists.

**Cross-measurement type interaction testing.** Significant associations between features from multiple measurement types were identified using two different models: an ‘unadjusted’ model of associations that are mainly due to dysbiosis, and an ‘adjusted’ model that emphasizes associations in addition to those that are dysbiosis-linked. Associations in both cases incorporated features from ten data sets: metagenomic species, species-level transcription ratios, functional profiles at the EC level (MGX, MTX and MPX), metabolites, host transcription (rectal and ileal separately), serology and faecal calprotectin.

To detect adjusted associations, we first obtained residuals of features from the above data types fit to a mixed-effects model including subjects as random effects as above for the differential abundance testing (or a simple linear model without the random effects when only baseline samples were used) and adjusting for age, sex, diagnosis, dysbiosis status, antibiotic and immunosuppressant use, and bowel surgery status. Residuals from subjects with fewer than four samples in their time series for the measurement type were ignored, and for measurements with no longitudinal samples (for example, serology and host transcriptomics measurements), the residualization was repeated with the first available samples using a simple linear model without random effects. This allowed the identification of significant (FDR  $P < 0.05$  for most measurement types,  $P < 0.25$  for serology) Spearman associations using HALLA 0.8.17 (hierarchical all-against-all association testing, <http://huttenhower.sph.harvard.edu/halla>, Supplementary Table 35). As subject-specific random effects and covariate effects were removed from these residuals, the resulting correlations are likely to be independent of all sources of

inter-individual variation as well as confounding effects due to the covariates. See Fig. 4c and Extended Data Figs. 7–9 for summary visualizations of these results. Similarly, unadjusted associations were identified using the same procedure, but without including dysbiosis as a covariate (Supplementary Table 36). Network visualization was done using Cytoscape<sup>96</sup> 3.6.0.

**Reporting summary.** Further information on research design is available in the Nature Research Reporting Summary linked to this paper.

## Data availability

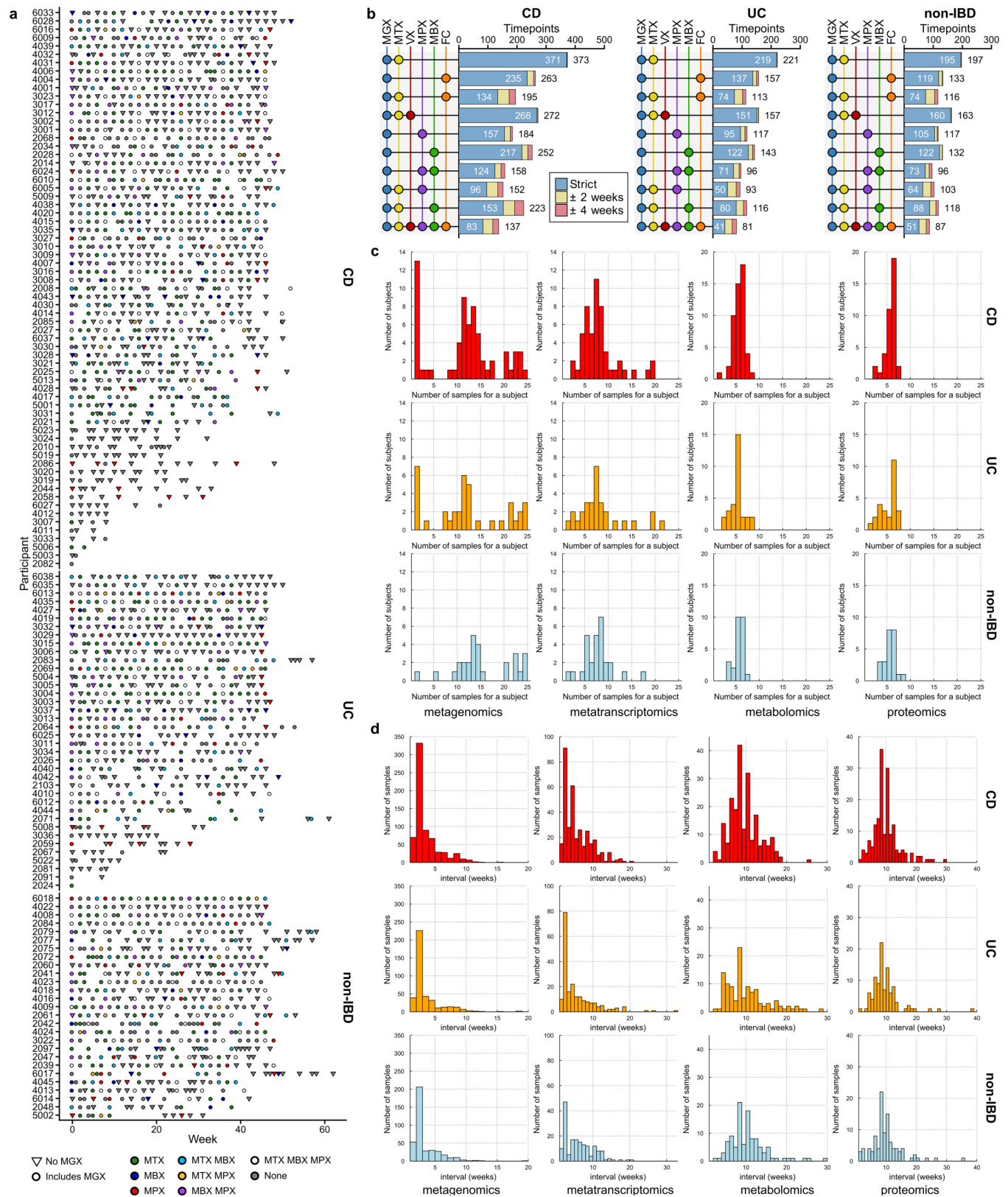
Protocols and data (both raw and summarized to data type-dependent profiles) are available at the IBDMDDB website (<https://ibdmdb.org>), the HMP DACC web portal (<https://www.hmpdacc.org/ihmp/>), and Qiita<sup>97</sup> (<https://qiita.ucsf.edu/>). Sequence data are available from SRA BioProject PRJNA398089. Expression data have been deposited in the NCBI Gene Expression Omnibus<sup>98</sup> and is accessible through GEO Series accession number GSE111889. Metabolomics data are available at the NIH Common Fund's Metabolomics Data Repository and Coordinating Center (supported by NIH grant U01-DK097430) website, the Metabolomics Workbench (<http://www.metabolomicsworkbench.org>), where it has been assigned Project ID PR000639. Mass spectrometry proteomics data have been deposited to the ProteomeXchange Consortium via the PRIDE<sup>99</sup> partner repository with the data set identifiers PXD008675 and 10.6019/PXD008675. Reprints and permissions information is available at [www.nature.com/reprints](http://www.nature.com/reprints).

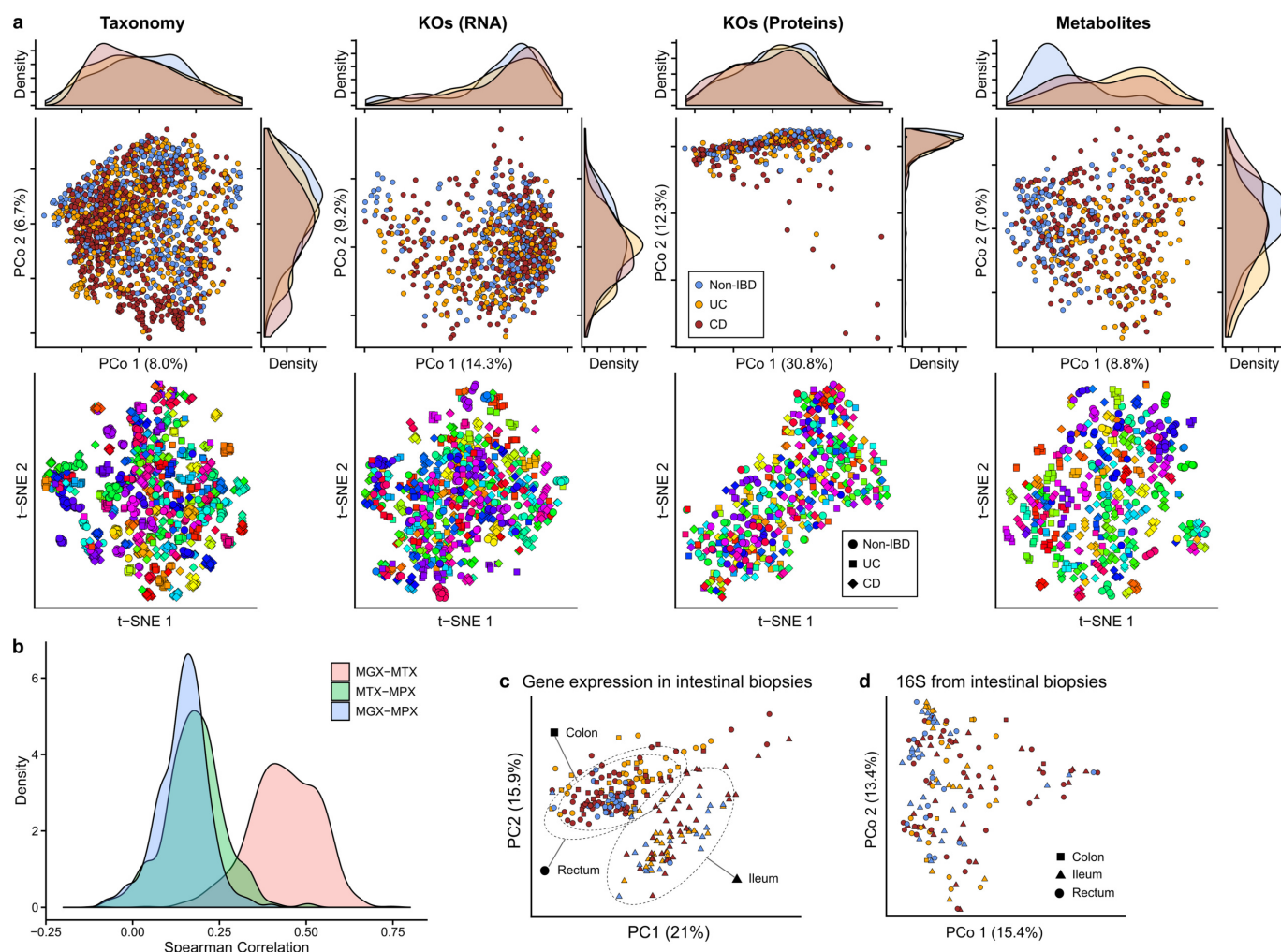
## Code availability

Bioinformatics workflows for metagenomics and metatranscriptomics data are available at [https://bitbucket.org/biobakery/hmp2\\_workflows](https://bitbucket.org/biobakery/hmp2_workflows). Analysis scripts are available at [https://bitbucket.org/biobakery/hmp2\\_analysis](https://bitbucket.org/biobakery/hmp2_analysis).

46. Franzosa, E. A. et al. Relating the metatranscriptome and metagenome of the human gut. *Proc. Natl Acad. Sci. USA* **111**, E2329–E2338 (2014).
47. Vogtmann, E. et al. Comparison of collection methods for fecal samples in microbiome studies. *Am. J. Epidemiol.* **185**, 115–123 (2017).
48. Lofftfield, E. et al. Comparison of collection methods for fecal samples for discovery metabolomics in epidemiologic studies. *Cancer Epidemiol. Biomarkers Prev.* **25**, 1483–1490 (2016).
49. Voigt, A. Y. et al. Temporal and technical variability of human gut metagenomes. *Genome Biol.* **16**, 73 (2015).
50. Jowett, S. L., Seal, C. J., Barton, J. R. & Welfare, M. R. The short inflammatory bowel disease questionnaire is reliable and responsive to clinically important change in ulcerative colitis. *Am. J. Gastroenterol.* **96**, 2921–2928 (2001).
51. Daperno, M. et al. Development and validation of a new, simplified endoscopic activity score for Crohn's disease: the SES-CD. *Gastrointest. Endosc.* **60**, 505–512 (2004).
52. Baron, J. H., Connell, A. M. & Lennard-Jones, J. E. Variation between observers in describing mucosal appearances in proctocolitis. *BMJ* **1**, 89–92 (1964).
53. Schirmer, M. et al. Dynamics of metatranscription in the inflammatory bowel disease gut microbiome. *Nat. Microbiol.* **3**, 337–346 (2018).
54. Shishkin, A. A. et al. Simultaneous generation of many RNA-seq libraries in a single reaction. *Nat. Methods* **12**, 323–325 (2015).
55. Zhu, Y. Y., Machleder, E. M., Chenchik, A., Li, R. & Siebert, P. D. Reverse transcriptase template switching: a SMART approach for full-length cDNA library construction. *Biotechniques* **30**, 892–897 (2001).
56. Clem, A. L., Sims, J., Telang, S., Eaton, J. W. & Chesney, J. Virus detection and identification using random multiplex (RT)-PCR with 3'-locked random primers. *Virology* **4**, 65 (2007).
57. Ajami, N. J., Wong, M. C., Ross, M. C., Lloyd, R. E. & Petrosino, J. F. Maximal viral information recovery from sequence data using VirMAP. *Nat. Commun.* **9**, 3205 (2018).
58. Kostic, A. D. et al. The dynamics of the human infant gut microbiome in development and in progression toward type 1 diabetes. *Cell Host Microbe* **17**, 260–273 (2015).
59. Kim, S. & Pevzner, P. A. MS-GF+ makes progress towards a universal database search tool for proteomics. *Nat. Commun.* **5**, 5277 (2014).
60. Thompson, L. R. et al. A communal catalogue reveals Earth's multiscale microbial diversity. *Nature* **551**, 457–463 (2017).
61. Caporaso, J. G. et al. Ultra-high-throughput microbial community analysis on the Illumina HiSeq and MiSeq platforms. *ISME J.* **6**, 1621–1624 (2012).
62. Human Microbiome Project Consortium. Structure, function and diversity of the healthy human microbiome. *Nature* **486**, 207–214 (2012).
63. Human Microbiome Project Consortium. A framework for human microbiome research. *Nature* **486**, 215–221 (2012).
64. Edgar, R. C. Search and clustering orders of magnitude faster than BLAST. *Bioinformatics* **26**, 2460–2461 (2010).
65. Edgar, R. C. UPARSE: highly accurate OTU sequences from microbial amplicon reads. *Nat. Methods* **10**, 996–998 (2013).
66. Pruesse, E. et al. SILVA: a comprehensive online resource for quality checked and aligned ribosomal RNA sequence data compatible with ARB. *Nucleic Acids Res.* **35**, 7188–7196 (2007).
67. Landers, C. J. et al. Selected loss of tolerance evidenced by Crohn's disease-associated immune responses to auto- and microbial antigens. *Gastroenterology* **123**, 689–699 (2002).
68. Targan, S. R. et al. Antibodies to CBir1 flagellin define a unique response that is associated independently with complicated Crohn's disease. *Gastroenterology* **128**, 2020–2028 (2005).
69. Fisher, S. et al. A scalable, fully automated process for construction of sequence-ready human exome targeted capture libraries. *Genome Biol.* **12**, R1 (2011).
70. Gu, H. et al. Preparation of reduced representation bisulfite sequencing libraries for genome-scale DNA methylation profiling. *Nat. Protocols* **6**, 468–481 (2011).
71. Mciver, L. J. et al. bioBakery: A meta'omic analysis environment. *Bioinformatics* **34**, 1235–1237 (2018).
72. Truong, D. T. et al. MetaPhlAn2 for enhanced metagenomic taxonomic profiling. *Nat. Methods* **12**, 902–903 (2015).
73. Franzosa, E. A. et al. Species-level functional profiling of metagenomes and metatranscriptomes. *Nat. Methods* **15**, 962–968 (2018).
74. Huang, K. et al. MetaRef: a pan-genomic database for comparative and community microbial genomics. *Nucleic Acids Res.* **42**, D617–D624 (2014).
75. Suzek, B. E., Wang, Y., Huang, H., McGarvey, P. B. & Wu, C. H. UniRef clusters: a comprehensive and scalable alternative for improving sequence similarity searches. *Bioinformatics* **31**, 926–932 (2015).
76. Wickham, H. *ggplot2: Elegant Graphics for Data Analysis* (Springer, New York, 2016).
77. Buchfink, B., Xie, C. & Huson, D. H. Fast and sensitive protein alignment using DIAMOND. *Nat. Methods* **12**, 59–60 (2015).
78. Oksanen, J. et al. vegan: Community Ecology Package. R package version 2.5-3. <https://CRAN.R-project.org/package=vegan> (2018).
79. Pinheiro, J. et al. nlme: Linear and Nonlinear Mixed Effects Models. R package version 3.1-108. <https://CRAN.R-project.org/package=nlme> (2013).
80. Robinson, M. D., McCarthy, D. J. & Smyth, G. K. edgeR: a Bioconductor package for differential expression analysis of digital gene expression data. *Bioinformatics* **26**, 139–140 (2010).
81. McCarthy, D. J., Chen, Y. & Smyth, G. K. Differential expression analysis of multifactor RNA-seq experiments with respect to biological variation. *Nucleic Acids Res.* **40**, 4288–4297 (2012).
82. Kanehisa, M., Furumichi, M., Tanabe, M., Sato, Y. & Morishima, K. KEGG: new perspectives on genomes, pathways, diseases and drugs. *Nucleic Acids Res.* **45**, D353–D361 (2017).
83. Ritchie, M. E. et al. limma powers differential expression analyses for RNA-sequencing and microarray studies. *Nucleic Acids Res.* **43**, e47 (2015).
84. The 1000 Genomes Project Consortium A global reference for human genetic variation. *Nature* **526**, 68–74 (2015).
85. Purcell, S. et al. PLINK: a tool set for whole-genome association and population-based linkage analyses. *Am. J. Hum. Genet.* **81**, 559–575 (2007).
86. Jostins, L. et al. Host-microbe interactions have shaped the genetic architecture of inflammatory bowel disease. *Nature* **491**, 119–124 (2012).
87. Liu, J. Z. et al. Association analyses identify 38 susceptibility loci for inflammatory bowel disease and highlight shared genetic risk across populations. *Nat. Genet.* **47**, 979–986 (2015).
88. Hall, A. B., Tolonen, A. C. & Xavier, R. J. Human genetic variation and the gut microbiome in disease. *Nat. Rev. Genet.* **18**, 690–699 (2017).
89. Enattah, N. S. et al. Identification of a variant associated with adult-type hypolactasia. *Nat. Genet.* **30**, 233–237 (2002).
90. Sheather, S. J. & Jones, M. C. A reliable data-based bandwidth selection method for kernel density estimation. *J. R. Stat. Soc.* **53**, 683–690 (1991).
91. Kenward, M. G. & Roger, J. H. An improved approximation to the precision of fixed effects from restricted maximum likelihood. *Comput. Stat. Data Anal.* **53**, 2583–2595 (2009).
92. Faith, J. J. et al. The long-term stability of the human gut microbiota. *Science* **341**, 1237439 (2013).
93. Kolde, R. *Pheatmap: pretty heatmaps*. R Package Version 1.0.10. <https://CRAN.R-project.org/package=pheatmap> (2012).
94. Gibbons, R. D., Hedeker, D. & DuToit, S. Advances in analysis of longitudinal data. *Annu. Rev. Clin. Psychol.* **6**, 79–107 (2010).
95. Minot, S. et al. The human gut virome: inter-individual variation and dynamic response to diet. *Genome Res.* **21**, 1616–1625 (2011).
96. Shannon, P. et al. Cytoscape: a software environment for integrated models of biomolecular interaction networks. *Genome Res.* **13**, 2498–2504 (2003).
97. Gonzalez, A. et al. Qiita: rapid, web-enabled microbiome meta-analysis. *Nat. Methods* **15**, 796–798 (2018).
98. Edgar, R., Domrachev, M. & Lash, A. E. Gene Expression Omnibus: NCBI gene expression and hybridization array data repository. *Nucleic Acids Res.* **30**, 207–210 (2002).
99. Vizcaino, J. A. et al. 2016 update of the PRIDE database and its related tools. *Nucleic Acids Res.* **44**, D447–D456 (2016).
100. Suzek, B. E., Huang, H., McGarvey, P., Mazumder, R. & Wu, C. H. UniRef: comprehensive and non-redundant UniProt reference clusters. *Bioinformatics* **23**, 1282–1288 (2007).
101. Bar-Joseph, Z., Gifford, D. K. & Jaakkola, T. S. Fast optimal leaf ordering for hierarchical clustering. *Bioinformatics* **17** (Suppl. 1), S22–S29 (2001).
102. Silverman, B. W. *Density Estimation for Statistics and Data Analysis* 48, eqn 43.31 (Chapman and Hall, 1986).
103. Wellcome Trust Case Control Consortium. Genome-wide association study of 14,000 cases of seven common diseases and 3,000 shared controls. *Nature* **447**, 661–678 (2007).



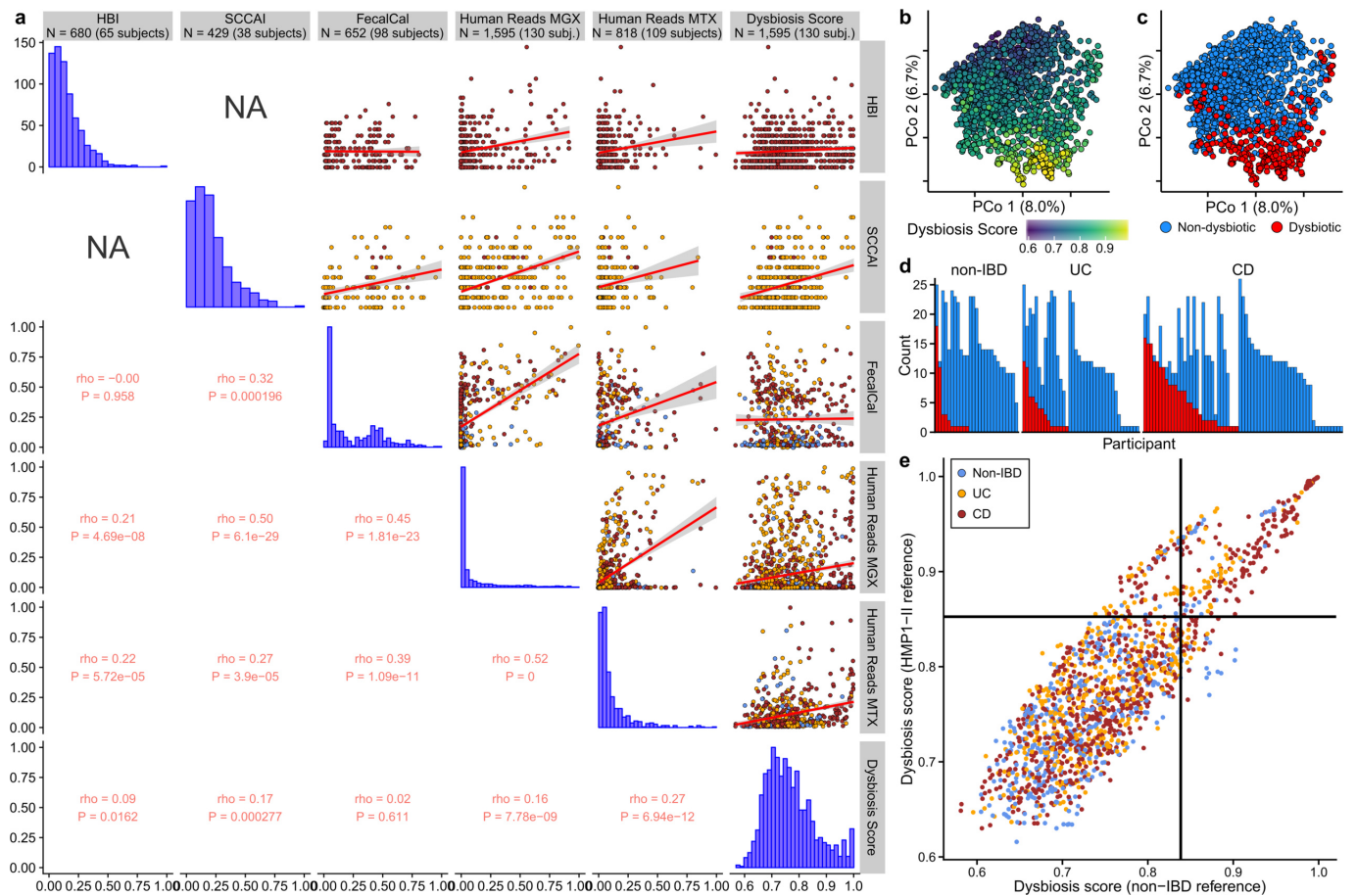




**Extended Data Fig. 2 | Within-individual stability is a major driver of microbiome differences across measurement types.** **a**, PCoA and t-SNE embeddings based on Bray–Curtis dissimilarity matrices from stool species abundances, transcripts, proteins, and metabolites. Marginal densities are shown for the PCoAs that show disease separation for some measurements. In the t-SNEs, each subject has been assigned a different hue, showing that small clusters generally represent individuals' time courses, as inter-individual differences are the greatest driver of microbiome variation across measurement types (Fig. 1f). Sample counts are shown in Fig. 1b. **b**, Distributions of correlations between functional profiles, captured as UniRef90<sup>100</sup> gene family abundances<sup>73</sup>,

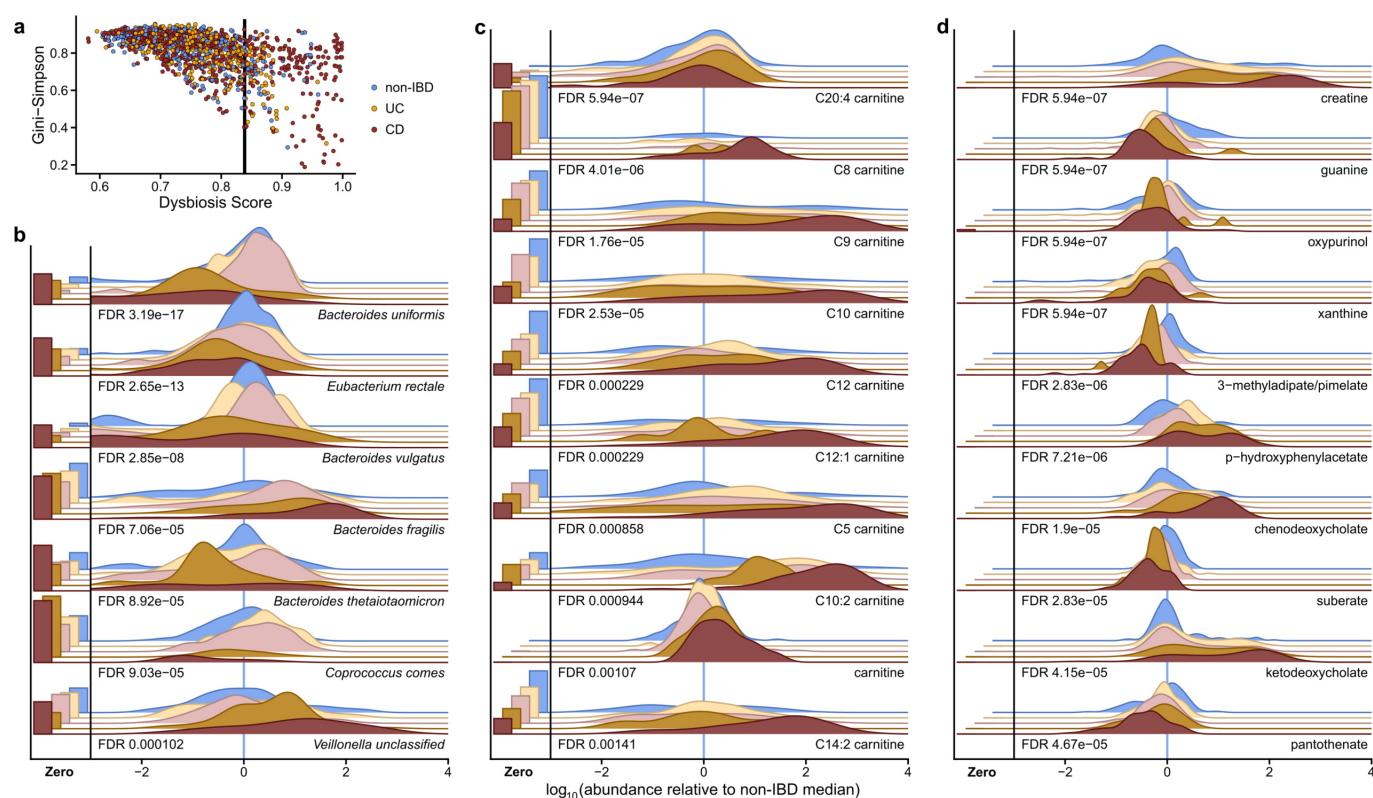
measured from paired metagenomes, metatranscriptomes, and metaproteomes (see Methods). **c**, Human transcriptional expression was mostly determined by biopsy location rather than IBD phenotype and inflammation ( $n = 249$  samples from 91 subjects). Ordination shows PCA on gene expression levels normalized by library sizes and represented as CPM. Ellipses indicate 95% confidence regions for the indicated sample types. **d**, Principal coordinates plot (Bray–Curtis on OTU profiles) of community profiles from biopsy samples shows that mucosal microbial communities do not differ significantly by biopsy location (shape), unlike human gene expression in epithelial tissue (Fig. 4b).





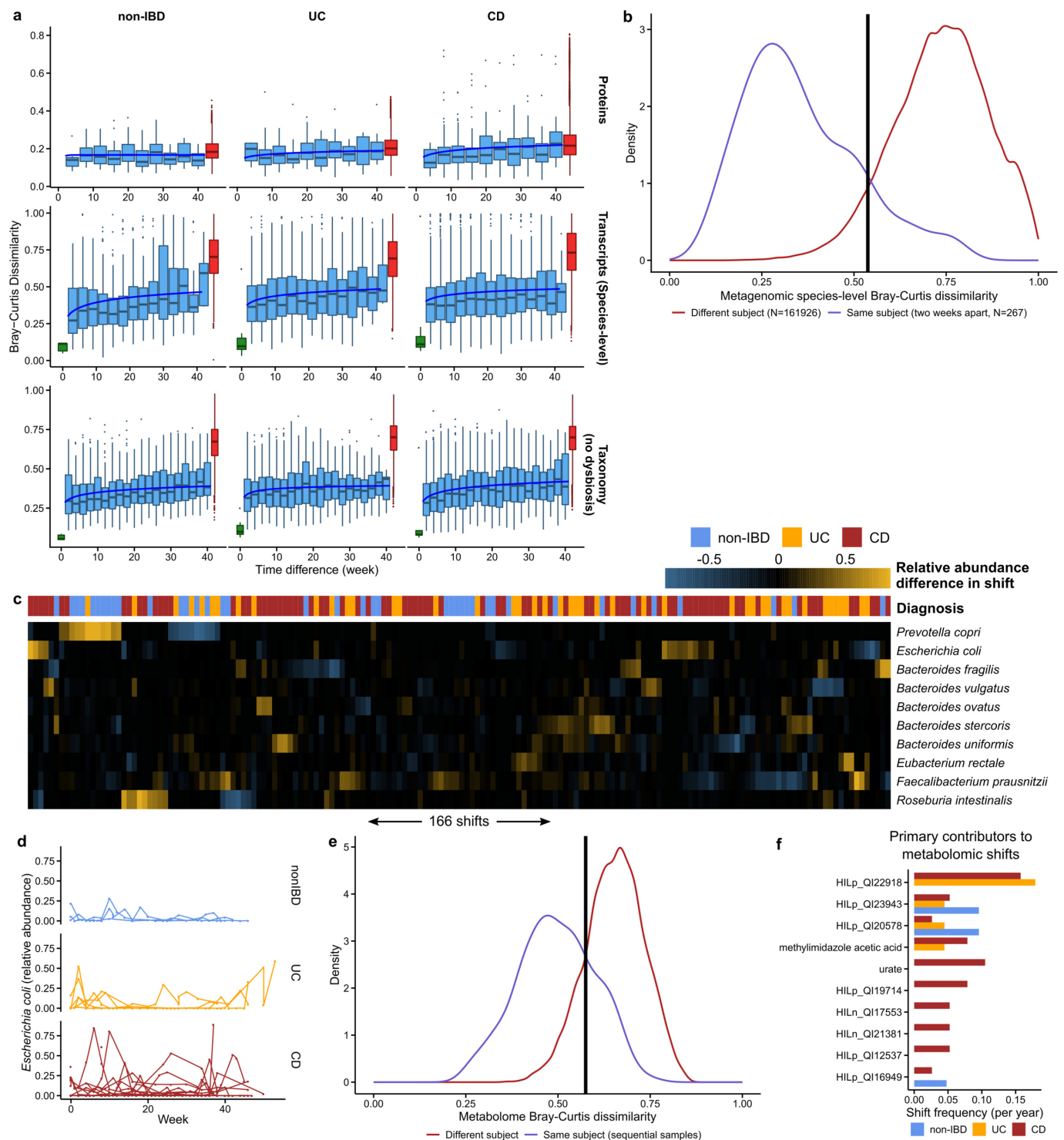
**Extended Data Fig. 3 | Patient-reported, molecular, and microbial disease activity measures.** **a**, Relationships between six measures of disease activity: the patient-reported HBI in CD, patient-reported SCCAI in UC, faecal calprotectin, the fractions of human reads from stool MGX and MTX, and a dysbiosis score defined here as departures from control population microbiome configurations (Fig. 2c). Rho values are Spearman correlations with ties broken randomly. Linear regression is shown (red line) with 95% confidence bound (shaded). Sample counts are presented in the title bar, though sample counts for a particular correlation may be less as samples must be paired. **b**, **c**, PCoA based on metagenomic species-

level Bray–Curtis dissimilarities ( $n = 1,595$  samples from 130 subjects), indicating dysbiosis score (b) and whether the sample was defined as dysbiotic (c). **d**, Number of dysbiotic samples per participant. Colour scheme as in c. **e**, Relationship between the dysbiosis score, when using the HMP1-II gut data set as reference ( $n = 553$  from 249 subjects), compared to the non-IBD data set. The threshold for the dysbiosis classification is also shown (black lines). The two scores are highly correlated (Pearson  $\rho = 0.86$ ; two-sided  $P < 2.2 \times 10^{-16}$ ), as are the resulting dysbiosis classifications (odds ratio of 56; Fisher's exact test  $P < 2.2 \times 10^{-16}$ ).  $n = 1,595$  samples from 130 subjects.



**Extended Data Fig. 4 | Significant microbial and metabolic perturbations during taxonomic dysbioses. a**, Alpha diversity (Gini-Simpson) as a function of the dysbiosis score for the sample (Pearson correlation  $-0.60$ ;  $P < 2.2 \times 10^{-16}$ ).  $n = 1,595$  samples from 130 subjects. **b**, Seven (chosen for space constraints) most differentially abundant species not shown elsewhere in this manuscript ( $n = 1,595$  samples from 130 subjects; Wald test; see Methods; full results in

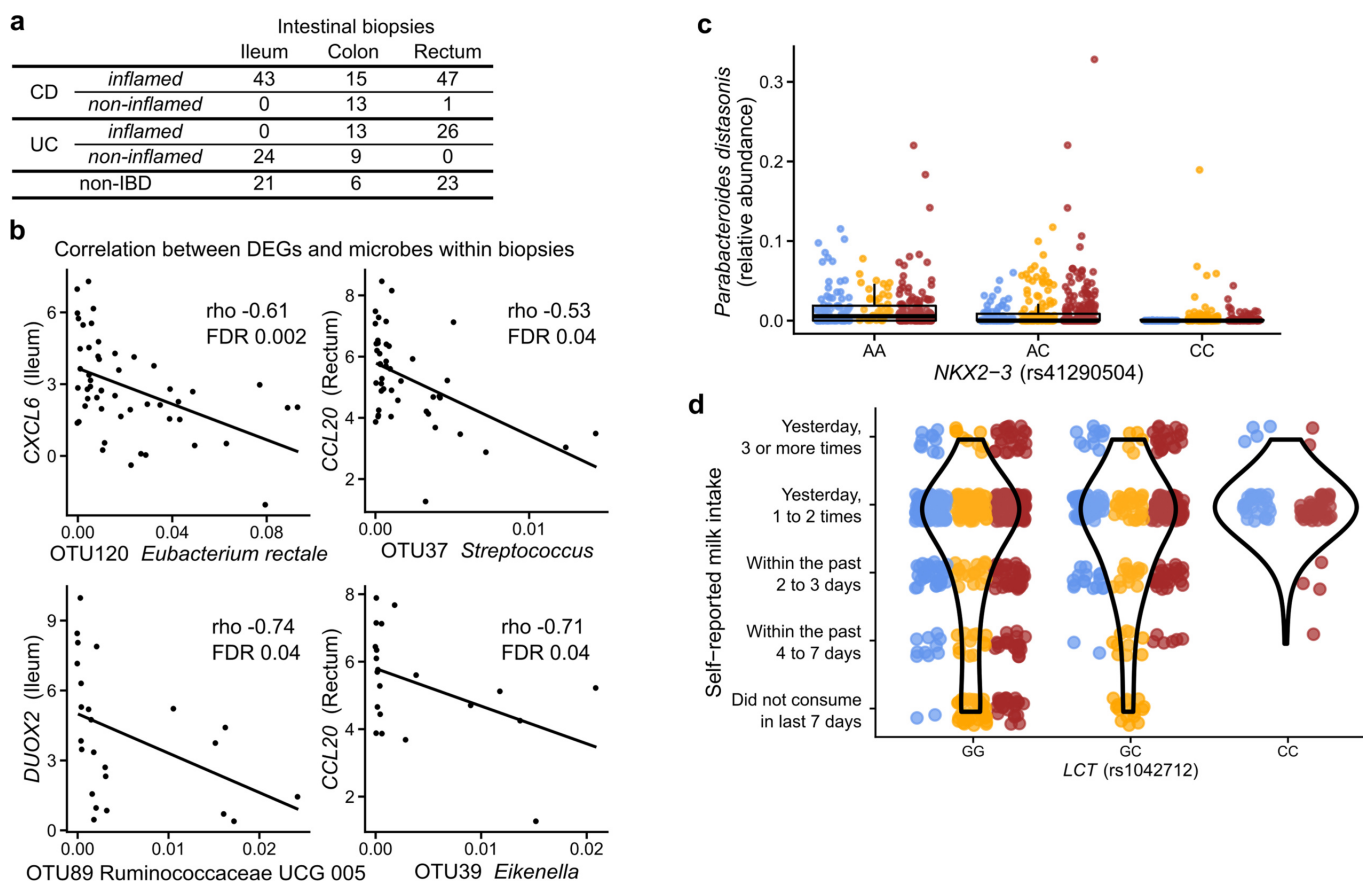
Supplementary Table 15). **c**, Top 10 differentially abundant acylcarnitines in dysbiosis ( $n = 546$  samples from 106 subjects; Wald test). Carnitine and acylcarnitines are more abundant in dysbiotic CD, whereas C20:4 carnitine is significantly depleted (Supplementary Table 16). **d**, Top 10 differentially abundant metabolites during dysbiosis not shown elsewhere in this manuscript ( $n = 546$  samples from 106 subjects; Wald test; full results in Supplementary Table 16).



Extended Data Fig. 5 | See next page for caption.

**Extended Data Fig. 5 | Detecting shifts in longitudinal microbiome multi-omics.** **a**, Distributions of Bray–Curtis dissimilarities as a function of time difference between samples for protein profiles, species-level transcriptional activity (see Methods), and species-level taxonomy (though excluding subjects with dysbiosis at any time point), otherwise as in Fig. 3a. Removing subjects with dysbiotic samples removes the extreme dissimilarities (near 1) observed in IBD subjects. Boxplots show median and lower/upper quartiles; whiskers show inner fences. **b**, Distribution of Bray–Curtis dissimilarities between samples from the same subject, two weeks apart versus those from different individuals, allowing us to define a ‘shift’ in the microbiome as a change more likely to have been drawn from the between-subject distribution than within-subject distances (corresponding to Bray–Curtis > 0.54). **c**, Relative abundance differences of the top ten microorganisms that contributed to each of the 183 detected taxonomic shifts among any two within-subject subsequent time points. Shifts are typically reciprocal (that is, losing a microorganism and regaining it later, or vice versa), and microorganism with frequent high-abundance shifts generally correspond to frequent contributors in Fig. 3b. Sample ordering is from a hierarchical clustering using average linkage followed by optimal leaf ordering<sup>101</sup>. **d**, As in Fig. 3c, but for *E. coli*

( $n = 322$  samples from 24 subjects; two-tailed Wilcoxon test of the absolute differences in relative abundances between consecutive time points  $P = 2.2 \times 10^{-4}$  for non-IBD to UC, and  $P = 0.029$  for non-IBD to CD), which is frequently implicated in gut inflammation. **e**, As in **b**, but showing Bray–Curtis dissimilarities of metabolomic profiles. Here, 22% (96 out of 440) of sample pairs exceed the shift threshold, whereas 13% (183 out of 1,413) exceed the threshold in **b**. If metagenomic profiles are sub-sampled to match the metabolomics samples, this increases to 14% (57 out of 398) of sample pairs, showing that if we increased the sampling rate, this measurement type would be likely to shift more than the metagenomes. **f**, As in Fig. 3b, but showing the primary contributors to metabolomic shifts, that is, the metabolite with the largest change in relative abundance during a shift. Note that other metabolites may still experience large changes in abundance (for example, for this reason, urate was not a primary contributor to any non-IBD shifts, though large changes are visible for one non-IBD individual in Fig. 3e). The full table of detected metabolomic shifts is given in Supplementary Table 30. Violin plot shows the density of points around that intake frequency; bandwidth chosen automatically by Silverman’s method<sup>102</sup>.

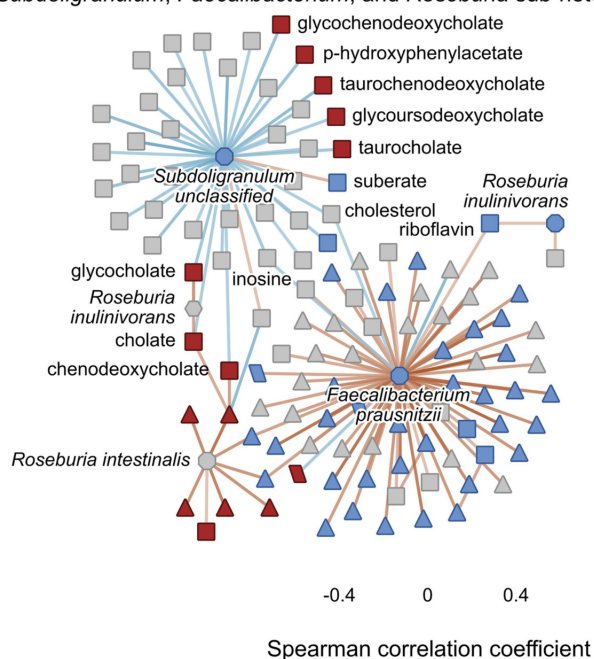


# Extended Data Fig. 6 | Mucosal communities and human genetics.

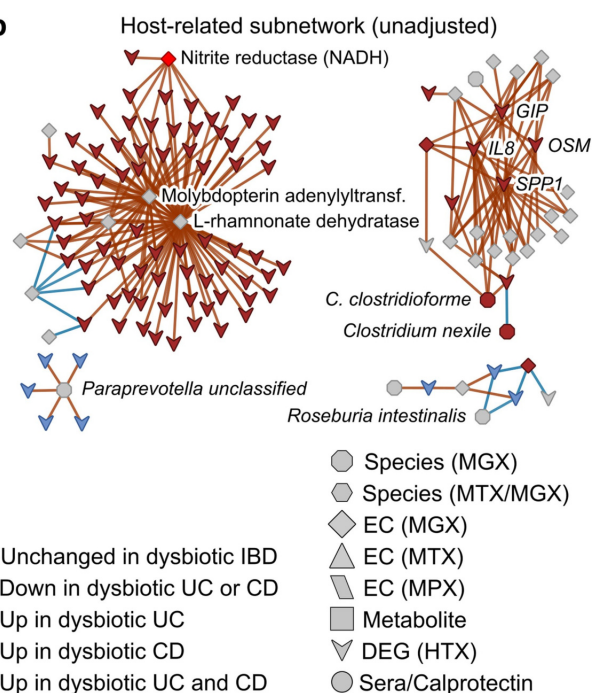
**a**, Number of biopsy samples available for each biopsy location and inflammation status. **b**, DEGs (Fig. 4a) with newly identified significant correlations with OTU abundances in biopsies (partial Spearman correlation conditioned on disease status, BMI, age at consent and sex; FDR  $P < 0.05$ ;  $n = 54$  in ileum and  $n = 52$  independent 16S–RNA-seq pairs; full table in Supplementary Table 33). **c**, A limited subset of the microbiome trended with genetic variants in targeted testing, including the strongest trend shown here of *Parabacteroides distasonis* with genotypes of *NKX2-3* (a known IBD-associated locus<sup>103</sup>; boxplots show median and lower/upper quartiles; whiskers show inner fences). This is the most significant association by  $P$  value among all tested associations between metagenomic taxa and five known IBD loci (nominal significance  $P = 0.006$ ; no associations passed FDR  $P < 0.05$ , mixed effect model with age, sex, antibiotic and immunosuppressant use and first 20 genetic principal components as covariates while specifying subjects as random

effects; Wald test;  $n = 84$  subjects of European ancestry with exomes and 960 metagenomes; full results in Supplementary Table 34). **d**, Association between rs1042712 SNP in the *LCT* locus and self-reported milk intake from dietary recall. Self-reported short-term milk intake (from dietary recalls accompanying stool samples) was significantly associated with the count of C alleles (29.8% allele frequency) at rs1042712 in the *LCT* gene locus using a linear mixed effect model accounting for age, sex, first 20 genetic principal components and with subjects as random effects ( $P = 0.028$ , linear mixed effect regression with Wald test, see Methods). All available data are plotted for unique subjects of European ancestry with exome data (per-genotype subject count (GG/GC/CC):50/26/8). Differences between IBD and non-IBD groups are not statistically significant (odds ratio 0.27; 95% CI 0.05–1.33;  $P = 0.10$ ;  $n = 84$  subjects of European ancestry with exomes and 960 dietary surveys; model: IBD (yes/no) ~ intercept + SNP + sex + age + PC1–PC20).

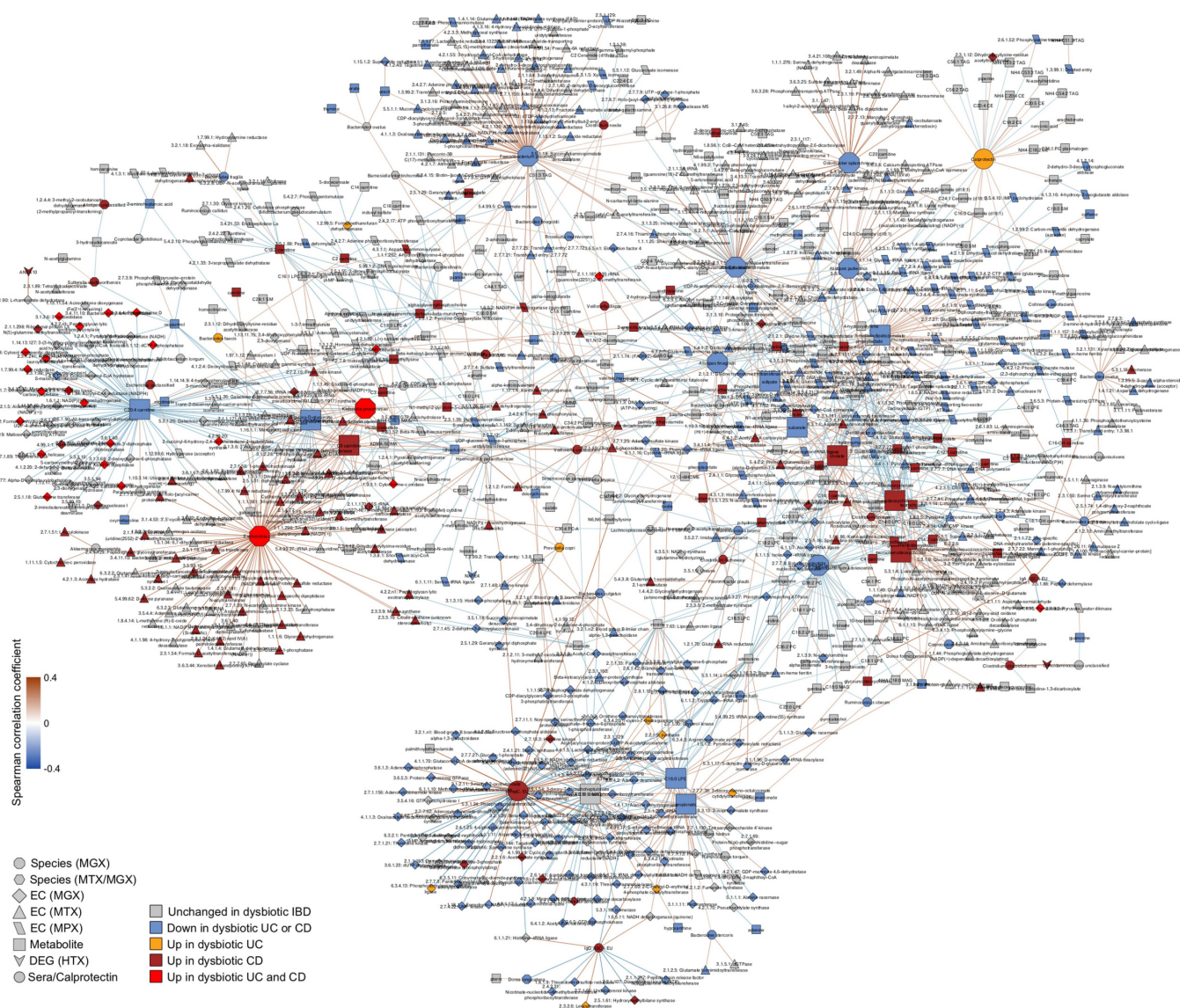


**a** *Subdoligranulum*, *Faecalibacterium*, and *Roseburia* sub-networks

**Extended Data Fig. 7 | Microbial and host-related subsets of the multi-omic association networks.** **a**, Subset of the network in Fig. 4c showing metagenomic abundances (octagons) and expression levels (hexagons) of *Subdoligranulum*, *Roseburia* spp. and *F. prausnitzii* and their neighbours (three functionally associated microbial hubs selected for further

**b**

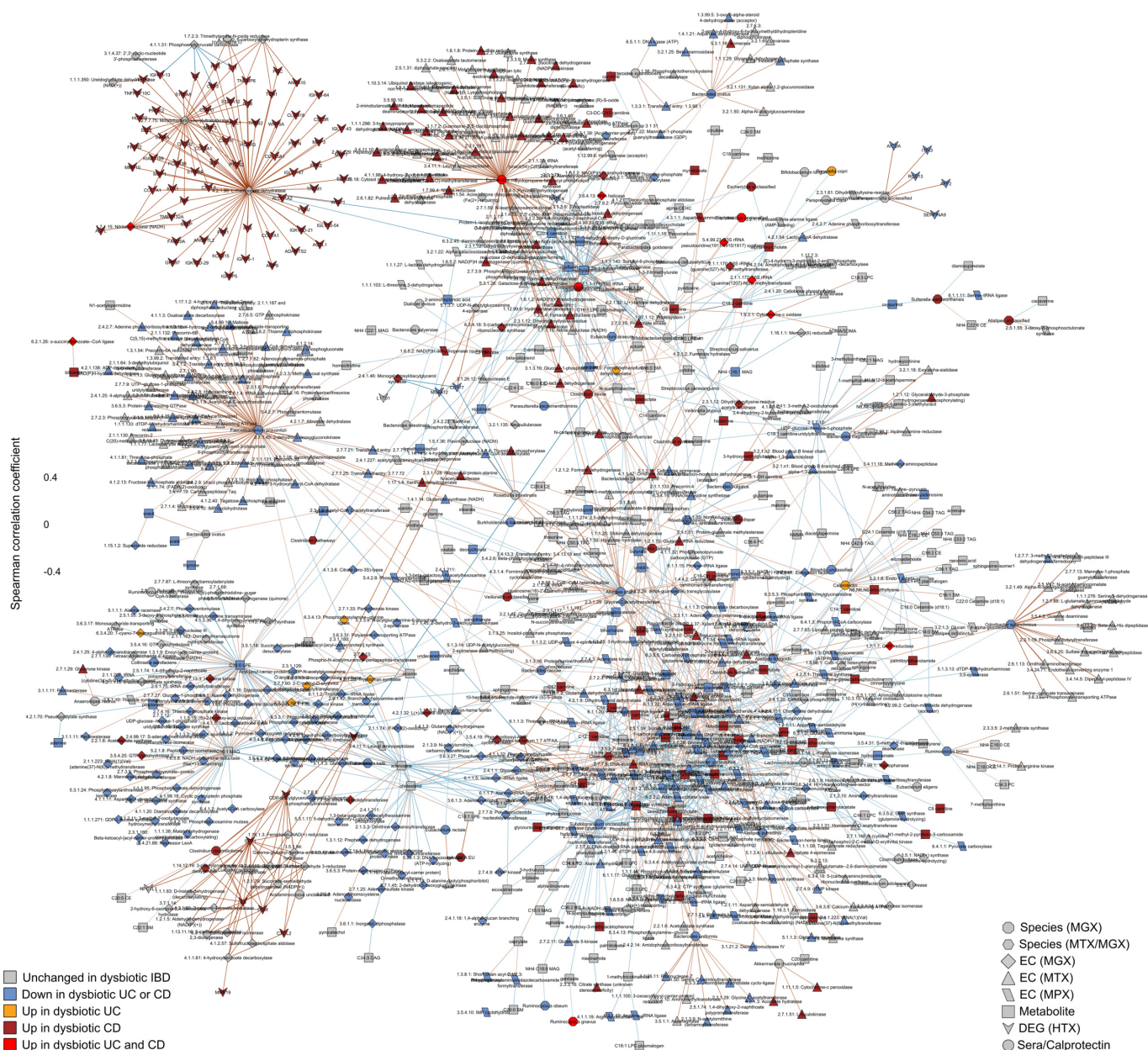
investigation based on anti-inflammatory associations in the literature, see text). **b**, The host expression-related subnetwork of the 'unadjusted' association network (Extended Data Fig. 9, Supplementary Discussion). Sample counts in Fig. 1b, c.



**Extended Data Fig. 8 | Significant covariation among multi-omic components of the gut microbiome and host interactors in IBD (adjusted).** Detailed labelling of the association network in Fig. 4c (intended for magnification). The network was constructed from ten data sets: metagenomic species, species-level transcription ratios, functional profiles at the EC levels (MGX, MTX and MPX), metabolites, host transcription (rectal and ileal separately), serology and faecal calprotectin. As in Fig. 4c, measurement types were approximately matched in time with a maximum separation between paired samples of four weeks. The top 300 significant correlations (FDR  $P < 0.05$ ) among correlations between features that were differentially abundant in dysbiosis were used to construct the network visualized here (for serology, a threshold

of FDR  $P < 0.25$  was used). Nodes are coloured by the disease group in which they are 'high', and edges are coloured by the sign and strength of the correlation. For this adjusted network, Spearman correlations were calculated using HALLA from the residuals of a mixed-effects model with subjects as random effects (or a simple linear model without the random effects when only baseline samples were used) after adjusting for age, sex, diagnosis, dysbiosis status, recruitment site, and antibiotics (see Methods). Appropriate normalization and/or transformation for each measurement type was performed independently before the model fitting (see Methods). Singleton node pairs were pruned from the network. Source associations are in Supplementary Table 35, sample counts in Fig. 1b, c.





**Extended Data Fig. 9 | Significant covariation among multi-omic components of the gut microbiome and host interactors in IBD (unadjusted).** The network was constructed from ten data sets: metagenomic species, species-level transcription ratios, functional profiles at the EC levels (MGX, MTX and MPX), metabolites, host transcription (rectal and ileal separately), serology and faecal calprotectin. As in Fig. 4c, measurement types were approximately matched in time with a maximum separation between paired samples of four weeks. The top 300 significant correlations ( $FDR\ P < 0.05$ ) among correlations between features that were differentially abundant in dysbiosis were used to construct the

network visualized here (for serology, a threshold of FDR  $P < 0.25$  was used). Nodes are coloured by the disease group in which they are 'high', and edges are coloured by the sign and strength of the correlation. For this unadjusted network, Spearman correlations were calculated using HALLA from the residuals of the same model as in Extended Data Fig. 8, though without adjusting for dysbiosis (see Methods). Appropriate normalization and/or transformation for each measurement type was performed independently before the model fitting (see Methods). Singleton node pairs were pruned from the network. Source associations are in Supplementary Table 36, sample counts in Fig. 1b, c.

Extended Data Table 1 | IBDMDB cohort characteristics

		Cedars-Sinai	Emory	Cincinnati	MGH	MGH Ped.	Total
Diagnosis	Subjects	33	11	33	38	17	132
	non-IBD	1	1	9	13	3	27
	UC	12	3	7	11	5	38
	CD	20	7	17	14	9	67
Sex	Female	24	6	16	15	3	64
	Male	9	5	17	23	14	68
Ethnicity	American Indian/Alaska Native					1	1
	Black or African American		6	2	2		10
	More than one race		3	1	1		5
	Other	1			3		4
	White	32	2	30	32	16	112
	Age (years)	45.0 ± 13.0 [26 - 76]	12.6 ± 3.8 [7 - 17]	12.9 ± 2.9 [6 - 17]	35.9 ± 14.5 [18 - 74]	13.9 ± 3.2 [6 - 17]	27.5 ± 17.3 [6 - 76]
	Height (cm)	169.7 ± 9.5 [152 - 188]	148.7 ± 10.7 [137 - 158]	157.9 ± 15.8 [112 - 182]	169.4 ± 11.4 [142 - 188]	164.1 ± 20.8 [114.3 - 193]	163.5 ± 15.5 [112 - 193]
	Weight (kg)	66.4 ± 13.0 [54.9 - 87.1]	43.9 ± 4.1 [41.0 - 46.8]	65.0 ± 23.5 [19.3 - 115.7]	71.8 ± 16.6 [37 - 100]	53.9 ± 18.6 [19.6 - 75.0]	65.1 ± 20.1 [19.3 - 115.7]
	BMI	28.4 ± 10.2 [19.5 - 50.2]	18.8 ± 3.2 [16.3 - 22.4]	21.1 ± 6.1 [13.5 - 35.6]	24.4 ± 5.1 [19.1 - 40.6]	19.1 ± 4.4 [13.5 - 28.4]	22.9 ± 7.1 [13.5 - 50.2]
	L1	1	2		8		11
	L1+L4			4		1	5
	L2	2			2	1	5
	L2+L4			1			1
	L3	9	1	5	2	2	19
	L3+L4		1	7		4	12
CD Montreal Location	N/A	8	3		2	1	14
UC Extent	Ulcerative proctitis			1		1	2
	Left-sided UC	2		2	1		5
	Extensive UC / Pancolitis	2	1	3	2	1	9
	N/A	8	2	1	8	3	22

Breakdown of the cohort by diagnosis, sex, ethnicity, physical characteristics, and disease location for each clinical site. Numeric data are summarized as mean ± s.d., with the range given by [min–max], and with blank cells for NA (not applicable). Subject counts for disease locations are subsets of the respective diseases.

## Life Sciences Reporting Summary

Nature Research wishes to improve the reproducibility of the work that we publish. This form is intended for publication with all accepted life science papers and provides structure for consistency and transparency in reporting. Every life science submission will use this form; some list items might not apply to an individual manuscript, but all fields must be completed for clarity.

For further information on the points included in this form, see [Reporting Life Sciences Research](#). For further information on Nature Research policies, including our [data availability policy](#), see [Authors & Referees](#) and the [Editorial Policy Checklist](#).

Please do not complete any field with "not applicable" or n/a. Refer to the help text for what text to use if an item is not relevant to your study. For final submission: please carefully check your responses for accuracy; you will not be able to make changes later.

### ► Experimental design

#### 1. Sample size

Describe how sample size was determined.

The target sample size calculated for at least  $n=72$  subjects with repeated measures was designed to have power of 0.9 to detect 1) between-group differences in taxon abundance (repeated measures ANOVA, group  $F > 0.4$ ), 2) differentially expressed transcripts (Edland's test for a linear mixed model with random slope,  $d > 0.07$ ), and 3) multi'omic correlations (Pearson correlation,  $r > 0.6$ ). Power calculations incorporated conservative Bonferroni p-value correction, with numbers of post-QC microbial features and within-sample correlations estimated from previous microbiome studies.

#### 2. Data exclusions

Describe any data exclusions.

Potential subjects were excluded from the study if they were unable or did not consent to provide tissue, blood, or stool, were pregnant, had a known bleeding disorder or an acute gastrointestinal infection, were actively being treated for a malignancy with chemotherapy, were diagnosed with indeterminate colitis, or had a prior, major gastrointestinal surgery such as an ileal/colonic diversion or j-pouch. These criteria were established prior to the study start. Samples were filtered based on data type-specific quality control measures. For metagenomes and metatranscriptomes, samples were required to have  $>1M$  reads and at least one species detected by MetaPhlAn2.

#### 3. Replication

Describe the measures taken to verify the reproducibility of the experimental findings.

The study was a large-scale clinical cohort and we did not attempt to replicate all aspects of sample collection and data generation. However, data and source code for computational tools used are available to the public and therefore all of our analysis can be reproduced using our methods or re-analyzed using other methods. When possible, we refer to existing literature that supports our findings. Multiple pilot studies as well as technical replicates covering a subset of samples are also available, and these data were successfully integrated into subsequent multi-batch analyses, ensuring that data generation methods produced reproducible results.

#### 4. Randomization

Describe how samples/organisms/participants were allocated into experimental groups.

Experimental groups could not be randomized as they depended on diagnosis. Participants were recruited into the three disease groups as available from each of the recruitment sites. Upon enrollment, an initial colonoscopy was performed to determine study strata. Subjects not diagnosed with IBD based on endoscopic and histopathologic findings were classified as "non-IBD" controls, including the aforementioned healthy individuals presenting for routine screening, and those with more benign or non-specific symptoms. This creates a control group that, while not completely "healthy", differs from the IBD cohorts specifically by clinical IBD status.

#### 5. Blinding

Describe whether the investigators were blinded to group allocation during data collection and/or analysis.

Samples were collected by clinical staff who were not blinded as they needed to examine patients to determine which experimental group they should be allocated to. All data were generated by investigators that were blinded to the metadata. Once data were generated, computational analysis was performed with all of the necessary clinical information to test between groups.

Note: all in vivo studies must report how sample size was determined and whether blinding and randomization were used.



## 6. Statistical parameters

For all figures and tables that use statistical methods, confirm that the following items are present in relevant figure legends (or in the Methods section if additional space is needed).

n/a Confirmed

- ☐ ☒ The exact sample size (*n*) for each experimental group/condition, given as a discrete number and unit of measurement (animals, litters, cultures, etc.)
- ☐ ☒ A description of how samples were collected, noting whether measurements were taken from distinct samples or whether the same sample was measured repeatedly
- ☒ ☐ A statement indicating how many times each experiment was replicated
- ☐ ☒ The statistical test(s) used and whether they are one- or two-sided  
*Only common tests should be described solely by name; describe more complex techniques in the Methods section.*
- ☐ ☒ A description of any assumptions or corrections, such as an adjustment for multiple comparisons
- ☐ ☒ Test values indicating whether an effect is present  
*Provide confidence intervals or give results of significance tests (e.g. *P* values) as exact values whenever appropriate and with effect sizes noted.*
- ☐ ☒ A clear description of statistics including central tendency (e.g. median, mean) and variation (e.g. standard deviation, interquartile range)
- ☐ ☒ Clearly defined error bars in all relevant figure captions (with explicit mention of central tendency and variation)

See the web collection on [statistics for biologists](#) for further resources and guidance.

## ► Software

Policy information about [availability of computer code](#)

### 7. Software

Describe the software used to analyze the data in this study.

Analysis of mass spectra: MSGF+ software v10072  
Sequence processing: Picard 2.9.4  
Metagenome and metatranscriptome profiles generated using bioBakery meta'omics workflow v0.9.0 (Preprocessing: KneadData 0.7.0; Taxonomic profiles: MetaPhlAn2 v2.6.0; Functional profiles: HUMAnN2 v0.11.0 with UniRef release 2014\_07, Diamond v0.8.22.84)  
Viral profiles: VirMAP  
16S analysis: USEARCH v7.0.1090  
Data analysis and plotting: R (main packages: edgeR, nlme, ggplot2, ggridges, pheatmap, vegan, tsne), Julia plots package  
Network construction and visualization: HALLA 0.8.17, Cytoscape 3.6.0

For manuscripts utilizing custom algorithms or software that are central to the paper but not yet described in the published literature, software must be made available to editors and reviewers upon request. We strongly encourage code deposition in a community repository (e.g. GitHub). *Nature Methods* [guidance for providing algorithms and software for publication](#) provides further information on this topic.

## ► Materials and reagents

Policy information about [availability of materials](#)

### 8. Materials availability

Indicate whether there are restrictions on availability of unique materials or if these materials are only available for distribution by a third party.

Remaining biospecimen aliquots from the project are available by request from the corresponding author.

### 9. Antibodies

Describe the antibodies used and how they were validated for use in the system under study (i.e. assay and species).

Antibodies were used for serology and the ELISAs we performed are not commercially available as kits or reagents (except for secondary antibodies).  
The primary antibodies are patient sera (validation not applicable).  
Conjugated polyclonal secondary antibodies are utilized, clone not applicable:  
Jackson ImmunoResearch Laboratories goat anti-human IgG-alkaline phosphatase; Cat # 109-056-098; 1:1000 dilution  
Jackson ImmunoResearch Laboratories goat anti-human IgA-alkaline phosphatase; Cat # 109-055-011; 1:1000 dilution

## 10. Eukaryotic cell lines

- State the source of each eukaryotic cell line used.
- Describe the method of cell line authentication used.
- Report whether the cell lines were tested for mycoplasma contamination.
- If any of the cell lines used are listed in the database of commonly misidentified cell lines maintained by [ICLAC](#), provide a scientific rationale for their use.

No eukaryotic cell lines were used.

No eukaryotic cell lines were used.

No eukaryotic cell lines were used.

No commonly misidentified cell lines were used.

## ► Animals and human research participants

Policy information about [studies involving animals](#); when reporting animal research, follow the [ARRIVE guidelines](#)

### 11. Description of research animals

Provide all relevant details on animals and/or animal-derived materials used in the study.

No animals were used.

Policy information about [studies involving human research participants](#)

### 12. Description of human research participants

Describe the covariate-relevant population characteristics of the human research participants.

Population characteristics are presented in Extended Data Table 1.

# Danone: The gut microbiome and probiotics – 100 years of shared history



## AUTHOR

Patrick Veiga, Silvia Miret and Liliana Jiménez  
Danone Nutricia Research, R.D. 128, 91767, Palaiseau, France

**D**anone was founded 100 years ago on a breakthrough concept of the time: that fermented foods and the bacteria they contained (not yet referred to as probiotics) could target the gut and its microbiome to bring health to all. One century later, Danone continues to place the gut and its microbiome at the core of its health strategy to deliver the company's mission "bringing health through food to as many people as possible". Today, the portfolio of the Danone Essential Dairy & Plant-Based division encompasses the traditional range of fermented dairy products and probiotics. The portfolio was recently broadened to include plant-based products, expanding the possibility to develop dairy and non-dairy ranges of healthy products that will contribute to nourish, enrich and protect the gut and its microbiome. Here we present the history of microbiology and Danone and reveal our research priorities for the coming years.

## DANONE WAS BORN DURING THE MICROBIOLOGY REVOLUTION

"The secret to longevity may lie in the microbiome and the gut"<sup>1</sup>. "Why the gut microbiome is crucial for your health"<sup>2</sup>. These



Figure 1. Danone yogurt was packaged and sold in ceramic pots in the early twentieth century. Source: Danone.

are two examples of headlines that were written over the past couple of years, but they could have been written one hundred years ago. By the end of the nineteenth century, the field of microbiology started to fulfil its first promises. Louis Pasteur discovered fermentation by lactic acid bacteria, which he described as beneficial bacteria to protect foods from spoilage. Despite the traditional use of fermentation in foods and beverages to improve storage time, safety, functionality, organoleptic quality and nutritional properties, it was Pasteur who demonstrated

that the lactate produced during fermentation inhibited the growth of pathogens and avoided food spoilage<sup>3</sup>. The idea that not all bacteria were prejudicial was a breakthrough at the time. The scientific world was shaken by the promise of modern microbiology, which saw the rise of vaccines, the isolation of beneficial bacteria and, later in the century, with the discovery in 1928 of penicillin by Alexander Fleming, the development of antibiotics. Microbiology was seen by many as uncharted scientific territory holding promises to improve people's lives.

Building on Louis Pasteur's legacy, in 1899 Henri Tessier, a paediatrician from the Institut Pasteur, discovered *Bifidobacterium bifidum* in faecal samples of breast-fed infants and reported that the bacteria could be used to help prevent babies from developing diarrhoea. The Russian-born biologist Élie Metchnikoff, recipient of the Nobel prize in physiology or medicine in 1908 for his work on phagocytosis, hypothesized that "there is a link between the gut flora and the senile degeneration"<sup>4</sup>. The gut microbiome and its metabolites were linked to intestinal processes

beyond food digestion and the absorption of nutrients. At the time, it was a breakthrough concept: the bacteria in our guts could dictate our fate. Metchnikoff also observed that food could be used to beneficially modulate the gut flora, in particular the bacteria contained in fermented foods<sup>4</sup>. His hypothesis was that if the lactate produced by bacteria during fermentation can inhibit the growth of harmful bacteria, then the same process could occur in the gut. Consequently, lactic acid bacteria could inhibit the 'putrefaction' and production of toxins in the gut. He worked to isolate pure cultures from a sample of Bulgarian fermented milk, among them *Lactobacillus bulgaricus* and *Streptococcus thermophilus*, the two species used today to produce yogurt.

The history of Danone begins in 1916, when Greek businessman Isaac Carasso took his wife and three children to Spain, his ancestral home. Much of Europe was experiencing the turmoil of the first world war and although Spain remained neutral, famine, malnutrition and poor living standards were present in many layers of society. Carasso was deeply affected by the levels of malnutrition and disease that he saw in Spanish children.

Carasso was open and curious about scientific developments and he was inspired by Metchnikoff's research into dairy ferments. Through experimentation and by trial and error, Carasso mixed fresh milk with ferments isolated at the Institut Pasteur to create in 1919, exactly 100 years ago, what became the first Danone yogurt. He named the yogurt after his son, Daniel, and in reference to his nickname 'Little Daniel'. The yogurt was packaged in porcelain pots (**Fig. 1**), which Carasso

hand-delivered as a health food to pharmacies across the city. In 1924, the production site was visited by the College of Doctors of Barcelona who complimented the product<sup>5</sup>.

From pharmacies, yogurt made it through to other channels accessible to a range of consumers and became a mainstream product. One decade later, Daniel joined the family business and successfully expanded Danone across France. In the late 1930s, with Europe once again on the brink of war, he decided to move to the United States. In the years following the first world war and, later, the second world war, yogurt was consumed as a way of providing healthy nutrients. The fermentation process means that yogurt contains higher quantities of vitamins B2, B6 and B12, and the nutrients calcium, potassium, zinc and magnesium than other dairy products such as milk<sup>6</sup>. Yogurt promotes adherence to dietary guidelines for many nutrients, particularly those of concern, such as calcium. During fermentation, the breakdown of lactose by enzymes present in *L. bulgaricus* and *S. thermophilus* reduces lactose levels and facilitates the consumption of dairy products by individuals who might be sensitive to lactose levels found in milk<sup>7</sup>. Recent population studies have suggested that yogurt might not only be a significant contributor in the provision of micronutrients but is also associated with a reduced risk of weight gain and increased satiety and that yogurt consumption might be linked to an overall healthier dietary and lifestyle pattern<sup>8</sup>.

Building on Pasteur's heritage, scientists in the twentieth century isolated other health-promoting strains from the human intestine among which

were *Escherichia coli* Nissle (1917), *Lactobacillus acidophilus* LB (1907) and *Lactobacillus casei* Shirota (1935). In 1974, Richard B. Parker proposed a definition of probiotics as "organisms and substances which contribute to intestinal microbial balance"<sup>9</sup>. An official definition was issued in 2001 by the Food and Agricultural Organization of the United Nations and the World Health Organization as constituting "live microorganisms that, when administered in adequate amounts, confer a health benefit on the host". Different types of bacteria (for example *Lactobacillus*, *Bifidobacterium*, *Streptococcus*, *Bacillus*) and yeast or mould (for example *Saccharomyces*, *Aspergillus*, *Candida*) are qualified as probiotics.

The first foodstuff to contain probiotics was probably fermented milk, but today many other matrices can contain probiotics. Danone started the production of two probiotic-containing fermented milks with *Bifidobacterium lactis* CNCM I-2494 (BFMP) and *L. casei* CNCM I-1518 (LFMP) in 1987 and 1994, respectively named Activia® and Actimel®. With the ambition to build and substantiate the health benefits of probiotics, a vast programme of studies was launched in the 1990s, resulting in more than 40 peer-reviewed scientific publications. The studied benefits of probiotic products range from reducing the incidence or duration of digestive discomfort symptoms, intestinal transit, common infection and illness, respiratory infection, gastrointestinal infection and prevention of diarrhoea following the use of antibiotics. Specifically, the results accumulated for BFMP showed a consistent and significant improvement of outcomes related to

gastrointestinal discomfort in healthy adults<sup>10,11</sup> and a decrease in the severity of symptoms in people with IBS-C<sup>12</sup>.

## THE SECOND MICROBIOLOGY REVOLUTION FED DANONE'S GUT HEALTH RESEARCH

Scientific discoveries often rely on the development of new technologies. The birth of modern microbiology at the end of the nineteenth and beginning of the twentieth century makes no exception. The first microbiology revolution was possible because of the development of new technological tools, such as the microscope. The advancements in genomics, proteomics and epigenomics have propelled the field into a second revolution that will allow researchers to understand the precise mechanisms of action of the bacteria in the gut. The metagenomics sequencing tools available today represent similar technological advancements because they allow scientists to rapidly capture the complexity of microbiomes and study invisible microorganisms without the need to isolate them.

At the forefront of this second revolution were the European and United States consortia of laboratories, MetaHIT (Metagenomics of the Human intestinal Tract, a project financed by the European Commission, 2008–2012) and Human Microbiome Project (2007–2013), respectively, which have led the way and developed bioinformatics tools and concepts that have unlocked microbiome research. Inspired by its microbiology heritage, Danone Nutricia Research contributed to this frantic endeavour by joining the MetaHIT consortium, which was seen by many as a scientific gamble at the time.

Building on the emerging gut-centred science, Danone Nutricia Research rapidly focused its research efforts on understanding the mode of actions of its major probiotic-containing product targeting gut health: BFMP. After a decade of a broad range of collaborations with leading academics including those from Washington University at St. Louis, U.S., Harvard T.H. Chan School of Public Health in Boston, U.S., the University of California, Los Angeles, U.S. (UCLA), Institut National de la Recherche Agronomique, headquartered in Paris, and the University of Gothenburg, Sweden, we are able to provide a working model capturing the different potential mode of actions of BFMP<sup>11</sup> (Fig. 2). The evidence supports the hypothesis that BFMP confers health benefits by modulating the activity of the gut microbiome and the components of the gut-brain axis. On the gut microbiome, we have evidence showing that BFMP stimulates the pathways leading to the production of beneficial short-chain fatty acids and decreases the production of intestinal gas<sup>13,14</sup>. On the gut-brain axis, results obtained in different studies support the idea that this product decreases the visceral hypersensitivity and modulates activity of the brain<sup>10,15</sup>.

During our research we found that not all individuals respond to BFMP to the same extent. Recently, we have shown that the decrease in intestinal gas production by BFMP was observed only in individuals exhaling high quantities of hydrogen<sup>14</sup>. We also observed evidence for two types of microbiomes: permissive and resistant<sup>16</sup>. The permissive microbiome was more susceptible to be modulated by BFMP than the resistant microbiome. Together,

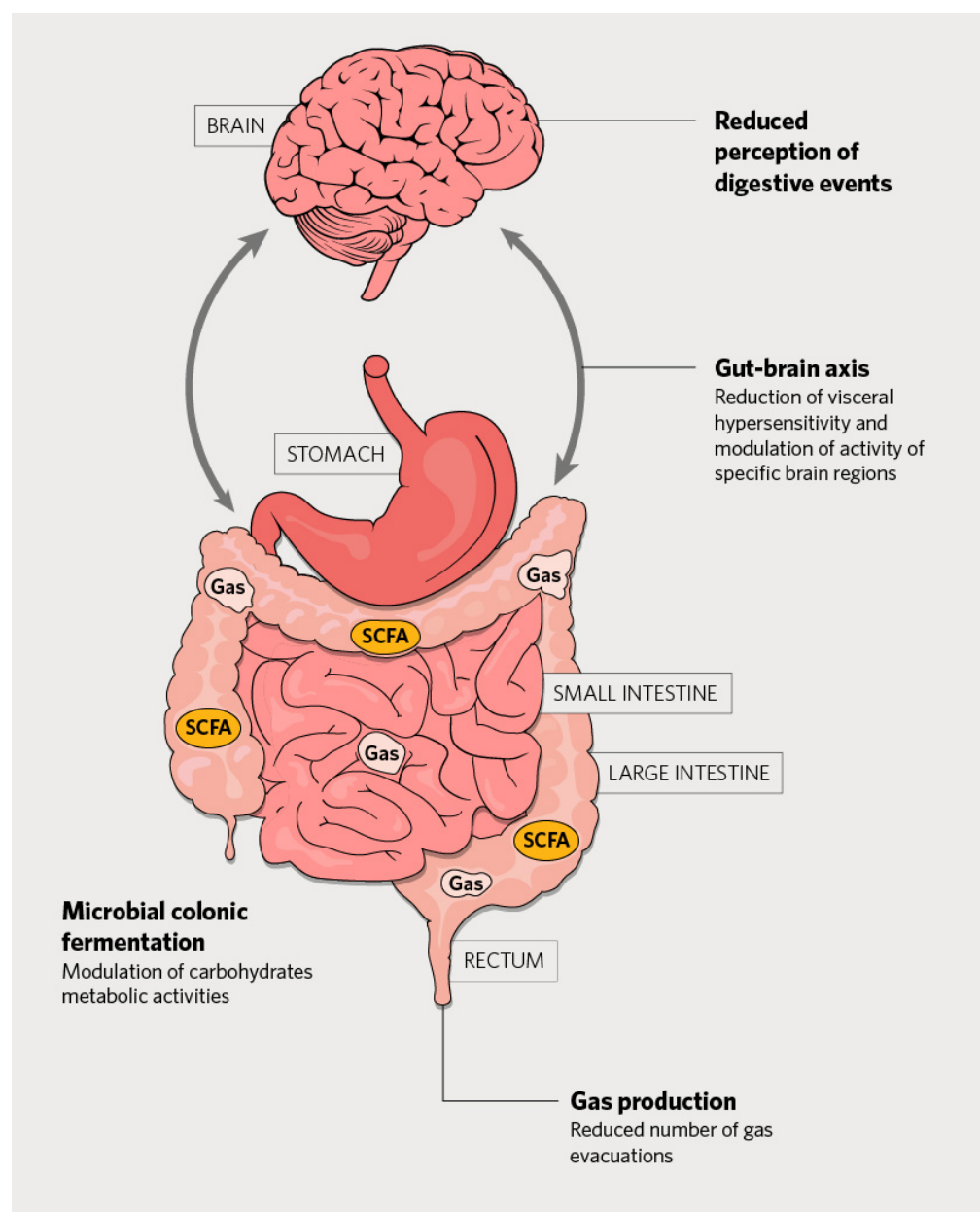


**Figure 2. The potential mode of action of BFMP (Activia®).** Source: Danone / Boris Le Névé.

the results open the avenue for the 'precision probiotics' era. In other words, probiotics that will be selected and tailored to an individual's phenotype, genetics and microbiome.

Future investigations should focus on the mechanistic understanding of the benefits of probiotics. Such understanding will not just impact gut health

but many aspects of health, from the neurological to the immune system, from paediatrics to geriatrics.

### 100 YEARS FROM NOW: CHALLENGES AND HOPES

In today's world, just as Isaac Carasso found 100 years ago, we face many challenges. In a world in constant and accelerated

change and continuous interconnections, human health is interconnected through effects of the environment, especially diet, the microbiome and the intrinsic and specific background of each individual.

### HEALTH THROUGH THE GUT

For decades, the scientific approach to health was



compartmentalized and focused on studying specific organs or cell types. Today, we are witnessing the emergence of a new era with the rise of integrative science, which defines health as the result of the adequate functioning of interconnected organs, organ systems or cell types. The intestine has been highlighted as one of the most interconnected organs because it is involved in mental, cardiovascular, metabolic, immune and musculoskeletal health and is essential for health and plays an important part in disease<sup>17</sup>.

Scientists are (re)discovering the gut as a cornerstone of human health and well-being because the function of the gut goes way beyond its primary function of digesting and absorbing nutrients. The gut is mediated by four different mechanisms: i) signalling molecules produced by the gut make it a virtual endocrine organ, arguably the largest that can contribute to circulating signalling molecules within the host; ii) bacteria-derived compounds (for example, short-chain fatty acids, lipopolysaccharides, vitamins, and polyphenol metabolites) able to cross the epithelial barrier contribute or interfere with the functioning of extra-intestinal organs or tissues; iii) immune cells primed in the intestine and homing in extra-cellular tissues and; iv) a nervous system able to transmit signals from the gut into the brain, interfering with its activity.

Because the gut is important to human health, it is not surprising that more studies suggest the potential benefits of probiotics beyond the gut to include the brain, cardiovascular, metabolic, bone, muscular and immune systems. In 2013, Danone Nutricia Research and collaborators from UCLA<sup>15</sup> published the first gut-brain probiotic clinical trial

in collaboration with scientists showing that a four-week intake of BFMP by healthy women affected the activity of brain regions that control central processing of emotion and sensation. More recently, we published a meta-analysis of 105 publications and demonstrated that the consumption of probiotics is associated with improvements in several metabolic risk factors in subjects with metabolic diseases<sup>18</sup>. Probiotics seem to be relevant candidates to bring health through the gut.

In line with our findings, we firmly believe in the concept of 'Health through the gut', which places the gut and its microbiome as an important target for health. More than one hundred years after Metchnikoff's insights, the idea that small molecules produced by the gut microbiome can modulate health is highly relevant and has catalysed a new gold rush in the gut microbiome field. The focus on health through the gut will allow the development of new solutions, including probiotics, to improve personal and hopefully contribute towards solving public health challenges.

### PRECISION PROBIOTICS

Scientific and technological advances in the gut microbiome field hold promises for a new way to select the next generation of probiotics, named hereafter 'precision probiotics'. Precision probiotics will bring to the gut activities or functions that are not provided by our gut microbiome or our own genes. Precision probiotics will be tailored to a recipient's diet, phenotype, lifestyle, age, gender, genetics and microbiome.

The first precision probiotics were *L. bulgaricus* and *S. thermophilus*, the bacteria used for yogurt fermentation, because they allow people who

are lactose intolerant to consume yogurt by providing the lactase (an enzyme missing in people who are lactose intolerant) to convert lactose into well tolerated glucose and galactose.

In the future, key species or functions of the gut microbiome will be identified by the scientific community, and probiotics will be a natural way to restore or support some of these functions. Probiotics could originate from our traditional lactic acid bacteria or *Bifidobacterium* but they will also come from bacteria isolated from the gut. *Akkermansia muciniphila* is a gut-isolated bacterium that holds promises in the area of metabolic health because research suggests it improves several metabolic parameters in obese and overweight individuals<sup>19</sup>.

### OPEN SCIENCE

There is huge potential for probiotics and the gut microbiome to contribute to public health, therefore one company and one research team will not suffice to explore and exploit all possibilities. A new way of thinking is required, and that involves multiple partners working together. The Danone vision is collaboration and openness that allows complementary factors to work together towards common goals.

To celebrate 100 years since the creation of its first yogurt, Danone has opened its collection of 1,800 strains for research purposes<sup>20</sup>. The 193 lactic and *Bifidobacterium* ferment strains, as well as Danone's collection of 1,600 other strains, have been made available to researchers around the world, with the sole aim of sharing our legacy to benefit all. The bacteria strains in Danone's collection may have a range of additional uses, many of which have not yet been explored

to their fullest potential. The strains could help to address a series of health, societal and environmental challenges<sup>20</sup>.

Additionally, and due to the complexity and diversity of the microbiome, Danone Nutricia Research decided to collaborate with world citizens and open the possibility for citizens to help understand the complexity and diversity of the world's gut microbiomes. Traditionally, research on the gut microbiome focused on populations from the Western world because we know the diet and how a variety of foods can modulate the gut microbiome. Danone Nutricia Research partnered with the University of California, San Diego, U.S. to understand the best ways of nourishing the gut microbiome. By launching The Human Diets & Microbiome Initiative (THDMI) we aim to discover the best diets and foods consumed by humans in different parts of the world that can benefit our guts. Because of the high variability in gut microbiome composition between individuals, it is necessary to achieve the recruitment of several cohorts across all geographical regions to enable a full mapping of the gut microbiome combined with dietary data. Most importantly, unlike other similar initiatives, this programme is using full metagenome sequencing, which is the latest sequencing technology, to assess the gut microbiome composition and function.

The THDMI programme has a public health educational vocation and will be conducted to contribute to promote healthy dietary habits. The THDMI initiative will give participants the opportunity to become citizen scientists and to contribute to the 'health through the gut' revolution.

## BRINGING IT ALL TOGETHER: THE GUT MICROBIOME AND DANONE SHARED HISTORY

The entrepreneurial spirit that inspired Isaac Carasso to search for solutions for malnourished children is as essential today as it was 100 years ago. And it is this spirit that propels us into the future at Danone. Entrepreneurs, in the purest sense, are those who identify a need – any need – and fill it. Every entrepreneur is a problem solver, someone who sees a problem affecting people and is driven to find a solution. Inspired by Carasso's entrepreneurship, openness and curiosity, research and innovation teams at Danone

Nutricia Research share the same passion for innovation. Danone researchers use their scientific and technological expertise to create products that best fit the Danone mission to bring health through food to as many people as possible. The science and technology for developing probiotics has moved at the same pace as the science in the field of the microbiome. The gut microbiome history reflects the Danone history for food and health.

## REFERENCES

1. McGill University. ScienceDaily, 31 May 2018. Available at: [www.sciencedaily.com/releases/2018/05/180531114611.htm](http://www.sciencedaily.com/releases/2018/05/180531114611.htm) [accessed 20 August 2019].

2. Robertson, R. Healthline, 27 June 2017. Available at: [www.healthline.com/nutrition/gut-microbiome-and-health](http://www.healthline.com/nutrition/gut-microbiome-and-health) [accessed 20 August 2019].
3. Berche, P. *Clin. Microbiol. Infect.* **18**, 1–6 (2012).
4. Cavaillon, J. M. & Legout, S. *Microbes Infect.* **18**, 577–594 (2016).
5. Viader, J. *HMIc: Història Moderna i Contemporània* **8** (2010).
6. van Hylckama Vlieg, J. E. T., Veiga, P., Zhang, C., Derrien, M. & Zhao, L. *Curr. Op. Biotechnol.* **22**, 211–219 (2011).
7. Savaiano, D. A. *Am. J. Clin. Nutr.* **99**, 1251S–1255S (2014).
8. Fernandez, M. A., Panahi, S., Daniel, N., Tremblay, A. & Marette, A. *Adv. Nutr.* **8**, 812–829 (2017).
9. Parker, R. B. *Anim. Nutr. Health* **29**, 4–8 (1974).
10. Waitzberg, D., Quilici, F., Miszputen, S. & do Carmo Friche Passos, M. *Nutr. Hosp.* **32**, 501–509 (2015).
11. Eales, J. et al. *Therap. Adv. Gastroenterol.* **10**, 74–88 (2017).
12. Agrawal, A. et al. *Aliment. Pharmacol. Ther.* **29**, 104–114 (2009).
13. Veiga, P. et al. *Sci. Rep.* **4**, 6328 (2014).
14. Le Nevé, B. et al. *PLoS ONE* **14**, e0214273 (2019).
15. Tillisch, K. et al. *Gastroenterology* **144**, 1394–1401.e1394 (2013).
16. Zhang, C. et al. *ISME J.* **10**, 2235–2245 (2016).
17. Hills, R. D. et al. *Nutrients* **11**, 1613 (2019).
18. Koutnikova, H. et al. *BMJ Open* **9**, e017995 (2019).
19. Depommier, C. et al. *Nat. Med.* **25**, 1096–1103 (2019).
20. Marking 100 years since the creation of its first yogurt, Danone opens access to its historical collection of 1,800 strains. Available at: [www.danone.com](http://www.danone.com) [accessed 20 August 2019].